

ELECTRONS IN MOLECULES

Electrons in Molecules

From Basic Principles
to Molecular Electronics

JEAN-PIERRE LAUNAY

Université Paul Sabatier, Toulouse

MICHEL VERDAGUER

Université Pierre et Marie Curie, Paris

OXFORD
UNIVERSITY PRESS

OXFORD

UNIVERSITY PRESS

Great Clarendon Street, Oxford, OX2 6DP,
United Kingdom

Oxford University Press is a department of the University of Oxford.
It furthers the University's objective of excellence in research, scholarship,
and education by publishing worldwide. Oxford is a registered trade mark of
Oxford University Press in the UK and in certain other countries

© Jean-Pierre Launay and Michel Verdaguer 2014

The moral rights of the authors have been asserted

First Edition published in 2014

Impression: 1

All rights reserved. No part of this publication may be reproduced, stored in
a retrieval system, or transmitted, in any form or by any means, without the
prior permission in writing of Oxford University Press, or as expressly permitted
by law, by licence or under terms agreed with the appropriate reprographics
rights organization. Enquiries concerning reproduction outside the scope of the
above should be sent to the Rights Department, Oxford University Press, at the
address above

You must not circulate this work in any other form
and you must impose this same condition on any acquirer

Published in the United States of America by Oxford University Press
198 Madison Avenue, New York, NY 10016, United States of America

British Library Cataloguing in Publication Data

Data available

Library of Congress Control Number: 2013938572

ISBN 978-0-19-929778-8

Printed and bound by
CPI Group (UK) Ltd, Croydon, CR0 4YY

Links to third party websites are provided by Oxford in good faith and
for information only. Oxford disclaims any responsibility for the materials
contained in any third party website referenced in this work.

Preface

Electrons in molecules . . . Both objects—electron and molecule—have a long, rich, and complex history. Both words began to be used as elusive concepts in the nineteenth century before gaining well-established scientific status at the turn of the twentieth century. Several tens of years of common endeavour, failures, and achievements by chemists and physicists, based on experimental and theoretical work, were necessary to reach consensus. The word ‘electron’ (from the Greek *élektron*, amber) was proposed by Stoney in 1894, to name the elementary negative charge of the particle, whereas ‘molecule’ comes from the diminutive of the Latin *moles* (mass), introduced in modern Latin by Gassendi as *molecula*. The emergence of the scientific concept of ‘molecule’, and its clear distinction from atoms and equivalents, was the result of big controversies (pros and cons in Karlsruhe Congress, 1860), but laid the foundations of the basic understanding of chemistry, molecular chemistry, and associated industrial synthetic processes. It opened the door to the understanding of complex, highly organized, and biological matter. Elucidation of the nature of the electron as a corpuscle and as a wave, and its role in atoms and molecules, gave rise to quantum mechanics. Today, everyone knows that molecules are quantum objects built from atoms sharing some of their electrons to establish chemical bonds.

Electrons in molecules . . . The title can also be read as ‘understanding the electronic structure and electronic properties of molecules’. Electrons are dividing their roles in a molecular entity: some ensure the chemical bonds and allow the stability of the molecules, while others are less bound to the atomic core and provide the molecules with their fancy properties—magnetic, electrical, photo-physical, colour, luminescence—allowing their use in molecular electronics, nanosciences, and so on . . . This book is based on the simple idea that such apparently different properties present a profound unity, relying on basic concepts of quantum mechanics and symmetry. This conclusion emerged from informal discussions which we had many years ago with numerous colleagues, and was fed by our teaching experiences at undergraduate and graduate levels.

The backbone of the book was designed accordingly. Chapter 1 briefly presents the basic quantum concepts as a common introduction to the broad domain encompassed by the properties. The molecular orbital approach is the red thread throughout the book, and its advantages and its limitations are carefully discussed. We then treat consecutively the magnetic properties (Chapter 2, ‘The localized electron’), electron transfer and electrical properties (Chapter 3, ‘The moving electron’), the photo-physical properties (Chapter 4, ‘The excited electron’), and finally, molecular electronics (Chapter 5, ‘The mastered electron’). So doing, we introduce the specific aspects of each of the

subjects, and try to enlighten them by returning systematically to the basic concepts. The goal is to better understand each topic and to show the transversal connections between many of them.

The book's content is shaped by a few specific features. First, it could be important to specify *what this book is not*: it is *not* a compilation of recent research results. There are many reviews in the specialized literature, which periodically updates the huge amount of data and results associated with the particular topics evoked here. We did not even consider the idea of being exhaustive in a given field. Each of the chapters could have been, and in some cases have already been, the subject of *several* books.

Second, we concentrate on *concepts* and use as little mathematics as possible. We try to give as much physical and chemical meaning as possible to the equations. We try to explain the logic and goal of calculations—the price being to skip some intermediate developments, which are left to the reader.

Third, we stress the importance of interdisciplinarity: to tackle ambitious challenges, we think deeply that in this domain one has to mix together chemistry, physics, and materials science. The book performs constant trips between these areas and between theory and experiment. Such a step appears compulsory to achieve the breakthroughs, allowing the progress of knowledge and the realization of practically useful materials and devices. Furthermore, in the recently popularized field of nanosciences, the division between physics and chemistry tends to vanish. But the round-trip ideas between chemist and physicist, between theoretician and experimentalist, are essential for adapting the molecule(s) to the instrument, or *vice versa*, and to be able finally to explore and demonstrate new phenomena.

Fourth, the book is fed by our lifelong experience of molecular chemists, synthesizing molecules and molecular assemblies specially designed to present given physical properties. A few quantum concepts constitute the background. Chemical synthesis provides the planned molecules (most often conceived after discussion to fit the needs of the physicist, the machine, or the demonstration). Beautiful physics experiments follow, with innovative setups and incredible enhanced sensitivities. Our book describes such experiments and their results, but stresses the contribution of molecular chemistry, which has sometimes been overlooked. It is indeed important to realize that this discipline has reached such a state of maturity that it can be considered as the science of elaborating three-dimensional objects of sub-nanometre size by rational design, with the possibility of predicting and fine-tuning their properties. A long time has passed since discoveries were made because a molecule was available on the shelf. Now, more and more, they are extensively designed before, and for, the experiment. The book is rich in many such examples. And when it happens that unexpected molecules arise, the curious scientist is always ready to foresee how they can be exploited to initiate new lines of research.

A fifth point is the importance of technology and instrumentation: huge progress has been made possible only because new equipment has been devised, such as the STM and its multiple variants, or the squid and its miniaturized evolutions. The race towards single-molecule properties, as opposed to the study of statistical ensembles, is now a strong motivation of research in all the fields covered in the book, as shown in the last chapter.

Such integrated content was conceived for an audience of students in chemistry, physics, and materials sciences, having a preliminary basic knowledge of the theory of symmetry and quantum mechanics. We taught most of the content of the book at undergraduate and graduate levels in chemistry and materials science courses in various places, French or foreign (European, Asian, and American) universities or French ‘grandes écoles’. Our goal is to provide fundamental knowledge and, above all, a solid *understanding* not only to beginners to boost their *curiosity* and *creativity* to design and obtain new materials with exciting new electronic properties, but also to already specialized researchers or engineers, to enlarge their vision to complementary fields and favour cross-fertilizing of other disciplines. We would always appreciate remarks and suggestions from our readers.*

* Every effort has been made to contact the holders of copyright in materials reproduced in this book. Any omissions will be rectified in future printings if notice is given to the publisher.

The content of our lectures varied systematically from one year to another to follow scientific trends and to integrate remarks and suggestions from our students and from our colleagues in neighbouring specialities. We are grateful to them. We also benefited from passionate discussions with coworkers and colleagues in our respective laboratories: Centre d’Elaboration de Matériaux et d’Etudes Structurales, CEMES (J.-P.L.) at Université Paul Sabatier in Toulouse, and Chimie Inorganique et Matériaux Moléculaires, CIM2 (M.V.) at Université Pierre et Marie Curie in Paris—both units of the Centre National de la Recherche Scientifique, the French institution supporting scientific research. Our colleagues will recognize their work, and fingerprints, here and there. Many thanks!

Thus, starting from our initial project, such exchanges and experiences transformed the book and its integrated content from principles to applications, resulting in a volume which, it appears, is unique in the literature at this level.

Our final word is directed to our families: our wives, Marie-Hélène and Jacqueline, and our daughters, sons, and grand-children, who endured, and sometimes accepted with incredulous smiles, the too long gestation of this volume.

Jean-Pierre Launay
Michel Verdaguer

Cordon, Escalquens, Palaiseau, Paris, Toulouse
September 2013

Abbreviations and symbols

1D	one-dimension
2D	two-dimension
3D	three-dimension
A	absorbance
A	acceptor
α	Coulomb integral
α	spin up
AC	alternating current
AFM	atomic force microscope
AM1	Austin model 1
AND	AND gate
AO	atomic orbital
β	decay coefficient
β	resonance integral
β	spin down
B3LYP	Becke 3-parameter Lee Yang Parr
BCS	Bardeen Cooper Schrieffer
BO	Bloch orbital
bpmp	2,6-bis[bis(2-pyridylmethyl)aminomethyl]4-methylphenol
bpy	2,2'-bipyridine
btz	bi-dihydrothiazine
BS	Broken Symmetry
C	carbon
C	constant
C_{2v} C_s	symmetry point group
C_{60}	C_{60} molecule
c, c_i, c_{ij}	coefficient
χ, χ', χ''	magnetic susceptibility
CAS-SCF	complete active space self consistent field
cat	catecholate
CDW	charge density wave
cgs	cgs unit system
CN ⁻	cyanide
CNDO	complete neglect of differential overlap
CNT	carbon nanotube
CO	carbon monoxide

Abbreviations and symbols

CO	charge order
CO	crystal orbital
CT	charge-transfer
D	Zero field splitting parameter
D	spectroscopic term
D, d	distance
D	donor
\tilde{D}	anisotropy tensor
Δ	ligand field parameter
D_{∞}, D_{2h}	symmetry point group
Δ_{oct}	octahedral ligand field parameter
δ_{rs}	Kronecker symbol
Δ_t	tetrahedral ligand field parameter
DFT	density functional theory
DNA	deoxyribonucleic acid
DOS	density of states
dpp	dipyridophenazine
Dq	ligand field parameter
e, e ⁻	electron
E	energy
E	identity operation
E	Zero field splitting parameter
e, e _g , E _g	symmetry labels
E _g	band gap
ε	monoelectronic energy
ε	permittivity
E°	standard potential (electrochemistry)
emu	electromagnetic unit system
EPR	electron paramagnetic resonance
ES	excited state
ESQC	elastic scattering quantum chemistry
EXAFS	extended X-ray absorption fine structures
Fe ₈	Fe ₈ iron complex
ϕ	atomic orbital
ϕ	polar angle
Φ	total wave function
FET	field-effect transistor
fsa or H ₄ (fsa)en	N,N' -(2-hydroxy-3-carboxybenzilidene)-ethanediamine)
γ	decay coefficient
g	g-factor
G	free enthalpy
g	gerade
GS	ground state
GVB	generalized valence bond
H	enthalpy
h, H	hamiltonian
h	Planck constant

HDVV	Heisenberg Dirac van Vleck
$h_{\text{eff}}, H_{\text{eff}}$	effective Hamiltonian
HL	Heitler London
HM	Hund Mulliken
HOCO	highest occupied crystal orbital
HOMO	highest occupied molecular orbital
i	complex number i ($i^2 = -1$)
i	inversion centre
INDO	intermediate neglect of differential overlap method
INHIBIT	INHIBIT gate
INS	inelastic neutron scattering
IP	Ionization potential
IR	infrared
IR	irreducible representation
ITRS	international technology roadmap for semiconductors
j, J_{ij}	coupling constant
$j, j_0, j_{ij}, J, J_{ij}$	two-centre two-electron integrals
j, J	orbital quantum number
j - j	j - j coupling
k, K, k_{ij}, K_{ij}	two-electron exchange integral
K	equilibrium constant
K	Kelvin
K	kinetic energy
k, k_B	Boltzmann constant
KCP	potassium tetracyanoplatinate
KS-DFT	Kohn-Sham orbitals in DFT
\mathbf{l}, \mathbf{L}	angular momentum operator
l, L	quantum number
λ	mean free path
λ	λ parameter
λ	wavelength
LCAO	linear combination of atomic orbitals
LD-LISC	ligand driven-light induced spin cross-over
LDOS	local density of states
LIESST	light induced excited spin state trapping
LMCT	Ligand metal charge transfer
LS	Russell Saunders coupling
LUMO	lowest unoccupied molecular orbital
LVCO	lowest vacant crystal orbital
LYP	Lee Yang Parr
M	magnetization
m	mass
M	molar, mole
M	molar mass
m	quantum number
M	transition dipole moment
μ_B	Bohr magneton
μ	magnetic moment

Abbreviations and symbols

μ_e	electron magnetic moment
μ_{eff}	effective magnetic moment
Mn_{12}	Mn_{12} manganese complex
MBPT	many-body perturbation theory
MCD	magnetic circular dichroism
MC-SCF	multiconfigurational SCF
MINDO	modified intermediate neglect of differential overlap
m_j, M_J	quantum number
m_l, M_L	quantum number
MLCT	metal ligand charge transfer
MMCT	metal metal charge transfer
MNDO	modified neglect of diatomic overlap
MO	molecular orbital
m_s, M_S	spin quantum number
M_S	magnetization at saturation
MWNT	multiwall nanotube
N_A	Avogadro constant
NDDO	neglect of differential diatomic overlap
NDR	negative differential resistance
NMR	nuclear magnetic resonance
O_h	octahedral symmetry point group
OLED	organic light-emitting diode
OR	OR gate
ox	oxalate
P	projection operator
P	probability
PB	Prussian blue
PBA	Prussian blue analogue
pba	1,3-propanebis(oxamate)
PIPT	photo-induced phase transition
phen	1,10-phenantroline
ptz	1-propyl tetrazole
PTZ	phenothiazine
py	pyridine
pz	pyrazine
PPP	Pariser Parr Pople
Ψ, ψ	wavefunction
q, Q	electric charge
Q	nuclear coordinate
R	gas constant
R	radial function
r	distance operator
r	radius
S	entropy
S	overlap integral
s, S	spin quantum number
s, S	spin angular momentum operator
S^2	spin operator

SALC	symmetry-adapted linear combination
SAM	self-assembled monolayer
SCF	self consistent field
SCM	single chain magnet
SI	Système International
SIM	single ion magnet
SMM	single molecule magnet
SO	symmetry orbital
SOMO	singly occupied molecular orbital
SDW	spin density wave
SH	spin-Hamiltonian
Σ	spin function
sq	semiquinone
SQUID	superconducting quantum interference device
STM	scanning tunnelling microscope
SWNT	single-walled nanotube
T	absolute temperature
Θ	Bloch orbital
θ	polar angle
t	time
t, T, t_{2g} , T_{2g}	symmetry labels
t	transfer integral
$T_{1/2}$	half-conversion temperature
T_c	critical temperature
T_C	Curie temperature
TCNQ	tetracyanoquinodimethane
T_d	tetrahedral symmetry point group
TD-DFT	time-dependent DFT
T(E)	transmission coefficient
tmen	tetramethyl 1,2-ethanediamine
TMMC	tetramethyl ammonium manganese chloride
TTF	tetrathiafulvalene
u	ungerade
U	two-electron repulsion integral (one-centre)
U	potential energy
UHV	ultra-high vacuum
UV	ultra-violet
V	electric potential
V	two-electron repulsion integral (two-centre)
V	Volt
v	speed
VSEPR	valence shell electron pair repulsion
VSIP	valence state ionization potential
VSM	Vibrating Sample Magnetometer
W	energy
W	energy bandwidth
W	watt
W_P	polaron energy

Abbreviations and symbols

χ	crystal orbital
XANES	X-ray absorption near edge structures
XMCD	X-ray magnetic circular dichroism
XOR	XOR gate
Y	angular function spherical harmonics
Z	partition function
Z	atomic number
Z_{eff}	effective atomic number
ZFS	Zero-field splitting

Basic concepts

1

In this chapter we establish, in a progressive way, how to describe the quantum properties of the constituents of matter—atoms, molecules, and extended molecular solids—with an emphasis on the behaviour of electrons, starting from first principles. Since the achievements of quantum mechanics, this step is in principle feasible. In this manner, Paul A. M. Dirac wrote: ‘The fundamental physical laws necessary to the mathematical theory of most parts of the physics and the whole of chemistry are completely known, and the difficulty is only that the exact applications of these laws lead to equations too complex to be solved exactly.’

It is true that the equation named after Schrödinger, under its stationary (1.1) or time-dependent (1.2) forms

$$\mathbf{H}\Psi_n = E_n\Psi_n \quad (1.1)$$

$$i\hbar\frac{\partial\Psi}{\partial t} = \hat{H}\Psi \quad (1.2)$$

allows theoretical determination of the eigenwavefunctions Ψ_n and the eigenenergies E_n which define the system and its change with time. In these formulae, \mathbf{H} is an operator which operates on the wavefunction Ψ , i is the complex number $i^2 = -1$, \hbar is the Planck constant, and the $\frac{\partial}{\partial t}$ operator is the partial derivative as a function of time t .

The ‘only’ difficulty, following Dirac, is that the operator must take into account *all* the interactions—in particular, the interactions between electrons—but *we are unable to write them analytically in an exact way*, two thirds of a century after Dirac. To solve the problem, *it is necessary to use some approximations*. It will be the purpose of the first part of this book to introduce some models useful to the description of the structure and the electronic structure of molecules and solids. These models will then be used to forecast the properties.

It is then possible to understand that the approximations realized, and the predictions made from them, should be compared in a systematic way to the experiments, source, and criterion of any model: the agreement model-forecasting experiment leads us to ascertain the validity of the model and presents the possibility of its safe use in a chosen experimental domain.

Conversely, the absence of agreement indicates the limit of the model and leads us to seek a more elaborate or different model for fitting the experiment and allowing us to foresee the properties in a new experimental field. This intellectual game is extremely fruitful. It is more and more practised by chemists, especially in materials science. References [1.1–1.5] will help the reader to become familiar with the most useful quantum models.

It is also easily understandable that the chemical reactivity of macroscopic sets of molecules and ions is extremely complex, as are the laws to obtain crystals with long-range order relying on very weak intermolecular interactions. Indeed, wide activity domains exist where systematic synthetic attempts are necessary to establish experimentally the correlations between structure and properties. From these attempts there sometimes arise structures (and properties) which cannot be *a priori* predicted or imagined. Far from being contradictory to a rational approach relying on the use of theoretical models, these endeavours complete and prepare more subtle new models and provide more exciting discoveries for tomorrow.

In some cases, some of these activities are styled *art* rather than *science*. The reader should not consider this comparison as pejorative, but rather, as a way to bring closer and to celebrate two major endeavours of human creativity.

1.1 Electron: an old, complex, and exciting story

The electron is the central theme of this book. Its name derives from a Greek word, *elektron*—amber—the electric properties of which are at the origin of the discovery of electricity (when you rub a piece of amber with some woven material, you produce electrons and positive charges which can be studied). It is known today that the electron can be described as a particle, having a very small size, an elementary mass ($m_e = 9.109534 \times 10^{-31}$ kg), a negative elementary charge ($e = -1.6021892 \times 10^{-19}$ Coulomb), and a spin ($s = 1/2$), associated with the elementary magnetic moment of the electron ($\mu_e = 9.284832 \times 10^{-24}$ J T⁻¹). The g Landé factor of the free electron is $g = 2 \mu_e/\mu_B = 2.0023193134$. μ_B is the Bohr magneton (see Chapter 2, Section 2.2.2). The electron is stable, and its lifetime is estimated to be 2×10^{22} years—longer than the age of the Universe, $1\text{--}2 \times 10^{10}$ years. As an elementary particle it is accompanied by its antiparticle, the positron, with the same mass but opposite charge. In atoms and molecules, the electron is moving with a speed v around the nuclei. Its kinetic energy is $K = mv^2/2$, its kinetic momentum is $p = mv$, and the corresponding associated wave has a wavelength $\lambda = h/p$. It can indeed be described as a wave—a property of quantum objects exhibiting wave/corpuscle duality. This property is currently used in electron microscopes, which frequently reveal important aspects of the structure of matter. The wavefunction $\Psi(x,y,z,t)$ associated with the electron allows us to describe all its properties. The square of the wavefunction Ψ^2 represents the probability density in an elementary volume $dv = dx dy dz$. These basic features of the electron are presented and discussed in many books of quantum mechanics, to which the reader is referred [1.1–1.4], and we shall use them when appropriate throughout this book. When accelerated, the electron

emits an electromagnetic radiation. When its speed is relativistic, the emitted radiation is called ‘synchrotron radiation’—white light from infrared to X-rays—a light source unsurpassed for the spectroscopic study of matter. The use of the properties of the electron, in the solid state and in devices, gave rise to a particularly active branch of physics and technology: electronics (electron-ics).

Today, therefore, the electron maintains an enviable scientific and social status, though this status has been obtained very slowly. It is difficult to speak of the ‘discovery’ of the electron, as the recognition of it as an elementary particle covers practically more than half of a century: characterization of the laws of electrolysis by Faraday (1833), implying ions; development of atomic theory, in which a mole of ions consists of the same number N_A of ions bearing an elementary charge; evaluation of the Avogadro constant N_A , particularly by Johann Loschmidt and George J. Stoney (1870–74)—the latter giving, in 1891, the name ‘electron’ to the elementary charge; recognition by Jean Perrin, in 1895, that cathodic rays are made of negative charges; determination of the charge/mass ratio, e/m , in 1897, by Joseph J. Thomson for the particles of cathodic rays, and by Pieter Zeeman for the ‘oscillating ion’; evaluation of the elementary charge, in 1901, by Max Planck (from the Boltzmann constant k_B , the gas constant $R = k_B N_A$, the Avogadro constant N_A , and the Faraday $F = N_A e . . .$); identification, at the same time, by Pierre and Marie Curie of the negative charge of the radioactive β rays for which Henri Becquerel measured the same e/m ratio than for the cathodic rays; and precise measurement of the charge e by Robert Andrews Millikan in 1909, which allows good determination of the Avogadro constant and of the mass of the electron. The history of the electron becomes, at this point, that of atomic quantum theory, with the models of Lorentz–Thomson, the planetary model of Ernst Rutherford where the electrons are at the periphery, the Bohr atom which uses the quantum model of Max Planck and Albert Einstein, the full development of quantum mechanics by Louis De Broglie, Erwin Schrödinger, Werner Heisenberg, Ernest Jordan, and Paul A. M. Dirac during 1924–25, and the introduction of the wavefunction Ψ quantified by the three quantum numbers n , l , and m . The parallel work of Alfred Landé, Wolfgang Pauli, George Uhlenbeck, and Samuel Goudsmit led to the introduction of a supplementary degree of freedom for the electron and the introduction of a fourth quantum number, the spin s , fully interpreted by Dirac’s relativistic equation.

The history of the electron, its evidence under the form of cathodic rays, the determination of its corpuscular properties (mass, charge, spin), and its description through the concepts of quantum and undulatory physics, were therefore at the centre of progress of chemistry and physics at the end of the nineteenth century and the beginning of the twentieth century, and one cannot overestimate their importance. It is extraordinary that the periodic table of the elements, fully based today on the atomic electronic structure and therefore on the existence of the electrons in atoms, was proposed by Dimitri Mendeleev in 1869, without previous knowledge of the existence of electrons!

We shall utilize only a small part of these extraordinary properties of the electron—essentially those related to quantum behaviour in atomic and molecular entities—and will proceed smoothly, step by step. The reader should

realize that the description of the polyelectronic macroscopic world—atomic, molecular, or in the solid state—implies different levels of sophistication. We can summarize the various levels as follows: first, neglecting the interelectronic repulsion, we can build a ‘one-electron world’, with atomic orbitals (atoms), molecular orbitals (molecules), or crystal orbitals (solids). Filling these orbitals with electrons, we reach *electronic configurations*. Second, taking into account interelectronic repulsion, and starting from electronic configurations, we obtain *states* (atomic, molecular, or solid). Third, by mixing the states we reach *configuration interaction states*.

We begin our journey in the ‘one-electron world’ with the simplest species involving electrons: atoms.

1.2 Electrons in atoms

Atoms are made of nucleons (neutrons and protons), building the nucleus, and electrons running around the nucleus. Contrary to the macroscopic (or classical) world surrounding us, the atomic world is quantized; it is a quantum world.

1.2.1 The electron in the simplest atom: hydrogen

The hydrogen atom ${}^1_1\text{H}$ is the simplest nuclide: a unique electron and a unique proton in the nucleus. In a static, non-quantum system, the electron will be attracted by and be precipitated on the nucleus and the atom will be over . . . Instead, the hydrogen atom is stable. The electron’s energy is determined by the Schrödinger eqn. (1.1), where the energy Hamiltonian \mathbf{H} is simply the sum of the kinetic energy $K(1)$ and the potential energy $U(1)$ of electron 1 in the potential field created by the central proton (or Coulombic field).

This equation has solutions only for discrete values of the energy E , termed eigenvalues, and the corresponding expressions of the wavefunctions are termed eigenfunctions. The atomic wavefunctions will be represented by ϕ in the whole book. Energies E_n are quantified by the quantum number n , the ‘principal’ quantum number ($n \geq 1$):

$$E_n = -2\pi^2 m e^4 Z^2 / h^2 n^2 \quad (1.3)$$

where m is the electron mass at rest, e the electron charge, Z the atomic number ($= 1$ for hydrogen), and h the Planck constant. The wavefunctions ϕ are also quantized and depend on three quantum numbers: n , l , secondary or orbital quantum number ($0 \leq l < n$) and m , magnetic quantum number ($-l \leq m \leq +l$): $\phi_{n,l,m}$.

Table 1.1 gives simplified expressions of the wavefunctions $\phi_{n,l,m}$ of the electron in the hydrogen atom, neglecting constant prefactors. They are expressed in the coordinate system shown in Fig. 1.1, which allows to write the wavefunction ϕ in a convenient way as the product of a radial function $R(r)$, depending only on r , the radial vector of the electron, and an angular function $Y(\theta, \varphi)$ which depends only on the two angles θ et φ : $\phi_{n,l,m} = R(r) \times Y(\theta, \varphi)$. The Y functions are termed *spherical harmonics*. The wavefunctions

Table 1.1 Simple analytical expressions and symmetry for some atomic s, p, and d orbitals. All quantities are given without their constant prefactors.

n	l	m	R(r)	Y(θ,φ)	Transformed Y	Wavefunction φ	Name	Sym
1	0	0	exp(-ζr)	1		exp(-ζr)	s	g
2	1	0	r exp(-ζr)	cos θ		z exp(-ζr)	p _z	u
2	1	-1	r exp(-ζr)	sin θ exp(-iφ)	sin θ cos φ	x exp(-ζr)	p _x	u
2	1	1	r exp(-ζr)	sin θ exp(iφ)	sin θ sin φ	y exp(-ζr)	p _y	u
3	2	0	r ² exp(-ζr)	3 cos ² θ - 1		(3z ² - r ²) exp(-ζr)	d _{z²}	g
3	2	-1	r ² exp(-ζr)	sin θ cos θ exp(-iφ)	sin θ cos θ cos φ	xz exp(-ζr)	d _{xz}	g
3	2	1	r ² exp(-ζr)	sin θ cos θ exp(iφ)	sin θ cos θ sin φ	yz exp(-ζr)	d _{yz}	g
3	2	-2	r ² exp(-ζr)	sin ² θ exp(-i2φ)	sin ² θ (cos ² φ - sin ² φ)	(x ² - y ²) exp(-ζr)	d _{x²-y²}	g
3	2	2	r ² exp(-ζr)	sin ² θ exp(i2φ)	sin ² θ sin φ cos φ	xy exp(-ζr)	d _{xy}	g

φ defined for a *one* electron system are termed *atomic orbitals*. In the hydrogen atom, *an orbital is an exact solution of the Schrödinger equation*.

The radial functions R(r) are of the form:

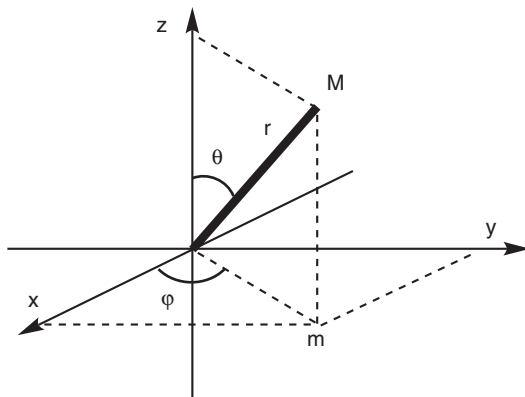
$$R(r) = \text{Constant} \times f(2Zr/na_0) \exp(-Zr/na_0) \quad (1.4)$$

where f(r) is a Laguerre polynomial and a₀ the radius of the electron orbit in Bohr's model. Exact expressions of the atomic orbitals, including numerical constants, Laguerre polynomials and radial functions can be found in the bibliography (see [1.1–1.2] for example). For computations, when the expressions of orbitals are written as A rⁿ⁻¹ exp(-ζr), they are termed Slater-type orbitals. Other approximate expressions can be used [1.1–1.2].

As can be seen in Table 1.1, the angular wavefunctions Y(θ,φ) emerging from the calculation are generally complex quantities, as are the corresponding wavefunctions. To represent geometrically the orbitals, one performs usually unitary transformations generating real wavefunctions, which is a valid procedure if the energies are the same. Noting that the dependence *versus* φ is of the form exp(imφ), this is achieved by combining 2 by 2 the angular functions Y_{l,m} and Y_{l,-m}:

$$(Y_{l,m} + Y_{l,-m})/2 \quad \text{proportional to } \cos(m\varphi) \quad (1.5a)$$

$$(Y_{l,m} - Y_{l,-m})/2i \quad \text{proportional to } \sin(m\varphi) \quad (1.5b)$$

**Fig. 1.1**

Cartesian (x, y, z) and spherical (r, θ, φ) coordinates.

Combining these transformed functions (column 6 of Table 1.1) with the radial function $R(r)$ gives expressions in which one recognizes Cartesian coordinates (column 7), and this is the basis of orbital denomination (for example, x leads to the p_x denomination, zx to d_{zx} , and so on).

In most of this book we will use these transformed (real) orbitals. However, in some cases we have to come back to the original complex orbitals, because they correspond to defined values of the m quantum number.

For the sake of clarity, the representation of the orbitals can be radial (see Section 1.3.6 for 3d orbitals) or angular (Fig. 1.2). In the figure, the lines are drawn for a constant value of the wavefunction (equi- ϕ curves). The positive values of the wavefunction are shown with a + sign or in shaded grey, whereas the negative values are shown by a - sign or white colour. This convention will be applied in the whole book.

The mathematical expressions and the graphical representations of the orbitals show the existence of nodal surfaces (geometrical locus of the points where $\phi_{n,l,m}$ equals zero). The total number of nodal surfaces is $n - 1$ (n if one includes the one always present at infinity). The number of nodal surfaces in radial wavefunction $R(r)$ is l (the secondary quantum number), and the number of nodal surfaces in the angular wavefunction $Y(\theta, \varphi)$ is therefore $n - 1 - l$. An important property of the atomic orbitals is their symmetry. An atom itself has important symmetry properties. In a rigorous way, in terms of group theory, one says that the eigenfunctions $\phi_{n,l,m}$ are basis functions for the irreducible representation $D^{(l)}$ of the three-dimensional group $O^+(3)$ (see [1.2]). More simply, they are often named after their symmetry properties—in particular, in the inversion operation (change x, y, z in $-x, -y, -z$), associated with the inversion centre at the nucleus: the s orbitals are spherical and symmetric in the inversion operation ($\phi_s(x, y, z) = \phi_s(-x, -y, -z)$) or even (*gerade* in German). So s orbitals are said to be *gerade* (or *g*). p orbitals are *ungerade*, or *u* ($\phi_p(x, y, z) = -\phi_p(-x, -y, -z)$). Then d orbitals are *g*, f orbitals are *u*, and so on. Such labels are shown in the last column of Table 1.1.

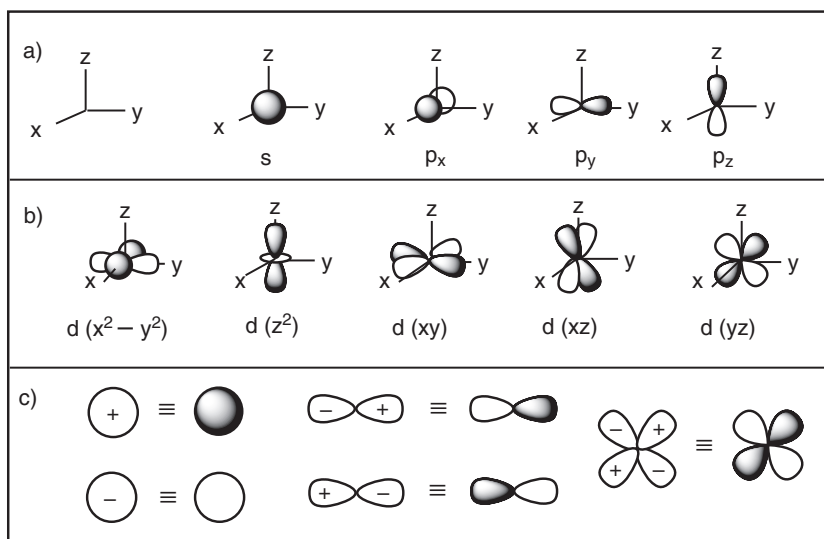


Fig. 1.2

Schematic angular representation of atomic orbitals: a) s and p orbitals; b) d orbitals; c) usual sign conventions.

Another important property of an orbital is its energy (see eqn. (1.3)). The energy of the orbital increases with n , or with the number of nodal surfaces of its wavefunction. The hydrogen atom is said to be in the ground state (the more stable state) when the electron is located in $\phi_{1,0,0}$, the orbital with the lowest energy (E_1) or 1s orbital. The electronic configuration is then written $(1s)^1$. The energy of the ground state of the hydrogen atom is found to be $E_1 = -21.8 \times 10^{-19}$ J or -13.6 eV. It is convenient to use electron-volts instead of Joules to avoid manipulating too small numbers, such as -21.8×10^{-19} . $E_1 = -13.6$ eV corresponds to the ionization potential in volts of the hydrogen atom (to obtain one proton H^+ and send the electron to infinity).

A final point concerns the spin of the electron. The hydrogen atom is paramagnetic. The spin of the electron is $s = 1/2$, with two projections ($m_s = \pm 1/2$, 'up', often called α , and 'down' or β). The spin multiplicity is defined as $2s + 1$ (here = 2; that is, a spin doublet). It is possible then to introduce the concept of spin-orbital, as the product of the orbital part $\phi_{n,l,m}$ and the spin part σ_s , where σ_s can take the values α or β).

$$\chi_{\text{spin-orbital}} = \phi_{n,l,m} \times \sigma_s \quad (1.6)$$

Beyond our simple presentation of quantum numbers l and s , the reader should remember that quantum mechanics defines them as angular momentum and vectorial quantities, and manipulate them with quantum operators. We shall return to this point in Sections 1.5 and 2.2.1.

1.2.2 The hydrogenoid ion

A hydrogenoid ion is an atomic entity with one electron and Z protons at the nucleus. The solutions of the Schrödinger equation are obtained in the same way as for the hydrogen atom. The number of protons Z is introduced in the expressions of the energies and of the wavefunctions, as shown in Table 1.1. and eqn. (1.3).

Two important consequences of the increase of the number of protons Z can be noted: (i) the stabilization of a given electronic energy level by a factor Z^2 ; the electron is 'going down' in energy (for example, for He^+ , $Z = 2$, $E_1 = -54.4$ eV); (ii) the contraction of the radial part of the wavefunction by a factor $\exp(-Z/n)$; the electron is more attracted by the nucleus and becomes closer to the nucleus. As in the hydrogen atom, the solutions are obtained exactly. The spin status is the same.

1.2.3 Helium and other atoms

Helium is the second element of the periodic table ($Z = 2$), with four nucleons, two protons, and two neutrons, and an electronic surrounding of two electrons: 4_2He

One electron more, and everything is changed! The mathematical equations for the energies and the wavefunctions are no more exactly solvable! The

reason for this is the repulsion energy between two electrons, e^2/r_{12} in atomic units, which leads to the Hamiltonian:

$$\mathbf{H} = \mathbf{h}(1) + \mathbf{h}(2) + e^2/r_{12} = \mathbf{K}(1) + \mathbf{U}(1) + \mathbf{K}(2) + \mathbf{U}(2) + e^2/r_{12} \quad (1.7)$$

$\mathbf{h}(1)$ is a one-electron Hamiltonian related to electron 1 only; $\mathbf{h}(2)$ deals only with electron 2. Both are the sum of a kinetic energy term \mathbf{K} and a potential energy term \mathbf{U} related to electron i : $\mathbf{h}(i) = \mathbf{K}(i) + \mathbf{U}(i)$. It is now impossible to determine the exact solutions, since the distance r_{12} between the two electrons depends on both electron coordinates, and furthermore, the electrons are indistinguishable. The problem can be solved only if an approximation is introduced.

A first idea would be to ignore the e^2/r_{12} term. Thus if the electrons had no interactions, the total energy would be twice the energy of an hydrogenoid system with $Z = 2$ —that is, 108.8 eV—while the true value is -79 eV [1.3], showing a quite large difference! This approximation is clearly inapplicable.

A better approximation is to consider that the two-electron term can be replaced by the sum of electronic terms $V(i)$: $e^2/r_{12} \approx V(1) + V(2)$. The Hamiltonian can then be written as an *effective* Hamiltonian: $\mathbf{h}^{\text{eff}}(i) = \mathbf{K}(i) + \mathbf{U}(i) + V(i)$. The total Hamiltonian is then the sum of two effective one-electron Hamiltonians:

$$\mathbf{H} = \sum_{1,2} [\mathbf{K}(i) + \mathbf{U}(i) + V(i)] = \sum_{1,2} \mathbf{h}^{\text{eff}}(i) = \mathbf{h}^{\text{eff}}(1) + \mathbf{h}^{\text{eff}}(2) \quad (1.8)$$

The Schrödinger equation can then be solved. The previous approximation is termed the ‘one-electron approximation’. The wavefunctions obtained in this frame are also termed orbitals, and in this case *an orbital is a solution of the Schrödinger equation in the one-electron approximation*.

We use here for the first but not the last time the concept of ‘effective’ Hamiltonian. We need to define it. An effective Hamiltonian is any operator whose energy spectrum reproduces that of the Hamiltonian operator for the state of interest [1.6]. ‘Effective’ is also used for physical quantities. An effective quantity is a fictitious physical quantity defined from an effective Hamiltonian and which is substituted to the fundamental one. It is most often defined empirically to fit experimental data effectively. We shall find many of them in this book (*effective* atomic number, quantum number, spin, g-factor, resonance integral β , and so on).

Relying on experimental results, chemists and physicists have defined approximations to express wavefunctions and energies of the electrons in the many-electron atom in a semi-empirical manner. The better known is the one by Slater which introduces an effective atomic number Z^{eff} , which is the atomic number Z diminished by a ‘screening constant’, σ . Z^{eff} is determined by the so-called ‘Slater rules’ where the σ_i for each electron depends on the electronic configuration and has semi-empirical values determined from experiments.

$$Z^{\text{eff}} = Z - \sigma = Z - \sum_i \sigma_i \quad (1.9)$$

An effective quantum number n^{eff} is sometimes defined and used, so that when replacing Z by Z^{eff} and n par n^{eff} in the expressions in Table 1.1. and eqn. (1.3),

wavefunctions and energies can be obtained in this one-electron approximation. A simple electrostatic image allows us to understand why σ and Z^{eff} can represent the interelectronic repulsion: an external (peripheral) electron moves in the electric potential created by Z protons, weakened or ‘screened’ by all the other electrons moving between the nucleus and the external electron.

The second electron in the helium atom occupies the same orbital $1s$ as the first one. The electronic configuration is $(1s)^2$. The situation follows the so-called ‘Aufbau principle’, or principle of stability: in the ground state the electrons occupy the lowest-energy orbitals. Regarding the total electronic energy of the atom, a more complete discussion of this problem is deferred to Section 1.5. (see also [1.2, 1.3]). Modern treatments of electron–electron repulsion utilize orbitals which are corrected from the average effect of other electrons. But the total electronic energy is no longer the sum of the individual electron energies. We nevertheless continue with the simple one-electron orbital picture as a starting point, and will introduce improvements and refinements later in the book.

The last comment concerns the spin and the magnetic properties. The helium atom is diamagnetic: the spins of the two electrons are opposite. If one is α , the second is β . This is our first encounter with an *electron pair*. Furthermore, the $1s$ orbital—as any orbital, atomic or molecular—can accommodate only two electrons. One says also that it is ‘full’ with two electrons. The situation is described by Pauli’s principle [1.1–1.4], which states in its simplest form that ‘two electrons cannot have the same four quantum numbers’ (a more sophisticated and strictly equivalent statement is that ‘the total polyelectronic wavefunction is antisymmetric—changes its sign—in the exchange of two electrons’). This means that

$$\Psi(1, 2, 3, \dots, i, j, \dots, N) = -\Psi(1, 2, 3, \dots, j, i, \dots, N) \quad (1.10)$$

We shall use this formulation in Section 1.5, but we can pause a while on this important point to understand better the interaction between electrons: since an atomic orbital is defined by three quantum numbers n , l , and m , the first electron described by the orbital can have a spin quantum number $m_s = (+ \text{ or } -) 1/2$. Instead, the spin of the second electron must have the opposite $m_s = (- \text{ or } +) 1/2$. The spin configuration is $\alpha\beta$ or $\beta\alpha$. Pauli’s principle is called an *exclusion* principle for that reason: it excludes from a given orbital electrons which have the same spin quantum number as the first electron. This is a *very strong exclusion* law. It is the basis of the formation of the famous ‘electron pair’ in an orbital. The two electrons have antiparallel magnetic moments so that they couple to reach a total spin of the atom $S = 0$ (that is, a spin singlet, $2S+1 = 1$, $M_S = 0$). The electron pair is diamagnetic, which is the basis of the diamagnetism of most molecular compounds. A rigorous way to determine S and M_S related to the atom is presented in Section 2.4.1.1.

In the lithium atom, $Z = 3$, ${}_3\text{Li}$, the third electron occupies the $2s$ orbital just above the ‘full’ $1s$. The electronic configuration is $(1s)^2(2s)^1$. The atom is paramagnetic ($S = 1/2$). And so on for other elements . . . We shall leave the ‘filling’ of atomic energy levels in the periodic table after a brief look at another fundamental question of interelectronic interaction. After the boron, $Z = 5$, ${}_5\text{B}$, with an electronic configuration $(1s)^2(2s)^2(2p_1)^1$, it is well known

that the electronic configuration of carbon ($Z = 6$, ${}^6\text{C}$) is $(1s)^2(2s)^2(2p)^2$ or $(1s)^2(2s)^2(2p_1)^1(2p_2)^1$; the first p electron occupies orbital $2p_1$ and the second p electron, 2, occupies a second p orbital ($2p_2$, same energy as $2p_1$), with its magnetic moment parallel to the one of electron 1. The atom is paramagnetic. The so-called ‘Hund’s rule’ is followed: the ground state is the highest spin multiplicity state. The coupling of the two spins $1/2$ gives rise to a spin $S = 1$ of the atom (a spin triplet, $2S + 1 = 3$, $M_S = 0, \pm 1$). It is important to realize that ‘Hund’s rule’ is due to electron repulsion and more precisely to the two-electron exchange integral k —defined in eqn. (1.58b)—which stabilizes the triplet state compared to the ground state, as we shall see in Section 1.5. In the $p_1(2) p_2(1)$ configuration, electrons 1 and 2 have been exchanged compared to $p_1(1) p_2(2)$. We shall find once more the exchange integral k on our way to ferromagnetic interactions (spins with parallel magnetic moments) when studying the case of two electrons on two centres in orthogonal orbitals having the same energy (see Chapter 2). The reader should consult [1.1–1.4] for more rigorous treatments of the previous presentation.

We can now deal with the next level of quantum organization of matter, which is central in this book: molecules.

1.3 Electrons in molecules

Molecules are built from atoms. One of the main achievements of quantum theory, after the understanding of atomic structure, was the explanation of the chemical bonding between atoms in the molecules. As for the atoms, other models of bonding existed before the quantum description. The most known—and the most popular until now—is the Lewis model. It is based on the use of the valence electrons of atoms, which combine in pairs to give bonding pairs when the electrons are shared between the atoms, or free pairs when they lie on one of the atoms. The simplest homodiatomic molecule, H_2 , is then described by the simple schemes $\text{H}\cdot\cdot\text{H}$ or $\text{H}-\text{H}$ (one bonding pair), the dioxygen molecule by $\langle\text{O}=\text{O}\rangle$ (two bonding pairs and two free doublets on each oxygen), the dinitrogen by $|\text{N}\equiv\text{N}|$ (three bonding pairs, one free pair on each nitrogen). For a given molecule, several bonding schemes are possible, called mesomeric formulae. Useful rules are available for choosing the most valuable bonding schemes to describe the molecule. In particular, the ‘octet rule’ foresees that a formula which corresponds to eight electrons surrounding each atom in the molecule (that is, completing the valence shell as an octet) is particularly stable—at least for atoms of the second row. The electron count is made by summing all the electrons in bonding pairs and free doublets around the given atom.

Another very appealing application of the Lewis model of localized bonds is the valence shell electronic pair repulsion model (VSEPR), designed by Ronald Gillespie, which is used to foresee the geometry of simple polyatomic molecules: the main parameter which imposes the geometry of a molecule is the repulsion between the pairs of valence electrons in the molecule. A quantum development of the localized bond approach has been developed with success by Walter Heitler and Fritz London or Linus Pauling, as a valence

bond theory with recent impetus from Sason Shaik and co-workers. Evidently, valence bond theory has been and is still very useful in organic chemistry. Nevertheless, in the following sections we shall focus on the model developed by Friedrich Hund and Robert Mulliken: the model of delocalized molecular orbitals, known as the theory of molecular orbitals—linear combination of atomic orbitals (MO-LCAO). It provides a convenient one-electron model to describe the electronic structure of the molecules, and comprises several levels of sophistication, taking more or less into account the important problem of interelectronic repulsion, discussed in Section 1.5. In Sections 1.3 and 1.4 we avoid the insoluble problem of the interelectronic repulsion—when several electrons are present—by using a one-electron ‘effective’ Hamiltonian, implying implicitly the interelectronic problem.

1.3.1 Dihydrogen molecule, H₂

The two atomic orbitals of the two hydrogen atoms 1 and 2 are termed ϕ_1 and ϕ_2 . In the following, we still use ϕ as the symbol for atomic orbitals and adopt ψ for molecular orbitals (MOs). The chemical bond arises from the existence of an overlap integral S between ϕ_1 and ϕ_2 . We shall work in the frame of the Born–Oppenheimer approximation; that is, the nuclei are fixed (since they are heavier than the electrons, they are moving much more slowly).

The one-electron overlap integral S for ϕ_1 and ϕ_2 is computed over all space, and can be expressed in two ways: a traditional one (using ϕ_i^* the conjugated complex of ϕ_i ; that is, if $\phi_i = a + i b$, $\phi_i^* = a - i b$, so that $\phi_i^* \cdot \phi_i = a^2 + b^2$) or the bra-ket notation introduced by Dirac, where $\langle \phi_i | = \phi_i^*$ (bra) and $|\phi_i\rangle = \phi_i$ (ket):

$$S_{12} = S = \langle \phi_1(1) | \phi_2(1) \rangle = \iiint \phi_1^*(1) \phi_2(1) dv \quad (1.11)$$

In these expressions the subscripted index refers to *atoms*, while the number in parentheses refers to *electrons*. The molecular orbitals ψ are linear combinations of ϕ_1 and ϕ_2 :

$$\psi = c_1 \phi_1 + c_2 \phi_2 \quad (1.12)$$

The coefficients c_i are termed molecular orbital coefficients. The probability density function ψ^2 , associated with ψ , integrated over the whole space, is:

$$\begin{aligned} \langle \psi | \psi \rangle &= c_1^2 \langle \phi_1 | \phi_1 \rangle + c_2^2 \langle \phi_2 | \phi_2 \rangle + 2 c_1 c_2 \langle \phi_1 | \phi_2 \rangle \\ &= c_1^2 + c_2^2 + 2 c_1 c_2 S_{12} \end{aligned} \quad (1.13)$$

since $S_{11} = \langle \phi_1 | \phi_1 \rangle = S_{22} = \langle \phi_2 | \phi_2 \rangle = 1$ and $S_{12} = S = \langle \phi_1 | \phi_2 \rangle$.

To determine the wavefunctions and their energies, two methods are available: the use of a secular determinant, or a direct calculation using the symmetry of the system (atoms 1 and 2 are equivalent). In the direct calculation, symmetry implies that atoms 1 and 2 bear the same electronic density so that $c_1 = \pm c_2$. ψ is normalized to unity. The coefficients are thus $c_{\pm} = \pm 1/\sqrt{2(1 \pm S)}$. The two molecular orbitals are then:

$$\psi_+ = \psi_{\text{bonding}} = \sqrt{\frac{1}{2(1+S)}} (\phi_1 + \phi_2) \quad (1.14a)$$

$$\psi_- = \psi_{\text{antibonding}} = \sqrt{\frac{1}{2(1-S)}} (\phi_1 - \phi_2) \quad (1.14b)$$

In the frame of Hückel theory, the energies E_{\pm} are determined with the help of the effective Hamiltonian \mathbf{H}^{eff} , written as:

$$\mathbf{H}^{\text{eff}} = \mathbf{H}^{\text{eff}}(1) + \mathbf{H}^{\text{eff}}(2) \quad (1.15)$$

Two one-electron integrals are defined, the Coulomb integral α and the resonance integral β :

$$\alpha = \langle \phi_1(1) | \mathbf{H}^{\text{eff}}(1) | \phi_1(1) \rangle = \langle \phi_2(2) | \mathbf{H}^{\text{eff}}(2) | \phi_2(2) \rangle \quad (1.16)$$

$$\beta = \langle \phi_1(1) | \mathbf{H}^{\text{eff}}(1) | \phi_2(2) \rangle = \langle \phi_2(2) | \mathbf{H}^{\text{eff}}(2) | \phi_1(1) \rangle \quad (1.17)$$

The α integral is negative, meaning that the atom itself is stable. The β integral is also negative here (but see in Section 1.3.3 the cases where β is >0).

Then are determined the energy values E_{\pm} of bonding and antibonding MOs:

$$E_{\pm} = \langle \psi_{\pm} | \mathbf{H}^{\text{eff}} | \psi_{\pm} \rangle / \langle \psi_{\pm} | \psi_{\pm} \rangle \quad (1.18)$$

That is:

$$E_+ = E_{\text{bonding}} = \frac{(\alpha + \beta)}{1 + S} \approx (\alpha + \beta) \quad (1.19a)$$

$$E_- = E_{\text{antibonding}} = \frac{(\alpha - \beta)}{1 - S} \approx (\alpha - \beta) \quad (1.19b)$$

In eqns. (1.19), the first expression does not neglect the overlap integral S compared to 1, whereas the last expression is written when neglecting S compared to 1.

On the other hand, when using the secular determinant method, based on the variation method (define the coefficients c_i which minimize the energy), one obtains the simultaneous equations [1.3]:

$$(H_{11} - E_i S_{11}) c_{1i} + (H_{12} - E_i S_{12}) c_{2i} = 0 \quad (1.20a)$$

$$(H_{21} - E_i S_{21}) c_{1i} + (H_{22} - E_i S_{22}) c_{2i} = 0 \quad (1.20b)$$

where $H_{ij} = \langle \phi_i | \mathbf{H}^{\text{eff}} | \phi_j \rangle$ and $S_{ij} = \langle \phi_i | \phi_j \rangle$.

The solutions are found when vanishing the determinant below (neglecting or not neglecting S , or S_{12} , compared to 1):

$$\begin{array}{cc} \left| \begin{array}{cc} H_{11} - E & H_{12} \\ H_{21} & H_{22} - E \end{array} \right| = 0 & \left| \begin{array}{cc} H_{11} - E & H_{12} - ES_{12} \\ H_{21} - ES_{21} & H_{22} - E \end{array} \right| = 0 \\ \text{(a) Determinant neglecting } S & \text{(b) Determinant with } S \end{array} \quad (1.21)$$

The solutions for the energies E_i are given by eqn. (1.22), obtained by equating the product of the extreme and the middle terms:

$$(H_{11} - E)(H_{22} - E) - (H_{12} - ES_{12})^2 = 0 \quad (1.22)$$

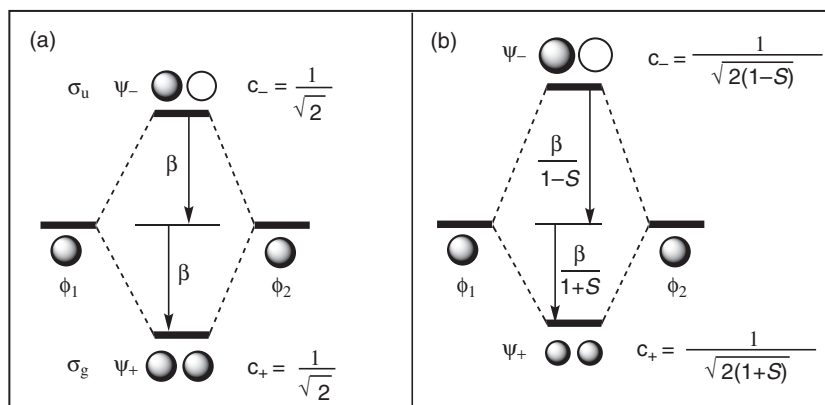


Fig. 1.3
Molecular orbitals energy diagrams of H_2 : (a) neglecting the overlap integral S compared to 1; (b) without neglecting S .

For the hydrogen molecule the energies are easily computed, since initial orbitals are degenerate (that is, have the same energy), $H_{11} = H_{22} = \alpha$; $H_{12} = H_{21} = \beta$ and $S_{12} = S_{21} = S$. One finds, of course, the same results as in the direct calculation (see eqns. (1.19)).

Figure 1.3 displays the energy diagram of the molecular orbitals of H_2 in the two hypotheses (neglecting or not neglecting S). One observes that when the overlap is not neglected, the antibonding MO is more destabilized (by $-\beta/(1-S)$) than the bonding MO is stabilized (by $\beta/(1+S)$); the MO coefficients of ϕ_1 and ϕ_2 are more important in ψ_- ($\psi_{\text{antibonding}}, \frac{1}{\sqrt{2(1-S)}}$) than in ψ_+ ($\psi_{\text{bonding}}, \frac{1}{\sqrt{2(1+S)}}$).

The ground state of the dihydrogen molecule corresponds to the occupation of the bonding orbital by the two electrons.

$$\psi_+ = \psi_{\text{bonding}} = \sqrt{\frac{1}{2(1+S)}}(\phi_1 + \phi_2) \quad (1.23)$$

The total wavefunction Ψ_+ is the product of the wavefunctions (1.23) written for electrons 1 and 2, which leads to:

$$\begin{aligned} \Psi_+ = \Psi_{\text{bonding}} &= [\phi_1(1) + \phi_2(1)][\phi_1(2) + \phi_2(2)]/2(1+S) \\ &= \{[\phi_1(1)\phi_1(2) + \phi_2(1)\phi_2(2)] + [\phi_1(1)\phi_2(2) \\ &\quad + \phi_1(2)\phi_2(1)]\}/2(1+S) \end{aligned} \quad (1.24)$$

We note that the wavefunction Ψ_{bonding} is the sum of four terms with equal weights. The first two correspond to an electron transfer between the two atoms with two electrons in the same orbital ϕ_1 or ϕ_2 . For the last two terms, the electrons remain in their orbitals or exchange their positions. The first two are termed *charge transfer* terms or *ionic* terms. They correspond to a delocalization of the electron of one atom to the other. We shall relate this expression to the valence bond one in Section 1.5, and in Chapters 2 and 3 we shall comment on its important meaning for physical properties.

How many bonds? Bond order

It is convenient to know how many ‘bonds’ are present between two atoms in a molecule. The number of bonds or *bond order* or *bond index* ω is defined as the

Basic concepts

difference between the number of bonding electrons N_{bonding} and the number of antibonding electrons $N_{\text{antibonding}}$ divided by two, since two electrons are necessary to build a bond:

$$\omega = \frac{N_{\text{bonding}} - N_{\text{antibonding}}}{2} \quad (1.25)$$

For the dihydrogen molecule, $\omega = (2 - 0)/2 = 1$. Since the bond is σ type, it can be said that in dihydrogen there is one σ bond (electronic configuration $1\sigma^2$).

Where stand the electrons? Population analysis

It is important to know ‘where the electrons are’ in a molecule: how many are on centre 1? . . . on centre 2? How many are shared between 1 and 2? To answer these questions, quantum chemists perform a ‘population analysis’.

If we take the general formulation of the orbital ψ in eqn. (1.12), $\psi = c_1 \phi_1 + c_2 \phi_2$, then the distribution of one electron in this orbital is given by eqn. 1.13 (with $\langle \psi | \psi \rangle = 1$), where c_1^2 is related to centre 1, c_2^2 is related to centre 2, and $2 c_1 c_2 S_{12}$ is a quantity associated with the interaction, termed the overlap population. If one wants to distribute the electron density on the two centres only, it is necessary to split the overlap population in two. Mulliken proposed to share equally between the two centres so that the electron density on centre 1 is $c_1^2 + c_1 c_2 S_{12}$, and on centre 2, $c_2^2 + c_1 c_2 S_{12}$. This is known as Mulliken population analysis.

To determine the electronic density on each atom of the molecule, it is simple to sum the contributions of all the atomic orbitals over all the molecular orbitals. For H_2 we can go further, analysing the overlap population in ψ_1 and ψ_2 by taking into account the value of the coefficients $c_{\pm} = \pm 1/\sqrt{2(1 \pm S)}$ in $\langle \psi | \psi \rangle = c_1^2 + c_2^2 + 2 c_1 c_2 S_{12}$. In ψ_+ the overlap population, found as $S/(1 + S)$, is positive, and the orbital is bonding. In ψ_- the overlap population $[-S/(1 - S)]$ is negative, and the orbital is antibonding.

Symmetry

A final comment deals with symmetry. The symmetries of the molecular orbitals are related to the symmetry of the molecule itself; that is, the one of the skeleton of the atomic nuclei. The molecular symmetry is described in the frame of the theory of symmetry or group theory. It relies on point group symmetry, which is the set of the *symmetry operations* (rotation θ , reflection σ , inversion i , and so on) around the *symmetry elements* (rotation axis $C_{\theta/2\pi}$, reflection or mirror plane σ , inversion centre i , and so on) transforming the molecule in itself, without macroscopic changes. A group is a mathematical being with perfectly defined properties, exactly adapted to the set of symmetry operations in a molecule or in a crystal. A point group is a group leaving at least one point of the molecule unchanged. Instead, a space group, based on operations on the crystal (translations of the molecules for example) leaves no point of the crystal unchanged. We consider here that the reader masters the necessary knowledge about symmetry theory. Many textbooks about symmetry are available at various levels of mathematical sophistication (see, for example, [1.7] and [1.8]). The systematic use of symmetry in the description of the electronic structure of solids can be found in chapter 2 of [1.9b]—a

companion book of the present volume. For the dihydrogen molecule the main geometry features are gathered in Fig. 1.4.

The *symmetry elements* are the internuclear axis z (rotation axis C_∞ , termed vertical), a reflection plane σ_h (termed horizontal), perpendicular to the z axis at M , the centre of the H_1 – H_2 segment, an infinity of reflection planes σ_v containing the vertical axis, and an infinity of rotation axes C_2 perpendicular to the z axis at M and the inversion centre i at M . The *symmetry operations*, leaving the molecule H_1 – H_2 unchanged, are the identity operation E (no change at all), an infinity of Φ rotations, whatever Φ , around the z axis; the rotation axis is termed C_∞ ; an infinity of reflections through the vertical reflection planes, therefore termed $\infty\sigma_v$; one reflection through the horizontal plane, termed σ_h ; the reflection operation interchanges H_1 and H_2 ; an infinity of π rotations (∞C_2) around the rotation axes perpendicular to the z axis at M : the C_2 operations interchange H_1 and H_2 ; inversion through the inversion centre, termed i : the i operation interchanges H_1 and H_2 . One of the most useful symmetry properties of the molecular orbitals of a molecule belonging to a given point group is that *the molecular orbitals build a basis for the irreducible representations (RI) of the point group*.

We summarize the symmetry properties of the wavefunctions of the dihydrogen molecule and related functions (x , y , z , $x^2 + y^2$, z^2 , ψ_1 or ψ_2) in Table 1.2: horizontally, the symmetry operations, assembled by nature (classes), corresponding to columns, and vertically the different objects corresponding to the symmetry labels. At the intersection we write a *character* which condenses the symmetry property of the object/function under the given symmetry operation: +1 if the object is unique and unchanged, –1 if the object is unique and changes its sign, 2 if the object is double (the pairs (x, y) or (xz, yz)) and unchanged, and so on.

Each line characterizes a given type of symmetry, and is termed an *irreducible representation (IR)* identified by a symmetry label: $\Sigma_g^+(A_{1g})$ (symmetric in all the symmetry operations or fully symmetric in particular in the C_∞ rotation (Σ label), in the inversion – g label, and so on); $\Sigma_u^+(A_{1u})$ (antisymmetric in the inversion – u label . . .), $\Pi_g(E_{1g})$, doubly degenerate, $\Pi_u(E_{1u})$, $\Delta_g(E_{2g})$, and so on. Completed with all the possible IRs, the table is termed a *character table*.

As for the molecular orbitals of the dihydrogen molecule, we derive the symmetry labels $\Sigma_g^+(A_{1g})$ for ψ_1 and $\Sigma_u^+(A_{1u})$ for ψ_2 . Applied to molecular orbitals, the symmetry labels are written as lower case subscripted symbols, σ_g^+ and σ_u^+ , which are shown in Fig. 1.3a.

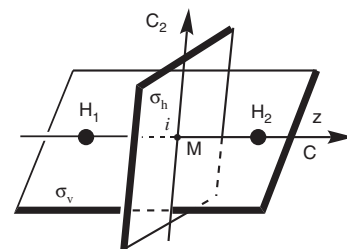


Fig 1.4

Symmetry elements for the dihydrogen molecule, H_2 .

Table 1.2 Part of the character table of the $D_{\infty h}$ point group.

$D_{\infty h}$	E	$2C_\infty^\Phi$...	$\infty\sigma_v$	σ_h	i	∞C_2	...Objects/Functions
$\Sigma_g^+(A_{1g})$	1	1	...	1	1	1	1	... $x^2 + y^2, z^2, \psi_1 = 1s_A + 1s_B$
$\Pi_g(E_{1g})$	2	$2\cos\Phi$...	1	0	2	0	... (xz, yz)
$\Delta_g(E_{2g})$	2	$2\cos 2\Phi$...	0	2	2	1	... $(x^2 - y^2, xy)$
$\Sigma_u^+(A_{1u})$	1	1	...	1	–1	–1	–1	... $z, \psi_2 = 1s_A - 1s_B$
$\Pi_u(E_{1u})$	2	$2\cos\Phi$...	0	2	–2	0	... (x, y)

We simply introduced here some definitions, notations, and the main results about the physical quantities that we shall use later. Detailed demonstrations and discussions are available in references [1.1–1.9], and character tables in [1.8b].

1.3.2 AB molecules

Here we consider briefly a slightly more complex system: an AB heterodiatom molecule ($A \neq B$), with an orbital ϕ_A , energy α_A , on A and ϕ_B , energy α_B , on B with $\alpha_A \neq \alpha_B$ ($\alpha_A > \alpha_B$). It is important, as many of the interesting molecular systems are built from atoms of different nature.

ϕ_A and ϕ_B are two non-degenerate orbitals. Energies and wavefunctions can be obtained by the secular equations (1.20), where $H_{11} = \alpha_A$, $H_{22} = \alpha_B$, $H_{12} = H_{21} = \beta$, and $S_{12} = S_{21} = S$. Energies follow from

$$(\alpha_A - E)(\alpha_B - E) - (\beta - ES)^2 = 0 \quad (1.26a)$$

After some calculations and approximations we obtain

$$(b) E_1 = \alpha_B - \frac{(\beta - \alpha_B S)^2}{\alpha_A - \alpha_B} \quad (c) E_2 = \alpha_A + \frac{(\beta - \alpha_A S)^2}{\alpha_A - \alpha_B} \quad (1.26b,c)$$

These expressions are obtained under the assumption that $|\beta|$ is $\ll |\alpha_A - \alpha_B|$, which occurs if the orbitals have very different energies, or if their coupling is small.

The molecular orbital coefficients can be computed from eqns. (1.20) and (1.27). Neglecting terms greater than second order in t and S , one finds:

$$\psi_1 = c_{1A}\phi_A + c_{1B}\phi_B \approx t\phi_A + (1 - tS - t^2/2)\phi_B \quad (1.27a)$$

$$\psi_2 = c_{2A}\phi_A + c_{2B}\phi_B \approx (1 - t'S - t'^2/2)\phi_A + t'\phi_B \quad (1.27b)$$

with

$$t = \frac{\beta - \alpha_B S}{\alpha_B - \alpha_A} \quad \text{and} \quad t' = \frac{\beta - \alpha_A S}{\alpha_A - \alpha_B} \quad (1.27c)$$

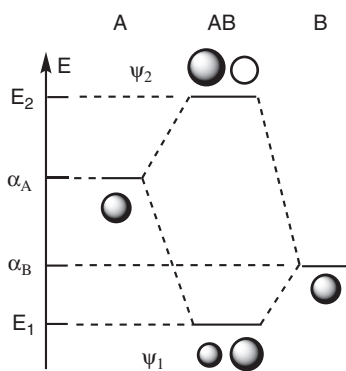
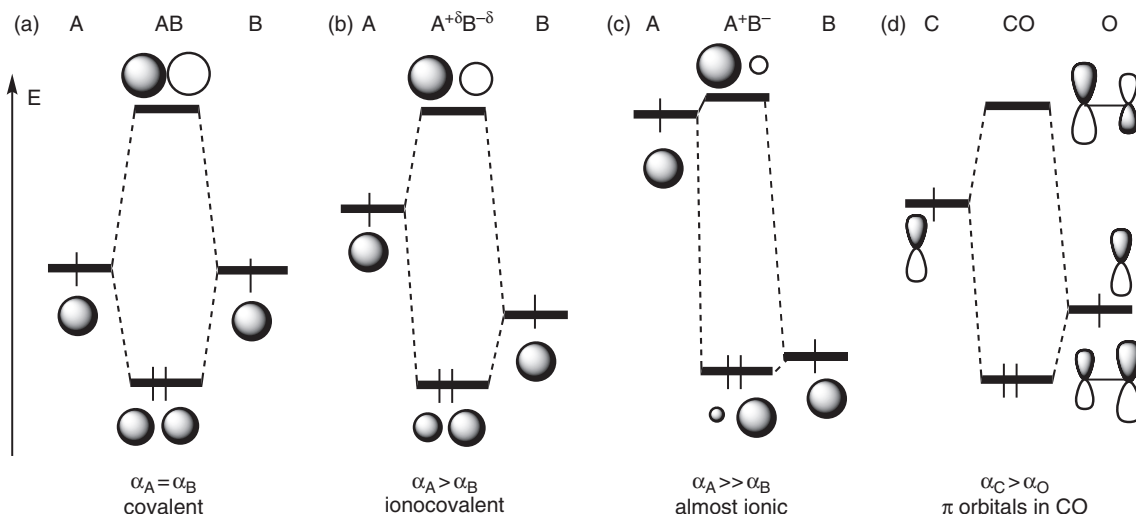


Fig. 1.5

Molecular orbitals energy diagram of an AB diatomic molecule.

t and t' are termed the mixing coefficients, since the bonding MO ψ_1 is mainly built from ϕ_B with some mixing of ϕ_A governed by t , whereas the antibonding MO ψ_2 is centred mainly on ϕ_A with some mixing of ϕ_B governed by t' . Figure 1.5 displays the molecular orbital energy diagram (MOED) and a scheme of the orbitals.

One can observe in eqns. (1.27) that the more important the energy difference $\alpha_A - \alpha_B$, the weaker are the mixing coefficients t and t' . Figure 1.6 illustrates qualitatively the change from a situation (a) where the electrons are shared equally by A and B ($\alpha_A = \alpha_B$, same electron density on A and B (electron— or charge—density is defined in Section 1.5.2); covalent bonding A–B, left) to a situation almost ionic (c), with a strong electronic density on the electronegative atom B—that is, a practically complete electron transfer from A to B ($\alpha_A \gg \alpha_B$; ionic bonding $A^+ B^-$)—through the intermediate case (b) with a partial electron transfer ($\alpha_A > \alpha_B$; ionocovalent bonding $A^{\delta+} - B^{\delta-}$, larger MOs coefficients in ψ_2 than in ψ_1). The previous inequalities are in line

**Fig. 1.6**

Changes in molecular orbitals of an AB molecule with the relative energies of atomic orbitals.

with negative values of the orbitals' energies. The different weights of A and B atoms in molecular orbitals is important in HX molecules (X halogen) and for π bonding in AB molecules such as CO or CN^- (d).

The resonance integral β is not so easy to evaluate. An approximate but explicit formula is given in the frame of extended Hückel framework (Section 1.5.2.2).

1.3.3 Dioxygen molecule, O_2

The dioxygen molecule is a widespread molecule, constituting 1/5 of the atmosphere. It is the basis of all aerobic life and combustion reactions, and combines with most of the known elements. It produces thermodynamically stable derivatives through reactions with high activation energies (slow reactions), due to its particular electronic structure, which therefore deserves particular attention. With the dioxygen molecule we arrive at a little more complex situation to build the molecular energy diagram: on each oxygen atom, six valence electrons are located in 2s, 2p_x, 2p_y, and 2p_z atomic orbitals. We can forget the 1s core electrons, which have no significant role in the bonding scheme and deal only with the 2s, 2p valence electrons. So we need to combine orbitals of various symmetries and energies. The point group symmetry is $D_{\infty h}$, with an inversion centre in the middle of the $\text{O}_A\text{--O}_B$ segment. The 2s and 2p_z are of σ symmetry (rotational symmetry around the internuclear axis z, O–O), whereas the p_x and p_y are of π symmetry (axis perpendicular to z axis). The 2s and 2p orbitals are far in energy ($E_{2s} = -33.86$ eV; $E_{2p} = -17.19$ eV). As a first approximation we can neglect the s–p interaction and combine the 2s orbitals together and the 2p_z together. This is shown in Fig. 1.8 to obtain a bonding

$1\sigma_g$ and an antibonding $1\sigma_u^*$ with $2s$, and a bonding $2\sigma_g$ and antibonding $2\sigma_u^*$ with $2p_z$:

$$\psi(1\sigma_g) = |1\sigma_g\rangle = 1\sigma_g = N(1\sigma_g)[2s(O_A) + 2s(O_B)] \quad (1.28)$$

Here and in the following equations, N is a normalization constant.

A word about the notations used: $1\sigma_g$ means the first molecular orbital, in order of increasing energy, built from valence electrons belonging to the σ_g irreducible representation (IR) of point group symmetry $D_{\infty h}$: σ , rotational symmetry around the z axis; g , gerade (symmetric in the inversion operation). $1\sigma_g$ is the in-phase (bonding) combination of the $2s(O_A)$ and $2s(O_B)$ orbitals. The out-of-phase combination of the $2s(O_A)$ and $2s(O_B)$ orbitals lead to the antibonding $1\sigma_u^*$ ($1\sigma_u$ means the first molecular orbital belonging to the σ_u IR; * is used to point out the MO antibonding character):

$$\psi(1\sigma_u) = |1\sigma_u\rangle = 1\sigma_u^* = N(1\sigma_u)[2s(O_A) - 2s(O_B)] \quad (1.29)$$

With the $2p_z$ and the same notations, we get similarly:

$$\psi(2\sigma_g) = |2\sigma_g\rangle = 2\sigma_g = N(2\sigma_g)[2p_z(O_A) - 2p_z(O_B)] \quad (1.30)$$

$$\psi(2\sigma_u) = |2\sigma_u^*\rangle = 2\sigma_u^* = N(2\sigma_u)[2p_z(O_A) + 2p_z(O_B)] \quad (1.31)$$

Note an important difference with the MOs built from the previous s orbitals and the H_2 case (Section 1.3.1). When the coordinate system is the same for the two atoms (see Fig. 1.7), the + sign of the $2p_z(O_A)$ orbital faces the - sign of the $2p_z(O_B)$ one (Fig. 1.7b). Thus the overlap integral S is now *negative*, and the resonance integral β is *positive*. Inspection of the molecular orbitals and calculation of their energies (still given by eqn. like (1.19)) show that $[2p_z(O_A) - 2p_z(O_B)]$ is now the bonding combination and $[2p_z(O_A) + 2p_z(O_B)]$ the antibonding one. Figure 1.7 gathers different important cases.













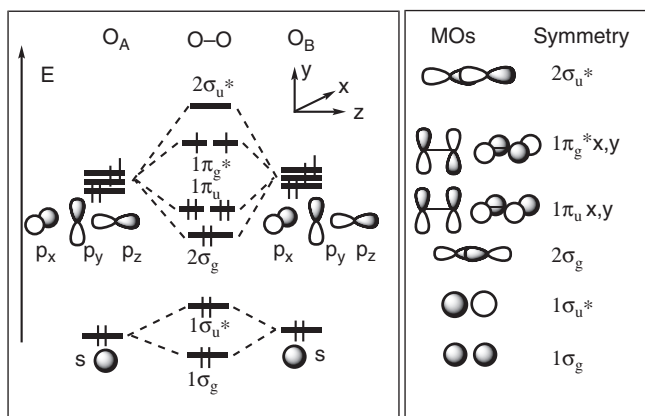
	(a)	A	B	S	β
	s			>0	<0
	p_z			<0	>0
		$p_z(A)$	$+p_z(B)$		
				>0	<0
		$p_z(A)$	$-p_z(B)$		
	p_y			>0	<0
	$d_{z,y}$			<0	>0
		$d_{zy}(A)$	$+d_{zy}(B)$		
				>0	<0
		$d_{zy}(A)$	$-d_{zy}(B)$		

Fig. 1.7

Signs of overlap S and resonance integral β between different kinds of orbitals centred on A and B in the coordinates system shown. Cases (b) and (e) correspond to negative S and positive β .

**Fig. 1.8**

Schematic molecular orbitals energy diagram of the dioxygen molecule: building, schemes, symmetry labels, and occupancy of the MOs.

We are now in a position to comment on the building of π symmetry MOs in Fig. 1.8: to get the two bonding MOs belonging to the π_u IR, we combine in phase the two $2p_x$ and the two $2p_y$ (Fig. 1.7d):

$$\psi(1\pi_u(x)) = |1\pi_u(x)\rangle = 1\pi_u(x) = N(1\pi_u(x)) [2p_x(O_A) + 2p_x(O_B)] \quad (1.32)$$

$$\psi(1\pi_u(y)) = |1\pi_u(y)\rangle = 1\pi_u(y) = N(1\pi_u(y)) [2p_y(O_A) + 2p_y(O_B)] \quad (1.33)$$

The notations are self-evident. As $2p_x$ and $2p_y$ are degenerate, so are the $1\pi_u(x)$ and $1\pi_u(y)$ MOs:

$$\psi(1\pi_u(x, y)) = |1\pi_u(x, y)\rangle = 1\pi_u(x, y) = N(1\pi_u(x, y)) [2p_{x,y}(O_A) + 2p_{x,y}(O_B)] \quad (1.34)$$

The out-of-phase combinations lead to:

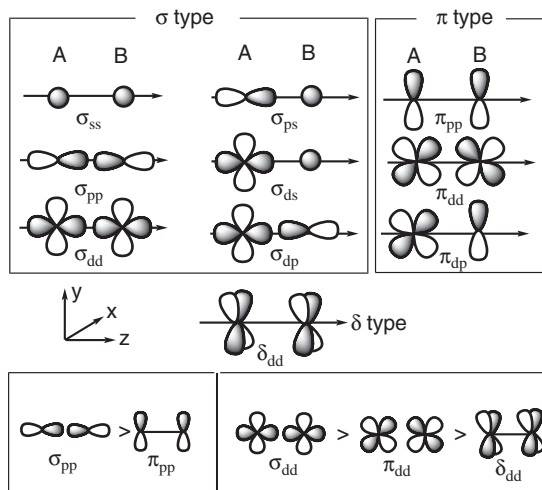
$$\psi(1\pi_g(x)^*) = |1\pi_g(x)^*\rangle = 1\pi_g(x)^* = N(1\pi_g(x)) [2p_x(O_A) - 2p_x(O_B)] \quad (1.35)$$

$$\psi(1\pi_g(y)^*) = |1\pi_g(y)^*\rangle = 1\pi_g(y)^* = N(1\pi_g(y)) [2p_y(O_A) - 2p_y(O_B)] \quad (1.36)$$

$$\begin{aligned} \psi(1\pi_g(x, y)^*) &= |1\pi_g(x, y)^*\rangle = 1\pi_g(x, y)^* \\ &= N(1\pi_g(x, y)) [2p_{x,y}(O_A) - 2p_{x,y}(O_B)] \end{aligned} \quad (1.37)$$

The relative energies of the $2\sigma_g$ and $1\pi_u$ MOs and of the $2\sigma_u^*$ and $1\pi_g^*$ MOs deserve some comment. Figure 1.8 shows that $2\sigma_g$ is below $1\pi_u$, whereas $2\sigma_u^*$ is above $1\pi_g^*$. In the absence of s-p interaction, this is a general situation: everything being equal, for a given orbital, the σ interactions are stronger than the π ones. Figure 1.9 illustrates this point and displays different possible interactions (σ , π , δ) between s, p, and d orbitals, and a qualitative ranking of the σ , π , and δ overlaps with the same distance between neighbours.

We can now establish and comment on the electronic structure of the dioxygen molecule. To find it, we need to place the twelve valence electrons in the MOs of Fig. 1.8, by using the basic principles of quantum chemistry. The first

**Fig. 1.9**

Types of orbital interaction ranked by symmetry (top) and by overlap magnitude (bottom).

four electrons are easily placed in $1\sigma_g$ and $1\sigma_u$, thanks to the Aufbau principle (the electrons occupy the more stable MOs). The resulting electronic configuration $(1\sigma_g)^2(1\sigma_u)^2$ is not bonding. The next six electrons can be accommodated in the $2\sigma_g$ and the $1\pi_u$ MOs, following the same principle. At this stage, the electronic configuration is $(1\sigma_g)^2(1\sigma_u^*)^2(2\sigma_g)^2(1\pi_{ux})^2(1\pi_{uy})^2$. Two electrons are left and two $(1\pi_{gx}^*)$ and $(1\pi_{gy}^*)$ degenerate MOs are available. Like in the case of the carbon atom (see Section 1.2.3.), we use Hund's rule (and exchange integral k) and the more stable configuration corresponds to the triplet state; the two electrons, with the same spin, occupy the two orbitals, which become half-occupied with a resulting molecular spin $S_{O_2} = 1$. The MO-LCAO model leads directly to the experimental result: a dioxygen paramagnetic molecule (contrary to the Lewis model). The electronic configuration is then $(1\sigma_g)^2(1\sigma_u^*)^2(2\sigma_g)^2(1\pi_{ux})^2(1\pi_{uy})^2(1\pi_{gx}^*)^1(1\pi_{gy}^*)^1$.

The dioxygen molecule exemplifies how the electronic structure determines magnetic properties, and in particular, how it is possible to force the rather uncommon situation where two electrons adopt parallel spins. This situation will be met with again in Section 1.5 and in Chapter 2 ('magnetic' orthogonal orbitals). It is not simply a quantum peculiarity. The triplet ground state of the dioxygen gives rise to many spin-forbidden reactions, which therefore presents high activation energies, explaining why living organisms and human beings are able to exist in a dioxygen atmosphere, even if they move around far above the thermodynamically stable state.

Bond order

The number of bonds in the dioxygen molecule is obtained from eqn. (1.25) and from the electronic configurations, with $N_{\text{bonding}} = 8$, $[(1\sigma_g)^2(2\sigma_g)^2(1\pi_{ux})^2(1\pi_{uy})^2]$ and $N_{\text{antibonding}} = 4$, $[(1\sigma_u^*)^2(1\pi_{gx}^*)^1(1\pi_{gy}^*)^1]$; that is, $(8 - 4)/2 = 2$. It can be detailed for σ and π bonds: $\omega_\sigma = (4 - 2)/2 = 1$ σ bond, and $\omega_\pi = (4 - 2)/2 = 1$ π bond. This is consistent with the Lewis picture, *except that* the paramagnetism is explained in a straightforward manner.

1.3.4 Water molecule, H₂O

The water molecule is one of the most common and most useful molecules on Earth. The main constituent of the oceans, seas, and rivers, it is the supporting medium of many biological systems, indispensable to life. Its acidobasic and redox properties and its physical properties rely on its electronic structure, and it will help us to take another step in the orbital description of matter and in understanding the relations between electronic structure and properties.

Figure 1.10 presents the geometrical structure: the two hydrogen atoms are bonded to the central oxygen atom ($d_{\text{OH}} = 95.7\text{pm}$); the molecule is bent with a H-O-H bond angle of 104.52° . The z axis bisects the H-O-H angle, and the x axis is perpendicular to the molecule plane. The point group symmetry is C_{2v} . To get the MOs of the molecule, it is convenient to use the symmetry of the valence electrons (Fig. 1.10). The valence orbitals are $1s(\text{H}_A)$ denoted $1s_A$, and $1s(\text{H}_B)$ denoted $1s_B$, $2s(\text{O})$, $2p_x(\text{O})$, $2p_y(\text{O})$, $2p_z(\text{O})$. The two hydrogen atoms H_A and H_B are equivalent in the molecule, and the oxygen is alone of its kind. The symmetry labels for the oxygen orbitals are found directly in the character table of the C_{2v} point group (Table 1.3).

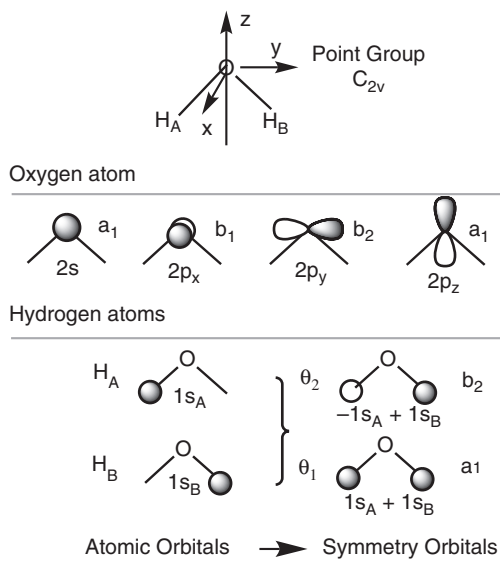
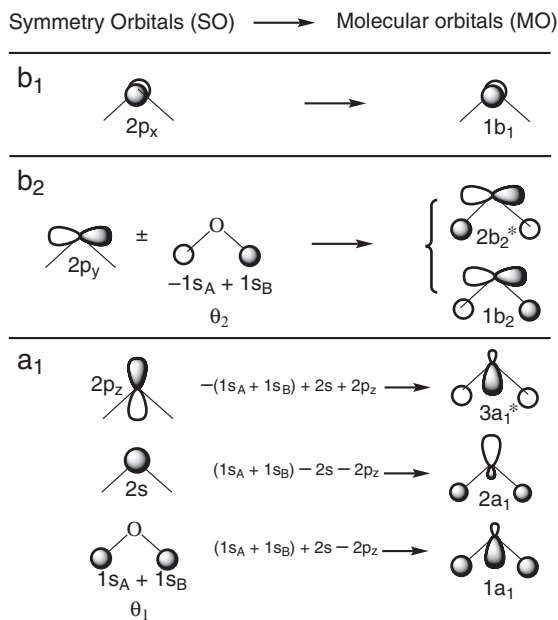


Fig. 1.10

Water molecule: symmetry of the valence orbitals. Building symmetry orbitals from atomic orbitals.

Table 1.3 Character table of the C_{2v} point group.

C_{2v}	E	C_2	$\sigma_v(xz)$	$\sigma_v(yz)$		
A_1	1	1	1	1	z	x^2, y^2, z^2
A_2	1	1	-1	-1		xy
B_1	1	-1	1	-1	x	xz
B_2	1	-1	-1	1	y	yz

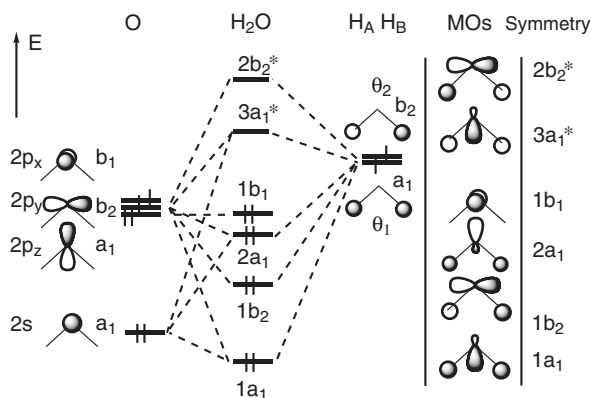
**Fig. 1.11**

Water molecule: building molecular orbitals from symmetry orbitals.

For the hydrogen atoms, each of the $1s_A$ or $1s_B$ considered alone is not a basis for an irreducible representation of the group; but their combinations $\theta_{\pm} = 1s_A \pm 1s_B$ are. The combinations adapted to the symmetry of the molecules are termed symmetry orbitals (SO), and in this book these will be termed θ . The symmetry labels of the basis orbitals are shown in Fig. 1.10.

We now need to find, for each irreducible representation, the appropriate combinations of basis orbitals to get the MOs. Figure 1.11 displays how the symmetry orbitals (SOs) can build the MOs: for symmetry b_1 there is only one atomic orbital (AO), which becomes one symmetry orbital (SO) and one molecular orbital (MO): $1b_1$; for symmetry b_2 there are two symmetry orbitals ($2p_y$ and θ_2), and their in-phase and out-of-phase combinations give two molecular orbitals (MOs): $1b_2$, bonding, and $2b_2^*$, antibonding; for symmetry a_1 the three symmetry orbitals ($2s$, $2p_z$, and θ_1) combine to give three molecular orbitals (MOs): $1a_1$, strongly bonding, $2a_1$, slightly bonding, $3a_1$, antibonding. This procedure emphasizes that molecular orbitals (MOs) can be built from symmetry orbitals (SOs), themselves built from atomic orbitals. In other words, molecular orbitals can be built by a stepwise method. Figure 1.12 displays the schematic molecular orbital energy diagram and the occupation of the orbitals by the electrons.

The electronic configuration is $(1a_1)^2(1b_2)^2(2a_1)^2(1b_1)^2$. The last two occupied orbitals (HOMO and HOMO-1) are $1b_1$ and $2a_1$ respectively, with two electrons in each. Orbital $1b_1$ is a pure $2p_x$ orbital of the oxygen, non-bonding, whereas the $2a_1$ orbital is slightly bonding (practically non-bonding), mainly composed of $2s$ and $2p_z$ oxygen orbitals with some admixture of the a_1 symmetry orbital of hydrogen atoms $\theta_1 = 1s_A + 1s_B$. These two MOs are at the origin of the important acidobasic properties of water. The two bonding

**Fig. 1.12**

Water molecule: schematic molecular orbitals energy diagram.

orbitals are $1a_1$ and $1b_2$, occupied by two electrons each. They ensure the stability of the molecule.

The occupation of orbitals, with four bonding electrons and four non-bonding electrons, has some relation with the traditional Lewis description (two free doublets and two O-H bonds). However, in the MO-LCAO description, each bonding pair is delocalized on the whole molecule, and contributes equally to the two OH bonds. Note that the MO method is the correct one to deal with electron energies (in particular, photoelectron spectroscopy shows that there are four different ionization potentials in H_2O), and that MOs respect the symmetry of the molecule, which is not the case for Lewis-type localized orbitals.

1.3.5 Organic molecular systems

There is no particular reason to separate the orbital description of organic molecules from others—inorganic ones. The same methods and rules apply with the same conclusions: methane, CH_4 , is described using the same principles as ammonia, NH_3 , or water, H_2O . Nevertheless, organic chemistry provides the quantum chemist with peculiar planar conjugated π systems, discrete or extended, where it is possible to derive simple analytical expressions of the energies and of the wavefunctions. This gives us the opportunity to make a step further towards the one-electron orbital description of the solid.

Hückel theory

The ideas at the basis of the Erich Hückel's theory are quite simple: in a planar polyene molecule, the $p\pi$ orbitals are antisymmetric with respect to the plane of the molecule. They do not mix with the σ orbitals framework and can be studied separately. The parameterization is particularly simple, of the 'all or nothing' type. Thus Coulomb energies for carbon atoms are taken as the same; that is, $H_{ii} = \alpha$ for all $p\pi$ basis orbitals. Resonance energies are considered as identical between adjacent $p\pi$ orbitals; that is $H_{ij} = \beta$, and are assumed to be zero as soon as atoms are not linked directly. Finally, overlap integrals S are neglected ($S \ll 1$). This simple form of Hückel theory is no longer used

for organic molecules, except for pedagogical purposes, because it gives the general trend in the shape and energies of orbitals during their progressive construction. It will be seen in Sections 1.4 and 1.5 that it corresponds to the ‘tight-binding’ method used to describe solid-state systems.

A step further is provided by extended Hückel theory, dealing with all valence electrons, in which the overlap S_{ij} is no more neglected and the resonance energies H_{ij} are approximated from overlap integrals. This method is described in more detail in Section 1.5.2.2. Within the extended Hückel method, one is no longer confined to planar molecules with σ/π separation, and the reintroduction of orbital overlaps produces more realistic energies, by strongly destabilizing antibonding orbitals. However, the method does not treat explicitly electron–electron repulsion (it is indirectly and crudely taken into account in the H_{ii} parameters). Thus the total electronic energy is simply the sum of the electron energies (which is not correct at all), and the triplet and singlet states arising from the same configuration have equal energies. Despite these defects, the extended Hückel method is the basis of a qualitative description of orbitals and makes the link between intuitive arguments (‘with the hands’) and sophisticated MO methods.

Qualitative approach of linear systems

The simplest π linear system is ethene, C_2H_4 , a planar symmetric molecule, with an internuclear C–C z axis. The π system consists of two $p\pi$ orbitals with axes perpendicular to the plane (let us say $2p_y$), both half-occupied by one electron. The expressions of the wavefunctions (eqns. (1.14)) and energies (eqns. (1.19)) derived from the same determinant (eqn. (1.21)) (neglecting S) are rigorously the same as for the dihydrogen molecule (see Section 1.3.1), *mutatis mutandis*; that is, replacing the $1s$ σ hydrogen orbital by the $2p_y$ π orbitals. The resulting MOs are bonding (antisymmetric in the inversion operation, u) and antibonding (symmetric, g). This is shown in Fig. 1.13 ($N = 2$). When we add a third $2p_y$ π orbital in a linear molecule, we obtain an allyl radical (Fig. 1.13, $N = 3$). By linear combination, the three MOs are respectively bonding (no node, u symmetry), non-bonding (one node on the central atom, g symmetry) and antibonding (two nodes, u symmetry), with appropriate MO coefficients, not shown. The MOs for larger N in Fig. 1.13 will be commented upon further in Section 1.4.

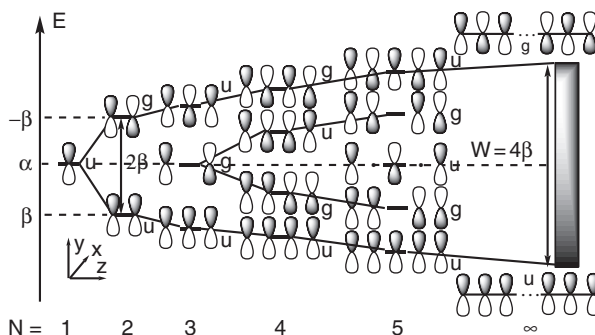


Fig. 1.13

Molecular orbitals of ethene ($N = 2$), allyl radical, and longer linear models.

Cyclic polyenes

The preceding observations can be extended to planar cyclic systems $(\text{CH})_N$ with very similar results. The point groups to be used are either the D_{nh} groups (σ_h is the molecular plane), or more simply but without loss of generality, the cyclic groups C_n . Figure 1.14 displays the MOs ψ_j built from the $2p_z$ π orbitals ϕ_n with axis z perpendicular to the molecular plane, their energy levels, and their symmetry labels in D_{nh} or C_n groups, for planar cyclic systems from C_3 to C_6 (benzene) (see character tables in references [1.7], [1.8], and [1.9]). The following observations hold:

- When the energy increases, the number of nodes increases by one on going from one ψ_j molecular orbital to the next higher in energy. The lowest MO presents no node. Degenerate MOs present the same number of nodes.
- The MO with the lowest energy is non-degenerate. The MOs at the highest energy are degenerate pairs for odd-membered rings and non-degenerate for even-membered ones.

These properties derive from the symmetry properties of the cyclic groups C_n : they all present a fully symmetric non-degenerate irreducible representation A (corresponding to the most stable and bonding level) and doubly degenerate irreducible representations E or $E_1, E_2 \dots$. When N is even, a non-degenerate irreducible representation B appears, which is antisymmetric with respect to the C_n rotations and corresponds to the most unstable and antibonding level.

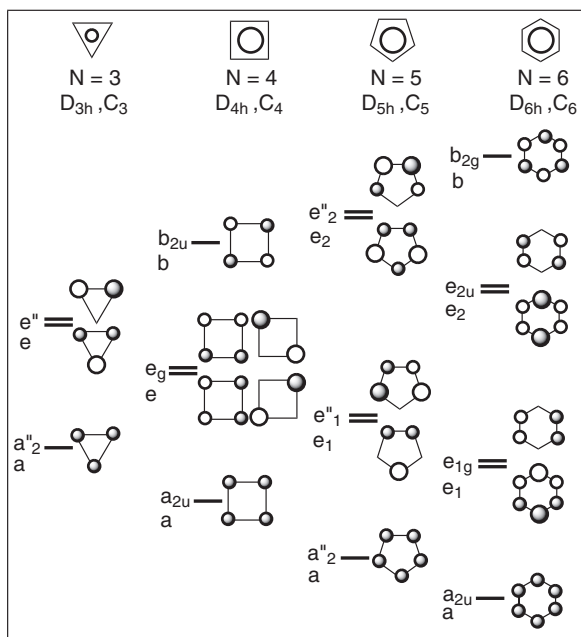


Fig. 1.14

Planar cyclic $(\text{CH})_N$ systems: energy levels and top view of π -type molecular orbitals ($N = 3-6$).

It is possible to determine the wavefunctions ψ_j and the energies E_j of systems with N atoms, each presenting one orbital (ϕ_n , half occupied), within the frame of Hückel's approximations:

$$\psi_j = \sum_{n=1}^N c_{n,j} \phi_n = \frac{1}{\sqrt{N}} \sum_{n=1}^N \left[\exp\left(\frac{2ij\pi(n-1)}{N}\right) \right] \phi_n \quad (1.38a)$$

$$E_j = \alpha + 2\beta \cos\left(\frac{2j\pi}{N}\right) \quad (1.38b)$$

In eqn. (1.38a), i is the complex number $i^2 = -1$. The j parameter takes the values $0, \pm 1, \pm 2, \pm 3, \dots, \pm(n'-1)$, n' (with $n' = N/2$, when N is even) according to the symmetry properties. The complex form of the wavefunction ψ_j comes from the irreducible representations E_i of the cyclic groups C_n , whose characters can be complex quantities. The energy levels E_j after eqn. (1.38b) are shown in Fig. 1.15, for N even (a) and odd (b). In c) is shown the Frost circle, with a $|2\beta|$ radius, whose usefulness is shown in d): an N -vertex polygon inscribed in the Frost circle with one of its vertices at the bottom allows us to derive easily the quantitative energy diagram for $N = 3-6$.

Stability of cyclic polyenes. Hückel $4n + 2$ rule

We have now to deal with the occupancy of the molecular orbitals. It should be clear from Fig. 1.15 a), b), and d) that the molecule will be the most stable, or will have a peculiar stability, when all the bonding and non-bonding levels are filled. Above the lowest bonding level, the other levels occur in pairs. If n pairs of these levels are occupied, $2n+1$ orbitals will be filled with $4n+2$ electrons. One can check that it works for $(\text{CH})_3^+$ and $(\text{CH})_4^{2+}$ (2 electrons, $n = 0$), $(\text{CH})_5^-$ and $(\text{CH})_6$ (six electrons, $n = 1$). We recognize the Hückel $4n+2$ rule (n integer, $0, 1, 2, \dots$). These peculiar electronic configurations are often termed *aromatic*.

By contrast, the cyclobutadiene molecule $(\text{CH})_4$ present a different behaviour because there are four π electrons, of which two occupy the a level and two the e levels, so that there is an incomplete filling of the e orbitals as a

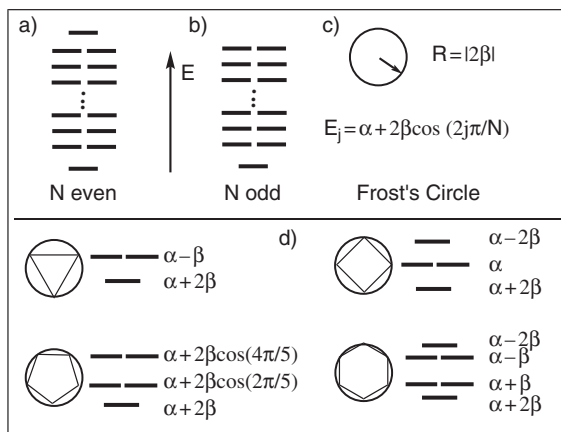


Fig. 1.15

Planar cyclic $(\text{CH})_N$ systems: use of the Frost circle to obtain the energy levels.

whole. With $4n$ electrons, the system is called *antiaromatic*. As a result of its peculiar electronic structure, it is subject to the Jahn–Teller effect, leading to a distortion with a loss of the highly symmetrical square structure. This effect is described in more detail in Section 1.3.7. We shall encounter a similar effect in the case of solids: Peierls distortion (Section 1.4.3), which occurs also when there is partial filling of a set of degenerate orbitals.

1.3.6 Coordination complexes

A coordination complex is a molecular entity resulting from the interaction of a metallic ion M with ions or molecules L , termed ligands:



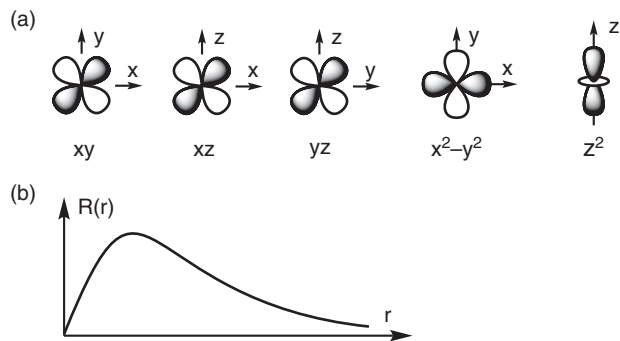
The ML_n complex can be charged or neutral.

Transition elements

We focus on the case where the metal ions M are transition elements, since they present distinct advantages for obtaining molecules with original properties and new materials. Their electronic configuration is $ns^2, (n-1)d^n$, and they have an incomplete d sub-shell in one of their oxidation states. Figure 1.16 shows their place in the periodic table.

s Elements										p Elements													
H																			He				
Li	Be																						
Na	Mg																						
K	Ca	Sc	Ti	V	Cr	Mn	Fe	Co	Ni	Cu	Zn	Ga	Ge	As	Se	Br	Kr						
Rb	Sr	Y	Zr	Nb	Mo	Tc	Ru	Rh	Pd	Ag	Cd	In	Sn	Sb	Te	I	Xe						
Cs	Ba	La	Hf	Ta	W	Re	Os	Ir	Pt	Au	Hg	Tl	Pb	Bi	Po	At	Rn						
Fr	Ra	Ac																					
										f Elements													
										Ce	Pr	Nd	Pm	Sm	Eu	Gd	Tb	Dy	Ho	Er	Tm	Yb	Lu
										Th	Pa	U	Np	Pu	Am	Cm	Bk	Cf	Es	Fm	Md	No	Lr
44,956	47,867	50,942	51,996	54,938	55,845	58,933	58,693	63,546	65,39														
Sc	Ti	V	Cr	Mn	Fe	Co	Ni	Cu	Zn														
21	22	23	24	25	26	27	28	29	30														
88,906	91,224	92,906	95,94	98,906	101,07	102,91	106,42	107,87	112,41														
Y	Zr	Nb	Mo	Tc	Ru	Rh	Pd	Ag	Cd														
39	40	41	42	43	44	45	46	47	48														
138,91	178,49	180,95	183,84	186,21	190,23	192,22	195,08	196,97	200,59														
La	Hf	Ta	W	Re	Os	Ir	Pt	Au	Hg														
57	72	73	74	75	76	77	78	79	80														

Fig. 1.16
d transition elements in the periodic table.

**Fig. 1.17**

Schematic angular (a) and radial (b) representations of 3d orbitals.

Table 1.4 Nodal surfaces in d orbitals.

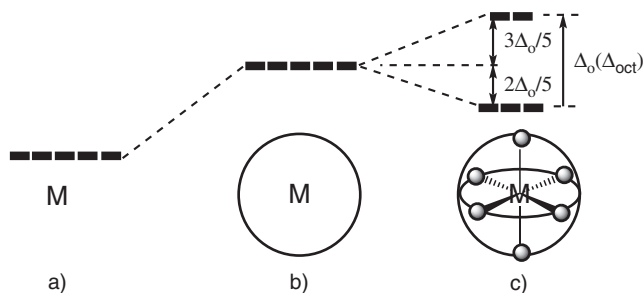
	Quantum number nd	Nodal surfaces: total	Radial part	Angular part
First line	3	2	0	2
Second line	4	3	1	2
Third line	5	4	2	2

d orbitals have a gerade symmetry, corresponding to the spherical harmonics xy , xz , yz , $x^2 - y^2$, and z^2 (quantum number $l = 2$). Their radial and angular representations are shown in Fig. 1.17. The total wavefunctions present $(n - 1)$ nodal surfaces, which are distributed as shown in Table 1.4 in the three lines of the periodic table.

As metals, the transition elements are well-known good conductors (copper is one of the most used metals for conducting wires), often magnetic (iron, cobalt, and nickel are well-known ferromagnetic compounds). A point of particular interest for us is the way that the d orbitals of the metallic ion M interact with the atomic or molecular orbitals of the neighbouring ligands L to produce the molecular complex ML_n . Several theoretical models have been proposed to describe the metal–ligand interaction. We reiterate only the main points, and suggest that the reader consult inorganic chemistry textbooks [1.10] or ligand field theory books [1.11].

Crystal field model

This is the simplest model, purely electrostatic in nature, which describes the molecules or anions L around the metallic ion as negative point charges or dipoles, stabilizing or destabilizing the d orbitals in a specific manner, depending on the symmetry. Figure 1.18 summarizes the main conclusions of the model for an octahedral complex: a uniform spherical distribution of six negative charges destabilizes the d orbitals in a uniform way (Fig. 1.18a, then b); starting from that, gathering the negative charges as six octahedral point charges removes the degeneracy and splits the d orbital energy into two sets (Fig. 1.18c): the two e_g orbitals (pointing along the $M-L$ directions) are destabilized, whereas the three t_{2g} orbitals (pointing between the $M-L$ directions) are stabilized. The difference in energy between the two sets of orbitals

**Fig. 1.18**

Crystal field in an octahedral complex: a) energy of the d orbitals in the free ion; b) under the influence of a uniform distribution of negative charges; c) under the influence of an octahedral distribution of charges.

is termed Δ_{oct} , or sometimes, and for historical reasons, $10 Dq$. A simple calculation, using the fact that the average orbital energy is conserved, leads to the stabilization energy of the t_{2g} orbitals $-2\Delta_{\text{oct}}/5$, whereas the destabilization of e_g orbitals is $3\Delta_{\text{oct}}/5$. The model deals only with the splitting of the energies of the d orbitals. It does not consider the nature of bonding between the metal and the ligand, but uses fully the symmetry properties of the crystal field.

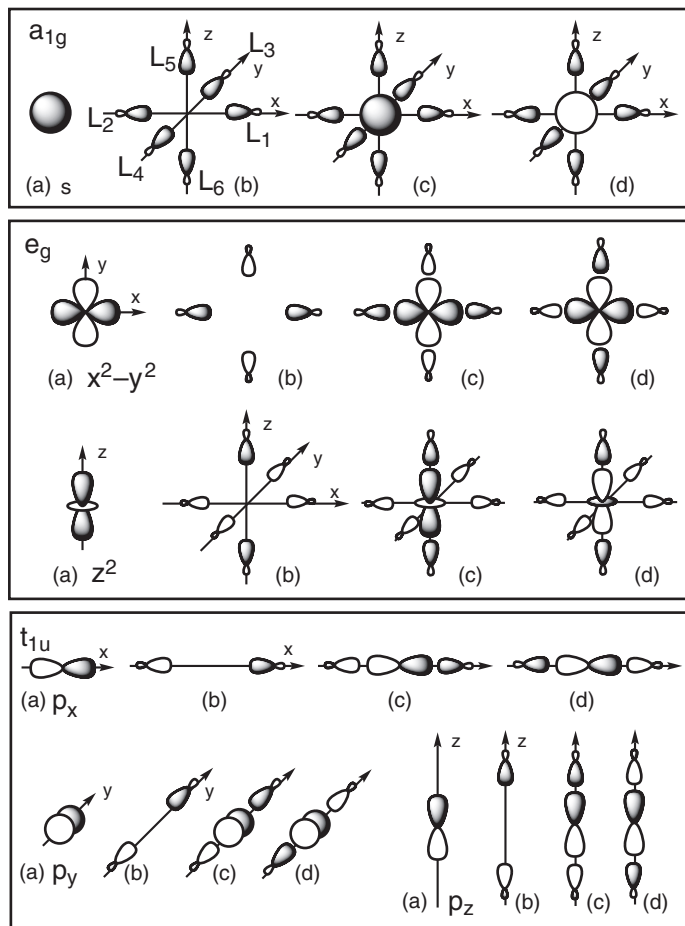
Molecular orbital model

The second model is the one of molecular orbitals, used in the preceding sections for molecules with s and p elements. The principles to obtain the MOs of a coordination complex are the same as before. The building of MOs is tightly bound to the symmetry properties of the molecular complex, and to the point group: O_h , T_d , D_{4h} , C_{4v} , and so on. MOs are a basis for the irreducible representations of the group, so that the derivation of the energy diagram is simplified [1.10–1.12].

Octahedral complex ML_6 (σ -type ligand L orbitals, with $M = Fe^{3+}$, electronic configuration d^5)

The point group is O_h , and the ligand disposition and numbering is shown in Fig. 1.19, with the x, y, z axes taken along the M–L bonds. The irreducible representations follow from the character table of the O_h group (Table 1.5). We start from fifteen initial orbitals—nine for the metal (five 3d orbitals, one 4s orbital and three 4p orbitals) and six σ orbitals brought by the ligands. For the metal, a direct reading of the table gives: $t_{2g}(xy, xz, yz)$; $e_g(x^2-y^2, z^2)$; $a_{1g}(4s)$; $t_{1u}(4p_x, 4p_y, 4p_z)$. For the ligands, it is necessary to build the symmetry orbitals as shown in Table 1.6.

We then perform the final combinations. It is found that a) the t_{2g} orbitals (xy, xz, yz) of the metal have no ligand counterpart: they remain unchanged in the complex; b) the sign of the participation of ligand orbitals l_i in the symmetry orbitals depends on the conventions adopted for the numbering of the ligand orbitals. The sign used here is in agreement with Fig. 1.19. Finally, fifteen MOs are found: three t_{2g} (π) purely metallic and non-bonding, twelve σ MOs obtained by the linear combination of six symmetry orbitals of the ligands (one a_{1g} , two e_g , three t_{1u}) and six from the metal with the same symmetry. In this σ set, six are bonding and six are antibonding. Figure 1.20 displays the energy diagram, the schematic representation of the MOs, and the symmetry labels. Regarding the electron count, for an Fe^{3+} complex the diagram must

**Fig. 1.19**

Axes, ligands numbering, symmetry orbitals, and molecular orbitals in an ML_6 octahedral complex (σ ligands). For a given symmetry: (a) metal orbitals; (b) symmetry orbitals of the ligands; (c) bonding orbitals of the complex; (d) antibonding orbitals.

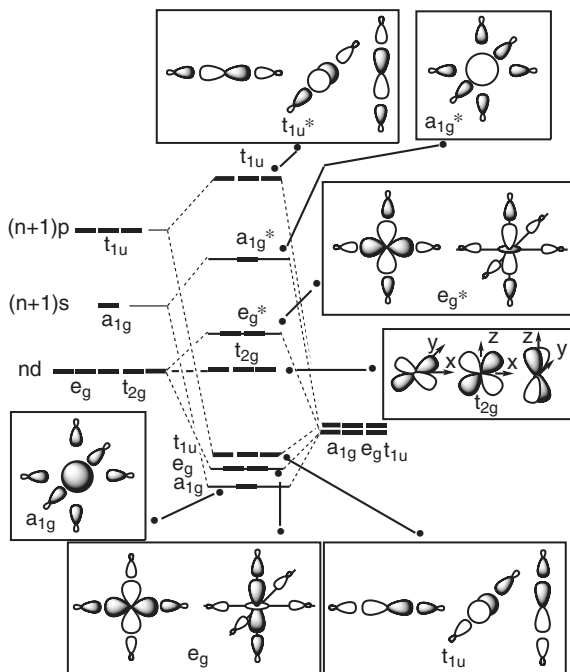
Table 1.5 Character table of the O_h point group.

O_h	E	$8C_3$	$6C_2$	$6C_4$	$3C_2$	i	$6S_4$	$8S_6$	$3\sigma_h$	$6\sigma_d$	
A_{1g}	1	1	1	1	1	1	1	1	1	1	$x^2 + y^2 + z^2$
A_{2g}	1	1	-1	-1	1	1	-1	1	1	-1	
E_g	2	-1	0	0	2	2	0	-1	2	0	$(2z^2 - x^2 - y^2, x^2 - y^2)$
T_{1g}	3	0	-1	1	-1	3	1	0	-1	-1	(xy, xz, yz)
T_{2g}	3	0	1	-1	-1	3	-1	0	-1	1	
A_{1u}	1	1	1	1	1	-1	-1	-1	-1	-1	
A_{2u}	1	1	-1	-1	1	-1	1	-1	-1	1	
E_u	2	-1	0	0	2	-2	0	1	-2	0	
T_{1u}	3	0	-1	1	-1	-3	-1	0	1	1	(x, y, z)
T_{2u}	3	0	1	-1	-1	-3	1	0	1	-1	

Table 1.6 Basis orbitals in an octahedral ML_6 complex.

Symmetry	Ligands L (Symmetry orbitals θ)	Metal M
$a_{1g}: \sigma$	$l_1 + l_2 + l_3 + l_4 + l_5 + l_6$	4s
$e_g: \sigma$	$(l_1 + l_2 - l_3 - l_4)$ and $(-l_1 - l_2 - l_3 - l_4 + l_5 + l_6)$	$x^2 - y^2, z^2$
$t_{1u}: \sigma$	$(l_1 - l_2), (l_3 - l_4)$ and $(l_5 - l_6)$	$4p_x, 4p_y, 4p_z$
$t_{2g}: \pi$	no	xy, xz, yz

Note that we use here and in Table 1.7 a different convention with respect to Fig. 1.7. The + and - signs in the above combinations denote bonding and antibonding combinations respectively, regardless of axis orientations.

**Fig. 1.20**

Molecular orbitals energy diagram of an ML_6 octahedral complex (σ ligands): schematic energy diagram and building lines; MOs schemes and symmetry labels.

accommodate seventeen valence electrons (twelve from the six ligands L, and five from the metal d^5). Thus all orbitals with predominant ligand σ character are filled, and there are five electrons in the orbitals with predominant metal d character—reminiscent of the ionic description of the system.

Two remarks arise from the comparison of the crystal field and the MO models: on the one hand, the two models remove the degeneracy of the d orbitals in the ligand field, Δ_{Oct} . On the other hand, the MO model gives the wavefunctions and the energies of the whole set of MOs, and not only the d ones. Inside the d domain the energy difference comes from the quantum non-bonding or antibonding character, and not from classical electrostatic arguments. For example, the e_g MOs centred on the metal are described clearly as antibonding (nodal surface between the metal and the ligands orbitals). They are often termed e_g^* to emphasize their antibonding character, frequently used in the following.

The ligands can be very different: water, halides X^- , ammonia NH_3 , amines RNH_2 , R_1R_2NH , $R_1R_2R_3N$, phosphine PH_3 and phosphines $R_1R_2R_3P$, complex biological ligands in metalloproteins . . . each ligand creates a different ligand field Δ_{oct} . Ligands giving rise to small Δ_{oct} are termed ‘low-field ligands’, and ligands giving rise to large Δ_{oct} are termed ‘high-field ligands’. An example of a ‘spectrochemical series’, for the Cr^{3+} ion, is:

Ligands	Cl^-	$< F^-$	$< H_2O$	$< NH_3$	$< CN^-$
Δ_{oct} values/ cm^{-1}	13200	15200	17400	21600	26600

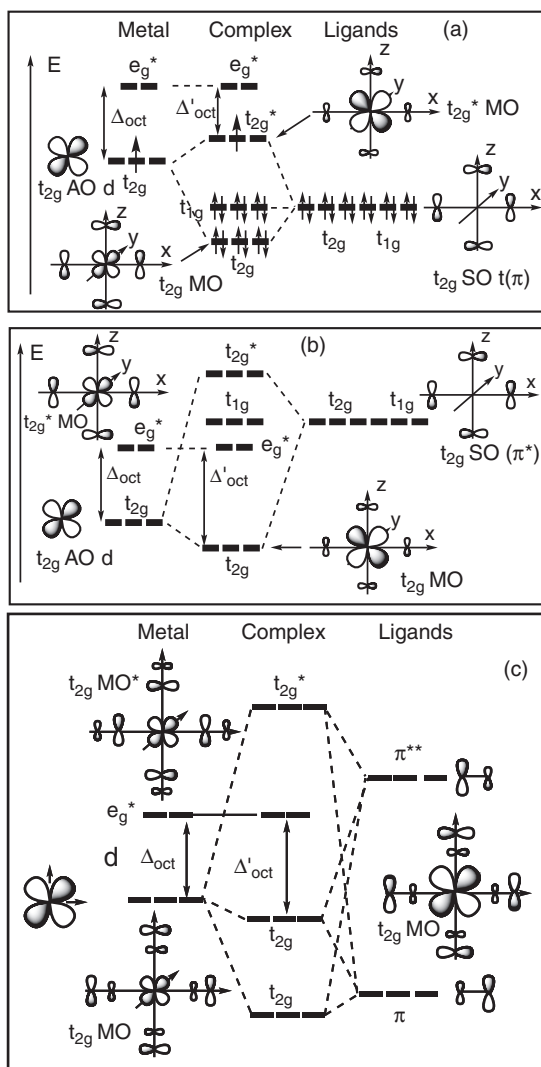
Complexes having only σ ligands are quite rare. Thus it is important to evaluate the rôle of the π bonding on the energy diagram of a ML_6 complex. It is valuable to do it starting from the energy diagram of a $ML_6(\sigma)$ complex and to see the modifications introduced by the change of ligand. Two parameters are important: the symmetry, as ever, and the relative energy of orbitals of the ligand and of the metal. For the relative energies, most often, the energies of the π occupied orbitals of the ligands lie lower in energy than the d orbitals (in other words, ligands are more electronegative than the metallic ions). When antibonding π^* orbitals are implied, they lie generally higher in energy than the d orbitals. For the symmetry, one introduces two π -type orbitals per ligand; that is, twelve supplementary orbitals, which are combined to θ symmetry orbitals as shown in Table 1.7 (the same work can be done for π^* orbitals).

The important point is the modification of the orbitals with preponderant d character by the new symmetry orbitals. In particular, the three t_{2g} d MOs, which are strictly metallic in the ML_6 complex with σ ligands, can combine here with the three t_{2g} symmetry orbitals of the π ligands to give six MOs—three bonding and three antibonding. Figure 1.21a specifies the nature of the interaction and shows that the ligand field is decreased to a Δ'_{oct} value (which happens, for instance, in halide complexes).

The observation holds also for ligands like CO or CN^- , whose π occupied MOs contribute to the destabilization of t_{2g} orbitals and decrease Δ_{oct} (Fig. 1.21a). Nevertheless, these ligands present also vacant high-energy π^* orbitals, which contribute on the contrary to stabilize the t_{2g} orbitals and to

Table 1.7 Symmetry orbitals of the ligands in an octahedral complex.

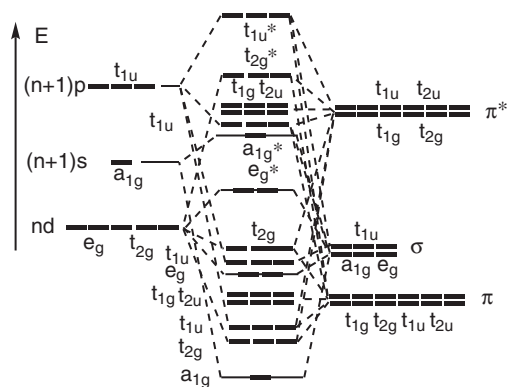
Symmetry	θ Symmetry orbitals of the ligands	Metal
$t_{1g}: \pi$	$(1_{1z} - 1_{2z}) - (1_{5x} - 1_{6x})$	No
	$(1_{3x} - 1_{4x}) - (1_{1y} - 1_{2y})$	No
	$(1_{5y} - 1_{6y}) - (1_{3z} - 1_{4z})$	No
$t_{2g}: \pi$	$(1_{1y} - 1_{2y}) + (1_{3x} - 1_{4x})$	xy
	$(1_{3z} - 1_{4z}) + (1_{5y} - 1_{6y})$	yz
	$(1_{5x} - 1_{6x}) + (1_{1z} - 1_{2z})$	zx
$t_{1u}: \pi$	$(1_{1x} + 1_{2x}) + (1_{3x} + 1_{4x}) - (1_{5x} + 1_{6x})$	$4p_x$
	$(1_{1y} + 1_{2y}) + (1_{3y} + 1_{4y}) - (1_{5y} + 1_{6y})$	$4p_y$
	$(1_{1z} + 1_{2z}) + (1_{3z} + 1_{4z}) - (1_{5z} + 1_{6z})$	$4p_z$
$t_{2u}: \pi$	$(1_{1z} + 1_{2z}) - (1_{3z} + 1_{4z})$	No
	$(1_{3x} + 1_{4x}) - (1_{5x} - 1_{6x})$	No
	$(1_{5y} + 1_{6y}) - (1_{1y} + 1_{2y})$	No

**Fig. 1.21**

Modification of the molecular orbitals energy diagram of an ML_6 octahedral complex in presence of a) π donor ligands, b) π^* acceptors ligands, and c) both π and π^* ligands.

increase Δ_{oct} , as shown in Fig. 1.21b. In fact, it is not possible to separate π and π^* effects; both are generally operating as shown in Fig. 1.21c. For ligands such as CO and CN^- , however, the π^* effect is by far the more important (the weight of carbon directly linked to the metal is much larger in the π^*), and this is why these ligands are ‘high-field’ ligands and lie at the right in the spectrochemical series.

Hence, the ligands σ , π and π^* allow (i) to tune quite precisely the ligand field Δ_{oct} around a transition metal ion in a complex, and (ii) to control therefore the reactivity of the complexes (acid–base, redox . . .) and the physical properties (spectroscopy, colour, magnetism . . .). The understanding of the symmetry and of the ligand field allows the chemist to finely control the properties thanks to the use of appropriate metallic ions and ligands. When adding

**Fig. 1.22**

Schematic molecular orbital energy diagram of a ML_6 octahedral complex with six π donor and π^* acceptor ligands.

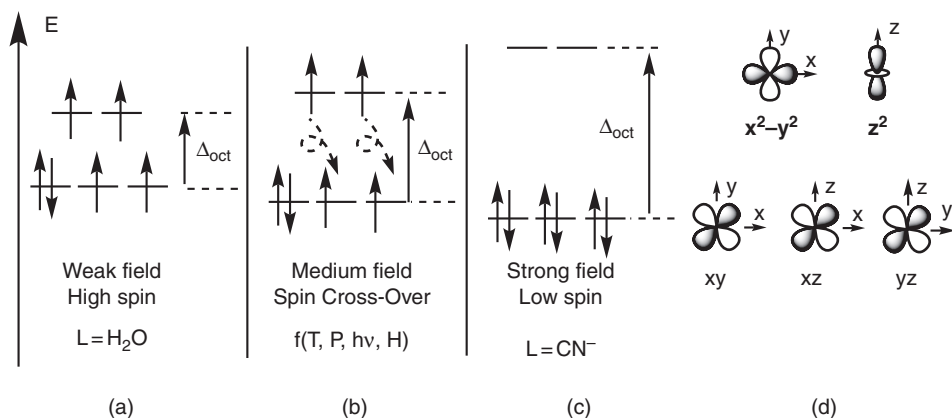
twelve π and twelve π^* MOs orbitals, symmetry t_{1g} , t_{2g} , t_{1u} , t_{2u} , the energy diagram presents the formidable aspect of Fig. 1.22, which is nevertheless easy to understand from the preceding arguments.

A particularly spectacular application in the field of materials is the spin cross-over phenomenon.

High-spin and low-spin complexes; spin cross-over

High-spin and low-spin situations arise from the two contradictory requirements: filling orbitals in the order of ascending energy (Aufbau principle), and having as many electrons as possible with parallel spins (see the case of O_2). For weak ligand fields Δ , the high-spin situation prevails, while for strong Δ it is the low spin.

Figure 1.23 displays the two possible situations for the ligand field in the case of octahedral complexes of the Fe^{II} ion, d^6 : left, the low-field situation is accompanied by a high spin state, $S = 2$. When the five orbitals are half-filled, the sixth electron is paired in one of the t_{2g} orbitals. Water, halogeno,

**Fig. 1.23**

Weak (a), medium (b), and strong (c) ligand fields in an ML_6 octahedral complex: electronic configuration of high-spin, spin cross-over, and low-spin states of the complex; (d) t_{2g} and e_g orbitals.

thiocyanato, or oxalato ligands favour such a high spin state: the hexaaqua iron(II) complex $[\text{Fe}^{\text{II}}(\text{H}_2\text{O})_6]^{2+}$ is high spin, $S = 2$.

On the right, the opposite situation is shown: high field and low spin, $S = 0$. Carbon monoxide CO, cyanide CN^- , and more generally π^* acceptors ligands—aromatic amines (2,2'-bipyridine, 1,10-phenanthroline . . .), phosphines . . . favour such a low-spin situation: the hexacyanidoferrate(II) complex $[\text{Fe}^{\text{II}}(\text{CN})_6]^{4-}$ or the deep red tris-1,10-phenanthroline iron(II) complex $[\text{Fe}^{\text{II}}(\text{phen})_3]^{2+}$ are low spin, $S = 0$.

In between there is a range of intermediate ligand fields for which the system can 'hesitate' between the two types of filling. This is a situation called spin equilibrium, spin cross-over, or spin transition. It is appealing from the point of view of applications, because it can be abrupt and present hysteresis as a result of cooperative effects. The spin cross-over is treated in detail in Section 2.4.3. The intermediate spin ($S = 1$) is rare but possible.

1.3.7 Influence of the electronic structure on the geometric structure: the Jahn–Teller effect

So far, we have started from a fixed molecular geometry and considered that it determines the electronic structure, using, in particular, symmetry and Group Theory arguments. However, the reverse can be true, because the geometry is determined by the simple fact that it must correspond to a minimum of the total energy of the molecule. Under certain circumstances this condition can lead to a loss of symmetry for electronic reasons linked to the orbital filling. This is the Jahn–Teller effect [1.13], presented in simplified form next.

Let us write the Hamiltonian of the molecule as

$$\mathbf{H} = \mathbf{K} + \mathbf{V}(\mathbf{Q}) \quad (1.40)$$

where \mathbf{K} is the kinetic energy operator and \mathbf{V} the operator corresponding to the interaction between charges (electrons and nuclei). \mathbf{V} depends on deformation coordinates \mathbf{Q} , and we limit the discussion to deformations which break the symmetry. A small deformation $\delta\mathbf{Q}$ around an initial position \mathbf{Q}_0 leads to a new \mathbf{V} potential which can be expressed in a Taylor series limited to second order:

$$\mathbf{V}(\mathbf{Q}) = \mathbf{V}(\mathbf{Q}_0) + (\partial\mathbf{V}/\partial\mathbf{Q})_{\mathbf{Q}_0}\delta\mathbf{Q} + \frac{1}{2}(\partial^2\mathbf{V}/\partial\mathbf{Q}^2)\delta\mathbf{Q}^2 + \dots \quad (1.41)$$

The energy change is then given by

$$\Delta E = \Delta E^{(1)} + \Delta E^{(2)} \quad (1.42a)$$

with

$$\Delta E^{(1)} = \langle \Psi_0 | (\partial\mathbf{V}/\partial\mathbf{Q}) | \Psi_0 \rangle \delta\mathbf{Q} \quad (1.42b)$$

$$\Delta E^{(2)} = \left[\frac{1}{2} \langle \Psi_0 | (\partial^2\mathbf{V}/\partial\mathbf{Q}^2) | \Psi_0 \rangle + \sum_i \frac{\langle \Psi_0 | (\partial\mathbf{V}/\partial\mathbf{Q}) | \Psi_i \rangle}{E_0 - E_i} \right] \delta\mathbf{Q}^2 \quad (1.42c)$$

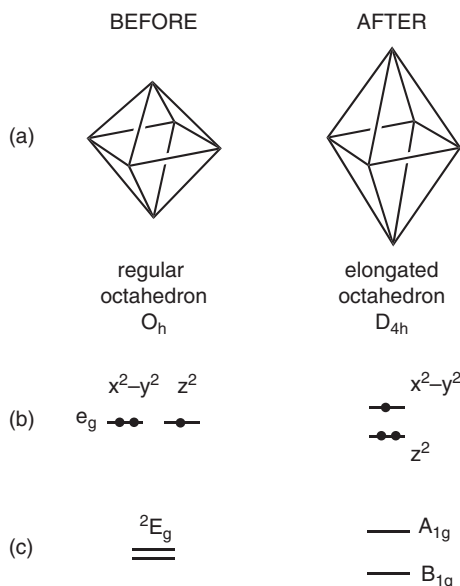
In these expressions, Ψ_0 is the ground-state wavefunction, while Ψ_i are excited states wavefunctions and the derivatives are taken for $\mathbf{Q} = \mathbf{Q}_0$.

First-order Jahn–Teller effect

Let us consider the first term $\Delta E^{(1)}$. If the integral $\langle \Psi_0 | (\partial \mathbf{V} / \partial Q) \Psi_0 \rangle$ is different from 0, a deformation δQ (either positive or negative) will necessarily stabilize the molecule. The problem can be analysed by group-theory arguments bearing on the symmetries of Ψ_0 and of the deformation. In 1937 it was demonstrated by H. A. Jahn and E. Teller that for non-linear molecules, if the electronic wavefunction Ψ_0 is degenerate, there exists at least one Q coordinate for which the previous integral is different from zero. Then the distortion (Jahn–Teller distortion) occurs necessarily. Once the distortion has occurred, the degeneracy is lifted.

Electronic degeneracy occurs in a system when degenerate orbitals are occupied by a different number of electrons. Many cases are found in transition-metal chemistry, the most typical being copper(II) with a d^9 electronic configuration. In a pure O_h symmetry, the configuration is $(t_{2g})^6(e_g)^3$, giving an unequal occupation of the two orbitals of the e_g set, as shown in Fig. 1.24

Thus the system *must* distort. Starting from the perfect O_h symmetry, if one performs an elongation of the two bonds along z , the z^2 orbital is stabilized with respect to $x^2 - y^2$ (and also xz and yz with respect to xy , but this is not important here). Thus the degeneracy is lifted, and orbital filling shows that the system has been stabilized, because there are two electrons in the stabilized orbital *versus* only one in the destabilized one. The converse is true for a compression, so in principle either a compression or an elongation of two opposite bonds could occur. However, experience shows that for the vast majority of Cu(II) complexes the Jahn–Teller effect is manifested as an *elongation* of the octahedron along one of its fourfold axes. Note that in the present case one can limit investigations to orbital analysis, but strictly speaking one should

**Fig. 1.24**

First-order Jahn–Teller effect in the example of Cu(II), with the situations before and after distortion: a) geometry of the octahedron; b) last orbitals with e_g symmetry and their filling; c) electronic states. The degenerate $(e_g)^3$ configuration gives rise to a degenerate 2E_g state subject to Jahn–Teller distortion—here an elongation along one of the octahedron axes, yielding D_{4h} symmetry. As a consequence, the degeneracy between z^2 and $x^2 - y^2$ is lifted, and their occupation is shown at right.

consider *electronic states*; that is, the total (polyelectronic) wavefunctions. (The relation between orbitals and states is developed in Section 2.4.1).

Second-order Jahn–Teller effect

When the electronic wavefunction is not degenerate the first-order term is zero, and thus the first derivative $\partial E/\partial Q$. But according to the sign of the second-order term $\Delta E^{(2)}$, the geometry can correspond to a minimum or a maximum, in this last case leading to a distortion. The different possibilities, including the first-order effect, are displayed in Fig. 1.25.

Unfortunately, the prediction is not as simple as previously, because there are several terms in $\Delta E^{(2)}$, and each case must be studied in particular. The complete analysis of the problem shows that $\Delta E^{(2)}$ can be negative if there is an excited state (energy E_i) of the proper symmetry not too high in energy, because its effect depends on $1/(E_0 - E_i)$. This is the second-order Jahn–Teller effect (often termed the pseudo-Jahn–Teller effect) [1.13] shown in Fig. 1.25c. If the excited state is too high, one has simply $\Delta E^{(2)} > 0$, and the high-symmetry structure is stable (Fig. 1.25a). Finally, we note in Fig. 1.25b,c the fundamental difference between Jahn–Teller effects: for first-order there is a curve-crossing, while for second-order effect there is an avoided crossing showing the influence of the upper (excited) level.

Cyclobutadiene C_4H_4 , evoked previously (see Section 1.3.5), is a special case of the second-order Jahn–Teller effect. The molecular orbitals and energies of regular square cyclobutadiene are shown in Figs. 1.14 ($N = 4$) and 1.15d. The three orbitals *a* and *e* have to accommodate four electrons, two of them being in the *e* set, which is incompletely filled. The complete derivation, based on the properties of electronic states, will not be presented here, though the reader can consult [1.13], and we shall discuss only the results. Four states, designated by their symmetry, are obtained: $^1A_{1g}$, $^1B_{1g}$, $^1B_{2g}$, and $^3A_{2g}$ (these capital-letter symbols designate electronic states by their symmetry, with the

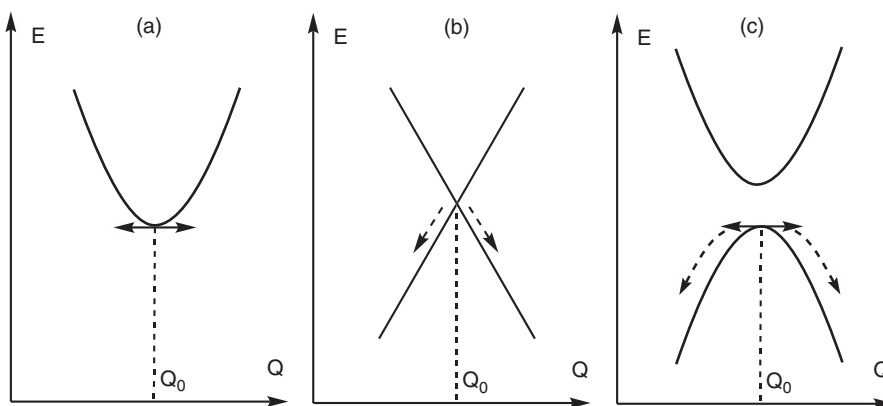
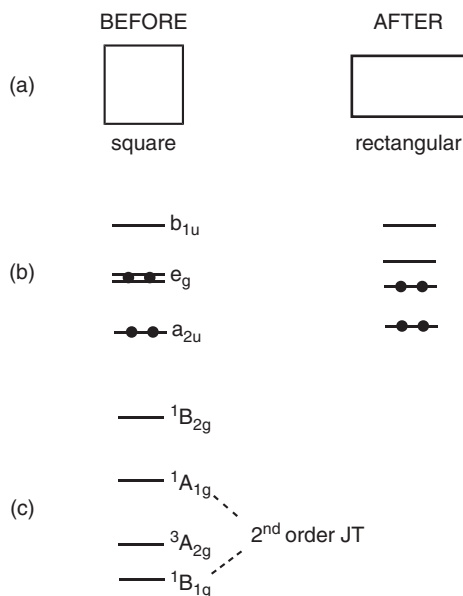


Fig. 1.25

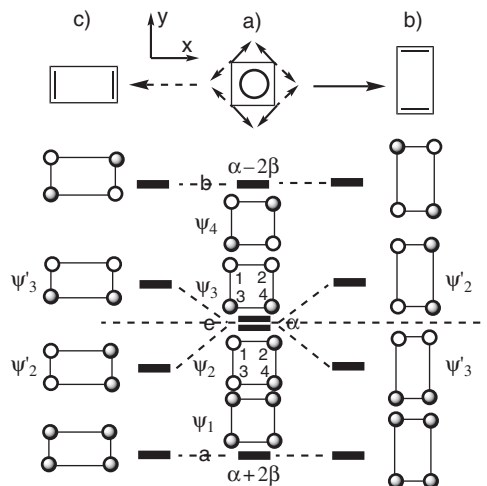
Energy as a function of a deformation coordinate Q around a high-symmetry geometry (Q_0): a) $\partial E/\partial Q = 0$, $\partial^2 E/\partial Q^2 > 0$, stable structure; b) $\partial E/\partial Q \neq 0$ with double value due to degenerescence, first-order Jahn–Teller effect; c) $\partial E/\partial Q = 0$, $\partial^2 E/\partial Q^2 < 0$ due to coupling with an excited state, second-order Jahn–Teller effect.

**Fig. 1.26**

The special second-order Jahn–Teller effect occurring in C_4H_4 , with the situations before and after distortion: a) geometry; b) π orbitals and their filling; c) electronic states. Note that exceptionally, the triplet state is not the ground state. See the text for discussion.

spin multiplicity $2S+1$ as upper index. Curiously, in the present case, the triplet state is *not* the ground state (this is one of the rare exceptions to Hund's rule). Of the singlet states, $^1B_{1g}$ is the lowest, and the system is *not electronically degenerate*. But the interaction with the nearby $^1A_{1g}$ state triggers a deformation, and it is found experimentally that C_4H_4 is rectangular (Fig. 1.26), with the short bonds presenting essentially double-bond character and the long ones essentially single-bond character.

A simplified (but alas not rigorous!) justification using orbitals can be presented as follows. Figure 1.27 gives some details about the possible distortions of the regular cyclobutadiene. In a) are shown the MOs and energies

**Fig. 1.27**

Jahn–Teller distortion in cyclobutadiene $(CH)_4$. For the initial symmetrical geometry (a), and the two possible distorted ones, (b) and (c), from top to bottom: geometry, molecular orbitals of the π framework.

of the non-distorted square molecule. At the top, the two most efficient normal modes of vibration are shown by black arrows and dotted arrows respectively. In b) are shown the MOs and energies of the distorted molecule after the black-arrows distortion: the square becomes a rectangle with longer y and shorter x dimensions. In c) is displayed the situation after the dotted-arrows distortion: the rectangle has now longer x and shorter y dimensions. The orbitals with a and b symmetry play no significant role in the process. Instead, the degenerate e orbitals, termed ψ_2 and ψ_3 in the figure, are determining. ψ_3 is stabilized to $\psi_{3'}$ in b), since the 1–2 and 3–4 bonding interactions become more bonding, whereas the 1–3 and 2–4 antibonding interactions become less antibonding. On the contrary, $\psi_{2'}$ is destabilized in b). Using the other mode of distortion in c), the opposite situation occurs: $\psi_{2'}$ is stabilized, whereas $\psi_{3'}$ is destabilized. Since one orbital is occupied and the other not, there is a net gain in energy, which is why the distortion occurs only for these non-equilibrated electron occupations.

As noted in Section 1.3.5, cyclobutadiene, and more generally the molecules with an electronic configuration $4n$ (n integer), present such distortions and are said to be ‘antiaromatic’ with alternating short and long bonds. We shall encounter a very similar phenomenon in solids with partly filled bands (Section 1.4.3), the most representative example being polyacetylene (Section 3.3.3).

1.4 Electrons in molecular solids

The next and last step in our exploration of the ‘one-electron’ world is the study of molecular objects placed in the solid state. As in preceding section we proceed step by step, starting by extending molecules to infinite, up to one-dimensional objects.

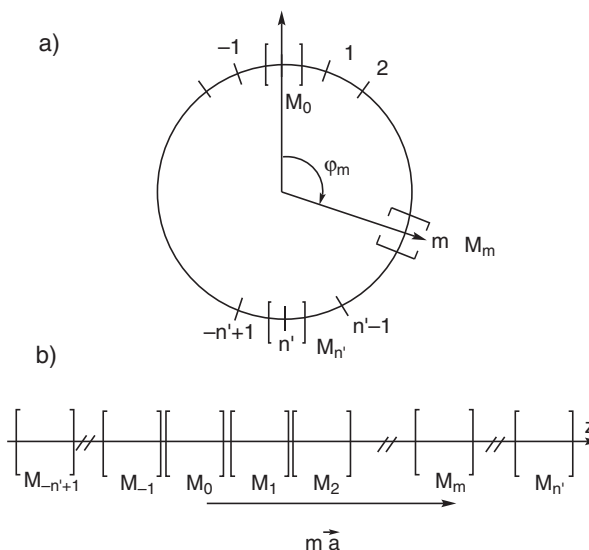
1.4.1 From molecular rings to infinite linear chains

We come back to the planar cyclic polyenes of Section 1.3.5. Figure 1.28a shows the system under consideration: a cyclic polyene, with repeating units M_m and numbered $0, \pm 1, \pm 2, \pm 3, \pm(n'-1)$, n' (n' being $N/2$ if N is even, or $N/2 - 1$ if N is odd). Each unit comprises a π atomic orbital ϕ_m having a Coulomb energy α and interacting only with the two first nearest neighbours $\phi_{m\pm 1}$ (resonance integral β). In a solid, the repeating units M_m are termed unit cells or cells, since by a set of translations they are able to build completely the solid (as will be seen).

The C_N rotation axis is perpendicular to the molecular plane. The symmetry operations are rotations. We name φ (or C_n^1) the elementary rotation angle transforming cell M_m in M_{m+1} , thus φ_m (C_n^m) rotation ($\varphi_m = m \varphi$) transforms cell M_0 in cell M_m , and so on. The point group symmetry is C_N , with N tending to infinite. Table 1.8 gives the C_N character table (for even N).

The basis of the representation is built from the N orbitals:

$$\Gamma_\phi = \{(\phi)_{n'-1}, \dots, (\phi)_0, \dots, (\phi)_{1-n'}(\phi)_{n'}\} \quad (1.43)$$

**Fig. 1.28**

Infinite planar polyene: a) cyclic, cyclic group C_N ; b) linear, obtained from the cyclic one when N tends to infinite (translation group).

Table 1.8 Point group symmetry C_n and irreducible representations.

C_n	E	C_2	C_n	C_n^{-1}	$C_n^m \dots$	C_n^{-m}	$C_n^{n'-1}$	$C_n^{-n'+1} \dots$
Γ_j	1	$(-1)^j$	$\exp(-\gamma)$	$\exp(\gamma)$	$\exp(-m\gamma)$	$\exp(m\gamma)$	$\exp[(1-n')\gamma]$	$\exp[(n'-1)\gamma]$
Γ_ϕ	N	0	0	0	0...	0	0	0...

where $\exp(\gamma) = \exp(2i\pi/n)$.

The characters of this (reducible) representation are shown in Table 1.8: N for the identity operation E , since the N orbitals remain unchanged; 0 for all other operations, since no orbital is transformed in itself by any of the rotations. The irreducible representations (IR) are Γ_j , where j is an integer running from 0, ± 1 , ± 2 , ± 3 , $\pm(n'-1)$ to n' . The character of the rotation C_n^m in the Γ_j IR is $\exp\left(\frac{2i\pi mj}{N}\right)$. It is then possible to get the N corresponding Γ_j IRs from the Γ_ϕ and the corresponding symmetry orbitals (in the solid, we shall name them Bloch orbitals, Θ , after Felix Bloch, a Swiss-American physicist, recipient of the Nobel Prize in 1952) from ϕ_m , using the usual projection procedures of group theory [1.7–1.8]:

$$\Gamma_\phi = \sum_{j=-n'+1}^{n'} \Gamma_j \quad (1.44)$$

$$\Theta_j = \frac{1}{\sqrt{N}} \sum_{m=-n'+1}^{n'} c_m \phi_m = \frac{1}{\sqrt{N}} \sum_{m=-n'+1}^{n'} \left[\exp\left(\frac{2i\pi mj}{N}\right) \right] \phi_m \quad (1.45a)$$

where $1/\sqrt{N}$ is a normalization factor, computed in the frame of the Hückel method (neglecting S). The symmetry (Bloch) orbitals are linear combinations of the atomic orbitals, with coefficients $\exp\left(\frac{2i\pi mj}{N}\right)$ depending on the

position m . The Θ_j functions take particularly simple expressions for $j = 0$ and $n' = N/2$ (remembering that $\exp(i\pi m) = (-1)^m$),

$$\Theta'_{j=0} = \frac{1}{\sqrt{N}} \sum_{m=-n'+1}^{n'} \phi_m = \frac{1}{\sqrt{N}} (\phi_{-n+1} + \cdots + \phi_{-1} + \phi_0 + \phi_1 + \cdots + \phi_{n'}) \quad (1.45b)$$

a fully bonding Bloch orbital, with no node, and conversely:

$$\begin{aligned} \Theta'_{j=N/2} &= \frac{1}{\sqrt{N}} \sum_{m=-n'+1}^{n'} (-1)^m \phi_m \\ &= \frac{1}{\sqrt{N}} (\phi_{-n+1} + \cdots - \phi_{-1} + \phi_0 - \phi_1 + \cdots - \phi_{n'}) \end{aligned} \quad (1.45c)$$

a fully antibonding Bloch orbital with $N - 1$ nodes. The orbitals are shown in Fig. 1.29.

The energies of Bloch orbitals are computed from

$$E_j = \frac{\langle \Theta_j | \mathbf{h} | \Theta_j \rangle}{\langle \Theta_j | \Theta_j \rangle} = \langle \Theta_j | \mathbf{h} | \Theta_j \rangle \quad (1.46a)$$

$$\begin{aligned} E_j &= \langle \Theta_j | \mathbf{h} | \Theta_j \rangle \\ &= \frac{1}{N} \left\langle \sum_{m=-n'+1}^{n'} \left[\exp\left(\frac{2i\pi m j}{N}\right) \right] \phi_m \right| \mathbf{h} \left| \sum_{m=-n'+1}^{n'} \left[\exp\left(\frac{2i\pi m j}{N}\right) \right] \phi_m \right\rangle \end{aligned} \quad (1.46b)$$

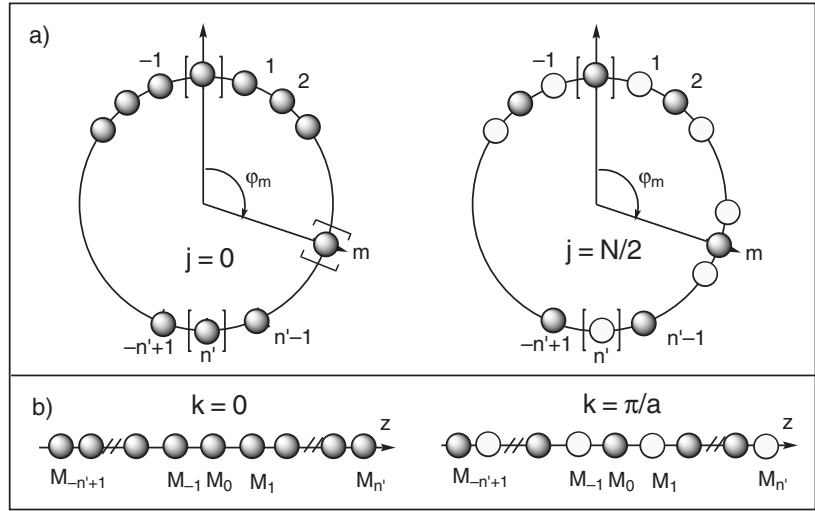
where \mathbf{h} is an effective one-electron Hamiltonian. Eqn. (1.46b) becomes simply, in the frame of the Hückel model:

$$E_j = \alpha + 2\beta \cos \frac{2\pi}{N} j \quad (1.46c)$$

since, for given j orbitals, there are N terms: $\langle \exp(\frac{2i\pi m j}{N}) \phi_m | \mathbf{h} | \exp(\frac{2i\pi m j}{N}) \phi_m \rangle = \alpha$ and $2N$ terms $\langle \exp(\frac{2i\pi m j}{N}) \phi_m | \mathbf{h} | \exp(\frac{2i\pi(m\pm 1)j}{N}) \phi_{m\pm 1} \rangle = \beta \cos(\frac{2\pi}{N} j)$. All the other terms imply pairs of orbitals ϕ_m and $\phi_{m\pm p}$ with $p > 1$, which are not interacting in our (simple Hückel) model ($\beta = 0$; $E = 0$). Eqn. (1.46c) is indeed a very simple expression of the energy: when N tends to infinite, the energy varies as a continuous cosine function from the energy value $\alpha + 2\beta$ ($j = -n' + 1$) to $\alpha - 2\beta$ ($j = n'$) through α ($j = 0$). The present case is an extrapolation to infinite of the finite cyclic polyenes of Section 1.3.5 and a convenient further step to the solid.

Towards linear chains

It is important to realize that when N tends to infinite, the ring's radius tends to infinite. The ring thus becomes a linear chain along some z axis (Fig. 1.29b). The elementary rotation φ is transformed in an elementary translation \vec{a} along z and $\varphi_m (= m \varphi)$ in a translation $\vec{r}_m = m \vec{a}$. Consequently there is an exact correspondence between the rotations in the molecular cyclic point group and the translations in the translation group. One should be careful about the conditions at the limits, since there is no discontinuity for the ring between the $-n' + 1$ and n' cells, while there is one in the chain, since $-n' + 1$ and n' cells

**Fig. 1.29**

Bloch orbitals for infinite polyenes; a) cyclic, at $j = 0$ and $j = \frac{N}{2}$; b) linear at $k = 0$ and $k = \frac{\pi}{a}$.

are found at the opposite ends of the chain. The so-called Born and Karman conditions, for infinite systems, allow cells $n' + 1$ and n' to interact and solve the problem. (Max Born was a German physicist, recipient of the Nobel Prize in Physics in 1954.)

We are now in a position to introduce new concepts with a closer look at the definition of the Bloch orbitals (eqns. 1.45). In the expression $\frac{2i\pi m j}{N}$, m can be replaced by $\vec{r}_m/\vec{a} = r_m/a$, since \vec{r}_m and \vec{a} are collinear. Then $\frac{2i\pi m j}{N} = \frac{2i\pi j}{Na} r_m$. Furthermore, we can remark that $k = \frac{2\pi}{Na} j$ is homogeneous to a reciprocal length (a^{-1}) and can be considered as the projection k of a vector \vec{k} on z (\vec{a}), so that $\frac{2i\pi m j}{N} = \frac{2i\pi j}{Na} r_m = i\vec{k}\vec{r}_m$. The quantity k , proportional to j , varies as $0, \pm \frac{2\pi}{Na}, \pm \frac{4\pi}{Na}, \dots, \pm \frac{2(n'-1)\pi}{Na}, \frac{\pi}{a}$. The expression of the Bloch orbital appears then as the one of a plane wave with wavevector \vec{k} :

$$\begin{aligned} \Theta_j &= \Theta_j(\vec{k}) = \frac{1}{\sqrt{N}} \sum_{m=-n'+1}^{n'} \left[\exp\left(\frac{2i\pi j}{Na} r_m\right) \right] \phi_m \\ &= \frac{1}{\sqrt{N}} \sum_{m=-n'+1}^{n'} \left[\exp\left(i\vec{k}\vec{r}_m\right) \right] \phi_m \end{aligned} \quad (1.47)$$

\vec{r}_m and \vec{a} are vectors in the real space. \vec{k} is a vector in the 'reciprocal space'. This point can be made even clearer if we introduce the vector \vec{a}^* defined by

$$\vec{a}^* \vec{a} = 2\pi \quad \text{or} \quad \vec{a}^* = \frac{2\pi}{a} \vec{a} \quad (1.48)$$

so that $\vec{k} = k_a \vec{a}^*$ (k_a is the projection of \vec{k} on \vec{a}^* with $k_a = \frac{a}{2\pi} k$ and varies as $0, \pm \frac{1}{N}, \pm \frac{2}{N}, \dots, \pm \frac{n'-1}{N}, \frac{1}{2}$). The \vec{a} vector defines the direct space and characterizes its periodicity. The \vec{a}^* vector defines the reciprocal space, the one of \vec{k} wavevectors and the periodicity of \vec{k} .

Coming back to the expression of Bloch orbitals (eqn. 1.47), using either variables j or \vec{k} , one observes that it describes a linear combination of atomic

orbitals ϕ_m (as for common molecules), weighted by a phase factor. For periodicity, check that when \vec{r}_m is replaced by $\vec{r}_m + \vec{a}$ or \vec{k} by $\vec{k} + \vec{a}^*$ the functions $\Theta_j(\vec{k})$ are unchanged.

The energies of the Bloch orbitals $\Theta_j(\vec{k})$ simply follow from eqn. (1.46a):

$$E_j(\vec{k}) = \frac{\langle \Theta_j | \mathbf{h} | \Theta_j \rangle}{\langle \Theta_j | \Theta_j \rangle} = \langle \Theta_j | \mathbf{h} | \Theta_j \rangle = \alpha + 2\beta \cos \frac{2\pi}{N} j = \alpha + 2\beta \cos(ka) \quad (1.49)$$

The last expression is particularly convenient to use, as will be shown later.

The $\Theta_j(k)$ wavefunctions at $k = 0$ (that is, $j = 0$) and $k = \frac{\pi}{a}$ (that is, $j = \frac{N}{2}$) are similar, *mutatis mutandis*, to those of (1.45b,c) and are shown in Fig. 1.29b.

Bands

The results already reached deserve some comments and allow the introduction of some new important concepts. The Bloch orbital $\Theta(k = 0)$ is fully bonding (no node). Its energy is $\alpha + 2\beta$, which is the lowest energy (in this case, β is *negative*). On the contrary, the Bloch orbital $\Theta(k = \frac{\pi}{a})$ is the most antibonding ($N - 1$ nodes). Its energy is $\alpha - 2\beta$, which is the highest energy. All the other Bloch orbitals lie between with intermediate energies, within the finite energy interval $W = 4|\beta|$, termed the bandwidth (shown already in Fig. 1.13). If the number N of orbitals is finite, k varies by regular discrete steps. Instead, if the number N of orbitals tends to infinite, k varies continuously and there is a vanishing energy difference ($\Delta\varepsilon = \frac{4\beta}{N}$) between two successive levels. Such a continuum of levels is called an energy band. The corresponding Bloch orbitals are orthogonal. \vec{k} is a wavevector, but defines also the symmetry of the corresponding Bloch orbital $\Theta_j(\vec{k})$ in the translation group. Hence, two different orbitals having different symmetries \vec{k} and \vec{k}' are orthogonal, and

$$\langle \Theta_j(\vec{k}) | \mathbf{h} | \Theta_{j'}(\vec{k}') \rangle = 0 \quad (1.50)$$

We suggest that the reader take time to grasp the real nature and important role of \vec{k} , in this book and in [1.9] and [1.14].

1.4.2 Brillouin zone, energy dispersion curve, Fermi level, and density of states

1.4.2.1 Brillouin zone, energy dispersion curve

The N $\Theta_j(\vec{k})$ or more simply $\Theta(\vec{k})$ Bloch orbitals are defined in a k space $[-\frac{\pi}{a}, \frac{\pi}{a}]$, which excludes $k = -\frac{\pi}{a}$, given our conditions at the limits. This space is termed *the (first) Brillouin zone* (after the French-American physicist Léon Brillouin). The point $k = 0$ is termed the zone centre and is represented by the greek symbol Γ . The point $k = \frac{\pi}{a}$ is the zone edge, represented by Z (when the axis of the system is Oz). The sinusoidal variation of the energy of the Bloch orbitals in the Brillouin zone is shown in Fig. 1.30. It is also known as the 'energy dispersion curve' or 'band diagram'. Above $k = \frac{\pi}{a}$ and below $-\frac{\pi}{a}$, the $\Theta(\vec{k})$ values are the same as inside the first Brillouin zone. Furthermore, the functions $\Theta(\vec{k})$ and $\Theta(-\vec{k})$ are degenerate (the points k and $-k$ are physically equivalent), and it is then possible to reduce the representation to the

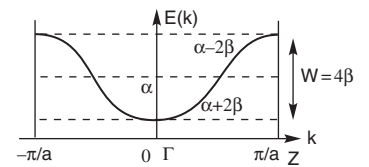
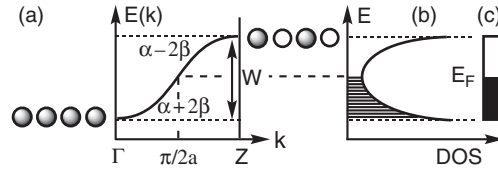


Fig. 1.30

Energy dispersion curve within the (first) Brillouin zone.

Fig. 1.31

a) Energy dispersion curve and Bloch orbitals at points Γ and Z ; b) density of states; c) schematic representation of an energy band and Fermi level E_F .



k interval $[0, \frac{\pi}{a}]$ of the first Brillouin zone, without loss of information, as shown in Fig. 1.31a.

1.4.2.2 Fermi level, density of states

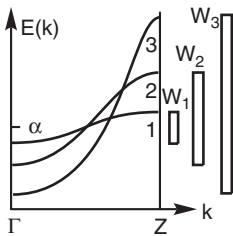
It is now appropriate to ‘fill’ Bloch orbitals with electrons as we did for the MOs. We apply once more the Aufbau principle. Each Bloch orbital accommodates two electrons at the maximum, so that the lowest $\frac{N}{2}$ levels are doubly filled and the above levels are vacant. The last occupied level is termed by chemists *the Fermi level* and its energy the Fermi energy, E_F , (after the Italian–American physicist Enrico Fermi, recipient of the Nobel Prize in Physics in 1938). The occupancy of the Bloch orbitals has fundamental consequences on the magnetic and electrical properties. Of particular interest for conductivity is the partial filling of a band which gives rise to a 1D conductor (Section 3.3), and for magnetism the filling of the N levels with one unpaired electron per level, which gives a 1D magnetic chain (Section 2.7.1).

Another important concept is *the density of states*, abbreviated as DOS, simply defined as the number of energy levels (or Bloch orbitals) ∂n per energy ∂E ; that is, $(\frac{\partial n}{\partial E})_E$. The DOS can be approximated as $\text{DOS} \propto 1/(\partial E/\partial k)_E$, the reciprocal of the slope of the dispersion energy curve (Fig. 1.31a): at $k = 0$ and $\frac{\pi}{a}$, the slope is close to zero (see Fig. 1.31b) and there are many energy levels for a given ∂E , whereas at $k = \frac{\pi}{2a}$ the slope is steep and the number of energy levels corresponding to the same energy variation ∂E is smaller; there is a minimum of the DOS at $k = \frac{\pi}{2a}$ (half of the band), as shown in Fig. 1.31b. A very simple representation of an energy band, as a mere rectangle, is given in Fig. 1.31c, with the filled levels in black and the Fermi level E_F at half-band.

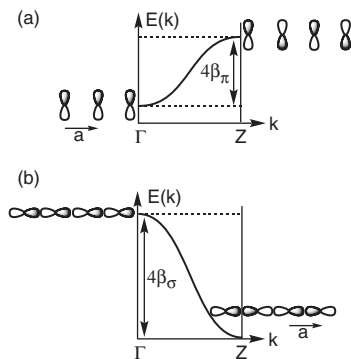
From the previous conclusions it is possible to realize that when the overlap S and the resonance energy β between two neighbouring orbitals vary, so does the bandwidth W . Figure 1.32 displays an example where the distance between nearest neighbours decreases from chain 1 to chain 3. Consequently, the bandwidth increases. It is also possible to observe on the scheme that when the overlap S is not neglected, the antibonding levels are more destabilized than the bonding ones are stabilized (as in dihydrogen, Fig. 1.3b).

We arrive at similar conclusions in Fig. 1.33 when the same neighbours (bearing p orbitals) are at the same distance (\bar{a}) but when the nature of the overlap varies (from π_{p-p} overlap in a) to σ_{p-p} overlap in b). The width is much larger for the σ overlap ($W_\sigma = |4\beta_\sigma| > W_\pi = |4\beta_\pi|$), as we expect from Fig. 1.9.

Nevertheless, the more important conclusion drawn from Fig. 1.33 is another one. In b), the chain is made of p_z orbitals (lying along the Oz axis). On the one hand, at $k = 0$, the Bloch orbital $\Theta_{k=0}(\phi_{-n+1} + \dots + \phi_{-1} + \phi_0 + \phi_1 + \dots + \phi_n)$ shows an antibonding interaction between nearest neighbours,

**Fig. 1.32**

Variation of overlap and bandwidth W with the distance between nearest neighbours. For the same orbitals, the bandwidth increases ($W_3 > W_2 > W_1$) when the distance decreases ($d_3 < d_2 < d_1$).

**Fig. 1.33**

Bandwidth W and nature of the overlap. Bands going ‘up’ (a) or ‘down’ (b).

contrary to what happens in a) between p_y orbitals (perpendicular to Oz). On the other hand, at $k = \frac{\pi}{a}$, the Bloch orbital $\Theta_{k=\pi/a}(\phi_{-n+1} - \dots - \phi_{-1} + \phi_0 - \phi_1 + \dots - \phi_n)$ is fully bonding. Due to the symmetry properties of the basis orbitals, the most antibonding orbital occurs now at $k = 0$, whereas the most bonding appears at $k = \frac{\pi}{a}$. The band is 'going down' instead of 'going up' as in Figs. 1.31 and 1.33a. This behaviour is found frequently, depending on the symmetry of the basis orbitals. As for the case of p_z - p_z interactions in the O_2 molecule (Section 1.3.3.) this comes from the fact that β is positive (Fig. 1.7).

We suggest that the reader consult references [1.5], [1.9], and [1.14] for further comments and detailed demonstrations.

1.4.3 Peierls distortion

Before studying more complex systems we would like to end this brief introduction on energy bands by looking more closely at what happens when a band is partially filled. We deal with a half-filled band for the sake of simplicity. Figure 1.34 summarizes the situation: (a) the energy dispersion curve, (b) four selected Bloch orbitals: the most bonding, $k = 0$ (no node, symmetric (S) in the reflection through plane Π), the most antibonding, $k = \frac{\pi}{a}$ ($N-1$ nodes, anti-symmetric (A) in the reflection), and the two frontier orbitals, the one below the Fermi level ($-1 + N/2$ nodes, (A)), and the one just above ($N/2$ nodes, (S)); (c) the band filling.

Please note that we represent schemes of Bloch orbitals as if they were real functions. In many cases, as other orbitals they are complex functions. They can or must be written as $\Theta = \Theta_{\text{real}} + i \Theta_{\text{imaginary}}$ ($i^2 = -1$). Only for $k = 0$ and $k = \pi/a$ are the functions real mathematical objects.

The frontier orbitals are practically degenerate: the orbital degeneracy is similar to the one introduced in Section 1.3.5. Then, as previously, the system is unstable. As in Sections 1.3.5 and 1.3.7 we have to find the distortion; that is, the appropriate lowering in symmetry (through some normal mode of vibrations) able to remove the electronic degeneracy. A simple one is a dimerization of the chain along the z -axis, as displayed in Fig. 1.35.

In (a) the situation is before distortion: a uniform distribution of the centres 1–8, with a translation vector \vec{a} from one cell to another. The Bloch orbitals are termed Θ_0 for $k = 0$, $\Theta_{\pi/a}$ for $k = \frac{\pi}{a}$ and Θ_2 and Θ_3 for the frontier orbitals, and the arrows at the top of the numbering show the directions of the displacements of the atoms in the dimerization which follows. In (b) is shown the situation after dimerization; atoms 1–2, 3–4, 5–6, and 7–8 are closer (enhanced overlap and interaction), whereas atoms 2–3, 4–5, and 6–7

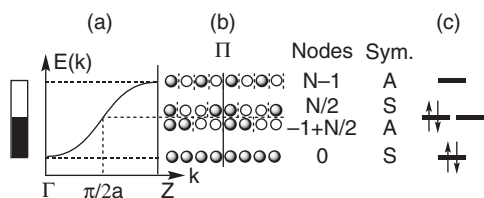
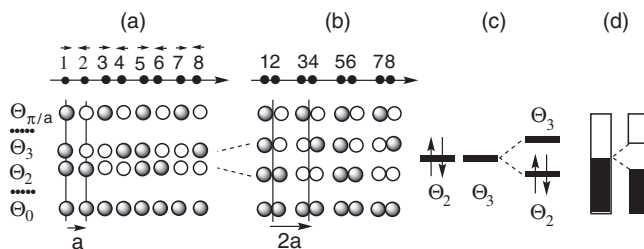


Fig. 1.34

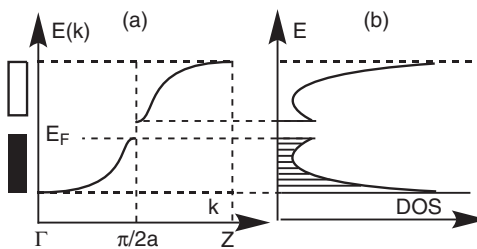
a) Energy dispersion curve; b) Bloch orbitals at points Γ and Z and around $k = \frac{\pi}{2a}$, their number of nodes and symmetry; c) occupancy of the orbitals.

Fig. 1.35

a) Bloch orbitals of the uniform 1D system; b) Bloch orbitals after dimerization; c) removal of the orbital degeneracy; d) opening of a gap at the Fermi level (schematic).

**Fig. 1.36**

After dimerization a gap opens at the Fermi level at $k = \frac{\pi}{2a}$: a) energy dispersion; b) density of states.



are farther (decreased overlap and interactions). The translation vector along the chain is now $2\vec{a}$.

It is easy to show that the ‘dimerization’ has no consequences for the energies of Θ_0 and $\Theta_{\pi/a}$. But for Θ_2 and Θ_3 important modifications occur. In Θ_2 the bonding interactions become stronger between 1–2, 3–4 etc, while the antibonding interactions become weaker between 2–3, 4–5, and so on, both factors stabilizing the Θ_2 orbital. The reverse holds for Θ_3 , which is destabilized. The overall result is the opening of a gap between the energies of Θ_2 and Θ_3 , at the Fermi level. As in the case of C_4H_4 (Sections 1.3.5 and 1.3.7), the system gains some energy because one of the orbitals is occupied, and the other not.

Anyway, this distortion gives rise to a forbidden energy band or gap for the electrons of the system, as shown in (c) and (d) with different graphical representations. Figure 1.36 depicts the new energy dispersion curve after distortion, using the same tools as before.

We shall see in Chapter 3 that such gap opening changes a 1D system from conducting to semiconducting. In molecules the phenomenon has been termed a Jahn–Teller distortion, while in the 1D solid it is usually termed a *Peierls distortion or transition* (after the German–British physicist Rudolf Peierls). It is described by physicists as the ‘opening of a gap at the Fermi level through electron–phonon coupling’, which is another way to talk about the influence of nuclear motions (phonons) on the electronic structure. The present orbital demonstration, due to Hoffmann [1.14], is more familiar to chemists.

1.4.4 Crystal orbitals: more than one orbital per cell

In our long way to the solid, the next step in complexity is the introduction in the 1D system of several orbitals per cell: in a metallic oxide it can be a d orbital of the metal and a p orbital of the oxide, and in a polyene it can be π orbitals of two non-equivalent carbon atoms. Generally, a cell will imply

several non-equivalent orbitals ℓ , ranging from 1 to N_0 . Each of the ℓ non-equivalent orbitals of the cell can be used to build N Bloch orbitals $(\Theta_\ell)_j$ or $\Theta_\ell(\vec{k})$, as shown in eqn. (1.47), leading to Bloch orbitals such as:

$$(\Theta_\ell)_j = \Theta_\ell(\vec{k}) = \frac{1}{\sqrt{N}} \sum_{m=-n'+1}^{n'} \left[\exp\left(\frac{2i\pi j}{Na} r_m\right) \right] (\phi_\ell)_m \quad (1.51)$$

In eqn. (1.51) the notation of the orbitals used in eqn. (1.47) are changed slightly to take into account the ℓ orbitals of a cell: atomic orbitals change from ϕ_m to $(\phi_\ell)_m$ and Bloch orbitals from Θ_j to $(\Theta_\ell)_j$ or $\Theta_\ell(\vec{k})$. It is now possible to build the crystal orbitals (COs) from linear combinations of the Bloch orbitals $\Theta_\ell(\vec{k})$. They are termed $X(\vec{k})$ throughout the book:

$$X(\vec{k}) = \sum_{\ell=1}^{N_0} c_\ell \Theta_\ell(\vec{k}) \quad (1.52)$$

The coefficients and the energies are computed by writing that $X(\vec{k})$ obeys the Schrödinger equation:

$$\mathbf{h}X(\vec{k}) = E(\vec{k})X(\vec{k}) \quad (1.53a)$$

or

$$\sum_{\ell=1}^{N_0} c_\ell(\vec{k}) [\mathbf{h}\{\Theta_\ell(\vec{k})\} - E(\vec{k})\Theta_\ell(\vec{k})] \quad (1.53b)$$

We obtain the coefficients $c_\ell(\vec{k})$ ($\ell = 1, \dots, N_0$) from the N_0 equations:

$$\sum_{\ell=1}^{N_0} c_\ell(\vec{k}) [\mathbf{H}_{\ell\ell'}(\vec{k}) - E(\vec{k})\mathbf{S}_{\ell\ell'}(\vec{k})] = 0 \quad (\ell' = 0, \dots, N_0) \quad (1.54a)$$

with

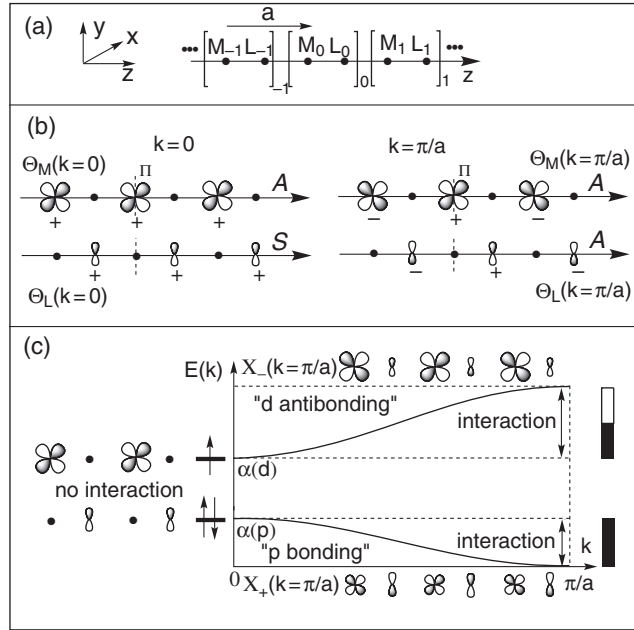
$$\mathbf{H}_{\ell\ell'}(\vec{k}) = \langle \Theta_\ell(\vec{k}) | \mathbf{h} | \Theta_{\ell'}(\vec{k}) \rangle \quad \mathbf{S}_{\ell\ell'}(\vec{k}) = \langle \Theta_\ell(\vec{k}) | \Theta_{\ell'}(\vec{k}) \rangle \quad (1.54b)$$

$$\left| \mathbf{H}(\vec{k}) - E(\vec{k})\mathbf{S}(\vec{k}) \right| = 0 \quad (1.54c)$$

where \mathbf{H} and \mathbf{S} are matrices of the Hamiltonians and overlaps related to the Bloch orbitals $\Theta_\ell(\vec{k})$ ($\ell = 1, \dots, N_0$). It is then possible to derive the energies $E(\vec{k})$ and, after normalization, the coefficients $c_\ell(\vec{k})$ ($\ell = 1, \dots, N_0$) of the crystal orbitals $X(\vec{k})$.

In the following we give a brief example to show that the building of crystal orbitals is less complex than it can appear from the previous equations. Suppose that we deal with a linear chain along Oz, built alternatively from one transition element M and one ligand L $-(M-L)_N$, with a translation vector \vec{a} (Fig. 1.37a).

The transition element M has a d_{yz} orbital able to interact (π interaction) with a neighbouring p_y orbital of a ligand L. In the chain, all the metals M are equivalent, and so are the ligands L. The energies of the atomic orbitals are $\alpha(d)$ and $\alpha(p)$ with $\alpha(d) > \alpha(p)$. We build the Bloch orbitals $\Theta_M(\vec{k})$ and $\Theta_L(\vec{k})$ at $k = 0$ and $k = \frac{\pi}{a}$ as before (Fig. 1.37b), and from them we want to obtain

**Fig. 1.37**

A 1D system with two orbitals per cell: a) description; b) Bloch orbitals (BOs) built from the equivalent AOs (metal and ligand) and their symmetry; c) crystal orbitals (COs) at $k = 0$ and π/a , built from the BOs and energy bands.

two crystal orbitals $X(\vec{k})$ particularly at $k = 0$ and $\frac{\pi}{a}$, from eqn. (1.52). As a rough approximation:

$$X(\vec{k}) \propto \left[\Theta_M(\vec{k}) \pm \Theta_L(\vec{k}) \right] \quad (1.55)$$

We observe that the symmetry of the Bloch orbitals upon the reflection through a plane perpendicular to Oz in M_0 (Π in Fig. 1.37b) is the same at $k = \frac{\pi}{a}$ (A) but is different at $k = 0$ (A for $\Theta_M(k = 0)$ and S for $\Theta_L(k = 0)$). There is therefore no interaction at $k = 0$ and an interaction at $k = \frac{\pi}{a}$. The two crystal orbitals at $k = 0$ are simply the initial Bloch orbitals $\Theta_L(k = 0)$ at energy $\alpha(p)$ and $\Theta_M(k = 0)$ at energy $\alpha(d)$. A scheme of the two $X_{\pm}(k = \pi/a)$ is given in Fig. 1.37c: one is bonding, with a larger weight for p than for d orbitals (see Section 1.3.2), and the other is antibonding, with larger weight for d than for p orbitals. It is then possible to draw the energy dispersion curve and to show the existence of two bands. The energy of the first one, $X_+(k)$, changes from non-bonding ($\alpha(p)$) at $k = 0$ to bonding at $k = \frac{\pi}{a}$, with a strong participation of the p orbitals of the ligand. It is occupied by the $2N$ -electrons of the ligand orbitals, and is termed a 'p bonding band'. It ensures the stability of the system. The energy of the other band $X_-(k)$ varies from non-bonding at $k = 0$ ($\alpha(d)$) to antibonding at $k = \frac{\pi}{a}$, with a strong participation of the d orbitals of the metal. It is half-filled with N -electrons of the d orbitals of the metal, and ensures the physical properties of the system.

1.4.5 Towards 3D systems

We have introduced some basic concepts in the frame of the 'one-electron' view of a 1D system. In particular, we have tried to show the deep similarity

Table 1.9 Comparison between the approaches of molecular and solid electronic structures.

Electronic structure of a molecule	Electronic structure of a 1D solid
N_0 orbitals (atomic or fragments), AOs ϕ_m	N_0 atomic orbitals to describe a cell m (N cells) $(\phi_l)_m$
Combining equivalent AOs to build N_0 symmetry orbitals, SOs, θ	Combining the equivalent AOs to build SOs or Bloch orbitals (BOs), $\Theta(k)$
Combining SOs θ with same IR to build molecular orbitals, MOs ψ	Combining BOs $\Theta(k)$ at each point k to build the crystal orbitals COs, $X(k)$

existing in building the useful wavefunctions to describe molecules and solids using symmetry properties. The steps are summarized in Table 1.9 (see also [1.9]).

Now, to describe *real* solids we should deal with two-dimensional (2D) or three-dimensional (3D) systems. In the last case we should work in a 3D direct space, based on three crystallographic axes \vec{a} , \vec{b} , \vec{c} instead of one. We should work also in a reciprocal space defined by three vectors \vec{a}^* , \vec{b}^* , \vec{c}^* such as $\vec{a}^* \cdot \vec{a} = 2\pi$, $\vec{b}^* \cdot \vec{b} = 2\pi$, $\vec{c}^* \cdot \vec{c} = 2\pi$, and the \vec{k} wavevector should have three components in this space. The Brillouin zone would become a surface or a volume, and the Fermi level a Fermi surface. But the basic concepts, elaborated here with 1D examples, would remain. We shall introduce the necessary modifications when appropriate in the book.

Nevertheless, before facing physical properties in the following chapters we need to tune our ‘one-electron’ view of the solid, rather optimistically, with some more delicate considerations on electronic repulsion and some of its consequences.

1.5 Effects of interelectronic repulsion

We now tackle the most difficult problem: the explicit introduction of interelectronic repulsion. The electrostatic (Coulomb) repulsion between two electrons, whatever their spins, impedes them to be in the same place; the positions of electrons are correlated, which can also be described as the electrons being surrounded by a *Coulomb hole*. In this section the goal is double: (i) to go beyond a qualitative description of the electronic structure to reach *quantitative results*, in particular on the wavefunctions and on the energy, taking into account interelectronic repulsions; and (ii) to introduce the spin dimension in the study of polyelectronic systems, through the example of two electrons on two centres and comparing their singlet ($\uparrow\downarrow$) and triplet ($\uparrow\uparrow$) behaviour.

1.5.1 Position of the problem

1.5.1.1 Hamiltonians

It is a well-known fact in quantum chemistry that the existence of the interelectronic repulsion renders impossible the exact solution of the Schrödinger equation for a polyelectronic system. Indeed, the general Hamiltonian for

an N-electron system in the frame of the Born–Oppenheimer approximation (fixed nuclei) can be written as a sum of three parts:

$$\mathbf{H} = \mathbf{H}_0 + \mathbf{H}_1 + \mathbf{H}_2 \quad (1.56a)$$

$$\mathbf{H}_0 = \sum_{i=1}^N \mathbf{h}(i) = \sum_{i=1}^N \mathbf{K}(i) + \mathbf{U}(i) \quad (1.56b)$$

$$\mathbf{H}_1 = \sum_{i=1}^N \sum_{j>i}^N \frac{e^2}{r_{ij}} \quad (1.56c)$$

$$\mathbf{H}_2 = \sum_{i=1}^N \zeta(i) \mathbf{I}(i) \mathbf{s}(i) \quad (1.56d)$$

We are already familiar with the one-electron part \mathbf{H}_0 , the sum of the kinetic \mathbf{K} and potential \mathbf{U} energies of single electrons i . \mathbf{H}_1 is related to interelectronic repulsion between two electrons i, j . It is our main concern here. Finally, \mathbf{H}_2 is the Hamiltonian related to spin–orbit interaction (ζ). Until now we have considered that there is no interaction between the orbital momentum of the electron, defined by its operator $\mathbf{I}(i)$ (and the quantum number $l(i)$) and the spin momentum operator $\mathbf{s}(i)$ (and the quantum number $s(i)$). But this is not the case, particularly when the atomic number Z is increasing. For low- Z atoms the \mathbf{H}_1 term is dominant over \mathbf{H}_2 , and \mathbf{H}_2 can be treated as a perturbation. For high- Z atoms the contrary is true. In the following, we centre on the Hamiltonian formulated as

$$\mathbf{H} = \mathbf{H}_0 + \mathbf{H}_1 \quad (1.57)$$

Due to the interelectronic repulsion term \mathbf{H}_1 , the system is not separable into one-electron descriptions. For example, in a two-orbital (ϕ_a and ϕ_b) and two-electron (1, 2) system, where exist electronic configurations such as $\phi_a(1)\phi_b(2)$ (electron 1 in ϕ_a and 2 in ϕ_b) or $\phi_a(2)\phi_b(1)$ (electron 2 in ϕ_a and 1 in ϕ_b) or $\phi_a(1)\phi_a(2)$ (both electrons 2 in ϕ_a), the calculations with the two-electron operator \mathbf{H}_1 ($= e^2/r_{12}$ in this case), imply new two-electron integrals such as those defined in Table 1.10.

All of them are positive, since the electrostatic repulsion between the two electrons destabilizes the system. The j integral corresponds simply to the self-repulsion of the electronic configuration where electron 1 is in ϕ_a and electron 2 is in ϕ_b . In physics it is often termed V . The integral is the same using the

Table 1.10 Definition of three two-electron integrals.

Definition	Usual name and other abbreviations	
$j = \langle \phi_a(1)\phi_b(2) e^2/r_{12} \phi_a(1)\phi_b(2) \rangle$	two-centre self-repulsion integral	(1.58a)
$k = \langle \phi_a(1)\phi_b(2) e^2/r_{12} \phi_a(2)\phi_b(1) \rangle$	exchange integral	(1.58b)
$j_0 = \langle \phi_a(1)\phi_a(2) e^2/r_{12} \phi_a(1)\phi_a(2) \rangle$	one-centre self-repulsion integral	(1.58c)

$\phi_a(2) \phi_b(1)$ configuration. The exchange integral k is more subtle. It corresponds to the repulsion of $\phi_a(1) \phi_b(2)$ with the configuration $\phi_a(2) \phi_b(1)$, where electrons 1 and 2 have changed their orbitals (hence the name ‘exchange’ integral). The j_0 integral corresponds to an excited configuration where the two electrons are in the same orbital (ϕ_a). The j_0 integral simply measures the self-repulsion of the $\phi_a(1)\phi_a(2)$ electronic configuration. The integral is the same using the $\phi_b(1) \phi_b(2)$ configuration. In physics it is often termed U .

Technically speaking, it is a many-body problem. No exact analytical solution exists, since r_{12} depends on both ϕ_a and ϕ_b , which precludes a separation of variables. However, it is possible to approach the exact solutions as much as possible by means of approximations. The only difficulty is to find the most efficient method; that is, a method for which the computing effort does not grow too rapidly with the complexity of the molecule.

It is useful to introduce here the concept of overlap density. The exchange integral k in eqn. (1.58b) can be rewritten:

$$\begin{aligned} k &= \langle \phi_a(1)\phi_b(2) | e^2/r_{12} | \phi_a(2)\phi_b(1) \rangle \\ &= e^2 \int \frac{\phi_a(1)\phi_b(1)\phi_a(2)\phi_b(2)}{r_{12}} d\vec{r}_1 d\vec{r}_2 = e^2 \int \frac{\rho(1)\rho(2)}{r_{12}} d\vec{r}_1 d\vec{r}_2 \end{aligned} \quad (1.59)$$

which evidences the product:

$$\rho(i) = \phi_a(i) \phi_b(i) \quad (1.60)$$

which is termed the *overlap density*, defined at each point in space.

1.5.1.2 Polyelectronic wavefunctions, the Pauli principle, and Slater determinants

In this section we state the general principles of construction of polyelectronic wavefunctions. First we return to the Pauli exclusion principle and propose a general formulation that will lead us to a useful tool to express N -electron wavefunctions: the Slater determinant.

The total N -electron wavefunction $\Psi(1,2,3 \dots i,j, \dots N)$ is a mathematical object whose square gives the probability to find simultaneously electrons 1,2,3, and so on, in different volume elements. It depends on the coordinates of the N -electrons, the spatial ones $r(i)$ and the spin ones $\sigma(i)$, that we term $x(i)$ (i varying from 1 to N). The spin functions are denoted α or β , corresponding to $m_s = 1/2$ (or spin up \uparrow) and $m_s = -1/2$ (or spin down \downarrow) respectively. As stated in Section 1.2.3, the electrons are indistinguishable, so that the interchange of two electrons i and j must not change the state of the system; that is, the square of the wavefunction must not change. Actually, since electrons are *fermions*, the wavefunction must be *antisymmetric with respect to the interchange of two electrons*, so that, taking $N = 2$ for simplicity:

$$\Psi(x(1), x(2)) = -\Psi(x(2), x(1)) \quad (1.61)$$

This expression (see also eqn. (1.10)) is related to the Pauli principle, since Ψ vanishes when the spatial and spin coordinates of the two electrons are the same.

When the spin-orbit coupling is absent (no \mathbf{H}_2 term in the Hamiltonian (1.56a)), the electronic wavefunction is an eigenfunction of a Hamiltonian

without spin variables. So, it can be written as a *spin-orbital*; that is, a product of a spatial wavefunction (ϕ for an atom, ψ for a molecule) eigenfunction of the Hamiltonian, by a spin function (σ for an atom, η for a molecule) to be defined. For an electron i , in a spatial molecular orbital $\psi_j(i)$, the molecular spin-orbital numbered j is

$$\chi_j(x(i)) = \chi_j(i) = \psi_j(i)\eta_j(i) \quad (1.62)$$

with $\eta_j(i) = \alpha(i)$ or $\beta(i)$.

At this stage the spatial wavefunction can be either an atomic orbital or a molecular orbital. The construction rules are perfectly general and apply to all methods—in particular, the MO and VB methods defined in the following.

The one-electron orbital approximation consists in building approximate spatial wavefunctions as the product of one-electron wavefunctions $\chi_j(i)$; that is, for two electrons, $\chi_i(1) \chi_j(2)$, where the subscript is the orbital numbering and the parentheses indicate the electron numbering. $\chi_i(1) \chi_j(2) \dots$ is termed a *Hartree product*. But this wavefunction would not obey the Pauli principle, because it is not antisymmetric with respect to the interchange of two electrons (as previously). Thus we build an antisymmetric wavefunction termed the *Hartree-Fock wavefunction* (Ψ_{HF}) as:

$$\Psi_{\text{HF}} = [\chi_i(1)\chi_j(2) - \chi_i(2)\chi_j(1)] \quad (1.63a)$$

Ψ_{HF} can be rewritten under the form of a *Slater determinant*:

$$\Psi_{\text{HF}} = \frac{1}{\sqrt{2!}} \begin{vmatrix} \chi_i(1) & \chi_j(1) \\ \chi_i(2) & \chi_j(2) \end{vmatrix} \quad (1.63b)$$

The rows are labelled by the N -electrons (1 to 2), whereas the columns are labelled by the N spin-orbitals (i, j). By generalization, for N -electrons, the antisymmetric wavefunction is then given by a Slater determinant with rank N :

$$\Psi_{\text{HF}} = \frac{1}{\sqrt{N!}} \begin{vmatrix} \chi_i(1) & \chi_j(1) & \dots & \dots & \chi_k(1) \\ \chi_i(2) & \chi_j(2) & \dots & \dots & \chi_k(2) \\ \dots & \dots & \dots & \dots & \dots \\ \chi_i(N) & \chi_j(N) & \dots & \dots & \chi_k(N) \end{vmatrix} \quad (1.63c)$$

It is easy to check that interchanging two electrons corresponds to interchanging two rows of the determinant (and therefore changing its sign): the Slater determinant meets the requirement of antisymmetry. Having two electrons in the same spin-orbital leads to two identical columns and the determinant is zero: only one electron can occupy a spin-orbital, which fulfils the Pauli principle. A convenient linear notation for a Slater determinant shows only the diagonal elements and includes the normalization constant:

$$\Psi_{\text{HF}} = \Psi = |\chi_i(1) \chi_j(2) \dots \chi_{k-1}(N-1) \chi_k(N)| = |\chi_1 \chi_2 \dots \chi_N| \quad (1.63d)$$

Such wavefunctions, built from orthonormal (that is, orthogonal and normalized) spin-orbitals are normalized. Furthermore, if a Hartree product is an electron-independent wavefunction (the electrons are fully independent), the antisymmetrized Slater determinant introduces some exchange effect: it is impossible to find two electrons with the same spin at the same place; that is, the motion of two electrons with parallel spins is *correlated*—but the motion of

electrons with antiparallel spins remains *uncorrelated*, so that a *single determinantal wavefunction is an uncorrelated wavefunction*. An electron is said to be surrounded by a *Fermi hole*, as demonstrated in [1.15]. The main origin of error in the Hartree–Fock approach is the absence of correlation among electrons bearing opposite spins. The *difference* between the exact energy, E_{exact} (non-relativistic), and the Hartree–Fock energy E_{HF} is then termed *correlation energy*, E_{corr} ($E_{\text{corr}} = E_{\text{exact}} - E_{\text{HF}}$). Its computation is the goal of all the post-Hartree–Fock treatments (see Section 1.5.2.3). We would like to emphasize that if the correlation between electrons (place, spin, and so on) are due to physical phenomena (Coulombic electronic repulsion, antisymmetry, the Pauli exclusion principle, and so on), the correlation energy is not a physical quantity but a measure of the energy error due to the neglect of correlation in a certain approximation.

We now have the necessary tools for the rational construction of a polyelectronic wavefunction. Its energy can be computed from the usual expression:

$$E = \langle \Psi | \mathbf{H} | \Psi \rangle / \langle \Psi | \Psi \rangle \quad (1.64)$$

where \mathbf{H} is the complete Hamiltonian now including interelectronic repulsion, and where the wavefunction itself can be improved by choosing extended basis sets of orbitals and through the variational procedure. Many strategies exist, however. The detailed description of even a part of the innumerable quantum methods that have been devised in the last eighty years would be a tremendous task, well beyond the scope of this book. Taking the risk of being extremely schematic, we present in Fig. 1.38 a considerably simplified landscape of the quantum methods.

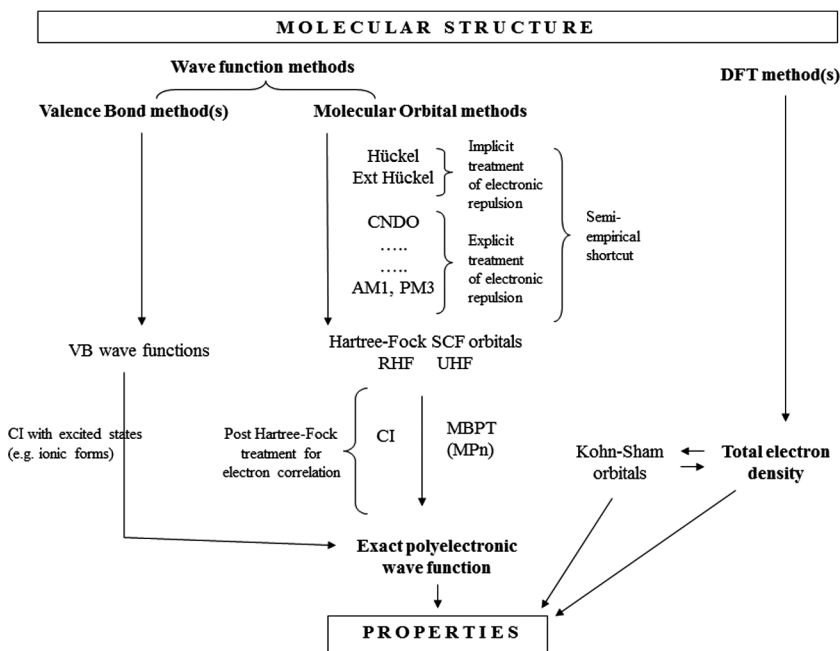


Fig. 1.38

Schematic chart of the quantum methods discussed in this section.

In the next two sections we shall concentrate on the two ‘historical’ methods: molecular orbitals and valence bond. In common, they try to write the true polyelectronic wavefunction, and then to extract properties through the convenient quantum-mechanical operators (Sections 1.5.2 and 1.5.3). A different approach, based on electronic density—and not centred on wavefunctions—the density functional theory (DFT), is presented in Section 1.5.4.

1.5.2 The quantitative molecular orbital (MO) method

The molecular orbital model relies on the definition of molecular orbitals as a combination of atomic or symmetry orbitals. The quantitative MO method, taking into account explicitly the interelectronic repulsion, requires two steps. First, the electronic repulsion is introduced under the form of a mean field; that is, a given electron is influenced by the *average* electronic density due to all other electrons. This is the basis of the *Hartree–Fock self-consistent field* procedure. The improvement is important but not sufficient, since it does not describe correlation effects, due to the *instantaneous* repulsion between electrons. Thus a second step is necessary, extending beyond Hartree–Fock treatments. Presently, this is the most demanding step in terms of computing power, since the length of calculations grows very rapidly with the number of electrons in the molecule.

1.5.2.1 The Hartree–Fock and self-consistent field (SCF) methods

Our problem is to find a set of N occupied spin–orbitals $\{\chi_a\}$ (noted a, b, \dots) that allows us to build a Slater determinant, obeying the Pauli principle:

$$|\Psi\rangle = \Psi = |\chi_a \chi_b \chi_c \dots \chi_N| \quad (1.65)$$

In the following, among the infinite number of spin–orbitals χ_j , the occupied orbitals χ_a are written with a, b, \dots, N indices and the unoccupied ones χ_r with r, s, \dots . The spin–orbitals χ_i are orthonormal; that is, $\langle \chi_a | \chi_b \rangle = \delta_{ab}$, where δ_{ab} is the Kronecker symbol, $\delta_{ab} = 1$ if $a = b$ and $= 0$ if $a \neq b$. We look for the best possible approximation to reach the ground state of the N -electron system, Ψ_0 , eigenfunction of the electronic Hamiltonian \mathbf{H} (1.57), with the lowest possible energy E_0 , applying eqn. (1.64). E_0 and Ψ_0 can be obtained by the variational method: χ_i and Ψ depend on various parameters, which can be optimized to satisfy the variational principle (∂E should be zero if we want E_0 to be the minimum of E):

$$\partial E = \partial \langle \Psi | \mathbf{H} | \Psi \rangle = 0 \quad (1.66)$$

In the Hartree–Fock approach the electronic repulsion is taken explicitly into account, while keeping the concept of spin–orbitals. The electron is assumed to evolve in the field created by all nuclei of the molecule and the *average* charge density created by all other electrons. The *charge density* $\rho(r)$, in a closed-shell molecule corresponding to a single determinant wavefunction, with N -electrons distributed in doubly occupied orbitals Ψ_i , is defined as:

$$\rho(r) = 2 \sum_{i=1}^{N/2} |\psi_i(r)|^2 \quad (1.67)$$

It is easy to find that the integral of the charge density over space is simply the number of electrons N :

$$\int_{\text{space}} \rho(r) dr = 2 \sum_{i=1}^{N/2} \int |\psi_i(r)|^2 dr = N \quad (1.68)$$

To present the essential arguments it is sufficient to take a two-electrons system (electrons 1 and 2, spin-orbitals χ_a and χ_b). Mathematically, each spin-orbital χ_a must be an eigenfunction of the Fock operator f :

$$f|\chi_a\rangle = \varepsilon_a|\chi_a\rangle \quad \text{or} \quad f\chi_a = \varepsilon_a\chi_a \quad (1.69a)$$

In the Hartree-Fock equation (1.69a), ε_a is the eigenvalue—the energy—of the spin-orbital $|\chi_a\rangle$, and f is the effective one-electron operator:

$$f(1) = h(1) + V^{\text{HF}}(1) = h(1) + \sum_{b \neq a} [\mathbf{J}_b(1) - \mathbf{K}_b(1)] \quad (1.69b)$$

$$h(1) = \mathbf{K}(1) + \mathbf{U}(1) = -\frac{1}{2}\nabla_1^2 - \sum_A \frac{Z_A}{r_{1A}} \quad (1.69c)$$

$$\mathbf{J}_b(1) \chi_a(1) = \left[\int \frac{\chi_b^*(2) \chi_b(2) dx(2)}{r_{12}} \right] \chi_a(1) \quad (1.69d)$$

$$\mathbf{K}_b(1) \chi_a(1) = \left[\int \frac{\chi_b^*(2) \chi_a(2) dx(2)}{r_{12}} \right] \chi_b(1) \quad (1.69e)$$

$h(1)$ is the one-electron operator describing the kinetic energy $\mathbf{K}(1)$ of electron (1) and its potential energy $\mathbf{U}(1) = -\sum_A \frac{Z_A}{r_{1A}}$ in the field of the various nuclei A .

$V^{\text{HF}}(1)$ is an effective one-electron operator, termed the Hartree-Fock potential. $V^{\text{HF}}(1)$ can be written as a difference of two operators $\mathbf{J}_b(1)$ and $\mathbf{K}_b(1)$, defined by their effect when operating on the spin-orbital $\chi_a(1)$. $\mathbf{J}_b(1)$ and $\mathbf{K}_b(1)$ are operators corresponding to the mean electrostatic repulsion of electron 1 with all the other electrons in spin-orbitals $\chi_b \neq \chi_a$.

Their significance can be commented upon briefly, as follows. \mathbf{J} and \mathbf{K} are reminiscent of the two-electron integrals j and k defined in relations (1.58), but are effective one-electron operators defined in eqns. (1.69d,e). $\mathbf{J}_b(1)$ is an operator acting on the spin-orbital $\chi_a(1)$, and represents the average local potential seen by the electron 1 at position r_1 , arising from an electron 2 in χ_b . $\mathbf{J}_b(1)$ is a Coulomb operator. $\mathbf{K}_b(1)$ is instead an exchange operator. It is also acting on the spin-orbital $\chi_a(1)$, but the average potential felt by electron 1 implies an 'exchange' between electrons 1 and 2, as shown in eqn. (1.69e).

In such a way, the description still uses one-electron functions, which are solutions of (almost) independent eigen equations. However, since the knowledge of a given one-electron wavefunction requires the detailed knowledge of *all other* one-electron wavefunctions, which themselves depend on the wavefunction of the considered electron, the system of equations can be solved only by an iterative procedure starting from a reasonable set of guessed wavefunctions. The procedure is then continued until a convergence is obtained, based on a criterion such as the difference between successive values of the energy. This method is known as the Hartree-Fock self-consistent field method.

Returning to N -electron systems, after the minimization of the energy of the determinant $|\Psi_0\rangle = |\chi_a \chi_b \chi_c \dots \chi_N|$, we obtain eigenvalue equations $\mathbf{f}|\chi_a\rangle = \varepsilon_a|\chi_a\rangle$ and an infinite set of eigenfunctions $\mathbf{f}|\chi_j\rangle = \varepsilon_j|\chi_j\rangle$ (with $j = 1, 2, \dots, \infty$). The energy ε_j (orbital energy) can be computed from:

$$\varepsilon_j = \langle \chi_j | \mathbf{f} | \chi_j \rangle \quad (1.70a)$$

Replacing the Fock operator \mathbf{f} by its expression (1.69b), one finds, after some calculations, that:

$$\begin{aligned} \varepsilon_i &= \langle \chi_i | \mathbf{f} | \chi_i \rangle = \langle \chi_i | \mathbf{h} + \sum_b (\mathbf{J}_b - \mathbf{K}_b) | \chi_i \rangle \\ &= \langle \chi_i | \mathbf{h} | \chi_i \rangle + \sum_b (\langle \chi_i | \mathbf{J}_b | \chi_i \rangle - \langle \chi_i | \mathbf{K}_b | \chi_i \rangle) \end{aligned} \quad (1.70b)$$

$$\varepsilon_i = \langle \chi_i | \mathbf{h} | \chi_i \rangle + \sum_b (\langle ib | ib \rangle - \langle ib | bi \rangle) \quad (1.70c)$$

Occupied orbitals:

$$\varepsilon_a = \langle a | \mathbf{h} | a \rangle + \sum_{b \neq a} (\langle ab | ab \rangle - \langle ab | ba \rangle) \quad (1.70d)$$

Vacant orbitals:

$$\varepsilon_r = \langle r | \mathbf{h} | r \rangle + \sum_b (\langle rb | rb \rangle - \langle rb | br \rangle) \quad (1.70e)$$

For occupied spin-orbitals, $\langle a | \mathbf{h} | a \rangle$ is the kinetic energy and the energy of attraction by all the nuclei, $\langle ab | ab \rangle$ is the two-electron Coulomb repulsion energy j , and $\langle ab | ba \rangle$ is the two-electron exchange repulsion energy k (running over the remaining $N - 1$ electrons in occupied spin-orbitals). For the unoccupied orbitals the result is the same but the interaction is now with all the N -electrons of the occupied orbitals as if an electron were added to Ψ_0 to give a $N + 1$ electronic configuration, ε_r being the energy of this supplementary electron.

It is, then, almost straightforward to compute the total electronic energy E_0 . A naïve conception would be to sum up the energies of the occupied orbitals:

$$\sum_a^N \varepsilon_a = \sum_a^N \langle a | \mathbf{h} | a \rangle + \sum_a^N \sum_b^N (\langle ab | ab \rangle - \langle ab | ba \rangle) \quad (1.71a)$$

but actually, using the standard procedure, $E_0 = \langle \Psi | \mathbf{H} | \Psi \rangle$:

$$E_0 = \sum_a^N \langle a | \mathbf{h} | a \rangle + \frac{1}{2} \sum_a^N \sum_b^N (\langle ab | ab \rangle - \langle ab | ba \rangle) \quad (1.71b)$$

$$E_0 = \sum_a^N \varepsilon_a - \frac{1}{2} \sum_a^N \sum_b^N (\langle ab | ab \rangle - \langle ab | ba \rangle) \quad (1.71c)$$

The factor $\frac{1}{2}$ in eqn. (1.71b) avoids counting twice the electron-electron repulsions present in eqn. (1.71a). Another form is eqn. (1.71c), which tells us that the total electronic energy is the sum of orbital energies *minus* the total repulsion energy, because adding orbital energies obtained by an SCF

procedure would count twice the electron–electron repulsions. If we apply relation (1.71b) to the case of the H_2 molecule, where $\Psi_0 = |\chi_1\chi_2|$ with two spin-orbitals ($\chi_1(1) = \psi_1\alpha = \psi_1$; $\chi_2(2) = \psi_1\beta = \bar{\psi}_1$; $N = 2$), we obtain simply for E_0 :

$$\begin{aligned} E_0 &= \langle \chi_1 | \mathbf{h} | \chi_1 \rangle + \langle \chi_2 | \mathbf{h} | \chi_2 \rangle + \langle \chi_1 \chi_2 | \chi_1 \chi_2 \rangle - \langle \chi_1 \chi_2 | \chi_2 \chi_1 \rangle \\ E_0 &= 2h + J_{12} - K_{12} \end{aligned} \quad (1.71d)$$

where the expressions are given for spin-orbitals. It is then useful to express the energies as a function of the spatial orbitals ψ , amenable to numerical computation. For the demonstration we use once more the simplest case of the H_2 molecule. Expression (1.71d) becomes, with ψ space orbitals:

$$\begin{aligned} E_0 &= \langle \psi_1\alpha | \mathbf{h} | \psi_1\alpha \rangle + \langle \psi_1\beta | \mathbf{h} | \psi_1\beta \rangle \\ &+ \langle \psi_1\alpha \psi_1\beta | \psi_1\alpha \psi_1\beta \rangle - \langle \psi_1\alpha \psi_1\beta | \psi_1\beta \psi_1\alpha \rangle \end{aligned} \quad (1.71e)$$

The operators are not acting on the spin functions α and β , which are orthonormal; that is:

$$\begin{aligned} \langle \alpha | \alpha \rangle &= \langle \beta | \beta \rangle = 1; \langle \alpha | \beta \rangle = \langle \beta | \alpha \rangle = 0, \langle \alpha \beta | \alpha \beta \rangle = 1, \\ \langle \alpha \beta | \beta \alpha \rangle &= 0 \end{aligned}$$

One obtains:

$$\begin{aligned} E_0 &= \langle \psi_1 | \mathbf{h} | \psi_1 \rangle \langle \alpha | \alpha \rangle + \langle \psi_1 | \mathbf{h} | \psi_1 \rangle \langle \beta | \beta \rangle + \langle \psi_1 \psi_1 | \psi_1 \psi_1 \rangle \\ &\langle \alpha \beta | \alpha \beta \rangle - \langle \psi_1 \psi_1 | \psi_1 \psi_1 \rangle \langle \alpha \beta | \beta \alpha \rangle \\ E_0 &= \langle \psi_1 | \mathbf{h} | \psi_1 \rangle + \langle \psi_1 | \mathbf{h} | \psi_1 \rangle + \langle \psi_1 \psi_1 | \psi_1 \psi_1 \rangle = 2h_1 + J_{11} \end{aligned} \quad (1.71f)$$

The expressions are related to spatial orbitals. We can observe that the exchange integral K has disappeared from the expression due to the orthogonality of the spins α and β . This is a general result: exchange integrals will be zero when spins are opposite. Thus for different spins the repulsion is J_{ij} , while for like spins it is $J_{ij} - K_{ij}$ (still positive). In other words, two electrons always repel each other, but less so when they have like spins.

Eqns. (1.71e) can be extended to the general case of an N -electron closed-shell Hartree–Fock function with $N/2$ space orbitals $|\Psi_0\rangle = |\chi_a \chi_b \chi_c \dots \chi_N| = |\psi_1 \bar{\psi}_1 \psi_2 \bar{\psi}_2 \dots \psi_{N/2} \bar{\psi}_{N/2}|$ (see [1.15] for a complete demonstration). The expression of the energy becomes:

$$E_0 = 2 \sum_{i=1}^{N/2} \langle \psi_i | \mathbf{h} | \psi_i \rangle + \sum_i \sum_j^{N/2} (2 \langle \psi_i \psi_j | \psi_i \psi_j \rangle - \langle \psi_i \psi_j | \psi_j \psi_i \rangle) \quad (1.71g)$$

$$E_0 = 2 \sum_{i=1}^{N/2} h_i + \sum_i \sum_j^{N/2} (2 J_{ij} - K_{ij}) \quad (1.71h)$$

If E_0 is not the sum of the orbital energies ε , what is the meaning of an orbital energy? A simple answer is that the orbital energy ε_d of a spin-orbital χ_d represents the negative of the ionization energy E_{ion} when one electron is withdrawn from the occupied spin-orbital χ_d to reach an $N - 1$ electronic

configuration with energy ${}^{N-1}E_d$. An equivalent equation can be derived for the fixation of one electron in a vacant orbital χ_t to obtain an $N + 1$ electronic configuration and determinant. The orbital energy ε_t is the negative of the fixation energy E_{fix} .

$$E_{\text{ion}} = {}^{N-1}E_d - {}^N E_0 = -\varepsilon_d \quad (1.72a)$$

$$E_{\text{fix}} = {}^N E_0 - {}^{N+1}E_t = -\varepsilon_t \quad (1.72b)$$

The two relations can be demonstrated at the expense of some calculations and within the approximation that the spin-orbitals remain the same in the ionization process (frozen orbital approximation). Eqns. (1.72) are the expression of Koopman's theorem. Nevertheless, if Koopman's theorem is a good first approximation for experimental ionization energies, it is not the case for fixation energies, since Hartree-Fock calculations on neutral molecules often give positive energies for vacant orbitals [1.15].

Eqn. (1.71h) has something else to tell us. To minimize the ground-state energy of the molecule, the composition of the orbitals should be such that the J_{ij} integrals are as small as possible and the K_{ij} as large as possible. How is this feasible? By nature, both J_{ij} and K_{ij} integrals are positive. K_{ij} is non-zero only for spin-orbitals with the same spin. According to their definitions, the integrals' magnitude depends on the sum of products such as $(c_{in}c_{jm}\phi_{in}\phi_{jm})^2$, where n and m are numbering the atoms of the molecule. J_{ij} and K_{ij} are non-zero if the molecular orbitals ψ_i and ψ_j have large coefficients on the same atoms of the molecule (c_{in} and c_{jn} , for example). Therefore, to minimize the energy of the molecule, spin-orbitals with the same spin tend to be centred on the same atoms to maximize K_{ij} , and spin-orbitals with opposite spins tend to segregate in different parts of the molecule to minimize J_{ij} . This observation is the basis of the mechanism of *spin polarization* defined in the following using the concept of unrestricted Hartree-Fock spin-orbitals (see Fig. 1.41) [1.15].

Density matrix ([1.15], p. 212)

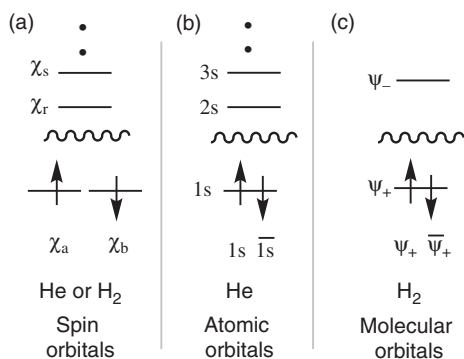
At this stage it is useful to introduce the concept of the *density matrix*, combining the expansion of a molecular orbital $\psi_i = \sum_{\mu=1}^N c_{\mu i} \phi_{\mu}$ with that of charge density:

$$\begin{aligned} \rho(r) &= 2 \sum_{i=1}^{N/2} \psi_i^*(r)\psi_i(r) = 2 \sum_{i=1}^{N/2} \sum_{\nu} c_{\nu i}^* \phi_{\nu}^*(r) \sum_{\mu} c_{\mu i} \phi_{\mu}(r) \\ &= \sum_{\mu\nu} \left[2 \sum_{i=1}^{N/2} c_{\mu i} c_{\nu i}^* \right] \phi_{\mu}(r) \phi_{\nu}^*(r) \end{aligned} \quad (1.73a)$$

or

$$\rho(r) = \sum_{\mu\nu} P_{\mu\nu} \phi_{\mu}(r) \phi_{\nu}^*(r) \quad \text{with } P_{\mu\nu} = 2 \sum_{i=1}^{N/2} c_{\mu i} c_{\nu i}^* \quad (1.73b)$$

$P_{\mu\nu}$ is the density matrix, related directly to the expansion coefficients c_i . It defines completely the charge density $\rho(r)$ and the results of the HF closed-shell calculations. The diagonalization of the matrix leads to eigenvectors which are termed *natural orbitals*, and to eigenvalues which are the *occupation*

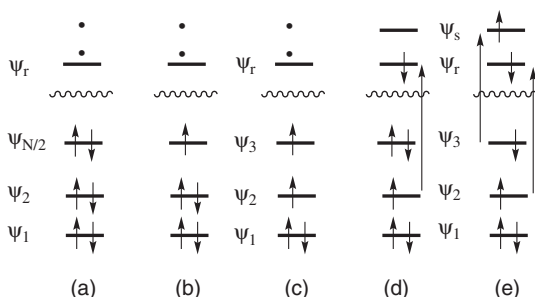
**Fig. 1.39**

Hartree-Fock ground-state determinants for a helium atom and an H₂ molecule: (a) spin-orbitals representation: $|\chi_a \chi_b\rangle$; (b) helium atom: $|1s \bar{1}s\rangle$; (c) H₂ molecule $|\psi_+ \bar{\psi}_+\rangle$. (Adapted from [1.15].)

numbers—useful intermediates in quantum calculations. The density matrix is used in the following to define the spin density and the related density matrices.

To summarize our steps up to now, the Hartree-Fock self-consistent field (HF-SCF) procedure provides us with the way to find the best (within a variational procedure) ground-state determinant $|\Psi_0\rangle = |\chi_a \chi_b \chi_c \dots \chi_N|$ and its energy E_0 , which is not the sum of the energy of the spin-orbitals ϵ_a . The spin-orbitals are $\phi_\bullet\sigma$ for an atom or $\psi_\bullet\eta$ for a molecule. For example, for a helium atom, $1s^2$ (see Section 1.2.3) and the dihydrogen molecule $\psi_+(1)\psi_+(2)$ (see Section 1.3.1), the Hartree-Fock ground-state determinants, following the spin-orbital scheme, are shown in Fig. 1.39. For helium, $\chi_a = 1s\alpha$ and $\chi_b = 1s\beta$, whereas for H₂, $\chi_a = \psi_+\alpha$ and $\chi_b = \psi_+\beta$ (Fig. 1.39a), where the nature of the spin (α , \uparrow and β , \downarrow) is made explicit. The number of vacant spin-orbitals χ_r depends on the number of orbitals in the basis set used in the Hartree-Fock calculation (for helium, with a minimum basis of one $1s$ orbital, there is no vacant χ_r ; in H₂, with a minimum basis set of two $1s$, they will be two vacant χ_r). Figures 1.39b (for He) and c) (for H₂) shows completely equivalent representations using spatial atomic (He) and molecular orbitals (H₂) and expressions of the determinant using the spatial orbitals and the bar notations for β spins.

At this point it is useful to introduce some new definitions (Fig. 1.40). When the HF-SCF determinant of an N -electron system with an even number of electrons can be written as $\Psi_0 = |\chi_1 \chi_2 \dots \chi_{N-1} \chi_N\rangle = |\psi_1 \bar{\psi}_1 \psi_2 \bar{\psi}_2 \dots \psi_{N/2} \bar{\psi}_{N/2}\rangle$ corresponding to a singlet state, we have a *closed-shell* HF-SCF ground-state determinant (Fig. 1.40a) in which all electrons

**Fig. 1.40**

(a) Closed-shell HF-SCF ground-state determinant, $|\Psi_0\rangle = |\psi_1 \bar{\psi}_1 \psi_2 \bar{\psi}_2 \dots \psi_{N/2} \bar{\psi}_{N/2}\rangle$; (b) open-shell HF-SCF doublet ground-state determinant, $|\Psi_0\rangle = |\psi_1 \bar{\psi}_1 \psi_2 \bar{\psi}_2 \psi_3\rangle$; (c) open-shell HF-SCF triplet ground-state determinant, $|\Psi_0\rangle = |\psi_1 \bar{\psi}_1 \psi_2 \psi_3\rangle$; (d) singly excited determinant, $|\Psi_2^r\rangle = |\psi_1 \bar{\psi}_1 \psi_2 \bar{\psi}_r \psi_3\rangle$; (e) doubly excited determinant, $|\Psi_{23}^{rs}\rangle = |\psi_1 \bar{\psi}_1 \psi_2 \bar{\psi}_r \psi_s \bar{\psi}_3\rangle$.

occupy orbitals as pairs with opposite spins. When the determinant corresponds to one unpaired electron (doublet, Fig. 1.40b) or a triplet (Fig. 1.40c), we have an *open-shell* ground-state determinant. When one (two) electron(s) is (are) promoted from one (two) χ_a occupied orbital(s) to one (two) virtual χ_r orbital(s), we have a singly (doubly) *excited* determinant (Figs. 1.40d and e).

The description of open-shell systems is more complicated than that of closed-shell systems, because one has to write the wavefunction as a combination of several Slater determinants. Unfortunately, this is the most interesting case for us, because a number of processes studied in this book, such as exchange magnetic coupling (in Chapter 2) or electron transfer (in Chapter 3), imply open-shell systems.

The determinants in Fig. 1.40 are said to be *restricted* determinants because the α and the β spins are constrained to have the same spatial orbital ψ ; that is, ψ and $\bar{\psi}$ have the same energy. This is also the case in Fig. 1.41a, related to a lithium atom. When ψ and $\bar{\psi}$ are allowed to have different energies and spatial definition, the determinant is *unrestricted* (Fig. 1.41b). This is an important step on the way to taking into account explicitly the interelectronic repulsion. Indeed, the $1s\alpha$ electron has an exchange interaction with $2s\alpha$, whereas the $1s\beta$ electron has not. Unrestricted spin-orbitals have different spatial orbitals which allow us to relax this constraint and lower the energy of the system. Figure 1.41(c, d) illustrates the case of an AB open-shell molecule with three electrons. The price to pay to accomplish this process is that the set of orthonormal spatial orbitals $\{\psi_i^\alpha\}$ is no more orthonormal to the set of orthonormal spatial orbitals $\{\psi_i^\beta\}$:

$$\langle \psi_i^\alpha | \psi_j^\alpha \rangle = \delta_{ij} \text{ and } \langle \psi_i^\beta | \psi_j^\beta \rangle = \delta_{ij} \text{ but } \langle \psi_i^\alpha | \psi_j^\beta \rangle \neq 0 = S_{ij}^{\alpha\beta} \quad (1.74)$$

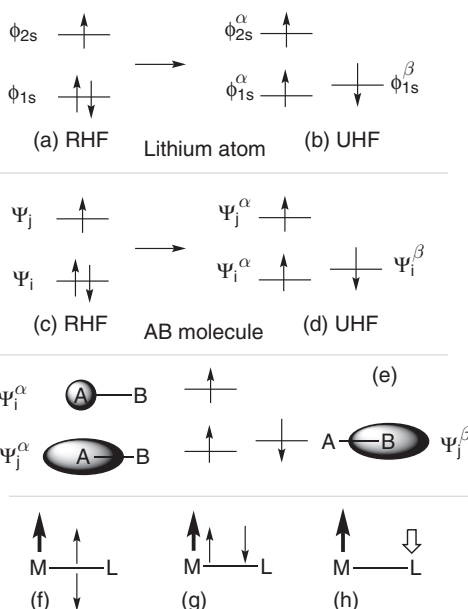


Fig. 1.41

Lithium atom. (a) Restricted Hartree-Fock (RHF) doublet determinant $|\Psi_{\text{RHF}}\rangle = |\phi_{1s}\bar{\phi}_{1s}\phi_{2s}\rangle$; (b) unrestricted Hartree-Fock (UHF) doublet determinant $|\Psi_{\text{UHF}}\rangle = |\phi_{1s}^\alpha\bar{\phi}_{1s}^\beta\phi_{2s}^\alpha\rangle$. AB molecule. (c) and (d): the same definitions in the AB molecule with a net spin $S = 1/2$; (e) spin polarization mechanism in AB, emphasizing the different spatial distribution of α and β spin-orbitals; (f-h) M-L metal-ligand bond with a net spin S in the metal orbital; (f) no spin polarization; (g) spin polarization of the bonding orbital M-L according to (e); (h) resulting spin polarization on the atoms M (positive) and L (negative).

Furthermore, in open-shell systems there is some *spin contamination* between the levels.

To comment further on Fig. 1.41(e–h) it is appropriate to introduce the concepts of *charge density* and *spin density*.

Charge density and spin density

Following IUPAC, the spin density is the unpaired electron density. An electron with a spin α (\uparrow) is described at some point (\mathbf{r}), by the molecular orbital $\psi_i^\alpha(\mathbf{r})$. The probability of finding this electron in the elemental volume $d\mathbf{r}$ is $|\psi_i^\alpha(\mathbf{r})|^2 d\mathbf{r}$. The electronic (charge) density is $|\psi^\alpha(\mathbf{r})|^2$. If there are N^α electrons with spin α , the total charge density of spin α is:

$$\rho^\alpha(\mathbf{r}) = \sum_i^{N^\alpha} |\psi_i^\alpha(\mathbf{r})|^2 \quad (1.75a)$$

The same relation applies for the N^β electrons with spin β (\downarrow):

$$\rho^\beta(\mathbf{r}) = \sum_i^{N^\beta} |\psi_i^\beta(\mathbf{r})|^2 \quad (1.75b)$$

Then the total *charge density* is the sum: $\rho(\mathbf{r}) = \rho^\alpha(\mathbf{r}) + \rho^\beta(\mathbf{r})$, and is always positive. By contrast, the *spin density* is the difference: $\rho^S(\mathbf{r}) = \rho^\alpha(\mathbf{r}) - \rho^\beta(\mathbf{r})$, and can be positive (in regions where there are more electrons with spin α than with spin β), or negative in the reverse case.

Let us consider the molecular system AB with three electrons and a net spin $S = 1/2$ (Fig. 1.41(e–h)) [1.16c]. In an unrestricted Hartree–Fock (UHF) approach, it is represented by three spin-orbitals (e). The unpaired electron (α spin) is in the SOMO ψ_i^α . We look at what happens when the α electron is located mainly on A. To minimize the energy of AB by increasing the exchange integrals K_{ij} , the presence of an α spin in the SOMO ψ_i^α ‘polarizes’ the ψ_j HOMO and favours more α spin density on A (ψ_j^α). At the same time, to minimize the energy by decreasing the repulsion integrals J_{ij} , there is more β spin density on B (ψ_j^β). The unrestricted Hartree–Fock procedure allows the spin-orbitals to have a *different spatial localization*, with ψ_j^α more centred on A and ψ_j^β more centred on B. When applied to an M–L metal–ligand situation with a net spin on the metal, the spin polarization of the bonding orbital M–L (g) is preferred to an equal distribution of α and β spins (f). It results in spin polarization on the atoms M (positive) and L (negative). Spin-polarized neutron diffraction NMR, XMCD are good methods for measuring the atomic spin densities (see Section 2.3.3).

The HF–SCF method can thus be stated as two variants: restricted Hartree–Fock (RHF), and unrestricted Hartree–Fock (UHF)—the latter being recommended for dealing with open-shell systems (see Chapter 2).

1.5.2.2 Semi-empirical computational methods: an overview

Before going further we present some approximate semi-empirical computational methods, whose objective is to shortcut the (long) process of computing SCF MO energies and wavefunctions. They speed up the calculations, so that larger systems can be studied. They differ in the way of computing, in a practical way, the numerous integrals associated with electronic repulsions. These

methods are listed in the following in order of increasing refinement. The first ones (Hückel and extended Hückel) do not compute these integrals at all, but compensate the error by an empirical choice of other parameters. They have been presented already in Section 1.3.5, and constitute the basis of simple reasoning based on the construction and filling of molecular orbitals.

Hückel method. This applies to π systems in planar molecules (butadiene, benzene . . .): a one-electron effective Hamiltonian is written without explicit treatment of the interelectronic repulsion. The π MOs are linear combinations of atomic orbitals (LCAO) and the energies computed from a secular determinant. Overlaps are neglected, and the electronic interaction (denoted β) is considered only between nearest neighbours. This method is now used mainly for pedagogical purposes.

Extended Hückel method. This applies to all molecules, planar or not. It was introduced by M. Wolfsberg and L. Helmholz in 1952 and given a strong impetus by R. Hoffmann in the 1960s, to become a widespread and popular method. It considers valence electrons only. The valence electrons Hamiltonian is a one-electron one (1.76a), again without explicit treatment of the interelectronic repulsion.

$$\mathbf{H} = \sum_{i \text{ valence}} \mathbf{H}_{\text{eff}}(i) \quad (1.76a)$$

$$\phi_s(\mathbf{r}) = A e^{-\zeta r} \quad \text{with} \quad A = A_{nlm}(\mathbf{r}, \theta, \varphi) = \frac{[2\zeta/a_0]^{1/2}}{[(2n!)]^{1/2}} r^{n-1} Y_{lm}(\theta, \varphi) \quad (1.76b)$$

$$\mathbf{H}_{\text{eff}}(i)\phi(i) = \varepsilon_i \phi(i) \quad (1.76c)$$

$$\sum_s [\mathbf{H}_{rs}^{\text{eff}} - \varepsilon_i S_{rs}] c_{si} = 0 \quad r = 1, 2, \dots \quad (1.76d)$$

$$H_{ij} = K S_{ij} (H_{ii} + H_{jj}) / 2 \quad (1.76e)$$

$$E_{\text{valence}} = \sum_i \varepsilon_i \quad (1.76f)$$

The MOs are LCAOs of valence Slater-type orbitals ϕ_s with semi-empirical A and ζ orbital exponents (eqn. (1.76b)). The energies are computed using secular equations, including all the overlaps between atoms (eqns. (1.76c) and (1.76d)). The H_{ii} parameters are the orbital energies taken as the valence-state ionization potential (VSIP, ionization potential of the atom in the valence state that it presents in the molecule). The H_{ij} parameters are computed through eqn. (1.76e) (with the K factor between 1 and 3, often = 1.75). There is no SCF step, and the total energy is the sum of orbital energies (eqn. (1.76f)).

The method is simple and efficient, and free user-friendly programmes are available. The method provides a very good approximation of the ‘shapes’ of MOs and a rough approximation of MOs energies. It has been extended to calculations of the band structure of solids with the term *tight-binding model* (see Section 1.4). It has been strongly criticized, since serious discrepancies are observed in the quantitative computations of distances, geometries, transition

energies, and even energies (the delocalization of electrons in the MOs is over-emphasized). However, it is still the basis of many qualitative reasonings about structures and reactivity of molecules (in particular, the Woodward–Hoffmann rules).

Pariser–Parr–Pople method (PPP). This is the simplest SCF method, of historical interest. It applies to planar systems, for which the σ/π separation is complete. The π system is treated with the two-electron repulsion terms, with the SCF procedure.

CNDO, INDO, and NDDO methods. These SCF methods were designed by Pople and coworkers, improving the two-electron PPP method. The goal is to reproduce the results of *ab initio* calculations with much less computational time. The methods treat only valence electrons, taking into account interelectronic repulsion but neglecting the differential overlap (NDO): for CNDO (complete neglect of differential overlap) the neglect is complete ($S_{rs} = \delta_{rs}$ and the repulsion integrals $\langle rs|tu \rangle = \langle rr|tt \rangle$, even on the same atom); each atom (except hydrogen) have several basis valence AOs; for INDO (incomplete neglect of differential overlap), the repulsion integrals on the same atom are taken into account, that improves the calculation when the electron spin distribution is important (calculation of EPR spectra . . .); for NDDO (neglect of diatomic differential overlap) the neglect bears on the overlap between AOs on different atoms; the method was further developed as MNDO (Modified NDO). Variants suitable for calculations of electronic spectra include some configuration interaction. They are suffixed with /S (for example, INDO/S).

MINDO, MNDO, AM1, MNDO-PM3, SINDO1, and ZINDO methods (Modified INDOs). These were implemented by Dewar and coworkers, not necessarily to reproduce the *ab initio* SCF results, but to compute molecular binding energies usable by chemists. The methods focus, therefore, on the modification of the preceding methods and on the choice of empirical parameters suitable for reproducing experimental physical quantities such as heats of formation, molecular geometries, and properties of ground-state organic molecules or potential-energy surfaces of chemical reactions. The MINDO/1, 2, 3 and MNDO and their derivatives AM1 (Austin Model 1) and PM3 (with new parametrization) derivatives are various generations of the programmes extending the accuracy of the calculations due to improved parameters defined for more chemical elements. They are contained in computer packages such as MOPAC and AMPAC. Results have been improving with time. The SINDO1 (symmetrically orthogonalized INDO) method was designed by Nanda and Jug, with symmetrically orthogonalized AOs and pseudo-potentials to simulate the inner-shell electrons. Finally, ZINDO methods (Zerner's intermediate neglect of differential overlap) was designed by M. C. Zerner to treat spectroscopic properties—in particular, for transition elements. The main criticism of these methods bears on the always present temptation of overparametrization.

1.5.2.3 Beyond Hartree–Fock: treatment of electron correlation

At the present stage we dispose of SCF MO computed with the best compromise between speed and accuracy. Is this the end of the story? Alas, no! It is a well-known weakness of molecular orbital theory that it does not describe electron correlation, due to the fact that it is a monodeterminantal method.

This is redhibitory in particular for weak interactions such as those occurring during a bond dissociation process. This can be realized readily when looking at the ground-state wavefunctions of the dihydrogen molecule $H_A H_B$, where the two electrons are paired in the bonding MO ψ_1 . At the Slater determinant, $|\chi_1 \chi_2| = |\psi_1 \eta_1 \psi_1 \eta_2|$ corresponds the spatial wavefunction Φ_+ :

$$\Phi_+ = N_+ \psi_1(1)\psi_1(2) = N_+ [\phi_a(1) + \phi_b(1)][\phi_a(2) + \phi_b(2)] \quad (1.77a)$$

$$\Phi_+ = N_+ \{[\phi_a(1)\phi_b(2) + \phi_b(1)\phi_a(2)] + [\phi_a(1)\phi_a(2) + \phi_b(1)\phi_b(2)]\} \quad (1.77b)$$

$$\Phi_+ = N_+ [\Phi_{\text{covalent}} + \Phi_{\text{ionic}}] \quad (1.77c)$$

The first term in eqn. (1.77b) is covalent (one electron per atom; see Section 1.5.3), whereas the second term is a sum of the ionic terms $H_A^+ H_B^-$ or $H_A^- H_B^+$, where the two electrons are on the same atom. The wavefunction Φ_+ is therefore the sum of two terms, with equal weight—one covalent Φ_{covalent} and one ionic Φ_{ionic} , as shown in eqn. (1.77c). The situation persists whatever the distance between H_A and H_B . The presence of the ionic terms leads to a wrong description of the real dissociation situation, which obviously corresponds to two neutral atoms, $H_A^\bullet + H_B^\bullet$. To alleviate this difficulty, the standard remedy has been for many years to write the wavefunction using several determinants (multiconfigurational SCF wavefunctions—MCSCF), or in other words, to perform configuration interaction (CI). Thus the total electronic wavefunction Ψ is developed as a function of several monodeterminantal wavefunctions Φ_i , corresponding to the ground-state determinant and to excited ones. In the case of a closed-shell singlet system, using the notations introduced before:

$${}^1\Psi = \sum_i \lambda_i {}^1\Phi_i = \sum \lambda_0 |{}^1\Phi_0\rangle + \lambda_1 |{}^1\Phi_2^r\rangle + \lambda_2 |{}^1\Phi_{23}^{rs}\rangle + \dots \quad (1.78)$$

where the λ_i coefficients can be obtained by a variational procedure. The process can be illustrated by returning to the H_2 molecule. The ground-state configuration and the singly and doubly excited states are shown in Fig. 1.42A.

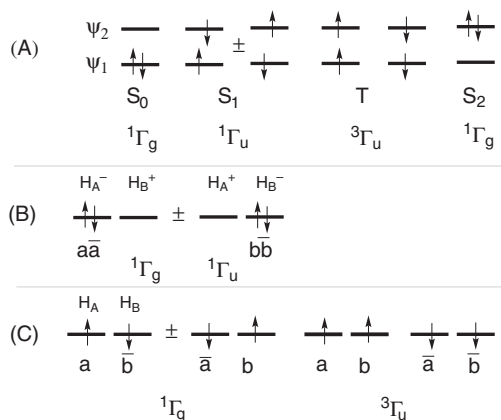


Fig. 1.42

Electronic configurations and states of an H_2 molecule as described in the frame of MO and VB models: (A) Hund-Mulliken (MO) scheme; (B) Heitler-London (VB) scheme, excited states; (C) Heitler-London (VB) scheme, ground state.

The only excited state which presents the same symmetry ${}^1\Gamma_g$ as the ground state is the doubly excited one which allows their interaction (Fig. 1.42):

$$\Phi_- = N_- \psi_2(1)\psi_2(2) = N_- [\phi_a(1) - \phi_b(1)][\phi_a(2) - \phi_b(2)] \quad (1.79a)$$

$$\Phi_- = N_- \{[\phi_a(1)\phi_a(2) + \phi_b(1)\phi_b(2)] - [\phi_a(1)\phi_b(2) + \phi_b(1)\phi_a(2)]\} \quad (1.79b)$$

$$\Phi_- = N_- [-\Phi_{\text{covalent}} + \Phi_{\text{ionic}}] \quad (1.79c)$$

The interaction of the two determinants (configurations, states) S_0 and S_2 should improve the wavefunction and ground state (${}^1\Psi = \Phi_+ + \lambda_2\Phi_-$), where the fraction of the ionic terms has been tuned.

For a closed-shell molecule with a large HOMO–LUMO separation, the dominating Φ describing the ground state is the one for which all electrons occupy the orbitals following the Aufbau principle. But things are more complicated when the HOMO–LUMO separation is weak and when considering excited states. For such cases, the mixture of one-determinant wavefunctions is so important that the notion of orbitals and their occupation tends to vanish. We shall discuss this point in Section 2.6.

Although it is theoretically possible to reach excellent approximations of the exact polyelectronic wavefunction and of the corresponding quantities (total electronic energy) by this procedure, in practice the calculations are extremely heavy. Many methods have been described in the literature to reach the best compromise between accuracy and practicability of computation, and the reader should consult books such as [1.15] and [1.16] for more details. Note that with present computational methods it is this post-Hartree–Fock step which is the most time-consuming. This derives from the fact that a correct treatment by configuration interaction can mix as many as 10^4 – 10^6 excited-state configurations with the ground-state configuration.

Perturbation technique

Perturbation relies on the simple idea that the problem to be solved is only slightly different from one which is already solved exactly. It starts with the partition of the Hamiltonian ($\mathbf{H} = \mathbf{H}_0 + \lambda\mathbf{V}$), where the reference part \mathbf{H}_0 corresponds to the already solved problem, and \mathbf{V} is a perturbation, small compared to \mathbf{H}_0 . λ is a parameter determining the strength of the perturbation ($\lambda = 0$, unperturbed, $\lambda = 1$, real system). The Schrödinger equation for the reference system is:

$$\mathbf{H}_0\Phi_i = E_i\Phi_i \quad i = 0, 1, 2, \dots \infty \quad (1.80a)$$

and for the perturbed system:

$$\mathbf{H}\Psi = W\Psi \quad (1.80b)$$

The solutions Φ_i of \mathbf{H}_0 build a complete orthonormal set. For the ground state and time-independent perturbation, when $\lambda = 0$, $\Psi = \Phi_0$, and $W = E_0$. When $\lambda \neq 0$, the energy W and the wavefunction Ψ are written as an expansion at different powers of λ :

$$\Psi = \lambda^0\Phi_0 + \lambda^1\Phi_1 + \lambda^2\Phi_2 + \lambda^3\Phi_3 + \dots \quad (1.80c)$$

Basic concepts

$$W = \lambda^0 W_0 + \lambda^1 W_1 + \lambda^2 W_2 + \lambda^3 W_3 + \dots \quad (1.80d)$$

We check that for $\lambda = 0$, $\Psi_0 = \Phi_0$, and $W_0 = E_0$, this is the zeroth order, unperturbed wavefunction Ψ_0 and energy W_0 . Ψ_1 and W_1 are the first-order corrections, Ψ_2 and W_2 the second-order corrections, and so on. Taking care of working with normalized wavefunctions $\langle \Psi | \Phi_0 \rangle = 1$, it is possible to use eqns. (1.80a)–(1.80d) to derive the n th-order perturbation equations by gathering the terms having λ at the same power:

$$\lambda^0 : \text{zeroth order} \quad \mathbf{H}_0 \Psi_0 = W_0 \Psi_0 \quad (1.80e)$$

$$\lambda^1 : \text{first order} \quad \mathbf{H}_0 \Psi_1 + \mathbf{V} \Psi_0 = W_0 \Psi_1 + W_1 \Psi_0 \quad (1.80f)$$

$$\lambda^2 : \text{second order} \quad \mathbf{H}_0 \Psi_2 + \mathbf{V} \Psi_1 = W_0 \Psi_2 + W_1 \Psi_1 + W_2 \Psi_0 \quad (1.80g)$$

$$\lambda^n : \text{nth order} \quad \mathbf{H}_0 \Psi_n + \mathbf{V} \Psi_{n-1} = \sum_{i=0}^n W_i \Psi_{n-i} \quad (1.80h)$$

The n th-order energy correction follows:

$$W_n = \langle \Phi_0 | \mathbf{V} | \Psi_{n-1} \rangle \quad (1.80i)$$

In this approach, the $(n-1)$ th wavefunction is needed to obtain the n th one. As the first-order equation has two unknowns, a further hypothesis is needed. In the frame of the Rayleigh–Schrödinger perturbation theory, the unknown first-order wavefunction Ψ_1 is expressed as a linear combination of the functions of the unperturbed Schrödinger equation Φ_i :

$$\Psi_1 = \sum_i c_i \Phi_i \quad (1.80j)$$

Hence (after eqn. (1.80f)):

$$(\mathbf{H}_0 - W_0) \sum_i c_i \Phi_i + (\mathbf{V} - W_1) \Phi_0 = 0 \quad (1.80k)$$

and, after multiplying eqn. (1.80k) on the left by $\Phi_j \neq \Phi_0$, and integrating:

$$W_1 = \langle \Phi_0 | \mathbf{V} | \Phi_0 \rangle \quad (1.80l)$$

$$c_j = \frac{\langle \Phi_j | \mathbf{V} | \Phi_0 \rangle}{E_0 - E_j} \quad (1.80m)$$

The energy's first-order correction is therefore an average of the perturbation \mathbf{V} on the unperturbed wavefunction Φ_0 . We can obtain similarly the expressions of W_2 and Φ_2 , using eqn. (1.80k):

$$\Psi_2 = \sum_i d_i \Phi_i \quad (1.80n)$$

$$(\mathbf{H}_0 - W_0) \sum_i d_i \Phi_i + (\mathbf{V} - W_1) \sum_i c_i \Phi_i - W_2 \Phi_0 = 0 \quad (1.80p)$$

$$W_2 = \sum_i c_i \langle \Phi_0 | \mathbf{V} | \Phi_i \rangle = \sum_{i \neq 0} \frac{\langle \Phi_0 | \mathbf{V} | \Phi_i \rangle \langle \Phi_i | \mathbf{V} | \Phi_0 \rangle}{E_0 - E_i} \quad (1.80q)$$

$$d_i = \sum_{j \neq 0}^n \frac{\langle \Phi_j | \mathbf{V} | \Phi_i \rangle \langle \Phi_i | \mathbf{V} | \Phi_0 \rangle}{(E_0 - E_i)(E_0 - E_j)} - \frac{\langle \Phi_j | \mathbf{V} | \Phi_0 \rangle \langle \Phi_0 | \mathbf{V} | \Phi_0 \rangle}{(E_0 - E_j)^2} \quad (1.80r)$$

And so on for higher-order perturbations, which increase in complexity. The main point is that the corrections can be expressed by applying the perturbation operator over unperturbed wavefunctions Φ_i and unperturbed energies E_i .

The consistency of the process at the different perturbation orders is checked through a diagrammatic representation proposed by Feynman. The advantage over configuration interaction is a faster convergence, since the successive corrections are usually ranked in order of decreasing energies. The method is used by physicists to describe large systems (with many bodies), and it is therefore commonly termed *many-body perturbation theory* (MBPT). The methods used most commonly are referred to as Møller–Plesset methods, with corrections to second or fourth order (MP2 and MP4 respectively), which are presented and used in Section 2.6.3.2.

1.5.3 The valence bond (VB) model: comparison with the MO model

1.5.3.1 The valence bond (VB) model

The valence bond model takes its origin in the concept of electron pair proposed by G. N. Lewis, in his pioneering work of 1916, to describe the chemical bond, in its quantum equivalent suggested by Heitler and London in 1927 for the hydrogen molecule, and its generalization to polyatomic molecules by Linus Pauling during the 1930s [1.17].

To present it, let us take again the example of the H_2 molecule. When the two atoms (A and B) are far away (at infinite distance), a first description corresponds to electron 1 in atomic orbital ϕ_a or a (A) with spin α , whereas electron 2 is in atomic orbital ϕ_b or b (B) with spin β (configuration $a1\uparrow b2\downarrow$). If electrons 1 and 2 are exchanged (but not the spins, configuration $a2\uparrow b1\downarrow$), the situation can be described by the determinant $|\bar{a}\bar{b}|$ (1.81a). Since the system is fully symmetric, there is no reason to constrain the α spin to be only on A, whereas spin β is only on B. The determinant $|\bar{a}b|$ (1.81b), where the spins are allowed to exchange (configurations $a\downarrow b\uparrow$), is as valid as the first one. Therefore, the Heitler–London function Ψ_{HL} is written as the sum of the two determinants (1.81c), with a normalization term, because the two orbitals a and b have an overlap integral S (or in other words, because the two determinants are not orthogonal). Then, Ψ_{HL} is written as the product of a space function by a spin function (1.81d):

$$|\bar{a}\bar{b}| = [a(1)b(2)\alpha(1)\beta(2) - a(2)b(1)\alpha(2)\beta(1)] \quad (1.81a)$$

$$|\bar{a}b| = [a(1)b(2)\beta(1)\alpha(2) - a(2)b(1)\beta(2)\alpha(1)] \quad (1.81b)$$

$$\Psi_{HL} = \frac{1}{\sqrt{2(1+S^2)}} (|\bar{a}\bar{b}| + |\bar{a}b|) \quad (1.81c)$$

$$\Psi_{HL} = \frac{1}{\sqrt{2(1+S^2)}} [a(1)b(2) + a(2)b(1)][\alpha(1)\beta(2) - \beta(1)\alpha(2)] \quad (1.81d)$$

An important remark is that Ψ_{HL} obeys the antisymmetry Pauli principle, the space function being *symmetric* under the interchange of electrons, whereas

the spin function is *antisymmetric*. A second remark is that Ψ_{HL} describes a *symmetric* singlet state, $S = 0$ (${}^1\Gamma_g$).

The corresponding energy E_{HL} (or E_+ , reminiscent of the + sign in the space function) can be found at the expense of some tedious but simple calculations (using expressions (1.57), (1.58), and (1.81d)), as:

$$E_{\text{HL}(S=0)} = E_+ = \langle \Psi_{\text{HL}} | \mathbf{h}(1) + \mathbf{h}(2) + \frac{e^2}{r_{12}} | \Psi_{\text{HL}} \rangle / \langle \Psi_{\text{HL}} | \Psi_{\text{HL}} \rangle \quad (1.82a)$$

$$E_+ = \{2\alpha + 2\beta S + j + k\} / (1 + S^2) \quad (1.82b)$$

We should remember that the one-electron Hamiltonian $\mathbf{h}(i)$ includes, in the potential part, the attraction of electron 1 by all the nuclei, so that α becomes equal to the energy of the hydrogen atom only at infinite distance.

A further insight into valence-bond theory can be gained by looking at the other electronic configurations and determinants which can be built: $|ab\rangle - |\bar{a}b\rangle$, $|a\bar{b}\rangle$, $|a\bar{a}\rangle$, and $|b\bar{b}\rangle$, shown in Fig. 1.42 and eqn. (1.83):

$$\Psi_- = \frac{1}{\sqrt{2(1-S^2)}} (|a\bar{b}\rangle - |\bar{a}b\rangle) \quad (1.83a)$$

$$\begin{aligned} \Psi_- &= \frac{1}{\sqrt{2(1-S^2)}} [a(1)b(2) - a(2)b(1)] [\alpha(1)\beta(2) + \beta(1)\alpha(2)] \\ &= \Psi_{-(S=1, M_S=0)} \end{aligned} \quad (1.83b)$$

We observe that Ψ_- obeys the antisymmetry Pauli principle, the space function being now *antisymmetric* under the interchange of electrons whereas the spin function is *symmetric*, so that Ψ_- describes the $M_S = 0$ component of an *antisymmetric* spin triplet state (u symmetry), $S = 1$, $2S + 1 = 3$ (${}^3\Gamma_u$). The $M_S = \pm 1$ components of the triplet are

$$|ab\rangle = \Psi_{-(S=1, M_S=1)} = \frac{1}{\sqrt{2(1-S^2)}} [a(1)b(2) - a(2)b(1)] [\alpha(1)\alpha(2)] \quad (1.83c)$$

$$|\bar{a}\bar{b}\rangle \Psi_{-(S=1, M_S=-1)} = \frac{1}{\sqrt{2(1-S^2)}} [a(1)b(2) - a(2)b(1)] [\beta(1)\beta(2)] \quad (1.83d)$$

$$|a\bar{a}\rangle = a(1)a(2) [\alpha(1)\beta(2) - \alpha(2)\beta(1)] \quad (1.83e)$$

$$|b\bar{b}\rangle = b(1)b(2) [\alpha(1)\beta(2) - \alpha(2)\beta(1)] \quad (1.83f)$$

The last two determinants (1.83e-f and Fig. 1.42B) describe two new configurations, termed charge transfer configurations since they correspond to an electron transfer from H_A to H_B or from H_B to H_A (or ionic configurations $H_A^+H_B^-$ or $H_A^-H_B^+$). They are true spin eigenfunctions. A simple linear combination leads to the states ${}^1\Gamma_g$ and ${}^1\Gamma_u$:

$${}^1\Gamma_g |a\bar{a}\rangle + |b\bar{b}\rangle = [a(1)a(2) + b(1)b(2)] [\alpha(1)\beta(2) - \alpha(2)\beta(1)] \quad (1.83g)$$

$${}^1\Gamma_u |a\bar{a}\rangle - |b\bar{b}\rangle = [a(1)a(2) - b(1)b(2)] [\alpha(1)\beta(2) - \alpha(2)\beta(1)] \quad (1.83h)$$

The states' energies, after calculations similar to those for E_+ , are written in eqns. (1.84a)–(1.84c) and allow us to compute the singlet-triplet splitting $E_{ST} = E_S - E_T = E_+ - E_-$:

Triplet ${}^3\Gamma_u$ (from eqn. (1.72b)):

$$E({}^3\Gamma_u) = E_- = \{2\alpha - 2\beta S + j - k\} / (1 - S^2) \quad (1.84a)$$

Singlet ${}^1\Gamma_g$ (from eqn. (1.72g)):

$$E({}^1\Gamma_u) = \{2\alpha + 2\beta S + j_0 + k\} / (1 + S^2) \quad (1.84b)$$

Singlet ${}^1\Gamma_u$ (from eqn. (1.72h)):

$$E({}^1\Gamma_g) = \{2\alpha - 2\beta S + j_0 - k\} / (1 - S^2) \quad (1.84c)$$

The singlet–triplet gap E_{ST} from eqns. (1.82b) and (1.84a) is:

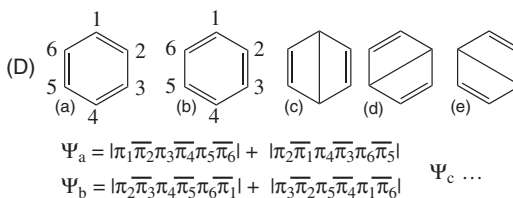
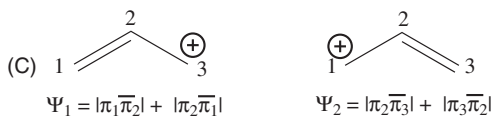
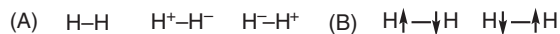
$$E_+ - E_- = [2k + 4\beta S - 2S^2(2\alpha + j)] / (1 - S^4) \quad (1.84d)$$

E_{ST} , at the first order in S , is: $E_{ST} \approx 2k + 4\beta S$ (1.84e)

We shall use these expressions, obtained very simply in the frame of the VB model, in Chapter 2. Particularly, the last expression of the singlet–triplet gap (1.84e)—an approximation at the first order in S —will be particularly useful for the understanding the magnetic properties. Remembering that integrals α , β are negative and integrals S , j , j_0 , and k are positive, it becomes obvious that the two states ${}^1\Gamma_g$ and ${}^3\Gamma_u$ arising from the ground-state determinants $|\bar{a}\bar{b}|$ and $|\bar{a}b|$ are far below in energy than the ionic states ${}^1\Gamma_u$ and ${}^1\Gamma_g$ resulting from electron transfer (since $j_0 \gg j, k$). Furthermore, among the lower ${}^1\Gamma_g$ and ${}^3\Gamma_u$, ${}^1\Gamma_g$ is the ground state, since βS is negative and $|2\beta S| > k$, when $S \neq 0$. The ground state of H_2 is a singlet, in agreement with experiment and common knowledge. In addition, when the molecule dissociates the VB energy E_+ tends to the energy of two separated hydrogen atoms, in contrast to the MO model, which gives a wrong dissociation energy. Nevertheless, the VB energy computed around the experimental equilibrium distance of H_2 is not fully satisfying: the wavefunction is too covalent, and the electrons are too localized. In some way we need to introduce some ionic configuration (H^+H^- or H^-H^+), as the exact opposite of the MO model. The combination with the excited ionic ${}^1\Gamma_g$ state of Fig. 1.42 is an obvious solution. This is discussed further in Section 1.5.3.3, where we compare the MO and VB approaches.

The VB model, corresponding to localized bonding, was extensively used for polyatomic molecules by Pauling and others. Figure 1.43 displays very simple examples of the VB description of chemical bonding through the so-called canonical structures. The total wavefunction Ψ is then written as a linear combination of the wavefunctions of the canonical structures. Even if these structures do not correspond to any physical reality, the representation in terms of localized bonding is anchored more strongly in the chemists' intuition and tradition than the delocalized MO scheme.

One can realize from these examples some of the drawbacks of the VB method, in its simplest expression, to implement calculations: for the H_2 molecule (one bond), when the MO model works with one determinant

**Fig. 1.43**

Valence-bond representations (canonical structures) of some simple molecules: (A) H₂ molecule, covalent and ionic forms; (B) H₂ molecule, making explicit the exchange of spins; (C) allyl radical and associated wavefunctions; (D) benzene molecule: the first two are the Kekulé structures with the associated wavefunctions, and the last three are the Dewar ones.

$\Psi_{\text{HF}} = |\chi_1 \chi_2|$, the VB model needs two: $\Psi_{\text{HL}} = \frac{1}{\sqrt{2(1+S^2)}} (|a\bar{b}| + |\bar{a}b|)$. With n bonds, the number of VB determinants reaches 2^n . Furthermore, contrary to the MO model where the MOs are orthogonal, the VB basis atomic orbitals $\phi_a, \phi_b \dots$ are non-orthogonal, and the non-zero overlap S increases the heaviness of the calculations.

1.5.3.2 Generalized valence bond (GVB)

The need to improve the VB model near the bonding equilibrium distance led to the introduction of a generalized VB model which basically consists (taking once more the useful example of the H₂ molecule) in replacing the simple Ψ_{VB} wavefunction (1.81d) by a slightly modified one, Ψ_{GVB} , in eqn. (1.85a) where the simple atomic wavefunctions a and b are replaced by non-orthogonal GVB wavefunctions f and g , expanded in a basis set of atomic orbitals. The expansion coefficients can be varied and chosen to minimize the energy E_{GVB} (forgetting the normalization constant and the spin part):

$$\Psi_{\text{GVB}} \propto f(1)g(2) + f(2)g(1) \quad (1.85a)$$

Let us take for example the following f and g functions:

$$f(i) = a(i) + \lambda b(i); g(i) = b(i) + \lambda a(i) \quad (1.85b)$$

It follows immediately that Ψ_{GVB} takes the new form (1.85c), where the ionic terms $a(1)a(2)$ and $b(1)b(2)$ are included:

$$\Psi_{\text{GVB}} \propto (1 + \lambda^2) [a(1)b(2) + a(2)b(1)] + 2\lambda [a(1)a(2) + b(1)b(2)] \quad (1.85c)$$

Other expressions have been proposed for $f(i)$ and $g(i)$, such as, following Coulson and Fischer:

$$f(i) = \cos\theta a(i) - \sin\theta b(i); g(i) = \sin\theta a(i) + \cos\theta b(i) \quad (1.85d)$$

The GVB method, first introduced by Coulson and Fischer and further developed by Goddard and coworkers, allows us to change the AOs during molecule formation due to the variation process to find the f and g wavefunctions. At large distance, f and g tend to a and b and give the right dissociation

energy. At bonding distance, the energy is improved. The GVB function is much simpler than the one including resonance structures, and is easier to compute. The GVB approach is one of the reasons of the revival of VB methods.

1.5.3.3 Comparison of VB and MO models

We can now compare briefly the molecular orbital and valence bond models [1.18]. We begin once more with the example of the H_2 molecule. We have shown that in the MO model the wavefunctions ψ_{\pm} are built as symmetry combinations $\psi_+ = N_+(\phi_a + \phi_b)$, $\psi_- = N_-(\phi_a - \phi_b)$, the electrons are allocated to the bonding orbital—in the general frame of the electronic configurations of Fig. 1.42A—and the two-electron wavefunction Φ arises as the product of the molecular spin-orbitals related to electron 1 and 2, $\Psi_{HF} = |\chi_1 \chi_2|$ with a space wavefunction Φ_+ or Φ_{MO} (1.77b) and (1.77c):

$$\begin{aligned}\Phi_{MO} &= N_+[\phi_a(1)\phi_b(2) + \phi_b(1)\phi_a(2)] + [\phi_a(1)\phi_a(2) + \phi_b(1)\phi_b(2)] \\ &= N_+[\Phi_{\text{covalent}} + \Phi_{\text{ionic}}]\end{aligned}$$

For a polyatomic molecule, Φ_{MO} spreads over all the atoms and is a basis for the point group irreducible representation of the molecule.

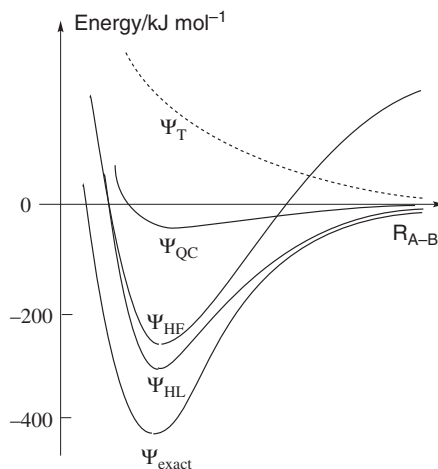
The spirit of the Heitler–London treatment is just the reverse: *first* build a two-electron wavefunction from atomic orbitals (simple Hartree product $\phi_a(1)\alpha\phi_b(2)\beta$), *then* perform a linear combination of two such products to take into account the symmetry with a space wavefunction:

$$\Phi_{HL} = N_+[\phi_a(1)\phi_b(2) + \phi_a(2)\phi_b(1)] = \Phi_{\text{covalent}} \quad (1.86)$$

The representation needs two determinants. For a polyatomic molecule (N atoms), Φ_{HL} is the weighted sum of 2^N such determinants.

When we deal with the simplest versions of the two models, therefore, a strong contradiction appears between the two: on one side (MO) the electronic structure of the molecule is described by molecular orbitals delocalized on the whole molecule, based on the group symmetry of the system, fitting rather well the ionization data. These results come from a polyelectronic monodeterminantal wavefunction, relatively easy to compute but taking only partially into account electron correlation and describing poorly the dissociation behaviour. On the other side (VB) the electronic description consists of bonds localized between two atoms, having good dissociation behaviour, but with a looser relation with symmetry. The large number of determinants and the overlap between the non-orthogonal basis orbitals make the quantum calculations much heavier. This is probably one of the reasons why the VB approach was eclipsed by its sister MO method for many decades. Figure 1.44 compares the potential energy curves as a function of the H_A – H_B distance for different wavefunctions: the antibonding triplet, the almost non-bonding case corresponding to the Hartree product (that is, without exchange), Hartree–Fock and its bad dissociation energy, Heitler–London and its weak representation of the bonding region, and the result of an ‘exact’ calculation very close to experiment.

Nevertheless, the contradiction is only apparent: we have seen that more advanced versions of the two models, elaborated to rub out the defects of the

**Fig. 1.44**

Variation of the energies of the ground state of the H_2 molecule as a function of R_{AB} (H_A-H_B) distance in the frame of different binding models: triplet state T, Hartree product (quasi-classical, QC), simple Hartree–Fock HF, simple valence bond (Heitler–London) HL, exact.

simplest formulations, converge to the same solutions. Upon proper correction the molecular orbital method can yield an almost exact polyelectronic wavefunction. This is schematized in Fig. 1.38, where two steps are shown: first the construction of the Hartree–Fock self-consistent field orbitals, then the correction by two possible post-Hartree–Fock treatments (either configuration interaction, CI, or many-body perturbation theory, MBPT). The configuration interaction process mixes the HF-SCF ground state with excited states of the same symmetry, decreases the weight of ionic terms, and gives the proper dissociation energy. The VB model, on its side, includes ionic functions (canonical structures) in the otherwise covalent wavefunction, and using a variational method improves the behaviour in the region of bonding distances. Finally, the two models converge to a space wavefunction such as:

$$\Phi = \lambda \Phi_{\text{covalent}} + \mu \Phi_{\text{ionic}} \quad (1.87)$$

with constants $\lambda \approx 0.75$ and $\mu \approx 0.25$, computed to give the ‘best’ wavefunction. More fundamentally, it can be demonstrated rigorously (see [1.15]) that a Hartree–Fock determinant (MO scheme) can be changed into other determinants by an infinity of unitary transformations which leave unchanged the total polyelectronic wavefunction, the energy, the charge density, and so on. Among the transformations, one corresponds to a localization process ending with *localized orbitals* essentially localized between two atoms (and a very weak contribution of the other atoms to ensure orthogonality). This is generally described through the hybridization process (sp , sp^2 , sp^3 . . .) of atomic orbitals in the frame of the VB scheme.

We will conclude with a brief historical survey which shows that science does not proceed linearly and is submitted, as many human activities, to ideological fluctuations. The MO and VB methods appeared historically almost at the same time. The valence bond model corresponds to a traditional representation of chemical objects by simple localized bonds, and it was widely disseminated by a charismatic Linus Pauling, able to rationalize most of the chemistry of his time in his beautiful book *The Nature of the Chemical Bond*

[1.17]. This model was thus extensively used and taught until the 1960s. After World War II the molecular orbital method began to take a leading position because of its direct relation with symmetry and as a result of easier and more systematic implementation on computing machines. In addition, several ‘failures’ were attributed to the VB model (used in its crudest form), such as the incorrect prediction of the triplet ground state of O_2 , while on the other hand it appears naturally in the frame of MO theory, or the stability of the cyclobutadiene molecule. During the 1970s the balance tilted clearly in favour of the MO model, but from about 1980 VB theory began to rise from its ashes and to offer an attractive alternative to MO theory. It was recognized in particular that most ‘failures’ of VB theory are in fact due to the use of an incomplete model. In particular, to the credit of the VB method, one can remark that the final wavefunction is built by linear combination of chemically meaningful structures. We have seen (relation (1.87) and Fig. 1.44) that at a sufficient level the MO and VB methods converge towards the same polyelectronic wavefunction. Thus, contrary to common belief, the two methods are actually equivalent. Today, choosing one rather than the other is mainly a matter of convenience, simplicity, and beauty of demonstration.

1.5.4 Density-functional theory (DFT) methods [1.19]

Density-functional theory is presently one of the most popular and successful quantum-mechanical approaches to electronic structure. It has proved a viable alternative to the usual SCF–MO method, which is hampered by the cumbersome treatment of electron correlation. The great advantage of DFT-based methods is to allow the treatment of large complicated molecules at a much lower computational cost [1.16b].

The basic principle of DFT relies on a central quantity: the total electron density $\rho(\mathbf{r})$, which has been shown by Hohenberg and Kohn to determine completely the ground-state electronic energy (the Hohenberg–Kohn theorem). It determines the total charge density through the use of a ‘functional’—a mathematical object which allows $\rho(r_1, r_2, \dots, r_N) \rightarrow \rho(\mathbf{r})$ passage and computation of the properties (see Fig. 1.38). (Note that if a function f is a rule to go from a variable x to a number $f(x)$, a functional F is a rule—or a mapping—to go from a function f to a number $F(f)$). Unfortunately, there is no universal functional. But, at the present time, after several decades of research, there are excellent enough approximations of the (still unknown) exact functional to allow an efficient implementation of the method. The first significant improvement of the DFT was the introduction of orbitals by Kohn and Sham (called Kohn–Sham orbitals—KS-DFT), which allow the exact introduction of an important component of the kinetic energy in the functional for non-interacting electrons. The rest of the kinetic energy remains to be introduced with the exchange correlation terms. Thus, KS orbitals can be considered as *molecular orbitals corrected for correlation*. An unrestricted version of the KS orbitals is available (UKS-DFT). In principle, they should not be used to predict ionization energies (though their relation with experimental quantities is still a subject of debate). As in the case of HF-SCF orbitals, the total electronic energy is not the sum of the occupied orbital energies.

Technically, most DFT methods use an iterative procedure in which one starts with an initial guess of $\rho(r)$ and then computes an effective potential, which allows the determination of one-electron orbitals. From these, a new electron density is computed and the process is repeated until convergence. This self-consistency is reminiscent of the Hartree–Fock SCF method, but the great difference is that there is *a priori* no need for post-treatment. The most difficult point in DFT methods is how to incorporate in the functional the interaction between electrons, exchange, and correlation. Different generations of DFT functionals have been elaborated to try to solve the problem: local density approximation (LDA—the density is treated as uniform electron gas); local spin density approximation (LSDA—with improvements and parametrizations proposed by Slater, Vosko, Wilk, and Nusair (VWN), and Perdew and Wang (PW)); gradient corrected methods by which the first derivative of the density is included as a variable (generalized gradient approximation, GGA, one of them proposed by Lee, Yang and Parr—LYP); inclusion of higher-order derivatives to improve the exchange and correlation (meta-GGA); and hybrid methods which introduce some parametrization for improving the exchange potential. A typical hybrid functional is the popular and widely used B3LYP proposed by Becke (B), starting with the LSDA model and successive corrections introduced by three parameters fitted from experimental data (B3LYP (for Becke-3–Lee–Yang–Parr)).

DFT methods can be applied to closed-shell or open-shell systems. For fundamental reasons, the calculation is valid for *ground-state properties*. But modifications known as time-dependent density-functional methods (TD-DFT) now allows the treatment of excited states. We shall see in Chapter 2 that for open-shell system the main drawback of DFT methods is that they are monodeterminantal, and unable to perform multideterminant calculations.

To summarize, one can state that wavefunction-based methods use an exact Hamiltonian operator and then approximations on the wavefunctions, whereas density-functional methods introduce approximation in the energy functional (Hamiltonian) and allow a free variation of the charge density.

1.6 A fundamental quantum effect: tunnelling

Before closing this chapter it appears useful to introduce a final quantum concept: quantum tunnelling, which is specific to quantum mechanics. In simple terms it states that a particle (typically an electron), present on one side of a given energy barrier U , has a non-zero probability to cross the barrier, *even if its energy $E < U$* . In classical mechanics, when a particle arrives on a barrier it is simply sent back after an elastic collision, with no chance to go through as long as $E < U$. In quantum mechanics the special properties of wavefunctions (their spatial extension) allow the crossing of the barrier. The tunnel effect is a *physics* concept, but is widely and implicitly used in *chemistry* because the chemical bond is one of its manifestations: in a molecular orbital, the electron(s) have to cross a zone of high potential energy between the atoms to go from one atom to the other.

The tunnelling phenomenon is central in some important magnetic or conducting properties of matter (Chapters 2, 3, 4, and 5). Here we present a qualitative introduction.

The process is introduced simply using Fig. 1.45. The electron is moving in a linear box along an axis x , with an energy E . It encounters an energy barrier U between $x = 0$ and a . Its wavefunction Ψ is described as a plane wave $A.e^{ikx}$: Ψ_A for $x < 0$, Ψ_B for $0 < x < a$, and Ψ_C for $x > a$. In part A there is an incident and a reflected wave, $\Psi_A = A_1.e^{ik_1x} + B_1.e^{-ik_1x}$ with $k_1^2 = 8\pi^2m_eE/h^2$ (where m_e is the rest mass of the electron). In part B (within the barrier) the wavefunction becomes $\Psi_B = A_2.e^{ik_2x} + B_2.e^{-ik_2x}$ with $k_2^2 = 8\pi^2m_e(U - E)/h^2$. In part C (beyond the barrier) the wavefunction is written $\Psi_C = A_3.e^{ik_1x}$. The only problem then is to choose the coefficients A_i, B_j to ensure the continuity of the wavefunctions and their first derivatives at the boundaries ($x = 0$ and a). We leave the details of the calculation to the reader to arrive at the expression of the probability P that the electron crosses the barrier, which is proportional to the square of the amplitude ratios of the associated wavefunctions: $P = |A_3/A_1|^2$, and then

$$P = \left[1 + \frac{1}{4} \left(\frac{k_2}{k_1} + \frac{k_1}{k_2} \right)^2 \sinh^2 k_2 a \right]^{-1} \quad \text{or} \quad P = \left[\frac{4}{\left(\frac{k_2}{k_1} + \frac{k_1}{k_2} \right)^2} \right] e^{-2k_2 a} \quad (1.88)$$

The expression at right is written in the limit $k_2 a \gg 1$. If a or $(U - E)$ tends to infinity (infinite width or height of the barrier), P tends to zero and the particle remains in the box. But for values such as $a = 1 \text{ nm}$ and $E = U = 1 \text{ eV}$, the probability P for the particle to cross the barrier becomes larger than 10^{-4} . Other quantum particles (protons . . .) can tunnel, but the tunnelling probability decreases exponentially with k_2 (eqn. (1.88)), hence with m , the mass of the particle. The tunnelling effect is then more important with the lighter electron. It is indeed observed in a nanometer-size insulating junction between two metals (Al–alumina–Al) or between a surface and a metallic tip (the basis of the principle of the scanning tunnelling microscope, STM) or between two superconducting wires (Josephson tunnelling), used in the modern and very sensitive superconducting quantum interference device (SQUID) magnetometers.

Tunnelling is also encountered in the famous double-well problem (Fig. 1.45b). In this case, two wells are located on the two sides of the barrier. By comparison with the case of Fig 1.45a, instead of travelling waves one can have *to a first approximation* stationary wavefunctions localized on one or the other well. But, unless the barrier is infinitely high or thick, they can interact, and localized wavefunctions are not eigenfunctions of the system.

Detailed study of the problem [1.20] shows the following (i and ii).

i) In a static description, energy levels located on each side of the barrier interact weakly, exactly in the same way as atomic orbitals produce molecular orbitals (see eqns. (1.14) and (1.19)). If we call Ψ_1 and Ψ_2 the (localized) wavefunctions in the absence of interaction, two new wavefunctions Ψ_+ and Ψ_- are then obtained. For a symmetrical system:

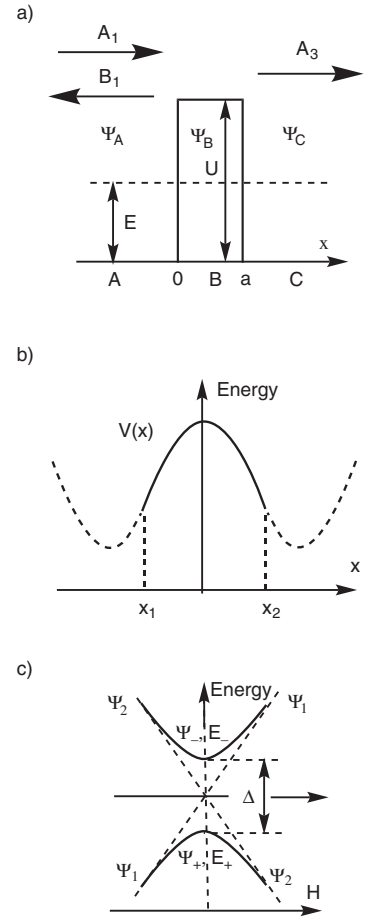


Fig. 1.45

a) A particle facing an energy barrier U . $A_1, B_1,$ and A_3 are respectively the incoming, reflected, and transmitted amplitudes (see the text); b) a system in a symmetric double potential well defined by the potential energy $V(x)$; depending on the physical problem, the x values outside the x_1-x_2 range may not be attained; c) mixing of the wavefunctions, avoided crossing and resulting tunnelling splitting Δ near the top of the barrier.

$$(a) \psi_+ = 2^{-1/2} (\psi_1 + \psi_2) \quad \text{and} \quad (b) \psi_- = 2^{-1/2} (\psi_1 - \psi_2) \quad (1.89)$$

These new levels, *now stationary eigenfunctions*, are separated by $\Delta = 2W$, where W is the coupling (see the β integral of MO theory) and Δ is the tunnel-splitting (Fig. 1.45c, central part).

ii) In a dynamic description, if at time zero the system is prepared in a non-stationary state, it will evolve in time according to the general law:

$$\psi(t) = c_+ \psi_+ \exp(-i E_+ t/\hbar) + c_- \psi_- \exp(-i E_- t/\hbar) \quad (1.90)$$

where E_+ and E_- are the energies of the stationary states, and c_+ and c_- are coefficients determined by initial conditions. One recognizes the combination of two oscillatory phenomena with slightly different frequencies, leading to a *beating process*. In particular, if the system is prepared at time zero in a pure localized state, then $c_+ = c_-$ and the system oscillates between ψ_1 and ψ_2 as a result of the alternating in-phase or out-of-phase combination of Ψ_+ and Ψ_- . The oscillation frequency ν is the difference between the frequencies of the two oscillatory processes appearing in eqn. (1.90), which are of the form (E_+/\hbar) and (E_-/\hbar) , and one obtains the Rabi formula:

$$\nu = \Delta/\hbar = 2W/\hbar \quad (1.91)$$

This oscillation process is at the heart of the tunnelling process in single-molecule magnets (Section 2.8), and intervenes also in two aspects of electron transfer: electron tunnelling (Section 3.2.1.2) and nuclear tunnelling (Section 3.2.1.3).

Another feature of the quantum tunnelling effect with the same kind of symmetric barrier is revealed in Fig. 1.45c. The system is evolving as a function of time under a given constraint H from a ground state described by a wavefunction Ψ_1 ($H < 0$) to a wavefunction Ψ_2 ($H > 0$). The corresponding energies are linear in H (the dotted lines in Fig. 1.45c). They cross at $H = 0$. If there is no tunnelling effect and if the system starts from $H < 0$, with increasing H , it remains described by the wavefunction Ψ_1 , an excited state when $H > 0$, and does not transform in Ψ_2 . Starting from Ψ_2 and decreasing H , it would remain Ψ_2 . But in quantum chemistry, when two functions of the same symmetry, like Ψ_1 and Ψ_2 , become close in energy (near $H = 0$), they combine to give rise to two new functions $\Psi_{\pm} = N_{\pm} (\Psi_1 \pm \Psi_2)$ with the corresponding energies E_{\pm} . The progressive mixing of the wavefunctions allows a smooth change from Ψ_1 to Ψ_2 , and the crossing is now avoided (the plain curves in Fig. 1.45c). The mixing is maximum at $H = 0$. The difference in energy, Δ (tunnel splitting), depends on Ψ_1 and Ψ_2 and their mixing (overlap).

For such a system the behaviour is dependent upon the rate of change of H . If H changes slowly, the Rabi oscillation appears fast and the system can 'equilibrate' by exploring the two states Ψ_1 and Ψ_2 . In other words, the smooth change between Ψ_1 and Ψ_2 is possible, and the system stays on the lower (dome-shaped) curve of Fig 1.45c. But if H changes rapidly, Rabi oscillations have not enough time to become established, and the wavefunction remains the initial one, Ψ_1 . The system then follows the ascending dotted line. These two types of behaviour will also be encountered in Chapters 2 and 3.

References

- [1.1] M. Karplus, R. N. Porter, *Atoms and Molecules*, W. A. Benjamin, Menlo Park, 1970.
- [1.2] M. Weissbluth, *Atoms and Molecules*, Academic Press, New York, 1978.
- [1.3] J. L. Rivail, *Éléments de Mécanique Quantique*, InterEditions, Editions du CNRS, Paris, 1989.
- [1.4] (a) J. P. Lowe, *Quantum Chemistry*, Academic Press, San Diego, 1993; (b) P. W. Atkins, R. L. Friedman, *Molecular Quantum Mechanics*, 4th edn., Oxford University Press, Oxford, 2005.
- [1.5] T. A. Albright, J. K. Burdett, M. Whangbo, *Orbital Interactions in Chemistry*, John Wiley, New York, 1985.
- [1.6] P. Durand, J.-P. Malrieu, in *Ab Initio Methods in Quantum Chemistry*, K. P. Lawley (ed.), Wiley, New York, 1987, vol. 1, chap. 6.
- [1.7] F. A. Cotton, *Chemical Applications of Group Theory*, John Wiley, New York, 1963.
- [1.8] (a) S. F. A. Kettle, *Symmetry and Structure*, John Wiley, New York, 1985. (b) *Tables for Group Theory*, by P. W. Atkins, M. S. Child, C. S. G. Phillips, in P. Atkins, J. de Paula, *Physical Chemistry*, 9th edn., Oxford University Press, Oxford, 2009.
- [1.9] (a) C. Iung, E. Canadell, *Description orbitale de la structure électronique des solides: 1. De la molécule aux composés 1D*, Ediscience International, Paris, 1997; (b) E. Canadell, M.-L. Doublet, C. Iung, *The Orbital Approach to the Electronic Structure of Solids*, Oxford University Press, Oxford, 2012.
- [1.10] (a) D. F. Shriver, P. W. Atkins, *Inorganic Chemistry*, 4th edn., Oxford University Press, Oxford, 1999; French edition: *Chimie Inorganique*, De Boeck Université, Louvain, 2001. (b) J. E. Huheey, E. A. Keiter, R. L. Keiter, *Inorganic Chemistry*, 4th edn., Harper Collins, New York, 1993; French edition: *Chimie Inorganique*, De Boeck Université, Louvain, 1996.
- [1.11] (a) B. N. Figgis, M. Hitchman, *Ligand Field and Its Applications*, Wiley-VCH, New York, 2000. (b) O. Kahn, *Structure électronique des éléments de transition, ions et molécules complexes*, PUF, Paris, 1977. (c) C. J. Ballhausen, *Introduction to Ligand Field Theory*, McGraw-Hill, New York, 1962.
- [1.12] Y. Jean, F. Volatron, J. K. Burdett, *An Introduction to Molecular Orbitals*, Oxford University Press, New York, 1993.
- [1.13] (a) I. B. Bersuker, *The Jahn–Teller Effect*, Cambridge University Press, Cambridge, 2010. (b) X. Assfeld, F. Volatron, *L'Actualité chimique*, Mars 2011, 26–34.
- [1.14] R. Hoffmann, *Solids and Surfaces: A Chemist's View of Bonding in Extended Structures*, VCH, New York, 1988.
- [1.15] A. Szabo, N. S. Ostlund, *Modern Quantum Chemistry*, McGraw Hill, New York, 1989.
- [1.16] (a) C. J. Cramer, *Essentials of Computational Chemistry, Theories and Models*, John Wiley, New York, 2002; (b) F. Jensen, *Introduction to Computational Chemistry*, John Wiley, New York, 2007. (c) J. Cano, E. Ruiz, S. Alvarez, M. Verdaguier, *Comments Inorg. Chem.* 20 (1998), 27–56.
- [1.17] L. Pauling, *The Nature of the Chemical Bond*, 3rd edn., Cornell University Press, Ithaca, New York, 1960.
- [1.18] R. Hoffmann, S. Shaik, P. Hiberty, A Conversation on VB versus MO Theory: a Never-Ending Rivalry? *Acc. Chem. Res.* 36 (2003), 750–6.
- [1.19] R. G. Parr, W. Yang, *Density-Functional Theory of Atoms and Molecules*, Oxford University Press, Oxford, 1989.
- [1.20] C. Cohen-Tannoudji, B. Diu, F. Laloë, *Mécanique quantique*, Tome I, Hermann, Paris, 1977, chap. 4.

2

The localized electron: magnetic properties

2.1 Introduction

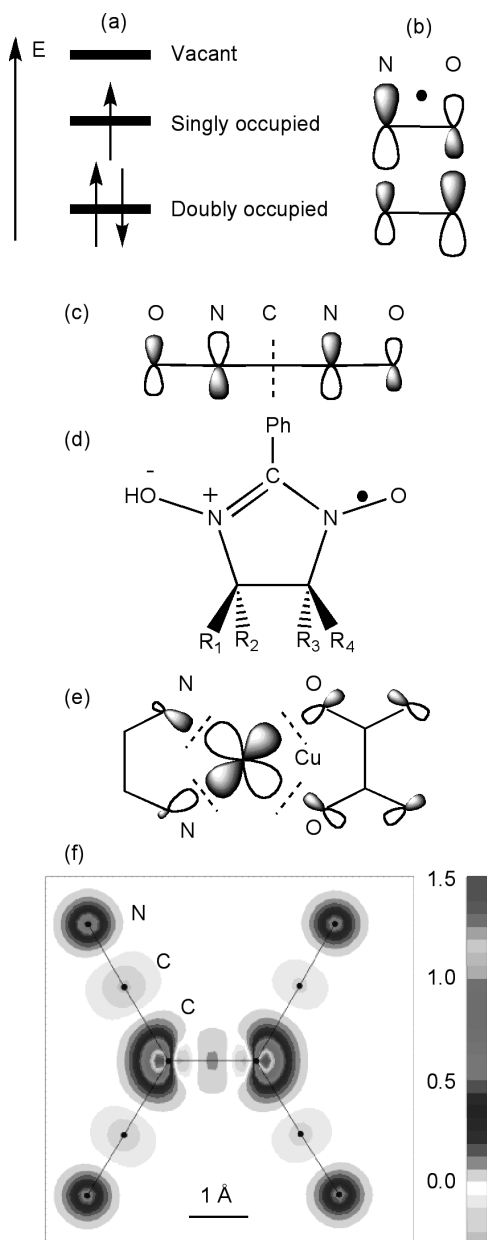
This second chapter is devoted to the magnetic properties of molecular compounds. This is an enormous domain, and we shall restrict ourselves to a few selected topics. We discard the study of diamagnetic systems, which represent most of the molecular systems, presenting only paired electrons (closed-shell molecules)—by far the most frequent in organic chemistry. We are interested instead in paramagnetic molecular systems; that is, systems presenting one or several unpaired electrons (or open-shell molecules) (Fig. 2.1). Let us recall briefly the nomenclature introduced in Chapter 1: HOMO is the highest occupied molecular orbital, LUMO the lowest unoccupied molecular orbital. We need a third category : the singly occupied molecular orbital (SOMO), carrying just one unpaired electron and responsible for the magnetic properties.

Localization, delocalization, electron transfer

Most of the chapter is devoted to so-called ‘localized electrons’—by which we mean that each unpaired electron and its ‘spin’ is localized on one part of an extended structure, called ‘site A’. The electron has no tendency to escape, to ‘jump’ on neighbouring sites B, contrary to the situation we shall encounter in Chapter 3 with electron transfer and conducting materials.

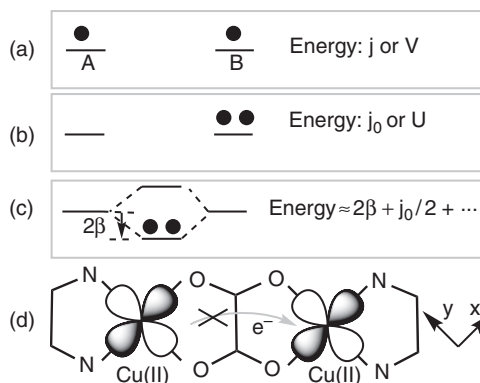
Electrons are localized when the two-electron repulsion integral on one centre j_0 (or U) is larger than the resonance integral β between the two neighbouring orbitals on A and B (see Section 1.5). Figure 2.2 distinguishes three cases: (a) one electron per orbital on sites A and B; the two-centre repulsion is j (or V); (b) one electron is transferred from A to B, the one-centre repulsion is j_0 (U); as the electrons are closer on one centre $j_0 \gg j$; U is a fundamental physical quantity to understand and to study magnetism in insulating materials, which is the case in this chapter; (c) the tendency of the electron to escape, to communicate with its neighbours, to establish bonds, is provided by the resonance integral β ; from the figure, it is easy to realize that the condition of electron localization is:

$$j_0 \gg |\beta| \quad (2.1)$$

**Fig. 2.1**

Different open-shell systems: (a) schematic molecular energy diagram emphasizing the frontier orbitals HOMO, SOMO, and LUMO. Representation of the SOMO in the case of (b) the molecular radical NO^\bullet ; (c–d) an organic radical nitronylnitroxide; (e) a 1,2-ethanediamine-Cu(II)-oxalate complex; (f) a tetracyanoethylene anion radical spin density map obtained by spin-polarized neutrons diffraction. (Courtesy of E. Ressouche.)

Let us take the example of a dinuclear complex of copper(II). Each copper has an electronic configuration d^9 , $S = 1/2$ (orbital x^2-y^2) (Fig. 2.2d). The two copper ions are surrounded by a terminal ligand (T, a diamine) and connected by a bridging ligand (B, oxalate): T–Cu(II)–B–Cu(II)–T is the ground state. The two copper are in oxidation state II and far apart ($\approx 5.2\text{\AA}$). The effective resonance integral between the two x^2-y^2 of Cu(II) is β ($< 0.1\text{eV}$). The one-centre repulsion integral j_0 is more than 5 eV. The electron transfer

**Fig. 2.2**

(a) Energies of two electrons on two centres A and B; (b) when gathered on one centre (b); (c) when engaged in a bond; (d) localized ground state of a copper(II) dinuclear complex.

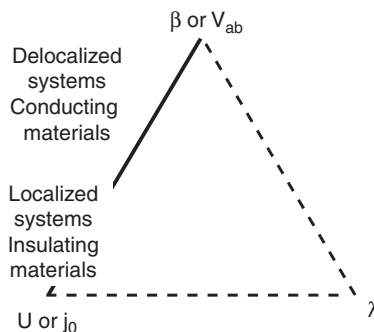
state $T-\{\text{Cu(III)}\}^+-\text{B}-\{\text{Cu(I)}\}^- -T$ (or the symmetric case) is an excited state, strongly destabilized by the one-centre repulsion j_0 on Cu(I). We have neglected the weak attractive ionic term $-e^2/R$. So the electrons ‘keep quiet’ on their respective sites.

Nevertheless, on this localized site (see the mononuclear complex 1,2-ethanediamine-Cu(II)-oxalate in Fig. 2.1e) the unpaired electron is described by a singly occupied molecular orbital (SOMO), sometimes called a *magnetic orbital* (discussed later). The wavefunction, and the corresponding spin density, are centred on the metal and partly *delocalized* on the ligands, particularly on the oxalate ligand (Fig. 2.1e). In a dinuclear metallic complex the delocalization of the spin density on the ligands is different from the electron transfer of one of the metallic centres to the other. We shall come to this point in Chapter 3. In the present chapter we deal with systems where U (j_0) is predominant, so that the properties of the localized electrons will be varied by tuning β . Figure 2.3 illustrates the changes of the properties when the $j_0 / |\beta|$ ratio varies.

The roots of the scientific domain called molecular magnetism can be found in magnetochemistry; that is, the study of magnetic properties of chemicals. The main goal of magnetochemistry was to use magnetic measurements to guess the unknown structure of molecules, especially molecular complexes [2.1]. Instead, in the 1980s *molecular magnetism* grew as a discipline dealing with the design, synthesis, study, and applications of new molecular magnetic

Fig. 2.3

Basic properties of materials according to the predominance of j_0 (U) versus β (V_{ab}). The λ parameter, located at the third summit, which introduces dynamics, will be defined in Chapter 3. See Fig. 3.11.



systems [2.2–2.6]. Deeply rooted in quantum chemistry and physics, it is now an important aspect of materials science and molecular spintronics.

This chapter briefly reviews the basics, and is organized as follows. The magnetic properties of the ‘naked’ electron itself are worthy of interest (Section 2.2). We introduce a few new quantum concepts and basic definitions concerning the controversial matter of units in magnetism (Section 2.3). We switch then to the properties of the electron located on a molecule or in a mononuclear complex. The spin cross-over phenomenon is explained in some details (Section 2.4). When the unpaired electrons belong to two (or several) centres, the story becomes even more exciting and more difficult and we propose a phenomenological approach to keep its description as simple as possible, Spin Hamiltonian (Section 2.5). We spend some time, then, with the basic understanding of why and how neighbouring electrons can ‘speak’ to each other and interact in a ferromagnetic $\uparrow\uparrow$ or antiferromagnetic $\uparrow\downarrow$ manner—through exchange interaction. Sections 2.6–2.8 describe the way to foresee magnetic properties and to synthesize new materials with predictable properties in a ‘programmed’ manner for objects of increasing size and complexity.

More information and deeper insights are found in references [2.2–2.6].

2.2 A new look at the electron

After a brief historical account of the electron in Section 1.1 and a phenomenological approach of its properties in Section 1.2, we introduce new tools for the description of this extraordinary elementary object, due to the Hamiltonian operator \mathbf{H} , its eigenfunctions (the electronic wavefunctions), and its eigenvalues (the energies). A complementary aspect is the total angular momentum, important for the discussion of the magnetic properties.

2.2.1 Orbital and spin angular momenta of the electron

When looking at the angular momentum properties of the electron, we actually find two: the orbital angular moment and the spin angular moment (and their sum).

Orbital angular momentum

The electron orbital angular moment can be introduced from the classical equivalent of a particle running perpendicular to a given axis z : speed \vec{v} , momentum $\vec{p} = m\vec{v}$, and angular moment $\vec{l} = \vec{r} \wedge \vec{p}$ (where \wedge is a vectorial product); see Fig. 2.4.

The z component of the angular moment reads therefore as in eqn. (2.2a). The other components follow by cyclic permutation:

$$(a) \quad l_z = x.p_y - y.p_x \quad (b) \quad l_x = y.p_z - z.p_y \quad (c) \quad l_y = z.p_x - x.p_z \quad (2.2a-c)$$

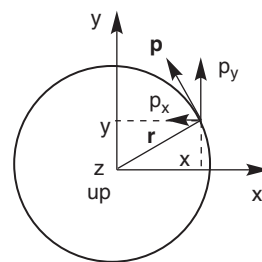


Fig. 2.4

Vectors \vec{r} and \vec{p} and their x and y components in a Cartesian frame x, y, z .

The localized electron: magnetic properties

The quantum quantities are obtained with the usual correspondences between classical and quantum coordinates (x to \mathbf{x}) and angular momenta (\mathbf{p} to \mathbf{p}) operators;

$$\begin{aligned} \text{(a) } \mathbf{L}_z &= -i\hbar \left(x \frac{\partial}{\partial y} - y \frac{\partial}{\partial x} \right) \\ \text{(b) } \mathbf{L}_x &= -i\hbar \left(y \frac{\partial}{\partial z} - z \frac{\partial}{\partial y} \right) \\ \text{(c) } \mathbf{L}_y &= -i\hbar \left(z \frac{\partial}{\partial x} - x \frac{\partial}{\partial z} \right) \end{aligned} \quad (2.3a-c)$$

The angular momentum is written as the sum of its components:

$$\vec{\mathbf{I}} = I_x \vec{\mathbf{i}} + I_y \vec{\mathbf{j}} + I_z \vec{\mathbf{k}} \quad (2.4)$$

where $\vec{\mathbf{i}}, \vec{\mathbf{j}}, \vec{\mathbf{k}}$, are the unit vectors on x, y, z .

The square of \mathbf{I} will be of particular interest later:

$$\mathbf{I}^2 = \mathbf{I}_x^2 + \mathbf{I}_y^2 + \mathbf{I}_z^2 \quad (2.5)$$

We then use the commuting properties to write the commutations relations, notated $[]$ as usual, of the orbital momentum operator:

$$[\mathbf{I}_x, \mathbf{I}_y] = i\hbar \mathbf{I}_z \quad [\mathbf{I}_y, \mathbf{I}_z] = i\hbar \mathbf{I}_x \quad [\mathbf{I}_z, \mathbf{I}_x] = i\hbar \mathbf{I}_y \quad (2.6)$$

$$[\mathbf{I}^2, \mathbf{I}_x] = 0 \quad [\mathbf{I}^2, \mathbf{I}_y] = 0 \quad [\mathbf{I}^2, \mathbf{I}_z] = 0 \quad (2.7)$$

The important conclusion is that even if the three components are non-commuting between them (eqn. 2.6), \mathbf{I}^2 commutes with each of its three components (eqn. 2.7). It follows immediately that \mathbf{I}^2 and one of its components can be known at the same time, and that they have in common a set of eigenfunctions. Such functions ϕ are defined for example by:

$$\mathbf{I}^2 \phi = a \phi \quad \mathbf{I}_z \phi = b \phi \quad (2.8)$$

The eigenvalues a and b are expressed by the quantum numbers l and m_l already introduced in a phenomenological—and abrupt—way in Section 1.2:

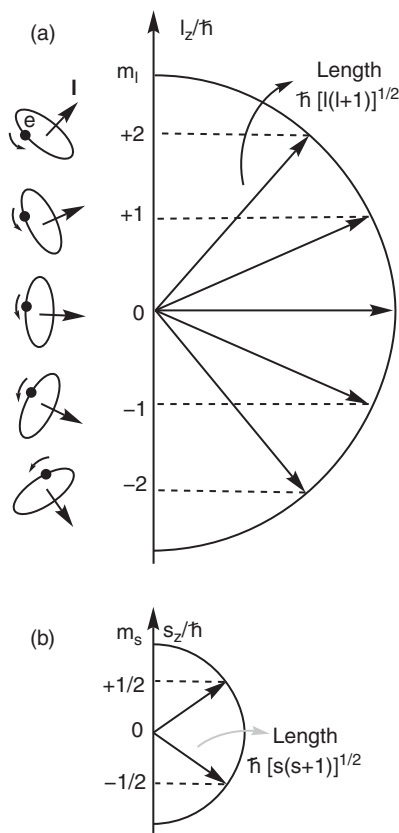
$$\mathbf{I}^2 \phi = [\hbar^2 l(l+1)] \phi \quad \text{with: } l = 0, 1, 2, \dots \quad (2.9)$$

and

$$\mathbf{I}_z \phi = [\hbar m_l] \phi \quad \text{with: } m_l = l, l-1, \dots, -l \quad (2.10)$$

The multiplicity of the orbital angular momentum is then $(2l+1)$. Orbital angular momenta are schematized in Fig. 2.5.

Neither the $\vec{\mathbf{l}}$ nor the $\vec{\mathbf{s}}$ vectors align completely with the z axis, because this would mean that their components along x and y would be simultaneously determined ($= 0$), in contradiction with the non-commuting rule (eqn. 2.6). The physical picture is based on *precession*: the $\vec{\mathbf{l}}$ vector of Fig. 2.5 has a definite projection along z , say $+l\hbar$, but its extremity precesses around z , so that its components along x and y are undetermined.

**Fig. 2.5**

(a) Orbital angular momentum, analogy with a current loop (running electron), orientation of \vec{l} , illustration of \vec{l} modulus and l_z projections when $l = 2$; (b) spin angular momentum, \vec{s} modulus and s_z projections.

l^2 eigenfunctions: a way to orbitals

At the expense of some more calculations, and using spherical polar coordinates, r , θ , and φ , it is possible also to establish that the spherical harmonics, $Y_{m_l}^1(\theta, \varphi) = Y_m^1(\theta, \varphi)$ introduced in Section 1.3 to define atomic orbitals, are also eigenfunctions of \mathbf{I}^2 and \mathbf{I}_z , and that:

$$\mathbf{I}^2 \{Y_m^1(\theta, \varphi)\} = [\hbar^2 l(l+1)] \{Y_m^1(\theta, \varphi)\} \quad (2.11)$$

$$\mathbf{I}_z \{Y_m^1(\theta, \varphi)\} = [\hbar m_l] \{Y_m^1(\theta, \varphi)\} \quad (2.12)$$

Indeed, the angular operators \mathbf{I}^2 , \mathbf{I}_z and the Hamiltonian operator \mathbf{H} commute; that is, they share a common set of eigenfunctions. The angular part of the atomic wavefunctions are therefore directly related to the angular momentum properties. The connection to the atomic orbitals is then simply realized by multiplying the spherical harmonics $Y_m^1(\theta, \varphi)$ by the radial part of the wavefunction $R_{n,l}(r)$: $\phi(r, \theta, \varphi) = R_{n,l}(r)Y_m^1(\theta, \varphi)$ (see Section 1.2.1.).

Spin angular momentum

The second part of the electron's angular momentum is more difficult to introduce, simply because it has *no classical* counterpart. The first experimental evidence of the existence of spin was provided by the experiment of Stern and

Gerlach in 1921 with silver atoms, but the interpretation in term of spin angular momentum waited some years, as told in *The Story of Spin* [2.7].

The theoretical solution of the problem—beyond the scope of this book—came later when Paul A. M. Dirac reconciled the theory of relativity (where time and space coordinates play equivalent roles) and quantum mechanics (where the time-dependent Schrödinger equation treats differently time and space coordinates) in the ‘Dirac equation’ by postulating (i) the existence of a positron, the antiparticle of electron, and (ii) the existence of an intrinsic angular momentum of the electron (in addition to the orbital angular momentum introduced by the Schrödinger equation), the spin angular momentum, whose properties fitted perfectly with the previously observed magnetic and spectroscopic experiments [2.8]. The image of a rotating particle (‘spin’), introduced by Goudsmit and Uhlenbeck in 1925, agreed by Pauli and still used frequently, is not strictly appropriate, because the electron has no measurable spatial dimension [2.7].

We can remark that even if the amount of energy related to the spin is in general tiny, its presence in quantum mechanics and therefore in physics and chemistry has enormous everyday consequences. For the while, we shall exploit the fact—without demonstration—that the spin angular momentum obeys the same basic rules as the orbital one, so that we can write equations similar to (2.9) and (2.10):

$$s^2 \phi_s = [\hbar^2 s(s+1)] \phi_s \quad \text{with: } s = 1/2 \quad (2.13)$$

and

$$s_z \phi_s = [\hbar m_s] \phi_s \quad \text{with: } m_s = s, -s; \text{ that is, } \pm 1/2 \quad (2.14)$$

where ϕ_s is a function of spin coordinates, s is a half-integer positive quantum number labelling the eigenvalues of s^2 , and m_s is a quantum number labelling the eigenvalues of the z component of the spin, s_z , along the z axis. In Chapter 1 we represented m_s either as $m_s = +1/2$, α or \uparrow , and $m_s = -1/2$, β or \downarrow . As before, the multiplicity can be written $(2s+1)$; that is, 2 (a doublet) for the isolated electron. As an electron can take different l , m_l , s , and m_s values in an atom, it is possible and convenient to write the eigenfunctions of the previous equations as $|l, m_l, s, m_s\rangle$, using Dirac bra-ket notation.

To complete our survey of the spin angular momentum, we suggest that the reader check the following results derived from eqns. (2.13) and (2.14):

$$s^2 |\alpha\rangle = \frac{3}{4} \hbar^2 |\alpha\rangle \quad s_z |\alpha\rangle = \frac{1}{2} \hbar |\alpha\rangle \quad s^2 |\beta\rangle = \frac{3}{4} \hbar^2 |\beta\rangle \quad s_z |\beta\rangle = \frac{1}{2} \hbar |\beta\rangle \quad (2.15)$$

Now, how does an electron behave when a magnetic field is applied?

2.2.2 Magnetic properties of one electron in an atom

For the one-electron atom one can define magnetic moment operators from the angular momentum operators by:

$$\boldsymbol{\mu}_l = -g_l \mu_B \mathbf{l} \quad \boldsymbol{\mu}_s = -g_s \mu_B \mathbf{s} \quad \boldsymbol{\mu} = \boldsymbol{\mu}_l + \boldsymbol{\mu}_s \quad (2.16a)$$

with eigenvalues:

$$\mu_l = -g_l \mu_B m_l \quad \mu_s = -g_s \mu_B m_s \quad (2.16b)$$

where

$$\mu_B = \frac{e\hbar}{2m_e c} \text{ (emu - cgs)} \quad \mu_B = \frac{e\hbar}{2m_e} \text{ (SI)} \quad (2.17)$$

μ_B is called the Bohr magneton, $-1 < m_l < +1$, $m_s = \pm 1/2$, $g_l = 1$, $g_s \approx 2$ so that:

$$\boldsymbol{\mu} = -\mu_B (\mathbf{l} + 2\mathbf{s}) \quad (2.18)$$

In a magnetic field (\mathbf{H}) or induction (\mathbf{B}), the energy Hamiltonian is then written:

$$\mathbf{H}_m = -\boldsymbol{\mu} \cdot \mathbf{H} \text{ (emu - cgs)} \quad \mathbf{H}_m = -\boldsymbol{\mu} \cdot \mathbf{B} \text{ (SI)} \quad (2.19)$$

These relations deserve some comments: (i) μ_B , the Bohr magneton, given by eqn. (2.17) is the natural unit for magnetic moments (the formula comes from a classical calculation for the current loop equivalent to an electron orbiting around the nucleus); its numerical value is $9.2740 \dots 10^{-24}$ A m² in SI system of units (and $9.2740 \dots 10^{-21}$ erg gauss⁻¹ in the cgs-emu system; see the next section); (ii) the orbital angular momentum \mathbf{l} gives rise to an orbital magnetic moment $\boldsymbol{\mu}_l$ defined as an *operator* in eqn. (2.16). So we are going from the simple classical physical image, where the electric current due to the moving electron ($-ev/2\pi r$) creates the orbital magnetic moment $\boldsymbol{\mu}_l$, perpendicular to the orbit plane, to the quantum situation in the atom where $\boldsymbol{\mu}_l$ is quantified by \mathbf{l} . Note that $\boldsymbol{\mu}_l$ becomes zero when the quantum number l is zero (ns electrons); (iii) the actual value of the spin magnetic moment $\boldsymbol{\mu}_s$ is about *twice as great* as would be anticipated from the angular momentum \mathbf{s} . For the spin, eqn. (2.16a) introduces a scalar quantity g_s termed the g-factor or Landé factor, which is *close to 2*, while for an orbital electronic momentum, $g_l = 1$.

This ‘anomaly’ is, of course, very intriguing. The g-factor (with a value of 2) was first introduced on an empirical basis by Landé to fit experimental data, and then by Thomas in 1926 [2.7]. In 1928, Dirac (Nobel Prize recipient in 1933) succeeded in combining special relativity with quantum mechanics, and predicted also a value of 2 for the g-factor. However, the exact value is slightly different ($g_e = 2 + \alpha/2\pi + \dots = 2.002319304\dots$, it is known to thirteen decimal places; in this formula, α is the fine structure constant $\alpha = \mu_0 e^2 c_0 / 2h = 1/137.036$). This was explained later by the theory of quantum electrodynamics of R. Feynman, J. Schwinger, and S.-I. Tomonaga (Nobel Prize recipients in 1965) [2.7]. The deviation with respect to 2.000 comes from the interaction of the electron with the surrounding electromagnetic field, *including its own field*; (iv) a final comment bears on the minus sign appearing in eqn. (2.16): it is due to the negative charge of the electron. This means that the magnetic moments of the electron (orbital and spin) are antiparallel to the respective angular momenta. When the electron is described by the 1s orbital of a hydrogen atom, without orbital angular momentum (l is zero), the magnetic properties arise only from the spin. We have thus to live with this strange concept, the spin, which is definitely different from a physical rotation of matter. But its magnetic moment exists and has tremendous consequences, even if it does not come from an equivalent electrical current.

2.2.3 The total angular momentum

Up to now we have introduced the magnetic moment operator μ_l generated by the angular momentum of the electron (due to its movement, and we therefore call it extrinsic) and the magnetic moment operator μ_s created by the spin angular momentum, which is an intrinsic property of the electron. Following Dirac, the two properties are independent of each other, at zeroth order. Nevertheless, at first order the magnetic moments associated with the angular and spin momenta \mathbf{l} and \mathbf{s} can interact. It can be seen as the tendency of one of the magnetic moments to align in the field created by the other, though the correct interpretation necessitates the more elaborate quantum relativistic theory. The interaction is known as spin-orbit coupling. This adds a first-order correction to all (energy) Hamiltonians proposed up to now, as:

$$\mathbf{H}_{\text{SO}} = \zeta \mathbf{l} \cdot \mathbf{s} \quad (2.20)$$

where ζ is a quantity termed the one-electron spin-orbit coupling constant (expressed in energy units). The spin-orbit coupling is a magnetic coupling in origin, concerning one given electron. We define, therefore, the total electronic angular momentum as:

$$\mathbf{j} = \mathbf{l} + \mathbf{s} \quad (2.21)$$

\mathbf{j} presents all the properties of a quantum angular momentum, hence:

$$\mathbf{j}^2 \phi = [\hbar^2 j(j+1)] \phi \quad \text{with } j \text{ values : } l+s, l+s-1, \dots, l-s \quad (2.22a)$$

$$\mathbf{j}_z \phi = [\hbar m_j] \phi \quad \text{with } m_j \text{ running from } j \text{ to } -j \quad (2.22b)$$

as l and s are quantum numbers labelling orbital and spin angular momentum (l integer, s half-integer), j labels the total angular momentum and takes either integer or half integer values ($j = 0, 1, 2, \dots$ or $j = 1/2, 3/2, 5/2, \dots$).

The angular momentum operators \mathbf{l} , \mathbf{s} , and \mathbf{j} of the electron and their mathematical properties (among them, commutation) will be particularly useful for describing the atomic electronic structure and the magnetic properties of many-electron atoms (see Section 2.4.1). First, however, we present a brief account of the fundamental physical quantities and units used in magnetism and molecular magnetism.

2.3 Physical quantities, definitions, units, and measurements

2.3.1 Physical quantities and definitions

This chapter is devoted to magnetic properties; that is, the behaviour of matter under the influence of a magnetic field.* In Section 2.2 we introduced some concepts to describe the interaction of the electron and the magnetic field. We give in the following a brief presentation of some important physical quantities and a few words on the problem of units. We also suggest referring to [2.9–2.13] and Chapter 1 in [2.3].

* In this chapter we shall use mainly the cgs-emu units system for magnetic quantities, because many quoted works still use it. We try nevertheless to recall the legal SI when useful. The correspondence between cgs-emu and SI units are recalled briefly at the end of this section.

We consider a small sample of volume dV subject to a magnetic field \vec{H} . It then acquires a magnetic moment (or magnetic dipole moment) $d\vec{\mu}_M$ and behaves as a tiny magnet. The magnetization \vec{M} is the magnetic moment per unit volume $\vec{M} = \frac{d\vec{\mu}_M}{dV}$. The interaction of this magnetic moment with \vec{H} (or \vec{B}) defining the z direction involves, for a unit volume, the magnetic energy E_{mag} :

$$E_{\text{mag}} = -\vec{H}\vec{M} = -HM_z(\text{cgs-emu}) \quad E_{\text{mag}} = -\vec{B}\vec{M} = -BM_z(\text{SI}) \quad (2.23)$$

which enters in the free enthalpy thermodynamic function G . We can define the free enthalpy state function G_{mag} , including the magnetic term, as (cgs-emu):

$$G_{\text{mag}} = U + PV - TS - HM \quad (2.24)$$

It can be shown easily that the magnetization is the partial derivative of G_{mag} related to H , T and P being constant:

$$M = -(\partial G_{\text{mag}}/\partial H)_{T,P} \quad (2.25)$$

The definition of magnetic susceptibility, which is a generic name for the system's response divided by the applied excitation, follows:

$$\chi = (\partial M/\partial H)_{T,P} \approx M/H \quad (2.26)$$

$$\chi = (\partial^2 G_{\text{mag}}/\partial H^2)_{T,P} \quad (2.27)$$

The magnetization \vec{M} is therefore the negative of the partial derivative of the free enthalpy with H , everything being equal; that is, it represents the rate of change in the free enthalpy with the magnetic field. The second derivative of G is the magnetic susceptibility χ per unit volume, which represents, therefore, an acceleration in the change of G . In many simple cases, when the applied field has weak values, the last expression on the right of eqn. (2.26), M/H , gives a useful approximation for χ . The susceptibility so defined is a dimensionless quantity, but it refers to a unit volume (see Section 2.3.2 on units). It is a common practice to use instead (i) the molar susceptibility χ_M given by χV_M , where V_M is the molar volume, or (ii) the mass susceptibility χ_{mass} by multiplying by the massic volume V_m .

2.3.2 Units in magnetism

Physical quantities and units are a frequent source of confusion and misunderstanding in the domain of magnetic studies [2.11–2.13]. There are several systems of units; but annoyingly, the physical quantities to which they refer have different definitions and can bear different names, despite the efforts of international committees such as IUPAC and IUPAP [2.12–2.13].

Philosophically, the coexistence of different systems is rooted in the birth and development of magnetism, which started with the concepts of magnetic poles (to which the cgs-emu system is well adapted) before the relation of magnetic fields with electrical currents was fully realized (this last case being well treated in the SI system). Thus the legal SI system is more modern and

better suited to electromagnetic machines. But at the microscopic scale, *not all magnetic moments can be associated with currents*, as shown by the strangeness of spin magnetic moments (see Section 2.2), and this is probably one of the reasons of the reluctance of the chemistry community to use the SI system.

We cannot give here an extensive account on these problems, and we restrict our discussion to the presentation of a few definitions in only two systems of units: *Système International d'Unités* (SI), and unrationalized cgs-emu (emu = **e**lectrom**m**agnetic **u**nits). In principle, only the first one should be used, but most people working in molecular magnetism still have a strong habit of working with the cgs-emu system.

The following simple considerations can prepare the reader to become familiar with both systems and to make easier the transition from cgs-emu to SI expressions and units. Three main difficulties must be overcome: (i) in the cgs-emu system, μ_0 , the permeability of vacuum is equal to 1 and is dimensionless, so it is most often omitted in the formulae; instead, in SI, μ_0 has a dimensioned value $4\pi \times 10^{-7} \text{ kg m s}^{-2} \text{ A}^{-2}$; (ii) the cgs-emu system is unrationalized, whereas SI is rationalized. 'Rationalization' was proposed to avoid having 4π factors in electromagnetic expressions in systems without spherical symmetry; (iii) the magnetization \vec{M} is defined in different ways (see in the following).

Let us recall and comment briefly on the definitions of the three fundamental vectorial quantities: \vec{H} , \vec{M} , and \vec{B} . If the field is generated by a current loop, the important quantity is \vec{H} (magnetic **field** strength), whose value at the centre of the loop is $I/2r$ (I , intensity; r , loop radius) and is expressed in A m^{-1} in the SI system. When matter is present there appears in each point a magnetization (magnetic moment per unit volume) denoted \vec{M} , whose unit is *also* A m^{-1} . Unlike the macroscopic magnetic moment $\vec{\mu}_M$ of the sample, \vec{M} is an intensive quantity. \vec{H} and \vec{M} combine to generate the magnetic **induction** (magnetic flux density) \vec{B} , which is the entity *really acting on matter* (for instance, by generating a force $q\vec{v} \wedge \vec{B}$ on a moving charge). The important relations are:

$$\vec{B} = \mu_0(\vec{H} + \vec{M}) \quad \text{with } \mu_0 = 4\pi 10^{-7} \text{ in SI} \quad (2.28a)$$

$$\vec{B} = \mu_0(\vec{H} + 4\pi\vec{M}) = (\vec{H} + 4\pi\vec{M}) \quad \text{since } \mu_0 = 1 \text{ in cgs-emu} \quad (2.28b)$$

For the two systems, one has the relation $\epsilon_0 \mu_0 c^2 = 1$.

In vacuum, \vec{B} and \vec{H} are proportional, and *even identical in the cgs-emu system*, which has favoured the sloppy habit of confusing the two. But in the presence of matter the distinction is important, and one should use the correct terms and notations: **field** for \vec{H} and **induction** for \vec{B} . Note also that the \vec{M} definitions, in SI and cgs-emu, differ by a factor 4π .

Table 2.1 is a minimal 'survival kit' for the domain, summarizing the properties of the main quantities.

The magnetic susceptibility is written as in Van Vleck's equation (2.45) in cgs-emu units, and with an additional prefactor μ_0 ($4\pi 10^{-7}$) in SI. Of course, for numerical conversions one has, in addition, to take into account the change in volume and mass units (see Table 2.1). Thus, for the frequently used

Table 2.1 Some important quantities, their definitions, units, and conversion coefficients between the unrationalized cgs-emu system and SI system. To derive the SI value from the cgs emu value, one has to multiply by the given coefficient; for instance 10^{-4} (first line, last column) means that 1 G corresponds to 10^{-4} T (or 10^4 G correspond to 1 T).

Nomenclature	Symbol	Unrationalized cgs emu	SI	Conversion coefficients
Magnetic induction, or Magnetic flux density	B	Gauss (G)	Tesla (T), or Weber m^{-2}	10^{-4} (1G = 10^{-4} T)
Magnetic field (strength)	H	Oersted (Oe)	A m^{-1}	$10^3/4\pi$
Magnetization	M	emu cm^{-3}	A m^{-1}	10^3
Permeability of vacuum	μ_0	dimensionless = 1	H m^{-1} ($\text{kg m s}^{-2} \text{A}^{-2}$)	$4\pi 10^{-7}$
Magnetic moment	m, μ	emu	A m^2	10^{-3}
Bohr magneton	μ_B	erg Oe^{-1}	J T^{-1}	10^{-3}
Volume susceptibility	χ	dimensionless	dimensionless	4
Molar susceptibility	χ_M	$\text{cm}^3 \text{mol}^{-1}$	$\text{m}^3 \text{mol}^{-1}$	$4\pi 10^{-6}$
Mass susceptibility	χ_{mass}	$\text{cm}^3 \text{g}^{-1}$	$\text{m}^3 \text{kg}^{-1}$	$4\pi 10^{-3}$

susceptibility standard $\text{Hg}[\text{Co}(\text{SCN})_4]$, for example, the numerical values of mass susceptibility are respectively $20.66 \cdot 10^{-8} \text{ m}^3 \text{ kg}^{-1}$ in SI and $16.44 \cdot 10^{-6} \text{ cm}^3 \text{ g}^{-1}$ in cgs-emu.

2.3.3 Magnetic measurements

The measurement of magnetic properties of matter can be performed by a variety of methods, each offering its own advantages and drawbacks. In recent years there has been tremendous progress in instrumentation, with huge gains in sensitivity. This tendency is general, in the frame of the strong motivation for going down to the nanoscale and the magnetic characterization of individual quantum objects. We will only briefly present and discuss some of the main methods. More can be found in [2.1, 2.4, 2.6, 2.10, 2.14].

One can broadly distinguish three classes of method (see Table 2.2). In macroscopic methods some physical quantity is measured outside the sample, and one relies on known macroscopic laws—for instance, electromagnetic induction—to know what happens inside the sample. In spectroscopic methods the interior of the sample is directly probed by using constraints (for example, \vec{H}) and particles (photons, neutrons, muons, and so on) which interact

Table 2.2 Classification of some magnetic measurement methods.

Macroscopic methods	Spectroscopic methods	Diffraction method
Torque or force measurement	EPR	Spin-Polarized
Faraday balance	X-ray magnetic circular dichroism	Neutron
Flux measurement	Muon spin resonance (relaxation)	diffraction
VSM	Inelastic neutron scattering	
SQUID		
Field measurement		
Hall probe, flux gate		
Thermodynamic measurement		
Heat capacity		

locally with the magnetic moments. There is resonance with energy absorption. Finally, in diffraction methods, there is also a local interaction but without resonance, and it concerns many identical sites at the same time.

Historically, the first and still widely used methods are of the macroscopic type, based on a torque or force measurement. One can quote Ohm's torsion balance, then the Gouy balance, using a cylindrical sample entering partially between the poles of a magnet. It was hampered by the need of a large quantity (several grammes) of matter. Later measurements used the Faraday balance, by which the sample is disposed in an inhomogeneous field with a gradient in the z (vertical) direction and a constant H $\partial H/\partial z$. It is then subject to a force related to the gradient of energy, itself given by eqn. (2.23).

$$F = -\text{grad } E = M \partial H/\partial z = \chi H \partial H/\partial z \text{ (cgs-emu)} \quad (2.29)$$

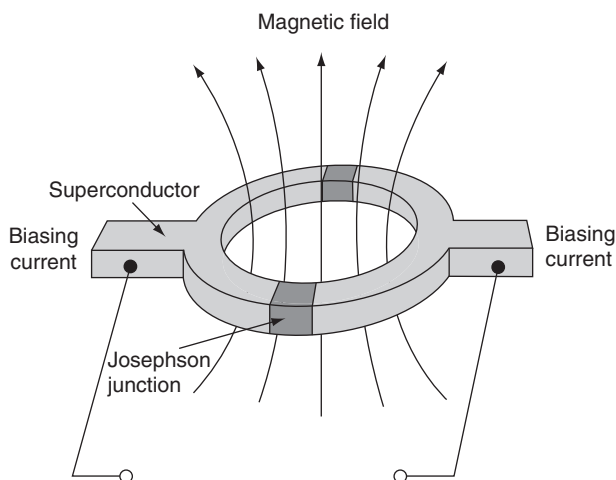
The measurement of χ thus relies on a *force* measurement, associated with a proper calibration. Twenty years ago the Faraday method was still the work-horse of magnetometry, due to its versatility. It requires only small amounts of matter (a few mg), is reasonably sensitive and of low cost, and is well adapted to measurements on a wide range of temperatures (from a few to several hundred K).

A recent development, particularly adapted to the domain of single-molecule magnets (SMM; Section 2.8) is AC susceptibility, which probes the dynamics of magnetization. When a weak magnetic field oscillating at a particular frequency ν (pulsation ω) is applied to the sample, the magnetic susceptibility becomes a complex quantity $\chi = \chi' + i \chi''$, where χ' is the in-phase component, and χ'' the out-of-phase one. If the magnetization follows instantaneously the drive field, or conversely does not follow at all, χ'' is zero. It takes large values only when the relaxation rate of magnetization is comparable with the AC pulsation. The experiment is generally performed at a fixed frequency and variable temperature (thus a variable rate of magnetization relaxation). A peak in the $\chi''(T)$ curve is then observed when the following condition $\omega = k$ is fulfilled, where $\omega = 2\pi\nu$ and k is the magnetization relaxation rate.

Another way of measuring magnetic properties is based on *flux* measurement by induction. In the vibrating sample magnetometer (VSM) method the sample vibrates rapidly between detection coils, and the change in magnetic flux induces an electromotive force. The system thus measures a magnetic moment. The method—which initially was not very sensitive—is well adapted to ferromagnetic materials, because they carry an important permanent magnetic moment, in particular to the determination of their hysteresis curve.

Flux measurement is, however, the realm of superconducting quantum interference devices (SQUID) methods. The heart of SQUID is a superconducting loop with two Josephson junctions (made of a very thin insulating barrier between two superconductors). Theory shows that the magnetic flux through the superconducting loop is quantized in units of the flux quantum Φ_0 , where $\Phi_0 = h/2e = 2.0679 \cdot 10^{-15}$ Wb (or $2.0679 \cdot 10^{-7}$ G cm²). The supercurrent can cross the Josephson junctions by the tunnel effect, but quantum interferences occur between the two possible pathways.

Due to the properties of Josephson junctions, if a constant bias current is maintained, as shown in Fig. 2.6, a voltage is measured at the terminals, which

**Fig. 2.6**

Scheme of the principle of a SQUID magnetometer. (Adapted from <<http://hyperphysics.phy-astr.gsu.edu/hbase/solids/squid.html>>)

oscillates as a result of quantization when the flux changes through the loop. If one moves the sample starting from a remote position (no flux) through the loop, it is then possible to count the number of quantum flux units due to the presence of the sample. The SQUID method can thus be considered as a special type of VSM with only a single passage of the sample, the SQUID loop acting as a very sensitive detector.

The SQUID method exhibits the highest sensitivity and is prone to extreme miniaturization, allowing the study of nano-objects or single-quantum objects. In addition, its response to perturbations is very fast. The drawbacks are its cost and complexity and the need for careful calibration (drift is frequent). A microSQUID version contains an array of miniaturized SQUIDs, and its sensitivity is still enhanced, but in a limited range in operation temperatures, because all relies on superconductivity. The magnetization reversal of a 3-nm cobalt nanoparticle (corresponding to 10^3 elementary spins) can be detected (that is, $10^{-5} \Phi_0/\sqrt{\text{Hz}}$). A review is available [2.15].

A nanoSQUID version based on carbon nanotubes (CNT-SQUID) exists. The main improvement is a much better flux coupling between the sample (the size of a molecule being 0.6 nm) and the 1nm^2 cross-section of the CNT junction) (see Section 5.2.9.2). Calculations show that it should have enough sensitivity to measure the magnetization reversal of a single high-spin Mn_{12} molecule; that is, $S = 10$ ($20 \mu_B$) (Section 2.8).

Magnetometers using field measurements are available but are less widely spread. Hall probes and microprobes are able to measure down to 10^{-6} Teslas, and flux gates down to 10^{-9} Teslas [2.10].

A few figures can help the reader to realize the enormous improvement of magnetic sensitivity measurements. With the Gouy balance, grammes were necessary, corresponding to $\approx 10^{21}$ Bohr magnetons. Routine measurements with a Faraday balance detected $10^{18} \mu_B$, with VSM $10^{16} \mu_B$, SQUID $10^{12} \mu_B$. These are rough estimations, since for each technique, more sophisticated methods can improve, in time, the sensitivity by orders of magnitude.

MicroSQUID (no more routine !) went down to $10^3 \mu_B$ and the nanoSQUID targets $20 \mu_B$.

We end this overview of macroscopic method by heat-capacity measurements, based on thermodynamics. It cannot rival the previous ones with respect to sensitivity, but it provides complementary information. The magnetic interaction between a field and a magnetic moment involves an energy (see eqn. (2.23)) which is finally exchanged with the surroundings as heat. The detected property is temperature, and in a typical measurement heat capacity is recorded as a function of temperature.

Mathematically, the heat capacity at constant magnetic field is given by:

$$C_H = -T \left(\frac{\partial^2 G_{\text{mag}}}{\partial T^2} \right)_H \quad (2.30)$$

In addition to magnetic interactions, the heat capacity of a sample contains several contributions, such as atoms and lattice vibrations, or free electrons contributions (if the sample is conducting). Thus one has to isolate the magnetic term by a proper modelization of the other terms or by reference measurements. Then the magnetic term is interpreted using magnetic models compatible with other experimental methods. The method is well adapted to cooperative phenomena such as long-range ordering occurring in phase transitions, because it gives a sharp heat capacity anomaly at the ordering temperature (critical temperature). It is a unique technique for determining the entropy and enthalpy variations across a transition. However, it demands very careful, accurate, and lengthy experiments, and relies on a proper modelization of the processes occurring inside the sample (see R. Burriel in [2.14] or M. Sorai in [2.6]).

We now consider spectroscopic methods. Here some local interaction occurs between a photon or a particle and the magnetic centre. There is a resonance process with energy absorption.

EPR: In electron paramagnetic resonance (EPR) one probes directly the paramagnetic centres. The energy of an electron spin in a magnetic field H is indeed split by the Zeeman interaction:

$$E = g_e \mu_B m_s H \quad (\text{cgs-emu}) \quad E = g_e \mu_B m_s B \quad (\text{SI}) \quad (2.31)$$

where g_e is the Landé factor, μ_B is the Bohr magneton, and m_s the spin projection ($m_s = +\frac{1}{2}$ or $-\frac{1}{2}$). The energy difference between the two states,

$$\Delta E = h\nu = g_e \mu_B H \quad (2.32)$$

can be matched by a quantum of electromagnetic radiation of frequency ν , giving rise to absorption. For a magnetic field of about 3000 G (0.3 T) the resonance occurs at a frequency of about 10 GHz, corresponding to a 3-cm wavelength (termed the X-band). The Landé factor g_e determines the position of the absorption signal. As seen previously, its value is 2.0023 for a pure electron spin, but spin-orbit coupling can introduce some orbital contribution, interactions with the nucleus spin often interfere, and g_e can deviate markedly from the spin-only value. It is often treated as a tensor. Note also that due to this possibility of orbital contribution the correct name for the method should be electron paramagnetic resonance (EPR) rather than electron spin resonance (ESR).

EPR is extremely rich in information, because the position of the signal depends on the orientation of the magnetic field with respect to the molecular axes, and also on the so-called hyperfine structure, resulting from the interaction between the electron magnetic moment and nuclear spins—for example, those of ^1H , ^{14}N , ^{31}P , ^{51}V , and so on. The quality and quantity of information is strongly enhanced by the use of different frequencies (Q- and W-bands) and high-field and high frequency (HF-EPR), since the data at each frequency provide a set of parameters which can be compared with those of other frequencies (Section 2.7). Spin Hamiltonian analysis (Section 2.5) is extremely useful here. Among the many books available we quote only one, directly concerned with molecular magnetism [2.16].

X-ray MCD. This is also a spectroscopic method, based on X-ray absorption. [2.17] It has been made possible through the unique properties of synchrotron radiation, which provides intense, tunable, and monochromatic X-ray beams. The method belongs to the general group of X-ray absorption methods for which there is electron excitation from an inner electronic orbital (core orbital, for instance 1s) towards either an empty state or a continuum of free electron states, depending on the photon energy. These possibilities correspond to XANES and EXAFS respectively. The absorption spectra exhibit edges characteristic of a given element and its core level. Synchrotron radiation can in addition provide circularly polarized beams. In such a case the absorption becomes sensitive to the magnetic state of matter through the Faraday effect. Magnetic circular dichroism is thus a difference measurement in which one compares the absorption for the two circular polarizations (clockwise or anti-clockwise), in the presence of a magnetic field parallel to the propagation direction of the radiation. Since an absorption edge is characteristic of a given element, selective information can be obtained by changing the X-ray wavelength. Using this specificity and the effect of the magnetic field, the X-ray MCD spectrum carries information on the local magnetic properties of the absorbing atoms—in particular, their spin and angular magnetic moment, a unique complementary data of the bulk macroscopic magnetization measurements. It is sensitive enough to measure monolayers of single-molecule magnets on surfaces.

Inelastic neutron scattering. The method is based on the inelastic scattering of neutrons, inelastic meaning that there can be an exchange of energy between the neutrons and the sample. Neutrons have a great penetrating power, because they are uncharged. Since they carry a spin ($S = \frac{1}{2}$) and thus a magnetic moment, they constitute efficient probes to study magnetic effects. The experiment necessitates a nuclear reactor and various devices to extract a neutron beam with homogeneous velocity (monochromatic beam), available in several countries. The neutron beam irradiates the sample with a given energy, and the scattered neutrons lose or gain some energy in the interaction with the sample. Exchanged energies can range from μeV (quantum tunnelling) to eV (electronic transitions). The method is used widely in studies of low-lying levels of single-molecule magnets [2.18].

Muon spin relaxation, rotation, resonance or μ -SR. Muons are particles similar to the electron or positron, with a spin $\frac{1}{2}$, but with a higher mass (about 207 times heavier) and a finite lifetime (2.2 μs). They are produced by particle

accelerators. As neutrons they can be spin-polarized—in this case with their magnetic moment aligned in the direction of propagation. Due to their higher mass, their penetration power is much greater than for electrons. Once thrown on the sample, positive muons (analogous to small protons) implant in the structure until they decay by emitting, in particular, a positron. Analysis of the direction of the positron's emission provides information on the interaction between the muon and the sample—in particular, the direction of the local magnetic field at the time of decay. The technique is expensive and is practiced in a few places only, but it is well adapted to magnetic and superconducting materials [2.19].

Spin polarized neutron diffraction. The method is based on diffraction; that is, the macroscopic response of an array of identical objects (atoms, molecules) arranged with a translation symmetry defining a lattice. In the well-known X-ray diffraction method, X-ray photons interact with core or valence electrons, and thus the scattering power of a given element increases with its atomic number Z . In neutron diffraction the wave-like nature of the particle allows also a diffraction process, because the associated wavelength can be tuned around 1–3 Å. But, besides their sensitivity to magnetic structures, neutrons have a complementary property with respect to X-rays: the neutron interacts with the nucleus and there is no systematic privilege to heavy elements. First, the neutron beam is polarized; that is, all neutron spins are aligned in the same direction (up or down). After interaction with a magnetized sample, the neutron signal is different for the two spin polarizations. The method is particularly adapted to the determination of ordering phenomena, through the appearance of superlattice peaks, in analogy with conventional X-ray diffraction. It is unbeatable for the determination of molecular spin densities (Fig. 2.1; J. Schweizer *et al.* in [2.14]) also produced by XMCD and NMR.

As seen previously, there are a wide variety of methods to probe the magnetic properties of matter. However the most commonly studied property is still susceptibility, in particular for paramagnetic systems. In the next section we study the relation between this macroscopic property of susceptibility and the microscopic quantities such as energy levels and molecular magnetic moments.

2.3.4 Understanding the susceptibilities: from Langevin to Van Vleck's formula

The reader is assumed to be familiar with elementary notions on magnetism of a substance; that is, diamagnetism (no unpaired spins, sample weakly repelled in a magnetic field), paramagnetism (the individual magnetic moments are independent, weak attraction in a magnetic field), ferromagnetism (the magnetic moments are interacting and kept parallel, strong attraction in a magnetic field), antiferromagnetism (identical magnetic moments are antiparallel), and ferrimagnetism (different magnetic moments are antiparallel and the resultant creates a remnant bulk moment). Precise definitions and developments can be found in many texts [2.2, 2.9, 2.10].

It took a long time for scientists to arrive at this classification of the magnetic properties. P. Curie studied experimentally the order–disorder (ferromagnetic–paramagnetic) transition at the ‘Curie’ temperature T_C , and

discovered what we know of today as the Curie law for ‘weakly magnetic’—today paramagnetic—materials, $\chi = C/T$ (with C , Curie constant). It took even more time to understand these changes with temperature. After a brief recall of the first attempts by P. Langevin, we derive a useful relation proposed by Van Vleck, which takes into account fully the quantum nature of magnetism [2.20].

In paramagnetic substances, the individual magnetic moments are uncoupled and interact independently with the magnetic field. The *classical* treatment of Langevin (1905) relates the two quantities: susceptibility and magnetic moment. It assumes that magnetic moments can orient in a continuous way and that there is a competition between the tendency for the lowest-energy configuration and thermal agitation. This competition is treated through Boltzmann statistics. The final result, valid for weak fields, is then for a sample with N_A (Avogadro’s constant) magnetic centres:

$$(a) \chi = N_A \frac{\mu^2}{3k_B T} \text{ (cgs-emu)} \quad (b) \chi = \mu_0 N_A \frac{\mu^2}{3k_B T} \text{ (SI)} \quad (2.33)$$

(a) in cgs-emu units; (b) in SI units, with $\mu_0 = 4 \pi 10^{-7}$. Boltzmann constant k_B is dimensioned, and denoted k in the following. Its value in SI is $1.380658(12) 10^{-23} \text{ J K}^{-1}$. Note that the ratio of numerical values of χ_{SI} and $\chi_{\text{cgs-emu}}$ is *not equal to* $4 \pi 10^{-7}$, because of the change in units between the two systems (see Table 2.1 for the conversion factors).

This explains the experimental Curie law (χ inversely proportional to T). It shows qualitatively the relation between susceptibility and magnetic moment. In particular, once the susceptibility is experimentally determined, it can be used ‘backwards’ to compute an effective magnetic moment μ_{eff} , thus providing a pictorial interpretation of the results. Despite that, Langevin’s equation is now only occasionally used, since it does not take in account the quantum nature of magnetic moments.

The modern way of treating theoretically paramagnetism, however, is to skip the magnetic moment concept and to relate directly the energy levels with susceptibility. This is made through the Van Vleck equation (1932) [2.20].

When a substance is subject to a magnetic field, to each magnetic centre can be associated a microscopic moment along z , denoted $\mu_{z,n}$ below and an energy level E_n . In similarity with eqn. (2.25):

$$\mu_{z,n} = - \frac{\partial E_n}{\partial H} \quad (2.34)$$

in cgs-emu. In SI, the expression would be $-\partial E_n / \partial B$.

The level occupation is governed by the Boltzmann distribution, so that the total macroscopic magnetic moment along z can be written, for one mole of substance:

$$\mu_{zM} = \mu_M \frac{N_A \sum_n \left(- \frac{\partial E_n}{\partial H} \right) \exp \left(- \frac{E_n}{kT} \right)}{\sum_n \exp \left(- \frac{E_n}{kT} \right)} \quad (2.35)$$

The localized electron: magnetic properties

To be more general, one can remark that the denominator is the partition function Z , a fundamental quantity in statistical physics:

$$Z = \sum_n \exp\left(-\frac{E_n}{kT}\right) \quad (2.36)$$

so that an expression equivalent to eqn. (2.35) is:

$$\mu_M = N_A kT \frac{\partial \ln Z}{\partial H} \quad (2.37)$$

and χ_M (molar magnetic susceptibility) can be computed from the partition function by:

$$\chi_M = \left(\frac{\partial \mu_M}{\partial H}\right)_{T,P,\dots} = N_A kT \frac{\partial^2 \ln Z}{\partial H^2} \quad (2.38)$$

Eqns. (2.37) and (2.38) are perfectly general and will be used later in the book. For the while, we come back to (2.35). As an approximation, Van Vleck proposed the development of the energies in powers of H :

$$E_n = E_n^0 + E_n^1 H + E_n^2 H^2 + \dots \quad (2.39)$$

where E_n^0 is the energy of the level number n with a zero applied magnetic field, while E_n^1 and E_n^2 are respectively the first-order and the second-order Zeeman coefficients. They can be obtained by a suitable analysis of the problem at the quantum level. Thus:

$$-\frac{\partial E_n}{\partial H} = -E_n^1 - 2E_n^2 H \quad (2.40)$$

Secondly, Van Vleck observed that generally the terms like $E_n^1 H$ in (2.39) (and *a fortiori* the second-order term) are small with respect to kT , so that one can write using this approximation:

$$\exp\left(-\frac{E_n}{kT}\right) = \left(1 - \frac{E_n^1 H}{kT}\right) \exp\left(-\frac{E_n^0}{kT}\right) \quad (2.41)$$

The molar macroscopic magnetic moment is then obtained as:

$$\mu_M = \frac{N_A \sum_n (-E_n^1 - 2E_n^2 H) \left(1 - \frac{E_n^1 H}{kT}\right) \exp\left(-\frac{E_n^0}{kT}\right)}{\sum_n \left(1 - \frac{E_n^1 H}{kT}\right) \exp\left(-\frac{E_n^0}{kT}\right)} \quad (2.42)$$

For usual magnetic fields, in paramagnetic systems, the macroscopic magnetic moment μ_M is linear in H and in addition $\mu_M = 0$ for $H = 0$. This corresponds to the observation that the susceptibility is constant, and to the fact that we exclude the case of substances with a permanent magnetization. We can thus simplify eqn. (2.42) by keeping only the terms linear in H , and noting that $\mu_M = 0$ at zero field requires that:

$$\sum_n E_n^1 \exp\left(-\frac{E_n^0}{kT}\right) = 0 \quad (2.43)$$

We finally obtain:

$$\mu_M = \frac{N_A H \sum_n \left[\frac{(E_n^1)^2}{kT} - 2E_n^2 \right] \exp\left(-\frac{E_n^0}{kT}\right)}{\sum_n \exp\left(-\frac{E_n^0}{kT}\right)} \quad (2.44)$$

and the Van Vleck equation for the molar susceptibility:

$$\chi_M = \frac{\mu_M}{H} = \frac{N_A \sum_n \left[\frac{(E_n^1)^2}{kT} - 2E_n^2 \right] \exp\left(-\frac{E_n^0}{kT}\right)}{\sum_n \exp\left(-\frac{E_n^0}{kT}\right)} \quad (2.45)$$

It is written in cgs-emu; in SI, the literal expression contains a prefactor μ_0 . The practical (numerical) conversion of cgs-emu values of χ_M to SI, must in addition take into account the change in units. The conversion coefficient is given in Table 2.1.

The equation is very general for paramagnetic systems. Its limitations are the absence of permanent magnetization (thus no long-range ordered ferro- or ferrimagnetic substance) and the condition of a weak applied field (or high temperature, H/kT small), meaning that we are far from *saturation* (the situation where all microscopic magnetic moments are aligned; see the end of this section). The treatment no longer uses the concept of microscopic magnetic moment. It is well adapted to molecular magnetism where the energy levels are obtained by successive perturbations calculations. For instance, one computes the eigenvalues of some zero-order Hamiltonian, and then introduces successive perturbations such as ligand field, spin-orbit coupling, and so on, ending with the effect of the magnetic field. Examples are given in the following sections.

As an application, we consider the case of a set of pure spin angular momenta S , without interaction. The possible energy levels come from a common level E_n^0 (the same for all centres), which is split by the Zeeman interaction (Fig. 2.7). To be more general and anticipate the case of many-electron atoms, we use the notation S instead of s and M_S instead of m_s . Thus:

$$E = E_n^0 + M_{S,n} g \mu_B H \quad (2.46)$$

where $g \approx 2$ and $M_{S,n}$ can take the values $-S, -S+1, \dots, +S$. Thus $E_n^1 = M_{S,n} g \mu_B H$.

It is possible to make an energy translation and put $E_n^0 = 0$ without changing the results, so that the susceptibility is given by:

$$\chi_M = N_A \frac{\frac{g^2 \mu_B^2}{kT} \sum_{M_S=-S}^{M_S=+S} M_S^2}{2S+1} = N_A \frac{g^2 \mu_B^2}{3kT} S(S+1) \approx \frac{n(n+2)}{8T} \quad (2.47)$$

For the simplified expressions, (i) we use the fact that the summation on M_S^2 in the numerator is identical to $S(S+1)(2S+1)/3$; (ii) we use the numerical values of the constants, $g = 2$ and the number of unpaired electrons ($n = 2S$), in cgs-emu units. We retrieve the famous Curie's law (χ is inversely proportional to T) and the relation between the Curie constant C and the number

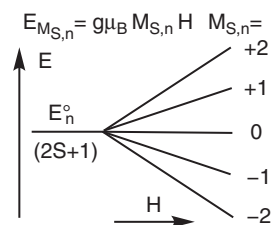


Fig. 2.7

Zeeman splitting of an energy level E_n^0 with a spin $S = 2$. The degeneracy $2S + 1 = 5$.

The localized electron: magnetic properties

n on unpaired electrons. Moreover, using eqn. (2.33) an *effective* magnetic moment can be computed. At a temperature T it is constant, and corresponds to a spin-only value.

$$\mu_{\text{eff}} = g\sqrt{S(S+1)}\mu_B = \sqrt{n(n+2)}\mu_B \quad (2.48)$$

For such a system the Van Vleck equation and the Curie law are valid only when H/kT is small. What happens when H/kT reaches higher values? Let us return to eqn. (2.37), giving the magnetization as a function of the partition function Z . In our system:

$$Z = \sum_{M_S=-S}^{M_S=+S} \exp(-M_S g \mu_B H/kT) = \frac{\sinh[(2S+1)x/2]}{\sinh(x/2)} \quad \text{with } x = g \mu_B H/k_B T \quad (2.49)$$

Performing now the calculation *without the Van Vleck approximation* eqn. (2.41), one obtains for the magnetization:

$$M = M_S B_S(y) \quad (2.50)$$

where M_S is $M_{\text{saturation}}$, the magnetization at saturation (not to be confused with a quantum number!) and y is an auxiliary variable. They are defined by:

$$M_S = n g \mu_B S \quad \text{and} \quad y = x S \quad (2.51)$$

where n is the number of paramagnetic centres in the considered volume. B_S is the Brillouin function, whose shape is displayed in Fig. 2.8.

$$B_S(y) = \frac{2S+1}{2S} \coth\left(\frac{2S+1}{2S}y\right) - \frac{1}{2S} \coth\frac{y}{2S} \quad (2.52)$$

The figure shows the phenomenon of saturation. If the $H/k_B T$ ratio is large enough, the magnetization is no longer proportional to H (hence the susceptibility is not constant), and the magnetization tends towards a limit, corresponding to the situation where all individual magnetic moments are

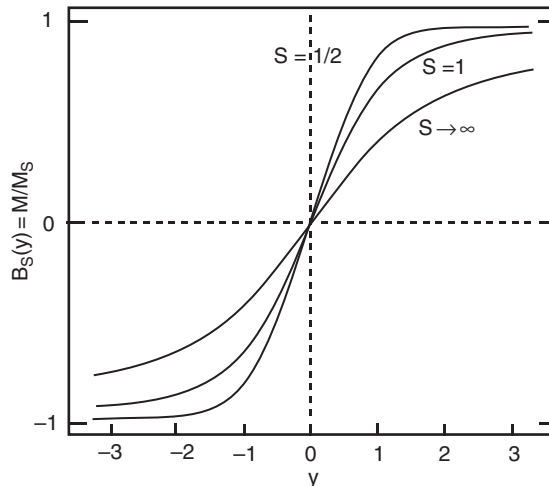


Fig. 2.8

Brillouin function governing the sample magnetization M as a function of the y parameter, itself proportional to the $H/k_B T$ ratio.

aligned in the field. However, this situation occurs only under extreme conditions. If we want $y > 2$ (the plateau on Fig. 2.8), with $S = 1/2$, $g = 2$, one needs from eqns. (2.50) and (2.52), H / T (cgs-emu) $> 30,000$; that is, for $T = 2$ K, a field of $H = 60,000$ Oe. In SI, $B/T > 3$ and $B = 6$ Teslas, achieved with modern superconducting magnets. Conversely, at room temperature and common magnetic fields (1 T), y is close to $2 \cdot 10^{-3}$, and the system is described by the linear (Van Vleck) regime. John Van Vleck was Nobel Prize recipient in 1977. [2.20b]

Saturation measurements allow determination of the number of unpaired spins, the properties of the ground state with eventually its change as a function of the magnetic field.

2.4 Many-electron atoms, mononuclear complexes, and spin cross-over

2.4.1 Many-electron atoms

The electronic structure of many electron atoms and of the mononuclear coordination complexes is determined by many factors, such as interelectronic repulsions, symmetry, and magnitude of the ligand field, spin-orbit coupling, and so on. The topic is extensively treated elsewhere (see the references in Chapter 1 and [2.21–2.26]), where the reader can find the detailed demonstrations. In this section we simply recall some main results and give them a physical/chemical meaning as much as possible.

The first step on our way to more complex systems is to use the angular momentum concepts introduced in the description of the unique electron (Section 2.2), adapted to a many-electron atom. The physical picture is based on the coupling of vectors (angular momenta) in ordinary 3D space, which gives a pictorial interpretation to the results. The coupling can be made in two ways: the LS (Russell–Saunders) coupling or the j–j coupling.

2.4.1.1 L–S or Russell–Saunders coupling

If the $\mathbf{L}s$ spin-orbit coupling is weak it is possible to obtain the angular momenta of the many-electron system through the vectorial sum of the n individual electron angular momenta—orbital on one side and spin on the other. We find:

- The x,y,z components of the orbital angular momentum \mathbf{L} as:

$$(a) \mathbf{L}_x = \sum_{i=1}^n \mathbf{l}_x(i) \quad (b) \mathbf{L}_y = \sum_{i=1}^n \mathbf{l}_y(i) \quad (c) \mathbf{L}_z = \sum_{i=1}^n \mathbf{l}_z(i) \quad (2.53)$$

- The orbital angular momentum \mathbf{L} as:

$$\mathbf{L} = \sum_{i=1}^n \mathbf{l}(i) \quad (2.54)$$

- And its square \mathbf{L}^2 as:

$$\mathbf{L}^2 = \left(\mathbf{L}_x^2 + \mathbf{L}_y^2 + \mathbf{L}_z^2 \right) \quad (2.55)$$

The localized electron: magnetic properties

The eigenvalues of \mathbf{L}^2 and L_z can be written, as in the case of *one* electron (eqns. (2.9) and (2.10)):

$$\mathbf{L}^2|L, M_L\rangle = \hbar^2 L(L+1)|L, M_L\rangle \quad (2.56)$$

$$L_z|L, M_L\rangle = \hbar M_L|L, M_L\rangle \quad (2.57)$$

L and M_L are quantum numbers labelling the operators \mathbf{L}^2 and L_z . L can take the values: 0, 1, 2, ..., and M_L runs from L to $-L$. The orbital degeneracy is therefore $2L + 1$. We need, of course, at this stage to tell how the quantum numbers l_i (for one electron i) and L (for many) are related. In the case of two electrons with quantum numbers l_1 and l_2 : L can take the values $l_1 + l_2, l_1 + l_2 - 1, \dots, |l_1 - l_2|$, sometimes named a Clebsch–Gordan series and schematized under the ‘vector sum rule’ shown in Fig. 2.9. If more than two momenta are present, the same rules apply by choosing a sequence: $l_1 + l_2$ to build l_{12} . Then $l_{12} + l_3$ gives l_{123} , and so on.

To the L quantum numbers are associated symbols, used to classify the *terms* of the atom.

$L =$	0	1	2	3	4	5	...
Term symbols:	S	P	D	F	G	H	...

Upper-case letters are used instead of the lower-case s, p, d, \dots symbols introduced for the one-electron systems (Chapter 1). *Mutatis mutandis*, we can apply the same treatment to the spin angular momentum and find the spin angular momentum \mathbf{S} as:

$$\mathbf{S} = \sum_{i=1}^n \mathbf{s}(i) \quad (2.58)$$

with similar relation as eqn. (2.53) for its components S_x, S_y, S_z .

The square \mathbf{S}^2 is:

$$\mathbf{S}^2 = (\mathbf{S}_x^2 + \mathbf{S}_y^2 + \mathbf{S}_z^2) \quad (2.59)$$

The eigenvalues of \mathbf{S}^2 and S_z can be written, as in the case of *one* electron (eqns. (2.13) and (2.14)):

$$\mathbf{S}^2|S, M_S\rangle = \hbar^2 S(S+1)|S, M_S\rangle \quad (2.60)$$

$$S_z|S, M_S\rangle = \hbar M_S|S, M_S\rangle \quad (2.61)$$

S and M_S are the quantum numbers labelling \mathbf{S}^2 and S_z .

As for L , a Clebsch–Gordan series allows linking of the quantum numbers s_i and S . For two electrons s_1 and s_2 , S can take the values $s_1 + s_2, s_1 + s_2 - 1, \dots, |s_1 - s_2|$; that is, $S = 1$ or 0 . If more than two spins are present we proceed

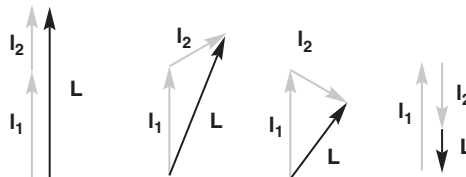


Fig. 2.9

Vectorial coupling of two orbital angular momenta \mathbf{l}_1 and \mathbf{l}_2 (grey vectors) to provide \mathbf{L} (vector triangle rule, adapted from [2.21]).

as for L: $s_1 + s_2$ gives s_{12} . Then $s_{12} + s_3$ builds s_{123} , and so on. Then, for three spins, $S = 3/2$ or $1/2$. It is obvious to generalize, and to find that S takes values $0, 1, 2, \dots$, for an even number of electronic spins and $1/2, 3/2, 5/2, \dots$, for an odd number. M_S runs by unit steps from S to $-S$: $S, S-1, \dots, -S$. The spin degeneracy is therefore $2S + 1$, which allows completion of the expression of a term L: ^{2S+1}L .

This constitutes a *spectroscopic term*. Until now, we have mainly discussed its vector properties, but it has a defined energy and, of course, a wavefunction. Unfortunately, this last one cannot generally be represented in a pictorial way, for two reasons: (i) except for the case of one electron the wavefunction is a many-electron wavefunction, and for n electrons it is a function of $3n$ space variables; (ii) the degeneracy—the number of different wavefunctions with the same energies—is usually very high, given by $(2S + 1)(2L + 1)$.

A term is thus a set of several electron wavefunctions. Although this mathematical object cannot be represented in ordinary 3D space, it has well-defined symmetry properties, which are used in the following. Its energy is a *total electronic energy*, not to be confused with orbital energies (see Section 1.5).

We use these concepts in the following sections. The demonstrations giving the terms of a given electronic configuration of a transition element, the microstates, the wavefunctions, and the energies in terms of Condon or Racah parameters, can be found in [2.22–2.24]. Those ‘free-ion’ energies will be our starting point in the $(3d^2)$ Tanabe–Sugano diagram in Fig. 2.12.

In many cases we want only to determine the ground term. Without calculations we can use the first two Hund’s rules, consecutively. Rule 1: the ground term belongs to the set of terms with the highest S ; Rule 2: among these terms the ground term is the one with the highest L . Thus, for a $(3d^2)$ configuration, among the available $^1S, ^1D, ^1G, ^3P$, and 3F terms the first rule selects 3F and 3P and the second rule allows to pick 3F . Note that Hund’s rules are used to select the ground term and *only the ground term*.

It is important to realize that this result comes from *purely electrostatic* effects. Thus Hund’s first rule (S_{\max}) means that a triplet state is more stable than a singlet with the same orbital occupancy. As seen in Section 1.5, this comes from the fact that in the triplet state electrons are on the average farther apart than in the singlet state, and thus they repel less than when they have opposite spins. For Hund’s second rule (L_{\max} , meaning that the two electrons occupy two high L orbitals), a classical picture consists of two electrons in approximately coplanar Bohr orbits, rotating in the same direction in order to maximize at any time their distance and avoid encounters [2.11, p. 32].

Finally, we introduce the total angular momentum operator \mathbf{J} , defined as:

$$\mathbf{J} = \mathbf{L} + \mathbf{S} \quad (2.62)$$

with the corresponding operators \mathbf{J} and its associated quantum number J , \mathbf{J}_z and its quantum number M_J (relations similar to the one of \mathbf{L}). The total quantum number J runs from $L + S$ to $|L-S|$ and M_J from J to $-J$ both by unit steps. The degeneracy is then $2J + 1$. As with j , J can take integer and half-integer values.

This coupling is known as the $L-S$ or Russell–Saunders coupling. As J implies spin–orbit coupling, it is usual to complete the preceding term

The localized electron: magnetic properties

formulation ^{2S+1}L using J as subscript $^{2S+1}L_J$, which defines a *level* or a *state* [2.21]. Hence, the free ion *terms*, created through electrostatic interactions, are split by spin-orbit coupling to create *states*.

The degeneracy of such a level is $2J + 1$. The energies of the levels are found using the spin-orbit Hamiltonian, applied to the many-electron atom:

$$\mathbf{H}_{\text{SO}} = \lambda \mathbf{L} \cdot \mathbf{S} \quad (2.63)$$

which is the many-electron counterpart of the one-electron spin-orbit Hamiltonian $\zeta \mathbf{l} \cdot \mathbf{s}$. λ is the many-electron spin-orbit coupling constant and has energy units. λ has the same value for all terms deriving from a given configuration and is related to ζ through:

$$\lambda = \pm \frac{\zeta}{2S} \quad (2.64)$$

We know that ζ is positive, so that eqn. (2.64) tells us that λ can be either positive or negative. Using definitions (2.56) and (2.60) and the Hamiltonian (2.63) applied to a term wavefunction ψ , defined by the quantum numbers L , S , and J , the spin-orbit splitting of the levels can be computed easily. We first identify $\mathbf{L} \cdot \mathbf{S}$ with $(\mathbf{J}^2 - \mathbf{L}^2 - \mathbf{S}^2)/2$ as usual, and we find the eigenvalue (energy) of the $^{2S+1}L_J$ state:

$$E(^{2S+1}L_J) = \langle \psi | \mathbf{H}_{\text{SO}} | \psi \rangle = \hbar^2 \frac{\lambda}{2} [J(J+1) - L(L+1) - S(S+1)] \quad (2.65)$$

The reader can check as an exercise that a similar expression is obtained for $E(^{2S+1}L_{J+1})$, and that the difference is:

$$E(^{2S+1}L_{J+1}) - E(^{2S+1}L_J) = \Delta E_{J+1,J} = \hbar^2 \lambda (J+1) = \lambda (J+1) \quad (2.66)$$

The last expression at the right is in atomic units ($\hbar = 1$), and is known as the Landé interval rule. With always the same ($3d^2$) configuration the 3F ground term gives rise to three states 3F_2 , 3F_3 , and 3F_4 levels with respective energies $(/\hbar^2) - 4\lambda$, $-\lambda$, and 3λ . The set of levels form a multiplet. The lowest state is determined by the sign of λ . Another Hund's rule (the third) helps us to find it: for a given term with a sub-shell half-filled or less, the level with the lowest J value lies lowest ($\lambda > 0$); with a sub-shell more than half-filled, the level with the highest J value lies lowest ($\lambda < 0$). See Fig. 2.10(a). The right-hand side of the figure is related to a ($3d^8$) configuration. One observes that the levels have been inverted, with the change of sign of λ . This is an illustration of a more general observation about the *electron and hole analogy*: the d^n (n electrons) and d^{10-n} (n holes) configurations give rise to the same ground term and states, but the states' order is reversed.

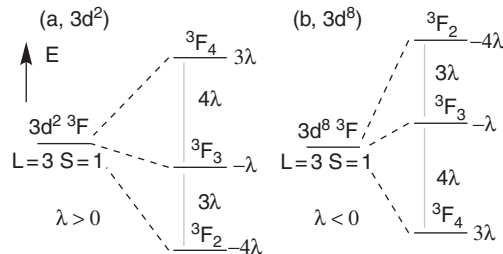


Fig. 2.10

Electron configuration, terms, and states: splitting of the 3F term by spin-orbit coupling for (a) d^2 ($\lambda > 0$, normal multiplet) and (b) d^8 configurations ($\lambda < 0$), inverted multiplet. (Adapted from [2.25].)

Landé g-factor

In many-electrons atoms the magnetic moment operator is an extension of the one of the electrons (eqn. 2.18):

$$\boldsymbol{\mu} = \mu_B (\mathbf{g}_L \mathbf{L} + \mathbf{g}_S \mathbf{S}) = \mu_B \mathbf{g}_J \mathbf{J} \quad (2.67)$$

where $g_L (=1)$, $g_S (=2)$ and g_J (given in the following) are the g-factors for orbital, spin, and total momenta. To determine g_J , the new Landé g-factor, we multiply eqn. (2.67) by \mathbf{J} :

$$\boldsymbol{\mu} \cdot \mathbf{J} = \mu_B (\mathbf{g}_L \mathbf{L} \cdot \mathbf{J} + \mathbf{g}_S \mathbf{S} \cdot \mathbf{J}) = \mu_B \mathbf{g}_J \mathbf{J} \cdot \mathbf{J} = \mu_B \mathbf{g}_J J(J+1) \quad (2.68)$$

and we use the properties of angular momenta to express $\mathbf{L} \cdot \mathbf{J}$ and $\mathbf{S} \cdot \mathbf{J}$:

$$\mathbf{L}^2 = (\mathbf{J} - \mathbf{S})^2 = \mathbf{J}^2 + \mathbf{S}^2 - 2\mathbf{J} \cdot \mathbf{S} \text{ or } \mathbf{J} \cdot \mathbf{S} = (\mathbf{J}^2 - \mathbf{L}^2 + \mathbf{S}^2)/2 \quad (2.69a)$$

with eigenvalues

$$\frac{1}{2} [J(J+1) - L(L+1) + S(S+1)] \quad (2.69b)$$

$$\mathbf{S}^2 = (\mathbf{J} - \mathbf{L})^2 = \mathbf{J}^2 + \mathbf{L}^2 - 2\mathbf{J} \cdot \mathbf{L} \text{ or } \mathbf{J} \cdot \mathbf{L} = (\mathbf{J}^2 + \mathbf{L}^2 - \mathbf{S}^2)/2 \quad (2.70a)$$

with eigenvalues

$$\frac{1}{2} [J(J+1) + L(L+1) - S(S+1)] \quad (2.70b)$$

By inserting these values in eqn. (2.68), we obtain:

$$g_J = g_L \frac{J(J+1) + L(L+1) - S(S+1)}{2J(J+1)} + g_S \frac{J(J+1) - L(L+1) + S(S+1)}{2J(J+1)} \quad (2.71a)$$

$$g_J = 1 + \frac{J(J+1) + S(S+1) - L(L+1)}{2J(J+1)} \quad (2.71b)$$

with $g_L = 1$ and $g_S = 2$. A detailed demonstration is given in appendix C of [2.11].

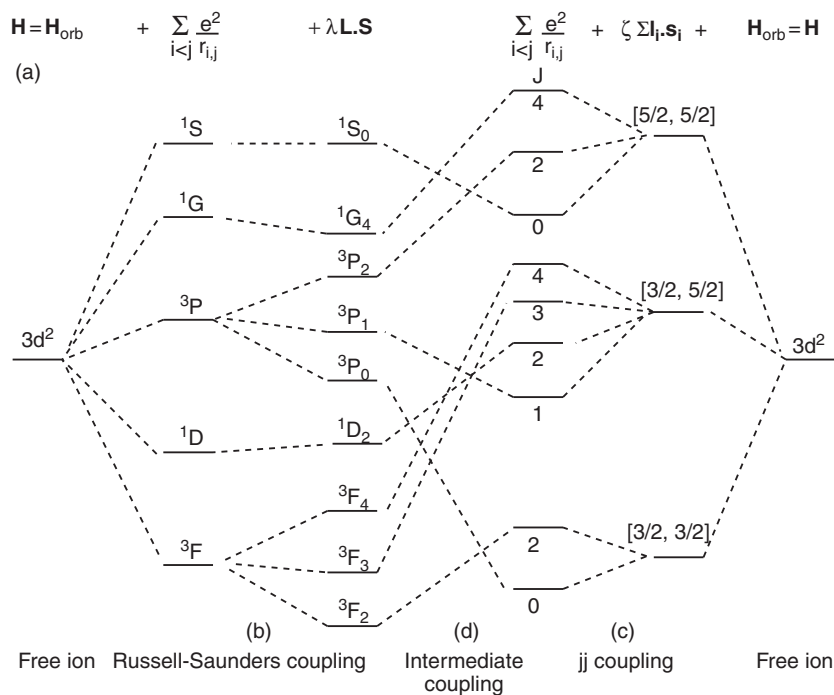
We have just described the L–S coupling when the interelectronic electrostatic repulsion which defines the terms is larger than the magnetic spin–orbit coupling. We move next to the reverse situation: the so-called j–j coupling.

2.4.1.2 j–j coupling

When the spin–orbit coupling is strong (this occurs in heavy atoms with large Z), l and s couple into j . l and s are no longer good quantum numbers, so the system must be described by j , defined in eqns. (2.21)–(2.22). The coupling of the individual $\mathbf{j}(i)$ leads to a total angular momentum \mathbf{J} :

$$\mathbf{J} = \sum_{i=1}^n \mathbf{j}(i) \quad (2.72)$$

where \mathbf{J} has the usual properties of an angular momentum. For heavy atoms (high Z), this coupling scheme must be followed; that is, it fits better with the experimental results. Let us illustrate the j–j coupling in our $(3d)^2$ example. From $l_i = 2$ and $s_i = 1/2$, we obtain $j_i = l_i \pm s_i = 5/2$ or $3/2$. Then we have three possible $(j_1 j_2)$ coupling and three energy levels: $(3/2, 3/2)$, $(3/2, 5/2)$, and

**Fig. 2.11**

Correlation diagram between the energy levels obtained with the Hamiltonian (a), through Russell–Saunders (LS) coupling (starting from the left, b) or j – j coupling (starting from the right, c); the middle situation (d) constitutes the intermediate coupling.

($5/2, 5/2$). This is schematized on the right-hand side of Fig. 2.11, which shows the successive application of the two perturbations (repulsion and spin–orbit) in different order and the correlation of their energy levels in an intermediate coupling situation. The scheme to be followed (LS or j – j) depends on the relative importance of the perturbation—electron repulsion or spin–orbit. As $\lambda \propto Z^4$, low- Z atoms should follow LS coupling (L and S are good quantum numbers), high- Z atoms should follow j – j coupling (J good quantum number), but in many cases one has to deal with an intermediate coupling. The j – j coupling scheme never occurs in its pure form. But the spin–orbit contribution becomes more and more important as the atomic number Z increases; that is, second and third transition series. In this book, all examples are treated with the LS model.

2.4.2 Mononuclear complexes, electronic structure

We now modify the preceding free-ion scheme by approaching different molecules or ions (ligands L) to the metallic atom. Here we enter into the domain of the electronic structure of coordination and organometallic compounds. Many textbooks are available, and therefore we do not reproduce material easily encountered elsewhere. Instead, we focus on a few points of interest for our future developments [2.22–2.26].

Here we deal only with central metallic atoms M to form metallic complexes ML_n . The ligands create an electrostatic field which modifies the metal energy levels. This is the crystal field approach directly related to the geometry

(symmetry) of the complex. When M–L bonds are introduced into the model, molecular orbital description allows us to define a more detailed ligand field model (introduced in Section 1.3.6). The examples chosen in this section are essentially octahedral complexes, with some indications of the related case of tetrahedral systems.

The most efficient way of treating the problem is to write the Hamiltonian with the different terms ranked by decreasing associated energies, so that, when possible, one can use perturbation expressions systematically. In addition, symmetry properties are used to simplify the treatment by providing convenient labels for the different states.

The Hamiltonian is thus written as:

$$\mathbf{H} = \mathbf{H}_{\text{orb}} + \mathbf{H}_{\text{e-e}} + \mathbf{H}_{\text{LF}} + \mathbf{H}_{\text{SO}} + \mathbf{H}_{\text{m}} \quad (2.73)$$

where \mathbf{H}_{orb} encompasses the effect of electron–nucleus attraction and mean electron–electron repulsion (thus defining the orbitals), $\mathbf{H}_{\text{e-e}}$ is the electron repulsion inside the valence shell (between 3d electrons for instance), \mathbf{H}_{LF} the ligand field term, \mathbf{H}_{so} the spin–orbit term, and finally \mathbf{H}_{m} the Zeeman term in presence of a magnetic field. As stated previously, these contributions are ranked by decreasing energies, but $\mathbf{H}_{\text{e-e}}$ and \mathbf{H}_{LF} can be of similar magnitudes. In Section 1.3.6 we saw the effect of the ligand field on *orbitals* (one-electron levels); that is, we have taken into account only \mathbf{H}_{orb} and \mathbf{H}_{LF} .

2.4.2.1 Ligand field action

Let us return to a $(3d)^2$ configuration and to the free-ion terms determined by interelectronic repulsion in the LS coupling scheme and before the intervention of spin–orbit coupling (Fig. 2.12 left). If the ligand field is now introduced (the \mathbf{H}_{LF} term of the Hamiltonian), the energies are modified and some degeneracies are lifted. How? The analysis of the problem is greatly simplified by the use of group theory. The precursor in this domain was H. Bethe, and the methodology is now well established [2.27].

In Table 1.5 we presented the character table for the O_h group, and used it to define the symmetries of *orbitals* (one-electron wavefunctions). On the one hand, MOs are a basis for the irreducible representations of the point group. On the other hand, the angular operators \mathbf{L}^2 , \mathbf{L}_z commute with Hamiltonian operator \mathbf{H} , so they share a common set of eigenfunctions. We can therefore use the symmetry for terms as we do for orbitals. The important result is that a given term behaves as an orbital characterized by the same l symbol: an S term behaves as s orbitals, P as p, D as d, and so on. Let us take the simple example of the O subgroup, retaining only the rotations of the O_h group. It can then be shown [2.27] that the character χ for a rotation of an angle φ is given by $\chi(\varphi)$:

$$\chi(\varphi) = \frac{\sin\left(L\varphi + \frac{1}{2}\right)}{\sin\frac{\varphi}{2}} \quad (2.74)$$

where L is the quantum number characterizing the term. When $\varphi = 0$, $\chi(\varphi) = 2L + 1$. Thus, considering the case of a D term ($L = 2$, $2L + 1 = 5$), the characters computed from eqn. (2.74) give a reduced version of Table 1.5 $O_h \rightarrow O$:

O	E	8C ₃	6C ₂	6C ₄	3C ₂
Γ_D	5	-1	1	-1	1

The representation Γ_D of the D term is reducible and can be reduced as $T_2 + E$, exactly in the same way as d orbitals transform as $t_2 + e$ [2.27]. As the complete O_h group contains, in addition, the inversion operation i , the exact result will be $T_{2g} + E_g$. Regarding the F ground term of a d^2 configuration, it is split into $A_2 + T_2 + T_1$. The final labels are then obtained by adding the subscript 'g' (all terms derived from a d^n configuration are symmetric—*gerade*—with respect to the inversion centre), and the superscript $2S + 1$, giving in this case ${}^3A_{2g} + {}^3T_{2g} + {}^3T_{1g}$. When dealing with optical spectroscopic properties it is enough to stop here, because the following perturbations (spin-orbit coupling and eventual magnetic field) have little or no consequences.

The resulting energy levels depend on the ligand field-splitting Δ_{oct} (or the related parameter D_q , defined by $\Delta_{oct} = 10 D_q$, for historical reasons and abridged as Δ in the following). More precisely, the behaviour depends on the ratio Δ/B , where B is Racah's parameter of interelectronic repulsion [2.22–2.23]. Finally, it is useful to display the results pictorially as a Tanabe–Sugano diagram [2.23], in which the energy is plotted in units of B against the Δ_{oct}/B ratio, the horizontal axis being the energy of the ground term taken as origin

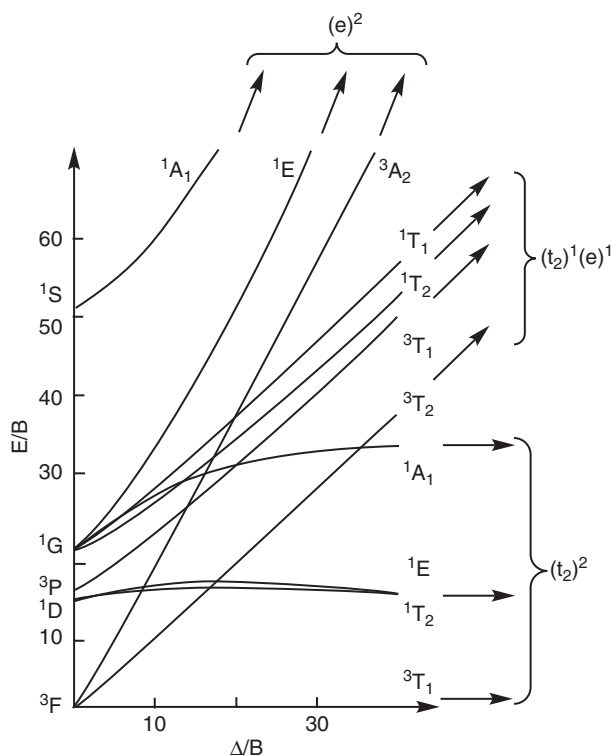


Fig. 2.12

An example of Tanabe–Sugano diagram. Case of a d^2 ion, showing for small Δ/B values the junction with free ions terms, and for strong Δ/B values the asymptotic behaviour towards configuration energies. Another example is given in Fig. 2.13 (d^6).

Table 2.3 Ground terms for d^1 to d^9 configurations in O_h symmetry.

$n \rightarrow$	1	2	3	4	5	6	7	8	9
Term	$^2T_{2g}$	$^3T_{1g}$	$^4A_{2g}$					$^3A_{2g}$	2E_g
HS Term				5E_g	$^6A_{1g}$	$^5T_{2g}$	$^4T_{1g}$		
LS Term				$^3T_{1g}$	$^2T_{2g}$	$^1A_{1g}$	2E_g		

(Fig. 2.12). Due to this choice of adimensional coordinates, the diagram is extremely versatile for a given configuration.

Table 2.3 lists the ground terms for configuration d^1 to d^9 . From d^4 to d^7 , two main types of configuration are possible: a ‘low spin’ one in which orbitals are filled according to the Aufbau principle, and a ‘high spin’ one in which one has the maximum of parallel spins. We shall return on this point in Section 2.4.3 on spin cross-over. As for the free ions, the left superscript is the spin multiplicity ($2S + 1$). Other intermediate spin configurations are not shown.

Tanabe–Sugano diagrams are extremely versatile. Thus, changing the ligand field symmetry from O_h to T_d is equivalent to changing the sign of Δ . Then the sequence of terms issued from a free-ion term is reversed. Changing the electronic configuration from d^n to d^{10-n} has the same effect, due to the electron-hole formalism (a d^9 system can be considered as a closed shell d^{10} system with one ‘electron hole’). As a consequence of these two equivalences, the Tanabe–Sugano diagram related to T_d d^n is identical to that of O_h d^{10-n} (except than one drops the u and g from the symmetry labels due to the absence of inversion centre in T_d : e, t_2 instead of e_g and t_{2g}).

The previous reasoning was based on the principle that the ligand field influence is a perturbation of the free-ion term energies. This is the ‘weak field approach’. But actually, the two types of effect are of comparable magnitude. So it is possible to start conversely from a ‘strong field approach’; that is, consider first the ligand field effect and then the electrostatic repulsion, and perform the correlation between the two approaches. The final result is still represented by the Tanabe–Sugano diagram. Thus for low Δ/B one finds the free-ion terms slightly perturbed by the ligand field. Conversely, for high Δ/B it can be noticed that the term energies corresponding to the same electronic configuration vary with the same slope (see Fig. 2.12, right-hand side). At very high Δ/B the relative energy difference between terms issued from the same configuration becomes negligible. The privileged way of reasoning is then to start from the configuration; that is, to assign electrons to orbitals and then introduce electronic repulsion as a perturbation.

When the symmetry is lower than O_h or T_d , one starts generally from the ‘strong field’ approach, which is more intuitive for chemists. Then one looks at the terms issued from each configuration, the analysis being simpler because there are much fewer orbital degeneracies.

2.4.2.2 Spin–orbit influence

We now consider the influence of spin–orbit, assumed to be weaker than ligand field and electrostatic repulsion effects because we are in the LS coupling scheme. As for the free ion, spin–orbit coupling can lift some remaining

The localized electron: magnetic properties

degeneracies. Again, group theory can help prediction of the behaviour, but a difficulty arises because the relevant formula for the rotation character is now given by eqn. (2.74), with J replacing L .

$$\chi(\varphi) = \frac{\sin\left(J\varphi + \frac{1}{2}\right)}{\sin\frac{\varphi}{2}} \quad (2.75)$$

Contrary to L , J can take half-integer values. Then a strange phenomenon occurs: if J is half-integer (say $J = \frac{1}{2}$; that is, $L = 0$, $S = \frac{1}{2}$), a 2π rotation *does not bring back the system identical to itself*. Instead, we have:

$$\chi(\varphi + 2\pi) = -\chi(\varphi) \quad (2.76)$$

This paradoxical result is rooted in the peculiar non-conventional nature of the spin and its imperfect physical representation. The mathematical treatment [2.27] (not presented here) uses ‘double groups’ with an additional operation, the 2π rotation R , which is distinct from identity and brings back the system to identity only after a 4π rotation.

In the theme of the book, the spin-orbit coupling will play a role by introducing small changes in energies (around 10^2 cm^{-1}), and also anisotropy in some properties. Indeed, the spin itself is an isotropic operator. For a pure spin the effects are the same regardless of the orientation of the spin with respect to the molecular axes. But the orientation of an angular orbital momentum is generally fixed by molecular structure. When the spin-orbit coupling mixes the two kinds of momentum, it communicates some anisotropy to the spin properties.

2.4.2.3 Other degeneracies

We have seen a number of effects (electrostatic repulsions, ligand field effect, spin-orbit coupling) leading to the progressive removal of electronic degeneracies. To these effects must be added the possible Jahn-Teller effect, which occurs when the electronic state is degenerate or when the ground state can mix with an excited state of suitable symmetry, and can also remove a degeneracy (see Section 1.3.7). Another important theorem, on the contrary, predicts when a degeneracy *cannot be lifted*. This is the case for doublet states ($S = \frac{1}{2}$) obtained from the occupation of a non-degenerate orbital by a single electron. Then the Kramers theorem states that this last degeneracy cannot be lifted by an electric interaction, but only by a magnetic field. The mathematical details are not given here, but this is a consequence of the time-reversal invariance at the microscopic scale.

If the total spin is greater than $\frac{1}{2}$ (for instance, $S = 1$ as in Ni(II) , d^8 , complexes), the Kramers theorem does not apply. Then the combined effects of ligand field and spin-orbit can partly remove the degeneracy. This is the ‘zero-field splitting’ (understood as ‘zero magnetic field splitting’), which is used in following sections.

2.4.2.4 Influence of a magnetic field: the Zeeman effect.

We end up with the smallest effect: the influence of the magnetic field H . For a paramagnetic system it can be assumed that the energy E_m of one of the states defined in Fig. 2.11 can be expressed as a power series of the magnetic field:

$$E_m = E_m^0 + E_m^1 H + E_m^2 H^2 + \dots \quad (2.77)$$

where E_m^0 is the energy in zero field, E_m^1 and E_m^2 are the first-order and second-order Zeeman coefficients respectively. At the first order in H , the Hamiltonian is:

$$\mathbf{H}_m = -\boldsymbol{\mu} \cdot \mathbf{H} = \mu_B g_J \mathbf{JH} = \mu_B (g_L \mathbf{L} + g_S \mathbf{S}) H \quad (2.78a)$$

(in cgs-emu, for SI put B in place of H).

The eigenvalues are accordingly:

$$E = \mu_B g_J M_J H \quad (2.78b)$$

with M_J varying from $-J$ to $+J$. The corresponding energy changes are in the range $\sim 1 \text{ cm}^{-1}$ per Tesla. The detailed study is dependent on the system under investigation, because the relative contributions of the orbital and spin momenta can be different from one case to another. The second-order coefficient even implies the other levels. See references [2.22, 2.24].

2.4.2.5 Quenching of orbital momentum

In coordination complexes the orbital magnetic moment related to d electrons can be manifested more or less according to the symmetry of the terms. There is a process called ‘quenching of orbital moment’ which occurs under certain circumstances and suppresses the contribution of the orbital moment. In such cases the magnetic properties are due to spin only, which incidentally simplifies greatly the behaviour.

The explanation is rooted in the basic properties of d orbitals. As seen in Section 1.2.1, in a free ion the d orbitals, solutions of the hydrogenoid Schrödinger equation, are initially obtained with angular parts of the form $\Theta(\theta) \exp(im_l \varphi)$, where m_l , the magnetic quantum number, can take the values $-2, -1, 0, 1, 2$. The corresponding wavefunctions can be denoted in Dirac form: $| -2 \rangle, | -1 \rangle, | 0 \rangle, | 1 \rangle$ and $| 2 \rangle$. To each of these orbitals is associated an orbital magnetic moment $m_l \mu_B$, but the problem is that we had to combine these ‘raw’ wavefunctions to generate real wavefunctions. Thus to a real orbital alone like $| d_{xy} \rangle$ one cannot associate an orbital magnetic moment. When the orbitals are degenerate, as in the free ion, the real orbitals can be recombined at will to generate orbitals presenting a magnetic moment. This process is not always possible in the presence of a ligand field. For instance, in O_h symmetry $| d_{xy} \rangle$ and $| d_{x^2-y^2} \rangle$ no longer have the same energy (t_{2g}, e_g are separated by Δ_{oct}) and cannot be recombined. Detailed study leads to a simple rule: terms with A or E symmetry have their magnetic moment ‘quenched’, while this is not the case for terms of T_1 or T_2 symmetry. But again, the spin-orbit coupling complicates this simple picture by introducing a mixing of the orbital and spin moments.

2.4.3 Spin cross-over: phenomenon and models

2.4.3.1 Introduction

We can apply these ligand field considerations to a very appealing phenomenon: the spin cross-over (also called spin transition), by which the metal complex can change its spin from a high-spin to a low-spin configuration. This phenomenon was discovered in 1931, and has been since the subject of a large

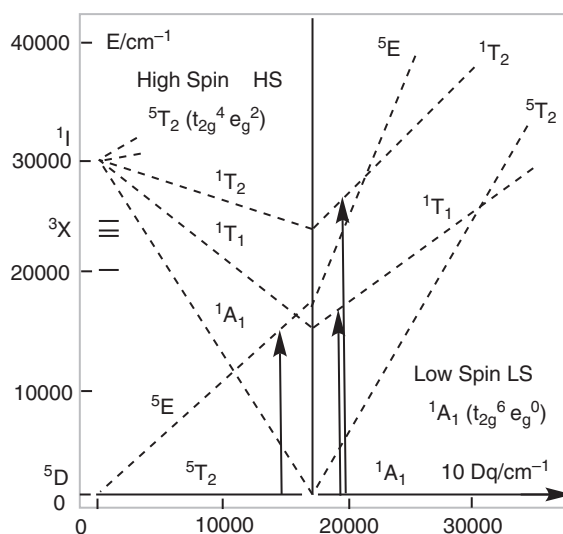
Table 2.4 Electronic configurations, term, spin, and mean pairing energy for some first row dⁿ HS and LS transition metal complexes.

d ⁿ	Ion	HS					LS				
		Configuration	Term	Spin	Π ^a	10Dq ^{HS b}	Configuration	Term	Spin	10Dq ^{LS c}	
d ⁴	Cr(II)	(t _{2g}) ³ (e _g [*]) ¹	⁵ E	2	23.5	13.9	(t _{2g}) ⁴ (e _g [*]) ⁰	³ T ₁	1	—	
d ⁴	Mn(III)	(t _{2g}) ³ (e _g [*]) ¹	⁵ E	2	28.0	21.0	(t _{2g}) ⁴ (e _g [*]) ⁰	³ T ₁	1	28 ^{c1}	
d ⁵	Mn(II)	(t _{2g}) ³ (e _g [*]) ²	⁶ A ₁	5/2	25.5	7.8	(t _{2g}) ⁵ (e _g [*]) ⁰	² T ₂	1/2	—	
d ⁵	Fe(III)	(t _{2g}) ³ (e _g [*]) ²	⁶ A ₁	5/2	30.0	13.7	(t _{2g}) ⁵ (e _g [*]) ⁰	² T ₂	1/2	35 ^{c2}	
d ⁶	Fe(II)	(t _{2g}) ⁴ (e _g [*]) ²	⁵ T ₂	2	17.6	10.4	(t _{2g}) ⁶ (e _g [*]) ⁰	¹ A	0	19.4 ^{c3}	
d ⁷	Co(II)	(t _{2g}) ⁵ (e _g [*]) ²	⁴ T ₁	3/2	22.5	9.3	(t _{2g}) ⁶ (e _g [*]) ¹	² E	1/2	15.5 ^{c4}	

^a Mean pairing energy $\Pi / 10^3 \text{ cm}^{-1}$ for the free ion (to be reduced by 70–80% in complexes—the nephelauxetic effect); ^b HS $10Dq / 10^3 \text{ cm}^{-1}$ ligand field energy in $[M(\text{H}_2\text{O})_6]^{n+}$ complexes; ^c LS $10Dq / 10^3 \text{ cm}^{-1}$ ligand field energy in selected complexes: ^{c1} $[\text{Mn}(\text{III})(\text{CN})_6]^{3-}$; ^{c2} $[\text{Fe}(\text{III})(\text{CN})_6]^{3-}$; ^{c3} $[\text{Fe}(\text{II})(\text{ptz})_6]^{2+}$; it is 33.5 for $[\text{Fe}(\text{II})(\text{CN})_6]^{4-}$; ^{c4} $[\text{Co}(\text{II})(\text{bpy})_3]^{2+}$. (Adapted from Y. Garcia [2.28] (vol. II, p. 49), [2.22], [2.30].)

number of studies. Recent reviews on this topic are available [2.3, 2.28–2.31]. Let us consider an octahedral complex of a transition metal with dⁿ electrons. For $n \leq 3$ only one configuration arises, (t_{2g})ⁿ; for $n \geq 8$ only one configuration is present: (t_{2g})⁶(e_g^{*})ⁿ⁻⁶. In these cases the concept of high and low spin has no real meaning. When we deal with $3 < n < 8$ we can find at least two electronic configurations, as shown in Table 2.4. Spin cross-over has been observed in the first line of transition elements with d⁴, Cr(II), d⁵, Fe(III), d⁶, Fe(II) and d⁷, Co(II). Rare examples are known in the second line and none in the third, due to high ligand field energies and weak spin pairing energy. Here we limit this simple analysis in terms of high/low spin, but matters can be more complicated with the occurrence of ‘intermediate spin’—in particular, when the symmetry is lowered [2.31].

A first description relies on the Tanabe–Sugano diagram (Section 2.4.2.1). The example for Fe(II), d⁶, is shown in Fig. 2.13, though for the sake of clarity,

**Fig. 2.13**

Simplified Tanabe–Sugano diagram for an octahedral Fe(II), d⁶ complex. Energy and terms are given as a function of the ligand field parameter 10Dq (see text). The Racah parameters used are $C = 4040 \text{ cm}^{-1}$ and $B = 917 \text{ cm}^{-1}$.

triplet terms are not shown. The only terms represented are the quintuplet (originating from the 5D free-ion term and giving the 5T ground term at low field) and the singlet (issued from the 1I free-ion term and giving the 1A_1 ground term at high ligand field). The ground terms are horizontal by convention. The arrows show the spin-allowed electronic transitions ($^5T \rightarrow ^5E$) in the high-spin regime and ($^1A_1 \rightarrow ^1T_1$ and $^1A_1 \rightarrow ^1T_2$) in the low-spin regime. In the case of the octahedral complex $[\text{Fe(II)}(\text{ptz})_6](\text{BF}_4)_2$ ($\text{ptz} = 1\text{-}n\text{-propyltetrazole}$) the spectroscopic data allow us to obtain $10Dq^{\text{HS}} = 11,800 \text{ cm}^{-1}$ (directly from the transition $^5T_2 \rightarrow ^5E$) and, from the transitions $^1A_1 \rightarrow ^1T_1$ and $^1A_1 \rightarrow ^1T_2$, $10Dq^{\text{LS}} = 19,410 \text{ cm}^{-1}$ and $B = 740 \text{ cm}^{-1}$. Note that there are *two* possible values (HS and LS) for the ligand field parameter (Hauser, in [2.28] vol. I, p. 49, [2.29]).

The occurrence of two values of $10Dq$ is explained by the diagram in Fig. 2.14, showing two wells of potential energy (such as enthalpy) as a function of a nuclear coordinate (for example, metal–ligand distances). The representation generally uses the harmonic oscillator model ($E = \frac{1}{2} kx^2$, where x is the variation of the metal–ligand distance from the equilibrium distance and k a force constant). Figure 2.14 represents the case of an Fe(II) complex in low- and high-spin forms ($d_{\text{Fe-L}}(\text{LS}) < d_{\text{Fe-L}}(\text{HS})$). The quantized vibration levels are represented in each well [$\nu_{\text{Fe-L}}(\text{LS}) > \nu_{\text{Fe-L}}(\text{HS})$]. The electronic interaction between the two systems, which allows the change from one to the other, is not represented: the two curves cross without mixing. In this scheme the lowest vibrational level of the HS form lies in enthalpy above the lowest vibrational level of the LS form by ΔH° , the zero-point enthalpy difference ($\Delta H^\circ = H^\circ_{\text{HS}} - H^\circ_{\text{LS}}$). The LS state is then the quantum-mechanical ground state. But if $\Delta H^\circ > 0$ and within the reach of thermal energies (kT), the HS state can become thermally populated when T increases, and the transition can occur—in particular, when taking into account the entropy factor and cooperativity (as in the following). Furthermore, the presence of an energy barrier shows that LS and HS are distinct chemical forms.

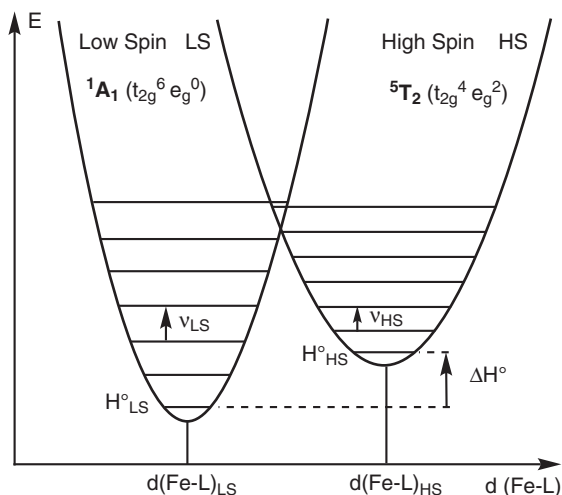


Fig. 2.14

Low-spin and high-spin potential energy wells of a Fe(II) complex as a function of the metal–ligand distance, including the vibrational levels in an harmonic oscillator model, with no interaction between the two systems.

The relation between the energy of both forms and the metal–ligand distances is straightforward. For the high-spin configuration, compared to the low-spin configuration, the e_{g}^* orbitals have a maximum occupation, thus the metal–ligand distances are larger and the ligand field parameter Δ_{oct} is weaker. In addition (this will be useful later), the metal–ligand vibrational frequency is lower, explaining the more closely spaced levels on the right-hand side of Fig. 2.14. For a given metal ion and a set of similar ligands, a useful approximate correlation exists between the ligand field Δ_{oct} and the metal–ligand distance r :

$$\frac{\Delta_{\text{oct}}^{\text{LS}}}{\Delta_{\text{oct}}^{\text{HS}}} = \left(\frac{r_{\text{HS}}}{r_{\text{LS}}} \right)^n \quad (2.79)$$

with $n = 5-6$. In the archetypal spin cross-over complex $[\text{Fe}(\text{II})(\text{ptz})_6](\text{BF}_4)_2$ quoted previously, the ratio is 1.64, in agreement with the usual Fe–N distances $r_{\text{HS}} \approx 216-220$ pm $r_{\text{LS}} \approx 196-200$ pm (from Hauser in [2.28] vol. I, p. 49).

It is frequently stated that the relative stability of the high-spin and low-spin forms depends on the comparison between Π , the mean pairing energy, and the ligand field parameter, and that spin cross-over occurs when they are of similar magnitude ($\Pi \approx 10\text{Dq}$). But since there are *two* such ligand field parameters, one has to look in more detail. Further insights can be gained with the representation of Fig. 2.15, where the zero-point enthalpy difference ΔH° between HS and LS states (Fig. 2.14) is plotted as a function of 10Dq for a model complex, $[\text{Fe}(\text{II})(\text{ptz})_6]^{2+}$, by varying the Fe–ligand distances, for example. Two lines divide the diagram: (i) the vertical representing the pairing energy Π , which does not vary so much with the spin state; Π is related to the cross-over point in the Tanabe–Sugano diagram (Fig. 2.13); (ii) the horizontal $\Delta H^\circ = 0$. Below this line ($\Delta H^\circ < 0$) the quantum-mechanical ground state is the HS state. Above this line ($\Delta H^\circ > 0$) it is the LS state. The variation of ΔH° as a function of 10Dq for the HS configuration (as 10Dq^{HS}) is displayed for low 10Dq values, and the similar curve for LS (as 10Dq^{LS}) is shown for high 10Dq values.

When $10\text{Dq}^{\text{HS}} < 10.000$ cm^{-1} , ΔH° is negative, the ground state is HS, and the LS state cannot be thermally populated (dotted line on 10Dq^{LS}). When $10\text{Dq}^{\text{LS}} > 23.000$ cm^{-1} , ΔH° is positive, and the ground state is LS. It is

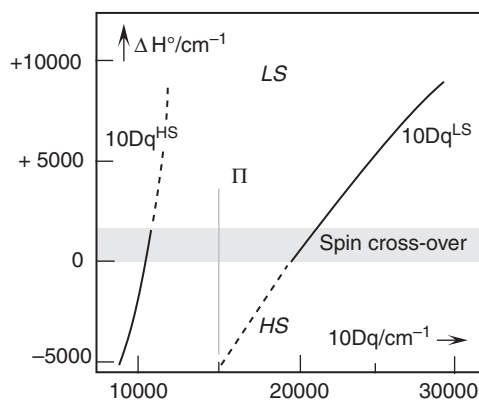


Fig. 2.15

Zero-point enthalpy ΔH° as a function of ligand field energy 10Dq drawn for the octahedral Fe(II), d^6 complex $[\text{Fe}(\text{II})(\text{ptz})_6](\text{BF}_4)_2$ and a Racah parameter reduced by 75% compared to the free ion value (nephelauxetic effect). The narrow grey area exhibits the zone where spin cross-over can occur (see text). (Adapted from Hauser in [2.28] vol. I, p. 49.)

possible to populate thermally the HS state without destroying the complex if ΔH° is not too large (say, $\Delta H^\circ \leq +2000 \text{ cm}^{-1}$). This zone, indicated in grey, corresponds to the situation where HS and LS states are both present and a spin cross-over can occur. Above this zone, ΔH° is too large for the HS state to be populated (dotted line on $10Dq^{\text{HS}}$). The spin cross-over transition can occur, therefore, in the narrow band of ligand field energies [$10Dq^{\text{HS}} \approx 10\text{--}12,500 \text{ cm}^{-1}$, $10Dq^{\text{LS}} \approx 19\text{--}22,000 \text{ cm}^{-1}$].

Thus the true condition for spin cross-over is $10Dq^{\text{HS}} \ll \Pi \ll 10Dq^{\text{LS}}$ —quite different from the simple assertion that $\Pi \approx 10Dq$. Such a conclusion can be extrapolated to other Fe–N octahedral complexes for the choice of proper ligand and the method used *mutatis mutandis* for other metal d^n ions ($d^4 < d^n < d^7$).

2.4.3.2 How do we follow the HS–LS cross-over?

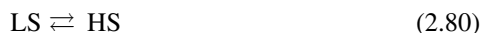
The transition can be followed using any technique sensitive to the change of one of the electronic, vibrational, and structural parameters during the transition [2.29]. The magnetic susceptibility measurement by SQUID magnetometry is by far the most basic and most used technique (see Section 2.3). It produces directly the HS/LS fractions. Heat capacity measurement is the only technique able to provide the thermodynamical parameters ΔH° and ΔS° . Mössbauer spectrometry is very useful to follow the spin state of iron(II) and iron(III) complexes through the isomer shift displacement and the quadrupole splitting. For each of the LS and HS states, infrared or Raman spectroscopy produces the change in vibrational states, whereas electronic spectroscopy produces the energy and intensity of the electronic transitions. The structural changes can be followed using single crystal X-ray or neutron diffraction when crystals are available and do not shrink at the transition. The local structure (surroundings of the metal ion) can be followed, whatever the shape of the sample, by X-ray absorption spectroscopy.

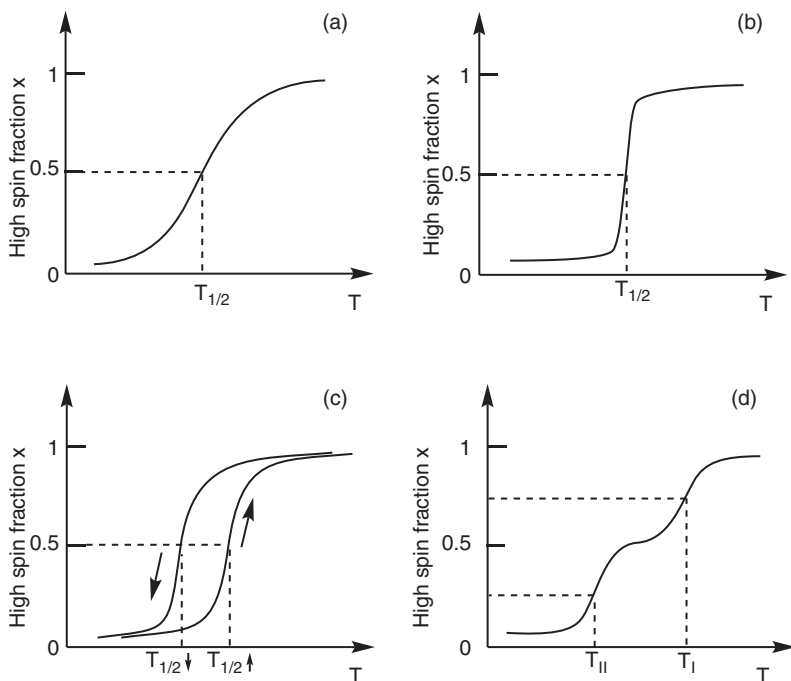
The most common way of depicting the spin transition is to plot the high-spin fraction x as a function of temperature. As will be seen in the following, it always increases with temperature, but the variation can take several forms (Fig. 2.16). One can have a gradual transition, or an abrupt one occurring in a small temperature interval (a few K). In some cases an hysteresis loop is observed; that is, the trajectories $x(T)$ are not the same when warming or cooling. Finally, there are examples of two-step transitions for which in a given temperature interval the high-spin fraction remains close to 50%.

2.4.3.3 Thermodynamics of the LS–HS equilibrium

The spin cross-over (spin transition) has been the subject of a large number of theoretical studies, some of which are presented in reviews such as [2.28, 2.30]. A first aspect to consider is the thermodynamics—in particular, the relative stabilities of the LS and HS forms. For the moment we compare these two forms as pure solids. (In Section 2.4.3.4 we will consider the possibility of solid solutions.)

The LS/HS conversion can be considered as a chemical equilibrium:



**Fig. 2.16**

Different behaviour types for a low-spin–high-spin transition: (a) smooth; (b) abrupt; (c) hysteresis; (d) two-step.

In the standard state (pure solids) the enthalpy, entropy, and free enthalpy changes are $\Delta H_{\text{LS} \rightarrow \text{HS}}^\circ$ ($= H_{\text{HS}}^\circ - H_{\text{LS}}^\circ$), $\Delta S_{\text{LS} \rightarrow \text{HS}}^\circ$ and $\Delta G_{\text{LS} \rightarrow \text{HS}}^\circ$, defined similarly. We note for simplicity, ΔH° , ΔS° , and ΔG° respectively. ΔS° is positive because it encompasses an electronic term $\Delta H_{\text{el}}^\circ$ and a vibrational term $\Delta H_{\text{vib}}^\circ$, both positive. The electronic term is linked to the degeneracy of electronic states. It is given by:

$$\Delta S_{\text{el}}^\circ = R \ln (\Omega_{\text{HS}} / \Omega_{\text{LS}}) \quad (2.81)$$

with

$$\Omega = \Omega_{\text{spin}} \Omega_{\text{angular}} = (2S + 1)(2L + 1) \quad (2.82)$$

At least, Ω_{spin} is larger for the HS state. $\Delta S_{\text{vib}}^\circ$ is positive because the vibrational states are more closely spaced and the bond lengths are higher in the HS form. Broadly speaking, the bonds are weaker in the HS form, allowing more degrees of freedom. In one of the most studied examples of iron(II) spin cross-over systems, $[\text{Fe}^{\text{II}}(\text{phen})_2(\text{NCS})_2]$, (phen = 1,10-phenanthroline), the transition occurs between ${}^5\text{T}$ ($2S + 1 = 5$; $2L + 1 = 3$) and ${}^1\text{A}$ ($2S + 1 = 1$; $2L + 1 = 1$) states, thus $\Delta S_{\text{el}}^\circ = R \ln (5 \times 3/1) = 13.38 \text{ J K}^{-1} \text{ mol}^{-1}$, while the total $\Delta S^\circ = 48.78 \text{ J K}^{-1} \text{ mol}^{-1}$, showing that most of the entropy change derives from the vibrational term (intra- and intermolecular).

In order to observe a thermal spin transition, ΔH° must be positive (as shown in Figs. 2.13 and 2.15), so that at low temperature the LS form is the most stable, while at high enough temperature $\Delta G^\circ = \Delta H^\circ - T \Delta S^\circ$ has a chance to become negative. $\Delta G^\circ = 0$ for a peculiar temperature that we denote $T_{1/2}$:

$$T_{1/2} = \Delta H^\circ / \Delta S^\circ \quad (2.83)$$

$T_{1/2}$ is the temperature for which the high and low spin fractions are equal to $1/2$. Note that when an hysteresis is present, $T_{1/2}$ cannot be measured directly, because it is inside the loop (see in the following). In the case of the previously mentioned $[\text{Fe}^{\text{II}}(\text{phen})_2(\text{NCS})_2]$ complex, $\Delta S^\circ = 48.78 \text{ J K}^{-1} \text{ mol}^{-1}$, $\Delta H^\circ = 8.60 \text{ kJ mol}^{-1}$, and $T_{1/2} = 176.29 \text{ K}$.

From a chemical point of view, the first and immediate factor controlling the $T_{1/2}$ temperature is the magnitude of the ligand field. Thus, let us consider the effect of substitution on the phen ligands of the $[\text{Fe}(\text{phen})_3]^{2+}$ complex [2.28]. The starting compound is LS at all temperatures. Incorporation of a methyl group in the 2-position of phenanthroline (adjacent to the N atom) reduces the ligand field, because steric interligand repulsions preclude the close approach of nitrogen to the metal. As a consequence, a spin cross-over is observed (that is, the HS state begins to be of comparable stability with the LS). With Cl, which is both bulky and electron-withdrawing, the ligand field still decreases and only the HS form is observed at all temperatures.

Another example is provided by the series derived from $[\text{Fe}(\text{py})_4(\text{NCS})_2]$, the latter being HS at all temperatures. Substituting two pyridine molecules by an 1,10-phenanthroline gives $[\text{Fe}(\text{py})_2(\text{phen})(\text{NCS})_2]$ with an increase of the average ligand field, leading to a spin cross-over at $T_{1/2} = 106 \text{ K}$. Substituting two more pyridine molecules to yield $[\text{Fe}(\text{phen})_2(\text{NCS})_2]$ still increases the ligand field and thus the LS domain, the $T_{1/2}$ temperature reaching 176 K.

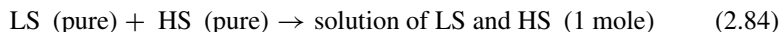
In some cases the ligand field can be manipulated by an external excitation. This happens in the ligand-driven light-induced spin cross-over (LD-LISC) process (see Section 4.5.2.3). If the system is just at the borderline of LS/HS, a photoisomerization of the ligand, changing its π -donor or acceptor character can change the ligand field strength just enough to trigger an LS–HS transition.

2.4.3.4 Spin cross-over with cooperativity, models, and examples

The phenomenon of spin cross-over occurs here in the solid state, and is strongly dependent on intermolecular interactions, giving rise to cooperativity. This means that the behaviour of a given site is dependent on the status of the neighbouring site. The experimental consequences are the more or less abrupt character of the transition, and in many cases the occurrence of an hysteresis. The transition, however, is still governed by thermodynamics and occurs around $T_{1/2}$, defined by eqn. (2.83).

The two forms, HS and LS, are actually isomers of the same species, and since their general structure is very similar we may expect them to be mutually soluble (at least in part) in the solid state. The relevant thermodynamic treatment of solid solutions [2.32] is very similar to that of liquid solutions. Before dealing with specific models of the spin cross-over, we will recall some basic concepts about solid solutions.

Calling LS and HS the two isomers, we have to evaluate the mixing quantities ΔS_{mix} , ΔH_{mix} , and ΔG_{mix} , corresponding to the process:



We can define X_{LS} and X_{HS} as the mole fractions, with $X_{\text{LS}} + X_{\text{HS}} = 1$. In the remaining, we shall use $X_{\text{HS}} = x$ and $X_{\text{LS}} = (1 - x)$ for simplicity. ΔS_{mix}

is > 0 , and thus $\Delta G_{\text{mix}} = \Delta H_{\text{mix}} - T\Delta S_{\text{mix}}$ is frequently negative and mutual solubility generally occurs.

For an ideal solution, $\Delta H_{\text{mix}} = 0$, while ΔS_{mix} is given by:

$$\Delta S_{\text{mix}} = -R X_{\text{LS}} \ln X_{\text{LS}} - R X_{\text{HS}} \ln X_{\text{HS}} = -R (1-x) \ln (1-x) - R x \ln x \quad (2.85)$$

Eqn. (2.85) can be obtained from a simple microscopic model in which molecules of LS and HS are arranged at random on the lattice nodes, which means that there is no privileged interaction between LS and HS molecules with respect to pure LS or HS.

When the solution is no longer ideal but the deviations to ideality are moderate, a frequently used model is that of regular solutions. In the definition given by J. S. Hildebrand in 1927, eqn. (2.85) is retained, but now $\Delta H_{\text{mix}} \neq 0$. A simple microscopic interpretation can be given by considering the scheme in Fig. 2.17, where $h_{\text{LS-LS}}$, $h_{\text{HS-HS}}$ and $h_{\text{LS-HS}}$ represent the elementary enthalpies (all negative) associated with the next-neighbours interactions.

Assuming that the distribution of molecules on the network nodes is still random, one obtains the following expression for the enthalpy of mixing per mole of mixture:

$$\Delta H_{\text{mix}} = \Gamma x (1-x) \quad (2.86a)$$

with

$$\Gamma = N_{\text{AZ}} [h_{\text{LS-HS}} - 1/2 (h_{\text{LS-LS}} + h_{\text{HS-HS}})] \quad (2.86b)$$

where N_{A} is Avogadro's constant and z is the number of neighbours for a given molecule. The Γ parameter determines the possibility of mixing. If $\Gamma < 0$ (LS-HS pairs more stable than the average of LS-LS and HS-HS pairs), ΔH_{mix} is negative, as $-T\Delta S_{\text{mix}}$ (always negative), and the mixture is always possible. If $\Gamma > 0$ (LS-HS pairs less stable than the average of LS-LS and HS-HS pairs), a competition exists between the enthalpy and entropy terms. The ΔG_{mix} curves = $f(x)$ are shown in Fig. 2.18 for various values of the Γ/RT parameter. Note that the entropic term always wins on the extreme range of compositions ($x \approx 0$ or 1), because of the form of eqn. (2.85), which presents vertical tangents at its extremities. For $\Gamma > 2RT$ (this limit is demonstrated later), the ΔG_{mix} curve presents two minima and a maximum for $x = 0.5$.

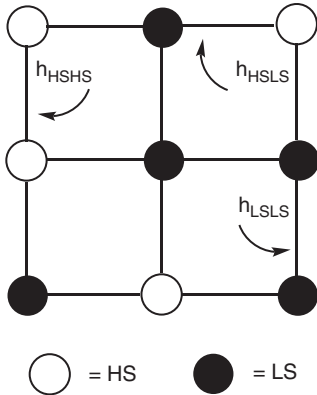
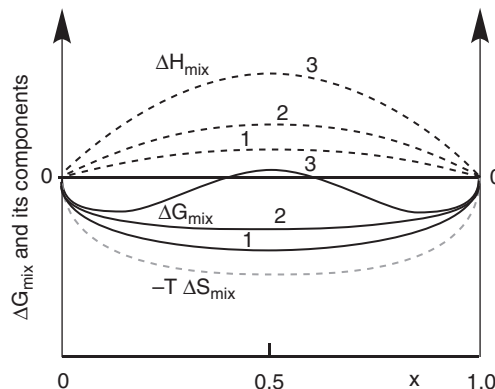


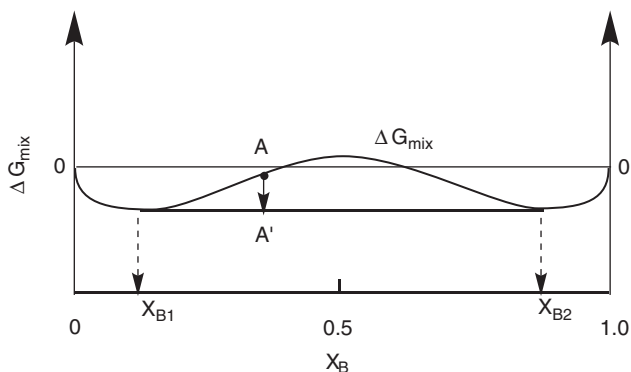
Fig. 2.17

Microscopic model for the calculation of the enthalpies.

Fig. 2.18

Variation of ΔG_{mix} and its components ΔH_{mix} and $-T\Delta S_{\text{mix}}$ (dotted lines) as a function of x for $\Delta H_{\text{mix}} > 0$. Numbers 1, 2, and 3 refer to increasing values of ΔH_{mix} . When ΔH_{mix} is large enough it wins on the entropic term in the central part of the diagram, but never at the extremities. Thus the ΔG_{mix} curve (plain lines) presents two minima and a maximum (see text). (Adapted from [2.32].)




Fig. 2.19

The demixing process. When the system is represented by a point like A, it evolves towards a more stable biphasic system represented by A'. A' resides on the common tangent to the two minima.

In such a situation a peculiar phenomenon may occur: demixing—that is, the separation in two phases. In the central part of the diagram a system represented by point A (see Fig. 2.19) is less stable than the one constituted by two phases with compositions X_{B1} and X_{B2} (point A' located on the common tangent). Thus miscibility occurs only between 0 and X_{B1} on one side and X_{B2} and 1 on the other side, and the system is biphasic between X_{B1} and X_{B2} .

We now consider the specific models of spin cross-over, which differ in describing intermolecular interactions [2.3, chapter 4].

Regular solution model (Slichter, Drickamer, 1972). Considering one mole of substance existing as x moles of high-spin form and $(1 - x)$ of low-spin form:

$$G = (1 - x) G_{LS}^{\circ} + x G_{HS}^{\circ} + \Delta G_{\text{mix}} = G_{LS}^{\circ} + x\Delta G^{\circ} + \Delta G_{\text{mix}} \quad (2.87)$$

The shape of the $G = f(x)$ curve is thus obtained from the curve giving ΔG_{mix} (see Figs. 2.18 or 2.19) by adding a linear ramp with slope ΔG° , as shown in Figs. 2.21 and 2.22. Since the HS and LS forms can interconvert, x varies until a minimum in free enthalpy is found. The minimum can be computed by putting to zero the derivative of eqn. (2.87):

$$\frac{\partial G}{\partial x} = \Delta G^{\circ} + \frac{\partial \Delta G_{\text{mix}}}{\partial x} = \Delta G^{\circ} + RT \ln \left(\frac{x}{1-x} \right) + \Gamma(1-2x) = 0 \quad (2.88)$$

There is no analytical solution for eqn. (2.88), only a graphical one, by considering that it is satisfied when the two functions $y_1(x)$ and $y_2(x)$ are equal:

$$y_1 = \ln(1-x)/x \quad (2.89)$$

$$y_2 = \frac{\Delta G^{\circ} + \Gamma(1-2x)}{RT} = \frac{\Delta H^{\circ} + \Gamma(1-2x)}{RT} - \frac{\Delta S^{\circ}}{R} \quad (2.90)$$

$y_1(x)$ has a well-known sigmoid shape, while $y_2(x)$ is a straight line. As shown in Fig. 2.20, when T varies, all y_2 curves pass through the point P of coordinates $x = 1/2 + \Delta H^{\circ}/2\Gamma$ and $y_2 = -\Delta S^{\circ}/R$, and at $T = T_{1/2}$ the y_2 line also passes through the point M, $x = 0.5$, $y_2 = 0$. Figure 2.20 schematizes the situation for different cases, $\Gamma > 0$ or < 0 , and various temperatures.

If $\Gamma = 0$ (the state of a molecule is independent of the state of its neighbours) there is only one intersection. When $\Gamma < 0$ (more attraction between HS-LS

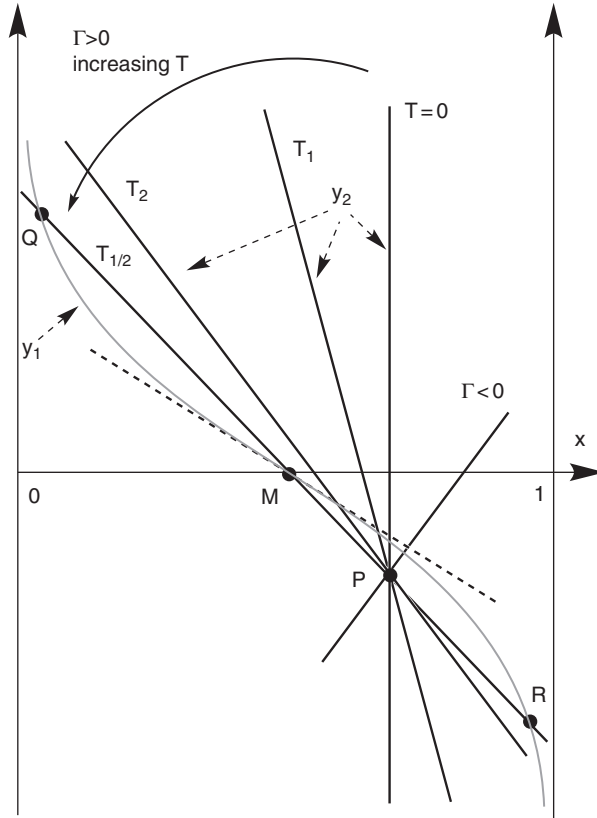


Fig. 2.20

Graphical solution of eqn. (2.88) by intersection of the curves $y_1(x)$ (grey curved line) and $y_2(x)$ (black straight lines) (see text). For $\Gamma < 0$ there is only one intersection. For $\Gamma > 0$ and large enough, multiple intersections can occur. The y_2 lines are shown for different increasing temperatures: $T = 0, T_1, T_2, T_{1/2}$. At $T_{1/2}$, for instance, the intersections occur at points Q, M, and R, corresponding respectively to minima, maxima, and minima in the $G(x)$ curves. Dotted line: tangent corresponding to the limiting case where demixing can begin to appear (see text).

pairs than between like pairs), there is also only one intersection, corresponding to a minimum in the $G(x)$ curve. The behaviour is relatively simple, and is depicted in Fig. 2.21.

When the temperature increases, $\Delta G^\circ (= \Delta H^\circ - T\Delta S^\circ)$ decreases and the abscissa of the minimum of $G = f(x)$ moves towards the right, as shown in the sequence of schemes in Fig. 2.22.

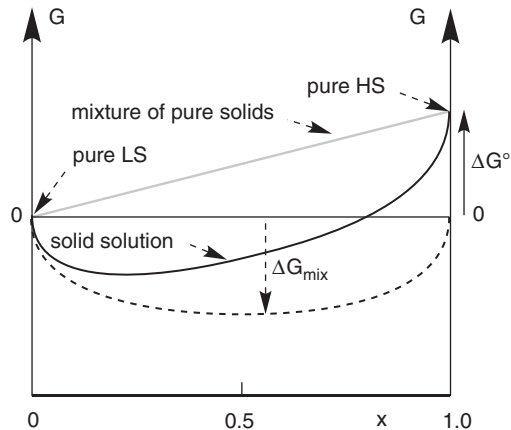


Fig. 2.21

Free enthalpy as a function of x for the case $\Gamma = 0$ or < 0 . Grey line: free enthalpy of the mixture of pure solids. Dotted line: free enthalpy of mixing. Plain line: free enthalpy of the solid solution.

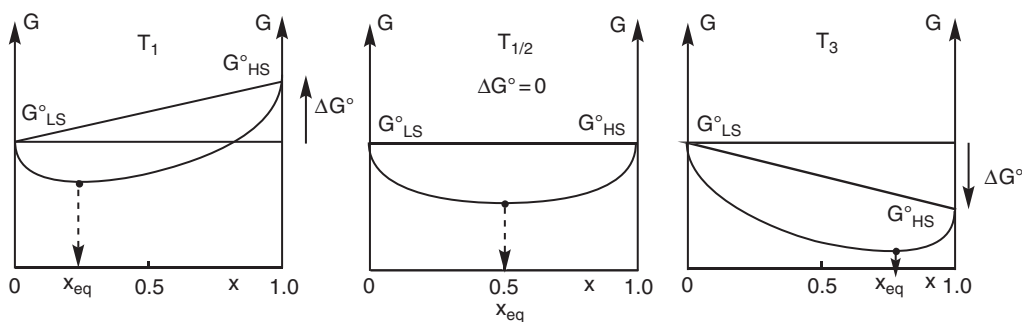


Fig. 2.22

Evolution of the $G = f(x)$ curves in the case where Γ is < 0 or 0 , for various increasing temperatures $T_1 < T_{1/2} < T_3$, corresponding to $\Delta G^\circ > 0, 0$ and < 0 . The abscissa of the equilibrium point x_{eq} moves smoothly to the right, corresponding to a gradual conversion of the LS form in the HS form.

The resulting $x = f(T)$ curve is shown in Fig. 2.23. The transition is gradual, without hysteresis. If $\Gamma = 0$ the situation is the same as in a gas phase or in solution, and corresponds to a Boltzmann population between two states, separated in energy by $\Delta H^\circ / N_A$ at the scale of one molecule.

Now we consider the case where Γ is positive. At the microscopic level it means that the LS molecules ‘prefer’ to be surrounded by LS molecules, and the same applies for HS. There is thus a cooperative effect favouring another kind of collective behaviour. In Fig. 2.20 it can be seen that since the slope of the $y_2(x)$ curve is $-2\Gamma/RT$, multiple crossings with the y_1 curve can occur if Γ is large enough. When both ΔH° and $\Delta S^\circ = 0$, point P is merged with point M, and a simple criterion for multiple crossing can be found: the limiting case is obtained when the y_2 curve is tangent to the y_1 curve at $x = 0.5$ (see dotted line on Fig. 2.20), and since $\left(\frac{\partial y_1}{\partial x}\right)_{x=0.5} = -4$, one obtains:

$$\Gamma = 2 RT \tag{2.91}$$

That is, for $\Gamma < 2RT$ only one extremum (a minimum) is observed in the $G(x)$ curve, while for $\Gamma > 2RT$ three extrema are observed (two minima and a maximum).

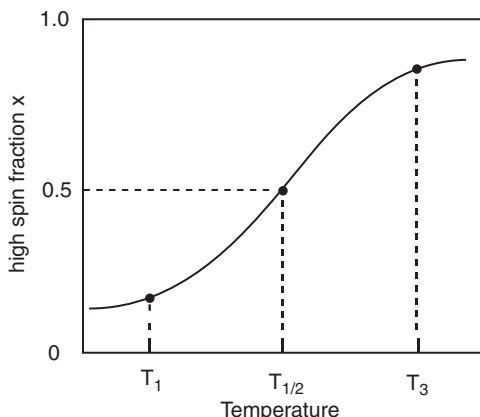


Fig. 2.23

Thermal variation of high spin fraction x , corresponding to the minima in Fig. 2.22.

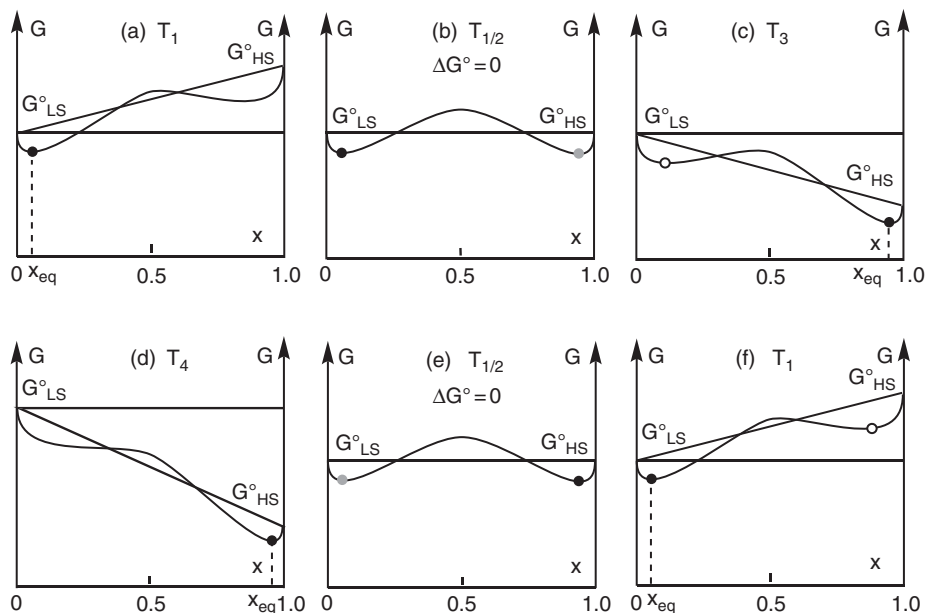


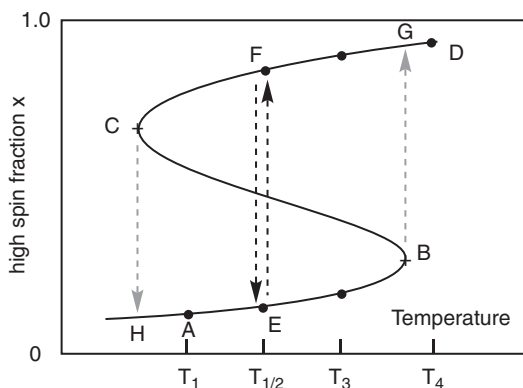
Fig. 2.24

Evolution of the $G(x)$ curves and position of the representative point of the system (black dot) for a system characterized by $\Gamma > 2 RT$ subject to an excursion in temperature: a–d) increasing $T_1 < T_{1/2} < T_3 < T_4$; d–f) decreasing $T_4 > T_{1/2} > T_3$. The grey dots represent the system at the same energy and the white dot a metastable state (see text).

In Fig. 2.24 the $G = f(x)$ curves are depicted for a system with $\Gamma > 2 RT$, subject to an excursion in temperature from low (T_1) to high (T_4) and back. It is useful to follow the events in Fig. 2.25, where the loci of the extrema of $G(x)$ are plotted *versus* T . Starting from T_1 (Fig. 2.24a, LS form more stable), the system is represented by the dot on the left-hand side of the diagram. At $T = T_2 = T_{1/2}$ (Fig. 2.24b), for which $\Delta G^\circ = 0$, the system can stay in the left-hand well, though the right-hand one has the same energy (grey dot). From then, two very different behaviours may arise.

Fig. 2.25

Loci of the extrema of x as a function of temperature for a strongly cooperative system ($\Gamma > 2 RT$). The AB and CD branches correspond to *minima* in the $G(x)$ curve, while the BC branch corresponds to a *maximum*. From low temperature to $T_{1/2}$ the lower branch is the more stable, while from $T_{1/2}$ to T_4 it is the upper branch. At $T = T_{1/2}$ the energies are the same. Grey dotted arrows: route without demixing; black dotted arrows: route with demixing.



If no demixing occurs, for a temperature like T_3 , the system can remain trapped in a metastable minimum (Fig. 2.24c, white dot); that is, the true thermodynamic equilibrium is not achieved (black dot). At a sufficiently high temperature, T_4 (Fig. 2.24d), the secondary minimum disappears and the system has no other choice than to move to the right and more stable minimum. In Fig. 2.25 the corresponding trajectory of the system is HAEB. Then, almost complete conversion to the HS state is achieved (point G). Returning from T_4 to T_3 , $T_{1/2}$, and T_1 occurs through the trajectory DGFC, and then the LS state arises (point H). There is an hysteresis effect; that is, the state of the system depends on its past history.

Hysteresis is a very important process, providing properties of bistability and memory, which are very appealing for applications. We return to this point later.

If demixing occurs, the system moves from one branch to the other as soon as the other one is more stable. In the $G(x)$ diagram (Fig 2.24) it can evolve under the central maximum, due to the demixing process (demixing may be seen as the thermodynamic equivalent of the tunnel effect of quantum mechanics). The trajectory in Fig. 2.25 is thus HAE followed by FGD, and the return occurs along the same path (DGF-EAH). The transition can be particularly abrupt.

Actually, real systems can behave intermediately between these two extreme behaviours—for instance, jumping from the lower to the upper branch on heating can occur somewhere between E and B in Fig. 2.25. This depends on factors such as grain size, frontier domains, and rate of nucleation, which are not included in the model, and this is one of the reasons why the occurrence and magnitude of the hysteresis is relatively hard to predict.

Domain model (Sorai, Seki, 1974) [2.3, chapter 4]

In this model it is assumed that LS and HS molecules are not distributed at random as in a solid solution, but form domains of the same spin (see Fig. 2.26). The domains are assumed to have uniform size and contain n molecules, with n typically between 10 and 100.

The mixing entropy is then given by:

$$\Delta S_{\text{mix}} = - (R/n) [x \ln x + (1 - x) \ln (1 - x)] \quad (2.92)$$

That is, n times less than in eqn. (2.85), because the number of possibilities has been reduced drastically by n , the number of molecule per domain. The ΔH_{mix} term is now zero, because there the short-range environment of a molecule is made of molecules of the same spin, as in pure solids (this assumption could, of course, be questioned if n is too small). Thus in eqn. (2.87) the main term is ΔG° . Exploiting $G = f(x)$ for different temperature curves, as previously, shows that the transition can be sharp (the larger n , the sharper the transition), but no hysteresis is predicted, which is the main drawback of this model.

Elastic model with internal pressure (Spiering, Gülich, 1982) [2.28, 2.29]

First, we recall the main modification associated with the spin change, apart from the magnetic property: due to the change in the number of electrons occupying the e_g^* antibonding orbitals, $\Delta n(e_g^*)$, there is an increase in metal–ligand distances from LS to HS. In the case of iron(II) complexes ($\Delta n(e_g^*) = 2$),

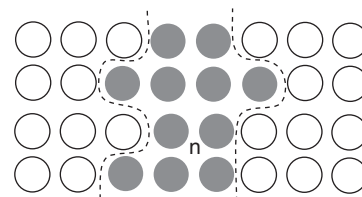
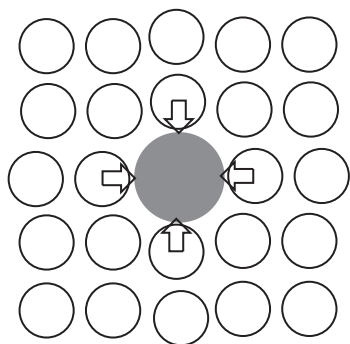


Fig. 2.26

Schematic representation of the domain model with n molecules of the same spin state (HS white spheres and LS grey ones).

**Fig. 2.27**

Scheme of a lattice network in which all molecules except one (in grey) are in the LS state. Their influence on the remaining HS molecule is equivalent to a pressure, hence the concept of ‘internal pressure’.

the increase can reach 21 pm, and correlatively the crystallographic cell dimensions increase also, as well as the molar volume. With cobalt(II), $\Delta n(e_g^*) = 1$ and the mean metal–ligand change is less—about 10 pm. Consequently, a simple explanation of cooperativity is based on intermolecular steric interactions; that is, the elastic energy due to the volume change accompanying the spin change. Thus, in the elastic model of Spiering and Gütllich, when most neighbours of a given molecule change their state, it is better for the last molecule to also change its state. Expressed differently, crystal packing is much easier and energetically more stable when all molecules have the same dimensions (Fig. 2.27).

In the example of Fig. 2.27—an isolated HS molecule surrounded by smaller LS molecules—the effect of the environment is to mimic the role of pressure. One can thus define an ‘internal pressure’ favouring the LS state, as in the case of a true external pressure (see Section 2.4.3.5). Mathematically, the enthalpic interaction term is written as $\Delta_{(x)} - \Gamma_{(x)} x^2$, instead of $\Gamma x(1-x) = \Gamma x - \Gamma x^2$ as in the regular solution domain (see eqn. (2.86a)). However, in this model Δ and Γ are functions of x , and the final result is qualitatively similar, in that the enthalpic term also passes through a maximum when x varies. Quantitatively there is a difference, because the elastic domain includes long-range interactions which are not taken into account in the regular solution model.

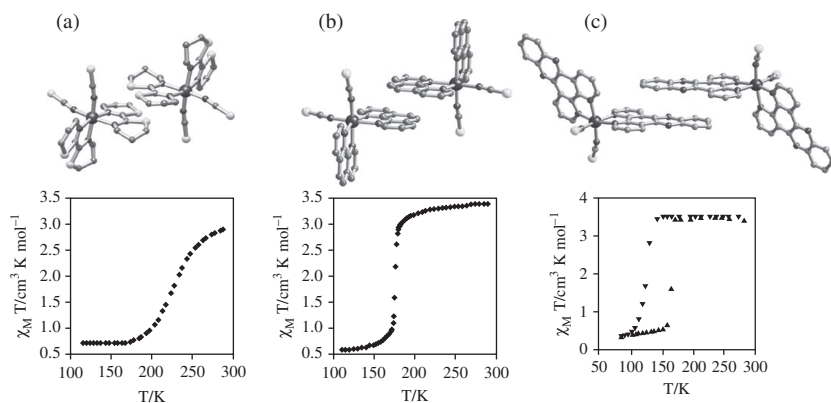
To conclude the discussion of models, we quote the recent model of Robert *et al.*, based on *ab initio* calculations [2.33]. Its main conclusion is that hysteretic effects appear to be governed by Madelung electrostatic energies. The important parameters are ΔQ , the amount of charge which is transferred between the metal and the ligands during the spin change, and $(\delta V_{HS} - \delta V_{LS})$, the fluctuation of the electrostatic Madelung potential difference in the crystal created by the environment of a given site. The authors propose that the Γ interaction parameter of the Slichter–Drickamer model (see previous) is given by $\Gamma = \Delta Q (\delta V_{HS} - \delta V_{LS})$ and therefore that their electrostatic model (in which Madelung energies play a role) complements usefully the description based on elastic-driven cooperativity. This is an interesting example of the contribution of modern quantum methods to the problem.

We now consider some examples in which the degree of cooperativity can be changed by chemical modifications.

The first idea is to change the nature of intermolecular contacts, which has been achieved on the general structure of $[\text{Fe}(\text{L})_2(\text{NCS})_2]$ complexes, where L is a bidentate α -diimine ligand such as 2,2'-bipyridine (bpy), 1,10-phenanthroline (phen), dipyrido [3,2-a:2'3'-c] phenazine (dpp), or 2,2'-bi-4,5-dihydrothiazine (btz). Except btz, these ligands are conjugated aromatic systems.

Contrasted behaviours are observed: thus with btz the transition is smooth, showing no cooperative effect. With bpy and phen the transition is abrupt, but without hysteresis. Finally, with dpp the transition is abrupt, with an hysteresis of around 40 K (Fig. 2.28).

The structural data show that the FeN_6 chromophore and its change upon spin conversion are very similar in all complexes, and thus the reasons for cooperativity must be sought elsewhere. Crystal packing analysis shows that

**Fig. 2.28**

Spin transition represented as $\chi T = f(T)$ curves for $[\text{Fe}(\text{L})_2(\text{NCS})_2]$ complexes with $\text{L} = \text{btz}$ (a), phen (b), and dpp (c). (Reproduced from [2.34].)

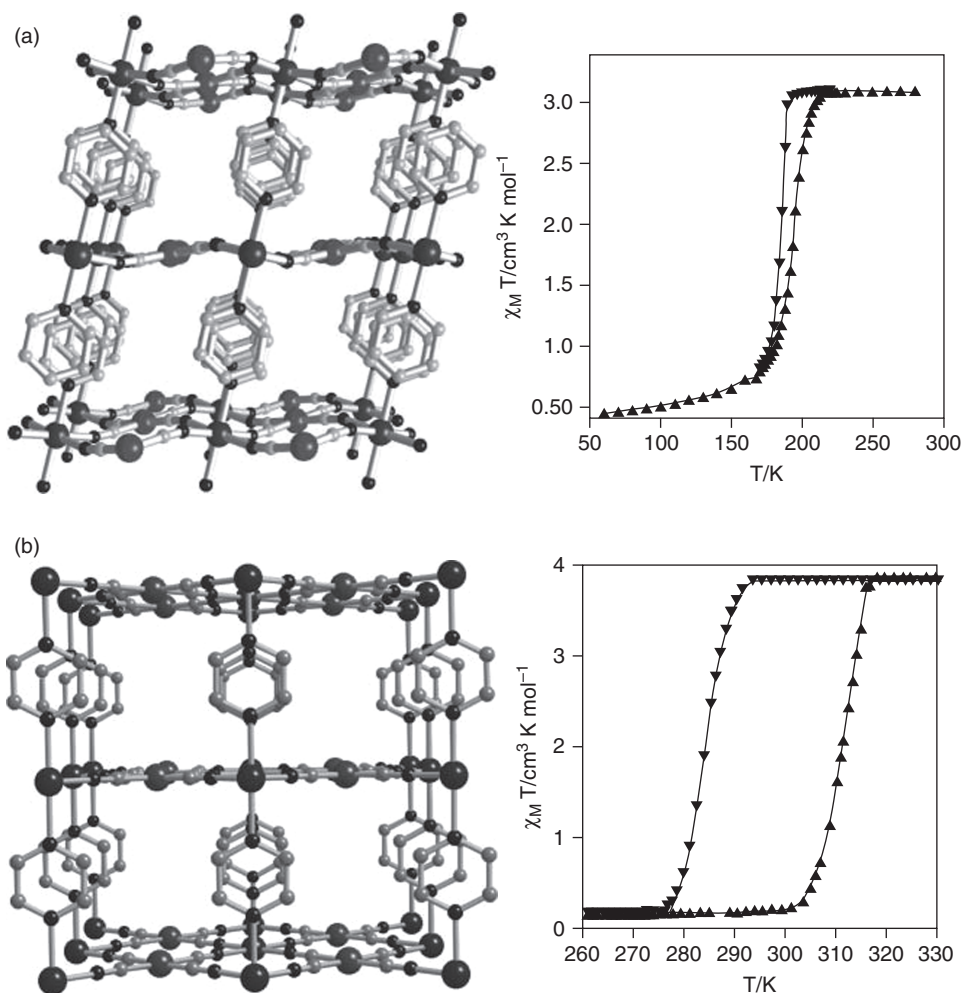
the intermolecular contacts are very limited with btz. For bpy and phen, some π - π stacking is present, and it is more important with dpp because of its extended aromatic character. This is, among others, a clear example of the influence of the intermolecular interactions on the nature of the transition. Large interactions favour abrupt transitions and the appearance of hysteresis. The exact mechanism is, however, still speculative.

Dimensionality of the lattice is also an important factor for cooperativity [2.34, 2.35]. Thus the 2D coordination polymer $[\text{Fe}(\text{py})_2\text{M}(\text{CN})_4]$ ($\text{M} = \text{Ni}(\text{II}), \text{Pd}(\text{II}), \text{Pt}(\text{II}), \text{py} = \text{pyridine}$) is built from alternate square planar diamagnetic $[\text{M}(\text{CN})_4]^{2-}$ anions and octahedral $\text{Fe}(\text{II})$ sites. Iron is surrounded by 4N of the cyanide ligands and 2N of axial pyridine ligands (see Fig. 2.29). The structure is thus made of metal-cyanide sheets with weak interactions with different sheets. For these compounds a sharp spin transition is observed, with an hysteresis of around 10 K.

Substituting pyridine by pyrazine allows linking of the different sheets by pillars connecting the iron atoms, thus yielding a truly 3D structure with formula $[\text{Fe}(\text{pz})\text{M}(\text{CN})_4]$ [2.34]. The comparison with the 2D structures shows an increase not only in the $T_{1/2}$ temperature but also in the width of the hysteresis loops (Fig. 2.29). The $T_{1/2}$ increase is attributed to the increased rigidity of the 3D lattice with respect to the 2D lattice, rather than to the ligand change, because pyrazine creates a smaller ligand field than pyridine. Regarding the width, when going from the 2D to the 3D structure, cooperativity necessarily increases, because the molecules are more connected and thus the influence of neighbours on a given site increases.

These 3D materials can also be transformed at will from one form to the other using light. This is the process of photo-induced phase transition (PIPT), described in Section 4.5.2.2.

A last effect influencing cooperativity is the size of crystallites constituting the sample. Thus samples of $[\text{Fe}(\text{pz})\text{Pt}(\text{CN})_4]$ have been prepared by a microemulsion method allowing the control of crystallites size in the nanometer range [2.34]. With two different sets of synthetic parameters it is possible to obtain samples with the same crystal structures but with crystallite sizes of either $230 \times 230 \times 55$ or $60 \times 60 \times 20$ nm. The width of the hysteresis loop is 22 and 10 K respectively, showing that cooperativity decreases with particle

**Fig. 2.29**

Structures of the 2D $[\text{Fe}(\text{py})_2\text{M}(\text{CN})_4]$ complex (a) and the 3D $[\text{Fe}(\text{pz})\text{M}(\text{CN})_4]$ complex (b), with the corresponding hysteresis loops. Although the structure in (a) appears 3D, since pyridine ligands are not bridging, the covalent backbone is only 2D. (Reproduced from [2.34].)

size. This point is a crucial one in all studies and applications of spin cross-over at nanometer size.

General remarks on hysteresis

From a practical point of view the consequences of hysteresis are important: for a given temperature there are two possible states—usually one stable and the other metastable—but since the rate of thermal conversion of the latter into the former is usually immeasurably slow, one can speak of *bistability*. The two forms have different properties (magnetic properties, of course, but also different colours), and it is thus possible to build display devices. Demonstrators have been realized (J. F. Letard, P. Guionneau, in [2.28, vol. 235, 221]).

Here we have shown that an excursion in temperature can trigger the conversion, but other physical parameters can be used. A photophysical excitation is possible, since the two forms usually have different absorption spectra, as shown by the LIESST or LD-LISC effects (see Chapter 4). But we can also rely on pressure, or the magnetic field itself, as shown in Section 2.4.3.5.

An interesting question concerns the possibility of observing bistability at the scale of one molecule. By comparison with the case of an interacting ensemble of molecules discussed previously, it seems very difficult and challenging. In the solid-state examples given previously, bistability is related to the extreme slowness of the thermodynamically allowed conversion from a metastable minimum to a stable one. At the scale of one molecule or a non-interacting population of molecules, one has to rely on the activation energy for the chemical reaction (isomerization) to keep the two states. Experimentally, however, it is found that the conversion of an LS to an HS form is very fast in solution (about $10^6 - 10^8 \text{ s}^{-1}$). Thus bistability—the possible existence of two different forms of one molecule for the same values of the external parameters—would be limited to a very short time in the case of spin transition systems. To date, in the domain of magnetic molecules, bistability with hysteresis has been observed only for sets of single magnet molecules at very low temperature (see Section 2.8).

2.4.3.5 Influence of other physical parameters (pressure, magnetic field, light)

Since the spin transition is accompanied by a volume change, it is sensitive to pressure—high pressures favouring the more dense LS state. One has, indeed:

$$(\partial G/\partial P)_T = \Delta V \quad (2.93)$$

with $\Delta V = V_{\text{HS}} - V_{\text{LS}} > 0$ for the LS \rightarrow HS reaction.

The effect is small, but it has been demonstrated clearly for many complexes. We give here the example of the $[\text{Fe}(\text{phen})_2(\text{NCS})_2]$ complex [2.34]. At room temperature the complex is 100% high spin, but upon application of a 1.3 GPa pressure ($1.3 \cdot 10^4 \text{ atm}$), an almost complete conversion to LS is observed (Fig. 2.30).

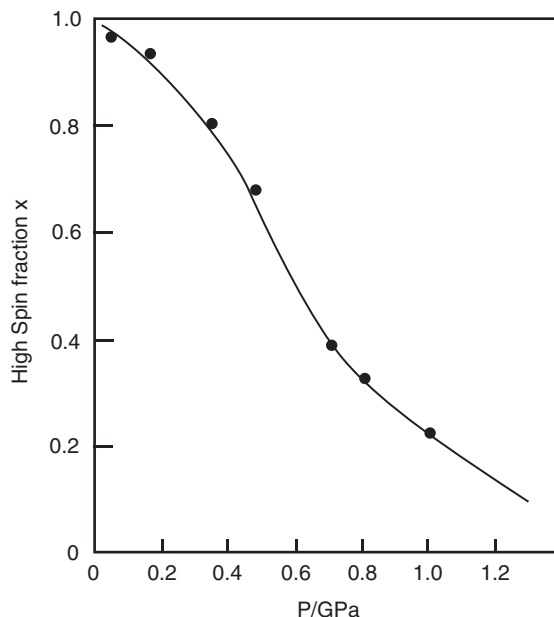
The magnetic field itself can have an influence because it introduces an additional term: $B M$ in the free enthalpy [2.28, vol. III]. Since the magnetization $M = \chi H$ ($M = \chi B/\mu_0$ in SI) is proportional to H (B), after integration between $H = 0$ and H , one obtains $-\chi H^2/2$ ($-\chi B^2/2 \mu_0$ in SI) for the extra term. Thus, in the presence of a magnetic field, ΔG° can be written as:

$$\Delta G^\circ = \Delta H^\circ - T\Delta S^\circ - (\Delta\chi)H^2/2 \quad [\dots(\Delta\chi)B^2/2\mu_0 \text{ in SI}] \quad (2.94)$$

where $\Delta\chi = \chi_{\text{HS}} - \chi_{\text{LS}}$ is > 0 . The new $(T_{1/2})_{\text{H}}$ temperature for $\Delta G^\circ = 0$, within an applied field H , is:

$$(T_{1/2})_{\text{H}} = (T_{1/2})_0 - (\Delta\chi)H^2/2\Delta S^\circ \quad [\dots(\Delta\chi)B^2/2\mu_0 \Delta S^\circ \text{ in SI}] \quad (2.95)$$

where $(T_{1/2})_0 = \Delta H^\circ/\Delta S^\circ$ is the $T_{1/2}$ temperature in the absence of magnetic field, and the second term is negative. Logically, the magnetic field expands the existence domain of the high-spin form by decreasing $T_{1/2}$. The expected effect is small (typically a 1.8 K change for 30 T from theoretical calculations). It is

**Fig. 2.30**

High-spin fraction x as a function of pressure for the $[\text{Fe}(\text{phen})_2(\text{NCS})_2]$ complex. (Adapted from [2.34].)

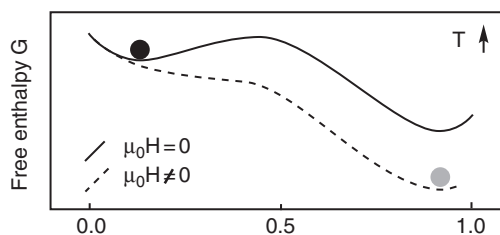
proportional to the square of H (B), hence high magnetic fields are valuable in revealing it.

In the region of the hysteresis curve a pulsed magnetic field can even trigger an irreversible conversion of one spin state into another. This has been observed in the case of $[\text{Fe}(\text{phen})_2(\text{NCS})_2]$, using pulsed magnetic fields (32 T with a duration of around 75 ms) [2.28, vol. III]. In the ascending part of the hysteresis loop, conditions for which the LS state is metastable, applying the strong magnetic field increases the proportion the HS state, and this change subsists after the end of the pulse. The thermodynamics of the phenomenon can be described by Fig. 2.31. At high magnetic field, either the bump in the $G(x)$ function has disappeared, or the ‘tunnelling’ (actually demixing) has been favoured, allowing the motion of the system towards the HS state, where it remains trapped after the end of the pulse.

A last physical parameter is light. By absorbing energy emanating from an electromagnetic radiation in the visible, the system can overcome the activation barrier at the molecular scale (see Fig. 2.14), or even surmount an energy maximum at the scale of an interacting ensemble of molecules. Several such processes are well documented, but are treated extensively in Chapter 4: these

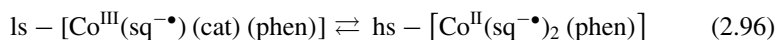
Fig. 2.31

Free enthalpy $G = f(x)$ curves for a point in the ascending part of the hysteresis loop. $B = \mu_0 H = 0$, plain curve and black dot; $B = B_{\text{max}}$, dotted curve and grey dot. (Adapted from Bousseksou *et al.* in [2.28, vol. III].)



are the light-induced excited spin state trapping (LIESST) in which one moves from a potential energy curve to another (Section 4.5.2.1), the photo-induced phase transition (PIPT) in which the excursion occurs from one branch to the other of an hysteresis curve (Section 4.5.2.2), and the ligand-driven light-induced spin cross-over (LD-LISC) where the photochemical transformation of a ligand triggers the spin cross-over (Section 4.5.2.3).

As a conclusion of this section, we mention that the spin cross-over process can also be found coupled to an electron transfer. Thus, in the complexes of general formula $[\text{Co}(\text{sq})(\text{cat})(\text{phen})]$, where cat is a catecholate dianion, sq is a semiquinone anion-radical (the 1-electron oxidized form of the latter), and phen is 1,10-phenanthroline, the following equilibrium has been established by Hendrickson and Pierpont ([2.28], vol. II):



Following an intramolecular electron transfer where Co^{III} oxidizes the catecholate²⁻ into semiquinone^{•-}, the central cobalt atom changes from low spin to high spin. As for spin cross-over, the process can be thermally activated but also triggered by light, and for polycrystalline samples, susceptibility studies show abrupt transitions typical of cooperative effects.

2.5 Spin Hamiltonian (SH) approach

The spin Hamiltonian approach is a method widely used for modelling spectroscopic data and computing energies of magnetic systems. It was first developed by Abragam, Pryce, Bleaney, Griffith, and Stevens to analyse the huge amount of data arising from electron paramagnetic resonance and nuclear magnetic resonance when these methods appeared after World War II [2.36]. As pointed out by Griffith: ‘The spin Hamiltonian is a convenient resting place during the long trek from fundamental theory to the squiggles on an oscilloscope which are the primary result of electron resonance experiments’ [2.23]. It was then developed by many others to reach its present status, schematized in Fig. 2.32.

Basically, there are two steps: (i) the spin Hamiltonian is written and empirical SH parameters are obtained from spectroscopic data; (ii) the SH parameters are related to the theoretical description of the electronic structure.

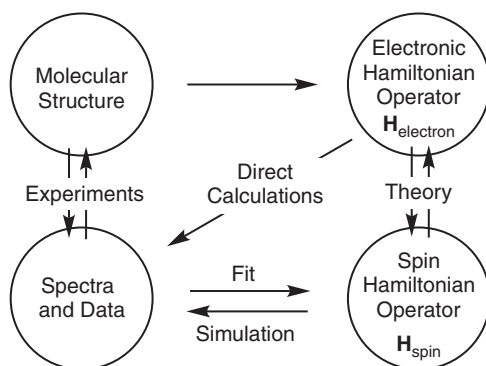


Fig. 2.32

The spin Hamiltonian (SH) approach between experimental data and theory. (Adapted from E. Solomon and F. Neese in [2.6, vol IV, p. 345].)

The feasibility of the SH approach relies on two bases: (i) the Pauli principle, which closely connects the spin part of a wavefunction to the orbital one; and (ii) the fact that the spin operators \mathbf{S}^2 and \mathbf{S}_z commute with the orbital Hamiltonian—that is, they have common eigenfunctions and eigenvalues. The spin Hamiltonian is an operator which is polynomial in \mathbf{S} (\mathbf{S} spin operator). It is acting on spin states $f(\mathbf{S}, M_S, I_N - I_N, \text{nuclear spin})$ that, in short, we denote as Σ . It recovers *effectively* the energies that can be computed from the orbital Hamiltonian (2.97a and b) ($E_S = E_{\text{orb}}$):

$$(a) \mathbf{H}_{\text{spin}}(\Sigma) = E_S \cdot \Sigma \quad (b) \mathbf{H}_{\text{orb}}(\psi) = E_{\text{orb}} \cdot \psi \quad (2.97)$$

To be efficient, it is necessary that the spin can be considered a pertinent parameter of the system (no orbital moment, no spin–orbit coupling, or weak enough to be considered a perturbation). If the spin Hamiltonian is suitably defined it allows the extraction of significant parameters and relating them to the orbital Hamiltonian eigenvalues E_{orb} and eigenfunctions ψ .

The second part of the task (connecting SH parameters to fundamental theory) is much more difficult than extracting parameters from data, and is beyond the scope of this book. We shall only approach the problem in some specific cases. More information is given by Solomon and Neese in [2.6, vol. IV, p. 345].

In the following we discuss a few examples of spin Hamiltonians: those related to one magnetic centre (Section 2.5.1), and those describing the interaction between centres (Section 2.5.2) [2.4], [2.16].

2.5.1 One-centre spin Hamiltonian

In many circumstances the Hamiltonian (2.98) has been used to *effectively* describe a molecule with an electronic spin operator \mathbf{S} and nuclear spin operators \mathbf{I}_i on different atoms i and their interaction with an external magnetic field (induction) \vec{B} :

$$\mathbf{H}_{\text{spin}} = \tilde{D}\mathbf{S} + \mu_B \mathbf{S}g\vec{B} + \sum_i \mu_N g_N \mathbf{I}_i \vec{B} + \sum_i \tilde{A}_i \mathbf{S} \mathbf{I}_i \quad (2.98)$$

The first term is the zero-field splitting, and \tilde{D} is a tensor; the second term is the Zeeman term, where μ_B is the Bohr magneton and g is a tensor; the third term describes similarly the interaction between the applied field and nuclear magnetic moment operators $\mu_N = \mu_N \cdot g_N \cdot \mathbf{I}$ (μ_N , nuclear magneton; g_N , nuclear g -factor considered as uniform; \mathbf{I} , nuclear spin operator), summed on all the i nuclei; and the fourth term is the hyperfine coupling between the electronic and nuclei spins, and \tilde{A} is the related tensor. Other terms are not shown (nuclear spin–spin coupling, quadrupole nuclear interactions, and Mössbauer isomer shifts). The empirical parameters to be determined from Hamiltonian in eqn. (2.98) (g -values, zero-field splittings, and hyperfine couplings) depend on the scientific field. The third and fourth terms, for example, are used widely in nuclear magnetic resonance (NMR) spectroscopy. We discuss only the first two terms—the most useful of them in the following of the chapter.

2.5.1.1 The Zeeman effect

We begin with the Zeeman effect, introduced in Section 2.4.2.4, and also comment briefly on a new quantity, g , introduced in eqn. (2.98), with the example of an EPR experiment which allows determination of the g -values. In Section 2.2.2 the g -factor is a scalar for a unique electron, g_e , or for the many-electrons atoms, g_j . In a molecule, the unpaired electron will experience not only the magnetic induction B_0 of the EPR spectrometer, but all the magnetic fields of the surroundings. The effective field experienced by the spin can be written $B^{\text{eff}} = B_0(1-\sigma)$. The resonance condition in the EPR experiment is $h\nu = g_e \cdot \mu_B \cdot B^{\text{eff}} = g_e \cdot \mu_B \cdot B_0(1 - \sigma) = g_{\text{eff}} \cdot \mu_B \cdot B_0$ (in SI units; see eqn. (2.31)), where g_{eff} is now an effective quantity defined by $g_{\text{eff}} = g_e (1 - \sigma)$. As the resonance depends on the orientation in the three directions of space of the induction and of the spin, the best way to link vectorial quantities, spin, and induction is a tensor, \tilde{g} . It is generally written as a 3×3 matrix and the Zeeman term expressed as a product of matrices (magnetic induction and spin). Without entering into mathematical details, the general 3×3 matrix corresponding to the \tilde{g} tensor can be transformed by a suitable axes change in a diagonal matrix with principal values of g , g_x , g_y , g_z , which can be related to g_e ($g_x = g_e + \Delta g_x$, and so on).

The g -values can then be compared with the measured spectroscopic values and correlated in a second step with the structural and electronic characteristics of the compound, often in terms of the spin-orbit coupling parameter λ and excitations' energies. For example, to obtain the g -values in pseudo-octahedral complexes, Gatteschi *et al.* [2.4] propose a perturbation treatment of the spin-orbit parameters for orbitally non-degenerate ground states using the following formula:

$$\mathbf{g} = g_e \mathbf{I} - 2\lambda \mathbf{\Lambda} \text{ or } \Delta \mathbf{g} = \mathbf{g} - g_e \mathbf{I} = -2\lambda \mathbf{\Lambda} \quad (2.99)$$

λ , the many electron spin-orbit constant, was defined in eqn. (2.64):

$$\Lambda = \sum_n \frac{\langle \Psi_g | \mathbf{L} | \Psi_{\text{exc}}^n \rangle \langle \Psi_g | \mathbf{S} | \Psi_{\text{exc}}^n \rangle}{E_{\text{exc}}^n - E_g} \quad (2.100)$$

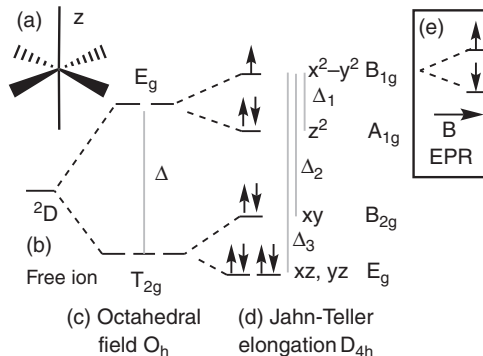
where Ψ_g is the wavefunction of the ground state with energy E_g , Ψ_{exc}^n is one of the excited states with energy E_{exc}^n and the sum runs over the n excited states, and \mathbf{L} is the orbital angular momentum operator. The elements of $\mathbf{\Lambda}$ are positive, and λ depends on the filling of the d^n configuration (< 0 if $n < 5$; > 0 if $n > 5$; see Section 2.4.1). For example, in a Cu(II) complex, d^9 , in an elongated octahedral geometry (square planar), a $x^2 - y^2$ ground state, the expressions of g_i are $g_x = g_e - 2\lambda/\Delta_3$, $g_y = g_e - 2\lambda/\Delta_3$, and $g_z = g_e - 8\lambda/\Delta_2$. The Δ_i are the excitation energies shown in Fig. 2.33 (electron jump from a doubly occupied orbital to the SOMO, Δ_2 from xy (B_{2g} excited state), Δ_3 from xz and yz (E_g excited state)). It should be remarked that $\Delta_3 = \Delta_{\perp}$, hence $g_x = g_y = g_{\perp}$ and $\Delta_2 = \Delta_{\parallel}$, hence $g_z = g_{\parallel}$. Frequently encountered values are $g_{\parallel} = 2.20$ and $g_{\perp} = 2.08$.

2.5.1.2 Zero-field splitting

We come now to the first term of eqn. (2.98), $\tilde{S}\tilde{D}\tilde{S}$, related to the zero-field splitting. \tilde{D} is a tensor, symmetric and real, with three orthogonal eigenvectors,

Fig. 2.33

Splitting of the energy levels of a $3d^9$ transition metal ion, Cu(II). See also Fig 1.24 in Section 1.3.7. (a) D_{4h} Structure; (b) free ion; (c) octahedral symmetry, O_h (ligand field Δ); (d) square planar symmetry D_{4h} after Jahn–Teller distortion (elongation along z) with orbitals fillings and symmetry labels; (e) further splitting by the Zeeman effect (EPR spectroscopy). In (d) $\Delta_1, \Delta_2, \Delta_3$ are the energies of the transitions in the electronic spectrum.



and \mathbf{S} is the spin operator. It is convenient to take the x, y, z coordinates axes parallel to the eigenvectors of \tilde{D} , so that:

$$\mathbf{H}_{\text{ZFS}} = \mathbf{S}\tilde{D}\mathbf{S} = D_{xx}\mathbf{S}_x^2 + D_{yy}\mathbf{S}_y^2 + D_{zz}\mathbf{S}_z^2 \quad (2.101a)$$

The D_{ii} are the diagonal components of \tilde{D} , and the \mathbf{S}_i are the components of spin operators.

Using the properties of spin operators and tensors, the spin Hamiltonian can be manipulated to obtain an expression easier to handle in a matrix form. The addition of a well-chosen constant (C) to the Hamiltonian shifts all the levels without changing the physical properties of the system:

$$C = -(D_{xx} + D_{yy}) (\mathbf{S}_x^2 + \mathbf{S}_y^2 + \mathbf{S}_z^2) / 2 = -(D_{xx} + D_{yy}) S(S + 1) / 2 \quad (2.101b)$$

$$\mathbf{H}_{\text{ZFS}} = D\mathbf{S}_z^2 + E (\mathbf{S}_x^2 - \mathbf{S}_y^2) \quad (2.101c)$$

with:

$$D = D_{zz} - (D_{xx} + D_{yy}) / 2 \text{ and } E = (D_{xx} - D_{yy}) / 2 \quad (2.101d)$$

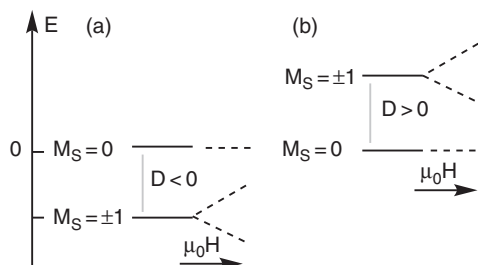
The same trick is used with the addition of a new constant $-D S(S + 1)/3$ in eqn. (2.101c):

$$\mathbf{H}_{\text{ZFS}} = D[\mathbf{S}_z^2 - D S(S + 1)/3] + E (\mathbf{S}_x^2 - \mathbf{S}_y^2) \quad (2.102)$$

Among other advantages, in eqn. (2.101a) (i): the trace of the Hamiltonian is zero; (ii) in cubic symmetry (where x, y, z are equivalent), $D_{zz} = D_{xx} = D_{yy}$, $D = 0$ (from eqn. (2.101d)); (iii) in axial symmetry (x, y equivalent), $D_{xx} = D_{yy}$, $E = 0$, and $D = D_{zz}$ (from eqn. (2.101d)); and in this case eqn. (2.101a) becomes:

$$\mathbf{H}_{\text{ZFS}} = D\mathbf{S}_z^2 \quad E_{\text{ZFS}} = D.M_S^2 \quad (2.103)$$

Given a spin S , its energy levels within this approximation are described by D only. The $(2S + 1)$ spin levels of the S multiplet are therefore split, even if there is no applied magnetic field, hence the term zero-field splitting (ZFS) given to the effect. The eigenvalues range from M_S to $-M_S$ and $E_{\text{ZFS}} = DM_S^2$ (M_S running from S to $-S$). For example:

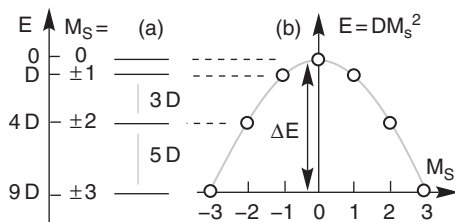
**Fig. 2.34**

Zero-field splitting for a uniaxial $S = 1$ system and Zeeman effect (dotted lines) after applying a magnetic induction $\mu_0 H$; (a) $D < 0$, the $M_S = \pm 1$ levels lie the lowest; (b) $D > 0$, the $M_S = 0$ level lies the lowest.

For $S = 1$, $M_S = 0$, $E_0 = 0$; $M_S = \pm 1$, $E_{\pm 1} = D$. For $S = 2$, $M_S = 0$, $E_0 = 0$; $M_S = \pm 1$, $E_{\pm 1} = D$; $M_S = \pm 2$, $E_{\pm 2} = 4D$. For $S = 3$, $M_S = 0$, $E_0 = 0$; $M_S = \pm 1$, $E_{\pm 1} = D$; $M_S = \pm 2$, $E_{\pm 2} = 4D$, $M_S = \pm 3$, $E_{\pm 3} = 9D$, and so on . . .

Figs. 2.34 and 2.35 display graphically some important consequences of the presence of zero-field splitting: in a uniaxial system (Fig. 2.34, $D \neq 0$, $E = 0$), the stabilization of the components $M_S = 0$ and ± 1 depends on the sign of D . When $D < 0$ (Fig. 2.34a) the components with the highest $|M_S|$ ($|M_S|_{\max} = S$) lie lowest, the spin tends to align along z , and the system presents ‘easy-axis anisotropy’. When $D > 0$ (Fig. 2.34b) the component(s) with the lowest $|M_S|$ ($|M_S|_{\min} = 0$ if S integer or $1/2$ if S half-integer) lie(s) lowest, the spin tends to orient in the xy plane, which is described as ‘easy-plane anisotropy’. The application of the magnetic field splits the degeneracy of the ± 1 levels (Fig. 2.34). For larger spins the splitting is larger (Fig. 2.35a). An important point is that when $D < 0$ it appears an energy barrier to reverse the spin from to $-M_{S\max}$ to $+M_{S\max}$ ($\Delta E = DM_{S\max}^2$ for integer spins, Fig. 2.35b). The reader can check that with a half-integer spin, $\Delta E = D(M_{S\max}^2 - 1/4)$. The presence of this barrier, directly related to the sign of D , its height, will have important consequences for the very peculiar objects termed single-molecule magnets (SMM), presented and discussed in Section 2.8. By contrast, when $D > 0$ there is no barrier. The sign of D and its magnitude will also be discussed in Section 2.8.

It is possible to play with the geometry of the complex and with the D and E values. First, it is obvious that E should be less than D . If not, the easy axis of anisotropy will change z to x . Using eqn. (2.101d) and playing with the components D_{xx} , D_{yy} , D_{zz} , and E/D , the reader can demonstrate as an exercise that (i) the maximum rhombicity (splitting between the three components D_{ii}) is achieved for $E/D = 1/3$ ($D_{xx} = 0$; $D_{yy} = -2D/3$; $D_{zz} = 2D/3$), and (ii) for $E/D = 1$ the anisotropy axis has simply changed. Therefore, it is wise to operate in conditions where $|E/D| < 1/3$.

**Fig. 2.35**

Zero-field splitting for a uniaxial $S = 3$ system when $D < 0$. (a) Energy levels and energy intervals; the highest M_S lie the lowest; (b) graph giving the variation of the energy $D.M_S^2$ of the M_S levels as a function of M_S with an energy barrier ΔE .

Besides this elementary presentation, the interested reader can find more in [2.4], section 2.1.1, on (i) the splitting of the M_S uniaxial level when the rhombicity (E/D) increases; (ii) the ZFS spin Hamiltonians with higher orders in S (S^4, S^6, \dots), often necessary to fit the energy levels; and (iii) the effects of a crystal field on magnetic anisotropy. Important recent developments in molecular magnetism rest on those anisotropy properties (Section 2.8).

2.5.2 Two-centre spin Hamiltonians with spin operators S_1 and S_2

In most cases the magnetic system comprises more than one spin, and the spin Hamiltonian must add to the individual spin Hamiltonians described previously the interaction between the neighbouring spins. Let us begin with the simplest system with two spins, S_1 and S_2 . The Hamiltonian is simply the sum of (i) the individual Hamiltonians of centre 1 (S_1) and 2 (S_2), and (ii) the Hamiltonian describing the interaction between the two spins. The latter is written:

$$\mathbf{H} = -\mathbf{S}_1 \cdot \mathbf{J}_{12} \cdot \mathbf{S}_2 \quad (2.104)$$

\mathbf{J}_{12} is the interaction matrix. Eqn. (2.104) can be written in a more readable form, to evidence three kinds of coupling between the two vector operators \mathbf{S}_1 and \mathbf{S}_2 (scalar, tensor, and vector products):

$$\mathbf{H} = -J_{12}\mathbf{S}_1\mathbf{S}_2 + \mathbf{S}_1\tilde{\mathbf{D}}_{12}\mathbf{S}_2 + \vec{d}_{12}\mathbf{S}_1 \wedge \mathbf{S}_2 \quad (2.105)$$

Isotropic Anisotropic Antisymmetric

where $J_{12} = -\text{Tr}(\mathbf{J}_{12})/3$. Tr is the trace of the interaction matrix (sum of the diagonal elements $J_{12}^{\alpha\alpha}$). $\tilde{\mathbf{D}}_{12}$ is a tensor, such as: $D_{12}^{\alpha\alpha} = \frac{1}{2}(J_{12}^{\alpha\beta} + J_{12}^{\beta\alpha}) - \frac{\delta_{\alpha\beta}}{3}\text{Tr}(\mathbf{J}_{12})$. \vec{d}_{12} is a vector, such as: $d_{12} = \frac{1}{2}(J_{12}^{\beta\gamma} - J_{12}^{\gamma\beta})$. α, β , and γ are the Cartesian components (x, y, z), and $\delta_{\alpha\beta}$ is the Kronecker symbol.

When $|J_{12}| \gg |D_{12}| \gg |d_{12}|$,

$$\mathbf{H} = -J_{12}\mathbf{S}_1\mathbf{S}_2 \quad (2.106a)$$

is the simplest possible, isotropic, Hamiltonian describing the interaction between two spins by a simple *scalar product*. As $\mathbf{S}_1\mathbf{S}_2 = S_1S_2\cos\theta$, it is sometimes called a *cosine* coupling. It was worked out successively by Heisenberg (1926), Dirac (1929), and Van Vleck (1932), and is known from the first letters of their names (HDVV Hamiltonian) [2.7]. Before working out the Hamiltonian we should warn the reader about different formulations by various authors ($\mathbf{H} = -2J_{12}\mathbf{S}_1\mathbf{S}_2$ or $+J_{12}\mathbf{S}_1\mathbf{S}_2$). In general there is no possible confusion, but it is always necessary to look at the Hamiltonian defining J_{12} before comparing different data in the literature. To find the solutions we use our usual tools. After introducing $\mathbf{S} = \mathbf{S}_1 + \mathbf{S}_2$ and its square $\mathbf{S}^2 = \mathbf{S}_1^2 + \mathbf{S}_2^2 + 2\mathbf{S}_1\mathbf{S}_2$, we obtain:

$$\mathbf{H} = -J_{12}\mathbf{S}_1\mathbf{S}_2 = -J [\mathbf{S}^2 - \mathbf{S}_1^2 - \mathbf{S}_2^2] / 2 \quad (2.106b)$$

The total spin S can take all the values comprised between $|S_1 - S_2|$ and $(S_1 + S_2)$. The corresponding eigenvalues in zero-field $E_S^{(0)}$ are:

$$E_S^{(0)} = -J_{12} [S(S + 1) - S_1(S_1 + 1) - S_2(S_2 + 1)] / 2 \quad (2.106c)$$

This equation holds, whatever the values of S_1 and S_2 .

For two spins $S_1 = S_2 = 1/2$, the two spin states S arising from the interaction are $S = 0$ (antiparallel magnetic moments, singlet) and $S = 1$ (parallel magnetic moments, triplet). The energy levels are then:

$$E_{S=0}^{(0)} = E_S^{(0)} = -3J/4 \quad (2.107a)$$

$$E_{S=1}^{(0)} = E_T^{(0)} = +J/4 \quad (2.107b)$$

The state of zero spin ($S = 0$) corresponds to a spin degeneracy $2S + 1 = 1$. It is a singlet S . The state of spin one ($S = 1$) corresponds to a spin degeneracy $2S + 1 = 3$. It is a triplet T . It is easy to find that:

$$E_S^{(0)} - E_T^{(0)} = J \quad (2.107c)$$

Fig. 2.36 shows the corresponding energy states. One can observe in the figure that when the singlet is at the ground state, J is negative. It is said that the coupling between the two spins is antiferromagnetic (Fig. 2.36a and b). When the triplet is at the ground state (Fig. 2.36c), J is positive and the coupling is said to be ferromagnetic.

J , coupling constant between the two spins, when defined by Hamiltonian (2.106a), is the energy difference between the singlet and the triplet states, and is a physical observable. The spin Hamiltonian approach provides it by a very simple calculation. We emphasize its usefulness in Bleaney and Bowers' study of the magnetic properties of copper acetate—an inescapable historical example in molecular magnetism (see Box 'Copper acetate'). Isotropic coupling tends to make the spins parallel (ferromagnetic coupling) or antiparallel (antiferromagnetic coupling).

This is, furthermore, a good example for achieving the second part of our programme, to go from the spin Hamiltonian to its theoretical orbital counterpart, using our preceding calculations (Sections 1.5.2.3 and 1.5.3.1). The reader will realize that there is an exact correspondence between the eigenvalues of the HDVV spin Hamiltonian and those obtained by the Heitler–London approach described in Section 1.5.3.1. Indeed, combining eqn. (1.84d) and eqn. (2.107c) we find:

$$J = E_S^{(0)} - E_T^{(0)} = [2k + 4\beta S - 2S^2(2\alpha + j)] / (1 - S^4) \quad (2.108a)$$

$$J = E_S^{(0)} - E_T^{(0)} \approx 2k + 4\beta S \quad (2.108b)$$

The latter equation is an approximation at first order in S . In many cases, when the overlap integrals S are negligible compared to 1, it is accurate enough. It is

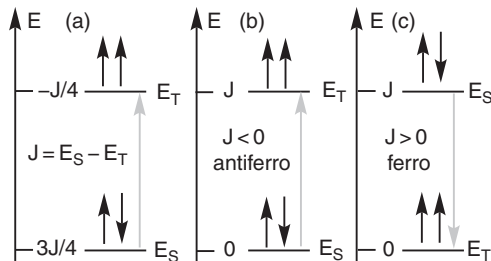


Fig. 2.36

Energy diagram of singlet and triplet states: (a) antiferromagnetic coupling; (b) antiferromagnetic interaction ($J < 0$) taking the singlet energy as origin of energy; (c) ferromagnetic coupling ($J > 0$). J is shown by the grey arrow.

The localized electron: magnetic properties

a very important relationship between J , the energy between the singlet and the triplet (spin approach), and the integrals describing the quantum interaction between two orbitals (orbital approach): S , the overlap integral, β , the resonance or transfer integral, and k , the two-electron exchange integral. Indeed, *the relation between J , a magnetic property, and k , β , and S electrostatic quantities depending on the structure of the molecule, is the fundamental bridge between magnetism and structure in the solid* and a key to build new molecular magnetic materials. This useful correlation will be found in the theoretical model by Kahn and Briat (See Section 2.6.1.1).

The second term in eqn. (2.105), anisotropic exchange, can be approached in the case of the so-called ‘strong exchange’ limit; that is, when $|J_{12}| \gg |D_1|, |D_2|, |D_{12}|, |d_{12}|, \dots$. This is a rather frequently encountered situation. In this case, Bencini and Gatteschi have shown [2.16] that it is possible to relate the spin Hamiltonian parameters of spin S (after coupling) to those of the original spins by the following relations:

$$g_S = c_1 g_1 + c_2 g_2 \quad (2.109a)$$

$$D_S = d_1 D_1 + d_2 D_1 + d_{12} D_{12} \quad (2.109b)$$

with:

$$\begin{aligned} c_1 &= (1 + c)/2; \quad c_2 = (1 - c)/2; \quad d_1 = (c_+ + c_-)/2; \\ d_2 &= (c_+ - c_-)/2; \quad d_{12} = (1 - c_+)/2 \end{aligned} \quad (2.109c)$$

Here, d_{12} is a coefficient, not to be confused with the antisymmetric vector \vec{d}_{12} .

And:

$$c = \frac{S_1(S_1 + 1) - S_2(S_2 + 1)}{S(S + 1)} \quad (2.109d)$$

$$c_+ = \frac{3[S_1(S_1 + 1) - S_2(S_2 + 1)]^2 + S(S + 1)[3S(S + 1) - 3 - 2S_1(S_1 + 1) - 2S_2(S_2 + 1)]}{(2S + 3)(2S - 1)S(S + 1)} \quad (2.109e)$$

$$c_- = \frac{4S(S + 1)[S_1(S_1 + 1) - S_2(S_2 + 1)] - 3[S_1(S_1 + 1) - S_2(S_2 + 1)]}{(2S + 3)(2S - 1)S(S + 1)} \quad (2.109f)$$

The full demonstration and examples of applications can be found in [2.4] and [2.16]. Anisotropic exchange tends to align the spins in a privileged direction in space.

When the strong exchange conditions are not realized or when the ground state is orbitally degenerate, the situation becomes much more difficult to describe. A possible shortcut is to write eqn. (2.106a) in a different way, evidencing the Cartesian components of the spins \mathbf{S}_1 and \mathbf{S}_2 in the scalar product, and introducing different values J_x , J_y , and J_z . Thus the following expression:

$$\mathbf{H} = -\mathbf{J}\mathbf{S}_1 \cdot \mathbf{S}_2 = -J [S_{1x}S_{2x} + S_{1y}S_{2y} + S_{1z}S_{2z}] \quad (2.110a)$$

is replaced by

$$\mathbf{H} = -[J_x S_{1x}S_{2x} + J_y S_{1y}S_{2y} + J_z S_{1z}S_{2z}] \quad (2.110b)$$

When J_x , J_y , and J_z are equal the exchange is isotropic: the coupling between the x , y , and z components of the spins are the same. But eqn. (2.110b) allows

Table 2.5 Isotropic and anisotropic exchange.

J_i values	Nature of exchange	Name
$J_x = J_y = J_z$	Isotropic	Heisenberg
$J_x \approx J_y \ll J_z$	Uniaxial (easy axis)	Ising
$J_x \approx J_y \gg J_z$	Planar (easy plane)	XY
$J_x \neq J_y \neq J_z$		XYZ

having different J_x , J_y , and J_z , which is a convenient way of describing an anisotropic exchange situation, frequently used by solid state physicists. Table 2.5 gathers different experimentally encountered situations.

The Ising situation corresponds to an easy axis of the magnetization: in a magnetic field the spins are aligned more easily in the z direction than in the two others; the XY situation corresponds to an easy plane of magnetization: the spin orients more easily in the XY plane than in the z direction. Other elegant approaches of exchange in the case of orbital degeneracy of the ground state have been proposed by Borrás–Almenar and Tsukerblat *et al.* in [2.6]. Exchange anisotropy is an important property in magnetic materials, as we shall see in Section 2.8.

The last term in eqn. (2.105) is antisymmetric exchange. This term describes the tendency of S_1 and S_2 to orient at 90° (See Fig. 2.64). It was developed by Dzyaloshinskii and Moriya. To occur, it needs systems with very low symmetry; but we do not tackle it in this book.

2.5.3 More than two centres

2.5.3.1 Uniform isotropic interaction between several spins: the Kambe method

After the simple case of two spins in interaction, we give the example of several spins (i or j from 1 to n), interacting between them with the same interaction, J_{ij} . We consider first that anisotropic and antisymmetric coupling can be neglected, so that we can generalize the Hamiltonian (2.106a) by summing $J_{ij} \cdot S_i \cdot S_j$ terms:

$$\mathbf{H} = - \sum_{i=1}^n \sum_{j>i} J_{ij} \mathbf{S}_i \mathbf{S}_j = -J \sum_{\text{neighbours}} \mathbf{S}_i \mathbf{S}_j \quad (2.111a)$$

where all the J_{ij} are equal. As before, we write the total spin operator and its square:

$$\mathbf{S} = \sum_{i=1}^n \mathbf{S}_i \quad \mathbf{S}^2 = \left(\sum_{i=1}^n \mathbf{S}_i \right)^2 = \sum_{i=1}^n \mathbf{S}_i^2 + 2 \sum_{\text{neighbours}} \mathbf{S}_i \mathbf{S}_j \quad (2.111b)$$

$$\mathbf{H} = -J \sum_{\text{neighbours}} \mathbf{S}_i \mathbf{S}_j = \frac{1}{2} \left[\mathbf{S}^2 - \sum_{i=1}^n \mathbf{S}_i^2 \right] \quad (2.111c)$$

Then, after Van Vleck [2.20a], the eigenvalues are:

$$E_s = \frac{-zJ}{2(n-1)} \left[S(S+1) - \sum_{i=1}^n S_i(S_i+1) \right] \quad (2.111d)$$

The localized electron: magnetic properties

where z is the number of neighbours, and n is the number of interacting spins.

To compute the susceptibility through the Van Vleck equation (2.45), we need to know the degeneracy of the levels S' that is, the number of times $\Omega(S')$ a level appears with a given spin S' . Van Vleck suggests the following solution:

$$\Omega(S') = \omega(S') - \omega(S' + 1) \quad (2.111e)$$

where $\omega(S')$ is the coefficient of S' in the following expansion:

$$(x^S + x^{S-1} + x^{S-2} + \dots + x^{-S+1} + x^{-S})^n \quad (2.111f)$$

It is easy to become familiar with the use of the last three equations to determine the energy levels and their degeneracy in a copper(II) binuclear complex: $S=1/2$, $n = 2$, $S' = 0$ or 1 , so that: $(x^{1/2} + x^{-1/2})^2 = x^1 + 2x^0 + x^{-1}$; $\omega(2) = 0$; $\omega(1) = 1$ and $\omega(0) = 2$. Then, $\Omega(1) = \omega(1) - \omega(2) = 1 - 0 = 1$, and $\Omega(0) = \omega(0) - \omega(1) = 2 - 1 = 1$. We find again the trivial result that the triplet energy is $E(S=1) = -J/4$; the singlet $E(S = 1) = 3J/4$; and both levels are non-degenerate.

The method was proposed first by K. Kambe [2.37] for trinuclear complexes of Fe^{3+} and Cr^{3+} , and can be found also in various places [2.25]. It can be applied to write concise analytical formula of the energy of the spin levels in high-symmetry systems when the coupling constant J is uniform among the neighbours. It can be used also in some cases with different coupling constants. To avoid lengthy equations we consider only a very simple system of three ions A_1, A_2, A_3 in a linear (or isosceles) molecule with spins S_1, S_2, S_3 , with an interaction J_1 between S_2 and S_1 and S_2 and S_3 , and an interaction J_2 between S_1 and S_3 . It is convenient to rename J_1 as J and J_2 as αJ . The spin Hamiltonian is then written:

$$\mathbf{H} = -J [\mathbf{S}_1 \cdot \mathbf{S}_2 + \mathbf{S}_2 \cdot \mathbf{S}_3 + \alpha \mathbf{S}_1 \cdot \mathbf{S}_3] \quad (2.112a)$$

The trick is to introduce an intermediate spin operator \mathbf{S}^* :

$$\mathbf{S}^* = \mathbf{S}_1 + \mathbf{S}_3 \quad \text{and} \quad \mathbf{S} = \mathbf{S}^* + \mathbf{S}_2 \quad (2.112b)$$

The choice of the intermediate spin is generally determined by the symmetry of the system, but it can be chosen arbitrarily. In any case, once chosen it is compulsory to keep the same coupling scheme during the whole calculation. Using the properties of \mathbf{S}^2 operators, the reader can easily find that the Hamiltonian, and its related eigenvalues $E(S, S^*)$, can be written as:

$$\mathbf{H} = -J [\mathbf{S}^2 - \mathbf{S}^{*2}(1 - \alpha) - \mathbf{S}_2^2 - \alpha (\mathbf{S}_1^2 + \mathbf{S}_3^2)]/2 \quad (2.112c)$$

$$E(S, S^*) = -J[(S(S+1) - S^*(S^*+1)(1-\alpha) - S_2(S_2+1) - \alpha S_1(S_1+1) - \alpha S_3(S_3+1)]/2 \quad (2.112d)$$

An even more compact equation is obtained when $S_1 = S_2 = S_3 = S_i$. The eigenvalues depend now on S^* and S . With the usual rules, $|S_2 - S_3| \leq S^* \leq S_2 + S_3$ and $|S^* - S_2| \leq S \leq S^* + S_2$. It is useful to build a table to find the values of S^* and S , to determine the various states (S, S^*) , their energies $E(S, S^*)$ and their degeneracies as before. The reader can check as an exercise that the energies of a three spin $1/2$ systems present the following

energies: $E(3/2, 1) = -J/2 + 3\alpha J/4$; $E(1/2, 1) = +J - \alpha J/4$; $E(1/2, 0) = +3\alpha J/4$.

Another powerful method useful for larger but highly symmetric clusters relies on the formalism of irreducible tensors, fully exploiting the symmetry of the spin system, and can be found in [2.4], section 2.5.

2.5.3.2 Exchange anisotropy in clusters

We close this section on spin Hamiltonians by extending the results obtained on the anisotropy of binuclear objects to cluster objects. The main goal is to relate the spin Hamiltonian parameters of the cluster to those of the individual constituents with closed-form equations. This can be done ‘easily’ only in the case of the strong exchange limit. Otherwise, it is necessary to apply more cumbersome computation methods. We simply give the principles, since more detailed calculations can be found in [2.4] section 2.5. Basically, the total spin is approached through intermediary spins as introduced in Section 2.5.3.1. If there are $n = 4$ spins one can write: $\mathbf{S}_{12} = \mathbf{S}_1 + \mathbf{S}_2$; $\mathbf{S}_{123} = \mathbf{S}_{12} + \mathbf{S}_3$; $\mathbf{S} = \mathbf{S}_{123} + \mathbf{S}_4$. $n - 2$ intermediate spins are needed. The $\tilde{\mathbf{g}}$ and $\tilde{\mathbf{D}}$ tensors for the different intermediates are written successively. The spin Hamiltonian for the spin–spin interaction of the whole system is composed of the sum of terms involving the individual local anisotropy $\tilde{\mathbf{D}}_i$ tensors and of terms implying the anisotropy interactions $\tilde{\mathbf{D}}_{ij}$ between spins i and j , as in eqn. (2.109b) for two centres:

$$\mathbf{H}_{ss} = \sum_{i=1}^n \mathbf{S}_i \tilde{\mathbf{D}}_i \mathbf{S}_i + \sum_{i=1, j>1}^n \mathbf{S}_i \tilde{\mathbf{D}}_{ij} \mathbf{S}_j \quad (2.113a)$$

$$\tilde{\mathbf{D}}_S = \sum_{i=1}^n d_i \tilde{\mathbf{D}}_i + \sum_{i=1, j>i}^n d_{ij} \tilde{\mathbf{D}}_{ij} \quad (2.113b)$$

$\tilde{\mathbf{D}}_S$ is the anisotropy tensor of the ground spin state S . The coefficients d_i and d_{ij} can be computed from the characteristics of the system. For example, Gatteschi *et al.* proposed the following simple formulae for the coefficients, in the case of a ferromagnetic coupling between n spins S_i (Section 2.5.2 of [2.4]):

$$(c) d_i = \frac{2S_i - 1}{n(2nS_i - 1)} \quad (d) d_{ij} = \frac{2S_i}{n(2nS_i - 1)} \quad (2.113c,d)$$

More than the details of the calculation, we are interested in the results of this spin Hamiltonian approach in simple anisotropic situations. For example, when identical individual spins have their anisotropy axis parallel, the single-ion participation in the D_S parameter of the ground spin is:

$$D_S = \frac{2S_i - 1}{2nS_i - 1} D_i \quad (2.114)$$

Then, within the spin ground state S , when D_S is negative, an energy barrier Δ will arise (see Section 2.5.1.2.). It will prove central in the physics of single-molecule magnets (Section 2.8). More generally, the spin Hamiltonian approach briefly introduced here will be used in different contexts throughout this chapter.

2.6 Orbital interactions and exchange

In the preceding section the spin Hamiltonian provided a tool for determining the spin states and the energy levels of a magnetic system. The coupling constant J was a phenomenological parameter; that is, it described only the coupling phenomenon, not the underlying mechanism. In the present section we propose describing and understanding in more depth the nature of the J coupling between two electrons. This fundamental problem has raised the interest of many scientists, from the beginning of quantum mechanics to the applied study of magnetic materials. The problem is not fundamentally different from the problem of bonding for which we provided solutions in Chapter 1. A famous book by J. Goodenough is indeed entitled *Magnetism and the Chemical Bond* [2.38].

But the focus here is not on the bond but on the magnetic properties, and more precisely on the singlet–triplet energy separation, J . And we know that the coupling's origin is not magnetic but electrostatic, orbital.

We start with the simple case of two unpaired electrons, involving two orbitals and two spins in a molecule. The two unpaired electrons considered will be named *active*, in opposition to all other electrons in the system, named passive, even if this is not strictly the case.

The two unpaired electrons are described by orbitals a and b having an overlap integral S . For the while, a and b are pure atomic orbitals of the $1s$ type, and the system is symmetrical (a and b have equal energies and the same nature). These two orbitals build the molecular orbitals ψ_1 and ψ_2 with energies ε_1 and ε_2 respectively, and $\Delta = \varepsilon_1 - \varepsilon_2$ (Fig. 2.37a):

$$\psi_1 = N_+ (a + b) \quad (2.115a)$$

$$\psi_2 = N_- (a - b) \quad (2.115b)$$

When the overlap is weak ($|\varepsilon_1 - \varepsilon_2|$ weak) the Heitler–London model (HL) was found to be preferred to the Hund–Mulliken (HM) scheme (see Section 1.5.3).

The different electronic configurations and states were given in Fig. 1.42. They constitute our starting point to present briefly, without extensive calculations, a few models of the exchange interaction in molecules.

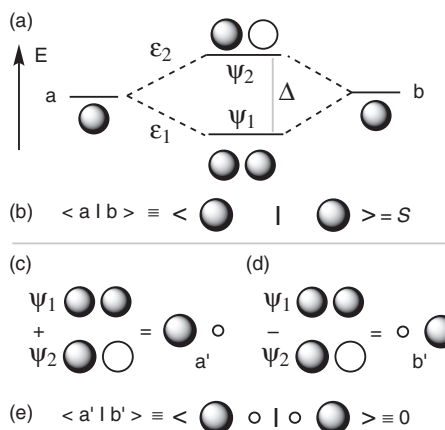


Fig. 2.37

(a) Two molecular orbitals ψ_1 and ψ_2 built from two basis orbitals a and b . ψ_1 and ψ_2 are orthogonal; (b) a and b orbitals have a non-zero overlap integral S ; (c) and (d) obtention of orthogonalized basis orbitals a' and b' from the linear combination of ψ_1 and ψ_2 ; (e) there is a unique solution corresponding to a' and b' having a zero overlap integral.

Copper acetate

Copper acetate can be considered a cornerstone in molecular magnetism and the first example of the study of magnetic exchange occurring within a molecule. The story began in 1951, before the crystallographic structure was known. Since then, the interpretation of the magnetic properties has attracted tremendous interest, and the saga continues with new materials based on the same structure.

In 1951, Guha published the temperature dependence of susceptibility [1]. Upon cooling, instead of presenting the Curie law, it showed a broad maximum near 250 K, and then dropped almost to zero. A year later, Bleaney and Bowers reported the decrease of the EPR signal intensity at low temperature, and concluded to an 'anomalous paramagnetism of copper acetate' [2]. Without knowing the structure, they proposed that 'isolated pairs of copper ions interact strongly through exchange forces, each pair forming a lower singlet state and an upper triplet state, the latter only being paramagnetic'. The 'anomalous' EPR results came from the triplet state, which behaves as a diradical (while the singlet state is EPR silent), and the decrease of both EPR signal and susceptibility at low temperature was nicely explained by the Boltzmann distribution over the different energy levels. The most relevant information is gathered in Fig. 1.

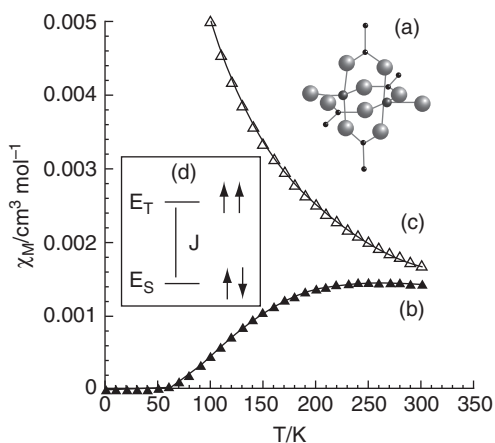


Fig. 1

Copper acetate: (a) structure; (b) recent susceptibility data (black triangles); (c) Curie law susceptibility behaviour for two spins without interaction; (d) the two-level spin model of Bleaney and Bowers.

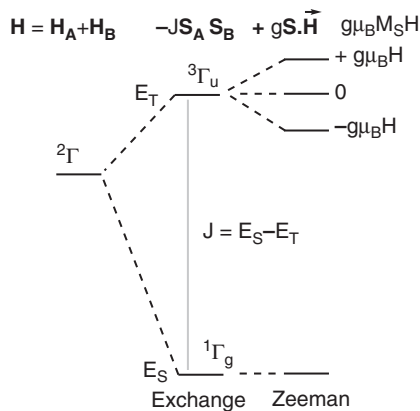


Fig. 2

Energy splitting in copper acetate through the successive action of exchange and Zeeman effect.

The susceptibility data can be fitted with a Bleaney–Bowers law and singlet–triplet gap value, $J = -296 \text{ cm}^{-1}$. Using the energy levels in Fig. 2, it is a good exercise for the reader to apply the Van Vleck equation and find the law proposed by Bleaney and Bowers (here in cgs-emu units):

$$\chi_M = \frac{2N_A g^2 \mu_B^2}{kT(3 + e^{-J/kT})}$$

The X-ray crystal structure, determined in 1953 by Van Niekerk and Schoening, confirmed the dinuclear nature of the compound [3]: the two copper(II) ions are bridged by four carboxylates (Fig. 1a). A water molecule is coordinated to each copper(II) achieving a square pyramidal geometry. The metal–metal distance is 2.64 Å. For that distance, and taking into account the orientation of $d_{x^2-y^2}$ orbitals, there is no significant direct overlap (contrary to the chromium(II) analogue, where the t_{2g} – t_{2g} overlap is so strong that the complex is diamagnetic). It is now recognized that the interaction occurs through the four bridging ligands.

Over the years, copper acetate has served as a reference compound to test exchange theories (not without a struggle!), computational techniques including ‘premières’ ([4] and see the following), and new types of experiment. Thus the singlet–triplet transition, which is unobservable by infrared or Raman spectroscopy because the corresponding transition is forbidden, was determined directly by inelastic neutron scattering in 1979 [5]. The result confirms magnetic measurements and provide a separation of $298 \pm 4 \text{ cm}^{-1}$. A nice summary of the magnetic story of copper acetate can be found in [4].

Today, the beautiful dinuclear structure is used as a precursor for materials—either magnetic frameworks where the copper pairs are substituted by dissymmetric AB pairs, or porous materials by replacing the acetate by extended carboxylates and water by bridging ligands, whereas theoreticians continue to unravel the details of the electronic structure. Guihéry *et al.* recently solved the calculation of the sign of zero-field splitting, $D = -0.335 \text{ cm}^{-1}$ [6].

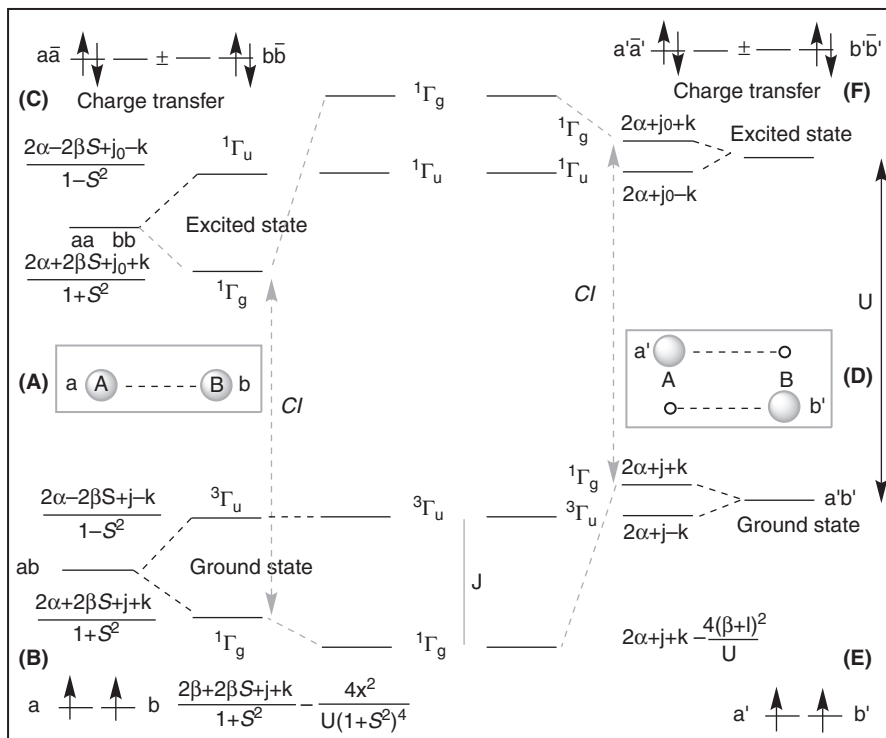
References

- [1] B. C. Guha, *Proc. Roy. Soc. A* 206 (1951), 353.
- [2] B. Bleaney, K. D. Bowers, Anomalous Paramagnetism of Copper Acetate, *Proc. Roy. Soc. (London) A* 214 (1952), 451.
- [3] J. N. Van Niekerk, F. R. L. Schoening, *Acta Cryst.* 6 (1953), 227.
- [4] P. de Loth, P. Cassoux, J. P. Daudey, J. P. Malrieu, *J. Am. Chem. Soc.* 103 (1981), 4007.
- [5] H. U. Güdel, A. Stebler, A. Furrer, *Inorg. Chem.* 18 (1979), 1021.
- [6] R. Maurice, K. Sivalingam, D. Ganyushin, N. Guihéry, C. de Graaf, F. Neese, *Inorg. Chem.* 50 (2011), 6229–36.

2.6.1 Basic theoretical background

2.6.1.1 Heitler–London model, non-orthogonal orbitals

We start here with the model by Kahn and Briat [2.3, 2.39], based on the Heitler–London scheme presented in Section 1.5.3.1. In Fig. 2.38, left-hand side, are shown the orbitals a on centre A and b on centre B (A); their overlap integral is $S = \langle a|b \rangle$; the electronic configurations and energies (B) provided

**Fig. 2.38**

Energies of the singlet and triplet states created by the interaction of non-orthogonalized orbitals a, b (A, B, C left) and orthogonalized ones a', b' (D, E, F right) in the frame of the Heitler–London model. In the middle are shown the orbitals a and b (A) and a' and b' (D). At the bottom are represented the low-lying configurations, energies, and states $[ab]$ (B) and $[a'b']$ (E). At the top, the excited states obtained by electron transfer from one site to the other, $a\bar{a}$ and $b\bar{b}$ (C) and $a'\bar{a}'$ and $b'\bar{b}'$ (F). In the centre are shown the energy levels obtained by configuration interaction (CI, grey arrows) between the ground and excited states of same symmetry (${}^1\Gamma_g$). The constant x which appears in (B) is defined in the text. (Adapted from [2.39].)

by eqns. (1.81) and (1.82a,b). Their interaction defines a ground-state singlet ${}^1\Gamma_g$ (E_S energy) and a triplet ${}^3\Gamma_u$ (E_T energy) (Figs. 1.42C and 2.38B). The coupling constant J is already defined as $(E_S - E_T)$. The electron transfer of one electron to the other orbital creates two singlet charge-transfer excited states, ${}^1\Gamma_g$ and ${}^1\Gamma_u$ (Figs. 1.42B and 2.38C).

In a second step, the two ground and excited states ${}^1\Gamma_g$ of same symmetry interact through configuration interaction (CI); they repel each other and give rise to slightly modified—and better—energy levels. Between the ground and the excited states the energy difference is $U = (j_0 - j)/(1 + S^2)$. The CI process stabilizes slightly the ground state by $-4x^2U/(1 + S^2)^4$ with $x = (\beta - \alpha S)(1 - S^2) + \ell(1 + S^2) - (j + k)S$; the calculation of the energy stabilization can be found in reference [2.39]. An improved J value is then obtained.

$$J = [2k + 4\beta S - 2S^2(2\alpha + j)] / (1 - S^4) - 4[(\beta - \alpha S + \ell - (j + k)S)^2 / U] \quad (2.116a)$$

The localized electron: magnetic properties

The two-electron integral ℓ (the repulsion between $a(1)b(2)$ and $b(1)b(2)$ configurations) is:

$$\ell = \langle a(1)b(2) \left| \frac{e^2}{r_{12}} \right| b(1)b(2) \rangle = \langle \phi_a(1)\phi_b(2) \left| \frac{e^2}{r_{12}} \right| \phi_b(1)\phi_b(2) \rangle \quad (2.116b)$$

The most important conclusion is that the Heitler–London model, with *a priori* non-orthogonal orbitals, provides the proper ground state $^1\Gamma_g$ without the need of configuration interaction. Eqn. (2.116a) provides the J value, which can be reduced at the first order in S (the overlap integral) as:

$$J = [2k + 4\beta S - 2S^2(2\alpha + j)] / (1 - S^4) \approx 2k + 4\beta S \quad (2.117a)$$

$$J = J_F + J_{AF} \quad (2.117b)$$

The term βS (< 0 when $S > 0$ and $\beta < 0$) can be substituted by equivalent quantities $\beta S \propto \beta^2 \propto S^2 \propto \Delta^2$ since $|\beta| \propto S$ (an approximation suggested by Mulliken) and $\beta \approx -|\Delta|/2$ (Δ is the energy difference between ψ_1 and ψ_2).

The sign of J is determined by the sum of a positive term, $2k$, favouring ferromagnetism and a negative one, $4\beta S$, favouring antiferromagnetic coupling.

2.6.1.2 Heitler–London model, orthogonalized orbitals

What happens if we use the *orthogonalized* orbitals a' and b' , instead of overlapping orbitals a and b ? The answer suggested by Girerd *et al.* [2.39] is shown on the right-hand side of Fig. 2.38. How do we obtain orthogonalized orbitals a' and b' ? We simply start from the bonding and antibonding molecular orbitals ψ_1 and ψ_2 of Fig. 2.37 (assumed to be the result of a quantum-chemical calculation of the complete system), and combine them with the following transformation maintaining orthogonality (eqns. (2.118a–c)):

$$a' = \sqrt{2}(\psi_1 + \psi_2)/2 \quad (2.118a)$$

$$b' = \sqrt{2}(\psi_1 - \psi_2)/2 \quad (2.118b)$$

and:

$$\langle a'|b' \rangle \equiv 0 \quad (2.118c)$$

The new orbitals a' and b' are orthogonal by definition, and they look as shown in Fig. 2.37c, d, e. (a' is centred mainly on A with a small antibonding—participation of B—and the opposite for b').

We can then compute the energy levels of the coupled system with a' and b' as basis orbitals. The energies are still given by eqns. (1.81) and (1.82a,b) by simply dropping the term in S since now the overlap integral S is zero. We should introduce a prime on all the integrals, S' , and so on, since they are defined with different orbitals and their values are different. Nevertheless, the change of basis orbitals, using such a unitary transformation, does not change the final energies of the system [2.39]. We drop the primes.

The energies of the ground states singlet $^1\Gamma_g$ and triplet $^3\Gamma_u$ are:

$$E(^1\Gamma_g) = 2\alpha + j + k \quad (2.119a)$$

$$E(^3\Gamma_u) = 2\alpha + j - k \quad (2.119b)$$

$$E_S - E_T = J = 2k (> 0) \quad (2.119c)$$

The result is drastically different. The triplet state is now the ground state! The interaction is expected to be ferromagnetic. As before, we can proceed further and take into account the configuration interaction between the two $^1\Gamma_g$ states of the ground and excited charge-transfer states. The lower $^1\Gamma_g$ state is strongly stabilized. The triplet state does not move, and we reach an energy scheme in agreement with the one obtained with non-orthogonal orbitals, due to the configuration interaction:

$$E_S - E_T = J = 2k - 4(\beta + \ell)^2/U \quad (2.119d)$$

The singlet–triplet gap is still the sum of a positive term (exchange integral k) and a negative one, introduced due to configuration interaction. The denominator in the stabilization term is U , and the difference in energy between the ground and the excited (charge transfer) states is, as usual, CI . The result allows us to understand the first quantum calculations of Heisenberg, who arrived, with orthogonal orbitals, at rigorously the same conclusion as eqn. (2.119c). $J = 2k$ is positive, and the interaction is ferromagnetic. It was necessary to await the thesis of L. Néel in 1932 to realize on an empirical basis that J could be negative and the interaction antiferromagnetic. The world was no longer a big magnet. It is also rewarding to note that the negative term in (2.119c) (which comprises the integral ℓ defined in eqn. (2.116b)) is very similar that of β^2/U introduced by Anderson to help solve the ‘great question of the sign of exchange interaction’.

2.6.1.3 Hund–Mulliken model, orthogonalized orbitals

Similar (and complementary) conclusions can be reached using the Hund–Mulliken model, as proposed by Hoffmann and coworkers [2.40]. One starts with the states obtained from molecular orbitals (scheme (a) in Fig. 1.42, where ψ_1 and ψ_2 are defined as in Fig. 2.37). The triplet state is uniquely defined ($\psi_1 \uparrow$ and $\psi_2 \uparrow$ and other triplet components). This is useful to allow an SCF calculation of the orbitals on the high-spin (triplet) state. It is more difficult to define the singlet ground state (GS), since in general it will be represented by linear combination of the two singlets S_0 and S_2 of same symmetry $^1\Gamma_g$ [2.40].

$$\Psi_{GS} = c_1\Psi_{S_0} + c_2\Psi_{S_2} \quad (2.120)$$

A strong interaction between orbitals a and b leads to a large energy difference $\varepsilon_1 - \varepsilon_2$ and $c_1 \gg c_2$ in eqn. (2.120). In such a case, the singlet state S_0 can be considered a good approximation for the ground-state singlet GS. But if the interaction is weak (small $\varepsilon_1 - \varepsilon_2$), it becomes clear that the ground-state singlet will obey eqn. (2.120) with $c_1 \approx c_2$. In other words, a configuration interaction will necessary be between S_0 and S_2 to obtain the appropriate ground state. Using the usual quantities (i) \mathbf{h}_i , the one-electron energy Hamiltonian for electron i in the system (kinetic and potential energies, nuclear repulsion); (ii) the usual Coulomb and exchange two-electron interactions (see Section 1.5).

$$h_i = \langle \psi_1(1) | \mathbf{h}_i | \psi_1(1) \rangle \quad (2.121a)$$

The localized electron: magnetic properties

$$J_{ij} = \langle \psi_i(1) \psi_j(2) \left| \frac{\mathbf{e}^2}{r_{ij}} \right| \psi_i(1) \psi_j(2) \rangle \quad (2.121b)$$

$$K_{ij} = \langle \psi_i(1) \psi_j(2) \left| \frac{\mathbf{e}^2}{r_{ij}} \right| \psi_i(2) \psi_j(1) \rangle \quad (2.121c)$$

We skip here the calculations (the diagonalization of the 2 x 2 matrix implying S_0 and S_2 , which can be found in [2.40] and [1.15]).

After reasonable approximations, neglecting non-significant weak terms [2.40], it arrives at:

$$E_T = h_1 + h_2 + J_{12} - K_{12} \quad (2.122a)$$

$$E_S = h_1 + h_2 + (J_{11} + J_{22})/2 - (1/2) [(2h_1 + J_{11} - 2h_2 - J_{22})^2 + 4K_{12}^2]^{1/2} \quad (2.122b)$$

$$E_S - E_T \approx -J_{12} + K_{12} + (J_{11} + J_{22})/2 - (h_1 - h_2)^2/2K_{12} \quad (2.122c)$$

where remain the main ingredients. As it is difficult to extract easily useful information from the last expression, R. Hoffmann and coworkers introduced orthogonalized localized orbitals a' and b' , as we did previously. They write the identities between the integrals J_{12} , K_{12} , ... (defined as previously from the molecular orbitals ψ_1 and ψ_2) and their equivalent $J_{a'b'}$, $K_{a'b'}$... (defined from the a' and b' orbitals):

$$J_{11} = (1/2) (J_{a'a'} + J_{a'b'}) + K_{a'b'} + 2 \langle a'a'|a'b' \rangle \quad (2.123a)$$

$$J_{22} = (1/2) (J_{a'a'} + J_{a'b'}) + K_{a'b'} - 2 \langle a'a'|a'b' \rangle \quad (2.123b)$$

$$J_{12} = (1/2) (J_{a'a'} + J_{a'b'}) - K_{a'b'} \quad (2.123c)$$

$$K_{12} = (1/2) (J_{a'a'} - J_{a'b'}) \quad (2.123d)$$

Then, the orbitals' energies ε_i are expressed as a function of the h_i (Section 1.5):

$$\varepsilon_1 = h_1 + J_{12} - K_{12} \quad \text{and} \quad \varepsilon_2 = h_2 + J_{12} - K_{12}, \quad \varepsilon_1 - \varepsilon_2 = h_1 - h_2 \quad (2.123e)$$

It comes after some new calculations and approximations:

$$J = E_S - E_T \approx 2K_{a'b'} - (\varepsilon_1 - \varepsilon_2)^2 / (J_{a'a'} - J_{a'b'}) \quad (2.124)$$

The singlet-triplet gap is once more the sum, or the competition, of a positive term J_F (always related to an exchange integral $K_{a'b'} > 0$) and a negative term J_{AF} built from the square of the energy difference between the molecular orbitals and the difference of two Coulomb integrals (in general, $J_{a'a'} > J_{a'b'} > K_{a'b'}$). It is easy to recognize under the name $K_{a'b'}$, $J_{a'a'}$, $J_{a'b'}$ and $\langle a'a'|a'b' \rangle$, our previous two-electron repulsion integrals k , j_0 , j , and l , defined on other quantum objects. When $\varepsilon_1 = \varepsilon_2$ the preceding result related to orthogonal orbitals is recovered: J is positive and the interaction is ferromagnetic. In series of compounds where $K_{a'b'}$, $J_{a'a'}$, $J_{a'b'}$ can be considered as constant (weak variation of the structure), J depends only on the square of $\Delta = \varepsilon_1 - \varepsilon_2$ —a quantity

easily accessible to simple molecular quantum calculations (extended Hückel MOs for example). In the case where the denominator is reasonably constant (a same system with smooth geometry changes, for example), it is possible to correlate J (the magnetic properties) to the geometry changes.

2.6.2 From hydrogen to transition metal complexes

2.6.2.1 Interaction between d orbitals

If we replace 1s orbitals by 3d orbitals, the problem and the conclusions are rigorously the same, in the frame of the HL scheme. This kind of exchange interaction has been called ‘direct exchange’ (with no need for intermediary ligand). But the symmetry begins to play a crucial role. Everything being equal—distance in particular—the overlap integral S is decreasing for σ , π , or δ overlaps, reaching zero for orthogonality, as shown in Fig. 2.39. This means that we can move with the same orbitals from a situation displaying strong antiferromagnetism to ferromagnetism, depending on symmetry.

2.6.2.2 Interaction through a monoatomic bridge in an A-X-B entity

To be closer to real problems we need to introduce a diamagnetic ligand between the two singly occupied orbitals (SOMO). Such a bridge raises a difficult problem: how could a diamagnetic ligand participate to the exchange? The A-X-B problem is still a controversial topic for some. Figure 2.40 sets the scene: the SOMOs are two $x^2 - y^2$ orbitals ϕ_A and ϕ_B of a Cu(II) ion, electronic configuration d^9 , and the ligand X is simply a p_x orbital. This example corresponds to an imaginary linear symmetric oxide bridge between two copper(II) ions, Cu(II)–O–Cu(II). We forget for the while the ancillary ligands necessary to allow the Cu(II) unpaired electron to be described by a $x^2 - y^2$ orbital (for example, in a square planar geometry). The σ overlap is chosen accordingly (see Section 1.3.6). An inversion centre is at the oxygen site in the middle of the two metallic ions. The symmetry is $D_{\infty h}$, but for simplicity we use the u and g notations related to the inversion operation.

We start from three *a priori* non-orthogonal orbitals, two $x^2 - y^2$ orbitals of the metallic ions, and a p_x orbital of the ligand. The p_x orbital (symmetry u) is lower in energy than the d orbitals, since the oxygen is more electronegative than the metals. To obtain the three molecular orbitals ψ_0 , ψ_1 , and ψ_2 it is helpful to build two u and g symmetry orbitals by a \pm combination of the d orbitals. The u symmetry orbital combines with the p_x orbital to give a bonding MO (ψ_0) and an antibonding one (ψ_2). The g symmetry orbital, unchanged, becomes the molecular orbital ψ_1 . The bonding MO ψ_0 is fully occupied with two electrons, and the two other MOs share two electrons. Figure 2.40 displays

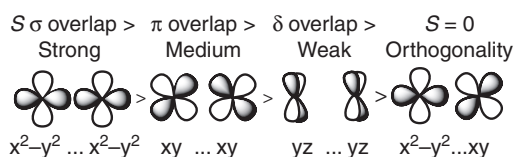
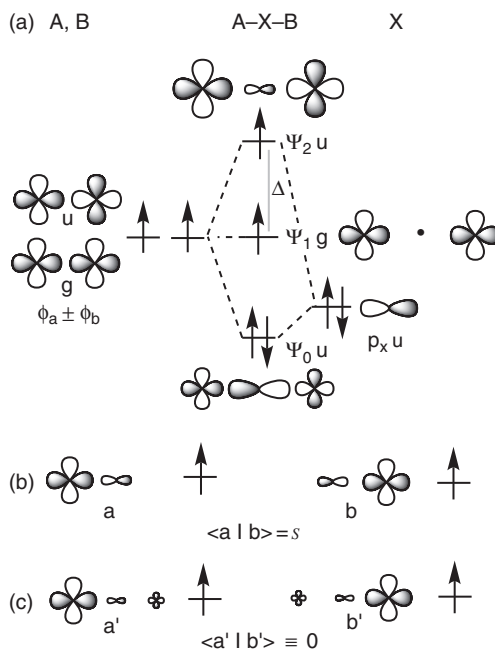


Fig. 2.39

Tuning the overlap between d orbitals with symmetry, from strong σ overlap to zero (orthogonality).

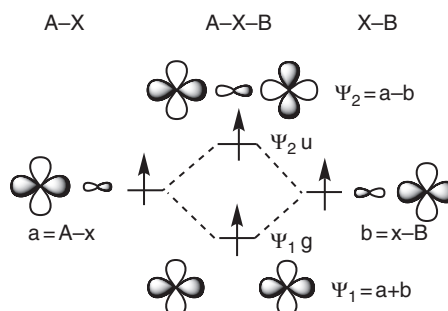
Fig. 2.40

Illustration of non-orthogonal and orthogonalized basis orbitals in the case of d orbitals and a bridging ligand X. (a) Three molecular orbitals ψ_0 , ψ_1 , and ψ_2 built from three non-orthogonal basis orbitals: the u and g symmetry orbitals built from ϕ_a and ϕ_b on the left and p_x on the right; ψ_0 , ψ_1 , and ψ_2 are orthogonal; (b) non-orthogonalized orbitals a and b and (c) orthogonalized orbitals a' and b' built from the linear combination of ψ_1 and ψ_2 . There is a unique solution corresponding to a zero overlap integral for a' and b' , since the overlap integral S is zero (c), which is not the case for a and b (b).



a triplet configuration $\psi_0(\uparrow\downarrow)\psi_1(\uparrow)\psi_2(\uparrow)$. Then the problem can be tackled as in the preceding HM and HL cases. Two singlets S_0 and S_2 are built from ψ_1 and ψ_2 and combine to give the ground state. The two molecular orbitals ψ_1 and ψ_2 can be localized and orthogonalized to give a' and b' , and the results for J are given by eqn. (2.124) (Hund–Mulliken situation, Section 2.6.1.3). On the other hand, to build ψ_1 and ψ_2 one can start alternatively from the two orbitals a and b, of the A-X and X-B fragments, centred on A and B and partially delocalized on the ligand oxide (obtained by ligand field theory) (Fig. 2.41). They are *a priori* non-orthogonal (they can be computed, for example, using a molecular orbital calculation of the Cu–O fragments). We are back to the Heitler–London situation (Section 2.6.1.1). The result for J is given by eqn. (2.117a). But if the a' and b' orbitals (HM) are clearly defined, it is not the case for a and b (HL), which are less rigorously defined.

The magnetic orbital concept allows use of the same expressions as for pure d orbitals, and this is the reason of its great heuristic power. Note, however,

**Fig. 2.41**

Two localized orbitals a and b interact to give molecular orbitals ψ_1 and ψ_2 (upper part of Fig. 2.40)

that in using expressions such as eqn. (2.117a), β is now an *effective* quantity (see Section 1.2.3). We shall re-encounter this concept of effective resonance integral in Chapter 3.

This situation is known in the literature as *superexchange* interaction; that is, exchange through a diamagnetic bridging ligand. We see that introducing the localized orbitals a' and b' or a, b , demonstrates that there is no difference *in nature* between 'direct exchange' between localized d orbitals (a, b or a', b') and 'superexchange'.

Superexchange

The concept of superexchange is defined by the IUPAC as an 'electronic interaction between two molecular entities mediated by one or more different molecules or ions'.

We meet it here for the first time in the frame of magnetic exchange interactions, but it will also occur in the case of electron transfer in Chapter 3. In both cases, the mediator entity plays a role by quantum-mechanical mixing of its wavefunctions with those of the terminal entities.

For magnetic exchange interactions we have to explain why two paramagnetic centres, which are too far to interact directly, can nevertheless present an exchange interaction. As seen previously, there are two ways to describe this indirect interaction:

- Use a full description of the system, as in the molecular orbital scheme of Fig. 2.40, starting from atomic orbitals. Here the role of the bridging ligand is taken into account explicitly, at the expense of some complexity.
- Use a reduced model as in Fig. 2.41. In this case one defines first magnetic orbitals, to take into account the partial delocalization between the ions and the bridging ligand, and then combines them as in the case of just two paramagnetic centres. The advantage of this (more pedagogical) approach is that there is no difference in nature between exchange and superexchange. The role of the bridging ligand is taken into account in the definition of magnetic orbitals.

Superexchange is described in a natural way by theory, because the process of mixing or perturbing wavefunctions is a common ingredient of quantum-mechanical methods. One has simply to avoid assigning too much importance to limiting forms or configurations, which have no real existence and actually contribute little to the overall state. An example of misconception is given later.

Using the simple qualitative scheme of Fig. 2.42 (three schematized versions of Fig. 2.40), we can illustrate an important aspect of the exchange phenomenon through the ligand concerning the electronegativity of the bridge X (F^- , Cl^- ,

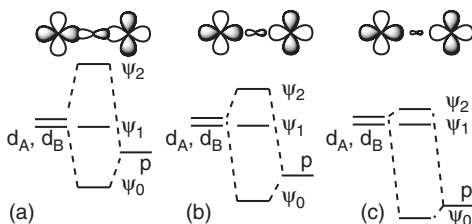


Fig. 2.42

Influence of the electronegativity of the bridging atom on the coupling: the larger the electronegativity, the weaker the interaction and the antiferromagnetic coupling.

Br^- , I^- or O^{2-} , S^{2-} , ..). Increase of electronegativity means that the p orbital energy decreases, and its interaction with the d orbitals (higher in energy) is weakened. Everything else being equal, the weight of the bridging orbital decreases in the ψ_2 orbital (Fig. 2.42 a, b, c, top). ψ_2 becomes less and less antibonding, the difference in energy between ψ_2 (ϵ_2) and ψ_1 (ϵ_1) decreases, and the antiferromagnetic component of the coupling is expected to decrease, as shown by eqn. (2.124).

Another important factor is the geometry. Figure 2.43 schematizes the situation for a bent AXB bridge with a 90-degree angle. The two localized orbitals a and b built from the d orbitals and suitable p orbitals of X do not overlap (Fig. 2.43c). They remain *as such* in the molecular entity (Fig. 2.43, centre). In the HL model, eqn. (2.117a) with $S = 0$ tells immediately that $J = 2k > 0$. In the HM model, $\epsilon_2 - \epsilon_1 = 0$, and eqn. (2.124) tells that $J = 2K_{a'b'} > 0$, and the coupling is ferromagnetic.

A final remark will deal with a frequently encountered misunderstanding. The exchange interaction through a bridge (or superexchange) is sometimes presented as shown in Fig. 2.44, considered as a crude pictorial representation of the superexchange mechanism, ‘explaining’ the antiferromagnetism observed in a linear A-X-B bridge. Basically, the phenomenon is explained by the fact that a spin ‘up’ on the metal A can interact with a spin ‘down’ of the p orbital, leaving a spin ‘up’ in the electron pair able in turn to interact with a spin down on B, as if it were possible and enough to separate an electron pair and to distribute the two spins in each of the two orbital lobes to understand exchange interaction. This is a misinterpretation of pioneering schemes, implying excited states with virtual electron transfer. We suggest that such a short cut be avoided.

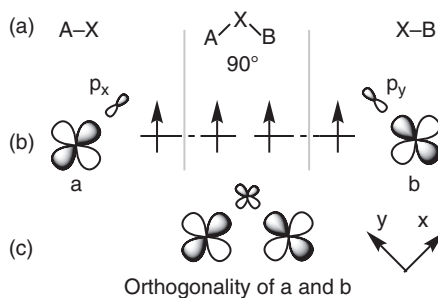


Fig. 2.43

Influence of the geometry: (a) the AXB entity is bent by 90° ; x, y axes are chosen as shown; (b) the localized orbitals a and b built from d x^2-y^2 orbitals and the suitable p orbitals of the bridging ligand; (c) orthogonality of the basis orbitals.

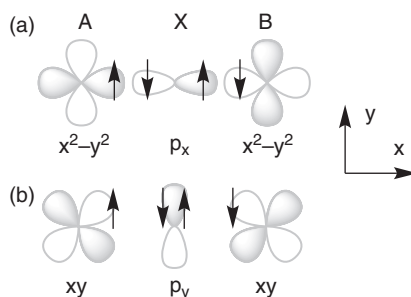


Fig. 2.44

A frequently encountered misunderstanding of magnetic superexchange.

2.6.2.3 Interaction through a molecular bridge

The final step is to replace the atomic bridge by a molecular one, which is crucial for understanding the magnetic systems studied in this chapter. We apply the same reasoning as before to the case of a dinuclear μ -oxalato copper(II) complex. The oxalate dianion, $[\text{C}_2\text{O}_4]^{2-}$, is the simplest dicarboxylate, and one of the favourite ligands among molecular magnetism chemists due to its very versatile bonding properties.

Kahn's model starts with non-orthogonal localized orbitals. The appealing feature is that such an orbital can be found in a mononuclear complex like the ethanediamine-oxalato-copper(II) complex, the structure of which is shown in Fig. 2.45a. It is one of the reasons why Kahn and coworkers named them 'natural magnetic orbitals' (NMO). The orbital is built from a molecular orbital of the oxalate dianion of adapted symmetry and a d orbital (Fig. 2.45b).

Two molecular orbitals arise, ϕ_{bonding} and $\phi_{\text{antibonding}}$ or ϕ_a . The higher in energy, ϕ_a , describes the unpaired electron. It presents a nodal surface between the metal and the oxygen atoms of the ligand. It is then antibonding. We shall see in this chapter that this is a common feature of SOMOs: being the highest in energy, they are quite often slightly antibonding or non-bonding. The unpaired

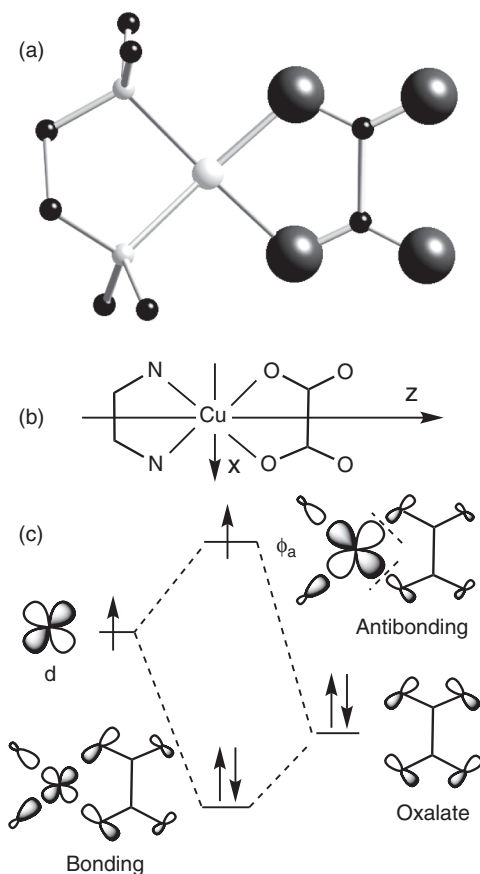


Fig. 2.45

'Natural' magnetic orbital (NMO) in a mononuclear complex of copper(II): (a) structure; b) symmetry of the molecular orbital; in a C_2 point group, with the chosen axes, the symmetry of the orbital is b_1 ; (c) molecular orbital energy diagram.

electrons *do not* participate to the bonding in the molecule. Another observation is that the ‘magnetic orbital’ is centred on the metal but widely delocalized on the ligand. The *spin density* is spread over the oxalate, including the oxygen atoms opposite to those directly bound to the metal.

The dinuclear complex (Fig. 2.46a) comprises two copper(II) cations bridged by the oxalate in a symmetric bis-bidentate way. Two terminal ethane-diamine derivative molecules bind the copper(II) trans to the oxalate. A water molecule completes the coordination of each copper in axial position, but it is not essential for our purpose, and we consider that the point group symmetry is C_2 .

2.6.2.4 Unsymmetrical molecule AB

Here we need to adapt the preceding singlet–triplet calculations (Section 2.6.1) to the AB unsymmetrical case. The system presents a magnetic orbital a_μ on site A and the orbital b_ν on site B, each occupied by one unpaired electron (spin operator s). μ and ν are the symmetry labels of the orbitals. The spin Hamiltonian is $\mathbf{H} = -J_{12}s_1.s_2$. The electronic Hamiltonian is $\mathbf{H} = \mathbf{h}(1) + \mathbf{h}(2) + \frac{e^2}{r_{12}}$ with $\mathbf{h}(1) \neq \mathbf{h}(2)$. The orbital energies are α_A and α_B (with $\delta_\mu = \alpha_A - \alpha_B$).

The overlap integral is $S_{\mu\nu} = \langle a_\mu(1)|b_\nu(2)\rangle$. The molecular orbitals of such an AB molecule were studied in Section 1.3.2. We can face two situations: (i) the symmetries of a_μ and b_ν are different ($\mu \neq \nu$), the orbitals are orthogonal, the overlap integral $S_{\mu\nu} \equiv 0$ and the AB molecular orbitals are identical to the original a_μ and b_ν ; (ii) the symmetries are the same ($\mu = \nu$). In this case, the overlap integral $S_{\mu\mu} \neq 0$, the two basis orbitals a_μ and b_μ build the two molecular orbitals ψ_1 and ψ_2 , shown in Fig. 2.47, with an energy gap Δ_μ .

Kahn’s HL and Hoffmann’s HM models (Sections 2.6.1 and 2.6.2) are based on the definition of a *pair* of symmetric, equivalent magnetic orbitals, centred on A and B. In the Hoffmann’s model this symmetry is compulsory; there is no general treatment when the sites A and B are different. For the HL model we report briefly the results given by Kahn [2.3, p. 189]. The calculations are lengthy, but the conclusion (when neglecting terms in S^2 in the development of J —which means that $S \ll 1$) is a simple extension of the symmetric case:

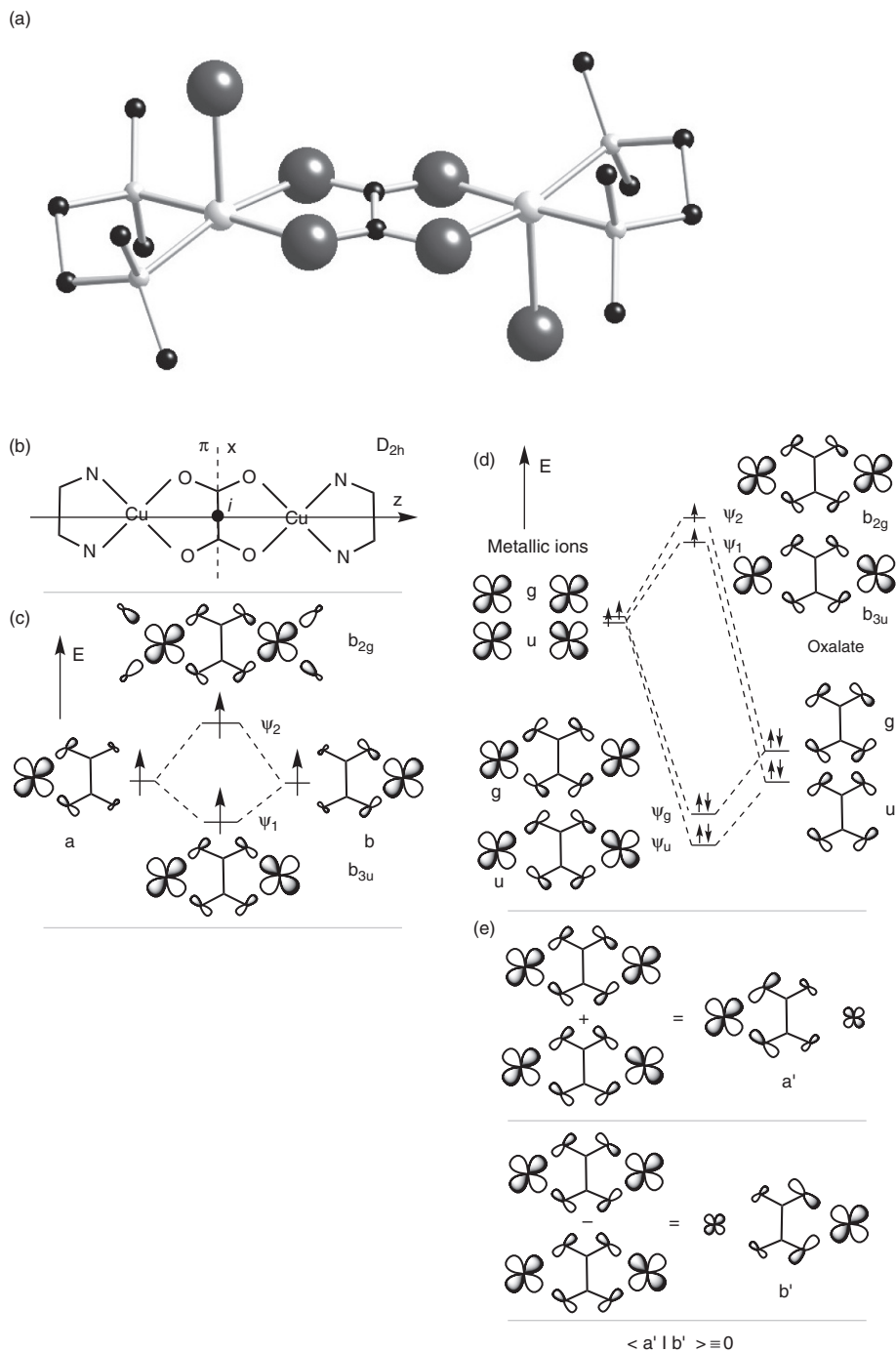
$$J = 2k_{\mu\nu} - 2[\Delta_\mu^2 - \delta_\mu^2]^{1/2} S_{\mu\nu} \quad (2.125a)$$

When compared with the expression for a symmetrical case (eqn. (2.117a))

$$J = 2k + 4\beta S \approx 2k - 4|\Delta|S/2 \approx 2k - 2|\Delta|S \quad (2.125b)$$

it is seen that the expression $-\left[\Delta_\mu^2 - \delta_\mu^2\right]^{1/2}$ plays the role of 2β . In other words, the quantities appearing in Fig. 2.47 can be used to define an effective β , which, in the unsymmetrical case, is no longer given directly by half the energy gap between a bonding and an antibonding orbital.

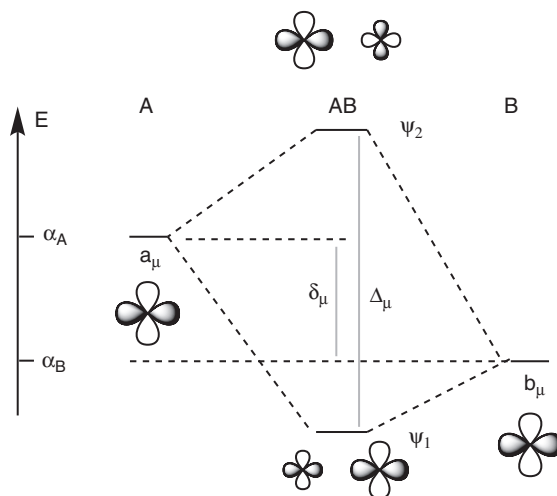
As for the symmetrical case, it is easy to recognize from eqn. (2.125b) that when $S_{\mu\nu} \equiv 0$ (orthogonality), $J = 2k_{\mu\nu} > 0$, and the interaction is ferromagnetic.

**Fig. 2.46**

(a) Structure of the dinuclear copper(II) complex (top view); (b) coordinates and symmetry, C_2 axis, mirror plane π and inversion centre i , D_{2h} point group; (c) molecular orbitals built from non-orthogonal localized orbitals (HL model); (d) molecular orbital energy diagram; the tails on the terminal ligand are not shown. The symmetry labels are those in the D_{2h} group or g and u for simplicity; (e) orthogonalized localized orbitals a' and b' (HM model).

Fig. 2.47

Schematic molecular orbital energy diagram in an A–B unsymmetrical molecule (simplified to a case of two d orbitals of different energies belonging to the same symmetry representation μ).



2.6.2.5 Interaction between several electrons per centre: concept of exchange pathway

We proceed further by examining dinuclear complexes having n_A unpaired electrons in a_i orbitals on centre A and n_B unpaired electrons in b_j orbitals on centre B with a total number of electrons $n = n_A + n_B$ and a total number of interactions $n_A \cdot n_B$. Only a qualitative analysis will be given here, but the full treatment can be found in [2.3, p. 186]. The magnetic behaviour can be analysed as follows: (i) on each centre, there is a magnetic exchange interaction between electron spins (for example, a local Hund rule if there are several quasidegenerate orbitals), so that a total local spin S_A or S_B can still be defined; (ii) by looking at the orbital overlaps, one can determine the J_{ij} couplings between electron pairs (one electron of site A with one electron of site B). The interactions are additive, and finally one can write:

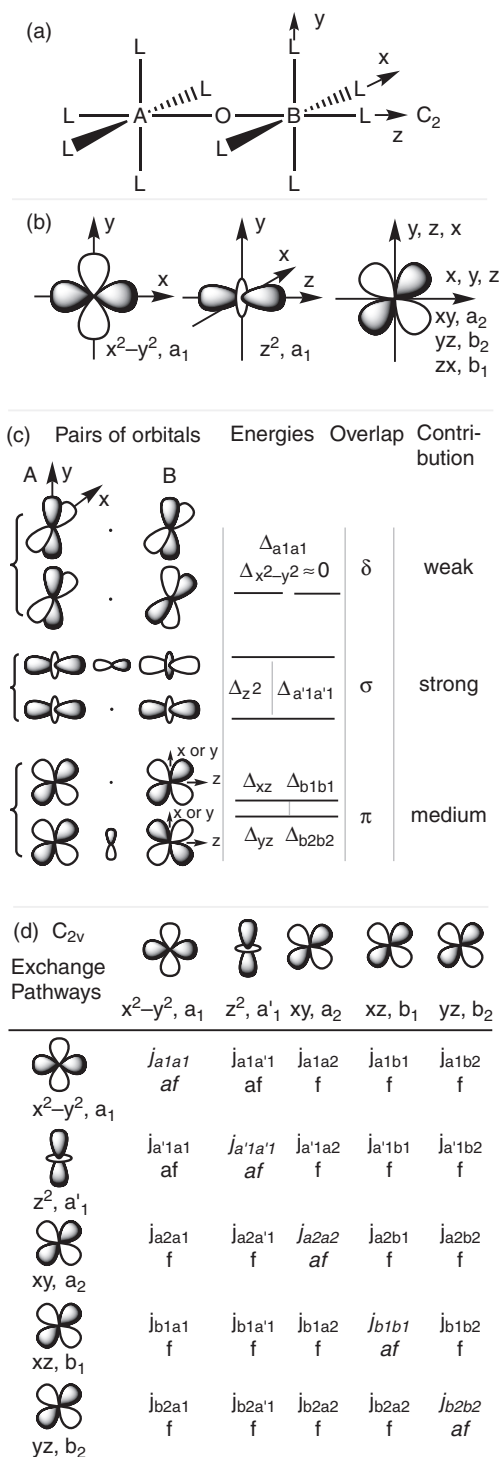
$$\mathbf{H} = -J \cdot \mathbf{S}_A \cdot \mathbf{S}_B \quad (2.126a)$$

$$J = \frac{1}{n_A n_B} \sum_{i=1}^{n_A} \sum_{j=1}^{n_B} J_{ij} \quad (2.126b)$$

J , the coupling between spins S_A and S_B , is defined as the sum of the J_{ij} , coupling for electron pairs i, j , divided by the number of exchange pathways. Note that the interaction energy scales as $J \cdot n_A \cdot n_B$.

We illustrate the concept of exchange pathway, interaction between pairs of orbitals in Fig. 2.48 for a dinuclear system AB with an oxo bridge (for cyanido, see Section 2.6.5.3).

We shall use this analysis in our study of polynuclear complexes in Section 2.6.5. The reader familiar with solid-state magnetism will have recognized in Fig. 2.48 a translation of the famous Goodenough–Kanamori rules (see the following).

**Fig. 2.48**

(a) Coordinates of a molecular dinuclear system AB with a μ -oxo bridge and an octahedral ligand field around transition metals A and B; (b) magnetic orbitals on A and B; the ligands orbitals are not shown for clarity; (c) building of the pairs of molecular orbitals from the magnetic orbitals on A and B, emphasizing their symmetry, the gap in energy, the nature of the overlap (σ , π , δ), the importance of their contribution to the antiferromagnetic coupling (see also Fig. 2.39); the xy pairs are not shown (the same conclusion as for the x^2-y^2 pairs); (d) table of the exchange pathways $j_{\mu\nu}$, with their symmetries and the nature of exchange (f as ferro- and af as antiferromagnetic). The antiferromagnetic pathways for pairs of identical orbitals are in italics.

2.6.3 Other models: from the pioneers to modern computations

2.6.3.1 The precursors: Kramers, Anderson, Goodenough, and Kanamori

We have developed at length Hoffmann's and Kahn's models, conceived for molecules, but previous exchange models, established for solids, inspired the molecular ones.

Kramers was the first, in 1934, to stress the role of a diamagnetic ligand to mediate the magnetic interaction between paramagnetic centres. Later, in 1950, P. W. Anderson (Nobel Prize recipient, 1977 [2.41]) exploited the idea of *virtual* electron transfer, which we can compare to configuration interaction with an excited charge transfer state. To describe the electronic structure of the solid, he used 'running waves' or *Bloch orbitals*—defined in Section 1.4.1 and used intensively in Chapter 3—the Bloch orbitals are defined by an SCF calculation in the ferromagnetic state); these wavefunctions are then localized and orthogonalized (and then named *Wannier orbitals*). They can be considered as a three-dimensional version of the Hoffmann ones. In the Anderson formalism the ferromagnetic term like $2 K_{a'b'}$ (eqn. 2.124) is called 'potential exchange', while the antiferromagnetic term like $-(\epsilon_1 - \epsilon_2)^2 / (J_{a'a'} - J_{a'b'})$ (formulated $-\beta^2/U$ by Anderson) is called 'kinetic exchange' because it is linked to the possibility of an electron on site a to delocalize on site b, and thus decrease its kinetic energy.

The model was later completed and refined by Goodenough and Kanamori.

One conclusion of Anderson is of particular interest: 'there is no distinction in principle between exchange caused by direct overlap of the wavefunctions on magnetic ions without intermediate atoms present, and exchange through non-magnetic groups; that is, between what used to be called 'direct' exchange and 'superexchange'.

The Goodenough–Kanamori rules

The 'rules' were coined by Goodenough using the same basic concepts as Anderson, and completing them (in a Hund–Mulliken approach) to find an explanation for the huge amount of magnetic properties of oxides, with n_A electrons on A and n_B electrons on B. Kanamori distilled the rules by using more systematically the symmetry and using a Heitler–London approach. At that time the rules gave an impressive valuable qualitative interpretation of most of the data. Goodenough emphasised (i) the 180-degree geometry (see Fig. 2.48) where the antiferromagnetic interaction is the largest (σ overlap between e_g orbitals (d^8 – d^8 , for example) and π overlap between the t_{2g} orbitals (d^3 – d^3 , for example) with our present notations, and (ii) the 90-degree geometry where orthogonality gives rise to ferromagnetic interactions (see Fig. 2.43). The real geometry is always more complex, especially in molecules. The reader can examine the *Goodenough–Kanamori* rules, having simply in mind the basic concepts of overlap and orthogonality between pairs of magnetic orbitals developed previously. The references to the original pioneering works can be found in Anderson [2.41] and Goodenough [2.38].

To summarize, five main models describing the exchange interaction between two transition metals through a diamagnetic ligand are gathered in Table 2.6.

Table 2.6 Models to describe the exchange interaction in transition metal derivatives.

Models Bonding/Exchange	Hund–Mulliken	Heitler–London
Solids	Anderson [2.41] Goodenough [2.38]	Kanamori [see 2.38, 2.41]
Molecules	Haÿ, Thibault, Hoffmann [2.40]	Kahn, Briat [2.3, 2.39]

In these approaches the configuration interaction used essentially excited states based on metal-to-metal charge transfer (MMCT) characterized by the one-site electron repulsion U . Other models have been developed since, using in particular ligand-to-metal charge transfer (LMCT) excited states both in the HL or HM approaches. Many references can be found in the recent reviews [2.42].

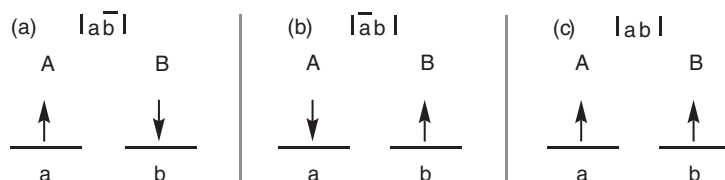
2.6.3.2 Numerical computation of J values

In the preceding sections we proposed heuristic solutions for understanding the main components of J ; that is, a qualitative approach. The problem is much more difficult when a quantitative output is searched, as close as possible to the experimental values. First, because beyond two electrons there is *no exact solution* to the electronic Hamiltonian, and the determination of the *correlation* energy between two electrons must be found by some *ersatz* or approximation. Second, one has indeed to determine a small energy difference (typically $1\text{--}300\text{ cm}^{-1}$) between singlet and triplet levels, while the total electronic energy of these states in a molecule can be $10^5\text{--}10^7$ times greater. These constraints constitute a strong motivation for the conception of smart methods using the most recent resources of computational chemistry.

Modern quantitative methods rely on either post-Hartree–Fock quantum treatments (also known as wavefunction theory, WFT) or density functional theory (DFT) calculations. As seen in Chapter 1, the post-Hartree–Fock treatment necessitates an extensive use of configuration interaction with excited states to improve the ground state (hence the introduction of many determinants), while DFT is basically a monodeterminantal method.

In both, the computation of the singlet ground state, *a priori* the easiest, is one of the difficult points. Let us return to the simple scheme of the ‘active electrons’ model limited to two magnetic orbitals a and b . Figure 2.49 displays three spin configurations or determinants.

We know that the singlet ground state is a linear combination of $|a\bar{b}|$ (a) and $|\bar{a}b|$ (b): ${}^1\Psi_0(M_s = 0) = \frac{|a\bar{b}| + |\bar{a}b|}{\sqrt{2}}$. Hence two determinants are needed to describe the singlet, which therefore necessitates a multideterminantal

**Fig. 2.49**

Three spin configurations and determinants. Note the lack of symmetry in (a) and (b).

approach (thus beyond Hartree-Fock). There is no such problem for the triplet (or more generally for a configuration where all the spins are parallel). For instance, the $M_S = 1$ component of the triplet is defined uniquely by the single determinant $|ab\rangle$ (Fig. 2.49c).

We begin with Hartree-Fock (WFT) treatments. In a seminal paper published in 1981, Malrieu and coworkers tackled the problem with the example of copper acetate (strongly antiferromagnetic, $J = -286 \text{ cm}^{-1}$) [2.43] [2.3 section 8.5]. They used *ab initio* methods based on the computation of SCF MO orbitals, followed by a configuration interaction (CI) with a Møller-Plesset perturbation treatment (see Section 1.5.2.2). The method was adapted to calculate *directly* the contribution of CI to the singlet-triplet energy difference, rather than use a brute force technique of computing independently the energies of the two states and making the difference. The beginning of their expression for J was similar to the Hay-Thibeault-Hoffmann (HTH) model, because they used orthogonalized magnetic orbitals (see Section 2.6.1.3) but went further by introducing various perturbative corrections. J was given by:

$$J = 2K_{ab} - \frac{(2h_{ab})^2}{J_{aa} - J_{ab}} + \text{other second - order terms} + \text{fourth - order terms} \quad (2.127)$$

in which one recognizes the first two terms of eqn. (2.124). Other second-order corrections are introduced, implying higher-energy configurations involving various kinds of charge transfer and ligand excitations. Finally, it was necessary to go to fourth order to approach experimental results.

The numerical results illustrate the difficulties of obtaining quantitative values. The ferromagnetic term $2K_{ab}$ (potential exchange) is computed as $+233 \text{ cm}^{-1}$, which is surprisingly high, taking into account the metal-metal distance. The next term (kinetic exchange) just compensates the first, and at this stage J is still slightly *positive*. Introducing the other second-order terms and the fourth-order terms yields at last a negative J value (-120 cm^{-1}), but still far from the experimental -286 cm^{-1} . The agreement is better in the case of oxalate-bridged system, the total value up to fourth order (-295 cm^{-1}) being closer to the experimental one (-385 cm^{-1}).

The method thus suffered from at least two difficulties: (i) the perturbation expansion of the CI is not unique, and (ii) where should the perturbation expansion be stopped? It was nevertheless the methodological starting point of many computational endeavours which are more and more successful even if they are demanding of computer time. Among them are the methods based on CASSCF (complete active space SCF) and their developments: definition of an active space (a few frontier orbitals including the singly occupied ones), computation using all the configurations of the active space compatible with space and spin symmetries, eventually completed by other selected configurations of the inactive space (DDCI, difference dedicated configuration interaction) [2.44, 2.45].

In the last twenty years, various alternatives have been devised, less demanding of machine time. One of the most fruitful is called the 'broken symmetry' approach, which can be declined in two variants: a simplified Hartree-Fock treatment and a DFT treatment.

The principle of the broken symmetry (BS) approach, introduced in 1981 by Noodleman [2.46], is to circumvent the previously mentioned difficulty in computing correctly the singlet energy. One defines a fictitious state, which is a mixed spin state. It has $M_S = 0$, but is not an eigenfunction of the triplet nor the singlet. It can be depicted schematically as one of the determinants (a) or (b) in Fig. 2.49.

Mathematically, the BS state is a determinant describing an electron on site A with spin ‘up’ and the other electron on site B with spin ‘down’. It is not symmetric (hence the name ‘broken symmetry’), because it associates a given spin state, say ‘up’, with one half only of the molecule, and thus presents a mixed spin symmetry. The great advantage of the broken symmetry state is that it can be computed from a simple SCF procedure taking into account only one determinant, without need of the CI step. Due to its mixed nature, its energy is in principle the average of the pure spin state energies:

$$E_{BS} = \frac{1}{2} (E_S + E_T) \quad (2.128a)$$

which would give:

$$J = E_S - E_T = 2 (E_{BS} - E_T) \quad (2.128b)$$

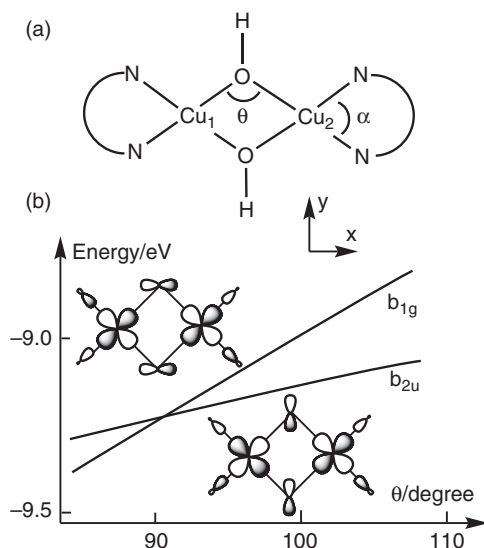
Technically, the BS state is computed at the unrestricted level, which suffers from ‘spin contamination’ (the computed levels are no more pure spin levels). We cannot enter into the conceptual and technical problems that arise, which are still an object of debate. Other expressions for J have been proposed (Yamaguchi, Ruiz, Caballol). The difficulties can be solved when some care is taken [2.47–2.49]. In these conditions, DFT calculations, with selected functionals, can be compared successfully with the most sophisticated *ab initio* calculations, in simple A-X-B models (H–He–H for example). If we return to the reference compound $[\text{Cu}_2(\text{acetate})_4]$ (see Box ‘Copper acetate’), a value of -299 cm^{-1} (experiment: -296) was obtained by DFT. Nowadays, DFT is used increasingly to tackle the computation of J values in extended polynuclear systems, at the moment unreachable by WFT calculations.

2.6.4 Ferromagnetic and antiferromagnetic coupling in dinuclear complexes with one spin per centre

In the two following subsections we present a few examples of real transition metal complexes where theoretical models allow understanding and predicting the magnetic properties. Our main tools in this heuristic approach are the concepts by Kahn and Hoffmann, condensed in eqns. (2.117) and (2.124). We start with very simple homometallic dinuclear complexes with one electron on each metallic centre where it is possible to tune, practically at will, the overlap between the magnetic orbitals. In the next section we proceed to the case of several electrons per centre.

2.6.4.1 Overlap and symmetry

A beautiful pioneering example was provided by the bis- μ -hydroxo copper(II) dinuclear complexes with the first attempts of ‘magneto-structural’ correlation between the bridging angle θ and the J values, by W. Hatfield and others,

**Fig. 2.50**

Exchange interaction in dinuclear bis- μ -hydroxo-copper(II) complexes. (a) schematic idealized planar structure; (b) variation of the singly occupied molecular orbital energies as a function of the bridging angle θ .

as already extensively presented in [2.2] and [2.3, p. 159sq]. When two copper(II) ions are bridged by two hydroxo groups (Fig. 2.50a), and when diamine terminal ligands N...N are varied to induce sterical constraint and modify the geometry around the copper(II), the N-Cu-N angle (α) is changing and induces large variations of the bridging Cu₁-X-Cu₂ θ angle. The J value varies accordingly, as shown by Table 2.7.

The phenomenon is explained nicely either by Kahn's or Hoffmann's models.

$$\begin{aligned}
 \text{(a) } J &= J_F + J_{AF} & \text{(b) } J &= 2k + 4\beta S \\
 \text{(c) } J &= 2K_{ab} - \frac{(\varepsilon_1 - \varepsilon_2)^2}{j_{aa} - j_{ab}} = 2K_{ab} - \frac{\Delta^2}{j_0 - j} & \text{(2.129)}
 \end{aligned}$$

The two singly occupied molecular orbitals are built from the ++ and -+ combination of the magnetic orbitals around Cu₁ and Cu₂ (Fig. 2.50) in a way completely similar to Fig. 2.46. In a D_{2h} point group they have b_{1g} and b_{2u} symmetry. The b_{1g} orbital comprises the 2p_x of the bridging oxygen, whereas the b_{2u} orbital includes the 2p_y oxygen orbital. When the θ angle varies, the energy of the two orbitals is changing, as shown in Fig. 2.50b (which was obtained by a simple semi-empirical extended Hückel calculation). Please note that in all the θ domain, the Hoffmann MOs (b_{1g} and b_{2u}) are of course orthogonal.

Table 2.7 Variation of the coupling constant J as a function of the bridging angle.

Compound	Cu ₁ -O-Cu ₂ / degrees	J / cm ⁻¹
[Cu(bpy)(OH)] ₂ (NO ₃) ₂	95.5	+172
[Cu(dmaep)(OH)] ₂ (ClO ₄) ₂	98.4	-2.3
[Cu(tmen)(OH)] ₂ (NO ₃) ₂	101.9	-367
[Cu(tmen)(OH)] ₂ Br ₂	104.1	-509

At some θ angle, slightly larger than 90 degrees, the energies are the same, and the MOs energy levels are degenerate. In eqn. (2.124), $\Delta = \varepsilon_1 - \varepsilon_2 = 0$ and $J = 2K_{ab}$. The triplet state is favoured by exchange interaction. When θ increases the antiferromagnetic term becomes larger, and can eventually become equal to the ferromagnetic one (this is practically achieved at 98.4° in Table 2.7, and then becomes preponderant). The interaction is then more and more antiferromagnetic. In terms of Kahn's model, the angle where the MOs energy levels are degenerate corresponds to the special situation where the *magnetic orbitals are orthogonal* (hence $S = 0$ and $J = 2k$ in eqn. (2.117a)).

Tunable exchange in copper(II) μ -oxalato dinuclear complexes [2.3, p. 167sq] Another textbook example is given by oxalate-bridged complexes which can be treated simply using Kahn's model. We can formulate this family of complexes as $\text{TCu(II)-Ox-Cu(II)T}$ (Ox = oxalate bridging ligand, T = various polyamines terminal ligand (en = 1,2-ethanediamine, tmen = N,N,N',N'-tetramethyl-1,2-ethanediamine, dien = diethylenetriamine)). The mononuclear tmenCu(II)Ox is shown in Fig. 2.45a. The schematic structures of the dinuclear complexes are shown in Fig. 2.51: **1** (a), **2** (b), **3** (c). The coupling constants J , fit from experimental susceptibilities, are very different for **1-3**: $J_1 = -385 \text{ cm}^{-1}$, $J_2 = -13 \text{ cm}^{-1}$, $J_3 = -75 \text{ cm}^{-1}$.

In the three complexes **1**, **2**, and **3**, the surrounding of the copper(II) can be described essentially by a square planar geometry formed by oxygen atoms of the oxalate and nitrogen atoms from the ligands at short distances ($\approx 2\text{\AA}$), ensuring the presence of ' x^2-y^2 ' type' magnetic orbitals. The presence in axial position of a water molecule (in **1**) or an oxygen atom of the oxalate (in **2** and **3**) at longer distance ($\approx 2.35\text{\AA}$) slightly modifies the copper geometry to square pyramidal but does not influence our simple semi-quantitative demonstration. The intramolecular Cu-Cu distances are close to 5.2 \AA in the three cases. Kahn's model allows a straightforward explanation of the tuning of the J values. We use the orbitals' overlaps displayed in Fig. 2.52 and the fact that in this model, $J = 2k + 4\beta S$; that is, $J \approx 4\beta S(\alpha S^2 \propto \beta^2 \propto \Delta^2)$ when neglecting k [2.50].

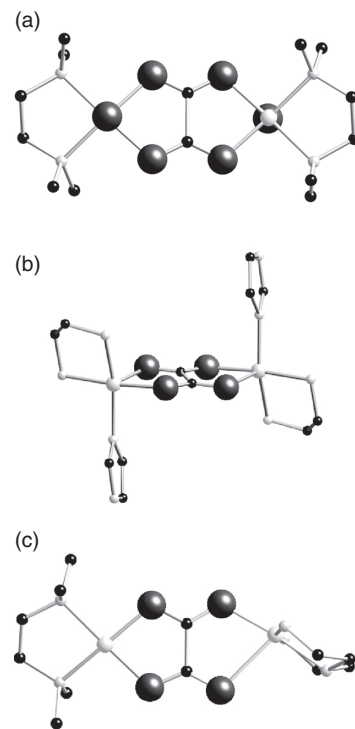


Fig. 2.51

Ball-and-stick structures of copper(II) complexes down the xy plane. a) dinuclear $\text{tmenCu(II)OxCu(II)tmen}$, **1**; b) dinuclear $\text{tmen-MeImCu(II)OxCu(II)MeIm-tmen}$, **2**; c) dinuclear $\text{tmenCu(II)OxCu(II)dien}$, **3**; Copper, medium grey sphere, oxygen, large black sphere, nitrogen, small grey sphere, carbon, small black sphere.

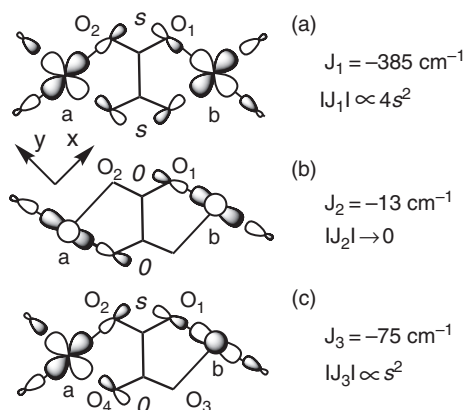


Fig. 2.52

Exchange interaction in dinuclear copper(II) μ -oxalato complexes. Schematic overlap, experimental and computed J values in (a) complex **1**, (b) complex **2**, (c) complex **3** (adapted from [2.50]).

In the symmetric dinuclear complex **1** [tmenCuOxCutmen]²⁺ (Fig. 2.51a), the two magnetic orbitals a and b are in the oxalato plane. They overlap significantly (integral overlap S_1) (Fig. 2.52a). If we define s as the overlap between the two atoms O₁ and O₂ on *one side* of the carboxylate bridge COO, $S_1 = 2s$ and $J_1 \propto 4s^2$. In the non-planar symmetric dinuclear complex **2**, [tmen-MeImCu(II)OxCu(II)MeIm-tmen]²⁺, (Fig. 2.51b), the two magnetic orbitals a and b are in planes roughly perpendicular to the oxalate bridge. They overlap very weakly (the overlap integral $S_2 \approx 0$) (Fig. 2.52b), and the coupling constant $J_2 \approx 0$. In the non-planar disymmetric dinuclear complex **3**, [tmenCu(II)OxCu(II)dien]²⁺, an intermediate situation occurs (Fig. 2.52c). The magnetic orbital a is in the oxalato plane, while b is in a perpendicular plane, so that they overlap only on one side of oxalate, $S_3 = s$, $J_3 \propto s^2$ should be $\approx J_1/4$ whereas the experimental ratio is $J_3 / J_1 \approx 5$.

Thus the model appears to work properly for understanding and foreseeing antiferromagnetic situations on a semi-quantitative basis. What about ferromagnetic coupling?

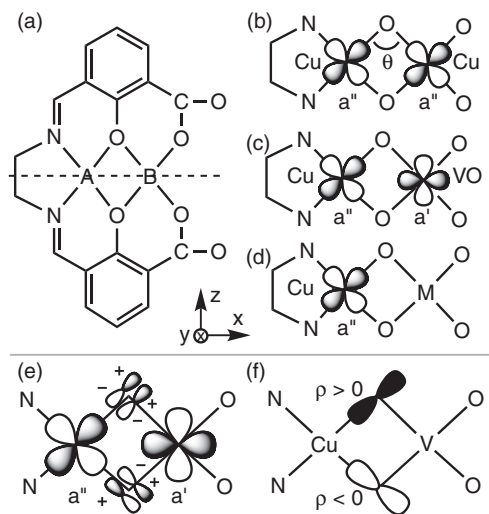
Symmetry, orthogonality, and ferromagnetic coupling

With the example of bis- μ -hydroxo copper(II) complexes, we showed that orthogonality of the magnetic orbitals and then ferromagnetic interaction could be achieved for a given θ angle, but this was (after Kahn) an *accidental* orthogonality. Orthogonality (and ferromagnetic interaction) can be achieved instead by a strict control of symmetry. An elegant approach was to use simple ions with one unpaired electron: copper(II), d⁹ and vanadyl(IV), d¹. We warn the reader not to confuse ‘ferromagnetism’, often used as a contraction of ‘ferromagnetic interaction’ between two neighbours, with ‘ferromagnetism’, the usual meaning of which is ‘long-range ferromagnetic order’ found in ferromagnets.

Ferromagnetic coupling in a copper(II)–vanadyl(IV) binuclear system [2.3, p. 174–81]

Here we use the very convenient ligand H₄(fsa)en (H₄(fsa)en = N,N'-(2-hydroxy-3-carboxybenzilidene)-ethanediamine) which presents two different binding sites A and B (Fig. 2.53a). It is not easy, but is possible, to fill the A site with a cation A (Cu^{II}, for example, d⁹) and the B site with different cations: Cu^{II} (Fig. 2.53b); V^{IV}O d¹, (Fig. 2.53c); M = Cr(III) d³; and Fe(III) d⁵ (Fig. 2.53d). We admit that the only symmetry element is the xy plane (‘horizontal’ plane in the C_h point group) (Fig. 2.53a). With A = B = Cu(II), the two magnetic orbitals have the same symmetry a'. As the θ angle = 100.2°, they overlap and the interaction is antiferromagnetic ($J = -650 \text{ cm}^{-1}$). In the CuVO(fsa)en complex (Fig. 2.53c), an axial methanol molecule coordinated to the copper(II) is, for clarity, not shown. The VO group is perpendicular to the mean plane of the molecule. The magnetic orbitals are x²-z², a', for V^{IV}O (symmetric in the reflection through the xy plane) and xz, a'', for Cu(II) (antisymmetric) (Fig. 2.53c).

These orbitals are orthogonal by symmetry, and thus both Kahn’s and Hoffmann’s models predict a ferromagnetic interaction. This is the case, and J is quite high ($J = +118 \text{ cm}^{-1}$). This result, obtained at the beginning of

**Fig. 2.53**

Interactions in AB(fsa)en complex. (a) Schematic structure of the molecule. The dotted line is the projection of xy symmetry plane. Also shown are the coordinates axes corresponding to point group C_h . Magnetic orbitals: (b) Cu–Cu, overlap and antiferromagnetism; (c) Cu–VO, orthogonality and ferromagnetism; (d) Cu–M with M = Cr(III) orthogonality and ferromagnetism; M = Fe(III), overlap and ferrimagnetism (Section 2.6.5.2); (e) Cu and VO magnetic orbitals emphasizing their delocalization on the oxygen bridges and the signs of the wavefunctions. The oxygen p orbitals belonging to the two magnetic orbitals have been artificially separated to better display their signs; (f) schematic representation of the overlap density pointing out the sign on the oxygen bridges.

the 1980s, was an important step in demonstrating the feasibility of ferromagnetic coupling at the molecular level, and by extension in complex objects. Furthermore, Kahn and Charlot provided a simple (pictorial) explanation of the magnitude of the J coupling constant. Looking at the expression of the exchange integral k , one realizes that k is related to the one-electron quantity $\rho(i)$, named overlap density, and defined in each point of space by the product $\rho(i) = a(i).b(i)$:

$$J = 2k = 2 \langle a(1) b(2) | e^2 / r_{12} | a(2) b(1) \rangle = \int \frac{\rho(1)\rho(2)}{r_{12}} dr_1 dr_2 \quad (2.130)$$

The delocalization of the two magnetic orbitals of Cu and VO is strong on the oxygen bridge; pay attention to the antibonding character of the two magnetic orbitals (Fig. 2.53e). The overlap density ρ is important around the two oxygen bridges (Fig. 2.51f), and then the ferromagnetic coupling J is important. Instead, when the spin density is delocalized on a large polyatomic bridge (oxalate, for example), orthogonality still creates ferromagnetism but the weak overlap density ρ gives only weak J values. It is amazing to observe that in the *ab initio* calculation of the CuVO complex ([2.3, p. 178_{sq}], the orthogonalized orbital a' and b' , related to Cu^{II} and $\text{V}^{\text{IV}}\text{O}$, have delocalization tails on the other metal, whereas the non-orthogonalized orbitals are orthogonal without need of the tails.

Our conclusion is therefore that ferromagnetic interaction can be achieved through orthogonality, and that the larger the overlap density (the smaller the bridge), the larger the effect. Other means to reach ferromagnetic coupling at the molecular level, through ‘double exchange’, are commented on in Section 3.2.2.4.

2.6.4.2 Influence of the energy of the bridge orbitals [2.51]

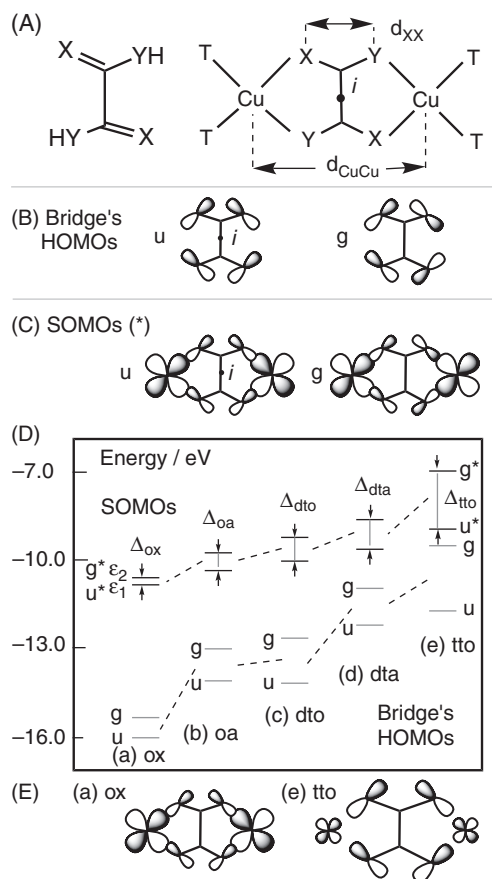
The second important parameter to understand the coupling constant between two unpaired electrons is the energy of the orbitals of the bridge. We already

had an answer for the case of a monoatomic bridge (Fig. 2.42): the closer the energy of the ligand is from the energy of the metallic orbitals, the larger the mixing with the d orbitals is and the larger the antiferromagnetic interaction is. *Mutatis mutandis*, the conclusion is the same for a molecular bridge, as shown in the following example. We compare oxalate-like bridges, oxamide (oa), dithiooxalate (dto), dithiooxamide (dta), and tetrathiooxalate (tto), forming dinuclear copper(II) complexes of similar structure (Fig. 2.54A). Extended Hückel calculations are performed on crystallographic geometries.

Fig. 2.54 displays the bridges' HOMOs (Fig. 2.54B), the SOMOs of the complex, obtained by the combinations (u and g) of the bridging HOMOs and of symmetry orbitals from the metals (+− and ++) (Fig. 2.54C) and the energies' changes (Fig. 2.54D). When the oxygen atoms of the oxalate bridge are progressively replaced by atoms of nitrogen and sulphur, less electronegative than oxygen (from left to right): (i) the bridges' HOMOs energies (Fig. 2.54D, bottom) increase and so does the difference between the energies of the bridge's g and u orbitals; (ii) the u and g bridging HOMOs interact more and more with the symmetry orbitals of the metals to give SOMOs of increasing energy; that is, the weight of the atoms of the bridge increases in the

Fig. 2.54

Influence of the energy of the orbitals of the molecular bridge on the J value. (A) Schematic structure of the bis-chelating bridges and of the dinuclear copper complexes. The bridges are: (a) X=Y=O, oxalate (Ox), (b) X=O; Y=NH, oxamide (Oa), (c) X=O, Y=S, dithiooxalate (dto), (d) X=S, Y=NH, dithiooxamide(dta), (e) X=Y=S, tetrathiooxalate(tto). (B) Scheme of the highest occupied molecular orbitals (HOMOs) of the bridge (u and g symmetry). *i* is the location of the inversion centre. (C) Scheme of the resulting antibonding (*) singly occupied molecular orbitals (SOMOs) (u and g). (D) Results of extended Hückel calculations on copper(II) dinuclear complexes. Lower: energy of the bridges' HOMOs (grey). The dotted lines are guides for the eyes. Upper: energy of the SOMOs. The small arrows and the grey vertical lines evidence the energy gap Δ between the u^* and g^* SOMOs. (E) Qualitative comparison of the two (u) SOMOs with oxalate (Ox) and tetrathiooxalate (tto) bridges emphasizing the larger participation of the bridge to the SOMO with sulphur (tto).



SOMOs ($O < N < S$); (iii) the energy gap $\Delta = \varepsilon_1 - \varepsilon_2$ between the SOMOs of the complex increases accordingly (Fig. 2.54D top). In the frame of the Hoffmann's model (J varies as $(\varepsilon_1 - \varepsilon_2)^2$), the computed trend explains nicely the experimentally observed antiferromagnetism and the enhancement of the absolute values of J from oxalate to tetrathiooxalate: $J_{\text{ox}} = -385 \text{ cm}^{-1}$, $J_{\text{oa}} = -580 \text{ cm}^{-1}$, $J_{\text{tta}} = -594 \text{ cm}^{-1}$, $|J_{\text{tto}}| > 1000 \text{ cm}^{-1}$.

2.6.5 Complexes with several spins per centre

A new step in our way to more elaborated magnetic molecular materials consists in introducing metallic ions with more than one electron on each centre. We use molecular bridges already known and the concept of exchange pathway introduced in Section 2.6.2.5. We deal first with dinuclear compounds and then polynuclear ones. In this way, we shall introduce the important concept of molecular ferrimagnetism and propose a rational approach to high-spin molecules.

2.6.5.1 Exchange pathways

The usefulness of this concept will be illustrated by the example of dinuclear μ -oxalato complexes of the general type A-Ox-B with A, B = Cu(II), Ni(II), Co(II), Fe(II), Mn(II). In our model (Fig. 2.55) the A and B ions and the oxalate bridge lie in the same plane. The surrounding of the two sites A and B is quasi-octahedral because of the presence of terminal ligands (not shown here). We use the symmetry point group C_{2v} to be able to describe the case $A \neq B$ without loss of generality. The coordinates' axes and the orbitals symmetry

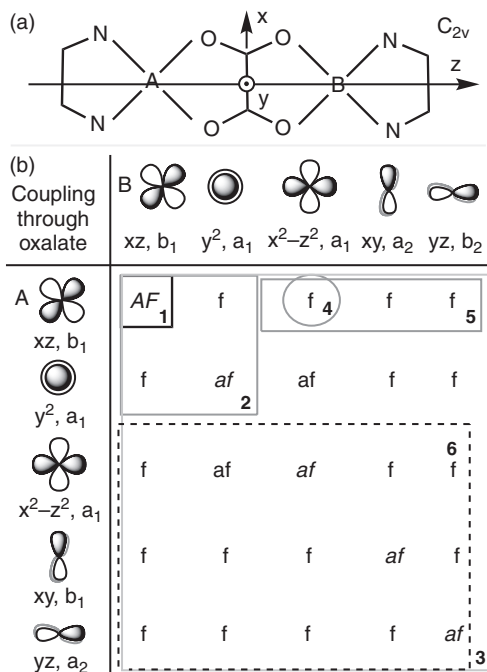


Fig. 2.55

(a) Coordinates of a molecular μ -oxalato dinuclear system AB and an octahedral ligand field around transition metals A and B; (b) table with the magnetic orbitals on site A (column) and B (row); the ligands' orbitals are not shown for clarity; the orbitals are represented as viewed down y; expectation of the contribution of the different exchange pathways to the coupling (notations af and f as in Fig. 2.48, AF means strong af); the boxes correspond to different experimental cases, homodinuclear Cu(II)-Cu(II), d^9-d^9 **1**, Ni(II)-Ni(II), d^8-d^8 , **2**, Mn(II)-Mn(II) or Fe(III)-Fe(III), d^5-d^5 , **3**. Also shown are boxes for heterodinuclear Cu(II)-V(IV)O, d^9-d^1 , **4**, Cu(II)-Cr(III), d^9-d^3 , **5** and Cr(III)-Mn(II), d^3-d^5 , **6**, used in Section 2.6.5.3.

Table 2.8 Structural and magnetic data for homometallic μ -oxalato dinuclear complexes. The values are the average for different terminal ligands.

A=B=	Mn(II)	Fe(II)	Co(II)	Ni(II)	Cu(II)	Zn(II)
d^n	d^5	d^6	d^7	d^8	d^9	d^{10}
$d_{AB} / \text{\AA} \approx$	5.6	na	5.4	5.4	5.2 (to 5.6)	–
$J / \text{cm}^{-1} \approx$	–2	–6	–10	–33(4)	–390(20)	0
$n_A n_B J \approx$	–50	–96	–90	–132	–390	0

(na: non available)

labels are different from Fig. 2.48. Furthermore, xy and yz are linear combinations of real orbitals. A very similar diagram would be obtained in the D_{2h} point group.

The experimental J for homodinuclear complexes are gathered in Table 2.8.

The J values—all negative—increase strongly from Mn(II) to Cu(II). This trend can be understood qualitatively using our preceding theoretical models. The interaction between two copper(II) ions (box 1 in Fig. 2.55b), with a strong $|J|$ value, was extensively discussed in Section 2.6.4.1. It relies on one exchange pathway implying a strong overlap of the xz magnetic orbitals through the oxalato bridge (noted AF in the figure). With two nickel(II) ions (box 2), the J value is much smaller than for Cu(II), $J_{AF}(\text{Ni-Ni}) \approx -33(4) \text{ cm}^{-1}$. $J(\text{Ni-Ni})$ corresponds to four exchange pathways ($n_A = 2$; $n_B = 2$): (i) xz – xz (b_1), antiferromagnetic, (af), as in the Cu(II) derivative; (ii) y^2-y^2 (a_1) also antiferromagnetic (af); and (iii) two ferromagnetic ones (f), xz – y^2 and y^2 – xz .

Following eqn. (2.125b) the coupling constant J can be written:

$$J = [j_{b_1b_1} + j_{a_1a_1} + j_{a_1b_1} + j_{b_1a_1}] / 4 \quad (2.131a)$$

with:

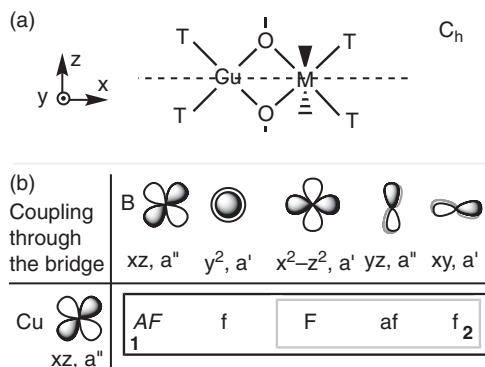
$$j_{b_1b_1} = 2k_{b_1b_1} - 2\Delta_{b_1}S_{b_1b_1}; j_{a_1a_1} = 2k_{a_1a_1} - 2\Delta_{a_1}S_{a_1a_1}; j_{a_1b_1} = j_{b_1a_1} = 2k_{a_1b_1} \quad (2.131b)$$

The competition implies two rather large negative antiferromagnetic terms and two rather weak ferromagnetic ones (exchange integrals k_{ij}). The observed experimental antiferromagnetism can therefore be understood. Why is it so weak compared to the copper derivative? The d orbitals of nickel are higher in energy than those of copper (minor Z), and interact less with oxalate HOMOs (then $|j_{b_1b_1}(\text{Ni})| < |j_{b_1b_1}(\text{Cu})|$), y^2 orbitals are spreading much less than the xz orbitals on the oxalate bridge, so $S_{a_1a_1} < S_{b_1b_1}$, $\Delta_{a_1} < \Delta_{b_1}$ and $|\Delta_{a_1}S_{a_1a_1}| < |\Delta_{b_1}S_{b_1b_1}|$. Similar considerations can be used to rationalize the other cases.

2.6.5.2 Molecular ferrimagnetism

Molecular ferrimagnetism is another efficient way to achieve molecular magnetic ground states. Note that we use here ‘molecular ferrimagnetism’ as a shortcut to designate actually ‘antiferromagnetic interaction between two spins of different magnitudes in a molecular system’.

The idea is *a priori* very simple. In nature, overlap is the general rule (and therefore antiferromagnetic coupling). It is then possible to use two

**Fig. 2.56**

Interactions in $\text{CuM}(\text{fsa})\text{en}$ complexes. (a) Scheme of the molecular bimetallic fragment and axes. (b) site A (column), copper(II) magnetic orbital a'' ; site B, row: box 1, complex $\text{Cu}(\text{II})\text{Fe}(\text{III})(\text{fsa})\text{en}$, five magnetic iron(III) orbitals, and expected contributions to the coupling constant J ; grey box 2, complex $\text{Cu}(\text{II})\text{Cr}(\text{III})(\text{fsa})\text{en}$, three magnetic orbitals of chromium(III). The notations are the same as in Fig. 2.55 (and F means strong ferromagnetic interaction).

spins $S_A(\downarrow)$ and $S_B(\uparrow)$ of different magnitudes on centres A and B, antiferromagnetically coupled, to get a ground spin state $S_{\text{GS}}(\downarrow \uparrow)$ which is still magnetic, $S_{\text{GS}} = |S_A - S_B|$. The total spin is lower than in the case of ferromagnetic coupling ($S_{\text{GS}} = S_A + S_B$) ($\uparrow \uparrow$), but it is non-zero. This is another example of a dialectic situation when a phenomenon (antiferromagnetic interaction) gives rise to its 'contrary' (magnetic ground state). The idea is not new, since it was evidenced in the late 1940s, by Néel, in perovskites, to characterize their three-dimensional *ferrimagnetic* ordering [2.52]. It was one of the achievements which lead him to be awarded the Nobel Prize. The concept of exchange pathway is particularly appealing for a straightforward interpretation of the first molecular ferrimagnetic example provided by Kahn: the $\text{Cu}(\text{II})(\text{CH}_3\text{OH})\text{Fe}(\text{III})(\text{H}_2\text{O})\text{Cl}(\text{fsa})\text{en}$ binuclear complex—a textbook example [2.3, p. 126]. The structure of the complex was given in Fig. 2.53d with A = Cu(II) and M = Fe(III). A chloride is bound to Fe(III) in the y direction, opposite to a water molecule. The point group is close to C_{2v} , with the model geometry and the axes shown in Fig. 2.56a and symmetry labels as in Fig. 2.55.

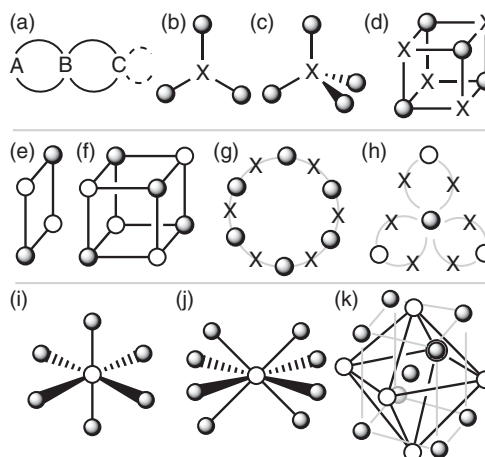
In $\text{CuFe}(\text{fsa})\text{en}$ there is one magnetic orbital on copper(II), xz , b_1 symmetry. The Fe(III) ion is high spin d^5 . Its five magnetic orbitals belong to symmetries $b_1(xz)$, $a_1(y^2)$, $a_1(x^2 - z^2)$, $a_2(xy)$, $b_2(yz)$. One of them, xz , b_1 , is strongly overlapping with the one of copper(II). It provides a strong antiferromagnetic pathway (AF), larger than the ferromagnetic ones (F or f). An antiferromagnetic coupling between the copper(II) and the iron(III) is thus observed ($J_{\text{CuFe}} = -78 \text{ cm}^{-1}$), with a ground state, $S_{\text{GS}} = 2$ ($5/2 - 1/2$). Note that actually the energetic effects depend on $n_A \cdot n_B \cdot J$, and since $n_A = 1$ and $n_B = 5$, the previous product amounts to -390 cm^{-1} . It is meaningful for the synthesis of future magnetic materials that ferrimagnetism in $\text{CuFe}(\text{fsa})\text{en}$ provides the same spin ground state $S_{\text{GS}} = 2$ ($3/2 + 1/2$) as ferromagnetic coupling in the $\text{Cu}(\text{II})\text{Cr}(\text{III})(\text{fsa})\text{en}$ complex (grey box 2 in Fig. 2.56b).

2.6.5.3 Polynuclear complexes and high-spin molecules

We now consider larger and larger systems, with the goal of producing molecules with higher and higher spin, with expected but original properties.

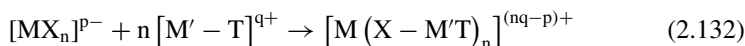
Fig. 2.57

Schematic structures and topology for high nuclearity and high spin molecules. (a) Linear; (b) triangular; (c) tetrahedral, ligand-centred; (d) tetrahedral, cubic; (e) square; (f) cubic; (g) ring; (h) propeller; (i) star: octahedral; (j) star: dodecahedral or square antiprism; (k) star or onion-shaped. A, B, C are different metallic spin bearers. X is a ligand. Shaded spheres: A. White spheres: B. Most of the metal coordination spheres of the metallic ions are not completed for clarity. In (k), a B_9A_6 complex, the grey spheres are B metal ions at the centre and capping the faces of the A_6 octahedron.



This is a way of bridging the gap between small molecules, generally binuclear systems seen previously, and extended solids (next section). Schematic structures of polynuclear systems are shown in Fig. 2.57.

There are many synthetic strategies for building large polynuclear systems: multistep synthesis, recipes from supramolecular chemistry, and even ‘serendipity’; that is, using the spontaneous and unexpected emergence of a complex structure from a simple combination of reactants. We just stress here the use of building blocks made of coordination complexes, playing thus the role of either ‘complex-as-ligand’ or ‘complex-as-metal’ (Fig. 2.58a, b, c). The corresponding synthetic process (Fig 2.58, d–e) is a simple Lewis acid–base reaction, and is written:



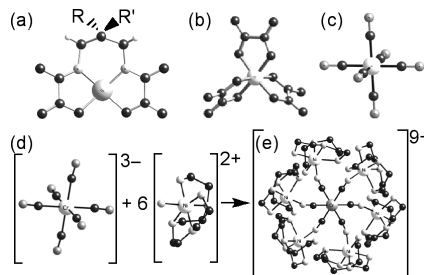
To avoid the formation of extended networks (Section 2.7) and stop the coordination process at the high-spin molecule stage, suitable terminal ligands T are introduced.

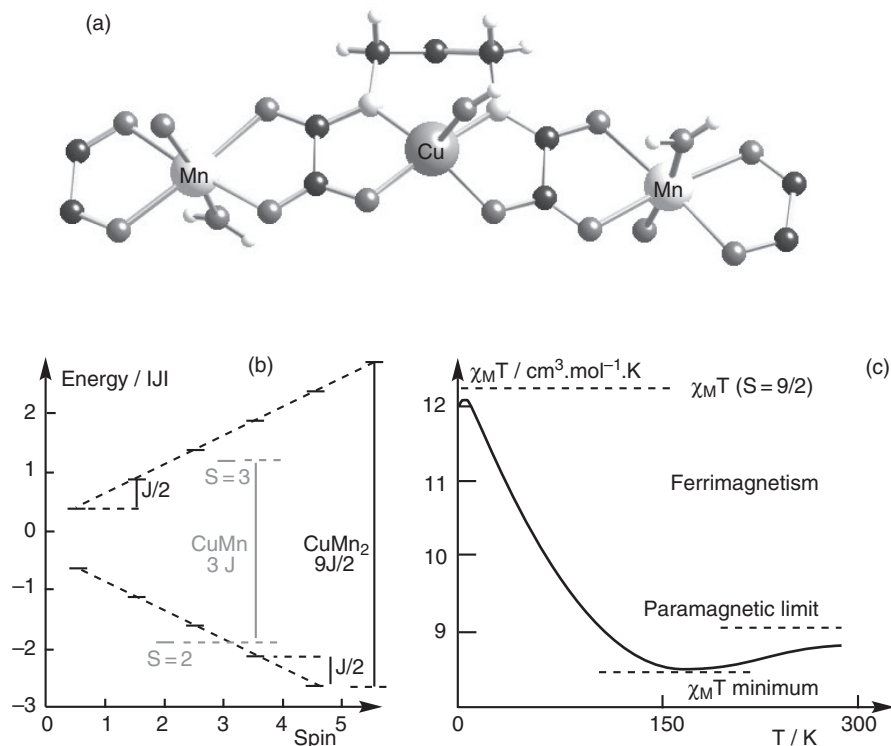
A first example is the T–Mn(II)[Cu(II)(pba)]Mn(II)–T trinuclear $Mn_1-Cu-Mn_2$ complex (T denotes ‘terminal ligand’, and pba is the abbreviation of 1,3-propanebis(oxamate)), or $\{CuMn_2\}$. The number of metallic neighbours of copper is 2, and the one of manganese is 1 (Fig. 2.59a).

The Cu–Mn coupling can be foreseen from Fig. 2.56. There are five exchange pathways through the oxamate ligand between the central xz d orbital

Fig. 2.58

Complexes used as ligands: (a) copper(II)1,3-propanebis(oxamate) dianion $[Cu(pba)]^{2-}$; (b) trisoxalatochromate(III) trianion (Λ enantiomer), $[Cr(Ox)_3]^{3-}$; (c) hexacyanidochromate(III), trianion $[Cr(CN)_6]^{3-}$; (d–e) Schematic Lewis acid–base reaction between an hexacyanidochromate(III) and metal(II) complexes to form cationic polynuclear complexes.



**Fig. 2.59**

Complex $\{\text{CuMn}_2\}$. (a) Ball and stick representation of the crystallographic structure; copper(II) large grey, manganese(II) large white, carbon, small black, oxygen, small dark grey, nitrogen small light grey balls; (b) spin state structure of $\{\text{CuMn}_2\}$ (black) and of $\{\text{CuMn}\}$ (light grey); horizontal bars represent the energy levels; dotted lines are guides for the eye; (c) experimental thermal variation of the molar magnetic susceptibility as $\chi_{\text{M}}T$ (adapted from [2.3, p. 223]).

on copper and the five d orbitals of manganese on each side of the copper: one is strongly antiferromagnetic (xz - xz), whereas the four others are weakly ferromagnetic. The Cu–Mn interaction is then expected to be antiferromagnetic with a ground spin configuration ($\uparrow\downarrow\uparrow$) and a spin ground state $S_{\text{GS}} = 2 \times 5/2 - 1/2 = 9/2$, which is indeed observed experimentally. This value is higher than the highest spin provided by nature in the periodic table, Gd(III), $S = 7/2$.

The spin Hamiltonian is:

$$\mathbf{H} = -J (\mathbf{S}_{\text{Mn1}}\mathbf{S}_{\text{Cu}} + \mathbf{S}_{\text{Cu}}\mathbf{S}_{\text{Mn2}}) = -J\mathbf{S}_{\text{Cu}} (\mathbf{S}_{\text{Mn1}} + \mathbf{S}_{\text{Mn2}}) = -J\mathbf{S}_{\text{Cu}}\mathbf{S}^* \quad (2.133a)$$

where we use Kambe's method introduced in Section 2.5.3.1. We define the intermediate spin operator $\mathbf{S}^* = \mathbf{S}_{\text{Mn1}} + \mathbf{S}_{\text{Mn2}}$ and the total spin operator $\mathbf{S}_{\text{T}} = \mathbf{S}_{\text{Cu}} + \mathbf{S}^*$. The Hamiltonian and the eigen energies are then written:

$$\mathbf{H} = -J S_{\text{Cu}} S^* = -(J/2) [S_{\text{T}}^2 - S^{*2}] \quad (2.133b)$$

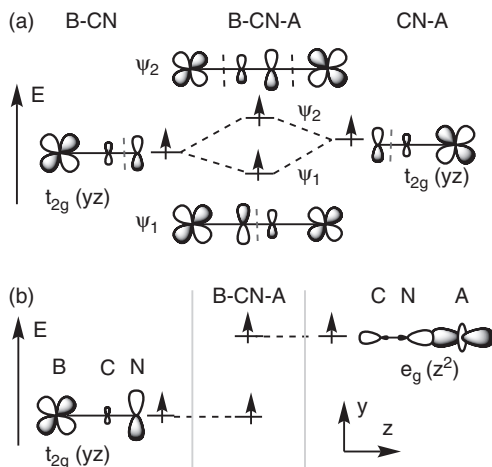
$$E(S_{\text{T}}, S^*) = -(J/2) [S_{\text{T}}(S_{\text{T}} + 1) - S^*(S^* + 1)] \quad (2.133c)$$

For each value of S^* , S_{T} spans values between $(S^* + S_{\text{Cu}})$ and $|S^* - S_{\text{Cu}}|$. The S^* values range from 5 to 0 by unit steps. For $S^* = 5$, $S_{\text{T}} = 11/2$ (energy $E(S_{\text{T}}, S^*) = E(11/2, 5)$) and $9/2$ (energy $E(9/2, 5)$). For $S^* = 4$, $S_{\text{T}} = 9/2$, and $7/2$, and so on, down to $E(1/2, 0)$. It is then easy to find the energy levels which range between $-23J/8$ and $+21J/8$ (Fig. 2.59b).

The spin-state structure (that is, the energy of the spin levels $E(S)$ as a function of their spin) is represented in Fig. 2.59 for the expected antiferromagnetic interaction. Also shown for comparison is the spin-state structure of a {CuMn} dinuclear complex with an antiferromagnetic interaction between copper (II) and manganese(II): the reader can easily find that in this case there are two spin states only: $S = 2$ (ground state, $E(2) = 7J/4$) and $S = 3$ (excited state, $E(3) = -5J/4$), separated by $3J$. In the case of {CuMn₂}, the most salient feature is that for each spin value there are two energy levels, and two branches—the lower one with energies ascending regularly by $|J|/2$ steps when the spin decreases by unit step from $9/2$ to $1/2$, and the upper branch ascending in the same way when the spin increases from $1/2$ to the highest spin $11/2$.

This spin-state structure and its Boltzmann distribution is the key for understanding the thermal variation of the molar susceptibility displayed as the $\chi_{\text{M}}T$ product in Fig. 2.59c, and in particular its curious minimum observed around 170 K. At very low T ($kT \ll |J|/2$), the only populated level is the $S_{\text{GS}} = 9/2$ ground state, corresponding to a number n of unpaired electrons, $n = 9$. The approximate value (with $g = 2$) of the $\chi_{\text{M}}T$ product using eqn. (2.51b) is $\chi_{\text{M}}T = n(n + 2)/8 = 12.375$ (in cgs-emu units, $\text{cm}^3 \cdot \text{mol}^{-1} \cdot \text{K}$). When the temperature increases, the excited levels on the lower branch of Fig. 2.59b begin to populate. As their spins are lower than $9/2$, the $\chi_{\text{M}}T$ product *decreases*. Conversely, if we start from the high temperature ($kT \gg 9J/2$), all the energy levels are equally populated. This state is precisely the paramagnetic limit; that is, the situation where the spin of copper(II) and manganese(II) behave independently. The corresponding approximate value of the $\chi_{\text{M}}T$ product is then (with a mean $g = 2$): $\chi_{\text{M}}T = (\chi_{\text{M}}T)_{\text{Cu}} + 2(\chi_{\text{M}}T)_{\text{Mn}} = [1 \times 3 + 2 \times 5 \times 7]/8 = 9.125$. When the temperature decreases, the first level to be depopulated is $S = 11/2$, and then those of the upper branch in Fig. 2.59b. As their spins are lower than $11/2$, *here also the $\chi_{\text{M}}T$ decreases*. There is thus a minimum somewhere in the $\chi_{\text{M}}T$ curve, and this constitutes a signature of extended ferrimagnetic compounds. The quantitative analysis of the curve using Van Vleck formula yields $J_{\text{CuMn}} = -36.6 \text{ cm}^{-1}$ [2.3, p. 223].

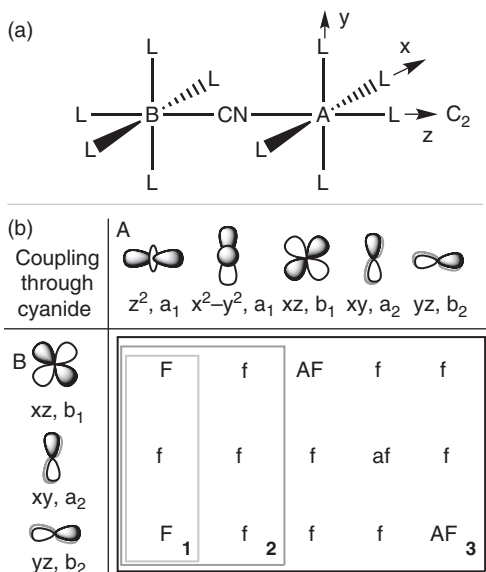
As a second example we consider systems built from hexacyanidochromate(III) $[\text{B}(\text{CN})_6]^{3-}$ (Fig. 2.58cd). Note the interest of chromium(III) precursors: the metal has a d^3 half-filled shell configuration which confers inertness to the complex; the three chromium(III) t_{2g} orbitals are spreading in the three x, y, z directions favouring exchange with neighbours. The hexacyanidochromate(III) is able to produce complexes with different nuclearities with a same metallic partner $\{\text{Cr}(\text{CN})_{6-n}(\text{CN-A-T})_n\}$ with $n = 1$ to 6 (A = Ni, T terminal polyamine, quite often tetra- or pentadentate) or different ones. The structure of a $\{\text{CrA}_6\}$ complex is shown in Fig. 2.58e. In such a way, in $\{\text{CrA}_6\}$, are

**Fig. 2.60**

Exchange in a linear cyanido-bridged B-CN-A unit. (a) Interaction between two overlapping orbitals and antiferromagnetism; (b) ferromagnetic exchange between two orthogonal magnetic orbitals.

obtained ground-state spins as different as $S = 9/2$, $\{\text{CrCu}_6\}$, Cr-Cu ferromagnetic interaction, $S = 15/2$, $\{\text{CrNi}_6\}$, also ferromagnetic interaction and $S = 27/2$ in the ferrimagnetic $\{\text{CrMn}_6\}$, with Cr-Mn antiferromagnetic interaction. These results can be understood easily with our usual tools.

Fig. 2.60a,b displays part of the molecular orbital energy diagrams for the B-CN-A unit, supposed linear. In the $\{\text{B}(\text{CN})_6\}^{\text{P-}}$ complex, cyanide is bound to B through carbon. The ligand field around B is very strong. The electronic configuration of B is limited to $d^{1-6} (t_{2g})^{1-6}$. For instance Cr(III), $(t_{2g})^3$, $S = 3/2$; Mn(III), $(t_{2g})^4$, $S = 1$; Fe(III), $(t_{2g})^5$, $S = 1/2$; Fe(II), Co(III) $(t_{2g})^6$, $S = 0$. Hence, the symmetry of the central B orbitals is always t_{2g} (or π) and a_2 , b_1 , b_2 if the BCNA unit is C_{2v} symmetry (Figs. 2.60 and 2.61). On the A(NC) side,

**Fig. 2.61**

Exchange pathways in cyanido-bridged B-CN-A complexes, analysed in C_{2v} symmetry point group. (a) Structural scheme and axes; (b) table of the exchange pathways and interactions for $\{\text{CrCu}_1\}$ (box 1, light grey), $\{\text{CrNi}_1\}$ (box 2, grey) and $\{\text{CrMn}_6\}$ (box 3, black). Capitals correspond to the stronger interactions.

the bonding is through the nitrogen of cyanide, which is a weak-field ligand. t_{2g} (π) and e_g (σ) orbitals are available, depending on the electronic configuration d^n . The two kinds of possible interactions are shown in Fig. 2.60. The overlap of the two π magnetic orbitals build two SOMOs, ψ_1 , and ψ_2 (Fig. 2.60a), and leads to antiferromagnetic interaction, whereas, when the magnetic orbitals are π and σ , they are orthogonal (2.60b), they remain unchanged, and ferromagnetic interaction results.

These considerations can be illustrated by the three complexes $\{\text{CrCu}_6\}$ $\{\text{CrNi}_6\}$ and $\{\text{CrMn}_6\}$, with the help of Fig. 2.61, similar to Fig. 2.48 (we suppose a C_{2v} symmetry of the B-CN-A unit, but the symmetry is indeed lower) [2.53]. In $\{\text{CrCu}_6\}$ the surrounding of copper is bipyramid trigonal, the magnetic orbital is z^2 (e_g , σ) and the interaction is between this orbital and the three t_{2g} (π) orbitals of chromium (Fig. 2.61, box 1) with three ferromagnetic exchange pathways (Experimental: $J_{\text{CrCu}} = +45.5 \text{ cm}^{-1}$). The spin ground state is $S_{\text{GS}} = 3/2 (\text{Cr}) + 6 \times 1/2 (\text{Cu}) = 9/2$. In $\{\text{CrNi}_6\}$ the interaction is between the three t_{2g} (π) orbitals of chromium and the two e_g (σ) orbitals of nickel(II). They are orthogonal. The interaction is expected ferromagnetic (Fig. 2.59, box 2) (Experimental: $J_{\text{CrNi}} = +17.3 \text{ cm}^{-1}$). The spin ground state is $S_{\text{GS}} = 3/2 (\text{Cr}) + 6 \times 1 (\text{Ni}) = 15/2$. For $\{\text{CrMn}_6\}$ the situation is shown in Fig. 2.61, box 3, with fifteen competing exchange pathways—six ferromagnetic as in $\{\text{CrNi}_6\}$, *mutatis mutandis*, and nine antiferromagnetic. An overall antiferromagnetic interaction is expected. Indeed, the experimental J value is $J_{\text{CrMn}} = -9.0 \text{ cm}^{-1}$. The spin ground state is $S_{\text{GS}} = [3/2 (\text{Cr}) - 6 \times 5/2 (\text{Mn})] = 27/2$ —an appealing ferrimagnetic situation, $[\downarrow(\uparrow)_6]$. The spin-state structure (not shown) is much more complex than in $\{\text{CuMn}_2\}$.

We finish this section with examples of very high spin molecules. The rational approach described previously with $\{\text{CrMn}_6\}$ lead to $S = 27/2$, far above the $7/2$ of the Gd(III) provided by nature, though still higher values have been obtained. Figure 2.62 displays some magnetization curves *versus* $\mu_0 H$.

The ferrimagnetic high-spin molecule $\{\text{Mo}_6\text{Mn}_9\}$ deserves a special comment. $\{\text{Mo}_6\text{Mn}_9\}$ stands for $[\text{Mn}(\text{II})[\text{Mn}(\text{II})(\text{MeOH})_3]_8(\mu\text{-CN})_{30}[\text{Mo}(\text{V})(\text{CN})_3]_6] \cdot 5\text{MeOH} \cdot 2\text{H}_2\text{O}$. [2.54]. A similar complex is $\{\text{W}_6\text{Mn}_9\}$. This

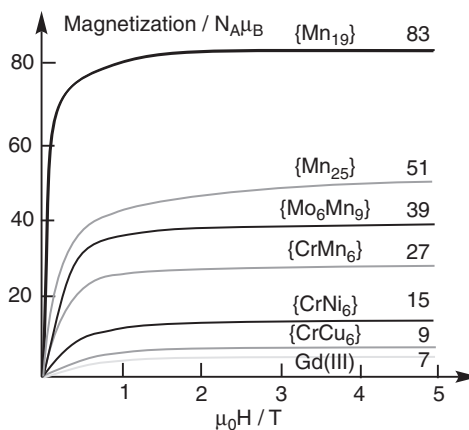
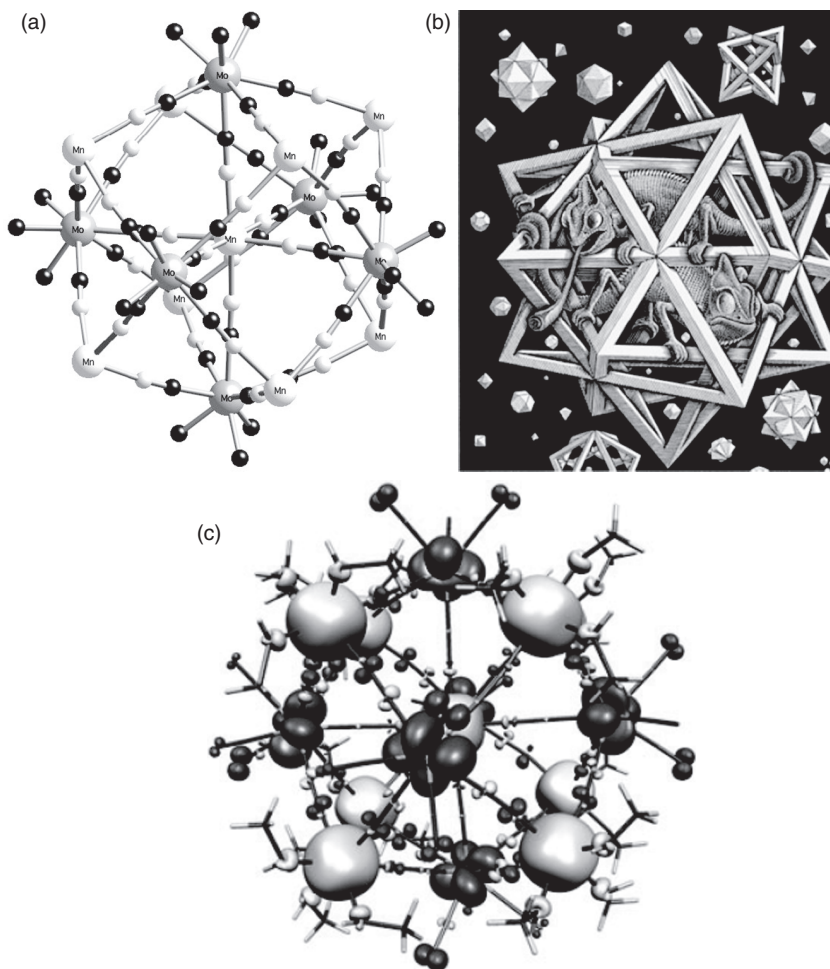


Fig. 2.62

Magnetization in Bohr magnetons *versus* $\mu_0 H$ of high-spin molecules described in the text. The curve of Gd(III) is given for comparison. The saturation value at high field gives directly the number of unpaired spins of the ground state (figure above the curves).

**Fig. 2.63**

Ferrimagnetism in $\{\text{Mo}_6\text{Mn}_9\}$. (a) Crystallographic structure; Mo large grey spheres; Mn, large white sphere, carbon, black, nitrogen light grey; external ligands are omitted for clarity. (b) Escher's view of the interweaving of an octahedron and a cube. See the polyhedron at the upper left the engraving. (M. C. Escher's *Stars* (1948) © 2013 The M. C. Escher Company, The Netherlands. All rights reserved. <<http://www.mcescher.com>>) (c) Spin density map, positive density is light grey, negative spin density, dark grey. (b and c reproduced from [2.54].)

is an example of the use of a second and third series of transition metal ion to the benefit of the larger spreading of the d orbitals with increasing Z to enhance the J values. The structure is shown in Fig. 2.63a. The building block is an octacyanometalate $[\text{Mo}(\text{V})(\text{CN})_8]^{3-}$, spin $S = 1/2$. A central $\text{Mn}(\text{II})$ ion, $S = 5/2$, is surrounded by an octahedron of $\text{Mo}(\text{V})$, the eight faces of which are capped by one $\text{Mn}(\text{II})$. The structure can be also described as a centred cube of $\text{Mn}(\text{II})$ capped by an octahedron of $\text{Mo}(\text{V})$. To design such a beautiful structure the scientist competes with the artist (Fig. 2.63b). The result is a ferrimagnetic molecule $\{\text{Mo}_6\text{Mn}_9\}$ or $\{\text{W}_6\text{Mn}_9\}$ with antiferromagnetic interactions $\text{Mo}(\text{V})\text{--Mn}(\text{II})$ and $\text{W}(\text{V})\text{--Mn}(\text{II})$. In $\{\text{Mo}_6\text{Mn}_9\}$, DFT calculations show that there is a distribution of negative J values from $\approx -20 \text{ cm}^{-1}$ for the central $\text{Mn}\text{--}\text{NC}\text{--}\text{Mo}$ linear units to $\approx -12 \text{ cm}^{-1}$ for the peripheral $\text{Mn}\text{--}\text{Mo}\text{--}\text{NC}\text{--}\text{Mo}$ bent ones. The experimentally determined ground state (magnetization and spin polarized neutron diffraction) is $S_{\text{GS}} = 39/2$, in line with the simple calculation: $S_{\text{GS}} = |-6 \times 1/2 (\text{Mo or W}) + 9 \times 5/2 (\text{Mn})| [(\downarrow)_6(\uparrow)_9]$. Figure 2.61 displays the DFT computed spin density—a beautiful illustration of the antiferromagnetic

coupling: spherical positive spin density of the d^5 manganese(II) ions and negative spin density of the unique Mo(V) unpaired electron in x^2-y^2 type orbital on the six Mo centres.

Finally, let us mention some very high spin values shown in Fig. 2.62 with a $\{\text{Mn}_{25}\}$ complex by Murugesu and Christou which paved the way to the present molecular spin record achieved with the ferromagnetic mixed valency aggregate $[\text{Mn}(\text{III})_{12}\text{Mn}(\text{II})_7(\mu_4\text{-O})_8(\mu_3\text{-}\eta_1\text{-N}_3)_8(\text{HL})_{12}\text{-}(\text{MeCN})_6]\text{Cl}_{12}\cdot 10\text{MeOH}\cdot\text{MeCN}$ ($\text{H}_3\text{L} = 2,6\text{-bis}(\text{hydroxy-methyl-4-methylphenol})$, $\{\text{Mn}_{19}\}$, with a $S_{\text{GS}} = 83/2$ by Powell [2.55]). In this very complex structure (not shown), the interactions between Mn(II) and Mn(III) are weakly ferromagnetic, but the large number of magnetic sites permits the very high spin ground state.

The next section illustrates the use of the same molecular building blocks in the construction of extended structures.

2.7 Extended molecular magnetic systems

Up to now we have dealt with zero-dimension (0D) systems; *i.e.* molecules and clusters where magnetic properties could be understood and described through a finite set of atoms, isolated from their surroundings. In fact, beyond the molecules exist extended lattices. Extended molecular magnetic lattices are objects whose magnetic properties present a dimensionality one (1D, chain), two (2D, planes) or three (3D, networks). In this section we present a few considerations to show how it is possible to fill the gap between the isolated molecule and the well-organized 3D solid. We start by a brief description on the complex specificity of the exciting 1D world. We present, then, an example of a new kind of 1D material displaying a cross-over to 3D behaviour, and, using our previous knowledge, we discuss the conditions to obtain a room-temperature molecule-based magnet.

2.7.1 The one-dimensional world: a Hamiltonian and synthesis factory

The one-dimensional world is an attractive common playground for mathematicians, physicists, chemists, experimentalists, and theoreticians. A simple reason is the possibility to solve *exactly* in 1D non-trivial physical problems too complex to solve in 3D. Significant examples can be found in [2.2] (de Jongh p. 1–35; J. C. Bonner, p. 157–205; W. Hatfield, p. 555–602), [2.3] (Chapter 11), [2.6] (vol. I, E. Coronado *et al.*, p. 1_{sq}, J.-P. Renard *et al.*, p. 49_{sq}).

We begin with a few definitions useful in the following section.

2.7.1.1 The magnetic chains zoo

A magnetic chain is a one-dimensional array of spin bearers S_i and $S_{j \neq i}$ with an interaction (coupling constant) J_{ij} between them. i and j define the positions of the spins in the chain. The mean direction of the chain is often chosen as the z axis.

- A *homospin or homometallic* chain is made of identical spins (radical or metallic). The usual spin Hamiltonian is the sum of terms $\mathbf{H}_{ij} = -J_{ij} \cdot \mathbf{S}_i \cdot \mathbf{S}_j$ (\mathbf{S}_i and \mathbf{S}_j are vector spin operators, $J_{i,i+1}$ the coupling constant). In most cases the exchange interaction occurs only between *nearest neighbours* (nn) \mathbf{S}_i and \mathbf{S}_{i+1} , since it is short-range. The conclusions of Section 2.6 relative to exchange are then fully valid here.
- A *uniform chain* is a chain where the *intrachain* coupling $J_{i,i+1}$ between identical spin bearers A_i is constant, $J_{\text{intra}} = J$. For example, if $(A)_N$ is a monometallic chain made of N spins, the Hamiltonian is written:

$$\mathbf{H} = -J \sum_{i=1}^{N-1} \mathbf{S}_i \mathbf{S}_{i+1} - g \mu_B \mu_0 H \sum_{i=1}^N S_i \quad (2.134)$$

The first term corresponds to an isotropic interaction. The second is the Zeeman term in the presence of an external field H , with our usual notations.

- *Nature of the coupling* (Fig. 2.64). The sign of J determines if the chain is ferromagnetic (F, $J > 0$) or antiferromagnetic (AF, $J < 0$).
- *Nature and magnitude of the spin*. The value of S_i determines if the chain can be treated as a *quantum chain* (defined by quantum spin operators \mathbf{S} , with well-defined M_S values—for low value of the spin) or as a *classical chain* (spin with an infinite value and presenting an infinite continuum of spatial orientations, as a classical vector). The spin S_i can take any value, half-integer or integer from $1/2$ [copper(II) or organic radical] (full quantum treatment for a spin $S_i = 1/2$, $m_S = \pm 1/2$) to $5/2$ [Fe(III), Mn(II)] or $7/2$ [Gd(III)] (quasi-classical treatment for $S_i = 7/2$, corresponding to eight values of M_S : $-7/2 \leq M_S \leq +7/2$). A copper(II) chain is a typical example of a quantum 1D object [*catena- μ -oxalato-Cu(II)*, $\{\text{Cu}(\text{Ox})_N$ or tetramethylammonium *catena-tris- μ -chlorocuprate(II)* $[\text{N}(\text{CH}_3)_4]^+ \{\text{CuCl}_3^-\}_N$]. The first one is neutral and the chains are close to each other. The second one is anionic and the chains are well separated by the bulky organic cations which ensure electroneutrality of the crystal.
- *Infinite and finite chains*. The chains can be described as infinite ($N \rightarrow \infty$) or finite; *i.e.* built from finite segments of spins. Only finite chains exist in the real world, since defects always interrupt the infinite chains,

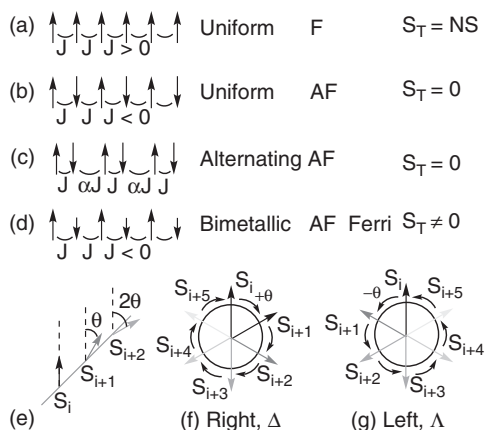


Fig. 2.64

Different kinds of chains. Spin structure, nearest-neighbour interaction (F or AF, name and total spin value for (a) uniform, ferromagnetic (F); (b) uniform antiferromagnetic (AF); (c) alternating, antiferromagnetic (AF); (d) bimetallic, antiferromagnetic between to successive spins (AF) hence ferrimagnetic, $S_T = N|S_A - S_B|$ (N number of pairs); (e-g) schematic illustration of the antisymmetric exchange; (f) right-handed helical configuration; (g) left-handed helical configuration.

create ‘ends of chains’, and perturb the ideal 1D behaviour. The longer segments ever observed comprise 10^4 spins in carefully grown crystals of tetramethylammonium catena-tris- μ -manganate(II) $[\text{N}(\text{CH}_3)_4]^+ \{\text{MnCl}_3^-\}_N$, TMMC. On the other hand, the hypothesis of infinite chains makes easier theoretical treatments. For example, a linear infinite chain can be considered as the limit of spins’ rings of radius R when $R \rightarrow \infty$. In this case the boundary conditions become $S_{N+1} \equiv S_1$. This presents a valuable way of computing the thermodynamic properties of chains by extrapolating results obtained in finite-size rings.

- *Fermions and bosons.* Another description focus of the value of the spin, half-integer (fermions) or integer (bosons). The thermodynamics of the chain is quite different in both cases. There is a continuum of spin energies for half-integer spins, but a gap opens between the singlet ground state and the first excited state (a triplet) for integer spins. This was conjectured by Haldane in the 1980s and later checked experimentally (J. P. Renard *et al.* in [2.6], vol. I, pp. 49–93). The physics of such a kind of ‘gapped’ system has been known since an important development in the study of ladders and strongly coupled electrons in superconductivity (see Section 3.3.4.4).
- *Alternating chains.* A chain of identical spins (homospin or homometallic) is said to be alternating when there is a periodic alternation of the J values: $J_1 = J$ between S_i and S_{i+1} , and $J_2 = \alpha J$ between S_{i+1} and S_{i+2} . An important phenomenon, theoretically documented and experimentally observed, is the spin–Peierls transition when a homometallic uniform chain (uniform J) becomes an alternating chain ($J, \alpha J$). The transition occurs at a spin–Peierls temperature T_{SP} when the vibrations (phonons) of the system couples with the exchange energy. An equivalent Peierls transition will appear in Chapter 3 for conducting systems.
- *Bimetallic chains.* The chain is said to be bimetallic when it is built from two ordered transition metals A and B: $(\text{A–B})_N$ (N number of pairs), with bridging ligands. Such species appeared only recently in the 1D zoo. We present a brief account on them in Section 2.7.2.
- *Anisotropic chains.* When the metal ion A presents a local anisotropy D_i and anisotropic exchange $D_{i,i+1}$ between neighbours, the chain is said to be anisotropic. The anisotropy in 1D also finds its origin in the through-space spin–spin magnetic dipolar interaction at any distance r between the spins (different along the chain and in other directions). This term is generally weak. It appears at low temperature when its energy becomes close to kT . The Hamiltonian (2.134) is then completed, as in eqn. (2.105), by a local anisotropy term such as:

$$\mathbf{H}_{\text{ani}} = D \sum_{i=1}^N (\mathbf{S}_i^z)^2 \quad (2.135)$$

Other terms describing the long-range *magnetic dipolar* interaction between the spin magnetic moments considered as point dipoles can be added. The dipolar term reads:

$$\mathbf{H}_{\text{dipolar}} = -\frac{4\mu_B^2}{a^3} \sum_{i=1}^{N-1} \sum_{r=i}^{N-1} \frac{1}{r^3} [\mathbf{S}_i \mathbf{S}_{i+r} - 3S_i^z S_{i+r}^z] \quad (2.136)$$

a is the repeating distance along the chain, and r.a the distance between spins i and i + r.

As for a pair of spins (eqn. 2.110), it is often simpler to describe the anisotropy by expressing the product $S_i \cdot S_{i+1}$, J, H (and eventually g) by their components along x, y, z. The Hamiltonian (2.134) then becomes:

$$\begin{aligned} \mathbf{H} = & - \sum_{i=1}^{N-1} [J_z S_i^z S_{i+1}^z + J_x S_i^x S_{i+1}^x + J_y S_i^y S_{i+1}^y] \\ & - g\mu_B \mu_0 \sum_{i=1}^N [H^z S_i^z + H^x S_i^x + H^y S_i^y] \end{aligned} \quad (2.137)$$

The names corresponding to various relative values of the effective J_z , J_x , J_y are as in Table 2.5. The most often used are the isotropic Heisenberg ($J_z = J_x = J_y$) and the Ising models ($J_z \neq 0$; $J_x = J_y = 0$). The dynamic properties of anisotropic chains are original, and will be considered in Section 2.8.

- *Chains with antisymmetric exchange.* The antisymmetric exchange already present in eqn. (2.105) can be introduced in the Hamiltonian by terms such as:

$$\mathbf{H}_{\text{anti}} = \vec{d}_{i,i+1} \cdot \mathbf{S}_i \wedge \mathbf{S}_{i+1} \quad (2.138)$$

This term is tilting the direction of neighbouring spins by an angle θ (or $-\theta$) (Fig. 2.64e). The spins in the chain are then adopting a canted configuration which can give rise to *helical magnetism*. The helical spins can turn right of left, depending on the θ value (Fig. 2.64f, g).

- *More Hamiltonians.* The Hamiltonian can be further modified (either to fit some set of data or to find an exact solution) by introducing other terms: *next-nearest neighbours* (nnn), interaction $\alpha J S_i \cdot S_{i+2}$ (generally, α is small $\ll 1$), quadratic terms, $\beta J (S_i \cdot S_{i+1})^2$ (where β is also small $\ll 1$), and so on, to infinity.
- *Interaction between chains.* In real systems, each chain has neighbours. The coupling constant between two neighbouring chains is called J_{inter} . The ratio $J_{\text{inter}}/J_{\text{intra}}$ determines how much the system is really 1D (the lower the ratio, the better 1D is a chain). One of the best 1D systems is $[\text{N}(\text{CH}_3)_4]^+ \{\text{MnCl}_3\}^-$ (TMMC) with a $J_{\text{inter}}/J_{\text{intra}} \approx 10^{-4}$. When $J_{\text{inter}}/J_{\text{intra}}$ is not $\ll 1$, the 1D properties can be hidden, and even a transition (cross-over) from 1D to 2D or 3D behaviours can occur, as we shall see soon (Fig. 2.73, Section 2.7.2).

2.7.1.2 Dynamics of 1D systems

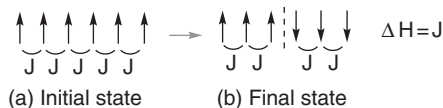
Besides thermodynamics, the most studied aspect of 1D chains—impossible to develop here—is their dynamics; that is, their behaviour when excitations are considered. We shall give an example in Section 2.8.

2.7.1.3 No long-range order in 1D at $T \neq 0K$

Low-dimensional physics, therefore 1D physics, is dimension-specific, and the 1D exact results cannot be simply extrapolated to other dimensionalities and to the real solid. For example, 1D thermodynamics implies that there is *no long-range order in 1D at $T \neq 0K$* , whereas the everyday life magnet (3D) is based on a long-range magnetic order between the spins.

Fig. 2.65

Ferromagnetic 1D chain with N spins. (a) Initial ordered state; (b) excited state with spin reversal in one position, costing an enthalpy J .



Let us take a ferromagnetic chain (Fig. 2.64a). The ground state should correspond to a configuration where all the spins S are aligned parallel, due to the ferromagnetic interaction $J_F > 0$ between neighbouring spins (Fig. 2.65a). The total spin is simply $S_{GS} = N.S$. An excited state can be built by reversing part of the spins (Fig. 2.65b). The enthalpy cost is the coupling constant, $\Delta H = J$. For any system, change is determined by the free enthalpy $\Delta G = \Delta H - T.\Delta S$, where ΔS is the entropy change. As the previous spin-reversing process can occur at $N-1$ positions along the chain, $\Delta S = k.\ln(N-1)$. Then:

$$\Delta G = \Delta H - T.\Delta S = J - kT.\ln(N-1)Z \quad (2.139)$$

which means that when the number of spins N is large enough (and clearly for $N \rightarrow \infty$), at a given temperature $T \neq 0$ K, the negative entropy term can become higher in absolute value than the positive enthalpy one, J . Then, $\Delta G < 0$. Spontaneously, the system abandons the ordered configuration (a) for a disordered one (b). There is no long range in 1D at $T \neq 0$ K. This demonstration, due to Landau, can be extended to 2D systems.

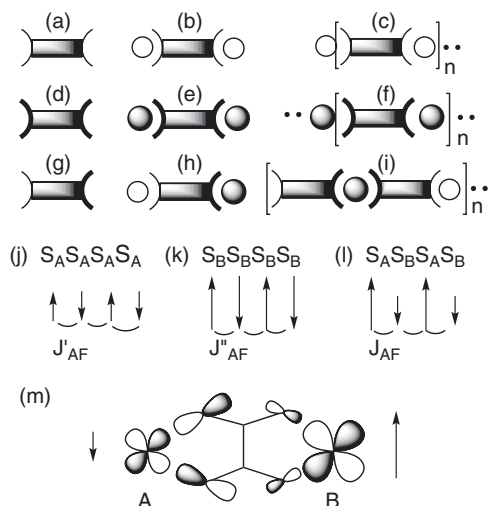
For a long time nevertheless, synthetic chemists thought that 1D chemistry could be a possible way to reach molecule-based magnets. It is rewarding to understand why and how this *a priori* impossible route proved successful.

2.7.2 Bimetallic ferrimagnetic chains: an improbable route to 3D magnets

2.7.2.1 From molecular engineering to 1D lattice fabrication

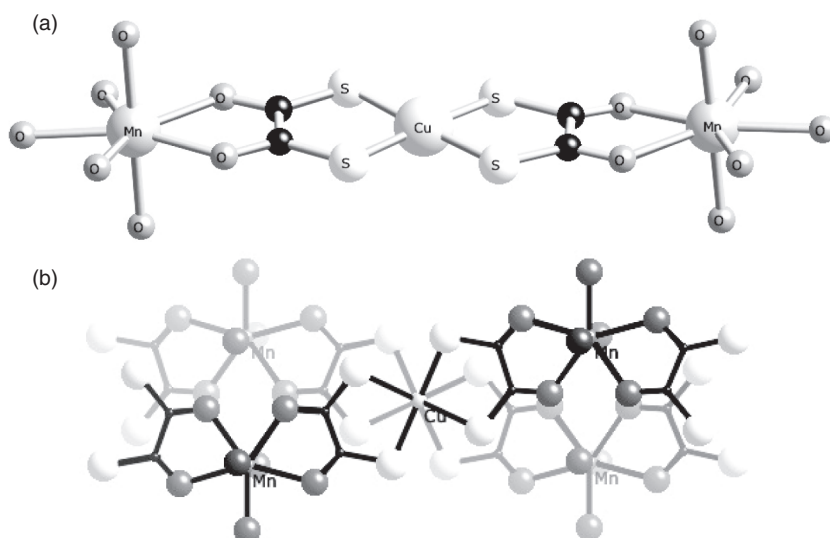
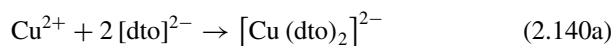
It is *a priori* simple to imagine how to build a 1D system using the bridging ligands of Section 2.6. For example, divalent cations A(II) combine easily with oxalate dianion to give *catena* μ -oxalato $[A-Ox]_n$ neutral chains. It works well. The reader can apply the arguments of Section 2.6.5.1 to foresee that anti-ferromagnetic chains are obtained. But it is a synthetic challenge to obtain a perfectly ordered bimetallic object $\{-A-X-B-X\}_n$ from a solution containing a mixture of A and B metallic ions and a bridging ligand X. The most probable is to obtain instead homometallic chains $\{-A-X-\}_n$ and $\{B-X\}_n$ or a random mixture of A/B inserted in a B/A chain. The general synthetic, spin and orbital strategies to get an ordered bimetallic chain are illustrated in Fig. 2.66a–i [2.3, Chapter 11], [2.56, 2.57].

An example of a suitable ligand is dithiooxalate, dto, encountered in Section 2.6.4.2 and Fig. 2.54, a possible suitable pair is Cu(II)–Mn(II), and the desired ordered bimetallic chain is Cu(II)(Mn(II)(S₂C₂O₂)(H₂O)_{7.5} (MnCu_{dto}), first synthesized by Gleizes in 1981. The structure consist of infinite chains (Mn(II))(H₂O)₃(O₂C₂S₂)Cu(II)(S₂C₂O₂) stretched along the b axis, stacking at van der Waals distances in the bc glide planes. A fragment of the structure of the chain is shown in Fig. 2.67a.

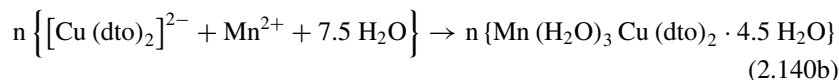

Fig. 2.66

Strategies towards ordered bimetallic ferromagnetic chains. Synthetic strategy: a symmetric bridging ligand X' (a) interacts with metal A (white ball) on both sides (b) and provides a homometallic uniform chain $(AX')_N$ (c). So does symmetric ligand X'' to give $(BX'')_N$ with metal B (grey ball) (d–f). A dissymmetric ligand X (g) leads to ordered heterometallic chains $(XAXB)_N$ (i) thanks to selective acid–base Lewis interaction at each side of the bridge (h). Spin strategy: (j) uniform antiferromagnetic chain with spin S_A (J'_{AF}) as in (c); with spin S_B (J''_{AF}) as in (f); (l) ordered bimetallic ferromagnetic chain (J_{AF}) with alternating spins S_A and S_B ($S_A \neq S_B$) as in (i). Orbital strategy (m): schematic overlap of two magnetic orbitals through the ligand.

The two sulphur atoms of the dto (in *cis* configuration) interact more readily with a Cu^{2+} ion than with an Mn^{2+} ion, which, on the contrary, binds preferentially to the oxygen atoms of dto. The *trans* bis-dithiooxalatecuprate(II) $[\text{dto-Cu-dto}]^{2-}$ reacts then with the Mn^{2+} ion, and in aqueous medium the neutral chain can precipitate (crystallize). This is well understood in the frame of hard and soft acid–base HSAB theory with privileged soft–soft (Cu–S) and hard–hard (Mn–O) interactions. This is now known as a ‘complex-as-ligand’ synthetic strategy. Eqns. (2.140) summarize the synthetic process:


Fig. 2.67

(a) Fragment of the ordered bimetallic $\{\text{MnCudto}\}$ chain emphasizing the precursor complex, $[\text{Cu(II)(dto)}_2]^{2-}$, and the soft–soft Cu–S and hard–hard Mn–O bonds; (b) stacks of CuS_4 units belonging to neighbouring chains down the *c* axis.



To derive the ferrimagnetic properties and 1D ferromagnetic spin structure, we still need to deploy the spin strategy of up and down unequal spins ($\downarrow \uparrow$)_n as shown in Fig. 2.66j–l. We use the considerations about overlapping magnetic orbitals of Cu(II) and Mn(II) (Fig. 2.66m), as in Section 2.6.5.2. {MnCudto} indeed presents all the features foreseen for a ferrimagnetic chain (experimental datapoints in Fig. 2.70): a minimum of χ_{MT} ($\approx 3.5 \text{ cm}^3 \text{ mol}^{-1} \text{ K}^{-1}$) at 130 K, and a strong increase at lower temperature up to 7.9 K ($\chi_{\text{MT}} \approx 11.5 \text{ cm}^3 \text{ mol}^{-1} \text{ K}^{-1}$). Unfortunately, at lower temperature, instead of the expected divergence a rapid decrease occurs—a sign of 3D antiferromagnetic ordering.

2.7.2.2 New magnetic objects, new Hamiltonians

We give in the following a brief account of the methods used to fit the magnetic data of these new systems [2.3, chapter 11], [2.56].

If the $(\text{CuMn})_{\infty}$ (or $\text{AB})_{\infty}$ infinite chain is considered as the limit of ordered bimetallic $(\text{CuMn})_n$ (or $\text{AB})_n$ rings when $N \rightarrow \infty$, the Hamiltonian for a ring N is written:

$$\mathbf{H} = -J \sum_{i=1}^{2N} \mathbf{S}_i \mathbf{S}_{i+1} \quad (2.141)$$

with $\mathbf{S}_{2N+1} = \mathbf{S}_1$; $\mathbf{S}_{2i-1} = \mathbf{S}_A = \mathbf{S}_{\text{Cu}}$ and $\mathbf{S}_{2i} = \mathbf{S}_B = \mathbf{S}_{\text{Mn}}$

When $J < 0$, the lowest energy level has $S_{\text{GS}} = n |S_A - S_B|$, the ring is ferrimagnetic, and the highest energy level has a spin $S_{\text{HS}} = n(S_A + S_B)$. Carrying out the same kind of calculations as in Section 2.6.5.3 (Fig. 2.59), it is possible to find the spin energy levels and to obtain the spin-state structures reported in Fig. 2.68.

For the two $(\text{CuMn})_n$ rings ($n = 2, 3$) the situation is more complex than for the trinuclear unit MnCuMn of Fig. 2.59, but the same qualitative conclusions can be drawn from Fig. 2.68. At very high temperature ($kT \gg |J|$) the spins S_A and S_B behave independently (which is equivalent to stating that all the energy levels are equally populated), the *paramagnetic limit* is reached, and the susceptibility χ_{M} per AB unit (in cgs-emu units) is:

$$(\chi_{\text{MT}})_{\text{HT}} = (N_A \mu_{\text{B}}^2 g^2 / 3k) [S_A(S_A + 1) + S_B(S_B + 1)] \quad (2.142)$$

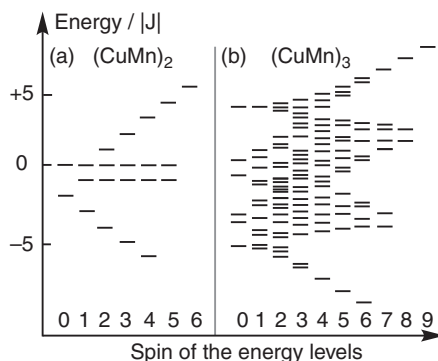
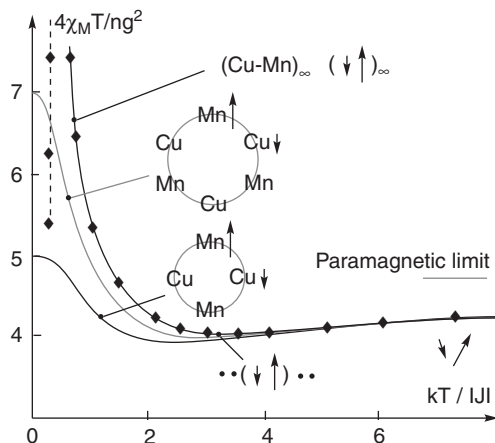


Fig. 2.68

Spin-state structure of ordered $(\text{CuMn})_n$ rings (a) with $n = 2$ and (b) $n = 3$. The ground state S_{GS} is magnetic. The presence of many levels having a spin $< S_{\text{GS}}$ allows us to understand the minimum in the $\chi_{\text{MT}} = f(T)$ curve (see Fig. 2.69).


Fig. 2.69

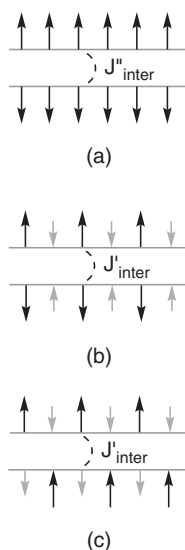
Reduced molar magnetic susceptibility per CuMn pair as a function of $kT/|J|$ for finite rings $(\text{CuMn})_n$ of increasing sizes ($n = 2, 3$) and for the infinite chain. Black diamonds are experimental data. The spin correlation is also shown schematically. The minimum in $\chi_M T$ is a signature of ferrimagnetism. The data at low T (dotted line) reveal the presence of weak interchain interactions.

where we assume that the local g factors g_A and g_B have the same value g . (With $N_A \mu_B^2 / 3k = 1/8$ and $g = 2$, check that for $A = \text{Cu}$ and $B = \text{Mn}$ $(\chi_M T)_{\text{HT}} = 4.75$). At very low temperature only the ground state is populated ($S_{\text{GS}} = n|S_A - S_B|$). The susceptibility, per AB unit, is then (cgs-emu):

$$\begin{aligned} (\chi_M T)_{\text{LT}} &= (N_A \mu_B^2 g^2 / 3k) [S_{\text{GS}} (S_{\text{GS}} + 1)] \\ &= (N_A \mu_B^2 g^2 / 3k) [n(S_A - S_B)^2 + |S_A - S_B|] \end{aligned} \quad (2.143)$$

The $(\chi_M T)_{\text{LT}}$ value tends to infinite for $N \rightarrow \infty$, since $(\chi_M T)_{\text{LT}} \propto n$ (Fig. 2.69). Following the same arguments as for the ferrimagnetic MnCuMn complex (Section 2.6.5.3), one arrives at the conclusion that in a ferrimagnetic chain, when T decreases, $\chi_M T$ decreases from the paramagnetic limit $(\chi_M T)_{\text{HT}}$, goes through a minimum, and then increases rapidly to diverge at low T . The minimum in $\chi_M T$ is the signature of a ferrimagnetic chain. The susceptibility for the chain is obtained by extrapolation of the susceptibility values for $(\text{CuMn})_n$ rings of increasing n . The correlation between the spins S_A and S_B provides another qualitative description of the ferrimagnetic chain. There is no correlation at high T (paramagnetic limit); when T decreases the correlation begins between two neighbouring spins S_A and S_B . At T_{min} , corresponding to the minimum of $\chi_M T$ $(\chi_M T)_{\text{min}}$, one can consider approximately that each S_A-S_B pair is correlated ($\downarrow \uparrow$) but that the pairs are not correlated between them. When $T < T_{\text{min}}$ the pairs begin to correlate ($\downarrow \uparrow \downarrow \uparrow$), ($\downarrow \uparrow \downarrow \uparrow \downarrow \uparrow$) and $(\downarrow \uparrow)_m$. m is the number of correlated pairs. The corresponding mean spin is $S_m = m|S_A - S_B|$, increasing at low T and reaching infinite when $(\downarrow \uparrow)_{m \rightarrow \infty}$, where $\chi_M T$ diverges. Such a trend allows us to understand that if there is (even a weak) antiferromagnetic interaction J_{inter} between z neighbouring chains, it exists at a critical temperature T_c , where $kT_c = J_{\text{inter}} \cdot z \cdot S_m (S_m + 1)$, below which an antiferromagnetic 3D ordering of the chains should occur (see Fig. 2.70b). The system is no more 1D. This cross-over from 1D to ordered AF 3D is a general feature (see Fig. 2.70a for uniform unimetallic chains). It is revealed by a drop of $\chi_M T$ curves at low T .

In some rare cases, exchange or long-range dipolar interactions (always present) can provide a ferromagnetic coupling between the chains (Fig. 2.70c,

**Fig. 2.70**

Spin strategy. (a, b) Antiferromagnetic interaction between two parallel neighbouring spin chains. (a) $(A)_n$ uniform chains, spin S_A (black arrow). The interaction J'_{inter} is between two spins S_A . The resulting spin is null. (b) $(A-B)_n$ uniform bimetallic chains, alternating large spin S_A (black) and small S_B (grey). On two neighbouring chains, similar spins are face to face (S_A-S_A and S_B-S_B). The interaction J'_{inter} is between two similar spins S_A . The resulting spin is null. (c) $(A-B)_n$ uniform bimetallic chains where one chain is displaced along the direction of the chain by $a/2$, half the unit cell. On two neighbouring chains, different spins are facing each other (S_A-S_B). The interaction J_{inter} is between two different spins S_A and S_B . The resulting spin is $p.m|S_A-S_B|$ (p number of chains, m number of pairs in the chains.)

commented on in the following). Other methods have been designed for the quantitative analysis of the magnetic data of ferrimagnetic chains. The interested reader can find a valuable summary of most of the original work in [2.3, chapter 11] and [2.6, vol. I, p. 1].

The strong decrease of $\chi_M T$ with T at low temperature in Fig. 2.69 is the sign of antiferromagnetic coupling between the chains and of the appearance of a 3D antiferromagnetic ordering. The ratio J_{inter}/J_{intra} was evaluated at 0.024. The chains are rather well isolated from each other, and behave as a quasi-1D ferrimagnetic chain at high temperature, allowing the observation of the $\chi_M T$ minimum. But at low temperature, weak interchain interactions (see Fig. 2.67b) are revealed and 3D ordering occurs.

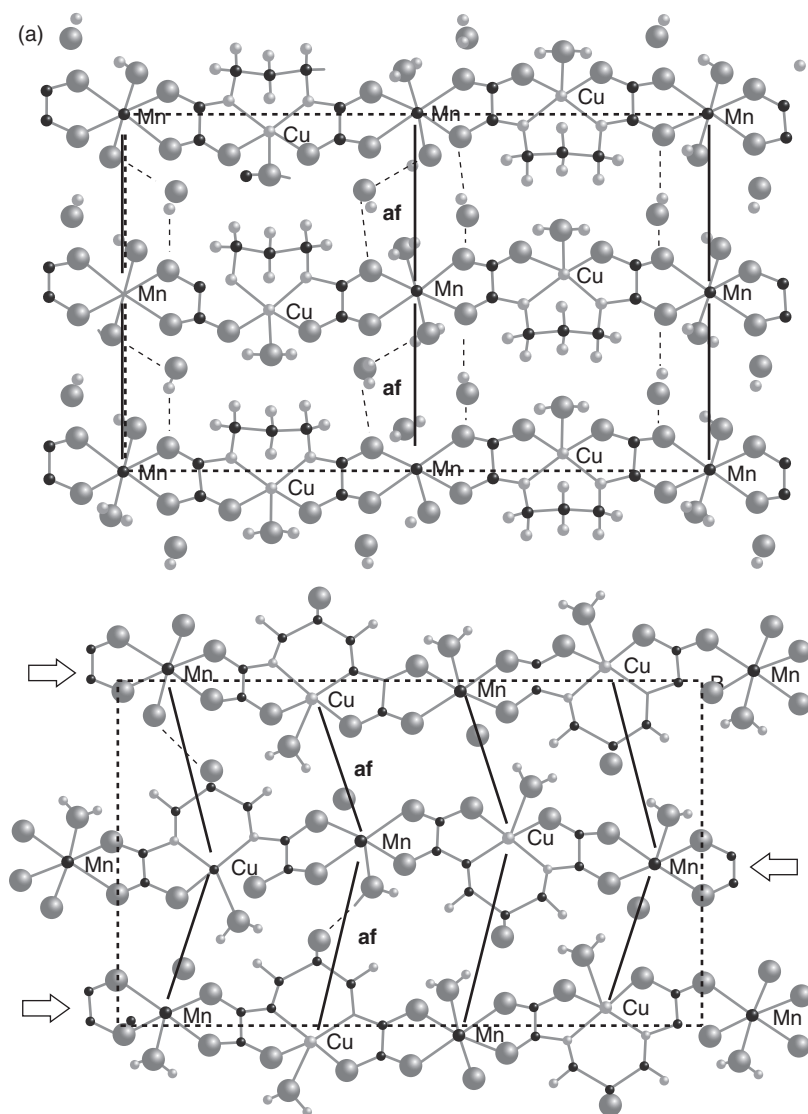
Deceivingly, but without surprise therefore, $\{\text{CuMndto}\}$ does not exhibit long-range ferrimagnetic ordering: (i) Landau's thermodynamics forbids long-range order in 1D; (ii) the AF interaction between the chains switches the system to a disappointing 3D antiferromagnet.

Can we go further and obtain 3D magnets through such a 1D chemical approach? If we understand that at some point a cross-over from 1D to 3D ferrimagnetism must be imagined and chemically prepared, a possible clever (and lucky) answer is discussed in the following.

2.7.2.3 From 1D lattice to crystal (supramolecular) engineering

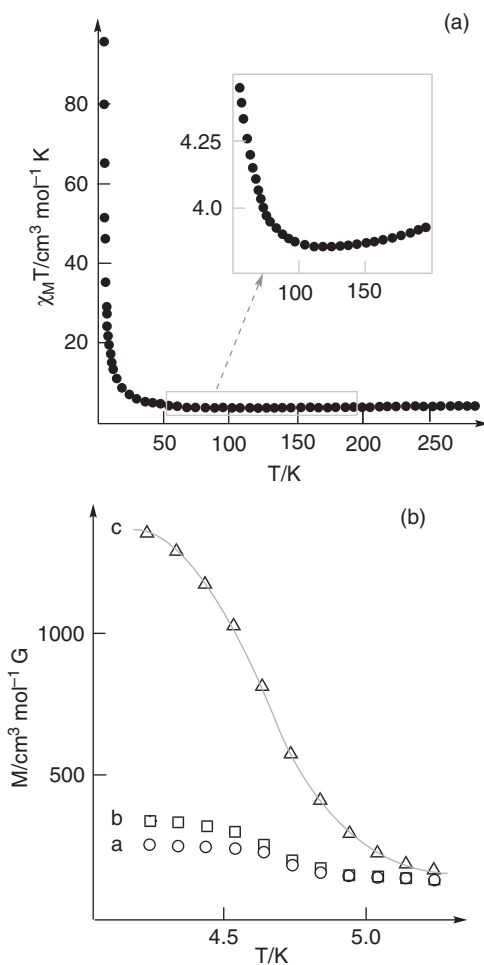
Instead of dto, the ligand 1,3-propylene-bis-oxamate (pba), already used to derive the finite $\{\text{MnCuMn}\}$ system (Section 2.6.5.3, Fig. 2.59), can be used—without introducing the terminal ligand—to prepare the infinite chain $\text{MnCu(pba)(H}_2\text{O)}_3 \cdot 2\text{H}_2\text{O}$ or $\{\text{MnCu(pba)}\}$. Its crystal structure is shown in Fig. 2.71a. The ordered Mn–Cu chains are aligned along the b axis with Cu–Mn distances 5.412 Å. The expected quasi-1D ferrimagnetic properties are indeed observed ($\chi_M T$ minimum at 115 K, χ_{TM} increase at low T , $J_{\text{CuMn}} = -23.4 \text{ cm}^{-1}$). Nevertheless, as for MnCu(dto) , weak interchain interactions due to hydrogen bonds and short Cu–Cu and Mn–Mn interchain distances (5.22 Å) in the a direction (Fig. 2.70b) provoke 3D antiferromagnetic ordering (Fig. 2.70b).

To overcome this difficulty, Kahn proposed shifting one of the chains by half a cell distance along the direction of the chain (Fig. 2.70c), so that different spins of two neighbouring chains are now facing each other. The ferrimagnetic configuration is extended to the neighbouring chain(s) and successively to the whole plane: in Fig. 2.70c, all the large (black) spins are aligned parallel (contrary to Fig. 2.70b) and antiparallel to all the small (grey) spins. This shift can be chemically achieved by introducing an OH group on the central carbon atom of the propylene bridge of the oxamate ligand, in an attempt to modify the hydrogen bond network in the crystal. This can be termed *crystal* or *supramolecular engineering*. The result is a new ferrimagnetic chain $\text{MnCu(pbaOH)(H}_2\text{O)}_3$ ($\text{pbaOH} = 2\text{-hydroxy-1,3-propylene-bis-oxamate}$) or MnCu(pbaOH) , the structure of which is displayed in Fig. 2.71b. It is very similar to MnCu(pba) , and the 1D ferrimagnetism is the same at high temperature. But now there is a short Cu–Mn distance (at 5.75 Å) in the a direction: the strategy to displace the chains was (partially) successful (Fig. 2.71b).

**Fig. 2.71**

Crystallographic structures of two closely related ferrimagnetic Cu–Mn chains down the *c* axis (*a*, vertical axis; *b*, horizontal axis). The bold lines schematize the largest antiferromagnetic interchain interactions in the *ab* plane. The thin dotted lines schematize the hydrogen bond network between the chains. (a) Structure of $\text{MnCu(pba)(H}_2\text{O)}_3 \cdot 2\text{H}_2\text{O}$. (b) Structure of $\text{MnCu(pba-OH)(H}_2\text{O)}_3 \cdot 2\text{H}_2\text{O}$. In (b), white arrows point out the displacement of the MnCu(pbaOH) chains compared to the MnCu(pba) chains. Compare with the ideal spin configurations in Fig. 2.70b, c.

Hydrogen bonds involving the OH group of pbaOH, close to copper and a water molecule coordinated to manganese, help in providing weak overlap and antiferromagnetic interaction between magnetic orbitals of copper(II) and manganese(II) belonging to neighbouring chains to finally provide the required ferrimagnetic planes. The magnetic consequence is the strong $\chi_{\text{M}}T$ increase at low temperature, $\chi_{\text{M}}T = 100 \text{ cm}^3 \text{ mol}^{-1} \text{ K}^{-1}$ at 4.3K (Fig. 2.72a), preliminary indication of a 3D ferrimagnetic order. Magnetization measurements *versus* temperature (Fig. 2.72b) confirm a ferrimagnetic long-range ordering with a Curie temperature $T_{\text{C}} = 4.6 \text{ K}$. The magnetization is strongly anisotropic, with an easy axis along *c*; that is, perpendicular to the chains. The molar magnetization per $\{\text{MnCu}\}$ unit *versus* applied magnetic induction (not shown) is close

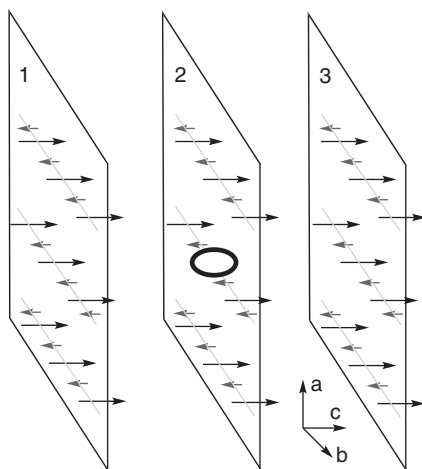
**Fig. 2.72**

Magnetic properties of MnCu(pbaOH). (a) Thermal variation of the product $\chi_M T$ per MnCu unit. The insert shows the expected minimum for a ferrimagnetic chain. Note the high $\chi_M T$ value at low T. (b) Thermal variation of the magnetization of MnCu(pbaOH) along the a (O), b (\square) and c (Δ) axes, in an applied magnetic induction of 10^{-3} T. The Curie temperature is $T_C \approx 4.6$ K. The magnetization is very anisotropic. c is the easy axis (the grey line is a guide for the eye). (Adapted from [2.57].)

to the value expected for a spin 2 $|S_{Mn} - S_{Cu}| = 2$, confirming the ferrimagnetic nature of the whole solid.

MnCu(pbaOH) can be considered the first molecule-based ferrimagnet obtained by rational design. The ordering temperature is low, but the compound was obtained through a rational, methodical step, rather than through serendipity, as the famous $V(\text{TCNE})_x$ by Manriquez and coworkers, obtained in 1991 when working on metallocene-based magnets [2.6] (G. T. Yee, J. S. Miller, in vol. V, p. 223–60).

An important aspect of the cross-over from 2D ferrimagnetism to 3D magnetic order is still missing. The synthetic strategy led us to ab ferrimagnetic planes (2D ferrimagnetism), but the interaction between the ab planes, necessary to reach 3D order, is still uncontrolled. The ab planes are not connected by hydrogen bonds, and exchange interactions should be very weak. Luckily, in the present case, the *magnetic dipolar* interaction (Hamiltonian (2.136)),

**Fig. 2.73**

Schematic spin configuration in a crystal of $\text{MnCu}(\text{pbaOH})$. 1D ferrimagnetic chain along b axis (grey lines). 2D ferrimagnetic ab planes 1, 2, 3 distant by $c = 5.023 \text{ \AA}$. The exchange interaction between the ab planes in the c direction is very weak. In plane 2 a hole (black circle) replaces a central manganese ion. At this point, all other spins of the crystal, acting as elementary dipoles, generate a magnetic field by magnetic dipolar effect. The long-range ordering of the spins in the crystal, ferrimagnetic or antiferromagnetic, depends on this dipolar field. If the dipolar field is parallel to the large (black) spins, the 3D order is ferrimagnetic (as shown and observed); if the dipolar field is antiparallel to the large spins, a final antiferromagnetic structure would result.

a weaker but long-range interaction, has the right influence. The geometry is such that the dipolar field created by the spins of a manganese unit (perpendicular to the ab plane) tends to align the magnetic moment of the next plane in the same direction (Fig. 2.73).

Thus the clever orbital, spin, and supermolecular strategy was very successful for the first two steps, 1D and 2D, but necessitated the help of an uncontrolled dipolar interaction to reach the required 3D ferrimagnetic order. Unfortunately, the dipolar interaction is beyond precise chemical control, because it depends on the geometrical distribution of the spins and their orientation *in the cell*. In Section 2.7.3 we shall encounter a genuine 3D strategy to rationally reach molecule-based magnets.

2.7.2.4 About order, dimensionality, and anisotropy

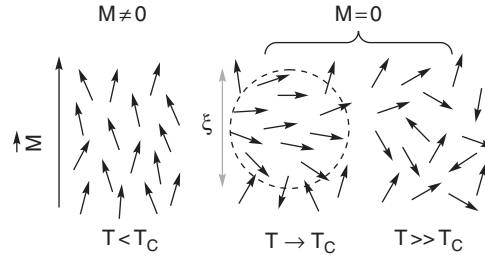
3D ordering (and magnetization reversal) is one of the most studied problems in solid-state magnetism. In the following we mention briefly some general principles governing the transitions between the paramagnetic state and the 3D ordered states such as ferromagnetic or antiferromagnetic.

We consider an ensemble of magnetic moments connected by a next-neighbour interaction J . At high temperature ($kT \gg (|J|)$) one has a disordered paramagnetic phase, and at low temperature ($kT \ll (|J|)$) an ordered magnetic phase. The two temperature ranges are separated by a critical temperature where $|J| \approx kT_c$. For ferro- or ferrimagnetic orders, T_c is the Curie temperature, T_C (named after Pierre Curie), and for antiferromagnetic order T_c is the Néel temperature, T_N , after Louis Néel).

In most cases such magnetic transitions are *not* accompanied by a change in the crystallographic structure, and belong to the category of *second-order transitions*. Let us recall that if the free enthalpy G depends on an external parameter x , when $\partial G/\partial x$ is discontinuous at the transition, it is first order;

Fig. 2.74

Microscopic picture of a ferromagnetic transition. The arrows represent individual magnetic moments. From right to left: $T \gg T_C$, paramagnetic disordered phase; $T \rightarrow T_C$ appearance of a correlation length; $T < T_C$, ferromagnetic ordered phase and appearance of a spontaneous magnetization M . (Adapted from J.-P. Renard [2.58].)



when the first derivative is continuous, but $\partial^2 G / \partial x^2$ is discontinuous, the transition is second order. In our case, $x = H$ (magnetic field), the first derivative (the magnetization; see Section 2.3.1) is continuous, and the second derivative (the susceptibility) is discontinuous at the transition.

From a microscopic point of view, Fig. 2.74 schematizes the situation in the paramagnetic phase (disordered phase, $M = 0$, correlation length $x \sim 0$) to the ferromagnetic phase (ordered, $M \neq 0$, correlation length diverges—a keystone of second-order transition). The magnetic system has spherical symmetry above T_C , and cylindrical symmetry below T_C . The symmetry breaking at $T = T_C$ is a general feature of phase transitions.

In literature—particularly in the physics domain—results are presented frequently as $1/\chi$ plots *versus* T (Fig. 2.75). For independent magnetic objects this corresponds to the Curie law, $\chi_M^{-1} = T/C$ (C Curie constant) (Fig. 2.75a). When there is an interaction, the Curie–Weiss modification $\chi_M^{-1} = (T - \theta)/C$ is used, but it has a weak theoretical justification and should be considered as essentially empirical. It is generally valid far from the critical temperature and allows the evaluation of θ by extrapolation. For a ferromagnetic order, $\theta > 0$ and is close to T_C (Fig. 2.75b). For an antiferromagnetic order, $\theta < 0$; T_N corresponds to χ_M^{-1} infinite (Fig. 2.75c). For a ferrimagnetic order, $\theta < 0$; T_C is obtained when χ_M diverges; that is, $\chi_M^{-1} = 0$ (Fig. 2.75d).

We now ask how a magnetic molecular system can transform in a magnetically ordered solid. At the microscopic level, two main parameters control this transition: (i) the dimensionality of the magnetic network

Fig. 2.75

Schematic thermal variation of the inverse of the molar susceptibility for Curie behaviour and different kinds of magnetic order (circled: spin configurations). (a) Curie behaviour (grey line). (b–d) Curie–Weiss behaviour: (b) Ferromagnetic order. (c) Antiferromagnetic order. (d) Ferrimagnetic order. Dotted lines are guide for the eye to evaluate θ and T_N .

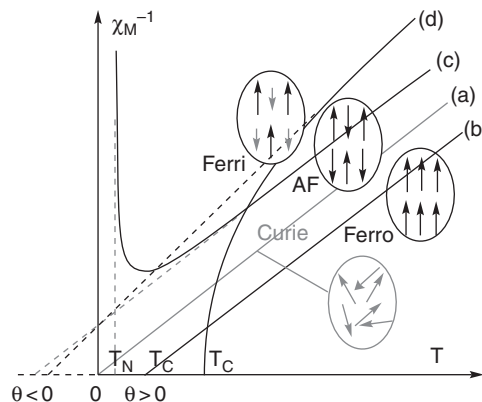


Table 2.9 Existence of long-range order at $T \neq 0\text{K}$ in a magnetic system with short-range interactions, as a function of its dimensionality and anisotropy.

Dimensionality/anisotropy	Name	1D	2D	3D
$J_z \gg J_x \approx J_y$	Ising	No	Yes	Yes
$J_x \approx J_y \gg J_z$	XY	No	KT ^a	Yes
$J_x = J_y = J_z$	Heisenberg	No	No	Yes

^a A special transition bearing the name Kosterlitz–Thouless. (Adapted from J.-P. Renard [2.58].)

(1D chains; 2D planes; 3D frameworks); (ii) the anisotropy of the interaction according to the relative values of the effective components of J : J_x , J_y , J_z . Table 2.9 summarizes—without demonstration—the most frequently encountered situations.

The conclusion is thus clear. 1D chains—first considered as a *conceptual* step between isolated molecules to magnetic ordered solid—are a *practical* dead-end. 2D planes can work within some constraints (Ising). The chemist willing to synthesize magnets should then create 3D networks, which present long-range order whatever the anisotropy. We present a few examples in the following.

Finally, if we want to increase as much as possible the critical temperature, a useful classical approximation relates the T_C temperature to the properties of the two subnetworks having spins S_A (Curie constant C_A) and S_B (C_B), a number of magnetic neighbours Z , and a coupling J . With our usual notations:

$$kT_C = Z|J| [S_A(S_A + 1)S_B(S_B + 1)]^{1/2}/N_A g^2 \mu_B^2 = Z|J| [C_A C_B]^{1/2}/N_A g^2 \mu_B^2 \quad (2.144)$$

Even approximate, eqn. (2.144) shows clearly that T_C can be maximized by increasing the number of magnetic neighbours Z , by increasing the magnitude of J and by increasing S_A and S_B [2.52].

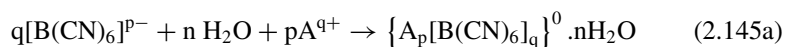
2.7.3 Three-dimensional frameworks, Prussian blue analogues

We reach here an enormous field, where the interaction between the spin bearers is directed in the three directions of space, building a *3D magnetic lattice*. To save space, we limit ourselves to a unique family, *a priori* very simple, synthesized from hexacyanidometalates, the Prussian blue analogues (PBA). Prussian blue itself is a blue pigment discovered in Berlin around 1704, first announced in a publication in 1710, and often considered as the first synthetic coordination compound: $\text{Fe}^{\text{III}}_4[\text{Fe}^{\text{II}}(\text{CN})_6]_3 \cdot 14\text{--}16\text{H}_2\text{O}$. The magnetic Prussian blue analogues (referred to in the following as MPB) are a ‘simple’ 3D extension of what we have already described about high-spin molecules based on hexacyanidometalates (Section 2.6.5.3). The main lines of the story can be found in [2.6, vol. V, 283sq].

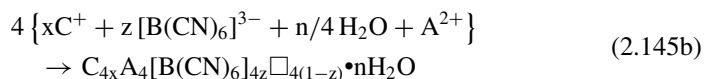
2.7.3.1 Formulation and structure

Prussian blue and its analogues can be synthesized easily by the reaction of the Lewis bases hexacyanidometalates $[\text{B}(\text{CN})_6]^{p-}$ with transition metal Lewis

acids A^{q+} in aqueous solution to give neutral three-dimensional networks $\{A_p[B(CN)_6]_q\}^0 \cdot nH_2O$:



The compounds are very insoluble and poorly crystalline, and comprise often extrinsic components (solvent, ions, and so on). Among the different ways of writing the MPB formulae (with A(II), B(III), and C(I)), we use $C_{4x}A(II)_4[B(III)(CN)_6]_{4z} \square_{4(1-z)} \cdot nH_2O$, (C^+ , alkali metal cation), where \square is a $[B(CN)_6]$ vacancy (check that $x + 2 = 3z$):



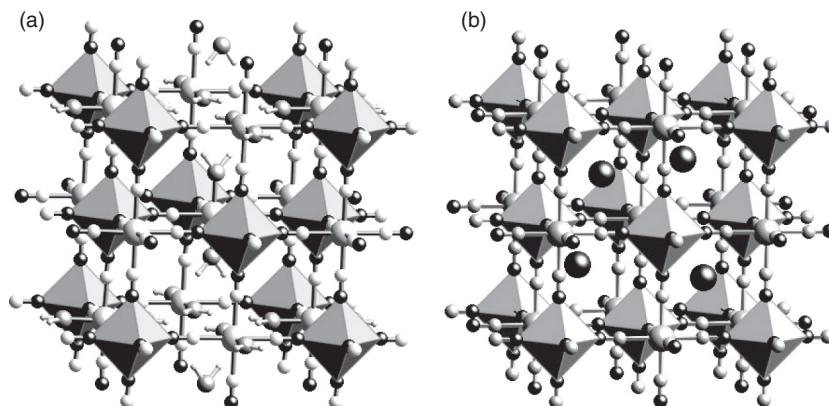
The equation is based on the cubic conventional cell shown in Fig. 2.76. For $x = z = 1$, the MPB adopt face-centred cubic (*fcc*) structures. The unit cell comprises eight octants corresponding to interstitial or tetrahedral sites. There are two types of octahedral metal site: strong ligand-field sites $[BCN)_6]$ and weak ligand-field sites $[A(NC)_6]$.

For $z < 1$, and therefore for Prussian blue, Lüdi and coworkers proposed, from powder diffraction and density measurements, that the A sites are fully occupied and the $[B(CN)_6]$ sites are fractionally occupied. Accordingly, the A centres surrounding the vacant $[B(CN)_6]$ sites have one (or more) water molecules in their coordination spheres, depending on the stoichiometry z (Fig. 2.76). Zeolitic water molecules and/or charge-balancing cations generally occupy the interstitial sites with an extensive hydrogen bond network.

In Prussian blue, $Fe^{III}_4[Fe^{II}(CN)_6]_3 \cdot 14-16H_2O$, the $[Fe(CN)_6]$ vacancies are most often disordered in the crystal, giving an apparent high-symmetry structure (*Fm3m*) with a fractional occupancy (3/4) of the $[Fe(CN)_6]$ sites. The

Fig. 2.76

Schematic ball-and-stick structure of a conventional cell of Prussian blue analogues: (a) $A(II)_4[B(III)(CN)_6]_{4z} \square_{4(1-z)} \cdot nH_2O$, $\{A_4B_{4z}\}$. $[B(CN)_6]$: grey octahedron. Other balls: A, large white; carbon, small black, nitrogen, small white; oxygen, medium grey. Coordination and zeolitic water molecules fill the $[B(CN)_6]$ vacancies. (b) $C_4A_4[B(CN)_6]_4 \square_0$ or $\{C_4A_4B_4\}$: C cation, large black balls in the tetrahedral cavities $\{C_4A_4B_4\}$.



presence of vacancies is *intrinsic* to PBAs whenever $z < 1$. It is *not* a ‘defect’ structure, as is often claimed. Some important properties are determined by these vacancies (discussed in the following).

The Prussian blue structural framework is closely related to that of perovskites ABO_3 , such as $CaTiO_3$, where the octahedral metal centres are connected by oxide ions instead of cyanide bridges. But the hexacyanido-metalate precursor exists in solution, which is not the case for the hypothetical $[Ti^{IV}O_6]^{4-}$ unit. Prussian blue and its analogues can therefore be considered as molecule-based materials. They are synthesized directly from preassembled molecular precursors in water.

Finally, from a preparative point of view, Prussian blue is obtained by the addition of an iron(III) salt to potassium hexacyanidoferrate(II). A long historical debate occurred about its relationship to a similar substance known as Turnbull’s blue, which was obtained by addition of an iron(II) salt to potassium hexacyanidoferrate(III). The problem was solved by Mössbauer spectroscopy, which revealed that the two compounds are actually identical: very rapid electron-transfer between the iron(II) and the hexacyanidoferrate(III) ions gives rise to the same mixed-valence PB compound with low-spin iron(II) (diamagnetic) in the C_6 environment and high spin iron(III) in the N_6 environment. The so-called ‘soluble forms’ of PB are actually colloidal suspensions of $K_xFe^{III}[Fe^{II}(CN)_6]_z \cdot nH_2O$. The intervalence origin of the bright blue colour of the mixed-valence PB is commented on in Section 3.2.2.2.

In such a context, Prussian blues (PBs) have stimulated an astonishing rebirth of interest in their magnetism and a revival of the chemistry of cyanide inorganic chemistry.

2.7.3.2 Magnetic Prussian blue analogues: the models

To design high- T_C MPBs, we combine in this section our knowledge of short-range interaction between nearest neighbours, governed by overlap and orthogonality (see Section 2.6) and the considerations resulting from eqn. (2.144). Prussian blue presents a ferromagnetic order at a deceiving $T_C = 5.6$ K. The J coupling constant is very small, because the distance between the Fe(III) spin-bearers ($S = 5/2$) across the $[NC-Fe(II)-CN]$ diamagnetic bridge is large (~ 10.4 Å). The ferromagnetic coupling is due to electron delocalization and double exchange (see Section 3.2.2). If we use instead systems where both A and B ions are magnetic, we have to choose the best combinations given by Fig. 2.61b, and also try to increase Z (we limit the discussion to exchange interaction between nearest neighbours) (2.6 Vol. V, 283sq).

The MPBs structure (Fig. 2.76) shows that the number of magnetic neighbours is always $Z_B = 6$ around the B site, and depends on the stoichiometry z for the A site: $Z_A = 6z$ (for example, $Z_A = 6$ for $z = 1$ in $\{C(I)_4A(II)_4B(III)_4\}^0$ a, and $Z_A = 4$ for $z = 2/3$ in $\{A(II)_4B(III)_{8/3}\}^0$ —a frequent case). It follows that the *mean* coordination sphere of A can be formulated as $A(NC)_{6z}(H_2O)_{6(1-z)}$ (that is, $A(NC)_6$ for $z = 1$ and $A(NC)_4(H_2O)_2$, for $z = 2/3$). This is another approximation. In reality, for a given stoichiometry, the A sites present a distribution of coordination spheres $A(NC)_{6-p}(H_2O)_p$ (p integer), as recently demonstrated by (paramagnetic) NMR. Nevertheless, we consider that the

mean number of magnetic neighbours depends on the stoichiometry and therefore on the amount of C^+ cation inserted in the structure. This can be governed by the C^+ concentration in the synthetic solution.

A wide range of results is presented in Table 2.10, and the main conclusions are developed in the following.

(1) When only e_g magnetic orbitals are present on A, all the exchange interactions with the t_{2g} magnetic orbitals present on $[B(CN)_6]$ are expected to be ferromagnetic. Thus, if a Prussian blue is prepared by adding a d^8 or d^9 A(II) cation such as Ni^{2+} or Cu^{2+} to a paramagnetic $[B(CN)_6]$ anion, a ferromagnet should result. (Compounds **10** and **11** in Table 2.10).

(2) When only t_{2g} magnetic orbitals are present on A, all the exchange interactions with the t_{2g} magnetic orbitals present on $[B(CN)_6]$ are expected to be antiferromagnetic. In this case, if the Prussian blue analogue is prepared by adding a d^2 or d^3 cation to a paramagnetic $[B(CN)_6]$ anion, a ferrimagnet should result. (Compounds **1** and **2** in Table 2.10.)

(3) When both t_{2g} and e_g magnetic orbitals are simultaneously present on A, ferromagnetic and antiferromagnetic interactions with the t_{2g} magnetic orbitals on $[B(CN)_6]$ coexist and compete. Here, the overall nature of the interaction is not so simple to predict. Usually, the nm antiferromagnetic interactions dominate and a ferrimagnetic order arises. (Compounds **3–7**, **9**, and **12** in Table 2.10.)

(4) Needless to say, when one of the ions (A or B) is diamagnetic and the partner paramagnetic, the resulting compounds are predicted (and shown experimentally) to be simple paramagnets in most of the accessible temperature range: for example, $[CsZn(II)Cr(III)]$, $[CsA(II)Co(III)]$ with A = Ni, Co, Fe, Mn [2.6, vol. V, 283sq].

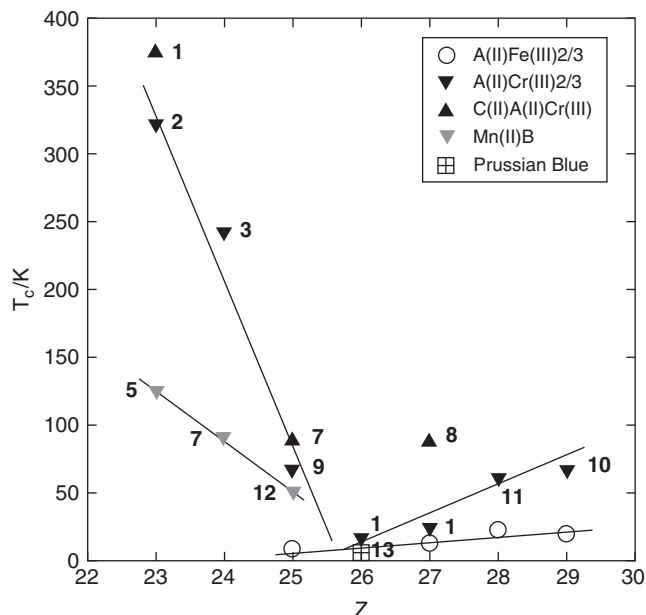
Looking in more detail at the results gathered in Table 2.10 and Fig. 2.77 [2.6, vol. V, 283sq], one can reach additional conclusions.

Table 2.10 Curie temperatures T_C of selected magnetic Prussian blues (decreasing T_C s).

Compound $C_xA_1[B(CN)_6]_z \cdot nH_2O$ ^(a)	Electronic structure	Ordering nature	T_C/K	N^o ^(b)
$K_1V^{II}_1[Cr^{III}(CN)_6]_1$	d^3-d^3	Ferri	376	1
$V_1[Cr^{III}(CN)_6]_{0.86} \cdot 2.8 H_2O$	d^3-d^3	Ferri	315	2
$Cr^{II}_1[Cr^{III}(CN)_6]_{2/3} \cdot 10/3 H_2O$	d^4-d^3	Ferri	240	3
$Cs_{2/3}Cr^{II}_1[Cr(CN)_6]_{8/9} \cdot 40/9 H_2O$	d^4-d^3	Ferri	190	4
$Cs_2Mn^{II}_1[V^{II}(CN)_6]_1$	d^5-d^3	Ferri	125	5
$(V^{IV}O)_1[Cr^{III}(CN)_6]_{2/3} \cdot 4.5 H_2O$	d^1-d^3	Ferri	115	6
$Cs_1Mn^{II}_1[Cr^{III}(CN)_6]_1$	d^5-d^3	Ferri	90	7
$Cs_1Ni^{II}_1[Cr^{III}(CN)_6]_1 \cdot 2-4 H_2O$	d^8-d^3	Ferro	90	8
$Mn^{II}_1[Cr^{III}(CN)_6]_{2/3} \cdot 5-6 H_2O$	d^5-d^3	Ferri	66	9
$Cu^{II}_1[Cr^{III}(CN)_6]_{2/3} \cdot 5-6 H_2O$	d^9-d^3	Ferro	66	10
$Ni^{II}_1[Cr^{III}(CN)_6]_{2/3} \cdot 4 H_2O$	d^8-d^3	Ferro	53	11
$Mn^{II}_1[Mn^{IV}(CN)_6]_1$	d^5-d^3	Ferri	49	12
$Fe^{III}_1[Fe^{II}(CN)_6]_{3/4} \cdot 3.7H_2O$	$d^5-d^6(LS)$	Ferro	5.6	13

^(a) The formulae given in the Table are adapted from the literature to be related to one A cation: $A_1[B(CN)_6]_z \cdot n H_2O$. We do not display explicitly the vacancies $A_1[B^{III}(CN)_6]_z \square_{1-z} \cdot n H_2O$.

^(b) References are given in [2.6, vol. V, 283sq]. First reports by Lüdi (13), Babel (7), Gadet (8–11), Mallah (3,4), Ferlay (2,6), and Girolami (1,5).

**Fig. 2.77**

Curie temperatures as a function of the atomic number Z in a few selected series of magnetic Prussian blues. $AB_{2/3}$ stoichiometry: B is kept constant and the Z of A is varied (\circ , B=Fe; \blacktriangledown , B=Cr). AB stoichiometry (\blacktriangle , B=Cr; A varies). AB stoichiometry, A is kept constant, the Z of B is changed (\blacktriangledown). Lines are guides for the eye.

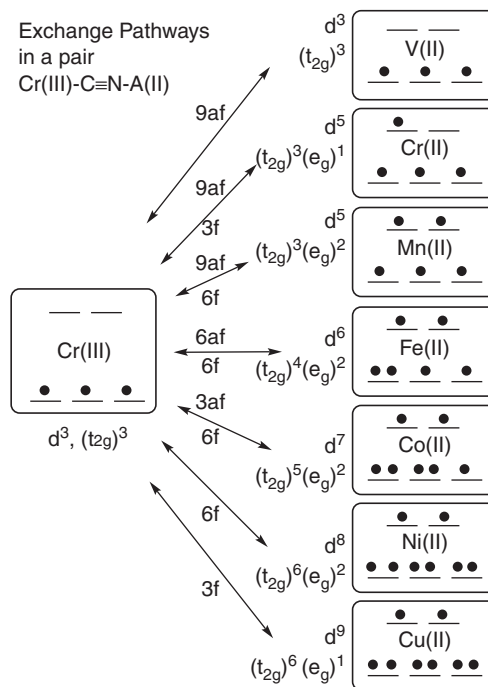
(5) If we compare, in Fig. 2.77, the T_C s of MPBs obtained in the $AB_{2/3}$ stoichiometry with B = Fe(III) (t_{2g})⁵, one unpaired electron (\circ) and B = Cr(III), (t_{2g})³, three unpaired electrons (\blacktriangledown), with the same metal A, the T_C s are clearly higher with Cr(III), since the three t_{2g} electrons are available for exchange in the x, y, and z direction (three j_{AB} pathways instead of one, J_{AB} is increased). Hence the interest in working with Cr(III) for higher T_C s.

(6) If we examine the influence of the stoichiometry for identical A–B pairs (compounds 1–2, 7–9, 8–11), the T_C s are higher in the A_1B_1 stoichiometry. This is fairly well understood using the $kT_C \propto Z |J|$ relation. A_1B_1 systems have six magnetic neighbours, while $A_1B_{2/3}$ have only four. The ratio of the T_C s should be 4/6. This is rather accurately satisfied for Mn_1Cr_1 (7, \blacktriangle , $T_C = 90$ K), $Mn_1Cr_{2/3}$ (9, \blacktriangledown , $T_C = 60$ K), Ni_1Cr_1 (8, \blacktriangle , $T_C = 90$ K), and $Ni_1Cr_{2/3}$ (11, \blacktriangledown , $T_C = 53$ K). Hence, for higher T_C s, the usefulness of working with an A_1B_1 stoichiometry.

2.7.3.3 High T_C magnetic Prussian blues

Taking into account the previous observations, to achieve really high T_C temperatures the best choice is to associate the $[Cr(III)(CN)_6]^{3-}$ with an A(II) partner. The electronic configurations and orbital pathways are gathered in Fig. 2.78, and the critical temperatures are presented in Table 2.11. A simple mixture of the precursors in aqueous solution leads to a $CrA_{2/3}$ stoichiometry.

The simplest idea would be to choose systems presenting only ferromagnetic interactions, with A = Cu (3f)(10) and Ni (6f)(11) (Fig. 2.78). The compounds are indeed ferromagnets, but with modest T_C (Table 2.11) and J . Actually, it is better to choose systems with *antiferromagnetic interactions*. This is at first sight surprising, since both Cr(III) and V(II) have a spin $S = 3/2$, but recall that the actual stoichiometry is $CrV_{2/3}$, and thus a *ferrimagnetic*

**Fig. 2.78**

Exchange pathways in a fragment Cr(III)-C≡N-A(II) of a magnetic Prussian blue. A is a metal of the first transition series. Left: electronic configuration and orbitals' occupancy of Cr(III). Right, electronic configuration and orbitals' occupancy of A(II), from Cu(II) to V(II). Centre, along the arrows, the nature of the exchange pathways (f ferromagnetic, af antiferromagnetic) and their numbers.

order $[(\uparrow)_1 (\downarrow)_{2/3}]$ results. In this logic one has to select the strongest antiferromagnetic couplings, thus choosing V(II), because it gives nine af pathways and no f pathways (Fig 2.78, top). Table 2.11 summarizes the situation. A Curie temperature above room temperature (315 K) is reached for compound **2**, due to a simple reasoning based on our heuristic rules [2.59].

The vanadium-hexacyanidochromate association can even lead to a higher T_C by simply applying eqn. (2.144) and enhancing the number of magnetic neighbours Z from 4 to 6, in inserting a caesium cation in the tetrahedral sites of the PB structure, $Cs_1V_1Cr_1$ compound **1**, which present the record temperature of 376 K, above the boiling point of water. Note that in this case the stoichiometry is V_1Cr_1 (which should lead to zero magnetization), but the ferrimagnetic behaviour is due to some V(III) impurity, some stoichiometry's deviation, and possibly a small difference between the g values of the metals.

Table 2.11 Experimental electronic structures, exchange interactions, long-range orders and Curie temperatures as a function of A in $A(II)_4[Cr(III)(CN)_6]_{8/3} \cdot xH_2O$.

A ^{II} ion	V, d^3	Cr, d^4	Mn, d^5	Fe, d^6	Co, d^7	Ni, d^8	Cu, d^9
Conf. $(t_{2g})^x(e_g)^{n-x}$	$(t_{2g})^3$	$(t_{2g})^3(e_g)^1$	$(t_{2g})^3(e_g)^2$	$(t_{2g})^4(e_g)^2$	$(t_{2g})^5(e_g)^2$	$(t_{2g})^6(e_g)^2$	$(t_{2g})^6(e_g)^1$
Interaction ^a	af	af	af	f^b	f^b	f	f
T_C / K	315	240	66	16	23	60	66

^a af = antiferromagnetic interaction and ferrimagnetic order, f = ferromagnetic interaction and order;

^b in disagreement with the too-simple heuristic model. See [2.6, vol. V, 283sq] for a deeper interpretation.

Is it possible to go still higher? Simple reasoning and DFT calculations show that with other selected pairs such as Mo(III)–V(II) (the Mo orbitals more diffuse than the Cr ones), one can expect higher J and T_C . Up to now, such attempts have been unsuccessful. The expected MPB material is not forming.

In this section we have tried to transform a set of molecules in a three-dimensionally ordered (classical) magnet by *optimizing the exchange interaction* between the spin bearers in the solid. On a completely different background we show in the next section how to transform one ion, one molecule, and one chain in a magnet, *without interaction* between the entities, by focusing on the *magnetic anisotropy* of the system.

2.8 Magnetic anisotropy and slow relaxation of the magnetization

In this section we introduce a new kind of magnetic object: the so-called *single-molecule magnet (SMM)*, *single-chain magnet (SCM)*, or *single-ion magnet (SIM)*. Such new compounds were discovered from 1993, and from that time the domain exhibits a quick development. The three kinds of molecules/systems present a common feature: a slow relaxation of the magnetization, without significant interaction between neighbouring species. This raises the hope of one day being able to store information on the ultimate, molecular, size. We present the basic features of the molecular anisotropy at the origin of the phenomenon.

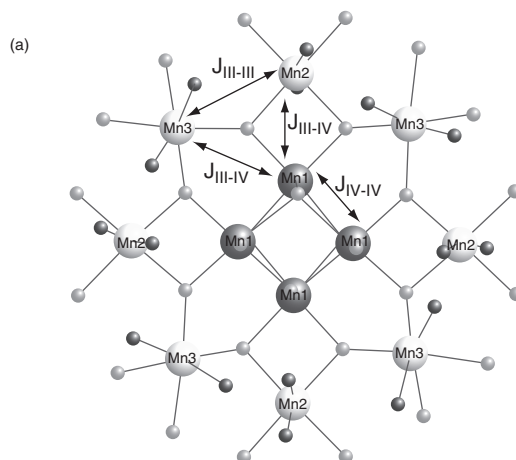
Several books and reviews are available [2.4, 2.60–2.63].

2.8.1 Single-molecule magnets (SMM)

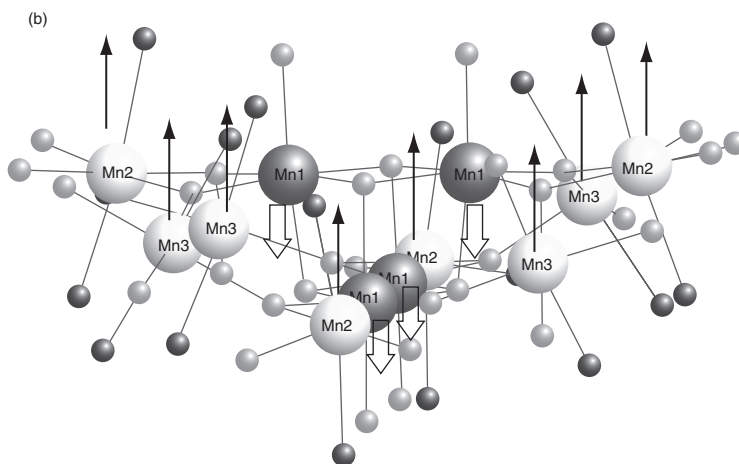
2.8.1.1 Discovery and main features: Mn_{12} [2.4, 2.62–2.64]

The story of single-molecule magnets began in 1993 with the study by Gatteschi *et al.* of an $\{\text{Mn}_{12}\}$ cluster [2.4, 2.64]. Actually, $\{\text{Mn}_{12}\}$ is a generic name for a family of compounds with the general formula $[\text{Mn}_{12}\text{O}_{12}(\text{O}_2\text{CR})_{16}(\text{H}_2\text{O})_4]$, where O_2CR is a carboxylate anion [2.62]. The compound is a mixed valence system with formal valence states $\text{Mn}^{\text{IV}}_4\text{Mn}^{\text{III}}_8$. (Such compounds are studied in detail in Section 3.2.2). The structure is organized around a central $\text{Mn}^{\text{IV}}\text{O}_4$ cubane core, around which are found the 8 Mn^{III} , additional O^{2-} bridges, and the sixteen carboxylate ligands (Fig. 2.79). The overall structure exhibits S_4 symmetry. Crystallographically, Mn^{IV} is denoted as Mn1, while the Mn^{III} ions are of two types with pseudo-octahedral environments: Mn2 surrounded by two oxo ligands and four oxygen atoms of carboxylate molecules, and Mn3 surrounded by two oxo ligands, three oxygen atoms of carboxylate ligands, and a water molecule.

In this structure, Mn^{IV} , d^3 has $S = 3/2$, while Mn^{III} , high-spin d^4 has $S = 2$. The latter is subject to a strong Jahn–Teller effect (see Section 1.3.7), because the e_g set contains only one electron. As for Cu^{II} , it is manifested most often as an elongation of the octahedron. This introduces a strong anisotropy in the magnetic properties through spin–orbit coupling. Importantly, the elongation axes make angles of 11° for Mn2 and 37° for Mn3 with the $S_4(z)$ axis

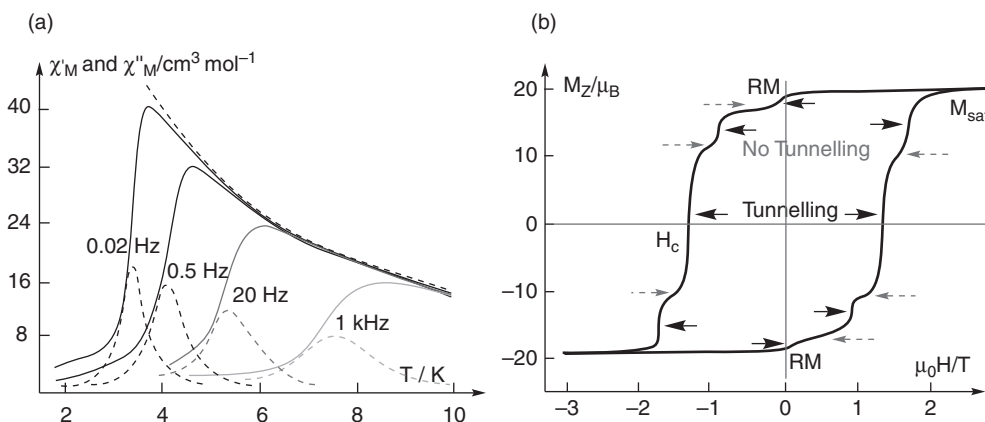
**Fig. 2.79**

Structure of the $\{Mn_{12}\}$ core, down (a) and roughly perpendicular (b) to the $S_4(z)$ axis. For clarity, the peripheral carboxylates are not shown. Large white spheres are Mn^{III} ions (Mn_2 and Mn_3). Large grey spheres are Mn^{IV} ions (Mn_1). The small grey spheres are oxygen atoms. The darkest ones underline the Mn^{III} Jahn–Teller axes (see text). In (a), the double-headed arrows indicate the exchange interactions between the different kinds of manganese ions. In (b), the spins $S = 2$ borne by Mn^{III} are schematized by long black arrows (up). The $S = 3/2$ of Mn^{IV} are shown by small open arrows (down).



(Fig. 2.79b), so that their general direction is close to the z axis, which is, by symmetry, a privileged axis for the overall anisotropy.

Regarding static magnetic properties, the different spin centres are coupled through oxygen and carboxylate bridges. Without entering into details (a complete analysis is presented in [2.65]), the four central Mn^{IV} are weakly ferromagnetically coupled ($J_{IV-IV} \approx +8K$) due to the $M-O-M$ angles near 90° (orthogonality; Section 2.6.3.1). The strongest interactions are antiferromagnetic between the central Mn^{IV} and the peripheral Mn^{III} ($J_{III-IV} \approx -120K$) (overlap between magnetic orbitals). Thus, although the interaction between Mn^{III} is antiferromagnetic ($J_{III-III} \approx -23K$), the spin structure consists of eight $S = 2$ ions with spin ‘up’, and four $S = 3/2$ ions with spin ‘down’; that is, a ferrimagnetic situation with $S = 16 - 6 = 10$ (Fig. 2.79b), as observed. The calculations [2.65] also give a first $S = 9$ excited state at 35 K above the ground state.

**Fig. 2.80**

Experimental magnetic properties of $\{\text{Mn}_{12}\}$. (a) AC susceptibility measurements at various frequencies as a function of temperature. The dotted line is the Curie law for the ground state $S = 10$ spin. The plain curves are the χ' susceptibilities. The dotted grey curves are the χ'' susceptibilities. (b) Hysteresis loop at 2.1 K of a single crystal with a magnetic field applied along the z anisotropic axis. M_{sat} is the magnetization at saturation, RM the remnant magnetization, H_c the coercive field. The black plain horizontal arrows point out the vertical steps due to quantum magnetic tunnelling, whereas the grey dotted arrows show the magnetization's plateaux when tunnelling is not allowed. (Adapted from Sessoli [2.61].)

Standard (static) magnetic susceptibility measurements show the signature of ferrimagnetic spin structure (not shown) [2.61]. Furthermore, magnetization measurements present the two peculiar phenomena illustrated in Fig. 2.80: (a) the appearance of a maximum in the AC susceptibility curves, announcing exciting dynamic properties; and (b) a remarkably wide hysteresis loop, reminiscent of a classical magnet accompanied by an unusual succession of plateaux and steps within the loop. The next two sections are devoted to simple explanations of these properties.

2.8.1.2 Anisotropy barrier and magnetization dynamics

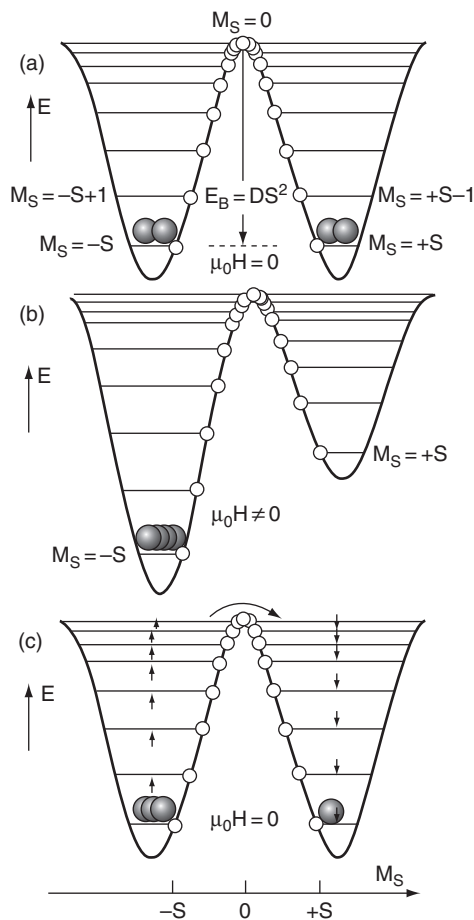
A technique of choice for studying the dynamics of magnetization is AC susceptibility (Section 2.3.3). When the magnetization instantaneously follows the oscillating field, χ' behaves as the static susceptibility, and χ'' is zero. A Curie law is observed (Fig. 2.80a, upper dotted line). When the field oscillates too quickly the magnetization follows with a delay, and the χ' signal departs from the Curie behaviour, presents a maximum, and tends to zero when T decreases. The most useful is the χ'' signal, because it presents a maximum when the relaxation rate k equals the AC pulsation ω and allows the determination of the anisotropy barrier through a study as a function of temperature. The results for the $\{\text{Mn}_{12}\}$ system are shown in Fig. 2.80a [2.62].

The non-instantaneous establishment of equilibrium magnetization is an indication of the presence of an energy barrier, due to zero-field splitting of the ground state and a negative D , as seen in Fig. 2.81. The Hamiltonian corresponding to a uniaxial anisotropy with an applied field H_z (Section 2.5) is:

$$\mathbf{H}_0 = D [S_z^2 - S(S+1)/3] + g\mu_B H_z S_z. \quad (2.146)$$

Fig. 2.81

Double-well energy representation of a spin state S having an easy axis magnetic anisotropy. Here, as in Fig. 2.35, the abscissa axis corresponds to M_S , varying only from $-S$ to $+S$ and the physically significant points are shown by white spheres. The superimposed double-well curve represents the classical potential energy as a function of the angle between the magnetic field and the easy axis. A grey ball represents a set of molecules in a given M_S state. $M_S < 0$ are in the left well. $M_S > 0$ are in the right well. (a) After cooling down in zero field: equal population in the two wells; (b) cooling down in an applied magnetic field populates the left well (Zeeman effect, up to magnetizations' saturation, M_{sat}); (c) returning to zero field at low temperature, the system is either trapped in the well (remnant magnetization RM close to the saturation value, M_{sat}) if $kT \ll E_B$ or, if kT is high enough, it tends to equilibrium through a series of thermally activated steps (small vertical arrows—Orbach process) and a slow relaxation of the magnetization. (Adapted from Sessoli [2.61].)



For $\{\text{Mn}_{12}\}$, $S = 10$, the energy of the spin levels ($-S \leq M_S \leq +S$) are $E(M_S) = D[M_S^2 - 110/3] + g\mu_B M_S H_z$ (Fig. 2.81):

In $\{\text{Mn}_{12}\}$ the two lowest energy states are $M_S = -10$ and $M_S = +10$, while the $M_S = 0$ state is the highest level (Fig 2.81a). Since S is an integer (Section 2.5) there is an energy barrier E_B , given by $E_B = |D|S^2$. With $D = -0.46 \text{ cm}^{-1}$ and $S = 10$, it amounts to 46 cm^{-1} (or 66 K in temperature units, by using the ratio E_B / k_B).

The relaxation rate of magnetization (or magnetization reversal rate) can be measured as a function of temperature from AC susceptibility data, and follows generally an Arrhenius law:

$$k = k_0 \exp(-E_B/k_B T) \quad (2.147)$$

with, in the case of Mn_{12} $k_0 = 4.8 \cdot 10^6 \text{ s}^{-1}$ and $E_B / k_B = 62 \text{ K}$ in the $2\text{--}10 \text{ K}$ temperature range. k_B is the Boltzmann constant. This value is very close to the barrier height expressed in K units, showing that in this temperature range the process is essentially thermally activated. In other words, one has to climb to the top of the barrier to perform the magnetization reversal. The slight

difference between the two values indicates that some other minor processes (tunnelling) are operating (see Fig 2.83a, process 2). For practical applications such a k_0 rate is too high (or the corresponding characteristic relaxation time τ_0 ($= 1/k_0$) is too small). At the common cryogenic temperature of 4.2 K (liquid He), the rate is still about 0.9 s^{-1} , thus a bit of information is kept for no longer than $\tau = 1 \text{ s}$. This is why huge efforts were and are made to find systems with higher barriers (see Section 2.8.1.4).

2.8.1.3 Remnant magnetization, hysteresis, and quantum tunnelling

When the temperature is low enough, the magnetization reversal rate can drop to very low values; for example, 10^{-7} s^{-1} at 2 K, corresponding to a characteristic time $\tau = 1/k$ of the order of *months*. Then, in our time-scale, the system is frozen and can be considered as a memory element (Fig. 2.81c). Experimentally it exhibits an hysteresis cycle when the magnetic field is swept in both directions, with a remnant magnetization RM (Fig. 2.80b), because the thermodynamic equilibrium is not established. Since the response involves the relaxation rate, the width of the hysteresis (characterized by the coercive field) increases when decreasing the temperature or when increasing the sweep rate (Fig. 2.82). At some temperature (depending upon the sweep rate), the hysteresis disappears (at 3.7 K in Fig. 2.82), because equilibrium is attained in the time-scale of the experiment.

Thus, the main characteristics of a classical magnet are obtained (remnant magnetization, coercive field). But contrary to other applications of magnetic molecules, SMM do not need to be associated in large number to constitute a material; they *are* the material. At variance with macroscopic magnets, the magnetization reversal does not rely on the motion of domain walls, but is a truly monomolecular process. But, while the motion of domain walls in a classical magnet can be immeasurably slow, for SMM it is extremely difficult to achieve $kT \ll E_B$ and to bring the magnetization reversal rate to or near zero.

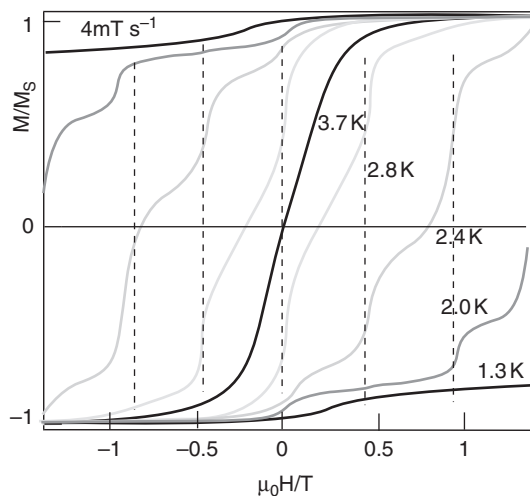


Fig. 2.82

Hysteresis curves of a $\{\text{Mn}_{12}\}$ single crystal with an applied magnetic field H_z , at a fixed sweep rate (4 mT s^{-1}) at different temperatures. (Adapted from Christou [2.62].)

The second obvious characteristic of the hysteresis curve (Figs. 2.80b and 2.82) is that it displays *steps*. These features are completely different from those observed in usual magnets whose origin is the reversal of magnetic domains. Here the steps occur when M'_S levels of the $S = 10$ manifold on one side of the double-well diagram are degenerate with M_S levels of the other side (Fig. 2.83c). When this happens, quantum tunnelling can occur, increasing the rate of magnetic relaxation, and a vertical step results on the hysteresis curve. The successive coincidences of energy levels of the right and left wells occur for $H = nD/g\mu_B$ (n integer = 0, 1, 2 . . . , as can be easily computed from the uniaxial \mathbf{H}_0 Hamiltonian, eqn. (2.146), giving the energy levels in presence of a magnetic field) (dotted lines in Fig. 2.82). The step height and the width of the overall hysteresis depend on the magnetic field sweep rate, allowing a detailed explanation taking into account the dynamics of the tunnel effect.

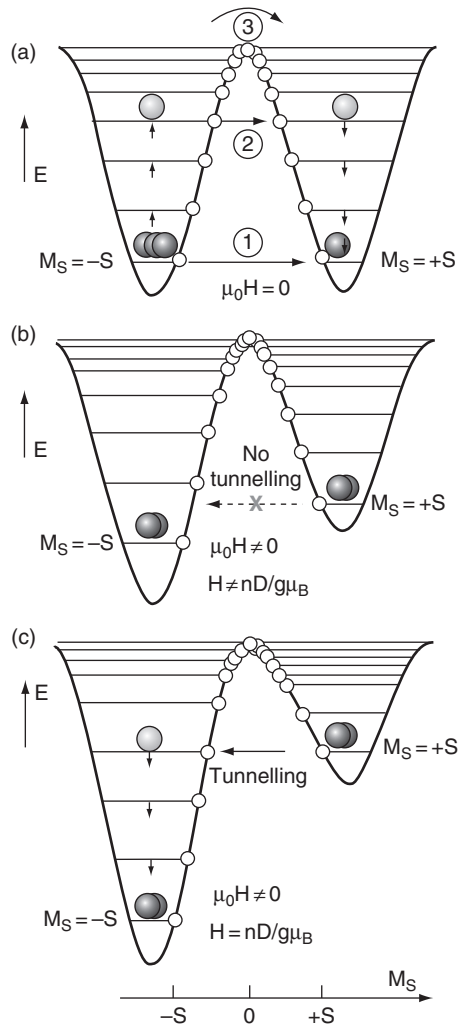
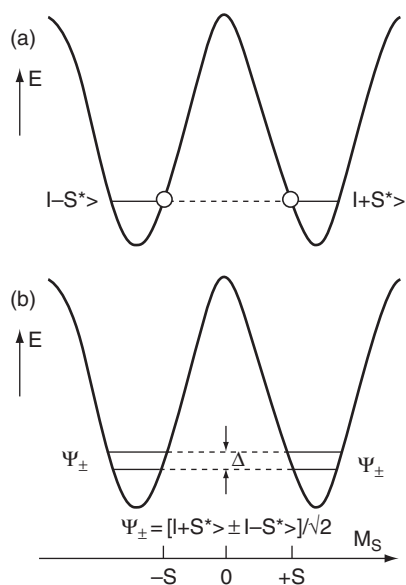


Fig. 2.83

Different magnetic relaxation processes. Same representation as in Fig. 2.81. (a) In zero magnetic field: 1, quantum tunnelling in the ground state; 2, quantum tunnelling between thermally excited states (grey balls); 3, relaxation through thermal activation. In a non-zero magnetic field, (b) without coincidence between the levels, no tunnelling (dotted arrow, magnetization plateau), (c) with energy coincidence between one level from the right manifold ($M_S = +S$) and one level of the left manifold ($M_S = -S + 3$), quantum tunnelling (horizontal plain arrow, step). (Adapted from [2.61].)

**Fig. 2.84**

Tunnel splitting in a double-well system. Same representation as in Fig. 2.81. (a) Non-interacting, perfectly localized energy states $|+S^*\rangle$ and $-S^*\rangle$; (b) interacting states Ψ_{\pm} , delocalized on the two wells, with tunnel splitting Δ . The splitting width Δ is exaggerated for clarity.

Quantum tunnelling can occur also in absence of a magnetic field, as shown in Figs. 2.83a and 2.84, which deserve a few comments. Assume that two levels are degenerate, but that the system has been prepared in one of the *localized* states; for example, $M'_S = +S$, denoted $|+S^*\rangle$ (right well). The corresponding state in the left well is $M_S = -S$, denoted $| -S^* \rangle$. This localized state $|+S^*\rangle$ is not stationary, and quantum oscillation begins to develop between states $|+S^*\rangle$ and $| -S^* \rangle$, with a frequency determined by the tunnel splitting Δ , as seen in Section 1.6 (Fig. 2.84).

The wavefunction $\Psi(t)$ is then given by:

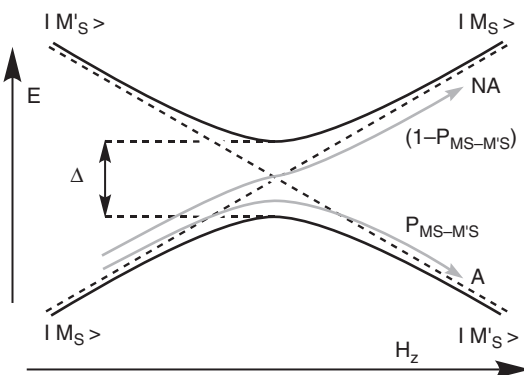
$$|\Psi(t)\rangle = |+S^*\rangle \cos(2\pi\nu t) + | -S^* \rangle \sin(2\pi\nu t) \quad (2.148)$$

with $\nu = \Delta / h$ (eqn. 1.91). In the absence of relaxation the oscillation should last indefinitely. The system would then be named *coherent*. In practice, however, this is not the case, because there is an exchange of energy with the environment. The main couplings to the surrounding ‘bath’ are (i) dipolar interactions with the spins of the different molecules (such interactions change when one of the surrounding molecules is switching its spin); (ii) the interaction of the electronic spin with the nuclear spins of the atoms of the molecule, when they exist. Of course, when the magnetic field is swept the degeneracy is rapidly lost and the system evolves towards the lowest localized energy state (Fig. 2.85).

The overall behaviour thus depends on the comparison of two time-scales: (i) the time during which the energy levels are almost in coincidence; and (ii) the period of quantum oscillations. If the sweep rate is fast, quantum oscillations do not have enough time to establish, and thus the system remains in the initial electronic state. If the sweep rate is small, quantum oscillations develop, so that the system explores permanently the two electronic states, and finally

Fig. 2.85

Energy of a pair of levels M_S and M'_S as a function of a magnetic field applied along z . The two levels are coupled by an interaction giving an avoided crossing in the centre with energy levels separated by the tunnel splitting Δ . The possible trajectories are denoted A (adiabatic) or NA (non-adiabatic). (Adapted from Sessoli [2.61]). See also Fig. 3.12.



evolves towards the most stable. These scenarios are depicted in Fig. 2.85. They are called, respectively, non-adiabatic and adiabatic processes.

Mathematically, the tunnelling probability P_{M_S, M'_S} to evolve from state $|M_S\rangle$ to $|M'_S\rangle$ can be computed [2.15], [2.61] in the frame of the Landau–Zener–Stückelberg model [2.66], and is given by:

$$P_{M_S-M'_S} = 1 - \exp\left(-\frac{\pi\Delta^2}{2\hbar g\mu_B |M_S - M'_S| (dH/dt)}\right) \quad (2.149)$$

where Δ is the tunnel splitting and dH/dt the sweep rate. One reaches the same conclusion as in the qualitative previous argument: for large dH/dt or small Δ (slow oscillations), $P \rightarrow 0$ (non-adiabatic process), and in the opposite situation, $P \rightarrow 1$ (adiabatic process). We shall encounter similar schemes and equations in the case of electron transfer in Section 3.2.1.2. An important property of the tunnel splittings Δ is that they are very small at the bottom of the wells (M_S large) and increase near the top of the barrier (M_S weak). Tunnel process 2 in Fig. 2.83a is expected to be more efficient than process 1, even if the thermal process 3 is predominant.

We now understand why the sweep rate can influence the hysteresis width in the pure tunnelling regime (no thermal activation). For fast sweep rates the equilibrium cannot be established at the first coincidence of M_S and M'_S levels, and the evolution is delayed until the next coincidence, generally more efficient because Δ and P are higher. This increases the hysteresis.

Returning to the situation in the absence of field (or weak AC field like in relaxation experiments), one can remark that at zero K there should be a residual magnetization reversal rate through tunnelling between the lowest $M_S = \pm S$ levels (Figs. 2.83 and 2.84), while the Arrhenius equation (2.147) would predict a zero rate. Thus the Arrhenius equation should break down at low temperatures, and the relaxation should become temperature-independent. Practically, this is not observed in $\{\text{Mn}_{12}\}$, because the tunnel splitting between $\pm S$ is much too small (it is estimated to be about 10^{-10} cm^{-1}). This derives from the fact that when a system obeys the Hamiltonian \mathbf{H}_0 , eqn. (2.146), the two localized levels $|+10^*\rangle$ and $|-10^*\rangle$ are orthogonal to each other. Thus the temperature-independent rate cannot be experimentally measured.

There is, however, a system for which the quantum tunnelling is observed *in the ground state*: $[\text{Fe}_8\text{O}_2(\text{OH})_{12}(\text{tacn})_6\text{Br}_8(\text{H}_2\text{O})_8]$ (tacn:1,4,7-triazacyclononane), abbreviated as $\{\text{Fe}_8\}$ [2.4, 2.61]. At variance with $\{\text{Mn}_{12}\}$, it presents a rhombic component described by the following perturbation Hamiltonian \mathbf{H}_1 (written with the corresponding Zeeman terms):

$$\mathbf{H}_1 = E \left[\mathbf{S}_x^2 - \mathbf{S}_y^2 \right] + g\mu_B H_x \mathbf{S}_x + g\mu_B H_y \mathbf{S}_y \quad (2.150)$$

with $0 \leq E/D \leq 1/3$. Such a Hamiltonian directly couples the M_S with $M_S \pm 2$ components ($M_S = 10$ with $M_S = 8$, $M_S = -10$ with $M_S = -8$, and so on, and finally $M_S = 10$ with $M_S = -10$ at the tenth order). The $\{\text{Fe}_8\}$ complex provides a wealth of information about the mechanisms of the tunnel effect in SMM (influence of dipolar interactions, hyperfine interactions, and so on) [2.4, 2.61]. The tunnel effect in the ground state will be encountered also in the case of electron transfer (Section 3.2.1.2).

2.8.1.4 How can the anisotropy barrier be increased?

To increase the barrier, DS^2 , there are several approaches: increase S , increase D , or both. The most appealing approach appeared first to increase S , since the barrier height should scale as S^2 . This explains the search for high-spin molecules (Section 2.6.5.3), and what we have learned about exchange interaction can be fully used here to produce ferromagnetic or ferrimagnetic states. The search for 1D compounds (Section 2.8.2) follows the same line of reasoning (increase S). As for D , an anisotropic molecular structure is a prerequisite. Eqns. (2.109) and (2.113) can be used. Ignoring the smaller exchange anisotropy terms $d_{ij} D_{ij}$ we find that D of the complex is the sum of the local anisotropy tensor terms D_i , weighted by d_i coefficients. Choosing transition-metal ions possessing large local D_i parameters [Cr(II), Mn(III), Co(II), lanthanides . . .] is a logical approach, but the difficulty is to assemble them so that the effects reinforce and do not cancel. Indeed, the d_i coefficients can take positive, negative, or zero values, depending on the topology of the complex, and it is therefore difficult to anticipate the D value. Furthermore, experiments and theory show that, everything being equal, D is not independent of S and can even scale as S^{-2} (see eqns. (2.109) and (2.113)). Thus, D should decrease with S , so that the $|D|S^2$ product could be, in fact, independent of S [2.67–2.68]. Hence the new endeavours to explore new systems, either 1D with SCMs, or mononuclear complexes (SIM) by optimizing the local anisotropy (choice of the ion and tuning of the structure) [2.69].

2.8.2 Single-chain magnets (SCM)

To reach a high spin, the single-molecule magnet approach uses several magnetic centres associated in a cluster. A related approach is to use a single-chain magnet. It can be expected that the large number of magnetic centres correlated within the chain will give a high-spin ground state S , and that, the structural anisotropy of the chain associated with Ising type magnetic anisotropy of the spins (that is, with spins S_i able to take only up and down orientation, ± 1 along z , for example), higher anisotropy barriers can be achieved. The domain was launched by Sessoli *et al.* in 2001 [2.70], soon followed by Miyashita and

Cl rac (who coined the SCM acronym), and Julve *et al.* Hundreds of SCM are now available [2.4, 2.60, 2.71].

Single-chain magnets (SCM) are 1D objects magnetically isolated from each other, presenting a slow relaxation of the magnetization. As shown in Section 2.7.1.3, they cannot present a long-range magnetic order, but they can exhibit a *short-range order*; that is, the occurrence of domains where the N spins are oriented in the same direction (Fig. 2.86a), interrupted by a reversed spin or by chain defects (\bullet). A finite magnetization can thus be frozen at low temperature in the absence of an applied magnetic field. The analysis of the slow relaxation of the magnetization, of the thermal activated behaviour, and of the quantum tunnel effect in SCM, relies on the anisotropic Ising model elaborated by R. J. Glauber [2.72] (recipient of the Nobel Prize in Physics, 2005). The main concept of Glauber's dynamics is the probability for a spin to flip within the chain, taking into account only the nearest-neighbours interactions, with an Hamiltonian of the kind $\mathbf{H} = -J \sum_{i=1}^{N-1} \mathbf{S}_i \mathbf{S}_{i+1}$. The essential features are shown in Fig. 2.86 in the case of a ferromagnetic coupling ($J > 0$). Starting with a system prepared in a saturated ferromagnetic configuration (by cooling in an applied magnetic field for example (Fig. 2.86a)), the complete reversal of the magnetization consists of several successive events. The first is the reversal of one spin in position i , S_i , which breaks two interactions with its two neighbours, at an energy cost of $4J$. Indeed, reversing the local magnetization necessitates struggle against J , a key parameter in this model, which tends to keep a spin in a given direction under the influence of exchange with its neighbours. The other steps, to flip the $S_{i\pm 1}$ spins, do not need further energy, since their neighbouring spins are now up and down (negative and positive interactions). The activation energy is then $\Delta = 4J$ (and $\Delta = 4JS^2$ when $S \neq 1$). The relaxation time is $\tau = \tau_0 \exp(4JS^2/kT)$, where τ_0 is the value for an isolated spin. Figure 2.86c displays the special case of a spin flip beginning at an end of chain, where the barrier is only $\Delta = 2J$ (or $2J S^2$). Finally, Figs. 2.86e–f show the probability of the reversal of S_i , $\omega_{S_i \rightarrow -S_i}$, as a function of: (i) α , the probability of reversal of an isolated spin, and (ii) $\gamma (= \tanh(2J/kT))$, a factor depending on the energy J the nearest neighbours interaction, in the three cases when the two neighbouring spins are both parallel to spin S_i (d), both antiparallel to spin S_i (f), and one parallel and the other antiparallel (e). The final result is an anisotropy barrier $4JS^2$, which can be much higher than in SMMs. Many other aspects of SCM dynamics are discussed in [2.4, 2.60 and 2.71].

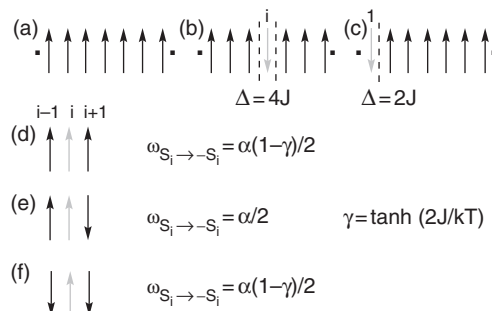


Fig. 2.86

Ising model of a single-chain magnet. (a) Finite segment of oriented spins. Activation energy to reverse a spin at site i within the chain (b) or at one end of chain ($i = 1$ or N) (c). (d–f) Probability ω to flip a spin (light grey) in the three possible configurations of the neighbouring spins. (Adapted from [2.4], section 15.2.)

2.8.3 Single-ion magnets (SIM)

In this approach we return to mononuclear complexes, but with several favourable factors due to *the use of rare-earth (RE) elements*. First, RE involve f orbitals—orbitals with a large angular momentum ($l = 3$) and many electrons, thus a high S . Second, the spin–orbit coupling is large (Z between 57 and 71; see third row of transition metals). When this is combined to the anisotropy of the ligand field, it can produce large negative D values.

The prototype is provided by sandwich complexes (also called ‘double-decker’) such as $[\text{Tb(III)Pc}_2]^{-0}$, (Pc = dianion of phthalocyanine) represented in Fig. 2.87. In the anionic form one has Tb(III), f^8 , and two Pc^{2-} ligands, while the neutral form contains also Tb(III), but one of the two ligands is formally oxidized by one electron, and the complex can be written $[\text{Tb(III)(Pc}^{2-})(\text{Pc}^{\bullet})]$. The RE metal environment is a square antiprism, conferring D_{4d} symmetry to the complex.

In the case of Tb(III), for the free ion, the eight electrons occupy seven degenerate f orbitals. The resulting ground term is characterized by $L = 3$ and $S = 3$, thus 7F . After the intervention of spin–orbit coupling the ground state has $J = 6$, and is written 7F_6 , in agreement with the rule for more than half-filled shells (Section 2.4.1.1) [2.73]. With rare earths and at variance with the case of transition metals, the ligand field is very weak and must be introduced *after* spin–orbit coupling. The action of the ligand field requires specific mathematical tools and is not detailed here, but can be found in [2.74, 2.75]. It lifts partially the $2J + 1$ degeneracy of the free-ion ground state (term), and the lowest substates have $J_z = \pm 6$, consistent with a negative D parameter.

This can be justified by a simple argument. Due to the strong spin–orbit coupling, the \vec{L} and S vectors are ‘locked’ in parallel position, while the ligand field acts only on \vec{L} by lifting the degeneracy between f orbitals. When filling the f^8 configuration, one puts first 1 electron in each orbital (thus at this stage all angular momenta cancel), but the eighth electron, responsible for the final L , enters the lowest energy orbital(s). With the environment of Fig. 2.87, these orbitals are $x(x^2 - 3y^2)$ and $y(3x^2 - y^2)$, because they lie in the xy plane [2.75], and since they are associated to $m_l = \pm 3$, there is a tendency for \vec{L} , and thus J , to align with z .

Finally, $[\text{TbPc}_2]^-$ presents attractive features for a single-ion magnet. Starting from the ground levels ($J_z = \pm 6$), the first pair of excited levels ($J_z = \pm 5$) lies more than 400 cm^{-1} above (Fig. 2.88). Without the tunnelling effect one should climb really high in energy to achieve a magnetization reversal. Even if the barrier is lower than what can be expected, as a matter of fact, the

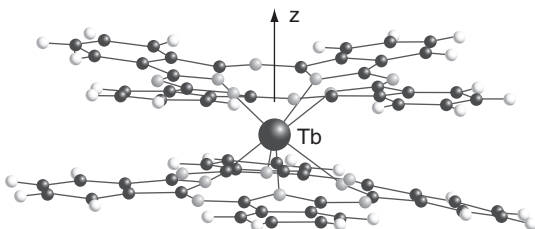
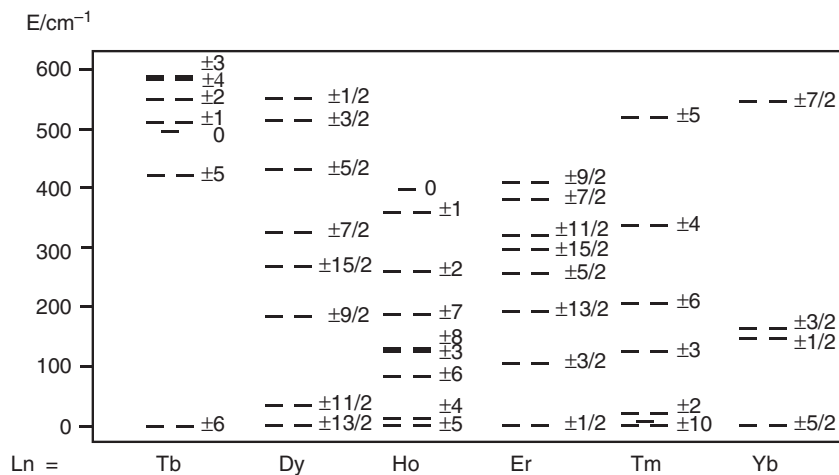


Fig. 2.87

Structure of a $[\text{TbPc}_2]^-$ sandwich compound (Pc = phthalocyanine), displaying the z anisotropy axis.

**Fig. 2.88**

Energy levels of the ground-state multiplets of $\{\text{LnPc}_2\}^-$. (Redrawn from [2.73b].)

maximum of χ'' at 1000 Hz is obtained for 40 K (*versus* 6 K for Mn_{12}), and for the neutral species the figure is even 50 K. $[\text{TbPc}_2]$ can be used as active element in a spintronic device described in Section 5.2.9. The use of lanthanides to create new quantum magnets—exploiting their very peculiar electronic structure (Fig. 2.88)—is emphasized in [2.74, 2.75] and many recent papers.

References

- [2.1] A. Earnshaw, *Magnetochemistry*, Academic Press, New York, 1968.
- [2.2] *Magneto-Structural Correlations in Exchange-Coupled Systems*, R. D. Willett, D. Gatteschi, O. Kahn (eds.), NATO ASI Series C, Vol. 140, Reidel, Dordrecht, 1983.
- [2.3] O. Kahn, *Molecular Magnetism*, VCH, New York, 1993.
- [2.4] D. Gatteschi, R. Sessoli, J. Villain, *Molecular Nanomagnets*, Oxford University Press, Oxford, 2006.
- [2.5] *Molecular Magnetism: New Magnetic Materials*, K. Itoh, N. Kinoshita (eds.), Kodansha, Tokyo, 2000.
- [2.6] *Magnetism: Molecules to Materials*, J. S. Miller, M. Drillon (eds.), 5 vols., VCH, New York, 2001–2005.
- [2.7] S. I. Tomonaga, *The Story of Spin*, University of Chicago Press, Chicago, 1997.
- [2.8] P. A. M. Dirac, *The Principles of Quantum Mechanics*, 4th. edn., Oxford University Press, Oxford, 1958.
- [2.9] B. I. Bleaney and B. Bleaney, *Electricity and Magnetism*, 3rd. edn., Oxford, Oxford University Press, 1976.
- [2.10] *Magnétisme*, E. du Trémolet de Lacheisserie (ed.), 2 vols., EDP Sciences, les Ulis, 2000.
- [2.11] S. Blundell, *Magnetism in Condensed Matter*, Oxford University Press, Oxford, 2001.
- [2.12] *Quantities, Units and Symbols in Physical Chemistry*, I. Mills, T. Cvitas *et al.* (eds.), IUPAC Physical chemistry Division, Blackwell, Oxford, 1993.
- [2.13] T. I. Quickenden, R. C. Marshall, *J. Chem. Ed.* 49 (1972), 114.
- [2.14] *Introduction to Physical Techniques in Molecular Magnetism: Structural and Macroscopic Techniques*, F. Palacio, E. Ressouche, J. Schweizer (eds.), Universidad Zaragoza, Zaragoza, Spain, 2001.
- [2.15] W. Wernsdorfer, *Adv. Chem. Phys.* 118 (2001), 99.

- [2.16] A. Bencini, D. Gatteschi, *EPR of Exchange Coupled Systems*, Springer-Verlag, Berlin, 1990.
- [2.17] *Neutron and Synchrotron Radiation for Condensed Matter Studies: Applications to Solid State Physics and Chemistry*, Hercules, J. L. Baruchel *et al.* (eds.), Springer-Verlag, Berlin, 1994.
- [2.18] H. Güdel, in E. Coronado *et al.* (eds), *Molecular Magnetism: From Molecular Assemblies to the Devices*, NATO ASI Series, Kluwer Academic Publishers, vol. E-321 (1996).
- [2.19] S. J. Blundell, *Contemp. Phys.* 40 (1999), 175.
- [2.20] (a) J. H. Van Vleck, *The Theory of Electric and Magnetic Susceptibilities*, Clarendon Press, Oxford, 1932; (b) Nobel Lecture, Quantum Mechanics, The Key to Understanding Magnetism, http://www.nobelprize.org/nobel_prizes/physics/laureates/1977/vleck-lecture.html
- [2.21] M. Gerloch, *Orbitals, Terms and States*, Wiley, Chichester, 1986.
- [2.22] C. J. Ballhausen, *Introduction to Ligand Field Theory*, McGraw-Hill, New York, 1962.
- [2.23] J. S. Griffith, *The Theory of Transition-Metal Ions*, Cambridge University Press, Cambridge, 1961.
- [2.24] B. N. Figgis, M. A. Hitchman, *Ligand Field Theory and Its Applications*, Wiley, New York, 1999.
- [2.25] F. E. Mabbs, D. J. Machin, *Magnetism and Transition Metal Complexes*, Chapman and Hall, London, 1973.
- [2.26] (a) *Comprehensive Coordination Chemistry II*, J. A. McCleverty, T. J. Meyer (eds.), vol. 2, Elsevier, Amsterdam, 2003; (b) *Comprehensive Inorganic Chemistry II*, J. Reedijk, K. Poeppelmeier (eds), Elsevier, Amsterdam, 2013.
- [2.27] F. A. Cotton, *Chemical Applications of Group Theory*, Wiley, New York, 1963.
- [2.28] *Spin Crossover in Transition Metal Compounds, I, II, III*, P. Gülich, H. A. Goodwin (eds.), *Topics in Current Chemistry*, vols. 233, 234, 235, Springer-Verlag, Berlin, 2004.
- [2.29] P. Gülich, A. Hauser, H. Spiering, *Angew. Chem. Int. Ed.* 33 (1994), 2024–54.
- [2.30] I. Krivokapic, A. Hauser *et al.*, *Coord. Chem. Reviews* 251 (2007), 364–78.
- [2.31] S. Alvarez, J. Cirera, *Angew. Chem. Int. Ed.* 45 (2006), 3012–20.
- [2.32] R. A. Swalin, *Thermodynamics of Solids*, John Wiley, New York, 1962.
- [2.33] M. Kepenekian, B. Le Guennic, V. Robert, *Phys. Rev. B* 79 (2009), 094428.
- [2.34] J. A. Real, A. B. Gaspar, V. Niel, M. C. Munoz, *Coord. Chem. Rev.* 236 (2003), 121–41; J. A. Real, A. B. Gaspar, M. C. Munoz, *Dalton Trans.* (2005), 2062–79.
- [2.35] C. Munoz, J. A. Real, *Coord. Chem. Rev.* 255, (2011), 2068–93.
- [2.36] A. Abragam, M. H. L. Pryce, *Electron Paramagnetic Resonance of Transition Ions*, Clarendon Press, Oxford, 1970.
- [2.37] K. Kambe, *J. Phys. Soc. Japan* 5 (1950), 48.
- [2.38] J. B. Goodenough, *Magnetism and the Chemical Bond*, Interscience Publishers, New York, 1966.
- [2.39] J. J. Girerd, Y. Journaux, O. Kahn, *Chem. Phys. Letters* 82 (1981), 534.
- [2.40] P. J. Hay, J. C. Thibeault, R. Hoffmann, *J. Am. Chem. Soc.* 97 (1975), 4884.
- [2.41] P. W. Anderson, in *Magnetism*, G. T. Rado, H. Suhl (eds.), vol. I, Academic Press, New York, 1963.
- [2.42] (a) J. Curely, B. Barbara, in *Structure and Bonding* 122, R. Winpenny (ed.) (2006) 207–50; (b) M. Verdager, V. Robert in *Comprehensive Inorganic Chemistry II*, J. Reedijk, K. Poeppelmeier (eds.), Elsevier, Amsterdam, Section 8.19, 1–59, 2013.
- [2.43] P. de Loth, P. Cassoux, J. P. Daudey, J.-P. Malrieu, *J. Am. Chem. Soc.* 103 (1981), 4007–16.
- [2.44] J. Miralles, O. Castell, R. Caballol, J.-P. Malrieu, *Chem. Phys.* 172 (1993), 33–43.
- [2.45] F. J. Neese, *Chem. Phys.* 119 (2003), 9428–43.
- [2.46] L. Noodleman, *J. Chem. Phys.* 74 (1981), 5737–43.

- [2.47] E. Ruiz, J. Cano, S. Alvarez, P. Alemany, *J. Comput. Chem.* 20 (1999), 1391–1400.
- [2.48] R. Caballol, O. Castell, F. Illas, I. de P. R. Moreira, J.-P. Malrieu, *J. Phys. Chem. A* 101 (1999), 7860–6.
- [2.49] J. J. Novoa, M. Deumal, J. Jornet-Somoza, *Chem. Soc. Rev.* 40 (2011), 3182–3212.
- [2.50] S. Alvarez, M. Julve, M. Verdaguier, *Inorg. Chem.* 29 (1990), 4500–07.
- [2.51] M. Verdaguier, M. Julve, O. Kahn, A. Gleizes, *Nouv. J. Chim.* 9 (1985), 325–34.
- [2.52] L. Néel, *Ann. Phys.* 3 (1948), 137–98.
- [2.53] V. Marvaud, C. Decroix, A. Scüller, C. Guyard-Duhayon, J. Vaisserman, F. Gonnet, M. Verdaguier, *Chem. Eur. J.* (2003), 1677–91.
- [2.54] E. Ruiz, G. Rajaraman, S. Alvarez, B. Gillon, J. Stride, R. Clérac, J. Larionova, S. Decurtins, *Angew. Chem. Int. Ed.* 44 (2005), 2711–15.
- [2.55] Powell, A. M. Ako, A. Powell *et al.*, *Angew. Chem. Int. Ed.* 46 (2006), 4926–9.
- [2.56] M. Verdaguier, A. Gleizes, J. P. Renard, J. Seiden, *Phys. Rev. B* 29 (1984), 5144–55.
- [2.57] O. Kahn, Y. Pei, M. Verdaguier, J. P. Renard, J. Sletten, *J. Am. Chem. Soc.* 110 (1988), 782–9.
- [2.58] J. P. Renard, in *Organic and Inorganic Low-Dimensional Crystalline Materials*, P. Delhaes, M. Drillon (eds.), NATO-ASI Series, B168, Plenum Press, New York, 1987.
- [2.59] S. Ferlay, T. Mallah, R. Ouahès, P. Veillet, M. Verdaguier, *Nature* 378 (1995), 701–3.
- [2.60] *Molecular Cluster Magnets*, R. Winpenny (ed.), World Scientific Books, Singapore, 2011.
- [2.61] D. Gatteschi, R. Sessoli, *Angew. Chem. Int. Ed.* 42 (2003), 268–97. A review with 241 references.
- [2.62] R. Bagai, G. Christou, *Chem. Soc. Rev.* 38 (2009), 1011–26. A review with sixty references.
- [2.63] A. Cornia, M. Mannini, Ph. Sainctavit, R. Sessoli, *Chem. Soc. Rev.* 40 (2011), 3076–91.
- [2.64] R. Sessoli, D. Gatteschi, A. Caneschi, M. A. Novak, *Nature* 365 (1993), 141–3.
- [2.65] N. Regnault, T. Jolicoeur, R. Sessoli, D. Gatteschi, M. Verdaguier, *Phys. Rev. B* 66 (2002), 409–14.
- [2.66] L. Landau, *Phys. Z. Sowjetunion* 2 (1932), 46; C. Zener, *Proc. Roy. Soc. London Ser. A* 137 (1932), 696; E. C. G. Stückelberg, *Helv. Phys. Acta* 5 (1932), 369.
- [2.67] O. Waldmann, *Inorg. Chem.* 46 (2007), 10035–7.
- [2.68] E. Ruiz, J. Cirera, J. Cano, S. Alvarez, C. Loose, J. Kortus, *Chem. Commun.* (2008), 52–4.
- [2.69] *Dalton Transactions*, Special Issue, ‘Frontier and perspectives in molecule-based quantum magnets’, M. Yamashita (ed.) 41 (2012), 13555sq.
- [2.70] A. Caneschi, D. Gatteschi, N. Lalioti, C. Sangregorio, R. Sessoli, G. Venturi, A. Vindigni, A. Rettori, M. G. Pini, M. A. Novak, *Angew. Chem. Int. Ed.* 40 (2001), 1760–3.
- [2.71] C. Coulon, H. Miyasaka, R. Clérac, in *Structure and Bonding*, Winpenny R. (ed.), Springer, Berlin, 122 (2006), p. 163.
- [2.72] R. J. Glauber, *J. Math. Phys.* 4 (1963), 294.
- [2.73] a) N. Ishikawa, M. Sugita, T. Ishikawa, S.-Y. Koshihara, Y. Kaizu, *J. Am. Chem. Soc.* 125 (2003), 8694–5; b) T. Ishikawa, *Polyhedron* 26 (2007), 2147–53.
- [2.74] L. Sorace, C. Benelli, D. Gatteschi, *Chem. Soc. Rev.* 40 (2011), 3092–3104.
- [2.75] J. D. Rinehart, J. R. Long, *Chem. Sci.* 2 (2011), 2078–85.

The moving electron: electrical properties

3

In Chapter 1 we saw that electrons are running in the field created by the nuclei, that their energy in the atom is quantized, and that their speed can be very high. Nevertheless, they remain localized around a given nucleus or in a given molecule (that is, a well-defined site). In the present chapter we introduce and study another kind of mobility of the electrons: from one site to another, which ensures conductivity in the case of a solid. This movement is a result, in most cases, of external perturbations (electric or magnetic fields, electromagnetic radiation, and so on). It depends on the interplay of a number of structural and electronic factors which are analysed in Section 3.1. In Section 3.2 we consider the case of electron transfer in discrete molecular systems, and in Section 3.3 the delocalization of electrons in solids with the resulting conducting properties.

3.1 Basic parameters controlling electron transfer

Electron transfer depends essentially upon three parameters: one is the electronic interaction between sites (this favours electron transfer), a second one is the change in geometrical structure of the surrounding induced by the presence or absence of an electron (this hinders electron transfer), and the third one (also unfavourable) is the interelectronic repulsion precluding the simultaneous presence of two electrons on the same site. The following discussion will be useful for the study of electron transfer in solution or in discrete molecular systems, as well as in extended solids. However, for reasons of simplicity the parameters will be defined using simple examples taken from discrete systems. Discrete systems will be in general of the $M^{n+} - M^{(n+1)+}$ type; that is, two neighbouring transition metal ions whose oxidation states differ by one unit. When the two ions are permanently linked by covalent bonds, they constitute a mixed valence compound—a type of compound which will play a crucial role in the concept of electron transfer (see Section 3.2.2).

3.1.1 The electronic interaction between neighbouring sites: the V_{ab} parameter

The basic reason for the possibility of electron transfer is the existence of an electronic interaction between different sites (atoms or nearby molecules). In the simplest case of the interaction between two atoms in vacuum, it is described by the resonance integral $\beta = \langle \phi_a | H | \phi_b \rangle$ as seen in eqn. (1.17). The interaction can be illustrated by a diagram, familiar to physicists, in which one plots the energy of an electron as a function of its position (Fig. 3.1).

In Fig. 3.1 are shown the electronic energy levels for each atom and for the complete system (molecule). For the latter, there is a splitting $2|\beta|$ (neglecting the overlap; see Section 1.3.1) between the bonding and the antibonding combination of atomic orbitals. The bonding and antibonding combinations are given by (neglecting overlap):

$$\psi_{\text{bond}} = \psi_1 = 2^{-1/2}(\phi_a + \phi_b) \quad (3.1a)$$

$$\psi_{\text{antibond}} = \psi_2 = 2^{-1/2}(\phi_a - \phi_b) \quad (3.1b)$$

A typical situation for electron transfer occurs when there is just one electron present in the system. Since the electron total energy is always below the potential energy in the region between A and B, it is said that the electron can move by tunnel effect between A and B. Actually, talking about the tunnel effect (here an *electronic* tunnel effect because Fig 3.1 deals with electron energies) is the same as talking about the birth of a chemical bond between A and B. For other aspects of tunnelling, see Sections 1.6 and 2.8.

Real systems are, of course, much more complex, for two reasons: (i) there is more than one electron, so that the quantum-mechanical description must involve total wavefunctions and energies instead of one-electron ones, and (ii) in most studied cases there is a bridging ligand linking the two metal sites, and the analysis must take into account the electronic delocalization on this ligand.

We temporarily get rid of difficulty (i) by assuming that in the system upon investigation the electronic interaction results from the mixing of only one orbital from each site—the one which is occupied by either one or zero electron. Below in energy are found occupied orbitals which do not play a role in a first approximation. We are thus brought back to a one-electron-two-orbitals analysis (Fig. 3.2). This approach has the immense advantage of allowing a pictorial approach based on orbital topologies. The problem will be discussed further in Section 3.2.2.6.

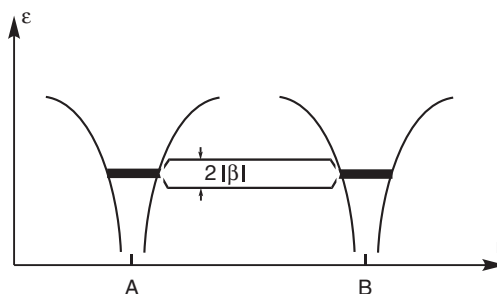


Fig. 3.1

Electron energy (denoted ϵ) for a system with two localization sites, A and B. Thin curved lines represent the potential energy, while bold horizontal lines represent the total energy. As a result of electronic interaction, the electron energies are split in two levels separated by $2|\beta|$.

We now consider difficulty (ii). As a result of the presence of the bridging ligand, the intervening orbitals have extensions on the bridge (as well as on ancillary ligands). Thus the problem must be analysed by considering the complete system. Let us take the example of two transition metal ions linked by a simple monoatomic bridge with just one active bridge orbital: many systems contain the centrosymmetric M–O–M framework, with a linear bridge considered formally as the oxide ion O^{2-} (Fig. 3.3). With the coordinate system of the figure, the d_{xz} orbitals of the metals can mix only with the p_x orbital of the oxide. Taking into account the electronegativity difference between metal and oxygen, one derives the qualitative diagram of Fig. 3.3, in which one recognizes the standard way of construction of molecular orbitals; that is, by building first symmetry-adapted linear combinations (SALC or SO) of d_{xz} orbitals, namely $2^{-1/2}(d_{xzA} + d_{xzB})$ and $2^{-1/2}(d_{xzA} - d_{xzB})$, and then allowing them to interact with oxygen. (See also Section 2.6.2.2 on exchange interaction where a similar reasoning was used for a linear M–O–M bridge but involving $d_{x^2-y^2}$ orbitals.)

Thus, in the upper part of the final diagram one recognizes two orbitals, ψ_1 , energy ε_1 , ψ_2 , energy ε_2 , with strong metal character and opposite symmetries u and g , as in the case of the two-site system (eqns. (3.1a) and (3.1b)). For a mixed valence situation there is only one electron in these orbitals. Calling them ψ_1 and ψ_2 , the electronic interaction is defined, by analogy as previously, by:

$$V_{ab} = |\beta| = 1/2(|\varepsilon_2 - \varepsilon_1|) \quad (3.2)$$

so that V_{ab} is always a positive quantity. This way of defining the electronic interaction is called the dimer-splitting method.

In this chapter we shall use either V_{ab} or β to characterize the electronic interaction. When using β we must keep in mind that it is an *effective quantity* because, as in Section 2.6.2.2, we are not dealing with the interaction between

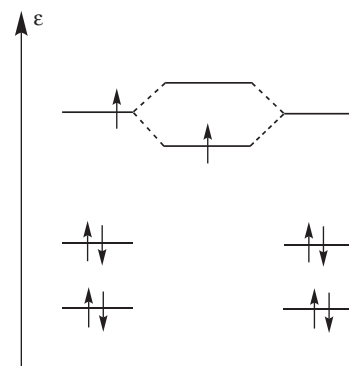


Fig. 3.2

A polyelectronic system in which only one orbital on each site plays a role in electron transfer.

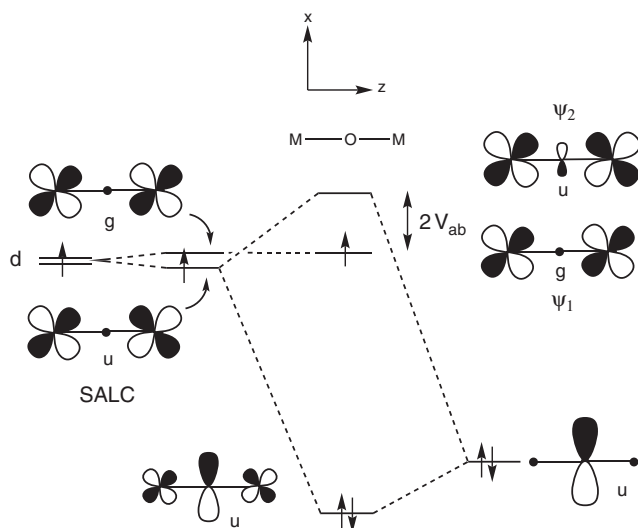


Fig. 3.3

Qualitative MO diagram for a mixed valence system with a linear oxygen bridge. The d orbitals of the two metals are assumed to bring just one electron (case of a vanadium(V)–vanadium(IV) system for instance). g and u refer to the gerade and the ungerade symmetry of the orbitals.

pure metal orbitals. Orbitals such as ψ_1 and ψ_2 could indeed be obtained by in-phase and out-of-phase combinations of localized orthogonal orbitals ψ'_a and ψ'_b (see orthogonal magnetic orbitals in Section 2.6.1.2); that is, orbitals with a strong weight on a metal atom and tails on the neighbouring ligands and even on the other metal site. Such orbitals are defined by:

$$\psi'_a = 2^{-1/2} (\psi_1 + \psi_2) \text{ and } \psi'_b = 2^{-1/2} (\psi_1 - \psi_2) \quad (3.3)$$

and with this definition

$$V_{ab} = | \langle \psi'_a | \mathbf{H} | \psi'_b \rangle | \quad (3.4)$$

where \mathbf{H} is the complete Hamiltonian of the molecule. Once again, we note the analogy with the problem of exchange interaction, except that in the present case the electronic filling is different because of the mixed valence nature.

The previous definitions can be used only for symmetrical systems. For non-symmetrical systems a more general procedure is necessary, because the splitting between MO levels such as Ψ_1 and Ψ_2 depends not only on $|\beta|$ but also on the initial energy difference between interacting orbitals (see Fig. 1.5). We can use a suitable effective Hamiltonian. We have already seen an example in Section 1.2.3, but here the purpose is different. The effective Hamiltonian adapted to electron transfer is defined in such a way that:

$$V_{ab} = \langle \phi_a | \mathbf{H}^{\text{eff}} | \phi_b \rangle \quad (3.5)$$

Note the difference compared with eqn. (3.4). Here the orbitals entering in the V_{ab} expression are *atomic orbitals* located on atoms A and B, but \mathbf{H} has been replaced by \mathbf{H}^{eff} , the definition of which is [3.1]:

$$\mathbf{H}^{\text{eff}} = \mathbf{P} \mathbf{U}^{-1} \mathbf{H} \mathbf{U} \mathbf{P} \quad (3.6)$$

where \mathbf{P} is the projection operator of the wavefunctions space on the subspace defined by ϕ_a and ϕ_b , and \mathbf{U} is an operator performing linear combinations of the wavefunctions (basis change) [3.1b]. \mathbf{U} is chosen in such a way that it minimizes the distance between some wavefunctions and the ϕ_a, ϕ_b subspace, or, in other words, it allows partitioning the Hamiltonian matrix. (The term 'distance' has no geometrical meaning here, but refers to the vectorial space of wavefunctions).

We shall not detail here the mathematics of this effective Hamiltonian, which can be found elsewhere [3.1]. We can just perform a qualitative checking, assuming that a molecular orbital calculation has been performed on the complete metal–ligand–metal system, giving MOs of the form:

$$\psi_i = c_{ia} \phi_a + c_{ib} \phi_b + \sum c_{iL} \phi_L \quad (3.7)$$

where ϕ_a and ϕ_b are pure atomic orbitals located on A and B (now A and B are no longer equivalent) and ϕ_L are orbitals belonging to the ligand. The effective coupling is then given by [3.2]:

$$V_{ab} = \left| \frac{c_{1a} c_{1b} - c_{2b} c_{2a}}{2(c_{1a} c_{2b} - c_{1b} c_{2a})} (\epsilon_1 - \epsilon_2) \right| \quad (3.8)$$

where indexes 1 and 2 refer to the two orbitals with the highest contributions coming from A and B. Thus, let us take the example of the combination of just

two orbitals with very different energies (ϕ_a much more stable than ϕ_b). Then one has:

$$c_{1a} \approx 1, c_{1b} \approx \kappa, c_{2a} \approx -\kappa, c_{2b} \approx 1 \quad (3.9a)$$

with κ a mixing coefficient $\ll 1$. Substituting in eqn. (3.8) gives

$$V_{ab} \approx |\kappa(\varepsilon_1 - \varepsilon_2)| \quad (3.9b)$$

showing that V_{ab} is now much lower than the energy difference ($\varepsilon_1 - \varepsilon_2$), in qualitative agreement with Fig. 1.5.

On the other hand, for a symmetrical system, the two selected orbitals are such that:

$$c_{1a} \approx 2^{-1/2}, c_{1b} \approx 2^{-1/2}, c_{2a} \approx 2^{-1/2}, c_{2b} \approx -2^{-1/2} \quad (3.9c)$$

and the substitution in eqn. (3.8) gives eqn. (3.2).

The effective Hamiltonian (3.6) is thus efficient and of general purpose. Its structure can be qualitatively justified as follows: the projection operator \mathbf{P} on the $\phi_a \phi_b$ subspace is equivalent to the operation of selecting in the complete MO diagram those orbitals (Ψ_1 and Ψ_2) which have strong weights on A and B. The \mathbf{U} operation, corresponding to a rotation in a vectorial space, corrects the energy calculation (\mathbf{H}) to take into account that Ψ_1 and Ψ_2 are unevenly distributed on ϕ_a and ϕ_b .

In this chapter we shall use mainly definition (3.2) based on the symmetry splitting of energy levels. For non-symmetrical systems, eqn. (3.2) cannot be used, and one has to fall back to the less intuitive formula (3.8). For the moment we use a definition of electronic coupling based on one-electron energies (hence the notation ε_i in all formulae). In Section 3.2.2.6 we shall say a few words about more advanced treatments, taking into account the polyelectronic nature of the wavefunctions.

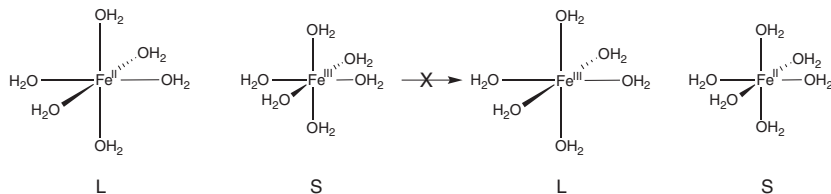
3.1.2 The structural change of the surrounding: the λ parameter

Electron motion from a localized site (such as a metal atom) to another is always accompanied by some structural change. The process is well documented for electron transfer in solution, and in what follows, the basic principles will be established from this example.

We consider the system formed by two hexaaqua complexes of Fe^{2+} and Fe^{3+} in close proximity. It is known, from X-ray structures in the solid state, that the iron–oxygen bond lengths are 1.99 Å for $[\text{Fe}(\text{H}_2\text{O})_6]^{3+}$, $(t_{2g})^3(e_g)^2$, and 2.12 Å for $[\text{Fe}(\text{H}_2\text{O})_6]^{2+}$, $(t_{2g})^4(e_g)^2$ [3.3]. This length variation with oxidation state is general in transition metal chemistry: frequently the addition of one electron populates an e_g^* antibonding orbital (see Section 1.3.6), and thus weakens the metal–ligand bonds. But even when a t_{2g} orbital is populated, there is also a weakening because of the general expansion of the electronic cloud, leading to an increase in metal–ligand distances. Anyway, owing to this difference the electron transfer is *impossible* with the initial ground-state geometry. Electron transfer must indeed obey two constraints: (i) since electronic motions are much faster than nuclear motions, the system geometry cannot

Fig. 3.4

(Left) initial geometry of the $[\text{Fe}(\text{H}_2\text{O})_6]^{3+} \dots [\text{Fe}(\text{H}_2\text{O})_6]^{2+}$ pair, showing (right) the impossibility to achieve an electron transfer at constant energy. S = 'small' (coordination sphere adapted to Fe^{III}); L = 'large' (coordination sphere adapted to Fe^{II}).

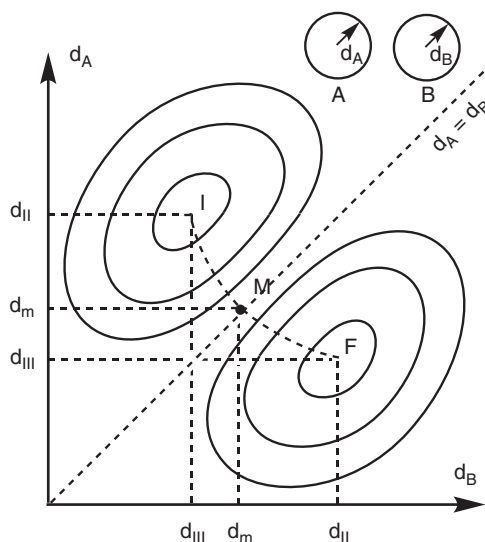


be modified during the electron transfer act; this restriction is very analogous to the Franck–Condon principle, which governs electronic transitions (see Section 4.2.3); (ii) also as a consequence of slow nuclear motion, the system has no time to exchange thermal energy with the surroundings; the system behaves as if isolated, and energy conservation prevails. But transferring an electron while keeping the initial geometry would result in the creation of a $[\text{Fe}(\text{H}_2\text{O})_6]^{3+}$ ion with the geometry of $[\text{Fe}(\text{H}_2\text{O})_6]^{2+}$ and *vice versa*, which is impossible at constant energy (see Fig. 3.4). Thus a change in geometry is a prerequisite for electron transfer.

A simple way to represent the nuclear state of the system consists in plotting the potential energy of the $[\text{Fe}(\text{H}_2\text{O})_6]^{3+} \dots [\text{Fe}(\text{H}_2\text{O})_6]^{2+}$ pair as a function of two variables, d_A and d_B , describing the bond lengths around the iron atoms labelled A and B (Fig. 3.5). The energy is then represented as contour lines. The initial state, corresponding to the $\text{Fe}_A^{2+}\text{Fe}_B^{3+}$ situation, is then associated to a point I ($d_A = d_{\text{II}}$; $d_B = d_{\text{III}}$) located away from the $d_A = d_B$ diagonal, and the final state $\text{Fe}_A^{3+}\text{Fe}_B^{2+}$ to a symmetrical point with respect to this diagonal, denoted F ($d_A = d_{\text{III}}$; $d_B = d_{\text{II}}$). Starting from these minimal energy situations, any modification of a bond length gives rise to an increase in energy, which is given, in the harmonic oscillator approximation, by $\Delta E = \frac{1}{2}k \Delta d^2$, where k is the force constant of the bond, and Δd the bond length change with respect to the equilibrium situation.

Fig. 3.5

Potential energy map for the $[\text{Fe}(\text{H}_2\text{O})_6]^{3+} \dots [\text{Fe}(\text{H}_2\text{O})_6]^{2+}$ pair as a function of d_A and d_B . I: Initial state corresponding to the $\text{Fe}_A^{2+}\text{Fe}_B^{3+}$ situation; F: Final state corresponding to the $\text{Fe}_A^{3+}\text{Fe}_B^{2+}$ situation; M: intermediate state. Note that the reaction trajectory $I \rightarrow M \rightarrow F$ is not generally linear.



To achieve electron transfer while obeying the previous constraints, one has to cross at some time the $d_A = d_B$ diagonal; that is, to bring the d_A and d_B distances to a common value, d_m . The problem is now to determine which d_m value will lead to the lowest energetic cost. Starting from the initial state, bringing all the Fe–O distances to a common value d requires the following energy:

$$\Delta E = (n/2) k_{\text{III}} (d - d_{\text{III}})^2 + (n/2) k_{\text{II}} (d_{\text{II}} - d)^2 \quad (3.10)$$

where n is the number of bonds around iron (here $n = 6$), k_{II} and k_{III} are the force constants in oxidation states II and III, and d_{II} and d_{III} are the corresponding equilibrium distances. Taking the derivative of eqn. (3.10) with respect to d , and searching for the extremum, yields:

$$d_m = \frac{k_{\text{II}} d_{\text{II}} + k_{\text{III}} d_{\text{III}}}{k_{\text{II}} + k_{\text{III}}} \quad (3.11)$$

That is, the best ‘compromise’ distance is a weighted average of the d_{II} and d_{III} distances corresponding to the two oxidation states. When the force constants are equal, one has the intuitive result:

$$d_m = \frac{d_{\text{II}} + d_{\text{III}}}{2} \quad (3.12)$$

If now we introduce the value of d_m in expression (3.10), we find, after rearrangement:

$$\Delta E = \frac{n k_{\text{II}} k_{\text{III}}}{2(k_{\text{II}} + k_{\text{III}})} (d_{\text{II}} - d_{\text{III}})^2 \quad (3.13)$$

which reduces, when $k_{\text{II}} = k_{\text{III}}$ to:

$$\Delta E = \frac{nk}{4} (d_{\text{II}} - d_{\text{III}})^2 \quad (3.14)$$

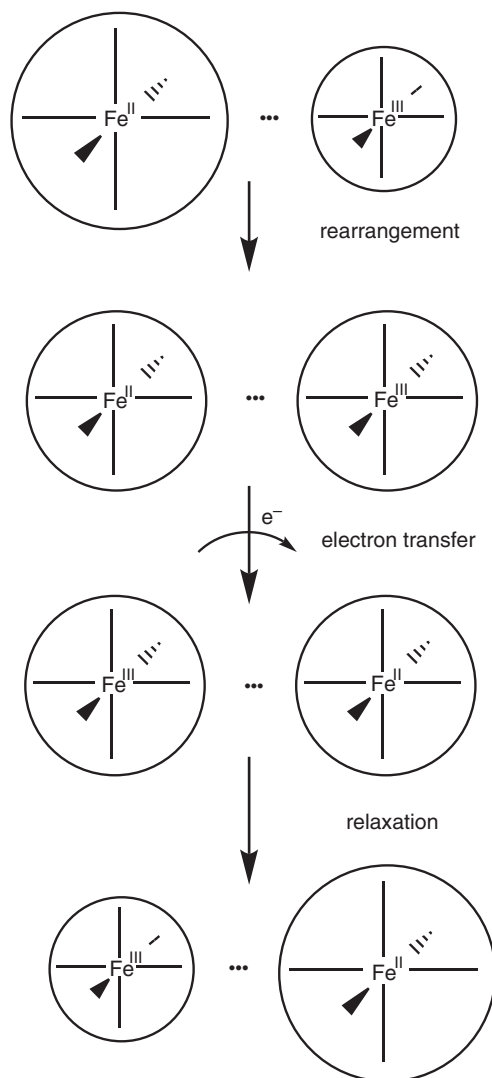
Thus, there is an activation energy which is proportional to the square of the difference $d_{\text{II}} - d_{\text{III}}$.

The interplay between structural rearrangement and electron transfer itself is illustrated in Fig. 3.6, showing the sequence of events: first the structural rearrangement leading to a ‘compromise’ geometry, which is symmetrical with respect to A and B sites, then electron transfer at constant geometry and energy, and finally a relaxation of the coordination spheres with adaptation to the new oxidation states.

However, to be complete one has to take into account an additional contribution to the activation energy coming from the solvent. In the same way as the metal–ligand distances are different around the Fe^{2+} and Fe^{3+} sites, the state of solvent polarization is different around the $[\text{Fe}(\text{H}_2\text{O})_6]^{3+}$ and $[\text{Fe}(\text{H}_2\text{O})_6]^{2+}$ entities, as a result of their charge difference. Solvent molecules are more strongly polarized around a 3+ charge than around a 2+ charge, due to the higher electrostatic field.

Thus the activation energy in solution contains two contributions, one due to the *internal* coordination sphere (the hexaqua complex itself), and one due to the *external* coordination sphere, namely the solvent, so that:

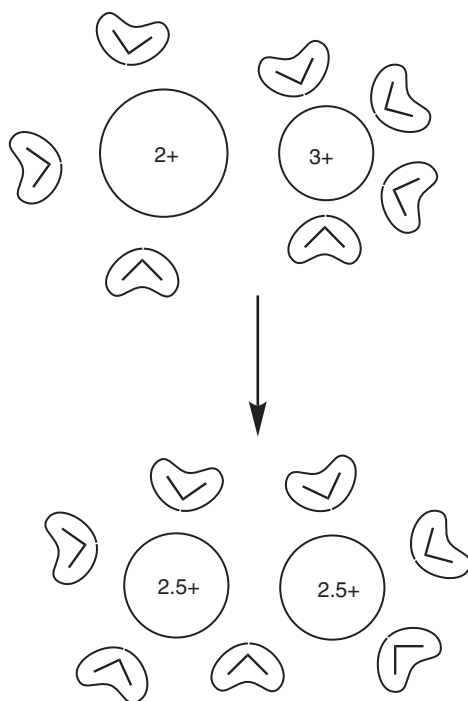
$$E_{\text{act}} = \Delta E = \Delta E_{\text{int}} + \Delta E_{\text{ext}} \quad (3.15)$$

**Fig. 3.6**

Sequence of events occurring during electron transfer.

ΔE_{int} is the term computed by eqn. (3.13) from microscopic quantities. On the contrary, to evaluate ΔE_{ext} a common practice is to use a 'macroscopic' model in which the solvent is considered as a continuous dielectric medium [3.4]. ΔE_{ext} derives from the interaction between the dielectric medium and the huge electric field created by charged species in their vicinities. Of course, such a model could be questioned, because it does not take into account explicitly the true molecular structure of the solvent around the ions, but this phenomenological approach has been successful for several decades in producing realistic estimations of the energies involved.

Thus the activation process can be imagined as follows at the level of the solvent: starting from the initial state, where the external coordination spheres present a polarization state adapted to the initial electronic configuration

**Fig. 3.7**

Rearrangement of external coordination spheres constituted by the solvent. For electron transfer to occur, the solvent must reach an 'average' polarization state, intermediate between the one prevailing around $[\text{Fe}(\text{H}_2\text{O})_6]^{3+}$ and the one around $[\text{Fe}(\text{H}_2\text{O})_6]^{2+}$. However, this concerns only the orientation polarization (see text).

(Fig. 3.7.), one has to reach an activated state where the polarization is a compromise between the one of a 2+ charge and the one of a 3+ charge; that is a 2.5+ / 2.5+ distribution (note the analogy of the previous argument with the case of the internal coordination sphere).

The calculation is complex, since we are dealing with a *non-equilibrium polarization*. One has indeed to distinguish two contributions to the solvent polarization energy: (i) an orientation contribution, due to the partial alignment of polar molecules along the strong electric field created by the charge, and (ii) an electronic contribution, due to the displacement of electrons inside the solvent molecules; that is, the electric polarization of solvent molecules themselves. The first process requires nuclear motions, which are slow with respect to the electronic motion, while the second process is fast and can adapt at any time to the motion of the transferred electron. Thus only the first component intervenes in the activation process, because it must be achieved *before* the electron transfer, for the same reasons as for the rearrangements of bond lengths. Concerning the electronic polarization, since it is fast, it can be modified *during* the electron transfer, and thus does not contribute to the activation energy.

Only an outline of the calculation will be given here. The interaction energy between a sphere of charge q and radius a , immersed into a dielectric medium of static dielectric constant ϵ_s is usually given by the Born expression:

$$E = \frac{1}{4\pi\epsilon_0} \frac{q^2}{2a} \left(1 - \frac{1}{\epsilon_s}\right) \quad (3.16)$$

Since this expression uses ϵ_s (ϵ 'static'), it encompasses the two components of the polarization. Now, if we are interested in the sole electronic polarization, we just have to replace ϵ_s by ϵ_{op} , which is the dielectric constant at optical frequencies ($10^{14} - 10^{15}$ Hz). This comes from the fact that at these very high frequencies of the electromagnetic field of optical radiations, only the electrons can follow the field changes, while the nuclear motions are frozen. ϵ_{op} is, of course, much lower than ϵ_s . From electromagnetic theory, ϵ_{op} equals the square of the index of refraction; that is, $(1.33)^2 = 1.77$ in the case of water. Thus it appears that the orientation contribution to the ion–solvent interaction must involve a difference term $(1/\epsilon_{op} - 1/\epsilon_s)$ called Pekar's factor [3.5]. Taking into account the detailed geometry of the system, the contribution of the solvation sphere to the activation energy is finally given by the following formula, due to Marcus [3.6] and Hush [3.7]:

$$\Delta E_{\text{ext}} = \frac{\Delta e^2}{4\pi\epsilon_0} \left(\frac{1}{\epsilon_{op}} - \frac{1}{\epsilon_s} \right) \left(\frac{1}{2a_A} + \frac{1}{2a_B} - \frac{1}{R} \right) \quad (3.17)$$

In this expression, Δe is the amount of charge transferred in the transition state; that is, $0.5 e^-$, a_A and a_B are the Van der Waals radii of the interacting ions (see Fig. 3.8), and R is their centre-to-centre distance (generally $R = a_A + a_B$).

Since the activation process implies two simultaneous and correlated changes, it is convenient to define a reaction coordinate Q , which describes *at the same time* the internal and external rearrangements. When this coordinate varies, the nuclei position changes gradually, and one evolves in a continuous way from the initial-state geometry to the final state one, the changes bearing simultaneously on the metal–ligand distances and on the solvent molecules orientation and disposition. This makes the Q coordinate difficult to visualize because, strictly speaking, the reaction path is a cross-section in a multidimensional diagram where the potential energy depends upon a large number of geometrical parameters. However, some feeling of the Q coordinate can be grasped from Fig. 3.9. An important guide for the following is that, for a given electronic configuration, the potential energy varies with Q according to a quadratic law of the form $m(Q - Q_i^\circ)^2$ or $m(Q - Q_f^\circ)^2$ (Fig. 3.9), where Q_i° and Q_f° are the equilibrium values for the initial and final state respectively, and m is a constant which does not need to be explained for the moment.

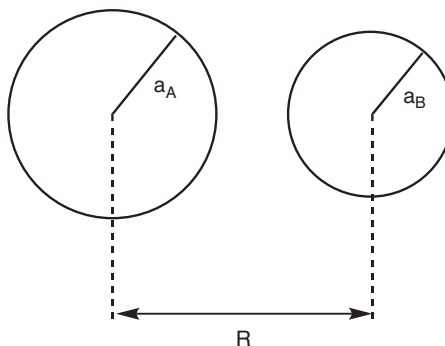
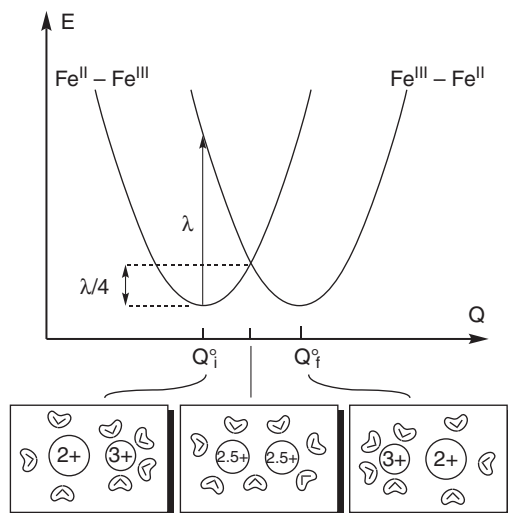


Fig. 3.8

Geometrical parameters used in the calculation of the solvent contribution in the Marcus–Hush model.

**Fig. 3.9**

Representation of the electron transfer by potential energy curves; namely, parabolae as functions of the reaction coordinate Q . As shown in the frames, moving along Q results in a concerted motion of the nuclei, those of the internal coordination sphere (expansion/contraction), and those of the solvent molecules. Q_i° and Q_f° are the equilibrium values for the initial and final state respectively. λ designates the 'vertical' rearrangement energy.

Remark: This quadratic dependence is obvious for the ΔE_{int} term, according to eqn. (3.10). Regarding ΔE_{ext} , all happens as if the solvent were polarized by a fictitious charge Δe (see eqn. (3.17)) able to vary continuously. This fictitious charge describes the solvent polarization state, and plays the same rôle as the bond lengths in ΔE_{int} . Now, the dependence of ΔE_{ext} upon Δe is also quadratic.

We now present the basic diagram universally used for describing electron transfer reactions. It is made of two displaced parabolae in the $E = f(Q)$ plane, one corresponding to each electronic configuration (Fig. 3.9). With respect to internal modes, it can be considered as a cross-section in Fig. 3.5 from I to F, and moving from left to right realizes the scenario of Fig. 3.6. To avoid a frequent misconception, it is important to realize that each parabola describes *the total energy of the whole system*, not the one of a subunit. (It is also important not to become confused with a figure like 3.1, in which the energy of *one* electron is plotted against a spatial coordinate.) The key parameter here is λ : it is the vertical distance in energy between the bottom of one parabola and the curve corresponding to the other electronic state.

Due to the parabolic nature of the curves, the difference in energy between the bottom of a curve and the crossing point is $\lambda/4$. Note that in the previous treatments, what we have computed in eqn. (3.13) (or (3.14)) and (3.17) was actually $\lambda/4$.

This type of diagram is extremely general, and can be used for any system, inorganic, organic, and even very complex systems such as proteins bearing redox groups. The internal geometry changes are, of course, more complex and harder to visualize than in the case of coordination complexes, though the general behaviour is the same.

In the solid state, a similar coupling between nuclear motion and electronic motion occurs: the presence of an extra electron on a given site generates a local distortion, and the electron can be 'self-trapped' by its own modification

of the medium, which considerably reduces its mobility. The association of the electron and its distortion constitutes a pseudo-particle called a *polaron*.

The concept of polaron was introduced by Landau in 1933 [3.8] and later discussed by Mott [3.9]. One can distinguish two situations: (i) polarons in molecular lattices, where the basic parameter is the bond length change upon addition/removal of one electron, and (ii) polarons in ionic lattices, which are described by phenomenological quantities, as in the previous case of the solvent.

For molecular lattices the treatment defines a polaron energy W_p , which is the change in energy when the system relaxes after the introduction of an additional electron. As previously, the energy change is a quadratic function of internuclear distances. Electron transfer between adjacent sites occurs by ‘hopping’ with an activation energy denoted W_H . The process is similar to the one depicted in Fig. 3.6. Each site distorts to adopt a ‘compromise geometry’, halfway between the geometries of the two oxidation states, and due to the quadratic law the energetic cost for a site is $\frac{1}{4} W_p$; but since there are two sites involved, the final result is:

$$W_H = \frac{1}{2} W_p \quad (3.18)$$

Comparison with Fig. 3.9 shows the correspondence between the solution-state model and the solid-state model:

$$W_p = \lambda/2 \quad (3.19)$$

In the solid-state literature, this process, by which the presence of an electron induces geometrical distortions, is called electron–phonon interaction, because the phonon is the quasi-particle associated with vibrations in solids.

For ionic lattices a simple picture can be presented if we consider the effect of introducing an additional charge on a given ion of the same sign. The nearby ions of opposite charge are attracted and move inwards, while the next ion neighbours are repelled and move outwards (Fig. 3.10).

In ionic lattices, polaron theory has been formulated in terms of static and optical dielectric constants ϵ_S and ϵ_{op} respectively, exactly in the same way as the polarization of a solvent. And as for the solvent, one has to separate the two components of polarization: the ion displacements (slow) and the electronic polarization (fast).

A simple calculation produces for W_p [3.9]:

$$W_p = -\frac{1}{2} \frac{1}{4\pi\epsilon_0} \left(\frac{1}{\epsilon_{op}} - \frac{1}{\epsilon_S} \right) \frac{e^2}{r_p} \quad (3.20)$$

where r_p is the polaron radius, defined approximately as the radius of the zone in which appreciable ion displacements occur. If r_p is of the same magnitude as the inter-ionic distance, then one has a *small polaron*, and this will be the case considered in this book. The other possibility is to have a much greater r_p , corresponding to a *large polaron*.

One can notice the analogy with eqn. (3.17)—in particular, the intervention of the Pekar factor.

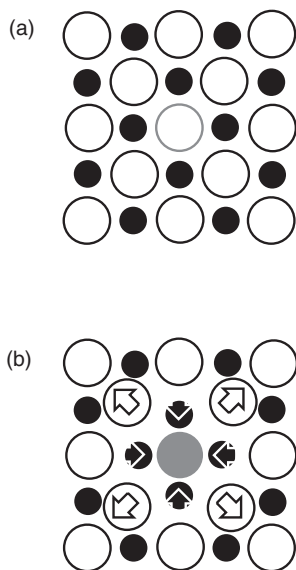
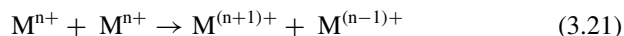


Fig. 3.10

Scheme of the motions of the ionic species associated to the formation of a polaron in an ionic lattice (white spheres are anions, black spheres are cations). (a) Initial positions of the ions; (b) an additional negative charge is introduced increasing the charge of the ion at the centre (grey sphere). The arrows show the resulting motions of the ions.

3.1.3 The interelectronic repulsion: the U parameter

The last important factor in electron transfer is the one-centre interelectronic repulsion parameter, already encountered in Chapters 1 and 2 and denoted as j_0 or U , and responsible *inter alia* for electron correlation. It is a major limiting factor for having electrons freely moving in a lattice or in a polycrystalline system, because transferring an electron from one site to a nearby site already occupied by another electron necessitates overcoming the one-centre interelectronic repulsion energy. A more ‘chemical’ way to formulate this problem is to note that in a system with localized valence states, moving an electron from one site to another one is a disproportionation process:



for which there is an energetic cost $\Delta E = U - V$, due to the proximity of charges. V , or j , is the electrostatic repulsion between charges located on adjacent sites, introduced in Section 1.5.1.

3.1.4 The interplay of parameters

The different situations resulting from the competition between the three parameters can be summarized with the ‘ternary diagram’ of Fig. 3.11, where the three summits correspond to the zone where a given interaction prevails.

In this chapter we shall study successively discrete systems; that is, systems with a limited number of electronic localization sites (generally studied in solution), and then extended solids.

For discrete systems the most typical examples involve two possible localization sites and just one exchangeable electron—for instance, two metallic sites with oxidation states differing by one unit. Thus the U parameter does not play any role, and the useful part of the diagram in Fig. 3.11 is the right one, showing the competition between V_{ab} and λ . There will be more or less electronic delocalization and mobility according to the relative values of V_{ab} and λ .

For extended systems the key experimental observable is conductivity, and thus the metallic, semi-conducting or insulating behaviour. Metallic conductivity occurs when V_{ab} is the dominant interaction, and standard band theory applies. In the mixed valence situation the role of U can be neglected because

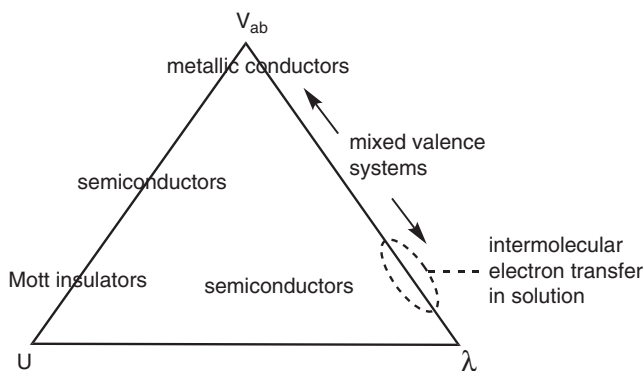


Fig. 3.11

Triangle representation of the competition between V_{ab} (or β), λ , and U (or j_0), with the consequences for the conductivity in solids.

the stoichiometry corresponds to less than one active electron per site, and the competition is between V_{ab} and λ , giving either a metallic or semiconducting character. In the homovalent situation, one cannot ignore U . When U predominates, the systems are called ‘Mott insulators’: despite the formation of incompletely filled bands, the energy cost for the electron to move from one site to another is too large, and the systems are not conducting. The fourth parameter, V , the two-centre repulsion energy, will play a role in Section 3.3.4.3 and will be commented on there.

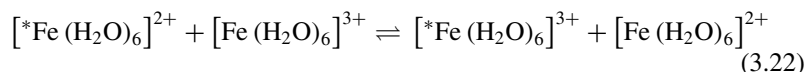
3.2 Electron transfer in discrete molecular systems

As a first step we will consider what happens in the transient association of two metal ions in different valence states. The electron transfer is then *intermolecular* and is generally studied in solution. As a second step we will study mixed valence compounds, where the two ions are permanently associated by a covalent link, so that the transfer is *intramolecular*.

3.2.1 Intermolecular transfer

3.2.1.1 Introduction

The simplest examples of intermolecular electron transfer are provided by self-exchange reactions, because they involve just one redox couple in which the reduced and the oxidized form exchange only one electron. The classical example is the following:

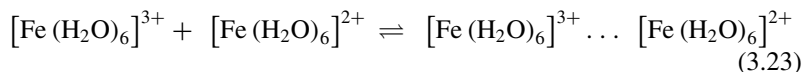


Since this reaction is accompanied by no net chemical change, one has to resort to special methods for monitoring, such as isotopic labelling, and here the * symbol designates a radioactive isotope of iron. Other methods, based on spectroscopy, are also possible (EPR, NMR, optical activity) [3.10]. Note that obviously, for such reactions the resulting free enthalpy change $\Delta G^\circ = 0$.

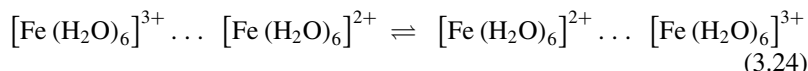
In the case of the $\text{Fe}^{3+/2+}$ system, discussed previously, the reaction is experimentally found second-order, with a rate constant of $1.1 \text{ mol}^{-1} \text{ l s}^{-1}$ at 25° C [3.3]. The activation energy is relatively high—greater than 50 kJ mol^{-1} [3.3, 3.11].

First of all, let us remark that the redox reaction between the $[\text{Fe}(\text{H}_2\text{O})_6]^{3+}$ and $[\text{Fe}(\text{H}_2\text{O})_6]^{2+}$ species must result from two consecutive processes:

- The association of reactants as an ion pair, with a very weak stability, as the ion charges are of same sign.



- The electron transfer reaction itself, with a first-order rate constant k_{et} :



If the first step is fast with respect to the second (fast pre-equilibrium situation), the overall rate constant is then given by:

$$k = K k_{\text{et}} \quad (3.25)$$

where K is the equilibrium constant of reaction (3.23). Expression (3.25) requires also that K be small, and this condition is fulfilled for ions bearing charges of the same sign. Throughout the rest of this chapter we shall concentrate on reaction (3.24), considered as the limiting step; that is, the one which determines the kinetics of the reaction.

The activation energy of electron transfer is due to the necessity of rearranging the internal and external coordination spheres, as shown in Section 3.1.2. The contributions of ΔE_{int} and ΔE_{ext} are frequently comparable, considering the following calculations. For the $[\text{Fe}(\text{H}_2\text{O})_6]^{3+} \dots [\text{Fe}(\text{H}_2\text{O})_6]^{2+}$ system, one has $d_{\text{II}} = 212$ pm, $d_{\text{III}} = 199$ pm, from reference [3.3], $k_{\text{II}} = 149$ N.m $^{-1}$, $k_{\text{III}} = 235$ N.m $^{-1}$ from reference [3.11], from which $d_{\text{m}} = 204$ pm, and finally $\Delta E_{\text{int}} = 27.8$ kJ.mol $^{-1}$. Regarding ΔE_{ext} , one has $a_{\text{A}} \approx a_{\text{B}} = 345$ pm, $R = 690$ pm, $\epsilon_{\text{s}} = 80$, and $\epsilon_{\text{op}} = 1.77$, leading to $\Delta E_{\text{ext}} = 27$ kJ.mol $^{-1}$. The total activation energy is then computed as $27.8 + 27 = 54.8$ kJ.mol $^{-1}$, close to the experimental value (57 kJ mol $^{-1}$) [3.11].

Remark: Later in this chapter we will assimilate ΔE and ΔG . There are indeed some justifications to such an approximation [3.11] [3.12] which is widely used in the literature: (i) in condensed phases, $\Delta E \approx \Delta H$, so the main problem is between ΔH and ΔG ; (ii) in the case of the solvent contribution, since the calculation deals with the macroscopic work of electrical forces, what is computed is actually ΔG , and in cases such as those referred to, this represents about 50% of the activation energy; (iii) the ΔS term is zero for symmetrical reactions such as exchange in eqn. (3.22). Nevertheless, the reactions with a strong ΔS° require a special adaptation of the theory.

The electron transfer is depicted in Fig. 3.12, which is a completed version of Fig. 3.9.

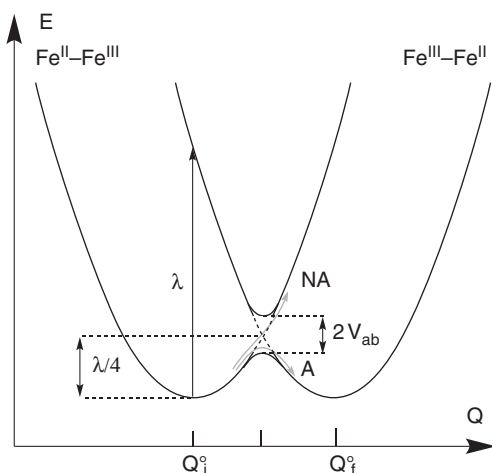


Fig. 3.12

Potential energy curves describing the electron transfer process, showing the avoided crossing with splitting $2V_{\text{ab}}$ in the central part. Two different trajectories are possible (grey arrows): in the adiabatic process (A) the system stays always on the lowest curve. In the non-adiabatic process (NA) it can go through the crossing zone while staying on the same initial potential energy curve (see also Fig. 2.85).

The activation process (see Fig. 3.12) consists in reaching the crossing zone of the $E = f(Q)$ curves. At the crossing point the geometrical structure is perfectly symmetrical, so that the electronic states are degenerate. However, due to the electronic interaction between the two electronic states, there is an ‘avoided crossing’ giving two new states with two new energies separated by $2 V_{ab}$ (see also Sections 1.6 and 2.8). In this section on intermolecular electron transfer, V_{ab} is small and the avoided crossing will not always be represented on the diagram. But it governs the possibility of electron transfer when reaching the central region.

One has to distinguish, indeed, two limiting cases (see Fig. 3.12): the ‘adiabatic’ case (A) when the system always stays on the lowest energy curve, and thus moves from one parabola to the other in the crossing region, and the ‘non-adiabatic’ case (NA) when the system remains on the initial (reactants) curve, so that no net electron transfer occurs. The calculation of the rate constant for step (3.24) must take into account these two eventualities. This will be performed in the following, using first two variants of a ‘semi-classical’ model, then a quantum model.

3.2.1.2 Rate in the semi-classical Marcus–Hush model

The simplest model is called ‘semi-classical’ because it is based on the concept of activation energy, itself computed with the previous expressions, into which enter only classical parameters (force and dielectric constants). The representative point of the system evolves on a potential-energy surface, and quantum aspects are introduced only in the activated complex zone. As will be shown in the following, there is a more rigorous but mathematically more cumbersome approach: the quantum model, in which quantum aspects are introduced from the beginning.

In the semi-classical model, the rate constant k_{et} of step (3.24) is computed from a variant of the activated complex theory:

$$k_{et} = \nu_n \kappa \exp\left(-\frac{\Delta G^\ddagger}{RT}\right) \quad (3.26)$$

where ΔG^\ddagger is assimilated to the total ΔE computed previously and ν_n is a nuclear vibration frequency. This is as an effective frequency taking into account both nuclear processes discussed previously [3.13, 3.14]:

$$\nu_n^2 = \frac{\nu_{ext}^2 \Delta E_{ext} + \nu_{int}^2 \Delta E_{int}}{\Delta E_{ext} + \Delta E_{int}} \quad (3.27)$$

This expression is indeed a weighted average based on the frequencies and reorganization energies associated with the intramolecular modes ν_{int} , ΔE_{int} (bond vibrations, typically 10^{13} sec^{-1}), and intermolecular, or external, modes ν_{ext} , ΔE_{ext} (solvent motion, typically 10^{12} sec^{-1}). A typical value for ν_n is $5 \cdot 10^{12} \text{ s}^{-1}$. ν_n can be seen as the number of times per second the system arrives in the crossing region. κ is the transmission coefficient; that is, the probability for the system to pass effectively from one parabola to the other, once in the curves’ crossing area (Fig. 3.12). As a matter of fact, reaching the crossing zone is not enough for the electron transfer to occur, because one needs in

addition that the two electronic states be connected by an electronic interaction. Think, for instance, what would happen if one metal site were on Earth and the other on the Moon: the system would still be described by a figure very close to 3.12(!), with a vanishingly small V_{ab} , but of course the rate of reaction would be immeasurably small! Thus κ can take any value between 0 and 1, depending on the electronic coupling occurring in the system.

Thus κ describes the possibility for an electron, initially localized on one site, to pass on the neighbouring site through empty space, or more generally through a region of high potential energy. This is an *electronic tunnel effect* (see also Sections 1.6 and 2.8), which should not be confused with the *nuclear tunnel effect*, evoked in the following (quantum model).

The theoretical treatment is generally based on Landau–Zener* formalism [3.15]: when the system, initially in the localized electronic state $\text{Fe}^{2+}\text{--Fe}^{3+}$ reaches the crossing zone, this state is no longer stationary. Calling ψ_A and ψ_B the wavefunctions describing respectively an electron localized on site A (initial state) and on site B (final state), the stationary wavefunctions now become, as a result of symmetry:

$$\psi_+ = 2^{-1/2}(\psi_A + \psi_B) \text{ and } \psi_- = 2^{-1/2}(\psi_A - \psi_B) \quad (3.28)$$

This is the origin of the avoided crossing in the energy diagram. The dynamic evolution can be described by a time-dependent wavefunction taking the form:

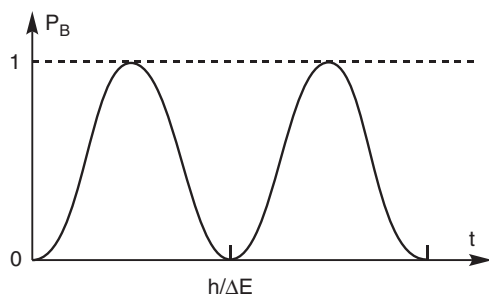
$$\psi(t) = c_+ \psi_+ \exp(-i E_+ t / \hbar) + c_- \psi_- \exp(-i E_- t / \hbar) \quad (3.29)$$

where E_+ and E_- are the energies of the (delocalized) stationary states, and c_+ and c_- are coefficients determined by initial conditions. The result is a beating process between the ψ_A and ψ_B states, with the frequency [3.16]

$$\nu = \Delta E / h, \text{ where } \Delta E = |E_+ - E_-| = 2 V_{ab} \quad (3.30)$$

Thus the system evolves periodically from the initial to the final state and *vice versa* (see Fig. 3.13). This behaviour is typical of any symmetrical two-state system when two equivalent states are coupled by some interaction.

Actually, this behaviour would be the real one if the nuclei were fixed exactly at a position corresponding to the intersection. But since the nuclei move rather than stay fixed, an irreversibility occurs; that is, there is a given probability for the system to evolve definitively from the electronic configuration of the reactants towards the one of the products. The net result depends on the amount of time the system stays in the crossing region. In fact, this is



*Although the name of Stückelberg is also associated to Landau and Zener in the case of magnetic properties (Section 2.8.1.3 and [2.66]), it is customary to quote only the first two names in electron transfer literature.

Fig. 3.13

Dynamic behaviour of a two-state system. P_B is the probability to find the system in state B, once it has been prepared in state A and allowed to evolve.

the same problem as encountered in Section 2.8.1.3 for Landau–Zener tunneling. The only difference is that in this earlier section the evolution along the abscissa could be controlled entirely by scanning the magnetic field H and its rate of change, while here the system evolves spontaneously by the effect of thermal motion. There is thus a probability P of conversion *per single passage* through the intersection, which is given by:

$$P = 1 - \exp\left(-\frac{4\pi^2 V_{ab}^2}{h v |s_A - s_B|}\right) \quad (3.31)$$

where s_A and s_B are the slopes of the surfaces in the intersection region ($s_A = -s_B$ for an exchange reaction), and v is the average velocity with which the system moves through the intersection region [3.11, 3.17]. One can note the analogy with eqn. (2.149).

The detailed calculation is more complicated because it must take into account multiple crossings and back transformations [3.11]. The complete treatment shows that κ , the true probability for electron transfer, is not equal to P but is given by:

$$\kappa = 2P / (1 + P) \quad (3.32)$$

The calculation can be continued by evaluating v by a Boltzmann averaged velocity, which introduces temperature into the model. The treatment, which is not detailed here, gives:

$$P = 1 - \exp\left(-\left(\frac{V_{ab}^2}{h v_n}\right) \left(\frac{\pi^3}{\lambda RT}\right)^{1/2}\right) \quad (3.33a)$$

where λ encompasses the two components of the activation energy [3.11]. Eqns. (3.26), (3.32), and (3.33a) allow the calculation of the rate constant in a range of situations, from adiabatic ($P \approx 1$, $\kappa \approx 1$) to strongly non-adiabatic ones (κ small, $\approx 2P$), where P is approximated by:

$$P = \left(\frac{V_{ab}^2}{h v_n}\right) \left(\frac{\pi^3}{\lambda RT}\right)^{1/2} \quad (3.33b)$$

A more ‘chemical’ derivation of this model has been proposed by Sutin *et al.* [3.13, 3.14], who define an ‘electronic frequency’, ν_{el} , which depends on the electronic coupling parameter V_{ab} :

$$\nu_{el} = \frac{2V_{ab}^2}{h} \left(\frac{\pi^3}{\lambda RT}\right)^{1/2} \quad (3.34)$$

Expression (3.34) takes into account the multiple crossings evoked previously [3.11, 3.17]. As a result, the electronic frequency is proportional to V_{ab}^2 , and not to V_{ab} as would be suggested by (3.30). Note that strictly speaking, ν_{el} is not a purely electronic factor, but encompasses nuclear parameters through the $(\lambda kT)^{1/2}$ denominator, because electronic and nuclear motions are intermingled. The final result for the probability κ , given in the following, reflects the competition between the electronic and the nuclear frequencies:

$$\kappa = \frac{2 [1 - \exp(-\nu_{el}/2 \nu_n)]}{2 - \exp(-\nu_{el}/2 \nu_n)} \quad (3.35)$$

Note the resemblance with eqn. (3.32). If $v_{el} \gg 2v_n$, then $\kappa \rightarrow 1$ (adiabatic limit). On the contrary, if $v_{el} \ll 2v_n$, then $\kappa \rightarrow v_{el} / v_n$. Once this value is reported in (3.26), the expression for the electron transfer rate becomes:

$$k_{et} = v_{el} \exp\left(-\frac{\Delta G^\ddagger}{RT}\right) \quad (3.36)$$

That is, the electron transfer rate is determined by the slowest process, the electronic frequency, itself proportional to V_{ab}^2 . This is the non-adiabatic limit, where κ is small, so that the electron transfer occurs rarely in the crossing region (see Fig 3.12). The full expression for k_{et} is then, from (3.34) and (3.36):

$$k_{et} = \frac{2V_{ab}^2}{h} \left(\frac{\pi^3}{\lambda RT}\right)^{1/2} \exp\left(-\frac{\Delta G^\ddagger}{RT}\right) \quad (3.37)$$

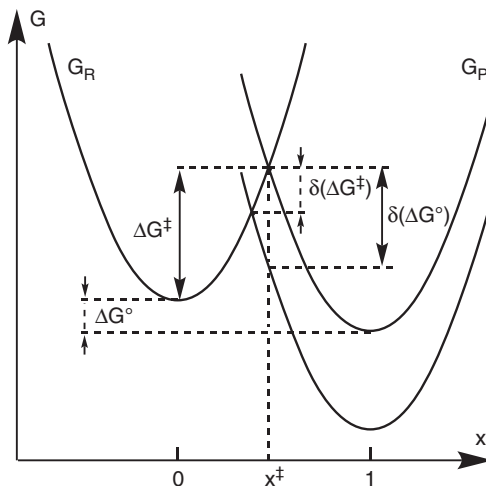
which could be also obtained from eqns. (3.33b), (3.32), and (3.26).

The semi-classical Hush–Marcus model is supported by a large amount of experimental data. Thus there is a clear relation between the self-exchange reaction rate and the parameters describing the internal reorganization—in particular, Δd (Table 3.1).

Note the remarkable case of the $[\text{Co}(\text{NH}_3)_6]^{3+/2+}$ system, with a particularly high Δd value, and thus an extremely low rate of reaction. This is due to the spin change from Co^{III} , $(t_{2g})^6$ ($S = 0$, ground term $^1A_{1g}$) to Co^{II} , $(t_{2g})^5(e_g)^2$ ($S = 3/2$, ground term $^4T_{1g}$) provoking a variation of two electrons in the population of e_g^* antibonding orbitals, and thus a high Δd . (A similar effect will be encountered in Section 4.5). The $[\text{Co}(\text{NH}_3)_6]^{3+/2+}$ system has been one of the most studied problems in electron transfer, because the process is frequently qualified as ‘spin-forbidden’. Actually this is a misnomer, since there is no change in the overall spin quantum number $S = 3/2$ for the complete system, and there are only local spin changes. The expected difficulty derives from the fact that three electrons are involved in the overall process, which raises the question of which occurs first: a local spin change or an electron transfer? It is now agreed that the electron exchange occurs via an excited state of Co^{II} , $(t_{2g})^6(e_g)^1$ ($S = 1/2$, 2E_g) which becomes more stable than the $^4T_{1g}$ state in the transition state region. Note that the activation energy has not been measured, due to the extreme sluggishness of the reaction. Only a theoretical estimation is given in Table 3.1. It is *lower* than one would expect for a direct mechanism without the $^4T_{1g}$ state. To summarize, it is now admitted that the spin-state change presents little intrinsic barrier to the electron transfer, and

Table 3.1 Parameters for self-exchange reactions [3.3] [3.18].

System	$\Delta d / \text{Å}$	$E_{act} / \text{kJ. mol}^{-1}$	$k / \text{mol}^{-1}.\text{s}^{-1}$	$\Delta S^\ddagger / \text{J. K}^{-1} \text{mol}^{-1}$
$[\text{Ru}(\text{bpy})_3]^{3+/2+}$	≈ 0	32	4×10^8	-28
$[\text{Ru}(\text{NH}_3)_6]^{3+/2+}$	0.04	43	6×10^3	-46
$[\text{Ru}(\text{H}_2\text{O})_6]^{3+/2+}$	0.09	46	20	-66
$[\text{Fe}(\text{H}_2\text{O})_6]^{3+/2+}$	0.13	46	1.1	-88
$[\text{Cr}(\text{H}_2\text{O})_6]^{3+/2+}$	0.20		$< 2 \times 10^{-5}$	
$[\text{Co}(\text{NH}_3)_6]^{3+/2+}$	0.22	> 68 (calc)	6×10^{-6} at 40°C (!)	

**Fig. 3.14**

Establishing Marcus cross-relation. G_R : reactants free enthalpy; G_P : products free enthalpy. Note that for a $\delta(\Delta G^\circ)$ change of the reaction free enthalpy, the activation free enthalpy changes by a smaller quantity $\delta(\Delta G^\ddagger)$, frequently one half of $\delta(\Delta G^\circ)$.

that its effect is essentially indirect, by inducing large structural differences between $[\text{Co}(\text{NH}_3)_6]^{3+}$ and $[\text{Co}(\text{NH}_3)_6]^{2+}$ [3.18].

The role of solvent on the reaction rate has been established clearly in the case of the $[\text{Cr}(\text{C}_6\text{H}_6)_2]^{+/0}$ system [3.19]. There is indeed a linear dependence of $\log k$ as a function of the Pekar factor $(1/\epsilon_{\text{op}} - 1/\epsilon_s)$.

We now consider the case of a 'true' chemical reaction, involving two different redox couples. The correlation with self-exchange rates of the two couples is due to Marcus. We start again from potential energy curves (Fig. 3.14), neglecting the avoided crossing, which is not necessary here. The potential energy curves of reactants (R) and products (P) are written respectively as:

$$E_R = A_R x^2 \quad (3.38)$$

$$E_P = A_P (1 - x)^2 + \Delta E^\circ \quad (3.39)$$

where x is a reaction coordinate describing in the same time the status of the internal coordination sphere, and the one of the solvent. The difference with the Q coordinate used in Section 3.1.2 is that now x is dimensionless, so that for $x = 0$ we have the nuclear configuration of reactants at equilibrium, while for $x = 1$ we have the configuration of products. This change in variables greatly simplifies the equations. ΔE° is the difference in energy between the relaxed reactants and products. As explained previously, we now identify all ΔE terms with ΔG [3.12].

A_R and A_P are constants characteristic of reactants and products respectively. In the following, they will be assumed equal and denoted as:

$$A_R = A_P = A \quad (3.40)$$

Finally, ΔG° will be assumed negative (products more stable than reactants). Thus to pass from the case of an exchange reaction ($\Delta G^\circ = 0$) to the case of a 'true' chemical reaction ($\Delta G^\circ < 0$), one has just to perform a vertical translation of the products curve with respect to the reactants curve.

It can be seen in Fig. 3.14 that the value of the reaction coordinate at the crossing point, x^\ddagger , is such that:

$$A x^{\ddagger 2} = A (1 - x^\ddagger)^2 + \Delta G^\circ \quad (3.41)$$

which leads to:

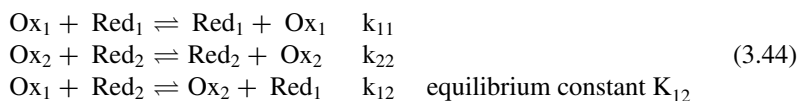
$$x^\ddagger = \frac{1}{2} \left(1 + \frac{\Delta G^\circ}{A} \right) \quad (3.42)$$

Introducing eqn. (3.42) into eqn. (3.38) yields the value of the activation free enthalpy:

$$\Delta G^\ddagger = \frac{1}{4} A \left(1 + \frac{\Delta G^\circ}{A} \right)^2 \quad (3.43)$$

In the case of an exchange reaction, $\Delta G^\circ = 0$, and thus $\Delta G^\ddagger = A/4$.

Let us consider now the two exchange reactions, and the corresponding redox chemical reaction:



One has:

$$\Delta G_{11}^\ddagger = A_{11}/4, \Delta G_{22}^\ddagger = A_{22}/4, \text{ and } \Delta G_{12}^\ddagger = \frac{1}{4} A_{12} \left(1 + \frac{\Delta G_{12}^\circ}{A_{12}} \right)^2 \quad (3.45)$$

The A_{ij} terms are determined by the rearrangements of the different species. Since the final reaction of eqn. (3.44) involves both couples, one can assume that:

$$A_{12} = \frac{1}{2} (A_{11} + A_{22}) \quad (3.46)$$

which leads to:

$$\Delta G_{12}^\ddagger = \frac{1}{2} \left(\Delta G_{11}^\ddagger + \Delta G_{22}^\ddagger \right) \left(1 + \frac{\Delta G_{12}^\circ}{2(\Delta G_{11}^\ddagger + \Delta G_{22}^\ddagger)} \right)^2 \quad (3.47)$$

Development of eqn. (3.47) leads to:

$$\Delta G_{12}^\ddagger = \frac{1}{2} (\Delta G_{11}^\ddagger + \Delta G_{22}^\ddagger) + \frac{1}{2} \Delta G_{12}^\circ + \frac{\Delta G_{12}^\circ{}^2}{8(\Delta G_{11}^\ddagger + \Delta G_{22}^\ddagger)} \quad (3.48)$$

In this expression the third term is usually small, because most common reactions are only weakly exoergic. Under these circumstances the free enthalpy of activation decreases as the reaction is more exoergic, with a linear dependence on ΔG_{12}° —a point to which we will return later.

Now, assuming the full adiabatic regime, and in the frame of activated complex theory, each rate constant can be written according to eqn. (3.26) with $\kappa = 1$. Taking the nuclear frequency factor ν_n as $(k_B T / h)$ (as usual in activated complex theories), and replacing ΔG_{12}° by $-RT \ln K_{12}$, one obtains, after some rearrangement:

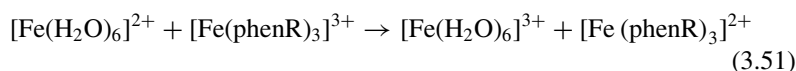
$$k_{12} = (k_{11} k_{22} K_{12} f)^{1/2} \quad (3.49)$$

where f is a corrective term given by:

$$\ln f = \frac{(\ln K_{12})^2}{4 \ln \left[k_{11} k_{22} / \left(\frac{k_B T}{h} \right)^2 \right]} \quad (3.50)$$

f is close to 1 for reactions with small ΔG° , which represent the majority of cases.

This constitutes the Marcus cross-relation [3.5, 3.20]. An experimental verification is possible at the level of eqn. (3.48), if one can vary the reaction ΔG° in an almost continuous way. This has been achieved with a series of reactions involving reactants of similar structures, for instance [3.21]:



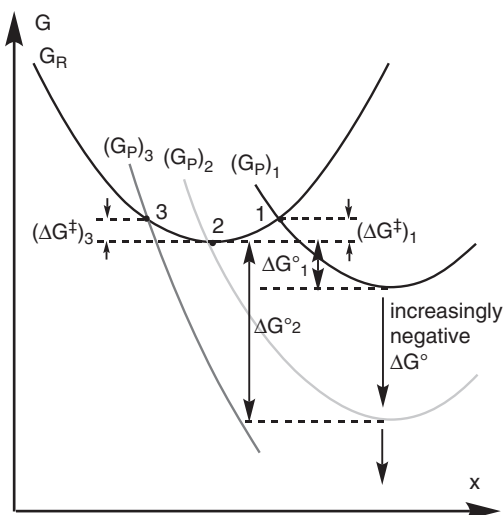
where phenR is an 1,10-phenanthroline ligand substituted by donor or acceptor groups. In this case, ΔG° can vary from -20 to -50 kJ mol^{-1} . The $\Delta G^\ddagger = f(\Delta G^\circ)$ curve is linear, with a slope very close to 0.5, [3.21] in agreement with eqn. (3.48) for small ΔG° . Note that this relation between ΔG° and ΔG^\ddagger can be found qualitatively from Fig. 3.14.

To end this section, we consider what happens when ΔG° has a large negative value. Then, from Fig. 3.15, it is clear that the activation energy must go to zero, and then increase again. Thus the rate of reaction must go through a maximum, and then decrease. This can also be established from eqn. (3.48), where the third term is no longer negligible. Such behaviour is contrary to intuition, because *the more the reaction is thermodynamically favoured, the slower it becomes*. This paradoxical prediction is termed 'Marcus inverted region behaviour'.

The decrease of reaction rates for highly exoergic reactions is more than an academic curiosity. It means that it is possible to store energy, at least

Fig. 3.15

Marcus inverted region. G_R and G_P represent the free enthalpy of reactants and products respectively. As ΔG° become more and more negative ($|\Delta G_1^\circ| < |\Delta G_2^\circ| < |\Delta G_3^\circ|$), the crossing point moves from 1 (G_P)₁, to 2 (G_P)₂ and then 3 (G_P)₃. For case 1 there is an activation free enthalpy $(\Delta G^\ddagger)_1$ (free enthalpy difference between the minimum of the G_R parabola and the crossing point with (G_P) ₁). For case 2 the activation free enthalpy is just zero (maximum rate). For case 3, $(\Delta G^\ddagger)_3$ increases again: this is the inverted region.



temporarily, and it has been soon suspected that it could be involved in the photosynthesis mechanism, where high-energy charge-separated species, created by the photon absorption, must not disappear too fast by an electron transfer back-reaction. However, the 'Marcus inverted regime', although predicted theoretically as soon as the end of the 1950s, was observed experimentally only from 1984 [3.5].

The study of highly exoergic reactions is indeed hampered by many difficulties. First, one has to generate extremely strong reductants or oxidants, hence very reactive, even in the inverted region, and whose existence is limited by the solvent electroactivity domain; that is, the range of redox potentials values for which side reactions with the solvent can be neglected. This point can be addressed by the transient generation of reactive species by either photochemistry or pulse radiolysis. But this is not enough. Since the studied reactions are still very fast, it is difficult to separate the electron transfer step *stricto sensu* from the previous step involving reactants encounter (see eqns. (3.23) and (3.24)). Thus several early attempts failed to observe the predicted decrease in rate constant, because people were actually measuring the reactant encounter step (eqn. (3.23)), which is diffusion-limited.

The problem could be solved only with the advent of studies involving an *intramolecular* electron transfer. The first well-characterized example was a biphenyl-steroid spacer-acceptor system (Fig. 3.16), in which the biphenyl moiety could be reduced radiolytically as an anion radical and could transfer its extra electron to the acceptor A through the steroid spacer [3.22]. Since then, many other series showing Marcus inverted behaviour have been identified, in compounds as diverse as proteins, reactive species generated in glasses, and inorganic complexes [3.5].

To give just one example, the photosynthetic reaction centre is a very complex protein, which is the siege of many successive electron transfer reactions, after the primary photochemical excitation. By proper modifications of amino acids of the structure, it has been possible to vary the ΔG° of some of these reactions, and to show that they occur in the inverted region [3.23].

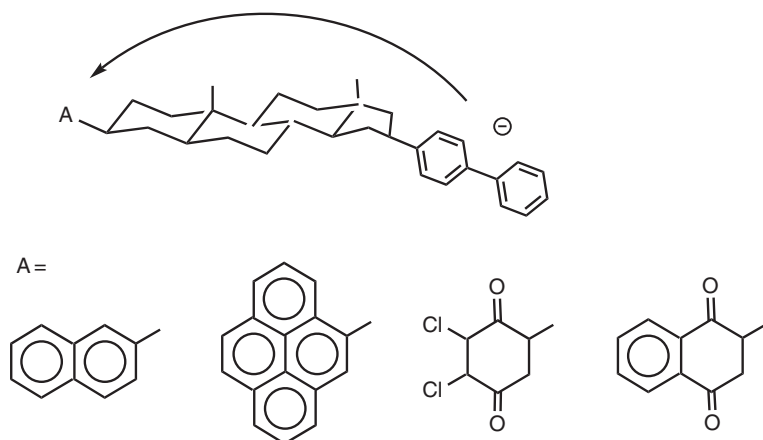


Fig. 3.16

The biphenyl-steroid spacer-acceptor series, showing for the first time Marcus inverted behaviour [3.22].

3.2.1.3 Quantum model

The previous semi-classical model (under its two variants) has the advantage of simplicity, and is prone to a pictorial representation in terms of displacements on potential energy curves. Unfortunately, reality is more complex. Many experimental results are not compatible with the concept of a constant activation energy, independent of temperature. In some cases [3.24], the rate at low temperature is greater than the value given by expression (3.26), and can even become *independent of temperature*, so that it does not vanish at 0 K (Fig. 3.17).

To describe this effect one must consider the possibility for the system to pass under the activation barrier. This necessitates taking into account explicitly the quantification of nuclear motions; that is, the existence of discrete vibrational levels. We thus consider that for each electronic configuration a or b (electron on site a or b respectively) there is a set of vibrational levels, solutions of the harmonic oscillator problem. The wavefunction describing the system is then the product of an electronic wavefunction, for instance Ψ_a^o , by a vibrational function Ψ_{aj}^v , where j is an index describing the vibrational state of configuration a.

Mathematically, the Hamiltonian describing the system can be written as:

$$H = H_0 + V \quad (3.52)$$

where H_0 corresponds to the two subunits without interaction, and V is the coupling term due to wavefunction overlap between the two sub-units. In the absence of interaction, $V = 0$, and the functions describing the system are of the form $\Psi_a^o \Psi_{aj}^v$ for the initial state (electron on a, and vibrational state j), and $\Psi_b^o \Psi_{bn}^v$ for the final state (electron on b, vibrational state n). Functions such as $\Psi_a^o \Psi_{aj}^v$ or $\Psi_b^o \Psi_{bn}^v$, which describe both the *vibrational* and *electronic* state of the system, are called *vibronic* functions.

Under the influence of V , the functions noted previously are no longer stationary. There can be an evolution from a $\Psi_a^o \Psi_{aj}^v$ level towards the $\Psi_b^o \Psi_{bn}^v$ level(s) of same energy. The electron transfer process can then be explained

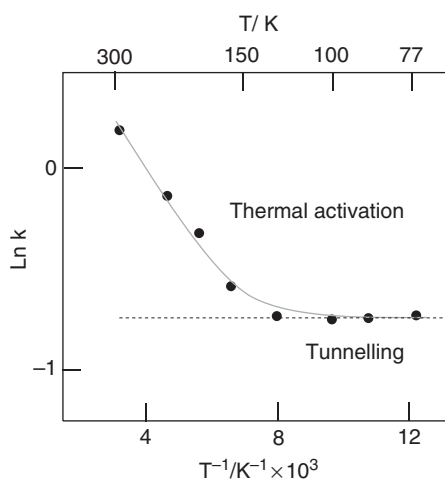
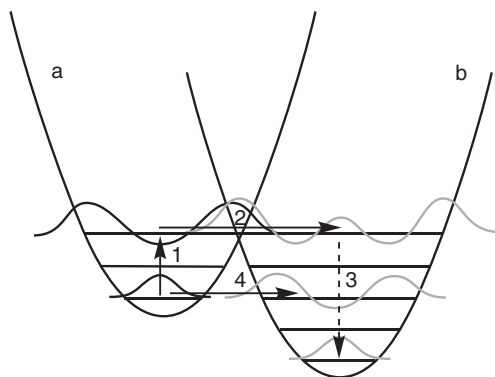


Fig. 3.17

An example of electron transfer reaction, the rate of which does not vanish at low temperature and displays instead a tunnelling effect. The reaction is a cytochrome c oxidation induced by flash photolysis. (Adapted from B. Chance *et al.* [3.24].)


Fig. 3.18

Quantum model showing the different vibrational levels associated with the initial (a) and final (b) configurations. There is electron transfer if the system evolves from one of the vibrational levels of 'a' (reactants) towards one of the levels of 'b' (products). The shape of the vibrational functions is shown for some levels only. Two types of process may occur, depending on conditions: i) at high temperature a thermal population of an excited vibrational level (1), followed by transfer in the crossing region (2) and finally vibrational relaxation (3); ii) at low temperature the transfer can occur only by direct nuclear tunnelling (4).

by the successive following steps: (i) fast Boltzmann equilibration between the different vibrational levels associated to the initial electronic configuration; (ii) passage from one of the vibrational levels associated with the initial electronic configuration towards the vibrational level of same energy belonging to the set of the final electronic configuration (this is the rate determining step); (iii) fast relaxation in the set of the final vibrational levels (see Fig. 3.18).

The rate of electron transfer is then given by the following general expression

$$k = \frac{2\pi}{\hbar} V_{ab}^2 \text{ (FCWDS)} \quad (3.53)$$

where FCWDS is the thermally averaged Franck–Condon weighted density of nuclear states. This expression comes from the so-called Fermi Golden Rule [3.25], which governs the rate of transition from a given initial state to a manifold of final states. For an elementary process such as evolving from the $\Psi_a^o \Psi_{aj}^v$ level towards one level of the other set, the Fermi Golden Rule states that the transition probability per unit time is given by:

$$k_{aj} = (2\pi/\hbar) V_{ab}^2 \rho_f(E_{bn}^o = E_{aj}^o) \quad (3.54)$$

where ρ_f designates the density of states for the final levels. ρ_f is a function of E_{bn}^o , the energy of the vibronic function of the product, defined by b and n, and we consider its value for $E_{bn}^o = E_{aj}^o$ to fulfil the requirement of electron transfer at constant energy.

The Fermi Golden Rule is a very general result, and will be encountered again in the treatment of energy transfer, in Section 4.4—in particular, eqn. (4.21).

In the present case, since we are concerned with a vibronic problem—that is, an interplay of electronic and nuclear factors—the density of states must be weighted by the nuclear Franck–Condon factors, *and* by thermal population. The Franck–Condon factors FC are of the form:

$$\text{FC} = \langle \Psi_{aj}^v | \Psi_{bn}^v \rangle \quad (3.55)$$

The moving electron: electrical properties

and thermal population is taken into account by the usual Boltzmann distribution factors for the reactants. Thus the FCWDS term is given by:

$$\text{FCWDS} = \frac{\sum_j \exp\left(-E_{aj}^0/kT\right) \langle \Psi_{aj}^v | \Psi_{bn}^v \rangle^2 \rho_f(E_{bn}^0 = E_{aj}^0)}{\sum_j \exp\left(-E_{aj}^0/kT\right)} \quad (3.56)$$

The final expression for the rate is thus [3.26]:

$$k = \frac{2\pi}{\hbar} V_{ab}^2 \frac{\sum_j \exp\left(-E_{aj}^0/kT\right) \langle \Psi_{aj}^v | \Psi_{bn}^v \rangle^2 \rho_f(E_{bn}^0 = E_{aj}^0)}{\sum_j \exp\left(-E_{aj}^0/kT\right)} \quad (3.57)$$

Inspection of the expression (3.57) leads to the following conclusions:

- The rate constant k is proportional to the square of V_{ab} , as in the non-adiabatic limit of the semi-classical treatment (eqn. (3.37)).
- Arrhenius' law is no longer followed: $\ln k$ is no longer a linear function of $1/T$, so that there is no more a constant, temperature-independent, activation energy.

Thus, the temperature dependence is now complicated, because the electron transfer can occur from levels of different energies. Transfer from the highest levels is favoured by the Franck–Condon overlap factor FC. The latter is optimal in the crossing area of the classical model (see Fig. 3.18), but this needs a temperature sufficiently high that the corresponding levels are thermally populated. This is a *thermally activated process*.

At very low temperatures the thermal population of these levels is not significant. The only possibility is then to pass directly from the lowest levels of the initial state towards a level of the final state. Since these levels have an energy *below* the top of the barrier, one has again a tunnel effect, but this is now a *nuclear tunnelling effect*, because the $E = f(Q)$ diagram involves nuclear coordinates. This is not to be confused with the *electronic tunnelling effect* (Section 3.1.1), which is already taken into account in the model through the V_{ab} parameter.

The nuclear tunnelling effect introduces into the global rate constant a component which is independent of temperature. This component always exists but is masked at high temperatures by the thermally activated process. Experimentally, the apparent activation energy, defined as:

$$E_{\text{act}} = -R \, d(\ln k)/d(1/T) \quad (3.58)$$

decreases at low temperature and tends towards zero, as observed in the case of the photochemical oxidation of cytochrome [3.27] (see Fig. 3.17).

A theoretical investigation of the model system $[\text{Fe}(\text{H}_2\text{O})_6]^{2+/3+}$ [3.11] has shown that at 300 K the transfer occurs essentially through the fifth excited vibrational level, the energy of which is close to the crossing point, in agreement with the classical concept of activation energy. On the contrary, at 100 K the reaction proceeds essentially through the lowest two vibrational levels, and thus occurs in the tunnel regime.

3.2.2 Intramolecular transfer: mixed valence compounds

Mixed valence compounds are, by definition, compounds containing the same element in different oxidation states. The existence of mixed valence was first noticed more than a century ago, due to their particular composition and their very specific properties such as additional colourations, as well as new electrical or magnetic properties [3.28]. In 1967, two simultaneous seminal articles (by Robin and Day, and also Allen and Hush) brought together the then available evidence [3.28b,c] and formulated the mixed-valence phenomenon with modern concepts. These articles laid the foundations for understanding the physical properties of such compounds and how the latter correlate with molecular and crystal structures.

The early recognized cases belonged to the solid state, typical examples being magnetite, Fe_3O_4 or Prussian blue. The extension of the mixed valence concept to *molecular systems* was triggered by the discovery, in 1969, of the Creutz-Taube complex $[(\text{NH}_3)_5\text{Ru-pz-Ru}(\text{NH}_3)_5]^{5+}$ (pz = pyrazine), which could be studied in solution [3.29]. This relatively simple compound raised in a particularly acute way the fundamental question of electron localization: since the overall charge is 5+ and the ligands are neutral, do we consider the ruthenium atoms as Ru^{2+} and Ru^{3+} , or two $\text{Ru}^{2.5+}$? Considerable efforts have been spent to address this question in the Creutz-Taube complex, and also in the large number of analogous compounds which have been synthesized since then. Figure 3.19 shows some other typical binuclear mixed valence systems,

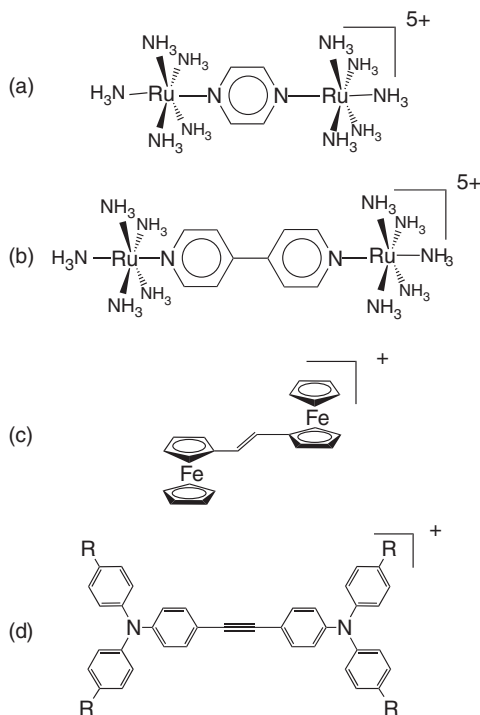


Fig. 3.19

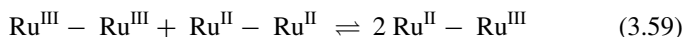
Examples of mixed valence compounds. (a) The Creutz-Taube complex; (b) another ruthenium binuclear system, with 4,4'-bipyridine as linker; (c) an organometallic bis-ferrocene system; (d) a purely organic mixed valence compound. These complexes contain formally a reduced site and an oxidized site. In case (d) the oxidized site is the whole triphenylamine moiety on one side.

and it can be seen that the phenomenon can be encountered not only in inorganic chemistry but also in organometallic chemistry and organic chemistry. Several reviews have gathered a large body of experimental and theoretical data over the last thirty years [3.13] [3.30].

We know now that the peculiar properties of mixed valence compounds arise from the possibility of electronic exchange, as in the ion pairs in solution noted in the previous paragraph. But with respect to the ion pairs, they exhibit two advantages: the permanent character of the association between the two redox centres, and the larger electronic coupling. However, before we deal with the electronic properties we have to look carefully at the circumstances under which mixed valence can form in solution—in particular, the thermodynamic and kinetic aspects.

3.2.2.1 Fundamentals: thermodynamic and kinetic aspects

Let us consider a homovalent binuclear complex of the symmetric type $[(\text{NH}_3)_5\text{Ru}^{\text{III}} - \text{L} - \text{Ru}^{\text{III}}(\text{NH}_3)_5]^{6+}$, where L is a neutral bridging ligand. We wish to prepare the mixed valence species resulting from the addition of one electron to the system—this addition resulting either from the action of a chemical reducing agent or from an electrochemical reduction. The two sites being identical, the addition of one equivalent of reducing agent does not guarantee the quantitative formation of the $\text{Ru}^{\text{II}} - \text{Ru}^{\text{III}}$ species; indeed, one can form, as well an equimolar mixture, $\text{Ru}^{\text{III}} - \text{Ru}^{\text{III}} + \text{Ru}^{\text{II}} - \text{Ru}^{\text{II}}$ corresponding to the same average oxidation state. Thus one has to worry about the situation of the comproportionation/disproportionation equilibrium:

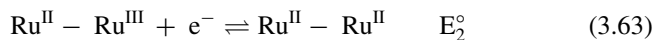
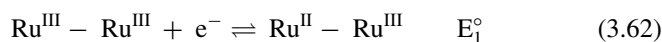


$$K_c = \frac{|\text{Ru}^{\text{II}} - \text{Ru}^{\text{III}}|^2}{|\text{Ru}^{\text{III}} - \text{Ru}^{\text{III}}| |\text{Ru}^{\text{II}} - \text{Ru}^{\text{II}}|} \quad (3.60)$$

Starting from this relation and from the law of conservation of matter, one can show that at half-reduction—that is, when one equivalent of reducing agent has been added per mole of binuclear complex—the proportion of mixed valence complex P is given by:

$$P = K_c^{1/2} / (2 + K_c^{1/2}) \quad (3.61)$$

In other respects, the K_c constant is linked to the difference between the two redox potentials relative to the equilibria:



with

$$(RT/F) \ln K_c = E_1^\circ - E_2^\circ \quad (3.64)$$

In principle, all K_c values are possible depending on the system. One observes, however, two general types of behaviour according to the nature of the bridge linking the metal atoms.

When the bridge is short enough, the two sites are in interaction and do not behave independently. This interaction arises from different effects [3.31], the main ones being:

- *The electrostatic effect* Reduction (*resp* oxidation) of one site consists in adding a negative (*resp* positive) charge, which renders the neighbouring site a little bit more difficult to reduce (*resp* oxidize). This effect is of *electrostatic* nature and thus depends on the distance between sites, and on the dielectric constant of the medium. A model taking into account the heterogeneity of the medium (composed of an intramolecular medium and of a solvent, with different local dielectric constants) has even been proposed.
- *The electronic effect* The partial delocalization from one site to another yields an extra stabilization (resonance energy). This phenomenon is of quantum nature and depends on the overlap between the different orbitals of the metals and of the bridge; it is more important for conjugated bridges, but can be neglected for saturated bridges.

In the vast majority of cases, this interaction, regardless its nature, makes E_1° markedly greater than E_2° ; that is, the reduction of the first site renders the second one more difficult to reduce. This is very analogous to the case of symmetrical diacids, such as H_2SO_4 or oxalic acid, for which pK_{a1} and pK_{a2} are different. As a consequence, the K_c constant is large and so is the proportion P of mixed valence compound at half-reduction. Finally if the difference $E_1^\circ - E_2^\circ$ is large enough, the reduction of the homovalent complex occurs by two distinct electrochemical processes, with the appearance of well-separated peaks in cyclic voltammetry. These conditions are, of course, favourable for the quantitative preparation of the mixed valence complex by partial reduction of the starting oxidized complex.

When the bridge becomes very long, the interactions of any nature between the metal sites vanish. Thus they behave independently, and simultaneously the $E_1^\circ - E_2^\circ$ difference becomes very small (but not null, as will be seen in what follows). Then one observes in cyclic voltammetry a single peak with a height corresponding to two electrons, which leads frequently to the erroneous conclusion that the reduction occurs by a direct two-electron process.



Actually this is not the case, as can be shown by the simple following demonstration. Let us consider a half-reduced solution. The sites being independent, each one has exactly one chance over two to exist as Ru^{II} , and one chance over two to exist as Ru^{III} . The proportion of homovalent derivatives is 25% for each of these species and 50% for the mixed valence species (this double proportion is explained by the fact that it can exist as $Ru^{III}-Ru^{II}$ or $Ru^{II}-Ru^{III}$). Putting into expressions (3.61) and (3.64), one obtains $K_c = 4$ and $E_1^\circ - E_2^\circ = 36$ mV. These values constitute the statistical limit.

Remark: Note the analogy with the case of symmetrical diacids, of the type $COOH-(CH_2)_n-COOH$, for which the ratio between acidity constants, which is the equivalent of the comproportionation constant, tends towards 4 (thus $pK_{a2} - pK_{a1} \rightarrow 0.6$) when n tends towards infinity.

Cyclic voltammetry

Cyclic voltammetry is an efficient way to study electrochemical processes. It consists in applying a triangular variation of potential to a stationary electrode. Starting from a reduced species (Red), if the applied potential increases and exceeds a given value, the current increases as a result of the onset of an electrochemical oxidation (Fig. 1). But, since the diffusion layer is not renewed, there is a depletion in electroactive substance near the electrode, so that the current passes through a maximum and then decreases. The major interest of the method is that the reaction product, the oxidized form (Ox), accumulates near the electrode, so that when the scan is reversed one can observe the electrochemical response of this form.

If the system is *reversible* (fast), one observes two peaks, located on both sides of the standard potential E° of the Red/Ox couple, with a separation ΔE_p given theoretically by $60/n$ mV, where n is the number of exchanged electrons.

If the system is *irreversible* (slow), the rate of the electrochemical reaction becomes noticeable only well after the standard potential E° , so that during the return scan one observes only the end of the oxidation process. The back-reduction of the formed product occurs then at a markedly different potential, located on the other side of E° (Fig. 1b).

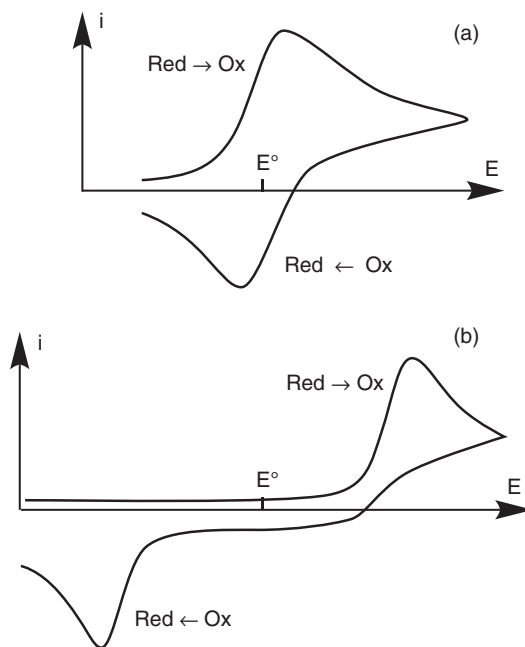
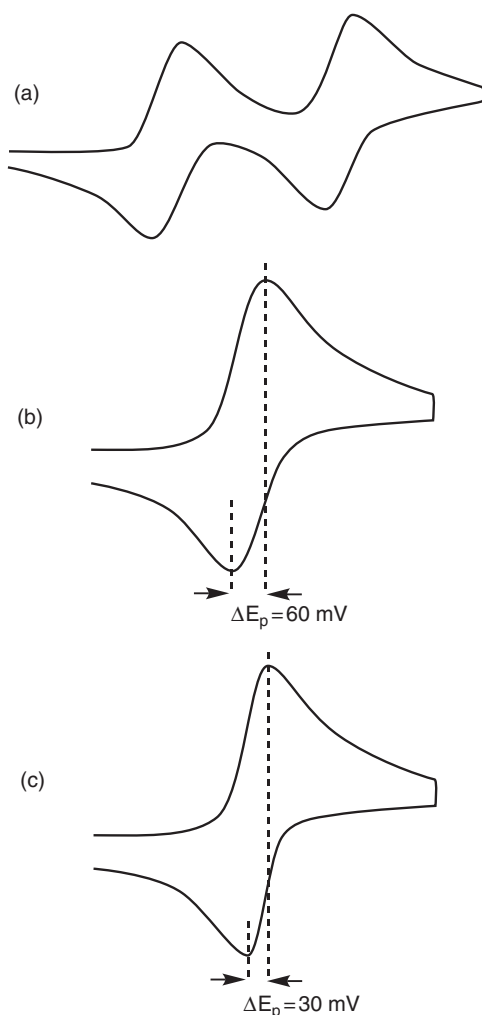


Fig. 1
Typical cyclic voltammetry curves for a fast (a) and slow (b) redox system.

Thus, even in this apparently unfavourable case, the proportion of mixed valence species still reaches 50%. From the point of view of electrochemistry, the height of the cyclic voltammetry wave corresponds to two electrons, *but the profile corresponds to one electron* (it will be, in particular, wider than a

**Fig. 3.20**

Cyclic voltammograms for several cases. (a) Two separated one-electron processes; (b) two one-electron processes occurring independently; (c) genuine two-electron process without intermediate. Note that the distinction between cases (b) and (c) relies only on the separation ΔE_p between anodic and cathodic peaks.

genuine two-electron wave, as shown in Fig. 3.20). Indeed, all happens as if one had a solution of mono-nuclear complex with a concentration twice the actual concentration in binuclear complex. The deconvolution of this wave in two one-electron waves has no meaning, the current additivity not being valid (see Box 'Cyclic voltammetry').

Thus in principle one can distinguish experimentally the case of 'two one-electron transfers between independent sites' from the case of 'direct two-electron transfer'. In practice, however, this distinction is difficult because it is based on the comparison of the curve profile in cyclic voltammetry, and particularly the separation ΔE_p between anodic and cathodic peaks, which is theoretically $60/n \text{ mV}$, where n is the number of exchanged electrons. This separation can be perturbed by other phenomena: the kinetics of electron transfer (if the transfer is not very fast, the ΔE_p gap is increased), and the uncompensated ohmic drop influence (which also increases ΔE_p).

Taking into account the previous considerations, one can ask the following question: can we have $K_c = 0$, or simply K_c below the statistical limit? This requires a particular mechanism, which ensures the following counter-intuitive behaviour: *the reduction (resp oxidation) of a site must make the neighbouring site easier to reduce (resp oxidize)*. First let us note that this is never observed for an extended bridge. For short bridges, such an effect may appear if the reduction process is accompanied by a chemical reaction or a structural rearrangement.

A last point to consider is the kinetic one. One could think that during the electrochemical reduction of a symmetrical complex presenting a weak interaction, it would not be possible to stop at the mixed valence stage, because this species, once formed, could immediately fix a second electron at almost the same potential. This is probably true at the electrode, but actually the totally reduced species diffuses towards the bulk solution where it reacts with the starting species to yield the mixed valence form according to the comproportionation reaction (3.59). The corresponding kinetics is generally very fast, as a consequence of the correlation established by Marcus between the rates of the electrochemical and chemical processes [3.32]. Thus, under usual conditions (working in solution at room temperature), the processes are driven by thermodynamics.

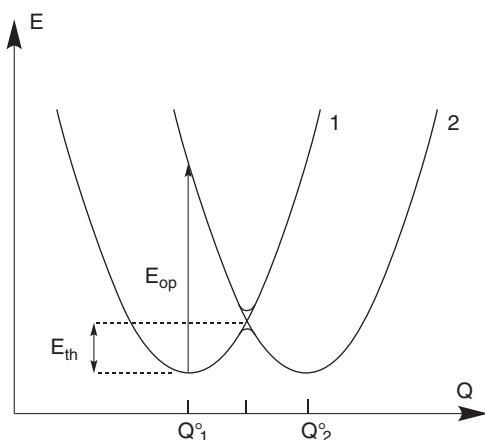
3.2.2.2 Thermal and optical transfers

A mixed valence compound is the equivalent of an ion pair as studied in Section 3.2.1, except that the two ions are connected by a covalent link. Thus the electron transfer is *intramolecular*. With respect to the ion pair case, the electronic coupling V_{ab} is stronger, which results in a larger splitting in the avoided crossing zone. However, as long as the electronic coupling is not strong enough, the lower potential energy curve still presents two minima. In the present paragraph we will assume that this condition is always fulfilled.

The stronger electronic coupling now makes possible a new phenomenon: an optical electron transfer (Fig. 3.21). In the diagram giving the potential energy as a function of the reaction coordinate, it is a transition qualified as ‘vertical’, because it occurs at constant nuclear coordinate, according to the Franck–Condon principle (see Chapter 4 on photophysics). During this transition one evolves from the potential energy curve related to one of the electronic configurations towards the other one, which corresponds indeed to an electron transfer. This transition is called ‘intervalence transition’, and it occurs at the energy λ defined previously.

Remark: Strictly speaking, this phenomenon is also possible in the case of ion pairs, but it is generally unobservable: first the electronic coupling is very weak and consequently the corresponding transition has a very low intensity (the intensity of the transition is discussed in Section 3.2.2.5), and secondly the effective ion pairs concentration is always very small.

There are thus two possible processes for electron transfer: a thermal one, with activation energy E_{th} , and an optical one (intervalence transition) with an energy $E_{op} = \lambda$. Due to the parabolic nature of the potential energy curves,

**Fig. 3.21**

The two types of electron transfer process in a mixed valence complex: thermal transfer and optical transfer. Labels 1 and 2 correspond to the two possible electronic states. The figure is the same as Figs. 3.9 and 3.12, but now λ corresponds to a real process. $E_{op} = \lambda$, and $E_{th} \approx \lambda/4$ if the avoided crossing can be neglected.

one has, for a symmetrical system when neglecting the avoided crossing effect, the very simple and popular relation:

$$\frac{E_{th}}{E_{op}} = \frac{1}{4} \quad (3.66)$$

Intervalence transitions are responsible for the colour of mixed valence species, which were first noticed more than a century ago [3.28]. Very often, the transition energy occurs in the 0.8–1.5 eV range, which corresponds to an absorption culminating in the red or the near infrared (with, in this last case, a ‘band-tail’ extending in the visible). As a consequence, mixed valence compound frequently exhibit a blue colour. Note that the energy of intervalence transitions is unusually small for electronic transitions. This derives from the fact that the fundamental state and the excited state are chemically equivalent, because in the case of a bimetallic mixed valence compound of ruthenium, one can write one state as $\text{Ru}^{\text{II}}\text{--Ru}^{\text{III}}$ and the other one as $\text{Ru}^{\text{III}}\text{--Ru}^{\text{II}}$. By contrast, a species such as $[\text{Ru}(\text{bpy})_3]^{2+}$ ($\text{bpy} = 2,2'$ -bipyridine) yields, after excitation, a state which can be written $[\text{Ru}^{\text{III}}(\text{bpy})_2(\text{bpy}^{\bullet})]^{2+}$, and is thus chemically very different from the ground state. Thus the transition involves a much larger energy (2–3 eV), as will be discussed in Chapter 4.

Historically, the first example of mixed valence species noted for its colour was the so-called Prussian blue, obtained as early as 1704, by grinding together animal wastes and sodium carbonate in iron pots. (Note that it was identified later as the first example of a coordination compound) [3.33]. We have already met this intriguing substance in Section 2.7.3 let us recall that it is a solid (during the preparation in solution, it is obtained as a colloidal suspension), and that it exhibits a cubic structure in which iron atoms are linked by cyanide ligands $\text{Fe}^{\text{III}}_4[\text{Fe}^{\text{II}}(\text{CN})_6]_3$, $\square_1 \cdot 15\text{H}_2\text{O}$, where \square denotes a $[\text{Fe}^{\text{II}}(\text{CN})_6]$ vacancy (see Fig. 2.76). Low-spin Fe^{II} atoms are in a carbon environment, while high-spin Fe^{III} atoms are surrounded by the nitrogen atoms of cyanide and by the oxygen of water molecules.

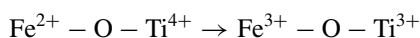
Note that, contrary to a common belief, the electronic structure of Prussian blue [iron(III) hexacyanidoferrate(II)] is the same, regardless of the method of

preparation; that is, either when $\text{Fe}^{3+}_{\text{aq}}$ is added to $[\text{Fe}^{\text{II}}(\text{CN})_6]^{4-}$ (method A), or when $\text{Fe}^{2+}_{\text{aq}}$ is added to $[\text{Fe}^{\text{III}}(\text{CN})_6]^{3-}$ (method B). The electronic structure agrees with method A. When the preparation is made by method B, a fast intramolecular electron transfer occurs to produce the same stable distribution of oxidation states [iron(III) hexacyanidoferrate(II)]. This final electronic structure has been proved by a number of physical methods, among which, Mössbauer spectroscopy produced the decisive arguments [3.34]: two absorptions with isomeric shifts characteristic of ferric ions and ferrocyanide were indeed observed.

The basic dinuclear unit necessary to understand the mixed valence properties is depicted in Fig. 3.22.

The deep blue colour of Prussian blue is due to an intervalence transition occurring at $14,100 \text{ cm}^{-1}$ [3.35, 3.28b]. The transition is very intense ($\epsilon \approx 10,000 \text{ L mol}^{-1} \text{ cm}^{-1}$ for the colloidal dispersion), and corresponds as a first approximation to the transfer of one t_{2g} electron of a Fe^{II} site to a t_{2g} orbital of the nearby Fe^{III} site. The two orbitals are indeed strongly overlapping through the bridging CN^- ligand. Actually, matters are a little more complicated, since each Fe^{II} is surrounded by six Fe^{III} ions. Thus the electron is actually transferred on a *linear combination of Fe^{III} t_{2g} orbitals* taking into account the symmetry of the system [3.28b]. From a practical point of view, since Prussian blue is extremely stable and non-toxic (ferrocyanide is very stable and inert), it has been for centuries one of the most-used blue pigments for painting, dyeing, decoration, and eye make-up, and is still in use by artists.

Many minerals exhibit colours due to intervalence transitions. (We quote them here, though they are more solid-state systems than molecular ones, because the short-range description of the mixed valence compounds is also applicable locally to three-dimensional solids). One can cite vivianite $\text{Fe}_3(\text{PO}_4)_2$, which contains theoretically Fe^{2+} , but the latter is always contaminated by a small amount of Fe^{3+} . In particular, a freshly cleaved crystal turns blue in air at the break. Some precious minerals (sapphire, beryl, garnet) also illustrate the mixed valence effect. Thus some blue sapphires are made of Al_2O_3 with a substitution of two Al^{3+} by Fe^{2+} and Ti^{4+} [3.36]. The colour is then due to the heteronuclear intervalence electron transfer:



Incidentally, the colour of sapphires can be modified by suitable oxidizing or reducing treatments.

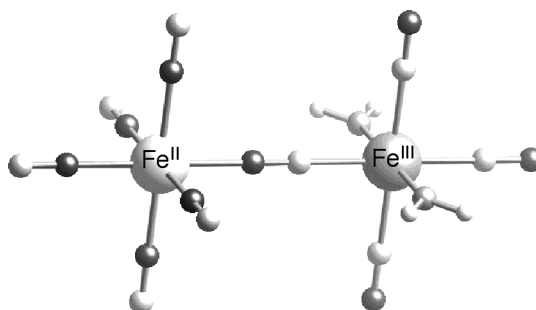
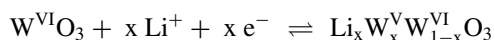


Fig. 3.22

Ball-and-stick representation of the binuclear unit $(\text{NC})_5\text{Fe}^{\text{II}}-\text{CN}-[\text{Fe}^{\text{III}}(\text{NC})_3(\text{H}_2\text{O})_2]$, part of the Prussian blue structure depicted in Fig. 2.76. Large balls: Fe^{II} (white), Fe^{III} (grey). Small balls: carbon (black), nitrogen (white), oxygen (grey). Two water molecules are bound to Fe^{III} .

In some cases the composition can be manipulated by an electrochemical process. This is in particular the case for tungsten bronzes, which can be generated at an electrode by the following reaction:



This converts the yellow WO_3 oxide into a blue tungsten bronze, with the possibility of realizing an electrochromic display device (Fig. 3.23) [3.37].

Blue colours, or more generally additional absorptions, are also encountered in partly reduced polyoxometallates, which are molecular compounds, but whose structure can be considered as oxide fragments. The more typical are of general formula $[\text{XM}_{12}\text{O}_{40}]^n$, $\text{X} = \text{Si}, \text{P}$, and so on . . . $\text{M} = \text{Mo}, \text{W}$ (for instance, the so-called Keggin structure) [3.38]. Once partly reduced, these species indeed present a coexistence of oxidation states VI and V for Mo or W. Their blue colour has been noted since 1826 and used for analytical purposes.

Mixed valence is also encountered in purely organic compounds (see example (d) in Fig. 3.19), in molecules bearing at least two groups able to undergo a 1-electron reduction or oxidation. Such redox groups can be triarylamines, triphenylmethane radicals, TTF units (TTF = tetrathiafulvalene), hydrazyl groups, and so on, and are generally linked by conjugated spacers [3.39]. The same basic processes as in inorganic mixed valence systems are observed—in particular, intervalence transitions. The main difference, however, is that there is more delocalization of the electron (or hole) on the molecular redox site. For instance, when a ruthenium redox group is oxidized the oxidation bears essentially on the ruthenium atom, while when a triarylamine redox site is oxidized the electron is taken out of an orbital with some weight on the nitrogen atom, but importantly tails on the adjacent groups (Fig. 3.24). This does not change the general behaviour, but complicates the quantitative analysis of the processes.

We shall see in Section 3.3 that the mixed valence formalism is also used to describe some molecular conducting solids.

3.2.2.3 The different classes of mixed valence compound

So far we have implicitly considered systems for which the electronic coupling is small. But actually, mixed valence compounds present a wide variety of behaviours according to the degree of mixing between the two electronic states. A very convenient, and still frequently used, classification was proposed in 1967 by Robin and Day [3.28b]. They distinguish three classes.

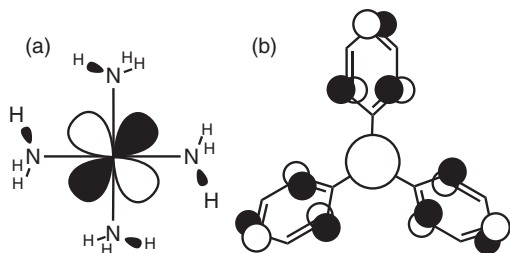


Fig. 3.23

Rear-view mirror equipped with a device using an electrochromic thin layer. (Information available at <http://mito-auto.com/> and <http://www.genlex.com/automotive/mirror-module>)

Fig. 3.24

Comparison of the delocalization in (a) a $\text{Ru}(\text{NH}_3)_5$ redox group, and (b) a triphenylamine redox group. The sketch shows the shape of the orbital in which an electron has been removed upon oxidation. In (a) the orbital is mainly localized on Ru (d_{xy}), with a very small admixture of σ orbitals of NH bonds. For (b), the main contribution comes from the $p\pi$ orbital of N (only one lobe visible since the drawing is along the C_3 axis), but important contributions are found on the phenyl rings (two lobes visible for each atomic orbital since the phenyl rings adopt a propeller shape). The notion of redox site is more difficult to define in case (b).

Class I. The properties (spectroscopic, magnetic, and so on) are simply the sum of the properties of constituent ions. This corresponds to the case where the electronic interaction is null or very weak.

Class II. The properties are those of constituent ions, who keep a certain individuality, but in addition new properties are observed. These new properties are generally colouration (due to intervalence transitions), and conducting properties in the case of extended systems. Here the electronic interaction is moderate.

Class III. The properties are entirely new, and one does not recognize the contributions of constituent ions. This last case corresponds to a very strong electronic interaction.

We now have to specify what is meant by weak, moderate, or strong interaction. The Robin–Day classification was initially qualitative, but later a rigorous formulation has allowed quantitative definitions [3.40]. Class I systems constitute a limiting case with few interest, and the more pertinent is the distinction between classes II and III. For that we consider a symmetrical two-site system (Fig. 3.25) presenting initially a very weak interaction. If the electronic interaction parameter V_{ab} increases, the splitting of the curves increases in the avoided crossing zone, and the central bump of the lowest curve in the $E_{\text{pot}} = f(Q)$ diagram finally disappears, so that the lowest potential energy curve present only

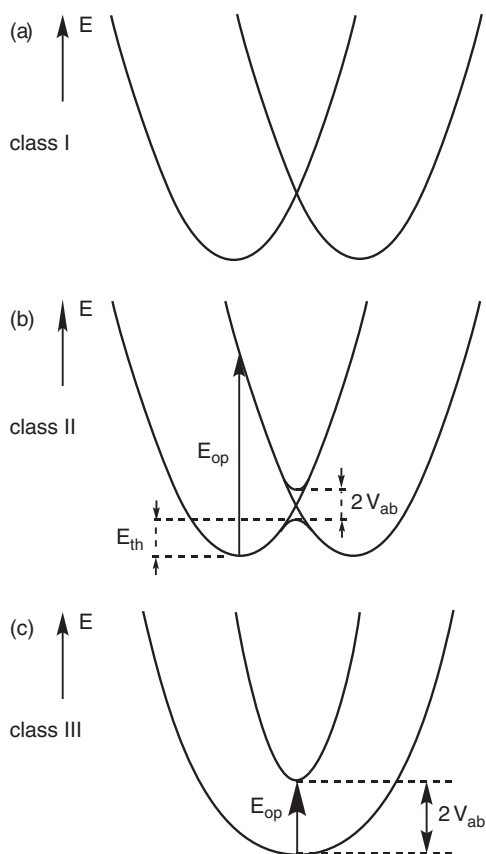


Fig. 3.25

Potential energy curves for the three classes of mixed valence compounds. (a) Class I, weak or null electronic interaction; (b) class II, moderate electronic interaction retaining the existence of two minima; (c) class III, strong electronic interaction making the activation barrier to disappear.

one minimum. We then define as class II the systems described by a curve of the type displayed in Fig. 3.25b, and as class III those displayed on 3.25c.

The evolution from one type to the other can be analysed by the following calculation, adapted from [3.40]. We consider a system made of two sub-units A and B, able to adopt oxidation states II and III (for instance, Ru^{II} and Ru^{III}). One of the electronic configurations is for instance $\text{A}^{\text{II}}\text{-B}^{\text{III}}$ and the other $\text{A}^{\text{III}}\text{-B}^{\text{II}}$. If there is no electronic interaction between these states they can be described by quadratic curves (see Section 3.1.2), and by wavefunctions ψ_a and ψ_b , and we can write their energies E_a for $\text{A}^{\text{II}}\text{-B}^{\text{III}}$ and E_b for $\text{A}^{\text{III}}\text{-B}^{\text{II}}$ as:

$$E_a = \lambda (x + 1/2)^2 \quad (3.67a)$$

$$E_b = \lambda (x - 1/2)^2 \quad (3.67b)$$

In these expressions we use again an adimensional x coordinate, as in eqns. (3.38) and (3.39), but now, to respect the symmetry of the problem, the minima of the curves are located at $x = 1/2$ and $x = -1/2$, instead of 0 and 1. λ is the vertical reorganization energy, corresponding to the intervalence band (see Fig. 3.26).

We now introduce the electronic interaction β between these two electronic states. This leads to new energies, which are obtained by diagonalizing the energy matrix.

β is the electronic interaction parameter, which can be positive or negative, as seen in Section 3.1.1. It mixes the two electronic states, and thus favours delocalization. On the other hand, λ encompasses all effects leading to localization; that is, the rearrangement of the internal coordination sphere, network vibrations (phonons) and of the solvent, when in solution. Following the general variational method, the eigenvalues of the energies are obtained by putting to zero the determinant:

$$\begin{vmatrix} \lambda(x + 1/2)^2 - E & \beta \\ \beta & \lambda(x - 1/2)^2 - E \end{vmatrix} = 0 \quad (3.68)$$

This leads to the following secular equation:

$$E^2 - E\lambda(2x^2 + 1/2) + \lambda^2(x^2 - 1/4)^2 - \beta^2 = 0 \quad (3.69)$$

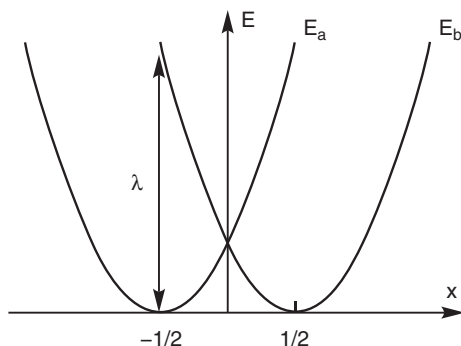


Fig. 3.26

Definitions of the parabolae for electronic states $\text{A}^{\text{II}}\text{-B}^{\text{III}}$ (E_a) and $\text{A}^{\text{III}}\text{-B}^{\text{II}}$ (E_b) before electronic interaction.

the solutions to which are:

$$E = \lambda (x^2 + 1/4) \pm (\lambda^2 x^2 + \beta^2)^{1/2} \quad (3.70)$$

The corresponding wavefunctions (unnormalized) are given by:

$$\psi_1 = - \frac{-\lambda x + (\lambda^2 x^2 + \beta^2)^{1/2}}{\beta} \psi_a + \psi_b \quad (3.71a)$$

$$\psi_2 = - \frac{-\lambda x - (\lambda^2 x^2 + \beta^2)^{1/2}}{\beta} \psi_a + \psi_b \quad (3.71b)$$

Thus for $x = 0$ (central part of the diagram in the avoided crossing zone), the wavefunctions are, after normalization, and if $\beta < 0$:

$$\psi_1 = 2^{-1/2} (\psi_a + \psi_b) \quad (3.72a)$$

$$\psi_2 = 2^{-1/2} (-\psi_a + \psi_b) \quad (3.72b)$$

Energies and a sketch of wavefunctions are given in Fig 3.27 for the most interesting case, a class II system, assuming that the redox sites are transition metal ions intervening by their d orbitals.

For $x = -1/2$, bottom of the left parabola, and for $|\beta| \ll \lambda$ one finds (unnormalized wavefunctions):

$$\psi_1 \approx -(\lambda/\beta)\psi_a + \psi_b \quad (3.73a)$$

$$\psi_2 \approx (\beta/\lambda)\psi_a + \psi_b \quad (3.73b)$$

so that the wavefunctions ψ_1 and ψ_2 are dominated by ψ_a and ψ_b respectively. The converse is true for $x = 1/2$. A better formulation for ψ_1 , giving symmetrical expressions for ψ_1 and ψ_2 , is:

$$\psi_1 \approx -\psi_a + (\beta/\lambda)\psi_b \quad (3.73c)$$

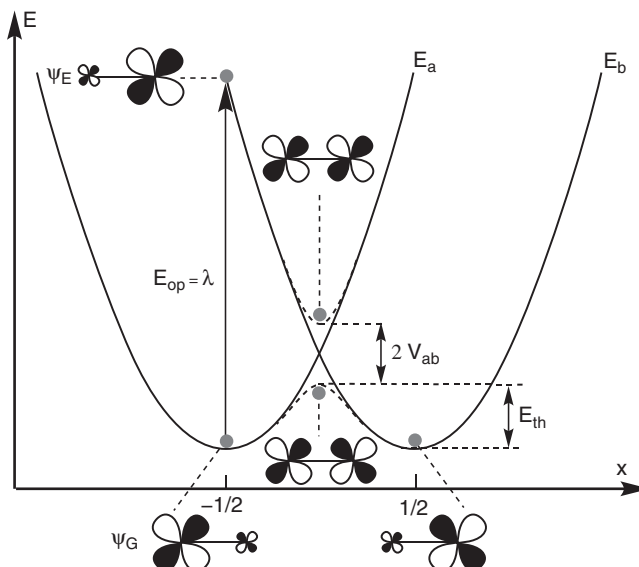


Fig. 3.27

Curves $E = f(x)$ before (plain) and after (dashed) taking into account the electronic interaction (V_{ab} parameter). The displayed case corresponds to class II. Sketches of the molecular orbitals involved in the different states are also given, neglecting any contribution from the bridging ligand. The optical intervalence transition ($E_{op} = \lambda$) from the ground-state function Ψ_G to the excited state one Ψ_E is also shown at $x = -1/2$. Ground and excited states are centred on A and B respectively.

showing that a key parameter is the ground-state delocalization coefficient δ ($\ll 1$), defined as:

$$\delta = |\beta|/\lambda = V_{ab}/\lambda \quad (3.73d)$$

Thus, for $x = \pm 1/2$ one clearly sees the charge transfer nature of the optical transition.

When V_{ab} increases, the lowest potential energy curve evolves from a two-minima curve towards a one-minimum curve. We call these situations class II and class III respectively. There is thus a simple mathematical criterion to define these classes: taking the derivative of the lowest potential energy curve (eqn. (3.70) with the $-$ sign), we obtain:

$$dE/dx = 2\lambda x - \lambda^2 x (\lambda^2 x^2 + \beta^2)^{-1/2} \quad (3.74)$$

This expression vanishes for $x = 0$ in all cases, and also for:

$$x = \pm \left(\frac{\lambda^2 - 4\beta^2}{4\lambda^2} \right)^{1/2} \quad (3.75)$$

which is possible only if $|\beta| < \lambda/2$.

The nature of the compound thus depends upon the competition between the electronic coupling, favouring delocalization, and the reorganization energy, favouring localization. For $|\beta| < \lambda/2$, one has a class II compound, and conversely for $|\beta| > \lambda/2$ a class III compound.

As long as the system is class II, the energy of the optical transition is λ (note that it does not depend at all on V_{ab}). The activation energy for the thermal process is given by:

$$E_{th} = \lambda/4 - |\beta| + \beta^2/\lambda \quad (3.76)$$

When $|\beta|$ (V_{ab}) is small, one recovers the classical relation $E_{th} = \lambda/4 = (1/4)E_{op}$. When $|\beta|$ increases while remaining small, the activation energy decreases in first approximation by the quantity $|\beta|$. But due to the second-order term in eqn. (3.76), the barrier disappears for $|\beta| > \lambda/2$, and not for $|\beta| > \lambda/4$, as could be anticipated from a naïve reasoning.

When the compound is class III there is no longer any conceivable thermal process, since the system is intrinsically delocalized. But the optical transition is still present, at an energy $2|\beta|$. In this case the optical transition corresponds to a transition between a fundamental state described by a wavefunction such as eqn. (3.72a) and an excited state such as eqn. (3.72b). Thus the charge transfer character of the transition has disappeared, since these two functions are equally distributed on the subunits A and B. However, it is in this case that the electronic transition presents the highest intensity (see Section 3.2.2.5).

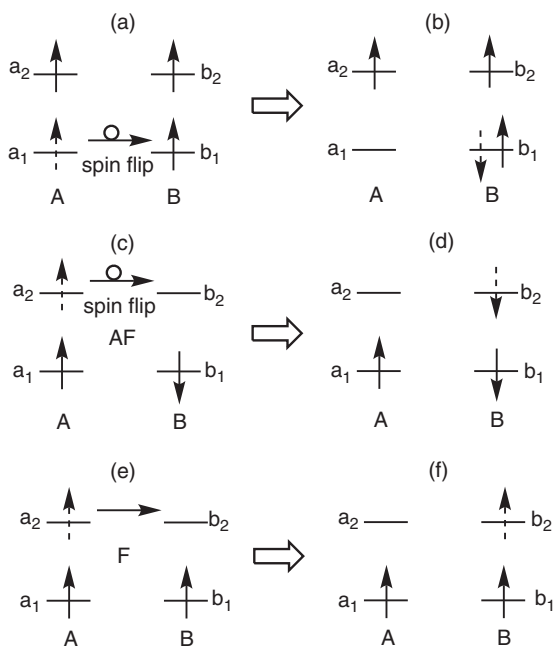
Remark: The previous model is similar to the semi-classical model used in Section 3.1.2, because it is based on the shape of potential energy curves, and does not take into account the quantification of nuclear motions. A vibronic model exists (the PKS model, [3.40]), which is more complete but mathematically more complex, and its study is outside the scope of this book.

3.2.2.4 Magnetic mixed valence systems

We now consider systems where the two subunits A and B bear magnetic moments [3.41]. The typical example is provided by the $\text{Fe}^{\text{II}}\text{-Fe}^{\text{III}}$ system, where Fe^{II} and Fe^{III} are both high-spin. Until now (see Section 3.2.1) this system has been treated in a simplified way, by just introducing an electronic interaction between the system states $\text{Fe}^{\text{II}}\text{-Fe}^{\text{III}}$ and $\text{Fe}^{\text{III}}\text{-Fe}^{\text{II}}$. But actually there are two effects in such a system: the magnetic exchange interaction and the electronic interaction (this term designating the one which is responsible of electron transfer). If the electronic interaction were zero the energy levels on each subunit would be described by a Heisenberg Hamiltonian $\mathbf{H} = -J \mathbf{S}_{\text{Fe}^{\text{II}}}\cdot\mathbf{S}_{\text{Fe}^{\text{III}}}$, with $S_{\text{Fe}^{\text{II}}} = 2$ and $S_{\text{Fe}^{\text{III}}} = 5/2$ S. This would give a spin-energy diagram $E(S)$ with states ranging from $S = 1/2$ to $S = 9/2$ and energies $E_{1/2} = -3 J/8$, $E_{3/2} = -15 J/8$, $E_{5/2} = -35 J/8$, $E_{7/2} = -63 J/8$, $E_{9/2} = -99 J/8$. The spin $S = 1/2$ or $9/2$ are the ground states according to the sign of J (see Fig. 3.29a,b, commented on later). Since there are two possible electronic configurations, $\text{Fe}_A^{\text{II}}\text{-Fe}_B^{\text{III}}$ and $\text{Fe}_A^{\text{III}}\text{-Fe}_B^{\text{II}}$, we have actually degenerate levels, which can be coupled by the electronic interaction.

To introduce useful definitions and formalism, let us consider a simpler system with two equivalent sites A and B, having each two kinds of orbitals a_1 and a_2 on A or b_1 and b_2 on B (a_1 and a_2 having different symmetry, $a_1 = b_1 = d_{x^2-y^2}$ and $a_2 = b_2 = d_{z^2}$, for example). The orbitals can be occupied by zero, one, or two electrons. If there is one electron per orbital, the most stable situation on each site is a $S = 1$ triplet state $a_1\alpha a_2\alpha$ and $b_1\alpha b_2\alpha$ for $M_S = +1$, and the other configurations for $M_S = 0$ and $M_S = -1$, because the on-site exchange interaction between the orthogonal orbitals a_1 and a_2 , or b_1 and b_2 is ferromagnetic. The local triplet state on A (and B) is stabilized by the exchange integral k between a_1 and a_2 (and b_1 and b_2) (see Sections 2.5.2 and 2.6.1) (Fig. 3.28a). Then the coupling between spins $S = 1$ on sites A and B to give the total spin S_T can be antiferromagnetic ($S_T = 0$ ground state), inexistent (two independent spin $S = 1$), or ferromagnetic ($S_T = 2$), depending on the overlap between the two sites. This four-electrons case with four singly occupied orbitals is not at all favourable to electron transfer, since it would imply not only a forbidden flip of the transferred electron—according to the Pauli principle—but also a strong one-centre two-electron repulsion U , due to the presence of two paired electrons in the same orbital leading to an highly excited state (Fig. 3.28b).

We shall learn much more from the case where the preceding system contains only three electrons and is mixed valence (Fig. 3.28c–f). On site A we have a triplet, spin $S = 1$, and on site B we have a doublet, $S = 1/2$. As previously, without electron transfer (electrons localized on sites A and B), we can have either no interaction (independent spins $S = 1$ and $S = 1/2$), antiferromagnetic AF interaction (Fig 3.28c, resulting spin $S_T = 1/2$), or ferromagnetic F interaction (Fig 3.28e, resulting spin $S_T = 3/2$). In the presence of electron transfer we have the two situations of Fig. 3.28d and f. In configuration (d) (antiferromagnetic interaction) the transferred electron has accomplished a spin flip (the on-site exchange interaction is much larger than the electronic interaction $|\beta|$), whereas in case (f) (ferromagnetic interaction) the transferred electron has kept its spin: we can qualitatively conclude that the electron transfer favours the ferromagnetic interaction and the high-spin ground state

**Fig. 3.28**

Spin configurations of two equivalent sites A and B with two different orbitals a and b, before electron transfer (left) and after electron transfer (right). The transferred electron is depicted by a dashed arrow. (a) Four unpaired electrons in four orbitals leading to (b) a highly excited state after electron transfer; (c–f) three-electron system with antiferromagnetic AF interaction (c–d) and an $S = 1/2$ ground state (c) and with a ferromagnetic F interaction (e–f), stabilizing an $S = 3/2$ ground state by electron transfer.

$S_T = 3/2$, in contrast to the localized electrons situation with a ground spin state $S_T = 1/2$. The system gains more delocalization energy when the two spins are parallel than when they are antiparallel. This spin dependence of the electron transfer process has been called ‘double exchange’ (Anderson [3.42]) or ‘spin-dependent delocalization’ (Kahn [3.43]). The physical reason of the larger delocalization for the highest spin state is that the transferable electron can move from one site to the other without spin flip, and the system gains exchange energy when there are many parallel spins (see Fig. 3.28).

The problem is simple only in appearance. It has been quantitatively tackled by many researchers: Zener, Anderson, Girerd, the Kishinev school, Malrieu, and their coworkers [3.42–3.45], among others, and the interaction model has been successively refined during the past sixty years. The following treatment describes, in a very simplified way, the approach proposed by Girerd [3.41].

It starts by the definition of a *complete electrostatic* Hamiltonian \mathbf{H}_R between orbitals on the two sites, including electron kinetic energy, electron attraction by nuclei, and electron–electron repulsion, since the exchange phenomenon (spin) and the electron transfer are both electrostatic in origin (see Sections 2.5.2 and 2.6.1 for exchange, and Section 3.2.1 for electron transfer). This complete Hamiltonian \mathbf{H}_R is quite heavy to manipulate, and it is wise to seek a simplified model Hamiltonian, keeping, if possible, the most important features of the problem. The approximations chosen to define the model Hamiltonians and the subsequent treatments lead, of course, to different results. An efficient model Hamiltonian \mathbf{H}_M is the so-called Hubbard–Anderson one. It relies on the use of the Hückel Hamiltonian \mathbf{H} as defined in Section 1.3.1, implying only one-electron integrals α and β (interaction energy between orbitals a (and b) located on sites A and B *i.e.* $\beta = \beta_{AB}$). A simplified

modelization of the electron–electron repulsion is implemented by introducing only the one-centre electron–electron repulsion integral U ($U = \langle a_i a_i | e^2 / r_{12} | a_i a_i \rangle = \langle b_i b_i | e^2 / r_{12} | b_i b_i \rangle$, with $i = 1, 2$). As in many cases, only the ground state and a few first excited states of the system are necessary for the description, and thus a perturbation treatment can be used to model the experimental properties. The model Hamiltonian \mathbf{H}_M is decomposed into two parts \mathbf{H}_0 (corresponding to one-centre terms, orbital energies α_i and repulsion energy U) and \mathbf{V} (corresponding to the interaction between orbitals on the two sites, β_{AB}). Thus $\mathbf{H}_M = \mathbf{H}_0 + \mathbf{V}$. \mathbf{V} , being weak, can be treated as a perturbation. The most interesting situation occurs when the ground state E_0 originating from Hamiltonian \mathbf{H}_0 is degenerate and is split by the perturbation \mathbf{V} : the energy gaps between the split levels corresponds to physical observables. This allows building an effective Hamiltonian \mathbf{H}_{eff} acting only on the ground state E_0 and reproducing the levels generated by \mathbf{V} . The final step is to put in correspondence the spin–orbitals functions of the ground state with the spin-only functions and to arrive at a spin Hamiltonian \mathbf{H}_S acting only on the spins and much easier to handle. We present a very brief account of the main results.

Starting from a perturbative treatment of the Hubbard–Anderson model Hamiltonian, Girerd [3.41] arrived at the following spin Hamiltonian:

$$\mathbf{H} = -J (\mathbf{S}_A \mathbf{S}_B \mathbf{O}_A + \mathbf{S}_A \mathbf{S}_B \mathbf{O}_B) + B \mathbf{T}_{AB} \quad (3.77)$$

where B is the electronic interaction parameter V_{ab} (or $|\beta|$) weighted by the spin multiplicity of the core spin S_0 (the local spin in the absence of transferable electron); that is:

$$B = V_{ab} / (2 S_0 + 1) \quad (3.78)$$

\mathbf{T}_{AB} , \mathbf{O}_A , and \mathbf{O}_B are operators with the following actions:

$$\mathbf{T}_{AB} |S_A, S_B, S\rangle^A = (S + 1/2) |S_A, S_B, S\rangle^B \quad (3.79)$$

$$\mathbf{T}_{AB} |S_A, S_B, S\rangle^B = (S + 1/2) |S_A, S_B, S\rangle^A \quad (3.80)$$

$$\mathbf{O}_A |S_A, S_B, S\rangle^A = |S_A, S_B, S\rangle^A \quad (3.81)$$

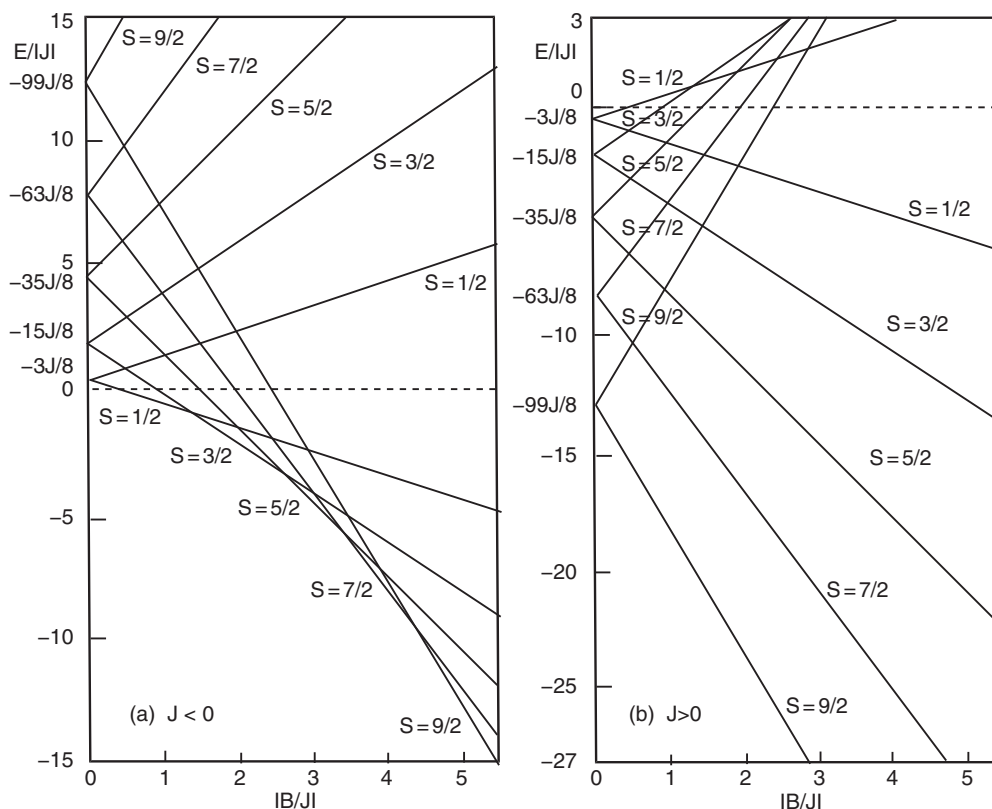
$$\mathbf{O}_A |S_A, S_B, S\rangle^B = 0 \quad (3.82)$$

and similar relations for \mathbf{O}_B . The ket symbol $|S_A, S_B, S\rangle^A$ represents a wavefunction with local spins S_A on site A and S_B on site B and total spin S , with an extra particle localized on site A (by particle, we mean an extra electron for half-filled or less than half-filled d^n configurations (without the transferable electron) and an extra hole for more than half-filled one). Thus \mathbf{T}_{AB} is a transfer operator, while \mathbf{O}_A or \mathbf{O}_B are occupation operators. The Hamiltonian has been called an exchange–double exchange Hamiltonian.

The eigenvalues of (3.77) are then:

$$E = -1/2 J S (S + 1) \pm B (S + 1/2) \quad (3.83)$$

There are thus two effects encompassed in eqns. (3.77) and (3.83): the first term is related to magnetic exchange (through the J term) and the second term to

**Fig. 3.29**

Eigenvalues E of the exchange–double exchange Hamiltonian in units of $|J|$ as a function of $|B/J|$. (a) For $J < 0$ (antiferromagnetic case); (b) for $J > 0$ (ferromagnetic case). (Adapted from Girerd [3.41].)

double exchange; that is, spin-dependent delocalization (through the B term). The remarkable effect of the double exchange term is to split the exchange energy levels in two, stabilizing one and destabilizing the other.

The combined effects of B and J are shown on Fig. 3.29 for the mixed valence $\text{Fe}^{\text{II}}\text{--Fe}^{\text{III}}$ system. On the left axis are displayed the ladder of spin energy levels computed from the exchange term only (Heisenberg Hamiltonian, no electron transfer, $B = 0$). When $|B|$ increases the spin levels are more and more split, and thus crossings between the spin states occur. For sufficiently large values of $|B|$ the $S = 9/2$ state becomes the ground state. It is important to realize that the situation depicted in Fig. 3.29 is valid only when the two configurations $\text{Fe}^{\text{II}}_{\text{A}}\text{--Fe}^{\text{III}}_{\text{B}}$ and $\text{Fe}^{\text{III}}_{\text{A}}\text{--Fe}^{\text{II}}_{\text{B}}$ have exactly the same energy; in other words, at the crossing point of the Hush–Marcus curves.

One of the interests of the previous treatment is that the model and spin Hamiltonians are rather simple to handle. They were, up to now, widely accepted. In a recent study of a simple mixed valence dinuclear compound $[\text{Ni}_2(\text{napy})_4\text{Br}_2]^+$ (napy denotes naphthypyridine), Malrieu and coworkers

[3.45] have used *ab initio* configuration interaction (time-consuming) calculations. They carefully analysed and compared their results (unfortunately impossible to reproduce in the limited space available here) with those resulting from the preceding perturbative treatment. They conclude that at least for this Ni_2 case the perturbative treatment cannot be applied safely, since the interaction between the ground state and the excited states is quite strong. Furthermore, the orbitals implied in the electron transfer process cannot be limited to the singly occupied 3d metallic orbitals, since the Ni 4s orbitals appear to play an unexpected important role. Therefore, their energy spacings and wavefunctions deviate significantly from those of the generally accepted model Hamiltonian. Additional calculations on other systems are therefore needed, and new exciting developments can be expected.

If now we take into account the effect of vibronic coupling, we start from two potential energy parabolae with spin S_1 , and two with spin S_2 ($S_2 > S_1$), as shown in Fig. 3.30. Then we couple each pair of parabolae by the $B(S + 1/2)$ interaction. The abscissa is defined in Fig. 3.30.

Several cases can appear, depending on the sign of J , as analysed in [3.41]. As an example showing the richness of behaviours, we consider the case of the $[\text{Fe}_2\text{bpmp}(\text{RCO}_2)_2]^{2+}$ complex, where bpmp is the anion of 2,6-bis[bis(2-pyridylmethyl)aminomethyl]4-methylphenol [3.46]. For this mixed valence $\text{Fe}^{\text{II}}-\text{Fe}^{\text{III}}$ complex, the J parameter is estimated as -10 cm^{-1} , and the ground state is assumed to be localized (class II). Taking into account that the effects of delocalization are smaller when the structure departs from symmetry, for x near to $\pm 1/2$ we have antiferromagnetically coupled Fe^{II} ($S = 2$) and Fe^{III} ($S = 5/2$) sites, with a total spin $S_T = 1/2$. But the electronic interaction, manifested in the avoided crossing zone, is larger for the higher spin states than for $S = 1/2$. Thus level crossings occur, giving the complex behaviour depicted in Fig. 3.31.

In such a system the activation energy for electron transfer is clearly much lower for the higher spin states. The electron transfer involves probably a complex mechanism, with thermal population of the higher spin states, followed by electron transfer and then spin conversion.

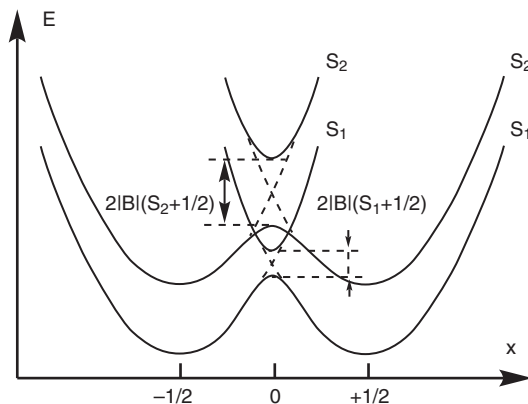
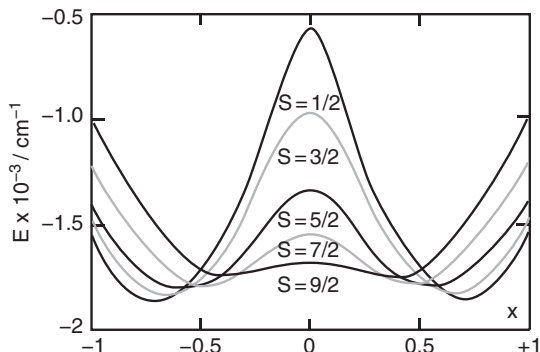


Fig. 3.30

Two pairs of potential-energy parabolae coupled by the electronic interaction. In this example the coupling is greater for the S_2 spin state than for S_1 , because $S_2 > S_1$. x is an adimensional coordinate as in Fig. 3.27.

**Fig. 3.31**

Assumed potential energy curves for the lowest states of $[\text{Fe}_2\text{bpmp}(\text{RCO}_2)_2]^{2+}$. x is an adimensional coordinate as in Fig. 3.30. (Redrawn from [3.41].)

An application: colossal magnetoresistance in $\text{Mn}^{3+}\text{--}\text{Mn}^{4+}$ systems

The interplay of magnetism and electron transfer is important for some applications in solid three-dimensional solid oxides. Our local approach, implying two neighbouring centres, can be used to understand the basic physics of some phenomena. Thus a number of solid oxides contain both high spin d^3 Mn^{4+} ($S = 3/2$) and high spin d^4 Mn^{3+} ($S = 2$) [3.47]. A typical example is $\text{Ln}_{1-x}\text{A}_x\text{MnO}_3$, where Ln^{3+} is a lanthanide, A^{2+} a divalent cation (Ba, Sr, Ca), and $0 \leq x \leq 1$. The structure is of the perovskite type with MnO_6 octahedra. There is thus the possibility of exchange magnetic coupling between Mn^{3+} and Mn^{4+} centres, and also of electron exchange leading to conductivity. Electron–phonon interaction also plays a role (see Sections 3.1.2 and 3.3.3 for the definition and use of this term), because the $\text{Mn}^{\text{III}}\text{O}_6$ octahedra are strongly distorted as a result of Jahn–Teller effect. (As already seen in Section 2.8.1.1, the Jahn–Teller effect is important in high-spin Mn^{III} because there is one electron in an antibonding orbital belonging to the e_g^* orbital set and the octahedral geometry is unstable due to orbital degeneracy.)

At both ends of the composition diagram of $\text{Ln}_{1-x}\text{A}_x\text{MnO}_3$, Mn is present respectively as Mn^{III} ($x = 0$) and as Mn^{IV} ($x = 1$). The compounds are then antiferromagnetic insulators. Between ($0 \leq x \leq 1$) the conductivity is important, due to the mixed valence composition. But the electron transfer is sensitive to the relative spin orientation of nearest neighbours Mn^{III} and Mn^{IV} centres: as seen previously, the electron transfer is easier when the spins are parallel (double exchange; see Fig. 3.28). Conversely, the electron transfer has an influence on the privileged type of magnetic coupling (ferro *versus* antiferro) because mobile electrons can play the role of ‘messengers’, forcing the spins to align. The final result is that in the intermediate x range ($0.15 < x < 0.50$) a ferromagnetic *and* metallic phase is observed at low temperature. In the regions close to the transition between phases the system is very sensitive to an additional perturbation, such as a magnetic field. Thus the conductivity increases dramatically upon application of a magnetic field, because it forces the parallel alignment of neighbouring spins. This effect has been called ‘colossal magnetoresistance’. The relations between structure (short and long ranges), electronic structure (Jahn–Teller, mixed valence), applications of a magnetic field, and physical properties are actively studied [3.47].

3.2.2.5 Experimental aspects: spectroscopic studies

The experimental study of mixed valence compounds must take into account the dynamic aspect of the investigation method. If the compound is class III, the only dynamical process is purely electronic—extremely fast—and all experimental methods point towards a total delocalization. But for a class II system there is a dynamical exchange between the two possible forms, corresponding to wells in the potential energy surface. These two forms are indeed genuine chemical species (isomers). The interchange process can be characterized by the intramolecular first-order rate constant k_{et} , or the corresponding characteristic time $\tau_{\text{et}} = 1/k_{\text{et}}$, both being generally dependent on temperature. τ_{et} represents the average time of residence of the extra electron on a given site. Now, to each spectroscopic method, one can assign a ‘characteristic time’ τ_{meth} , which represents the average equivalent duration of the interaction between the radiation and the system [3.48]. The experimental result depends on the relative magnitudes of τ_{et} and τ_{meth} :

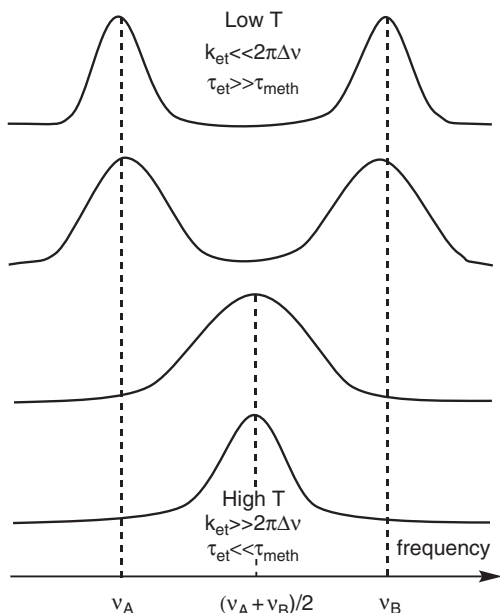
If $\tau_{\text{et}} \gg \tau_{\text{meth}}$ the electron has not enough time to jump during the equivalent duration of the interaction, and the experiment concludes that the state is ‘localized’, in the same way as a short-time flash freezes the motion in a photograph.

If $\tau_{\text{et}} \ll \tau_{\text{meth}}$ the electron has time enough to perform a large number of transfers back and forth between the two sites, and the experiment concludes that the state is ‘delocalized’, as a photograph of a rapidly moving object taken with a long exposure gives only the object’s average position. Hence, the same situation can be considered as ‘localized’ or ‘delocalized’, depending on the characteristic time of the measurement method. Thus one has to be careful in interpreting experimental data. In particular, when a method shows equivalent sites it is not possible to decide immediately between the two possibilities: either the system is class III, or is class II with $\tau_{\text{et}} \ll \tau_{\text{meth}}$.

We have now to specify in more detail the definition of the ‘characteristic time of a method’ (see also Box ‘Time-scales of investigation methods’). In the following, we will consider mainly the case of resonance methods, the most typical being EPR and NMR spectroscopies, which can be treated by a common formalism [3.49]. If there are two localization sites, denoted A and B, they can be associated with two different resonance signals with frequencies ν_A and ν_B respectively. In the case of EPR, for instance, the unpaired electron does not exhibit the same resonance frequency when it passes from an initial site to a site with a different orientation or with a different hyperfine coupling. In the case of NMR one generally follows the resonance of a nucleus close to the metallic site on which electron transfer occurs, using the influence of the metal oxidation state on the nearby NMR active nucleus. A related case is Mössbauer spectroscopy, where the absorption frequencies in the γ domain are dependent on the oxidation state of the considered element.

The interconversion between the two chemical species A and B corresponding to the two possible electron localizations introduces a new relaxation pathway, which modifies the signal shape. The detailed theory of resonant absorption in the presence of this new process shows that the characteristic time of the method is given by:

$$\tau_{\text{meth}} = \hbar/\Delta E = 1/(2\pi \Delta \nu) \quad (3.84)$$

**Fig. 3.32**

Thermal variation of the shape of the signals characteristic of two species, A and B, in the presence of a dynamic exchange.

where ΔE is the difference in energy resonances between the two A and B states, and $\Delta\nu$ is the difference between the two resonance frequencies [3.50a].

Thus, in the case of NMR, τ_{meth} is not equal to the reciprocal of the NMR frequency, but is proportional to the reciprocal of the *difference* in chemical shifts observed for the A and B states. As a consequence, τ_{meth} is not constant for a given spectrometer, but depends on the system under investigation. The case of Mössbauer spectroscopy is different: here the time-scale of the method is given by the lifetime of the nuclear excited state.

Consider now a system for which the k_{et} constant can be varied, for instance, by a change in temperature, so that one can cross the temporal ‘window’ associated with the investigation method, then the following behaviours are observed successively (Fig. 3.32):

- For $k_{\text{et}} \ll 2\pi \Delta\nu$ ($\tau_{\text{et}} \gg \tau_{\text{meth}}$ at low temperature), two signals at frequencies ν_A and ν_B are observed, as if the sample were constituted by a mixture of two species without interconversion.
- When k_{et} increases and becomes close to $2\pi \Delta\nu$, the signals widen and then coalesce. The unique resulting signal is located midway between ν_A and ν_B . Then it narrows.
- Finally, when $k_{\text{et}} \gg 2\pi \Delta\nu$ a single sharp signal remains. Its characteristics (position, width) are the averages of those of A and B signals.

In the intermediate zone where $k_{\text{et}} \approx 2\pi \Delta\nu$, detailed analysis of the signal shape by numerical simulation can yield the rate constant k_{et} . Conversely, when k_{et} is much lower or much greater than $2\pi \Delta\nu$, the signal shape is independent of k_{et} .

Time-scales of investigation methods

Each experimental method can be characterized by its time-scale—the effective duration during which the system is probed. The situation is analogous to the case of photography, where, according to the shutter speed or the duration of the flash, a photograph of a moving object can be sharp or blurred. In many cases the time-scale is defined by the difference in frequency between two signals characteristic of two distinct chemical forms (see eqn. (3.84)).

The table summarizes the time-scale of some common spectroscopic techniques.

Method	Characteristic time scale (s)	Remarks
NMR	10^{-3} to 10^{-8}	(1)
Mössbauer	10^{-7} to 10^{-10}	(2)
EPR	10^{-7} to 10^{-11}	(1)
Infrared, Raman	10^{-12} to 10^{-13}	(3)
Visible–ultraviolet	10^{-14}	(4)
Solvent effects	10^{-10}	(5)
Dielectric relaxation	10^4 to 10^{-6}	(6)

(1) For NMR and EPR, there are strictly speaking several time scales, depending on the investigated system, and even on the part of the spectrum which is examined. They are estimated from the frequency shifts (spreading of the spectrum) of signals influenced by the electron transfer. The frequency shifts can be due to differences in chemical shifts or to couplings (case of NMR), to the anisotropy of the g factor or the presence of hyperfine lines (case of EPR), or finally to the modulation of relaxation times (all techniques).

(2) In Mössbauer, one uses the lifetime of the excited absorbing nucleus, rather than the spectrum spreading.

(3) Usually and approximately evaluated from the average duration of a vibration, but recent experiments show that the same formalism as for NMR is valid [3.52]. This time scale corresponds more or less to the class II / III distinction, because nuclear motions cease to follow electronic motions when the latter exceed a critical frequency which is of the order of the molecular vibrations frequency.

(4) Evaluated from the reciprocal of the frequency of electromagnetic radiation in the visible–ultraviolet.

(5) This concerns the solvent effect on the position of intervalence transitions. If such a dependence exists, it means that the solvent molecules (reorientation time near 10^{-10} s) have enough time to reorient between two electron transfers, and thus can contribute to E_{op} . [3.13]

(6) This is the dielectric response of a material disposed between the two plates of a capacitor submitted to an alternate voltage of variable frequency. The modern variant is called ‘time-domain reflectometry’ [1]. The frequency range can be extremely wide (from 10^{-4} Hz to 10^6 Hz), but the method is sensitive to any cause of dipolar relaxation (polar groups motion, counter ions motion, and so on), and not only to electron transfer.

Reference

- [1] B. C. Bunker, R. S. Drago, M. K. Kroeger, *J. Am. Chem. Soc.* 104 (1982), 4593.

One of the earlier examples of a dynamic study of electron transfer in a mixed valence system was provided by europium sulphide Eu_3S_4 , not a molecular compound. This solid contains formally Eu^{2+} and Eu^{3+} in a 1:2 ratio, and the two valence states produce Mossbauer signals of ^{151}Eu at different isomeric shifts. At low temperature (80 K), two types of signal are obtained in the expected 1:2 ratio, while at room temperature a single signal is observed at an average position of the chemical shift (Fig. 3.33) [3.51].

Since the electron transfer process is thermally activated, changing the temperature realizes the different cases discussed previously; that is, $\tau_{\text{et}} >$, \approx or $<$ τ_{meth} , with $\tau_{\text{meth}} = 8.8$ ns, fixed by the lifetime of the nuclear excited state. By proper analysis of the signal shape, it is even possible to determine the rate

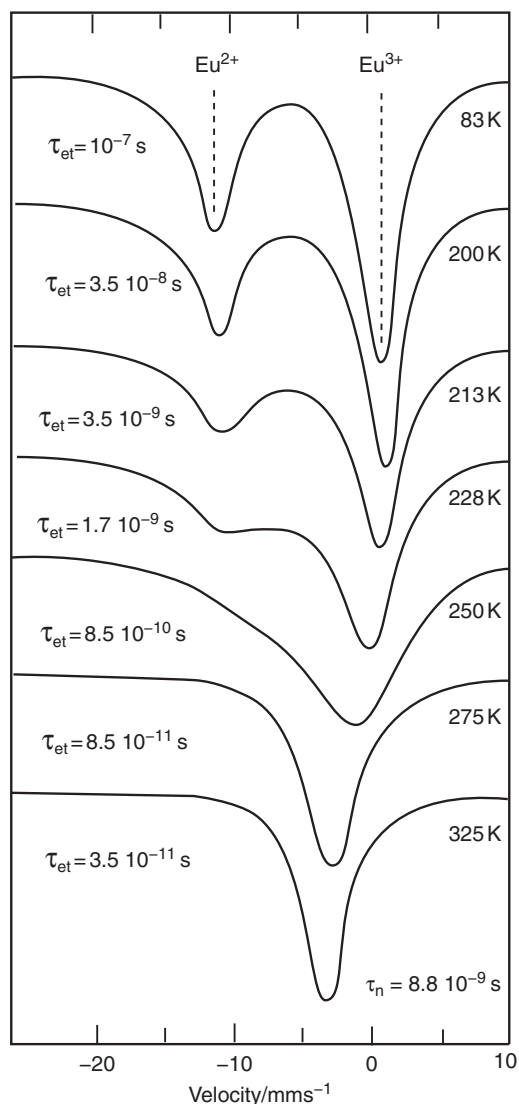
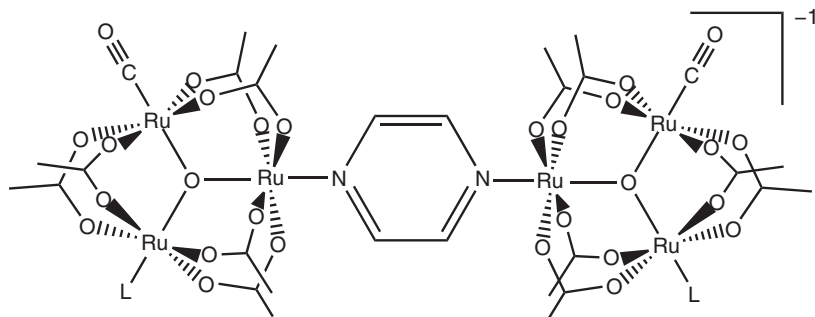


Fig. 3.33

Mössbauer spectrum of Eu_3S_4 as a function of temperature. $\tau_n = 8.8$ ns is the lifetime of the nuclear excited state (time-scale of the method). (Adapted from [3.51].)

Fig. 3.34

Structure of a mixed valence compound built from two trinuclear Ru_3O units, with ancillary CO ligands and a pyrazine bridge. (Adapted from Kubiak [3.52].)



constant, which is found to vary from around 10^7 s^{-1} at 80 K to 10^{10} s^{-1} at room temperature.

Infrared spectroscopy has been used only recently for the dynamic study of mixed valence systems. In the series of compounds depicted in Fig. 3.34, two trinuclear moieties of the Ru_3O type are linked by a bridging ligand, and one of the ruthenium atoms bears an ancillary carbonyl ligand [3.52]. The mixed valence effect arises from the possibility of reducing one of the trinuclear units. Interestingly, the carbonyl ligand displays an infrared stretching band, the frequency of which changes by about 50 cm^{-1} , according to the oxidation state of the moiety to which it is attached.

Varying the bridging ligand, or even the solvent, modifies the rate of intramolecular electron transfer between the trinuclear moieties and realizes the sequence of broadening and coalescence, as for other methods (Fig. 3.32). However, such examples are extremely rare in vibrational spectroscopy. Since the frequencies associated with vibrational motions are very high, as are the differences in frequency between two oxidation states, the range of rate constants probed by dynamic infrared studies can be extremely high and thus complementary with respect to other methods. In the present examples, intramolecular rate constants between 10^{12} and $5 \times 10^{12} \text{ s}^{-1}$ have been determined [3.52]. Another advantage of the infrared method (or more generally of vibrational methods, like Raman spectroscopy) is to probe the process of nuclear motions—the very process which is responsible for the eventual valence trapping. Thus if a system appears ‘delocalized’ by the vibrational study, the rate of electron transfer is so fast that the system is very probably of class III nature.

One of the most frequently used methods for the study of mixed valence compounds is ultraviolet–visible–near-infrared spectroscopy, since the characteristic intervalence transitions appear in this domain. This method can be qualified as ‘fast’, with a characteristic time near 10^{-14} s . This method plays a particular role, however, since the photon energy is high enough to promote electron transfers, and thus modify the system upon investigation. Therefore, rather than dealing directly with dynamic aspects, electronic spectroscopy in the domain of intervalence transitions (visible–near-infrared) is a way of obtaining information on the degree of electronic coupling, as shown in the following.

In the case of a class II system the *intensity* of the intervalence transition carries some information on the ground-state delocalization, and thus on the electronic coupling parameter V_{ab} . The root of the theoretical treatment, due to Hush [3.53], is in fact an adaptation of Mulliken's charge transfer theory. The molecule is reduced to its two terminal sites, A and B; that is, the partial delocalization on the bridging ligand is not explicitly introduced, which constitutes a rough approximation. The electronic coupling is assumed to be small with respect to λ . Under these conditions, the wavefunctions describing the ground state $|\Psi_G\rangle$ and the excited state $|\Psi_E\rangle$ are of the form (3.73b) and (3.73c):

$$|\Psi_G\rangle = -|\Psi_a\rangle + (\beta/\lambda)|\Psi_b\rangle \quad (3.85a)$$

$$|\Psi_E\rangle = (\beta/\lambda)|\Psi_a\rangle + |\Psi_b\rangle \quad (3.85b)$$

The intensity of the transition depends on the transition moment, defined by:

$$M = \langle \Psi_G | \mathbf{er} | \Psi_E \rangle \quad (3.86)$$

where \mathbf{er} is the dipole moment operator, and M is an integral over space. When developing eqn. (3.86), quantities such as $\langle \Psi_a | \mathbf{r} | \Psi_a \rangle$ and $\langle \Psi_b | \mathbf{r} | \Psi_b \rangle$ appear, corresponding to these \mathbf{r} values when the wavefunction is Ψ_a or Ψ_b ; these values are separated by R , the metal-metal distance (the significance of R is discussed in what follows). Thus one finds:

$$M = e(|\beta|/\lambda)R = e(V_{ab}/\lambda)R \quad (3.87a)$$

or, alternatively,

$$V_{ab} = M\lambda/eR \quad (3.87b)$$

To make the link with experimental quantities such as extinction coefficient, band position, and so on, one makes use of an intermediate quantity, the oscillator strength of the transition, denoted f . It is defined as [3.50b]:

$$f = \left(\frac{4m_e c \epsilon_0}{N_A e^2} \ln 10 \right) A \quad (3.88)$$

where m_e and e are the electron mass and charge, c the velocity of light, ϵ_0 the permittivity of vacuum, N_A the Avogadro constant, and A the area of the absorption curve $\int \epsilon(\nu) d\nu$, where ν is the frequency. For a Gaussian band profile, this area is given by:

$$A = (1/2) (\pi / \ln 2)^{1/2} \epsilon_{\max} \Delta\nu_{1/2} \approx 1.06 \epsilon_{\max} \Delta\nu_{1/2} \quad (3.89)$$

where ϵ_{\max} is the maximum molar absorption coefficient, and $\Delta\nu_{1/2}$ the width at half-maximum of the transition (in frequency units).

The oscillator strength is also related to the transition dipole moment by [3.50b]:

$$f = \frac{8\pi^2 m \nu}{3 h e^2} |M|^2 \quad (3.90)$$

Finally, by combining eqns. (3.87b) and (3.90), one obtains an expression of V_{ab} which depends on the experimental parameters ϵ_{\max} , ν_{\max} , and $\Delta\nu_{1/2}$ (the band position and width in frequency units). This is Hush's equation [3.53]:

$$V_{ab} = h \left[3 h C \epsilon_0 (\ln 10) / 4\pi^2 N_A e^2 \right]^{1/2} (\pi / \ln 2)^{1/4} \frac{\sqrt{\epsilon_{\max} \bar{\nu}_{\max} \Delta \bar{\nu}_{1/2}}}{R} \quad (3.91)$$

Combining all numerical factors and expressing the band position and width in wavenumbers yields the practical formula:

$$V_{ab} = \frac{2.05 \cdot 10^{-2} \sqrt{\epsilon_{\max} \bar{\nu}_{\max} \Delta \bar{\nu}_{1/2}}}{R} \quad (3.92)$$

In this frequently used expression, V_{ab} is now in cm^{-1} , and the parameters of the intervalence band are in the usual units: ϵ_{\max} in $\text{L mol}^{-1} \text{cm}^{-1}$, and $\bar{\nu}_{\max}$ and $\Delta \bar{\nu}_{1/2}$ in cm^{-1} . The definitions are recalled in Fig. 3.35. Since the intervalence band overlaps frequently with band tails originating from other transitions such as metal-to-ligand and ligand-to-metal transitions, a deconvolution of the mixed valence compound spectrum is often necessary.

Curiously, although eqn. (3.91) relies on a number of rough approximations, and in particular ignores partial delocalization on the bridging or ancillary ligands, its range of validity is wider than expected. It has been shown that it remains valid even for relatively strong couplings [3.54].

However, a known difficulty in the use of eqn. (3.91) is the value of the R parameter, which represents an effective distance between the localized donor's and acceptor's charge centroids. It is usually taken as the through-space geometrical distance between sites A and B, but delocalization effects (extensive wavefunction mixing in the ground and excited states) and polarization effects (changes in electron distribution) can introduce marked differences. This difficulty is discussed in the 'generalized Mulliken-Hush model' (GMH) model [3.55]. According to this model, a more rigorous formulation is obtained by using the following expression for V_{ab} instead of (3.87b):

$$V_{ab} = M\lambda / \Delta\mu_{ab} \quad (3.93)$$

where $\Delta\mu_{ab} = \mu_a - \mu_b$ is the diabatic change in dipole moment; that is, the difference in dipole moments for two non-interacting sites (full localization). The previous treatment leading to eqn. (3.91) was valid for a full transfer on one electron along a distance R (thus $\Delta\mu_{ab} = eR$) but in the frame of the GMH model one uses instead:

$$\Delta\mu_{ab} = [(\Delta\mu_{12})^2 + 4(M)^2]^{1/2} \quad (3.94)$$

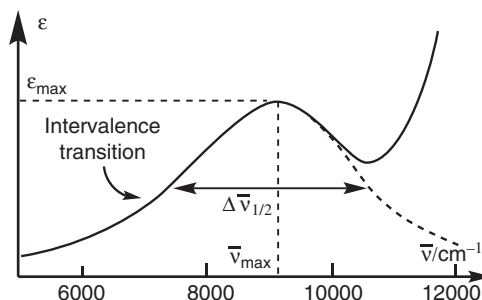


Fig. 3.35

Parameters defining the intervalence band: position (in wavenumbers), maximum molar absorption coefficient, and full width at half-maximum (in wavenumbers).

where $\Delta\mu_{12}$ is the difference between eigenvalues of the adiabatic dipole moment matrix [3.55]. The interest of eqn. (3.94) lies in the fact that $\Delta\mu_{12}$ and M can be evaluated experimentally, respectively from Stark effect measurements [3.56] and from the intensity of the intervalence transition. Once $\Delta\mu_{ab}$ is known from these measurements one can define an effective distance by $R_{\text{eff}} = \Delta\mu_{ab}/e$. Note, however, that this more rigorous procedure has been used very scarcely, due to the paucity of Stark effect experiments.

In the case of a class III mixed valence compound, the transition occurs between fully delocalized levels, given by eqns. (3.72a) and (3.72b). In this case, V_{ab} is not obtained from the band intensity, but merely from the band position: it is simply one half of the optical transition energy (see Fig 3.25). The transition moment is then given, from (3.86), by:

$$M = eR/2 \quad (3.95)$$

which is much larger than in eqn. (3.87a), since in this last expression the ground-state delocalization coefficient V_{ab} / λ is necessarily small. Thus, in a class III system, while there is no more thermal transfer, one observes a particularly intense electronic transition. But it does not correspond to a charge transfer, since the initial and final levels are fully delocalized with equal weights on the two sites, and is actually similar to a bonding-to-antibonding transition.

This difference of nature of the transitions can be used as a criterion for the class II/class III distinction. For a class II system, as a consequence of eqns. (3.17) and (3.66), the energy of the intervalence transition must depend on the solvent, and this has been experimentally established [3.13, 3.57]. On the contrary, for a class III system there is no appreciable charge redistribution during the electronic excitation, and thus the solvent influence on the transition is very small.

Another criterion to distinguish class II from class III systems is based on the bandwidth of the intervalence transition. In a class II compound (see Figs. 3.21 and 3.25b) the vertical transition reaches the excited state curve in a region where the slope of the $E = f(Q)$ curve is large. Thus, as a result of fluctuations in the initial Q value, there is an important dispersion in the transition energy. The detailed calculation was performed by Hush, and gives the energy bandwidth $\Delta E_{1/2}$ of the transition as:

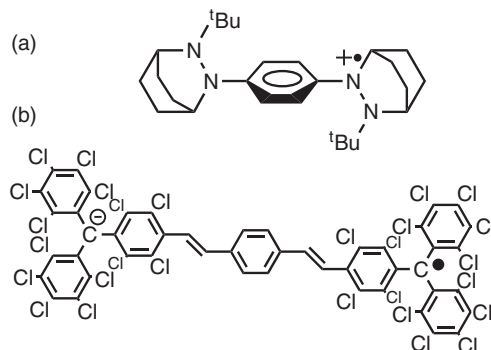
$$\Delta E_{1/2} = [16 kT (\ln 2) \lambda]^{1/2} \quad (3.96)$$

That is, numerically at 298 K, when the band position and width are in cm^{-1} :

$$\Delta \bar{\nu}_{1/2} = [2310 \bar{\nu}_{\text{max}}]^{1/2} \quad (3.97)$$

By contrast, in a class III compound the vertical transition reaches the upper curve on a rather flat region (Fig. 3.25c), and the corresponding band is much narrower.

We can now discuss in more detail the properties of some systems for which the simultaneous determination of E_{th} and E_{op} has been possible. The best examples are found in organic mixed valence systems, using EPR spectroscopy to determine the rate of intramolecular electron transfer, and from its variation

**Fig. 3.36**

Two examples of mixed valence compounds for which the simultaneous determination of E_{op} and E_{th} is available. a) half-oxidized bis-hydrazines [3.58]; b) half-reduced perchlorinated bi-radical [3.59].

with temperature, the activation energy for the thermal process. Two examples are shown in Fig. 3.36.

In the case of the bis-perchlorinated radicals (Fig. 3.36b) the partial reduction generates a monoradical, which can be considered formally as the association of an EPR-active radical on one side and an EPR-silent carbanion on the other side [3.59]. For this system, all parameters can be experimentally determined. Thus an intervalence transition is observed near 1400 nm, corresponding to $E_{op} = 0.78$ eV. From the intensity of the transition, a value of $V_{ab} = 0.015$ eV is obtained, using Hush's equation (see eqn. (3.92)). The thermal electron transfer can be monitored by EPR, because of the hyperfine splitting due to the coupling with a vinylic proton on each side. At low temperature (200 K) the EPR spectrum presents two lines, showing that the unpaired electron interacts with only one proton; that is, it is localized on only one half of the molecule. When the temperature is raised, the spectrum evolves gradually towards a three-line spectrum, characteristic of an interaction with two equivalent ^1H nuclei, meaning that the electron transfer becomes fast in the EPR time-scale. The detailed analysis of the spectrum by computer simulation gives the electron transfer rate constant (found in the range 10^7 – 10^8 s^{-1}), and from its variation with temperature, an activation energy $E_{th} = 0.117$ eV can be obtained. This value is appreciably lower than one fourth of the optical energy ($E_{op}/4 = 0.197$ eV). Even taking into account the effect of V_{ab} which decreases the thermal activation energy (see eqn. (3.76)), the agreement is not perfect. The conclusion is thus that eqn. (3.66) is certainly a rough approximation and reality is more complicated. For instance, as seen previously, quantum effects (nuclear tunnelling) can exist and would perturb the extraction of the barrier height from the relation between the rate constant and temperature. Another possibility, which has been proposed in the literature, is that the potential energy curves depart from the ideal harmonic oscillator model [3.58].

In the methods mentioned previously the electron transfer is not followed in real time. The rate is obtained from a spectrum which is recorded for a duration which can be as long as several minutes or hours. Conversely, in *time-resolved studies* one tries to follow instantaneously the system evolution between an initial and a final state. This necessitates several conditions:

- (i) The analysis method must be 'fast' in order to monitor instantaneously the composition of the mixture. One uses almost exclusively visible-ultraviolet absorption, or fluorescence emission, making use of the almost instantaneous response of photosensitive detectors (diodes, photomultipliers).
- (ii) The initial and final states must have different spectroscopic characteristics, which implies an unsymmetrical system. In most of the cases this introduces an energy difference between the two states.
- (iii) It is necessary to be able to define precisely the 'zero time': the system, initially in the more stable state, is rapidly brought in in the other possible (less stable) electronic state, from which it will relax towards the fundamental state, by an electron transfer reaction. This preparation step is crucial, and is usually achieved through ultra-fast laser-pulse techniques.

There have been very few well-characterized examples of time-resolved intramolecular electron transfer in mixed valence systems. Note that it is not in general possible to trigger the electron transfer by excitation on the intervalence transition, and one has rather to perform an excitation on a higher-energy charge transfer transition. One of the best examples is provided by ruthenium-osmium binuclear systems with a rigid spacer [3.60] (Fig. 3.37).

The starting complex exists as $\text{Ru}^{\text{II}}\text{-L-Os}^{\text{II}}$, where L is the bridging ligand, which incorporates a bicyclo[2.2.2.]octane unit in order to reduce the electronic interaction, and thus slow down any intramolecular reaction. The mixed valence $\text{Ru}^{\text{II}}\text{-L-Os}^{\text{III}}$ species can be formed quantitatively by chemical oxidation with 1 equivalent of oxidant, since Os^{II} is easier to oxidize by 0.4 V than Ru^{II} for the same environment. Upon excitation of the Ru^{II} chromophore on a metal-to-ligand charge transfer band (MLCT), an electron is transferred from Ru^{II} to a symmetry-adapted combination of π^* orbitals of neighbouring ligands, thus generating an excited state which can be considered as $\text{Ru}^{\text{III}}(\text{bpy}^{\bullet-})$ anion radical (see Section 4.3.1). The high-energy electron can then move to the remote Os^{III} site, thus generating temporarily the *mixed valence isomer* $\text{Ru}^{\text{III}}\text{-L-Os}^{\text{II}}$, which is thermodynamically unstable with respect to $\text{Ru}^{\text{II}}\text{-L-Os}^{\text{III}}$ (see the sequence of events on Fig. 3.38). Finally, back-electron-transfer is observed with a rate constant $1.0 \times 10^6 \text{ s}^{-1}$ [3.60]. This sequence of events was followed by time-resolved absorption spectroscopy which allowed identification of the $\text{Ru}^{\text{III}}\text{-L-Os}^{\text{II}}$ intermediate species.

As mentioned previously, there are few studies of this type. This is because many processes can compete with electron transfer, in particular energy transfer, and also non-radiative deactivation. The observation of time-resolved intervalence electron transfer is not a routine experiment, but requires the fine-tuning of many parameters in a carefully chosen system.

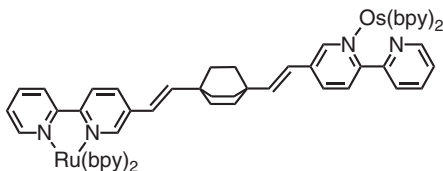
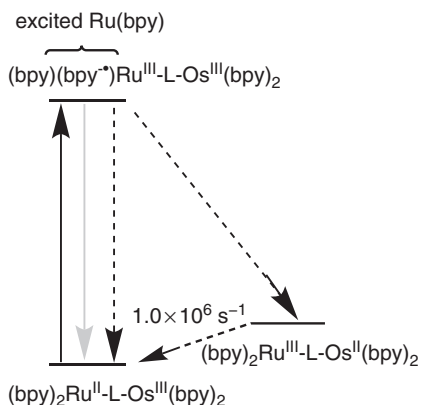


Fig. 3.37

Structure of a rigid Ru-Os binuclear complex.

**Fig. 3.38**

Reaction scheme following the excitation of the $Ru^{II}-L-Os^{III}$ binuclear complex on a Ru^{II} -to-ligand charge transfer transition. Plain black arrow, excitation; plain grey arrow, luminescence; dashed arrows, radiationless processes.

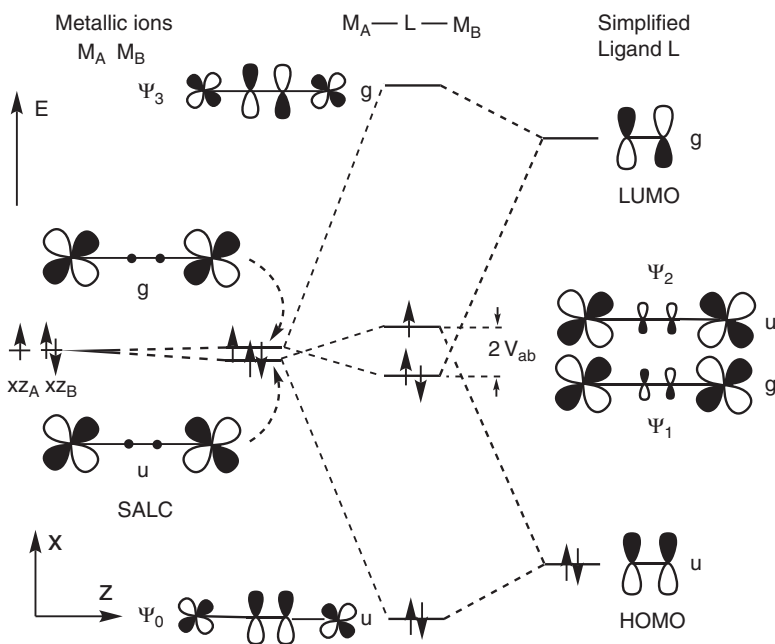
3.2.2.6 The electronic interaction and mechanism of electron transfer in mixed valence systems

At this stage it is useful to discuss in more detail the electronic interaction in mixed valence compounds, and more generally in strongly coupled systems. This has important consequences for the detailed mechanism by which an electron is transferred through a bridge, and addresses contemporary issues on the long-range transmission of electronic effects.

As discussed in Section 3.1.1, in a one-electron model, such as the extended Hückel model, V_{ab} is simply taken as half the energy difference between two orbitals having high weights on the metal atoms, and presenting opposite symmetries, such as ψ_g and ψ_u in Fig. 3.39. Although crude, this method gives very satisfactory orders of magnitudes of the electronic coupling, and is particularly well adapted to qualitative chemical-based discussion. It is important to notice that the interaction is measured by the *difference* in energy between these two orbitals, and not by the properties of a single orbital, even when it shows an important delocalization on the bridging ligand.

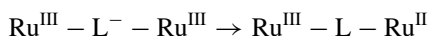
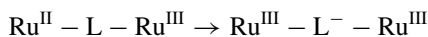
To be more specific, let us consider the typical example of a system bridged by a conjugated organic ligand. As in Section 3.1.1, we start from the symmetry-adapted linear combinations of d_{xz} orbitals, and look at their interaction with the HOMO and the LUMO of the ligand. We restrict ourselves to the π system shown in Fig. 3.39. (Compare also with Figs. 2.40 and 3.3)

In general, for conjugated systems the energy of the metal orbitals falls in the HOMO-LUMO gap, and the HOMO and LUMO have opposite u and g symmetries (Fig. 3.39). Thus in the example represented the $(d_{xzA} + d_{xzB})$ combination is stabilized by a bonding interaction with the LUMO, while the $(d_{xzA} - d_{xzB})$ combination is destabilized by an antibonding interaction with the HOMO. These effects add up to produce a splitting. However, it remains modest because the mixing is relatively weak due to the energy difference between metal and ligand orbitals. Thus the ground-state description contains a contribution of a configuration in which either the metal is oxidized and the ligand is reduced, or the reverse. This mechanism increases dramatically the coupling with respect to the case of a direct (through space) interaction of the metal orbitals. This is called *superexchange*—a general concept already met with in Chapter 2 (see Section 2.6.2.2, Box ‘Superexchange’).


Fig. 3.39

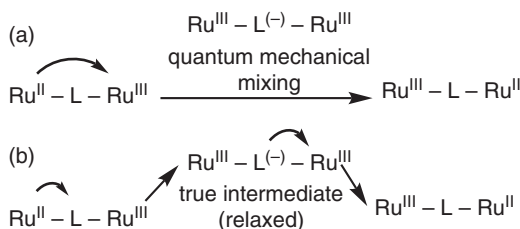
Molecular orbital energy diagram of a mixed valence system bridged by a conjugated ligand. At left, the d_{xz} orbitals of metals A and B build two symmetry-adapted linear combinations (SALC), u and g. They are assumed to bring three electrons (as in a ruthenium(II)–ruthenium(III) system). At right are shown the u and g MOs of the π ligand, reduced to the coordinating atoms. In the middle are shown the energies and schemes of the Ψ_i MOs of the M_A-L-M_B fragment. Count the number of nodes in the MOs' schemes.

If the metal orbitals are closer in energy to one of the frontier orbitals (say the ligand's LUMO), then the mixing increases rapidly, and consequently the V_{ab} coupling, though mainly one of the ligand orbitals contribute to the effect. The large increase of V_{ab} is called *resonance*. Taking the example of a $Ru^{II}-L-Ru^{III}$ mixed valence system, it means that the $Ru^{III}-L^- - Ru^{III}$ configuration is increasingly important in the description of the ground state. As a limiting case, it may happen that this configuration becomes a true intermediate. Then the electron transfer becomes a two-step process:



The intermediate now has a transient existence. This means that the bond lengths have time to relax and adapt to the electronic state, and this species corresponds to a local minimum in a potential energy surface.

Thus when the electronic mixing with the bridge is important, there are two possible mechanisms, whose characteristics are summarized in Fig. 3.40:


Fig. 3.40

The two possible mechanisms for electron transfer through a bridge. (a) Single step, superexchange mechanism, implying a quantum-mechanical mixing with an intermediate configuration; (b) two-step mechanism with transient formation of a real intermediate.

- A single step, superexchange mechanism, in which the intermediate configuration is only virtual, *i.e.* it participates in the quantum mechanical description of the initial and final ground states, with a variable weight.
- A two-step mechanism, also called ‘sequential’, or ‘chemical mechanism’, or ‘hopping-type mechanism’, in which the intermediate configuration is ‘real’, *i.e.* it can be observed experimentally as a transient state.

Considerable work has been devoted to the distinction between these two types of mechanisms [3.4, 3.61, 3.62]. A recent problem was raised by the properties of DNA, and the possibility that this fundamental molecule, support of heredity, could have special electronic properties favouring long distance electron transfer. (See Box ‘Electron transfer through DNA’).

The duality between both mechanisms will also be encountered in Section 5.2.2 when a molecule will be inserted between two ultra-thin metallic conductors, so as to mediate the passage of an electrical current.

Decay law of V_{ab} with distance

A final concern is the question of the decrease of V_{ab} with distance. Since V_{ab} determines the electron transfer rate in the non-adiabatic regime (eqn. (3.37)), this question has strong implications in various domains of chemistry, biology, physics, nanosciences, and so on, and will be evoked again in Chapters 4 and 5. The experimental study of series of compounds with different lengths has allowed some progress in this direction. The V_{ab} coupling can be determined by the intervalence band method, using Hush’s eqn. (3.92), provided that the coupling is large enough, which requires in practice a conjugated bridge [3.30].

It is generally found that the V_{ab} coupling decreases with the distance R between redox sites according to an exponential law, with a decay coefficient γ depending on the bridge and defined by:

$$V_{ab} = V_{ab}^{\circ} \exp(-\gamma R) \quad (3.98)$$

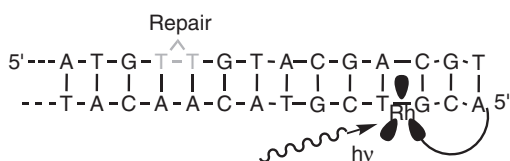
Thus, according to eqn. (3.98), in the non-adiabatic regime the intramolecular electron transfer rate constant varies also according to an exponential law, but with a doubled decay coefficient, because k varies as V_{ab}^2 (see eqns. (3.37) and (3.57)):

$$k = k^{\circ} \exp(-2\gamma R) \quad (3.99)$$

Curiously, for many compounds with diverse structures the γ decay coefficient falls in a rather narrow range: 0.07 to 0.10 \AA^{-1} [3.30c]. This is a rather slow rate of decay, and is much smaller than if the interaction between the redox sites occurs through empty space (in such a case γ would be about 0.5 \AA^{-1}) (Fig. 3.41). The big challenge for achieving long-range electron transfer is to realize simultaneously a strong initial coupling V_{ab}° and a weak attenuation factor γ , but these requirements are in a first approximation mutually exclusive [3.30c]. Looking more closely, however, there are interesting deviations of this general law, and some groups, such as anthracene, are particularly efficient as bridge components to ensure a strong interaction between terminal sites. The search for more efficient structure is an active field of research.

Electron transfer through DNA

The electronic properties of DNA have received considerable attention since 1993, when the first measurements showed that it could be the sieve of electron transfer reactions [1]. Modified DNA molecules were prepared with a photosensitive metal complex such as $\text{Rh}(\text{phi})_2(\text{dmb})$, ($\text{phi} = 9,10$ -phenanthrenequinone diimine, $\text{dmb} = 4,4'$ -dimethyl-2,2'-bipyridine), which is used as an intercalator within the π stack of DNA pairs. Upon photophysical excitation the tethered complex acts as a hole generator; that is, it can receive an electron from a distant place such as a thymine dimer. This constitutes a model for the biologically important reaction of thymine dimer repair. (A thymine dimer is a pair of abnormally chemically bonded adjacent thymine bases. Oxidation of the thymine pair breaks the dimer, thus restoring their normal mode of bonding).



Several other modifications of DNA have been performed by grafting various photosensitive groups and detecting chemical reactions at distance, either by strand cleavage or by generation of cation radicals [2]. The nucleobases do not have the same redox properties (guanine is more easily oxidized than adenine and the pyrimidine nucleobases), making possible the selective oxidation of guanine by adapted excited acceptors, electronically coupled to the DNA, which do not also oxidize adenine. Continuous improvement of detection methods led to the resolution of the enormous initial discrepancies between different measurements.

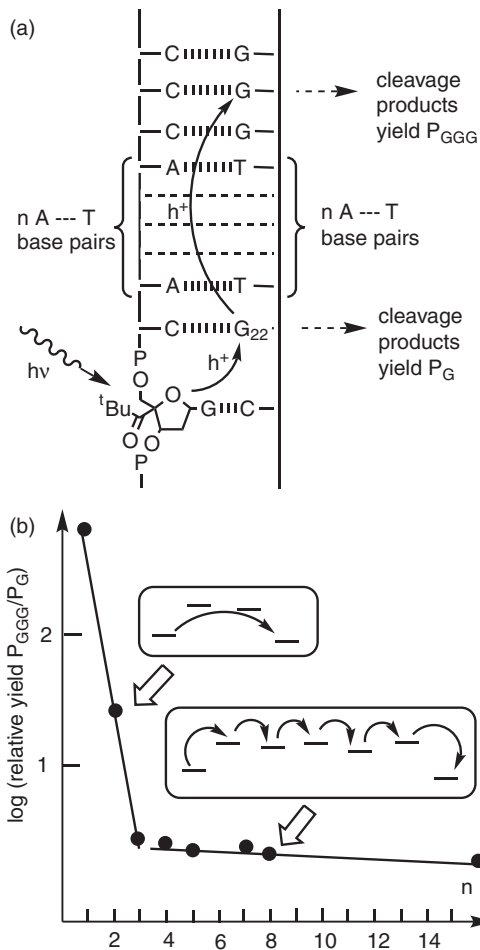
An intriguing fact was that for some systems the electron transfer rate constant k_{et} decreased very slowly with distance. This was shown indirectly by the yield of a given reaction occurring at distance, away from the centre of a local excitation. Thus, in a modified DNA double strand containing an acylated photosensitive intercalator, the photochemical excitation generates a cation radical and the positive charge can migrate until it is trapped by a remote triplet of guanine bases. The effect is observable at distances of up to 50 Å. Since the stacked base pairs present weak electronic couplings between the π systems, one expects a rapid rate of decay of the V_{ab} interaction between donor and acceptor with distance, at least more rapid than in the following examples with conjugated bridges (see, in particular, Fig. 3.41).

Theoretical investigations agree that electron transfer is actually a hole transfer mechanism, for which oxidizable bases such as guanine present in the DNA strands must play a role. The superexchange mechanism would lead to a rapid attenuation of k_{et} with distance, and thus present interpretations favour a 'hopping mechanism' using several intermediates including some unavoidable disorder [3]. Thus the hole (actually a polaron—a hole + distortion) would migrate by a series of diffusive steps ending on the final site. Calculations show that this would indeed lead to a much slower rate of decay than by direct superexchange.

An improvement of the model, due to Renger and Marcus [3b], is to consider that in the intermediate species the hole is not located on a single base but rather delocalized on several bases. This increases the effective size of the polaron and renders the system less sensitive to static disorder.

Fig. 1

Scheme of the intercalator rhodium complex-DNA-thymine dimer. The thymine dimer is shown in light grey. Following the photoexcitation of the tethered intercalated rhodium complex, oxidative repair of the thymine dimer occurs at 26 Å distance. (Adapted from Genereux and Barton [1b].)

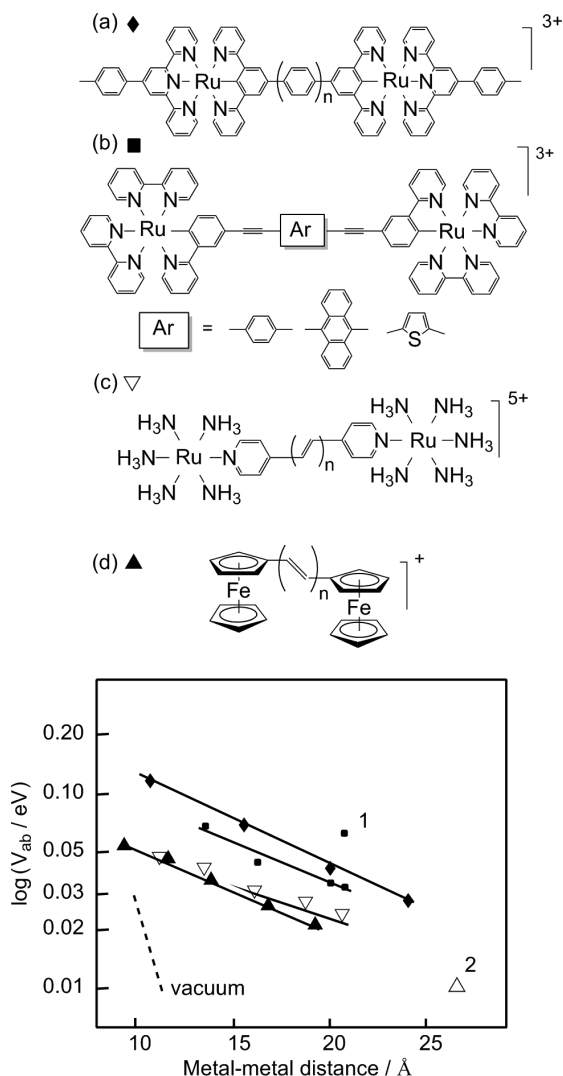
**Fig. 2**

Long-distance hole transfer in a modified DNA double strand: (a) structure of the synthetic double strand, with a photosensitive acylated group, generating a positive charge, and subsequent reactions; h^+ designates a hole; (b) decay law of the relative yield of long-distance products as a function of the number n of A–T pairs, showing the two regimes, superexchange for $n < 3$, hopping for $n > 3$. (Adapted from Giese [2b].)

References

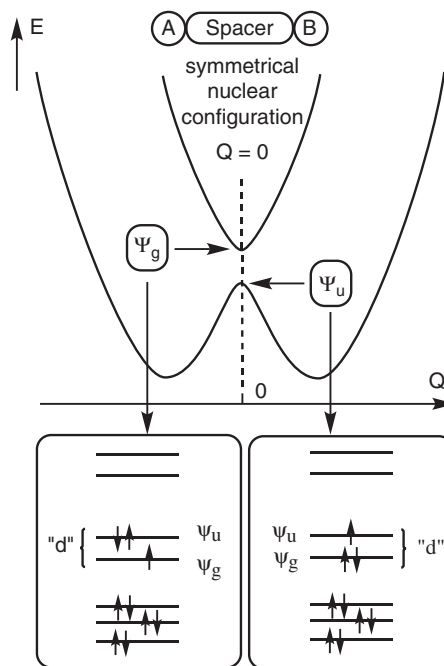
- [1] a) C. J. Murphy, M. R. Arkin, Y. Jenkins, N. D. Ghatlia, S. H. Bossmann, N. J. Turro, J. K. Barton, *Science* 262 (1993), 1025; b) J. C. Genereux, J. K. Barton, *Chem. Rev.* 110 (2010), 1642.
- [2] a) D. Ly, L. Sani, G. B. Schuster, *J. Am. Chem. Soc.* 121 (1999), 9400; b) B. Giese, J. Amaudrut, A.-K. Köhler, M. Spormann, S. Wessely, *Nature* 412 (2001), 318.
- [3] a) M. Bixon, J. Jortner, *J. Am. Chem. Soc.* 123 (2001), 12556; b) T. Renger, R. A. Marcus, *J. Phys. Chem. A* 107 (2003), 8404.

A last question about electronic interaction is of theoretical nature. Up to now we have used qualitative mono-electronic models. But to be more precise on the role of the bridging ligand, we should take into account the polyelectronic nature of the wavefunctions. We consider what happens at the avoided crossing point, when the system's geometry is perfectly symmetrical.


Fig. 3.41

The decay of the electronic interaction V_{ab} with distance. (Upper) structure of the studied molecular systems; (lower) corresponding typical decay laws, with a comparison with vacuum. Special cases: 1: complex of the type b) with anthracene in the spacer; 2: bis ferrocene of the type d) with three phenylene and four vinylene as spacer.

In principle one should compute the total energy of the mixed valence system for the two possible electronic states at $Q = 0$ (see Fig. 3.42, showing in particular the distinction between *total* wavefunctions such as Ψ_g , Ψ_u , and *one-electron* wavefunctions such as ψ_g , ψ_u). This rigorous approach necessitates the full many-electron treatment with evaluation of total electronic energies, including correlation effects. At this level, two variants can be considered: (i) from adiabatic energy splitting (dimer splitting)—calculating the energy difference between the two possible electronic states—and (ii) from the direct calculation of the matrix element $\langle \Psi_a | \mathbf{H} | \Psi_b \rangle$, where Ψ_a and Ψ_b represent diabatic total electronic wavefunctions. These wavefunctions correspond to the unperturbed basis states $\text{Ru}^{\text{II}}\text{-Ru}^{\text{III}}$ and $\text{Ru}^{\text{III}}\text{-Ru}^{\text{II}}$, and can be obtained by a symmetry-broken SCF calculation [3.63]. They derive in particular from symmetry-adapted wavefunctions such as Ψ_g , Ψ_u by the standard unitary transformation $\Psi_{\pm} = 2^{-1/2}(\Psi_g \pm \Psi_u)$ [3.64].

**Fig. 3.42**

Definition of the electronic interaction at the crossing point ($Q = 0$) in the 'dimer splitting' method. 'd' designates molecular orbitals with preponderant d character centred on A and B metal sites. Ψ_g and Ψ_u are total polyelectronic wavefunctions, and the associated rectangular frames show the electronic filling of one-electron wavefunctions ψ_g and ψ_u (molecular orbitals). The electronic filling corresponds to a system such as $\text{Ru}^{\text{II}}-\text{Ru}^{\text{III}}$.

There are, however, only a few examples of exact calculation, at the *ab initio* SCF level with account of electron correlation, or even at simpler DFT level. This comes from the fact that for such complicated molecules with many electronic and nuclear degrees of freedom, several artefact solutions may appear in the calculations. Thus in *ab initio* SCF methods, anomalous symmetry breaking of the Hartree–Fock solutions can appear even for a perfectly symmetrical system, while conversely, DFT methods tend to favour artificially delocalized structures [3.65]. This is why, for lack of something better, simple methods based on orbital semi-empirical models are still very useful today for a basic illustration of the phenomena.

3.3 Conductivity in extended molecular solids

3.3.1 Conductivity: definitions, models, and significant parameters

So far, we have considered mainly discrete mixed valence molecules, typically with two redox sites, which were essentially studied in solution, so that no macroscopic electronic conduction could occur. We now examine the transport properties in extended systems in the solid state (mixed valence or not). Metallic conducting materials (most of them are non-molecular, metals, alloys, oxides) allow electron motion in a circuit, giving rise to a transport of electric charge Q (in Coulomb, C), during a time t (in seconds, s), corresponding to an electrical current with intensity I (in ampères, A):

$$Q = I \cdot t \quad (3.100)$$

This occurs when a potential difference U (in volts, V) is applied to the system. Ohm's law relates the electric parameters, intensity I and applied potential U , to the resistance of the material R (in ohms, Ω):

$$U = R \cdot I \quad (3.101)$$

The inverse of the resistance is the conductance C (in siemens, S or ohm^{-1} , Ω^{-1}). The resistivity ρ of a material having a length l and a uniform section s (Fig. 3.43a) is defined by:

$$R = \rho \frac{l}{s} \quad (3.102)$$

and is expressed in ohm cm . The conductivity is simply the inverse of the resistivity:

$$\sigma = 1/\rho \quad (3.103)$$

It is expressed in $\text{ohm}^{-1} \text{cm}^{-1}$, $\Omega^{-1} \text{cm}^{-1}$. Since $I = U/R = Us/\rho l = U\sigma (s/l)$, the conductivity measures the ability of a material to conduct the current: everything being equal, the intensity I increases with σ . Another familiar expression of Ohm's law, expressed in terms of the current density j ($j = I/s$) and the applied electric field $E (= U/l)$, is thus easily derived:

$$j = \sigma E \quad (3.104)$$

The current density can be expressed alternatively as a function of n , the number of charge carriers per unit volume (in cm^{-3}), the charge q of the carriers, and the drift velocity v of the charge carriers:

$$j = nqv \quad (3.105)$$

If we define the mobility of the carriers as u ($u = v/E$) (in $\text{cm}^2 \cdot \text{V}^{-1} \cdot \text{s}^{-1}$), the conductivity is expressed by:

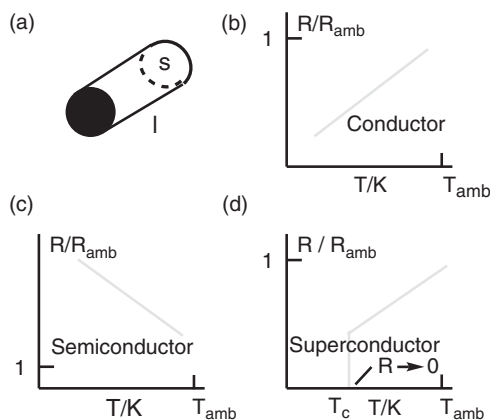
$$\sigma = j/E = nqu \quad (3.106)$$

The expression will prove useful for identifying the nature of the charge carriers, electrons ($q = e$, negative) or holes (q positive, also noted h), or both (see Section 3.3.2.2). If there are several types of carrier, the contributions are additive.

From the conductivity point of view, one can distinguish four important categories of materials: insulators, semiconductors, conductors, and superconductors. The four categories are distinct not only through the value of the conductivity, which increases from insulators to superconductors, but also by the thermal variation of the conductivity.

We shall return in more detail on these behaviours in the corresponding sections, and the reader is prompted to refer to physics textbooks. At present, we need only to state the following:

- The insulators have a very weak conductivity ($\sigma < 10^{-6} \Omega^{-1} \text{cm}^{-1}$, for example), without important change with temperature.
- The semiconductors have a medium conductivity ($10^{-6} \Omega^{-1} \text{cm}^{-1} < \sigma < 1 \Omega^{-1} \text{cm}^{-1}$) and the conductivity is thermally activated (Fig. 3.43c).

**Fig. 3.43**

Useful definitions for electrical properties. (a) Length and section of a sample. Ratio R/R_{amb} (resistance/ambient resistance) versus temperature for (b) a conductor; (c) for a semiconductor; (d) for a superconductor.

$$\sigma = \sigma_0 \exp\left(-\frac{E_A}{RT}\right) \quad (3.107)$$

- The conductors have a large conductivity ($1 \Omega^{-1} \text{ cm}^{-1} < \sigma < 10^6 \Omega^{-1} \text{ cm}^{-1}$), and furthermore, the conductivity increases when the temperature decreases (Fig. 3.43b and Section 3.3.2).

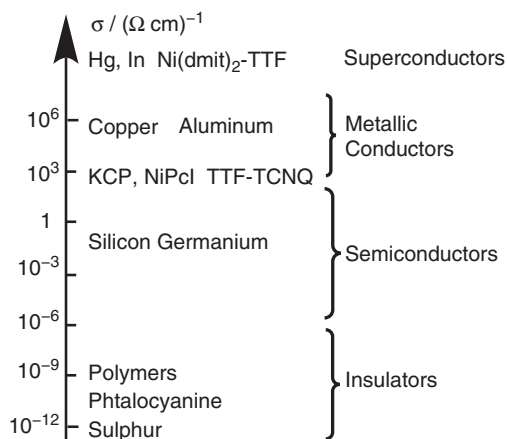
$$\sigma = \frac{\sigma_{\text{Tref}}}{T^\alpha} \text{ with } \alpha > 1 \quad (3.108)$$

where σ_{Tref} is the conductivity at a given reference temperature T_{ref} .

- The superconductors have, *a priori*, an infinite conductivity below a critical temperature T_c (zero resistivity!) (Fig. 3.43d).

The problem for the chemist is that molecular systems in the solid state are generally insulating. Obtaining a high conductivity with molecular materials represents a challenge, but the issue is important for potential applications (low-density conductors, for example, are very appealing), and have given rise to many research endeavours, some of them distinguished by the Nobel Prize in Chemistry in 2000 (A.J. Heeger, A.G. MacDiarmid, and H. Shirakawa). Many molecular conducting systems have now been found, and it is possible to establish and use some rules to produce molecular materials exhibiting remarkable conducting properties (Fig. 3.44).

It is useful to investigate conduction phenomena, having in mind the discussion in Section 3.1 concerning the resonance integral β (termed V_{ab} in Section 3.2), the one-centre electronic repulsion integral U (termed j_0 in Chapter 2), and λ parameters (Figs. 2.3 and 3.11). The resonance integral β is sometimes termed the transfer integral t in the context of conducting materials, but in this section we will retain the notations β , U , and λ . Two general situations can lead to conduction: (i) the extended system can be described by sufficiently wide bands (β relatively large and $|\beta| \gg U$), with an incomplete filling, leading to metallic conduction. This is the standard ‘band model’, and in this case the role of U is ignored. From the beginning the description utilizes delocalized levels, so that the λ parameter also disappears. One can consider in this case that the delocalization of electrons proceeds via a tunnelling mechanism from one site to another; (ii) the extended system can be


Fig. 3.44

Conductivity of molecular systems compared to traditional materials: the conductivity spans an incomparable range of values.

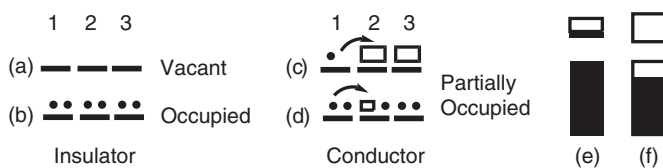
of mixed valence composition. In such a case, the one-centre repulsion U is small and does not play a role (see Fig. 3.11), and the properties depend on the competition between β and λ , as in the case of discrete mixed valence systems discussed previously. Note that in these systems the starting point for the description is the reverse of the band model: instead of using delocalized levels from the beginning, we start from localized levels. Then β favours conduction, while λ hinders it. The conduction occurs by ‘hops’ between localized states, as in class II molecular discrete systems, and the electron transfer is thermally activated—the typical behaviour of a semiconductor.

More complex situations can exist. For instance, systems described by *narrow bands* (weak β and $|\beta| \approx U$ or $|\beta| \ll U$) present a particular behaviour. In such cases, even the two-centres repulsion integral V (or j as defined in Chapter 2) can also play a role. We deal with such narrow-band systems in Section 3.3.4.

3.3.2 Extended metallic molecular systems and band theory

Here we are dealing with solids which are *metallic*; that is, with a conductivity which is high and obeys eqn. (3.108): the conductivity increases when the temperature decreases.

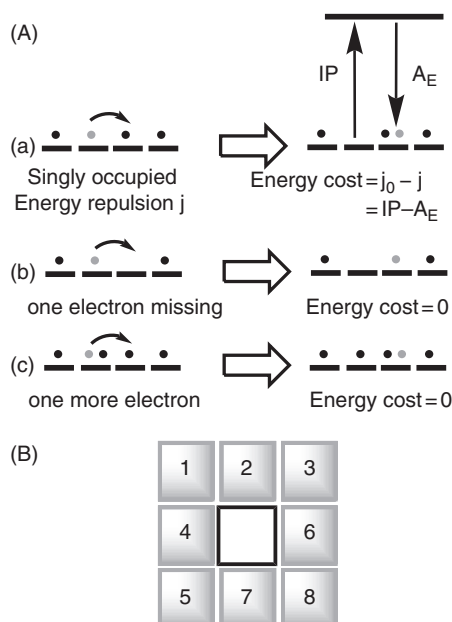
In this case the useful tool is the band model. In the following we present a brief account of it, as an extension of the molecular orbital approach to the solid, with the same advantages and limits as before. The work by Hoffmann and coworkers [1.14] and the recent book by Canadell *et al.* [1.9b] are particularly illuminating in bridging the gap between the molecule and the solid. Simple schemes of electron transfer between centres in a solid are shown in Fig. 3.45 and Fig. 3.46.


Fig. 3.45

Schematic description of insulator and conducting materials. Three sites, 1, 2, 3, with one orbital per site: (a) no electron (vacant orbitals), no conduction; (b) two electrons per orbital, no conduction; (c) one electron in three orbitals: the conduction becomes possible, through electron mobility; (d) five electrons and one hole in three orbitals: the conduction becomes possible, through hole mobility; (e) and (f) ‘band’ representation of cases (c) and (d): the conduction occurs due to partially occupied bands.

Fig. 3.46

(A) Schematic electron transfer in 1D systems and cost in energy: at left, before electron transfer; at right, after electron transfer. (a) One electron per orbital. The electron transfer energy cost is the difference between the one-centre electronic repulsion integral $U(j_0)$ and the two-centre electronic repulsion integral, $V(j)$. When an electron is withdrawn (b) or added (c), there is no energy cost for the electron transfer; the transferred electron is in grey. (B) A mechanical analogy to stress simply the importance of holes: it is possible to displace the grey numbered squares (electrons) only if at least one of the positions is vacant (hole). (Adapted from A.J. Heeger, A.G. MacDiarmid, H. Shirakawa [3.66].)

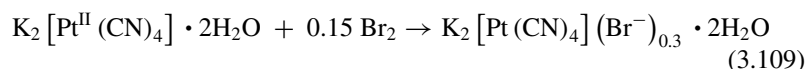


The two figures reveal the nature of the species allowing the conduction (electron or hole), the energy cost for the electron transfer, in terms of the two-electron repulsion integrals U and V , and suggest a link to the quantities IP , the standard ionization enthalpy, and A_E , the electronic affinity (or better, the negative of the standard enthalpy for electronic fixation), better known among chemists.

We deal hereunder with three examples: oxidized potassium tetracyanidoplatinate (KCP), doped polyacetylene, and 1D organic conductors. We rely on simple ideas on the electron–electron interactions, on the electronic structure of the molecules, and on the structure of the materials to show how it is possible to obtain molecular materials exhibiting the expected conductivity. The interested reader may consult the general references [1.9, 1.14, 3.66–3.70] to acquire a deeper insight (and different approaches) of the field.

3.3.2.1 KCP: oxidized potassium tetracyanidoplatinate

KCP is the abbreviation for oxidized potassium tetracyanidoplatinate (*kalium tetracyanoplatinat* in German), which is representative of a wide family of compounds with formula $C_2 [Pt(CN)_4] (X^-)_x \cdot nH_2O$ ($C = K, Rb, Cs$; $X = Cl, Br, FHF$; $x = 0.2 - 0.4$; $n = 0 - 7$). The system was first investigated by Knop as early as 1842, and approached by Levy in 1912, but it was Krogmann, in 1968, who was responsible for the main progress. The compounds are often denoted as Krogmann salts. One of the typical solid known as KCP is $K_2 [Pt(CN)_4] (Br^-)_{0.3} \cdot 2H_2O$. The other compounds in the family present slight variations in the properties (to be discussed), but the basic features remain the same. $K_2 [Pt(CN)_4] (Br^-)_{0.3} \cdot 2H_2O$ is produced either by chemical oxidation of a solution of potassium tetracyanidoplatinate, $K_2 [Pt^{II}(CN)_4]$, by dibromine:



or by electrocrystallization. Fine black needles with a metallic lustre grow slowly on a platinum anode when crossed by a controlled constant current.

Whereas $\text{K}_2 [\text{Pt}^{\text{II}} (\text{CN})_4] \cdot 2\text{H}_2\text{O}$ is an insulator ($\sigma = 5 \cdot 10^{-7} \Omega^{-1} \text{cm}^{-1}$), $\text{K}_2 [\text{Pt} (\text{CN})_4] (\text{Br}^-)_{0.3} \cdot 2\text{H}_2\text{O}$ (KCP) is a metallic conductor at room temperature. The conductivity parallel to the z axis $\sigma_{\parallel} = \sigma_z \approx 300\text{--}800 \Omega^{-1} \text{cm}^{-1}$ at room temperature (depending on the samples), and increases when T decreases. KCP becomes a semiconductor at lower temperatures (around 270 K), with an activation energy $\Delta E = 70 \text{ meV}$. Furthermore, the conductivity is highly anisotropic, being much larger along the z axis (stacking axis of the molecules) than in the perpendicular plane: $\sigma_{\parallel}/\sigma_{\perp} \approx 10^5$ (see Fig. 3.47). The striking change in electrical properties can be interpreted in a rather simple way, using the band-structure description, providing some illuminating insights into our study of conducting molecular materials.

The first observation is that in both compounds the structure is made of $[\text{Pt}(\text{CN})_4]$ anionic units stacked along the z axis in a staggered configuration. The potassium ions and the water molecules are located between the stacks. The angle between successive Pt–CN units along z is around 16° in $\text{K}_2[\text{Pt}^{\text{II}}(\text{CN})_4] \cdot 2\text{H}_2\text{O}$ and 45° in KCP. Two important differences occur in the oxidized KCP structure: 0.3 bromide ions appear between the $[\text{Pt}(\text{CN})_4]$ stacks, and the Pt–Pt distance decreases strongly from 350 pm to 289 pm (indeed, close to the Pt–Pt distance in platinum metal, 277.5 pm). The anisotropy of the structure is clearly related to the anisotropy of the conductivity, with a prominent role of the z axis. Without loss of generality, for interpretation of the electrical properties it is possible to simplify the description of the system by making the two approximations shown in Fig. 3.48f,g, as suggested by Hoffmann [1.14]. First, the real staggered conformation in (d, e) can be replaced by the eclipsed model in (f); the cell parameter along the z

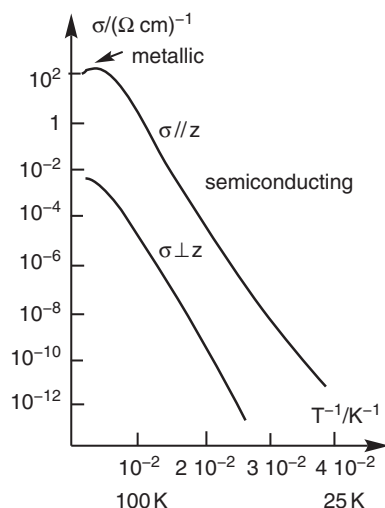
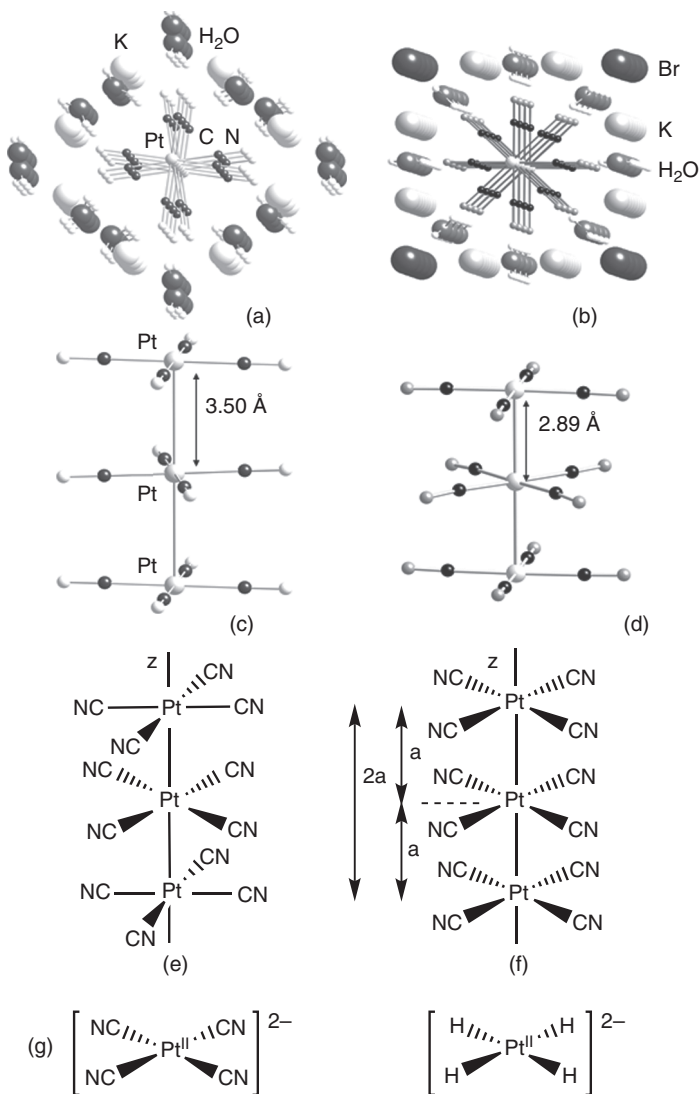


Fig. 3.47

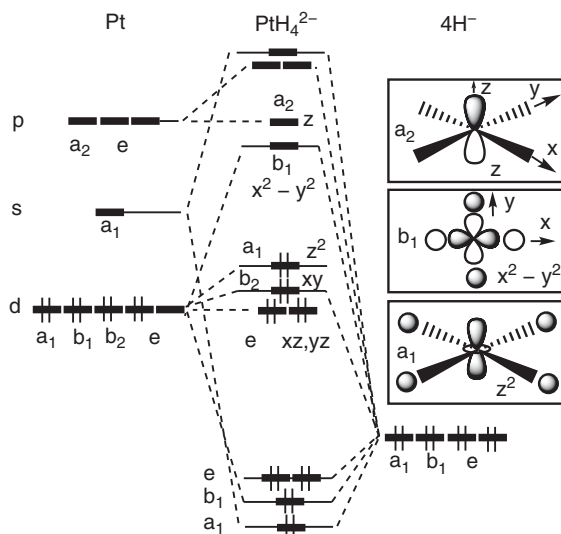
Variation of the conductivity (log scale) versus $1/T$ of a single crystal of KCP measured parallel to the z axis (σ_{\parallel}) and in a perpendicular direction (σ_{\perp}). (Adapted from [3.70].)

**Fig. 3.48**

Crystallographic structures down the z axis: (a) $\text{K}_2[\text{Pt}^{\text{II}}(\text{CN})_4] \cdot 2\text{H}_2\text{O}$; (b) $\text{K}_2[\text{Pt}(\text{CN})_4](\text{Br}^-)_{0.3} \cdot 2\text{H}_2\text{O}$. Perspective views of the stacks: (c) $\text{K}_2[\text{Pt}^{\text{II}}(\text{CN})_4] \cdot 2\text{H}_2\text{O}$; (d) $\text{K}_2[\text{Pt}(\text{CN})_4](\text{Br}^-)_{0.3} \cdot 2\text{H}_2\text{O}$. Schematic structures: (e) staggered stacks of $\text{K}_2[\text{Pt}(\text{CN})_4](\text{Br}^-)_{0.3} \cdot 2\text{H}_2\text{O}$ (cell parameter $2a$); (f) eclipsed model structure (cell parameter a); (g) $[\text{Pt}^{\text{II}}(\text{H})_4]^{2-}$ model in which the cyanides have been replaced by hydrides.

axis changes accordingly from $2a$ to a . Second, the cyanide ion CN^- in the real $[\text{Pt}^{\text{II}}(\text{CN})_4]^{2-}$ complex is replaced by the hydride H^- (Fig. 3.48g). The square planar model $[\text{Pt}^{\text{II}}(\text{H})_4]^{2-}$, D_{4h} symmetry results. Its electronic structure is shown in Fig. 3.49. The symmetry labels shown are those of the C_{4v} point group, for simple reasons that will appear soon. The metal brings eight d electrons, and the ligands also eight (two electrons per hydride). In the molecule, the sixteen electrons occupy the four bonding MOs (a_1 , b_1 , e), ensuring the bonding, the three non-bonding xy (b_2), xz , and yz (e) d orbitals and the slightly antibonding dz^2 (a_1).

The molecular orbitals of the precursor interact in the solid to build the symmetry orbitals, or Bloch orbitals defined in Section 1.4 by eqns. (1.44), with energies defined by eqn. (1.46). It is obvious from the structure that the only


Fig. 3.49

Schematic molecular orbital energy diagram of square planar $[\text{Pt}^{\text{II}}(\text{H})_4]^{2-}$, D_{4h} symmetry (the symmetry labels correspond to C_{4v} ; see text). At left are the atomic levels of $5d^8$ Pt(II), and at right are the four symmetry orbitals of the four hydride ions, and in the centre are the molecular orbitals of $[\text{Pt}^{\text{II}}(\text{H})_4]^{2-}$. The significant MOs for the discussion are shown at right, including the highest doubly occupied MO, based on Pt $5dz^2$.

significant interactions take place along the z axis and not in the perpendicular plane. The band structure arises from the overlap of the molecular orbitals centred on the metal. We begin with the interaction of the z^2 MOs. We name α_{z^2} the energy of the z^2 MOs in the complex, and $\beta_{z^2z^2}$ the resonance energy between two neighbouring z^2 MOs along the z axis. The Bloch orbitals built from the overlap of the z^2 MOs are shown in Fig. 3.50: one recognizes, at $k = 0$, the fully bonding Bloch orbital $\Theta_{k=0}(z^2)$ with no node, at energy $\alpha_{z^2} + 2\beta_{z^2z^2}$ and, at $k = \pi/a$, the fully antibonding orbital, $\Theta_{k=\pi/a}(z^2)$ with $N - 1$ nodes, at energy $\alpha_{z^2} - 2\beta_{z^2z^2}$.

$$\begin{aligned}\Theta'_{k=0} &= \frac{1}{\sqrt{N}} \sum_{m=-n'+1}^{n'} (1)^m \phi_m \\ &= \frac{1}{\sqrt{N}} (\phi_{-n'+1} + \dots + \phi_{-1} + \phi_0 + \phi_1 + \dots + \phi_{n'})\end{aligned}\quad (3.110a)$$

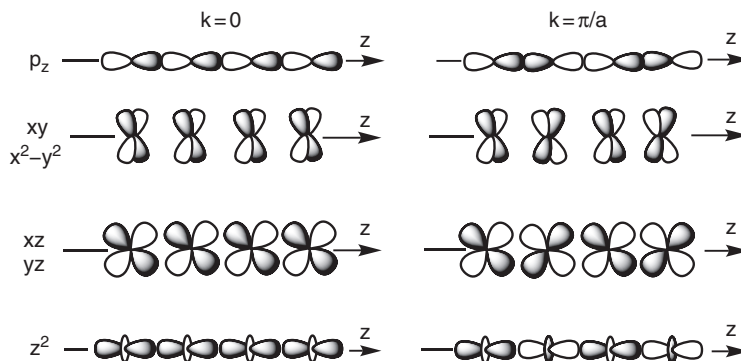
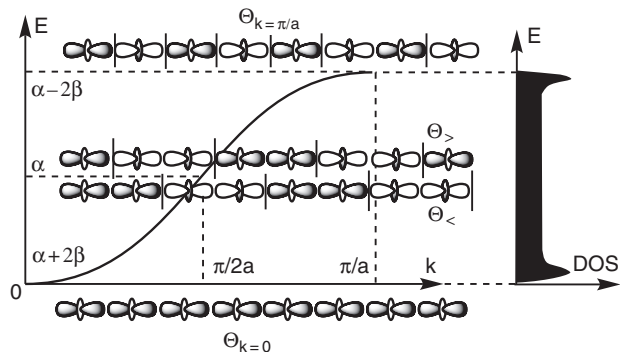
$$\begin{aligned}\Theta'_{k=\pi/a} &= \frac{1}{\sqrt{N}} \sum_{m=-n'+1}^{n'} (-1)^m \phi_m \\ &= \frac{1}{\sqrt{N}} (\phi_{-n'+1} - \dots - \phi_{-1} + \phi_0 - \phi_1 + \dots - \phi_{n'})\end{aligned}\quad (3.110b)$$

Furthermore, Fig. 3.50 displays the two Bloch orbitals just below $k = \pi/2a$ ($N/2 - 1$ nodes) and just above ($N/2$ nodes), practically non-bonding. These orbitals will play an important role later. The Bloch orbitals built from the other metal-centred orbitals are shown in Fig. 3.51.

Two qualitative observations should be made here: (i) the overlap decreases from σ overlap ($p_z-p_z > z^2-z^2$) to π overlap ($xz-xz$, $yz-yz$) and δ overlap [$xy-xy$ and $(x^2-y^2)-(x^2-y^2)$]; the width of the corresponding Bloch orbitals will behave accordingly, very wide for p_z , wide for z^2 , narrow for xz and yz , and very narrow for xy and x^2-y^2 ; (ii) the z^2 , xy and x^2-y^2 Bloch orbitals

Fig. 3.50

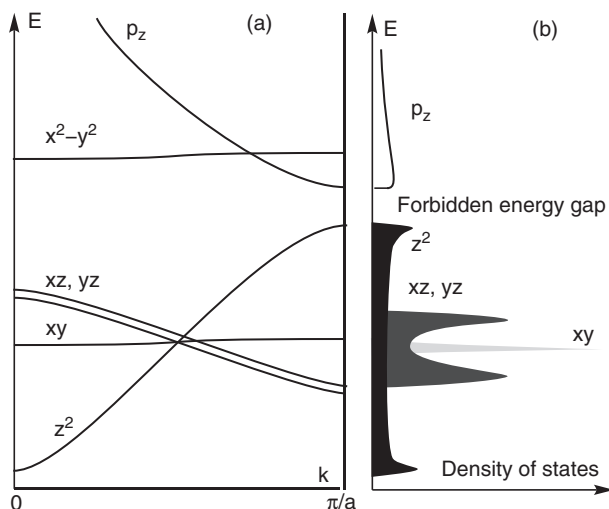
Bloch orbitals generated by the z^2 orbitals and energy dispersion curve. The stacking axis z is horizontal; α denotes α_{z^2} , and β denotes β_{z^2} . At the bottom, the $\Theta_{k=0}(z^2)$ Bloch orbital is fully bonding, whereas at the top of the band the $\Theta_{k=\pi/a}(z^2)$ is fully antibonding. The Bloch orbitals around $k = \pi/2a$ ($\Theta_{<}$ and $\Theta_{>}$) are practically non-bonding. At right, a scheme of the density of states.

**Fig. 3.51**

Bloch orbitals generated by the metal-centred orbitals; at left, centre of the Brillouin zone, $k = 0$; at right, border of the Brillouin zone, $k = \pi/a$. The stacking axis z is horizontal.

are bonding at $k = 0$ and antibonding at $k = \pi/a$, and they will run ‘up’; the p_z , xz , and yz Bloch orbitals behave at the opposite, and the bands will run ‘down’. Both effects are illustrated in the dispersion energy curve of Fig. 3.52a, based on semi-empirical extended Hückel calculations. The p_z band is so wide that the bottom at $k = \pi/a$ lies below the energy of the very narrow x^2-y^2 band, above the top of the z^2 band. One can observe that the energy values of the bands at $k = \pi/2a$ correspond to energy levels in the isolated complex (Fig. 3.50).

Our qualitative approach allows us to find the main features of the band diagram, but the relative position of the z^2 and the p_z band needs calculations to be established. We then fill in the bands, according to the electronic structure of the complex, as shown in Fig. 3.49: the electrons of the d orbitals fill four d bands. The highest occupied level, or Fermi level, is the top of the z^2 band, whereas the lowest unoccupied level is the bottom of the p_z band. Between the two there is a forbidden energy gap. Calculations show that the gap is wide so that the compound is an insulator. We have reached a first step in our interpretation of the properties of $K_2[Pt^{II}(CN)_4] \cdot 2H_2O$: the d bands are filled, bonding and antibonding levels are occupied, and do not contribute to the bonding scheme, so that there is no d–d bonding along the stack, which allows us to understand the rather large Pt–Pt distance, in the range of Van der Waals interactions. The forbidden energy $5dz^2-6p_z$ gap explains the insulating properties of the material.

**Fig. 3.52**

(a) Energy dispersion curves for Bloch orbitals generated by the metal-centred orbitals; at left, centre of the Brillouin zone at $k = 0$; at right, border of the Brillouin zone at $k = \pi/a$; (b) density of states and filling of the bands. (Adapted from Hoffmann [1.14].)

We now turn to the oxidized material, KCP, $\text{K}_2[\text{Pt}(\text{CN})_4](\text{Br}^-)_{0.3} \cdot 2\text{H}_2\text{O}$. A simple analysis of the formal oxidation state of platinum (using the common oxidation states for the other elements, +1 for potassium, -1 for bromide and cyanide) leads to an unusual non-integer number, $\text{Pt}^{+2.3}$: platinum appears to have been partially oxidized. Using a local view of oxidation states, it could be interpreted by the presence of some Pt(III) or Pt(IV) in the stacks. Nevertheless the band structure is more appealing: the oxidation corresponds to the withdrawing of electrons of the filled bands and more precisely to withdrawing of electrons at the top of the highest occupied band which is z^2 . The band then becomes partially occupied, which is one of the conditions of conduction: the partial oxidation of platinum leads to a partial occupancy of the band and to an easy interpretation of the high-temperature metallic conducting properties of KCP (Fig. 3.45f). Furthermore, the band which is partially emptied is the z^2 band. The conduction is important, and metallic, along the z axis only, and allows explaining in a straightforward way the anisotropy of the conductivity. The band model has something else to reveal: the structural change upon oxidation. The levels at the top of the z^2 band are antibonding levels: emptying them strengthens the z^2 - z^2 bonding in the z direction, and the decrease of Pt-Pt distance follows.

KCP is the prototype of a large family of similar compounds which exhibit a metallic character with conductivities reaching $2300 \Omega^{-1} \text{cm}^{-1}$ at 300 K in some cases.

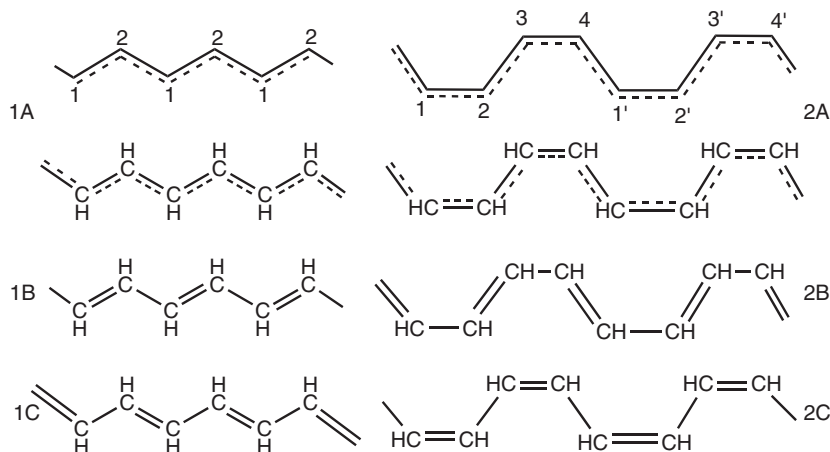
When the temperature decreases, KCP and all these one-dimensional conductors undergo a transition to a semiconducting state (termed a Peierls transition). We study this important feature and more complex phenomena in Section 3.3.3.3.

3.3.2.2 Conducting polymers: the case of doped polyacetylene

The discovery of the metallic conduction of doped polyacetylene was an important event in the field of organic materials. For the first time, it was

Fig. 3.53

Different representations of bonding in polyacetylene: at left, *trans*-polyacetylene; at right, *cis*-polyacetylene: 1A and 2A: regular structures; 1B and 1C equivalent alternant structures for the *trans*-isomer; 2B and 2C non-equivalent alternant structures for the *cis*-isomer.



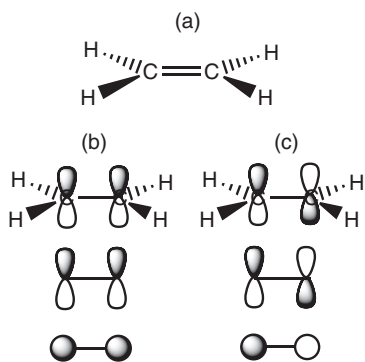
shown in a convincing manner that organic matter can behave as a metal, without metallic elements and without conducting d electrons. KCP was indeed the first evidenced conducting molecular material, but we have seen that the mechanism of the conductivity implies essentially the metal d_{z^2} orbitals. With polyacetylene, only carbon and hydrogen atoms are implied. Polyacetylene is a polymer (or plastic, in everyday language) with formula $-(CH)_n$. It exists under various isomer forms. The pure *cis* and *trans* isomers are shown in Fig. 3.53. Generally, ‘plastics’ are used around conducting metallic wires to insulate the metal from the environment. But in the present case, by a simple redox reaction, the conductivity of the ‘plastic’ can be multiplied by a factor of one billion (10^{12}), and becomes as conducting as some metals. This important step in the chemistry of molecular materials was distinguished in 2000 by the Nobel Prize in Chemistry [3.66].

In the following we try to use the band theory concepts introduced previously as a first approximation to explain simply the conducting properties of doped polyacetylene.

Regular *trans*-polyacetylene

We first address *trans*-polyacetylene, and more precisely the regular form shown as 1A in Fig. 3.53, supposed to be a planar crystalline ribbon without interaction between the chains. Indeed, one can understand that even if the chains are individually good conductors, the overall conductivity will be limited by the fact that the electrons have to ‘jump’ from one chain to the next. Hence, the chains have to be ordered and well packed. The orbitals of interest are the valence carbon π orbitals. Each atom has one such orbital in a plane perpendicular to the polymer ribbon ($2p_y$). For the sake of simplicity we represent the orbitals viewed from the top, as shown in Fig. 3.54 for ethylene (a), π bonding orbitals (b), and π^* antibonding (c). We illustrate the building of the crystal orbitals—as shown in Section 1.4—and their dispersion energy curves in Fig. 3.55.

An ideal regular *trans*-polyacetylene (1A), with a partially occupied band (half-filled with one electron per carbon) should therefore be a *metallic* conductor. Indeed, such an ideal compound *does not exist*. *Trans*-polyacetylene

**Fig. 3.54**

Conventional representations of ethylene (a) and π orbitals: π bonding (b) and π^* antibonding (c).

The discovery of polyacetylene

The discovery came from work in Shirakawa's laboratory in the Tokyo Institute of Technology in the 1970s. A new catalytic procedure allowed control of the amount of *cis*- and *trans*- polyacetylenes in the black film deposited in the reaction vessel: with an excess of catalyst, *trans*-polyacetylene appeared as a silvery film, whereas, in different conditions, *cis*-polyacetylene was obtained as a copper-coloured film. The discovery is narrated in the Nobel committee documents, as follows:

'In another part of the world, chemist MacDiarmid and physicist Heeger were experimenting with a metallic-looking film of the inorganic polymer sulphur nitride, $(\text{SN})_x$. MacDiarmid referred to this at a seminar in Tokyo. Here the story could have come to a sudden end, had not Shirakawa and MacDiarmid happened to meet, accidentally, during a coffee break. When MacDiarmid heard about Shirakawa's discovery of an organic polymer that also gleamed like silver, he invited Shirakawa to the University of Pennsylvania in Philadelphia. They set about modifying polyacetylene by oxidation with iodine vapour. Shirakawa knew that the optical properties changed in the oxidation process, and MacDiarmid suggested that they ask Heeger to have a look at the films. One of Heeger's students measured the conductivity of the iodine-doped *trans*-polyacetylene and . . . eureka! The conductivity had increased ten million times! In the summer of 1977, Heeger, MacDiarmid, Shirakawa, and coworkers published their discovery in the article "Synthesis of electrically conducting organic polymers: Halogen derivatives of polyacetylene $(\text{CH})_n$ ".' *Journal of the Chemical Society, Chemical Communications*.

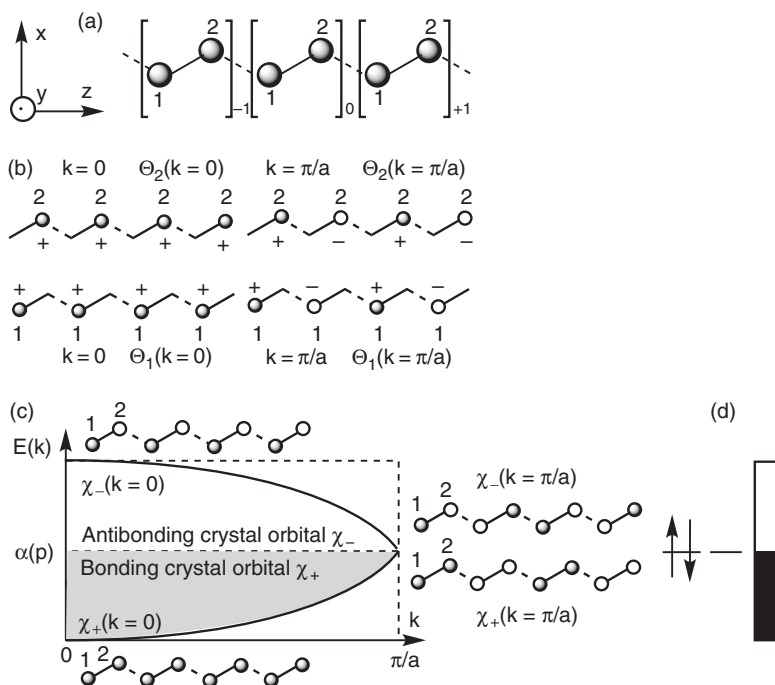


Fig. 3.55

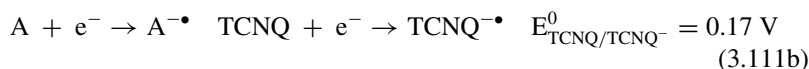
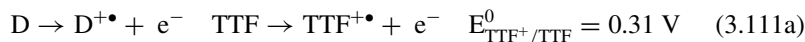
Crystal orbitals in regular *trans*-polyacetylene: a) axes, numbering scheme of the two different sites in the cell and neighbouring cells; (b) Bloch orbitals built from atoms 1, at $k=0$ $\Theta_1(k=0)$ and at π/a $\Theta_1(k=\pi/a)$ and from atoms 2, $\Theta_2(k=0)$ and $\Theta_2(k=\pi/a)$; (c) crystal orbitals $\chi_{\pm}(k) = N_{\pm} [\Theta_1(k) \pm \Theta_2(k)]$ and their dispersion energy curves; (d) occupancy of the crystal orbitals and degeneracy of $\chi_+(\pi/a)$, highest occupied level of $\chi_+(k)$ and of $\chi_-(\pi/a)$, lowest vacant level of $\chi_-(k)$.

exists instead as the alternant 1B and 1C semiconducting forms (Fig. 3.53), as a result of the Peierls distortion in a 1D system with a half-filled band (see Section 1.4.3). This process is very general, and is discussed in more detail in Sections 3.3.3.1 and 3.3.3.2.

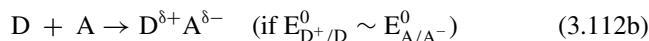
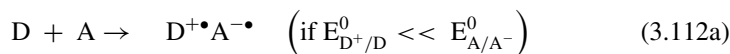
3.3.2.3 Charge transfer salts (TTF-TCNQ and related systems)

Another class of molecular conductors (or semiconductors) is provided by the charge transfer salts. By ‘charge transfer salts’ we mean molecular solids made of electrons donors D and acceptors A. They are essentially made of planar molecules. Such molecules exhibit a strong tendency to stack along one dimension in the solid state. The most typical components are tetrathiafulvalene (TTF) and tetracyanoquinodimethane (TCNQ) and their combination TTF-TCNQ, but many other examples can be found, as shown in Fig. 3.56. The constituent units are closed-shell systems, with an extended system of π delocalized electrons. The electron donors D can be oxidized (the case of TTF), while electron acceptors A can be reduced (the case of TCNQ).

The oxidized and reduced species are charged and open-shell species. The oxidized donor is written $D^{+\bullet}$; a cation-radical, and the reduced acceptor $A^{-\bullet}$, an anion-radical. The possible reactions and the standard redox potentials *versus* SCE (saturated calomel electrode) for the TTF-TCNQ system in acetonitrile are given in the following:

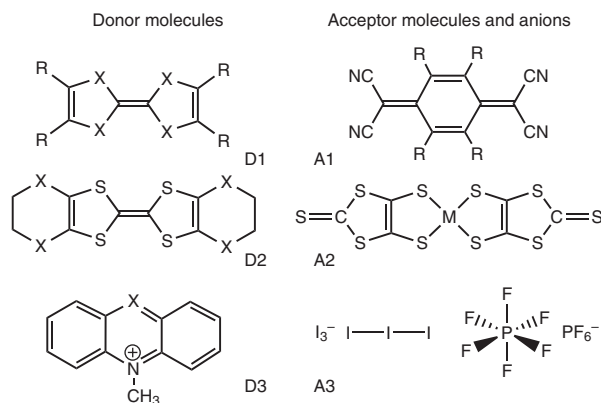


From these constituents, many types of 1D system can be prepared. When the donor and acceptor are associated, the question arises of the possible redox reaction. Although we are in the solid state we can make use, for qualitative purposes, of the standard redox potentials $E_{D^{+}/D}^0$ and $E_{A/A^{-}}^0$ in solution, and then:



Thus, depending on the relative values of the redox potentials, the electron transfer can be complete ($\delta = 1$, $D^{+}A^{-}$, ionic situation), ineffective ($\delta = 0$, DA, D and A remain unchanged, neutral situation) or partial (δ , $D^{\delta+}A^{\delta-}$, partial charge transfer). δ is the fraction or degree of charge transfer, sometimes termed DPO, degree of partial oxidation.

The latter situation is by far the more interesting in giving rise to conducting properties, as we shall see soon. In the solid, these planar molecules can lead to 1D structures in which the π electronic clouds interact weakly, thus producing narrow bands (the typical bandwidth is 0.5–1 eV). The stack can be considered as a mixture of neutral and charged molecules ($D/D^{+\bullet}$; $A/A^{-\bullet}$), a molecular mixed valence state, reminiscent to the situation of platinum in KCP.

**Fig. 3.56**

At left, donor molecules D: (D1) R = H, X = S, Tetrathiafulvalene (TTF); R = H, X = Se, tetraselenofulvalene (TSF); R = methyl, X = S, tetramethyltetra-thiofulvalene (TMTTF); R = methyl, X = Se, tetramethyltetraselenofulvalene (TMTSF); R,R = trimethylene, X = S; hexamethylenetetra-thiafulvalene (HMTTF); R,R = hexamethylene, X = Se, hexamethylenetetraselenofulvalene (HMTSF); R,R = benzene, X = S, dibenzotetrathiafulvalene DBTTF; R,R = benzene, X = Se, dibenzotetraselenofulvalene DBTSF. (D2) X = S, bis(ethylenedithio)tetrathiafulvalene BEDTTF or ET; X = O, bis(ethylenedioxo) tetrathiafulvalene BEDOTTF. (D3) X = CH, N-methylacridinium (NMA) X = N, N-methylphenazinium (NMP). At right, acceptor molecules A: (A1) R = H, tetracyanoquinodimethane (TCNQ); R = F, tetrafluorotetracyanoquinodimethane (TCNQF₄); central ring = naphthalene: tetracyanonaphthoquinodimethane (TNAP). (A2) [M(dmit)₂], M = Ni(II), Pd(II), Pt(II); dmit = 4,5-dimercapto-1,3-dithiol-2-thione. (A3) anions: triiodide I₃⁻; hexafluorophosphate, PF₆⁻.

The crystallographic structures vary, but in many cases the donor–acceptor D–A combination produces segregated stacks (D^{δ+})_n and (A^{δ-})_n, or alternated ones (D^{δ+}A^{δ-})_n (Fig. 3.57a,b). Segregation occurs in solid TTF–TCNQ with distinct stacks of TTF^{•+} and TCNQ^{•-} moieties, as shown in Fig. 3.57c,d.

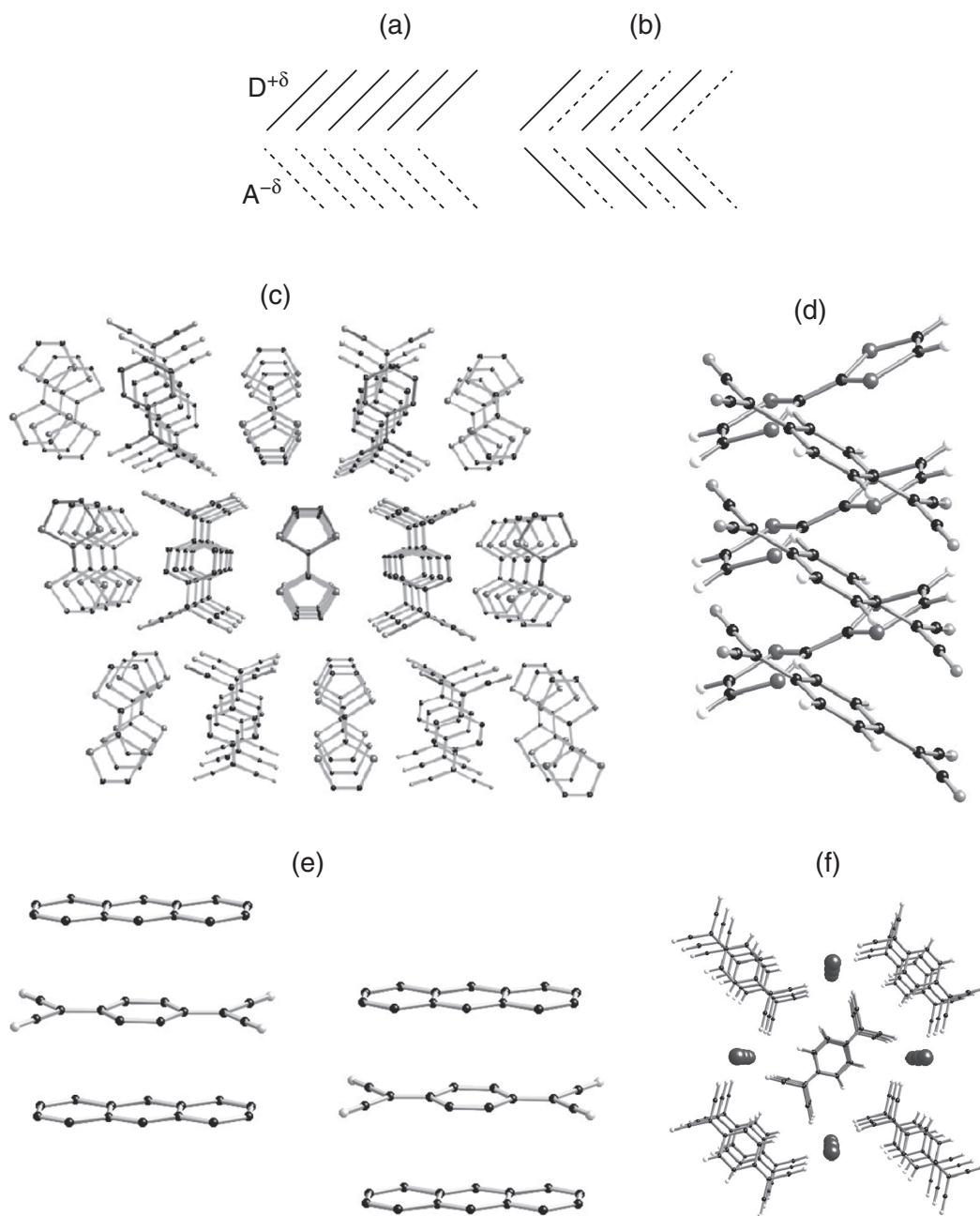
Alternation occurs in anthracene–TCNQ, where there is no electron transfer (Fig. 3.57e). The molecules build a molecular solid in which all the components are neutral. The main source of crystal stability is the van der Waals energy. Conversely, in the case of K⁺TCNQ⁻ (Fig. 3.57f) the electron transfer is complete (D⁺A⁻)_n; the primary interactions are ionic, and they ensure the stability of the solid with Madelung energy.

Figure 3.58 shows the conductivity *versus* temperature curve for a number of 1:1 TCNQ salts. Some compounds, such as the ionic alkaline salts, present a low conductivity in the 10⁻²–10⁻⁴ Ω⁻¹ cm⁻¹ range, increasing with temperature, characteristic of semiconductors.

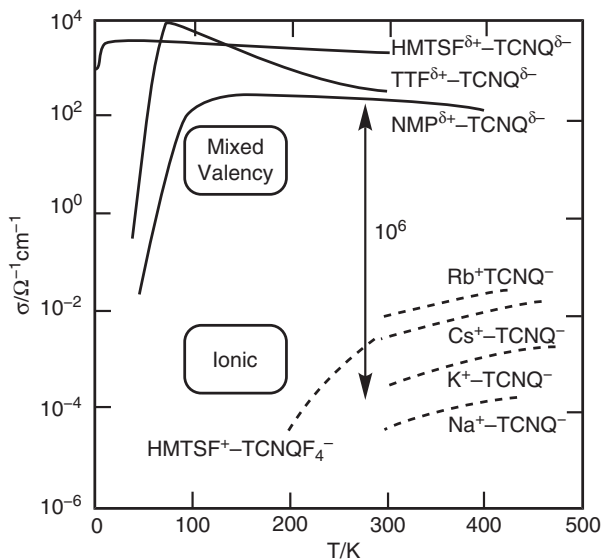
Other systems, such as TTF–TCNQ, or HMTSF–TCNQ (HMTSF is hexamethylenetetra-selenofulvalene) exhibit a much higher conductivity, near 10²–10⁴ Ω⁻¹ cm⁻¹, increasing with temperature, and thus can be ranked as metals. They are named ‘mixed valency’ in Figs. 3.58 and 3.59. Some others, such as anthracene–TCNQ (not shown), present no electron transfer and are practically insulators.

A first simple explanation of these differences is based on the redox potentials of the two molecules associated in the 1:1 salts. The room-temperature conductivity of the compounds (as pellets) is displayed schematically in Fig. 3.59 as a function of the standard redox potential of the donor D. The figure reveals, remarkably, a classification in three groups, according to the possibility of charge transfer ρ between the donor D and the TCNQ acceptor, due to a redox process: the ionic compounds, for which the transfer is complete ($\rho = 1$), are semiconducting or insulating; the ‘mixed-valency’ ones, for which the electron transfer is partial ($0 < \rho < 1$), are metallic conductors, and finally, the neutral ones, in which no charge transfer occurs ($\rho = 0$), are insulating.

Why we encounter such a clear-cut situation is not easy to answer. Indeed, the amount of electron transfer and the energy of the solid are determined not only by the redox properties of the components in solution, but also by the

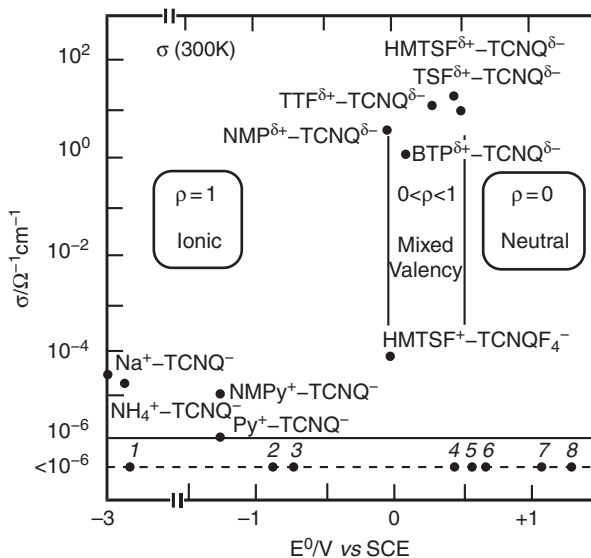
**Fig. 3.57**

Stacks of donor-acceptor solids: (a) segregated [donor $D^{+\delta}$ (plain line) and acceptor $A^{-\delta}$ (dotted line)]; (b) alternated; (c) perspective view of the TTF-TCNQ structure down the b axis, demonstrating the segregation of TTF and TCNQ stacks; (d) view of TTF-TCNQ down the a axis, displaying the dihedral angle between TTF and TCNQ stacks; (e) view of anthracene-TCNQ, a neutral molecular solid with alternated (mixed) stacking of anthracene and TCNQ down the b axis; (f) perspective view of $K^+TCNQ^{\bullet-}$, an ionic solid; the TCNQ $^-$ segregated stacks are down the a axis.


Fig. 3.58

Thermal variation of the conductivity of 1:1 charge transfer complexes based on TCNQ. Abbreviations as in Fig. 3.56. Na⁺, K⁺, Rb⁺, Cs⁺: alkali cations. (Adapted from Torrance [3.67].)

Madelung energy of the crystal (not discussed until now). We shall address these questions in more detail in Section 3.3.3. But it is rewarding at this stage to observe that (i) the neutral systems are almost insulating ($\sigma \leq 10^{-6} \Omega^{-1} \text{cm}^{-1}$) because they correspond to filled molecular orbitals and bands; (ii) the ionic systems exhibit only a slightly higher conductivity (10^{-6} – $10^{-4} \Omega^{-1} \text{cm}^{-1}$), though they correspond to a half-filled band, because they correspond to solids with a large Madelung energy created by the ionic components, with electrons localized due to large interelectronic repulsive interactions U and narrow bands (we shall see in Section 3.3.4 that they are termed Mott insulators); (iii) only


Fig. 3.59

Conductivity of 1:1 TCNQ-based charge transfer complexes as a function of the standard redox potential of the donors. Abbreviations as in Fig. 3.56, and as follows: 1, TEA⁺ (triethylammonium); 2, NMQ_n⁺ (N-methylquinolinium); 3, NMPz⁺ (N-methylpyrazinium); 4, TTFH₂⁺; 5, DBTTF⁺ (dibenzotetrafulvalenium); 6, TTFH₄⁺; 7, perylene⁺; 8, pyrene⁺ or anthracene⁺; BTP = 4,4'-bithiopyrazinium; HMTSF = hexamethylene-tetraselenofulvalene; NMP⁺ = N-methylphenazinium; NMPy⁺ = N-methylpyridinium; Py⁺ = pyridinium; TSF = tetraselenofulvalene. (Adapted from Torrance [3.67].)

the ‘mixed valency’ systems present a high conductivity, above $1 \Omega^{-1} \text{ cm}^{-1}$, because electron transfer can occur between the oxidized and reduced sites of a same entity (see Figs. 3.45 and 3.46). The evidence of the role of partial electron transfer for creating metallic conductivity in charge transfer salts was an important step in the understanding and design of new molecular metals in the 1980s. An archetypal example is TTF-TCNQ, which highlights the most important features of conducting mixed valence systems.

The TTF-TCNQ system

‘TTF-TCNQ is the first molecular crystal to show a conductivity approaching that of conventional metals at room temperature and exhibiting a metal-like behaviour on cooling’, wrote Jérôme [3.69j]. But how do we obtain it?

When mixing TTF and TCNQ neutral molecules in an organic solvent such as tetrachloromethane or acetonitrile, a black solid soon appears. TCNQ was first synthesized by Melby and Acker and coworkers in 1962, TTF and TTF chloride were prepared by Wudl and coworkers in 1970, and TTF-TCNQ was discovered by Heeger, Ferraris and coworkers in 1973. In the solid state, both pure TTF and TCNQ produce crystallographic structures with one-dimensional stacks. TTF-TCNQ single crystals can be grown easily using electrocrystallization, allowing detailed physical studies. The crystallographic structure corresponds to a monoclinic system, space group P21/c, with crystallographic parameters: $a = 122.9 \text{ pm}$; $b = 382 \text{ pm}$; $c = 184.2 \text{ pm}$; and $\beta = 104.49^\circ$. Views of the structure down the b and a axes are shown in Fig. 3.57c,d.

The electronic properties are strongly dependent on δ —the degree of charge transfer from the donor to the acceptor—which is determined largely by the redox properties of TTF and TCNQ in solution. As seen before, the standard redox potential for $\text{TTF}^{+•}/\text{TTF}$, $E^\circ_{\text{TTF}^+/\text{TTF}}$ is 0.31 volts. Here we can forget the second oxidation step giving TTF^{2+} , stabilized by aromaticity in the two rings, as shown in Fig. 3.60. The standard redox potential for $\text{TCNQ}/\text{TCNQ}^{•-}$, $E^\circ_{\text{TCNQ}/\text{TCNQ}^{•-}}$ is 0.17 volts. The thermodynamically favoured reaction is thus reaction 2 in eqn. (3.113).

When starting from TTF and TCNQ in solution, the equilibrium is initially displaced far to the left, but owing to the insolubility of the TTF-TCNQ salt the equilibrium is displaced smoothly to grow crystalline TTF-TCNQ (or better, $\text{TTF}^{\delta+}-\text{TCNQ}^{\delta-}$).

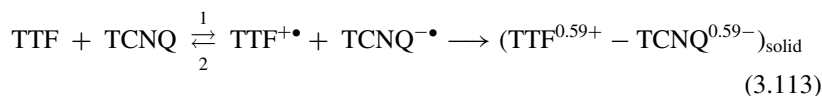
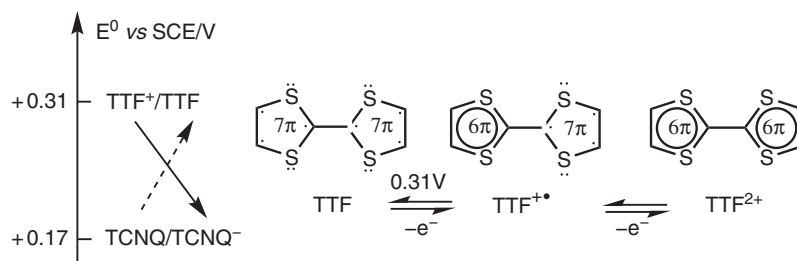


Fig. 3.60

(a) Scheme of the standard redox potentials of TTF and TCNQ and the related thermodynamically favoured reaction (arrows); (b) electronic structure of different oxidation states of TTF and reversible redox reactions.



The electric properties of TTF-TCNQ in solid state are shown in Fig. 3.58. Above about 60 K, TTF-TCNQ is a good molecular metallic conductor. The conductivity is metallic and highly anisotropic, with a value in the $500\text{--}10^3 \Omega^{-1} \text{cm}^{-1}$ range (the exact value depending on the quality of the crystals). Below this temperature the conductivity decreases in a complex way, since several transitions occur, but the general behaviour is one of a semiconductor. As in the preceding examples, one-dimensional Peierls instabilities appear (discussed in Section 3.3.3).

Electronic structure of TTF-TCNQ and interpretation of the metallic conductivity

An important parameter necessary to understand the charge transfer δ is the band structure. We begin with the components: TTF and TCNQ. The energy diagrams of the molecular orbitals of neutral TTF and TCNQ are shown in Fig. 3.61. The two orbitals of interest are the HOMO of TTF, filled, which becomes half-occupied in $\text{TTF}^{+\bullet}$, and the LUMO of TCNQ, empty, which becomes half-filled in $\text{TCNQ}^{\bullet-}$.

In the solid there are uniform molecular stacks along the *b* axis. The overlap between two adjacent molecules is schematized in Fig. 3.62A. The overlap between the π molecular orbitals along the stacking direction is of σ type (axial) and rather strong. The consequences for the Bloch orbitals are shown in Fig. 3.62B–D for TTF and TCNQ at the centre ($k = 0$) and the edge ($k = \pi/b$) of the Brillouin zone.

At the centre of the Brillouin zone, at $k = 0$ (Fig. 3.62B,C), the Bloch orbitals are built from the in-phase (+ +) combination of the molecular orbitals; the interaction between two successive TTF HOMOs is antibonding (column a) whereas the interaction between two successive TCNQ LUMOs is bonding (column b). At the edge of the Brillouin zone, at $k = \pi/b$ (D), the Bloch orbitals are built from the out-of-phase (+ -) combination of the molecular orbitals; the interaction between two successive TTF HOMOs is bonding (a), whereas the interaction between two successive TCNQ LUMO

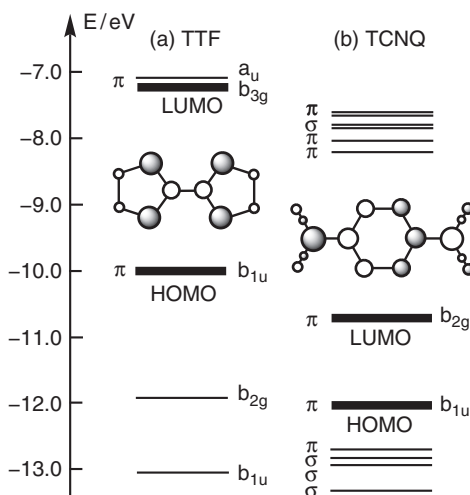
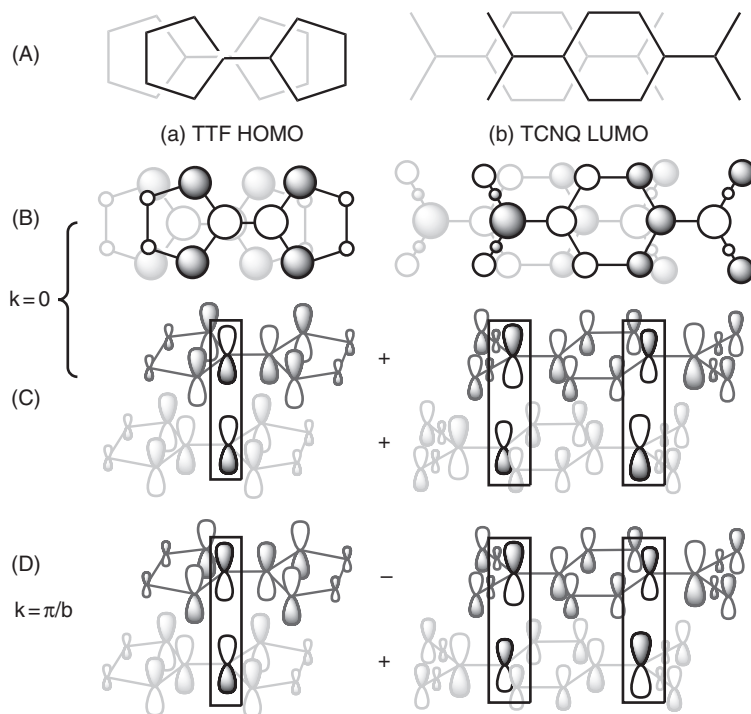


Fig. 3.61

Schematic molecular orbital energy diagram of (a) TTF, with the scheme of its HOMO; (b) TCNQ, with the scheme of its LUMO.

**Fig. 3.62**

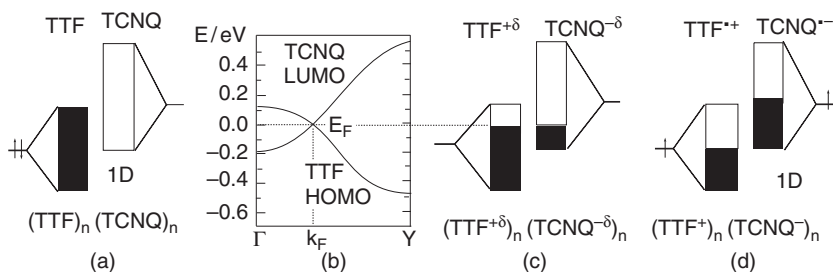
(a) At left, TTF; (b) at right, TCNQ. (A) Molecular overlap along the stacks (b axis). (B) Schematic overview and (C) perspective view of the overlap between the wavefunctions of two neighbouring molecules at the centre of the Brillouin zone ($k = 0$). (D) Perspective view of the overlap at the edge of Brillouin zone ($k = \pi/b$). The rectangles point out the locations of maximum overlap.

is antibonding (b). The resulting resonance integral β is different for TTF and TCNQ, giving rise to the energy bandwidths, ranging from 0.4 to 0.8 eV ($\approx 38\text{--}76 \text{ kJ mol}^{-1}$).

Detailed explanation based on semi-empirical calculations and band structure are presented in Fig. 3.63. At the Brillouin zone centre ($k = 0$) we have the bottom of the LUMO TCNQ band (bonding) and the top of the HOMO TTF band (antibonding). At the Brillouin zone edge ($k = \pi/b$) we have the reverse situation (top of the LUMO TCNQ band, antibonding, and bottom of the HOMO TTF band, bonding). Then, when k increases from the centre of the Brillouin zone ($k = 0$) to the edge ($k = \pi/b$), the LUMO TCNQ's band *runs up*, whereas the HOMO TTF's band *runs down* (it is also said to be inverted). Given the initial energies of the TTF's HOMO and the TCNQ's LUMO (note that the energies are different for neutral molecules in the gas phase and the partially charged units in the solid—stabilized for $\text{TTF}^{+\delta}$ and destabilized for $\text{TCNQ}^{-\delta}$) and the values of the resonance (transfer) integrals β within the stacks ($\beta_{\text{TTF}} \approx 0.11 \text{ eV} \approx 10 \text{ kJ mol}^{-1}$) ($\beta_{\text{TCNQ}} \approx 0.19 \text{ eV} \approx 18 \text{ kJ mol}^{-1}$), the two bands cross at the Fermi level E_{F} , at wavevector k_{F} . The Fermi level is thus determined by the partial charge transfer from TTF to TCNQ stacks. The available charge density δ for the conduction is determined by the value of k_{F} , and is written simply as:

$$2k_{\text{F}} = \delta\pi/b \quad (3.114)$$

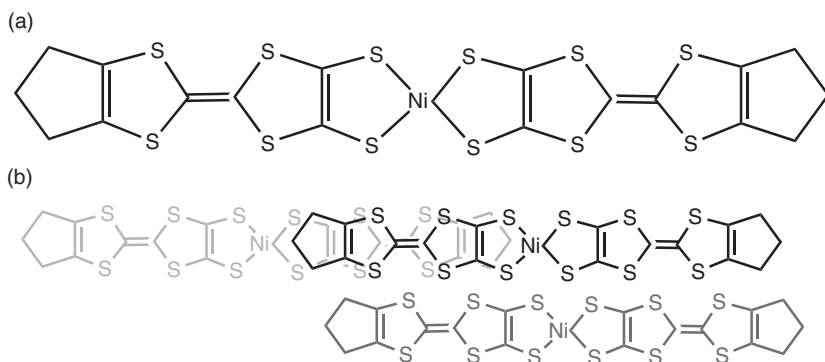
where b is the unit cell length.

**Fig. 3.63**

Band structure and electron transfer in TTF-TCNQ: (a) schematic representation of the bands built from the TTF's HOMO (occupied) and the TCNQ's LUMO (empty); (b) energy dispersion curves of the relevant two frontier orbitals: the TCNQ LUMO curve runs *up* and the TTF HOMO curve runs *down*; they cross at the Fermi level (energy E_F and wavevector k_F); (c) band scheme with electron transfer adjusted at the Fermi level ($\text{TTF}^{\delta+}-\text{TCNQ}^{\delta-}$); (d) band scheme with an hypothetical one-electron transfer ($\text{TTF}^{+\bullet}-\text{TCNQ}^{-\bullet}$). (Adapted from Canadell and Whangbo [3.68] and Jérôme [3.69].)

Thus, each stack can be considered as a mixture of neutral TCNQ and charged TCNQ^- for one, and TTF and TTF^+ for the other; that is, in a mixed valence state.

Finally, we can note that owing to the inverted behaviour of the TTF and TCNQ bands, *there is a unique k_F vector, common to the two bands*, because the number of states between the Γ point and k_F is the same for the HOMO and the LUMO bands. The main features allowing the phenomenon are that (i) the two bands run in different ways (up and down); (ii) the energy of the top of the donor's band is above the one of the bottom of the acceptor's LUMO band, so that their dispersion curves cross. To generalize the phenomenon we need systems having LUMO's donor and HOMO's acceptor close in energy, and their bandwidths larger than this energy difference. This can be provided by large flat molecules presenting at the same time extended delocalized bonds and appropriate intermolecular contacts. Canadell even predicted that a *single component molecular metal* could be achieved in this way, using the bands related to the LUMO and HOMO of the same molecule. We show in Fig. 3.64 an extraordinary *neutral* molecule, $[\text{Ni}^{\text{II}}(\text{tmdt})_2]^0$ (tmdt = trimethylenetetrafulvalenedithiolate), synthesized and studied by A. and H. Kobayashi *et al.* [3.69e], which indeed behaves in the solid as a single-component molecular metal ($400 \Omega^{-1} \text{cm}^{-1}$ at room temperature and a metallic behaviour down to 0.6 K!), without any need of a donor or an acceptor partner! Similar systems are described in [3.69e].

**Fig. 3.64**

A single-component molecular metal. The $\text{Ni}(\text{tmdt})_2$ (tmdt = trimethylenetetrafulvalenedithiolate) molecule: (a) molecular scheme; (b) schematic contacts and overlaps in the solid, within the stacks (black and light grey), within a plane (black and dark grey). (Adapted from Kobayashi *et al.* [3.69e].)

This is a nice example of the interplay between theory and experiment in molecular materials, when the lucid predictions of theoreticians encounter the ingenious skills of synthetic chemists.

The previous analysis is somewhat simplified, and more details on the subtleties of the behaviour of these systems can be found in texts such as [1.9] [3.68] [3.69a–c,j]. Clearly, the gross behaviour is determined by the previous band structure, but we have now to refine the model by introducing two effects which compete with the band formation and tend to hinder conductivity. As stated in the introduction (Section 3.3.1), they are: (i) the coupling of distortions (static aspect) or even vibrations (dynamic aspects) with the electronic structure. The stabilization of one-dimensional systems at low temperature by electron–phonon coupling is one of the major sources of complexity of conducting molecular systems. The resulting Peierls instabilities are studied in Section 3.3.3; (ii) the interelectronic repulsion energy U (or j_0). In a system like TTF-TCNQ it could be approximated from electrochemical or optical data and found to be 1.3 eV in a solution of TCNQ^{•-} and 1.0 eV in the solid state: in other words, U is of the same order of magnitude or even slightly larger than the bandwidth of the TCNQ HOMO (0.7–0.8 eV). In the next section we approach the first effect: the role of Peierls instability.

3.3.3 Peierls instability in 1D: electron–phonon interactions

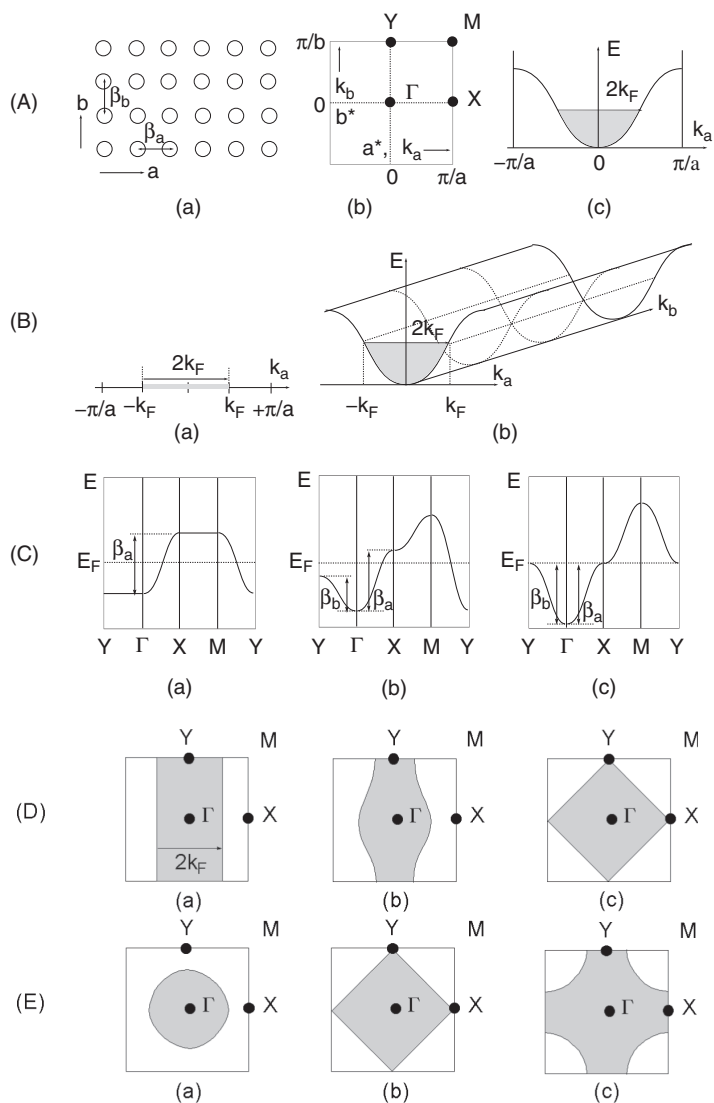
The Peierls distortion is based on a very general process: the influence of electronic filling on bond lengths. The distortion is unavoidable because upon distortion an occupied orbital is stabilized while a vacant orbital is destabilized. This simple way of reasoning was introduced in Section 1.4.3. We now look in more detail at the consequences upon conductivity; namely, the transition of a metallic to a semiconducting regime. We need to introduce a few more concepts to achieve an overall clearer picture: Fermi surface, nesting vector, and charge density wave (CDW).

3.3.3.1 Fermi surface, nesting vector, charge and spin density waves

Fermi surface

The concept is a simple extension of what we have already termed a Fermi level. It is conveniently introduced when examining an array of molecules stacking along the a direction (intermolecular distance, a) and also along the b direction (intermolecular distance, b) [Fig. 3.65, Part A(a)]. The resonance integral β resulting from the overlap S of a given molecular orbital of the molecules in the a direction is denoted β_a , and the resonance integral in the b direction is denoted β_b . The wavevector along a^* is k_a , and along b^* is k_b . The first Brillouin zone is shown in Fig. 3.65, Part A(b). Part A(c) of the figure displays the energy dispersion curve for a 1D system, pointing the $2k_F$ wavevector at the Fermi level for a half-filled band between $-\pi/2a$ and $+\pi/2a$. We admit, without demonstration, that the energy dispersion expression for the 2D system can be extrapolated from the 1D system (eqn. (1.49)) through:

$$E_j(\vec{k}) = \alpha + 2\beta_a \cos(k_a a) + 2\beta_b \cos(k_b b) \quad (3.115)$$


Fig. 3.65

Fermi surface in 1D and 2D systems: (A) (a) 2D array of molecules (white spheres) and resonance integrals in a and b directions; (b) first Brillouin zone with the characteristic points Γ ($k_a = 0, k_b = 0$), X ($k_a = \pi/a, k_b = 0$), Y ($k_a = 0, k_b = \pi/b$) and M ($k_a = \pi/a, k_b = \pi/b$); (c) 1D Energy dispersion curve along k_a . (B) 1D Energy dispersion curve: (a) k_a frame; k_a - k_b frame. (C) 1D to 2D Energy dispersion curves: (a) purely 1D; (b) 1D with weak interactions between chains; (c) purely 2D; the horizontal dashed lines show the Fermi level for the half-filled band. (D) Fermi surfaces corresponding to (C). (E) Fermi surfaces of an ideal 2D system with a band less than half-filled (a), exactly half-filled (b), more than half-filled (c). Light grey surfaces represent occupied levels. (Adapted from Canadell and Whangbo [3.68].)

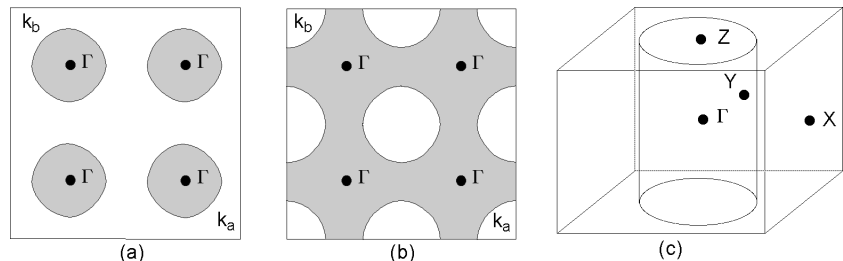
A third term, $2\beta_c \cos(k_c c)$, should be added for the 3D case. It is then a trivial task to draw the energy dispersion curves corresponding to $\Gamma \rightarrow X \rightarrow M \rightarrow Y \rightarrow \Gamma$ pathway for different significant cases, as shown in Fig. 3.65, part C: (a) a strictly 1D case with interactions only in the a direction ($\beta_a < 0, \beta_b = 0$); (b) imperfectly 1D, with an interaction in the b direction, weaker in magnitude than in the a direction ($\beta_b < \beta_a < 0$), and (c) fully 2D with interactions of the same magnitude in both directions ($\beta_a = \beta_b < 0$). The convention $\beta_b < 0$ denotes a bonding interaction, whereas $\beta_b > 0$ should denote an antibonding interaction (but is not treated here). In case (a), $\beta_b = 0$, so the curve is dispersionless for $\Gamma \rightarrow Y$ and $X \rightarrow M$. The horizontal dashed lines show the Fermi level for a half-filled band.

It is convenient to introduce a slightly different representation, as in Part B of Fig. 3.65, which shows for a perfect 1D system in a k_a frame (a) or a k_a - k_b frame (b) that there is no dispersion in the b^* direction, and that below the Fermi level, for a half-filled band, there are wavevectors q (grey zone) joining occupied levels. The k_a - k_b representation is fully developed in part (D) in the case of a half-filled band for 1D (a), 1D with interchain interaction (b), and 2D (c). The grey surface represents wavevectors corresponding to occupied levels, and the white zone to wavevectors of vacant levels. The grey zone (filled levels) represents half of the total surface. Part (E) is related to the pure 2D system with a band less than half filled (a), half filled (b), and more than half filled (c). The boundary surfaces between the grey and the white zone—between wavevectors corresponding to occupied levels and wavevectors of vacant levels—are known as *Fermi surfaces*. The wavevectors on the Fermi surface are the Fermi vectors k_F . Figure 3.66 represents several Brillouin zones in the reciprocal space of a 2D system with a band less than half filled (a) and more than half filled (b), so that it becomes obvious that the corresponding Fermi surfaces are closed loops. Fermi surfaces as that of case (a) are often called electron Fermi surfaces, whereas the Fermi surfaces of case (b) are called hole Fermi surfaces. A Fermi surface corresponding to a 3D system built on a, b, c axes where $\beta_a = \beta_b < 0, \beta_c = 0$, and a reciprocal space a^*, b^*, c^* with a first Brillouin zone Γ -X-Y-Z, is shown in Fig. 3.66c. The topology of the Fermi surfaces varies with the dimensionality of the system: 1D Fermi surfaces in a 1D representation are simply two points at $\pm k_F$ (Fig. 3.65, case B,a). If we introduce the 2D k_a - k_b representation they are two isolated parallel lines perpendicular to $\Gamma \rightarrow X$ (Fig. 3.65, cases D, a-b). In a 3D representation (k_a - k_b - k_c) they will be two planes perpendicular to $\Gamma \rightarrow X$. 2D Fermi surfaces in a 2D representation are closed loops (Fig. 3.65, cases E and Fig. 3.66a,b). In a 3D representation the Fermi surface of Fig. 3.66a will become the cylinder of Fig. 3.66c).

The Fermi surfaces can be used to illustrate important properties dealing with the conductivity of the system. The current carriers in metals are the electrons at the Fermi level. When a dispersion energy curve in a given wavevector direction ($\Gamma \rightarrow X$ in Fig. 3.65, cases Ca,b, or $\Gamma \rightarrow X, \Gamma \rightarrow Y$ in Fig. 3.65, case Cc) crosses the Fermi energy level, there are electrons with metallic properties along that direction. The larger the Fermi surface, the larger the number of carriers and the larger the conductivity. Finally, Fermi surfaces can be used to explain electronic instabilities, when the bands are partially filled, which is precisely our concern in this section. The crucial concept here is one of *nesting*.

Fig. 3.66

Closed loops of 2D Fermi surfaces in a 2D representation over four Brillouin zones: (a) less than half-filled band (electron Fermi surface); (b) more than half-filled (hole Fermi surface); (c) in a 3D representation the Fermi surface in (a) transforms in a cylinder. (Adapted from E. Canadell and M. Whangbo [3.68].)



Fermi surface nesting

First we give the definition: when a fraction of a Fermi surface can be translated by a wavevector q so that it can be superimposed on another fragment of the Fermi surface, it is said that the Fermi surface is *nested*. For example, the 1D Fermi surface of an ideal 1D system in Fig. 3.67a, consisting of two parallel lines, is nested by an infinite number of vectors q . To determine whether the surface is nested or not, it is often useful to consider several neighbouring Brillouin zones, as in Fig. 3.67b, where two Brillouin zones along $\Gamma \rightarrow Y$ are necessary to evidence the nesting vector q , or as in Fig. 3.67c, where four Brillouin zones, along $\Gamma \rightarrow X$ and $\Gamma \rightarrow Y$, are necessary to evidence the two orthogonal sets of parallel lines, which allows finding many nesting vectors.

The importance of nesting is related to the fact that a metallic system with a nested Fermi surface presents an electronic instability which leads to a metal-to-insulator or metal-to-semiconducting transition due to the opening of a gap at the Fermi level, as shown in Section 1.4.3. Indeed, we arrive here at the same basic results as in Section 1.4.3, with new tools, new concepts, and a deeper understanding. Below the transition there is no more Fermi surface (since the occupied and vacant states are separated in energy)! Let us examine the 1D metallic system in Fig. 3.68a. We relate an occupied Bloch orbital Θ_k^o to a vacant one $\Theta_{k'}^o$ with a nesting vector $q (= k - k')$. Θ_k^o and $\Theta_{k'}^o$ are eigenfunctions of the Hamiltonian H^o in the metallic state. When we apply some perturbation (V) to the system—for example, a distortion related to the vibrations (phonons)—the eigenfunctions of the new Hamiltonian $H^o + V$ are no more the eigenfunctions of H^o , Θ_k^o , and $\Theta_{k'}^o$, but a combination of them (c is a complex mixing coefficient):

$$\Theta_k \propto \Theta_k^o + c\Theta_{k'}^o \quad (3.116a)$$

$$\Theta_{k'} \propto -c\Theta_k^o + \Theta_{k'}^o \quad (3.116b)$$

As in Section 1.4.3, with a half-filled band we arrive at the situation sketched in Fig. 3.68. The mixing of the occupied Θ_k^o and unoccupied $\Theta_{k'}^o$ levels leads to new Bloch orbitals, named Θ_k and $\Theta_{k'}$, separated in energy. The interaction is the largest when k and k' belong to the Fermi level ($q = k - k' = 2k_F$) and the Bloch orbitals Θ_k^o and $\Theta_{k'}^o$ are degenerate. A gap opens at the Fermi level as shown in Fig. 3.68. Its value is 2Δ , with $\Delta = \langle \Theta_k^o | V | \Theta_{k'}^o \rangle$ (at k_F).

We can now compute the new electronic density associated to Θ_k and $\Theta_{k'}$. We express therefore $\langle \Theta_k | \Theta_k \rangle$ and $\langle \Theta_{k'} | \Theta_{k'} \rangle$:

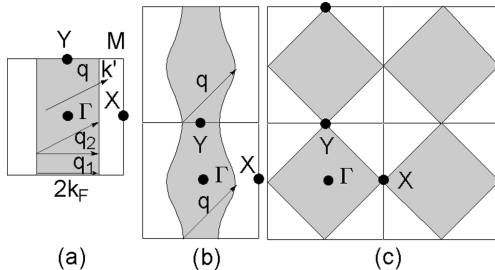
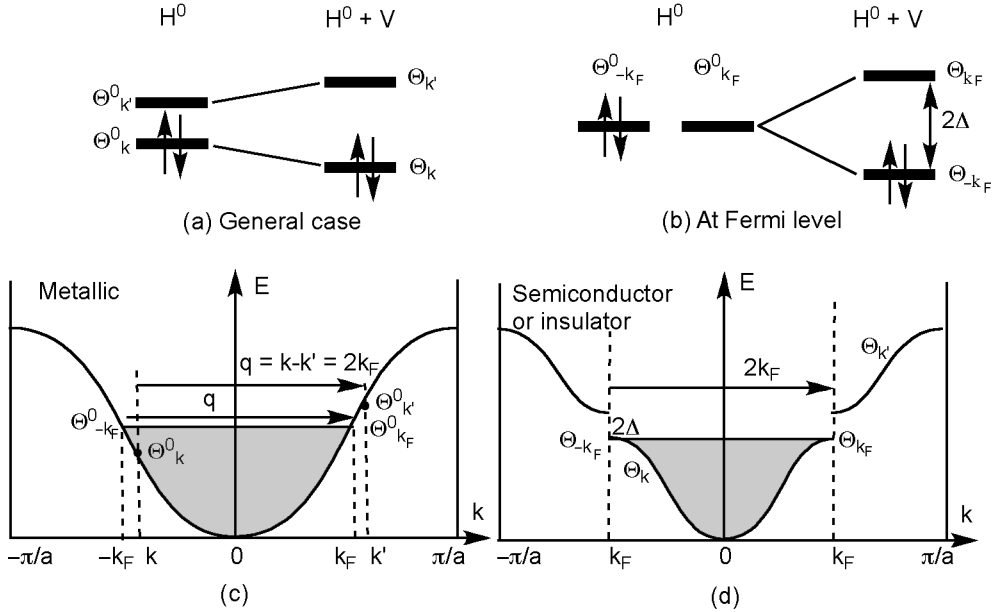


Fig. 3.67

(a) 1D Fermi surface of an ideal 1D system, examples of nesting vectors among an infinity (q_1 and q_2 at the Fermi surface). q is relating an occupied state k and an unoccupied one k' ; (b) 1D Fermi surface of a non-ideal system (with lateral interaction) and nesting vector q ; (c) 2D Fermi surface showing two orthogonal sets of parallel lines and the possibilities of many nesting vectors. (Adapted from Canadell and Whangbo [3.68].)

**Fig. 3.68**

Different aspects of a Peierls distortion from metallic to semiconducting states. Under a V perturbation, (a) combination of occupied (k) and vacant (k') Bloch orbitals in the general case when the levels are non-degenerate; (b) particular case when k and k' are at the Fermi level with degenerate Bloch orbitals. For a system with a half-filled band ($k_F = \pi/2a$) (occupied levels in grey): (c) energy dispersion curve in the metallic state; (d) energy dispersion curve in the semiconducting state (opening of a gap at the Fermi level, no more Fermi surface). (Adapted from Canadell *et al.* [1.9].)

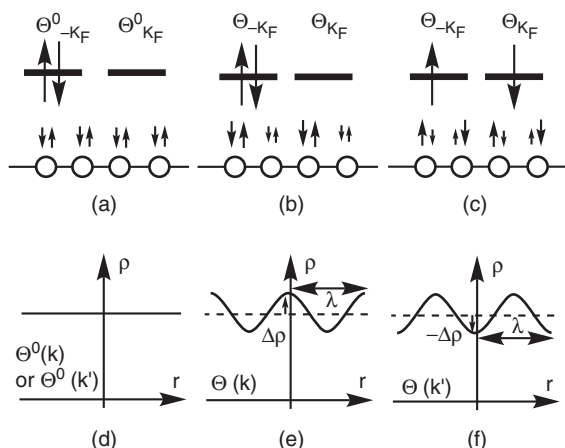
$$\begin{aligned} \langle \Theta_k | \Theta_k \rangle &= \langle (\Theta_k^0 + c\Theta_{k'}^0) | (\Theta_k^0 + c\Theta_{k'}^0) \rangle \\ &= \langle \Theta_k^0 | \Theta_k^0 \rangle + c^2 \langle \Theta_{k'}^0 | \Theta_{k'}^0 \rangle + 2c \langle \Theta_k^0 | \Theta_{k'}^0 \rangle \end{aligned} \quad (3.117a)$$

$$\langle \Theta_k | \Theta_k \rangle = \langle \Theta_k^0 | \Theta_k^0 \rangle + c^2 \langle \Theta_{k'}^0 | \Theta_{k'}^0 \rangle + \Delta\rho = \rho^0 + \Delta\rho \quad (3.117b)$$

$$\langle \Theta_{k'} | \Theta_{k'} \rangle = \langle (-c\Theta_k^0 + \Theta_{k'}^0) | (-c\Theta_k^0 + \Theta_{k'}^0) \rangle = \rho^0 - \Delta\rho \quad (3.117c)$$

$$\begin{aligned} \Delta\rho &= 2c \langle \Theta_k | \Theta_{k'} \rangle = (2c/N) \sum_m \langle \phi(r_m) | \phi(r_m) \rangle \cos[r_m(k - k')] \\ &= (2c/N) \sum_m \langle \phi(r_m) | \phi(r_m) \rangle \cos(qr) \end{aligned} \quad (3.117d)$$

We introduce ρ^0 , the charge density before perturbation, and $\Delta\rho$, the change in charge density induced by perturbation, defined in eqn. (3.117d). In the same equation we use the expression of the Bloch orbital Θ_k^0 introduced in eqn. (1.45), as a sum of $\phi(r_m)\exp(ikr_m)$ terms. The orbital $\phi(r_m)$ is an orbital ϕ located at site m , position r_m along the a axis, and $\exp(ikr_m)$ is its coefficient. The main conclusion is that the modulation of charge density follows a cosine law, $\cos(q \cdot r + \varphi)$: it represents a charge density wave (CDW), shown schematically in Fig. 3.69e–f. To derive the total modulation of the charge density one must, of course, integrate over all the occupied levels Θ_k . Another conclusion from


Fig. 3.69

(a) Schematic representation of the uniform charge density in the metallic state; (b) scheme of the modulation of the charge density in the semiconducting state compared to metallic, and appearance of a charge density wave (CDW); (c) scheme of the modulation of the spin density after the appearance of a spin density wave (SDW); the length of an arrow represents the magnitude of the (up or down) spin density; (d) non-distorted metallic system, uniform charge density ρ^0 in Bloch orbitals Θ_k^0 and $\Theta_{k'}^0$; (e–f) after distortion, charge density wave; λ is the wavelength; (e) $\Delta\rho$ in the occupied Bloch orbital Θ_k ; (f) $-\Delta\rho$ in the vacant Bloch orbital $\Theta_{k'}$. Observe the phase opposition between (e) and (f). (Adapted from Canadell *et al.* [1.9].)

eqns. (3.117b,c) is that when there is a local charge density enhancement in a Bloch orbital Θ_k ($\Delta\rho$) there is a charge density depletion in $\Theta_{k'}$ ($-\Delta\rho$).

In 1D systems the Fermi surface is fully nested; that is, the superposition of surfaces occurs on *all* the surface, not only on a fragment. Then the mixing of the (k, k') pairs of Bloch orbitals operates on a wide range of k values around the Fermi level, hence a favourable condition to open a band gap. As we shall see in what follows, perfect nesting is much less frequent in 2D or 3D systems.

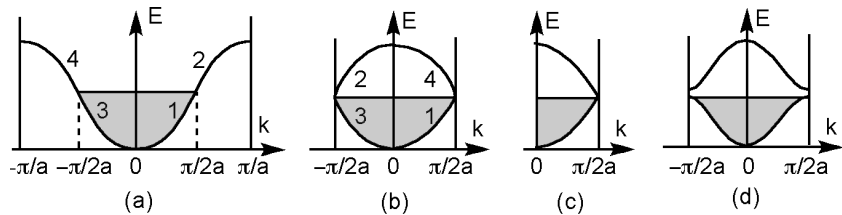
We have introduced in Fig. 3.69c, without demonstration, the case where the two electrons each occupy a different orbital—one spin up the other down. This leads to a modulation of the spin density in the chain called a spin density wave (SDW). SDW is favoured by the same circumstances as the CDW wave: low temperature, low dimensionality, and high density of states at the Fermi level. It occurs when $|\beta| \ll U$, inducing a strong electron correlation in the chain. This type of wave is more difficult to observe than a CDW—in particular because the structural changes are less important than in the CDW case (see Section 3.3.4.4).

We now generalize the previous discussion. The illustrations in Fig. 3.68c–d deal with the half-filled band case, when $k_F = \pi/2a$ and the initial band is split into two bands. But the Peierls instability in 1D is a very general process, not limited to half-filled bands. Due to the full nesting, the instability can occur for *any* q value (Fig. 3.67a). If a band has a partial electronic filling δ , the Fermi level is at $k_F = \pi\delta/a$ and the Peierls instability will occur at k_F with a wavelength of the charge density wave $\lambda = 2a/\delta$. It is called a $2k_F$ distortion, since $q = 2k_F$. When $\delta = 1/n$ the band will split into n bands and the system will suffer an n -merization. The Fermi level will be between the lowest split band (occupied) and the second (vacant). If $\delta = (n-1)/n$, the system suffers an n -merization also (n bands), but the Fermi level is between the $(n-1)$ th split band (last occupied) and the n th (vacant). When such partial filling occurs followed by an n -merization, it is convenient to introduce a more compact representation of the Brillouin zone, as shown in Fig. 3.70 and Fig. 3.71.

Figure 3.70a displays the usual energy dispersion curve, from $-\pi/a$ to $+\pi/a$, for one centre (orbital) per unit cell and half-filled band. In Fig. 3.70b the same

Fig. 3.70

Representations of energy dispersion curves of a half-filled system: (a) one orbital per cell, interval $]-\pi/a, \pi/a]$; (b) two orbitals per cell, interval $]-\pi/2a, \pi/2a]$; (c) two orbitals per cell, interval $]0, \pi/2a]$; (d) two orbitals per cell, interval $]-\pi/2a, \pi/2a]$, Peierls distortion. The occupied levels are grey. (Adapted from Canadell *et al.* [1.9].)



dispersion curve is drawn for a double cell (two centres—and orbitals—per cell, hence $a' = 2a$), from $]-\pi/2a$ to $+\pi/2a]$. The dispersion curves appear as if they have been folded from Fig. 3.70(a). A more accurate treatment shows the correspondence between the 1, 2, 3, 4 parts of the dispersion curves as indicated in the Fig. 3.70ab. Figure 3.70c still reduces the representation of the dispersion to the $]0, \pi/2a]$ interval, due to symmetry. Figure 3.70d represents the gap opening when using the double cell representation, in the interval $]-\pi/2a, \pi/2a]$.

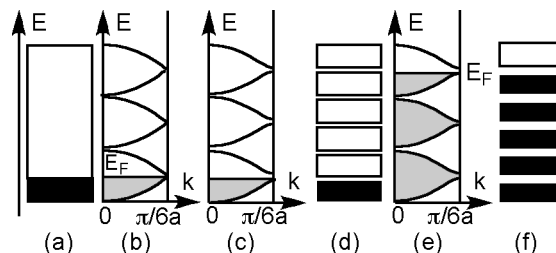
Figure 3.71 uses extensively the representation with a cell containing six centres with one orbital per centre, and a reduced energy dispersion diagram (interval $]0, \pi/6a]$) (b), Peierls hexamerization, in the case of a partial band filling $\delta = 1/6$ (a–d) or $5/6$ (e–f). These schemes will be useful for studying the Peierls transition in KCP (which follows). It is important to realize that in general the combination between two Θ_k^0 and $\Theta_{k'}^0$ Bloch orbitals having different energies leads to an antibonding situation. Only the combination between occupied and vacant Bloch orbitals close in energy (hence close to the Fermi level) has a stabilizing influence. This occurs only at the gap opened at the Fermi level [$\delta = 1/6$ (c–d) or $5/6$ (e–f)]. The Peierls instability will therefore be observed only when the electronic stabilization at the Fermi level exceeds all the destabilizing interactions, including the repulsive nucleus–nucleus interactions. This is an aspect of the competition between β and λ parameters.

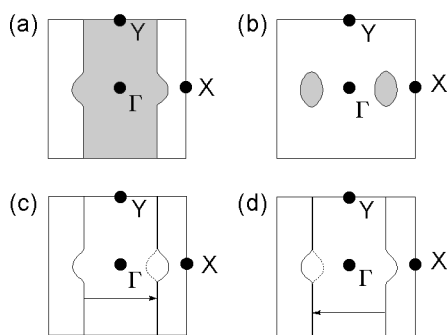
Interesting situations can arise when the nesting of the Fermi surface is not complete, as shown in Fig. 3.72. Here, upon translation, the coincidence does not occur on the entire surface. In this case the Fermi surface does not disappear completely. The Fermi surface is smaller, it presents less carriers, and the metallic conductivity will decrease but will not be suppressed.

The last but not the least point is the observation that the Peierls transition appears at $k_F = \pi\delta/a$. The corresponding crystallographic distortion associated with the charge density wave is detected easily by high-resolution X-ray

Fig. 3.71

Representations of energy dispersion curves of a partially filled system ($\delta = 1/6$, a–d) or $\delta = 5/6$ (e–f): (a) traditional bar representation with E_F at $1/6$ of the bandwidth; (b) six centres (orbitals) per cell, interval $]0, \pi/6a]$, E_F at $1/6$ of the bandwidth; (c) six centres per cell, interval $]0, \pi/6a]$ with Peierls instability, hexamerization, E_F just below $1/6$ of the bandwidth; (d) traditional bar representation of case (c); (e) $\delta = 5/6$, six centres per cell, interval $]0, \pi/6a]$ with Peierls instability, hexamerization, E_F just below $5/6$ of the bandwidth; (f) traditional bar representation of case (e). The occupied levels are in grey in the dispersion curves and in black in the bar representations. (Adapted from Canadell *et al.* [1.9].)



**Fig. 3.72**

Incomplete Fermi surface nesting: (a) Fermi surface presenting different curvatures; (b) formation of Fermi pockets after partial Fermi surface nesting as shown in (c) and (d). (Adapted from Canadell and Whangbo [3.68].)

diffraction measurements. Since $\lambda = 2a/\delta$, the determination of λ allows derivation of the band filling δ , hence the charge transfer ρ in DA charge transfer complexes or the degree of partial oxidation (DPO) for cyanidoplatinates complexes such as KCP. It is then possible to compare them with value arising from chemical analysis. When $\delta = p/n$ (irreducible fraction, p and n integers, $p < n$), the distortion is said to be commensurate. If not, the distortion is said to be incommensurate. This distinction is important because commensurate distortions have a tendency to ‘lock’ on fixed positions in the lattice, while incommensurate ones are more mobile.

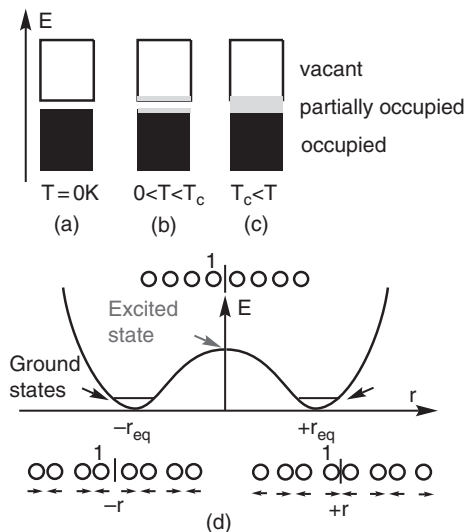
At this stage it is interesting to note that the influence of distortions on the electronic structure is a very general phenomenon which we have encountered already in the discussion of molecular mixed valence compounds (see Section 3.2.2.3). The main difference is that in molecular mixed valence compounds the distortion concerned a *single metallic site*, and thus the fate of *one* electron, which was either trapped or delocalized. In the case of the Peierls distortion, *two* adjacent sites are concerned by a concerted motion, and thus a *pair of electrons* is localized (see, for instance, the ultimate case of the infinite H_∞ chain, actually giving H_2 molecules). This arises from the fact that while mixed valence systems are generally open-shell systems with an odd number of electrons, 1D conjugated systems are closed-shell ones with an even number of electrons. But it is possible here also to build a nuclear coordinate describing the state of the molecular skeleton, as with the Q coordinate in Section 3.1.2. The energy change upon reorganization could also be denoted as λ through a proper definition, and enters in the general discussion on the β , λ , and U competition presented at the beginning of the present chapter.

Peierls instability and the role of temperature

Most of the demonstrations proposed previously assume that the temperature is $T = 0$ K, so that a $\Theta(k)$ orbital, below E_F , is doubly occupied (occupancy $f = 1$), and a $\Theta(k')$ orbital, above E_F , is vacant (occupancy $f = 0$). When the temperature is different from zero, the population of the levels follows the Fermi–Dirac distribution function:

Fig. 3.73

Peierls instability and temperature: (a) at $T = 0$ K the system is distorted and semiconducting; (b) at $0 < T < T_c$ the levels near Fermi energy becomes partially populated, since electrons are excited from the lower valence band to the upper conduction one. The system remains distorted and semiconducting; (c) above T_c the partially occupied levels fill the gap and build a band, the regular geometry becomes more stable, and the system is metallic; (d) total energy of the system along a distortion $\pm r$ applied to atoms labelled 1. (Adapted from Canadell *et al.* [1.9].)

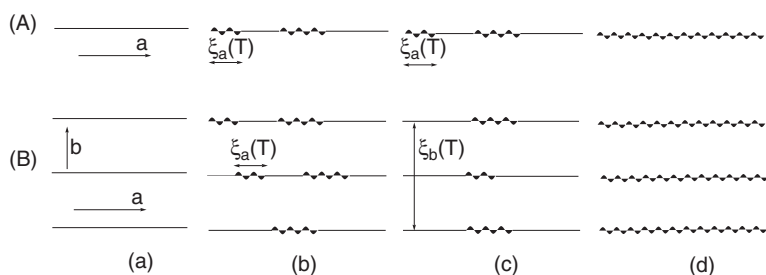


$$f(E) = \frac{1}{1 + \exp\left(\frac{E - E_F}{k_B T}\right)} \quad (3.118)$$

The most concerned levels are those near the Fermi level; that is, with an energy E , such as $E_F - 4 k_B T < E < E_F + 4 k_B T$, which are precisely those of interest for the Peierls instability. Since at $T > 0$ K, $f(E) < 1$ for $E(k) < E_F$ and $f(E) > 0$ for $E(k') > E_F$, the interaction between $\Theta(k)$ and $\Theta(k')$, maximum at $T = 0$ K will be reduced at higher temperature. We illustrate the role of the temperature in Fig. 3.73 with a band representation (a–c) and with the total energy of the system (electronic + nuclear) when some distortion $\pm r$ is applied to atom 1 (d). The competition is between the stabilization of the electronic energy, which favours a dimerization (the two potential wells of Fig. 3.73d), and the nuclear repulsion (and rigidity of the system), opposite to any displacement. At $T = 0$ K the system is distorted, semiconducting, and the gap is open (a). It is in the lowest vibrational level of one of the two potential wells. When the temperature increases the excited vibrational levels become populated, and the top of the valence band and the bottom of the conduction bands become partially populated (b). At a given critical temperature T_c the loosely bound dimers become a uniform chain at the top of the energy barrier ($r = 0$). The energy gap disappears (c). Note the analogy between Fig. 3.73d and Fig. 3.25b (class II compound).

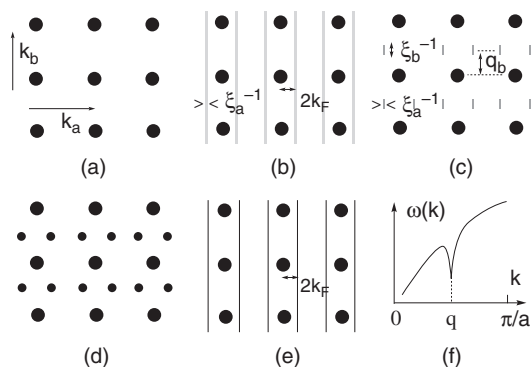
Fluctuations and charge density wave instabilities

Here we focus on another important role of the temperature, due to the dynamic fluctuations which occur in the system, even above the critical temperature T_c . It affects the dynamics within one chain, as shown on Fig 3.74(A), and also the instabilities in the solid, when the chains are weakly interacting Fig 3.74(B). In (A) is shown the situation of one metallic chain, assumed isolated, running in the a direction; (a) at high temperature, T_{high} , chain in the metallic state;



(b) at a given lower temperature, T_a and above the Peierls critical temperature, $T_{\text{Peierls}} < T_a < T_{\text{high}}$, it appears at different places in the chain, in the a direction, a beginning of charge density wave (CDW). There is a dynamic formation of small segments of the chain with a mean correlation length $\xi_a(T)$, depending on the temperature. Typically, ξ_a is varying as T^{-1} (increases when T decreases); (c–d) when decreasing the temperature the CDW is fully formed at T_{Peierls} together with the opening of the gap. In (B) is shown the situation of weakly interacting chains: (a–b) at high temperature, same situation as previously, independent chains; (c) when decreasing the temperature, at $T < T_{\text{Peierls}}$, interchain interactions manifest themselves, and correlation occurs between the CDW segments of neighbouring chains with a correlation length $\xi_b(T)$, perpendicular to the chains; (d) a 3D order eventually appears at a temperature termed T_{3D} . The appearance of the Peierls transition or of the 3D ordered state depends on the relative value of the intra- and interchain interactions.

Experimental techniques such as single-crystal X-ray diffuse diffraction and vibrational spectroscopy allow us to follow the previous dynamic fluctuations, as shown in Fig. 3.75. In (a), the diffraction spots corresponding to the perfect single crystal of Fig. 3.74a can be observed (T_{high}); in (b), at $T_{\text{Peierls}} < T_a < T_{\text{high}}$, diffuse lines perpendicular to k_a appear at $\pm 2k_F$ due to the dynamic creation of CDW fragments, with correlation length ξ_a . The width of the lines is given by ξ_a^{-1} ; in (c), at $T_{3D} < T < T_{\text{Peierls}}$, with non-negligible interchain interactions, interchain correlations appear along k_b ; the diffuse lines transform into diffuse spots centred at $2k_F, q_b$; the width of the spots is given by ξ_b^{-1} ; (d) a 3D order appears with condensation of the CDW along k_a , and interaction between the CDW along k_b , distinct from the 1D CDW only (e).


Fig. 3.75

(a) Bragg peaks of the single crystal at high T ; (b) $T < T_a$, appearance of diffuse lines at $\pm 2k_F$ perpendicular to k_a (dynamic CDW fragments, correlation length ξ_a); (c) diffuse spots at points $(2k_F, q_b)$ due to the interchain correlation between chains; (d) superlattice peaks due to a 3D order; (e) appearance of a 1D CDW; (f) 'Kohn anomaly' at wavevector $q = 2k_F$. (Adapted from Canadell and Whangbo [3.68].)

Finally, the right-hand part of Fig. 3.75f displays the ‘Kohn anomaly’ which appears in the phonon spectrum $\omega(k)$ when $q = 2k_F$. The phonon spectrum can be determined experimentally via X-ray, neutron, or electron diffuse scattering. The CDW formation is associated with a lattice vibration (phonon) ω at wavevector $k = q = 2k_F$. When the CDW appears the vibration ‘softens’, giving rise to the peak at $\omega(q)$, as shown.

We now examine more closely the 1D conductors of the preceding section when they become semiconducting. A large part of the discussion will be devoted to polyacetylene, which has been the subject of a huge amount of investigation, owing to its central position as a prototype of conducting polymers.

3.3.3.2 Alternant *trans*-polyacetylene

We begin by the alternant *trans*-polyacetylene, since it is a beautiful example of Peierls instability: the regular structure (Fig. 3.53, 1A) does not even exist! The electronic structure of the alternant *trans*-polyacetylene can be deduced easily from that of the regular case. It is possible to foresee, in Fig. 3.55, from the orbital degeneracy of $X_+(\pi/a)$, the highest occupied level of $X_+(k)$, and of $X_-(\pi/a)$, the lowest vacant level of $X_-(k)$ (Fig. 3.55c), that the regular system is not stable and is ready to experience a Jahn–Teller effect, as explained in Section 1.4.3 (which is another way to talk about the Peierls transition). The alternant configuration is preferred, even at room temperature (Fig. 3.76). The structure shows alternating ‘long’ (144 pm) and ‘short’ (136 pm) bonds (a). These values are between the usual values for simple (154 pm) and double

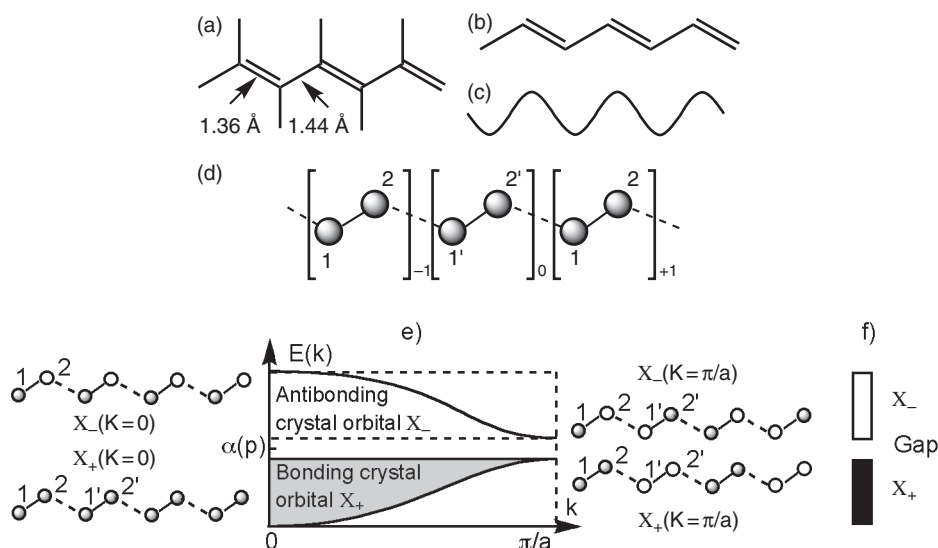


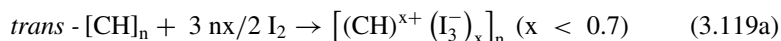
Fig. 3.76

Alternant *trans*-polyacetylene: (a) Bond lengths; (b) schematic structure; (c) charge density wave of π electrons; (d) numbering scheme of the two different sites in the cell and neighbouring cells; (e) crystal orbitals $X_{\pm}(k) = N_{\pm} [\Theta_1(k) \pm \Theta_2(k)]$ and their dispersion energy curves; the degeneracy of $X_+(\pi/a)$ and of $X_-(\pi/a)$ of the regular compound is removed; (f) bar representation of band energies and evidence of the gap.

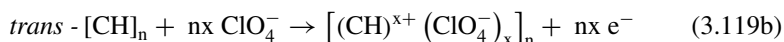
(132 pm) carbon–carbon bonds. Alternation is a very general phenomenon: the dihydrogen molecule (extreme case of alternation) is more stable than a regular hydrogen chain. Figure 3.76 also displays the alternant scheme (b), the charge density wave of π electrons (c), the numbering scheme (d), and the electronic structure of the alternant *trans*-polyacetylene (d–f). It can be compared usefully with Fig. 3.55 for regular (hypothetical) *trans*-polyacetylene. The energy dispersion diagram is obtained as previously, using two resonance integrals—one of them, β_{12} , for 1–2 interactions, and the other, $\beta'_{21'}$, for 2–1' interactions. Since $|\beta_{12}| > |\beta'_{21'}|$, the crystal orbitals $X_+(\pi/a)$ and $X_-(\pi/a)$ are no longer degenerate, and a gap opens at $k = \pi/a$. The forbidden energy gap evidenced in the usual bar representation (f) allows us to understand why, without doping, alternant *trans*-polyacetylene is a *semiconductor*.

Let us insist on the following idea. It is frequently believed that the presence of delocalized double bonds ('conjugated' double bonds) is a sufficient condition for obtaining conducting materials. This is indeed not true, as exemplified by undoped alternant *trans*-polyacetylene.

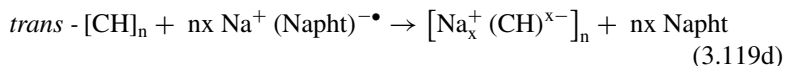
We now understand why several kinds of doping can, in principle, transform the semiconducting alternant *trans*-polyacetylene into a conductor. First, we begin with redox processes: oxidation of polyacetylene withdraws electrons from the top of the filled band of the material (that we can term the highest occupied crystal orbital, HOCO) and creates positive holes. With the diiodine I_2 , reduced to the tri-iodide I_3^- , we obtain:



The process is accompanied by a jump of the conductivity σ from $\approx 10^{-5} \Omega^{-1} \text{cm}^{-1}$ to $\approx 10^3 \Omega^{-1} \text{cm}^{-1}$. When the polymer is stretched before doping, conductivities parallel to the stretching and chain direction can reach $10^5 \Omega^{-1} \text{cm}^{-1}$. Doping can also be realized by electrochemistry by immersing a *trans*- $[\text{CH}]_n$ film linked to an anode in a solution of support-electrolyte such as LiClO_4 in propylene carbonate.



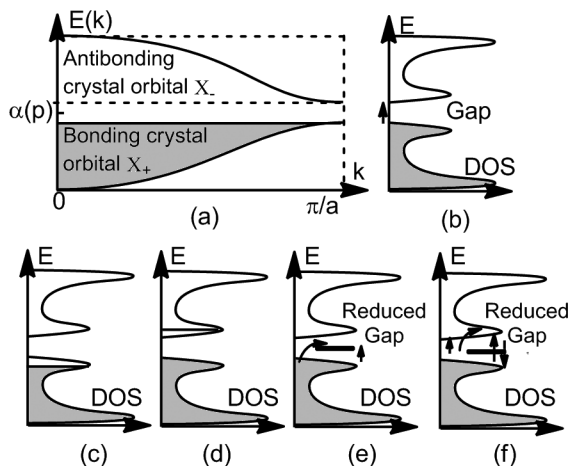
Oxidation, by halogen or by electrochemistry, and creation of positive holes is known as *p*-doping (*p* as positive). Conversely, reduction injects electrons into the bottom of the upper empty band, which we can term the lowest vacant crystal orbital (LVCO). It creates negative centres in the polymer. With liquid sodium amalgam or sodium naphthalide, $\text{Na}^+(\text{Napht})^{-\bullet}$, we obtain:



The reduction process can also be performed electrochemically, with the polymer connected to a cathode in a solution of LiClO_4 in tetrahydrofuran. Reduction and creation of negative carriers is known as *n*-doping (*n* as negative). In the salts formed in this way, and in a perfectly organized solid, the polymer becomes conducting. The interpretation using an ideal version

Fig. 3.77

Band theory and doping in alternant polyacetylene models: (a) energy dispersion curve with opening of a gap; (b) density of states of the undoped semiconducting material (valence band fully occupied, conduction band empty); (c) density of states after p -doping (oxidation empties the HOCO at the top of the valence band); (d) density of states after n -doping (reduction fills the LVCO at the bottom of the conduction band); (e) reduced gap with localized acceptor levels; (f) reduced gap with localized donor levels. Small black vertical arrows schematize the energy gap.



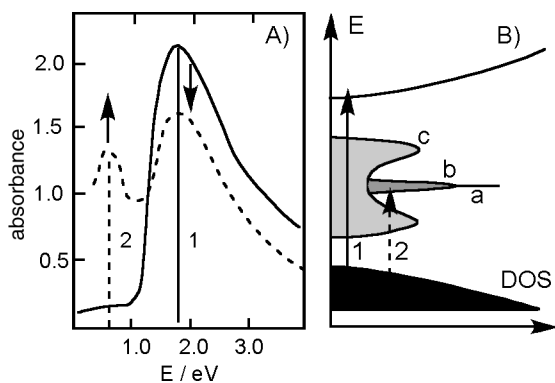
of band theory is shown in Fig. 3.77c,d: doping induces partially filled bands and conduction; and the conductivity can be increased by a factor 10^{10} !

If we examine more closely the chains themselves, the width of the valence and conduction bands is large (≈ 5 eV), and the interchain band dispersion is weak (≈ 0.3 eV), demonstrating good 1D behaviour. The forbidden energy band gap E_g , from absorption measurements, is evaluated at 1.4–1.7 eV (excitation of one electron from the valence to the conduction band). These figures can be obscured by extrinsic impurities within the gap. The activation energy E_a from conductivity measurements (corresponding to the energy gap E_g) can be found as low as 0.3–0.5 eV, and the onset of photoconductivity as 0.8 eV (the energy of the photon necessary for the material to become conducting). Tight binding and DFT calculations confirm the large width of the valence and conduction bands, the weak interchain band dispersion, and the forbidden energy gap.

As for the doped materials, the main point is the enormous increase of the conductivity upon doping. Important complementary information derives from optical and spectroscopic conductivity and other transport measurements (thermoelectric power and the Hall effect).

Figure 3.78 shows optical results in the infrared–visible range, and their interpretation. In (A), in the undoped material the onset of absorption occurs at 1.4–1.7 eV, whereas in the doped material a new transition appears around 0.7 eV. The intensity of transition 1 decreases when the intensity of transition 2 increases with the doping level (following the small vertical arrows). In the band scheme (Fig. 3.78B), transition 1 corresponds to a HOMO-LUMO (or HOCO-LVCO) transition, from the top of the valence band to the bottom of the conduction band. Also shown in (B) are the ‘localized’ states present within the gap (or ‘midgap’ states). They are created by defects in the undoped polymer, such as neutral solitons (Fig. 3.79): they are perfectly localized; Fig. 3.78B case a. They can also be created by doping.

The width of the midgap states increases with doping ($c > b$). Depending on the nature of the doping (n or p), the midgap states can be filled or empty. Transition 2 is a transition between these states and the bands of the polymer

**Fig. 3.78**

(A) Optical absorption for the undoped (continuous line) and doped with 10% AsF_5 (dotted line) material; (B) schematic density of states around the Fermi level, with different filled localized midgap states a, b, and c (see text). (Adapted from Roth and Bleier [3.71].)

(either valence band-midgap when the midgap states are acceptors (empty) (the situation shown in the figure), or midgap conduction band when the midgap states are donors (filled). Transition 2 is hence at lower energy than transition 1 [3.66, 3.70].

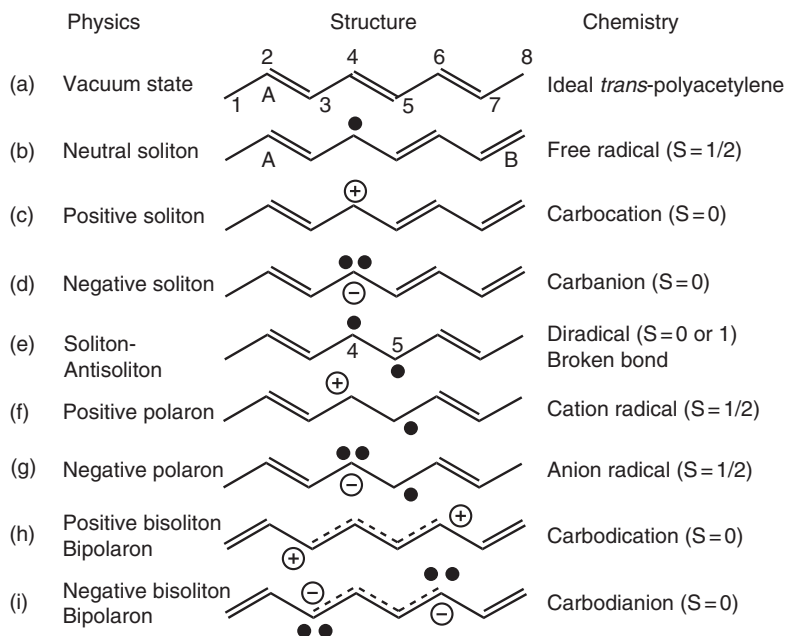
The transport measurements are sample dependent. The thermal variation of the conductivity follows quite well, in general, the expression $\sigma = \sigma_0 \exp[-(T_0/T)^\gamma]$ with $\gamma = 1/3$. The conductivity is much higher for oriented, stretched films $\geq 2000 \Omega^{-1} \text{cm}^{-1}$, and increases rapidly with doping, due to the decrease of activation energy from 0.5 eV to 0.02 eV (at 20% doping). In some cases, *metallic* conductivity is reached. This last statement can appear contradictory with the previous ones—but it is not. We shall examine this point subsequently (Fig. 3.83).

We turn now to another fruitful model using the topological consequences of the existence of bond alternation in real polyacetylene. Bond alternation can give rise to a special class of defect, named *solitons*—the subject of intense research. The possible defects which might occur in a polyacetylene chain are summarized in the glossary/dictionary in Fig. 3.79. The figure makes the linguistic link between the chemists' and physicists' communities, each bringing its own cultural background—chemical bonding and reactivity for the former, and semiconductor physics for the latter.

Figure 3.79(a) shows a chain of an ideal *trans*-polyacetylene, 'in vacuum' (without interaction between the chains). The ground state of *trans*-polyacetylene is degenerated: two ground-state configurations are possible—the one represented where the double bonds 'run down' from even to odd carbons (A configuration), and the one where the double bonds 'run up' from odd to even (B configuration) (b). When the two ground states are present (b), one at each end of a chain with an odd number of carbon atoms, a 'defect' in the conjugation scheme is present with one unpaired electron surrounded by two single bonds. This is known as a neutral *soliton*, with a spin $1/2$. Such a creature is described by physicists as a 'dangling bond' or a 'quasi-particle' (named using the postfix '*on*'—solit-*on*). The soliton is moving without any loss in energy. It obeys a non-linear equation with a non-dispersive shape-conserving motion. If such a development is outside the scope of this book, it is useful to examine nevertheless how it modifies the picture that we have of

Fig. 3.79

Solitons and polarons—a schematic ‘microscopic’ view of some events implied in the conductivity of *trans*-polyacetylene. A and B designate the two possible organizations of the alternation (configurations). Centre: representation of the species in a chain; (a) numbering of the carbon sites; (b–i) different species, black dots are electrons, electrostatic charges are shown by their sign. Left, physicist’s description. Right: chemist’s nomenclature. The spin state is shown in parentheses. See text. (Adapted from Roth and Bleier [3.71].)

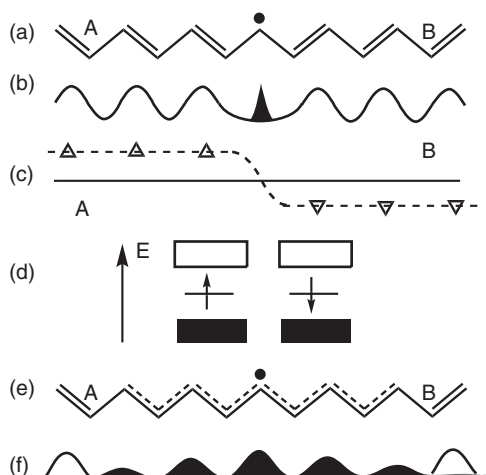


trans-polyacetylene. When the neutral soliton’s electron is removed by oxidation, a positive soliton appears (carbocation, singlet state) (c), whereas upon reduction a negative soliton is created (carbanion, also singlet state) (d).

Figure 3.80 displays some important features of the *neutral* soliton (a), in terms of charge density wave (b), where the soliton appears as a peak in the density wave, alternation parameter (c), where the soliton marks the inversion of the alternation parameter from positive (associated with the A configuration) to negative (B configuration), and energy bands (d), where the isolated soliton creates a level exactly at the centre of the forbidden energy gap (‘midgap’ level), occupied either by a spin up or a spin down. This localized description

Fig. 3.80

Neutral soliton in *trans*-polyacetylene: (a) ‘localized’ representation as an unpaired electron between two different alternating bonds segments; (b) charge density wave representation; (c) alternation parameter; (d) creation of a midgap energy level with spin up or down, within the forbidden energy gap; (e–f) two different delocalized representations, as a wall between two chain segments with opposite configurations of alternating bonds. See text. (Adapted from Roth and Bleier [3.71].)



should be adapted, as calculations have shown that solitons are not exactly localized but extend over approximately fifteen atoms where the alternation parameter is tuned, acting as a ‘wall’ between two different conjugation segments A and B (as shown in e and f). It can be understood that when electrons are removed from the chain there are some bond length changes where the oxidation takes place. The doping modifies the *geometrical* structure. Note that in (f) the soliton’s charge density peaks only at the even sites.

When the neutral soliton’s electron is removed by oxidation, a positive soliton appears (carbocation, singlet state) Fig. 3.79(c), whereas upon reduction a negative soliton is created (carbanion, also singlet state) Fig. 3.79 (d). Figure 3.79 and 3.81 extend the soliton’s concepts to positive (c) and negative (d) solitons. One can observe the significant changes in charge and spin (if spin, no charge, and if charge, no spin). The midgap level can be empty (positive soliton), and behaves as an acceptor level for electron transfer from the filled valence band (Figs. 3.78B and 3.81a (3)). It can be doubly occupied (negative soliton) (Fig. 3.81a (4)), which allows electron transfer to the conduction band. Both cases contribute to decrease the energy of the transitions in the optical spectrum (Fig. 3.78A). On the other hand, the variation of the alternation parameter remains the same in all kinds of soliton (Fig. 3.81d (2–4)).

Continuing our examination of the different species in *trans*-polyacetylene, we return to Fig. 3.79e), which displays a diradical or broken bond, also termed by physicists as a soliton–antisoliton pair. Indeed, a soliton is able to move along the chain on even sites; for example, (4, 6, 8), as shown in Fig. 3.82a, whereas an antisoliton can move only on odd sites (7, 9 . . .). Thus the two kinds of soliton cannot interchange. The oxidation of the pair gives a cation radical (Fig. 3.79f), with a positive charge on one site and a radical on the neighbouring site. This is a *positive polaron*, having a spin $\frac{1}{2}$. The *negative polaron* is obtained likewise by the chain reduction (g).

How can solitons and polarons be created? Neutral solitons are defects occurring in chains with an odd number of sites, as prepared (solitons can be created, for example, when a chain changes from *cis* to *trans* configuration). Positive and negative solitons are obtained from the neutral ones by (electro-) chemical oxidation or reduction respectively. The two kinds of species appear through weak doping (*p*-doping for positive polaron, *n*-doping for negative polaron). Positive (negative) polarons are obtained similarly from the ideal chain through weak oxidation (reduction). Further doping allows the creation

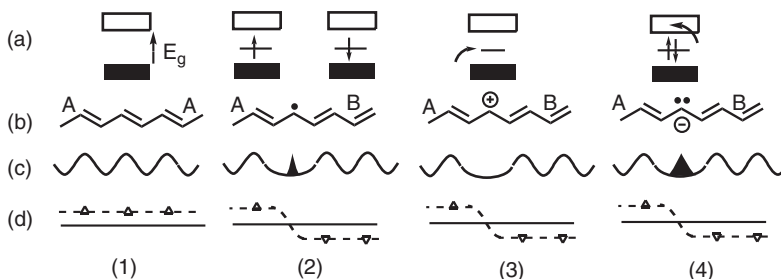


Fig. 3.81

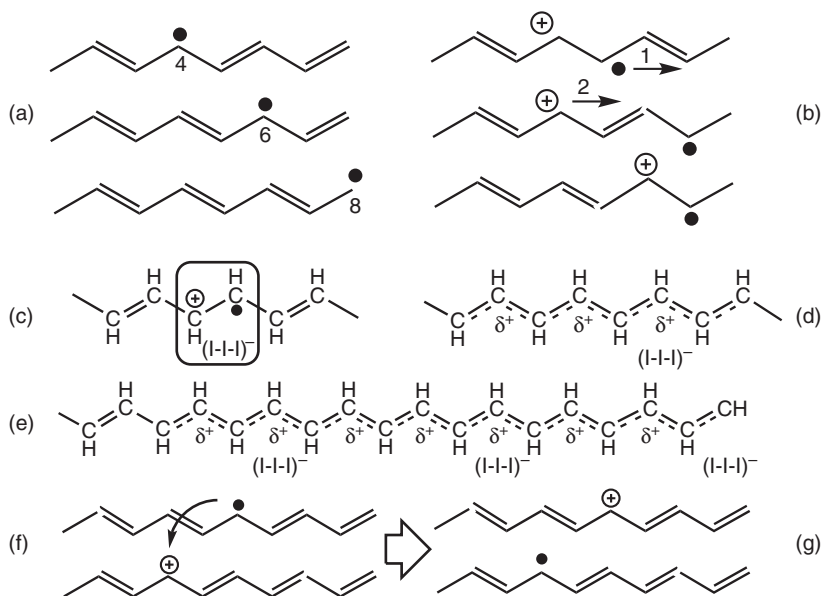
Solitons in *trans*-polyacetylene: (1) ideal chain; (2) neutral soliton ($S = 1/2$); (3) positive soliton ($S = 0$); (4) negative soliton ($S = 0$). (a) Energy band scheme; (b) structure of the chain; (c) charge density wave representation; (d) alternation parameter. See text. (Adapted from Roth and Bleier [3.71].)

of several polarons that in turn can combine into bipolarons (or bisolitons), positive or negative, all having a singlet state. In bipolarons, electrostatic interactions between the charges occur and should be taken into account.

As for the role of these species for the transport properties, we need examine their mobility (Fig. 3.82):

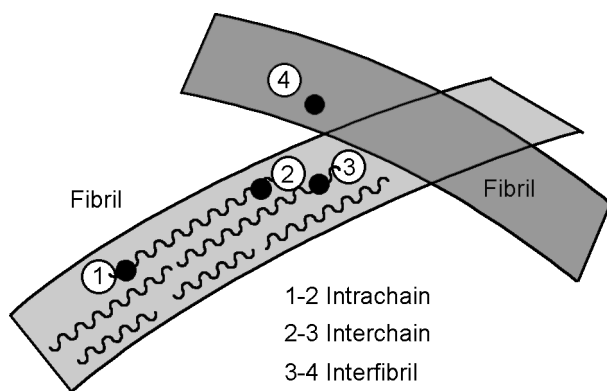
Fig. 3.82

Movements of solitons and polarons: (a) a soliton can move freely on one kind of site; the alternation parameter is displaced accordingly; (b) displacement of a positive polaron; (c–d) at low doping level the polarons interact with the associated counterion (here I_3^-) with limited mobility: (c) localized, and (d) delocalized representation, showing the decrease of bond alternation towards regular *trans*-polyacetylene; (e) at heavier doping, polarons can interact between themselves, providing a wider domain of regular chain with metallic conductivity, and less interactions with the dopant; (f–g) possible mechanism for interchain electron transfer: interaction between a neutral soliton on one chain and a positive soliton on a neighbouring chain.



The displacement of neutral solitons is free, not thermally activated, but has no influence on the conductivity, as solitons are neutral (a). The displacement of a positive polaron (b) should contribute to the intrachain mobility (through holes), and a displacement of a negative polaron should contribute through electrons. Nevertheless, since they are charged species, their interaction with the counterions of the dopant present between the chains limits their mobility, at low doping level, as shown in (c), even if the decrease of the bond alternation (d) weakens the electrostatic interaction. Heavier doping creates more polarons. It extends the segments where the alternation configuration becomes closer to that of regular *trans*-polyacetylene. The doping modifies the *geometrical* structure (bond lengths) and modifies the *electronic* structure by increasing the width of the midgap states, by mixing them with the valence and conduction bands (as shown in Fig. 3.78B). Finally, schemes (f) and (g) in Fig. 3.82 provide examples of the possibility of interchain charge transfer due to the interaction of a neutral and charged solitons located on neighbouring chains.

The previous developments illustrate the enormous experimental and theoretical endeavours and skills involved in conducting polyacetylene. But, as frequently observed in materials science, the properties of bulk samples depend not only on the molecular structure but also on the presence of defects and impurities, and on the processing method. The polyacetylene chains run

**Fig. 3.83**

Schemes of possible conductivity pathways in real polyacetylene. Different chains (wavy lines) run parallel in a fibril (curved grey ribbon). Dots 1 to 4 represent probes that could allow measurement of the conductivity, intrachain (1-2), interchain (2-3), interfibril (3-4).

parallel to each other and are organized in fibrils, which can themselves be aligned parallel by stretching and special preparation treatments (Fig. 3.83).

Thus we are faced with the problem of conductivity in an heterogeneous medium, as schematized in Fig. 3.83. The only resistance which can be really measured is R_{1-4} , between dots 1 and 4, the sum of the different resistances $R_{1-2} + R_{2-3} + R_{3-4}$. It depends, of course, in a complex way, on the structure (disorder, stretching ..) and level of doping.

As a conclusion to this section about polyacetylene, we can stress again the long conceptual journey necessary to link the molecular structure and the properties of the real bulk material, where unexpected effects such as fibril contacts and presence of impurities play a big role. But the effort has been worthwhile, due to interest in the conducting polymers for applications. The simple fact that the same system can provide *n*-doped and *p*-doped materials by simply changing the dopant opens the route to *p-n* junctions and to all the related applications developed in the traditional semiconductor industry.

3.3.3.3 Peierls instability in KCP derivatives and other conducting materials

We return to the example of KCP, as it remains to be understood why the compound becomes a semiconductor at lower temperatures.

The same principles as in polyacetylene are valid, since the Peierls distortion is a general process in 1D conductors, resulting from competition between the stabilization of the electronic structure and the stiffness of the material. In KCP, each platinum has lost 0.3 electron (formal oxidation state $\text{Pt}^{2.3}$), the dz^2 band is 0.15 emptied; the Fermi level is then at $k_F = 0.85$ and the structural change associated with the transition is now an *n*-merization, with $n = 1/0.15 = 6.6667$, which is not an integer. It is said that the distortion is incommensurate. To simplify, we take $n = 6$, and obtain the band diagram in Fig. 3.71f, showing the existence of a gap at the Fermi level. Experimentally, the Peierls distortion occurs below 150 K, with loss of the metallic character [3.69a]. The distortion can be revealed by accurate X-ray diffraction measurements [3.69k, 3.72].

In other 1D conducting material like TTF-TCNQ, the Peierls transition is even observed twice, at $T_{\text{Peierls}}(\text{TCNQ})$ on the TCNQ stacks and at T_{Peierls}

(TTF) on the TTF ones, giving rise to a rich and complex physics, beyond the scope of this book [3.69].

3.3.4 Beyond the one-electron description: narrow-band systems or no band at all

Until now in this Section 3.3 we have privileged a one-electron view based mainly on molecular orbital (band) theory where the resonance integral, whatever its name (β , V_{ab} , or t —transfer integral) was much larger than the other electronic effects, the interelectronic repulsion integrals, U (one centre, alias j_0), and V (two centres, alias j), or the electron–phonon interaction λ . The band picture relying on the delocalized molecular orbital model was satisfying. We were even able to understand in this frame that in one-dimensional or quasi-one-dimensional conducting materials the conducting state (relying on β) is not stable due to the competition of β with electron–phonon interaction (λ). Even when a band is partially filled the metallic conduction can disappear due to Peierls distortion and charge density waves (CDW). Reality is, of course, more complex: (i) the world is not one-dimensional, and (ii) other instabilities and important phenomena occur when β competes with the other electronic effects (U , V , λ). ‘Competition’ means that β is becoming close in energy to one, or several, of the λ , U , and V parameters. In these cases we deal with weak $|\beta|$ values (around or below 1 eV), and therefore with systems described by not-very-wide bands or *narrow bands*, or even systems where the band model (molecular orbital theory) collapses. For example, if $|\beta| \ll U$, electrons become localized on one site (Mott–Hubbard localization; see Section 3.3.4.1). The valence bond description is then a better model, as we showed in Chapter 2 for magnetic properties.

This scientific area has undergone an incredible burst over in the past forty years, both experimentally and theoretically (quasi-particles, Fermi liquids, Luttinger liquids . . .). A wide variety of structures, physical behaviour, and theoretical models—as a function of composition, temperature, and pressure—is available. For the more exotic materials—and some of the most promising, including superconductors—challenges remain in synthesis and new physical tools or interpretation [3.69].

To compute the energy of the systems, the Hamiltonian should be built to describe the different aspects:

$$\mathbf{H} = \mathbf{H}_{\text{kin/pot}}(\beta) + \mathbf{H}_{\text{e-e}}(U, V, \dots) + \mathbf{H}_{\text{e-ph}}(\lambda) + \mathbf{H}_{\text{exch}}(J, D \dots) \quad (3.120)$$

where $\mathbf{H}_{\text{kin/pot}}$ is the kinetic and potential energy term, $\mathbf{H}_{\text{e-e}}$ is the electron–electron repulsion Hamiltonian, $\mathbf{H}_{\text{e-ph}}$ is the electron–phonon energy Hamiltonian, and \mathbf{H}_{exch} is the exchange energy Hamiltonian.

The first term on the right is proportional to the resonance integral β between nearest neighbours i and $i \pm 1$ (one-electron band description). The second term, introduced by Mott and Hubbard, depends on the repulsion integrals U , for the doubly occupied sites $n_{i\uparrow\downarrow}$, and on V , for neighbouring singly occupied sites by electrons with spin σ and σ' , $n_{i\sigma}n_{(i+1)\sigma'}$. The third term relies on the λ electron–phonon interactions and the phonon energy, suggested by Peierls. The fourth term is the exchange term that we used extensively in

Chapter 2, following Heisenberg, Dirac, and van Vleck. This Hamiltonian is often termed the extended Mott–Hubbard Hamiltonian, since it includes repulsion terms (leading to Mott and Hubbard electron localization). It is also known as Peierls–Hubbard, due to electron–phonon terms (leading in particular to Peierls distortion).

We cannot deal with all these cases. Rather than formal mathematical developments which can be found in [3.69a–c, 3.73], we present some examples, beginning with simple cases, where just one effect enters in competition with the resonance integral β : β and U in Section 3.3.4.1; β and λ in Section 3.3.4.2. Then, in Section 3.3.4.3 we consider a more complex case where several effects compete. Finally, in 3.3.4.4 we present some perspectives opened by the organic metals and superconductors. We hope, with these simple considerations, to allow the interested reader (i) to grasp the spectacular interplay between chemistry and physics in the field, (ii) to enter in a more specialized literature, and (iii) to synthesize or to study, at some time, exciting new materials.

3.3.4.1 Mott insulators

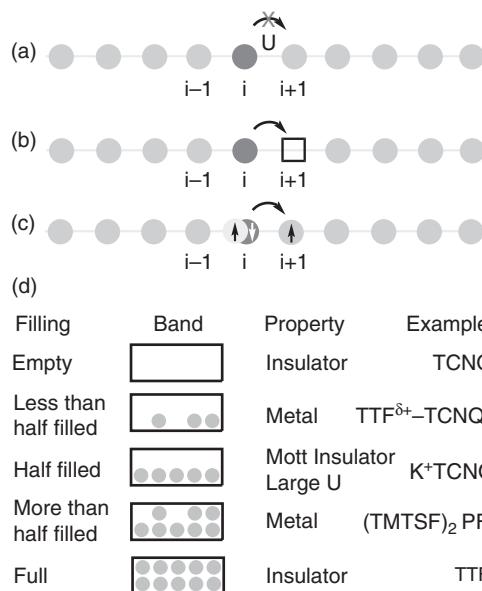
This case corresponds to the Hamiltonian in eqn. (3.120), limited to the first two terms:

$$\mathbf{H}_{\text{Hubbard}} = \mathbf{H}_{\text{kin/pot}} + \mathbf{H}_{\text{e-e}} = \beta \sum_{i,j=i+1} n_{ij} + U \sum_i n_{i\uparrow\downarrow} + V \sum_i n_{i\sigma} n_{(i+1)\sigma^+} \quad (3.121)$$

$\mathbf{H}_{\text{kin/pot}}$ corresponds to the potential energy and kinetic energy gained by electron jump from one site i to its nearest neighbour $j = i + 1$, and $\mathbf{H}_{\text{e-e}}$ describes the one-centre repulsion U when two electrons with different spins are present on the same site i . This very simplified way to write the Hamiltonian retains the basic physical features and avoids the usual introduction of second quantization notations. The first part of the Hamiltonian leads to a description in the frame of band theory, but the second part would require the introduction of the ‘split band’ concept; that is, the definition of two sub-bands separated by U , each one being filled by one electron per orbital with same spins, the spins being opposite from one band to the other. For reasons of space limitation we shall not use it here, as since a too brief introduction could induce conceptual dangers for the reader. This approach can be found in [2.11], [3.74].

We begin with the ionic compound $\text{K}^+\text{TCNQ}^{\bullet-}$, the structure of which is depicted in Fig. 3.57 and the electrical properties in Fig. 3.58. At high temperature, above $T_C = 395 \text{ K}$, the $\text{TCNQ}^{\bullet-}$ anion radicals are uniformly stacking, building a narrow band. On each $\text{TCNQ}^{\bullet-}$ radical lies an electron. The band is half-filled, but $\text{K}^+\text{TCNQ}^{\bullet-}$ is an insulator. We need to consider the one-centre repulsion integral U and the two-centre one, V . The transfer of one electron from site i to site $i + 1$ costs an energy $U - V$ (Fig. 3.84a).

If $|\beta| \ll U - V \ll U$, the state with one electron localized on each site is the more stable; it is the ground state (an estimate of U is $\approx 4 \text{ eV}$, and $V \approx 3 \text{ eV}$). When U imposes such *electron localization*, the system is a *Mott insulator* (Fig. 3.84a). In this case we return to the situation encountered with most of the compounds of Chapter 2 (the localized electron). Depending on

**Fig. 3.84**

(a) Mott insulators for half-filling; a grey sphere represents a site with one electron; U impedes the electron transfer from site i to the $i \pm 1$ one; (b) with one electron fewer (site $i + 1$ vacant, shown by a square) or (c) one electron more than half filled (a pair of electrons on site i , the arrows represent the spins), the electron transfer costs no energy and is allowed; (d) overview of the different cases of band fillings and conductivity.

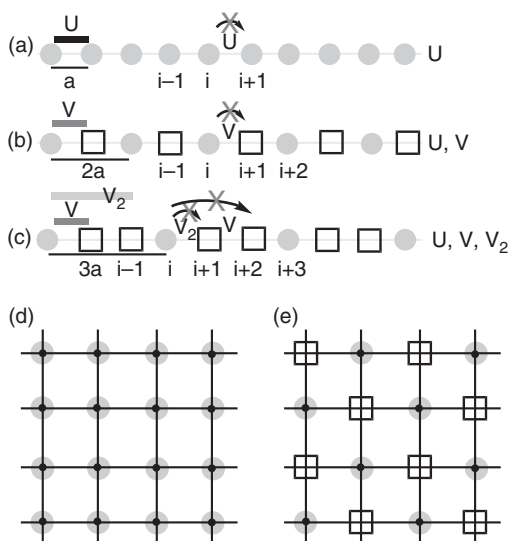
exchange, the interaction between the spins leads either to a ferromagnetic, antiferromagnetic, or random chain. As soon as the compound presents a site without an electron (b) or with two spins (c), the model foresees that electron transfer from site i to $i \pm 1$ is allowed, as it costs no energy, and there is hope of again having a conductor as generalized in (d).

We can analyse the problem in another way. Let us return (see Section 1.4) to a simpler 1D chain, in which each unit bears one electron—for instance, the *hypothetical* regular and infinite hydrogen chain $(\text{H}^\bullet)_n$ or $.. \text{H}^\bullet .. \text{H}^\bullet ..$ —and see what happens when we stretch uniformly all bonds. Obviously, if the $\text{H}^\bullet ... \text{H}^\bullet$ distance becomes very large, the electrons must remain localized on each H atom, and no conduction can be expected, though the band made with 1s orbitals is half-filled. Where is the mistake? It comes from the use of a band model, which is for solids the counterpart of the simple molecular orbital model, and we saw in Section 1.5.2.3 that the method is no longer valid for large $\text{H}^\bullet ... \text{H}^\bullet$ separations and weak β . We are in a situation where $\beta \ll U$, and in such a case the valence-bond method is better adapted (see Section 1.5.3.1).

Let us roughly estimate U in the case of the hydrogen chain. It is simply the energy necessary to transfer one electron from an atom to the other, thus creating H^+ and H^- . We have already seen (Fig. 3.46) that for an H_2 molecule, $U - V = \text{IP} - A_E \approx U$ (IP is the ionization potential, A_E the electron affinity, and when the ions are far enough, $V \ll U$). In the case of dihydrogen, $\text{IP} = 13.6$ eV, $A_E = 0.8$ eV, and thus $U = 12.8$ eV, which is a huge quantity, much higher than the usual values of β resonance integrals. In the chain there are two neighbours for each H^\bullet site, and thus the cost in energy for the electron transfer, by pair, is $U - 2V \approx 12$ eV (see also Section 3.3.4.3). The effects of electrostatic repulsion are not at all negligible, and explain simply the electron localization!

We have seen, nevertheless, that the major instability in this case is due to electron–phonon interaction (the stable system is the ‘dimerized chain’—the dihydrogen molecule). In molecular compounds able to produce 1D systems, such as TTF and TCNQ, the $U-V$ quantity is much lower, of the order of 1 eV (as seen previously), because the orbitals containing the active unpaired electrons are spread over many atoms; but anyway, the $U-V$ value is frequently of the same magnitude as $|\beta|$. It was enough to explain the electron localization in $K^+TCNQ^{\bullet-}$. A final remark is necessary to point out the important role of temperature when vibrations and phonons are concerned. Below $T_c = 395$ K, the $TCNQ^{\bullet-}$ anion radical stacks undergo a Peierls dimerization. The narrow band is split, and the system is semiconducting (Fig. 3.58). The two neighbouring radicals couple antiferromagnetically ($\uparrow\downarrow$) to produce a singlet ground state. The situation is very reminiscent of that described in Fig. 3.73, but here the high-temperature state is not a conductor but a Mott insulator.

Is half-filling (one electron, one hole per site) the only band filling giving rise to Mott insulators? No. We can consider the situation of a 1/4th filling or 1/6th filling (either with electrons or holes), and more generally to any filling commensurate with the structure (Fig. 3.85). For one electron per site at distance a (Fig 3.85a), corresponding to a $\rho = 1$ charge transfer (ionic situation) in a charge transfer salt, the electrons (and also spins) are localized on each site. A transfer on the neighbouring sites $i \pm 1$ costs $U-V$. For a quarter-filled band (Fig 3.85b), with $\rho = 1/2$, the transfer from site i to site $i \pm 1$ costs an energy V which localizes the electrons on one site over two ($i, i + 2, \dots$), every $2a$, achieving a charge density having a $2a$ periodicity. Considering now 1/6th filling (Fig 3.85c), with $\rho = 1/3$, the Mott insulator situation is achieved with one charge every three sites (i and $i + 3$, distant of $3a$) if the interelectronic repulsion integral V_2 between two next nearest neighbours (i and $i \pm 2$) is operative and efficient. In simple cases the band filling is determined by


Fig. 3.85

(a–c) 1D Mott insulators taking into account, U , V , and V_2 with (a) electron half-filling (order imposed by U), (b) 1/4 filling (order imposed by V , repulsion between sites $i + 1$ and $i + 2$), (c) 1/6 filling (order imposed by V_2 —repulsion between $i + 1$ and $i + 3$ —and V —repulsion between $i + 2$ and $i + 3$). (d–e) 2D Mott insulators; with electron half-filling (d), or 1/4 filling with a charge ordered (CO) state (e). A grey sphere corresponds to a one-electron site, and \square to a vacant site. Similar schemes apply for holes. (Adapted from Fukuyama [3.69b] and Giamarchi [3.69c].)

the stoichiometry of charge transfer salts. For D_2X salts (D, donor, X, anion), the quarter-filled case is realized with a hole (three electrons and one hole per two molecules, $\rho = 1/2$). D_4X composition should produce an eighth-filled case, and so on (see Section 3.3.4.4 on superconductors). The 2D charge-ordered (CO) state is presented in Figs. 3.85d (for half-filling) and 3.85e (for quarter-filling).

The main conclusion here is that for narrow-band 1D systems with a charge transfer commensurate with the structure, U , V , V_2 , and so on, must be taken into account to understand why Mott insulators arise, and obtain a clear picture of their electronic structure. The longer the interaction range, the higher the commensurability presented by a Mott insulator.

Other good examples of insulators produced by electron localization and large U values are provided by some transition-metal oxides—typically, MO with $M = Mn$ to Ni . The nickel oxide NiO has a rocksalt structure. The Ni^{2+} ions are in an octahedral environment, with the configuration $(t_{2g})^6(e_g)^2$. The e_g set being half-filled, it gives rise to a half-filled band, and thus metallic conductivity is anticipated in a one-electron picture. In reality, pure stoichiometric NiO has negligible conductivity due to large U and electron localization [3.75].

3.3.4.2 Semiconducting systems and mixed valence

The band model also fails when $\beta < \lambda$, without the direct influence of U and V . The appropriate simplified Hamiltonian after eqn. (3.120) is:

$$\mathbf{H} = \mathbf{H}_{\text{kin/pot}} + \mathbf{H}_{\text{e-ph}} \quad (3.122)$$

Many examples can be found in molecular or solid-state chemistry. This situation is encountered in particular in many transition-metal oxides when they exhibit non-stoichiometry with a mixed valence composition [3.75]. In this case, the existence of different valence states makes the geometry of the sites different, and the translational symmetry is lost. Such systems are thus extended analogues of class II binuclear mixed valence compounds, and cannot be described with the band model. When two different valence states, such as V^{5+} and V^{4+} , are present (this occurs, for instance, in non-stoichiometric V_2O_5 , which contains small quantities of V^{4+}), it can be considered that a V^{4+} site corresponds to one extra electron. Thus the presence of an extra electron distorts the corresponding site and expands the metal–oxygen distances, and the electron can be considered as ‘self-trapped’ by its own modification of the medium, which considerably reduces its mobility. The association of the electron and its distortion constitutes a *polaron*—a concept introduced in Section 3.1.2, and characterized by its energy W_p .

The structural consequence of oxidation or reduction has also been encountered in the case of polyacetylene, where the Peierls distortion is indeed influenced by electronic filling (doping). In polyacetylene, however, the distortion involves at least two centres and leads to dimerization, while in polaron formation only one centre is involved. On the other hand, the mixed valence situation is a way of escaping the deleterious influence of U . When there is less than one electron per site, the transfer of an electron is possible at a much lower cost (see Figs. 3.46 and 3.84b). There is no longer an influence of U —only the influence of the relaxation of the surrounding medium.

In these solids, conduction occurs by discrete jumps of electrons between localized states (hopping), and the process is thermally activated, giving rise to semiconducting behaviour. The conductivity in such solids depends, therefore, on the number of charge carriers and their mobility, as seen in eqn. (3.106). The mobility u is related to the diffusion coefficient D of the carrier, through Einstein's equation:

$$D = \frac{k_B T}{e} u \quad (3.123)$$

where k_B is Boltzmann's constant. Note that Einstein's equation connects conductivity—in which the charge carriers are subject to an electric field and have an overall motion—to diffusion, which is a purely random process. In the diffusion process, a particle (here the electron) stays for an average time τ on a site, and then executes a random jump on a nearby site located at a distance a (Fig. 3.86). The process is said to be Markovian, which means without memory between two jumps (drunken-sailor walk). For a one-dimensional system, D is given by:

$$D = \frac{a^2}{2\tau} \quad (3.124)$$

where the factor 2 arises from the two directions of motion when leaving a site i to site $i - 1$ or $i + 1$ (it would be 6 for a 3D system). The average residence time on a site is related to the rate constant of the hopping process ν_h by:

$$\tau = 1/\nu_h \quad (3.125)$$

ν_h is a first-order rate constant (the hopping frequency), identical to the rate k_{et} which governs the electron transfer in solution between the precursor and successor complexes (see eqn. 3.26). By combining eqns. (3.123)–(3.125) with (3.106) we obtain for a 1D system:

$$\sigma = \frac{1}{2} n e^2 a^2 \frac{\nu_h}{k_B T} \quad (3.126)$$

and the same equation with a factor of 1/6 for a 3D system.

Thus eqn. (3.126) relates conductivity (a macroscopic quantity) to the dynamic process of hopping between two sites (a microscopic quantity). Note that ν_h can be measured independently—for instance, by EPR or dielectric relaxation. As far as 'n' is concerned, it is actually the concentration in *pairs* associating an occupied and a vacant site, because electron transfer is only possible under these conditions. Thus for a mixed valence solid containing n_T total metal sites, of which a fraction α are in one of the valence states, the n value in eqn. (3.126) is:

$$n = n_T \alpha(1 - \alpha) \quad (3.127)$$

Accordingly, the hopping conduction is thus impossible for a homovalent system ($\alpha = 0$ or 1). For these systems, either there are no charge carriers (empty band), or the electrons are localized by electron–electron repulsions described by the U factor (narrow half-filled band, Mott insulators). There is a close analogy between solids containing small polarons and molecular mixed valence

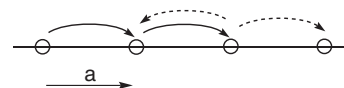
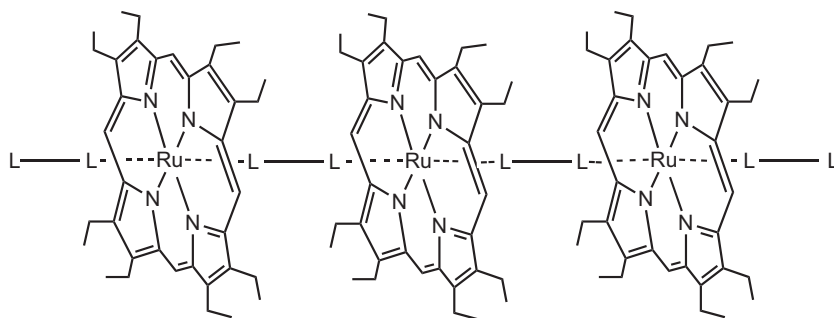


Fig. 3.86
Markovian process consisting of a series of independent jumps, without memory.

Fig. 3.87

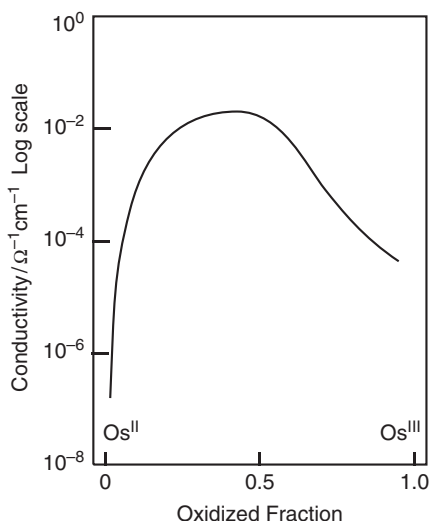
The 'shish-kebab' structure. The macrocycle can be either a substituted phthalocyanin or porphyrin, while the metal is Fe, Ru, Os. Axial ligands L-L are either pyrazine or 4,4'-bipyridine, and so on. (Adapted from Collman [3.76].)



systems. Thus an optical excitation of a polaron can send an electron out of its trap to a neighbouring site, at constant nuclear geometry. This necessitates the energy $\lambda = 2 W_p$ (see eqn. (3.19)), and the process can be termed an inter-valence transition. In the same way, there is also a thermally activated process: the 'hopping frequency' ν_h entering into eqns. (3.125) and (3.126) is temperature dependent according to an exponential law $\exp(-E_a/kT)$, with a hopping activation energy E_a equal to $W_p/2$; that is, one fourth of the optical energy, as in molecular systems.

These considerations can be extended to inorganic complexes, such as the 'shish-kebab' polymers made of metallic macrocycles linked by axial ligands, allowing some electron delocalization in one dimension (Fig. 3.87).

For these compounds the conductivity is extremely low in the purely reduced state of the metallic ion M^{II} , and increases upon partial oxidation to M^{III} , by doping. The occurrence of a hopping mechanism is nicely demonstrated by the evolution of the conductivity which passes through a maximum as a function of the fraction of oxidized centres (Fig. 3.88), in agreement with eqn. (3.127), thus showing that both oxidation states are necessary for conduction. The values, however, remain low compared to conductors. On the two extreme parts

**Fig. 3.88**

Evolution of conductivity as a function of the fraction of oxidized centres in $[\text{Os}(\text{OEP})(\text{pz})]_n$. (Adapted from Collman *et al.* [3.76].)

of the curve the conduction is extremely small, because the hopping process is no longer possible, and there is no alternative mechanism for current transport. For the M^{II} composition (d^6 , t_{2g}^6 in pseudo-octahedral environment), the band created from the metal t_{2g} levels is full. For the M^{III} composition, (d^5 , t_{2g}^5 in a pseudo-octahedral environment), one has a partially filled band. As it is extremely narrow, the situation is that of a Mott insulator ($U \gg |\beta|$).

In this example the conductivity was measured on pressed pellets of powdered material. It can be influenced by intramolecular as well as intermolecular electron transfer, and also by interparticle contact resistances. This problem is reminiscent of that of fibril contacts in polyacetylene (Section 3.3.3.2). However, the dependence upon the nature of the axial bridging ligand correlates well with their known ability to mediate electron transfer, so that it is reasonable to conclude that conductivity is determined in large part by intramolecular processes occurring along the 'shish-kebab' chain.

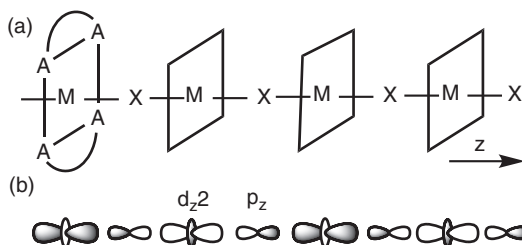
We conclude by quoting two other examples of hopping conduction in compounds with a mixed valence composition. In non-stoichiometric iron oxide $Fe_{1-x}O$, for which several iron sites are vacant, the charge compensation is realized by the existence of Fe^{3+} sites; the exact formula is written $Fe^{2+}_{1-3x}Fe^{3+}_{2x}\square_xO$ (\square is an iron vacancy). Thus Fe^{3+} sites can be considered as additional positive charges in small concentration in a 'sea' of normal Fe^{2+} sites. The conductivity is thermally activated and is proportional to the concentration of Fe^{3+} sites. The reverse situation is provided by TiO_2 and V_2O_5 —two oxides which contain mainly Ti^{4+} and V^{5+} , but with small amounts of the lower valence states, Ti^{3+} and V^{4+} respectively. In these cases there are thus extra electrons, stabilized by the polaron effect.

Such systems are, however, difficult to characterize from a structural point of view, because polarons are species which are present in small concentrations. A nice example illustrating the geometrical differences on a given site as the result of the presence or absence of an electron is provided by $K_3[MnO_4]_2$. This mixed valence double salt is made of alternating MnO_4 tetrahedra of two types, with Mn–O bond lengths similar to those in the structure of $K[Mn^{VII}O_4]$ and $K_2[Mn^{VI}O_4]$ (mean distances 160.7 and 164.6 pm respectively) [3.77a]. This is a class I mixed valence system, because the electronic interaction between Mn atoms is extremely small. Thus extra electrons corresponding to $[Mn^{VI}O_4]^{2-}$ are trapped, and the compound is semiconducting. The hopping frequency $\nu_h = 10^5 \text{ s}^{-1}$ can be measured directly by dielectric relaxation (see Box 'Time-scales of investigation methods'), and is in good agreement with the value obtained from the conductivity by the use of the 3D version of eqn. (3.126) [3.77].

Note that the $K_3[MnO_4]_2$ structure also provides a model of the ion pair involved in outer-sphere electron transfer exchange in solution, and detailed study shows the profound unity of the solid-state and solution processes [3.77].

3.3.4.3 Competition between $|\beta|$, λ , and U

In this section we consider a more complex situation where several parameters—the resonance integral $|\beta|$, the reorganization energy λ (electron–phonon interaction), the on-site Coulomb interaction U , and finally the

**Fig. 3.89**

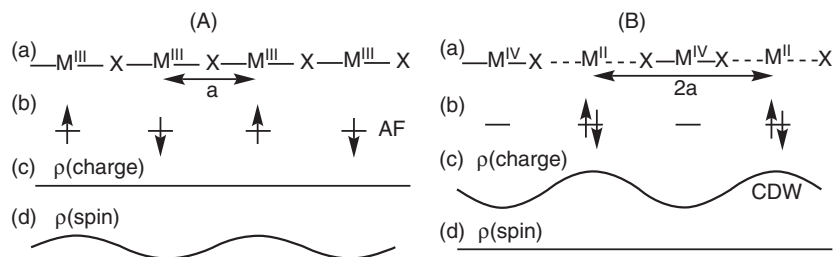
Schematic structure of $[M(AA)_2X]^{2+}$ chains (a) and relevant metallic d_{z^2} and halogen bridge p_z orbitals (b).

inter-site Coulomb energy V —compete or cooperate with one another. In a first simplified reasoning, we discard this last one.

A typical example is provided by $[M(AA)_2X]^{2+}$ chains aligned along the metal–metal direction z , where $M = Pt, Pd,$ or Ni with a mean d^7 filling, $X =$ halide (Cl^-, Br^-, I^-) in axial position, and AA = a chelating equatorial ligand such as 1,2 ethanediamine providing a square surrounding perpendicular to the chain (Fig. 3.89a) [3.78]. The alternating relevant $M(d_{z^2})$ and $X(p_z)$ orbitals are shown in (3.89b), in a bonding overlap situation. Electroneutrality is provided by anions between the chains (not shown). In the following, we abridge $[M(AA)_2X]^{2+}$ to $\{MX\}$.

The chain can exist as univalent $(M^{III}-X^{-1}-M^{III}-X^{-1})_n$ units built by alternating half-occupied $M(d_{z^2})^1$ and filled $(p_z)^2$ orbitals ($M = Ni; X = Br; AA =$ chxn, cyclohexanediamine; counter ion bromide; $Ni-Ni = 516$ pm, $Ni-Br = 258$ pm) (Fig. 3.90 A), class III in the Robin–Day classification. It can also be mixed valence $(M^{II}-X^{-1}-M^{IV}-X^{-1})$ units, built by alternating filled $M^{II}(d_{z^2})^2$, filled $(p_z)^2$, empty $M^{IV}(d_{z^2})^0$, and filled $(p_z)^2$ orbitals ($M = Pt, Pd; X = Cl, Br, I; AA =$ chxn, counter ion bromide; $Pt-Pt = 576$ pm, $Pt-I = 272$ and 296 pm) (Fig. 3.90), Robin–Day class II. $\beta, \lambda,$ and U can vary by choosing M and X , or by ‘doping’ (substituting M with M' , or X with X').

We start with the uniform symmetrical chain $(M^{III}-X^{-1}-M^{III}-X^{-1})_n$ ($M = Ni, X = Br$), with all metal–halogen distances equal and bridging halogens located mid-way of the metal atoms (Fig. 3.90A). In a band model the chain should be metallic, because M^{III} corresponds to a $(d_{z^2})^1$ configuration with half-filled band. But with nickel bridged by bromide, the repulsion parameter U (evaluated to be 5.5 eV) wins both λ and β , compelling the chain to be uniform (no break of symmetry) (Fig. 3.90Aa), and the d_{z^2} unpaired Ni(III) electrons to be localized (b). The system is an insulator. (Rather than a Mott insulator, it is said to be a charge transfer insulator, as a charge transfer absorption from bromide to metal has been identified in the optical conductivity

**Fig. 3.90**

(A) Univalent uniform $(M^{III}-X^{-1}-M^{III}-X^{-1})_n$ chain, for instance with Ni . (B) Mixed valence dimerized $(M^{IV}-X^{-1}-M^{II}-X^{-1})_n$ chain, for instance with Pd or Pt . (a) Structure; (b) electronic structure; (c) charge density; (d) spin density.

spectrum.) Overlap occurs between neighbouring localized d_{z^2} Ni(III) orbitals (Fig. 3.89b), through the bridging halogen p_z orbitals, giving rise to strong antiferromagnetic (AF) interaction ($J \approx -2700$ K) with alternating up and down spins (Fig. 3.90Ab). Of course, the charge density on the nickel is uniform (c).

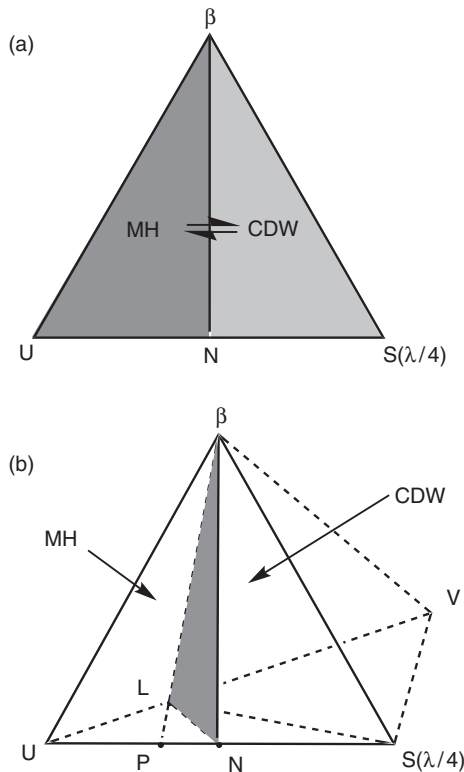
With platinum or palladium chains (Fig. 3.90B) we still have a mean d^7 filling, but such a filling can be subject to polaron-type distortion. Given the choice of softer, less electronegative, metallic constituents, the balance is now in favour of λ , as the U repulsion integral is weakened compared to nickel (1.5 eV for Pd, 1eV for Pt). There is now the possibility of transferring one electron from one metal to the other, thus generating M^{IV} and M^{II} , provided that stabilization of these oxidation states by distortion of the coordination spheres occurs. The situation is reminiscent of the examples studied in Section 3.3.4.2, except that there is a two-electron difference between the oxidation states.

Considered in more detail, the halide is displaced towards the more positive metallic ion M^{IV} building octahedral sites around M^{IV} and nearly square-planar ones around M^{II} (a). A gap is open, the conductivity is very weak, the system is semiconducting, and a charge density wave appears (c). The spin density on the metal is obviously zero (d). The energy gap, opened by the distortion, changes with the metal and the bridging halide, everything being equal, {Pt-Cl}: 2.8 eV, {Pt-Br}: 1.88 eV, {Pt-I}: 1.53 eV, {Pd-Cl}: 1.94 eV, {Pd-Br}: 1.61 eV as do the M...M and the alternating M-X...M distances (the larger the gap, the larger the distortion and the larger the λ parameter). To give an example, in the least distorted {Pt-I} derivative, $d = \text{Pt-Pt} = 567.2$ pm; $l_1 = \text{Pt}^{IV}\text{-I} = 296$ pm; $l_2 = \text{Pt}^{II}\text{-I} = 272$ pm, and the distortion parameter $(l_1 - l_2)/d \approx 0.042$.

These different behaviours can be rationalized by using an extension of the diagram in Fig. 3.11 (using β instead of V_{ab} to conform to current literature). We add the V parameter, so that the resulting diagram is a tetrahedron, constituting a phase diagram (Fig. 3.91). The theoretical treatment by Nasu [3.73d], using a mean field theory, delimitates zones in which either the Mott-Hubard (MH) or the CDW situations are the most stable. As a first approximation, the border is defined by a plane passing through the apex of the tetrahedron (β) and two points corresponding to situations $U = 2V$ (point L) and $U = S$ (point N). In this treatment the S parameter corresponds actually to $\lambda/4$. There are also intermediate regions where the two phases can exist (one stable and the other metastable), but they are not shown here.

Broadly speaking, when the system is dominated by U, the MH situation prevails. When S or V are important, the CDW situation is obtained. The first case is achieved for Ni derivatives (all atoms Ni^{III}), while the second is obtained for Pt (present as $\text{Pt}^{II}\text{-Pt}^{IV}$ chains). As will be seen in the following, Pd is an intermediate case for which the MH-CDW transition has been observed.

In fact, the general characteristics of the tetrahedral phase diagram can be recovered using potential energy curves of the type seen in Section 3.2.2.3. To simplify, we neglect the influence of β . We then have three parabolae corresponding to the electronic configurations $M^{II}\text{-}M^{IV}$, $M^{IV}\text{-}M^{II}$, and $M^{III}\text{-}M^{III}$ (Fig. 3.92). At the centre of the diagram ($Q = 0$, symmetrical nuclear

**Fig. 3.91**

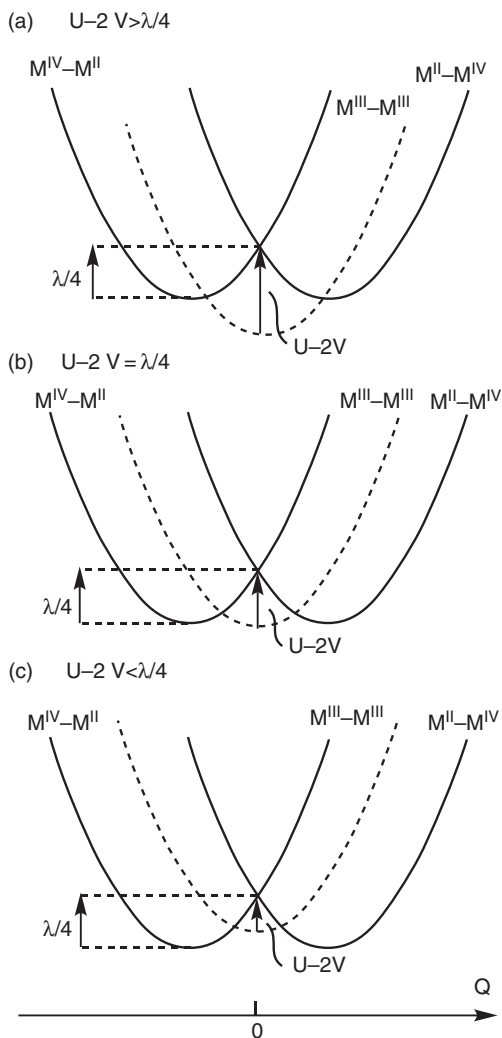
Schematic ground-state domains of the 1D MX system as a function of β , U , and λ parameters (a), or β , U , λ , and V ($V/U < 0.5$) (b). The conventions are the same as in Fig. 3.11. In (a) is shown the division of the domain by the line βN (where $U = \lambda/4$) separating charge density wave (CDW) systems (light grey surface on the right) from Mott-Hubbard (MH) localized systems (grey surface at left). The double arrow corresponds to the transition found in the palladium complexes (see text). In (b) is shown the schematic division of the domains by the βNL plane (where $U = 2V$) (grey) separating CDW (at right) and MH systems (at left). (Adapted from [3.73d].)

configuration), the most stable situation is $M^{III}-M^{III}$, but the others can be stabilized by the polaron distortion, $\lambda/4$. At $Q = 0$ the difference between $M^{III}-M^{III}$ and $M^{IV}-M^{II}$ or $M^{II}-M^{IV}$ is $U-2V$, because in an infinite chain where all the centres participate to electron transfer, for each $M-M$ pair, there is one U interaction and two V interactions. We see that electrostatic repulsions intervene only by the $U-2V$ parameter, which is certainly positive, and that the diagram depends only on the competition between $U-2V$ and $\lambda/4$. It is easily seen in Fig. 3.92 that for $U-2V > \lambda/4$ the $M^{III}-M^{III}$ state is the more stable, while for $U-2V < \lambda/4$ it is the $M^{II}-M^{IV}$ state. This last situation is sometimes called the ‘negative U effect’, because the *bottom* of the $M^{II}-M^{IV}$ is *below* the one of $M^{III}-M^{III}$. In our opinion this expression should be avoided. In fact, the effect of U has been simply overwhelmed by the effect of V and λ .

The previous conditions fit nicely with the conclusions of the tetrahedral phase diagram (Fig. 3.91).

Based on this diagram, the *fine chemical tuning* of the U/λ ratio allowed going from one case to the other, using one of the two following strategies:

- Strategy 1 allows movement from an MH state to a CDW state by decreasing U through a progressive doping of the MH $[\text{Ni}^{III}(\text{chxn})_2\text{Br}]^+$ chain ($U = 5.5$ eV for Ni) by palladium ($U = 1.5$ eV for Pd), keeping the same 1D structure up to $x = 1$ ($[\text{Pd}^{II}(\text{chxn})_2\text{Br}, \text{Pd}^{IV}(\text{chxn})_2\text{Br}]^+$). In the doped system $[\text{Ni}^{III}_{(1-x)}\text{Pd}_x(\text{chxn})_2\text{Br}]^+$ the MH to CDW transition appears around


Fig. 3.92

Potential energy curves for the three possible electronic configurations of an M-M pair within an infinite chain. (a) $U-2V > \lambda/4$, $M^{III}-M^{III}$ ground state, $M = Ni$; (b) $U-2V = \lambda/4$, two possible ground states $M = Pd$; (c) $U-2V < \lambda/4$, $M^{II}-M^{IV}$ ground state, $M = Pd, Pt$.

$x = 0.9$. Below $x = 0.9$, Pd^{III} is observed in an MH state, whereas above $x = 0.9$ the dimerized CDW $Pd^{II}-Pd^{IV}$ is favoured. The Pd-Pd distance at the transition is 526 pm.

- Strategy 2 consists in moving from a CDW state to an MH state by decreasing λ due to a steric trick: the anions ensuring the electroneutrality around the Pd-Br chain, $[Pd^{II}(en)_2Br]^+$ ($en = \text{ethanediamine}$), are dialkylsulphosuccinates, which present long organic tails (alkyl varying from butyl to octyl) which can bring closer and closer the palladium ions in the chain when the temperature decreases. With a pentyl derivative the Pd-Pd distance varies from 531 pm at room temperature to 521 pm at 160 K. The steric constraint is enough to produce the first-order phase transition (that is, with a structural change) CDW to MH at 206 K. Once again the Pd-Pd distance at the transition is 526 pm, which appears as the limit between the

two phases (corresponding to line βN in Fig. 3.91a or to the plane βNL in Fig. 3.91b).

Even if we did not describe the many experimental techniques—including STM ones—and the different theoretical endeavours which allow us to arrive at such a degree of understanding, the reader can realize how the interplay between experimentalists and theoreticians is fruitful for analyzing such complex systems. For more details, see [3.78].

3.3.4.4 Other kinds of instability in 1D organic conductors: towards superconductivity

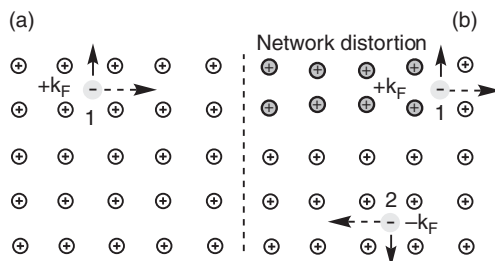
As seen previously, the detailed description of the synthesis and physical behaviour of 1D conductors is an extremely wide subject. We end this section on narrow-band systems with an evocation of a last challenge: reaching superconductivity with molecular materials.

Superconductivity is a peculiar state of matter discovered in Kammerling-Onnes' laboratory in Leiden in 1911. It opened the possibility of transporting electricity with zero energy loss, and led to important industrial applications. A century after its discovery, mastery of superconductivity remains an important scientific and technological challenge, especially at high temperature. Let us begin with a brief reminder about conventional superconductivity, before presenting a few examples of molecular superconductors. Superconductivity is characterized by a zero value of the resistance below a critical temperature T_c (Fig. 3.43d). It is accompanied by the Meissner effect (strong expulsion of magnetic lines of flux from the superconducting matter). Application of a magnetic field suppresses the Meissner effect at some critical field H_c , in ways different for class I and II conventional superconductors. (This nomenclature derives from the phenomenological Ginzburg-Landau model. In 2003, Abrikosov and Ginzburg shared the Nobel Prize with Leggett.) A satisfying microscopic interpretation of superconductivity at very low temperature was given by Bardeen, Cooper, and Schrieffer (Nobel Prize recipients in 1972), and is known as the BCS model.

In the BCS model, superconductivity appears at low temperature when the electrons condense in a particular state: Cooper pairs, made of two electrons, 1 and 2, travelling in opposite directions but linked by an attractive interaction despite the electron-electron repulsion (which is not easy to see in real space! Nevertheless, see an attempt in Fig. 3.93). The attractive interaction results from the electron-phonon interaction and its time-lag with respect to the

Fig. 3.93

A naive sketch of a Cooper pair formation in a conventional low-temperature superconducting material. (a) Electron 1 (light grey sphere, negative charge, spin up) located at the Fermi surface, moves in a 3D array of ionic species (crossed white balls, positively charged) with a wavevector $+k_F$; (b) electron 1 distorts the ionic network (grey balls) and electron 2, also at the Fermi level, with a wavevector $-k_F$ (moving in the opposite direction, negative charge, spin down) creates a Cooper pair through a weak, long-distance electron-phonon interaction.



perturbation due to a travelling electron. Thus, if the lattice distorts to accommodate the passage of one electron, it is possible that a second electron could be attracted by this distortion, even though the first electron has gone, and move more easily. This provides an *indirect* attraction between the two electrons. Superconductivity is a weak, long-distance effect due to the coupling of two electrons (spin $1/2$, fermions) into a Cooper pair (a boson, spin $S = 0$).

Until 1986 the known superconductors were metals or metallic alloys with a critical temperature around 23 K. In 1986 a major and unexpected breakthrough was the discovery of the so-called ‘high-temperature’ cuprate superconductor ($T_c = 35$ K in a lanthanide copper oxide) by Bednorz and Muller (Nobel Prize recipients in 1987). This triggered an incredible burst of activity in the physicists’ and chemists’ community in the 1980s–90s, culminating with a record temperature of 138 K. But it was a failure for the BCS theory, unable to explain such high critical temperatures by the indirect electron–phonon attraction evoked previously. Thus, a century after its discovery, and despite huge theoretical endeavours, no universal model for superconductivity is available. Cuprate oxides are therefore considered as *unconventional* superconductors.

Let us return to organic superconductors, which are also considered as unconventional. Actually, the first molecular organic superconductor was discovered in 1979, shortly before the discovery of cuprates (but of course, part of the interest shifted on the latter because of their ‘high T_c ’). The key molecular compound is tetramethyltetraselenofulvalenium hexafluorophosphate $(\text{TMTSF})_2(\text{PF}_6)$ (Jerôme in [3.69]), which is a metallic conductor from ambient to 12 K (with a very high conductivity of $10^5 \Omega^{-1} \text{ cm}^{-1}$), and becomes a superconductor at 0.9 K under 9 kbar (Fig. 3.94). It is part of the $(\text{TMTSF})_2\text{X}$ family built from different anions ($\text{X} = \text{PF}_6$, AsF_6 (octahedral), ClO_4 , ReO_4 (tetrahedral) and NO_3 , triangular). They are known as Bechgaard

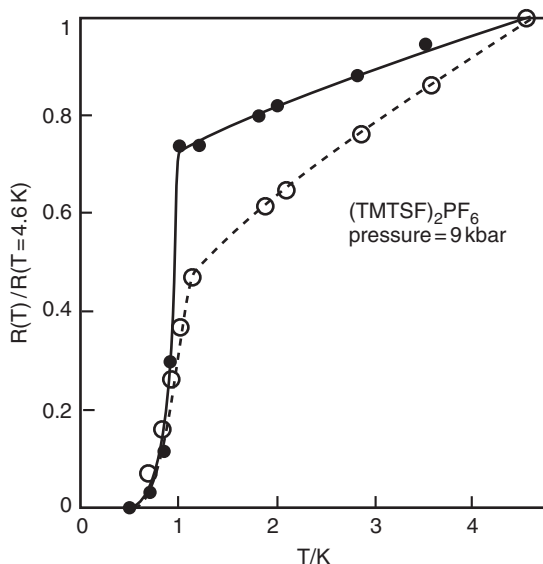
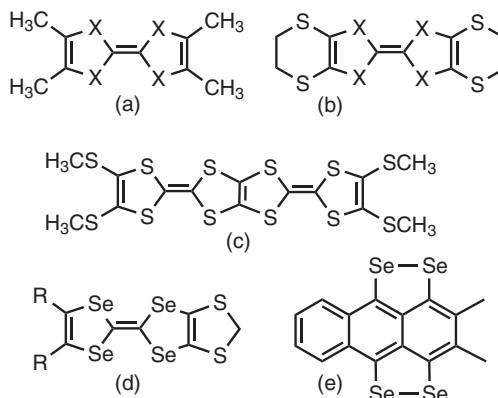


Fig. 3.94

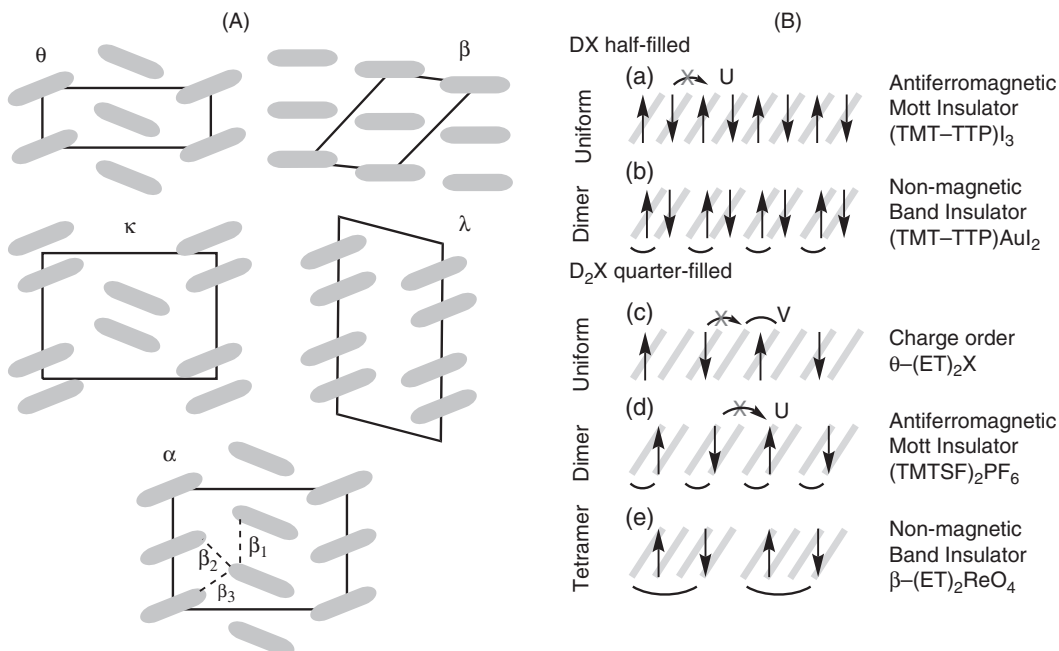
1980s first evidence of molecular superconductivity in the Bechgaard salt organic conductor $(\text{TMTSF})_2(\text{PF}_6)$. The two curves correspond to two different samples. (Adapted from Jérôme [3.69].)

Fig. 3.95

Donor molecules used to build organic metals and superconductors. (a) TMTTF (X = S), TMTSF (X = Se); (b) ET or BEDT-TTF (X = S) and BETS (X = Se); (c) TTM-TTP; (d) MDT-TTF; (e) DM TSA. *Abbreviations:* TMTTF = tetramethyltetrathiafulvalene; TMTSF = tetramethyltetraseleno fulvalene; ET or BEDT-TTF = bis(ethylene-dithio)tetrathiafulvalene; BETS = bis(ethylene-dithio)tetraselenofulvalene; (c) TTM-TTP = 2,5-bis(4,5-bis(methylthio)-1,3-dithiol-2-ylidene); (d) MDT-TTF = methylenedithiotetraselenafulvalene; (e) DM TSA = 2,3-dimethyltetraselenoanthracene. (Adapted from Mori [3.69a].)



salts, and the parent derivatives based on the tetramethyltetrathiafulvalenium salt $(\text{TMTTF})_2\text{X}$ are known as Fabre salts (Fig. 3.95). Their crystal structures are very different, and are named after some typical stackings, as shown in Fig. 3.96. Both the molecular and the crystal structure are at the origin of the conducting and physical behaviours, since they control the molecular orbitals

**Fig. 3.96**

(A) Some typical frequent molecular phases of organic conductors, named with Greek letters: θ -phase, β -phase, κ -phase, and so on. The molecules are grey cylinders. For one of the phases are shown the intermolecular contacts giving rise to different intra- and interstack resonance integrals β_i between the HOMOs, essential for building the energy dispersion curves and for obtaining the Fermi surface. (B) Some examples of the physical properties of organic materials D_nX as a function of stoichiometry, band filling, and n-merization. Abbreviations as in Fig. 3.95.

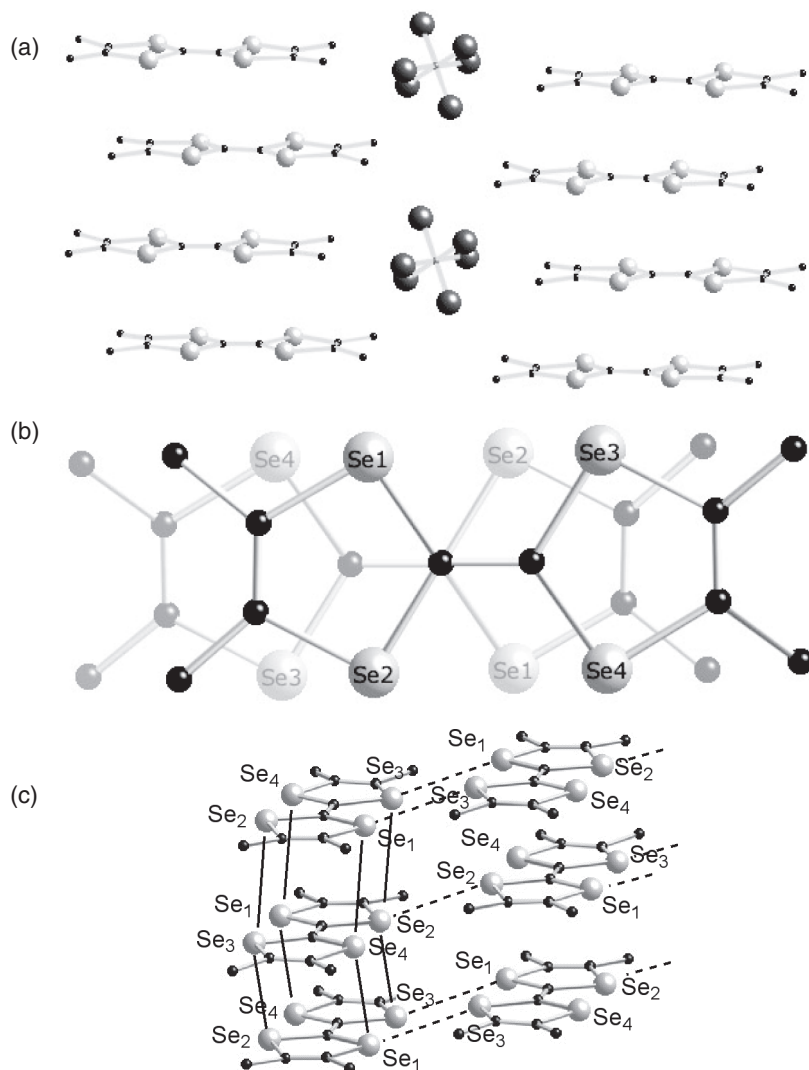
(here HOMO) and the intermolecular resonance integrals β between them. Some of them are sketched in the Fig. 3.96.

The low-temperature physics of these metallic conductors is extremely rich and therefore intricate. Figure 3.96B shows some typical examples of the physical properties related to the stoichiometry, the band filling, and the distortion of the 1D system (dimer, tetramer, and so on). As for the magnetic properties, they are readily understood using the models defined in Chapter 2: overlap between magnetic orbitals on neighbouring sites leads to antiferromagnetic interaction. At room pressure the superconductivity does not appear systematically, and most of the ground states are insulating. This is the case for $(\text{TMTSF})_2\text{PF}_6$, which undergoes a sudden metal–insulator transition at 12 K, contrary to the perchlorate derivative, which becomes directly superconductor at ambient pressure (the only one). The reader is now familiar with such instabilities in organic conductors: Peierls transition, charge density wave (Section 3.3.3.1), and Hubbard electron localization (Section 3.3.4.1). Superconductivity represents a new kind of instability, which we present in the case of $(\text{TMTSF})_2\text{PF}_6$.

According to the stoichiometry there is one positive charge shared by two TMTSF molecules. In D_2X systems, contrary to the donor–acceptor DA salts, only the organic donor molecules D contribute to the conductivity, and we need to concentrate on them. $(\text{TMTSF})_2\text{PF}_6$ crystallizes in the triclinic system. The TMTSF molecules are stacking along the a axis with the hexafluorophosphate anion on the side, as shown in Fig. 3.97a,b. The P–P distance of 702 pm corresponds to the a parameter. A slight dimerization in the molecular stack is observed, assigned to the periodicity of the TMTSF molecules—twice that of the anions. The closest intermolecular contacts are shown in Fig. 3.97c. Within the stacks, down a , they are Se1–Se4–Se1... and Se2–Se3–Se2... contacts. The mean intrastack Se–Se distance is 383 ± 5 pm. Contacts are present along b , such as Se1–Se3, Se3–Se1, Se2–Se2, and Se3–Se3. The mean interstacks Se–Se distance is 366 ± 1 pm, and Se3–Se3 is 375 pm. In the c direction the contacts are less important, some being through the fluorophosphate.

This information, along with the anisotropy of the single-crystal room-temperature conductivity ($\sigma_{a\parallel} = 510$; $\sigma_{b\perp} = 1.5$; $\sigma_{c\perp} = 0.015$ in $\Omega^{-1} \text{ cm}^{-1}$), shows that $(\text{TMTSF})_2\text{PF}_6$ is a fairly good 1D organic metal at room temperature. At the same time, they indicate the existence of several short interstack distances, which will appear of the utmost importance (i) to avoid the deleterious 1D Peierls distortion and (ii) to allow the appearance of superconductivity.

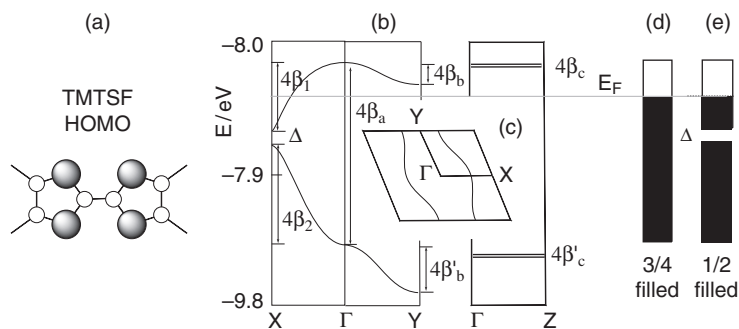
The electronic structure is determined by the highest occupied molecular orbital (HOMO) of TMTSF (Fig. 3.98a) and its resonance integrals with its neighbours, parallel to the stacks ($\beta_{\parallel a}$, along a ; indeed β_1 and β_2) or perpendicular ($\beta_{\perp b}$, along b and $\beta_{\perp c}$ along c). The energy dispersion curves and the Fermi surface of $(\text{TMTSF})_2\text{PF}_6$ are shown in Fig. 3.98b,c. They were obtained from three-dimensional tight-binding calculations based on ambient temperature and pressure crystallographic structure, and interpreted in a simplified orthorhombic model. The salient features are that the bandwidths are anisotropic, $4\beta_{\parallel a}$ (495 meV) \gg $4\beta_{\perp b}$ (70 meV) $>$ $4\beta_{\perp c}$ (2 meV), so they are large in the ΓX domain (a^*) and medium for ΓY (b^*). For ΓZ (c^*) the dispersion

**Fig. 3.97**

Schematic structure of $(\text{TMTSF})_2\text{PF}_6$. (a) Perspective view of the stacking of the TMTSF molecules along the a axis; (b) overlap of two neighbouring molecules down the a axis with numbering of the selenium atoms; (c) closest molecular contacts: intrastack along the a axis (plain lines) and interstacks roughly perpendicular to the a axis, along b (dashed lines).

curves are flat. The Fermi level is determined by the charge on the TMTSF molecule: one positive charge on two molecules means three electrons and one hole in the two HOMOs, which corresponds to a three-quarter filling of the band. The dimerization's gap Δ opening at X is small: 66 meV. It is located below the Fermi level. It transforms the $3/4$ filled system (d) in a formally $1/2$ filled one (e). The Fermi surface Fig. 3.98c is rather flat and almost perfectly nested, since $\beta_{\perp b}$ is much smaller than $\beta_{\parallel a}$. This creates a perfect situation for an instability.

Based on previous experiences, the reader (and at the end of the 1970s, the scientific community) should foresee that the instability is a CDW. It is not. There is no fluctuation above T_c , and no detectable Peierls distortion, but conversely, peculiar magnetic properties. The instability appears to be a rare spin density wave (SDW) (see Section 3.3.3.1). The functions $\Theta_{\mathbf{kF}}$ and $\Theta_{-\mathbf{kF}}$

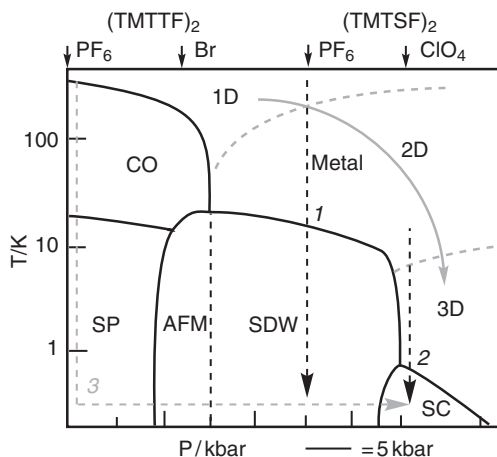

Fig. 3.98

Electronic structure of $(\text{TMTSF})_2\text{PF}_6$. (a) HOMO. (b) Schematic energy dispersion curves; (c) Fermi surface [$\Gamma = (0,0,0)$, $X = (a^*/2,0,0)$, $Y = (0,b^*/2,0)$, $Z = (0,0,c^*/2)$]; (d–e) schematic band filling. In (d) the dimerization within the stacks is not considered (3/4 filling). In (e) the dimerization gap is included (half-filling of the upper band). (Adapted from Canadell et al. [1.9],[3.79].)

describing the two electrons at the Fermi level (one spin up, the other down) combine and create a modulation of the spin density in the chain, or in other words, ‘itinerant antiferromagnetism’. Since there is no important Peierls distortion but antiferromagnetic coupling of electrons, this state appears as a good precursor state for superconductivity. Application of 9 kbar pressure and 0.9 K temperature finally led to the goal, as shown in Figs. 3.94 and 3.99.

Over the years a wealth of data have been gathered on similar compounds, which can be summarized in a phase diagram in a temperature–pressure space (Fig. 3.99). Many electronic states can appear, and superconductivity is only one among many others. It is important to notice that the abscissa is a *relative pressure* axis. A given compound is characterized by a given abscissa, which can be changed by application of pressure. Changing the compound’s formula (for example, substituting PF_6^- by Br^-) has an effect similar to a change in the real pressure. In the metallic state, decreasing the temperature and increasing the pressure (the curved arrow in Fig. 3.99) changes the nature of conductivity from 1D to 2D and 3D. It does so by increasing the interstack contacts in the b and c directions and therefore avoiding 1D instabilities ($\sigma_{\perp b}$ and $\sigma_{\perp c}$ are increasing with P , as does $\sigma_{\parallel a}$). The influence of the pressure on the resonance integrals β has been estimated as $\text{dln } \beta / \text{d}P = 2.2$ (% kbar $^{-1}$).

The main lessons drawn from the diagram are that (i) superconductivity appears in the same area as spin density wave (SDW). Unfortunately, the


Fig. 3.99

Generic experimental phase diagram of the $(\text{TMTTF})_2\text{X}$ and $(\text{TMTSF})_2\text{X}$ or D_2X organic metals. The pressure scale is not absolute but relative: the black arrows at the top indicate the room-pressure situation for four derivatives. The dotted black vertical arrows show, for $(\text{TMTSF})_2\text{PF}_6$, the way to arrive at the SDW state at room pressure (point 1) and to achieve superconductivity under 9 kbars at 0.9 K (point 2). The plain curved grey arrow emphasizes the dimensionality changes of the conductivity (from 1D to 3D; the limits between dimensionalities are shown by dashed curved grey lines). Only $(\text{TMTTF})_2\text{PF}_6$ presents all the identified phases (follow the light grey dotted line at left and arrow 3). This allows drawing the present generic phase diagram for D_2X derivatives. (Adapted from Jérôme [3.69].)

latter is an insulating state and must be avoided, but at the microscopic level one could hope to discover some hidden analogy between the SDW or other instabilities and the formation of Cooper pairs; (ii) the 3D character of conductivity appears necessary. Regarding this last condition, the standard recipes have in common the introduction of some additional dimensionality in the system; that is, to increase the interaction between neighbouring chains, because this is antagonistic to the Peierls distortion in particular. The following tools have been used:

- Chemically modify the structure to have less 1D character; for instance, by introducing polarizable atoms such as sulphur and selenium at the periphery of the molecules (see Fig. 3.97c). These atoms interact and introduce some interaction between chains. This is efficient even if the relation between the molecular structure and the crystal structure is not at all direct.
- Work under pressure to increase the overlap between adjacent chains (see Fig. 3.96). This has proved necessary for many 1D organic conductors to obtain superconductivity. Practical applications, of course, would need to eradicate the high pressure.

Thus at the present time, superconductivity in quasi-1D organic systems has reached modest critical temperatures (about 10 K for κ (ET)₂Cu(NCS)₂ system, far from the record molecular superconductivity in the three-dimensional cubic Cs₃C₆₀ molecular system ($T_c = 38$ K at 7 kbar). But perhaps more important, it represents a huge playground for physicists and chemists to test new concepts in a rational way. To take just one example: mathematically, Cooper pairs are built with mixtures of wavefunctions describing occupied pairs and unoccupied ones. Thus there is a mixing of band levels above and below the Fermi level (at $\pm k_F$), as for the formation of CDW and SDW. As a consequence, Cooper pair formation, CDW, and SDW tend to occur under the same conditions, in particular at low temperature, and which one effectively appears is determined by subtle characteristics of the system and delicate effects of temperature and pressure. As remarked previously, however, the CDW and SDW lead to a metal–insulator transition, while we seek just the reverse, thus the path is narrow between success and failure! In other respects, reality appears more complex than suggested by the simple concepts and schemes presented here. Over the last twenty years, many other ‘exotic’ systems have appeared, with other kinds of competition at play between U , V , and λ parameters. For example, when anions are magnetic, such as $X = \text{Fe}^{\text{III}}\text{Cl}_4^-$, magnetic field-induced superconductivity has been observed [3.69f]; and when X takes the shape of an anionic oxalato-based two-dimensional magnetic network, molecular conducting magnets or superconducting magnets are obtained [3.69h].

We think that quasi-1D organic systems can contribute efficiently to solving the superconductivity problem, because of the extreme flexibility of molecular chemistry, playing with the precursors, the stoichiometry (band-filling), the counterions, and so on. Once superconductivity is better understood, this type of chemistry will be in a good position to build, on demand, the architectures necessary for stabilizing Cooper pairs or probably other strange entities that might appear necessary.

References

- [3.1] a) C. Joachim, J.-P. Launay, *Chem. Phys.* 109 (1986), 93; b) P. Durand, *Phys. Rev. A* 28 (1983), 3184.
- [3.2] S. Woitellier, J.-P. Launay, C. Joachim, *Chem. Phys.* 131 (1989), 481.
- [3.3] B. S. Brunschwig, C. Creutz, D. H. Macartney, T.-K. Sham, N. Sutin, *Farad. Disc. Chem. Soc.* 74 (1982), 113.
- [3.4] R. D. Cannon, *Electron Transfer Reactions*, Butterworths, London, 1980.
- [3.5] a) G. Grampp, *Angew. Chem. Int. Ed. English* 32 (1993), 691; b) R. A. Marcus, *Nobel Lecture in Angew. Chem. Int. Ed. English* 32 (1993), 1111.
- [3.6] R. A. Marcus, *Ann. Rev. Phys. Chem.* 15 (1964), 155.
- [3.7] N. S. Hush, *Trans. Farad. Soc.* 57 (1961), 557 and 155.
- [3.8] L. D. Landau, *Phys. Z. SowjetUnion* 3 (1933), 664.
- [3.9] I. G. Austin, N. F. Mott, *Advances in Physics* 18 (1969), 41.
- [3.10] A. G. Lippin, *Redox Mechanisms in Inorganic Chemistry*, Ellis Horwood, New York, 1994.
- [3.11] B. S. Brunschwig, J. Logan, M. D. Newton, N. Sutin, *J. Am. Chem. Soc.* 102 (1980), 5798.
- [3.12] R. A. Marcus, N. Sutin, *Comments Inorg. Chem.* 5 (1986), 119.
- [3.13] C. Creutz, *Progr. Inorg. Chem.* 30 (1983), 1.
- [3.14] N. Sutin, *Progr. Inorg. Chem.* 30 (1983), 441.
- [3.15] L. Landau, *Phys. Z. SowjetUnion* 2 (1932), 46; C. Zener, *Proc. Roy. Soc. London Ser A* 137 (1932), 696.
- [3.16] C. Cohen-Tannoudji, B. Diu, F. Laloë, *Mécanique Quantique*, Tome I, Chap IV, Hermann, Paris, 1977.
- [3.17] R. A. Marcus and P. Siddarth, in *Photoprocesses in Transition Metal Complexes, Biosystems and Other Molecules*, E. Kochanski (ed.), Kluwer, Dordrecht, 1992, p. 49.
- [3.18] A. G. Lippin, *Redox Mechanisms in Inorganic Chemistry*, Ellis Horwood, New York, 1994, pp. 60, 78, 89; R. G. Endres, M. X. LaBute, D. L. Cox, *J. Chem. Phys.* 118 (2003), 8706.
- [3.19] T. T.-T. Li, M. J. Weaver, C. H. Brubaker Jr, *J. Am. Chem. Soc.* 104 (1982), 2381.
- [3.20] R. D. Cannon, *Electron Transfer Reactions*, Butterworths, London, 1980, p. 206.
- [3.21] M. H. Ford-Smith, N. Sutin, *J. Am. Chem. Soc.* 83 (1961), 1830.
- [3.22] J. R. Miller, L. T. Calcaterra, G. L. Closs, *J. Am. Chem. Soc.* 106 (1984), 3047.
- [3.23] C. C. Moser, J. M. Keske, K. Warncke, R. S. Farid, P. L. Dutton, *Nature* 355 (1992), 796.
- [3.24] *Tunneling in Biological Systems*, B. Chance, D. C. DeVault, H. Frauenfelder, R. A. Marcus, J. R. Schrieffer, N. Sutin (eds.), General Discussion, p. 439, Academic Press, New York, 1979.
- [3.25] V. May and O. Kühn, *Charge and Energy Transfer Dynamics in Molecular Systems*, 2nd edn., Wiley-VCH, Weinheim, 2004, p. 95.
- [3.26] P. F. Barbara, T. J. Meyer, M. A. Ratner, *J. Phys. Chem.* 100 (1996), 13148.
- [3.27] D. De Vault, B. Chance, *Biophys. J.* 6 (1966), 825; J. Jortner, *J. Chem. Phys.* 64 (1976), 4860.
- [3.28] a) P. Day, N. S. Hush, R. J. H. Clark, *Phil. Trans. Roy. Soc. A* 366 (2008), 5; b) M. B. Robin, P. Day, *Adv. Inorg. Chem. Radiochem.* 10 (1967), 247; c) G. C. Allen, N. S. Hush, *Progr. Inorg. Chem.* 8 (1967), 357.
- [3.29] C. Creutz, H. Taube, *J. Am. Chem. Soc.* 91 (1969), 3988.
- [3.30] a) R. J. Crutchley, *Adv. Inorg. Chem.* 41 (1994), 273; b) B. S. Brunschwig, N. Sutin, *Coord. Chem. Rev.* 187 (1999), 233; c) J.-P. Launay, *Chem. Soc. Rev.* 30 (2001), 386; d) D. M. D'Alessandro, F. R. Keene, *Chem. Soc. Rev.* 35 (2006), 424.
- [3.31] J. E. Sutton and H. Taube, *Inorg. Chem.* 20 (1981), 3125.
- [3.32] R. A. Marcus, *J. Phys. Chem.* 67 (1963), 853.

- [3.33] a) M. Verdaguer, G. Girolami, in *Magnetism: Molecules to Materials. V*, J. S. Miller and M. Drillon (eds.), Wiley-VCH, Weinheim, 2004, chap. 9; b) A. Kraft, *Bull. Hist. Chem.* 33 (2008) 61.
- [3.34] M. Shatruk, C. Avendano, K. R. Dunbar, *Progr. Inorg. Chem.* 56 (2009), 155.
- [3.35] M. B. Robin, *Inorg. Chem.* 1 (1962), 337.
- [3.36] R. G. Burns, D. A. Nolet, K. M. Parkin, C. A. McCammon, K. B. Schwartz, in *Mixed Valence Compounds*, D. B. Brown (ed.), NATO ASI Series, D. Reidel, Dordrecht, 1980, p. 295; J. L. Emmett, T. R. Douthit, *Gems and Gemology* 29 (1993), 250; see also the Caltech server on minerals: <<http://minerals.gps.caltech.edu>>
- [3.37] G. A. Niklasson, C. G. Granqvist, *J. Mater. Chem.* 17 (2007), 127.
- [3.38] M. T. Pope, in *Polyoxometallate Molecular Science*, J. J. Borrás-Almenar, E. Coronado, A. Müller, M. T. Pope (eds.), Kluwer Academic Publishers, Dordrecht, 2003, p. 3.
- [3.39] C. Lambert and G. Nöll, *J. Am. Chem. Soc.* 121 (1999), 8434; S. F. Nelsen, in *Electron Transfer in Chemistry, Vol 1*, V. Balzani (ed.), Wiley-VCH, Weinheim, 2001, chap. 10; J. Bonvoisin, J.-P. Launay, W. Verbouwe, M. Van der Auweraer, F. C. De Schryver, *J. Phys. Chem.* 100 (1996), 17079; C. Rovira, D. Ruiz-Molina, O. Elsner, J. Vidal-Gancedo, J. Bonvoisin, J.-P. Launay, J. Veciana, *Chem. Eur. J.* 7 (2001), 240.
- [3.40] S. B. Piepho, E. R. Krausz, P. N. Schatz, *J. Am. Chem. Soc.* 100 (1978), 2996.
- [3.41] G. Blondin, J.-J. Girerd, *Chem. Rev.* 90 (1990), 1359.
- [3.42] P. W. Anderson, H. Hasegawa, *Phys. Rev.* 100 (1955), 675.
- [3.43] O. Kahn, *Molecular Magnetism*, VCH, New York, 1993, p. 337.
- [3.44] M. I. Belinskii, B. S. Tsukerblat, N. V. Gerbeléu, *Sov. Phys. Solid State* 25 (1983), 497; S. A. Borshch, I. N. Kotrov, I. B. Bersuker, *J. Chem. Phys.* 3 (1985), 1009.
- [3.45] N. Guihéry, J.-P. Malrieu, *J. Chem. Phys.* 119 (2003), 8956; C. Boilleau, N. Suaud, R. Bastardis, N. Guihéry, J.-P. Malrieu, *Theor. Chim. Acta* 126 (2010), 231.
- [3.46] A. S. Borovik, V. Papaefthymiou, L. F. Taylor, O. P. Anderson, L. Que, *J. Am. Chem. Soc.* 111 (1989), 6183.
- [3.47] B. Raveau, *Phil. Trans. Roy. Soc. A* 366 (2008), 83, and references therein.
- [3.48] R. S. Drago, *Physical Methods in Chemistry*, W. B. Saunders, Philadelphia, 1977, section 4.5, and *Physical Methods for Chemists*, 2nd edn., Surfside Scientific Publishers, Gainesville, 1992.
- [3.49] *The Time Domain in Surface and Structural Dynamics*, G. J. Long and F. Grandjean (eds.), Kluwer Academic Publishers, Dordrecht, 1988.
- [3.50] P. W. Atkins, *Physical Chemistry*, 4th edn., Oxford University Press, Oxford, 1990, a) p. 555; b) p. 503.
- [3.51] D. B. Brown and J. T. Wroblewski, in *Mixed Valence Compounds*, D. B. Brown (ed.), NATO ASI Series, D. Reidel, Dordrecht, 1980, p. 243 (quoting the original reference: O. Berkooz, M. Malamud, S. Shtrikman, *Solid State Comm.* 6 (1968), 185.)
- [3.52] C. H. Londergan, C. P. Kubiak, *Chem. Eur. J.* 9 (2003), 5962.
- [3.53] N. S. Hush, *Coord. Chem. Rev.* 64 (1985), 135.
- [3.54] C. Creutz, M. D. Newton, N. Sutin, *J. Photochem. Photobiol. A* 82 (1994), 47.
- [3.55] R. J. Cave, M. D. Newton, *Chem. Phys. Letters* 249 (1996), 15.
- [3.56] L. N. Silverman, P. Kanchanawong, T. P. Treynor, S. G. Boxer, *Phil. Trans. Roy. Soc. A* 366 (2008), 33.
- [3.57] K. D. Demadis, C. M. Hartshorn, and T. J. Meyer, *Chem. Rev.* 101 (2001), 2655.
- [3.58] S. F. Nelsen, R. F. Ismagilov, D. R. Powell, *J. Am. Chem. Soc.* 119 (1997), 10213.
- [3.59] J. Bonvoisin, J.-P. Launay, C. Rovira, J. Veciana, *Angew. Chem. Int. Ed. English* 33 (1994), 2106.
- [3.60] L. De Cola, V. Balzani, F. Barigelletti, L. Flamigni, P. Belser, A. von Zelewsky, M. Frank, F. Vögtle, *Inorg. Chem.* 32 (1993), 5228.

- [3.61] E. G. Petrov, Y. V. Shevchenko, V. I. Teslenko, V. May, *J. Chem. Phys.* 115 (2001), 7107; M. Bixon, J. Jortner, *J. Am. Chem. Soc.* 123 (2001), 12556.
- [3.62] B. P. Paulson, J. R. Miller, W.-X. Gan, G. Closs, *J. Am. Chem. Soc.* 127 (2004), 4860.
- [3.63] M. D. Newton, *Chem. Rev.* 91 (1991), 767.
- [3.64] M. D. Newton, in *Electron Transfer in Chemistry, Vol 1*, V. Balzani (ed.), Wiley-VCH, Weinheim, 2001, chap. 1; C. J. Calzado, J.-P. Malrieu, J. F. Sanz, *J. Phys. Chem. A* 102 (1998), 3659.
- [3.65] L. Rodriguez-Monge, S. Larsson, *J. Phys. Chem.* 100 (1996), 6298; S. B. Braunschweig, O. Wiest, *J. Phys. Chem. A* 107 (2003), 285.
- [3.66] A. J. Heeger, A. G. MacDiarmid, H. Shirakawa, Nobel Lectures, Chemistry 1996–2000, Ingmar Grenthe (ed.), World Scientific Publishing Co, Singapore, 2003.
- [3.67] J. B. Torrance, *Accounts Chemical Research* 12 (1979), 79.
- [3.68] E. Canadell, M. H. Whangbo, *Chem. Rev.* 91 (1991), 965.
- [3.69] *Special issue of Chemical Reviews* 104 (2004), P. Batail (ed.), with review articles by (a) T. Mori, 4947; (b) H. Seo, C. Hotta, H. Fukuyama, 5005; (c) T. Giamarchi, 5037; (d) J. M. Fabre, 5133; (e) A. Kobayashi, E. Fujiwara, H. Kobayashi, 5243; (f) H. Kobayashi, H. Cui, and A. Kobayashi, 5265; (g) C. Rovira, 5289; (h) P. Day, E. Coronado, 5419; (i) T. Enoki and A. Miyazaki, 5449; (j) D. Jérôme, p. 5565; (k) S. Ravy, 5609; (l) K. Miyagawa, K. Kanoda, A. Kawamoto, 5635; (m) C. Coulon, R. Clérac, p. 5655; (n) M. Dressel and N. Driehko, 5689; (o) S.J. Blundell, 5717; (p) M. V. Kartsovnik, 5737.
- [3.70] *Molecular Metals*, NATO Conference Series, W. H. Hatfield (ed.), Plenum Press, New York, 1979.
- [3.71] S. Roth, H. Bleier, *Adv. Phys.* 36 (1987), 385.
- [3.72] R. Comes, M. Lambert, H. Launois, H. R. Zeller, *Phys. Rev. B* 8 (1973), 571.
- [3.73] (a) N. F. Mott, *Pure Appl. Chem.* 52 (1979), 65; (b) J. Hubbard, *Proc. Roy. Soc. London A* 276 (1963), 238; (c) D. Jérôme, H. J. Schulz, *Adv. Physics* 42 (1982), 299; (d) K. Nasu, *J. Phys. Soc. Jpn* 53 (1984), 427, and references therein.
- [3.74] P. A. Cox, *The Electronic Structure and Chemistry of Solids*, Oxford University Press, 1986, chap. 5.
- [3.75] (a) L. Smart, E. Moore, *Solid State Chemistry: An Introduction*, 3rd edn., Taylor and Francis, Boca Raton, 2005; (b) J. B. Goodenough, *Metallic Oxides: Progress in Solid State Chemistry* 5 (1971), 267, Pergamon Press, Elmsford.
- [3.76] J. P. Collman, J. T. McDevitt, C. R. Leidner, G. T. Yee, J. B. Torrance, W. A. Little, *J. Am. Chem. Soc.* 109 (1987), 4606–14.
- [3.77] (a) R. D. Cannon, U. A. Jayasooriya, C. Tilford, C. E. Anson, F. E. Sowrey, D. R. Rosseinsky, J. A. Stride, F. Tasset, E. Ressouche, R. P. White, R. Ballou, *Inorg. Chem.* 43 (2004), 7061; (b) R. D. Cannon, *Electron Transfer Reactions*, Butterworths, London, 1980, chap. 9; (c) D. R. Rosseinsky, K. C. Quillin, in *Mixed Valency Systems*, K. Prassides (ed.), Kluwer, Dordrecht, 1991, p. 401.
- [3.78] (a) M. Yamashita, T. Manabe, T. Kawashima, H. Okamoto, H. Kitagawa, *Coord. Chem. Rev.* 190–92 (1999), 309–330; (b) M. Yamashita, S. Takaishi, *Chem. Comm.* 46 (2010), 4438; (c) K. Nasu, Y. Toyozawa, *J. Phys. Soc. Jpn.* 51 (1982), 2098 and 3111; (d) J. T. Gammel, A. Saxena, I. Batistic, A. R. Bishop, S. R. Phillpot, *Phys Rev B* 45 (1992), 6408 and 6435; (e) M. Yamashita, S. Takaishi, in *Comprehensive Inorganic Chemistry*, chap. 4.24, J. Reedijk, K. Poepelmeier (eds.), Elsevier, Amsterdam, 2013.
- [3.79] L. Balicas, K. Behnia, W. Kang, E. Canadell, P. Auban-Senzier, D. Jérôme, M. Ribault, J. M. Fabre, *J. Phys I* 4 (1994), 1539.

4

The excited electron: photophysical properties

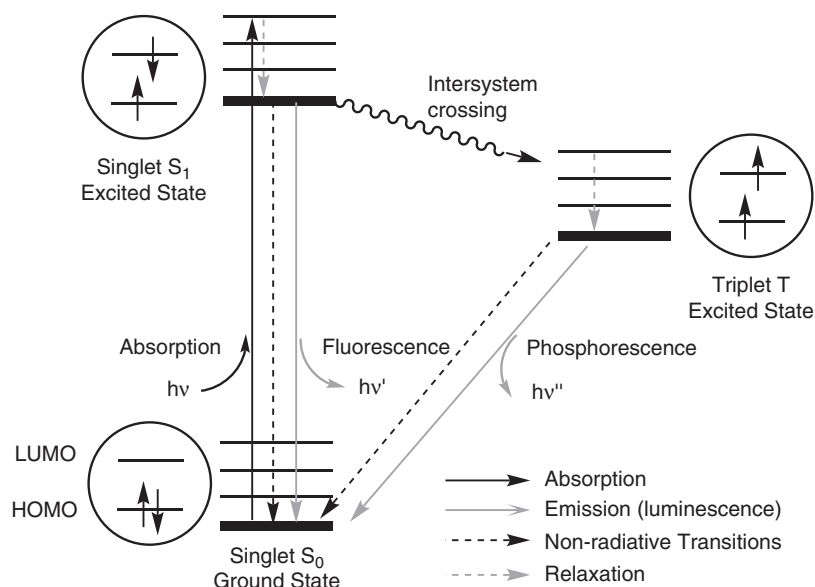
4.1 Introduction

After localized electrons and magnetism (Chapter 2), and delocalized electrons, electron transfer, and conductivity (Chapter 3), in this chapter we consider the process of electronic excitation and its consequences. Electronic excitation results in most cases from the absorption of a photon, and the resulting state can generally (but not always) be described by an electronic configuration where the arrangement of electrons does not follow the Aufbau principle. Therefore, in the first part we will recall a few basic concepts in photophysics—in particular, absorption and emission and the properties of excited states. Then we will consider successively *excited state electron transfer*, *energy transfer*, and *photomagnetism*.

There are many photoprocesses which can occur after an electronic excitation, because the system is in a high-energy state. Rather than being exhaustive, we shall concentrate more on photophysical processes than on photochemical ones (leading to chemical products). We shall focus on intramolecular processes, which are easier to handle, because they do not require an association or diffusion step of reactants, and they can occur inside a cleverly designed molecule or supramolecule. But we shall also provide some examples of more complex systems. We shall use the expression chromophore (from the Greek, ‘colour bringer’) to design a group (part of a molecule, molecule) whose electronic transition energy (corresponding to a characteristic ‘colour’) is transferable from one compound to another.

First, we shall present the problems related to the spin of the excited states, taking the simple example of a molecule with an even number of paired electrons (singlet ground state) and no orbital degeneracy: here the excited state can be a singlet or triplet. The overall scheme (singlet ground state, excited singlet and triplet states) can be described by the so-called Jablonski diagram, which features most of the important photophysical basic phenomena (Fig. 4.1).

Second, we shall consider the case of *excited state electron transfer*. In this process, an electron moves away from the excited chromophore, thus leaving behind him an electron hole (usually a positive charge). If the system is initially neutral, there is thus a *charge separation*. The corresponding systems are potentially appealing for energy conversion: excited state electron transfer

**Fig. 4.1**

Energies of the different states after a photophysical excitation (Jablonski diagram). The diagram shown here corresponds to the very frequent case of a singlet ground-state molecule. A few vibrational levels are shown for each electronic state.

occurs in photosynthesis as well as in artificial light harvesting systems, or in new molecular-based devices such as organic light-emitting diodes.

Third, another important process after excitation is *energy transfer*. As previously, the distribution of the electrons among the various energy levels is modified in the process, but there is no net charge modification on the different parts of the molecule. Thus only energy, not matter, is transferred. Of course, since the energetic state of the molecule depends on the status of electrons, there is a relation between energy transfer and electron transfer. In some cases we shall see that the two processes are actually intermingled.

Finally, a last topic will be *photomagnetism*, which can be considered as a simple extension of the Jablonski diagram. When the photoexcitation is followed by a cross-over to another spin state, the new spin state can become a *metastable state*; that is, a state which is trapped for some time in a potential well, unable to overcome an activation barrier to return to the ground state. Photomagnetism—a very recent discipline—is indeed developing rapidly, with the hope of photocontrolled high-density storage of information. We shall present some trends and examples, extending the scope of the chapter.

4.2 Fundamentals in photophysics: absorption, emission, and excited states

The fundamental concepts of absorption, emission, and excited states can be found in a number of textbooks [4.1]. They are most easily introduced starting from the example of closed-shell systems. For instance, the vast majority of organic molecules present a configuration in which two spin-paired electrons occupy the highest occupied molecular orbital (HOMO), and somewhere

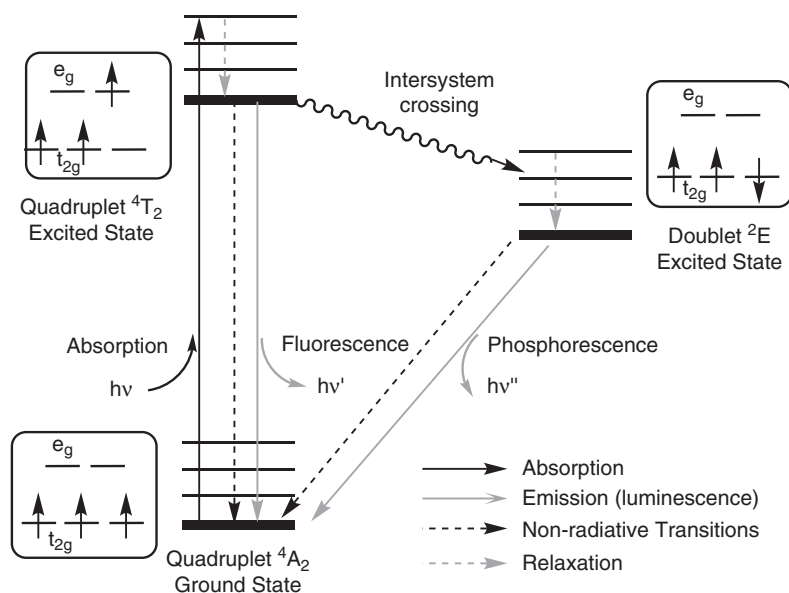
above in energy lies the LUMO (see Fig. 4.1). This electronic configuration is the lowest-energy one, in agreement with the Aufbau principle, and corresponds to a singlet ($S = 0$) ground state. Note that in the following it will be important (i) to make the distinction between the energies of orbitals and the total energy of the resulting state, and (ii) to notice that for all electronic states (excited or not) there are several possible vibrational levels. The interval between these levels is of the order of vibrational wavenumbers (10^2 – 10^3 cm^{-1})—much less than the interval between different electronic levels (10^4 – 10^5 cm^{-1}).

4.2.1 Energy levels

Upon excitation by photon absorption, the system can reach a high-energy (excited) state. In many cases this is the result of an electron promotion to a higher-energy orbital, here from the HOMO to the LUMO. For reasons that will be explained subsequently, in a first step we reach a *singlet* excited state; that is, there has been an electron promotion without spin flip.

The singlet excited state, S_1 , and more generally any excited state, can evolve according to different possibilities. First of all, it relaxes by molecular motions or interaction with the surrounding (solvent) molecules, and rapidly reaches the lowest vibrational level. Then (i) it can return to the ground state with photon emission. When the excited state has the same spin state as the ground state, the process is called *fluorescence*. It occurs at a slightly lower energy (higher wavelength) than the absorption process, because of the *relaxation* process (see Fig. 4.1); (ii) it can return to the ground state without photon emission. This is a *non-radiative* process. In such a case the energy is dissipated as heat along the different intramolecular vibration modes and/or processes involving the surrounding (solvent) molecules; (iii) it can transform finally into a different excited state with a different spin. This is called *inter-system crossing*. The simplest and the most typical of such processes is the conversion to a triplet state (Fig. 4.1). As seen in Chapter 1, for two electrons in two degenerate orbitals the triplet state is more stable than the singlet state, because of the exchange term k . From the triplet state we can return to the ground state by either a non-radiative process or a radiative process. This last case is called *phosphorescence*. As a result of the relative position of excited states, phosphorescence occurs at a lower energy (higher wavelength) than fluorescence. Fluorescence and phosphorescence are encompassed in the general term *luminescence*.

An important property of excited states is their lifetime. For an excited singlet state it is typically a few nanoseconds, while for triplet states it is longer—typically a few microseconds, though it can reach seconds. The lifetime determines the possibility of the excited state evolving and transforming before disappearing. This is particularly important for photochemical transformations, but they are not considered here, the present chapter being devoted essentially to photophysical transformations. The most direct consequence of the difference in lifetimes is to make the time-scales of fluorescence and phosphorescence also different. Fluorescence disappears very rapidly after the end of excitation, while phosphorescence remains for a longer time.

**Fig. 4.2**

Jablonski diagram for an open-shell system—here the hexaaqua-chromium(III) coordination complex, $[\text{Cr}(\text{H}_2\text{O})_6]^{3+}$.

When dealing with open-shell systems the general principles and definitions remain the same. To be more concrete, we shall consider the case of a coordination complex such as the octahedral hexaaqua-chromium(III) $[\text{Cr}(\text{H}_2\text{O})_6]^{3+}$, with three unpaired d electrons (t_{2g}^3 configuration, $S = 3/2$, quartet ground state ${}^4A_{2g}$, Fig. 4.2). The difference between state and term has been stressed in Chapter 2. Throughout this entire chapter we shall use the terminology ‘state’, which is commonly used in molecular photochemistry, even if a symbol like ${}^4A_{2g}$ is *stricto sensu* a ‘term’ from the point of view of atomic spectroscopy. The excitation by promotion of an electron to an e_g orbital produces a ${}^4T_{2g}$ state. By an intersystem crossing (with spin-flip) one can reach a lower-energy excited state which is a doublet, 2E_g . Emission from ${}^4T_{2g}$ to ${}^4A_{2g}$ is called fluorescence (no spin change), and from 2E_g to ${}^4A_{2g}$, phosphorescence (with spin change). For compounds containing heavy elements, such as heavy transition metals, there is, however, some difficulty in defining rigorously a spin state, because the spin-orbit coupling is important and allows mixing of states having different spins, and thus prevents distinguishing fluorescence from phosphorescence.

In the absence of chemical reactions, excited states, whatever their nature, decay by a combination of radiative and non-radiative processes. Thus they present a finite lifetime τ , related to the radiative and non-radiative constants k_r and k_{nr} by:

$$\tau^{-1} = k_r + k_{nr} \quad (4.1)$$

Another important definition in photochemistry or photophysics is the *quantum yield*. This is the probability (usually expressed in percentage) that an excited state evolves according to a given process. Thus the quantum yield for emission Φ_m is given by:

$$\Phi_m = \frac{k_r}{k_r + k_{nr}} \quad (4.2)$$

In the same way, one can define quantum yields for other processes, such as intersystem crossing, or photochemical reactions.

In transition metal complexes, several types of electronic transition may occur. They are broadly sorted according to the nature of the molecular orbitals involved in the excitation process (Fig. 4.3). Thus transitions between molecular orbitals with predominant d character are called d-d transitions. Other types of transition imply an electron transfer from a predominant ligand orbital L (more properly from a symmetry orbital, combination of ligand-based orbitals) towards metallic d orbitals (M). They are called ligand-to-metal charge transfer (LMCT) transitions. The reverse case is a metal-to-ligand charge transfer (MLCT) transition. Finally, there is a possibility of ligand-centred transitions (Fig. 4.3). In polynuclear complexes containing M–Bridge–M' units metal-to-metal charge transfer (MMCT), transitions are also important.

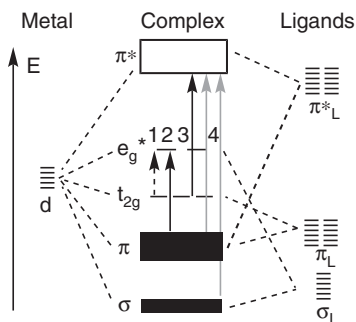


Fig. 4.3

Different types of transition in a coordination complex: 1, d-d; 2, LMCT; 3, MLCT; 4, ligand-centred.

4.2.2 Transition probabilities

The absorbance A_λ of a substance at wavelength λ is:

$$A_\lambda = \log_{10} \frac{I_0}{I} = \epsilon_\lambda c l \quad (4.3)$$

where I and I_0 are the light intensities before and after absorption respectively; ϵ_λ , the molar absorption (or extinction) coefficient— $L \text{ mol}^{-1} \text{ cm}^{-1}$; c , the concentration— mol L^{-1} ; l , the length of optical path— cm . A is dimensionless. The curve $A_\lambda = f(\lambda)$ or $\epsilon_\lambda = f(\lambda)$ is termed the absorption spectrum of the substance. The relations between the wavelength λ , the period T , the frequency ν , and the wavenumber $\bar{\nu}$ of the electromagnetic wave and the celerity of the light c are well known ($\lambda = cT = c/\nu$; $\nu = 1/T$; $\bar{\nu} = 1/\lambda = \nu/c$). For a given transition between ground and excited levels, G and E , the oscillator strength f_{EG} is the area under the curve between two wavenumbers $\bar{\nu}_1$ and $\bar{\nu}_2$ surrounding the transition:

$$f_{EG} = \frac{4\epsilon_0 m_e c^2 \ln 10}{N_A e^2} \int_{\bar{\nu}_1}^{\bar{\nu}_2} \epsilon(\bar{\nu}) d\bar{\nu} \quad (4.4)$$

Note that this equation was given in a slightly different form in Chapter 3 (eqn. (3.88)) because there the area was expressed with frequencies instead of wavenumbers.

Absorption and emission obey *selection rules*. The interaction of the ground or excited state with the electromagnetic radiation of light is due essentially to the electric vector component. The detailed theory of the interaction can be found in textbooks [4.1], and here we provide just a few, very simple, guidelines. The mathematics is in fact quite simple: the intensity of a transition is proportional to the square of the transition dipole moment M , which is given by:

$$M = \langle \Psi_{gr} | \mathbf{O}_{dip} | \Psi_{ex} \rangle \quad (4.5)$$

where the wavefunctions— Ψ_{gr} for the ground state and Ψ_{ex} for the excited state—are the product of a space function by a spin function, $\Psi = \Phi \Sigma$, while \mathbf{O}_{dip} is the electric dipole operator, $\mathbf{e} \cdot \mathbf{r}$, with components $e \cdot \mathbf{r}_x$, $e \cdot \mathbf{r}_y$, and $e \cdot \mathbf{r}_z$.

Developing eqn. (4.5), one finds:

$$M = \langle \Phi_{\text{gr}} \Sigma_{\text{gr}} | \mathbf{O}_{\text{dip}} | \Phi_{\text{ex}} \Sigma_{\text{ex}} \rangle = \langle \Phi_{\text{gr}} | \mathbf{O}_{\text{dip}} | \Phi_{\text{ex}} \rangle \langle \Sigma_{\text{gr}} | \Sigma_{\text{ex}} \rangle \quad (4.6)$$

because the electric dipole operator does not act on the spin wavefunctions.

A first immediate consequence is the following: the transition moment is different from zero only if the spin functions Σ_{gr} and Σ_{ex} are the same for the ground and excited states. If we use the convention α for spin up (\uparrow) and β for spin down (\downarrow), we obtain the simple relations:

$$\langle \uparrow | \uparrow \rangle = \langle \alpha | \alpha \rangle = 1 \text{ and } \langle \beta | \beta \rangle = \langle \downarrow | \downarrow \rangle = 1 \quad (4.7a)$$

$$\langle \uparrow | \downarrow \rangle = \langle \alpha | \beta \rangle \text{ and } \langle \downarrow | \uparrow \rangle = \langle \beta | \alpha \rangle = 0 \quad (4.7b)$$

With respect to this rule, singlet-to-singlet transitions are allowed, while singlet-to-triplet transitions are forbidden. The experimental consequence is that the transition from a singlet to a triplet has very weak intensity, and is generally not observed (Fig. 4.1). As far as emission is concerned, the spin interdiction acts as a bottleneck and strongly reduces the probability of transition. This is why phosphorescence has a much longer lifetime than fluorescence.

If we now consider the simplified version of eqn. (4.5) in which the spin parts of the wavefunctions have been removed:

$$M = \langle \Phi_{\text{gr}} | \mathbf{O}_{\text{dip}} | \Phi_{\text{ex}} \rangle \quad (4.8)$$

we are able to understand the additional condition (besides the spin condition) necessary for a transition to be allowed. The integral in eqn. (4.8) must be different from zero. The analysis of the problem is facilitated by the use of group theory. The electric dipole moment operator can be characterized by a defined symmetry, that of the x, y, z coordinates; that is, for instance t_{1u} in octahedral symmetry. For expression (4.8) to be non-zero it is necessary that the direct product of the irreducible representations Γ , associated with the Φ_{gr} and Φ_{ex} wavefunctions and the \mathbf{O}_{dip} operator, contains the totally symmetric representation A_1 (see Chapter 1). This necessitates that the direct product $\Gamma(\Phi_{\text{gr}}) \otimes \Gamma(\Phi_{\text{ex}})$ is the same or contains the same symmetry as the dipolar electric operator.

The rule allows a simple and pictorial interpretation, taking as an example the case of an octahedral complex (O_h point group). A transition from a s (a_{1g}) to a p (t_{1u}) orbital is allowed (Fig. 4.4). Conversely, a transition from a d orbital to another d orbital is forbidden. In O_h symmetry the d orbitals are centrosymmetric (gerade, g), so their direct product $g \otimes g$ is also of g symmetry, while the dipolar electric operator is of u symmetry. This very important and general result is known as the Laporte rule.

In transition metal complexes displaying octahedral symmetry and more generally having an inversion centre, d - d transitions are thus forbidden by the

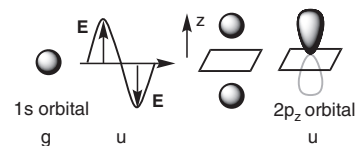


Fig. 4.4

Schematic representation of an electron in a $1s$ orbital (g symmetry) submitted to the dipole of the electric field E of an electromagnetic wave oscillating along z (u symmetry): it gives rise to an electronic distribution with a mirror symmetry in the xy plane, as a p orbital (u symmetry).

Laporte rule (and in some cases also by the spin conservation rule), and thus exhibit a low intensity.

Typical values of the extinction coefficients for d–d transitions ϵ_λ are about $10\text{--}100\text{ L mol}^{-1}\text{ cm}^{-1}$ if there is no spin restriction. Charge transfer transitions, on the other hand, are generally allowed. The detailed inventory of the states shows that in the manifolds of states coming from the ground and excited configurations, one can generally find a couple of states with the right symmetry to produce a non-zero transition dipole moment. Thus the corresponding extinction coefficients for allowed LMCT or MLCT transitions are in the range $10^3\text{--}10^4\text{ L mol}^{-1}\text{ cm}^{-1}$.

4.2.3 Nuclear relaxation after excitation

As noted previously, the energy of the states depends also on the vibrational state, and more generally on the instantaneous geometry of the system. This is taken into account, either by displaying the vibrational progression on the energy diagram (Fig. 4.1), or by plotting the total energy as a function of a nuclear coordinate (Fig. 4.5). This gives potential energy curves, or more generally potential energy surfaces when several nuclear coordinates are involved. Usually, there is a simple potential energy surface for the ground state, with a single minimum, which means that the molecule has a defined geometry. In the excited state the situation is generally more complex, as there are frequently different electronic configurations with nearby energies. Several potential energy curves (or surfaces) arise with their own minimum, and they are connected by avoided crossing interactions (cf Sections 3.2.1.1 and 3.2.2.3). We now have a more complete tool for interpreting the different processes occurring after an excitation.

First, in the energy *versus* nuclear coordinate representation (Fig. 4.5) an electronic transition is *vertical*. It occurs, indeed, at constant geometry as a result of the Franck–Condon principle, which states that nuclei have no time to move during the transition (nuclei are much more massive than electrons) [4.2]. Now, in the excited state, since the distribution and localization of electrons is different, the energy minima do not generally occur for the same abscissa

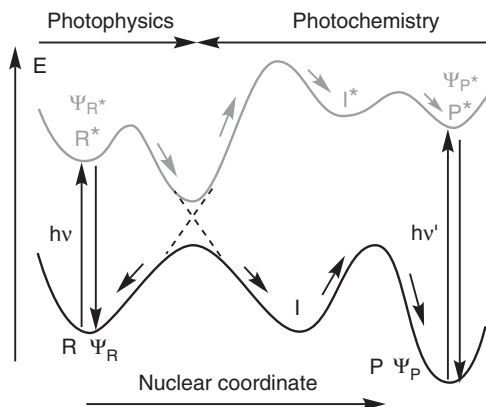


Fig. 4.5

Potential energy surfaces as a function of nuclear coordinate for the ground state (black) and excited state (grey). Chemistry works in the ground state (from reactant R to product P). Photophysics plays with excited states (R^* , P^*) after photoexcitation ($h\nu$ or $h\nu'$). Photochemistry provides products P through excited species R^* , intermediates I^* or P^* .

than in the ground state. For example, if the excited electron were initially in a bonding orbital, the bond is weakened and the equilibrium distance is increased. Therefore, a vertical transition reaches an excited vibrational state, and the system then relaxes to the energy minimum with a different geometry. This explains the relaxation process, responsible for the shift in fluorescence energy. With respect to the reactivity of the excited states, it can be considered an exploration of the different possibilities offered by the manifold of excited state surfaces.

In the following we shall look mainly at two general classes of photophysical processes. In both cases we move from one excited-state potential energy curve to another one. Actually, since the two curves are connected by non-crossing zones, it is more correct to say that we move from a local minimum to another one. In one case the two excited states differ by the formal charges borne by different sub-moieties constituting the molecule: this corresponds to *excited state electron transfer*, with variants such as *charge separation* and *charge recombination*. In another case the excited states do not differ in an obvious way by electron motion, but by distribution of the electronic energy. This corresponds to *energy transfer*.

4.3 Electron transfer in the excited state

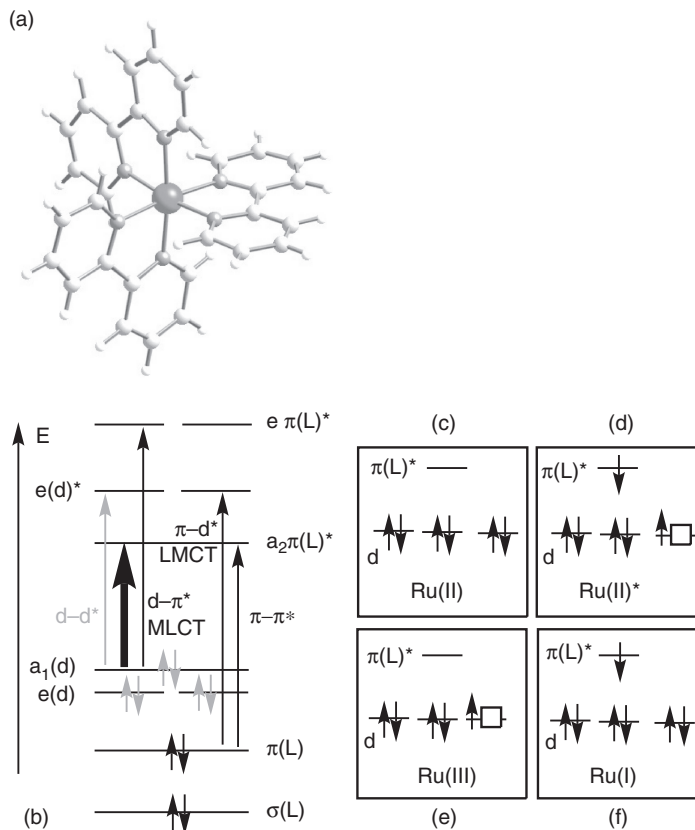
In this section we describe a number of electron transfer reactions in the excited state. This is by no means an exhaustive inventory, and we have selected a few representative examples. From the point of view of theory, excited state electron transfer obeys the same general rules as more conventional electron transfer and the general treatment in Chapter 3 is valid. Only Section 4.3.6, devoted to ultra-fast electron transfer, will introduce new concepts.

4.3.1 Properties of the excited state: the example of $[\text{Ru}(\text{bpy})_3]^{2+*}$

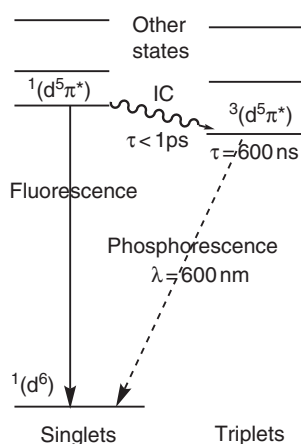
To explain the properties of excited states we consider in detail a very instructive example from coordination chemistry, $[\text{Ru}(\text{bpy})_3]^{2+*}$, where bpy = 2,2'-bipyridine [4.3]. This is a complex with pseudo- O_h symmetry (actually D_3 ; see Fig. 4.6), where the low oxidation state of ruthenium is stabilized by the π -acceptor ligand 2,2'-bipyridine, giving a $(t_{2g})^6$ low-spin configuration.

The absorption spectrum is dominated by a metal-to-ligand charge transfer transition (MLCT) occurring in the visible near 452 nm (in CH_3CN), and providing an intense orange colour ($\epsilon = 13,000 \text{ L mol}^{-1} \text{ cm}^{-1}$). The d-d transitions are not observed, due to their much lower intensity, and occur at higher energy than the MLCT, which is, incidentally, a rather unusual situation: in $[\text{Ru}(\text{bpy})_3]^{2+}$ the energy of the metal-centred $e(d)^*$ orbitals is above the one of the ligand-centred $a_2 \pi(L)^*$ orbitals (Fig. 4.6b).

Upon excitation a singlet state is first obtained $^1(d^5\pi(L)^*)$ or $^1(d^5\pi^*)$, but is converted rapidly ($\tau < 1\text{ps}$), due to spin-orbit coupling, into a triplet state $^3(d^5\pi^*)$, with vibrational relaxation (Fig. 4.7). The triplet state is indeed split in three low-lying states separated by 30 cm^{-1} and mixed with higher singlet

**Fig. 4.6**

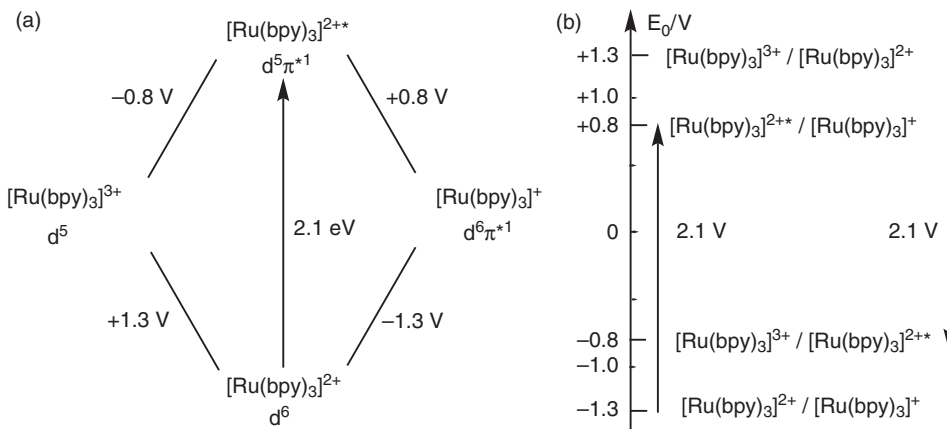
a) Crystallographic structure of $[\text{Ru}(\text{bpy})_3]^{2+}$; b) energy scheme of the molecular orbitals of $[\text{Ru}(\text{bpy})_3]^{2+}$, d^6 : on the left, the d metal-centred MOs named after their symmetry in the D_3 symmetry point group; the six electrons are paired—black grey; on the right the ligand-centred MOs; arrows show the electronic transitions; from the left: forbidden $d-d^*$ (light grey), allowed MLCT $d-\pi^*$ (bold arrow) and LMCT $\pi-d^*$, ligand to ligand $\pi-\pi^*$; * means antibonding level, as usual; c–f) schematic electronic configuration of $[\text{Ru}(\text{bpy})_3]^{2+}$ using the frontier orbitals: three d orbitals and the $a_2 \pi(L)^*$ ligand orbital: c) Ru(II); d) excited Ru(II)*; e) Ru(III); f) Ru(I). \square schematizes an electronic hole.

**Fig. 4.7**

Basic features of the luminescence of $[\text{Ru}(\text{bpy})_3]^{2+}$.

states. This excited state has been the subject of a large number of studies because of its appealing properties: it is strongly luminescent and emits at 600 nm (red emission), and has very interesting chemical properties that are detailed subsequently. The first problem is to understand its electronic structure.

The molecular orbital theory states that the MLCT transition involves an electron motion from one of the a_1 or e orbitals towards a *symmetry combination* of the LUMOs of the three equivalent bpy ligands, $a_2 \pi^*(L)$. Thus the excited state could be viewed as a ruthenium(III) species with a collectively reduced set of ligands; that is, three bpy sharing a negative charge. Actually, detailed experimental studies have shown that the system distorts in the excited state, and loses its threefold symmetry, with localization of the excited electron on one particular bpy ligand. The final state is thus better written as $[\text{Ru}^{\text{III}}(\text{bpy})_2(\text{bpy}^-)]^{2+*$, where the asterisk denotes an electronically excited state. This way of writing stresses the important characteristics of the excited state: it is a species in which *charge separation* has occurred—one hole on the ruthenium, one electron on one ligand—which heralds the simultaneous occurrence of an oxidizing character (through Ru^{III}) and a reducing character (through bpy^-). This is shown schematically in Fig. 4.6c–f.

**Fig. 4.8**

Redox potentials involving the ground and the excited states of $[\text{Ru}(\text{bpy})_3]^{2+}$. (a) different species and redox couples; (b) scale of redox potentials.

The excited state is easily monitored by its characteristic luminescence at 600 nm. The corresponding energy, 2.1 eV, represents the useful energy content of the excited state. Another important characteristic is the lifetime, found to be 600 ns, in well-degassed solutions. In non-degassed solutions the presence of dioxygen partially quenches the luminescence and reduces the lifetime. This 600-ns lifetime is long enough to permit specific reactions of the excited state, which are quite different from the reactions of the ground state. Thus an excited state can be considered as an isomer of the ground state, with its own geometry, and more important, its own reactivity.

The reactivity of the excited state is followed by the disappearance (quenching) of luminescence when a suitable reagent is added. With $[\text{Ru}(\text{bpy})_3]^{2+*}$ this occurs when adding oxidants ($[\text{Fe}(\text{CN})_6]^{3-}$, $\text{Fe}^{3+}_{\text{aq}}$, methylviologen) as well as reductants ($[\text{Fe}(\text{CN})_6]^{4-}$, ferrocene, $\text{Eu}^{2+}_{\text{aq}}$), because of the ubiquitous nature of the excited state (reducing *and* oxidizing). It is thus possible to define redox potentials involving the excited state, as shown in Fig. 4.8.

We note that for ground-state species ($[\text{Ru}(\text{bpy})_3]^{3+/2+/1+}$ sequence, lower part of Fig. 4.8a) the redox potentials lie in the 'normal' order; that is, the most oxidized species correspond to the highest potential. Thus $[\text{Ru}(\text{bpy})_3]^{2+}$ is stable with respect to disproportionation into $[\text{Ru}(\text{bpy})_3]^{3+}$ and $[\text{Ru}(\text{bpy})_3]^{+}$. But when the excited state $[\text{Ru}(\text{bpy})_3]^{2+*}$ is involved the potentials are 'reversed', showing the high reactivity compared to $[\text{Ru}(\text{bpy})_3]^{2+}$; it becomes both (i) more reducing, due to the $a_2 \pi(\text{L})^*$ electron, and (ii) more oxidizing, due to the d hole (Fig. 4.6d). At pH = 8 it can therefore oxidize water ($E = -0.76\text{V}$) and reduce CO_2 ($E = -0.67\text{V}$). Such properties will be used in variants of $[\text{Ru}(\text{bpy})_3]^{2+}$, described in the next section.

4.3.2 Molecular photodiodes

A compound in which photoinduced charge separation occurs can be considered a molecular photodiode. A photodiode is a semiconducting device

based on a p-n junction (a junction made from p and n semiconductors; see Section 3.3.3.2), and such that upon irradiation at a suitable wavelength the junction generates electron-hole pairs which are then dissociated by the internal electrical field. With molecular systems, as well as with semiconducting devices, the game is to achieve a large spatial separation between electrons and holes, in order to avoid recombination, and to use them independently. Two such systems are presented in Fig. 4.9a,b and different molecular donors and acceptors in Fig. 4.9c.

Starting from the $[\text{Ru}(\text{bpy})_3]^{2+}$ structure, an obvious development is to graft acceptor and donor groups which could react within the molecule with the bpy^- and the Ru^{III} moieties respectively [4.4]. Thus the triad $[\text{PTZ}-\text{Ru}^{\text{II}}-\text{MV}^{2+}]$ has been prepared (Fig. 4.9a). PTZ is phenothiazine (donor) and MV^{2+} is methylviologen (acceptor), grafted on different bpy ligands. Excitation of the $\text{Ru}^{\text{II}}(\text{bpy})_3$ chromophore triggers a series of intramolecular electron transfers that eventually produce a charge-separated state $[\text{PTZ}^{\bullet+}-\text{Ru}^{\text{II}}-\text{MV}^{\bullet+}]$ (\bullet^+ denotes a cation radical). This species is still 1.14 eV above the ground state and has a lifetime of 160 ns. Note that the back electron transfer occurs in the inverted region (Section 3.2.1.2, Fig. 3.15), which is certainly a factor slowing down the reaction.

In the previous example the topology is not completely mastered, because many isomers are possible, and even when a separation is performed one has to cope with the existence of many conformers (Fig. 4.9a). A better design starts from the related $[\text{Ru}(\text{tpy})_2]^{2+}$ moiety, where $\text{tpy} = 2,2':6'2''$ -terpyridine, because it is possible to functionalize the terpyridine units in the 4' position [4.5], so that the donor and acceptor groups lie on opposite directions at 180° from each other, with a rigid geometry (Fig. 4.9b, with $\text{M} = \text{Ru}$).

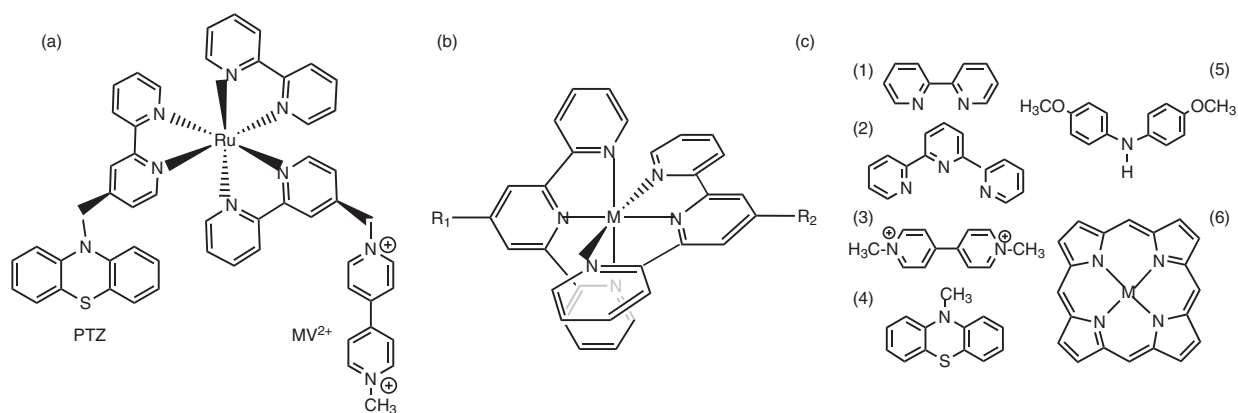


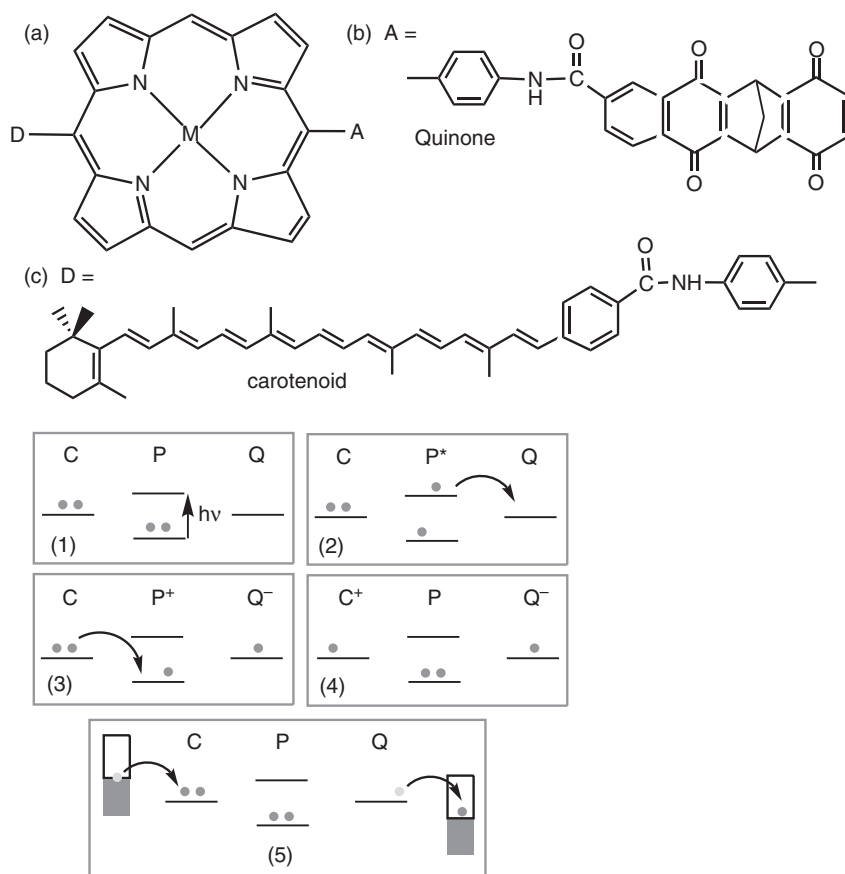
Fig. 4.9

Examples of molecular photodiodes based on polypyridine metal complexes. a) triad based on $[\text{Ru}(\text{bpy})_3]^{2+}$ (with PTZ on the left and MV^{2+} on the right); b) triads based on a $[\text{M}(\text{tpy})_2]^{3+}$ complex with R_1 and R_2 substituents on two perpendicular terpyridine ligands, in 4' positions; c) Ligands, donors and acceptors for the synthesis of photoactive triads: (1) 2, 2'-bipyridine, bpy; (2) terpyridine, tpy; (3) Methylviologen dication, MV^{2+} ; (4) methyl-phenothiazine, Me-PTZ; (5) di(*p*-anisyl)amine, DPAA; (6) metalloporphyrin, MPp, $\text{M} = \text{zinc, ZnPp}$, $\text{M} = \text{gold, AuPp}$.

The unsubstituted $[\text{Ru}(\text{tpy})_2]^{2+}$ moiety is not luminescent at room temperature because the lifetime of the possible triplet emitting state (the energy after relaxation is about 2 eV) is too short (250 ps only). This derives from the fact that the d–d excited states are only slightly above the triplet metal-to-ligand ($^3\text{MLCT}$) state, and thus provide an efficient pathway for radiationless deactivation, once thermally populated. Thus the situation appears at first sight worse than in the case of the $[\text{Ru}(\text{bpy})_3]^{2+}$ chromophore. Nevertheless, interesting triads $[\text{R}_1\text{--Ru--R}_2]$ have been prepared; for instance, $[\text{DPAA--Ru--MV}^{2+}]$. They are studied at low temperature to limit the effect of the radiationless deactivation. After excitation of the $[\text{Ru}(\text{tpy})_2]^{2+}$ unit a series of electron transfer reactions yields the $[\text{DPAA}^{+\bullet}\text{--Ru--MV}^{+\bullet}]$ charge-separated state, with an energy of 1.15 eV above the ground state and a lifetime of 27 ns. More spectacular results are obtained starting from the $[\text{Ir}(\text{tpy})_2]^{3+}$ chromophore (Fig. 4.9b, with $\text{M} = \text{Ir}$) [4.5b]. Iridium(III), d^6 , is isoelectronic with Ru(II). Iridium has two advantages with respect to ruthenium: the ligand field states are much higher in energy, and so is the $^3\text{MLCT}$ state. Thus they are much less prone to compete with the formation of the interesting charge-separated state. Starting from this structure, the grafting in 4' positions of $\text{R}_1 =$ a zinc porphyrin, ZnPp , and $\text{R}_2 =$ a gold porphyrin, AuPp (Fig. 4.9c), acting respectively as electron donor and electron acceptor, provides a triad molecule with an edge-to-edge distance of 20 Å between the two porphyrin rings. After excitation of the $\text{Ir}(\text{tpy})_2$ chromophore, electron transfers occur to give a fully charge-separated species denoted formally $\text{ZnPp}^+\text{--Ir--AuPp}^-$ with a unity quantum yield. The energy of this charge-separated state is 1.35 eV, and its lifetime is 450 ns.

Another beautiful example is provided by carotene–porphyrin–quinone triads (C–P–Q), where the porphyrin P (Fig. 4.10a) is the photosensitizer, the carotene C (Fig. 4.10c) the electron donor, and the quinone Q (Fig. 4.10b) the electron acceptor [4.6]. The mechanism is shown in Fig. 4.10d. As for ruthenium complexes, the porphyrin is a closed-shell molecule (see box 1 in Fig. 4.10d) which, once excited, acts as an oxidant and a reductant (box 2). After a series of electron transfers one finally obtains a $\text{C}^{+\bullet}\text{--P--Q}^{\bullet}$ charge-separated state (box 4), where the electron and the ‘hole’ (positive charge) are separated by more than 20 Å. When the molecule is connected to two wires, the diode function is achieved (box 5). With such a distance it is possible to build a prototype of a device performing the actual use of the photochemical energy, as follows.

For this purpose, in a demonstrative experiment, triad molecules of the C–P–Q type were embedded in the wall of a vesicle; that is, the lipid bilayer of a liposome. The triads have a preferential orientation and span the membrane, with the carotene part inside the vesicle. After excitation the $\text{C}^{+\bullet}\text{--P--Q}^{\bullet}$ state with charge separation can undergo electron transfer with a soluble quinone which can fix a proton and transport it from the outside to the inside of the liposome. The final result is the building of a proton motive force—the same process that occurs in natural photosynthesis. Thus *in fine* these ‘photodiodes’ do not provide electrical energy as their semiconductor analogues, but *chemical* energy. But the primary process after excitation is a genuine electronic process.

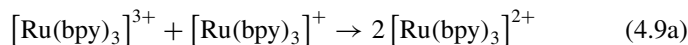
**Fig. 4.10**

(a-c) The carotene-porphyrin-quinone triad (CPQ); (d) schematic mechanism of electron-hole separation: (1) photoexcitation; (2) the photoexcited state P* acts as a reductant (electron transfer to the quinone acceptor); (3) the carotenoid donor C transfers an electron to the cationic porphyrin P⁺, acting as an oxidant, (4) achievement of the state with charge separation, C^{+•}-P-Q^{-•}; (5) possible restoration of the initial state C-P-Q due to metallic conductors at different potentials.

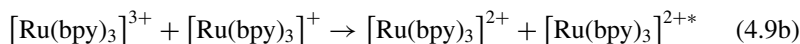
4.3.3 Light-emitting diodes (LED)

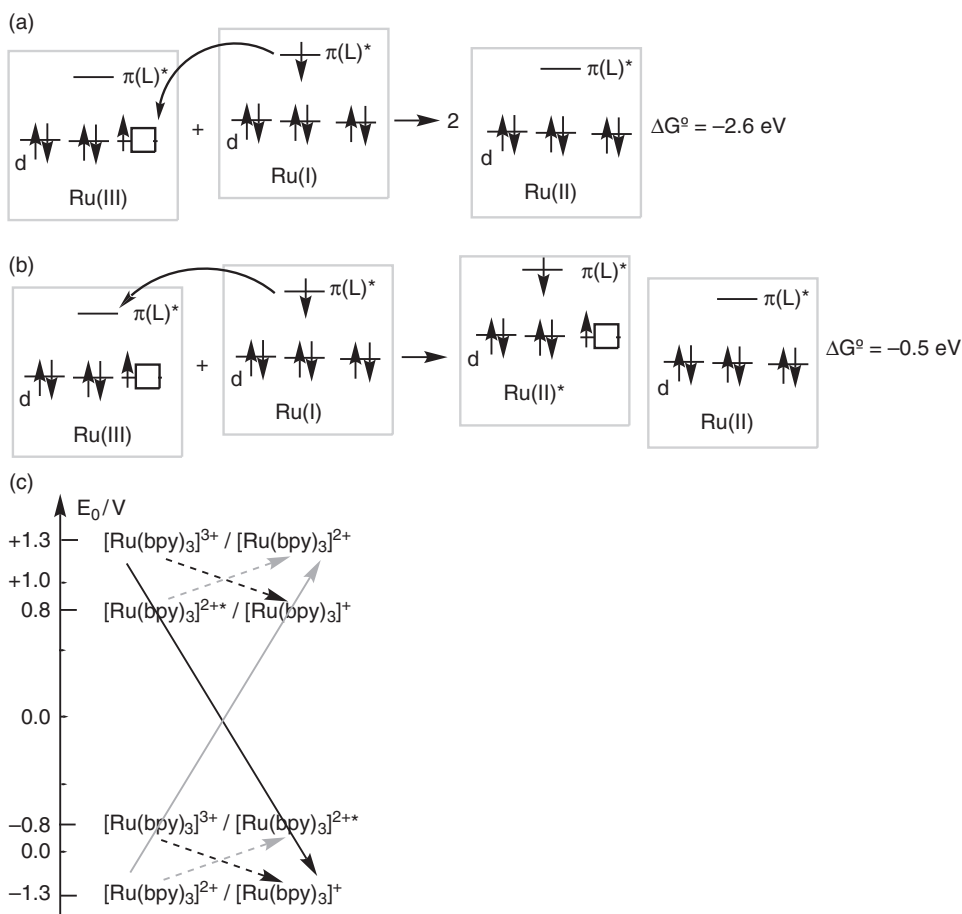
Light-emitting diodes function in the reverse way with respect to photodiodes: electrons and holes are injected from opposite ends of the device, and their recombination generates light. Once again the [Ru(bpy)₃]²⁺ component can be used as a model of a molecular light-emitting diode. This is the domain of chemiluminescence or electrochemiluminescence.

Let us consider what happens when the oxidized and the reduced form of [Ru(bpy)₃]²⁺ are mixed. Clearly, looking at the potentials displayed in the lower part of Fig. 4.8a, and at Fig. 4.11, the reaction:



is thermodynamically allowed ($\Delta G^\circ = -2.6$ eV), and will be the final overall transformation (Fig. 4.11a,c). But another reaction is possible, though it has a smaller driving energy ($\Delta G^\circ = -0.5$ eV) (Fig. 4.11b,c):



**Fig. 4.11**

Reaction of $[\text{Ru}(\text{bpy})_3]^+$ and $[\text{Ru}(\text{bpy})_3]^{3+}$: (a,b) molecular orbital reactions schemes and (c) thermodynamic interpretations of the chemiluminescence.

The molecular interpretation of eqn. (4.9b) is very simple: an electron transfer occurs from the singly occupied molecular orbital (SOMO) of $[\text{Ru}(\text{bpy})_3]^+$ (this is essentially a π^* bpy orbital) towards a vacant $\pi^*(\text{bpy})$ orbital of $[\text{Ru}(\text{bpy})_3]^{3+}$, thus generating the excited state $[\text{Ru}(\text{bpy})_3]^{2+*}$ (see Fig. 4.11b). The $a_2 \pi^*(\text{bpy})$ orbital in $[\text{Ru}(\text{bpy})_3]^{3+}$ is at a lower energy than in $[\text{Ru}(\text{bpy})_3]^+$, because of the stabilization by the larger positive charge on ruthenium, and this difference provides the driving energy for the reaction. Interestingly, reaction (4.9b) occurs with a 100% efficiency at the expense of reaction (4.9a); that is, there is a strong kinetic preference, certainly because reaction (4.9a) has a large negative ΔG° value, and is slowed down by the Marcus inverted region (see Section 3.2.1.2).

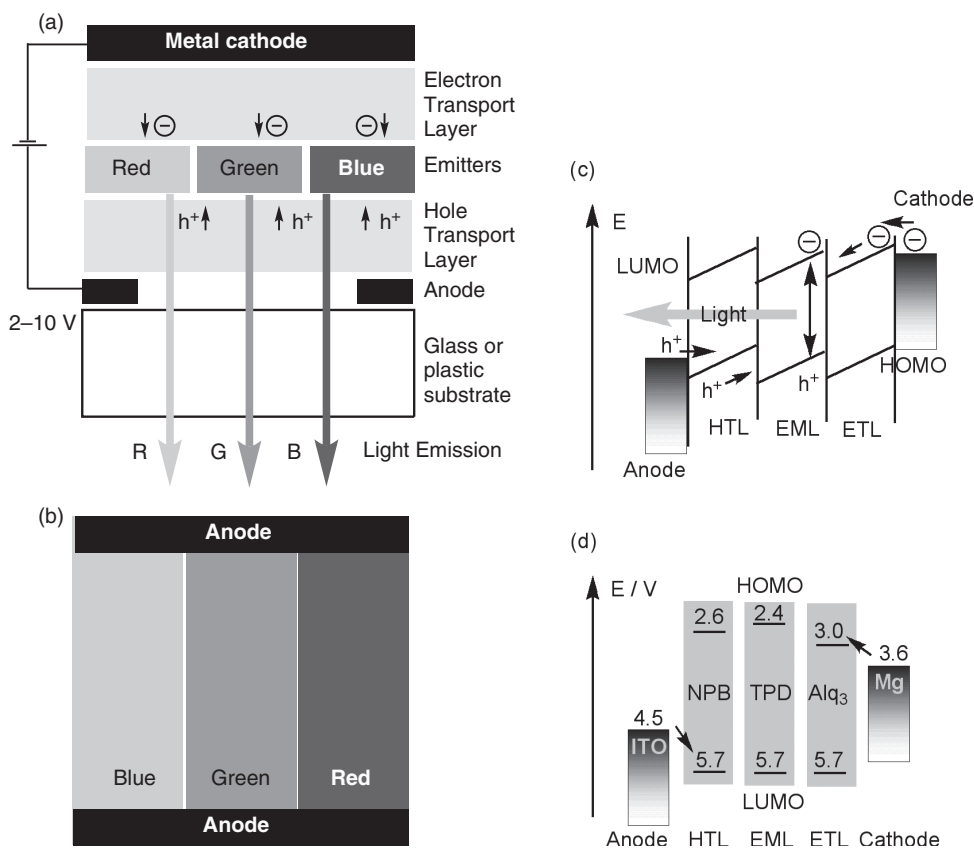
From a practical point of view, reaction (4.9b) can be achieved by mixing the oxidized and reduced forms of $[\text{Ru}(\text{bpy})_3]^{2+}$, these forms being prepared independently by passing the complex on a PbO_2 column for oxidation, or by

reacting it with borohydride for reduction. Other possibilities involve the oxidation of $[\text{Ru}(\text{bpy})_3]^+$ by the very reactive $\text{SO}_4^{\bullet-}$ species, itself generated from $\text{S}_2\text{O}_8^{2-}$, and several variations adapted to classroom demonstrations have been described. These experiments constitute examples of *chemiluminescence*—luminescence originating from a chemical reaction. Another possibility is to generate these forms electrochemically by cycling the potential of a platinum electrode at a frequency of around 0.2 Hz between the reduction and the oxidation potentials of $[\text{Ru}(\text{bpy})_3]^{2+}$ (from 2.4 to 1.8 V), thus providing an example of *electrochemiluminescence*—luminescence produced by an electrochemical reaction. The beautiful red luminescence appears on the electrodes. It is weak, but can be seen clearly in a darkened room.

The concept of the light-emitting diode has now become popular because of commercial applications based on the organic light-emitting diode (OLED). The subject began in the 1960s, and then major progress was made by teams at Kodak using small organic molecules [4.7a], and later by Friend's Cambridge Group, using polymers [4.7b]. Considerable improvements have been achieved recently from the point of view of colour gamut, luminance efficiency, and device reliability. The use of OLED for flat panel displays is now a commercial reality, including television screens (Sony, Samsung), and are said to offer significant advantages over the known solutions such as liquid crystal displays (LCD) and plasma panels.

OLED devices function according to the same general principle of electron–hole recombination as the luminescent systems described previously. For practical reasons, however, their structure is more complex. An OLED is an electrically driven light-emitting device designed from organic molecules or polymers. OLEDs are based on extremely thin layers (10–100 nm) of different organic materials, so they can be considered as supramolecular systems. The detailed technological description of these arrangements is clearly outside the scope of this book, and the reader is invited to consult texts such as [4.7c]. Briefly, a typical OLED device is made in most cases of three layers: (i) an electron transport layer (ETL), bringing electrons from the cathode; (ii) a hole transport layer (HTL), bringing holes from the anode; and (iii) between, an emitting material layer (EML) in which recombination of holes and electrons takes place with fluorescence emission (singlet–singlet) or phosphorescence emission (triplet–singlet). The layers are sandwiched between two electrodes which allow injection of charges and application of a small potential difference (2–10 volts) to facilitate transport and enhance light emission intensity. The general design of an OLED is shown in Fig. 4.12a,b. The transparent anode lies on a transparent substrate (rigid glass or flexible plastic), ensuring mechanical strength and transparency. The scheme of the energy levels of the different layers is shown in Fig. 4.12c, whereas typical energy values are shown in Fig. 4.12d. This figure uses the concept of 'work function', defined in Section 5.2.2.1.

Some of the main characteristics of an OLED are the colour emitted/wavelength (nm), the luminance (the luminous flux/lumen (lm); that is, the luminous intensity/candela (cd) in a given solid angle/steradian (sr), cd.sr), the quantum efficiency Z —the ratio of the number of emitted photons per number of charge carriers—the luminous efficiency—the ratio of the luminous

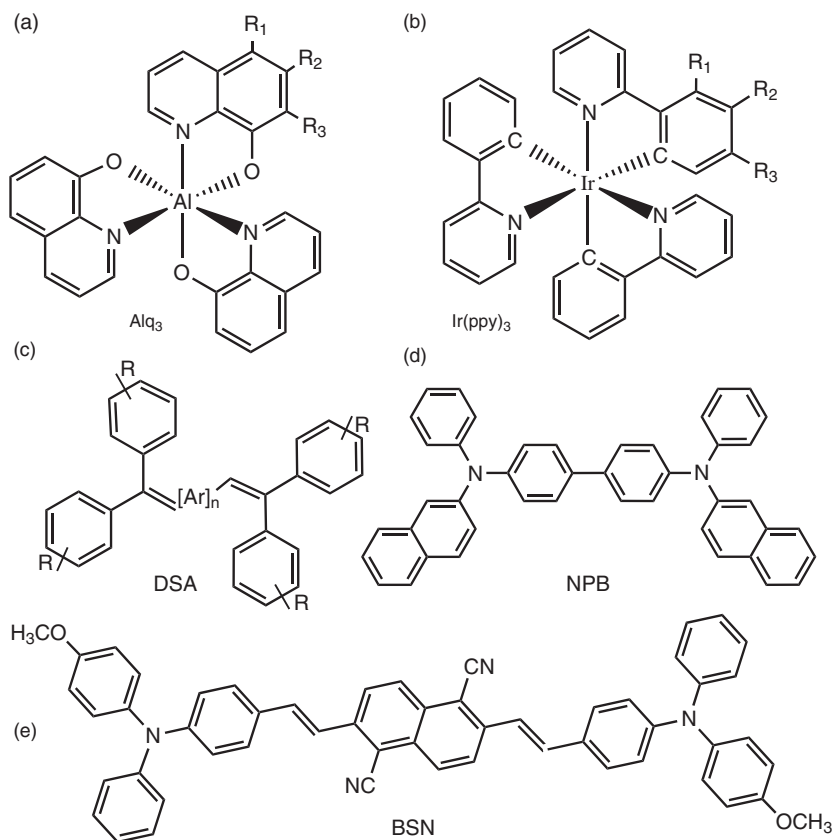
**Fig. 4.12**

Organic light-emitting diode (OLED): a) sandwich structure displaying RGB (red, green, blue) emission; \ominus are electrons, h^+ are holes; b) emitting face; c) schematic energetic scheme emphasizing the electrodes work functions ϕ (darkened surfaces), the changes in energy of the LUMO and HOMO of the molecular material of the hole transport (HTL) of the emitting material (EML) and of the electron transport (ETL) layers; arrows show the direction of the charges' displacement; the double arrow indicates the recombination of holes and electrons with light emission from the emitting layer EML; d) typical values of metallic electrodes work function ϕ and LUMO and HOMO energies of molecular components (ITO: indium tin oxide; for other abbreviations, see Fig. 4.13); arrows emphasize the energy barriers to overcome for holes' and electrons' injection from electrodes to the transport layers.

flux emitted per consumed electric power—and the stability in time. These characteristics (some fundamental, some technical) depend strongly on (i) the properties of the individual components that can be worked out separately and (ii) the overall structure of the cell. Considerable work is underway to optimize these characteristics.

The flexibility of molecular chemistry was essential for adjusting the materials properties and ensuring rapid progress in the field. Some molecular materials with best performances are displayed in Fig. 4.13.

The electron transport material is generally tris(8-hydroxyquinolinato) aluminum (Alq₃) (Fig. 4.13a). It is also a green emitter. Hole transport materials are frequently based on polyaromatic amines, such as NPB

**Fig. 4.13**

Organic molecules used in OLEDs: a) fluorescence green emitter (and electron transport material), tris-(8-hydroxyquinolato)aluminum complex, Alq_3 ; b) phosphorescence emitter, tris(2-phenylpyridine)-iridium, $\text{Ir}(\text{ppy})_3$; in both cases substituents R_1 , R_2 , R_3 are used to finely tune the properties of the complexes; c) blue emitter: distyrylarylene derivatives (DSA); d) hole transport materials and blue emitter: N,N' -bis(1-naphthyl)- N,N' -diphenyl-1,1'-biphenyl-4,4'-diamine (NPB); e) Red emitter: derivative of 1,1'-dicyano-bis-styrylnaphthalene (BSN).

(Fig. 4.13d) or the parent N,N' -diphenyl- N,N' -bis(3-methylphenyl)(1,1'-biphenyl)-4,4'-diamine (TPD). Finally, for the emitting material itself one uses luminescent organic dyes such as red-emitting BSN (Sony) (Fig. 4.13e), green-emitting coumarins 10-(2-benzothiazolyl)-1,1,7,7-tetramethyl-2,3,6,7-tetrahydro-1H,5H,11H-[1]benzo-pyrano[6,7,8-ij]quinolizin-11-one, known as C-545T, and blue-emitting NPB or DSA (Idemitsu Kosan Co) (Fig. 4.13c,d), with a proper choice to generate the basic red, green, and blue (RGB) colours, and white when combined. There is a large variety of possible dyes. Dopants are also used to tune the properties (adjust emission wavelengths, increase quantum and luminous efficiencies). More recently, it was found that emission from a triplet state—phosphorescence—is a better solution than fluorescence, because it gives a higher yield of conversion. Heavy transition-metal complexes present important spin-orbit coupling and easier singlet-triplet crossing, and allow the formation of triplet excitons. Many systems based on iridium compounds have been described (Fig. 13b).

4.3.4 Photovoltaic devices

The process of photoinduced charge separation in molecular systems, treated in Section 4.3.2, has led to another important practical development in the form of

photovoltaic cells using sensitizing dyes. The starting point is the structure of transition-metal complexes of the $[\text{Ru}(\text{bpy})_3]^{2+}$ family, but the device is actually supramolecular, as it associates different components in interaction in the form of layers or liquids. The major contribution and development began during the 1980s with the impetus of Michael Grätzel at the Ecole Polytechnique Fédérale de Lausanne [4.8a].

The $[\text{Ru}(\text{bpy})_3]^{2+}$ structure itself is not well adapted, because charge separation is not directional, the three bpy ligands being chemically equivalent. In the related neutral complex $[\text{Ru}(\text{bpy})_2(\text{NCS})_2]$, (NCS is the N-bonded thiocyanate) on the other hand, some directionality is found. The LUMO is localized on the bpy ligands, while the HOMO has comparable contributions on the ruthenium atom and the thiocyanate ligands (Fig. 4.14).

If the excited complex is near an electrode one may think of collecting electrons (or holes). But near a metallic electrode a rapid quenching (deactivation) of an excited state occurs. This is not the case near a semiconductor electrode.

The major breakthrough from Grätzel's team was the idea of adsorbing this complex on a semiconductor in the form of nanocrystalline TiO_2 —‘nanocrystalline’ meaning that TiO_2 is present in the form of particles of 10–30 nm diameter. The fixation is easily done by using functionalized bpy ligands; for instance 4,4'-dicarboxy-2,2'-bipyridine (dc bpy), which permit anchoring of the complex on the surface of TiO_2 (see Fig. 4.15a). The use of nanocrystalline TiO_2 ensures a high effective surface, and thus an intimate interaction between the metallic complex (qualified in the following as the ‘dye’) and the semiconductor. Thus when $[\text{Ru}(\text{dc bpy})_2(\text{NCS})_2]$ is excited, the excited electron can jump in the conduction band of the semiconductor, because its energy is high enough, and also because of the spatial proximity between the modified bpy ligand and the surface. To use energy it is then necessary to collect the holes. Noting that the NCS groups point in the opposite direction, the idea was to soak the system by an electrolyte containing a reducing substance such as the iodide I^- , to play the role of a redox shuttle through the I_3^-/I^- couple. In the final device (Fig. 4.15b) the TiO_2 semiconductor is contacted by a transparent electrode (usually tin oxide), and on the solution side a counterelectrode closes the circuit. The reaction scheme corresponding to the exchange of one electron is shown in Fig. 4.15c.

Note that the energy scale in Fig. 4.15b is a hybrid representation of the one-electron energies of the valence and conduction band of TiO_2 and of the redox standard potentials (plotted upside down) of the redox semi-equation (that corresponds to free enthalpy energies, as $\Delta G^\circ = -nFE^\circ$).

The first realization of this principle was reported in 1988, and over the years, many improvements have been achieved on the practical realization of the cell. The most significant parameter is the overall conversion efficiency of the dye-sensitized cell, that is, the solar-to-electric energy conversion efficiency, η_{global} , defined as the ratio of the electrical power obtained (output) divided by the intensity of the incident light (input). Its definition is:

$$\eta_{\text{global}} = P_{\text{max}}/I_s \quad (4.10a)$$

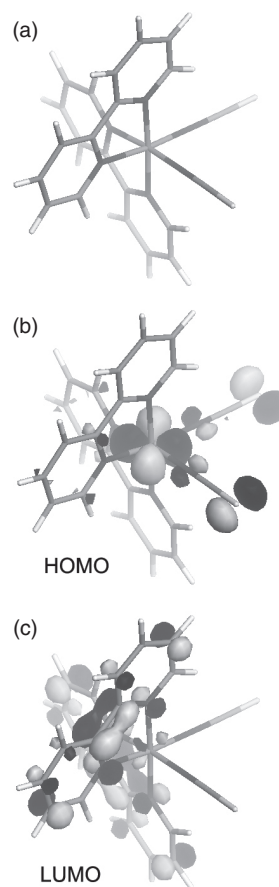
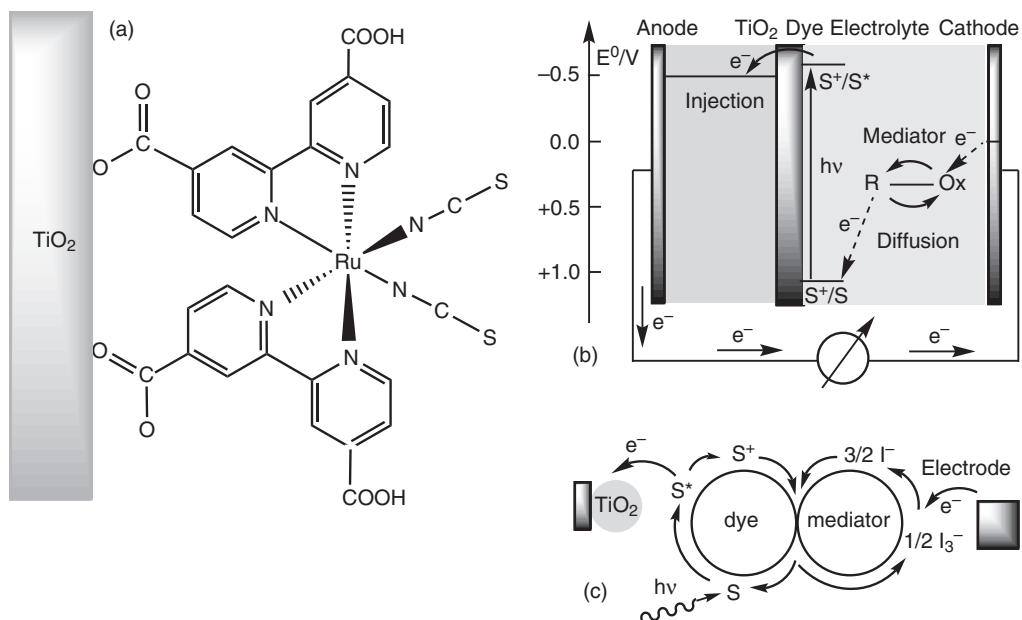


Fig. 4.14 Structure of $[\text{Ru}(\text{bpy})_2(\text{NCS})_2]$ (a), and schemes of the HOMO (b) and of the LUMO (c).

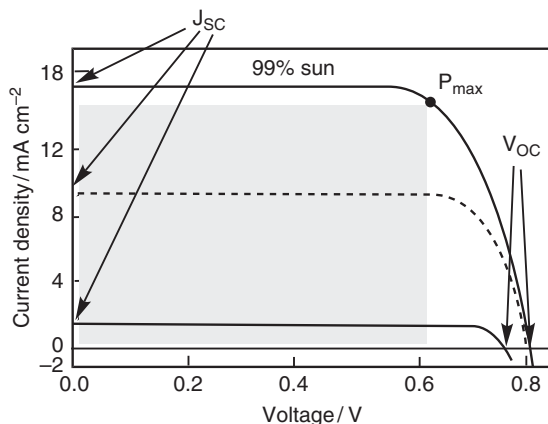
**Fig. 4.15**

Principle of the photovoltaic cell using $[Ru(dcbpy)_2(NCS)_2]$ as a sensitizing dye: (a) the dye molecule bonded to a TiO_2 nanoparticle; (b) the general setup showing also the energy levels and the electron flow generated by the photon absorption; the energy scale corresponds to the standard potential of the redox couples; the anode is a conducting transparent glass; (c) reaction scheme for a one photon absorption and one electron flow.

where P_{max} is the maximal electrical power output, and I_s is the intensity of the incident light. P_{max} is empirically obtained from the expression:

$$P_{max} = I_{sc} V_{oc} ff \quad (4.10b)$$

where I_{sc} is the photocurrent density measured at short circuit, V_{oc} is the open-circuit photovoltage, and ff is the fill factor of the cell. This last term is lower than 1 to take into account that the maximum electrical power is obtained neither under open-circuit nor short-circuit conditions (see Fig. 4.16).

**Fig. 4.16**

Density current vs voltage curves for different light intensities showing the short-circuit current density J_{sc} , the open-circuit voltage V_{oc} , and the working point ensuring the maximum power P_{max} , when the J.V product (grey area) is maximum. As can be seen, P_{max} is lower than the $J_{sc} \cdot V_{oc}$ product, in agreement with eqn. (4.10b).

Typical values are $J_{SC} = 16\text{--}22 \text{ mA/cm}^2$, $V_{OC} = 0.7\text{--}0.86 \text{ V}$, $ff = 0.65\text{--}0.8$, $I_s = 1,000 \text{ W/cm}^2$ (corresponding to full sunlight) giving η_{global} about 11%, barely below the 15% efficiency of commercial silicon solar cells. Note that for these strongly coloured systems, all the incident light is absorbed, and in addition the quantum yield is very good: each absorbed photon generates about 0.8 electron.

A solid-state version of the dye-sensitized photovoltaic cell—avoiding the liquid electrolyte—has been built. It uses the same TiO_2 –ruthenium dye association, but the electrolyte is replaced by a hole transport material (see Section 4.3.3). The efficiency is only 3–4% at the moment, but progresses in this area can be rapid.

Photovoltaic cells based on ruthenium dyes seem to have a bright future. The main component, TiO_2 , is cheap and non-toxic (it is the main component of white paints, and even toothpaste). Ruthenium is, of course, much more expensive, but the necessary quantity for a device is very limited. Thus it should be possible to build photovoltaic cells with a very competitive price compared to silicon cells. Durability tests have shown that the dye can sustain 10^8 excitation/oxidation/reduction cycles, corresponding to solar years of solar exposition. The last problems to solve are degradation by heat and ultraviolet radiation, and the sealing of the liquid electrolyte cell; but prototypes have been built by Solaronix (Switzerland), Konarka (USA), Aisin Seiki (Japan), and RWE (Germany) [4.9]. Demonstration materials are commercialized—even tiles for buildings equipment.

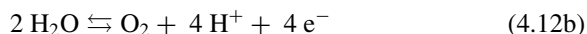
4.3.5 Harnessing photochemical energy: towards water photolysis

Harnessing chemical energy from photophysics is an extremely appealing perspective, in the general spirit of mimicking photosynthesis. Among the different chemical transformations that can be envisioned, the photolysis of water into hydrogen and oxygen is considered as the Holy Grail. The unique advantage of hydrogen is, of course, its ability to be burned, either directly or in a fuel cell, without producing pollutants or greenhouse gases. The hydrogen produced from sunlight could be used directly as a fuel for transportation purposes, and more generally to feed the ‘hydrogen economy’. It could be used, for instance, in the catalytic reduction of carbon dioxide to produce fuels such as methane or methanol.

Photochemical water photolysis, however, represents an extremely difficult challenge, because it is a multi-electron process, implying no less than four electrons for one molecule of dioxygen and a large molecular reorganization from reactants to products, so that no satisfactory solution has been found yet. As every first-year student knows, the dissociation reaction:



can be written in solution as the sum of the two formal half-reactions:



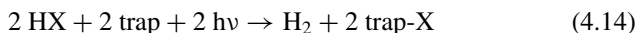
and thus in principle a photochemical charge-separation process could be convenient, electrons feeding reaction (4.12a), and holes reaction (4.12b). The total free enthalpy necessary to realize the strongly endoergic reaction (4.11) is computed easily from the standard potential of the O_2/H_2O system (+1.23 V with respect to the standard hydrogen electrode):

$$\Delta G^\circ = 4 \times 1.23 = 4.92 \text{ eV} \quad \text{i.e. } +474.8 \text{ kJ mol}^{-1} \quad (4.13)$$

This is a quite large value, and efforts have been devoted to the independent realization of the two half-reactions (4.12a) and (4.12b).

Reaction (4.12a) is the easiest part of the problem (or the least difficult!), because once electrons are available one is brought back to the problem of catalyzing the electrochemical evolution of dihydrogen, for which macroscopic solutions exist; for instance, the use of platinum catalysts. But we want to use an integrated molecular system which would collect photochemical energy and perform hydrogen evolution.

Noting that the evolution of one molecule of dihydrogen necessitates two electrons, and taking into account the known ability of precious metals to catalyse hydrogen evolution, an interesting solution is based on the use of dinuclear complexes such as $Rh_2(dfpma)_3$ [4.10], where $dfpma = \text{bis}(\text{difluorophosphino})\text{methylamine}$, $\text{MeN}(\text{PF}_2)_2$. A photocatalytic cycle has indeed been described which realizes H_2 generation from HX ($X = \text{Cl}$ or Br), according to the overall reaction:

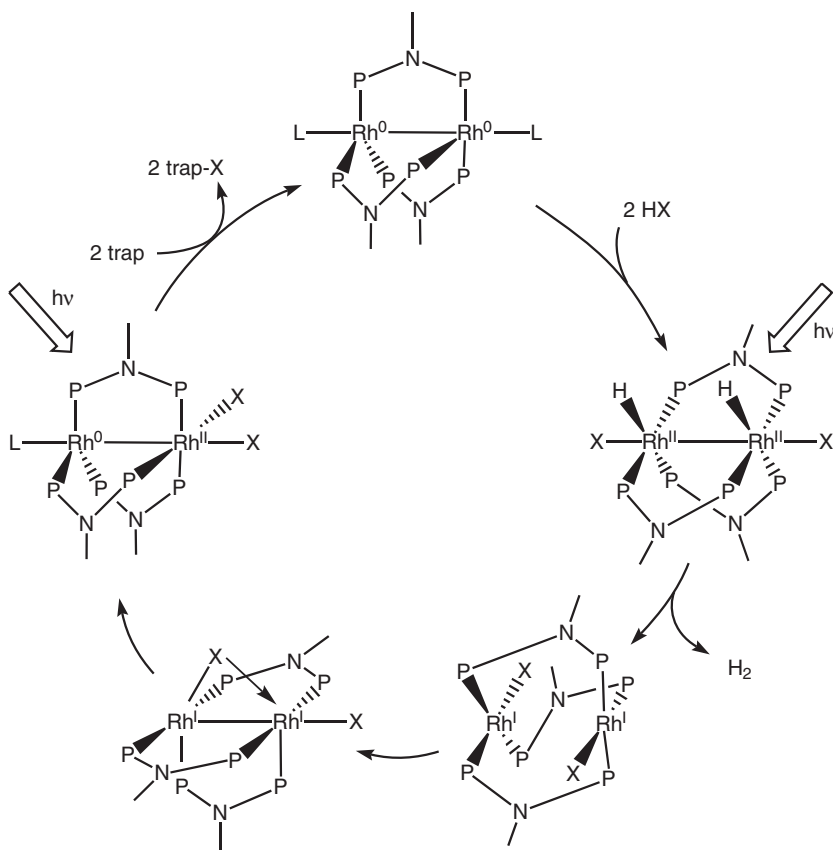


where 'trap' designates a molecule able to trap the halide, for instance THF, dihydroanthracene, or 2,3-dimethylbutadiene. The catalyst is a dinuclear $Rh(0)$ complex presenting a metal-metal bond (Fig. 4.17).

In a first step, HX adds to the Rh^0-Rh^0 core to produce the Rh^I-Rh^I dihydride dihalide, which photoeliminates H_2 . This gives a reactive intermediate formulated Rh^I-Rh^I , which is unstable with respect to internal disproportionation into $Rh^0-Rh^I(X)_2$. The key point is here the ability of the halogen to move from one rhodium atom to the other. A new photoexcitation of $Rh^0-Rh^I(X)_2$ leads to halogen elimination (captured by the trap) and regeneration of the Rh^0-Rh^0 complex, thus completing the cycle. The overall efficiency is only 1%. It is limited by the halogen elimination step from the binuclear core.

The second half-reaction (4.12b) is more difficult to achieve, because it involves two water molecules and the concerted removal of four electrons and four protons. Nature solved this problem by using a unique metalloenzyme, called the photosystem II water-oxidizing complex, which is coupled to the photosynthetic centre.

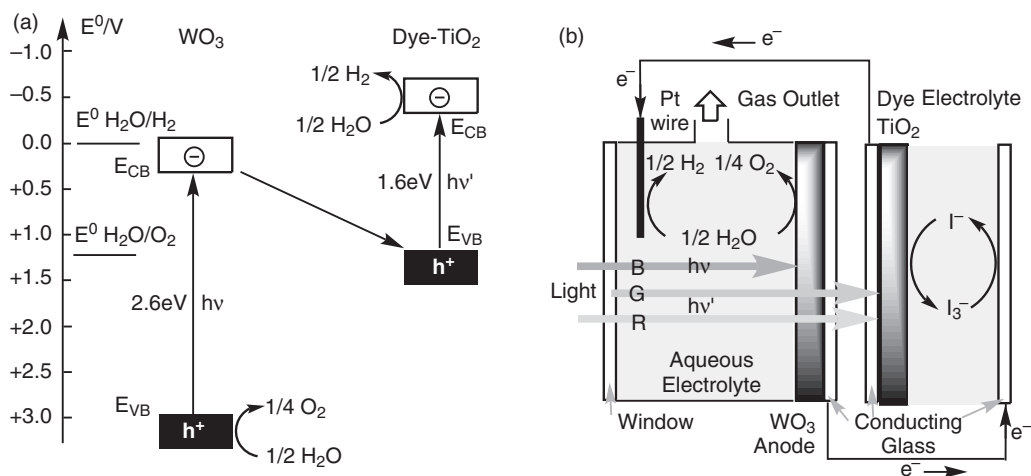
At the present time, no unique molecular system performing both reactions (4.12a) and (4.12b) and their coupling with a photochemical step has been found. To date, the only practical achievement for artificial photochemical water photolysis is again a supramolecular system based on a combination of dye, semiconductor, and electrodes, as with the dye-sensitized solar cell

**Fig. 4.17**

The photocatalytic cycle for H_2 evolution from HX , catalysed by $\text{Rh}_2(\text{dfpma})_3$. See text. (Adapted from [4.10b].)

described in Section 4.3.4. Actually it even uses *two cells* connected in series constituting a tandem system. The use of a macroscopic setup made of two cells connected by metallic conductors is a method of accumulating the necessary number of electrons. Note that natural photosynthesis also uses two photochemical systems mounted in tandem, called photosystem I and photosystem II [4.11].

The general principle of the artificial tandem cell is presented in Fig. 4.18: (a) energy scheme, and (b) schematic setup [4.12]. It is as follows. The two cells are transparent, allowing light to reach the photosensitive layers, Ru-dye sensitized TiO_2 (cell on the right of 4.18b) and WO_3 (cell on the left of (4.18b)). The ruthenium-sensitized cell of the type described in Section 4.3.4 provides electrons in the conduction band of TiO_2 . The electrons' energy is high enough to allow the reduction of protons to H_2 (reaction (4.12a)). But the generated holes do not have enough energy to oxidize water. In a second cell a thin transparent film of nanocrystalline WO_3 (or Fe_2O_3) absorbs photons and generates electrons and holes (note that the electrons are tungsten(V) centres—negative polarons as encountered in Section 3.3.3.2 and Fig. 3.79). The valence-band holes can oxidize water (reaction (4.12b)), while

**Fig. 4.18**

The tandem cell: (a) Energy levels for the two cells, for the excitation of two electrons by absorption of two photons ($h\nu$ and $h\nu'$). \ominus and e^- indicate electrons, and h^+ represents holes. The scale corresponds to standard electrode potentials at $\text{pH} = 0$ (indeed, $\Delta G^\circ = -nFE^\circ$), and one-electron energies for the bands. The valence band is shown with a black rectangle, and its higher energy level is E_{VB} . The conduction band is shown with an unfilled rectangle, and its lower energy level is E_{CB} . The oblique black arrow shows the macroscopic electronic connection between the two cells; (b) general setup of the cell; at right, the Ru-sensitized TiO_2 cell, already presented; at left, the second cell equipped with a nanocrystalline photosensitive WO_3 thin layer and a platinum wire. The two cells are connected by macroscopic wires, allowing the circulation of electrons. High-energy light (blue, B) is absorbed by WO_3 . Other energies, green (G) and red (R), reach the first cell.

the electrons are fed in the first photosystem by the macroscopic connection (Fig. 4.18). The total balance shows that for the production of one dioxygen molecule, *eight* photons are used—four in each cell.

The tandem photolysis cell indeed provides hydrogen and oxygen under visible light illumination. The conversion efficiency is, however still modest: only 4.5%. Work is in progress to improve the device [4.8a].

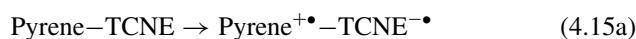
4.3.6 Ultrafast electron transfer

Until now, we have used the same theoretical concepts for electron transfer as in Chapter 3. In particular, the rate of electron transfer can be computed, if necessary, from the activation barrier, with a pre-exponential term taking into account non-adiabatic effects. But a specificity of photoinduced electron transfer is to provide access to very reactive species formed immediately after the photophysical excitation. Such species can undergo ultrafast electron transfer reactions, which present original characteristics.

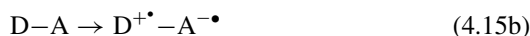
The underlying assumption in most expressions for the electron transfer rate encountered so far is that the excited initial state is at vibrational equilibrium. This is the basic reason of the single-exponential decay of the initial state, which is observed in the vast majority of cases, and allows the definition of a first-order rate constant. But with the very short pulses of some photophysical experiments (a few femtoseconds, for instance), the initial state (which is actually the first excited state) can be prepared out of vibrational equilibrium.

At time zero the system is then in a superposition of vibrational states, corresponding to a wave packet which is not a stationary solution of the vibrational Schrödinger equation. This wave packet has its own dynamics, and moves on the potential energy surface of the excited state. This motion can lead to a modulation of the reaction rate, and thus to discrepancies with respect to the usual one-exponential law of first-order reactions.

One of the systems studied most extensively is TCNE-pyrene [4.13], which belongs to the category of donor-acceptor (D-A) complexes in solution. The interaction between the donor and the acceptor is strong enough for the system to behave as a unique supramolecule, and thus only first-order kinetic processes have to be considered. Excitation is performed with a laser pulse of only 35 fs in a charge transfer band at 810 nm, corresponding to the excitation:



That is:



This charge transfer band is the equivalent of the intervalence transition in mixed valence systems (see Section 3.2.2.2). After excitation the system is analysed with a weaker probe beam at the same wavelength, to monitor the charge recombination bringing back the system to the ground state. As a first approximation, the $\text{D}^{\bullet+} - \text{A}^{\bullet-}$ excited state has a lifetime in the ps range (thus a rate constant for deactivation of the order of 10^{12} s^{-1} !), but the decay is more complicated and cannot be described by a single exponential. A detailed quantitative analysis shows the necessity of using a four-level model, the ground and the excited state presenting at least two vibrational levels each (see Fig. 4.19).

The first excited state ES, $\text{D}^{\bullet+} - \text{A}^{\bullet-}$ or $|b\rangle$, is obtained through a pump process at 810 nm from the vibrational and electronic ground state GS, D-A, or $|a\rangle$ with a charge transfer (CT). The excited ES relaxes to a (vibrationally) relaxed excited state, RES, $|c\rangle$. The back electron transfer (ET) leads to a (vibrationally) excited (hot) ground state, HGS, $|d\rangle$ that relaxes in turn to the ground state.

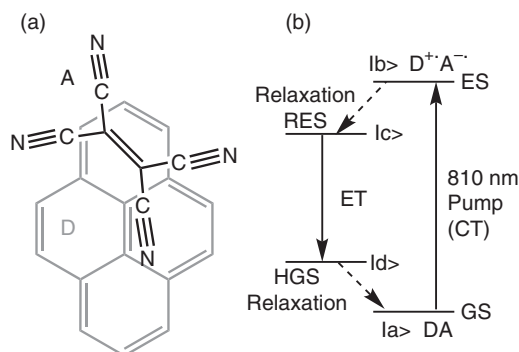


Fig. 4.19

Pyrene-TCNE complex: (a) structure in the solid state, pyrene, donor D (grey) and tetracyanoquinodimethane, acceptor A (black); (b) four-level model used to analyse the back electron transfer $\text{D}^{\bullet+} - \text{A}^{\bullet-} \rightarrow \text{D-A}$. (Adapted from [4.13].)

When the data are quantitatively analysed with the four-level scheme of Fig. 4.19, it is found that small oscillations are superimposed on the general decay. Their period is about 200 fs, corresponding to a wavenumber of 170 cm^{-1} —a value which has been assigned to a vibrational mode of the complex.

A simple simulation model reproduces this behaviour. It is based on the potential energy curves of Fig. 4.20.

It is assumed that at time zero the initial excited position distribution is given by the bell-shaped curve 2 in Fig. 4.20, arising from the vertical excitation from the ground state, curve 1, at the origin of the vibrational coordinate. (Note that curve 2 is *not* an eigenfunction of the harmonic oscillator!) Then the ‘wave packet’ oscillates back and forth in the excited state well ($D^{+\bullet}-A^{\bullet-}$), with a frequency of the order of the classical frequency of the harmonic oscillator. At any time, the system has a probability to jump on the D–A energy curve, by borrowing some energy from other vibrational modes. The jump probability per unit time is chosen as:

$$P(\Delta E) = P_0 \exp(-\Delta E/C) \quad \text{for } \Delta E > 0 \quad (4.16a)$$

$$P(\Delta E) = 0 \quad \text{for } \Delta E < 0 \quad (4.16b)$$

where ΔE is the difference $E_{DA} - E_{D^{+\bullet}-A^{\bullet-}}$ and C is a constant. Thus with this model the back electron transfer can occur only in the left part of the diagram, when the energy of D–A is *above* the energy of $D^{+\bullet}-A^{\bullet-}$ —a situation which is achieved periodically in time. When the D–A energy is *below* the energy of $D^{+\bullet}-A^{\bullet-}$ the rate is assumed to be zero, because at this time-scale there is no simple way to remove the excess energy. This simple model reproduces the general behaviour; that is, the exponential rise of the D–A population, with superimposed oscillations. This constitutes a well-characterized example of a vibrationally coherent electron transfer.

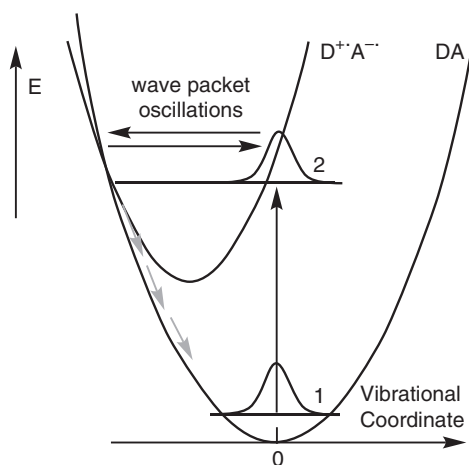
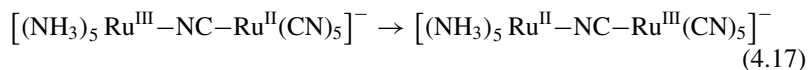


Fig. 4.20

Model used in the simulation, with the motion of the wavepacket on the potential energy surface of the initial excited state. **1** designates the vibrational eigenfunction in the ground state, associated to the potential energy curve of DA; **2** is the non-stationary wave packet belonging to the $D^{+\bullet}-A^{\bullet-}$ manifold, created immediately after excitation. The conversion of $D^{+\bullet}-A^{\bullet-}$ into DA occurs on the left hand side of the diagram where the diabatic potential energy curves cross. (Adapted from [4.13b].)

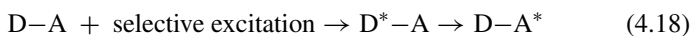
Ultrafast electron transfer has also been studied in mixed valence systems; for instance, $[(\text{NH}_3)_5\text{Ru}^{\text{III}}-\text{NC}-\text{Ru}^{\text{II}}(\text{CN})_5]^-$. This is a cyanide-bridged class II system, in which the sites are chemically non-equivalent [4.14]. The distribution of oxidation states is as indicated, because ruthenium(II) is more stabilized by the strongly acceptor cyanide ligands than by the ammonia ligands, and, of course, there is a higher energy state which can be populated by excitation on the intervalence transition:



The excitation can be performed with a 20-fs pulse at 800 nm, and the subsequent behaviour followed with a probe at various wavelengths. The return to the ground state by back electron transfer occurs according to a complex kinetic law involving several exponentials, the main one corresponding to a lifetime of about 85 fs. But as previously, one finds superimposed oscillations with frequencies corresponding to vibration modes of the molecular system, these vibrations being observed independently by Raman resonance spectroscopy. Even less clearly characterized than in the pyrene-TCNE complex, vibrationally coherent electron transfer also appears to be present.

4.4 Energy transfer

Here we consider the process of intramolecular energy transfer which occurs in a bichromophoric molecule, when one of the chromophores (the donor D) is selectively excited (to D^*) and transfers part of its energy to the other chromophore (acceptor A).



Note that such a possibility implies that the chromophores are *weakly coupled*, otherwise we would have to consider the energy levels of a single supramolecule, and any excitation would necessarily involve the two chromophores. The energy transfer processes are very important in several scientific domains: (i) they occur naturally in the photophysical process of photosynthesis; (ii) energy transfer allows the efficient capture of solar energy, by the so-called antenna effect, where a large number of chromophores can be excited, and then transfer their energy to the active site where the true photophysical reaction (a charge separation) occurs; (iii) energy transfer and the resultant quenching of the donor's fluorescence and enhancing of the acceptor's fluorescence is also widely used in biology to determine distances between D and A—proteins' conformation changes.

The exact analysis of the energy transfer is very complex, and more details can be found in several general references [4.15]. Different mechanisms have been suggested at different levels of sophistication. We present as simply as possible two of them (Förster and Dexter) before illustrating them with examples.

4.4.1 Theoretical treatment of energy transfer

We define the molecule as made of two parts: an *energy* donor D and an *energy* acceptor A. These denominations correspond to their behaviour with respect to energy transfer, not (necessarily) to the usual definition of *electron* donor or acceptor groups, used previously. In zero-order approximation the initial and final states in reaction (4.18) can be written as:

$$|\Psi_i\rangle = |\Psi_D^* \Psi_A\rangle \quad (4.19a)$$

$$|\Psi_f\rangle = |\Psi_D \Psi_{A^*}\rangle \quad (4.19b)$$

meaning that in the initial state the D site is excited (hence the *) and A is in its ground state, while the reverse is true for the final state. In expressions (4.19a,b), Ψ_i and Ψ_f are polyelectronic wavefunctions including the spin functions Σ and the vibrational functions Ψ^v (see the case of electron transfer reactions, Section 3.2.1.3). Thus we can write:

$$|\Psi_D\rangle = |\Psi_D^{\text{el}} \Psi_{Dj}^v \Sigma_D\rangle \quad (4.20a)$$

$$|\Psi_{D^*}\rangle = |\Psi_{D^*}^{\text{el}} \Psi_{D^*j'}^v \Sigma_{D^*}\rangle \quad (4.20b)$$

$$|\Psi_A\rangle = |\Psi_A^{\text{el}} \Psi_{Ak}^v \Sigma_A\rangle \quad (4.20c)$$

$$|\Psi_{A^*}\rangle = |\Psi_{A^*}^{\text{el}} \Psi_{A^*k}^v \Sigma_{A^*}\rangle \quad (4.20d)$$

where each total wavefunction is written as the product of a polyelectronic wavefunction (Ψ^{el}) by a vibrational function (Ψ_j^v), and a spin function (Σ). The vibrational function is characterized by an index j for the donor and k for the acceptor.

We postulate that there is an interaction between the D and A sites because they belong to the same molecule, and we can define a coupling operator \mathbf{V} . Its expression is complicated because it contains all terms such as the interaction of an electron of D with nuclei or other electrons of A, and *vice versa*, and it will be detailed later. The transition between $|\Psi_i\rangle$ and $|\Psi_f\rangle$ is a *non-radiative* transition, and can be treated by the same formalism as for electron transfer (see Section 3.2.1.3); that is, the rate is given by using Fermi's Golden Rule:

$$k = \frac{2\pi}{\hbar} V_{\text{EnT}}^2 \rho \quad (4.21)$$

where V_{EnT} (EnT for 'energy transfer') is the electronic coupling matrix element, and ρ the density of states. A very simplified scheme of the energy transfer and its main photophysical consequences are shown in Fig. 4.21.

The rate is thus proportional to the square of the matrix element:

$$V_{\text{EnT}} = \langle \Psi_i | \mathbf{V} | \Psi_f \rangle \quad (4.22)$$

which plays the same key role as V_{ab} in electron transfer theories. However, for historical reasons the development of the theory of energy transfer reactions was slightly different.

The first quantitative treatment of energy transfer between two chromophores was performed by Förster in 1948. At that time, the typical system

particular, for their spin functions. Thus the spin factor in (4.24) can be rewritten as:

$$\langle \Sigma_{D^*} | \Sigma_D \rangle \langle \Sigma_A | \Sigma_{A^*} \rangle \quad (4.26)$$

This term is non-zero (see eqn. (4.7a,b)) only if:

$$\Sigma_{D^*} = \Sigma_D \text{ and } \Sigma_A = \Sigma_{A^*} \quad (4.27)$$

This leads to a selection rule with a simple interpretation: things happen as if there is a local transition on D, which must be spin-allowed, and simultaneously, a spin-allowed transition on A. Since many chromophores have a singlet ground state (organic molecules or closed-shell coordination complexes) (Fig. 4.21a), it means that in this approximation of very weakly interacting systems, singlet–singlet energy transfer is allowed, while singlet–triplet energy transfer is forbidden.

The second condition is represented by the electronic factor. The \mathbf{V} operator acts only on electronic wavefunctions and describes the Coulomb interaction between the initial $|\Psi_{D^*} \Psi_A\rangle$ and the final $|\Psi_D \Psi_{A^*}\rangle$ states. It is usually represented as a Taylor expansion of interactions between electrical multipoles, plus an exchange term:

$$\mathbf{V} = \text{dipole–dipole term} + \text{dipole–quadrupole term} + \dots + \text{exchange term} \quad (4.28)$$

In the Förster treatment it is assumed that the local transitions on both chromophores are strongly allowed, so that the dipole–dipole interaction dominates the expansion. Another important approximation is that the donor and acceptor are widely separated, so that the exchange term, due to electronic repulsion, can be neglected (see Section 2.6). Looking only at the dipole–dipole term, the operator \mathbf{V}_{dd} can be written, from the classical expression of the interaction energy between two dipoles:

$$\mathbf{V}_{dd} = \frac{\vec{\mu}_D \vec{\mu}_A - 3(\vec{\mu}_D \cdot \vec{R})(\vec{\mu}_A \cdot \vec{R})}{R^3} \quad (4.29)$$

where $\vec{\mu}_D$ and $\vec{\mu}_A$ are vectors corresponding to dipole operators centred on D and A, and \vec{R} is the vector associated with the dipole–dipole distance R.

The electronic matrix element is then computed from:

$$\langle \Psi_{D^*}^{el} \Psi_A^{el} | \mathbf{V}_{dd} | \Psi_D^{el} \Psi_{A^*}^{el} \rangle \quad (4.30)$$

Since the operator appears as the product of independent local operators μ_D and μ_A , expansion of eqn. (4.30) yields an expression in which appear the *transition dipole moments*:

$$\mathbf{V}_{EnT} = \frac{\vec{M}_D \vec{M}_A - 3(\vec{M}_D \cdot \vec{R})(\vec{M}_A \cdot \vec{R})}{R^3} \quad (4.31)$$

where \vec{M}_D and \vec{M}_A are now the transition moments *vectors*:

$$\vec{M}_D = \langle \Psi_{D^*}^{el} | \vec{\mu}_D | \Psi_D^{el} \rangle \quad (4.32a)$$

and

$$\vec{M}_A = \langle \Psi_A^{el} | \vec{\mu}_A | \Psi_{A^*}^{el} \rangle \quad (4.32b)$$

Introducing the angles θ_T between the transition moment vectors, θ_D and θ_A between the transition moment vectors of D and A and the R vector (Fig. 4.22), the expression can be rewritten:

$$V_{\text{EnT}} = \frac{\|\vec{M}_D\| \|\vec{M}_A\| (\cos \theta_T - 3 \cos \theta_D \cos \theta_A)}{\vec{R}^3} \quad (4.33)$$

where $\|\vec{M}_D\|$ and $\|\vec{M}_A\|$ are the moduli of the transition moments vectors. There is thus an *orientation factor*, which will play an important role in the rate of reaction, and is discussed later.

We now consider the Franck–Condon term. Actually, in the final rate expression it is obtained by the summation of the square of terms like $\langle \Psi_{D^*j}^v | \Psi_{A^*k'}^v \rangle$; that is:

$$\sum \left(\langle \Psi_{D^*j}^v | \Psi_{A^*k'}^v | \Psi_{Dj}^v | \Psi_{A^*k'}^v \rangle \right)^2 \quad (4.34)$$

Since the vibrations on sites D and A are independent, eqn. (4.34) can be written as:

$$\sum \left(\langle \Psi_{D^*j}^v | \Psi_{Dj}^v \rangle \langle \Psi_{A^*k'}^v | \Psi_{A^*k'}^v \rangle \right)^2 \quad (4.35)$$

It would be extremely difficult to compute theoretically this factor. The originality of the Förster treatment was to approximate it by the spectral overlap integral between the normalized spectra (in nm) of the donor emission and of the acceptor absorption:

$$\int_{\bar{\nu}_1}^{\bar{\nu}_2} f_{D^*}(\bar{\nu}) f_A(\bar{\nu}) d\bar{\nu} \quad (4.36)$$

This is the Förster spectral overlap integral.

It satisfies, incidentally the principle that the energy transfer must occur at constant energy of the whole D–A system. This condition is justified by the same arguments as for electron transfer (Section 3.2.1.3); that is, the much faster rate of electronic motions with respect to nuclear motions.

Finally, keeping only the part of the \mathbf{V} term given by eqn. (4.29) and with all the previous assumptions, the rate of energy transfer is found as [4.15c]:

$$k = \text{const} \left[\frac{\|\vec{M}_D\| \|\vec{M}_A\| (\cos \theta_T - 3 \cos \theta_D \cos \theta_A)}{\vec{R}^3} \right]^2 \frac{\Phi_D}{\tau_D} \int_0^\infty f_{D^*}(\bar{\nu}) f_A(\bar{\nu}) d\bar{\nu} \quad (4.37)$$

where Φ_D is the quantum yield of fluorescence of D^* , and τ_D its lifetime in the absence of A. This expression contains the interaction term between transition dipole moments, multiplied by the Förster spectral overlap integral. The distance dependence is as R^{-6} , where R is the donor–acceptor distance. The form of eqn. (4.37) is amenable to a simple interpretation: a *virtual emission–absorption* process (Fig. 4.23).

The Förster process (Fig. 4.23b) is qualified as virtual because it should not be confused with the ‘trivial’ mechanism, consisting of the real emission of a

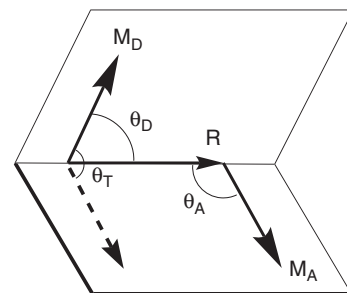
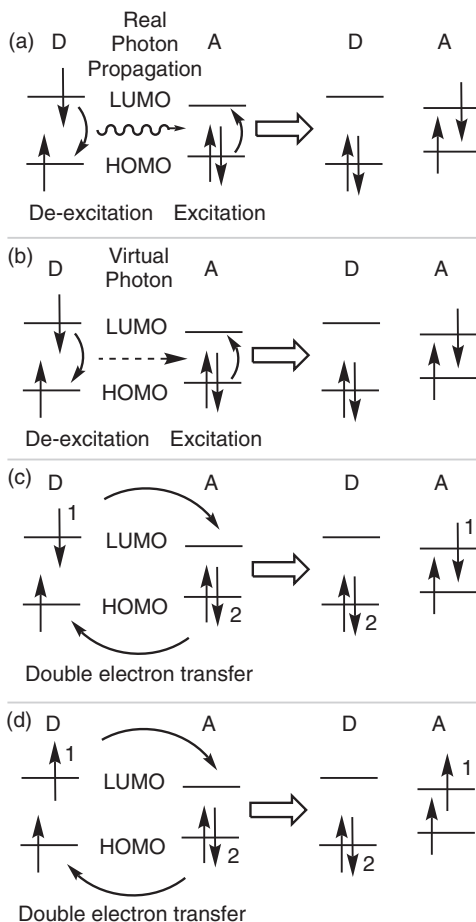


Fig. 4.22

Definition of the angles describing the orientation of the transition dipole moments.

**Fig. 4.23**

The different processes for energy transfer between donor and acceptor chromophores: (a) the 'trivial process': emission, real photon propagation (laws of optics) and then absorption; (b) the virtual photon emission-absorption process (Förster); (c) the double electron transfer process (Dexter) for a singlet-singlet transfer. The numbering of electrons 1 and 2 corresponds to eqn. 4.39. (d) Dexter triplet-triplet transfer.

photon, its propagation, and then its absorption (Fig. 23a). In the trivial mechanism the donor and acceptor are far from each other (at a large distance when compared to the wavelength of the exchanged radiation), and there is a light-propagation step according to the laws of optics and Maxwell's propagation equations. These conditions are not fulfilled here, due to the small distance between donor and acceptor.

When the local transitions are spin forbidden—for example, in the case of triplet excited states in organic chemistry—the Förster mechanism is theoretically impossible. In particular, it is not possible to determine the Förster spectral overlap integral because of the very weak intensity of the spin-forbidden absorption band of the acceptor. If at the same time the distance between chromophores is reduced, one has to take into account the overlap between electronic wavefunctions of the donor and the acceptor. In other words, the separation of the molecule as made of a donor and an acceptor becomes less clear, and the wavefunction of the two parts interact in a quantum-mechanical way.

A more complete treatment of energy transfer was therefore introduced by Dexter in 1953, and it encompasses the Förster treatment as a special case.

Under such circumstances, the additional terms in the development of \mathbf{V} must be considered (see eqn. (4.28)). An important consequence results from the introduction of the exchange term:

$$\langle \Psi_{D^*}^{\text{el}} \Psi_A^{\text{el}} | e^2/r_{12} | \Psi_{A^*}^{\text{el}} \Psi_D^{\text{el}} \rangle \quad (4.38)$$

Due to this term we are no longer constrained to the rule that the spin state must remain the same on each sub-unit. Now the spin functions of the two chromophores can change simultaneously; that is, we can have $\eta_D^* = \eta_A^*$ and $\eta_A = \eta_D$, allowing in particular transitions which are locally forbidden such as triplet–triplet energy transfer.

In the Dexter treatment we introduce one-electron wavefunctions such as the HOMO and LUMO on each chromophore. The electronic matrix element takes the form:

$$\langle \psi_D^{\text{LUMO}}(1) \psi_A^{\text{HOMO}}(2) | \mathbf{V} | \psi_A^{\text{LUMO}}(1) \psi_D^{\text{HOMO}}(2) \rangle \quad (4.39)$$

Expression (4.39) implies configurations which differ by the transfer of an electron from the LUMO of the donor to the LUMO of the acceptor, and at the same time the transfer of an electron in the reverse direction at the level of the HOMOs (Fig. 4.23c). Thus the Dexter mechanism can be considered as a *double electron transfer*.

The rate law is then given by the same formula as in electron transfer theory (see eqn. (3.37), but with λ and V_{ab} parameters adapted to the present case):

$$k_{\text{et}} = \frac{2V_{\text{ab}}^2}{h} \left(\frac{\pi^3}{\lambda RT} \right)^{1/2} \exp(-\Delta G^\ddagger/RT) \quad (4.40)$$

Thus energy transfer by this mechanism presents some common characteristics with the more usual electron or hole transfer processes. In particular, it is thermally activated. The variation with the free enthalpy of reaction ΔG° is similar, with an acceleration for small $|\Delta G^\circ|$, followed by a decrease when entering the ‘inverted region’. It is even possible to show, in an approximate way, the common roots between electron transfer and Dexter energy transfer. Eqn. (4.39) is indeed formulated as a resonance integral (see Section 1.3), and as such it requires that the wavefunctions overlap in space. Assuming that the \mathbf{V} operator does not vary too rapidly with distance, one can write the coupling matrix element (eqns. (4.21) and (4.22)):

$$V_{\text{EnT}} = \text{const} \times \langle \psi_D^{\text{LUMO}}(1) \psi_A^{\text{HOMO}}(2) | \psi_A^{\text{LUMO}}(1) \psi_D^{\text{HOMO}}(2) \rangle \quad (4.41a)$$

$$V_{\text{EnT}} = \text{const} \times \langle \psi_D^{\text{LUMO}}(1) | \psi_A^{\text{LUMO}}(1) \rangle \langle \psi_A^{\text{HOMO}}(2) | \psi_D^{\text{HOMO}}(2) \rangle \quad (4.41b)$$

This introduces overlap integrals corresponding to electron and hole transfer. With the same argument as previously, these integrals can be considered as proportional to the corresponding electronic couplings, and thus:

$$V_{\text{EnT}} = \text{const}' \times V^{\text{ET}} \cdot V^{\text{hT}} \quad (4.42)$$

where V^{ET} and V^{hT} are the matrix elements corresponding to electron transfer and hole transfer respectively. This expression, although approximate and formulated with an unknown constant, will be useful when the question of the decay of the rate constant for energy transfer with distance is raised later.

To conclude this section let us note that for complex molecules the detailed structure and role of the bridging unit between chromophores should be explicitly taken into account. For electron transfer reactions this was achieved by introducing the concept of *superexchange* (see Section 3.2.2.6), in which one mixes configurations where the bridge is oxidized or reduced. For energy transfer it should be possible, in a similar way, to mix configurations in which the bridge is excited.

The theory of intramolecular energy transfer does not seem to have been pushed as far as the theory of electron transfer. But such effects involving the bridge are likely to exist, and could explain some peculiarities evoked in Section 4.4.2.

As a final comment on Section 4.4.1, let us note that in the frame of molecular electronics, energy transfer could be used to realize data treatment at the molecular scale (see Chapter 5). For such a goal, it would be helpful to devise a ‘photonic switch’ or an ‘energy switch’ allowing the dynamical control of energy transfer. While it does not seem easy to achieve switching in a system where energy transfer occurs by the Förster (dipole–dipole) mechanism, it is conceivable with the Dexter mechanism, because of its relation with electron transfer processes (Chapter 5). In particular, the chemical nature, degree of conjugation, and so on, of the spacer separating the donor and the acceptor plays a role. This is why a current challenge is the rational construction of donor–acceptor systems where energy transfer occurs via the Dexter mechanism.

4.4.2 Some examples

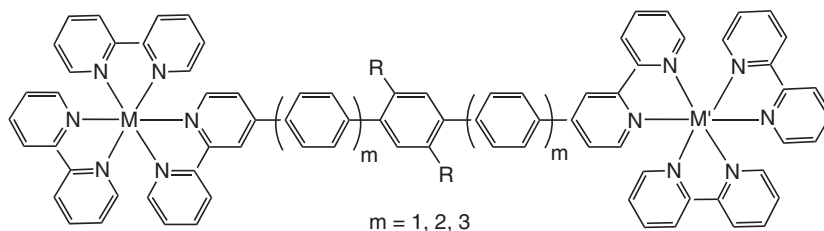
4.4.2.1 Ru–Os binuclear complexes

Energy transfer has been established in a large variety of bichromophoric compounds, and we have selected here only a few representative examples, with a particular focus on long-distance energy transfer and the possibility of controlling it by the chemical nature of the link between the two chromophores.

In the field of transition-metal binuclear complexes, ruthenium–osmium systems are particularly interesting [4.16]. Such systems, with the general formula $[(bpy)_3M-(ph)_n-M'(bpy)_3]^{4+}$ ($M = Ru(II)$, $M' = Os(II)$, $ph = 1,4$ -phenylene), have been described, with values of $n = 3, 5, 7$ (Fig. 4.24). They constitute rod-like compounds of nanometric dimensions, since for the longest spacer the metal–metal distance amounts to 4.2 nm. The photophysical behaviour is dominated by emission from essentially triplet states from the ruthenium or osmium units, so the emission process will be qualified as phosphorescence.

Fig. 4.24

Structure of the ruthenium–osmium heterodinuclear complexes. The central phenylene group bears R substituents for solubility reasons. For $m = 1, 2,$ and 3 , the number of phenylene units linking the $M(bpy)_3$ moieties is $3, 5,$ and 7 respectively.



The occurrence of energy transfer is demonstrated by a comparison with similar homodinuclear compounds Ru–Ru or Os–Os. Both chromophores absorb at about the same wavelength near 435 nm, but emission wavelengths are different, Ru emitting near 620 nm and Os near 740 nm. In the heterodinuclear system, the phosphorescence of the Ru unit is partially quenched, and there is a corresponding sensitization of the Os unit; that is, its emission intensity at 740 nm is increased. This phenomenon is typical of the occurrence of an energy transfer in the Ru–Os (D–A) complex between the Ru*–Os (D*–A) to the Ru–Os* (D–A*). The rate constant for energy transfer can be obtained from a comparison of the phosphorescence lifetimes τ° and τ of the ruthenium-based component in Ru–Ru and Ru–Os respectively, according to:

$$k_{\text{EnT}} = (1/\tau) - (1/\tau^\circ) \quad (4.43)$$

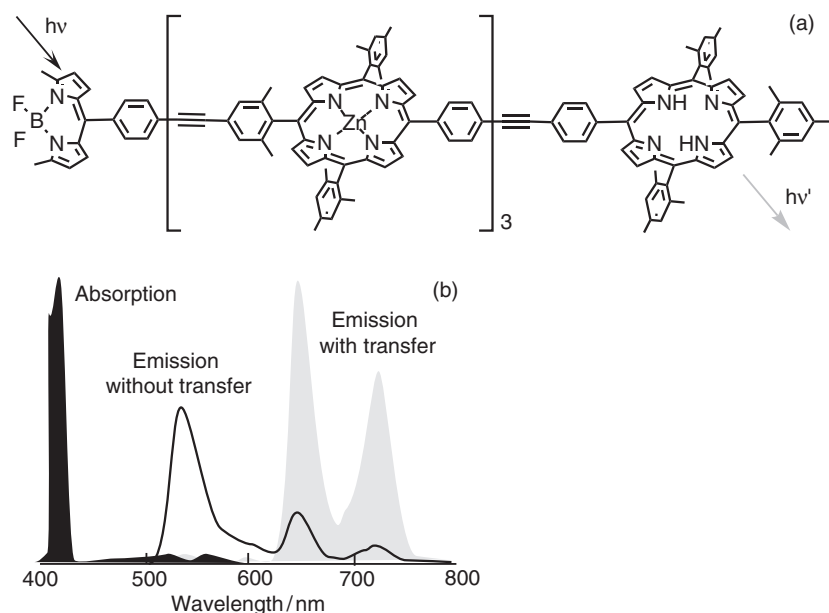
This provides values of k_{EnT} for the different complexes, $k_{\text{EnT}} = 6.7 \times 10^8 \text{ s}^{-1}$ for $n = 3$, $k_{\text{EnT}} = 1.0 \times 10^7 \text{ s}^{-1}$ for $n = 5$, and $k_{\text{EnT}} = 1.3 \times 10^6 \text{ s}^{-1}$ for $n = 7$. The analysis can now be performed in comparison with Förster and Dexter theories. It is found that the rate constant calculated by Förster theory is 2–3 orders of magnitude smaller than the observed rate constant, which is not surprising, as the emission processes are essentially singlet–triplet transitions (phosphorescence) and are thus forbidden. Thus energy transfer can safely be attributed to the Dexter (double electron exchange) mechanism. The rate of decay of k_{EnT} with distance is 0.32 \AA^{-1} . As for electron transfer, it can be related to the rate of decay of the electronic coupling matrix element (see Chapter 3 and eqn. (4.42)).

Related systems are known where the terminal units are terpyridine (tpy). As mentioned previously, their advantage over bpy systems is to present a more rigid conformation, but the emission lifetimes are shorter, and these systems must be studied at lower temperatures (150 or 77 K). As for bpy-based heterodinuclear systems, there is an efficient energy transfer process from the ruthenium moiety to the osmium moiety. It is interesting to notice that the insertion of a saturated unit such as bicyclooctane (bco) in the bridging ligand causes a dramatic reduction in the energy transfer rate (even when the increase in distance is taken into account), which can be related to the electronically ‘insulating’ character of the bco group, in agreement with the double electron transfer mechanism.

4.4.2.2 Photonic wires from porphyrins

Energy transfer is also found in organic systems, such as porphyrins [4.17]. The most attractive example is provided by a large molecule in which up to three Zn-tetraphenylporphyrin moieties are attached by diarylethyne spacers, with a dipyrromethene dye at one end acting as absorber, and a free base porphyrin at the other end acting as emitter (Fig. 4.25). The structure extends over 90 \AA , and is soluble.

As previously, the absorption spectrum is essentially the superposition of the spectra of the component parts. Excitation at 485 nm concerns mainly the dipyrromethene dye. The emission is dominated by the free base porphyrin at 650 and 720 nm, while dipyrromethene alone would emit at 534 nm. Here the excited states are singlets and the emission is thus qualified as fluorescence.

**Fig. 4.25**

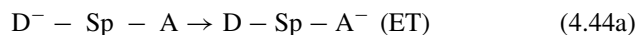
(a) Array of three Zn-tetraphenylporphyrins bridging a dipyrromethene dye at one end and a free base porphyrin at the other; (b) absorption spectrum of the dipyrromethene dye (a.u.) (black filled curve); emission spectra of the dipyrromethene dye (black line) and of the free porphyrin (filled grey curve). (Adapted from ref. [4.17].)

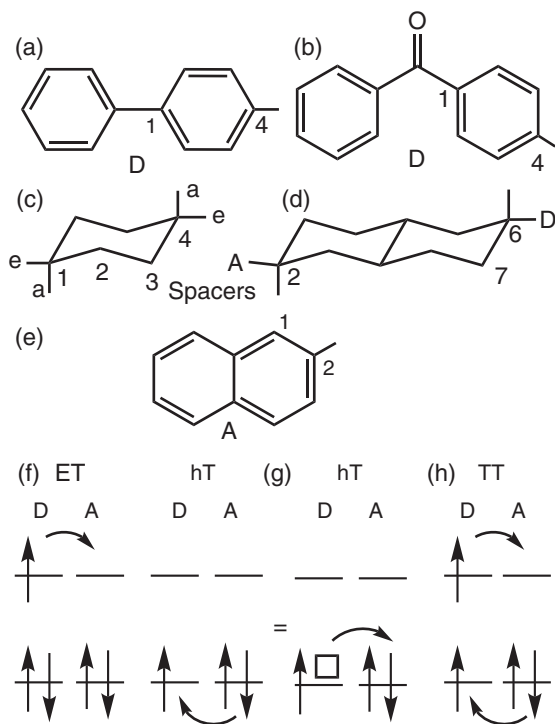
Since the transitions are allowed, a first analysis according to Förster theory can be envisioned. However, a direct (through-space) coupling mechanism between the two remote ends would be predicted at much slower rate than actually observed. Another possibility is to consider a variant of the Förster mechanism: a stepwise energy transfer along the array of intermediate Zn-tetraphenylporphyrins. Even in this case, the observed rate is still much higher than the one computed from the model. Thus one is left with the general idea that the coupling is a through-bond mechanism involving the diarylethyne link, of the Dexter type. Note that this is only a part of the answer: the original Dexter treatment is a two-site treatment and suffers the same drawbacks as simple treatments of electron transfer neglecting the explicit role of the bridge. Here also, it would be necessary to go beyond a two-site description and use concepts similar to superexchange in electron transfer (see Section 3.2.2.6).

4.4.2.3 Relation between triplet transfer and electron and hole transfer

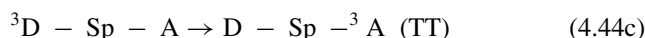
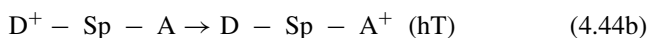
The last example we present is based on a particularly versatile structure of the D–Spacer–A (D–Sp–A) type, which allows electron transfer (ET), hole transfer (hT), and triplet transfer (TT) studies in the same series (Fig. 4.26) [4.18]. Here D is the donor group, 4-biphenyl (Fig. 4.26a) for the electron transfer and hole transfer studies, and 4-benzophenonyl (Fig. 4.26b) for the triplet transfer studies, the spacers Sp are cyclohexane or *trans*-decalin (Fig. 4.26c,d), with different regio- and stereochemical attachments, and A is the 2-naphthyl group, (Fig. 4.26e).

The different possible processes are thus:



**Fig. 4.26**

D-Sp-A systems for electron, hole, and triplet transfer studies. (a) 4-biphenyl and (b) 4-benzoquinone donors; (c) cyclohexane spacer with atoms numbering, axial *a*, and equatorial *e* substitution positions; (d) *trans*-decalin spacer with the general structure of the system (here is a 2,6*ee* A-Sp-D); (e) 2-naphthyl acceptor; (f, g, h) schemes of electron transfer (ET, (f)), hole transfer (hT, (g)), two equivalent representations), and triplet transfer (TT, (h)).



where 3D or 3A designates a donor or acceptor group excited in the triplet state (Fig. 4.26h). For the ET reactions the negative species are generated by pulse radiolysis. For the hT, the positive species are also generated by pulse radiolysis, but in the presence of 1,2-dichloroethane, which produces cation-radicals. Finally, TT reactions are studied by flash photolysis with transient absorption measurements, by monitoring the decay of the triplet benzophenone state and the build-up of the triplet naphthalene state.

Since the rate constants are proportional to the square of coupling elements, eqn. (4.42) leads to a relation between the rate constants k_{ET} , k_{hT} , and k_{TT} :

$$k_{TT} = C \times k_{ET} \times k_{hT} \quad (4.45)$$

where C is an unknown constant. In the present series, a good fit between observed k_{TT} values and those predicted from eqn. (4.45) is obtained when taking $C = 4.0 \times 10^{-10}$ s. The fit is valid over five decades. This equation also predicts that there is a relation between the rates of decay with distance, when each rate constant is written as (see Section 3.2.2.6):

$$k = k_0 \exp(-\beta R) \quad (4.46)$$

Thus the β coefficients (not to be confused with resonance integrals!) are expected to be related by:

$$\beta_{TT} = \beta_{ET} + \beta_{hT} \quad (4.47)$$

The reader is invited to go back to the electron transfer mechanisms developed in Section 3.2.2.6 on mixed valence systems, to better grasp the present developments.

Remark: A difficulty has been noticed in the literature concerning the use of eqn. (4.45). k_{ET} and k_{HT} refer to electron or hole transfer reactions, which are thermally activated and thus depend on solvent reorganization energies, themselves introducing an extra distance dependence (Chapter 3, eqns. (3.15)–(3.17)). On the other hand, k_{TT} is found to be much less solvent-dependent—a fact attributed to the almost non-polar nature of the excited triplet state.

4.4.2.4 Antenna effect and light harvesting

Light harvesting is a process which occurs in natural photosynthesis. A number of pigments are located near the reaction centre where the initial charge separation is performed. The role of these pigments is to collect light and funnel absorbed energy to the reaction centre. In this way the effective cross-section for light absorption is greatly enhanced, as each photon passing near the reaction centre has a greater probability of being captured. This is called the *antenna effect*.

The process of light harvesting is based on energy transfer between chromophores. A simple representation is given in Fig. 4.27. It is generally assumed that energy transfer in antenna systems occurs via the Förster mechanism, and thus implies singlet excited states.

A major conceptual advance occurred in 1995 with the precise resolution of the structure of a purple bacteria light-harvesting antenna complex called LH2 [4.20, 4.21]. It is made of two circular arrangements of bacteriochlorophyll

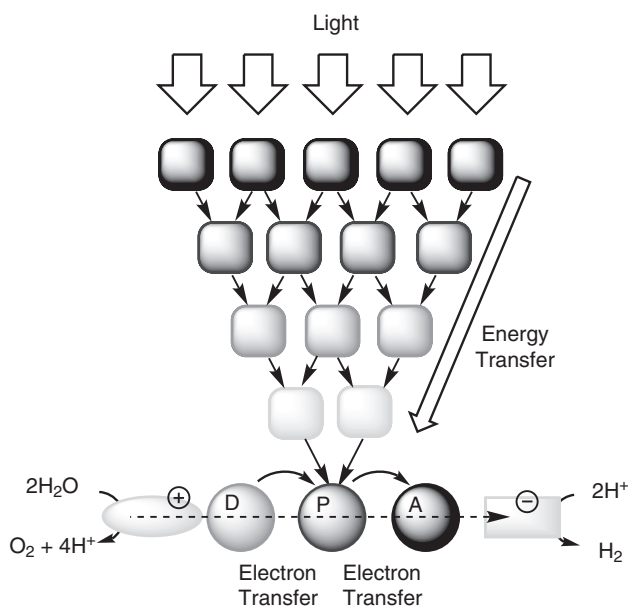
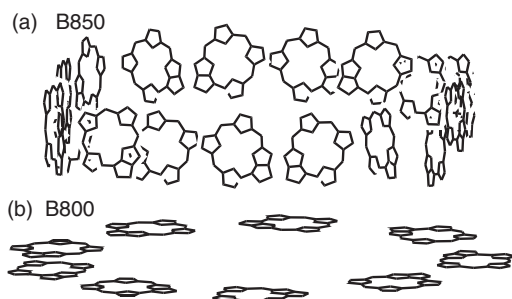


Fig. 4.27

Schematic representation of the antenna effect. The chromophores must have different energy levels so that a predetermined energy gradient is built into the system. The energy is finally absorbed in the reaction centre, where a series of electron transfers lead to electron–hole separation and eventually to a chemical process such as water-splitting. (Adapted from [4.19].)

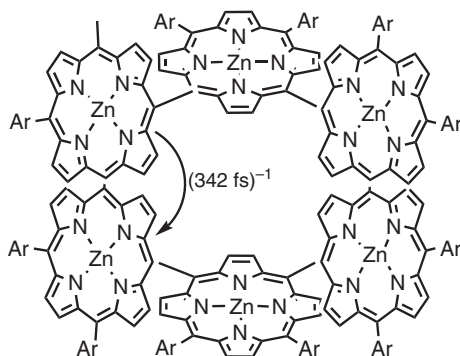
**Fig. 4.28**

The pigments arrangement in the LH2 antenna complex of purple bacteria, showing the two rings of bacteriochlorophylls: (a) the upper (B850) contains eighteen pigments, and the lower (B800) contains nine pigments. (Adapted from reference [4.21].)

molecules—one ring called B850 (from the wavelength absorption) and the other B800 (see Fig. 4.28). Extremely fast energy transfer (less than 1 ps) is observed from B800 to B850. Then energy is transferred to another, larger antenna complex, called LH1, which also has a ring structure, and finally to the reaction centre. The circular structure of these units has a distinct advantage: since energy can migrate from one chlorophyll to the other along the rings, this ensures that at some time the proper orientation for energy transfer to another ring or the reaction centre is achieved (see Section 4.4.1 for the geometric requirements).

Thus natural photosynthesis provides a proof-of-principle of a successful antenna system, but many other molecular assemblies are conceivable and are investigated presently. The realization of artificial systems able to achieve the antenna effect is presently a big challenge. One has to associate a large number of chromophores, in many cases through self-assembly, and in addition there must be several types of chromophore with a controlled relative disposition, so that energy transfer is directional. In the following we give only a few examples, but extensive reviews are available [4.22].

A large number of cyclic porphyrin arrays constituting macrocycles have been prepared, by inspiration, from the natural arrays [4.22b] discussed previously. As usual for macrocyclic compounds, the synthetic problem is to favour intramolecular cyclization with respect to polymerization. While the larger arrays are obtained by elegant template synthesis, the smaller ones can be obtained by direct synthesis under high-dilution conditions. This is the case for the cyclic tetramer depicted in Fig. 4.29.

**Fig. 4.29**

Cyclic porphyrin array in which ultra-fast energy transfer has been observed. (Adapted from reference [4.22b].)

Energy transfer has been observed in this system by either transient absorption spectroscopy or transient absorption anisotropy measurements (the last method relies on the depolarization of the emission signal when energy hops from a site to another one with a different orientation). Energy transfer (Förster mechanism) is extremely rapid, with a rate constant around $(340 \text{ fs})^{-1}$, which rivals the one observed between B800 and B850 in the natural cyclic antenna system. In the present case, however, there is no preferential direction for energy transfer.

Another approach is based on metal–organic dendrimers. Returning to the chemistry of ruthenium and osmium, one can prepare dendrimers in which each metal is coordinated to 2,2'-bipyridine, playing the role of a terminal capping ligand, or 2,3-bis(2'-pyridyl) pyrazine, playing the role of a bridging ligand (see Fig. 4.30) [4.19]. Dendrimer chemistry presents distinct advantages over conventional multistep synthesis, because it is based on simple repetitive reactions, allowing precise control of the size and the composition. A simple dendrimer made of three ruthenium polypyridyl units around a central osmium moiety is depicted in Fig. 4.30.

In this tetranuclear species, energy transfer occurs from the ruthenium to the osmium site in less than 200 fs, and again the leading mechanism seems to be singlet–singlet energy transfer by the Förster mechanism.

Finally, we present a beautiful example obtained by conventional multistep synthesis [4.23]. The molecule, represented in Fig. 4.31, is built around a central benzene ring from which six arms expand. Two arms bear anthracene units (A_1 , Fig. 4.31b), two other boron dipyrromethene units (A_2 , Fig. 4.31c), and the last two zinc tetraarylporphyrins (A_3 , Fig. 4.31a). The rationale is that the absorptions of the three chromophores cover a large part of the ultraviolet–visible spectrum, and furthermore that energy transfer can occur from anthracene, A_1 to dipyrromethene and from dipyrromethene, A_2 to Zinc tetraarylporphyrin, A_3 .

The energy is transferred to a C_{60} unit coupled to the previous structure by means of two pyridyl groups which can coordinate with the zinc atoms. Transient studies of the complete assembly have shown that energy transfer indeed occurs in the predicted way and generates a singlet excited porphyrin. Electron transfer then occurs, yielding the charge-separated state $Zn\text{-TPP}^+ C_{60}^{\bullet-}$ with a quantum yield of unity. The lifetime of the charge-separated state is 230 ps.

4.5 Photomagnetism

4.5.1 Introduction

In this chapter's introduction we emphasized that a photoexcitation occurs always at constant spin, and that the spin change can follow subsequently due to a forbidden slow intersystem crossing. In this section we focus on some examples related to magnetic molecular materials, where the photoexcitation is followed by a durable change in the magnetic properties of the system. This change of magnetic properties through light absorption is known as photomagnetism, which recently has seen a spectacular revival involving everyday applications.

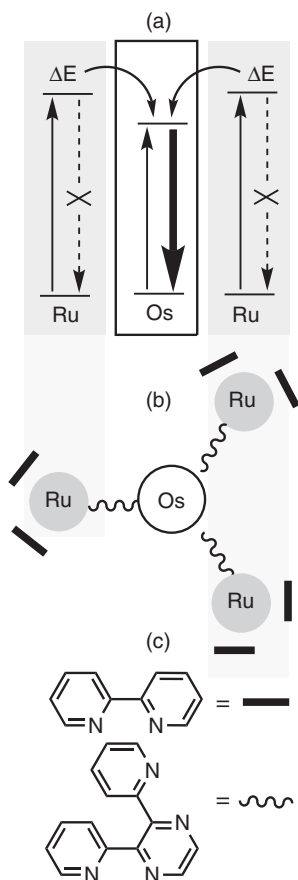
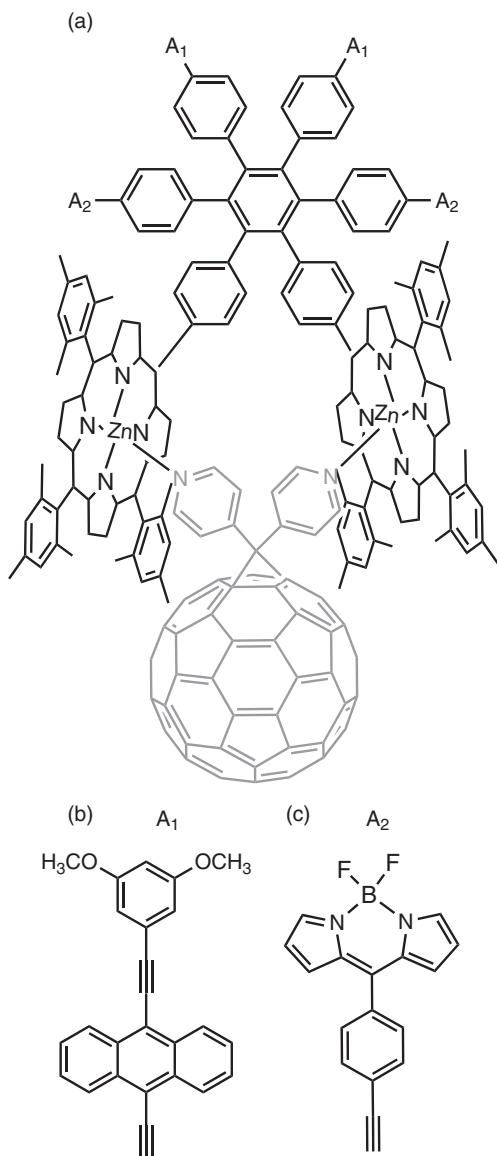


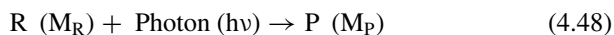
Fig. 4.30

Scheme of an OsRu₃ polynuclear complex, precursor of a larger family of dendrimers. (a) The upper part shows energy levels and the process of energy transfer from Ru to Os site; (b) OsRu₃ structure; (c) terminal capping ligands are 2,2'-bipyridine (black bars), and bridging ligands are 2,3-bis(2'-pyridyl) pyrazine (wavy lines). (Adapted from [4.19].)

**Fig. 4.31**

(a) The hexad antenna coupled to a charge-separation unit. On the six arms starting from the central benzene ring are two substituted anthracene units (A_1) (b), two boron dipyrromethene units (A_2) (c), and two zinc tetraarylporphyrins (A_3). A C_{60} derivative is linked by two pyridyl groups to the zinc porphyrins. (Adapted from [4.23].)

Photomagnetism can be defined as a process that changes the magnetism of a system after absorption of photons. The system can consist of molecules, more or less in interaction, in solid state or in solution. If R (reactant) is the initial molecule and P the final one (product), molecular photomagnetism can be schematized as:



where M_R and M_P are the (different) magnetizations of the reactant (R) and of the product (P) respectively. Photomagnetism is thus the transformation of matter by light and should be distinguished from magneto-optics, which

is the reverse process—the transformation of light by matter (change in light polarization—Faraday and Kerr effects—and so on).

Here we apply the knowledge and the rules introduced in Section 4.2: (i) as a first approximation, there is no direct spin–photon interaction; (ii) the photoexcitation is mainly an interaction between the electric field of the incoming radiation and the electrons in the occupied orbitals of the molecules; (iii) the first reached excited state has the same spin as the ground state; (iv) a change of spin may occur later after vibrational relaxation and through forbidden intersystem crossings (Figures 4.1 and 4.2).

We apply these observations to two classes of compound: (i) the spin cross-over systems introduced in Section 2.4.3, and (ii) polymetallic systems (either molecular or 3D inorganic solid-state structures) in which the basic excitation is followed by a metal–metal charge transfer.

In both cases, magnetic properties are modified. This area of photo-switchable materials is giving rise to many exciting scientific and possibly technological developments. Indeed, the molecular switch is one of the functions that the chemist must master in molecular electronics (see Chapter 5). We therefore provide the reader with very recent results.

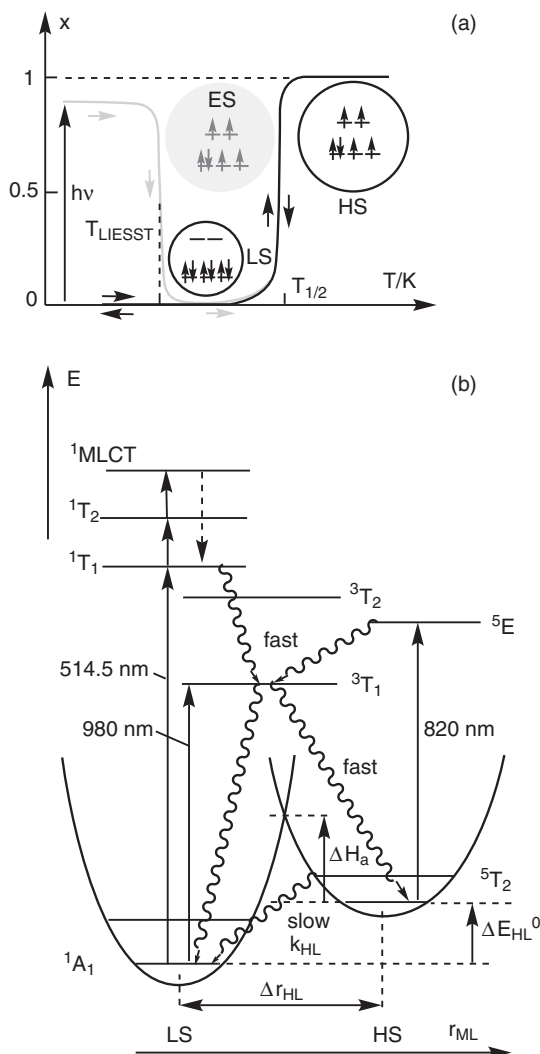
4.5.2 Photomagnetism in spin cross-over systems

We recall here the definition of Section 2.4.3: a spin cross-over is the spin change of a transition metal complex (from high spin (HS) to low spin (LS) or the contrary). It can occur under the influence of temperature, pressure, light, or magnetic field.

The first observation of a photomagnetic process in a molecular spin cross-over system was made in solution by McGarvey *et al.* as a transient state. Then Decurtins, Gülich, and Hauser, studying the electronic spectroscopy of the spin cross-over system $[\text{Fe}^{\text{II}}(\text{ptz})_6](\text{BF}_4)_2$ (ptz = 1-propyl-tetrazole) discovered serendipitously the effect as a metastable state at low temperature (1984) (Figs. 4.32 and 4.33). They termed it ‘light-induced excited spin state trapping’ (LIESST), as it corresponds to the trapping of an excited high-spin state by an activation energy barrier between the excited state and the ground state, impeding the system to revert to the ground state [2.28–2.29] [4.24a].

4.5.2.1 Light-induced excited spin-state trapping (LIESST) effect

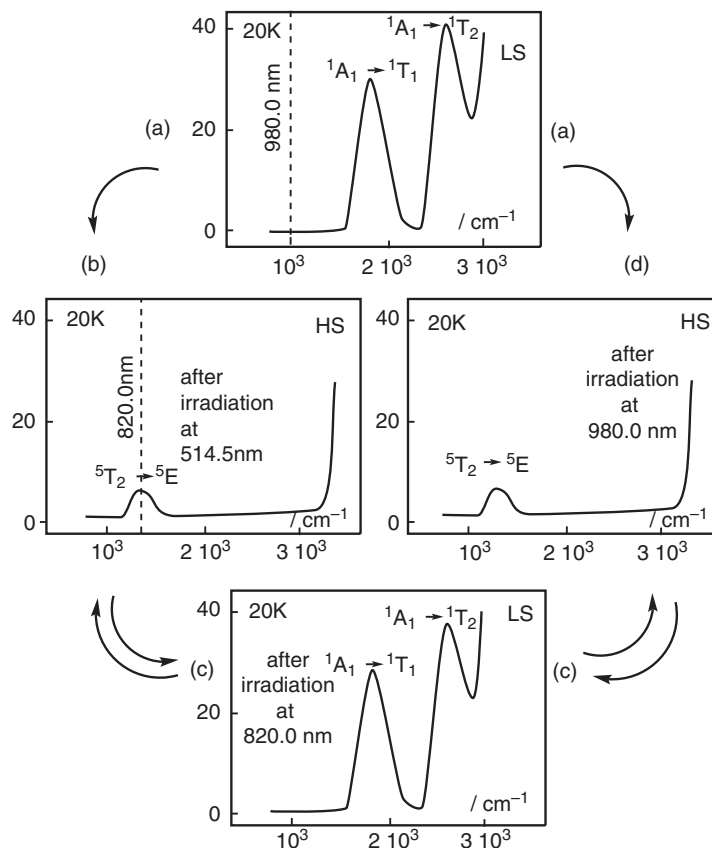
The $[\text{Fe}^{\text{II}}(\text{ptz})_6]^{2+}$ complex is a d^6 iron(II) octahedral complex, as already introduced in Section 2.4.3. The complex presents an abrupt spin cross-over transition at $T_{1/2} = 135$ K marked by a deep change in colour—practically colourless in the HS state and bordeaux red in the LS state. Figure 4.32a displays the magnetic properties as the $\chi_{\text{M}}T$ product *versus* temperature. When exciting at low enough temperature (20 K) colourless hexagonal plates of the compound, 1 mm thick, in the singlet–singlet absorption band using a 450W Xenon lamp (green light) the excited state is created. After 1 hour the conversion is complete and the new state remains ‘trapped’ for weeks. When heated, the excited state relaxes to the low spin state and the susceptibility curve merges with the initial curve. The temperature at which half of the high-spin excited

**Fig. 4.32**

Mechanism of the LIESST and reverse-LIESST effects in the $[\text{Fe}^{\text{II}}(\text{ptz})_6](\text{BF}_4)_2$ complex, d^6 . (a) High spin (HS) fraction as a function of temperature. Black curve, usual spin cross-over to low-spin (LS). In grey, excited state after irradiation (ES). Spheres represent schematically the electronic structure and the volume of the species (HS, LS, ES). Small arrows indicates the direction of temperature changes. (b) Energy levels and potential energy curves for the $1A_1$ ($S = 0$) $(t_{2g})^6$ and $5T_2$ ($S = 2$) $(t_{2g})^4(e_g^*)^2$ states versus the metal–ligand distance r_{ML} . A triplet intermediate spin state $3T_1$ ($S = 1$) $(t_{2g})^5(e_g^*)^1$, is also shown (see text). The dashed arrow corresponds to vibrational de-excitation, and wavy arrows to forbidden intersystem crossings. (Adapted from [2.29].)

state has relaxed to low spin is known as T_{LIESST} . The phenomenon has been investigated thoroughly and the mechanism deserves some comments.

We recall the spin states in Fig. 4.32b. We emphasize the photoexcitation from ground state singlet S_0 ($1A_1$) to excited singlet S_1 ($1T_1$) and the subsequent steps up to the trapped quintet $5T_2$. The low spin state S_0 $(t_{2g})^6$ has a lower enthalpy H_{LS}^0 than that of the quintet ($S=2$) $(t_{2g})^4(e_g^*)^2$, $\Delta H_{HL}^0 (= H_{HS}^0 - H_{LS}^0 > 0, \approx 450 \text{ cm}^{-1})$. The metal-to-ligand distance in the quintet state is larger than that in the singlet (with an average mean change in iron(II) complexes $\Delta r_{HL} = r_{HS} - r_{LS} \approx 0.2 \text{ \AA}$). We have already seen in Section 2.4.3 that these two important energetic and structural features are related directly to the population of the e_g^* antibonding orbitals: when depopulating the e_g^* orbitals, the bond order increases and so does the bonding energy, whereas the bonding order increases and the metal–ligand distance decreases.

**Fig. 4.33**

Single crystal electronic spectra of $[\text{Fe}^{\text{II}}(\text{ptz})_6](\text{BF}_4)_2$, at the origin of the discovery of LIESST effect: (a) normal spectrum of the LS complex at 20K; (b) from (a), after irradiation into the spin-allowed $^1\text{A}_1 \rightarrow ^1\text{T}_1$ transition, at 514.5 nm: spectrum of the HS species—LIESST HS state; (c) after subsequent irradiation from (b), into the spin-allowed $^5\text{T}_2 \rightarrow ^5\text{E}$ transition, at 820 nm: spectrum of the LS species—reverse-LIESST LS state; (d) starting again from (a), with an irradiation at 980.0 nm, into the spin-forbidden $^1\text{A}_1 \rightarrow ^3\text{T}_1$ transition: spectrum of the HS species. (Adapted from [2.29].)

These combined features (change in energy, important change in geometry—metal—ligand distances) build up an energy barrier ΔH_a between the potential wells of the excited quintet $^5\text{T}_2$ and of the ground singlet, $^1\text{A}_1$, able to trap the quintet as a *metastable* state.

Thus the LIESST effect begins with the allowed transition (black arrow on the left, $\lambda = 514.5$ nm) from the low-spin $(t_{2g})^6 S_0$ singlet, $^1\text{A}_1$, to the excited S_1 singlet $(t_{2g})^5(e_g^*)^1$, $^1\text{T}_1$, then to the intermediate triplet $^3\text{T}_1$ ($S = 1$) $(t_{2g})^5(e_g^*)^1$, and then to the quintet $^5\text{T}_2$ ($S = 2$). When the system is in the triplet state $^3\text{T}_1$, it can revert to the initial singlet $^1\text{A}_1$ (and the photon is lost) or move to the quintet $^5\text{T}_2$. The metastable quintet $^5\text{T}_2$ ($S = 2$) $(t_{2g})^4(e_g^*)^2$ is 'trapped' by the activation energy barrier ΔH_a , hence achieving the LIESST. The reverse-LIESST effect has been observed: it starts with photoexcitation (black arrow on the right, $\lambda = 820$ nm) from the trapped $^5\text{T}_2$ quintet to the excited ^5E which can evolve to the triplet $^3\text{T}_1$, and then to the initial singlet $^1\text{A}_1$ with the same bifurcation problem (if the system is going back to the quintet, the photon is lost). The different spectroscopic terms have been identified by their energy (or the wavelength of photoexcitation as shown later). The observed electronic spectra are shown in Fig. 4.33.

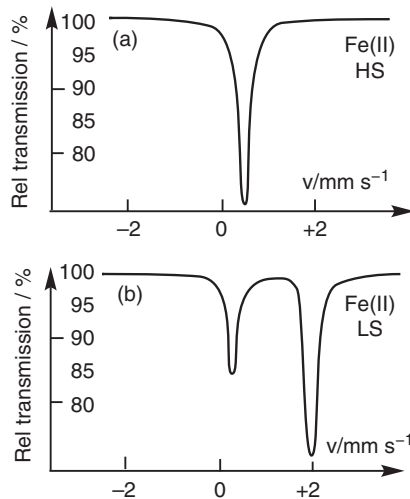


Fig. 4.34

Single-crystal Mössbauer spectra of $[\text{Fe}^{\text{II}}(\text{ptz})_6](\text{BF}_4)_2$: (a) HS spectrum; (b) LS spectrum. In a LIESST and reverse-LIESST experiment, HS spectrum (a) is observed in situations (b) and (d) of Fig. 4.33, and LS spectrum (b) in situations (a) and (c) of Fig. 4.33 (Adapted from [2.29].)

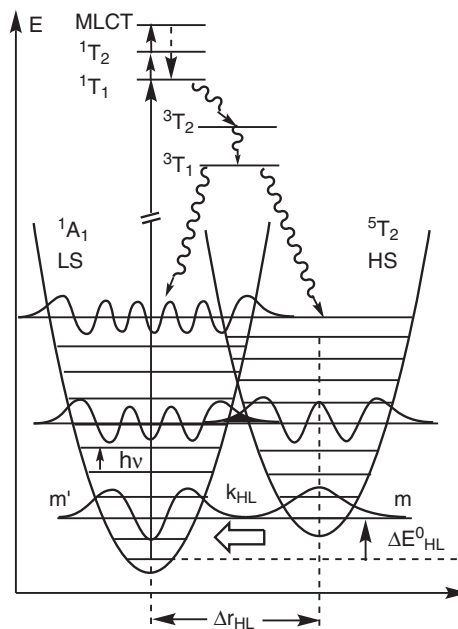
The same demonstration can be made using the Mössbauer spectra of LS and HS species and their appearances and disappearances with irradiation at different energies. They are very distinct, as shown in Fig. 4.34.

Understanding the relaxation of the HS state to the LS state is important both for fundamental reasons and possible applications [2.28].

In solution, with pulse laser excitation, it is possible to measure the rate constant k_{HL} of the HS \rightarrow LS relaxation. Activated Arrhenius behaviour, $k_{\text{HL}}(T) = A \exp(-E_a/kT)$, is observed. For iron(II) complexes, activation energy barriers E_a are in the range 1,000–1,500 cm^{-1} and the pre-exponential factors A of 10^7 – 10^9 s^{-1} . In the solid, also in iron(II) complexes, the E_a values are 2,500–3,000 cm^{-1} for small values of the zero-point energy difference ΔE_{HL}^0 . The lifetimes τ vary considerably with the systems, and furthermore, at very low temperatures the relaxation process is no longer thermally activated but becomes temperature-independent, revealing a tunnelling mechanism. In such cases, the relaxation is not a classical adiabatic one (at vibrational equilibrium and passing over the barrier). Instead, the relaxation proceeds through the nuclear tunnelling effect from the metastable high-spin state to the suitable vibrational levels of the singlet state: (i) at low temperatures it goes exclusively through the lowest vibrational state of the quintet, and (ii) at higher temperature through different thermally populated vibrational levels, as shown in Fig. 4.35. This is why it is termed a non-adiabatic multi-phonon process.

4.5.2.2 Photo-induced phase transitions (PIPT)

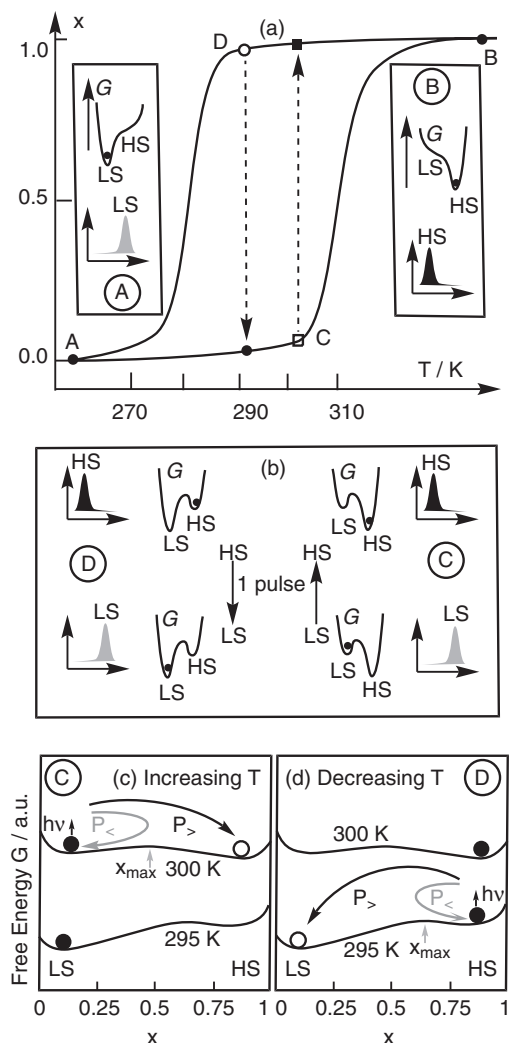
These considerations apply at low temperature, when the thermal quantum kT is much lower than the vibrational quantum. At high temperature the LIESST effect is no longer operative. Nevertheless, different systems presenting spin cross-over temperatures and wide hysteresis around ambient reveal another important phenomenon related to a photo-induced phase transition (PIPT). It is observed when the intensity of the irradiation light overcomes a given threshold, $P_{\text{threshold}}$.

**Fig. 4.35**

Low-temperature HS→LS relaxation through tunnelling processes, implying different vibrational levels of the HS state (m) and of the LS state (m') (Cf. Fig. 3.18). The potential energy curves of the high-spin and low-spin states are given *versus* a reaction coordinate chosen as the metal–ligand distance (in the frame of the single configurational coordinate model). Curly arrows show the way that the HS metastable state arises from the MLCT excited state.

It is peculiarly spectacular on single crystals of $\text{Fe}^{\text{II}}(\text{pyrazine})[\text{Pt}^{\text{II}}(\text{CN})_4]$ (see Section 2.4.3.4. Figure 2.29) [4.25]. The compound crystallizes in the space group P/mmm at high and low temperature with a contraction of the cell parameters at low temperature. Figure 4.36a displays the hysteresis loop, the Raman spectra, and the free-energy scheme at points A (LS) and B (HS). The $\chi_{\text{M}}T$ values in the hysteresis loop vary from $3.81 \text{ cm}^3 \text{ K mol}^{-1}$ at 340 K (corresponding to $S = 2$) to 0.16 at 270 K (a virtually complete transformation to $S = 0$). The hysteresis width is 24 K. The Raman spectra (signal *versus* wavenumber $\bar{\nu}$ in the $650\text{--}700 \text{ cm}^{-1}$ range) displays a ‘marker’ band characteristic of the LS state at 682 cm^{-1} (point A, left) and of the HS state at 650 cm^{-1} (point B, right). We know from Section 2.4.3 that within the hysteresis loop the system can exist in a stable state and a metastable state. This is shown schematically in Fig. 4.36c,d (see also Fig. 2.24) by the two shallow minima in the free-energy scheme separated by a maximum located at x_{max} ($x_{\text{max}} \approx 0.47$ at 300 K and ≈ 0.65 at 295 K).

Departing from A (LS) and increasing the temperature, one reaches point C (□, mainly trapped in LS state as shown in Fig. 4.36b,c). At the opposite, departing from B (HS) and decreasing the temperature, one reaches point D (○, trapped in HS state as shown in Fig. 4.36 b,d). The irradiation by a Nd:YAG laser (one pulse of 4 ns, $\lambda = 532 \text{ nm}$, pulse energies 1mJ for a spot size of 0.4 mm^2) transforms the system to HS state in C and to LS in D. In this case the applied irradiation power is above the threshold power, $P_{\text{applied}} > P_{\text{threshold}}$ (curved black arrows in Fig. 4.36c,d). Instead, when the irradiation power is below the threshold, $P_{\text{applied}} < P_{\text{threshold}}$, the system relaxes rapidly to the initial state (short curved grey arrows in Fig. 4.36c,d). The threshold power $P_{\text{threshold}}$ is needed to transform, at the microscopic level in the solid,

**Fig. 4.36**

(a) Hysteresis loop for the spin cross-over in the $\text{Fe}^{\text{II}}(\text{pyrazine})[\text{Pt}^{\text{II}}(\text{CN})_4]$ compound as x , the fraction of the high-spin HS species versus temperature. At left, schematic Raman spectrum (signal versus wavenumber $\tilde{\nu}$ in the 650–700 cm^{-1} range) and the free enthalpy scheme at point A (low spin ground state), where the black dot localizes the ground state of the system. At right, the same data at point B (high-spin ground state). (b) Transitions induced by one laser pulse at points D and C (metastable states) with the related Raman spectra and free enthalpy scheme before and after the pulse: C, ascending temperature, the system is trapped in the low-spin state, and changes to high spin by a single laser pulse; D, descending temperature, the system is now trapped in the high-spin state, and a single laser pulse is enough to change it to low spin. (c) Free enthalpy versus HS fraction x in the ascending branch of the hysteresis loop (point C): after excitation by light, the system reverts to the LS state (grey arrows) if the power threshold is not reached ($P_<$), or goes to the HS state when the power threshold is overcome ($P_>$) (black arrows); black sphere, thermal population; white sphere, population after one laser shot; (d) analogous phenomenon in the descending branch (point D).

enough molecules from the metastable to the ground state, and hence to build a large enough nucleus of the new phase, stabilized by the lattice distortions accompanying the change in spin state and to allow the macroscopic change to occur. A simple way of describing the process is to tell that at point C the HS fraction must become higher than x_{max} for the system to cross the free-energy maximum and turn HS; and at point D the LS fraction must become higher than $(1-x_{\text{max}})$ for the system to cross the free-energy maximum and turn LS.

A complete analysis should take into account the possibility of demixion; that is, the formation of two phases. In such a case the dot representing the system energy can lie below the maximum in the $G = f(x)$ curve.

An amazing point is that it is possible to induce at will $\text{LS} \rightarrow \text{HS}$ or $\text{HS} \rightarrow \text{LS}$ bidirectional transitions with the same light (wavelength $\lambda = 532 \text{ cm}^{-1}$). This

is simply due to the fact that even if the colours of the two phases are different they both absorb at this wavelength.

To conclude, one can stress that such cooperative photo-induced phase transitions are highly non-linear, with a threshold effect on the light intensity. In the example studied the bidirectional transitions occur around room temperature over a substantial range of bistability with magnetization and colour changes. This presents interesting prospects for applications in memory devices and/or optical switches.

4.5.2.3 Ligand-driven light-induced spin cross-over (LD-LISC effect)

A variant of spin cross-over consists in provoking the spin change by an electronic excitation on a photoisomerizable ligand. For example, a *cis-trans* double bond photoisomerization can vary the ligand field around the metal ion sufficiently to achieve the spin cross-over. This is termed the ligand-driven light-induced spin cross-over (LD-LISC) after Zarembowitch [4.24b].

Figure 4.37 illustrates the phenomenon, which occurs in the temperature range where the two isomers of the complex have different spin states (here for $T < T_{1/2}$).

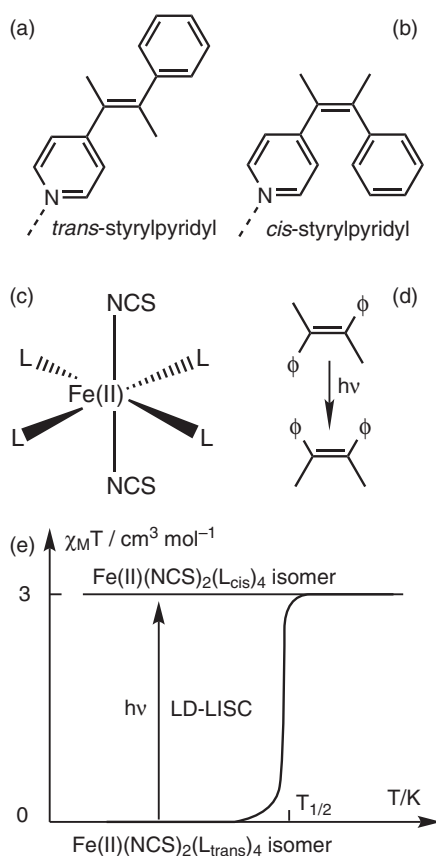
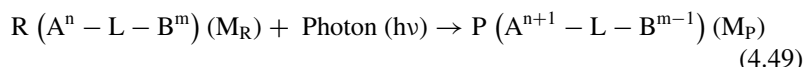


Fig. 4.37

Ligand-driven light-induced spin cross-over: (a) L_{trans} and (b) L_{cis} isomers of the styrylpyridyl ligand L ; they can bind to Fe^{II} through the pyridyl nitrogen; (c) a *trans*- $\text{Fe}^{\text{II}}(\text{NCS})_2(\text{L})_4$ complex; the complex can be synthesized either from the L_{cis} or L_{trans} ligand isomers; it presents the LD-LISC effect; (d) *trans-cis* photoisomerization of the styrylpyridyl; (e) schematic magnetic susceptibility of *trans*- $\text{Fe}^{\text{II}}(\text{NCS})_2(\text{L}_{\text{cis}})_4$ (no spin cross-over) and *trans*- $\text{Fe}^{\text{II}}(\text{NCS})_2(\text{L}_{\text{trans}})_4$ (with a spin cross-over at $T_{1/2}$) and LD-LISC effect below $T_{1/2}$.

4.5.3 Photomagnetism originating from metal–metal charge transfer

In polymetallic AB complexes the change in the magnetization of matter upon irradiation can occur also when excitation is followed by an electron transfer from one metallic centre A to the other, B. The initial compound (reactant R) is a bimetallic system (A^n-L-B^m , L being a bridging ligand, A^{n+} and B^{m+} two different transition metal ions in n and m oxidation states, or A^nB^m). The irradiation forms an excited state $[A^nB^m]^*$ with spin conservation, which relaxes down to a metastable state ($A^{n+1}B^{m-1}$) in a series of steps including electron transfer, and subsequent spin changes such as $[A^{n+1}B^{m-1}]^*$ (see Fig. 4.38). For example:



The electron transfer and spin change are generally accompanied by important geometrical changes around the transition metals: going to low spin and/or higher oxidation decreases the metal–ligand distance. Thus it is possible to describe the process by using an energy diagram with one of the metal–ligand distances (M–L) as reaction coordinate (Fig. 4.38).

The reader should realize that this process needs not only the presence of the bimetallic AB pair but also a solid to trap the metastable state due to intermolecular and/or three-dimensional interactions. Furthermore, in many cases the intensity of the irradiation must overcome a *threshold* value to achieve the transformation. Most of the examples of photomagnetism with electron transfer imply cyanide as a bridging ligand.

4.5.3.1 Photomagnetism in molecular polynuclear complexes

We start with the *a priori* most simple, zero-dimensional (0D) molecular solids where the intermolecular cooperative magnetic effects are not essential for determining the photomagnetic properties [4.26–4.28]. The spin scheme of a general photo-induced electron transfer A^mB^n to $A^{m+1}B^{n-1}$ is shown in Fig. 4.39a,b. It is important to realize that it modifies the oxidation states and the spins of the individual metallic ions A and B but not necessarily the total spin

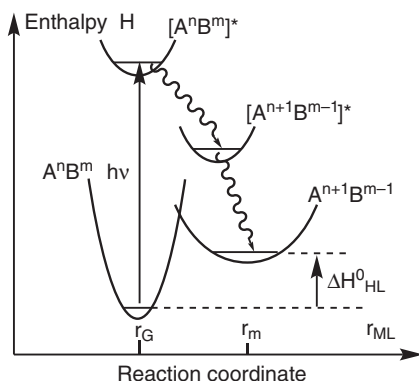


Fig. 4.38

Simplified four-state potential-energy diagram for a metal–metal charge transfer from the ground state A^nB^m to the metastable $A^{n+1}B^{m-1}$. The wavy arrows represent forbidden intersystem crossings. The reaction coordinate is the metal-to-ligand distance r_{ML} (r_G in the ground state and r_m in the metastable state).

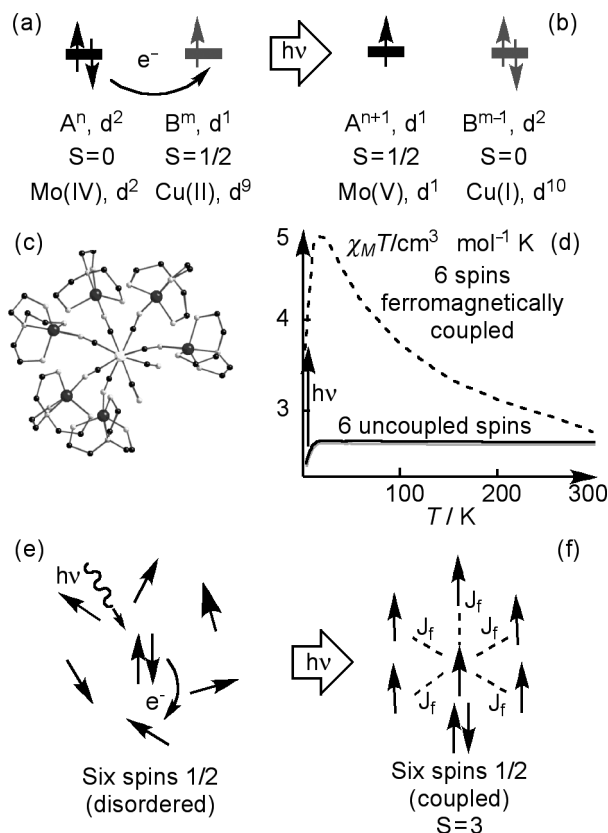
**Fig. 4.39**

Photo-induced electron transfer from a bimetallic pair $\text{Mo}^{\text{IV}}\text{Cu}^{\text{II}}$ (a) to $\text{Mo}^{\text{V}}\text{Cu}^{\text{I}}$ (b); (c) crystallographic structure of the molecular cation $\{\text{MoCu}_6\}^{8+}$; (d) magnetic properties of $\{\text{MoCu}_6\}$ before irradiation at 5 K (black lower curve); after irradiation at 406 nm (dashed upper curve) when increasing temperature; after annealing at room temperature (grey lower curve); spin structure of $\{\text{MoCu}_6\}$: (e) before irradiation, uncoupled Cu^{II} ions in $[\text{Mo}^{\text{IV}}(\text{Cu}^{\text{II}}\text{tren})_6]$ and (f) after irradiation, ferromagnetically coupled Mo^{V} and Cu^{I} ions in the mixed valency $S = 3$ $[\text{Mo}^{\text{V}}(\text{Cu}^{\text{I}}\text{tren})(\text{Cu}^{\text{II}}\text{tren})_5]$ (f).

of the system. To change the total spin, a peculiar spin topology is required where many unpaired electrons are coupled by exchange interactions.

We focus on two recent textbook examples: the heptanuclear $[\text{Mo}^{\text{IV}}(\text{CN})_2(\text{CN}-\text{Cu}^{\text{II}}-\text{L})_6]^{8+}$ ($\text{L} = \text{tren}$) complex (noted $[\text{Mo}(\text{Cutren})_6]^{8+}$ and abbreviated as $\{\text{MoCu}_6\}$) (Fig. 4.39), and the octanuclear $[(\text{pzTp})\text{Fe}^{\text{III}}(\text{CN})_3]_4[\text{Co}^{\text{II}}(\text{pz})_3\text{CCH}_2\text{OH}]_4$ cubic complex ($\text{pzTp} = \text{tetrapyrazolylborate} = \text{L}$, $(\text{pz})_3\text{CCH}_2\text{OH} = 2,2,2\text{-tris(pyrazolyl)ethanol} = \text{L}'$, abbreviated as $\{(\text{FeL})_4(\text{CoL}')_4\}$ or $\{\text{Fe}_4\text{Co}_4\}$) (presented in Fig. 4.42).

The first one is obtained when octacyanomolybdate(IV), $[\text{Mo}^{\text{IV}}(\text{CN})_8]^{4-}$ is reacted with $\text{Cu}^{\text{II}}-\text{L}$ ($\text{L} = \text{tris}(2\text{-aminoethyl})\text{amine}$ or tren) complex in a suitable stoichiometry. An heptanuclear complex arises, the structure of which is shown in Fig. 4.39c. It bears eight positive charges. The Mo^{IV} ion sits at the centre of the complex, surrounded by six $\text{Cu}^{\text{II}}-\text{L}$ groups, N-coordinated to cyanido ligands and by two cyanides. Eight anions (in this case perchlorates) ensure the electroneutrality of the solid. Solutions of the compound present optical absorptions in the visible–ultraviolet range corresponding to the ligand-field bands of $[\text{Mo}(\text{CN})_8]^{4-}$, to the d–d transition of the $\text{Cu}(\text{II})$ ions, and also a band around 500 nm identified as an intervalence *metal-to-metal* charge transfer (MMCT) corresponding to a $\text{Mo}^{\text{IV}}-\text{Cu}^{\text{II}} \rightarrow \text{Mo}^{\text{V}}-\text{Cu}^{\text{I}}$ transition. The central Mo^{IV} ion in the $[\text{Mo}(\text{CN})_8]^{4-}$ complex is diamagnetic, d^2 ,

($S_{\text{Mo}} = 0$). The six Cu(II) ions are paramagnetic ($S_{\text{Cu}} = 1/2$). The magnetic properties of $[\text{Mo}(\text{Cutren})_6]$ in the solid, before irradiation, are those of six quasi-non-interacting paramagnetic Cu^{II} ions: a Curie law in the whole range of temperature and a decrease of the $\chi_{\text{M}}T$ product at very low temperature, due to weak $\text{Cu}^{\text{II}}-\text{Cu}^{\text{II}}$ exchange interactions through the $\text{NC}-\text{Mo}^{\text{IV}}-\text{CN}$ bridge.

Then, at 5 K the solid is irradiated in the region of the MMCT band ($\lambda = 406$ nm), and its magnetization increases steadily up to saturation. After a few hours the irradiation is stopped and the magnetic properties are measured in the dark, with increasing temperature. The $\chi_{\text{M}}T$ product experiences a drastic change, a much higher value, and then a slow decrease with increasing temperature up to ambient (Fig. 4.39d). This behaviour reveals a strong ferromagnetic interaction between the spin carriers, and the formation of a spin ground state $S = 3$ molecule. After a few hours of annealing at 300 K, the compound recovers its initial properties. The photomagnetic process is reversible (grey curve in Fig. 4.39d, superimposable to the initial Curie law).

The effect is explained simply by (i) a photo-induced electron transfer from Mo^{IV} (d^2 , $S = 0$) to Cu^{II} (d^9 , $S = 1/2$) leading to Mo^{V} (d^1 , $S = 1/2$) and Cu^{I} (d^{10} , $S = 0$); (ii) the presence of a central paramagnetic Mo^{V} ion able to switch ON the exchange interactions between the central Mo^{V} and the peripheral Cu^{II} not implied in the electron transfer and (iii) the formation of a metastable species $[\text{Mo}^{\text{V}}(\text{Cu}^{\text{I}}\text{tren})(\text{Cu}^{\text{II}}\text{tren})_5]^{8+}$ with $S = 3$ (Fig. 4.39).

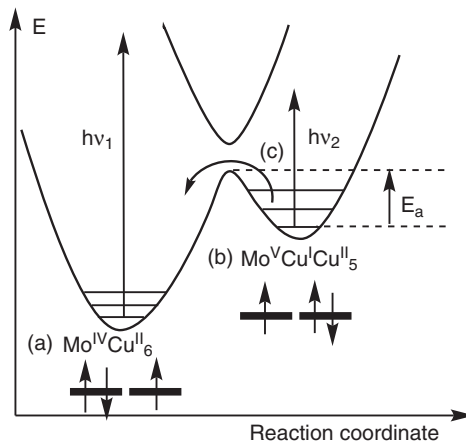
Orthogonality of the magnetic orbitals of Mo^{V} and Cu^{II} ions explains the short-range $\text{Mo}^{\text{V}}-\text{Cu}^{\text{II}}$ ferromagnetic coupling (Section 2.6.1). The coupling constant J_{MoCu} is quite high, around $+100$ cm^{-1} . The photo-induced metastable state has a remarkably long lifetime (days at low temperature, $T < 10$ K). It relaxes thermally to the ground state only at room temperature, indicating the presence of a very high activation energy barrier E_{th} . The process can be repeated many times without apparent fatigue. Even if the exact nature of the long-lived metastable state is not fully known yet, its existence and high stability can be understood from (i) the structural reorganization around the photo-induced Cu^{I} ; (ii) the intermediate geometry of the molybdenum coordination sphere, between square antiprism and dodecahedron where dz^2 and dx^2-y^2 orbitals are close in energy; and (iii) the schematic potential diagram of a class II mixed valency compound (Fig. 4.40).

The overall explanation given previously, evidently oversimplified, was nevertheless confirmed by different experimental techniques (X-ray absorption spectroscopy—near edge structures, XANES, and extended fine structures, EXAFS—probing the oxidation states and the hole created on photo-produced Mo(V), X-ray magnetic circular dichroism at the molybdenum $L_{2,3}$ edges—probing the spin on Mo(V), solid-state EPR and DFT theoretical calculations). Under X-ray irradiation, a Mo^{IV} triplet (d^2 , $S = 1$) has been evidenced.

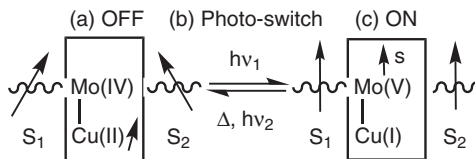
$[\text{Mo}^{\text{IV}}(\text{Cu}^{\text{II}}\text{tren})_6]$, the first photomagnetic ‘high-spin’ molecule, can be considered as the prototype of an OFF/ON photoswitch embedded in photomagnetic supramolecular assemblies (Fig. 4.41). Other MoCu complexes have since been developed.

Fig. 4.40

Schematic potential-energy diagram in the solid state for $[\text{Mo}^{\text{IV}}(\text{Cu}^{\text{II}}\text{tren})_6]$ and $[\text{Mo}^{\text{V}}(\text{Cu}^{\text{I}}\text{tren})(\text{Cu}^{\text{II}}\text{tren})_5]$: (a) initial state; (b) irradiation with blue light ($h\nu_1$) produces an excited charge-transfer state; (c) the metastable complex $[\text{Mo}^{\text{V}}(\text{Cu}^{\text{I}}\text{tren})(\text{Cu}^{\text{II}}\text{tren})_5]$ is trapped at low temperature. The activation energy barrier (E^{\ddagger}) can be overcome either thermally or optically (light $h\nu_2$). In the spin structures, only the copper centre concerned with the electron transfer is represented.

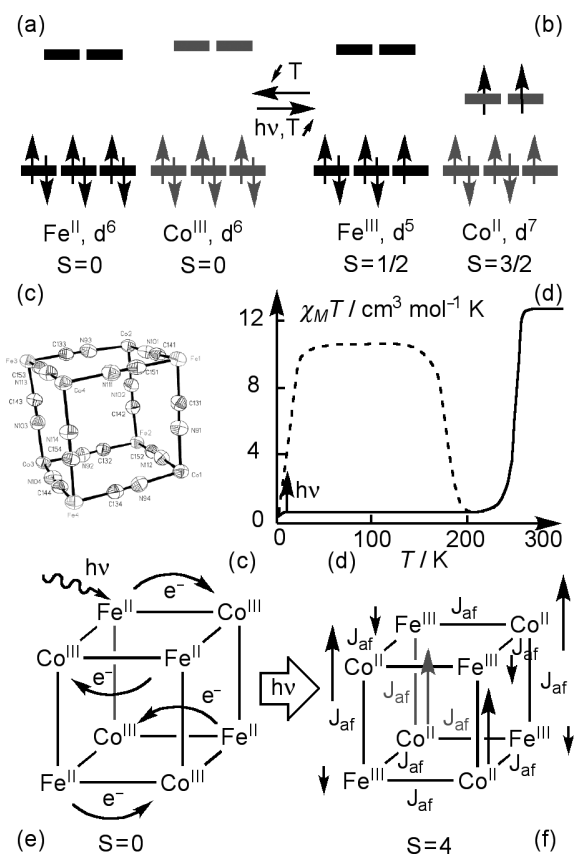
**Fig. 4.41**

A molecular photo-switch between two magnetic components: (a) OFF position, isolated spins S_1 and S_2 . (b) The photo-induced electron transfer from Mo^{IV} to Cu^{II} creates a spin s on Mo and switches ON the exchange interaction. (c) ON position, the magnetic fragments are coupled (here ferromagnetically, $S_T = S_1 + s + S_2$).



Our second example of a photomagnetic molecular complex is the octanuclear $[(\text{pzTp})\text{Fe}^{\text{III}}(\text{CN})_3]_4[\text{Co}^{\text{II}}(\text{pz})_3\text{CCH}_2\text{OH}]_4$, abbreviated as $\{\text{FeL}_4(\text{CoL}')_4\}$ or $\{\text{Fe}_4\text{Co}_4\}$. It is an amazing and beautiful molecular cube $\{\text{Fe}_4\text{Co}_4\}$, with alternation of Co and Fe at each corner and cyanide connectors on each edge. Iron and cobalt ions are in octahedral surroundings, $\text{Fe}(\text{CN})_3(\text{N}-\text{L}_1)_3$ and $\text{Co}(\text{N}-\text{L}_2)_6$. The cubes are well isolated by anions, ensuring the electroneutrality, and by bulky ligands around the metallic centres: the tetrapyrazolylborate (pzTp) for the Fe corners, and the 2,2,2-tris(pyrazolyl)ethanol for the Co corners (Fig. 4.42c). The space group is $P21/c$. The mean $\text{Fe}^{\text{III}}-\text{C}$ distances are around 1.92 Å, and the mean HS $\text{Co}^{\text{II}}-\text{N}$ are 2.06 Å. The $\text{C}-\text{Fe}-\text{C}$ and $\text{N}-\text{Co}-\text{N}$ angles are close to 90° (88° and 92°). The $\text{Fe}-\text{Co}$ distances are 5.11 Å (edge) and 8.89 Å (cube diagonal), and the $\text{Fe}-\text{Fe}$ are 7.46 Å (face diagonal).

The χ_{MT} value, $12.7 \text{ cm}^3 \text{ K mol}^{-1}$, corresponds to four quasi-isolated low-spin, LS Fe^{III} , and four high-spin, HS Co^{II} . The Fe^{III} are low-spin ($S = 1/2$) due to the strong octahedral ligand field of C-bonded cyanides, whereas the Co^{II} are high-spin, HS ($S = 3/2$), due to the weak ligand field allowed by the N-bonded cyanides. At room temperature the complex is then $\{[\text{LS Fe}^{\text{III}}]_4[\text{HS Co}^{\text{II}}]_4\}$. The spin structure of a $\text{Fe}^{\text{III}}-\text{Co}^{\text{II}}$ pair is shown in Fig. 4.42b. When the crystals are cooled slowly, several spectacular changes occur between 265 and 255 K: the colour is modified, from red to green; the χ_{MT} value almost vanishes (approaching $0.57 \text{ cm}^3 \text{ K mol}^{-1}$ at 200 K); at 90 K the mean $\text{Fe}-\text{C}$ distances are around $1.90(\pm 0.02)$ Å, and the mean HS $\text{Co}-\text{N}$ are $1.90(\pm 0.01)$ Å—a shrinking of 0.16 Å compared to room temperature! The $\text{Fe}-\text{Co}$ distances are 4.96 Å (edge) and 8.54 Å (cube diagonal), and the $\text{Fe}-\text{Fe}$ are 7.02 Å (face diagonal). The space group remains $P21/c$. The


Fig. 4.42

Electron transfer in the molecular cube $\{\text{Fe}_4\text{Co}_4\}$: (a) low-temperature ground state; (b) high-temperature or photo-induced metastable state; (c) molecular skeleton of the $\{\text{Fe}_4\text{Co}_4\}$ box (the external ligands are omitted for clarity); (d) thermal variation of the magnetic susceptibility as $\chi_M T = f(T)$ in the dark state (plain curve) when T decreases, and in the light-induced state (dashed line) when T increases; (e) scheme of electron transfer upon irradiation in the low-temperature ground-spin state ($S = 0$); (f) proposed spin structure in the metastable state ($S = 4$, with an antiferromagnetic $\text{Fe}^{\text{III}}\text{-Co}^{\text{II}}$ interaction).

phenomenon is perfectly reproducible when cycling in temperature without detectable thermal hysteresis. These changes are consistent with the formation of a diamagnetic $\{[\text{LSFe}^{\text{II}}]_4[\text{LSCo}^{\text{III}}]_4\}$ cluster and an intramolecular electron transfer from each Fe^{III} to one Co^{II} neighbour. The diamagnetic spin structure is shown in Fig. 4.42a. Infrared and electronic spectroscopies confirm these interpretations.

When the crystals are irradiated by an halogen white light at 30 K and 575 mW cm^{-2} for 20 h, another spectacular change occurs: the $\chi_M T$ increases to a value $> 10 \text{ cm}^3 \text{ K mol}^{-1}$ between 30 and 180 K, close to that expected for a metastable $\{[\text{LSFe}^{\text{III}}]_4[\text{HSCo}^{\text{II}}]_4\}$. Above 180 K the $\chi_M T$ value decreases down to that of the low-spin $\{[\text{LSFe}^{\text{II}}]_4[\text{LSCo}^{\text{III}}]_4\}$ cluster. Above 200 K the magnetic properties merge with those obtained when slowly decreasing the temperature. A remarkable feature is that the relaxation of metastable state to the low-spin state is thermally activated with a characteristic relaxation time $\tau = \tau_0 \exp(-E_a/kT)$ ($\tau_0 = 2.6 \cdot 10^{-8} \text{ s}$ and an energy barrier $E_a/k = 4455 \text{ K}$). In other words, the lifetime of the metastable state at 180 K is roughly ten years. This remarkable high lifetime demonstrates the possible interest of purely molecular compounds for photomagnetic information storage. The intriguing properties exhibited by the compound when it is rapidly

cooled from ambient to 5K are not concerned with photons, and we do not deal with them here.

4.5.3.2 Photomagnetism in three-dimensional frameworks

The two preceding examples, dealing with molecular solids, allowed us to understand how an electron can be transferred from one site to another by a photon within a molecule, and the magnetic consequences. In both cases the link between the two spin bearers A and B was a cyanide ligand: A^n-NC-B^m . What happens when the same pairs of metallic ions are embedded in a solid $(-A^n-NC-B^m-CN-)_{\infty}$? One can expect, as we have seen in Section 2.7.3, long-range cooperative phenomena and spectacular changes in the long-range magnetic order (enhancement of magnetization in the magnetically ordered phase and of the Curie temperature). This is also an active branch of research. Different three-dimensional $Mo^{IV}-Cu^{II}$ photomagnetic compounds have been characterized, but we present only examples dealing with the Fe–Co pair in some Prussian blue analogues—the structural framework of which is familiar (Section 2.7.3).

The first photomagnetic effect with electron transfer was reported by Hashimoto and coworkers in 1996 in Prussian blue analogues, far before the molecular cases of Section 4.5.3.1. [4.29]. The compound was formulated $K_{0.4}Co_{1.3}[Fe(CN)_6]_1 \cdot 5H_2O$, which becomes $K_{1.2}Co_4[Fe(CN)_6]_{3.1} \cdot 15.4H_2O$ in a formulation related to the face-centred cubic conventional cell, close to $\{C_1Co_4Fe_3\Box_1\}$ in an abridged way. The Japanese team showed that the magnetization and the magnetic ordering temperature T_C of this compound increased under irradiation by visible light at low temperature (Fig. 4.43). The metastable state can relax either optically (not shown) or thermally at high relaxation temperature, T_{relax} (Fig. 4.43c). This discovery opened a new field of investigation. ‘Molecular electronics emerges in molecular magnetism’ was a comment [4.30].

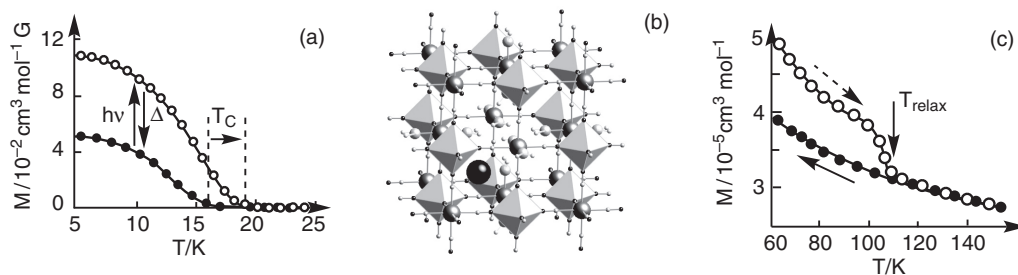


Fig. 4.43

(a) Photomagnetic effect in a CoFe Prussian blue analogue (●, before irradiation; ○, after irradiation). Note the remarkable enhancement of the magnetization and of the Curie temperature T_C after irradiation. (adapted from [4.29]). (b) Schematic conventional cell representation of the compound $\{C_1Co_4[Fe_3\Box_1]\}$; Fe ions are at the centre of light grey octahedra, cobalt ions are large dark grey spheres; carbon, small black spheres; nitrogen and hydrogen, small grey spheres; oxygen, medium grey spheres; alkali cation (caesium), large black spheres. (c) Field cooled magnetization (●, before irradiation); magnetization of the metastable state when increasing temperature, showing the relaxation at $T_{relax} \approx 110K$ (○).

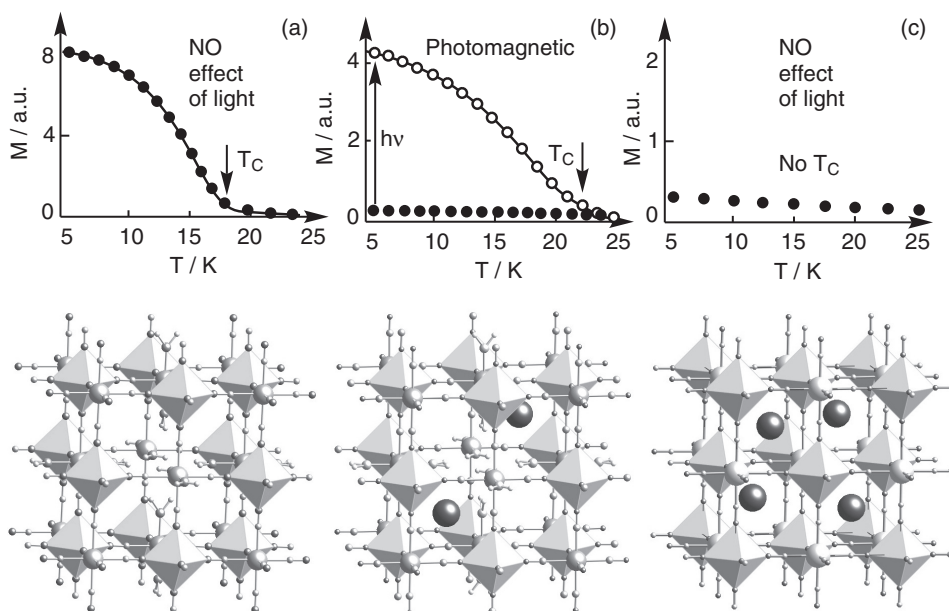
The simple argument proposed by Hashimoto to explain the photomagnetism of their compound was that for some reason a few $\text{Co}^{\text{III}}\text{-NC-Fe}^{\text{II}}$ diamagnetic pairs should exist in the compound among the $\text{Co}^{\text{II}}\text{-NC-Fe}^{\text{III}}$ ones, so that photons can provoke an electron transfer:



The number of magnetic centres in the sample is therefore enhanced upon irradiation, leading to the observed increase of the magnetization. The same argument was used with success twelve years later for the $\{\text{Co}_4\text{Fe}_4\}$ molecular cube. Furthermore, the increase of the Curie temperature T_C is understood following the same argument, as we have seen in Section 2.7.3 that after Néel $T_C \propto z |J|$, (where z is the number of magnetic neighbours and J the coupling constant between neighbours). The increase in z increases T_C .

After this first finding, many studies were undertaken to answer several questions. Are there really $\text{LS Co}^{\text{III}}\text{-Fe}^{\text{II}}$ diamagnetic pairs? What is their origin? How can they be created? How can the photomagnetic properties be improved? To make a long story short [4.31–4.33], we need to return to the chemistry and structure of Prussian blue analogues. We have already written that charges are very important in inorganic synthesis, and there is probably no better example to illustrate this point than photomagnetic Prussian blue analogues. When one mixes aqueous solutions of $\text{K}_3[\text{Fe}^{\text{III}}(\text{CN})_6]$ and $\text{Co}^{\text{II}}\text{Cl}_2 \cdot 6\text{H}_2\text{O}$, a pale brown *neutral* compound precipitates $\{\text{Co}^{\text{II}}_3[\text{Fe}^{\text{III}}(\text{CN})_6]_2 \cdot n\text{H}_2\text{O}\}^0$ or $\{\text{Co}^{\text{II}}_4[\text{Fe}^{\text{III}}(\text{CN})_6]_{8/3} \square_{4/3} \cdot 4n/3 \text{H}_2\text{O}\}^0$ when reported to the conventional cell, abbreviated as $\{\text{Co}^{\text{II}}_4\text{Fe}^{\text{III}}_{8/3} \square_{4/3}\}$, where \square denotes a $[\text{Fe}^{\text{III}}(\text{CN})_6]$ vacancy (see Section 2.7.3). An even shorter abbreviation is $\{\text{Co}_4\text{Fe}_{8/3}\}$. The Co:Fe 3:2 stoichiometry is simply determined by the charges of the precursors. In the vacant $[\text{Fe}^{\text{III}}(\text{CN})_6]$ sites, water molecules replace $-\text{NC}$ ligands in the coordination sphere of cobalt. Other water molecules, termed zeolitic, fill the vacancy loosely bound by hydrogen bonds. The reader can check from the structure that the octahedral surrounding of Fe(III) is always $\text{Fe}(\text{CN}-\text{Co})_6$ (six magnetic neighbours for iron), and the mean coordination of octahedral Co^{II} is $\text{Co}^{\text{II}}(\text{NC})_4(\text{H}_2\text{O})_2$ (four magnetic neighbours for Co).

The $[\text{Fe}^{\text{III}}(\text{CN})_6]$ vacancies can be ordered or random, so that $\text{Co}^{\text{II}}(\text{NC})_4(\text{H}_2\text{O})_2$ is a mean formula (the cobalt surrounding can be also $\text{Co}^{\text{II}}(\text{NC})_5(\text{H}_2\text{O})_1$ or $\text{Co}^{\text{II}}(\text{NC})_3(\text{H}_2\text{O})_3$). When the synthesis is achieved by mixing the precursors $\text{C}_3[\text{Fe}^{\text{III}}(\text{CN})_6]$ and $\text{Co}^{\text{II}}\text{Cl}_2 \cdot 6\text{H}_2\text{O}$, in the presence of a controlled excess of C^+ cation, alkali cations are inserted into the structure. They sit on the tetrahedral positions 8g. For x C^+ cations entering, $x/3 [\text{Fe}^{\text{III}}(\text{CN})_6]^{3-}$ should leave to ensure electroneutrality of the solid (in an ideal scheme where no other ions are implied in the synthesis). The stoichiometry and the number of vacancies vary (ideally) with the fraction x of inserted cations: $\{\text{C}_x\text{Co}^{\text{II}}_4[\text{Fe}^{\text{III}}(\text{CN})_6]_{(8+x)/3} \square_{(4-x)/3} \cdot n'\text{H}_2\text{O}\}^0$. A brief calculation leads to a mean cobalt(II) coordination sphere $\text{Co}^{\text{II}}(\text{NC})_{(4+x/2)}(\text{H}_2\text{O})_{(2-x/2)}$. The number of inserted cations can vary from 1 to 4, depending on the synthesis conditions (the larger x , the larger must be the excess of cation in the synthetic pot). When x reaches 4 we obtain $\{\text{C}_4\text{Co}_4\text{Fe}_3 \square_0\}$; that is, no more vacancies, a $\text{Co}(\text{NC}-\text{Fe})_6$ surrounding, and no more coordinated water.

**Fig. 4.44**

Schematic structure (upper, same symbols as in Fig. 4.43) and (photo)magnetic properties (lower) of Co–Fe Prussian blue analogues with inserted caesium cations. (a) in $\{\text{Co}_4\text{Fe}_{8/3}\square_{4/3}\}$; (b) in $\{\text{Cs}_2\text{Co}_4\text{Fe}_{10/3}\square_{2/3}\}$; (c) in $\{\text{Cs}_4\text{Co}_4\text{Fe}_4\square_0\}$ (Cs in 8g sites). Note the changing scales on the magnetization axis. (Adapted from [4.31].)

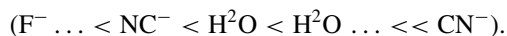
Accordingly, a series of compounds has been prepared by varying the number of inserted cations (and vacancies) and the nature of the cations. Their photomagnetism was experimentally characterized. On one side of the series, with no cation, the compound $\{\text{Co}_4\text{Fe}_{8/3}\square_{4/3}\}$ is a paramagnet down to a Curie temperature of 15–16 K, below which it orders as a ferrimagnet (Fig. 4.44a). Long-range ferrimagnetic order originates from antiferromagnetic interaction through the cyanide between the high-spin Co^{II} $S = 3/2$ and the low-spin Fe^{III} $S = 1/2$ due to the overlap of t_{2g} orbitals of cobalt and iron (see Section 2.7.3). The compound presents no $\text{Co}^{\text{III}}\text{--NC--Fe}^{\text{II}}$ diamagnetic pairs and no photomagnetic effect. On the other side, with a very high cation content the compound $\{\text{Cs}_{3.9}\text{Co}_4\text{Fe}_{11/3}\square_{1/3}\}^0$ has been prepared: (i) it is practically diamagnetic (indeed, very weakly paramagnetic); (ii) its exact composition is $\{\text{Cs}_{3.9}\text{Co}^{\text{II}}_{0.4}\text{Co}^{\text{III}}_{3.6}[\text{Fe}^{\text{II}}_{0.9}\text{Fe}^{\text{III}}_{0.1}(\text{CN})_6]_{11/3}\square_{1/3}\}^0$, which means that 90% of the initial $\text{Co}^{\text{II}}/\text{Fe}^{\text{III}}$ centres have been transformed in $\text{Co}^{\text{III}}/\text{Fe}^{\text{II}}$ by electron transfer; and (iii) it is not photomagnetic (Fig. 4.44c).

This finding is not so surprising: it means that the presence of diamagnetic pairs is a *necessary* but *not a sufficient* condition to give rise to photomagnetism. We are faced with the interesting but intriguing situation of a family of compounds $\{\text{C}_x\text{Co}_4[\text{Fe}(\text{CN})_6]_{(8+x)/3}\square_{(4-x)/3}\bullet n/\text{H}_2\text{O}\}^0$, where the two extremes of the series, $\{\text{C}_0\text{Co}_4[\text{Fe}_{8/3}\square_{4/3}]\}$ and $\{\text{C}_4\text{Co}_4[\text{Fe}_4\square_0]\}$ are non-photomagnetic, whereas the intermediate $\{\text{C}_1\text{Co}_4[\text{Fe}_3\square_1]\}$ (with one inserted alkali cation and one vacancy, or two as in Fig. 4.43b) is said to contain photo-active $\text{Co}^{\text{III}}\text{Fe}^{\text{II}}$ pairs.

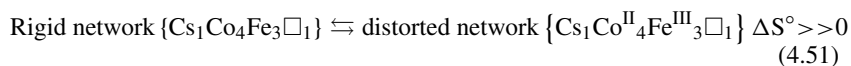
Many studies were therefore realized to characterize the photomagnetism of cobalt–iron Prussian blue analogues with intermediate cation content $\{C_xCo_4[Fe(CN)_6]_{(8+x)/3}\square_{(4-x)/3}\bullet n/H_2O\}^0$: the crystal structure (long-range by X-ray diffraction, short-range by X-ray absorption), the electronic structure—oxidation and spin state—(near-edge X-ray absorption), the magnetic properties (macroscopic with SQUID measurements, and local with X-ray magnetic circular dichroism at the cobalt, iron, and caesium edges). The emerging general conclusion is very similar to that of the molecular Co_4Fe_4 cube. There is i) the formation of diamagnetic $Co^{III}-Fe^{II}$ pairs in the ground state when decreasing the temperature, (ii) phototransformation at low temperature of the diamagnetic $Co^{III}-Fe^{II}$ pairs to metastable $Co^{II}-Fe^{III}$ paramagnetic ones, and (iii) relaxation of the $Co^{II}-Fe^{III}$ metastable state to the ground state $Co^{III}-Fe^{II}$ when increasing again the temperature.

First, let us look at the formation of the photomagnetic pairs $Co^{III}-Fe^{II}$ in the ground state. The creation of photomagnetic pairs $Co^{III}-Fe^{II}$ depends on (i) the inserted cation fraction x for a given cation, as shown for caesium in Fig. 4.45a. When x increases, the faster the $\chi_M T$ product decreases with temperature, the larger the electron transfer and the more diamagnetic pairs are present; (ii) on the nature of the cation for a given x (Fig. 4.45b, with $x = 1.8$). Caesium and rubidium are fitting better in the octants (sites 8g), and are more efficient in favouring electron transfer than the loosely bound sodium. Potassium (not shown) is intermediate.

It has been demonstrated in the very active photomagnetic $\{Cs_{0.7}Co_4Fe_{2.9}\square_{1.1}\}$ caesium derivative that the formation of the $Co^{III}-Fe^{II}$ pairs is accompanied by a displacement of the cation from a position near the vacancy to the centre of the octant (Fig. 4.46a–b). The electron transfer is partial and affects the cobalt and iron ions surrounding caesium. The whole Co–Fe network is associated cooperatively with the transfer: at room temperature (Fig. 4.46b) the structure is flexible and distorted, the rigid $[Fe(CN)_6]$ blocks are tilted, and the $Co^{II}-NC-Fe^{III}$ units are bent (the Co–N–C angle is around 167° ; Fig. 4.46d). At low temperature the rigid $[Fe(CN)_6]$ blocks rotate, the network becomes compact and more rigid (Fig. 4.46a), and the $Co^{III}-NC-Fe^{II}$ units become linear (Fig. 4.46c). The local contraction of the cobalt–neighbours distances ($\Delta d \approx 0.18 \text{ \AA}$) is followed by the consequent shrinking of the cubic cell parameter ($\Delta a \approx 0.35 \text{ \AA}$). On the other hand, precise spectroscopic measurements demonstrate that the ligand field around the cobalt, taking 1 for $\{Co^{II}(H_2O)_6\}$ as reference, is 0.55 for $Co^{II}(NC-Fe)_4(H_2O)_2$, in $\{CoCo_4[Fe_{8/3}\square_{4/3}]\}$, 0.7 for $Co^{II}(NC-Fe)_5(H_2O)_1$ and 2.4 for $Co^{III}(NC-Fe)_5(H_2O)_1$ in $\{Rb_{1.8}Co_4Fe_{3.3}\square_{0.7}\}$. This confirms that the N-bonded cyanide is a weak field ligand in the spectrochemical series



Thus we can write the following chemical equilibrium:



where in $\{Cs_1Co_4Fe_3\square_1\}$, both the cobalt and the iron are in two oxidation states. The creation of diamagnetic pairs is therefore entropy-driven, strongly related to the molecular vibrations and networks phonons.

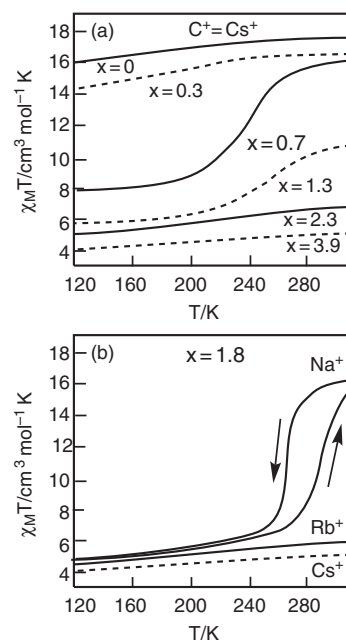
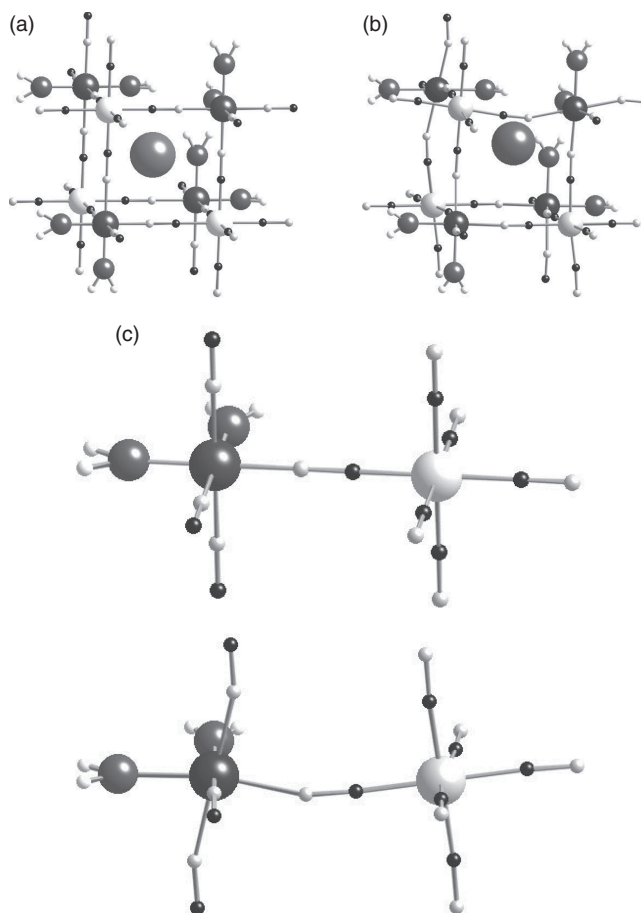


Fig. 4.45

Thermal variation of the molar susceptibility of cobalt–iron Prussian blue analogues $C_xCo_4Fe_{(8/3+x/3)}\square_{4/3-x/3}$ as a function of the inserted cation C^+ : (a) same caesium cation, $C^+ = Cs^+$, at different x fractions; (b) same fraction, $x = 1.8$, and different cations C^+ : Na^+ , Rb^+ , Cs^+ .

**Fig. 4.46**

Structural aspects of the creation of diamagnetic $\text{Co}^{\text{III}}\text{-Fe}^{\text{II}}$ pairs in the $\{\text{Cs}_1\text{Co}_4\text{Fe}_3\Box_1\}$ Prussian blue analogue. Octant's schematic structure: (a) low-temperature rigid $\text{Co}^{\text{III}}\text{-Fe}^{\text{II}}$ phase, and (b) high-temperature distorted $\text{Co}^{\text{II}}\text{-Fe}^{\text{III}}$ phase; Co-NC-Fe units; (c) linear $\text{Co}^{\text{III}}\text{-NC-Fe}^{\text{II}}$, and (d) bent $\text{Co}^{\text{II}}\text{-NC-Fe}^{\text{III}}$.

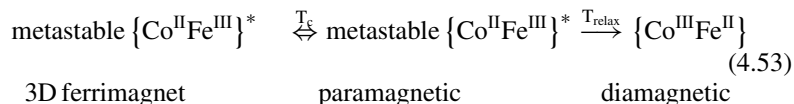
Let us now consider the photomagnetic transformations. They rely also on the previous structural and electronic analysis. The wavelength of excitation is not crucial, since the absorption spectrum of CoFe Prussian blue analogues is very broad (a lamp with $\lambda = 750 \text{ nm} \approx 1.5 \text{ eV}$ is used most often). In experiments utilizing synchrotron radiation over a range of energy much higher—several thousand eV—the excitation is also obtained. The quantum yield is difficult to measure, and is not known up to now. The diamagnetic pairs $\{\text{Co}^{\text{III}}\text{Fe}^{\text{II}}\}$ are excited to $\{\text{Co}^{\text{III}}\text{Fe}^{\text{II}}\}^*$, and the electron transfer occurs to the $\{\text{Co}^{\text{II}}\text{Fe}^{\text{III}}\}^*$ excited state, which then relaxes to the metastable state $\{\text{Co}^{\text{II}}\text{Fe}^{\text{III}}\}$ (Fig. 4.43c).



The process is accompanied by an important structural reorganization, with increase of the cobalt–ligand distances and of the unit cell parameter. A large energy is needed for such a solid's expansion. It explains why, when most of the cobalt–iron $\text{Co}^{\text{III}}\text{-Fe}^{\text{II}}$ pairs are tightly bound in a compact crystal such as $\{\text{Cs}_{3.9}\text{Co}_4\text{Fe}_4\Box_{0.1}\}$ with practically no available vacancies, the photomagnetic process does not occur (Fig. 4.44c): the unit cell is too stiff, and the expansion

of cobalt coordination sphere is too costly in energy. Instead, the presence of enough vacancies allows smooth expansion of the coordination sphere of cobalt, and permits the system to reach the metastable state after the electron transfer (Fig. 4.44b).

The photomagnetic response depends strongly (i) on the fraction of a given inserted cation; (ii) on the nature of the cation, for a given stoichiometry, in a way close to the thermal electron transfer (Fig. 4.46). The most efficient photomagnetic CoFe solid is close to $\{\text{Cs}_1\text{Co}_4\text{Fe}_4\Box_1\}$; that is, one cation and one vacancy per conventional cell (Fig. 4.46a.b). When the thermally driven electron transfer occurs with an hysteresis loop (Fig. 4.45b), it is possible to trigger the system within the hysteresis loop with a laser from low-spin to high-spin. The transition can be one-phase or two-phase, depending on the cation content, as revealed by powder synchrotron X-ray diffraction. In one-phase transitions (in $\{\text{Cs}_{0.7}\text{Co}_4\text{Fe}_{2.9}\Box_{1.1}\}$ for example), the network changes its cell parameter continuously during the photo-induced electron transfer within the same crystallographic phase. In two-phase transitions (in $\{\text{Rb}_{1.8}\text{Co}_4\text{Fe}_{3.3}\Box_{0.7}\}$ for example), the initial $\{\text{Co}^{\text{III}}\text{Fe}^{\text{II}}\}$ phase with a small cell parameter disappears progressively during excitation at low temperature to give a new $\{\text{Co}^{\text{II}}\text{Fe}^{\text{III}}\}$ phase, with a longer cell parameter. During the photoexcitation the system is biphasic. When the temperature is increased in absence of irradiation, the metastable phase $\{\text{Co}^{\text{II}}\text{Fe}^{\text{III}}\}$ feeds the ground state $\{\text{Co}^{\text{III}}\text{Fe}^{\text{II}}\}$ phase, which remains the only one at the relaxation temperature T_{relax} . The magnetic consequences of the thermal relaxation of the metastable state $\{\text{Co}^{\text{II}}\text{Fe}^{\text{III}}\}^*$ also merit interest. They are summarized as follows:

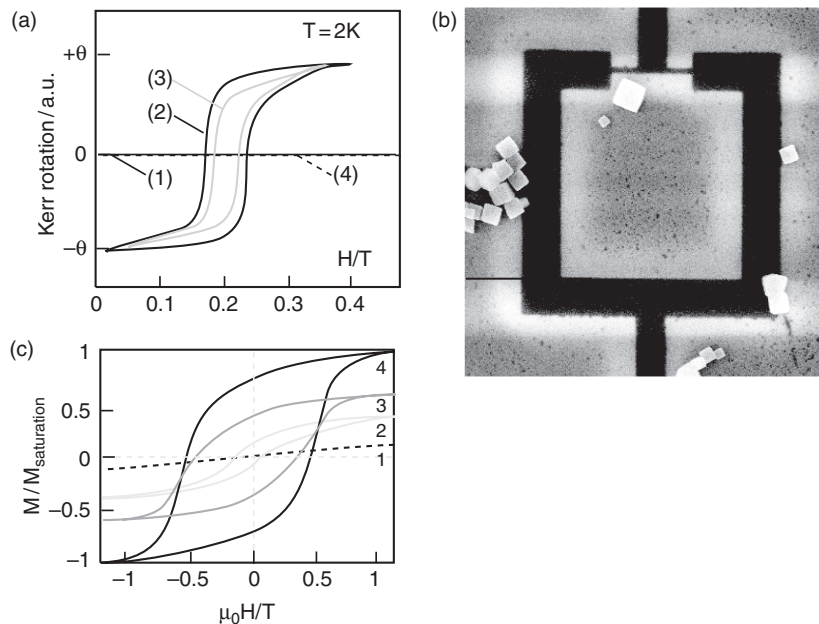


The increase of temperature after obtaining the metastable $\{\text{Co}^{\text{II}}\text{Fe}^{\text{III}}\}^*$ ferrimagnet phase at low temperature provokes two distinct events: (a) above the Curie temperature T_C , the appearance of a metastable paramagnetic phase (Fig. 4.43a); this step is reversible if the sample is not heated above the relaxation temperature T_{relax} ; (b) at T_{relax} , the relaxation to the diamagnetic phase $\{\text{Co}^{\text{III}}\text{Fe}^{\text{II}}\}$ (Fig. 4.43c); this step is irreversible. No quantitative data concerning the dynamics of the phenomenon is available.

The interest of such systems is obvious for photomagnetic information storage. Figure 4.47 reports the results of two unpublished experiments. Figure 4.47a shows a Kerr effect experiment. The Kerr effect is the rotation of linearly polarized light when reflected by a magnetized substance. The θ rotation angle is proportional to the magnetization. The experiment was realized by Ferré *et al.* (Paris-Sud University) on a powdered sample of diamagnetic $\{\text{Rb}_{1.8}\text{Co}_4\text{Fe}_{3.3}\Box_{0.7}\}$. The spot of the irradiation laser is used either to read only (low power, 0.7 mW mm^{-2}) or to read *and* write the information (high power, 70 mW mm^{-2}). The curves shown are the sum of signal recorded during two hours at a temperature of 2 K. Before irradiation, curve 1 is flat (plain line, read only at low power); the sample is not magnetized. Curve 2 (plain black line, read *and* write process, high power) displays a hysteresis curve typical of a soft magnet. Curve 3 (plain grey line, read only, low

Fig. 4.47

(a) Kerr measurements demonstrating a rewritable photomagnetic memory in microcrystalline CoFe Prussian blue analogue $\{\text{Rb}_{1.8}\text{Co}_4\text{Fe}_{3.3}\square_{0.7}\}$ (adapted from Ferré, Orsay, see text for nature of curves 1–4); (b) scanning electron microscope image of nanoparticles of $\{\text{Rb}_{1.8}\text{Co}_4\text{Fe}_{3.3}\square_{0.7}\}$ on a microSQUID; the size of the white cubic particle near the two Josephson junctions is ≈ 100 nm; (c) hysteresis curves recorded after different irradiation times: 1 (dashed) before irradiation; 2 (light grey) after 30 min irradiation; 3 (dark grey), after 100 min; 4 (black) saturation after twelve hours. (b and c from Wernsdorfer, Grenoble; personal communication. Courtesy of J. Ferré, Orsay).



power) demonstrates that the magnetic information was stored and can be read (memory effect). Finally, curve 4 (dashed line, partly hidden by curve 1, read only), recorded above T_{relax} shows that the photomagnetic information has been erased thermally. This is a first example of a rewritable photomagnetic memory. Nevertheless, before it can be used as a useful device a solution to the crucial problem of low critical temperature must be found.

On the other hand, efforts have been developed to obtain such photomagnetic systems at the nanoscale and check their photomagnetic properties. We select only one spectacular result. Figure 4.47b shows a scanning electron microscope image of cubic nanoparticles of CoFe Prussian blue analogues (≈ 100 nanometers), prepared by controlled crystal growth and lying on a microSQUID. Figure 4.47c displays the signal of this unique microSQUID, and demonstrates that photomagnetism can be induced on nanoparticles of such size. From curve 1 before irradiation (very weakly paramagnetic) to curve 4 (after twelve hours) a transition to a three-dimensional ordered magnet is observed. There is still a long way to go to produce a photomagnetic device allowing the storage of bits of information at the submicronic scale at room temperature, but demonstrative experiments now exist at low temperature.

We have now reached the end of this chapter. The reader can realize that the domain of non-linear optics is missing. In this area, the response of the system is no longer linear with the applied electromagnetic field beyond a given beam power. With cleverly designed polar and polarizable molecules, the absorption of a photon is followed by the emission of light with double or triple frequency (second or triple harmonic generation), among other aspects. But this is not the place to develop this point, which can be found elsewhere [4.34].

Instead, we have described and tried to explain the basic principles of photophysics controlling the excitation of electrons in molecules. We illustrated

them through a few selected phenomena: electron–hole separation, electron and energy transfer, and photomagnetism, which are crucial for basic knowledge and applications (light-emitting diodes, photovoltaic devices, harnessing photochemical energy, harvesting light energy, displays or/and magnetic recording). All these areas are developing very rapidly. We shall use this knowledge in the next chapter, which is devoted to molecular electronics, or the mastered electron.

References

- [4.1] (a) N. J. Turro, J. C. Scaiano, V. Ramamuthy, *Principles of Molecular Photochemistry: An Introduction*, University Science Books, Sausalito, 2009; (b) *Photophysics of Molecular Materials*, G. Lanzani Ed., Wiley-VCH, New York, 2006.
- [4.2] P. W. Atkins, *Physical Chemistry*, 5th edn., Oxford University Press, Oxford, 1994, p. 592.
- [4.3] (a) R. J. Watts, *J. Chem. Ed.* 60 (1983), 834–42; (b) W. L. Wallace, A. J. Bard, *J. Phys. Chem.* 83 (1979), 1350–7; (c) E. Bolton, M. M. Richter, J. Selco, *J. Chem. Ed.* 78 (2001), 47–8.
- [4.4] J. A. Treadway, P. Chen, T. J. Rutherford, F. R. Keene, T. J. Meyer, *J. Phys. Chem. A* 101 (1997), 6824–6.
- [4.5] (a) J.-P. Sauvage, J.-P. Collin, J.-C. Chambron, S. Guillerez, C. Coudret, V. Balzani, F. Barigoletti, L. De Cola, L. Flamigni, *Chem. Rev.* 91 (1994), 993–1019; (b) I. M. Dixon, J.-P. Collin, J.-P. Sauvage, L. Flamigni, *Inorg. Chem.* 40 (2001), 5507–17.
- [4.6] (a) T. A. Moore, D. Gust, *et al.*, *Nature* 307 (1984), 630–2; (b) M. R. Wasielewski, *Chem. Rev.* 92 (1992), 435–61.
- [4.7] (a) C. W. Tang, S. A. VanSlyke, *Appl. Phys. Lett.* 51 (1987), 913–5; (b) J. H. Burroughes, R. H. Friend, *et al.*, *Nature* 347 (1990), 539–41; (c) L. S. Hung, C. H. Chen, *Mat. Science Eng.* R39 (2002), 143–222.
- [4.8] (a) M. Grätzel, *Inorg. Chem.* 44 (2005), 6841–51; (b) M. Grätzel, *Acc. Chem. Res.* 42 (2009), 1788–98; (c) S. Fantacci *et al.*, *J. Am. Chem. Soc.* 125 (2003), 4381.
- [4.9] <<http://www.solaronix.ch/>>; <<http://www.konarka.com/>>; <<http://www.dyesol.com/>>
- [4.10] (a) A. F. Hayduk, D. G. Nocera, *Science* 293 (2001), 1639–41, (b) J. L. Dempsey, A. J. Esswein, D. R. Manke, J. Rosenthal, J. D. Soper, D. G. Nocera, *Inorg. Chem.* 44 (2005), 6879–92.
- [4.11] (a) R. E. Blankenship, *Molecular Mechanisms of Photosynthesis*, Blackwell Science, Oxford, 2002; (b) <<http://www.life.illinois.edu/govindjee/>>
- [4.12] M. D. K. Nazeeruddin, M. Grätzel, in *Comprehensive Coordination Chemistry*, Elsevier, Amsterdam, 2004, chap. 9.16.
- [4.13] (a) K. Wynne, G. D. Reid, R. M. Hochstrasser, *J. Chem. Phys.* 105 (1996), 2287–97; (b) K. Wynne, R. M. Hochstrasser, *Adv. Chem. Phys.* 107 (1999), 263–390.
- [4.14] P. J. Reid, C. Silva, P. F. Barbara, L. Karki, J. T. Hupp, *J. Phys. Chem.* 99 (1995), 2609–16.
- [4.15] (a) T. Förster, *Ann. Phys.* 6 (1948), 55; (b) D. L. Dexter, *J. Chem. Phys.* 21 (1953), 836–50; (c) P. Piotrowiak, in *Electron Transfer in Chemistry*, V. Balzani (ed.), vol. 1, part 1, Wiley-VCH, Weinheim, 2001, pp. 215–37; (d) A. Tramer, in *Photoprocesses in Transition Metal Complexes, Biosystems and Other Molecules*, E. Kochanski (ed.), Kluwer Academic Publishers, Dordrecht, 1992, pp. 1–47.
- [4.16] B. Schlicke, P. Belser, L. De Cola, E. Sabbioni, V. Balzani, *J. Am. Chem. Soc.* 121 (1999), 4207–14.
- [4.17] R. W. Wagner, J. S. Lindsey, *J. Am. Chem. Soc.* 116 (1994), 9759–60.

- [4.18] G. L. Closs, M. D. Johnson, J. R. Miller, P. Piotrowiak, *J. Am. Chem. Soc.* 111 (1989), 3751–3.
- [4.19] S. Serroni, S. Campagna, F. Puntoriero, F. Loiseau, V. Ricevuto, R. Passalacqua, M. Galletta, *C. R. Acad. Sciences, Chimie* 5 (2003), 883–93.
- [4.20] G. McDermott, S. M. Prince, A. A. Freer, A. M. Hawthornthwaite-Lawless, M. Z. Papiz, R. J. Cogdell, N. W. Isaacs, *Nature* 374 (1995), 517–21.
- [4.21] G. Trinkunas, J. L. Herek, T. Polivka, V. Sundström, T. Pullerits, *Phys. Rev. Lett.* 86 (2001), 4167–70.
- [4.22] (a) M. R. Wasielewski, *Acc. Chem. Res.* 42 (2009), 1910–21; (b) Y. Nakamura, N. Aratani, A. Osuka, *Chem. Soc. Rev.* 36 (2007), 831–45.
- [4.23] D. Gust, T. A. Moore, A. L. Moore, *Acc. Chem. Res.* 42 (2009), 1890–8.
- [4.24] (a) S. Decurtins, P. Gütlich, C. P. Köhler, H. Spiering, A. Hauser, *Chem. Phys. Lett.* 105 (1984), 1; (b) C. Roux, J. Zarembowitch, B. Gallois, T. Granier, and R. Claude, *Inorg. Chem.* 33 (1994), 2273.
- [4.25] S. Cobo, D. Ostrovskii, S. Bonhommeau, L. Vendier, G. Molnár, L. Salmon, K. Tanaka, A. Bousseksou, *J. Am. Chem. Soc.* 130 (2008), 9019–24.
- [4.26] J.-M. Herrera, V. Marvaud, M. Verdaguer, J. Marrot, M. Kalisz, C. Mathonière, *Angew. Chem., Int. Ed.* 43 (2004), 5468.
- [4.27] D. Li, R. Clérac, O. Roubeau, E. Harte, C. Mathonière, R. Le Bris, S. M. Holmes, *J. Am. Chem. Soc.* 130 (2008), 252.
- [4.28] C. Mathonière, M. Verdaguer, B. Sieklucka, V. Marvaud, A. Bleuzen, *Inorg. Chem.* 48 (2009), 3453–66.
- [4.29] O. Sato, T. Iyoda, A. Fujishima, K. Hashimoto, *Science* 272 (1996), 704.
- [4.30] M. Verdaguer, *Science* 272 (1996), 698–9.
- [4.31] A. Bleuzen, C. Lomenech, V. Escax, F. Villain, F. Varret, C. Cartier dit Moulin, M. Verdaguer, *J. Am. Chem. Soc.* 122 (2000), 6648–52.
- [4.32] V. Escax, A. Bleuzen, M. Verdaguer, C. Cartier dit Moulin, F. Villain, *J. Am. Chem. Soc.* 123 (2001), 12536–43.
- [4.33] O. Sato, *Acc. Chem. Res.* 36 (2003), 692–700.
- [4.34] R. W. Boyd, *Nonlinear Optics*, 2nd ed., Academic Press, San Diego, 2003.

The mastered electron: molecular electronics

5

5.1 Introduction and historical account

As we have seen in previous chapters, there are many ways to control the behaviour of electrons in molecules, by playing with magnetic effects, electrical fields, or excitations with photons. Mastering electron behaviour in molecules can become a reality leading to an ambitious goal: molecular electronics. *Molecular electronics unifies the richness of molecular chemistry and electronics.*

In a broad sense, the topic can be defined as the manipulation of electrical, optical, or magnetic signals in devices made from molecules. The concept appeared in the 1980s, boosted by the continuous miniaturization of electronic circuits (see Box ‘Moore’s law’). This led to the idea that instead of going down, ‘top down’ (shrinking more and more electronic circuits by the progress of lithography), it was time to start from the bottom, ‘bottom up’, by building perfectly controlled atomic assemblies—molecules—and then associating them to realize circuits. But an even more important motivation came from the extreme richness of molecular chemistry, compared to the apparent simplicity of conventional inorganic materials used in microelectronics, such as silicon, germanium, III–V semiconductors, and so on. This richness suggests many possibilities of reaching qualitatively new functions by associating several properties [5.1, 5.2, 5.3]. We describe in this chapter the endeavours to master electrons, extending to the tiny and to the complex.

Moore’s law

At the dawn of electronics, transistors and other components were fabricated and assembled one by one. Then came the era of integration—the realization of many transistors in parallel by a planar process on a silicon chip. After only a few years of this new mode of fabrication, in 1965 Gordon Moore (who later was to be one of the founders of Intel) formulated his famous ‘law’: ‘The number of transistors integrated on a chip doubles every two years’. The extraordinary aspect of this prediction is that it was formulated only three years after the beginning of integration, but remained valid for more than forty years.

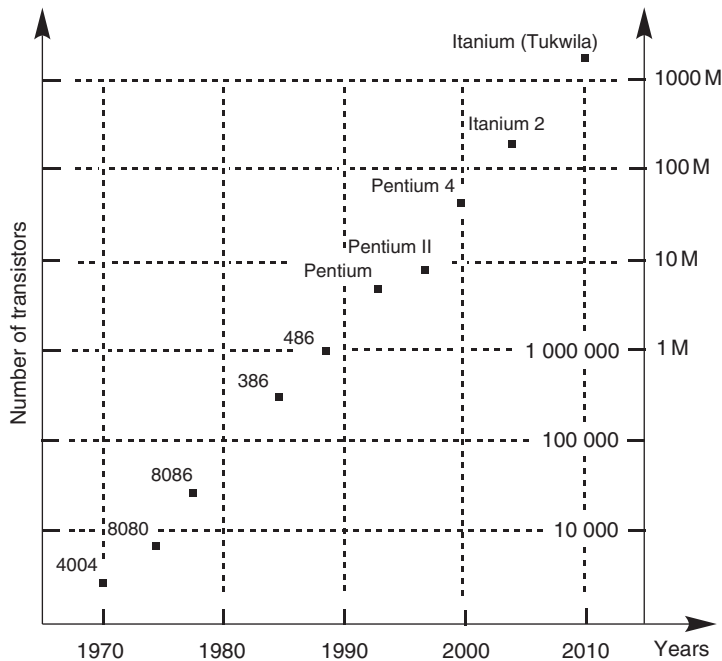


Fig. 1
Increase over the years in the number of transistors integrated on a chip (log scale), with the name of popular processors.

The increase in the number of transistors integrated on a chip was essentially due to the decrease in size of each component (the size of the silicon wafer on which circuits are realized did not increase very much). Thus an alternative formulation of Moore's law could be: 'The minimum feature size one can realize on a silicon chip (and thus the size of a typical transistor) decreases by

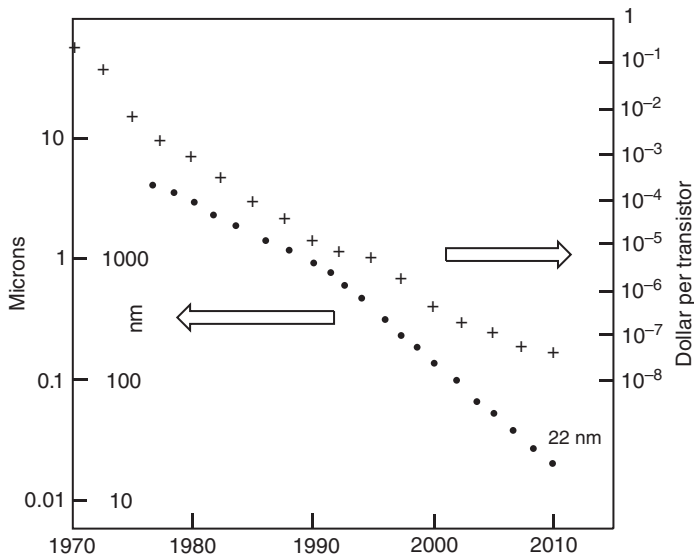


Fig. 2
Decrease of the transistor dimension (log scale) and of the average transistor price with time. (Adapted from Intel: www.intel.com/technology/mooreslaw.)

a factor of two every four years'. From the beginning of the integration era to now, the minimum feature size has decreased from several tens of microns to 65 nm for present processes. This continuous decrease has been the result of a series of technological improvements rather than the result of a unique scientific breakthrough. At the same time as dimensions decreased, the energy consumption per logic operation also decreased, as well as the cost per transistor.

Of course, there must be some physical limits to the continuous reduction in size, and no exponential law can last forever. After several decades of apparent insouciance, the semiconductor industry is increasingly concerned by the approach of physical limits. Thus it is recognized that problems such as crosstalk (defect of insulation of the devices), interconnections, energy dissipation, and quality of the materials are more and more difficult and costly to solve. The opinion of experts is expressed periodically in the International Technology Roadmap for Semiconductors (ITRS). Presently, in addition to new progress in scaling—'more Moore' (a 22-nm size is now realized)—the roadmap opens the way to a new step—'more than Moore'—with functional diversification based on the improvement of integration (with 'system on chip' (SoC) combined with 'system in package' (SiP)). Another related aspect of the evolution of the semiconductor industry concerns cost and investments for new factories. Processes are more and more demanding in terms of complexity and accuracy. It is admitted now that the cost of a new factory doubles at each generation of processes—over a period of three years—and could become prohibitive. In 2010 it reached around \$5 billion—a figure greater than the Gross National Product of many countries.

Thus, for both fundamental and financial reasons, no exponential can go on for ever.

Over the last ten years the interest in molecular electronics has also been boosted by the general motivation about nanosciences and nanotechnologies. These topics share with molecular electronics the same motivation for size reduction, for the most precise control of the objects to be built (ideally at the atomic scale), and the pervasive occurrence of quantum effects. Molecular electronics can now be considered as a branch of nanosciences, and takes full advantage of the existence of nanotechnologies.

Meanwhile, molecular electronics is dealing with more and more complex systems, programming either several functions in the same molecule (molecular chemistry) or self-assembling building blocks with the desired functions (supramolecular chemistry).

The definition of molecular electronics presented here encompasses two limiting cases, which have been frequently amalgamated in the past: (i) the achievement of electronic functions using *molecular materials*—a large number of molecules, the behaviour of any practical device being largely determined by cooperative effects—and (ii) the achievement of functions based on *single molecules*. There is an intermediate case (iii) in which one uses an ensemble of molecules, but without interaction between themselves. In this last case, a large number of molecules is necessary to obtain sufficient signal, as the system is usually probed by some kind of spectroscopic technique, giving rise to an average response.

In this chapter we privilege the second approach, which constitutes the heart of molecular electronics. Implementing an electronic function at the scale of

a unique molecule is an important and exciting scientific challenge. It necessitates the maximum control of the molecule's behaviour, of its interaction with the macroscopic world, and a full understanding of the quantum nature of its response. The third approach will also be considered, as it allows linking in a precise way the properties of the molecule to the desired function, and frequently constitutes an intermediate step between the elaboration of new molecules and their use in single molecule experiments. Such molecular systems gathering several functions are of peculiar interest.

From an historical point of view, mastering the behaviour of electrons is an intrinsic goal of chemistry, from its very beginning. Thus electronic effects (breaking and building bonds, concept of donor or acceptor groups, polarization, conjugation) have been in the background of chemists' knowledge for a very long time. But the objective has long been to control reactivity. The advent of conducting polymers in the 1960s showed that organic macromolecules—considered at that time as insulating—could contain mobile electrons, and that metallic conductivity was not restricted to metals. This is well explained by the band model (see Sections 1.4 and 3.3), and seems trivial more than forty later, but at that early time it was a conceptual revolution.

As far as molecular materials are concerned (approach (i)), the subject is indeed extremely wide, and could justify a whole textbook. Let us mention that molecules, as molecular assemblies, are already and increasingly used in electronics, under different forms: liquid crystals for displays, polymers for lithographic photoresists, organics for light-emitting diodes (Section 4.3.3), and so on. A new scientific area is developing under the name of 'organic electronics'. We invite the reader to consult more detailed and extensive references on these subjects [5.4]. Regarding electric properties of molecular and macromolecular materials, after several decades of research, the field has now reached maturity. Thus molecular semiconductors are a reality and can be used in diverse applications such as thin-film transistors, solar cells (Section 4.3.4), gas sensors, and so on [5.5]. A particularly important application is in light-emitting diodes based on conjugated polymers. The effect was discovered inadvertently in 1989, and has since been subject to tremendous development [5.6]. It was presented in Section 4.3.3. The great interest of these materials resides in their ease of processing by methods adapted to the deposition on a flexible substrate, such as painting or spin-coating (that is, applied on a fast-rotating substrate to spread a thin layer of the liquid by centrifugal effect). It is probable that they will find increasing applications in many common objects such as cell phone displays, or even large panels for traffic signals.

However, using an organic conductor or semiconductor instead of silicon for its bulk properties does not change radically the concepts of electronics. A big leap was achieved in 1974, when Aviram (from IBM, Yorktown Heights) and Ratner (then at the University of New York) proposed the idea of a *molecular rectifier*, constituted by a single molecule connected to two ultra-thin metallic electrodes [5.7].

Although it was not noticed immediately, it proved to be a really revolutionary idea, because it was the first detailed application of the concepts of electronics to a single molecule—an object which cannot be characterized by bulk properties such as resistance, relying on statistical physics. The

generalization of this approach occurred a few years after, in particular under the impulsion of Carter [5.8], who made a plethora of propositions for ‘molecular electronic devices’ performing the basic functions of electronics, such as transmission, rectification, switching, amplification, and information storage. During the larger part of the 1980s, however, it was impossible to test the *individual* properties of molecules, so that most of the propositions remained ‘thinking experiments’ (*‘gedanken experiments, expériences de pensée’*).

In 1981 the appearance of the scanning tunnelling microscope (STM), invented by Binnig and Rohrer (recipients of the Nobel Prize in Physics in 1986 [5.9], together with Ruska, the inventor of the more conventional electron microscope), was another breakthrough. The STM is based on the tunnel current arising between a metallic surface and the apex of a metallic tip brought in close proximity to it. Two important consequences result from this setup: (i) the system fully uses the quantum nature of electrons, which can cross the void between the metallic conductors, though they do not have enough energy in the classical model, and (ii) the size of the active part of the device is extremely small, of molecular dimensions. These characteristics were soon recognized as the first practical opportunity to study electron transport through unique molecules, by allowing the realization of metal/molecule/metal junctions of controlled dimensions. But in addition, it turned out that the STM tip is not only an *observation* tool but also a *fabrication* tool (Fig. 5.1). Thus, in 1991 Eigler started a pioneer work by imaging and manipulating a single xenon atom [5.10]. The extension to molecules appeared soon afterwards, with the STM study of the current through a C_{60} molecule [5.11a]. Now, twenty years after these breakthroughs, a huge number of molecules have been studied under the tip of an STM, the most precise results being obtained under ultra-high vacuum (UHV) at low temperatures. Molecules have been specially elaborated to present specific functions and behave as mechanical or electronic elements, or even to permit selective bond formation by local activation of a specific group [5.11b]. A special effort is devoted to switches [5.11c]. It is also possible, by using a magnetic tip, to perform the spin-mapping of atomic or molecular deposits [5.11d]. These realizations pave the way for molecular nanotechnology, including chemistry at the nanoscale.

It is important to stress at this point that a molecule is a quantum object and that any kind of macroscopic tool to observe it will have direct consequences on the properties of the molecule and will, more or less, modify them. The reader will realize soon that in many cases what is observed is not the property of the initial molecular system itself but *the property of the system in*

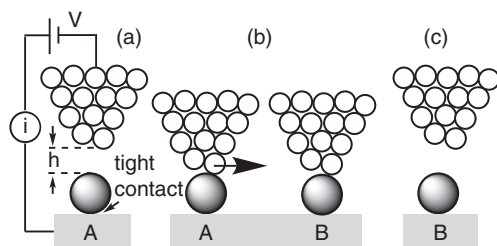


Fig. 5.1

Schematic drawing of an STM tip: (a) the tip acts as an observation tool measuring a tunnelling current i in site A, giving information on the tip-to-object distance, h ; (b) the tip acts as a manipulating tool, displacing an atomic or molecular object from site A to site B on the surface; (c) the tip is ready to measure at site B.

interaction with the measuring tool. This intrinsic drawback was predicted a long time ago by pioneers in quantum mechanics, and is now experienced daily by the scientists working in this field.

Returning to the metal/molecule/metal junctions, their realization with a STM is, of course, a laboratory demonstrator for fundamental studies. Their practical mass fabrication requires a planar process. Several methods based on microelectronics processes have been proposed [5.12, 5.13], and are described in Section 5.2.1.

We begin this chapter with the concept of ‘hybrid molecular electronics’, in which molecules are connected through metallic conductors. As we shall see, in the last ten years the basic functions of electronic devices (namely transmission, rectification, switching) have been really achieved with a device made of just one molecule. Then we shall expand the discussion to assemblies of active, ‘smart’ molecules, either in solution or in the solid state. Finally, in the conclusion, we shall discuss the possible evolution of the subject, and the trends that can be forecast already.

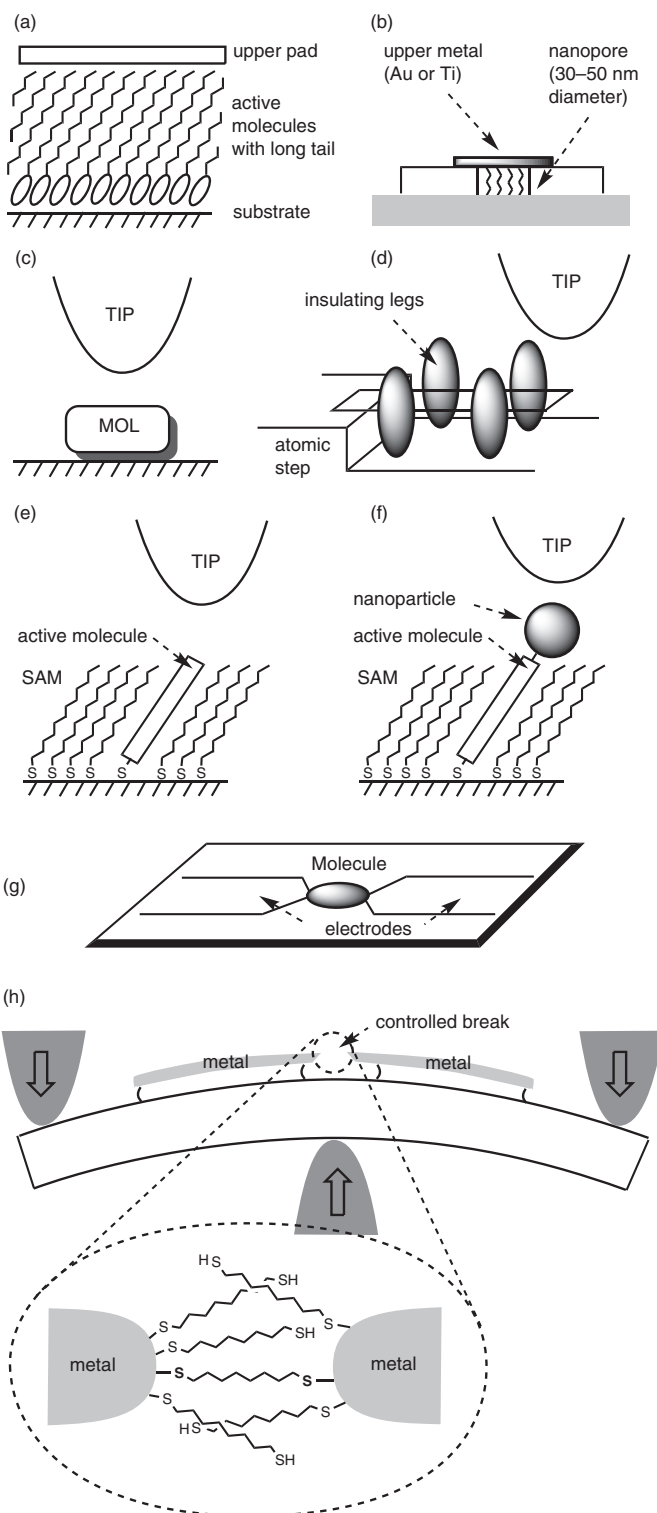
5.2 Hybrid molecular electronics

We call *hybrid molecular electronics* [5.14] a situation in which molecular components made of single molecules are used to process signals, but they are still connected to metallic conductors of very small dimensions (nanometer-sized or below). The metallic pads ensure the connection between the different molecular elements. In this situation, electrons cross the molecular system but usually do not reside in it: they jump from one metallic conductor to the other, where they are thermalized. The process is a variant of the electronic tunnelling effect, because the energy levels of the molecular system are usually too high, when compared to the Fermi levels of the two metallic connections. But, as in the electron transfer process (Section 3.2), the chemical nature of the molecule plays a role to facilitate electron transport.

5.2.1 Realization of metal–molecule–metal connections

Realizing a metal–molecule–metal unit in a controlled way, to address ideally a single molecule, is a great challenge. On the one hand, molecules are very small objects, with sizes of typically a few nanometers. On the other hand, until a recent date, most artificial structures that could be elaborated, using, for instance, microlithography, were far larger—typically several hundreds of nanometers. The situation has changed in the last fifteen years, and there are now several available techniques for realizing metal–molecule–metal connections. They are illustrated in Fig. 5.2 and are discussed briefly next. Since the useful parts of the electrodes which interact with the molecule are necessarily of nanometric dimensions, the metal–molecule–metal system is called, in the following, a *nanojunction*.

Broadly speaking, the connection methods can be divided into two groups: ‘vertical configuration’ and ‘horizontal configuration’ methods—‘vertical’ and ‘horizontal’ referring to the orientation of the current flow with respect to

**Fig. 5.2**

Processing of metal–molecule–metal connections (nanojunctions). (a) Using Langmuir–Blodgett films; (b) nanopore method; (c) using the tip of an STM (direct connection, rarely used); (d) with a molecule blocked on an atomic step (it must be equipped with insulating legs); (e) with molecules embedded in a self-assembled monolayer (SAM); (f) through gold nanoparticles ensuring contact; (g) planar connection to nanoelectrodes; (h) break junction technique. (See text.)

the substrate surface. Another important classification distinguishes methods involving a statistical ensemble of many molecules addressed in parallel, and methods allowing measurements on a single molecule.

We begin with ‘vertical’ methods. The first attempts were based on Langmuir–Blodgett (LB) films, using amphiphilic molecules, usually made of a polar (hydrosoluble) head and a long aliphatic tail. The molecules orient in a parallel way at a water–air interface, and are then deposited on a conducting substrate. Depositing a conducting pad on the top of the film allows the electrical connection (Fig. 5.2a). However, even when reducing the lateral dimensions of the pad, the measurement bears on a large number of molecules. The method is thus sensitive to defects of the LB layers—in particular, those acting as short-circuits.

A related method relies on the preparation of a nanopore (30–50 nm in diameter) in a thin layer of an insulating substance deposited on a metal electrode. Molecules are then deposited and spontaneously fill the nanopore in an organized way, with in principle few or no defects. Then an upper electrode is evaporated on the top of the structure (Fig. 5.2b). The number of addressed molecules is typically a few thousand [5.15].

The use of the scanning tunnelling microscope (STM) is the main basis of methods allowing single molecule measurements. Since the tip can be positioned with an extreme accuracy (less than 0.1 nm), it can be positioned just above the desired molecule, itself lying on the conducting substrate. The advantage is that the geometry of the system can be known precisely, and in some respect can be modified, for instance, by varying the tip–substrate distance h (Fig. 5.1a and 5.2c). A drawback is that most molecules slip on surfaces. In addition, it is difficult to stabilize accurately the tip position, except at very low temperatures. Finally, the junction is asymmetric, since the contact of the molecule is tighter with the substrate than with the STM tip, and this can have deep consequences for the behaviour of the junction.

Due to the mobility of molecules, the ‘direct’ STM method (Fig. 5.2c) is rarely used, and several variants or refinements have been described. Thus one can design molecules which can spontaneously adsorb on atomic steps, and thus stay still there. Atomic steps exist on most crystalline surfaces, giving rise to terraces. Their occurrence and properties are well known, so it is possible to adapt the shape of the molecules to the step geometry (Fig. 5.2d). The molecules are usually built from a planar ‘conducting’ board equipped with ‘insulating’ and bulky ‘legs’ [5.16]. The advantage of this method is that the metal–molecule connection is perfectly defined, even at the atomic scale. The quality of the contact (in other words, the nature of the interaction between the tool and the object) is indeed a key point in many studies.

Another way to immobilize molecules is to embed them in a self-assembled monolayer (SAM). Usually the SAM is made of alkanethiols deposited on gold. The thiol function makes an extremely strong covalent bond with the gold atoms of the surface, and the alkyl chains pack together in a compact way (Fig. 5.2e). The alkyl chain being saturated does not contribute appreciably to electron transport. Thus, if an active molecule, equipped with a thiol function, is introduced during the SAM formation, it is enclosed in the SAM in a ‘vertical’ position. The other molecular end can then be approached by the STM tip.

A variant of the SAM method makes use of nanoparticles. Molecules bearing two thiol functions, one at each end, are dispersed in a SAM of alkanethiol. A solution containing gold nanoparticles is then deposited, which leads to the attachment of a nanoparticle on the outer thiol function. Finally, the nanoparticles are individually contacted by a gold-coated tip of an atomic force microscope (Fig. 5.2f). The great advantage of this method is to yield highly reproducible contacts [5.17].

Vertical methods based on the STM are, of course, extremely efficient for demonstration purposes, but they rely on a complex system unsuitable to mass fabrication and studies. Several other methods have been proposed, taking advantage of the progress in micro- and even nano-fabrication. They can be qualified as ‘horizontal’ or ‘planar’ because the two electrodes are in the plane of the substrate.

The most direct method can be called ‘planar’ in the spirit of the planar realization of most electronic devices. The molecule is deposited on an insulating substrate (usually SiO_2) on which two small metallic electrodes have been prepared by electron-beam (e-beam) lithography (Fig. 5.2g). The challenge is, of course, to put the molecule in the right place, with the right orientation. Regarding electrodes, they must be extremely small. But the resolution of electron-beam lithography is hampered by many factors: the size of the electron beam, the effect of secondary electrons in the e-beam writing process, the imperfections of the resist, and the grain structure of the deposited metal. Pushing the method to its extreme limits has allowed the realization of junctions in the 5 nm size range [5.18]. The method is convenient only for very long molecules—in particular, carbon nanotubes—because the exact distance between electrodes cannot be accurately fixed. Note that the electrodes must be *buried* in the insulating substrate, otherwise the molecule fixation, and its detection, for instance, by STM, are always problematic.

In the break junction method (Fig. 5.2h) one starts from an ultra-small metal wire at the surface of an insulating substrate. The sample is then progressively curved by the progressive action of a piezoelectric actuator (grey cones in Fig. 5.2h). The small wire (light grey) breaks eventually, and the size of the gap can be controlled in an extremely accurate way by the flexion [5.19]. Molecules are then deposited by wetting the junction with a solution. Frequently, one uses elongated molecules bearing thiol functions at each of their ends, so that they attach to gold electrodes. The length of the molecules (determined by the chemical synthesis) must, of course, match the length of the gap, which can be tuned by the operator. Adjusting the experimental parameters while monitoring the electrical response of the system can lead to conditions where just *one* molecule (shown by bold S in Fig. 5.2h) is connected between the two electrodes.

Electromigration is a related technique in which a gold nanowire (prepared by e-beam lithography) is covered with molecules of interest. Then the wire is broken by electromigration (that is, by application of a ‘large’ current, like for a fuse) [5.20]. The experiment is performed in parallel on many junctions, so that some interelectrode gaps are bridged by a single molecule. The measurements are then made only on *these* bridged junctions (which are identified by their special electrical response), and the others are discarded.

5.2.2 Principles of electrical conduction in nanosystems

5.2.2.1 Parameters defining the problem

The molecule lies between two metal electrodes and is assumed to be in interaction with the two. The interaction will be generally considered as weak, so that it is still possible to recognize the properties of the molecule. One can apply a potential difference V between the two electrodes ($V = E_{>0} - E_{<0} > 0$), which is called the *bias voltage*. The junction is then said to be polarized. A general description of the system is based on the scheme shown in Fig. 5.3.

The Fermi energies E_{F1} and E_{F2} are also called electrochemical potentials μ_1 and μ_2 . The difference between these energy levels is related simply to the electrical potential difference by:

$$(E_{F1} - E_{F2}) = (\mu_1 - \mu_2) = eV \quad (5.1)$$

From now on, the symbol e designates the absolute value of the elementary charge: $1.6 \cdot 10^{-19}$ C. The molecule is characterized by a series of electronic levels (orbitals), with energies denoted ε_i , some of the orbitals being occupied and others not. To simplify in a first step, we consider only the case of a closed-shell molecule. The usual convention for *one-electron* energies is to refer them to the level of an electron in vacuum, away from the molecule and with zero kinetic energy. Thus the energies of occupied molecular orbitals are necessarily *negative* (the molecule is stable). They can be determined by photoelectron spectroscopy. The energy of the highest occupied molecular orbital (HOMO) corresponds, after a change in sign, to the first ionization potential of the molecule. Typical values for HOMO energies of stable molecules are in the range -8 to -12 eV.

In the same way, the vacant levels can be probed by electron attachment experiments. The energy of the lowest unoccupied molecular orbital (LUMO) is related to the electron affinity of the molecule. Typical values of LUMO energies are in the range -2 to 0 eV. Positive values are due to interelectronic repulsion U . Above zero energy the anion radical formed by electron attachment is not stable.

Regarding electrodes, they are described by the band model (see Sections 1.4 and 3.3). The important parameter is the Fermi energy E_F . The Fermi energies of two electrodes made of the same metal are equal when the

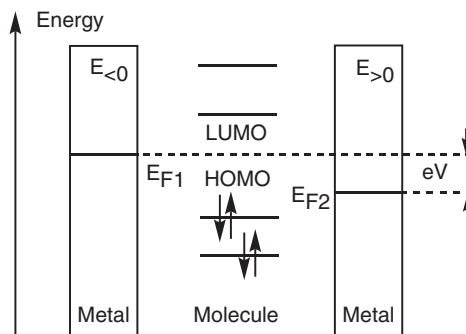


Fig. 5.3

Energy levels of the electrodes (Fermi levels E_F) and of the HOMO and LUMO frontier molecular orbitals. Typical disposition for a small bias voltage with the right electrode as positive terminal. Increasing the voltage moves downwards the levels of the right electrode with respect to the left one, due to the electron's negative charge.

junction is not polarized. Using the same convention as for molecular levels, the Fermi energy is *negative*. It corresponds, after a change in sign, to the energy necessary to extract an electron and send it to infinity with a zero kinetic energy (often called the work function of the metal, as in Section 4.3.3). In the case of gold, a frequently used metal, $E_F = -5.3$ eV.

Thus a very frequent energy situation is the one depicted in Fig. 5.3, where the Fermi levels of the electrodes fall in the gap between the HOMO and LUMO of the molecule.

Figure 5.3 is obviously an oversimplified scheme, because actually the molecular levels are modified by their interaction with the electrodes. This effect corresponds to the *chemisorption* phenomenon. Each molecular level (orbital) interacts with many levels of the electrodes. The result is a series of orbitals which can be analysed, as usual, for solid-state structures, from the density-of-states diagram, by performing a decomposition of the total density of states into contributions of fragments [5.21]. The result is termed the ‘local density of states’ (LDOS). It is the density of states weighted by the fraction of its squared wavefunction that resides on a given fragment. A common practice is to plot the LDOS in abscissa and the energy in ordinate (Fig. 5.4). Looking at the contribution coming from the molecule, two effects arise from chemisorption: a shift and a broadening.

There is an energy shift because of the orbital interaction of the molecule with the surface (bonding and antibonding—only the bonding domain is shown here), and in addition a small transfer of charge generally occurs, which modifies the levels by electrostatic effect.

The broadening is due to the large number of metallic levels corresponding to a given molecular level, distributed around an average value. In this process the symmetry of the metal–molecule contact obviously plays an important role.

The broadening is defined by its width at half-height Γ , as shown in Fig. 5.4 [5.22]. The larger the interaction, the larger the broadening (this is reminiscent of the general trend when atomic orbitals combine to give molecular orbitals; see Chapter 1). Thus Γ , which has the dimensions of an energy, is a measure of the coupling strength of a given molecular level with the electrode.

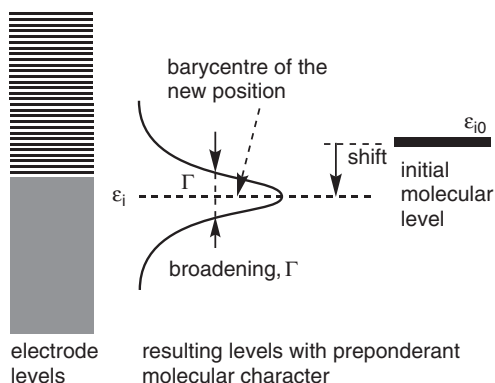


Fig. 5.4

Energy level shift and broadening Γ of a molecular level (orbital) due to chemisorption.

Molecular levels can be shifted as the result of charging effects. We have seen in Section 1.5.1.1 that one-electron energies are dependent on interelectronic repulsion energies of the form:

$$U = \langle \psi(1) \psi(2) | e^2 / r_{12} | \psi(1) \psi(2) \rangle \quad (5.2)$$

if the two electrons 1 and 2 reside in the same molecular orbital ψ . This integral was written in a slightly different form in eqn. (1.58c) for atomic orbitals and denoted as $j_0 = U$.

When the molecule is in equilibrium with a metal surface we are faced with a new problem, since the population of an orbital varies with the molecule–surface interaction and with the bias voltage. A given level with energy ε_{i0} can be occupied by a fractional number of electrons $2 f_0$, where f_0 is the Fermi function (the factor 2 coming from the spin α or β). The concept of fractional occupation is at first sight surprising, but recall that the molecular and electrode levels are mixed, so that the Fermi statistics applies indirectly to the molecular levels.

If the number of electrons is changed to a non-equilibrium value N , we need to evaluate the new repulsion energy term. As an approximation we can consider that it appears as a repulsion energy of the form $U (N - 2 f_0)$, where U is now a combination of terms as in eqn. (5.2), as many electrons and average effects are involved. This energy destabilizes the system if $N > 2 f_0$ and makes the addition of other electrons more difficult. It is thus equivalent to consider that the level floats up or down, according to [5.22]:

$$\varepsilon_i = \varepsilon_{i0} + U (N - 2f_0) \quad (5.3)$$

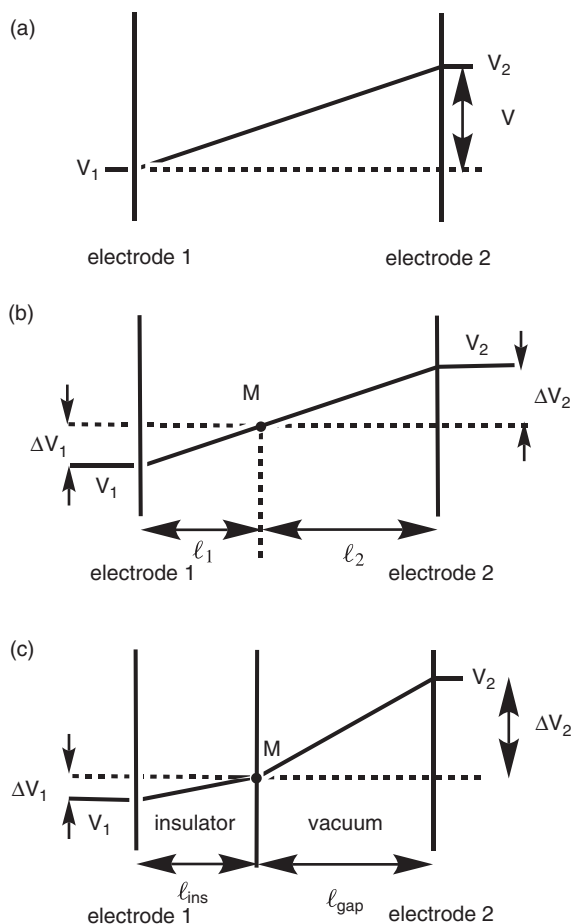
Eqn. (5.3) is in fact a ‘trick’, used for lack of something better. We should remember that in a complex system where electron–electron repulsion is present, the total energy is not the sum of one-electron energies (see Section 1.5), and thus the most stable state does not necessarily correspond to the situation where the lowest-energy orbitals are occupied. By introducing an electronic repulsion term in the energy level, as in eqn. (5.3), we restore significance to the simple reasoning based on electron occupation of the lowest levels. This convention will be used in the following, and U will play a role when successive additions (or removal) of electrons are considered.

Regarding Γ (Fig. 5.4), another physical meaning can be given. Γ (the dispersion on the energy level) can be related to τ , the lifetime of the state in the junction (the time it takes for an electron placed in this level to escape into the metal) according to:

$$\Gamma = \hbar / \tau \quad (5.4)$$

In the following we call ε_i the centre of the distribution of the molecular energy levels, after their interaction with the electrodes (see Fig. 5.4). Note that if the interaction is too great it will be difficult or even impossible to define ε_i . Generally, one of the ε_i values is close to E_F , and the corresponding level will play an important role in the transport.

Another parameter necessary for a correct description of the metal–molecule–metal interaction is the electrostatic potential across the junction. It is necessary, because the potential defines the state of polarization of the

**Fig. 5.5**

Three cases of electrostatic potential distribution inside nanojunctions. (a) No substance in the gap (vacuum); (b) a molecule considered as a point-like object in vacuum; (c) a molecule deposited on an insulating substance and approached by an STM's tip (electrode 2).

molecule under the influence of the strong electric field E existing in the nanojunction. In a simple planar model, this electric field scales as V/ℓ , where ℓ is the distance between the electrodes, in the range of nanometers (hence very small). Thus E can be very large, and this has an effect on the electrical response.

If there is nothing in the gap between the electrodes, the potential is a simple linear ramp between the potentials V_1 and V_2 of the two electrodes, themselves related to the Fermi levels E_{F1} and E_{F2} (Fig. 5.5a). When a molecule is introduced somewhere between the two electrodes (Fig. 5.5b), the problem is more complex. A crude approach is to consider the molecule as a point-like object which does not modify the potentials in the junction, and to apply the classical rules of electrostatics. Calling ℓ_1 and ℓ_2 the distances between the molecule and the electrodes 1 and 2, the voltage drop divides into two parts ΔV_1 and ΔV_2 , with $\Delta V_1 + \Delta V_2 = V$, where V is the bias voltage (Fig. 5.5b).

The two voltage drops, ΔV_1 and ΔV_2 , between each electrode and the molecule are given, in absolute values, by:

$$\Delta V_1 = \left(\frac{\ell_1}{\ell_1 + \ell_2} \right) V = \eta V \quad (5.5)$$

$$\Delta V_2 = \left(\frac{\ell_2}{\ell_1 + \ell_2} \right) V = (1 - \eta) V \quad (5.6)$$

which defines the *voltage division factor* η —a dimensionless quantity, the value of which is between 0 and 1. The η factor tells us to which actual potential the molecule is submitted.

Another frequent situation is the following (Fig. 5.5c, left): the molecule is deposited on a thin layer of an insulating substance (NaCl, Al₂O₃) covering a conducting substrate, and is approached by the tip of an STM (Fig. 5.5c, right). The curvature of the tip can generally be neglected, so that the situation is the same as with planar electrodes. Again we use a macroscopic treatment, now with the intervention of the relative dielectric constant of the insulator ϵ_r [5.23]. Calling ℓ_{ins} the thickness of the insulator and ℓ_{gap} the distance between the insulator and the STM tip, simple electrostatics shows that the total voltage drop V now divides into:

$$\Delta V_{\text{ins}} = \left(\frac{\ell_{\text{ins}}}{\ell_{\text{ins}} + \epsilon_r \ell_{\text{gap}}} \right) V \quad (5.7)$$

$$\Delta V_{\text{gap}} = \left(\frac{\epsilon_r \ell_{\text{gap}}}{\ell_{\text{ins}} + \epsilon_r \ell_{\text{gap}}} \right) V \quad (5.8)$$

Of course, if $\epsilon_r = 1$ one recovers the case of the linear ramp. Note that the electric field is much lower by a factor ϵ_r across the insulator than across a vacuum. To provide some orders of magnitude, $\epsilon_r = 8$ for bulk alumina and $\epsilon_r = 5.5$ for bulk sodium chloride.

Eqns. (5.5)–(5.8) and Fig. 5.5 are acceptable approximations for molecules lying ‘flat’ in the junction or on a substrate, so that most parts of the molecule are at the same electrostatic potential. This condition is achieved for many planar molecules deposited either on a metal or on an insulating substrate.

The situation is quite different in the case of a long molecule chemically connected by one end to electrodes. In this case the long axis is generally perpendicular to the surface, so that the molecule experiences fully the voltage drop, and polarization effects become important (Fig. 5.6). The simple notion of voltage division factor is no longer valid. Since most used molecules are conjugated—that is, they contain delocalized electrons—we can assume that they are easily polarized. Thus, according to the classical laws of electrostatics, most of the voltage drop should occur at the interfaces and only a small fraction along the molecule [5.24]. But this is a very crude approach. A more

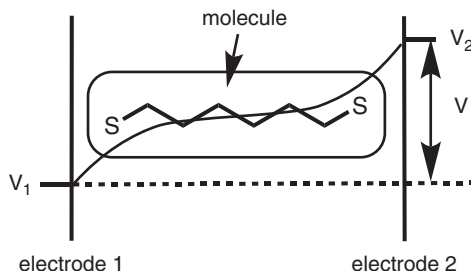


Fig. 5.6

Electrostatic potential across the junction for a long molecule chemically connected roughly perpendicular to electrodes.

rigorous treatment is necessary by solving the Schrödinger and Poisson equations for the complete system (electrodes bearing their charge, and molecule) by a self-consistent procedure, because, as seen in Section 1.5, the electrons in the molecule are subject to the field and electrostatic repulsions of all other electrons. The result gives the wavefunctions, the electronic density, and the electrostatic potential at each point of the junction.

5.2.2.2 The different mechanisms

We now have all the necessary ingredients for an overview of the different mechanisms by which a current can be transported through the metal–molecule–metal junction. We have defined four pertinent parameters describing the metal–molecule–metal junction, the Fermi energy E_F , the molecule–electrode interaction Γ , the orbital energy, ε_i and the interelectronic repulsion energy U , *assuming, however, that the coupling with electrodes is small enough, so that the molecule retains its individuality*. The different mechanisms possible appear in Fig. 5.7.

A first important classification of the transport regimes is to distinguish between 1-step and 2-step processes.*

On the one hand, in *1-step* transport (Fig. 5.7b), for each electronic event, an electron crosses the junction directly from one electrode to the other. It never localizes on the molecule, though, as will be seen, the molecular levels play a role by increasing the efficiency of the process. The process is elastic; that is, without energy exchange inside the junction. This results in a particular structure in the current noise—the random variation in the current for a fixed voltage. In the present case the frequency analysis reveals a ‘shot noise’ structure. This is typical of a system in which the current is transported by elementary charges (electrons) arriving in a random way, with a fixed probability per unit time and independence between successive events.

On the other hand, *2-step* transport (Fig. 5.7c) corresponds to two independent and successive electronic events; for instance, an electron transfer from electrode 1 to the molecule (which is temporarily reduced), and then an electron transfer from the molecule to electrode 2. During the interval between these events, the molecule temporarily bears a negative charge. (Alternatively, one can have first the right-side electron transfer, then the left-side electron transfer, and in such a case a positive charge appears temporarily on the molecule). The interval between the two transfers is randomly distributed in time. Incoherent transport is qualified as *inelastic*, because when a charge localizes on the molecule there is a relaxation of the molecular geometry. Thus some energy is dissipated inside the junction and the electron loses its phase. The structure of the noise is different.

Looking in more detail, one can identify four different regimes according to the values of Γ (the coupling) and E_G , the energy difference between the Fermi energy and the closest frontier orbital. E_G varies at the opposite of the thermodynamic tendency of the molecule to undergo a true loss or gain of electron (oxidation or reduction) at the contact of the electrode.

The four regimes [5.25] are displayed in Fig. 5.8, showing also the occurrence of 1-step and 2-step transports.

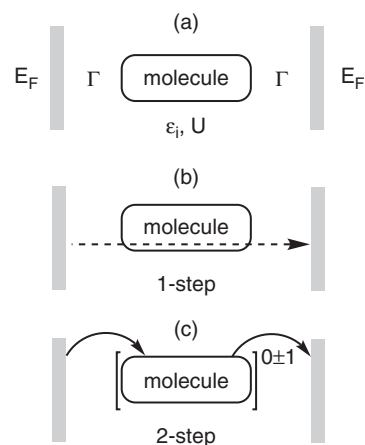
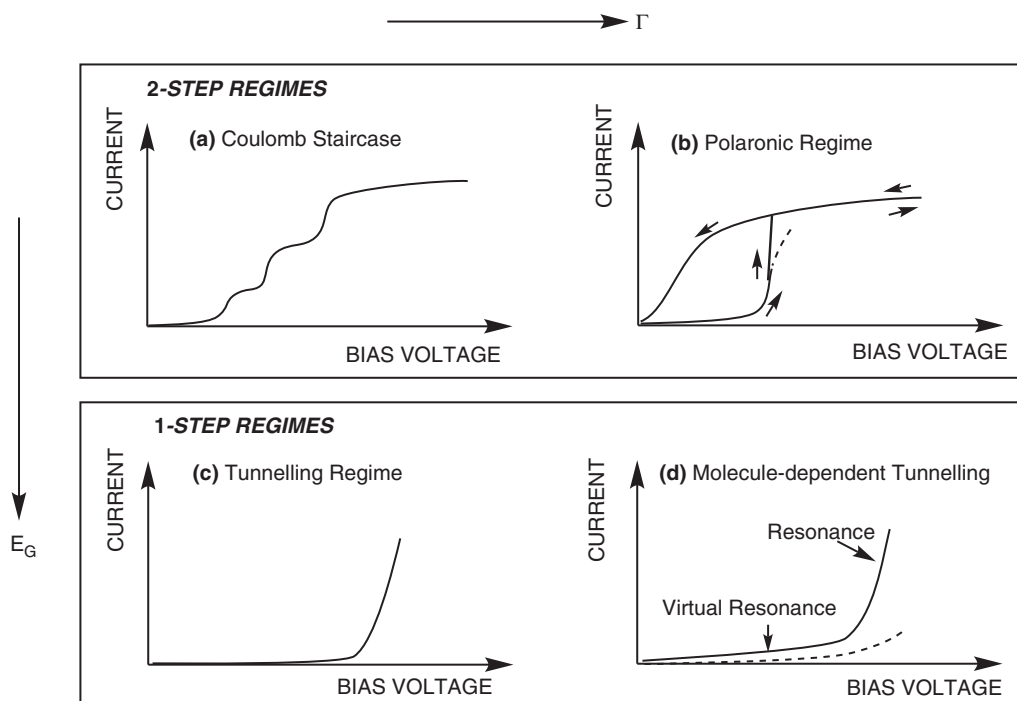


Fig. 5.7

(a) The four important parameters defining the transport regime, E_F , Γ , ε_i , U . The two classes of transport: (b) 1-step; (c) 2-step.

*Many authors use the expression ‘coherent’ and ‘incoherent’ for 1-step and 2-step respectively. ‘Coherent’ then means that the wavefunction associated with the travelling electron *keeps its phase* for the whole process, which is the case in the 1-step mechanism but not for 2-step. However there could be confusion with the notion of coherence between *different electrons*. Due to this possible misunderstanding, we avoid here this nomenclature.

**Fig. 5.8**

The different transport regimes according to E_G and Γ values. (a) Low E_G and Γ : Coulomb staircase; after a first electron exchange to or from the molecule, the transport is *temporarily* blocked by intervention of the U parameter; (b) low E_G and high Γ : polaronic (vibronic) regime; after electron exchange, the molecule relaxes to adapt its geometry to its new redox state; (c) High E_G and low Γ : tunnelling regime with little or no intervention of the molecular levels; (d) high E_G and Γ : molecule-dependent tunnelling. With respect to the previous case, the molecule plays a greater role by partial mixing of its levels with the electrode ones (see superexchange in Sections 2.6.2.2 and 3.2.2.6). The dotted line represents the current in the absence of molecule. (Adapted from [5.25].)

- (a) Low E_G and low Γ , *Coulomb staircase*. The molecule keeps its individuality and electrons move one by one. Since E_G is small, a finite voltage difference can bring molecular and electrode levels in coincidence, and true oxidation or reduction can take place. But since Γ and E_G are both weak, the behaviour can be dominated by an additional parameter, which is U . Once the molecule has been oxidized (respectively reduced) it is impossible to remove (respectively add) another electron, unless the bias voltage is increased and imposes it again. This gives a succession of steps in the current, corresponding to a so-called *Coulomb staircase*. Actually, the Coulomb staircase behaviour was discovered and conceptualized for metallic nano-islands embedded inside a junction. The phenomenon is frequently called ‘Coulomb blockade’, but we use here the denomination Coulomb staircase, more related to the experimental manifestation. In the present case we are concerned with molecules which exhibit different electronic structures, since they are not metallic. But as molecules are much smaller than these metallic nanoparticles, the two-electron repulsion is stronger and the concept of Coulomb staircase can be extended to molecules.

- (b) Low E_G and high Γ , *polaronic regime*. This case is the closest to a conventional chemical reaction. Electron addition or removal is easy, and the resulting charged species stabilizes itself by vibrational relaxation of the geometry. There is thus a genuine oxidation or reduction generating a product at thermodynamic equilibrium. The process is thus related to the Marcus–Hush theory of electron transfer in solution, and also to the mechanism of charge transport in mixed valence solids (see Section 3.3.4.2). Alternative designations are *hopping-type mechanism* or *sequential tunnelling*. In the polaronic regime there is an activation energy, because of the nuclear motion in the vibrational relaxation process. When working at low temperature on a single molecule this can lead to an hysteresis in the current–voltage curve as shown on the figure.
- (c) High E_G and low Γ , *tunnelling regime*. The molecule keeps its individuality. Since E_G is large, the bias voltage necessary to perform electron injection or removal becomes prohibitive. In the accessible voltage range one observes generally only a small tunnel current. This is the *tunnelling regime*. This transport regime was first formalized by Landauer in 1957 ([5.26], and subsequently discussed here), but at this time the junction was considered as just an energy barrier, without explicit introduction of a molecule.
- (d) High E_G and high Γ , *molecule-dependent tunnelling*. Since E_G is large we are in a tunnel regime, but amplified by the strong molecule–electrode interaction Γ . It is qualified as *molecule-dependent tunnelling*. Note that in this regime the strong Γ makes the separation of the system in two subsystems (the molecule and the electrodes) increasingly difficult. Thus the theoretical description, which is a modification of the original Landauer treatment, must consider the metal–molecule–metal nanojunction as a whole.

In the *molecule-dependent tunnelling regime* one can further distinguish two modes of transport according to the magnitude of the voltage bias. When the bias voltage is sufficiently large there is coincidence between at least one molecular level and one Fermi energy, giving rise to a large increase in current. This is called *resonant tunnelling*. For low bias voltage the molecular levels and Fermi energy level are not in coincidence, but a weak quantum mechanical mixture of levels is still possible. Such electronic interaction between two entities mediated by one molecule has been termed *superexchange* (in Section 2.6.2.2 and Section 3.2.2.6). The electron transport is qualified as *virtual-resonant tunnelling*.

With respect to the basic distinction, tunnelling and molecule-dependent tunnelling regimes are 1-step processes, while the Coulomb staircase and polaronic regimes are 2-step. 1-step tunnelling occurs for small molecules, because the tunnel effect is direct and there are few energy levels and degrees of freedom available on the molecule. Conversely, for larger and more complex molecules the system will more easily find a relaxation pathway which localizes the electron. For the same reason the temperature favours the 2-step mechanism, because thermal energy is available for a geometrical distortion (Section 3.1.2). Regarding bias voltage, at low bias 1-step tunnelling is the only

Table 5.1 The main classes of process for electron transport through a nanojunction.

	1-step	2-step
Energy exchange in the junction?	No (Elastic)	Yes (inelastic)
Other names	Direct tunnelling (coherent)	Hopping-type, sequential tunnelling, chemical mechanism (incoherent)
Conditions of occurrence	Small molecules, low temperature Preferably low bias voltage	Large molecules or nanoparticles, high temperature, frequently high bias voltage
Theoretical description	Scattering theory [5.26] or non-equilibrium Green function [5.27]	Rate equations
Sub-categories	—Tunnelling regime —Molecule-dependent tunnelling, with: —Non-resonant tunnelling (small bias) —Resonant tunnelling (large bias)	—Hopping, Coulomb staircase (for molecules) —Coulomb Blockade (for nanoparticles, carbon nanotubes)

possibility, because the molecular energy level does not line up with the Fermi levels of the electrodes (see Fig. 5.3). For high bias voltages, both processes, 1-step and 2-step, are theoretically possible.

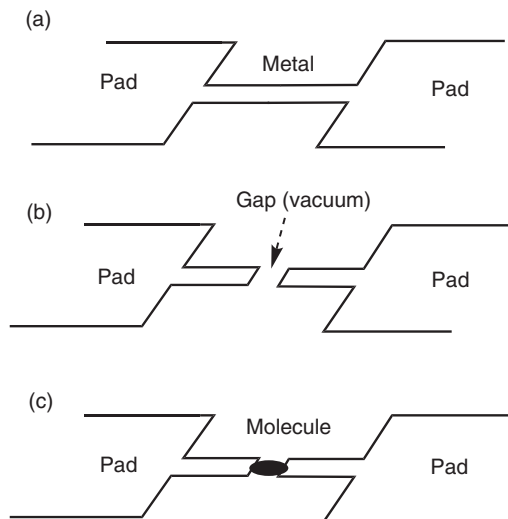
Finally, one can remark that Coulomb staircase and Tunnelling are regimes in which the role of the electronic structure of the molecule is minored, and the treatment uses essentially physical concepts. By contrast, the polaronic regime is based on the chemical concepts of oxido-reduction and molecular vibration. Finally, the molecule-dependent tunnelling regime mixes concepts from physics (the tunnel effect) and chemistry (electronic structure of the molecule). The main characteristics of the 1-step and 2-step cases are summarized in Table 5.1.

We now examine the theoretical treatments in more details. 1-step tunnelling is generally treated by a formalism initiated by Landauer [5.26], linking classical and quantum aspects through the definition of a transmission coefficient. On the other hand, 2-step tunnelling, being a sequential process, is usually treated by rate equations for the two-electron transfers. These rate equations are then combined using a stationary state principle, in analogy to the case of two consecutive chemical reactions.

5.2.2.3 1-step transport

In 1-step transport the tunnel effect involves the total system constituted by the electrodes and the molecule. Since it is a quantum process the size and geometry of the elements, including the symmetry of their contacts, play an important role and must be defined carefully.

We consider the basic architecture: the *nanojunction*. Let us start from a small continuous metallic wire of nanometric dimensions, connected to two metallic macroscopic pads (Fig. 5.9a). At the pad-to-nanowire connection there is a constriction, which will play a crucial role later. Then the inner wire is cut to leave a gap, which defines the nanojunction, the two ends being separated by empty space (Fig. 5.9b). Finally, the gap is bridged by a single molecule (Fig. 5.9c). In some cases this corresponds to the actual geometry of the system—for instance, in the planar junction method evoked previously in section 5.2.1. In other cases (methods based on the STM) it is not obvious to

**Fig. 5.9**

The basic architecture of a nanojunction, showing conceptual steps. The outer metallic wires (pads) are of macroscopic dimensions. The inner wires are nanometer-sized: (a) no gap; that is, a continuous nanowire connecting the two pads; (b) existence of a vacuum gap; (c) gap bridged by a molecule.

identify the metallic pads and the nanowires. But there is nevertheless a constriction somewhere between the macro- and nanometric conductors, and we admit that the same general theory is valid.

With normal macroscopic metallic wires, Ohm's law $V = R I$ is valid (eqn. (3.101)), and the conductance G of a sample (Section 3.3.1) is given by:

$$G = R^{-1} = \frac{s}{\rho l} \quad (5.9)$$

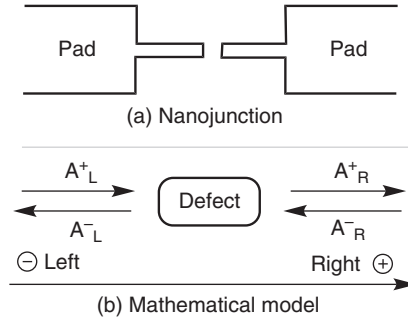
where s and l are respectively the section and the length of the sample, and ρ its resistivity. The resistivity is a *bulk property*, independent of the geometrical dimensions of the sample. Actually this behaviour comes from statistical arguments: in the solid, electrons are permanently scattered by the surrounding defects and impurities which are assumed to be distributed in a random way. This is an inelastic process, for which energy is dissipated as heat, and this is the reason for the existence of a resistance to the electron flow.

At very small scales, however, matters become more subtle, because the inelastic processes do not occur homogeneously in space. Thus, in the case of Fig. 5.9, in the inner metallic nanowires (constriction), the classical treatment is no longer valid, because of the intervention of the wavelength associated with the electron. We have thus to define the critical dimension below which new phenomena occur. Actually, there are three dimensions to consider: the Fermi wavelength λ_F associated with conduction electrons, the mean free path λ_m , and the coherence length λ_ϕ ([5.14, 5.28]; and see Box 'Characteristic lengths').

In this section we consider the case where the sample dimensions are of the same magnitude as λ_F but much smaller than λ_m and λ_ϕ . Under these conditions the quantum effects due to the constriction are present, but the electron can propagate through the sample without experiencing scattering that could change its momentum or its phase. This is the situation of *ballistic transport*. It occurs in mesoscopic systems with micrometric dimensions, which were

Fig. 5.10

Model of a nanojunction (including the nanometric wires). (a) Scheme; (b) mathematical model: the nanojunction is considered as a defect for the propagation of electronic plane waves arriving from or to the large metallic pads. The incoming amplitudes are denoted A_L^+ and A_R^- , while the outgoing ones are denoted A_R^+ and A_L^- . (see text)



intensively studied in the 1980s. The leading contribution was initiated by Landauer from 1957 [5.26], and was later refined with Büttiker [5.29].

The Landauer treatment considered the nanojunction as a defect for the propagation of electrons arriving from the macroscopic conductor to the sample. In the following it is, however, better to use the plane waves associated with the moving electrons. They can be either transmitted or reflected (Fig. 5.10). In the most general case we can have incoming waves arriving from opposite directions, as well as outgoing waves leaving the sample. The amplitudes are denoted, for instance, A_L^+ for an incoming wave arriving from the left and propagating in the positive direction, A_R^- for a wave arriving from the right in the negative direction, and so on. The incoming wave from the left (A_L^+) is partially transmitted with an amplitude ($t_L A_L^+$), whereas the wave entering from the right (A_R^-) is partially reflected with an amplitude ($r_R A_R^-$). The transmission coefficient t_L and the reflection one r_R take values between 0 and 1. In these conditions, an outgoing wave—for example, the one with amplitude A_R^+ —is the sum of two contributions: the partial transmission of wave A_L^+ and the partial reflection of wave A_R^- :

$$A_R^+ = t_L A_L^+ + r_R A_R^- \quad (5.10)$$

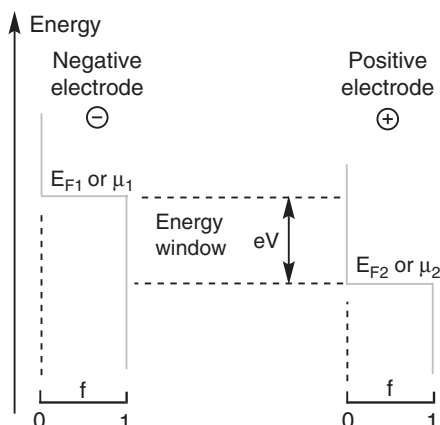
This is written more compactly by using a scattering matrix which relates the outgoing waves to the incoming waves:

$$\begin{bmatrix} A_R^+ \\ A_L^- \end{bmatrix} = \begin{bmatrix} t_L & r_R \\ r_L & t_R \end{bmatrix} \begin{bmatrix} A_L^+ \\ A_R^- \end{bmatrix} \quad (5.11)$$

Nanojunction with a continuous nanowire

Let us consider first the case of a continuous nanowire as represented in Fig. 5.9a. In the external metallic pads one can define two electrochemical potentials for the electrons μ_1 ($= E_{F1}$, the Fermi energy) and μ_2 ($= E_{F2}$). The application of a bias potential V makes the electrochemical potentials different, and an electron flow results.

To simplify the discussion we choose the temperature at 0 K, so that the Fermi functions on each electrode are perfect staircases with values $f = 1$ below E_F and $f = 0$ above (Fig. 5.11). As for electron transfer (Chapter 3), electron tunnelling occurs between two levels only when the energy of the filled level is the same as the energy of the vacant one. Thus it is easy to see that electron tunnelling occurs only in the narrow energy window of width

**Fig. 5.11**

Energy levels for a junction with a continuous nanometric wire, submitted to a bias potential V . The Fermi functions f of the metals (grey curves) are represented as perfect staircases, which is valid only for $T = 0$ K.

$\Delta E = eV$ for which the levels are filled on one side and vacant on the other side. Since the nanowire is continuous, we assume that there is a perfect transmission ($t_L = 1$ for a wave arriving from the left), and so all levels in the energy window contribute to electron transport.

A current is a charge transported per unit time. Thus, in a simple model [5.30] the current flowing through the nanowire can be written as:

$$I = 2e (v_F/L) (\mu_1 - \mu_2) (\partial n / \partial E) \quad (5.12)$$

where v_F is the velocity of electrons at the Fermi level (see Box ‘Characteristic lengths’), L is the nanowire length, and $(\partial n / \partial E)$ is the density of states (number of levels at energy E within a ∂E gap). (v_F/L) represents the inverse of the transit time of an electron in the nanowire, μ_1 and μ_2 are the electrochemical potentials in electrodes 1 and 2, and $(\mu_1 - \mu_2) (\partial n / \partial E)$ represent the total number of levels (orbitals) involved in the energy window. The factor 2 is introduced because two electrons with opposite spins can be associated with each orbital.

We expand $\partial n / \partial E$ as:

$$(\partial n / \partial E) = (\partial n / \partial k) (\partial k / \partial E) \quad (5.13)$$

In the frame of the free-electron model in one dimension, $(\partial n / \partial k)$ is evaluated easily, since for a row of N sites there are N equally spaced levels between $k = -\pi/a$ and $+\pi/a$, and thus

$$(\partial n / \partial k) = Na / 2\pi = L / 2\pi \quad (5.14)$$

The factor $(\partial k / \partial E)$ can be related to the Fermi velocity v_F as shown in the Box ‘Characteristic lengths’, and one obtains:

$$(\partial k / \partial E)_F = 1 / \hbar v_F \quad (5.15)$$

The difference in electrochemical potentials of electrons is proportional to the bias voltage, according to eqn. (5.1).

Characteristic lengths and useful relations in the free electron model

Three characteristic lengths play a role in the nanojunction problem: λ_F , λ_m and λ_ϕ . The first one, λ_F , the Fermi wavelength, is given by:

$$\lambda_F = \frac{h}{\sqrt{2mE_{\text{kin},F}}}$$

where $E_{\text{kin},F}$ is the kinetic energy of electrons at the Fermi level, in the frame of the free electron model [1.9, 5.28]. This equation is found easily from the energy E expressed as a function of the momentum $p = mv$ ($E = p^2/2m$) and from the de Broglie expression of the wavelength λ associated with a particle with momentum p ($\lambda = h/p$). Note that $E_{\text{kin},F}$ is *positive*, while the total (kinetic + potential) energy at the Fermi level E_F (defined in Section 1.4.2) is *negative*.

The mean free path λ_m is the average distance an electron can travel between two collisions with impurities or defects which change its momentum. It is, of course, determined by the purity and perfection of the sample. Finally, the third characteristic length is the coherence length λ_ϕ , corresponding to the length over which the associated wave of the electron retains its phase. The Fermi wavelength λ_F has values of the order of 0.1 nm in metals (as the interatomic distances), while λ_m and λ_ϕ are much larger (10^2 nm) [5.14, 5.28].

The kinetic energy $E(k)$ and the momentum p of the electrons are quantified, and vary as shown in eqns. (a)–(d).

$$E(k) = \hbar^2 k^2 / 2m \quad (\text{a})$$

$$p = mv_F = \hbar k \quad (\text{b})$$

$$\partial E / \partial k = \hbar^2 |k| / m = \hbar v_F \quad (\text{c})$$

$$\partial k / \partial E = 1 / \hbar v_F \quad (\text{d})$$

This last equation is crucial for the estimation of the current through the nanojunction.

Substituting eqns. (5.13)–(5.15) in eqn. (5.12), we finally obtain:

$$I = 2e \left(\frac{V_F}{L} \right) e V \left(\frac{L}{2\pi} \right) \left(\frac{2\pi}{\hbar v_F} \right) = \frac{2e^2}{h} V \quad (5.16)$$

and for the conductance:

$$G = \frac{I}{V} = \frac{2e^2}{h} \quad (5.17)$$

Thus, although there is no apparent obstacle to electron propagation, the conductance is not infinite, but equals $(2e^2/h)$; that is, $77.4 \cdot 10^{-6} \Omega^{-1}$, the *conductance quantum*. The inverse, $12.9 \text{ k}\Omega$, represents the *resistance quantum*.

This surprising result arises from the fact that the junction is so small that there is no inelastic scattering event inside it. Electrons cross the junction in the so-called *ballistic* regime without losing energy. Energy losses by collisions occur only in the macroscopic leads. Thus, the incompressible resistance quantum is some kind of contact resistance occurring at the constriction, which is impossible to avoid because we measure V , the voltage difference

between the two macroscopic conductors. If we could measure V directly on the small inner wires—with the 4-probe method, commonly used for measuring single crystals conductivities—we would obtain an infinite conductance (a zero resistance).

The quantization with the numerical value close to $13 \text{ k}\Omega$ has indeed been observed for a structure made of a chain of a few gold atoms suspended between electrodes [5.31].

Eqn. (5.17) is valid for a one-dimensional wire sample in which only one transversal quantum mode exists. One has indeed to take into account the lateral confinement of the electron wave. As usual in quantum physics, it gives rise to several standing modes with different energies (analogous to the well-known quantum problem of the particle-in-a-box [1.4]). These modes are called channels, and they contribute to the overall electron transport in a parallel way. When the lateral dimension of the wire is of the order λ_F , there is usually one channel available. For a three-dimensional (macroscopic) wire the detailed analysis of the problem shows that the number N_{ch} of possible channels increases with the wire section s ($N_{\text{ch}} \propto s$). There is thus a gradual transition towards the macroscopic situation in which the conductance is proportional to the section s of the conductor (eqn. (5.9)).

Nanojunction with a vacuum gap

Now let us assume that the nanowire is broken by a vacuum gap (Fig. 5.9b). Then the passage of an electron from the left-hand part to the right-hand part of the system is governed by a transmission coefficient $T(E)$, itself given by the square of the relevant scattering matrix element. Thus for a propagation from the left to the right:

$$T(E) = |t_L|^2 \quad (5.18)$$

Since the process occurs with electrons at energies close to the Fermi energy E_F , the transmission coefficient is generally denoted $T(E_F)$. Taking into account the existence of several channels and the influence of the $T(E)$ factors, we finally reach Landauer's equation:

$$G = \frac{2e^2}{h} \sum_{i=1}^{N_{\text{right}}} \sum_{j=1}^{N_{\text{left}}} T_{i,j}(E_F) \quad (5.19)$$

where $T_{i,j}$, function of E_F , is the transmission coefficient from the left channel i to the right channel j , and the summation operates on all couples of channels. The $T_{i,j}$ coefficients are obtained from the squared scattering matrix elements of eqn. (5.11). If there is no gap in the nanowire, then all $T_{i,i} = 1$ while cross terms are zero and the conductance is proportional to the number of channels.

The Landauer equation is the cornerstone of the treatment of 1-step transport. It will be used most frequently in a simplified form corresponding to the case where there is just one channel to consider; that is, without the summation over the i and j indices.

Nanojunction with a molecule in the gap

By this stage we have simply taken into account the tunnel effect which occurs through the empty space across the gap and determines the $T(E)$ value

($T(E) < 1$). When a molecule bridges the gap between the two nanoelectrodes (Fig. 5.9c) the $T(E)$ factor is determined by the complete system ‘molecule + nanowires’. The theory must take into account explicitly the structure of the molecule, as well as the details of the connections to the nanowires. This was the subject of intensive research throughout 1988–2000, but only a simplified account is presented here.

The general procedure is to compute the scattering matrix elements by a quantum-mechanical method, taking into account explicitly the detailed structure of the metal–molecule–metal nanojunction. A particularly efficient method—elastic scattering quantum chemistry (ESQC)—has been described by Joachim and Sautet [5.32]. In its original form it is based on an extended Hückel description of the system; that is, without taking into account explicitly the interelectronic repulsion. However, as for the case of electron transfer processes (see the evaluation of the V_{ab} couplings in Section 3.2.2.6), the method has proved very efficient in reproducing the experimental results available.

During the same period another type of method was also developed: the ‘non-equilibrium Green function’ (NEGF) [5.27]. It is, however, less intuitive than the scattering method, and will not be presented here. The interested reader can consult [5.33] for a recent implementation combining the NEGF method with a DFT description of the system.

For a molecule bridging the gap, the $T(E)$ factor is usually computed as a function of the energy E of incoming electrons (corresponding to the Fermi level E_F of the electrode from which the electron is issued), leading to the diagram in Fig. 5.12.

In the figure, $T(E)$ (displayed horizontally) has been calculated for a large range of E values, assuming that the position of E with respect to the molecular energy levels can be tuned by a proper choice of the metallic electrodes, or by modifying the molecule. But for a particular situation, there is of course only one E value to consider ($= E_F$), which is represented by the dotted horizontal line in Fig. 5.12.

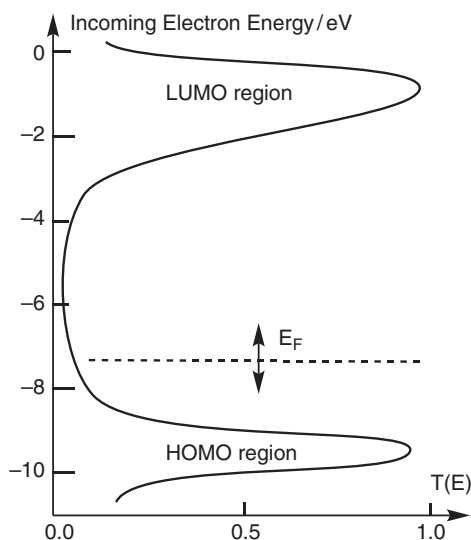


Fig. 5.12

Computed probability of the transmission of the electrons $T(E)$ as a function of the energy E of incoming electrons. The $T(E)$ factor is extremely small when the Fermi energy is away from the values of molecular energy levels. It approaches 1 when E_F matches a molecular orbital value (HOMO or LUMO), giving rise to resonance. Note that the calculation is performed for the complete system, including the electrodes.

Figure 5.12 introduces an important distinction into the general frame of 1-step transport when it implies a molecule: we can have *resonant tunnelling* or *non-resonant tunnelling*. Resonant tunnelling corresponds to the case where the Fermi level of at least one electrode matches one of the molecular ε_i levels. The corresponding $T(E_F)$ is large. Conversely, for non-resonant tunnelling the Fermi level does not match molecular levels, and the corresponding $T(E_F)$ is small, which corresponds to the case displayed in Fig. 5.12. The reason for these different behaviours is the same as in Section 3.2.2.6 for the metal–metal coupling mediated by a bridging ligand: a weak or zero energy difference between partners (either metal and ligand in Section 3.2.2.6, or bulk metal and molecule here) considerably increases the mixing of orbitals, and thus increases the interaction. In Fig. 5.12 the peaks in $T(E)$ correspond to the intervention of either the HOMO or the LUMO in the tunnelling.

From an experimental point of view, the type of tunnelling depends essentially on the applied bias voltage. As already pointed out, most systems correspond to the case of Fig. 5.3; that is, their Fermi levels fall in the HOMO–LUMO gap of the molecule. Thus, for a small bias voltage $T(E_F)$ is small (no resonance) and practically constant in the energy window, and from eqn. (5.19) the conductance G is constant. This gives rise to a linear current–voltage curve. The first well-characterized example of this behaviour was observed for a single C_{60} molecule adsorbed on gold and contacted by the tip of a STM [5.11a]. The junction resistance was found as $54.8 \text{ M}\Omega$, corresponding to a $T(E_F)$ factor of $2.3 \cdot 10^{-4}$.

For high bias voltages the situation is more complicated than that depicted by Fig. 5.3, because the two electrodes are at markedly different potentials, so that, from Fig. 5.12, $T(E)$ cannot be considered as constant. Thus one has to integrate contributions to electron transport over a range of energy levels for the whole system. In addition, the description of the molecule must encompass the effect of the strong electrical field between electrodes. Thus T depends now on *two* parameters—the electron’s energy E and also the bias voltage V —and will be denoted $T(E, V)$, which means that the curve in Fig. 5.12 deforms as a function of V .

The equation for the current is then [5.34]:

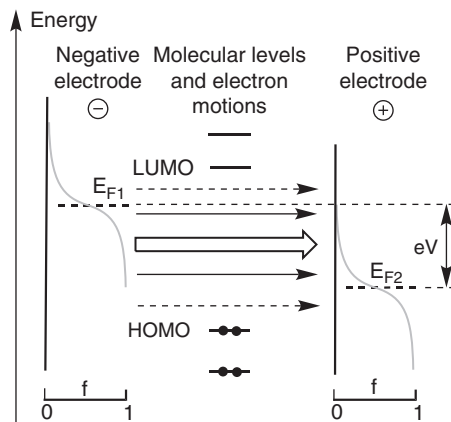
$$I(V) = \frac{2e}{h} \int_{-\infty}^{+\infty} T(E, V) [f(E - E_{F1}) - f(E - E_{F2})] dE \quad (5.20)$$

where f is the Fermi function for each electrode. The integration is performed in principle for the whole range of one-electron energies ($-\infty$ to $+\infty$). For a high bias voltage there is a chance that one of the Fermi levels will line up with a molecular level, giving rise to resonance.

Assuming that $T(E, V)$ is known, eqn. (5.20) gives the current. Note that the integration is effective only in an ‘energy window’, as in Fig. 5.11. The present situation is depicted in Fig. 5.13, and differs from the simplified case of Fig. 5.11 in two ways: (i) the energy window is much wider, and (ii) we consider a non-zero temperature; that is, the Fermi functions are S-shaped instead of perfect staircases. Thus the factor $[f(E - E_{F1}) - f(E - E_{F2})]$ entering into eqn. (5.20) varies smoothly. The contribution to the overall current is represented schematically in Fig. 5.13 by thick, plain, or dotted arrows.

Fig. 5.13

Energy levels in the high bias voltage regime, with the Fermi functions f of the two electrodes (grey curves). The horizontal arrows schematize the electron motions contributing to the current in eqn. (5.20), and the 'energy window' where electron tunnelling occurs. The contributions are qualitatively ranked in the following way: thick white arrow (strong contribution), plain arrows (medium), dashed arrows (weak).



Imaging molecular orbitals

A spectacular and unexpected repercussion of STM studies on molecules is the imaging of molecular orbitals. Let us recall that molecular orbitals were introduced by Mulliken in 1932 (see Sections 1.3 and 1.5.2). Although they are extremely useful for the prediction of reactivity, for a long time they have been considered by theoreticians merely as intermediates in the construction of the total wavefunction. It is even claimed frequently that they have no physical existence, the only rigorously accessible quantities being the total electronic energy and density.

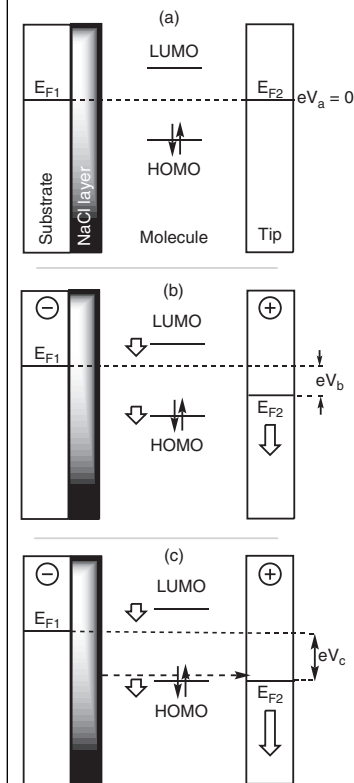
Of course, the *energies* of the molecular orbitals are (approximately) observable due to Koopman's theorem (see Chapter 1), but until recently their shape and symmetry has escaped direct determination.

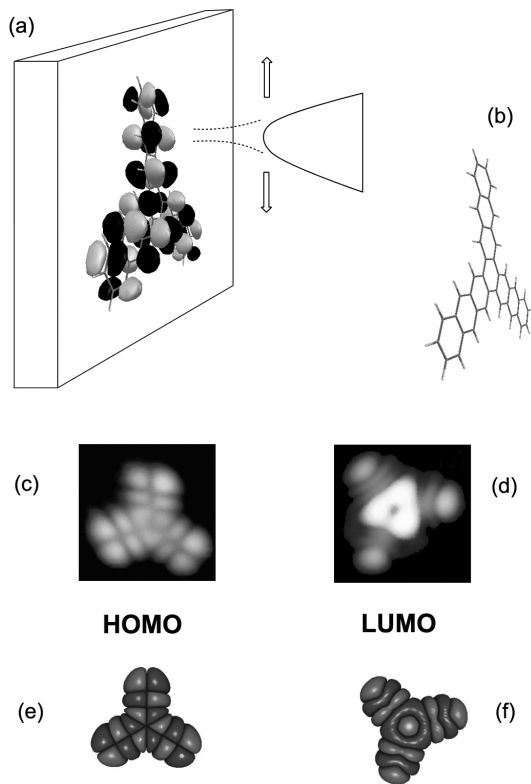
In 2005, molecular orbitals were observed by STM for planar molecules deposited on a metal substrate, Cu(111), itself covered by an ultrathin (two atoms thick) layer of NaCl [1]. The role of NaCl is to decouple partially the molecule from the metal substrate levels, so that the electronic levels of the molecule keep their individuality; that is, the shift and broadening appearing in Fig. 5.4 are then minimal. When polarizing the junction, as shown in Fig. 5.5c, the energy levels of the molecule follow the levels of the metal substrate. Thus the first coincidence occurs with the Fermi energy of the tip. Once the coincidence is achieved or nearly achieved, efficient electron transport occurs, essentially by molecule-dependent tunnelling (with possibly some contribution by the polaronic mechanism).

This provides a simple rule: with a positive tip there is a mixing of the tip orbitals at the Fermi level with the HOMO, and with a negative tip the mixing occurs with the LUMO. Hence the process is sensitive to the position of the tip with respect to the lobes and nodes of the orbital. Consequently, the tip 'images' the relevant molecular orbital. As a first approximation, one sees the square of the wavefunction ψ^2 .

Fig. 1

Evolution of the energy levels upon application of an increasing voltage bias $V_a (= 0)$ (a) $< V_b$ (b) $< V_c$ (c) with the tip positive. Due to the NaCl layer the molecular levels remain close to the substrate level (Fig. 5.5c). They go down much less (short thick arrows) than the Fermi energy of the tip E_{F2} (long thick arrow). Therefore, the first coincidence occurs between the HOMO and the Fermi level of the tip, giving rise to a strong increase in current.



**Fig. 2**

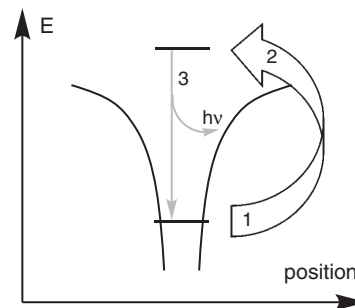
(a) Position of the tip in front of a planar molecule deposited on a NaCl/Cu(111) substrate. (b) Molecular skeleton of the studied molecule, decastaphene, showing its three-fold symmetry. (c) and (d) STM images for different bias voltages corresponding to the HOMO and LUMO; (e) and (f) comparison with computed orbitals. Adapted from [2].

Later experiments have shown that in some cases it is possible to get rid of the NaCl layer [3]. Thus, depositing pentacene molecules *directly* on Au(111) yields images not only of the HOMO, but also, for higher voltages, of the lower-energy occupied orbitals HOMO-1 and HOMO-2.

A completely different method for imaging molecular orbitals was described in 2004. It is based on a tomographic reconstruction using femtosecond laser pulses [4, 5].

The principle is based on the highly non-linear behaviour of a molecule subject to excitation by an intense (10^{16} W/cm²) and ultrashort (30 femtosecond) laser pulse. The very high electrical field exceeds the field that binds electrons to the molecule, and a special kind of ionization—tunnel ionization—occurs, though the laser frequency is in the infrared range. The oscillating laser field returns the electron to the molecule, and recombination occurs with emission of a photon in the soft-X-ray range. During the recombination step, interference occurs between the wavefunction of the returning electron and the one of bound states, providing information on the orbital shape.

Practically, the molecule (in the gas phase) is first oriented by a previous laser pulse (a common and well-mastered technique), and the experiment is thus performed for a definite orientation. Associating several such experiments for different orientations allows 3D reconstruction of the molecular orbital. Basically, the method concerns the HOMO, but remarkably, since it is based on an interference process,

**Fig. 3**

Ionization and recombination process. 1: tunnel ionization; 2: electron returning under the influence of the intense laser field; 3: recombination with photon emission in the soft X-ray range.

it produces the complete wavefunction, *including its phase*. In addition, recent experiments [5] also provide access to the HOMO-1.

References

- [1] J. Repp, G. Meyer, S. M. Stojkovic, A. Gourdon, C. Joachim, *Phys. Rev. Lett.* 94 (2005) 026803.
- [2] O. Guillermet, S. Gauthier, C. Joachim, P. de Mendoza, T. Lauterbach, A. Echavarren, *Chem. Phys. Lett.* 511 (2011) 482.
- [3] W.-H. Soe, C. Manzano, A. De Sarkar, N. Chandrasekhar, C. Joachim, *Phys. Rev. Lett.* 102 (2009) 176102.
- [4] J. Itatani, J. Levesque, D. Zeidler, H. Niikura, H. Pépin, J. C. Kieffer, P. B. Corkum, D. M. Villeneuve, *Nature* 432 (2004) 867.
- [5] S. Haessler, J. Caillat, W. Boutu, C. Giovanetti-Teixeira, T. Ruchon, T. Auguste, Z. Diveki, P. Breger, A. Maquet, B. Carré, R. Taïeb, P. Salières, *Nature Physics* 6 (2010) 200.

5.2.2.4 Transport through the 2-step process

In the two-step process a charge appears temporarily on the molecule. It is facilitated by two factors which have been neglected so far in the Landauer or more generally in scattering treatments: electron–phonon coupling (the fact that a charge can modify its environment and thus can self-trap), and electrostatic repulsion effects. These effects manifest themselves for large and/or complex molecules or entities (metallic nanoparticles, carbon nanotubes). When the leading effect is electron–phonon coupling the *hopping-type transport* operates; when the leading effect is electrostatic repulsions the *Coulomb staircase* regime applies. These two situations will now be detailed successively.

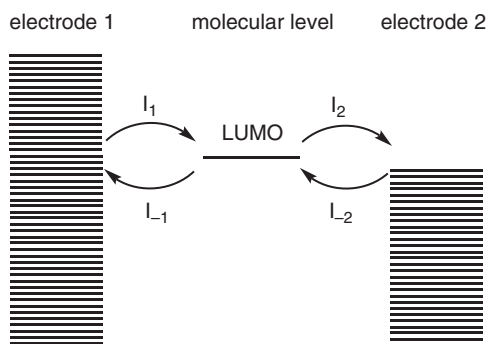
2-step process, hopping type (Fig. 5.8b)

A simple argument for the occurrence of the *hopping-type* mechanism is based on time-scale considerations [5.35]: when the molecule is long enough, the tunnelling time becomes large and can be of the order of vibration periods, allowing the molecular structure to react by vibronic coupling. This is the same problem as in the case of intramolecular electron transfer, with the opposition between superexchange and stepwise electron transfer (see Section 3.2.2.6).

Thus, instead of ‘flying’ as a phantom from one electrode to the other, the electron can ‘materialize’ on the molecular site, which distorts to accommodate the charge. The hopping-type mechanism is analogous to the formation of a small polaron in the case of an ionic solid (see Section 3.1.2), and corresponds to the so-called ‘chemical mechanism’ encountered also in Section 3.2.2.6.

The experimental signature for the hopping-type mechanism is a marked temperature dependence of the current, because there is an activation energy to overcome. As in Section 3.1.2 the activation process concerns not only the molecule itself but also its environment if there is a polarizable medium in the vicinity.

From a theoretical point of view, the hopping-type mechanism is amenable to a treatment using rate constants. In the following, adapting [5.12] and [5.22], we consider a simple case where the molecule is involved by just one vacant level (the LUMO). The couplings with electrodes 1 and 2 generate

**Fig. 5.14**

Electron currents I , associated with the hopping-type mechanism: simple model implying two electrodes and only one vacant level (LUMO) on the molecule.

four possible electron transfers: from electrode 1 to the molecule (generating M^-) (process 1), from the charged molecule to 2 (process 2), and the reverse processes (see Fig. 5.14).

Using eqn. (5.4) and simple probability considerations, we can write the electron current associated with process 1 (transfer of an electron from electrode 1 to the molecule):

$$I_1 = e(\Gamma_1/\hbar)f_1P_M \quad (5.21a)$$

where Γ_1 is the coupling with the electrode 1 (electron donor), and $f_1 = f_1(E)$ is the Fermi function of the same electrode, for the energy E of the molecular orbital. P_M is the probability for the molecule to exist in the *neutral* state (that is, its original state before receiving an electron, which is also its final state after releasing an electron).

Equation (5.21a) translates the fact that the transfer needs an occupied state on the electrode and a vacant state on the molecule. In the same way as the processes denoted I_2 , I_{-1} , and I_{-2} in Fig. 5.14, one can associate partial currents given by:

$$I_2 = e(\Gamma_2/\hbar)(1 - f_2)(1 - P_M) \quad (5.21b)$$

$$I_{-1} = e(\Gamma_1/\hbar)(1 - f_1)(1 - P_M) \quad (5.21c)$$

$$I_{-2} = e(\Gamma_2/\hbar)f_2P_M \quad (5.21d)$$

After some time, a stationary state is established, for which:

$$I_1 + I_{-2} = I_{-1} + I_2 \quad (5.22)$$

From eqn. (5.22) and the definitions of the partial currents, one easily obtain the P_M probability:

$$P_M = \frac{\Gamma_1(1 - f_1) + \Gamma_2(1 - f_2)}{\Gamma_1 + \Gamma_2} \quad (5.23)$$

The overall current is given by:

$$I = 2(I_1 - I_{-1}) = 2(I_2 - I_{-2}) \quad (5.24)$$

where the factor 2 takes into account the spin degeneracy.

Substituting P_M in expressions of I_1 and I_{-1} in the first part of eqn. (5.24), and using eqn. (5.21) and equivalent forms, gives, after some rearrangements:

$$I = 2 \frac{e}{\hbar} \frac{\Gamma_1 \Gamma_2}{\Gamma_1 + \Gamma_2} (f_1 - f_2) \quad (5.25)$$

Note that this derivation is the exact analogue of the treatment of two consecutive chemical reactions in homogeneous phase under the assumption of the stationary state, except that the probability P_M (for the molecule to be neutral) enters into the equations instead of the concentration of an intermediate species, because we are working on a single molecule.

Eqn. (5.25) shows that the current is extremely small when the molecular level lies outside the energy window defined by the Fermi levels of the two electrodes. For sufficient bias voltage the current increases when the coincidence of levels begins, and then saturates to the value:

$$I_{\max} = 2 \frac{e}{\hbar} \frac{\Gamma_1 \Gamma_2}{\Gamma_1 + \Gamma_2} \quad (5.26)$$

The resulting I–V curve can be computed from eqn. (5.25) and from assumptions regarding the relative positions of the Fermi level of the electrodes and the molecular level. This necessitates knowledge of the voltage division factor (when the concept is applicable). A typical curve is depicted in Fig. 5.15.

If the voltage becomes sufficiently high, a second level can enter the window, and a second step occurs. The previous model is a simplified one, but reproduces most of the physical behaviour for 2-step hopping-type transfer. However, the temperature dependence is not correctly reproduced. Temperature enters into eqn. (5.25) via the Fermi functions, but this is not enough. The role of vibrations is lacking. It can be introduced by considering that just before the onset of a current rise the molecular level is near to coincidence with a Fermi level. Then, any thermally induced fluctuation could bring the molecular level into the energy window, and thus strongly increase the current (Fig. 5.16).

For long molecules consisting of several repeat units which can stabilize either an electron or a positive charge, the site-to-site hopping process can become the leading process when compared to direct inter-electrode tunnelling (the 1-step process). Theoretical calculations show that the rate of decay of the current with distance r is slow, and should be described by a polynomial law as $1/(A + B r)$ [5.35, 5.36]. By contrast, the 1-step tunnelling implies a decay with distance according to an exponential law (see Section 5.2.3). Thus, for long distances only the hopping mechanism survives.

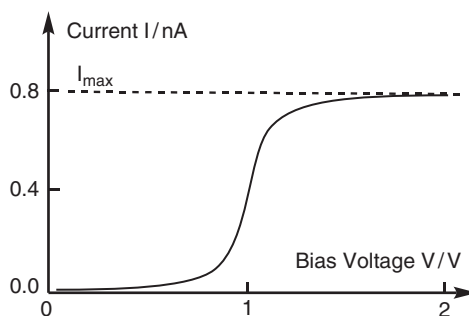
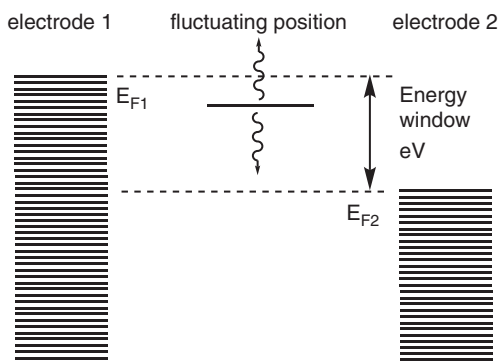


Fig. 5.15

Current (nA) versus bias voltage (V) for typical values of the parameters: $\Gamma_1 = \Gamma_2 = 3.3 \cdot 10^{-6}$ eV, symmetrical voltage division factor (0.5), $E_G = 0.5$ eV, $k_B T = 0.025$ eV. (Adapted from Bourgoïn *et al.*, [5.12].)

**Fig. 5.16**

Thermally activated process described by a fluctuation of the molecular energy level (vibrations, and so on).

Transport through 2-step process: the Coulomb staircase (Fig. 5.8a)

We now turn to the other sub-category of the 2-step process. In the Coulomb staircase regime, the leading effect is electrostatic. Actually, these effects were first described for structures larger than molecular nanojunctions, typically for metallic nanoparticles (1–10 nm) embedded in an insulator, or for carbon nanotubes (length about 100 nm) coupled to electrodes. In the following, we call them ‘islands’ rather than ‘molecules’. Due to the size of these systems the behaviour is intermediate between nanosized systems and mesoscopic ones.

The conditions for observing a typical Coulomb staircase are:

- A metallic structure for the island between the electrodes. Thus, contrary to the case of molecules, there is no quantification of the energy levels.
- An extremely weak coupling (Γ) of the island with the electrodes. The charge of the island cannot vary smoothly, but must take an integer value.

The fundamental qualitative explanation of a Coulomb staircase is as follows: the coupling being very small and the system of large dimensions, no direct (1-step) tunnelling is possible, and we can have only sequential tunnelling. The island being large, it can present several discrete charge states ($0, \pm 1, \pm 2, \dots$). Each of these charge states appear successively at a given threshold voltage, for which the current increases. Before the first threshold the current is zero. The corresponding I–V curve thus exhibits, under certain conditions, the characteristic Coulomb staircase shape (Fig. 5.8a) [5.37].

The basic quantitative interpretation is due to Likharev, and is referred as the *orthodox theory* [5.38]. It is a mixture of quantum and classical treatments, as it relies on the macroscopic concept of capacitance, though it is applied to a system of mesoscopic dimensions (typically 100 nm). When one electron only has been added (or removed), there is a charging energy E_c :

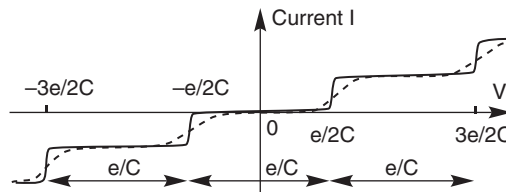
$$E_c = e^2/2C \quad (5.27)$$

where C is the capacitance of the capacitor made by one of the electrodes and the island. For very small structures, E_c can be important and much greater than kT . Charging the island necessitates providing at least this energy, which is supplied by the bias voltage V . Thus there is a threshold voltage V_t , given by:

$$V_t = E_c/e = e/2C \quad (5.28)$$

Fig. 5.17

The Coulomb staircase. Plain curve: Current-potential curve at low temperature showing well-defined steps. Dashed curve: smoothed steps observed at higher temperature.



Generalizing the argument to multiple charging explains the step-like pattern of the I–V curve (Fig. 5.17).

The detailed theory, however, requires the junction to be strongly asymmetric for observation of the characteristic Coulomb staircase shape (Fig. 5.17). The potential difference between two steps (abscissa) is e/C . In addition, this theoretical shape is obtained only at low temperature. At high temperature the thermal energy overcomes the charging energy. Then the steps disappear progressively and are replaced by a smoother curve (Fig. 5.17).

An interesting consequence of Coulomb blockade that can be used to identify the phenomenon is the reduction in shot noise. In normal shot noise the time interval between the successive passages of one electron is distributed at random, but in the situation of Coulomb staircase, on a current step (Fig. 5.17), when an electron has been added to the particle by tunnelling from electrode 1, the junction is blocked for a given time until the electron is removed by tunnelling to electrode 2. There is thus a silent period after a pulse, and the noise is reduced with respect to the uncorrelated situation [5.37].

The Coulomb blockade effect has aroused great interest in relation to the possibility of building *one-electron devices* such as transistors, switches, and so on. Since the system is of larger dimensions than usual nanojunctions, it is generally possible to introduce a third electrode in the vicinity of the central island. By playing with the potential of this third electrode one can tune the charge state of the island by capacitive influence and bring the system from a state of Coulomb blockade (no current) to a state where a current can flow. This is basically a one-electron transistor. Other devices include single-electron traps, turnstiles, pumps, and oscillators, with applications in supersensitive electrometry, DC current standards, temperature standards, and detection of infrared radiation, and in a prospective way, digital logic gates [5.38].

The main difficulty is, however, the necessity to work at very low temperature to ensure the condition $kT < e^2/C$. With the normal systems used in Coulomb blockade experiments (size ≈ 100 nm) the capacitance C has values of the order of 10^{-16} F, leading to operating temperatures below 10 K. Decreasing the dimensions to about 1 nm reduces the capacitance, and has raised the possible temperature to room temperature [5.37].

The concept of a Coulomb blockade has been expanded to the case where a molecule, rather than a metallic ‘island’, is present in the nanojunction [5.39]. However, several important differences must be taken into account when transferring the Coulomb blockade reasoning to molecules. (i) Electrostatic effects are much larger in molecules than in ‘islands’ (though the precise comparison is difficult because the notion of capacitance has no unique-molecule counterpart). Thus, for molecules, the successive charging states ($0, \pm 1, \pm 2, \dots$) are

generally not observed, because they would occur for unrealistic bias voltage values. (ii) In molecules, the energy levels (molecular orbitals) are discrete and separated by relatively large energies. (iii) Finally, molecules being much smaller than ‘islands’, the 1-step Landauer-type process is possible and frequently overcomes the blockade’s process.

Thus, the explanation of Coulomb blockade for molecules relies on the use of energy levels (orbitals) rather than capacitance, with proper modification of the simple model to introduce charging (electrostatic) effects. Broadly speaking, the energy interval between steps (E_{add}) is:

$$E_{\text{add}} = E_c + \Delta E \quad (5.29)$$

where E_c is the charging energy defined previously, and ΔE is the separation between molecular levels.

A typical situation is represented in Fig. 5.18. We assume that a single vacant level is located near the Fermi levels of the electrodes. This vacant level is theoretically able to accommodate two electrons. Upon application of a moderate bias, coincidence will occur with the transfer of one electron from the

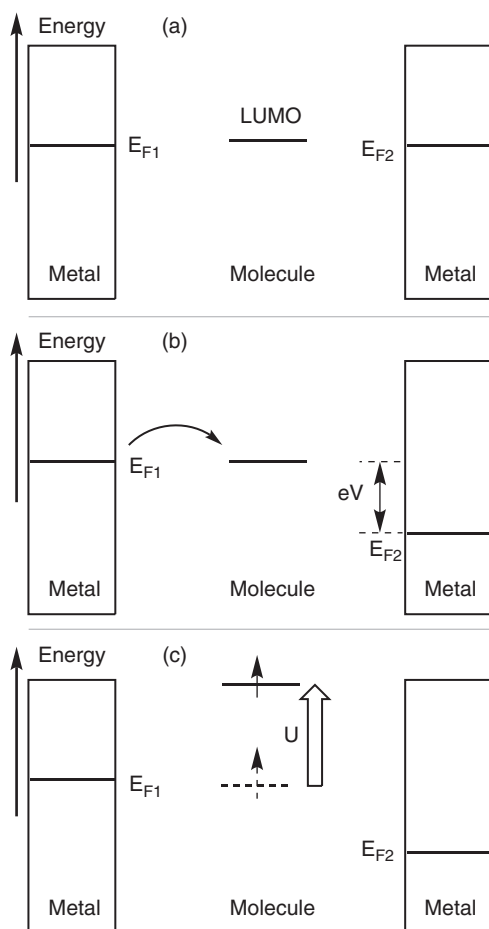


Fig. 5.18

Energy levels for a Coulomb blockade situation with a molecule in the nanojunction. (a) Initial situation at zero bias, with a molecular vacant level close to the Fermi levels of electrodes; (b) application of a moderate bias, leading to level coincidence, and electron transfer from one electrode to the vacant level; (c) after electron transfer (reduction to the anion-radical state), the level floats up, due to the electron repulsion U , preventing further electron addition.

negative electrode to the molecule, which is thus reduced to an anion-radical. However, as soon as this event has happened the molecule is more difficult to reduce, due to the intervention of the electronic repulsion term (which we still call U , as in eqn. (5.2), but which is actually a sum of bielectronic integrals, because there are many electrons). As explained previously, we can consider that the molecular level floats up and exits from the energy window between E_{F1} and E_{F2} , precluding the further charging of the molecule to the dianion state. In other words, all occurs as if *the molecular level could accommodate only one electron*.

5.2.2.5 A special case of 1-step process: the Kondo resonance effect

When the molecular level is initially occupied by one electron, and thus bears a spin magnetic moment, a special effect, *Kondo resonance*, can occur. The effect is reminiscent of the Kondo effect observed in metals containing magnetic impurities (Mn^{2+} in a copper or gold wire, for example). The phenomenon was observed by de Haas in 1934 [5.40a] as a minimum in the thermal variation of the resistance (the resistance increases at low temperature), together with a decrease of the magnetic susceptibility of the impurity (Fig. 5.19a). The effect was first interpreted in 1964 by Kondo [5.40b] as a scattering of the conduction electron by the impurity with an antiferromagnetic interaction between the isolated impurity and the conduction electron. The Kondo Hamiltonian is written $\mathbf{H} = -J \mathbf{S}_{\text{impurity}} \cdot \mathbf{S}_{\text{conduction}}$, where J is the coupling constant, $\mathbf{S}_{\text{impurity}}$ is the spin of the impurity, and $\mathbf{S}_{\text{conduction}}$ is the spin of the conducting electron. The interaction between the two electrons allows explanation of the minimum. The temperature of the minimum is often called the Kondo temperature, T_K .

The model was further refined by Friedel and also by Anderson using a magnetic impurity model and the ‘simple’ Hamiltonian [5.41]:

$$\mathbf{H} = \mathbf{H}_{\text{impurity}}(U) + \mathbf{H}_{\text{conduction}}(k) + \mathbf{H}_{\text{interaction}}(V) \quad (5.30)$$

where $\mathbf{H}_{\text{interaction}}(V)$ is the Kondo Hamiltonian evoked previously. V is the interaction between the localized impurity and the conducting electron. Over the past twenty years the Kondo effect has undergone a revival, because quantum dots and magnetic molecules can be described in this frame as magnetic impurities. Surprisingly, while in bulk metal the Kondo effect *decreases* the conductivity, in the case of a nanojunction it *increases* the conductance at low temperature by suppressing the Coulomb blockade (Fig. 5.19). We give hereunder a very simplified image of a phenomenon which would be too long to explain in detail.

We now reduce the problem to two electrons, one of which is localized on the molecule’s SOMO ψ_{mol} (magnetic impurity or scattering impurity), and the other is the conducting electron within the electrode (or tunnelling between the left and right electrodes), described by a Bloch function $\Theta_{\text{cond}}(k)$ (Sections 1.4 and 3.3.2). The situation is shown in Fig. 5.20, reminiscent of the

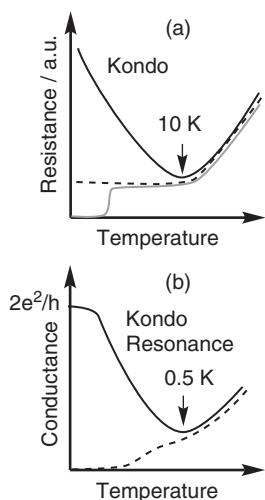
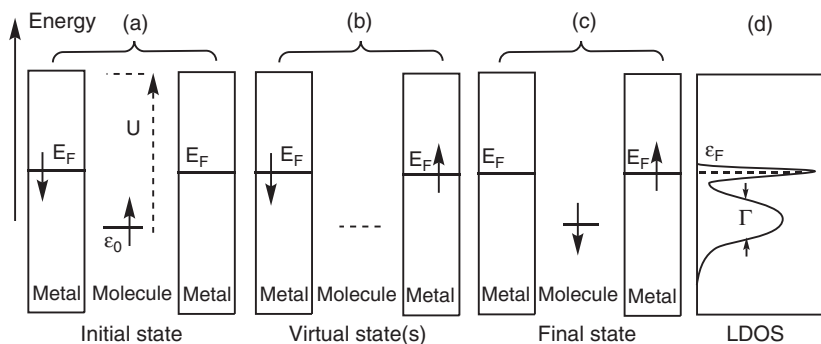


Fig. 5.19

Low-temperature many-body effects on metals and quantum dots with opposite Kondo effect consequences. (a) *resistance* in a macroscopic metal: plain curve, metal with magnetic impurities, *Kondo effect increases the resistance* at low T ; dashed curve, pure metal behaviour, resistance saturates to a constant value depending on defects amount; grey curve, superconductor, *resistance* tends to zero; (b) *conductance* in a nanojunction with a molecule or a quantum dot as ‘impurity’ in the gap: plain curve, magnetic impurity in the gap, *Kondo resonance increases the conductance* up to the quantum conductance limit $2e^2/h$; dashed line, non-magnetic impurity, the *conductance* tends to zero.

**Fig. 5.20**

The Kondo resonance effect in a nanojunction. Energy levels scheme. (a) Initial state, $|\uparrow, \downarrow\rangle$, showing the singly occupied molecular level which is not in resonance with the Fermi levels; (b) one of the virtual states of higher energy, $|0, \uparrow\downarrow\rangle$; (c) final state after tunnelling, $|\downarrow, \uparrow\rangle$; (d) local (projected) density of state on the molecule. The Kondo resonance effect is responsible of the appearance of a sharp extra peak at the Fermi energy, and thus the current can flow for zero bias voltage. (Adapted from L. Kouwenhoven, L. Glazman, *Physics World*, January 2001, p. 33.)

magnetic impurity model of Anderson. We have already encountered the two-electrons-two-orbitals problem in Section 1.5.3, and we know that four states can arise: one $S = 1$ triplet and three $S = 0$ singlet states. In the following we use the Dirac notation $|\psi_{\text{mol}}, \Theta_{\text{cond}}(\mathbf{k})\rangle$ using the corresponding spins. (The left position in the ket corresponds to the electron in the molecule, the second to the electron in the electrodes). The triplet has the following basis set: $|\uparrow, \uparrow\rangle$, $|\downarrow, \downarrow\rangle$, $|\uparrow, \downarrow\rangle + |\downarrow, \uparrow\rangle$ (Section 1.5.3). It plays no part in the tunnelling process, because two like spins cannot be together on one centre, due to the Pauli exclusion principle (or Fermi hole: an electron creates around it a hole where the presence of a like spin is strictly forbidden). So we are dealing only with the singlet states, based on an antiferromagnetic interaction as in the Kondo effect in metals, which necessitates a good wavefunction overlap between the wavefunctions of the molecule and of the conductors.

The singlet basis set is $|\uparrow, \downarrow\rangle - |\downarrow, \uparrow\rangle$, $|\uparrow\downarrow, 0\rangle$, $|0, \uparrow\downarrow\rangle$. The situation depicted in Fig. 5.20 corresponds to this singlet situation with a zero applied bias. The singly occupied molecular level is located below the Fermi level of the electrodes at energy ϵ_0 (Fig. 5.20a, with a spin \uparrow , for example). At the Fermi level of the electrode, the electron spin is opposite \downarrow . There is no possible electron transfer from the electrodes to the molecular level, because of the repulsion term U (dashed arrow in Fig. 5.20a). The energy of the doubly occupied molecular level would be $2\epsilon_0 + U$. Thus the current should be theoretically blocked. But a special interaction can take place. We know that to determine the exact ground state of the system, configuration interaction is needed between the original and excited states of proper symmetry. In the present case the interaction between the molecule (ψ_{mol}) and the electrodes ($\Theta_{\text{cond}}(\mathbf{k})$) is denoted V . The $\eta = V/U$ ratio is assumed to be $\ll 1$ (weak interaction). The calculation leads to the ground-state wavefunction Ψ_0 :

$$\Psi_0 = (1/2)^{-1/2} [(1 - \eta^2)^{-1/2} (|\uparrow, \downarrow\rangle - |\downarrow, \uparrow\rangle) + \eta(|\uparrow\downarrow, 0\rangle + |0, \uparrow\downarrow\rangle)] \quad (5.31)$$

The presence in Ψ_0 of the excited (virtual) states $|\uparrow\downarrow, 0\rangle$ and $|0, \uparrow\downarrow\rangle$ allows stabilization of the ground state. The other crucial consequence for tunnelling is the appearance of the so-called Kondo resonance at the Fermi level.

The Kondo resonance is a many-body interaction which couples the initial and final states ((a) and (c) in Fig. 5.20). The coupling occurs through higher-energy excited (virtual) states such as that shown in Fig. 5.20b, described by $|0, \uparrow \downarrow \rangle$. The levels available for tunnelling are then described by a Bloch orbital, depending on k , where a density of states (DOS) can be defined. (In fact, many of them, since there are many Bloch orbitals concerned on the electrodes.) Particularly interesting is the local density of states (LDOS) of the molecule (the participation of the molecule to the DOS), which exhibits not only the broadened peak around energy ε_0 , as seen before, but also *an additional narrow peak, precisely at the Fermi energy* (Fig. 5.20d). This feature, known as the Kondo resonance, is important, because the electron tunnelling is determined by the density of states at the Fermi level. All happens as if (part of) the molecular level had moved upwards and put in resonance with the electrode Fermi levels. The experimental consequence is an increase in conductance for zero bias. Of course, this mechanism would be impossible if the molecular level were occupied by two electrons with opposite spins, which is why Kondo resonance requires a molecule with an odd number of electrons. As we shall see in Section 5.2.9.1, molecules present, in addition, advantages over quantum dots for the observation of the Kondo resonance: (i) the phenomenon is now well established in molecules (present in open-shell radicals and not in the corresponding closed-shell species); (ii) the Kondo resonance temperature T_K is much higher for molecules.

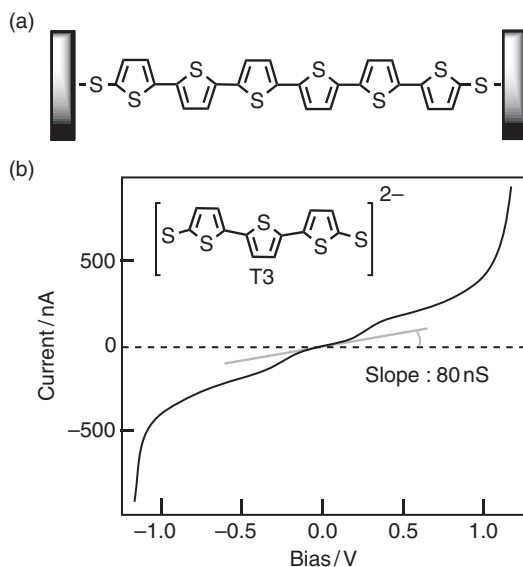
In the next section we consider examples of molecules and the corresponding functions which have been realized in the hybrid architecture. We start with very simple components of the two-terminal type, and then try to expand to three-terminal devices, which are, of course, much more promising for data treatment because they can mimic switches and transistors.

5.2.3 Molecular wires

The molecular wire is conceptually the simplest system: the molecule must play the rôle of an electron pipe; that is, it must facilitate as much as possible the electron transfer from one metallic pad to another (Fig. 5.21). Usually, molecular wires work in the 1-step regime.

From the beginning, researchers have explored the possibilities of π -conjugated oligomers, using the large body of studies on conducting polymers as guidelines. One should note, however, several important differences in the case of such polymers: (i) in the present case the molecular wire must be of defined length; (ii) there is no ‘doping’; (iii) the desired properties must be really intramolecular, and should not depend on collective or intermolecular effects (compare with doped polyacetylene; Section 3.3.2.2).

Experimental studies frequently use long molecules functionalized by thiol groups, to ensure a strong covalent fixation on gold electrodes, and the connection is performed by the breakjunction technique (Fig. 5.2h) or a variant ([5.12, 5.17, 5.42]). The transport usually occurs in the molecule-dependent tunnelling regime, with non-linear I - V curves for high bias voltages, due to resonance effects.

**Fig. 5.21**

(a) A molecular wire between two electrodes. The wire is made of several repeat units, here thiophene moieties; (b) the bis-thiol-terthiophene dianion (T3) and a typical current-voltage curve for a gold-T3-gold junction, showing the linear regime at low bias voltage. (Adapted from [5.42].)

The case of bis-thiol-terthiophene (T3, Fig. 5.21b) constitutes a typical example. The molecule has been connected to two gold electrodes using the break junction technique, and after a number of control experiments necessary for showing that the electrodes were linked by just one molecule, the current voltage curve shown in Fig. 5.21 is obtained [5.42]. It is symmetrical, and presents step-like features. The interpretation is different according to the imposed bias voltage.

At low bias (< 0.1 V), the I - V curve is linear, with a very weak (but non-zero) slope. The slope is the junction conductance, and the most typical value obtained for several samples is 80 nS (one nano-Siemens, $\text{nS} = 10^{-9} \Omega^{-1}$). We are here in the molecule-dependent tunnelling regime with virtual resonance (Fig. 5.8d); that is, the tunnelling is increased by partial mixing of the electrode levels with one molecular level—here the HOMO. This can be reproduced by calculation, using the Landauer formula (eqn. (5.19) with just one channel), with a value of the transmission coefficient $T(E)$ computed by the ESQC technique. $T(E)$ depends on the incident electron energy, as in generic Fig. 5.12. The quantitative simulation requires two pieces of information: (i) the exact geometry, including the contact's geometry, because it determines the overall $T(E)$ curve, and (ii) the E_F value.

Regarding the geometry, the critical parameter is the Au-S bond length, which has been taken as 1.9 \AA (190 pm) according to structural studies, but could actually be larger [5.42]. The E_F energy is close to the HOMO energy, and the difference $E_F - E_{\text{HOMO}}$ is estimated to be in the 0.0–0.7 eV range. With $E_F - E_{\text{HOMO}} = 0.6$ eV, a nanojunction conductance of 87 nS is obtained, as observed experimentally [5.42].

For large bias voltage (> 0.1 V) the I - V curve is no longer linear, and steps appear. They are not placed regularly, contrary to the case of the Coulomb

blockade/Coulomb staircase regime (Fig. 5.8a), and so the possible interpretations are either the molecule-dependent tunnelling regime with resonance (Fig. 5.8d) or the polaronic model (Fig. 5.8b) [5.42]. In the first case, the current can be computed from eqn. (5.20) and again the $T(E)$ curve. In the second case, the current is calculated by sequential tunnelling formalism of the type given by eqn. (5.25), but with additional parameters describing the contact barriers at both ends of the molecule. The best agreement is obtained with the polaronic model (sequential tunnelling; Fig. 5.8b).

This example, however, shows the difficulty of reaching firm conclusions regarding the exact transport mechanism, because several adjustable parameters have to be used. In addition, it is possible to evolve smoothly between the two invoked mechanisms, which are only limiting cases. Both are based on the oxidizable character of the T3 molecule, with relatively high-energy HOMO. The question is thus to know whether a true redox reaction occurs, generating transiently the $T3^{+\bullet}$ cation radical, or if its lifetime is so short that only level mixing can be invoked. Reality could be intermediate between these possibilities. Finally, as a sufficiently advanced theoretical description (self-consistent quantum calculations), the exact energy of a molecular level depends on the charge state, and this introduces an argument similar to the Coulomb blockade mechanism.

For molecular wires an important question concerns the decay of the efficiency of the electron transport with length. This is best studied by using weak bias voltage—that is, in the non-resonant tunnelling regime—because the efficiency is characterized by a single number, either $T(E_F)$ or the junction conductance. Under these conditions the conductance of the metal/molecule/metal nanojunction varies generally with the length L of the molecule according to a decreasing exponential law [5.43]:

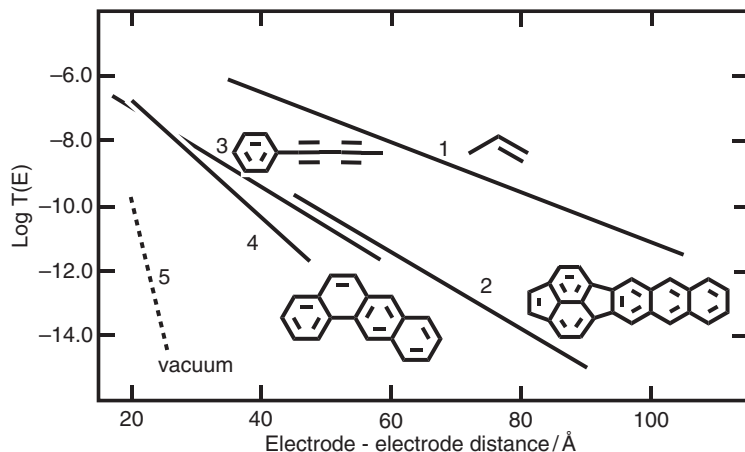
$$G = G_0 \exp(-\gamma' L) \quad (5.32)$$

The exponential coefficient γ' is a parameter, expressed in \AA^{-1} ($1 \text{\AA}^{-1} = 10 \text{ nm}^{-1}$), which characterizes the G decay provoked by the increase of the length of the molecule. One wishes, of course, to have γ' as small as possible.

This problem was first tackled by theory, which can probe a large number of different chemical structures—in particular, oligomeric structures consisting of the repetition of a given moiety [5.44]. Thus systematic calculations by the ESQC method show that the γ' factor is in the $0.2\text{--}0.6 \text{\AA}^{-1}$ range for conjugated systems, *versus* $0.6\text{--}1.0 \text{\AA}^{-1}$ for aliphatic chains, and about 2.3\AA^{-1} for a tunnelling through empty space (thus confirming that tunnelling is much more efficient through the molecule than through vacuum); see Fig. 5.22. The G_0 conductance is determined by the degree of coupling of the molecule with the electrodes.

The variation in conductance can be extremely large for apparently similar conjugated structures. Theory can thus help to identify the best chemical structures; that is, those presenting a high conductance for a given length and/or a weak γ' factor [5.44].

From the experimental point of view, carotenoid polyenes with five to eleven conjugated double bonds have been connected to electrodes and show a γ'

**Fig. 5.22**

Theoretical calculation of the $T(E)$ transmission coefficient as a function of distance, for different chemical structures. $\text{Log } T(E)$ is plotted as a function of the inter-electrode distance for several representative chemical structures made of identical repeat units (oligomers). 1: Polyene; 2: Oligo (cyclopenta-naphthofluoranthene); 3: Oligo (phenylbutadiyne); 4: Oligo (benzoanthracene); 5 (dashed): transmission through vacuum. (Adapted from [5.44].)

parameter of 0.22 \AA^{-1} , and this can be reproduced by electronic structure calculations [5.45]. But a more systematic characterization is possible by using a polymer chain deposited on a substrate, and for which one extremity can be grasped and lifted progressively by the tip of an STM [5.46]. It is then possible to study the conductance of a single chain as a continuous function of the effective length (Fig. 5.23). The result shows a general exponential decay of the conductance with a γ' factor of 0.38 \AA^{-1} —a value consistent with theoretical calculations.

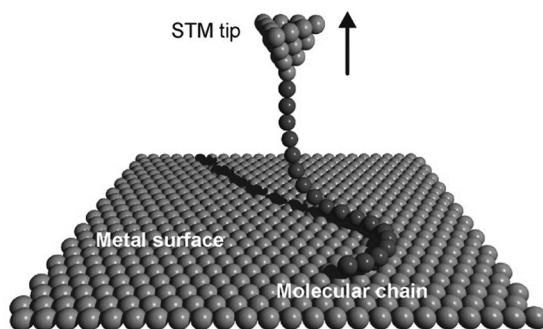
Finally, it is interesting to draw a parallel with electron transfer studies in mixed valence compounds—in particular, those containing long conjugated bridges, since the motivation is also to select systems with the smallest attenuation with distance (see Section 3.2.2.6) [5.47]. Actually, a relationship between intramolecular electron transfer in solution in a donor–bridge–acceptor system (DA) and molecular conduction in a nanojunction containing the same molecule can be established theoretically [5.48].

$$G = \frac{8e^2}{\pi^2 \Gamma_D^L \Gamma_A^R F} k_{\text{et}} \quad (5.33a)$$

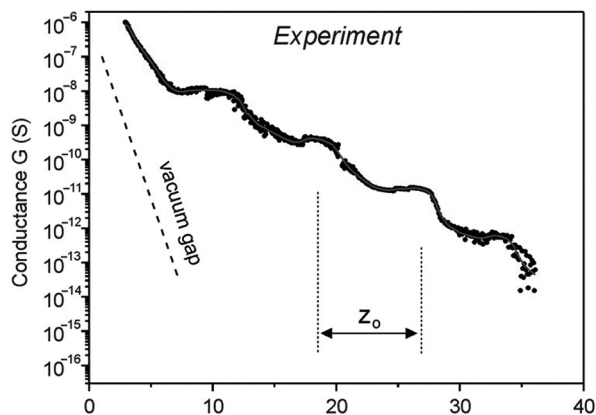
where G is the conductance of the nanojunction, k_{et} is the intramolecular electron transfer rate constant, Γ_D^L and Γ_A^R are couplings of the donor part with the left electrode and the acceptor part with the right electrode, and F is the thermally averaged Franck–Condon-weighted density of nuclear states (see Section 3.2.1.3). Using typical values of the couplings Γ_D^L and $\Gamma_A^R \approx 0.5 \text{ eV}$ and $F \approx 0.02 \text{ (eV)}^{-1}$ yields an approximate numerical relation between G and k_{et} :

$$G \approx 10^{-17} k_{\text{et}} \quad (5.33b)$$

where the conductance G is in Ω^{-1} and the rate constant k_{et} is in s^{-1} . This relation shows the interest of studying mixed valence binuclear systems (Section 3.2.2), as a way to prepare studies on molecule bridged nanojunctions. In the case of mixed valence compounds, however, the results are usually expressed in terms of decay rate γ of the V_{ab} factor with length. Since a rate is

**Fig. 5.23**

Determination of the conductance of a polymer chain as a continuous function of its effective length. Up: disposition with the STM tip grasping one end of the chain; down: conductance (in log scale) as a function of distance. The oscillations on the decay are due to the successive detachment of monomer units (at a distance Z_0) from the surface. (From L. Lafferentz, F. Ample, H. Yu, S. Hecht, C. Joachim, L. Grill, *Science* 323 (2009), 1193.) <<http://www.sciencemag.org/content/323/5918/1193.full>> (Reprinted with permission from AAAS.)



proportional to V_{ab}^2 (Section 3.2.1.2), and taking into account eqn. (5.32), the γ' factor of nanojunctions should be compared with 2γ .

Experimentally, we can compare, for a polyene chain, the $\gamma' = 0.22 \text{ \AA}^{-1}$ value quoted previously with the corresponding $2\gamma = 0.14 \text{ \AA}^{-1}$ value of the corresponding mixed valence system (from $\gamma = 0.07 \text{ \AA}^{-1}$; Section 3.2.2.6). Although the numerical agreement is not very good in this case, the general tendency of a weak decay is observed.

As for mixed valence systems, geometrical isomerism plays a role here. Thus, in a break junction where the active molecule is connected to the electrodes by thiophenyl groups, the conductance is sensitive to the position of the thiol group, with a much higher value for the *para* isomer with respect to the *meta* [5.49]. In a parallel way, a *para* connection gives a much higher V_{ab} coupling than a *meta* [5.50].

5.2.4 Molecular diode (rectifier)

In the same spirit as silicon electronics began with the p-n junction, molecular electronics' original goal was the search for molecular rectification [5.7]. The diode (rectifier) is indeed a simple device which can be associated with resistors to realize logic circuits.

The story of the molecular rectifier, from its conception to its realization after many attempts, is emblematic and highly instructive, as it illustrates the scientific way of coping with difficulties, and reorienting the subject when necessary. The original proposition by Aviram and Ratner (1974) was a 'gedanken experiment' involving an hypothetical molecule of the type donor- σ -acceptor, where the donor was of the tetra-thiafulvalene type, the acceptor was a tetracyanoquinodimethane moiety, and σ was a rigid saturated spacer [5.7]. The molecule was assumed to be contacted by two metallic wires, and simple reasoning suggested that the response would be different according to the polarity (Fig. 5.24). Thus the donor was modelled by a site with an occupied level just below the Fermi level of the electrodes (TTF-type), and the acceptor by a site with a vacant level just above (TCNQ-type) (see Fig. 5.24b).

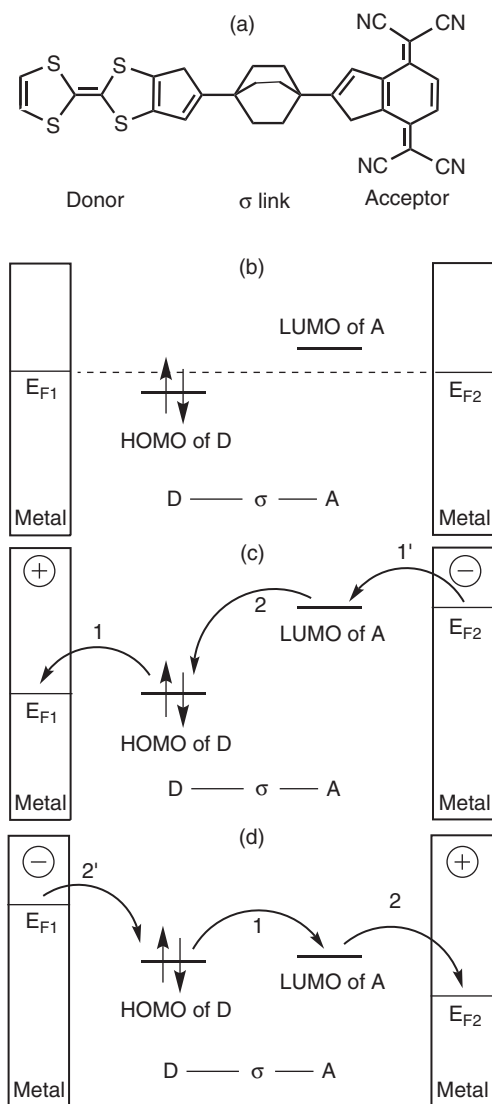


Fig. 5.24

Aviram and Ratner's molecular rectifier: concept and principle. (a) The prototype molecule; (b) representation as one-electron energy levels at zero bias; (c) behaviour on a given polarization; (d) behaviour on reverse polarization.

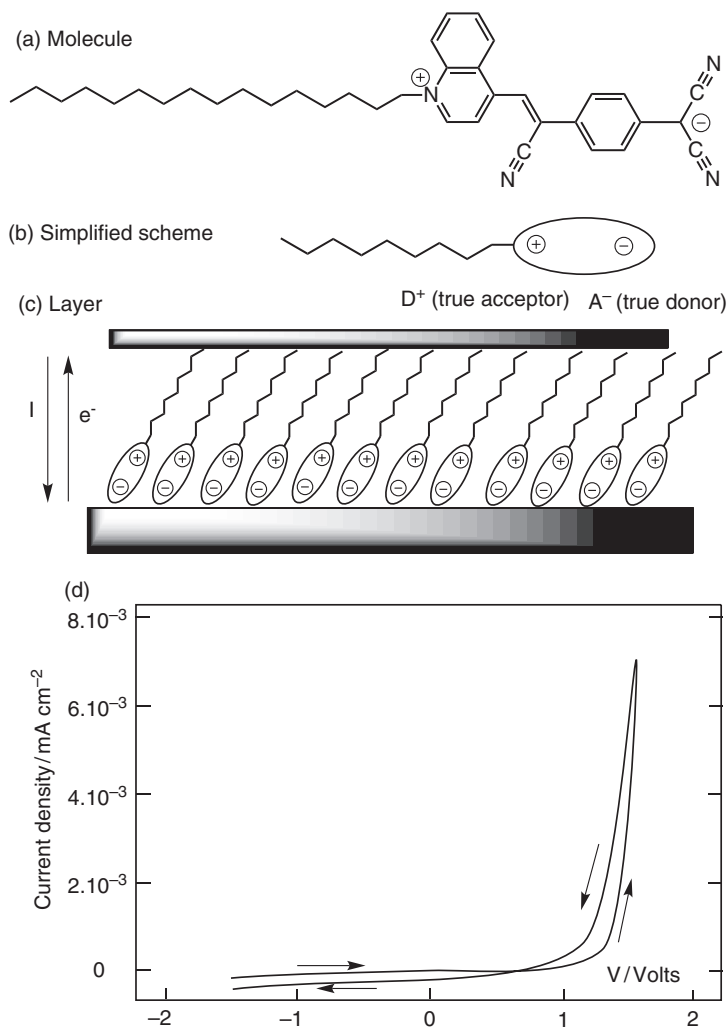
The effect of polarization was predicted by assuming that a shift of a Fermi level induces a smaller shift of the nearby molecular level, and that the threshold voltage is determined by the first coincidence between molecular and/or Fermi levels.

Thus upon the polarization depicted in Fig. 5.24(c)—that is [electrode (anode) (+) – D – A – (cathode) electrode (–)]—the first coincidence occurs between the Fermi level of the negative electrode and the LUMO of A, and also between the HOMO of D and the Fermi level of the left electrode (processes 1' and 1 in Fig. 5.24(c)). This generates the $A^- - D^+$ configuration, which is clearly unstable with respect to the A – D configuration, and inelastic intramolecular tunnelling (process 2) can occur, thus achieving the transfer. With the reverse polarization (d)—that is, [electrode (cathode) (–) – D – A – (anode) electrode (+)]—the transfers on both ends are blocked until the voltage is such that an intramolecular electron transfer occurs, producing the $A^- - D^+$ configuration (process 1 in Fig. 5.24(d)). After that, electron transfers 2 and 2' at both electrodes complete the process. In their original paper, Aviram and Ratner predicted that the easier polarization, corresponding to the lower threshold, would be depicted by (c); that is, with an electron flow in the A–D direction.

The realization of Aviram and Ratner's proposition proved extraordinarily difficult, and it took several decades before convincing results could be reported. Note, incidentally, that the molecule represented in Fig. 5.24(a) was never synthesized. The first results were obtained on Langmuir–Blodgett monomolecular films. In this technique it is necessary to prepare amphiphilic molecules; that is, molecules with a polar head (hydrophilic, with affinity for a polar solvent like water), and a long saturated hydrocarbon chain (hydrophobic, with affinity for non-polar media). These molecules can orient at an air–water interface, and can be transferred on a conducting substrate (Fig. 5.2a). After that, it is necessary to deposit by evaporation a top electrode, without disrupting the film nor creating a short circuit. Although the electrical measurements involve more than one molecule, it is admitted that the results are representative, because the molecules work in parallel.

A typical and much studied molecule is $C_{16}H_{33}$ -Q-3CNQ (Tail-D-A) [5.51], consisting of a donor (the quinolinium Q) and an acceptor (the tricyanoquinodimethane 3CNQ) group (Fig. 5.25a). Due to the requirements of the Langmuir–Blodgett technique, one end of the molecule (here the quinolinium) is functionalized by a long aliphatic chain (the tail), which at first sight should not play a role in the electronic behaviour. But matters are not so simple, as will be discussed later. In the ground state the molecule exists in the zwitterionic state [Tail– $D^+ \bullet$ – $A \bullet$], because the intramolecular electron transfer has already occurred. Thus the true donor is D^- , and the true acceptor is D^+ , but this should not change the general principle of functioning.

The best experimental evidence for rectification with this molecule was obtained by depositing a Langmuir–Blodgett film on an aluminum Al substrate (the surface of which, being, of course, coated with a thin layer of alumina, Al_2O_3 , formed spontaneously). A top Al electrode is evaporated on it, and contacts are realized with a drop of gallium/indium Ga/In eutectic. The I–V curve is clearly asymmetric, demonstrating the rectifying character of the junction (Fig. 5.25) [5.52].

**Fig. 5.25**

Molecular diode. (a) The $C_{16}H_{33}\text{-Q-3CNQ}$ molecule; (b) molecular model; (c) Langmuir–Blodgett film disposed between two aluminium electrodes; (d) current–voltage curve showing rectification. The voltage V refers to the polarity of the upper metal pad—the one contacting the tail side of the molecule. In (c) is shown the privileged direction for the current and the electron flux. (Adapted from Metzger [5.52].)

One has to note, however, that the direction of electron flow for the favourable polarization is from A^- to D^+ , this notation taking into account the zwitterionic nature of the molecule in the ground state. But A^- is, strictly speaking, the true donor, and D^+ the true acceptor, so that the system actually works as in Fig. 5.24d; that is, *in the reverse way with respect to the Aviram–Ratner prediction*. This seems to be a general result, according to studies on several kinds of molecules [5.39, p 338]. In fact, there is no simple way of predicting which polarization will produce the lowest threshold, because this depends in a complex and subtle way on the positions of the HOMO and LUMO with respect to the Fermi levels, and also on the repartition of the electrical potential inside the junction.

But is this rectification really due to the cleverly designed electronic structure of the molecule? This has been questioned for several reasons. First, the bridge linking the donor and the acceptor groups is a conjugated one, instead

of a saturated one in the original suggestion of Aviram and Ratner. An important consequence is that it is difficult or even impossible to identify a donor and an acceptor. The HOMO and LUMO are strongly delocalized on the two sites, so that the molecule behaves as a single entity. A second problem is due to the (apparently anodyne) presence of the long aliphatic chain. It decouples the active part of the molecule (the D–A moiety) from one of the electrodes, and, moreover, it influences the voltage division factor, so that the D–A moiety stays at a potential close to the one of the other electrode. The situation is actually similar to that of Fig. 5.5c. Under such circumstances, the behaviour is determined by the coincidence of either the HOMO or the LUMO with the Fermi level of the strongly coupled electrode. In other words, the rectification effect does not seem to arise from the donor–acceptor structure of the molecule (a simpler molecule would work as well). It could derive from the asymmetry of the interactions of the molecule with the electrodes.

In recent times, molecular rectification has been observed, at last, on single-molecule nanojunctions. The molecules were made of two conjugated π -systems linked by a C–C single bond (Fig. 5.26). The two π -systems were made different by proper substitutions—one containing an unsubstituted phenyl group, and the other a fluorine substituted phenyl group (hence more acceptor). The molecule was equipped with thiol functions at each end, for connection to gold electrodes in the break junction disposition (Fig. 5.2h) [5.53]. Importantly, the central part of the molecule consists in a 2,2'-dimethylbiphenyl unit, for which the presence of the methyl groups induces a large torsion angle between benzene rings (75°), thus minimizing the electronic coupling between the donor and acceptor parts.

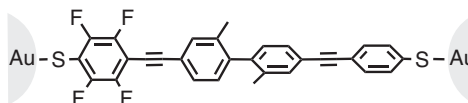
Experiments have shown a rectification when imposing ± 1.5 V bias voltage, with a rectification ratio (ratio of the currents for opposite polarities) of 4.5. No rectification is observed in control experiments with analogous *symmetrical* molecules [5.53].

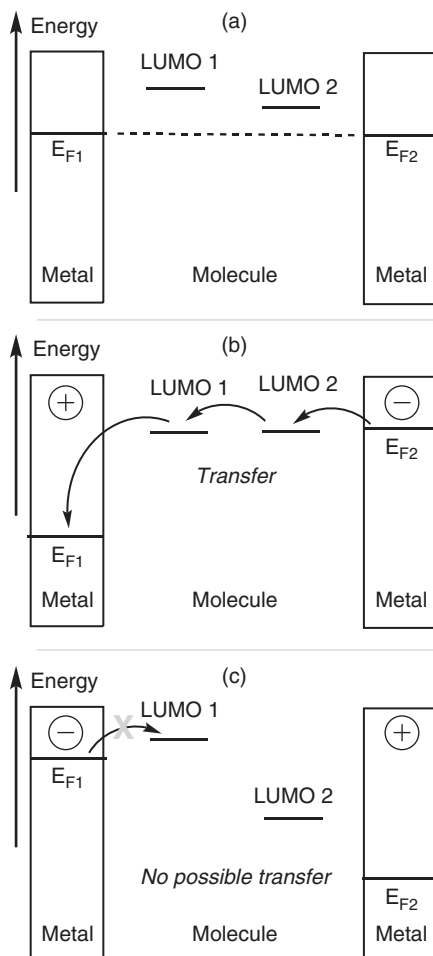
This last result is probably the most convincing evidence of a rectification effect, at the molecular level, because the connections with the electrodes and the general architecture are symmetrical. With respect to Aviram and Ratner's original concept, there are, however, subtle differences: the two parts of the molecule are chemically similar, and operate probably through their LUMO; that is, their more or less pronounced acceptor character. Theoretical calculations suggest that rather than being constituted of a donor and an acceptor group, the system can in some respects be considered as made of two weakly coupled quantum boxes (or dots) that have different polarizabilities [5.53]. But a simple model based on two acceptor levels (LUMO) of different energies can explain qualitatively the rectifying effect, as shown in Fig. 5.27.

For one of the polarizations, level coincidences may occur and allow an electron transfer via the LUMOs, while for the opposite bias this is more difficult.

Fig. 5.26

A single-molecule rectifier made of two different conjugated π systems, in a break junction.



**Fig. 5.27**

A simple model of the rectifying molecule made of two subunits with LUMOs of different energies. (a) No bias; (b) bias with the right electrode negative, allowing the electron transfer; (c) opposite bias does not allow the transfer.

To conclude this molecular rectifier saga, it can be remarked that after thirty years of research the original concept has been modified substantially. The general topology is still a two-site molecule, and the rectification effect has indeed been obtained with a unimolecular device including the electrodes. But the detailed interpretation is now different, and more in agreement with recent progresses in concepts and theory.

5.2.5 Memory effect and negative differential resistance in two-terminal devices

In molecular electronics, another important property and function to achieve is the storage of a bit of information on a molecule.

Some two-terminal devices exhibit interesting effects such as hysteresis (memory) or negative differential resistance (NDR). Hysteresis means that the current–voltage curve is different according to the direction of the voltage

scan—the system’s behaviour depends on its past history. Negative differential resistance means that the current–voltage curve exhibits parts where the slope dI/dV is negative. In both cases the spectacular changes in electronic properties are qualified as ‘switching effects’. Note that these behaviours have been known since the beginning of the electronics era on solid devices. Thus NDR has been used in a variety of devices such as memory cells, oscillators, microwave components, and even logic circuits.

In the case of molecular nanojunctions these effects are generally assigned to an important structural change in the bridging molecule itself; for instance, a mechanism of the polaron type or a change in the molecule–metal geometry.

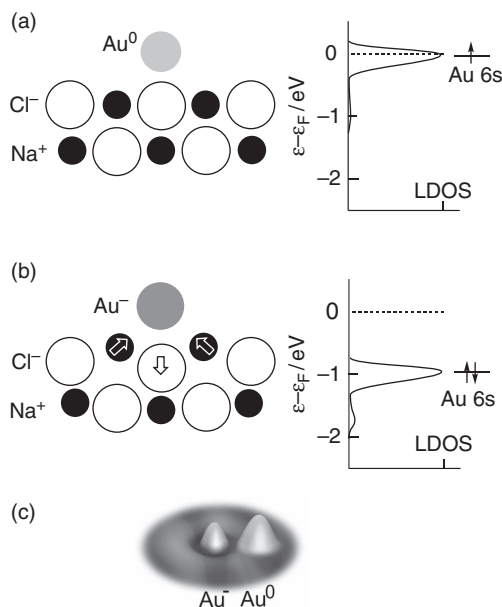
As a first example we consider experiments performed with a STM microscope and molecules, or even atoms, deposited on an insulating substrate. Under such conditions the coupling of the molecule with both electrodes is weak (see Fig. 5.7c), so that it retains its electronic identity. In addition, a given charge state can be generated by a voltage pulse and retained for some time, even after the end of a perturbation (memory effect).

Thus gold atoms can be adsorbed on a sodium chloride film (two atomic layers in thickness) deposited on a metal substrate (Fig. 5.28). The individual gold atoms can be seen in STM as protrusions. Applying a negative voltage pulse to the tip, when it is just above a gold atom, causes the transformation of this atom into the anion Au^- , which appears upon subsequent imaging also as a protrusion like neutral Au, but with a smaller contrast. Most importantly, both states are stable, after the end of the pulse, in the time-scale of the experiments [5.54].

The interpretation is straightforward in the frame of the hopping-type mechanism, taking into account the voltage division factor of Fig. 5.5c and eqns. (5.7) and (5.8) (see also the Box on ‘Imaging molecular orbitals’). First, let us

Fig. 5.28

The mechanism of ‘trapping’ of the reduced state Au^- by lattice distortion. A gold atom is deposited on an ultrathin NaCl substrate (two atomic layers only), itself lying on Cu(111), not shown. (a) Initial state: cross-section of the NaCl layers with one neutral Au^0 atom. Right part: projected (local) density of states LDOS of the 6s orbital of Au, showing its proximity with the copper Fermi level, in agreement with the $6s^1$ configuration. (b) After ionization to Au^- state. Note the motion of Na^+ and Cl^- ions (plain arrows, polaron formation). Right part: resulting stabilization of the gold 6s level, allowing the existence of the $6s^2$ configuration. (c) 3D picture from the STM experiment of Au^0 and Au^- . Note the apparent larger size of neutral Au (see text). ((a) and (b) adapted from [5.54]; (c): courtesy of J. Repp and G. Meyer.



note that gold has a relatively low-lying vacant state (a 6s orbital), and thus an intrinsic facility to produce Au^- (this is also shown by its special chemistry [5.55]). When a bias voltage is applied, the effective electrostatic potential experienced by the gold atom stays close to the Fermi level of the substrate. Thus the level coincidence arises on the vacuum side of the junction, and if the tip is negative one obtains a gold atom reduction. Once the gold atom has been charged to an Au^- anion, a relaxation of the surroundings (the NaCl layer) occurs. The atomic motions are the same as in small polaron formation in ionic crystals (Section 3.1.2); that is, positive charges are displaced towards the newly created Au^- , and negative charges are repelled. This relaxation strongly stabilizes the 6s atomic orbital of gold, so that the Au^- state is trapped. The calculation shows in particular that the 6s level has been so lowered (about 1 eV) that it is now out of resonance with the Fermi levels of the electrodes [5.54]. The current through the junction is thus decreased, and in subsequent imaging the Au^- ion appears different from Au^0 , because in the imaging process the tip is moved so as to recover a determined current. Note that due to this compensating motion of the tip, the apparent size of Au^- decreases (Fig. 5.28c), contrary to the prediction based on chemical knowledge.

To return to the neutral state, an activation energy must be overcome, as in the case of electron transfer in ionic solids or in solution. In the present case this activation energy is so large that no back-conversion of Au^- into Au was observed in the time-scale of the experiment (several hours).

An analogous experiment has been described in the case of a molecule, bis-dibenzoylmethanato-copper [5.56]. As previously, it is deposited on a NaCl bilayer grown on Cu(111). The molecule is initially neutral with copper in the Cu(II) state (d^9), and can be driven by a proper voltage pulse into the negatively charged state corresponding to Cu(I), d^{10} . But here the main source of stabilization after the charge transfer is intramolecular: the initial Cu(II) complex is square planar, while the Cu(I) complex is tetrahedral. Charge and geometrical changes of the complex on the surface have been established by a combination of scanning tunnelling imaging before and after the pulse, and dynamic force microscopy, which is sensitive to the charge of the molecule (Fig. 5.29).

Another and quite different type of two-terminal system with memory effect is based on molecular motions rather than electron motions. This occurs with special molecules called rotaxanes. A rotaxane is a molecule with both characteristics of a wheel (*rota* in Latin) and an axle. In a normal rotaxane the axle is threaded across the wheel, and they cannot dissociate without breaking a covalent bond (Fig. 5.30), because there are stoppers at the ends of the axle. A related but simpler system is called ‘pseudo-rotaxane’: in this case, there is no stopper, so the two parts can disassemble. For a review about rotaxanes and the beautiful chemistry of their preparation, the refer is referred to [5.57].

In the rotaxane, when the axle is long enough, the wheel can behave as a shuttle. The shuttle is usually in close interaction (usually by donor–acceptor interaction) with a part of the axle, called a recognition site, or more simply a station. An interesting extension of the concept gives rise to [2] rotaxanes with two stations (Fig. 5.30). They constitute, therefore, a two-state system, in principle adapted to a binary coding of information. The interest of such systems is that the interaction between the two parts is a chemical process, but

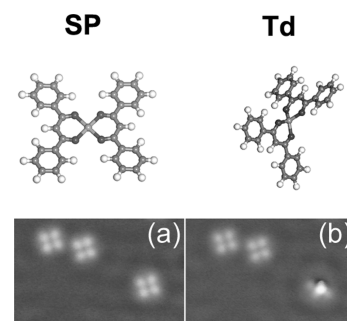
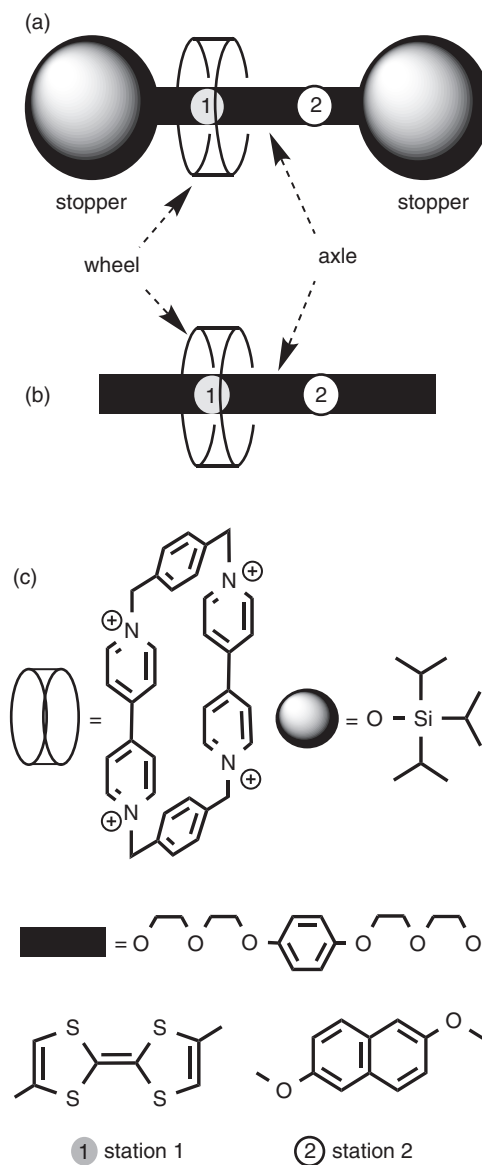


Fig. 5.29

Switching of a copper complex by reduction. Upper: models of the two forms, square planar (SP) Cu(II) and tetrahedral (Td) Cu(I). Lower: (a) STM pictures of three molecules; (b) STM picture when one of the molecules has been switched by a -2 V voltage pulse applied to the STM tip. (Reprinted with permission from T. Leoni, O. Guillermet, H. Walch, V. Langlais, A. Scheuermann, J. Bonvoisin, S. Gauthier, *Phys. Rev. Lett.* 106 (2011), 216103. <<http://prl.aps.org/abstract/PRL/v106/i21/e216103>>.

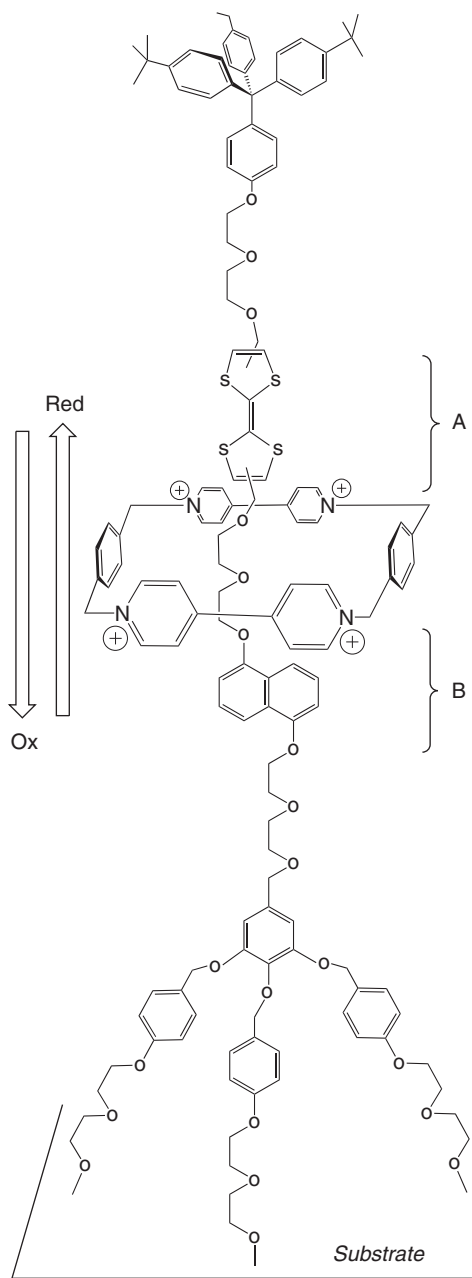
(Copyright 2011 by the American Physical Society.)

**Fig. 5.30**

(a) A rotaxane and (b) a pseudo-rotaxane, both bearing two stations, 1 and 2; (c) chemical definitions of the schematized components. The wheel is generally a strongly acceptor cyclic system (here with four pyridinium sites), while the stations are donors. In the example shown, station 2 has a fixed donor power, while station 1 (a TTF moiety) can lose its donor character by oxidation.

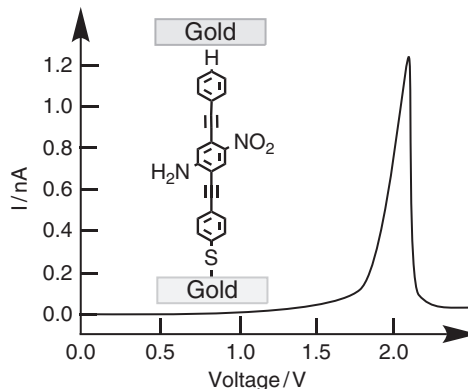
since they cannot fully separate, the motion of the shuttle from one station to the other is actually a monomolecular reaction analogous to an isomerization. Such molecules have been studied first in solution, where the acceptor/donor character of a moiety can be reversed by electrochemistry, and have then been transferred and used in solid-state devices.

Rotaxane molecules have been deposited as Langmuir–Blodgett (LB) monolayers on a polycrystalline silicon substrate, and covered by a Ti/Al top electrode, thus giving a two-terminal device of monomolecular thickness (Fig. 5.31). Electrical characterization shows a switching effect under

**Fig. 5.31**

A molecular shuttle with two stations linked to a substrate. The motion is controlled by the electrochemical oxidation of the TTF unit (station A). See text. (Adapted from [5.58].)

the form of an hysteresis curve, associated with the existence of two possible conformations with different electron transport properties [5.58]. Note that the perturbation is here an oxidation/reduction of a moiety, transforming, for instance, a donor station (TTF) into an acceptor (TTF⁺). This is basically an electrochemical process, requiring in solution the intervention of a counter

**Fig. 5.32**

Negative differential resistance (NDR) effect observed with phenylene-ethynylene molecules bearing amino and nitro groups and deposited between two gold contacts in a nanopore. (Adapted from [5.59].)

ion. It is not clear how such a process occurs in the solid-state device based on a monolayer.

Although several control experiments show that a two-station structure is necessary to obtain a switching effect, the exact interpretation remains obscure, because the molecules contain several other flexible parts, and their exact orientation in the LB layer, as well as the geometry of the contacts with the interfaces, are not readily accessible to experiment.

Another interesting (and intriguing) case is provided by molecules of the phenylene ethynylene type used in a nanopore cell (see Fig. 5.2b), where they form a self-assembled monolayer (SAM) with close packing in the same orientation. It is then possible to contact the ensemble of molecules (around 1,000) between the bottom metallic substrate and an evaporated upper electrode. Due to the small size of the pore (30–50 nm), a defect-free ensemble can be expected. The current–voltage curve exhibits the NDR effect, with an abrupt fall of the current from about 1 nA to 1 pA in a very narrow potential range (Fig. 5.32) [5.59].

The interpretation of this effect is not totally established. It has been suggested that it is due to a conformational change, phenylene groups adopting for a given voltage a perpendicular conformation with almost total decoupling between the phenylene units. Another possibility, supported by theoretical calculations, is that a charge injection occurs, followed by molecular relaxation (the hopping mechanism; see Section 5.2.2.2). After relaxation the molecular level (for instance, the LUMO) is no longer in the ‘energy window’ between E_{F1} and E_{F2} , so the current decreases abruptly [5.36, 5.60].

5.2.6 Two-terminal devices under constraint (pressure, light)

The next step in complexity is to achieve the control of the current by realizing a three-terminal device. This task is by no way trivial, and we begin with examples in which this control is not performed by a third electrode but indirectly by an effect other than electrical.

5.2.6.1 C₆₀ molecule: a molecular transistor under pressure

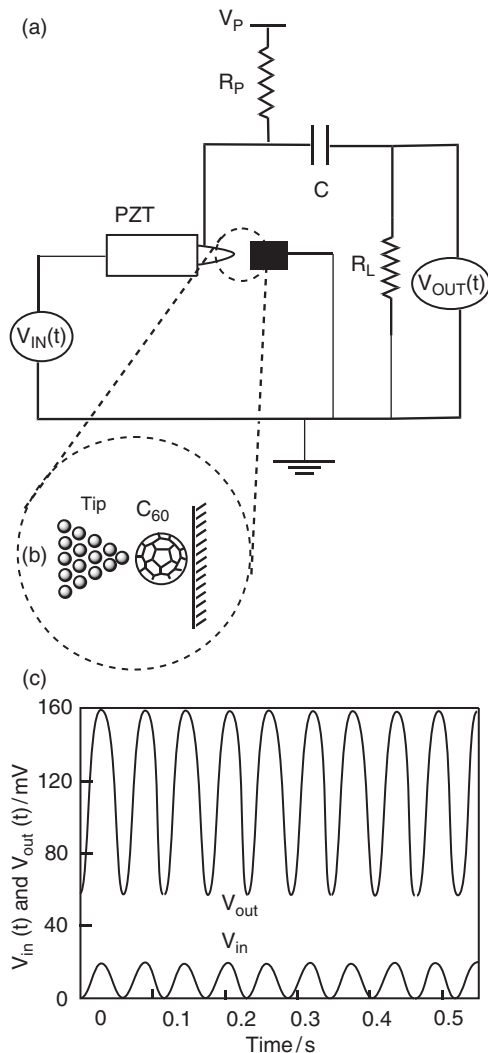
A C₆₀ molecule adsorbed on a metallic surface can be addressed by the tip of a STM. Under these conditions and for small bias voltages, a weak current flows through the junction by the tunnelling effect. The $T(E_F)$ factor (Section 5.2.2.3 and Fig. 5.12) is very small—around $2.3 \cdot 10^{-4}$ —but if the STM tip-to-C₆₀ distance is varied, the $T(E_F)$ changes drastically. Thus an increase of three orders of magnitude is observed when going from a situation where the C₆₀ molecule is weakly perturbed by the tip, with a relaxed geometry, to a situation where C₆₀ is constrained, and thus deformed [5.61]. This peculiarity can give rise to an amplifier effect when the complete experimental setup is considered. The STM tip position is indeed controlled by a piezoelectric actuator. (Piezoelectricity is the property of some substances to create charges under application of a mechanical stress or, at the opposite, to deform under the application of an electrical field. This can be used to generate displacements of extreme precision.) By modulating the command voltage of the piezoelectric actuator (input), a change occurs in the tip position, and thus in the current. This last change can be easily converted in a voltage change by means of a resistor, thus providing the output (Fig. 5.33; see also the Box ‘Field-effect transistor’ p 442 for electrical definitions). It is found that the device exhibits gain; that is, a small change in the input (20 mV, for example) leads to a larger change in the output (100 mV) [5.61]. Actually, this is one of the two examples of molecule-based devices exhibiting gain, the other being the carbon nanotube device described in Section 5.2.8.

A deeper study shows that this amplifying effect is due to unique properties of the C₆₀ system with degenerate manifolds of frontier orbitals (h_u HOMO and t_{1u} LUMO). A simple four-orbital model can be built with two orbitals from each set presenting opposite symmetries with respect to the electrodes. They contribute to the tunnel effect, but for symmetry reasons their contributions cancel in an almost perfect way in the normal (relaxed) C₆₀. Compressing C₆₀ lifts the degeneracy, and thus suppresses the cancellation. This explains the great sensitivity of the C₆₀ system towards a change in geometry, and thus the amplifying effect [5.61].

Of course, this result constitutes only a proof of principle. It shows that it is possible to reach gain with a single-molecule device, but the total setup including the STM apparatus is of huge dimensions! An integrated system in which a C₆₀ molecule would be located between two planar electrodes and compressed by a microcantilever has been proposed [5.62].

5.2.6.2 Photochromic molecules: switching under irradiation

Another method of controlling a current is to use photons in order to perform a photoisomerization, as it occurs in photochromic molecules. These molecules have been widely studied and used as components for molecular materials, but they will be used here at the single molecule scale. Among the extreme variety of photochromic systems, the family of dithienylcyclopentenes has been particularly studied because they present distinct advantages (see Box ‘Switching and memory’) [5.63]. They will also be encountered in Section 5.3.1.

**Fig. 5.33**

The C_{60} amplifier. (a) Complete circuitry. PZT: piezoelectric actuator fed by $V_{in}(t)$ voltage; R_P : polarization resistance; R_L : load resistance; $V_{out}(t)$ is read at the terminals of the load resistance. (b) Expanded view of the C_{60} surrounding. (c) Plots of $V_{in}(t)$ and $V_{out}(t)$ upon application of the $V_{in}(t)$ sinusoidal voltage showing a gain of 5. (Adapted from [5.61b].)

To study single-molecule switching, a dithienylcyclopentene derivative has been equipped with thiols functions to allow fixation on gold electrodes. The connection to electrodes was realized by a variant of the breakjunction technique, in which a gold surface is covered by the dithiolated molecules, and a STM gold probe tip is repeatedly approached and retracted (Fig. 5.34). Analysis of the current allows identification of the precise moment when the gap is bridged by just one molecule. This method allows the precise electrical characterization of the photochromic molecule in the two isomeric states [5.65]. The nanojunction resistance is $526 \text{ M}\Omega$ for the open form (OFF) *versus* $4 \text{ M}\Omega$ for the closed one (ON), starting from isomers prepared previously. The *in situ* conversion, using the appropriate radiation, was observed in both directions.

Switching and memory using photochromism: the example of dithienylcyclopentenes

Switching and memory are frequently related, as one wishes that a given bit of information is retained after the application of a perturbation. Photochromism—the process by which a given substance changes its colour upon irradiation—is widely used for this purpose, because at the molecular level it is frequently the result of photoisomerization. Thus it implies that a molecule can exist under two states, with the appealing possibility of coding binary information (0 for one isomer and 1 for the other). Bistability results if the two isomers are stable under the same conditions and do not interconvert spontaneously once formed. An additional constraint for potential applications is that the number of possible cycles between the two states before degradation or side reactions occur must be as high as possible.

Here we consider the example of diarylethenes—in particular, dithienylcyclopentenes, which can undergo photocyclization/ring reopening processes under irradiation.

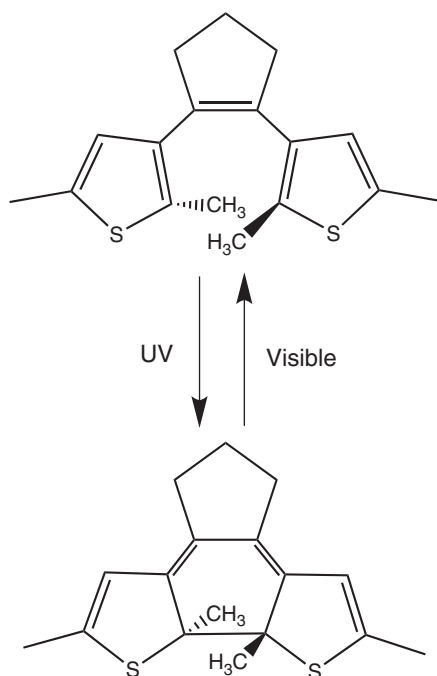


Fig. 1

Switching between the two isomers of the diarylethene moiety, in this case dithienylcyclopentene.

Basically, they are made of two thiophene units linked to a double bond, itself embedded in a cyclopentene ring to block the *cis* configuration [5.63]. Their photochemical characteristics are particularly well adapted to switching and memory at the molecular scale. First, the two isomers—‘open’ and ‘closed’—are inert (kinetically stable), though one of them—generally the ‘open’—is thermodynamically more stable. Thus the state of the molecule can be considered as representing a bit of information. Second, the photochemical transformation is reversible and can be achieved in both directions, cyclization being triggered by ultraviolet light and

reopening by illumination in the visible, with high quantum yields in both cases. Thus the two states can be kept almost indefinitely and converted one into the other at will under the influence of light. The difference in absorption spectra arises from their different electronic properties: one isomer can be considered as consisting of two weakly coupled thiophene units, the other as a conjugated octatetraene. This is a third and precious feature, which can be used to control an electron transfer or transport across the molecule—the ‘open’ isomer being ‘insulating’ while the ‘closed’ isomer is ‘conducting’.

Dithienylcyclopentenes have been proposed as molecular optical memories. Note, however, that if the nature of the memory effect is indeed monomolecular, it is not in general possible to store one bit of information on a unique molecule, because the smallest dimensions of a light-beam are far larger than the size of the molecule. Thus most applications involve a macroscopic ensemble. In addition, to produce a practical optical memory system one should have a non-destructive readout capability. This means that reading the state should not alter the message, which is impossible in practice because the usual way of reading is by using optical absorption. To circumvent this difficulty, ingenious systems have been devised in which a combination of effects is needed for writing, while a simple irradiation is sufficient for reading [5.63]. (See also Section 4.5.3.2 and Fig. 4.47a.)

Of course, an electrical conversion of the molecules would be more practical and more in the spirit of electronics. The ultimate limit of addressing a single molecule is easier to reach using electrons rather than photons. It is interesting in this context to note that some diarylethene compounds can also be interconverted by an oxidation–reduction sequence [5.64].

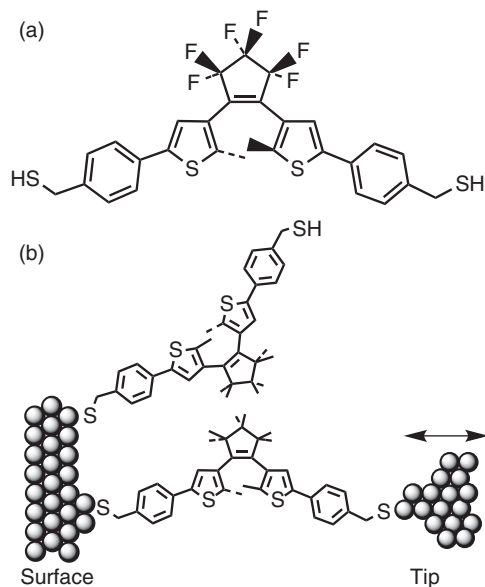


Fig. 5.34

The dithienylcyclopentene switch connected to two electrodes. (a) The molecule is functionalized with thiol groups for fixation on gold; (b) the measurement is performed with a STM version of the break junction allowing a precise manipulation of the interelectrode distance (double arrow close to the tip). (Adapted from [5.65].)

Thus the photochemically induced switching of a single molecule in a nan-junction has been demonstrated, despite the fact that the presence of metallic conductors can quench the excited states (see Section 4.3.4) and thus perturb the isomerization process. In some cases, using a slightly different molecule, switching can occur in only one direction [5.66].

5.2.7 Three-terminal devices: field-effect transistor (FET)

True three-terminal devices present the topology of a transistor, with a gate electrode controlling the electron transport between the source and the drain by applying a potential difference (see Box 'Field-effect transistor').

Realizing a field-effect transistor with a molecule as the active unit is extremely difficult, because the three electrodes and the molecule must be in close proximity and accurately positioned with respect to each other. Some examples are now available where the source and drain electrodes are deposited on an insulating SiO₂ layer surmounting the third electrode, the gate [5.67]. The gap between source and drain is created and adjusted by electromigration, and a molecule able to undergo a redox process (for instance, a C₆₀ or a cobalt complex) is deposited in the junction (Fig. 5.35). Such devices can be termed *single-molecule transistors*, though the question of the electrical gain (which should be > 1) is not always addressed.

The general principle is based on the energy levels' disposition, such as in Fig. 5.35a,b. Manipulating V_{SD} shifts one of the electrode levels with respect to the other, with an intermediate variation for the molecular levels (as in Fig. 5.24, for instance), while manipulating V_G shifts the molecular energy levels as a whole with respect to both electrodes. Thus level coincidence giving rise to a current can be achieved either by a V_{SD} or by a V_G variation. The final result is presented in Fig. 5.35c, showing in the V_{SD}, V_G plane, the zones where current flow occurs. If the molecule is large enough, several characteristic diamond-shaped patterns are observed, corresponding to successive charge states of the molecule. Note that the diamonds are of different sizes because the levels are generally not equidistant. Inside these patterns, frequently called 'Coulomb diamonds', the current is blocked. (Actually, this terminology, stressing the role of electrostatic repulsion, arises from the quantum dot literature and is not strictly valid here. In the present case involving molecules, the spacing of molecular levels depends, in addition, on the electronic structure.)

At the boundary of a diamond the current starts to flow, and this is commonly detected by a peak in differential conductance dI/dV (where V = V_{SD}). Outside the diamond the current is almost constant as a function of V_{SD} (see, for instance, Fig. 5.17). Note, finally, that in Fig. 5.35c the slopes of the ascending and descending boundaries are not the same. This asymmetry derives from the asymmetry in the electronic circuit, because V_G (strictly speaking V_{GD}) is defined with respect to one particular electrode.

New effects occur when the junction contains a magnetic molecule, and are presented in Section 5.2.9.

Field-effect transistor

The field-effect transistor (FET) is the workhorse of modern digital electronics. The principle and topology are very simple. The main current crosses the device, made of semiconducting material, between two electrodes, called 'source' and 'drain' respectively. A third electrode, called 'gate', controls the source-drain current by an electrical field effect. The voltages V_{SD} and V_{GD} (denoted V_G) are shown in Fig. 1. The source-drain current I_{SD} can be converted to an output voltage V_{out} by inserting a load resistance in the circuit (not shown here, but in Fig. 5.33). The important electrical characteristics are (i) the transconductance dI_{SD}/dV_G , and (ii) the gain, defined as V_{out}/V_G . One wishes to have the gain > 1 , and this achieved in the C_{60} example in Section 5.2.6.1.

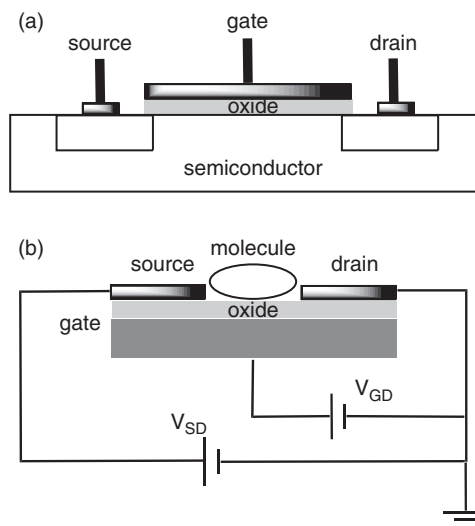


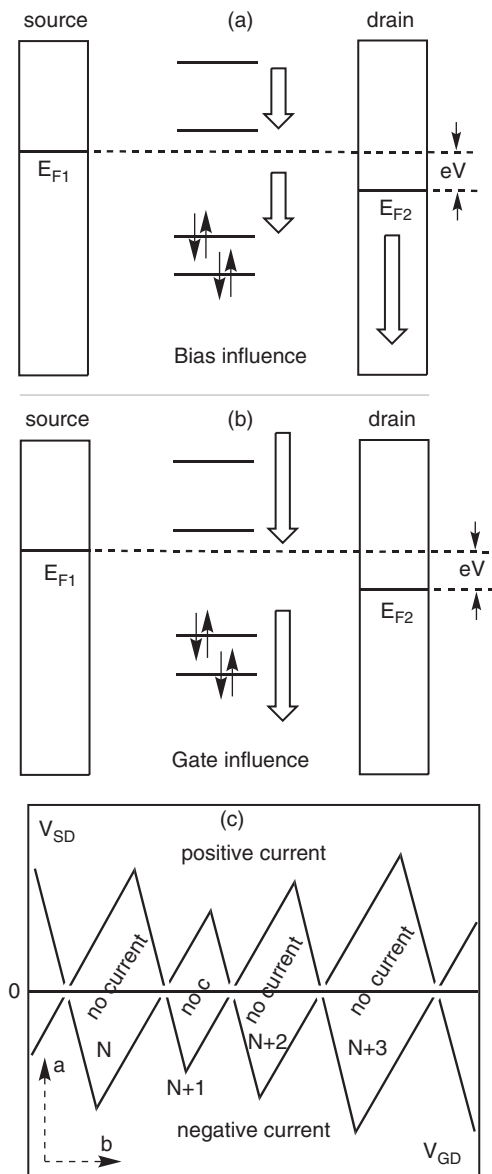
Fig. 1

(a) Scheme of a conventional field-effect transistor; (b) transistor with a single molecule as active part. The latter device, which is much smaller, is built so that a gate electrode (silicon) is capacitively coupled to the molecule through an insulating oxide layer (silica, SiO_2). The source-drain electrode gap can be adjusted by electromigration. Note that the gate voltage (V_{GD}) is defined with respect to one electrode, the drain, but is frequently denoted V_G for short.

The picture shows the usual silicon/silicon oxide realization, and the slightly different disposition when the active part is a molecule.

In both cases the gate electrode is electrically insulated from the others, and thus is crossed by a negligible current. The two basic parameters are thus the source-drain voltage, V_{SD} , and the gate voltage, usually measured with respect to the drain electrode, V_{GD} , which determines the electrical field in the device. This way of functioning is different from conventional transistors, where the third electrode acts by introduction of charge carriers.

Conventional FET are based on silicon semiconductors with a layer of SiO_2 performing the necessary insulation of the gate, hence the denomination metal-oxide-semiconductor field-effect transistor (MOSFET). Under normal conditions the electrons or holes cross the device from source to drain in a limited region of the semiconductor, called the channel. Applying a suitable voltage to the gate pinches the channel and thus modulates the current, as the action of a gardener crushing a garden-hose. As will be seen subsequently, the functioning of the single molecule transistor is markedly different due to the much smaller size and the quantization of charge states of the molecule.

**Fig. 5.35**

Principle of the single-molecule transistor. (a) Effect of an increase in bias voltage V_{SD} : the electron energies decrease strongly for the right electrode (drain, positive electrode) while the molecular levels exhibit an intermediate variation (long and short thick arrows respectively). (b) Effect of a variation in gate voltage V_G : only the molecular levels are affected. (c) Representation of the current in the V_{SD}, V_G plane. No current occurs inside the diamond-shaped regions corresponding to successive charging states of the molecule. Changing V_{SD} or V_G (moves along a or b) can trigger the current. Outside the diamonds, the current is constant as a function of V_{SD} . The boundary lines thus correspond to a strong peak in dI/dV .

5.2.8 Nanotubes, graphene, and devices

Carbon nanotubes constitute an important class of nanometer-sized objects which deserves a specific treatment. They were discovered as early as 1952 [5.68a], forgotten, and born again in 1991 with Iijima [5.68b]. They were soon the object of intense research, due to their unique mechanical and electrical properties combined with their good chemical stability. In recent years, several devices based on these objects have been realized because their length can reach hundreds of *microns*, so that it is relatively easy to connect them

to microelectrodes—typically 100 nm wide and 15 nm thick. But at the same time, carbon nanotubes can be considered as a special class of large molecules and can be studied with the tools of molecular chemistry.

The structure of carbon nanotubes is apparently extremely simple [5.69]. Let us assume that we take a graphene sheet (graphene is a single layer of graphite) and roll it into a cylinder with a typical diameter of about 1.4 nm. This produces a nanotube. Carbon nanotubes can exist as single-walled nanotubes (SWNT) made of one cylinder, or multi-walled nanotubes (MWNT) made of concentric cylinders. In the following we shall consider only the case of SWNT, because their behaviour can be more precisely related to their structure.

Actually, there are several ways to roll the graphene sheet, depending on the orientation of the cylinder axis (or its circumference) with respect to the lattice parameters. The orientation is defined by the unit vectors \vec{a}_1 and \vec{a}_2 , and a set of two numbers (m, n) which define a lattice vector $\vec{C}_h(n, m)$ (see Fig. 5.36a).

In the nanotube (Fig. 5.36a) the lattice vector is folded along the circumference. The origin and the end of the lattice vector are joined together. When

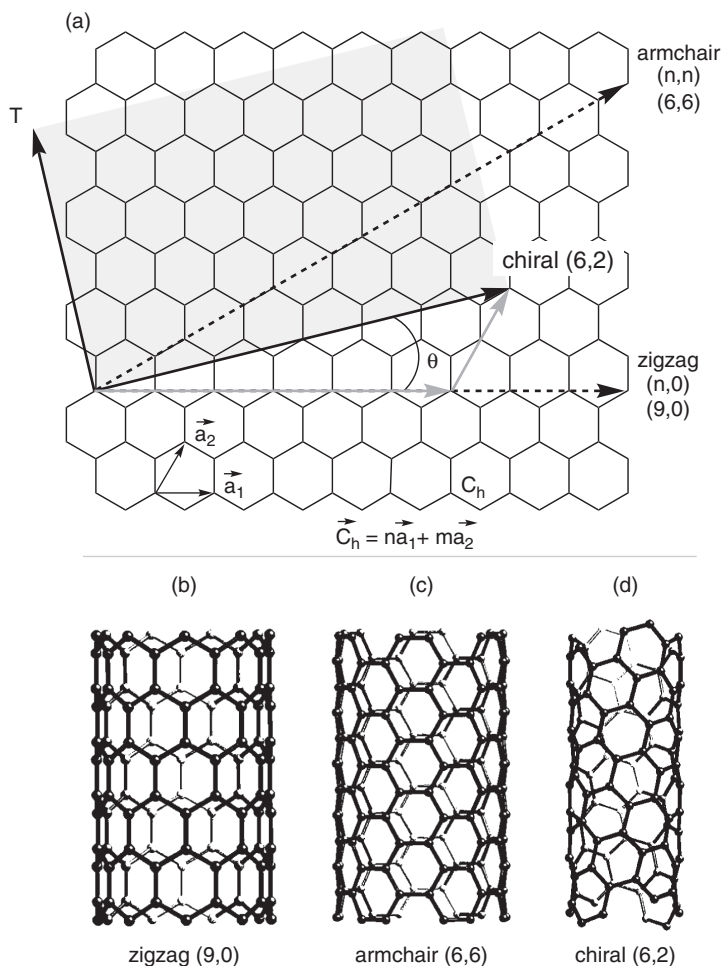


Fig. 5.36

(a) Flat graphene sheet with the indications of the unit vectors, \vec{a}_1 and \vec{a}_2 and lattice vectors. The lattice vector $\vec{C}_h(n, m)$ defines the circumference once folded, and the cylinder axis is perpendicular. Different ways of rolling a graphene sheet to make a carbon nanotube are shown: zigzag nanotube with the zigzag axis $\vec{C}_h(9, 0)$ (horizontal dashed arrow), armchair nanotube with the armchair axis $\vec{C}_h(6, 6)$ (tilted dashed arrow), a chiral nanotube $\vec{C}_h(6, 2)$ (bold plain arrow and grey surface; the grey plain arrows show the construction of the 6, 2 vector). The bold arrow T defines the longitudinal axis of the (6, 2) chiral nanotube. The chiral angle θ is defined with respect to the zigzag axis. At bottom, the corresponding schematic drawings of (b) the zigzag (9, 0) tube (semiconducting), (c) the armchair (6, 6) tube (conducting), and (d) the chiral (6, 2) tube. (Drawings made with the applet www.nanotube.msu.edu/tubeASP/)

the two numbers are equal—that is, or a (m,m) nanotube—one has the so-called ‘armchair’ structure, because the atoms around the circumference draw an armchair pattern. For (m,0) nanotubes the structure is called ‘zigzag’, with reference to the pattern of atoms around the circumference. Finally, one has also ‘chiral’ nanotubes, in which the rows of hexagons spiral along the nanotube axis. The nanotubes presenting the same m/n ratio are of the same type, and differ only in their diameter.

The electronic structure of carbon nanotubes is extremely peculiar. Armchair tubes are expected to be metallic, whereas most zigzag and chiral nanotubes are semiconducting. The precursor graphene sheet also has very exciting properties which, in some way, allow us to understand the relationship between structure and properties in nanotubes. A rigorous treatment of the band structure of graphene can be found in [1.9b], chapter 9. Here we present only a brief account of the salient points.

Using the tools introduced in Sections 1.4.2 and 3.3.2, we start from the hexagonal lattice in real space, with repeat vectors \vec{a} and \vec{b} (Fig. 5.37a; note that they are different from \vec{a}_1 and \vec{a}_2 in Fig. 5.36), and we build the related reciprocal lattice of the graphene layer with repeat vectors \vec{a}^* and \vec{b}^* (Fig. 5.37b) and the energy dispersion curve (Fig. 5.37c). For most values of k there is a gap, but the conduction and valence bands touch each other at point K ($k_a = k_b = 1/2$ in adimensional coordinates) (Fig. 5.37b, c). As we have seen in Section 3.3.2, when the filled valence band and the empty conduction band are touching, the energy gap is zero and the system should be metallic. As this occurs here in a very limited portion of the band diagram, the compound is called a *semi-metal*—a category intermediate between a true metal and a semiconductor.

In the contact region the shape of the dispersion curve with a conical intersection (Fig. 5.37d) confers a very high mobility on the charge carriers (electrons and holes). This can be grasped from the quasi-free electron model [1.9, 5.28], in which one can define an effective mass of the carriers given by $m^* = \hbar^2 / (\partial^2 E / \partial k^2)$. Thus at the conical intersection shown in Fig. 5.37d, the

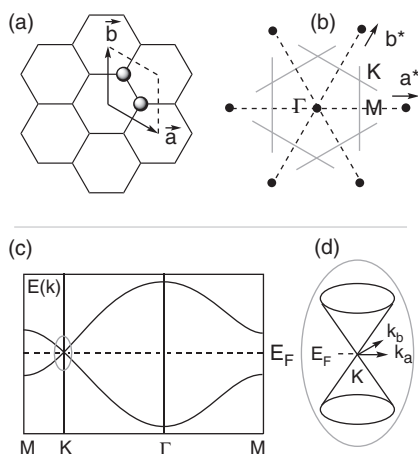


Fig. 5.37

Hexagonal graphene layer. (a) Real-space fragment of the layer with the repeat vectors \vec{a} and \vec{b} ($a = b$, with an angle 120°) defining the repeat unit with two carbon atoms (filled spheres). (b) Reciprocal lattice of the layer with repeat vectors \vec{a}^* and \vec{b}^* ($a^* = b^*$, making an angle of 60°), the first Brillouin zone (grey lines) and the Γ , M , and K points of the Brillouin zone ($\Gamma(0,0)$, $M(1/2,0)$, and $K(1/2,1/2)$). (c) Energy dispersion curve (π -type) of graphene. (d) Enlargement of the contact region (grey ellipse) near point K , showing the conical intersection. (Adapted from [1.9b], chap. 9.)

curvature being infinite, the effective mass tends towards zero. For undoped graphene, the Fermi level corresponds precisely to this intersection.

When the graphene sheet is rolled to produce a nanotube, the detailed way of connecting the sheet can tilt the balance towards either a metallic (no energy gap in K) or a semiconducting state (gap). Generally speaking there is extreme sensitivity of the nanotube electronic structure to the geometrical nature and even diameter of the nanotube. A simple rule is that (m,n) nanotubes with $m - n = 3p$ (where p is an integer, including zero) are metallic (the bands 'touch'), the others are semiconducting (there is a gap between the valence occupied and the conduction vacant bands). Thus all armchair tubes (m, m) are metallic, while for zigzag and chiral nanotubes, the properties depend on the exact values of n and m . Statistically, in a random sample, after purification, 1/3 of nanotubes are found to be metallic and 2/3 semiconducting.

Carbon nanotubes can be obtained by a variety of methods, which will not be detailed here. One can quote arc discharge between carbon electrodes, laser ablation, chemical vapour deposition from hydrocarbon gases with catalytic growth, and so on. Extensive details can be found in [5.69].

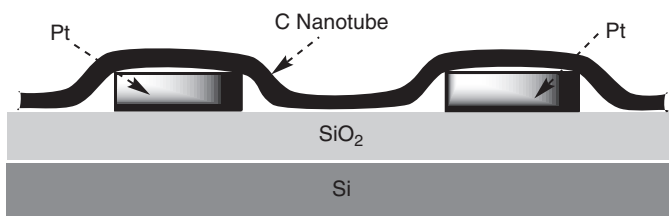
Many devices using carbon nanotubes have been realized by connecting them to electrodes. The simplest technique is to deposit, in a random way, the nanotubes (as a suspension in a solvent) on an array of metallic electrodes, and then choose the best samples. In some cases their position can even be adjusted using the tip of an AFM. Of course, this can be convenient for demonstration purposes, but not for mass production requiring a controlled mode of deposition. Intense research is thus devoted to the processes, allowing systematic building of circuits made of nanotubes. Such processes use methods or a combination of methods such as self-assembly, the local functionalization of a substrate to use the selective affinity of nanotubes for certain zones, 'combing' methods to align nanotubes, and so on. The reader can consult texts such as [5.70] for recent advances in this rapidly evolving field.

Several words of caution are, however, necessary: besides their intrinsic drawback—that is, the great heterogeneity of crude samples—carbon nanotubes frequently contain impurities, the most problematic for magnetic measurements being ferromagnetic impurities introduced by the usual catalysts. Purification is thus a fundamental necessity. Regarding the devices made of nanotubes, they suffer from the impossibility of predicting the nature (metallic or semiconducting) of a given nanotube, and the difficulty to master the contact resistance with the electrodes. We now present some examples of devices.

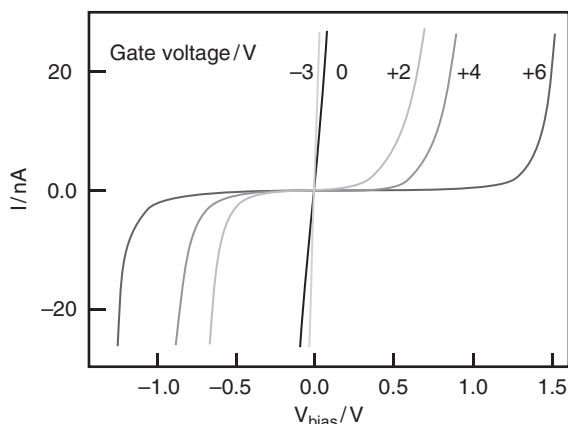
Field-effect transistor (FET)

This device was realized in 1998, using a SWNT [5.71] (Fig. 5.38) with the same topology as for single molecule transistors (see Box 'Field-effect transistor' and Fig. 5.35), though the principle of operation is different.

The SWNT transistor necessitates a *semi-conducting* nanotube. At the present time there is no way of knowing in advance whether a given nanotube will be metallic or semiconducting, and thus one has to fabricate a large number of devices and then identify which ones are functional. When the nanotube is metallic, the current voltage curves $I - V_{\text{bias}}$ are linear and do not depend on

**Fig. 5.38**

A field-effect transistor made of a single semi-conducting carbon nanotube. The nanotube lies above the Pt source and drain (in grey) and the Si/SiO₂ gate. (Adapted from [5.71].)

**Fig. 5.39**

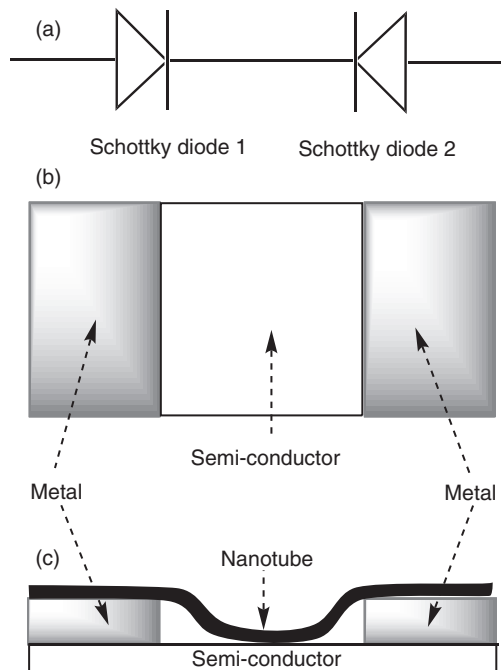
Current-voltage curves $I = f(V_{\text{bias}})$ for a device of the type shown in Fig. 5.38, recorded at room temperature at different applied gate voltages. (Adapted from [5.71].)

the gate voltage. When the nanotube is semi-conducting, the $I - V_{\text{bias}}$ curve is strongly non-linear and depends very much on the gate voltage, as shown in Fig. 5.39. Such systems could exhibit a gain > 1 [5.71].

The interpretation is based on the analogy with conventional semiconductor devices. Since the contact resistance between the nanotube and the metal is expected to be large, the device is described as two Schottky diodes connected back to back (Fig. 5.40) [5.71]. (A Schottky diode is a metal-semiconductor junction. It is used for its rectification properties with a very fast response.) Then classical theory explains the transistor effect by the influence of the gate potential on the central part of the nanotube (away from the contacts), giving rise to either accumulation or depletion of holes. Accumulating holes, for negative gate voltage, increases the conductance [5.71]. Note that due to the large size of the device and length of the nanotube (300 nm), the terminology has shifted towards concepts of conventional, or at least mesoscopic, electronics. The only difference with the usual metal-oxide-semiconductor (MOS) devices is that the nanotube is not intentionally doped.

Single-electron transistors (SET)

Carbon nanotubes can also be used to make single-electron transistors (SET), using the Coulomb blockade effect (Section 5.2.2.4 and Fig. 5.17). In this case one needs a nanotube presenting metallic conductivity, which is deposited on two electrodes (source and drain), thus defining the useful length, which can be more than 100 nm [5.72]. A third electrode (the gate) is present below the nanotube. Since the nanotube is metallic and the contacts with the electrodes

**Fig. 5.40**

Analogy between the semi-conducting nanotube connected to two electrodes and two Schottky diodes connected back to back. (a) Schottky diodes. (b–c) Carbon nanotube device, (b) top view, (c) side view.

are highly resistive, we are in the situation of Coulomb blockade, the nanotube playing the role of the ‘small’ metallic island. The I – V curve shows distinct steps, the position of which is sensitive to the potential of the third electrode. The general behaviour is explained by the orthodox theory of Coulomb blockade, which implies that the conductance is sensitive to the presence or absence of only one additional electron on the nanotube, hence the expression ‘single-electron transistor’.

The first realized device worked at an extremely low temperature (5 mK) [5.72]. We recall that low temperatures are frequently necessary in Coulomb blockade experiments, in order to have $kT \ll e^2/2C$ (see Section 5.2.2.4), and more generally in experiments involving very small energies (see also Section 2.8).

In this first experiment the capacitance was relatively large, since it used a 3- μm long nanotube contacted on a large fraction of its length on the metallic wires. In a later experiment a contacted nanotube was deformed in two places using the tip of an AFM, thus generating extra tunnel barriers. This defined a 20-nm effective length for the metallic island, and extremely small area contacts and thus capacitances. The operating temperature has then been raised to room temperature [5.73].

Graphene devices

Graphene itself could be considered as a promising material to generate devices. As stated previously, it exhibits a peculiar band structure with an extremely high mobility for electrons and holes. The interest for this material rose abruptly as soon as simple methods were devised to generate single

monolayers, the simplest being peeling off a graphite sample with the aid of adhesive tape. Of course, more sophisticated and controllable methods exist, such as the use of a silicon wafer as substrate or epitaxial growing by thermal decomposition of silicon carbide [5.74]. Let us recall that in 2010 the Nobel Prize in Physics was awarded to A. K. Geim and K. S. Novoselov for their contribution to the study of this unique, truly 2D, material.

In principle, it should be possible to carve a circuit in a graphene sheet by using nanometer-size ‘burners’ such as the FIB (focused ion beam). The main advantage of this material is that it is theoretically possible to use it for both the nanometer-size active part, playing, for instance, the role of a field-effect transistor, and the macroscopic contacts. This would avoid the creation of an interface between different materials, in contrast to the other kinds of connection. However, at the present time the realization of a circuit like that depicted in Fig. 5.41 is still speculative.

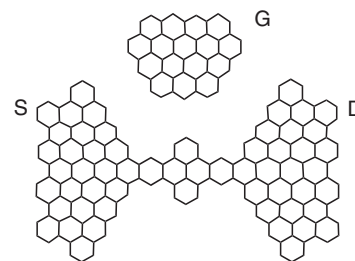


Fig. 5.41

Speculative concept of a circuit with source (S), drain (D), and gate (G) electrodes which could be cut out from a graphene sheet. (Adapted from [5.74a].)

5.2.9 Molecular spintronics

5.2.9.1 Spintronics: a recent discovery

Until now in this chapter we have considered the properties of the electron focusing on its charge, and the current that it creates through a nanojunction. Indeed, the electronic charge has been for a long time the unique property exploited by mainstream electronics. Most electronic devices are based on electrical current detection. Affairs began to move twenty years ago when scientists considered the electron not only as a charged particle but also as a spin bearer.

This was following an earlier idea by Mott (Nobel Prize recipient in 1977), suggesting that the electron flow in a magnetic metal consists of two fluids whose electronic spins have opposite directions. Let us say, to simplify, that the conduction is ensured by two channels, one with spins up (\uparrow, α), the other with spins down (\downarrow, β). Fig. 5.42 illustrates the basic ideas.

In a metal (Fig. 5.42, part a1), a conducting electron is moving from one scattering centre to another with a mean free path λ and a relaxation time τ (a1). This gives rise to the resistance R (b1). Looking at the spin, most of the scattering events (\bullet) occur without spin flip up to the point where the spin flips ($*$). The spin mean free path λ_{sf} (relaxation time τ_{sf}) is the sum of all the distances covered between two spin-flip events $\lambda_{sf} = \sum_0^{\tau_{sf}} \lambda$. This allows us to

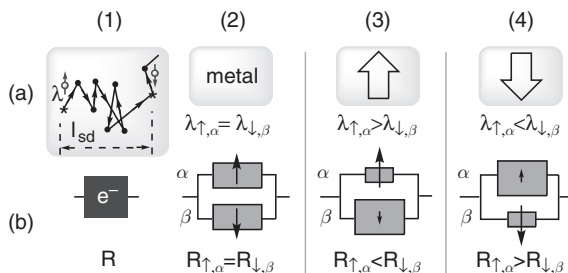


Fig. 5.42

Two-channels model and spin polarization. (a) Mean free paths λ for up (\uparrow, α) and down (\downarrow, β) spins in metals, non-magnetic (1, 2), or magnetic (3, 4). In (1) the (\uparrow, α) electron is moving between scattering centres, without spin flip (\bullet) or with spin flip ($*$). The scattering for equivalent (\downarrow, β) electron is not shown, for clarity. In (3, 4) the white open arrows indicate the direction of the majority spins in the material. (b) Equivalent electrical circuit: resistor R for electrons in a non-magnetic medium (2) and in magnets (3, 4). The surface of the grey boxes is proportional to the resistance. The size of black arrows schematizes the magnitude of the spin-polarized currents.

define the *spin diffusion length* $l_{sd} \propto \sqrt{\lambda\lambda_{sf}}$, which is smaller than λ_{sf} because the trajectory can be folded (a1). This length is an important quantity if one wants to retain unchanged the spin polarization through a layer of width e (l_{sd} must be $\gg e$).

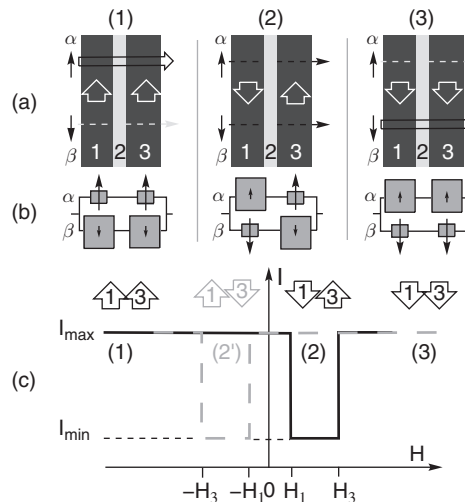
In a non-magnetic metal the spin mean free path λ_{sf} is the same for α and β spins, $\lambda_{1,\alpha} = \lambda_{1,\beta}$, and therefore $R_{1,\alpha} = R_{1,\beta}$ (Fig. 5.42, parts 2,a,b), and so behaves the conductance G . No polarization. In a magnetic metal (parts 3,4), most of the spins are aligned parallel, as they are coupled by exchange. A direct consequence is that the spin mean free path of the majority spins becomes larger than that of the minority opposite spins, and the resistance becomes weaker (parts 3,4a, b). A current flowing through the metal is spin-polarized, and its polarization changes with the magnetization (from (3) to (4)).

Such a phenomenon was first observed in magnetic multilayers, in which conducting ferromagnetic layers are separated by a thin conducting non-magnetic layer. The current through the device is strongly reduced when the configuration of the magnetizations of the conducting layers changes from parallel to antiparallel. The effect was named *giant magnetoresistance (GMR)*, and one of the resulting devices a *spin valve*. GMR is due to the polarization of the spin current by the magnetic layers. A very simplified image is shown in Fig. 5.43, using the example of a spin valve.

In (1,ab), the mobile (α, \uparrow) spins parallel to the majority spins present a large $\lambda_{\uparrow,\alpha}$ in both layers 1 and 3, a weak $R_{\uparrow,\alpha}$, and a large conductance (1b). The (α, \uparrow) current is large (open horizontal arrow). The conducting (β, \downarrow) spins encounter the opposite situation (large resistance in both layers 1 and 3), and the corresponding (β, \downarrow) current is very weak (grey dashed horizontal arrow). The overall resistance R_p (p for parallel configuration), is weak and the conductance G_p is large. In (2,ab) the magnetization is flipped in layer 1. Therefore α spins meet a small resistance in layer 1 but a large one in layer 3 (2b). The overall situation is analogous for β spins (2b). Then, both α and β currents are weak (dashed black horizontal arrows, 2a), as is their sum. The overall

Fig. 5.43

Principle of GMR and of a spin valve device. Two magnetic conducting layers 1 and 3 (dark grey) are separated by a thin non-magnetic metallic spacer [(2), light grey]. (a) Three states of the device with different configurations of the majority spins in the magnetic layers (white vertical arrows), parallel (up, up) in (1), antiparallel in (2), and once again parallel in (3) (down, down). The horizontal arrows schematize the magnitude of the polarized current (α, \uparrow or β, \downarrow spins) (open white > black dashed > grey dashed). (b) Equivalent electrical circuit. (c) Usual 'butterfly' shape of the intensity I as a function of the applied magnetic field, H , in a spin valve. The black plain curve corresponds to an increasing magnetic field, the grey dotted line to a decreasing field. H_1 and H_3 are the coercive field of the magnetic layers 1 and 3 (see text).



resistance R_{ap} (ap for antiparallel configuration) is large, and the conductance G_{ap} is weak. In (3ab), both layers have flipped their magnetization. The situation is symmetrical to (1), and the same reasoning shows that R_{p} is weak and G_{p} large.

In Fig. 5.43 part (c) it is possible to follow the overall current through the device in the three configurations (1), (2), (3) when the applied magnetic field varies: at large negative field and parallel configuration (1), the intensity is large (I_{max}); when the field becomes positive and reaches the coercive field H_1 of layer 1 (supposed to be less than the one of layer 3, $H_1 < H_3$), the magnetization in layer 1 flips and creates an antiparallel configuration, and the current decreases strongly to I_{min} (2). A new increase of the field allows reaching coercive field H_3 , and it is the turn of magnetization of layer 3 to flip. The new parallel configuration (3) is accompanied by an intensity jump to I_{max} . The performance of such devices can be measured by the magnetoconductance ratio, defined as:

$$R = (G_{\text{p}} - G_{\text{ap}}) / G_{\text{ap}} \quad (5.34)$$

Initially less than 20%, the ratio jumped to 80% in tunnel junctions (when the metallic spacer is replaced by semiconducting ones) with record values of 500%. We do not discuss the various aspects of the performances. We simply note that the discovery of GMR boosted quasi-immediate technological applications in magnetic devices and computing hardware (magnetic random access memories (MRAM), magnetic heads, and hard disks, for instance) and the academic recognition of the discoverers, with the Nobel Prize awarded to Fert and Grünberg in 2007 [5.75a]. The field developed rapidly, and today covers many phenomena under the name ‘spintronics’ [5.75].

Spintronics can be defined as the science of injecting, manipulating, and detecting electronic spins and its applications—a spin-based electronics. One important aspect of spintronics consists in the use of the quantum property of the electron spin to store and treat information.

5.2.9.2 Molecular spintronics: a new research domain

If the ideas and the advantages of molecular electronics (this chapter) and spintronics are merged, we can envision what can become *molecular spintronics*—the manipulation of spin and charges in electronic devices containing one or more molecules; that is, molecule-based spintronics.

Introducing molecules in the spintronics game introduces new degrees of freedom and considerably enlarges the range of possibilities: (i) magnetic electrodes with different kinds of magnetization sandwiching molecules or molecular layers, conducting, semiconducting, or insulating; (ii) non-magnetic electrodes with the infinite variety of magnetic molecules or molecular sheets. We shall not treat systems involving conventional ferromagnetic materials as electrodes, but this is an area rich in development. Let us quote only the example of apparently trivial molecules such as benzene, cyclopentadiene, or cyclooctatetraene, free or metallated phthalocyanines lying on a magnetic surface below a magnetic tip producing a spin-polarized tunnel current. The molecules appear able to tune the spin polarization and even to reverse it, depending on which part of the molecule is addressed by the current. Such

a property—evidenced by combined spin-polarized STM (SP-STM) experiments and DFT studies—is due to a unique property of the hybrid states created by the molecule–substrate interaction [5.76].

Next we concentrate on systems with non-magnetic electrodes, but using magnetic molecules. The most interesting are those for which the magnetic state of the molecule can be translated into an electrical effect [5.77]. We have already introduced the mechanism of the Kondo resonance effect (Section 5.2.2.5), when a spin, and not only a charge, is present on the molecule inside a junction made from non-magnetic electrodes. We present a few examples.

Cobalt(II/III) complex

Let us consider a cobalt complex, able to evolve between two oxidation states: low-spin Co(II) (d^7 , $S = 1/2$) and low-spin Co(III) (d^6 , $S = 0$), inserted as a unique molecule between two electrodes [5.78a,b]. When the results are presented as a map of the differential conductance (dI/dV) versus the source-drain bias voltage V_{SD} and the gate voltage V_G , a special behaviour appears when compared with a closed-shell molecule. For positive values of V_G there is a zone of high differential conductance centred on $V_{SD} = 0$. (A similar case on a more complex system is shown in Fig. 5.44.)

This arises from a combination of Coulomb blockade and Kondo resonance effects [5.78a]. Negative values of V_G favour the Co(III) state of the complex, while positive values favour the Co(II) state. On the Co(III) side, normal behaviour (diamonds) is observed, but for V_G positive enough, Co(II) being paramagnetic ($S = 1/2$), gives rise to the Kondo resonance effect (see Fig. 5.20); that is, a large differential conductance at zero bias.

A signature of the Kondo resonance effect is provided by the magnetic field dependence of the resonance peak $dI/dV = f(V)$. This has been observed with a cobalt complex of the previous type: while at zero magnetic field, the resonance Kondo peak is centred on $V_{SD} = 0$, applying a magnetic field up to 10 T shows a peak splitting (Zeeman splitting) varying linearly with B [5.78b].

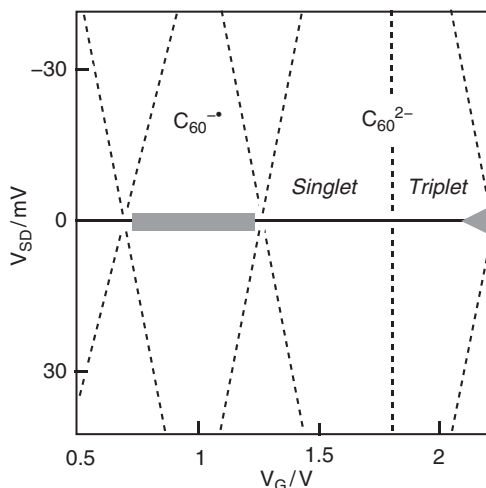


Fig. 5.44

Map obtained from the differential conductance $dI/dV = f(V_{SD}, V_G)$ for a device containing a single C_{60} molecule, with the ‘diamonds’ corresponding to $C_{60}^{\bullet-}$ and C_{60}^{2-} . The diamond corresponding to C_{60}^{2-} is split in two by a vertical line separating the existence domains of the singlet and triplet states. The dark grey zones are the domains of the Kondo resonance effect, manifested as a high conductance at zero bias. It occurs in the $C_{60}^{\bullet-}$ diamond (at left), and also at the limit of the C_{60}^{2-} triplet domain (extreme right). (Adapted from [5.79].)

C₆₀ molecule in a nanojunction

The Kondo resonance effect is not limited to $S = 1/2$ system, and can occur for larger spin systems, with the same ingredients at work: the many-body interaction between delocalized conduction electrons and the magnetic moment of the object in the nanojunction. Thus C_{60} , when introduced in a nanojunction, can exist as C_{60} , $C_{60}^{-\bullet}$, or even C_{60}^{2-} , according to the gate voltage [5.79] (Fig. 5.44). When C_{60} is present as $C_{60}^{-\bullet}$, the simple Kondo resonance is observed. But for C_{60}^{2-} , the situation is more complex, because singlet and triplet states may occur (note that the LUMO of C_{60} is degenerate with t_{1u} symmetry, so that the triplet state is normally the more stable). Curiously, the singlet–triplet gap is sensitive to the electric field, so that the relative stabilities of both states can be manipulated by the gate voltage (Fig. 5.44). Again a Kondo resonance is observed—this time at the limit of the triplet domain.

Spintronic devices using single-molecule magnets

We conclude this section with a description of a very peculiar molecular spin valve built from a nanotube decorated by single-ion magnets. Such experimental study necessitates new experimental setups adapted to the detection of individual magnetic moments. We begin with a description of the setup.

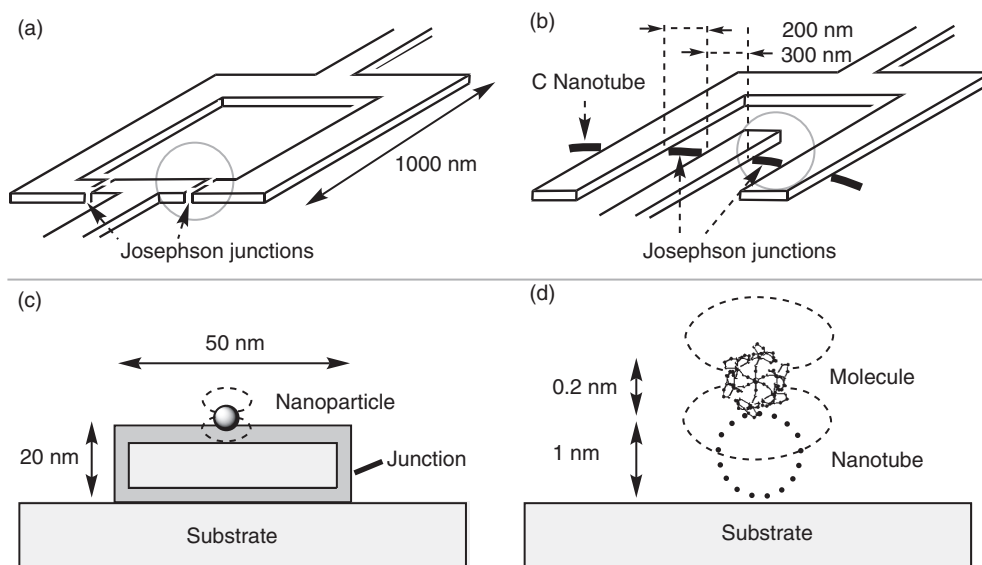
The NanoSQUID device

The extremely small diameter of carbon nanotubes can be exploited for an original application: the ‘nanoSQUID’. Let us recall that a SQUID circuit (superconducting quantum interference device) is made from a loop of superconducting wire with two tunnel junctions called Josephson junctions [5.80] (Fig. 5.45a,b) (See Section 2.3.3 and Fig. 2.6). The SQUID circuit can be used as an extremely sensitive magnetometer.

A SQUID circuit has been realized by bridging aluminum wires (superconducting below 1.2 K) with a single carbon nanotube realizing both tunnel junctions (Fig. 5.45b) [5.81]. The great advantage of this ‘nanoSQUID’ resides in the extremely small diameter of the nanotube (typically 1 nm), with the possibility of depositing a magnetic particle directly onto it. Since the dimensions of the nanotube are comparable to those of the magnetic object, the field lines of the latter can penetrate the loop more deeply, thus increasing considerably the sensitivity (Fig. 5.45c, d). It is predicted that the device would have enough sensitivity to detect the magnetization reversal associated with a spin 10 (a single Mn_{12} molecule, for example).

Molecular spin valve with two single-ion magnets

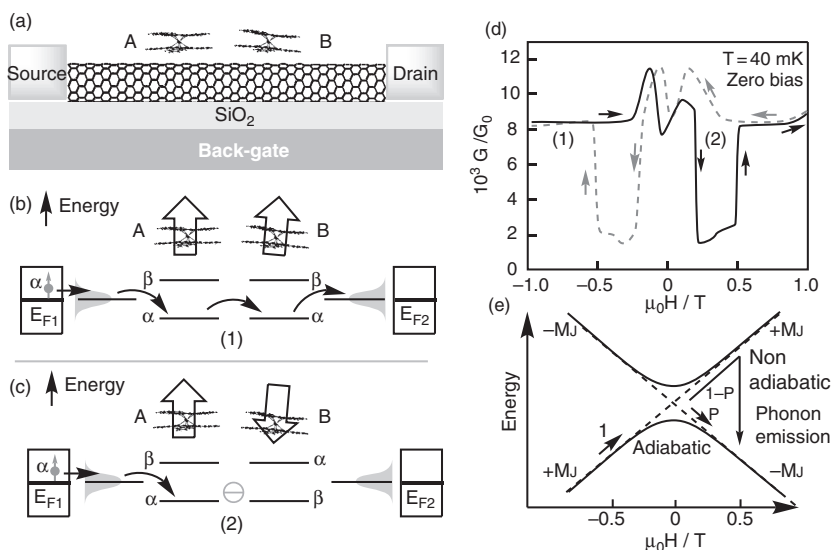
In Section 2.8.3 we introduced the properties of $[Tb(III)Pc_2]^{-/0}$ as a single-ion magnet (SIM). Recall that the anionic form contains closed-shell Pc^{2-} phthalocyanine ligands, while in the neutral form one of the Pc rings has lost one electron, hence creating a spin $1/2$ delocalized in the π system. In the presence of a magnetic field the highly anisotropic $J = 6$ spin system can be ‘up’ or ‘down’, corresponding to $J_z = +6$ or -6 for the Tb(III), the z axis being defined by the easy magnetization axis of the molecule. This property can be used to control a current by grafting several such units on a carbon nanotube. For this purpose, one of the phthalocyanine rings has been substituted

**Fig. 5.45**

MicroSQUID and NanoSQUID. (a) MicroSQUID circuit (see also Fig. 4.47b). (b) NanoSQUID circuit. The junctions are made of a carbon nanotube on which electrodes have been deposited. They define two Josephson junctions. (c) MicroSQUID, lateral view: interaction of the magnetic flux (dashed) lines of a magnetic particle and the microjunction. (d) NanoSQUID, lateral view: interaction between the magnetic flux (dashed) lines of a high-spin molecule and the nanotube junction, showing more penetration inside the junction. Note the differences in sizes. (Adapted from [5.81].)

with six hexyl and one pyrene group to ensure anchoring on the carbon nanotube by strong Van der Waals forces. These molecules are then deposited on a SWNT in a FET arrangement [5.82] (Fig. 5.46a). There is an average of four molecules on a SWNT segment of 300 nm. The most interesting behaviour is obtained when there are two such molecules bound to the nanotube. When the magnetic field is swept, beginning with negative values, the $J = 6$ spin of the molecules can adopt three configurations: parallel either ($\uparrow\text{up}, \uparrow\text{up}$) (Fig. 5.46b) or ($\downarrow\text{down}, \downarrow\text{down}$) (not shown), and between, antiparallel ($\uparrow\text{up}, \downarrow\text{down}$) (Fig. 5.46c) or ($\downarrow\text{down}, \uparrow\text{up}$) if they do not switch from ‘up’ to ‘down’ (reverse their magnetization) for the same magnetic field.

Therefore, there is a range of magnetic fields for which the $J = 6$ spins are antiparallel. The situation is fully comparable to that of a conventional spin valve (Fig. 5.43). Each of the molecules induces localized states in the SWNT nanotube through exchange interactions, resulting in a splitting of these levels according to the orientation of the $J = 6$ spin of the nearby molecule. There is a stabilization of either the α channel (molecules A and B in Fig. 46b, and molecule A in Fig. 5.46c) or the β channel (molecule B in Fig. 5.46c). The level splitting is estimated to be around 4 cm^{-1} (corresponding to 6 K). Note that since neutral forms of the complex are used, the interaction between the Tb(III) $J = 6$ spin and the nanotube electrons is relayed by the $S = \frac{1}{2}$ radical present on the phthalocyanine rings.

**Fig. 5.46**

Molecular spin valve. Compare with Fig. 5.43. (a) Scheme of the device realized with a SWNT carbon nanotube inside a FET structure, with two grafted TbPc₂ units. The substituted groups are not shown, for clarity. (b) Energy levels of the local states on the nanotube when the two TbPc₂ units have parallel $J = 6$ spins (white arrows), showing the possibility of electron transport for an ‘up’ (α, \uparrow) spin (small grey arrow) (configuration (1)). The broadening Γ of the molecular levels is represented by the grey area. (c) Case of antiparallel $J = 6$ spins on TbPc₂ showing the energy mismatch (configuration (2)). No electron transport is possible, regardless of the electron spin. (d) Conductances during a magnetic field excursion, showing the hysteresis and the large magnetoconductance ratio. Black curve and arrows: increasing field; grey dashed curve and arrows: decreasing field. G_0 is the quantum conductance unit. (e) Scheme of the Landau–Zener tunnelling processes. (Adapted from [5.82].)

If an electron with a spin ‘up, α ’, for instance, tries to cross the junction when the $J = 6$ spin on TbPc₂ are parallel and up (Fig. 5.46b), configuration (1), it will then encounter two α levels at the same energy, thus allowing its migration to the other electrode with the help of the broadening Γ due to the interaction of the nanotube and the electrode (estimated at 1.6 cm^{-1} or 2.3 K). But when the $J = 6$ spins are antiparallel on the two TbPc₂, there is an energy mismatch between the levels in the nanojunction configuration (2) (Fig. 5.46c), and the current is blocked. This conclusion is fully valid for an electron with a spin ‘down, β ’, starting from the appropriate configuration (3) (down, down) of the $J = 6$ spins on TbPc₂.

The conductance values when sweeping the magnetic field are shown in Fig. 5.46d. The fact that during a magnetic field excursion the spin flips do not occur at the same place results from (i) slight differences in molecule position and/or orientation on the nanotube, and (ii) the possibility of two kinds of process, either adiabatic or non-adiabatic, as shown in Fig. 5.46e. As seen in Sections 2.8.1.3 and 3.2.1.1, in the adiabatic process the system stays on the lowest energy curve, with a probability P , while in the non-adiabatic process, of probability $(1-P)$, it stays on the initial curve. But in this second case it can jump down later to the lowest curve by exchanging energy with the environment by phonon emission. This introduces a lag in the spin flip, which can be different from one molecule to the other. The tunnel probability P is given by the Landau–Zener formula (eqn. (2.149)). As a result of (i) and (ii), the electrical response presents an hysteresis.

To summarize: the system *operates as a molecular spin valve, where the two SIM molecules play the role of the ferromagnetic electrodes*. The conductances are very weak (see Fig. 5.46d), but the magnetoconductance ratio, defined by eqn. (5.34), amounts to 300%—an important value. The result is promising,

but is obtained at the very low temperature of 40 mK. It vanishes rapidly when T increases (600 mK for the presented example).

5.3 Behaviour of ensemble of molecules

In this paragraph we concentrate on the properties of macroscopic sets of molecules, without reference to the problem of connecting them to electrodes. The goal is to identify a number of interesting behaviours that can be promising for molecular electronics. There are three reasons for this: first, such molecules can be considered as a reserve bank for future one-molecule studies; second, studying an ensemble rather than a single molecule provides an easier characterization, because the experimental signal (spectroscopic, electrochemical, magnetic, and so on) is larger; third, in some cases the behaviour is cooperative—it relies on the existence of interactions between molecules.

5.3.1 Systems studied in solution

Molecular wire

The molecular wire function can be tested in solution using mixed valence complexes with long conjugated spacers, as seen in Section 3.2.2. From a topological point of view, a molecular mixed valence compound resembles a nanojunction in which the metal electrodes are reduced to one metal atom only. We recall the basic conclusion of Section 3.2.2.6, eqn. (3.98): the electronic coupling between metal sites (which determines the rate of intramolecular electron transfer) decreases with distance according to an exponential law, with a γ coefficient in the 0.07–0.10 Å⁻¹ range for diverse conjugated structures.

Molecular wires are also encountered in Section 4.4.2.

Memory element

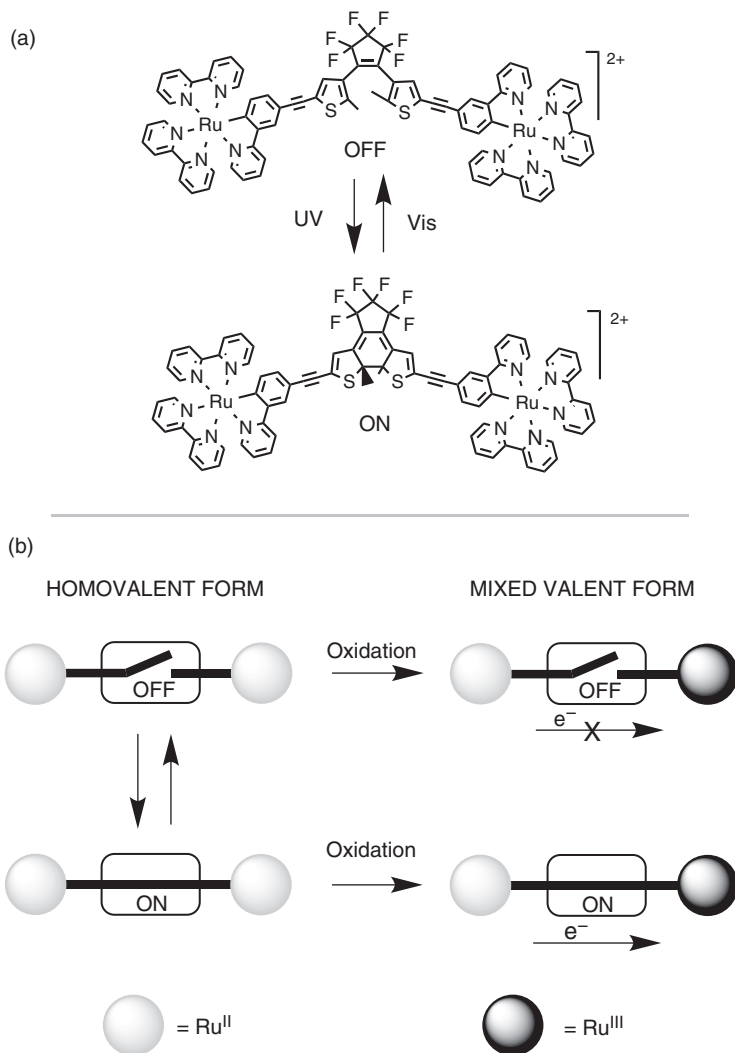
This corresponds to the large class of photochromic compounds which can indeed be used for erasable optical memory. (The subject has been discussed in Box ‘Switching and memory’, in Section 5.2.6, for the case of dithienylcyclopentenes.)

Molecular switch

There are many definitions of molecular switches. Here we shall use a simple one, borrowed from the electrotechnical domain: a switch is an ensemble of pieces whose function is to stop and/or establish the electrical current in a circuit. At the molecular scale and in solution (where no *stricto sensu* circuit is possible), a molecular switch can be built by associating a mixed valence structure and a memory element. This produces a bistable system which remains in the same state in the absence of perturbation.

The insertion of a photochromic diarylethene moiety in the structure of a molecular mixed valence compound has been realized in 2000 [5.83a]. The diarylethene links two cyclometallated ruthenium complexes (Fig. 5.47).

The starting form (‘open’) is prepared in the Ru^{II}–Ru^{II} homovalent state. Upon partial oxidation the Ru^{II}–Ru^{III} mixed valence form is generated, for

**Fig. 5.47**

A molecular switch made of a dithiolenyl moiety inserted in a binuclear structure. (a) The photoisomerization process, performed in the homovalent $\text{Ru}^{\text{II}}\text{-Ru}^{\text{II}}$ state; (b) the sequence of operations, showing switching. The V_{ab} coupling between ruthenium sites is measured in the mixed valence $\text{Ru}^{\text{II}}\text{-Ru}^{\text{III}}$ state.

which the effective coupling between ruthenium sites (V_{ab}) can be determined from the parameters of the intervalence band (see Section 3.2.2.5). It does not exhibit a detectable V_{ab} coupling, as a consequence of its non-conjugated structure. The photochemical conversion of the open form into the closed one is possible in the $\text{Ru}^{\text{II}}\text{-Ru}^{\text{II}}$ homovalent state, and after partial oxidation to the $\text{Ru}^{\text{II}}\text{-Ru}^{\text{III}}$ mixed valence form an appreciable V_{ab} coupling (0.025 eV) is then observed, in agreement with the conjugated character of this isomer. The system has thus been driven from an ‘insulating’ (OFF) to a ‘conductive’ (ON) state, by analogy with a conventional electrical switch.

Many other ways of controlling, or at least modulating, an intramolecular electron transfer have been described in the literature [5.83b].

Logic gates

The complexity of some molecules provides access to a richness of behaviours mimicking logic functions. For this purpose, molecules must have been designed in a very precise way, so that in some respect they are 'programmed' to realize a specific and complex operation. Here we do not limit discussion to electronic properties, as other types of excitations or responses (chemical, photophysical) are possible.

Some molecules can achieve logic functions of the type AND, OR, XOR, and so on [5.84]. In these gates the system responds to two independent binary inputs, with an output given by a rule called the 'truth table', as shown here.

IN1	IN2	OUT		
		AND	OR	XOR
0	0	0	0	0
0	1	0	1	1
1	0	0	1	1
1	1	1	1	0

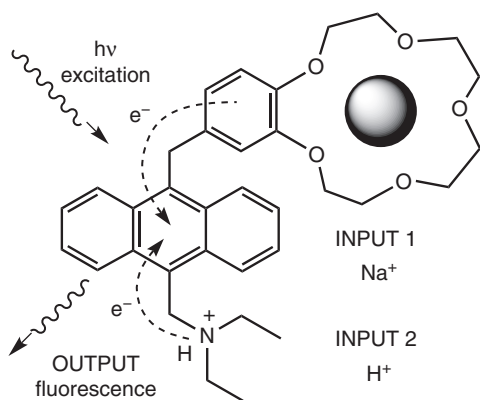
The AND function requires the 2 input to equal 1 for returning 1 on the output, while the OR function requires that 1 or the other input equals 1. For XOR (exclusive OR), *only one* of the input, *but not both*, must equal 1.

A more complex gate, called INHIBIT, presents three inputs. It returns 1 on the output only if the first two inputs equal 1 (as in the AND function), but also if the third input equals 0.

IN1	IN2	IN3	OUT INHIBIT
0	0	0	0
0	1	0	0
1	0	0	0
1	1	0	1
0	0	1	0
0	1	1	0
1	0	1	0
1	1	1	0

The AND gate can be realized from a fluorophore such as anthracene, onto which two chemically sensitive groups have been grafted. These groups have the potential to quench the fluorescence of the chromophore by photoinduced electron transfer (PET) (Fig. 5.48).

The system works as follows. Under normal conditions (no reagent added), once the system is excited there are two possible PET, and each one alone can quench the fluorescence. Thus no fluorescence (output) is observed. To produce fluorescence one has to block the two PET by complexation with Na⁺

**Fig. 5.48**

An AND gate built from a disubstituted anthracene moiety, with Na^+ and H^+ as inputs. Fluorescence of the anthracene moiety occurs *only* if both Na^+ and H^+ are present, because they block the two possible intramolecular electron transfers (dashed arrows), which would quench the excited state. (Adapted from [5.84].)

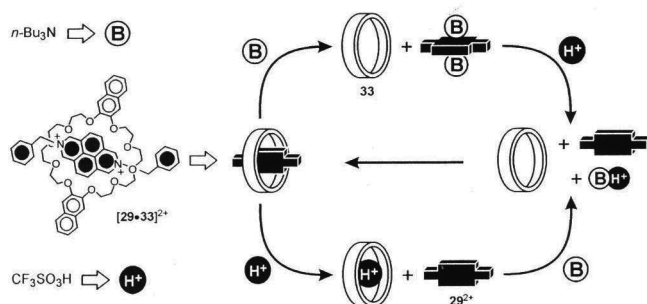
(on the crown ether site) AND H^+ (on the amine site), these reagents being considered as INPUT1 and INPUT2.

The OR gate is relatively easy to implement. For instance, one can use again a fluorescent molecule, with a non-selective complexation site able to fix, for instance, Ca^{2+} OR Mg^{2+} . Luminescence occurs only when the coordination site is occupied, whatever the nature of the cation, hence the OR function.

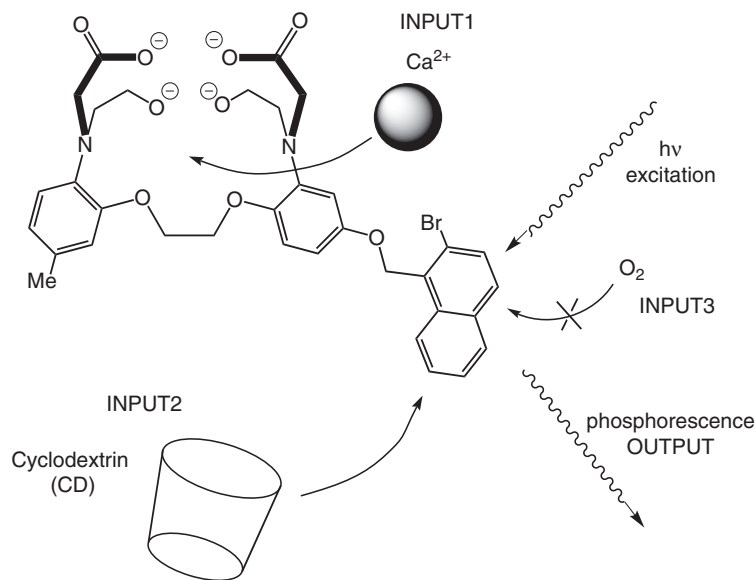
The XOR logic function is more difficult to achieve: the system must respond when one OR the other input is activated, *but not both*. The proposed solution is to use a pseudorotaxane (see the definition of a pseudo-rotaxane in Fig. 5.30), made of a diazapyrenium thread and a crown ether macrocycle (Fig. 5.49) [5.84]. The basic property of the pseudorotaxane, compared to the rotaxane, is that it can disassemble. The OUTPUT is provided by the state of the system (threaded = 0, unthreaded = 1). The INPUTs are provided by reactants which have affinity for the diazapyrenium or the crown ether.

Thus one OR the other reactant leads to disassembling. But when both are present they simply react on each other in solution, and their effects cancel!

Finally, let us consider the complex function INHIBIT. The related molecule is made of a phosphorescent bromonaphthalene unit linked to a polyaminoacid receptor (Fig. 5.50) [5.84]. This receptor is able to quench the phosphorescence of bromonaphthalene unless the linked receptor is occupied by a cation like Ca^{2+} . But in addition, phosphorescence requires that the bromonaphthalene is shielded from the outside medium by complexation with a cyclodextrin, and

**Fig. 5.49**

An XOR gate based on the threading/rethreading of a pseudorotaxane. The inputs are an acid ($\text{CF}_3\text{SO}_3\text{H}$) and a base ($n\text{-Bu}_3\text{N}$). (Reproduced from [5.85], vol. 3, p. 528, Fig. 24.)

**Fig. 5.50**

An INHIBIT gate made of a phosphorescent bromonaphthalene unit linked to a polyaminoacid receptor. The inputs are Ca²⁺ (INPUT 1), a cyclodextrin (CD) (INPUT 2), and O₂ (INPUT 3). Phosphorescence is observed only if Ca²⁺ and CD are present, but O₂ is absent. (Adapted from [5.84] vol. 5, p 167.)

it also needs the absence of molecular oxygen which is a powerful quencher (Fig. 5.50). To summarize, phosphorescence (OUTPUT = 1) is observed only if Ca²⁺ and cyclodextrin are present (INPUT1 = INPUT2 = 1) and if O₂ is absent (INPUT3 = 0).

Of course, many more systems can appear as a result of chemists' imagination to answer such kinds of problems. But the real challenge is in using these systems in a practical way. The demonstrations are made on large ensembles of molecules in solution, while it would be necessary to realize the function at the single molecular scale. Furthermore, it is extremely difficult in the present state of the art to discern how the inputs and outputs, which consist in the presence or absence of a reactant, could be transferred from one gate to the other.

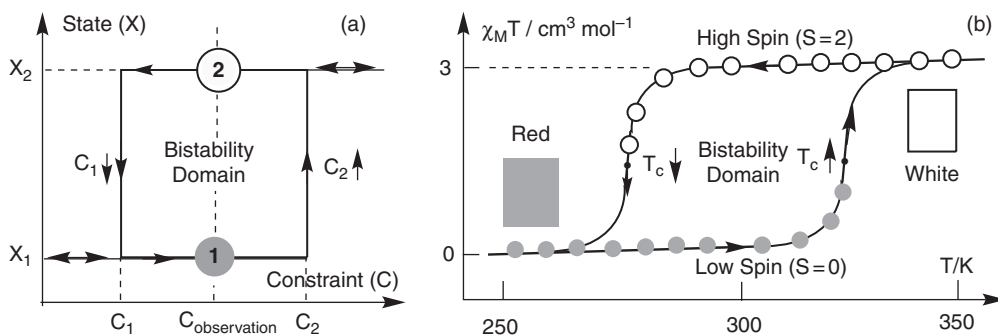
5.3.2 Systems studied in the solid state

Devices based on spin cross-over

Spin cross-over systems can be used to store information. In Section 2.4.3 we presented the basic features of the spin cross-over phenomena and the conditions to produce bistable systems, and in Section 4.5.2 how the spin transition can be triggered by photons (LIESST and LD-LISC effects). Note, however, that the appearance of hysteresis in the spin cross-over process requires *cooperativity*, and thus cannot be scaled down to the level of a unique molecule. For the moment, the possible practical uses are more oriented towards display devices rather than information storage. We address here one such example.

The property which is exploited is bistability; that is, the ability of the given system to exist in two stable states under identical external conditions (T, P, and so on), as shown in Fig. 5.51.

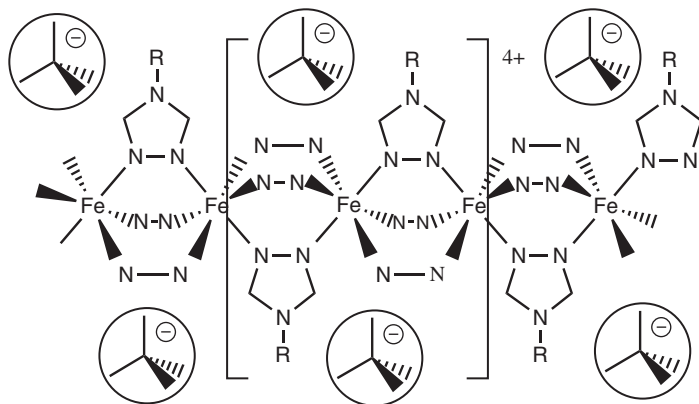
Figure 5.51a shows a general scheme of the bistability phenomenon: starting from low values of the applied constraint C and increasing C, the system is in

**Fig. 5.51**

Bistable systems. (a) General case: between $C_1 \downarrow$ and $C_2 \uparrow$, the system presents two stable states, X_1 and X_2 , defining a bistability domain; (b) thermal variation of the molar susceptibility of a spin cross-over Fe(II) system presenting a wide hysteresis around room temperature. (Adapted from Kahn *et al* [5.86].)

state X_1 and remains as such up to the value $C_2 \uparrow$ of the constraint. For $C > C_2 \uparrow$ it changes to state X_2 . Then, decreasing C , the system remains in state X_2 down to the constraint value $C_1 \downarrow$ when it changes to state X_1 . We recognize an hysteresis, and between $C_1 \downarrow$ and $C_2 \uparrow$ the state of the system depends on its past history: we have a bistability with a memory effect. It is convenient to define special values of the constraint C , $C_2 \uparrow$ (up) (same amount of states X_1 and X_2 when increasing C), and $C_1 \downarrow$ (down) (same amount of states X_1 and X_2 when decreasing C).

Figure 5.51b is an experimental illustration of the general scheme applied to the magnetic susceptibility of the Fe(II) spin cross-over system schematized in Fig. 5.52. The external constraint is the temperature T . The property used to describe the system is the spin state: high spin, spin $S = 2$ at high temperature, low spin, $S = 0$ at low temperature. The ordinate is the $\chi_M T$ product of the molar susceptibility χ_M multiplied by the temperature T . The high and low spin values of $\chi_M T$ are easy to find from the Curie law ($\chi_M T = n(n + 2)/8$, n number of unpaired electrons; see Section 2.3.4 and eqn. (2.47)). The bistability domain is centred on room temperature (300 K), with a wide hysteresis

**Fig. 5.52**

Schematic structure of a spin cross-over system built from a cationic chain of tris- μ -(R-triazole)iron(II) and insulating anions [5.86].

(≈ 50 K). The hysteresis loop is smoother than the theoretical one, for the reasons given in Section 2.4.3. The important point for practical application is that around room temperature the system presents a wide bistability domain, with either a white colour (when deriving from high temperature) or Bordeaux red (when deriving from low temperature). All the conditions are fulfilled to use this molecule-based system, at room temperature, in a display device.

Fig. 5.52 shows the chemical structure: a chain of iron(II) cations, bridged by three neutral triazole ligands, with an aliphatic chain R as a substituent [5.86]. The repeating unit along the chain is made of two Fe(II) ions and six triazole ligands. The chain is therefore cationic, and negative counter ions ensure the electroneutrality of the system and isolate the chains from each other. Iron(II) was chosen since it presents frequently high-spin and low-spin states, especially with triazole ligands, which provide an intermediate ligand field propitious to the appearance of spin cross-over at relatively high transition temperature. In addition, the triazole bridges neighbouring iron atoms, conferring a polymeric structure to the system.

Note that the behaviour requires intermolecular interactions of the proper sign (Section 2.4.3). In the present case it is likely that the polymeric nature of the system plays a role by introducing some elastic interaction between neighbouring metallic ions. Organic substituents R and anions are two further parameters introducing additional flexibility into the chemistry of the whole system. Other devices exploit the room-temperature bistability of the systems presented in Section 2.4.3.4 and Fig. 2.29.

5.4 Towards quantum computing

Quantum computation is the subject of intense research activity. It is based on the intrinsic quantum behaviour of small objects, including molecules. Note that conventional electronics uses, of course, the quantum properties of matter, but the data are treated under the form of macroscopic variables such as currents and voltages. In a quantum calculation the data are treated under the form of quantum states, which can combine in a complex and subtle way. At the heart of the processing is the time evolution of a state under the influence of the evolution operator $e^{-\frac{i\mathbf{H}t}{\hbar}}$. Mathematically, this translates as:

$$|\Psi(t)\rangle = e^{-\frac{i\mathbf{H}t}{\hbar}} |\Psi(0)\rangle \quad (5.35)$$

where $|\Psi(0)\rangle$ is the state at time zero and $|\Psi(t)\rangle$ the state at time t , while \mathbf{H} is the system's Hamiltonian. As the subject of quantum computation is extremely wide and is evolving rapidly, the reader is advised to consult basic introductory texts such as [5.87]. Here we simply present an overview, and mention some fundamental features of the process.

5.4.1 Standard quantum computing

The most frequent implementation of quantum computing is based on the preparation of the system in a given non-stationary quantum state $|\Psi(0)\rangle$, then its free evolution as a function of time, and finally the 'reading' of the result at

a given precise time. This standard approach relies on the concept of the qubit (quantum bit). At variance with classical bits, which can take only the binary values of 0 or 1, qubits can exist in a superposition of states such as $\alpha |0\rangle + \beta |1\rangle$, where α and β are coefficients that can take any values, subject to the normalization condition $\alpha^2 + \beta^2 = 1$.

A second important difference is that two or more qubits can be put in *entangled* states by a proper mastery of state superpositions [5.87]. In the entangled state, two qubits cannot be separated and thus cannot be described independently. An example is provided by the two $s_1 = 1/2$ and $s_2 = 1/2$ spins of a singlet state described by $|\Psi\rangle = (|\uparrow\downarrow\rangle - |\downarrow\uparrow\rangle)/2^{1/2}$. Only the total quantum state can be specified completely, but not the one of the components. Entanglement is crucial, because it allows the system to explore several possibilities at the same time. The detailed theory shows indeed that after its evolution the system has performed the equivalent of a large number of classical calculations occurring in parallel. In practice, to generate entangled states, it is necessary to play with couplings between the subsystems in order to entangle or disentangle at will.

Qubits can be implemented with different physical systems: quantum dots, ion traps, single-photon devices and cavities, superconducting devices, and a few chemical systems. The most popular among chemists are ensembles of *nuclear spins*, addressed by NMR. Pulsed NMR techniques allow preparation of nuclear spins in superposition of states, with a specific addressing of different nuclei, and the dynamic evolution of nuclear spins is well isolated from their environment. To date, the best achievement relies on a molecule presenting seven qubits, under the form of seven ^{13}C or ^{19}F nuclei in different magnetic environments, and with proper couplings. Once properly manipulated, this system is able to factorize the number 15 as 5×3 by using the so-called Shor algorithm [5.89]. These experiments are possible only on a macroscopic ensemble of identical molecules present in a standard NMR tube.

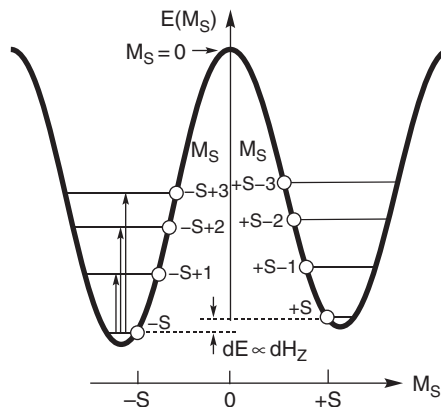
However, to facilitate the interface with the outside world it is more appealing to rely on molecular *electronic* properties. Since electronic spins are then concerned, the general experimental setup would be based on pulsed ESR techniques.

Paramagnetic molecules with spins $1/2$ could constitute a first class of systems relatively easy to understand because of the conceptual proximity with NMR experiments familiar to chemists. In a magnetic field, the states \uparrow and \downarrow can code 0 and 1, and the system can be prepared in a non-stationary state by a suitable pulse of microwave or radio-frequency radiations. In this spirit, some clusters, such as Cr_7Ni , have been proposed [5.88]. Cr_7Ni is a ring with antiferromagnetically coupled metal centres: 7 Cr(III) ($S=1/2$) and 1 Ni(II) ($S=1$). The resulting spin is $1/2$ (it is an example of molecular ferrimagnetism; see Section 2.6.5.2). It is possible to prepare a dimer of such units, and spin entanglement between the $1/2$ spins of the rings has been demonstrated through magnetic susceptibility at 50 mK.

Another class is provided by high-spin molecules which present a number of advantages. As seen in Section 2.8, some of them present the behaviour of single-molecule magnets, they exhibit coherence times up to hundreds of ns, and, their energy spectrum being richer, the selective generation of arbitrary

Fig. 5.53

Energy levels of an Mn_{12} single-molecule magnet in the presence of a small magnetic field dH_z , so that the M_S and $-M_S$ states have slightly different energies. A suitable complex pulse allows the excitation in a state which is a superposition of several M_S states such as $M_S = -S + 1, -S + 2,$ and $-S + 3$ (plain vertical arrows). Representation as in Fig. 2.81. (Adapted from [5.90].)



superpositions of spin eigenstates is theoretically possible. As a conceptual example we can consider the case of an Mn_{12} single-molecule magnet (see Section 2.8.1 and Fig. 2.81) placed in a weak magnetic field (Fig. 5.53). We consider only levels of the left-hand part of the diagram, which are (slightly) stabilized by the magnetic field with respect to the levels of the right (Zeeman effect).

At very low temperatures (around 1 K), the system is present in the $M_S = -S$ state (for Mn_{12} , $S = 10$) and transitions are possible towards states $M_S = -S + 1, -S + 2, -S + 3,$ and so on. An important point is that the levels *are not equidistant* (at variance with the case of the harmonic oscillator; see Section 2.5.1.2 and Fig. 2.35). Thus selective population of the different excited states is possible by using different frequencies. But quantum calculations requires more than that: actually, by using a complex pulse of several frequencies, it is possible to place the system in a superposition of states. After that, theory shows the possibility of starting the calculation by a universal single pulse, and then read the result by stimulated emission or absorption, which would produce information on the nature of the populated levels [5.90]. This system is theoretically capable of implementing the Grover algorithm [5.91]—a quantum procedure allowing the efficient search of an item in an unsorted database.

However, quantum computing is plagued by the fundamental problem of *decoherence*. Since quantum computation is based on fragile interference effects, it is of paramount importance that the spontaneous evolution occurs in a way retaining the *coherence* of the state superpositions. But this coherence is easily lost by the interaction with environment (atomic motions, interaction with nuclear spins, and so on). Some systems nevertheless present promising behaviour; for instance, the V_{15} cluster, with two very close ground states $S = 1/2$ and with an excited state $3/2$ just above. But this cluster must be ‘wrapped’ by interaction with a cationic surfactant to separate the magnetic units from each other and avoid the decoherence by magnetic dipolar effects. Upon spin-echo experiments [5.92], Rabi oscillations between sublevels (see the two-state system behaviour in 1.6) have been observed for durations of a few hundreds of ns at 4K.

Research is very active in this field, but at the present time the effects heralding quantum computing are obtained only with complex equipment and procedures necessary to prepare the initial state. In addition, there is no realistic solution to ‘cascade’ the qubits components; that is, to use the output of one to be the input of another. We now present a recently proposed alternative approach.

5.4.2 Quantum Hamiltonian computing

A different way of performing quantum computation with a single molecule has been proposed under the name of ‘quantum Hamiltonian computing’ (QHC) [5.93]. Here the molecule is not divided into qubits. Moreover, the input information is not introduced as an electronic property (for instance, an electron spin state), but in the Hamiltonian driving the intramolecular quantum evolution, by way of control of the geometry. Finally, the result is read at specific places of the molecule under the form of an electron flux. The difference between normal quantum computing and quantum Hamiltonian computing is made apparent in Fig. 5.54.

An advantage of quantum Hamiltonian computing is that it is well adapted to the treatment of data through electrical currents. The input and output could consist in a flux of electrons, thus ensuring the averaging of individual quantum events as well as quantum-to-classical conversion [5.93].

The following example of dinitro[1,3]anthracene (Fig. 5.55) shows how it could function as a half-adder—an elaborate logic gate with two inputs and two outputs, able to process two binary numbers. One of the outputs constitutes the sum modulo 2 of the input bits (corresponding to the function XOR), while the other is the carry, and thus takes the value 1 only if both inputs have the value 1 (corresponding to the function AND). The truth table is therefore as follows:

Input Bit 1	Input Bit 2	Output XOR	Output AND
0	0	0	0
0	1	1	0
1	0	1	0
1	1	0	1

In this molecule the (classical) input would be introduced as values of the θ_1 and θ_2 angles between the respective planes of NO_2 groups and the anthracene plane. (It is assumed that these angles can be controlled experimentally; for

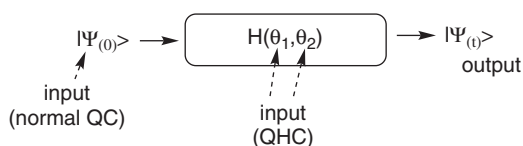
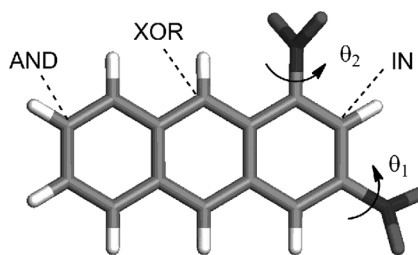


Fig. 5.54

Two kinds of quantum computing. In normal quantum computing (QC) the input is introduced in the form of an initial state $|\Psi(0)\rangle$, which evolves in time under the influence of the system’s Hamiltonian (fixed) according to eqn. (5.35). The output is provided by the state $|\Psi(t)\rangle$, measured at some later time t . In quantum Hamiltonian computing (QHC) the Hamiltonian depends on structural parameters such as bond angles (θ_1 and θ_2). The input consists in modifying these parameters while $|\Psi(0)\rangle$ is fixed.

Fig. 5.55

The quantum Hamiltonian half-adder gate. In this theoretical work, a dinitro[1,3]anthracene molecule is studied from the point of view of its dynamical response to an electron uptake according to the position of the NO₂ groups. The NO₂ dihedral angles are assumed to be externally fixed at either 0 or 90°, coding binary inputs 0 and 1 respectively. After an electron introduction in location IN, the time evolution can be read by the appearance of the electron at locations AND and XOR, corresponding to the half-adder operation. (adapted from [5.93])



instance, using the tip of an STM). The code is that $\theta = 0$ corresponds to 0 and $\theta = 90^\circ$ corresponds to 1. Then the system is prepared in a non-stationary state by injecting, for instance, an electron in a particular location, noted $|\phi_{in}\rangle$. The quantum evolution is then computed as a function of time, and the electron moves along the system of π orbitals in an almost periodic way, with from time to time localization in a given location such as $|\phi_{AND}\rangle$ and $|\phi_{XOR}\rangle$ (Fig. 5.55). The result of calculation can be read in these particular locations, for instance, if $\theta_1 = 0^\circ$ and $\theta_2 = 90^\circ$ (code 0 1), the electron has a high probability of appearing in the output $|\phi_{XOR}\rangle$, and never appears in the location denoted $|\phi_{AND}\rangle$ [5.93].

The main advantage of QHC is the possibility of implementing it in an extremely small volume, and thus take full advantage of the monomolecular nature of the device, with the possibility of addressing the system by an electron flux and thus to partially restore a classical behaviour. Nevertheless, this approach relies on the connection of a molecule to several electrodes at the atomic scale—another future challenge.

5.5 Conclusion and perspectives

Molecular electronics is a topic which is constantly evolving. (Its spin variant, molecular spintronics, is in its infancy). Since the first prospective ideas in the 1970s, many achievements have been realized. The more concrete ones belong to hybrid molecular electronics, which has developed in a way parallel to silicon electronics. This has been the opportunity to set up cutting-edge experiments at the frontier of technical possibilities—in particular, the measurements involving single molecules, but the results are there: we can now test real devices and investigate their usefulness in realizing larger circuits.

There are, however, considerable difficulties ahead. The reliability of each molecular device cannot be guaranteed. To give an example, the authors of the beautiful result on the molecular spin valve (Section 5.2.9) [5.82] reveal that among the 130 investigated devices, twenty-five showed a magnetic molecular signal, and seven could be studied in detail. Associating a large number of devices necessitates extreme control of their disposition and interaction. At present there is no process adapted to mass fabrication and precise interconnection, which would be (at a lower scale) the equivalent of microelectronic processes. But is it really useful and necessary to mimic the architecture of conventional silicon-based circuits? If we return to the original motivation, the

size reduction, we have to consider the considerable improvements achieved by the conventional technology in the past decades. And if we take into account the total size of a hybrid device, *including the necessary connection wires* (electron reservoirs), the gain with respect to silicon devices is not so great. The International Roadmap for Semiconductors predicts (in 2012) transistor dimensions of 14 nm in the near future, with the conventional technology. Of course, most proposed molecules are much smaller, with a typical size of 2–3 nm, but the connection wires are usually several times larger than these values.

Incidentally, conventional silicon electronics is also facing problems, showing that the absolute limit in miniaturization will soon knock on physical limits. Besides, it is agreed now that size reduction ('more Moore'; see Box 'Moore's law' p 397) cannot be the sole motivation for molecular electronics. Since 2005 the International Roadmap for Semiconductors has recognized the interest in introducing more complex and integrated functions (the 'More than Moore' approach). In this respect, molecules are the candidates of choice for fulfilling these requirements.

Molecular electronics could present an advantage over silicon electronics in terms of cost of manufacturing. The semiconductor industry is confronted with a huge increase in costs for each new generation of processes. In this respect, molecular electronics relies on molecular chemistry, which utilizes much cheaper methods of deposition. The selective affinity of molecules for certain substrates gives rise to self-assembling processes, and any chemical transformation is a highly parallel process, since it involves a large number of molecules. These advantages are quoted frequently in the literature, but it is fair to say that at the present time these ideas are mostly speculative.

But we have to consider also the possibility of novel types of architectures. Since the advent of molecular electronics this has also been the subject of much speculation and debate. The concept of an *integrated architecture* has emerged initially from the work of Forrest Carter [5.8]. The principle is to connect directly the components, without the intermediate metallic wires; but in this situation the fundamental principle of conventional electronics disappears: the components are no longer independent, and we cannot decompose a large circuit into elements. More annoyingly, there is nothing like an intrinsic characteristic of a part of a circuit, such as a current–voltage curve, nor even a physical variable, such as a voltage, which can be transferred from one component to another. Instead, the circuit is embedded in a large single molecule, and the total system must be devised from the beginning, and then studied and modelled. This possibility could be called *monomolecular electronics* [5.14].

The evolution towards monomolecular electronics can be seen as parallel to the evolution which occurred in the 1950s, when electronics moved from discrete components to integrated circuits. In principle, it should be possible to conceive such molecular integrated circuits. Several logic and computing functions would be integrated in a large and extremely complex molecule, and only the final result would be accessible from the outside world. This huge challenge is the subject of current research. It will certainly change drastically our way of thinking. To quote just one example, it can be shown that the usual rules of association of circuits are no longer valid: thus the conductances of

two elements mounted in parallel are not additive [5.14]. Tackling this type of problem will require considerable effort, but it begins to be affordable, given the considerable progress of numerical calculations.

Quantum computing is also a possible avenue for molecular electronics, but is still very speculative. (Note that the vast majority of experimental studies in quantum computing make use of *physical* devices, not molecules). As for the rest of the molecular electronics domain, the problem of selective and precise addressing of molecules, and moreover, in this case, molecular quantum states, represents a formidable challenge.

As a conclusion, it is interesting and instructive to remark that the progress of science is composed of many discontinuous advances, impediments, and temporary blockades in the domains of theory, experiment, and concepts. When new results are obtained, ideas evolve, new concepts emerge, and new experiments are planned and realized. In the case of molecular electronics, although we do not have in hand yet a truly molecular computer, the subject has triggered considerable progresses in the techniques and understanding of processes at the nanometric scale. The large body of accumulated data is also indicative of the huge potential of molecular chemistry and its ability to provide really new structures. The most important of these is the constant appearance of new and eventually unplanned results, increasing common knowledge, refining the presently accepted models or imposing the adoption of new ones, and leading to endlessly new avenues of discovery.

References

- [5.1] *Molecular Electronics*, J. Jortner, M. Ratner (eds.), Blackwell Science, Oxford, 1997.
- [5.2] *Les Nanosciences*, M. Lahmani, C. Dupas, P. Houdy (eds.), Berlin and Paris, 2004.
- [5.3] Molecular Electronics Special Feature, *Proceedings of the National Academy of Sciences* 102, no. 25 (2005).
- [5.4] (a) *Handbook of Liquid Crystal Research*, P. J. Collings, J. S. Patel (eds.), Oxford University Press, Oxford (1997); (b) *Organic Electronics: Materials, Manufacturing and Applications*, Hagen Klauk (ed.), Wiley-VCH, 2006; (c) *Organic Electronics: Materials, Processing, Devices and Applications*, F. So (ed.), CRC Press, 2009; (d) *Organic Photovoltaics: Mechanism, Materials, and Devices*, S. Sun, N. S. Sariciftci (ed.), Taylor and Francis, London, 2005; (e) *Printed Organic and Molecular Electronics*, D. Gamota *et al.* (eds.), Springer, Berlin, 2004; (f) *Flexible Flat Panel Displays*, G. P. Crawford (ed.), Wiley, New York, 2005.
- [5.5] *Molecular Semiconductors*, J. Simon and J.-J. André, Springer-Verlag, New York, 1985.
- [5.6] J. H. Burroughes, D. D. C. Bradley, A. R. Brown, R. N. Marks, K. Mackay, R. H. Friend, P. L. Burns, A. B. Holmes, *Nature* 347 (1990), 539–41.
- [5.7] A. Aviram, M. Ratner, *Chem. Phys. Lett.* 29 (1974), 277–83.
- [5.8] *Molecular Electronic Devices*, F. L. Carter (ed.), Marcel Dekker, New York, 1982; *Molecular Electronic Devices II*, F. L. Carter (ed.), Marcel Dekker, New York, 1987.
- [5.9] G. Binnig, H. Rohrer, Nobel Lecture, 8 December 1986. <http://nobelprize.org/nobel_prizes/physics/laureates/1986/rohrer-lecture.pdf>

- [5.10] D. M. Eigler, C. P. Lutz, W. E. Rudge, *Nature* 352 (1991), 600–03.
- [5.11] (a) C. Joachim, J. K. Gimzewski, R. Schlittler, C. Chavy, *Phys. Rev. Lett.* 74 (1995), 2102; (b) L. Grill, *J. Phys. Condens. Matter* 20 (2008), 053001; (c) S. J. van der Molen, P. Liljeroth, *J. Phys. Condens. Matter* 22 (2010), 133001; (d) R. Wiesendanger, *Rev. Mod. Phys.* 81 (2009), 1495.
- [5.12] J.-P. Bourgoin, D. Vuillaume, M. F. Goffman, A. Filoramo, in [5.2], chap. 13.
- [5.13] J.-P. Bourgoin, *Lecture Notes in Physics*, Springer-Verlag 579 (2001), 105.
- [5.14] C. Joachim, J. K. Gimzewski, A. Aviram, *Nature* 408 (2000), 541–8.
- [5.15] J. Chen, L. C. Calvet, M. A. Reed, D. W. Carr, D. S. Grubisha, D. W. Bennett, *Chem. Phys. Lett.* 313 (1999), 741.
- [5.16] F. Moresco, A. Gourdon, *Proc. Natl. Acad. Sciences USA* 102 (2005), 8809.
- [5.17] X. D. Cui, A. Primak, X. Zarate, J. Tomfohr, O. F. Sankey, A. L. Moore, T. A. Moore, D. Gust, G. Harris, S. M. Lindsay, *Science* 294 (2001), 571.
- [5.18] V. Rousset, C. Joachim, S. Itoua, B. Rousset, N. Fabre, *J. Phys III* 5 (1995), 1983–89.
- [5.19] M. A. Reed, C. Zhou, C. J. Muller, T. P. Burgin, J. M. Tour, *Science* 278 (1997), 252.
- [5.20] T. Taychatanapat, K. I. Bolotin, F. Kuemmeth, D. C. Ralph, *Nano Lett.* 7 (2007), 652–6.
- [5.21] R. Hoffmann, *Solids and Surfaces: A Chemist's View of Bonding in Extended Structures*, VCH, New York, 1988.
- [5.22] M. Paulsson, F. Zahid, S. Datta, in *Nanoscience, Engineering and Technology Handbook*, W. Goddard, D. Brenner, S. Lyshevski, G. Iafrate (ed.), CRC Press, 2003.
- [5.23] N. P. Guisinger, N. L. Yoder, M. C. Hersam, *Proc. Nat. Acad. Sc.* 102 (2005), 8838.
- [5.24] A. Nitzan, M. A. Ratner, *Science* 300 (2003), 1384–9.
- [5.25] A. Troisi, M. A. Ratner, *Small* 2 (2006), 172–81.
- [5.26] R. Landauer, *Phil. Mag.* 21 (1970), 863.
- [5.27] Y. Xue, S. Datta, M. A. Ratner, *Chem. Phys. Special Issue*, ‘Transport in Molecular Wires’, 281 (2002), 151.
- [5.28] (a) N. W. Ashcroft, N. D. Mermin, *Solid State Physics*, Saunders, Fort Worth, 1976; (b) C. Kittel, *Introduction to Solid State Physics*, J. Wiley, 3rd edn., New York, 1968.
- [5.29] M. Buttiker, Y. Imry, R. Landauer, S. Pinhas, *Phys Rev B* 31 (1985), 6207–15.
- [5.30] J. N. Patillon, D. Mailly, in [5.2], chap. 12.
- [5.31] H. Ohnishi, Y. Kondo, K. Takayanagi, *Nature* 395 (1998), 780.
- [5.32] P. Sautet, C. Joachim, *Chem. Phys. Lett.* 185 (1991), 23.
- [5.33] A. R. Rocha, V. M. Garcia-Suarez, S. Bailey, C. Lambert, J. Ferrer, S. Sanvito, *Phys. Rev. B* 73 (2006), 085414.
- [5.34] S. Datta, *Quantum Transport: Atom to Transistor*, Cambridge University Press, Cambridge, 2005.
- [5.35] A. Troisi, M. A. Ratner, in *Molecular Nanoelectronics*, M. A. Reed, T. Lee (eds.), American Scientific Publishers, 2003, chap. E.
- [5.36] C. Joachim, M. Ratner, in [5.3], p. 8801.
- [5.37] H. Birk, M. J. M. de Jong, C. Schönenberger, *Phys. Rev. Lett.* 75 (1995), 1610–3.
- [5.38] K. K. Likharev, *Proceed. IEEE* 87 (1999), 606.
- [5.39] *Introducing Molecular Electronics*, G. Cuniberti, G. Fagas, K. Richter (eds.), *Lecture Notes in Physics*, Springer-Verlag, Berlin, 2005.
- [5.40] (a) W. J. de Haas, J. de Boer, G. J. van den Berg, *Physica* 1 (1934) 1115–1124; (b) J. Kondo, *Progr. Theor. Phys.* 32 (1964) 37.
- [5.41] P. W. Anderson, Nobel Lecture: <http://nobelprize.org/nobel_prizes/physics/laureates/1977/anderson-lecture.html>
- [5.42] C. Kergueris, J.-P. Bourgoin, S. Palacin, D. Esteve, C. Urbina, M. Magoga, C. Joachim, *Phys. Rev. B* 59 (1999), 12505–12513.
- [5.43] M. Magoga, C. Joachim, *Phys. Rev. B* 56 (1997), 4722.

- [5.44] M. Magoga, C. Joachim, *Phys. Rev. B* 57 (1998), 1820; A. Lahmidi, C. Joachim, *Chem. Phys. Lett.* 381 (2003), 335.
- [5.45] J. He, F. Chen, J. Li, O. F. Sankey, Y. Terazono, C. Herrero, D. Gust, T. A. Moore, A. L. Moore, S. M. Lindsay, *J. Am. Chem. Soc.* 127 (2005), 1384–5.
- [5.46] L. Lafferentz, F. Ample, H. Yu, S. Hecht, C. Joachim, L. Grill, *Science* 323 (2009), 1193.
- [5.47] J.-P. Launay, *Chem. Soc. Rev.* 30 (2001), 386; J.-P. Launay, C. Coudret, in *Electron Transfer in Chemistry*, V. Balzani (ed.), Wiley-VCH, Weinheim, 2001, vol. 5, chap. 1.
- [5.48] A. Nitzan, *J. Phys. Chem. A* 105 (2001), 2677.
- [5.49] M. Mayor, H. B. Weber, J. Reichert, M. Elbing, C. von Hänisch, D. Beckmann, M. Fischer, *Angew. Chem. Int. Ed.* 42 (2003) 5834.
- [5.50] C. Rovira, D. Ruiz-Molina, O. Elsner, J. Vidal-Gancedo, J. Bonvoisin, J.-P. Launay, J. Veciana, *Chemistry Eur. J.* 7 (2001) 240.
- [5.51] A. S. Martin, J. R. Sambles, G. J. Ashwell, *Phys. Rev. Lett.* 70 (1993), 218.
- [5.52] R. Metzger, *Acc. Chem. Res.* 32 (1999), 950–7.
- [5.53] M. Elbing, R. Ochs, M. Koentopp, M. Fischer, C. von Hänisch, F. Weigend, F. Evers, H. B. Weber, M. Mayor, *Proc. Nat. Acad. Sc.* 102 (2005), 8815.
- [5.54] J. Repp, G. Meyer, F. E. Olsson, M. Persson, *Science* 305 (2004), 493.
- [5.55] J. E. Huheey, E. A. Keiter, R. L. Keiter, *Inorganic Chemistry: Principles of Structure and Reactivity*, Harper Collins College Publishers, 1993, chap. 18.
- [5.56] T. Leoni, O. Guillermet, H. Walch, V. Langlais, A. Scheuermann, J. Bonvoisin, S. Gauthier, *Phys. Rev. Lett.* 106 (2011), 216103.
- [5.57] (a) *Catenanes, Rotaxanes, and Knots: A Journey Through the World of Molecular Topology*, J. P. Sauvage, C. Dietrich-Buchecker (eds.), Wiley-VCH, Weinheim, 1999. (b) A. Harada, A. Hashidzume, H. Yamaguchi, Y. Takashima, *Chem. Rev.* 109 (2009) 5974; (c) X. Ma, H. Tian, *Chem. Soc. Rev.* 39 (2010) 70.
- [5.58] Y. Luo, C. P. Collier, J. O. Jeppesen, K. A. Nielsen, E. Delonno, G. Ho, J. Perkins, H. R. Tseng, T. Yamamoto, J. F. Stoddart, J. R. Heath, *Chem. Phys. Chem.* 3 (2002), 519.
- [5.59] J. Chen, M. Reed, A. Rawlett, J. Tour, *Science* 286 (1999), 1550.
- [5.60] M. Galperin, M. A. Ratner, A. Nitzan, *Nanolett.* 5 (2005), 125.
- [5.61] (a) C. Joachim, J. K. Gimzewski, H. Tang, *Phys. Rev. B* 58 (1998), 16407; (b) C. Joachim, J. K. Gimzewski, *Chem. Phys. Lett.* 265 (1997), 353.
- [5.62] S. Ami, C. Joachim, *Nanotechnology* 12 (2001), 44.
- [5.63] M. Irie, *Chem. Rev.* 100 (2000), 1685–1716.
- [5.64] G. Guirado, C. Coudret, J.-P. Launay, M. Hliwa, *J. Phys. Chem. B* 109 (2005), 17445.
- [5.65] J. He, F. Chen, P. A. Liddell, J. Andréasson, S. D. Straight, D. Gust, T. A. Moore, A. L. Moore, J. Li, O. F. Sankey, S. M. Lindsay, *Nanotechnology* 16 (2005), 695–702.
- [5.66] D. Dulic, S. J. van der Molen, T. Kudernac, H. T. Jonkman, J. J. D. de Jong, T. N. Bowden, J. van Esch, B. L. Feringa, B. J. van Wees, *Phys. Rev. Lett.* 91 (2003), 207402.
- [5.67] H. Park, J. Park, A. K. L. Lim, E. H. Anderson, P. Alivisatos, P. L. McEuen, *Nature* 407 (2000), 57.
- [5.68] (a) L. V. Radushkevich, V. M. Lukyanovich, *Soviet J. Phys. Chem.* 26 (1952) 88–95 (available in Russian at <<http://nanotube.msu.edu/HSS/2006/4/2006-4.pdf>>); (b) S. Iijima, *Nature* 354 (1991), 56; S. Iijima, T. Ichihashi, *Nature* 363 (1993), 603.
- [5.69] H. Dai, *Surf. Science* 500 (2002), 218.
- [5.70] T. Druzhinina, S. Hoepfener, U. S. Schubert, *Adv. Mater.* 23 (2011), 953–70.
- [5.71] S. Tans, A. Verschueren, C. Dekker, *Nature* 393 (1998), 49.
- [5.72] S. J. Tans, M. Devoret, H. Dai, A. Thess, R. Smalley, L. Geerligs, C. Dekker, *Nature* 386 (1997), 474.
- [5.73] H. W. C. Postma, T. Teepen, Z. Yao, M. Grifoni, C. Dekker, *Science* 293 (2001), 76.

- [5.74] (a) A. K. Geim, A. H. MacDonald, *Physics Today*, August 2007, 35–41; (b) C. Soldano, A. Mahmood, E. Dujardin, *Carbon* 48 (2010) 2127–50; (c) <http://www.nobelprize.org/nobel_prizes/physics/laureates/2010>
- [5.75] (a) <http://www.nobelprize.org/nobel_prizes/physics/laureates/2007/>; (b) *Handbook of Magnetism and Advanced Magnetic Materials* vol. V, H. Kronmüller, S. Parkin (eds.), Wiley, New York, 2007; (c) C. Chappert, A. Barthélémy, in [5.2], chap. 14.
- [5.76] (a) N. Atodiresei, J. Brede, P. Lazic, V. Caciuc, G. Hoffmann, R. Wiesendanger, S. Blügel, *Phys. Rev. Letters* 105, (2010) 066601; (b) J. Brede, N. Atodiresei, S. Kuck, P. Lazic, V. Caciuc, Y. Morikawa, G. Hoffmann, S. Blügel, R. Wiesendanger, *Phys. Rev. Letters* 105 (2010), 047204.
- [5.77] (a) L. Bogani, W. Wernsdorfer, *Nature Materials* 7 (2008) 179; (b) S. Sanvito, *Chem. Soc. Rev.* 40 (2011) 3336.
- [5.78] (a) D. Natelson, L. H. Yu, J. W. Ciszek, Z. K. Keane, J. M. Tour, *Chem. Phys.* 324 (2006) 267–75; (b) G. D. Scott, D. Natelson, *ACS Nano* 4 (2010) 3560–79.
- [5.79] N. Roch, S. Florens, V. Bouchiat, W. Wernsdorfer, F. Balestro, *Nature* 453 (2008), 633–8.
- [5.80] R. Kleiner, D. Koelle, F. Ludwig, J. Clarke, *Proc. IEEE* 92 (2004), 1534.
- [5.81] J.-P. Cleuziou, W. Wernsdorfer, V. Bouchiat, T. Ondarçuhu, M. Monthiou, *Nature Nanotech.* 1 (2006), 53–9.
- [5.82] M. Urdampilleta, S. Klyatskaya, J.-P. Cleuziou, M. Ruben, W. Wernsdorfer, *Nature Materials* 10 (2011), 502.
- [5.83] (a) S. Fraysse, C. Coudret, J.-P. Launay, *Eur J. Inorg. Chem.* (2000), 1581. (b) J.-P. Launay, C. Coudret, C. Joachim, ‘Molecular Switches’, in *Dekker Encyclopedia of Nanoscience and Nanotechnology*, M. Dekker (2004), 2145.
- [5.84] A. P. de Silva, N. D. McClenaghan, C. P. McCoy, in *Electron Transfer in Chemistry*, V. Balzani (ed.), Wiley-VCH, Weinheim, 2001, vol 5, chap. 5.
- [5.85] M. Venturi, A. Credi, V. Balzani, in *Electron Transfer in Chemistry*, V. Balzani (ed.), Wiley-VCH, Weinheim, 2001, vol. 3, chap. 6.
- [5.86] O. Kahn, E. Codjovi, *Phil. Trans. Roy. Soc. Series A* 354 (1996), 359–79.
- [5.87] A. Steane, *Rep. Progr. Phys.* 61 (1998), 117; D. P. DiVincenzo, *arXiv:quant-ph/0002077v3*.
- [5.88] F. Troiani, M. Affronte, *Chem. Soc. Rev.* 40 (2011), 3119; A. Candini, G. Lorusso, F. Troiani, A. Ghirri, S. Carretta, P. Santini, G. Amoretti, C. Muryn, F. Tuna, G. Timco, E. J. L. McInnes, R. E. P. Winpenny, W. Wernsdorfer, M. Affronte, *Phys. Rev. Lett.* 104 (2010), 037203.
- [5.89] L. M. K. Vandersypen, M. Steffen, G. Breyta, C. S. Yannoni, M. H. Sherwood, I. L. Chuang, *Nature* 414 (2001), 883–7.
- [5.90] M. N. Leuenberger, D. Loss, *Nature* 410 (2001), 789–93.
- [5.91] L. K. Grover, *Phys. Rev. Lett.* 79 (1997), 325–8.
- [5.92] S. Bertaina, S. Gambarelli, T. Mitra, B. Tsukerblat, A. Müller, B. Barbara, *Nature* 453 (2008), 203.
- [5.93] I. Duchemin, C. Joachim, *Chem. Phys. Lett.* 406 (2005), 167–72; C. Joachim, N. Renaud, M. Hliwa, *Advanced Mater.* 24 (2012), 312–7.

Index

- 1-step process, 401–404, 420, 422
 - 2-step process, 114, 261, 401–404, 414, 417
 - 1D, one-dimension, 44, 46, 48, 49,
172–180, 183, 185, 199, 200, 270, 278,
285–289, 291, 293–298, 303, 306–309,
314–322
 - 2D, two-dimension, 49, 123, 172–175,
176, 182–185, 286–289, 291, 307,
321, 449
 - 3D, three-dimension, 48, 123, 172–183,
185, 287, 291, 295, 309, 311, 316, 321,
366, 383

 - A**
 - AB unsymmetrical molecules, 16–17, 60, 150,
152
 - Abragam A., 127, 203
 - absorbance, 330, 353
 - absorption
 - general process, 90, 92, 464
 - in EPR, 92
 - electronic (UV-vis-near IR), 125, 237, 239,
255, 259, 298–299, 312, 439–440
 - in photophysics, 227, 326–331, 333, 344,
348, 353, 355–356, 359–366, 374, 382
 - γ rays (Mossbauer), 238
 - in NMR, 250
 - X-ray, 93, 113, 375, 381
 - molar absorption (extinction) coefficient,
255–256, 330–332
 - activation energy
 - high-spin low-spin, 125, 366, 368
 - in electron transfer, 211, 213–214, 216,
218–220, 222–223, 226, 228, 230, 236,
243, 248, 258
 - in Glauber mechanism, 200
 - in nanojunctions, 403, 414, 433
 - in photo-induced electron transfer,
375–377
 - of conductivity, 271, 298, 310
 - AC susceptibility, 90, 193
 - adiabatic, 198, 219–225, 257, 265, 455
 - AFM, *see* Atomic Force Microscope
 - allyl radical, 24, 70
 - AND gate, 458, 465
 - Anderson, P.W., 143, 154, 203, 245, 324, 420,
469–470

 - angular momentum operators, 50, 81–86,
99–104
 - orbital (**L**, **L**), 50, 81–83, 99, 108, 129, 201
 - spin (**s**, **S**), 50, 83–86, 97, 100
 - total (**j**, **J**), 86, 101, 103, 201
 - see also* operator, sub-entry spin angular
momentum
 - anisotropy, 132, 191
 - and crystal field, 132
 - and exchange, 131–135, 137, 174, 185
 - and long-range order, 185
 - and magnetization dynamics, 191–195
 - and zero-field splitting, 131
 - easy axis, 131, 135, 181, 194
 - easy plane, 131, 135
 - in chains, 174, 199
 - in clusters, 137
 - in conductivity, 271, 275, 281, 303
 - in lanthanides, 201
 - in single chain magnets, 199
 - in single ion magnets, 201
 - in single molecule magnets, 191–199
 - Ising, *see* Ising anisotropy
 - D parameter, tensor, 128–132, 134,
137–138, 199
 - g parameter, tensor, 129
 - single-ion, 128–132
 - two-centre, 134
 - structural., 174*sq*, 191*sq*, 199*sq*, 201*sq*,
272*sq*, 276*sq*, 278*sq*
 - uniaxial, 131, 135, 193
 - XY, 135, 185
- anisotropy barrier, 131, 193*sq*, 199–202
- antenna effect, 351, 362–363, 365
 - see also* light harvesting
- antiaromatic, 27, 39
- antibonding (orbitals)
 - definition, 12
 - in Bloch or crystal orbitals, 24, 41–45, 48
 - in complexes, 29–32, 121, 209, 223, 272,
334
 - in exchange interaction, 142, 145, 148–150,
161–162
 - in Jahn-Teller or Peierls distortion, 39, 46,
249
 - in KCP, 273–275, 292
 - in polyacetylene, 277
 - in spin cross-over complexes, 121, 367

- antibonding (orbitals) (*cont.*)
 in TTF-TCNQ, 284
see also bonding
- antiferromagnetic
 coupling, interaction, 133, 140–152,
 153–156, 157–172, 173–183, 188–192,
 244–247, 311–316, 377, 380.
 in a chain, 173, 176, 179
 in Kondo effect, 420
 Mott insulator, 249, 318
 order, 178–180, 183–185
- antiferromagnetism, 8, 94, 145, 148, 161–164,
 169, 321
- antisymmetric
 exchange, 135, 173, 175
 Hamiltonian, 132, 135
 orbitals, 23–25, 45, 160
 wavefunction, 9, 51, 68
- antisymmetry, 52, 67
- approximation
 Born–Oppenheimer, 11, 50
 Hartree–Fock, 52–63
 Hückel, E., 12, 26
 Koopman, 58
 LDA, LSDA (DFT), 74
 mean-field, 54, 313
 MO-LCAO, 11
 Mulliken, R., 142
 one-electron, 4, 8, 23, 39, 52, 74
 tight-binding, 24, 62, 319
 Van Vleck, J.H., 96, 98
see also semi-empirical methods
- approximate, approximated
 density of states, 44
 Franck–Condon factor (Förster theory),
 355
 probability for electron transfer, 222
 radial functions, 5
 relation between G and k_{et} , 425
 resonance integral, 17, 24
 time scales, 252
- aromatic, 26, 35, 122, 282, 341
- Arrhenius law, 194, 198, 230, 369
- atomic force microscope (AFM), 395, 446,
 448
- atomic number (Z), 4, 8, 50, 94, 104, 189
- atomic orbital (AO)
 definition, 5, 9
 symmetry, 6, 21
 linear combination, 11, 24, 29, 40, 62, 164,
 207, 260
- Au, *see* gold
- Aufbau principle, 9, 20, 34, 44, 65, 107, 326,
 328
- Austin Model (AM1), 63
- Aviram, A., 390, 427–430, 468
- Avogadro constant (N_A), 3, 95, 116, 255
- avoided crossing, 37, 75, 198, 219–224, 237,
 240–242, 248, 264, 332
- B**
- bacteriochlorophyll, 362
- ballistic transport, 405, 408
- band
 model, 39–45, 268–275, 304, 306, 308, 312,
 396
 narrow, 269, 278, 304–308, 316
 splitting by Peierls distortion, 45–46,
 286–304
 width, W, 43–44, 278, 284–286, 292, 319
see also conduction band, intervalence
 transition, valence band
- Bardeen Cooper Schrieffer (BCS) model, 316
- Becke, 3-parameter Lee Yang Parr (B3LYP)
 functional 74
- Becquerel, H., 3
- Bednorz, 317
- benzene, 25, 62, 70, 364, 430, 451
- Bethe, H., 105
- bias
 current, 90–91
 voltage, 396–399, 402–408, 411–413,
 416–424, 427, 430–433, 437, 443, 446,
 452
- bi-dihydrothiazine (btz), 122
- binuclear, *see* dinuclear
- bistability, 121, 124, 372, 439, 460–462
- Bleaney–Bowers, 127, 133, 139
- Bloch, F., 40
- Bloch Orbital (BO), 40–49, 154, 272–277,
 283–286, 289–292
- Bohr, N., 3, 101
- Bohr magneton (μ_B), 2, 85, 89, 91, 128, 170
- Boltzmann constant (k_B), 3, 95, 194, 309,
- bond
 alternation, 299, 302
 chemical, 11, 67–77, 138, 203, 206
 covalent, 11–23, 205, 394, 433
 delocalized, conjugated, 285, 296, 424, 430
 dissociation, 64, 69–72
 length (electron transfer), 209–216, 261,
 311
 length (Peierls distortion), 286, 296,
 301–302
 length (spin cross-over), 114
 localized, 10, 69, 72
see also bonding, Valence Bond, MO theory
- bond order or index, 13, 20, 367
- bonding, 12
 and exchange interaction, 138–147,
 149–155
 and spin polarization, 60

- in coordination complexes, 29–34, 272–275, 367
- in H_2 molecule, 11–15, 63–65, 71, 297, 306
- in Jahn-Teller or Peierls distortion, 35–39, 45
- in Molecular Orbital theory, 54–67
- in polyacetylene, 275–278
- in TTF-TCNQ bands, 283–285
- in Valence Bond theory, 67–72
- in water molecule, 22
- pair, 10, 23
- π bonding, 17, 32, 48, 276
- see also* antibonding, Bloch orbital, Crystal orbital
- Born, M., 42, 213
- Born–Karman condition, 42
- Born–Oppenheimer approximation, 11, 50
- boron atom, 9
- boron dipyrromethene, 364
- bra-ket (or Dirac) notation, 11, 84
- break junction, 393, 395, 423, 426, 430, 438, 440
- bridge(d)
 - carboxylate, 140, 160, 192
 - conjugated, 233, 260, 262, 425
 - cyanide, 169, 187, 351
 - hydroxo, 158
 - molecular, 149–151, 161, 395, 405, 410, 425, 438
 - monoatomic, 145, 147–148, 207, 312
 - oxalate, 150, 156, 159, 162–164
 - oxide, oxo, 145, 152, 191, 207
- bridging angle, 157–158
- bridging ligand, 79, 140, 146–148, 159, 174, 176, 206, 232, 242, 254, 259, 262, 311, 359, 364, 373, 411
- Brillouin
 - function, 98
 - zone, 43–44, 49, 274, 283–291, 445
 - first Brillouin zone, 43–44, 286–288, 445
- Brillouin, L., 43
- Broken Symmetry (BS), 156–157, *see also* DFT, unrestricted Hartee–Fock
- C**
 - C_{60} , 322, 364–365, 391, 411
 - C_{60} amplifier, 437–438, 441
 - C_{60} Kondo effect, 452–453
 - carotene, 337, 424
 - carbon
 - atom, 20, 23, 46, 180, 299, 445
 - graphite, 444, 449
 - see also* C_{60} , graphene
 - carbon monoxide ligand, 17, 32–35, 254
 - carbon nanotube, *see* nanotube
 - Carter, F., 391, 467
 - cgs-emu units, 85, 86–89
 - chain
 - alternating, 174
 - anisotropic, 174, 199
 - antiferromagnetic, 173, 176
 - bimetallic, 174, 176, 180
 - classical, 173
 - ferromagnetic, 173, 176, 180
 - ferrimagnetic, 173, 176–183
 - finite, 173
 - homometallic or homospin, 173, 176
 - infinite, 173, 176, 178–180, 314
 - magnetic, 44, 172–183
 - quantum, 173
 - uniform, 173–180, 294
 - see also* 1D
 - channel
 - in FET, 442
 - in nanojunctions, 409, 423
 - in spintronics (α , β), 449, 454
 - character, 15, 40, 105, 108
 - see also* group theory
 - character table, 15, 21, 25, 29, 39, 105
 - characteristic time, 195, 250–254
 - see also* time scale
 - charge (q, Q), *see* electron
 - recombination, 333, 349
 - separation, 326, 333–338, 342, 346, 351, 362, 365
 - charge density, 54, 58, 61, 72, 284, 290–295, 301, 307, 312
 - wave (CDW), 286, 290–292, 294–297, 300, 312–315, 320–322
 - charge transfer (CT)
 - configuration, 13, 68, 140–143, 154–156, insulator, 312
 - transition, 243, 255–257, 259, 349
 - salt, 278–285, 293, 304–308
 - see also* ligand-to-metal, metal-to-ligand, metal-to-metal charge transfer
 - charge order(ed), 307, 318
 - chemical mechanism (electron transport or transfer), 262, 404, 414
 - chemical reaction, 125, 224, 236, 262, 329, 340, 403, 416
 - chemiluminescence, 338–340
 - chromium, *see* Cr
 - chromophore, 122, 259, 326, 336, 351, 354–359, 362–364, 458
 - class (mixed valence), 240–243
 - class I, 240, 311
 - class II, 240–243, 248–257, 269, 294, 308, 312, 351, 375
 - class III, 240–243, 250–257, 312
 - closed-shell, 59–65, 74, 107, 278, 293, 327, 337, 354, 396, 422, 452–453
 - CO, *see* carbon monoxide, charge order, crystal orbital

- Co (Cobalt), 27
cobalt(II), Co(II), Co^{II}, 110, 164, 190, 379, 452
 Kondo effect in cobalt complex, 452
cobalt(III), Co(III), Co^{III}, 169, 188, 452
Co(sq)(cat)(phen) complex, 127
cobalt, *see* Co
coercive field, 193, 195, 450
coherence, 401, 463
coherence length, 405, 408
commutation, 82, 86
commuting operators, 82, 105, 128
complete active space self consistent field (CASSCF), 156
complete neglect of differential overlap (CNDO), 63
complex as ligand, as metal, 166, 177
 see also coordination complex
complex wavefunction, 5, 26, 40–43, 47, 76, 221, 290, 462
comproportionation, 232–233, 236
conductance, 267, 405, 408–411, 420–426, 447–451, 455, 467
 transconductance, 442
 differential, 441, 452
 quantum, 408, 420, 455
conduction, 266–270, 284, 298, 309–311, 396, 420, 425, 449
 band, 294, 298–302, 343, 347–348, 445–446
 electron, 405, 420, 453
 metallic, 268, 275, 304
 spin-polarized, 449–452
conductivity, 44, 217, 249, 266–315, 420
 metallic, 217, 282, 299, 302, 308, 390, 447
 see also superconductivity
conductor, 28, 217, 268, 276–279, 306, 316–319, 390–392, 405, 409
 metallic, 217, 269, 271, 277, 283, 297, 392
 one-dimensional (1D), 44, 270, 275, 296, 303, 321
 see also semiconductor, superconductor
configuration interaction (CI), 4, 63–67, 72, 141–143, 154–156, 248, 421
cooperativity, 111, 115, 122, 460
coordination complex, 27–35, 99, 109, 166, 329–330
coordination sphere, 187, 210, 375, 379, 383
 external, 211
 internal, 211, 213, 215, 224, 241
Cooper pair, 316, 322,
copper, *see* Cu
correlated electrons, 49, 52
correlated spins, 179, 199
correlation
 between ligand field approaches, 107
 between charge density waves, 295
 electron, 53, 63, 71, 73–74, 217, 266, 291
 energy, 53, 155
 length, 184, 295
 magneto-structural, 157, 202
Coulomb
 blockade or staircase, 402–404, 414, 417–420, 424, 447, 452
 diamonds, 441–443, 452
 energy (α), 12, 23, 39
 hole, 49
 one-electron integral, 12
 repulsion, *see* electron repulsion
covalent bond, 16, 205, 394, 433
covalent term, wavefunction, 64–72
Cr (chromium), 27
Cr(II), Cr^{II}, chromium(II) acetate, 140
Cr(III), Cr^{III}, chromium(III), 160, 163, 165, 168, 188–190, 329, 463
 [Cr(III)(CN)₆]³⁻, 166, 169, 188–190
 Cr(III)-Cu(II) complex, 161–165
 Cr(III)-Mn(II) complex, 163
 [Cr(III)(ox)₃]³⁻, 166
 CrCu₆, CrMn₆, CrNi₆ complexes, 169
critical temperature (T_c), 92
 in magnetic ordering, 179, 183–185, 189, 383
 in Peierls distortion, 294
 in superconductivity, 268, 316
Creutz-Taube complex, 231
crystal field, 28–31, 104, 132
crystal orbital (CO), 4, 46–49, 277, 296
Cu (copper), 27
Cu(II), Cu^{II}, copper(II), 36, 130, 136, 145, 163, 173, 374
 acetate, 133, 139, 156
 bis- μ -hydroxo complex, 157–159
 Cu(II)-Cr(III) complex, 161–165
 [Cu(II)(dto)₂]²⁻ complex, 177, *see also* MnCudto chain
 Cu(II)-Fe(III) complex, 165
 Cu(II)-Mn(II) complexes, 166–168
 [Cu(II)pba]²⁻, 166–168, *see also* MnCupba chain
 [Cu(II)pbaOH]²⁻, 180–183, *see also* MnCupbaOH chain
 Cu(II)-V(IV)O complex, 160
 dibenzoylmethanato complex, 433
 μ -oxalate complex, 79, 149–151, 159–164, 173
 μ -oxamide, dithiooxamide,
 tetrathiooxamide complex, 162
 in Prussian blue analogues, 189
Curie law, 95–98, 139, 184, 193, 375, 461
Curie temperature (T_c), 94, 181–183, 188–190, 378–380, 383
Curie, M., 3
Curie, P., 3, 94, 183
Curie–Weiss law, 184,

- cyanide bridge, ligand, 123, 166–170, 187, 238, 287, 272–275, 351, 373–381
see also hexacyanidochromate, hexacyanidometalates, octacyanido complex, Prussian blue
- D**
- D parameter, 130–132, 140, 174, 193, 194, 199, 201
- D tensor, 128–129, 132, 137, 199
see also anisotropy
- Δ , Δ_{oct} , *see* ligand field parameter or splitting
- Day P., 231, 239, 312, 323, 325
- De Broglie L., 3, 408
- decastarphene, 413
- decay
 of conductance, 416, 424–426
 of electronic interaction, 262–265, 359, 425
 of excited state (photochemistry), 329, 348–350, 361
 of rate constant, 262, 264, 357–359, 361
- decoherence, 464, *see also* coherence
- degeneracy, 28, 31, 36, 45, 97, 100–102, 108, 114, 131–136, 197, 201, 249, 277, 296, 326, 415, 437
 electronic degeneracy, 36, 45
 energy level degeneracy, 136
 orbital degeneracy, 45, 100, 135, 249, 296, 326
 spin degeneracy, 101, 133, 415
- degenerate
 atomic orbitals, 13, 19, 109, 201
 Bloch orbitals, 43, 45, 289
 electronic state, term or configuration, 36, 38, 108, 134, 220, 244, 246, 299
 irreducible representations, 15, 25
 magnetic sublevels, 196–197,
 molecular orbitals, 20, 25, 36, 39, 159, 328, 437, 453
- delocalized electrons, 278, 400, 453
- demixion, demixing, 117–121, 126, 371
- density functional theory (DFT), 73, 77, 155–157, 171, 191, 266, 298, 375, 410, 452
 electron density in DFT, 73
see also broken symmetry, functional, Kohn Sham orbital
- density matrix, 58
- density of states (DOS), 43–46, 229, 291
 at the Fermi level, 291, 422
 in KCP, 274–275
 in nanojunctions, 407, 422
 in polyacetylene, 298–299
 local (LDOS), 352, 397, 432
- deoxyribonucleic acid (DNA), 263–264
- Dexter model, 351, 356–359, 385
- diamagnetic, 9, 140, 188
 atom, 9
 [Fe₄Co₄] cluster, 377
 iron(II) complex, 187
 ligand, 145–147, 154
 [M(CN)₄]²⁻ complex, 123
 [Mo(CN)₈]⁴⁻ complex, 374
 pair in Co-Fe system, 379–383
- diamagnetism, 9, 94
 diamond-shaped, 441–443, 452
- diarylethene, 439, 456–457
- difference dedicated configuration interaction (DDCI), 156
- dimer splitting, 207, 265–266
- dimerization, 45, 294, 307, 319–321
see also Peierls transition
- dinuclear, binuclear complexes, 152, 157, 163–166
 Cu(II)–Cu(II), 79–80, 136–137, 140, 149–151, 157–163
 homodinuclear, 163
 heterodinuclear, 160–169
 mixed valence Rh–Rh, 346–347
 mixed valence Ru–Os, 259, 358–359
 mixed valence Ru–Ru, 231–233, 456–457
 μ -oxalato complexes, 149–151, 163
see also chromium, cobalt, copper, iron, manganese, mixed valence, nickel
- dipyridophenazine (dpp) dipyrido, β , 2-a:2'3'-c] phenazine 122
- Dirac notation, 421
- Dirac, P.A.M., 1, 3, 11, 84–86, 109, 132, 202
- direct exchange, *see* exchange
- dispersion, *see* energy dispersion
- disproportionation, 217, 232, 335, 346
- dithienylcyclopentene, 437–440, 456
- dithiooxalate (dto), 162, 176
- dithiooxamide, 162
- domain
 magnetic domain, 195–196, 200
 model, 121
 walls (in ferromagnetism), 195, 200
- doping (n, p), 297–303, 308–314, 422
- double exchange, *see* exchange
- double-well, 75, 194–197
see also mixed valence, single molecule magnet, spin cross-over
- Dq parameter, 29, 106, 110–113, *see also* ligand field
- drain (electrode), 441–443, 447, 449, 452, 455
- Drickamer, H., 117, 122
- Dzyaloshinskii, 135
- E**
- E parameter, 130–132, 199
see also zero-field splitting, anisotropy
- easy axis, 131, 135, 181, 194, 453
see also Ising, anisotropy

- easy plane, 131, 135
- effective
- atomic number (Z_{eff}), 8
 - coupling, 208, 457, *see also* electronic interaction
 - Hamiltonian (H_{eff}), 8, 11, 62, 208, 246
 - magnetic moment, (μ_{eff}), 95, 98
 - mass (electron), 445
 - quantity, 8, 129, 147, 207
 - resonance integral (β_{eff}), 79, 146, 150, 207
see also V_{ab} parameter
- e_g orbitals, 25, 28–34, 36, 38, 110, 154, 169, 188, 190, 209, 223, 308, 329, 367
- E_g character, state or term, 30, 106, 129
- eigen
- state, 464
 - value, 1, 4, 55–58, 81–85, 97, 100–103, 109, 129–136, 241, 246, 257
- vector, 58, 129
- wavefunction, 1, 3–6, 51–56, 68, 75, 81–84, 105, 128, 157, 289, 350
- Einstein, A., 3, 309
- elastic model, 121, 410
- elastic process, 74, 401, 404, 410, 462
- elastic scattering quantum chemistry (ESQC), 410, 423–424
- electrochemiluminescence, 338–340
- electrochromic, 239
- electromagnetic radiation, 3, 92, 126, 205, 252, 330
- electromigration, 395, 441
- electron
- charge, 2–4
 - discovery, 2*sq*
 - in atoms, 4*sq*
 - in discrete molecular systems, 218*sq*
 - in molecular solids, 39*sq*, 266*sq*
 - in small molecules, 10*sq*
 - mass, 4, 255
 - spin, 2–4, 63, 92, 421, 451, 455, 465
- electron correlation, 53, 63, 71, 73, 155, 217, 266, 291
- electron density, 11, 14, 16, 54, 61, 73, 289, 401
see also charge density, spin density
- electron-electron repulsion, *see* electron repulsion
- electron exchange, 10, 50, 56, 134, 223, 249, 359, 402
- electron-hole formalism, 107
- electron-hole pair
- recombination, 340
 - separation, 336, 338, 362, 385
- electron paramagnetic resonance (EPR), 63, 89, 92, 127, 129, 139, 203, 218, 250, 252, 257, 309, 375
- electron-phonon coupling, interaction, 46, 216, 249, 286, 304–307, 311, 316, 414
- electron repulsion, 9, 24, 49*sq*, 53–57, 63, 78, 104, 144, 155, 244–246, 270, 304, 309, 316, 398, 402, 419, *see also* two-electron repulsion
- electron transfer
- in discrete molecular systems, 218*sq*
 - in the excited state, 333*sq*
 - optical *vs* thermal, 236*sq*
 - partial electron transfer in organic metals, 278*sq*
- electron transport, 340–342, 391–394, 401–414, 417, 422–424, 435, 441, 455
- electronegative, electronegativity, 16, 32, 145–148, 162, 207, 313
- electronic configuration, 4, 326–328
- in atoms, 7–10
 - in bonding theory, 50–51, 56–58, 63–68, 71–72
 - in complexes, 29–37, 79, 101, 107, 110, 145, 169–170, 189–190, 244, 313–315
 - in electron transfer, 212–215, 221, 228, 241
 - in exchange theory, 138–141
 - in excited states, 332–335
 - in polyenes, 26, 38
 - in small molecules, 14–23,
- electronic interaction, 62, 111, 147, 205–207, 220, 240–248, 259–266, 311, 403
- electronics, 3, 387, 390, 432, 440, 447, 449, 462, 468
see also microelectronics, molecular electronics, organic electronics, silicon electronics
- energy barrier, 74–76, 111, 131, 137, 193–195, 198–201, 223–230, 236, 240, 243, 258, 294, 341, 366–369, 375–377, 403
- energy (E , W)
- charging energy, 417–419
 - energy gap, 150, 162–163, 246, 274, 294, 297, 300, 313, 445
 - energy transfer, 351–364
 - solar energy, 343–346, 351, 385, 390
 - total electronic energy *vs* orbital energy, 9, 24, 56–57, 73, 101
 - transition energy, 237, 257, 301, 326
see also activation energy, band, Fermi energy, kinetic energy, Madelung energy, potential energy, potential energy surfaces, repulsion energy
- energy dispersion curve, 43–46, 48, 274, 277, 285–288, 290–292, 296–298, 318–321, 445

- enthalpy (H), 92, 111–118, 176, 270, 367, 373
see also free enthalpy
- entropy (S), 92, 111, 114–119, 121, 125, 176, 219, 381
- ethene (ethylene), 24, 276
- exchange
 anisotropic, 132–135, 173–175
 antisymmetric, 132, 135
 direct, 145, 147, 154
 double, 161, 187, 245–249
 isotropic, 132–135, 173–175
 interaction, 60, 81, 138, 143, 145, 147, 154, 157–159, 173, 182, 187–192, 199, 207, 244, 374–376, 454
 kinetic, 154, 156
 potential, 154, 156
see also superexchange
- exchange-double exchange operator, 246
- exchange operator, 55
- exchange pathway, 152, 163–170, 190
- exchange reaction, 218, 222–225
- excited electron, 326*sq*
- excited state, 326*sq*, 333*sq*
 electron transfer, 236*sq*, 333*sq*
 in configuration interaction, 64*sq*, 71–73, 141*sq*, 155*sq*
 in Jahn-Teller effect, 35*sq*, 108
 in photomagnetism, 373*sq*
 in [Ru(bipy)₃]²⁺, 333–340
 in tunnelling effect, *see* tunnelling effect
see also ground state
- exclusion principle, 9, 51, 53, 421
see also Pauli
- extended Hückel method, 24, 62, 145
- extended X-ray absorption fine structures (EXAFS), 93, 375
- F**
- Faraday, M., 3
 balance, 89–91
 effect, 93, 366
- Fe (iron), 27
- Fe(II), Fe^{II}, iron(II), 34, 35, 110–111, 163, 169, 187, 190, 210, 212, 237, 244–248, 372, 377, 379–382, 461
 [Fe(phen)₃]²⁺, 35, 114
 Fe(phen)₂(NCS)₂, 114, 125
 [Fe(ptz)₆]²⁺, 110, 366–369
 Fe(py)₂M(CN)₄, 123
 Fe(py)₂(phen)(NCS)₂, 115
 Fe(py)₄(NCS)₂, 115
 Fe(pz)₂M(CN)₄, 123–124
 mixed valence II/III in Prussian Blues, 185–188, 237–238
 [tris-μ(triazole)Fe]²⁺ chain, 461–462
- Fe(III), Fe^{III}, iron(III), 110, 160, 165, 169, 189, 210, 215, 237, 244–248, 322, 374, 376–383
 dinuclear iron(III) complex, 163
 Fe₈ complex, 199
 heterodinuclear copper(II)-iron(III) complex, 165
- Fermi, E., 44
- Fermi
 energy, level, 43–46, 49, 284–292, 294, 299, 303, 316, 320–322, 392, 396, 399, 401, 403, 406–407, 409–412, 416, 419, 421, 427–430, 432, 446
 function, 398, 406, 411, 415
 hole, 53, 421
 nested surface, 289, 291, 320
 surface, 49, 286–293, 316–321
 wavelength, 405, 407
- Fermi-Dirac distribution (or Fermi function), 293, 411
- Fermi Golden Rule, 229, 352
- ferrimagnet, 181, 188, 380, 383
- ferrimagnetic, 97, 165, 168–171, 173–184, 188–190, 192, 199, 380
 ferrimagnetic chain, 173–183
- ferrimagnetism, 94, 161–191, 463
 molecular, 163, 164*sq*, 463
 signature of, 167, 179, 193
- ferromagnetism, 94, 142, 145, 160
- ferromagnetic, 28, 90, 94, 154, 167, 172, 183, 187–190, 247, 306, 446, 455
- chain, 173, 176–180
 coupling, interaction, 10, 81, 133, 137, 143, 148–150, 157–161, 164, 169, 179, 187, 199, 244, 375
 exchange pathways, 164, 169
 materials, 90, 184, 188, 249, 450, 455
 order, 160, 178, 180, 184, 187–191
 state, 154, 170
 term, 156
- Feynman, R., 67, 85
- field-effect transistor (FET), 442, 446–449, 454
- fluorescence, 259, 327–329, 331–334, 340, 342, 351–353, 355, 359, 458–459
- flux quantum, 90
- Fock operator, 55
see also Hartree-Fock
- Förster mechanism, 351–364, 385
- Franck-Condon
 factor, 229, 353, 355, 425
 principle, 210, 236, 332
- free enthalpy (G), 87, 114, 117, 125, 176, 183, 218, 224–226, 343, 346, 357, 371
- frontier orbitals, 45, 79, 156, 261, 285, 334, 437

- Frost circle, 26
 functional, 73, 157, *see also* DFT, LYP, Becke
 3-parameter Lee Yang Parr
- G**
- g-factor, 2, 8, 85, 103, 128, 179, 252
 nuclear, 128
 gadolinium, *see* Gd
 gain (electronic device), 437, 441, 447
 gate (electrode), 441–443, 447, 449, 452–455
 Gd (gadolinium), 27
 Gd(III), Gd^{III}, gadolinium(III), 27, 167, 170,
 173
 generalized Mulliken Hush (GMH) model,
 256
 generalized valence bond (GVB), 70
 gerade, 6, 18, 28, 106, 207, 331
 Gillespie, R., 10
 Glauber, J., 200
 model, 204
 gold
 atoms, 336, 394, 409, 432
 electrodes, 395, 422, 430, 436, 440
 nanoparticles, 393, 395
 surface, 394, 397, 440, 411, 413
 work function, 397
 Goodenough, J., 138, 154, 155, 203, 325
 Goodenough–Kanamori rules, 152–154
 Goudsmit, S., 3, 84
 Gouy balance, 90–91
 graphene, 443–446, 448–449
 Griffith, J. S., 127, 203
 ground state (GS)
 and Hund's rules, 10
 and perturbation technique, 65
 definition, 7, 9, *see also* Aufbau principle
 determinant, 59, 64, 69
 in DFT, 73–74
 in electron transfer theory, 242–248, 255,
 257, 260–262
 in exchange interaction, 133–135, 137,
 141–143, 146, 155
 in ferromagnetic molecules, 164
 in Hartree–Fock SCF method, 54, 58–60
 in high-spin molecules, 167–172
 in Jahn–Teller effect, 35, 38
 in Kondo resonance, 421
 in magnetic chains and rings, 174, 176, 178
 in Peierls distortion, 294
 in photophysics, 326–329, 332, 335–336,
 349–352, 354, 366, 371, 373, 375, 377,
 381, 383
 in post-Hartree–Fock, 64, 65
 in single chain magnets, 199
 in single ion magnets, 201
 in single molecule magnets, 192, 196, 199
 in spin cross-over, 110–112
 in Tanabe–Sugano diagrams (term), 106
 in Valence Bond model, 69, 72
 in Zeeman effect, 129
 of 1D MX systems, 314
 of Co(II) and Co(III) complexes, 223
 of dinuclear Cu(II) complexes, 79
 of H₂, 13
 of molecular diodes, 428
 of Mott insulators, 305, 307
 of O₂, 20
 of organic superconductors, 319
 of polyacetylene, 299
 see also excited state
 group theory, 6, 14, 35, 40, 77, 105–108, 203,
 331
- H**
- H₂ dihydrogen molecule, 10–15, 24, 44,
 57–59, 64, 67–72, 293, 297, 306,
 345–348, 362
 H₄(f_{sa})_n, 160, 165
 H₂O
 coordinated, 32, 34, 140, 150, 159, 181,
 186, 191, 237, 379
 hydrogen bonds, 181
 molecule, 21–23
 photolysis, splitting, 345–347, 362
 solvent, 214, 428
 Haldane, F. D. M., 174
 Hamiltonian, 4, 8, 35, 49, 81, 83, 105, 127
 effective, 8, 11, 41, 208
 exact, 74
 exchange–double exchange, 246
 Heisenberg (HDVV), 132, 135, 185, 244,
 247
 Hubbard–Anderson, 245
 Hubbard, Mott–Hubbard, Peierls–Hubbard,
 305
 Hückel and extended Hückel, 62
 model, 245–248
 one-electron, 8, 41, 68,
 see also effective Hamiltonian, spin
 Hamiltonian
 harmonic oscillator, 111, 210, 228, 258, 350,
 464
 Hartree product, 52, 71
 Hartree–Fock method, 54–61, 71
 post-Hartree–Fock, 53, 63–67, 72, 155–157
 Hay–Thibeault–Hoffmann model, 143–144,
 155–158
 heat capacity, 89, 92, 113
 Heeger, A. J., 268, 270, 277, 282, 325
 Heisenberg, W., 3, 132, 135, 143
 Heisenberg Dirac Van Vleck Hamiltonian
 (HDVV), 132, 135, 244, 247, 305
 Heisenberg model, 175, 185
 Heitler, W., 10
 Heitler–London (HL) model, 64, 67, 71, 133,
 138, 140–142, 146, 154

- helium atom, 7–9, 59
Helmholtz, L., 62
heterodinuclear, *see* dinuclear
heterometallic
 dinuclear, 160, 163–165
 chain, 176–183
 see also chain, dinuclear
hexaqua iron(II), (III), 209–211, 213, 218, 219, 223, 226, 230
hexacyanidochromate(III), 166, 168
hexacyanidometalates, 185
high field (ligand), 32–35, 110
high field (magnetic), 93, 125, 170
high spin (HS)
 molecule, 165–172, 185, 375, 454, 463
 state, 34, 110–114, 366, 369, 371, 461
 see also low spin
high T_c superconductor, 317
high T_C Prussian blue analogue, 189
highest occupied molecular orbital (HOMO), 78
 in molecular devices, 396, 410–413, 423, 427–430
 HOMO-LUMO gap, 65, 260, 285, 298, 397, 411
 TTF HOMO, 283–285
Hildebrand, J. S., 116
Hoffmann, R., 46, 62, 77, 143, 154–158, 203, 269, 271, 275, 469
Hohenberg–Kohn theorem, 73
homodinuclear, *see* dinuclear
homometallic
 dinuclear, 157, 164
 chain, 173–177
 see also chain, dinuclear
hopping mechanism, 216, 262, 309–311, 403, 414–416, 432, 436
Hubbard, J., 245, 304, 314, 319, 325
Hückel method, 12, 23, 26, 40, 41, 62
 $4n + 2$ rule, 26
 see also extended Hückel
Hund–Mulliken (HM) model, 11, 64, 138, 143–146, 148, 150, 154, 412
Hund’s rules, 10, 20, 38, 101, 152
Hush, N. S., 214, 220, 223, 231, 255–258, 262, 323
 Hush–Marcus model, 214, 220, 223, 247, 403
hydrogen atom, 4–7, 85
hydrogen chain, 297, 306
hydrogen bond, 180–182, 186, 379
 see also H₂O
hydrogenoid ion, 7, 109
hydroxo bridge, 157–160
hyperfine coupling, 93, 128, 199, 250, 252, 258
hysteresis
 in memory devices, 402, 431, 435, 455
 in molecular magnets, 193, 195–196, 198
 in Prussian blue analogues, 383
 in spin cross-over, 113–115, 120–127, 369–371, 460–462
- I**
imaginary susceptibility (χ''), 90, 193
indistinguishable (electrons), 8, 51
inelastic neutron scattering (INS), 89, 93, 140
inelastic transport, process, 401, 404, 408, 428
infrared (IR), 3, 113, 140, 237, 252, 254, 298, 377, 413, 418
INHIBIT gate, 458–460
INPUT (in logic gates), 459
insulating layer (NaCl in STM studies), 399, 412, 432
intermediate neglect of differential overlap (INDO) method, 63
international technology roadmap for semiconductors (ITRS), 389
intersystem crossing, 327–330, 364, 366, 373
intervalence transition, 236–242, 252, 254–259, 262, 310, 351, 374, 457
inversion centre, 6, 14, 17, 106, 145, 151, 162, 331
ionic
 bonding, 16, 278
 compounds (in organic metals), 278–281, 305, 307
 terms, states or configurations, 13, 64, 68–72
ionization potential, 7, 62, 306, 396
ionocovalent bonding, 16
iron compounds, *see* Fe
irreducible representation (IR), 6, 15, 18, 22, 25, 29, 40, 71, 105, 331
 see also character tables
Ising anisotropy, 135, 175, 185, 199
isotropic exchange, *see* exchange
- J**
j, J angular momentum operator (total), 86, 101, 103
j, J quantum number, 86, 101, 103, 201
Jablonski, 326–329
Jahn–Teller effect, 35–39, 46, 77, 296
 1st order, 36, 130, 191, 249
 2nd order (pseudo Jahn–Teller), 37
j–j coupling, 103–104
Jordan, E., 3
Josephson junctions, 90–91, 384, 453–454
junction, 75, 91, 394–396, 398–404, 407, 411, 418, 423, 428, 433, 437, 441, 447, 451, 454
 break, 393, 395, 423, 426, 430, 438, 440

- junction (*cont.*)
 metal-molecule-metal, 391–394, 397, 401, 403, 410
 p-n, 303, 336, 426
see also Josephson junction, nanojunction
- K**
 Kahn, O., 77, 150, 160, 165, 180, 202–204, 245, 324, 461, 471
 Kahn–Briat model, 134, 140–143, 149–157
 Kambe method, 135–137, 167, 203
 kinetic energy, 2, 4, 8, 35, 55, 73, 154, 245, 305, 396, 407
 kinetic exchange, *see* exchange
 Kohn anomaly, 295
 Kohn–Sham orbital, 73
 Kondo effect, 420–421
 Kondo resonance, 420–422, 452
 Koopman’s theorem, 58, 412
 Kramers, H. A., 154
 Kramers theorem, 108
- L**
I, L angular momentum (orbital), 81–86, 99–101, 103, 129, 201
 λ parameter, 209–217, 219, 236, 241, 255, 257, 311, 313
see also electron-phonon coupling, polaron energy
 λ mean free path, *see* mean free path
 l, L quantum number (orbital), 4, 6, 50, 100, 105
 λ wavelength
 CDW, 291
 electromagnetic (UV-vis), 328, 330, 336, 340, 342, 349, 351, 353, 355, 359, 363, 368, 371, 382
 electron (de Broglie), 2, 405
 Fermi, 405, 408
 neutron, 94
 X-ray, 93
 Laguerre polynomial, 5
 Landau–Zener–Stückelberg model, 198, 204, 221–222, 323, 455
 Landauer, R., 403–409, 414, 419, 423, 469
 Landé, A., 3
 (g)-factor, 2, 85, 92, 103
 interval rule, 102
 Langevin, P., 94
 Langmuir–Blodgett (LB), 393, 428, 434
 lanthanide, 27, 199, 201, 249, 317
see also gadolinium, terbium
 Laporte rule, 331
 Lewis acid-base interaction, 166, 177, 185
 Lewis model, 10, 20, 23, 67
- lifetime of
 a state in a junction, 398
 excited state (photophysics), 328, 331, 334–337, 349, 351, 364
 muon, 93
 nuclear excited state, 251–253
 the electron, 2
see also excited state, metastable state
 ligand driven-light induced spin cross-over (LD-LISC), 372
 ligand-to-metal charge transfer (LMCT), 155, 256, 259, 330, 332–334
 ligand field, 31–34, 105–108, 109–115, 130, 153, 163, 201, 337, 372, 374, 376, 381
 ligand field splitting (Δ), 32–35, 106–108, 109–115, 130
 light emitting diode (LED, OLED), 338–342
 light harvesting, 327, 362
see also antenna effect
 light induced excited spin state trapping (LIESST), 366–369, 460
 linear combination of atomic orbitals (LCAO), 11, 20, 23–34, 42, 62
 lithium atom, 9, 60
 {LnPc₂}[−] 202, *see also* TbPc₂
 Local Density Approximation (LDA), 74
 Local Spin Density Approximation (LSDA), 74
 localized electrons, 78*sq*, 80, 245, 326
 logic gates, 418, 458–460, 465
see also AND, INHIBIT, INPUT, OR, OUTPUT, XOR
 London, F., 10
see also Heitler–London model
 Lorentz–Thomson model, 3
 low field (ligand), 32, 34, 111
 low spin (LS)
 molecule, 34–35, 107, 110–114, 123, 187, 237, 333, 366–369, 376, 380, 452, 461
 state, 34, 109–114, 115–125, 366–369, 370–372, 377–383
see also high spin
 lowest unoccupied molecular orbital (LUMO), 78, 79
 in molecular devices, 396, 410–415, 419, 427–431, 436, 453
 HOMO-LUMO gap, 65, 260, 285, 298, 397, 411
 TCNQ LUMO, 283–285
 LS coupling, *see* Russell Saunders
 luminescence, 260, 327–329, 334–335, 340, 459
see also chemiluminescence, electrochemiluminescence, fluorescence, phosphorescence
 LYP functional, 74

M

- MacDiarmid, A. G., 268, 270, 277, 325
- Madelung energy, 122, 279, 281
- magnet, 87, 90, 143, 175, 182, 191, 193, 195, 322, 384
- molecule-based, 172, 176sq, 182, 185–191
 - single molecule, 191–199, 204, 463
 - single ion, 201, 453
 - single chain, 199
 - soft, 383
- magnetic anisotropy, *see* anisotropy
- magnetic circular dichroism (MCD), 93
- X-Ray magnetic circular dichroism (XMCD), 61, 89, 93, 375, 381
- magnetic domain, *see* domain
- magnetic energy, 87
- magnetic exchange, *see* exchange interaction
- magnetic field, 85–89
- and Zeeman effect, 108sq, 128–131, 173, 194, 198, 464
 - dipolar effect, 174, 182
 - in molecular spintronics, 449–455
 - in quantum computing, 463
 - influence on spin cross-over, 125–127
 - see also* coercive field, Zeeman effect
- magnetic flux density, 88
- magnetic induction, 88, 129, 131, 181
- magnetic interaction, 92, 152, 154
- dipolar, 174, 182
 - exchange, *see* exchange interaction
- magnetic moment, 84–86, 85–90, 92–98, 103, 109, 128, 183, 420, 453
- effective, 95, 98
 - electron, 2, 93
- magnetic orbital, 80, 146–150, 153–165, 169, 177, 181, 188, 192, 208, 319, 375
- magnetic susceptibility, 87–90
- and magnetic order, 184
 - definition, units, 87–89
 - in Fe₄Co₄ systems, 377
 - Kondo effect, 420
 - in LD-LISC effect, 372
 - in LIESST effect, 366
 - in Kambe treatment, 135
 - measurement, 90, 94
 - of (CuMn)_n ring,
 - of copper acetate, 139
 - of polynuclear systems,
 - of ferrimagnetic CuMn systems, 167, 178–182
 - of paramagnetic systems (Van Vleck), 94–98
 - of Prussian Blue analogues, 381
 - of single molecule magnets, 193
 - of spin cross-over systems, 113, 123, 366, 372, 461
- magnetization
- and spin cross-over, 125–127
 - anisotropy, 134, 181–184, 199–201
 - at saturation, 98, 193, 170
 - definition, 87–91, 93–97
 - dynamics, 193, 198, 200
 - in photomagnetic systems, 365, 372–375, 378–383
 - in Prussian blue analogues, 190
 - in spin valve, 449–453
 - local vs macroscopic, 93
 - permanent, 96
 - plateaux, 193
 - remnant, 94, 193–195
 - reversal, 91, 183, 194, 198, 200, 453
 - see also* Brillouin function, hysteresis, spin-polarized, tunnelling, Van Vleck equation
- magnetochemistry, 80
- magnetoresistance: colossal, 249, giant 450
- magneto-structural correlation, 157, 202
- manganese, *see* Mn
- many-body perturbation theory (MBPT), 67, 72
- Marcus, R. A.,
- cross-relation, 224–226
 - inverted region, 226, 331, 336, 339, 357
 - see also* Hush-Marcus model
- mean free path (λ), 405, 408, 449
- Mendeleev, D., 3
- metal-molecule-metal, 392–393, 398, 401, 403, 410
- metal-to-ligand charge transfer (MLCT), 259, 330, 333, 337, 370
- metal-to-metal charge transfer (MMCT), 155, 330, 374
- metastable state
- in LIESST, 368–372
 - in photomagnetism, 327, 366, 373–378, 381–383
 - in spin cross-over, 120, 124–126
- methylviologen, 335
- microelectronics, 387, 392
- Millikan, R., 3
- mixed valence, 231, 325
- classes, 239–240
 - definition, 231
 - electronic interaction in, 260
 - experimental study, 250–260
 - in dinuclear Rh-Rh, 346–347, Ru-Os, 259–260, Ru-Ru, 231–233, 351, 456–457
 - in K₃[MnO₄]₂, 311
 - in M(AA)₂X chains, 312
 - in Mn₁₂, 191
 - in MoCu₆, 374
 - in non-stoichiometric oxides, 311
 - in organic compounds, 239
 - in Prussian Blue analogues, 187

- mixed valence (*cont.*)
 in Ru-CN-Ru, 351
 in TTF or TCNQ stacks, 279, 281, 285
 intervalence transitions in, 255–257
 isomer, 259
 magnetic, 244–249
 molecular orbitals, 207, 261
 molecular switch, 456
 molecular wire, 456
 Ru-Os, 259
 semi-conducting, 308–309
 stability (comproportionation), 232–236
 thermal and optical transfer, 237
 mixed valency, *see* mixed valence
 ML₆ complex, 29–34
 Mn (manganese), 27
 Mn(II), Mn^{II}, manganese(II), 110, 163–168, 181–183
 Mn(II)Cr(III) complex, 163
 MnCu₂O chain, 176–180
 MnCu₂O and MnCu₂O·OH chain, 180–183
 MnCu₂O·Mn trinuclear complex, 166, 178–180
 Mn₆Mo₉ complex, 170–172
 mixed valence II/III complexes Mn₂₅, Mn₁₉, 172
 μ-oxalato complex, 163
 in Prussian blue analogues, 188–190
 Mn(III), Mn^{III}, manganese(III), 110, 169
 in [Mn(CN)₆]³⁻, 110, 172
 mixed valence III/IV complex, *see* Mn₁₂
 Mn₁₂ complex, 91, 191–198, 202, 453, 464
 Mo (molybdenum), 27
 Mo(IV), Mo^{IV}, molybdenum(IV), 378
 [Mo^{IV}(CN)₈(Cu^{II}tren)₆]⁸⁺, 374–376
 Mo(V), Mo^V, molybdenum(V), 378
 [Mo^V(CN)₈(Cu^ICu^{II}₅tren)₆]⁸⁺, 374–376
 Mo₆Mn₉ complex, 170–172
 modified intermediate neglect of differential overlap (MINDO), 63
 modified neglect of diatomic overlap (MNDO), 63
 molecular
 diode (rectifier), 390, 426–431
 electronic devices, 391, 468
 shuttle, 433–435
 switch, 366, 456, 471
 transistor (amplifier), 437
 wire, 422–424, 456, 469
 see also single molecule
 molecular electronics, 358, 366, 378, 387–468
 and spintronics, 451–455
 hybrid molecular electronics, 392–456
 in solution, 456–470
 perspectives, 466–468
 solid state devices, 460–462
 molecular ferrimagnetism, 163–172, 176–183, 463
 molecular magnetism, 80, 86, 88, 93, 97, 132, 139, 149, 202, 324, 378
 molecular orbital (MO)
 basic theory (H₂ and AB), 11–17
 building MO of simple molecules and coordination complexes., 17–35
 comparison with VB method, 71–73
 imaging MO, 412–413
 quantitative MO method, 54–67
 weakness of simple MO theory, 64, 304–308
 see also Bloch Orbitals, Crystal Orbitals, Highest Occupied, Lowest Unoccupied, Singly Occupied Molecular Orbital
 molecular solid, 1, 39–49, 266–322, 373
 molecular spintronics, 81, 449–455, 466
 molecule i-vi, 10–39
 see also AB, H₂, H₂O, O₂, organic molecules, coordination complexes
 molecule-dependent tunnelling, 402–404, 412, 422–424
 Møller-Plesset method, 67, 156
 molybdenum, *see* Mo
 monomolecular electronics, 467
 Moore's law, 387–389, 467
 Moriya, 135
 Mössbauer spectroscopy, 113, 128, 187, 238, 250–253, 369
 Mott, N. F., 449
 Mott-Hubbard Hamiltonian, 304–305
 Mott insulator, 217, 281, 304–309, 311–314, 318
 Müller, K. A., 317
 Mulliken, R., 11, 14, 142, 412
 β – Δ approximation, 142
 see also Hund-Mulliken model
 multiwall nanotube (MWNT), 444
 muon spin relaxation, 89, 93

N
 N₂ molecule, 10
 nanocrystalline, 343, 347
 nanojunction
 general formalism, 392–395, 399, 403–412, 417–422
 in spintronics, 449–451, 455
 Kondo effect, 420–422
 with C₆₀, 453
 with molecular diode, 429–431
 with molecular switch, 438, 440
 with molecular wire, 423–426
 nanometer size, 75, 123, 358, 384, 392, 399, 404–407, 443, 449, 468
 nanoparticles, 384, 393, 395, 402, 404, 414, 417
 nanopore, 393, 436

- nanoscale, 89, 384, 391
nanoscience, 468–471
nanotechnology, 391, 471
nanotube, 395, 404, 414, 417, 443–449
 electronic structure, 445
 in SQUIDs, 91, 453
 multi-walled (MWNT), 444
 properties (metallic, semi-metallic, semi-conducting), 446
 single-walled (SWNT), 444, 446, 454
 structure (armchair, chiral, zigzag), 444–446
 use in devices, 446–448, 453–455
nanowire, 395, 404–410
narrow band, 278, 289, 304–308
Nasu K., 313, 325
natural magnetic orbital (NMO), 149
near-infrared, 237, 254
Néel, L., 143, 165, 204, 379
 temperature (T_N), 183
negative differential resistance (NDR), 431, 436
nesting, 286–293, *see also* Fermi surface
neutron diffraction, 61, 89, 94, 113, 171
neutron scattering, *see* inelastic neutron scattering
Ni (nickel), 27
Ni(II), Ni^{II}, nickel(II), 108, 123, 170, 188, 190, 279, 285, 463
 in μ -oxalato complex, 163
 in Prussian blue analogues, 188–191
Ni(III), Ni^{III}, nickel(III), 312
nickel, *see* Ni
nitronyl nitroxide, 79
nodal surface, 6, 28, 31, 149
node in wave function, 24, 41, 43, 45, 261, 273, 412
non-adiabatic, 198, 222, 262, 348, 369, 455
non-bonding orbitals, 22–31, 48, 71, 149, 272–274
non-commuting operator, 82
non-orthogonalized (orbitals), 141, 146, 161
non-orthogonal orbitals, 71, 140–146, 149, 151, 161
non-radiative, 259, 327–329, 352
normalization constant, 18, 40, 52, 67, 70
nuclear
 g-factor, 128
 magnetic moment, 128
 magneton, 128
 spin operator, 128
nuclear magnetic resonance (NMR), 61, 94, 128, 187, 250–252, 463
- O**
O₂ molecule, 10, 17–20, 335, 345, 348
octet rule, 10
octacyanido complex, 170, 374
octahedral, 28–35, 110–113, 129–130, 153, 163, 166, 186, 191, 249, 308, 311, 313, 329, 366, 376, 379
O_h (symmetry), 29–36, 105–109, 130, 331, 333
one-dimensional, 172, 275, 282, 283, 286, 304, 309, 409
 see also 1D
one-electron
 energy, 209, 343, 396, 398, 411, 427
 integral, 245
 model, approximation, 8, 11, 23, 39, 48–50, 52, 260, 304
 transistor, 418
 wavefunction, 55, 105, 266, 357
 see also Hamiltonian
open-shell, 59–61, 74, 78, 278, 293, 329, 422
operator, 1, 7
 dipolar electric (or dipole moment), 255, 331
 evolution, 462
 exchange, 55
 kinetic energy, 35
 magnetic moment, 84–86, 103
 nuclear magnetic moment, 128
 occupation, 246
 one-electron, 55
 orbital angular momentum (\mathbf{l} , \mathbf{l}^2 , \mathbf{L} , \mathbf{L}^2), 81–85, 99–102, 105, 129, 201
 perturbation, 65–67
 projection, 208, 209
 spin angular momentum (\mathbf{s} , \mathbf{s}^2 , \mathbf{S} , \mathbf{S}^2), 83, 84, 100–102, 128–132, 135–137, 150, 167
 spin Hamiltonian, 127*sq*
 total angular momentum (\mathbf{j} , \mathbf{J} , \mathbf{J}^2), 101–103
 two-electron, 50
 V coupling (Förster theory), 352–354
 vector, 132, 173
 see also Fock operator
optical density, *see* absorbance
optical electron transfer, 236–239
OR gate, 458–459
Orbach process, 194
orbital
 atomic, 5, 6, 83
 complex orbital, 5, 40–42, 47, 76, 221, 290, 462
 exponent, 5, 62
 magnetic, *see* magnetic orbital
 molecular, *see* molecular orbital (highest occupied, lowest unoccupied, singly occupied)
 see also Bloch Orbital, Crystal Orbital
orbital angular momentum, *see* angular momentum
organic electronics, 390, 468

- organic light-emitting diode (OLED), 340–342
 organic metal, 278*sq*, 282*sq*, 305, 318–321
 organic molecules, 23–24, 327, 340–342
see also polyenes
- orthogonal orbitals, 10, 20, 43, 52, 70, 138, 142, 144, 146, 150, 158–161, 169, 208, 244
 orthogonality, 57, 72, 142, 145, 148, 150, 154, 160–161, 187, 192, 375
 orthogonalized orbitals, 19, 63, 138, 141–146, 151, 154, 156, 161
 ortho-phenanthroline, *see* 1,10-phenanthroline
 oscillator strength, 255, 330
 OUTPUT (in logic gates), 459
- overlap, 11–13, 18–20, 67, 70, 238, 421
 and band-width, 43–48
 and conductivity, 273, 283–286, 319–322
 and energy transfer (spectral overlap), 355–356
 and magnetism, 138, 140–145, 152–161, 164–172, 176–192, 319, 380
 and mixed valence, 238, 312
 density, 51, 161
 differential overlap (neglected), 63
 Franck–Condon factor, 230
 integral, 11–13, 18, 23, 67, 133, 138–142, 145, 150, 160, 357
 population, 14
 treatment in semi-empirical methods, 62
see also spectral overlap integral
- oxalate, oxalato ligand, 35, 79, 149–151, 156, 159–166, 173, 176, 322
 oxamide ligand, 162
 oxo ligand and bridge, 152, 191
 polyoxometallate, 239, 324
- P**
- π -acceptor, 33–35, 115, 333
 pairing energy, 110, 112
 paramagnetic, 7, 9, 10, 20, 78, 108, 139, 147, 154, 375, 452, 463
 in photomagnetic systems, 373*sq*, 380–381, 383–384
 limit, 167, 178–179
 paramagnetic-ferromagnetic transition, 94, 183–184, 187, *see also* Curie
 susceptibility (Van Vleck), 94–98,
see also electron paramagnetic resonance,
 exchange, Kondo effect, open-shell,
 Zeeman effect
- paramagnetism, 20, 94, 139
 Pariser–Parr–Pople (PPP) method, 63
 partition function, Z, 95–98
 Pauli principle, 9, 51–54, 67, 84, 128, 244, 421
 Pauli, W., 3, 84
 Pauling, L., 10, 67, 69, 72, 77
 π -donor, 33, 115
- Peierls transition (distortion), 45, 278, 286, 290–296, 303–305, 319–322
see also spin-Peierls transition
- Pekar factor, 214, 216, 224
 periodic table, 3, 7, 9, 27, 167
 permeability (magnetic), 88, 89
 Perrin, J., 3
 perturbation (method), 65–67, 72, 97, 105–107, 129, 156, 246–249, 289
 1, 10-phenanthroline (phen), 35, 114, 122, 126, 226
- phenothiazine (PTZ), 336
 phosphorescence, 327–329, 331, 334, 340, 342, 358, 459
 photocatalytic, 346
 photochemical, 227, 230, 326, 330, 345–347, 439, 457
 photochemistry, 329, 332, 345, 385
 photodiodes, 335–338
 photo-induced phase transition (PIPT), 369, 372
 photolysis, 228, 345–348, 361
 photomagnetic, 366, 373, 375–384
 photomagnetism, 364–369, 373, 378–385
 photonic switch, 358
 photonic wire, 359
 photophysical, 263, 326–386, 327, 329, 332–333, 348, 351, 358
 photophysics, 236, 326–332, 384–385
 photosynthesis, 227, 327, 337, 345, 347, 351, 362, 385
 photosynthetic reaction center, 227, 346
 photovoltaic, 342–345, 385, 468
 efficiency, 343, 345–346, 348
 photochromic, 437, 438, 456
 photochromism, 439
 Planck constant, 1, 4
 Planck, M., 3
 point group, 14, *see also* character table
- polaron (small polaron), 216, 263, 300–302, 308–314, 347, 414, 432–433
 bipolaron, 300
 energy, 216, 308, 310
 negative, 300–302, 347
 polaronic regime, 402–404, 412, 424
 positive, 263, 300–302
- polyacetylene, 275*sq*
 alternant polyacetylene, 296–303
 doped and regular polyacetylene, 275–278
 polyelectronic wave function, 9, 37, 49, 51, 53, 65, 71–73, 266, 352
- polyenes
 carotenoid, 424
 cyclic, 25, 53, 39–43
 linear, 23, 40, 53, 425
- population analysis (Mulliken), 14
 porphyrin, 310, 336–338, 359, 363–365

- positron, 2, 84, 93
 potassium tetracyanoplatinate (KCP), 269–271, 275–276, 292, 303
 potential energy (U), 4, 8, 55, 63, 74, 75, 111, 206, 210, 214, 221, 304–305, 408
 potential energy curves, surfaces, 63, 71, 206, 332
 in electron transfer, 210, 215, 219, 224, 236, 349
 in magnetic mixed valence systems, 248–250
 in mixed valence systems, 240–243, 250, 258, 261, 313–315
 in photomagnetic systems, 373, 376
 in single molecule magnet, 193–197
 in spin crossover, 111, 126, 367, 370–372
 potential exchange, 154, 156
 precession, 82
 principal quantum number (n), 4
 probability density, 2, 11
 propyltetrazole (ptz), 110–112, 366–369
 Prussian blue (PB), 231, 237–238
 analogue (PBA), 185–191, 378–384
 cobalt-iron, 378–384
 pyrazine ligand (pz), 123, 231, 254, 310, 370
 pyridine ligand (py), 115, 123
- Q**
 quantum computing, 462–466
 quantum model, 3
 of electron transfer, 228–230
 quantum number, 3–9, 28, 50, 82, 84–86, 98–106, 109, 223, 353
 effective, 8
 magnetic quantum number (m_l , M_L), 4–6, 9, 81–85, 100, 109, 201
 orbital, secondary, 4, 6, 50, 82, 99, 109
 principal, 4
 spin, 7, 9, 84, 98, 100, 223
 total quantum number (m_j , M_J), 101, 109
 quantum oscillation, 197–198, 221
 quantum tunnelling, 74–76, 93, 195–197, 199–200
 quantum yield, 329, 337, 345, 355, 364, 382
 qubit, 463, 465
 quenching
 of luminescence or excited state, 335, 343, 351
 of orbital momentum, 109
 quinone, 337, 361
- R**
 Rabi formula, 76
 Rabi oscillation, 76, 464
 see also quantum oscillation
 Racah parameter, 101, 106, 110, 112
 radial function, 4–6
 see also orbital exponent, Slater orbital
 rate constant
 electron transfer, 218–222, 225, 227, 230, 250, 254, 258, 262, 263, 309, 425
 energy transfer, 357–359, 361, 364
 excited state electron transfer, 348
 high spin-low spin relaxation, 369
 rationalized units, 88
 reaction
 chemical, 63, 125, 224, 236, 262, 340, 403, 416
 coordinate, 214, 224, 236, 370, 373, 376
 real wavefunction, 5, 6, 45, 109
 reciprocal space or lattice, 42, 49, 288, 445
 reflection plane, 14, 45
 regular solution model, 117–122
 remnant magnetization, 193–195
 repulsion
 energy (U, V), 8, 56, 217, 218, 246, 286, 398, 401
 integrals, 50, 61, 63, 78, 144, 246, 268–270, 304, 307, 313
 see also electron repulsion, two-electron repulsion
 resonance integral (β), 8, 12, 17, 39, 44, 78, 134, 206, 268, 284, 286, 297, 304–306, 311, 318, 321, 357
 see also V_{ab} , transfer integral
 restricted determinant, 60
 restricted Hartree-Fock (RHF), 60
 Robin-Day classification, 231, 239, 312
 rotation axis, 14, 39
 rotation operation, 39–41, 105, 108
 rotaxane, 433, 459
 Ru (ruthenium), 27
 Ru(II), Ru^{II} , ruthenium(II)
 mixed valence II/III complexes, 231–233, 241, 254, 259–261, 265, 351, 456
 PTZ-Ru-MV²⁺ triad, 336
 [Ru(bpy)₂(NCS)₂], 343–344
 [Ru(bpy)₃]²⁺, 223, 237, 333–340
 [Ru(tpy)₂]²⁺, 336–337
 Ru(III), Ru^{III} , ruthenium(III)
 [Ru(bpy)₃]³⁺, 223, 333–339
 see also Creutz-Taube complex
 Russel–Saunders coupling, 99, 101, 104
 ruthenium, *see* Ru
 Rutherford, E., 3
- S**
 S^2 spin operator, 84, 100, 102, 128, 132, 135
 saturation (magnetism), 97–99, 170, 193–194, 375, 384
 scanning tunnelling microscope (STM), 391–395, 399, 404, 411–413, 425–426, 432, 437–440, 452, 466

- scattering, 296, 420, 449
 neutron scattering, 89, 93, 140
 of electrons in nanojunctions, 404–406,
 408–410, 414, 420
 X-ray scattering, 94
- Schottky diode, 447
- Schrödinger, E., 3
 equation, 1–8, 47, 49, 65, 84, 109,
 349, 401
- screening constant, 8
- second order transition, 183
- secondary (orbital) quantum number, 4, 6
- secular determinant, equations, 11, 16, 62
- selection rules, 330–332, 354
- self-assembled monolayer (SAM), 393–395,
 436
- self-consistent field (SCF), 54–56, 59, 61–64,
 72–74, 143, 154, 156, 265
- self-repulsion integral, 50
- semi-empirical methods, 53, 61–63
- semiconductor, 217, 267–269, 271, 278, 283,
 297, 299, 303, 336, 343, 346, 387, 389,
 442, 445, 447, 467
- sequential mechanism, 262, 403, 417, 424
- shell
 closed, 59, 60, 64, 74, 107, 278, 293, 337,
 354, 396, 422, 452
 half-filled, 168
 open, 59, 60, 63, 74, 78, 278, 293, 329, 422
 sub-, 27, 102
 valence, 10, 105
- Shirakawa, H., 268, 270, 277, 325
- shot noise, 401, 418
- shuttle, *see* molecular shuttle
- silicon electronics, 345, 387–390, 426, 442,
 466
- single chain magnet (SCM), 191, 199–201
- single electron transistor, 418, 447
- single ion magnet (SIM), 191, 201, 453
- single molecule in molecular electronics, 389,
 392, 394, 403, 416, 430, 437, 438–443,
 446, 465, 467
- single molecule magnet (SMM), 90, 93, 131,
 191–200, 453, 464
- singlet, 9, 49, 64, 111, 133, 136, 146, 155–157,
 174, 307, 359, 362, 452–453
 singlet-singlet absorption, emission,
 transfer, 327–329, 331, 340, 353–355,
 364, 380
 state, 24, 38, 59, 68, 101, 139, 141–143,
 300–302, 326–328, 333, 366–369, 421,
 463
- singlet-triplet
 crossing, 327–329, 342
 gap, splitting, 69, 138, 140, 143, 150, 156,
 453
 transfer, 354
- transition, 140, 331, 359
- singly occupied molecular orbital (SOMO),
 61, 78–80, 129, 145, 149, 158, 162, 339,
 421
- Slater
 determinant, 51, 54, 60, 64
 orbital, 5, 62
 rules, 8
- Slichter, C., 117, 122
- solid solution, 118, 121
- soliton, 298–302
- Sorai and Seki model, 92, 121
- source (electrode), 441–443, 447, 449
- space function, 67
- space group, 14
- spacer, 227, 239, 259, 265, 353, 358–361, 427,
 456
- spectral overlap integral, 353, 355
- spectrochemical series, 32, 381
- spectroscopy, *see* infra-red, UV, visible
- spectroscopic term, 100–102, 105–107,
 110–11, 329
- spherical
 coordinates, 5, 83
 harmonics, 4, 28, 83
 symmetry, 6, 28, 88, 184
- spin angular momentum (s , s^2 , S , S^2), *see*
 operator
- spin contamination, 61, 157
- spin conservation rule, 332
- spin cross-over, $34sq$, 109–127, 203, 366–372,
 460–462
- spin density, 61, 74, 79, 150, 161, 171, 291,
 312–314, 321
- spin density wave (SDW), $286sq$, 291,
 320–322
- spin diffusion length, 450
- spin flip, 200, 244
- spin function, 51, 57, 67, 331, 352, 354,
 357
- spin Hamiltonian (SH), 127–138, 150, 167,
 173, 246
- spin mean free path, 449
- spin multiplicity, 7, 10, 38, 107, 246
- spin-orbit, 7, 50–52, 108,
 constant, 50, 102, 129
 coupling, 51, 86, 92, 97–109, 128, 191, 201,
 329, 333, 342
 Hamiltonian, 50, 102
 splitting, 102–104
- spin-orbital, 7, 52–61, 71, 86, 246,
- spin-Peierls transition, 174, *see also* Peierls
- spin-polarized
 current, 449–452
 muons, 93
 neutron diffraction, *see* neutron diffraction
 STM (SP-STM), 452

- spin polarization
 mechanism, 58–61
 of current, 449–452
 of neutrons, 94
- spin quantum number, *see* quantum number
- spin transition, *see* spin cross-over
- spintronics, 449–451
see also molecular spintronics
- spin valve, 450, 453–456, 466
- Stark effect, 257
- state, *see* excited state, ground state,
 spectroscopic term
- Stern–Gerlach experiment, 83
- Stevens, 127
- Stoney, G., 3
- strong field, 34, 107
- superconducting quantum interference device
 (SQUID, micro- and nano-), 75, 89–92,
 113, 381, 384, 453
- superconductivity, 91, 174, 316–319, 321
- superconductor
 definition and properties, 267–269, 317
 in SQUID devices, 90
 organic, 317–322
- superexchange
 in electron transfer, 260–263, 358, 360, 402
 in magnetic exchange interaction, 147, 154
- susceptibility, *see* magnetic susceptibility
- symmetry
 element, 14–15, 160
 operation, 14–15, 39
see also character table, group theory, point
 group
- symmetry-adapted linear combination
 (SALC), 207, 260, *see also* symmetry
 orbital
- symmetry orbital (SO), 21, 29–32, 40, 49, 145,
 162, 272, *see also* Bloch orbitals
- synchrotron radiation, 3, 93, 203, 382
- Système International (SI), units, 85–89, 97
- T**
- t, t_{2g} orbital, 28, 31–34, 36, 107, 109–111,
 140, 154, 168–170, 188–190, 209, 223,
 238, 308, 311, 329–330, 333, 367, 380
- T_{2g} character, state or term, 30, 106, 130
- Tanabe–Sugano, 106, 110, 112
- tandem cell, 347
- Tb (terbium), 27
- Tb(III), Tb^{III} , terbium(III), $[Tb(III)Pc_2]^{-/0}$,
 201, 453
- T_d symmetry, 107, 433
- Teller, *see* Jahn–Teller
- term, *see* spectroscopic term
- terminal ligand, 79, 150, 158, 163, 166, 168,
 180, 359, 364
- terthiophene, 423
- tetracyanoethylene (TCNE), 182, 349
- tetracyanoethylenide, 92
- tetracyanoquinodimethane (TCNQ), 278–286,
 303, 305–307, 427
- tetrathiafulvalene (TTF) and variants,
 278–286, 303–304, 317–321, 427, 434
- tetrathiooxalate, 162
- thermal electron transfer (E_{th}), 236, 240, 242,
 257, 375, 383
- thiol, 394, 422, 426, 430, 438, 440
- Thomson J. J., *see* Lorentz–Thomson
- three-dimensional, 49, 165, 185, 322, 378, 384
see also 3D
- tight-binding model, 24, 62, 319, *see also*
 Hückel method
- time-dependent DFT (TD-DFT), 74
- time-domain reflectometry, 252
- time scale, 195, 197, 250, 252, 258, 328, 350,
 414, 432
see also characteristic time
- TiO₂ nanoparticles, 343–345, 347
- TMMC (tetramethylammonium-manganese
 chloride or catena-tris- μ -manganate(II)
 chloride), 174
- T** operator, 246
- total angular momentum, *see* angular
 momentum
- transfer integral, 134, 268, 304
see also resonance integral, V_{ab} parameter
- transistor
 single molecule transistor (amplifier), 437,
 441, 443
see also field effect transistor (FET), one-
 electron or single electron transistor
- transition (dipole) moment, 255, 257, 330, 355
 vector, 355
- transmission coefficient
 in electron transfer, 220
 in nanojunction theory, 404, 406, 409, 425
- triad, 336–338
- triplet, 10, 24, 49, 59, 111, 146, 150, 155–157,
 174, 331, 337, 340, 342, 375, 421
 ground state, 20, 59, 73
 state, 20, 38, 68, 71–73, 101, 133, 136–144,
 159, 244, 326–329, 333, 354–362, 367,
 452
- triplet-singlet emission, *see*
 phosphorescence
- triplet-triplet transfer, 356–357
see also singlet, singlet-triplet
- tungsten, *see* W (tungsten)
- tunnel(ling)
 current or regime, 391, 402–404, 420–422,
 451
 effect, process, 74–76, 90, 121, 126, 406,
 409, 412, 418, 420–422, 424, 428, 437,
 455

- tunnel(ling) (*cont.*)
 electronic, 206, 221, 230, 268, 392, 406, 412
 junction (or barrier), 448, 451, 453, *see also* nanojunction
 magnetic quantum, 93, 193, 195–201
 molecule-dependent, 402–404, 412, 422–424
 non-resonant, 404, 411, 424
 nuclear, 221, 228–230, 258, 369
 resonant, 402–404, 411
 sequential, 403–404, 414, 417, 424
 1-step, 404, 416
see also scanning tunnelling microscope (STM)
 two-dimensional, 49, 322
see also 2D
 two-electron repulsion integrals, 50, 78, 304–307, 311–316,
 exchange (k), 10, 20, 50, 57, 61, 134, 143, 164, 244
 one-centre repulsion (U, j_0), 50, 78–80, 217, 244–246, 268–270, 304–316, 419–421
 two-centre repulsion (V, j), 50, 78, 218, 270, 304–316
- U**
 U parameter, *see* two-electron repulsion
 Uhlenbeck, G., 3, 84
 ultrafast electron transfer, 348–351
 ultrafast energy transfer, 363
 ultra-high vacuum (UHV), 391
 uncorrelated electrons, 53
 ungerade, 6, 207
 unit cell, 39, 284
 units
 cgs-emu, 85–89
 in magnetism, 86–89
 Système International (SI), 85–89, 97
 unrationalized units, 88–89
 unrestricted
 determinant, 60
 Hartree–Fock, 58, 60, 73, 157
 U operator, 208
 UV ultraviolet, 252, 254, 259, 345, 353, 364, 374, 439, 457
 UV-visible-near IR, 254
- V**
 V (vanadium), 27
 Vanadium (II), V(II), V_{II} , 189–191
 Vanadium (IV), V(IV), V_{IV} , 207, 308, 311
 V coupling operator, 352–358
 V parameter, *see* two-electron repulsion
 V_{ab} parameter (integral), 80, 206–209, 217–223, 230, 236, 240, 242, 246, 255–258, 260, 262, 265, 304, 425, 457
see also effective resonance integral
 valence band, 294, 298–299, 301, 347
 Valence Bond
 generalized (GVB), 70
 model, theory, 67–73
 valence shell electronic pair repulsion (VSEPR) model, 10
 Van Vleck, J. H., 132, 135, 203, 305
 equation, 95–99, 136, 140, 168
 vanadyle, *see* Vanadium (IV)
 variational method, 12, 53, 59, 64, 72, 241
 vertical transition, 257, 333
 vibrating sample magnetometer (VSM), 89–91
 vibrational function, 228, 352
 vibronic functions, 228
 visible, 126, 237, 333, 348, 353, 378
 visible-near IR, 254, 298
 visible-UV, 252, 259, 364, 374, 440
 voltage division factor, 400, 416, 430, 432
 $V(\text{TCNE})_x$, 182
- W**
 W (tungsten), 27
 Tungsten(V), W(V), W_V W_6Mn_9 , 170
 Tungsten(VI), W(VI), W_{VI} WO_3 , 239, 347
 Wannier orbitals, 154
 water, *see* H_2O
 wavefunction, 1–4, 6, 51, 68, 75, 81–84, 105, 128, 157, 289, 350
 in atoms, 4sq, 5, 7sq, 109
 in coordination complexes, 28sq
 in molecular solids, 39sq
 in organic chemistry, 23sq
 in small molecules, 10sq, 17sq
see also atomic, Bloch, Crystal, Molecular Orbital, one-electron
 wavevector, 42, 49, 284–286, 288, 295, 316
 weak field, 34, 107, 170, 381
 Wolfsberg, M., 62
 work function, 340, 397
- X**
 x^2-y^2 orbital, 5, 28–30, 34, 36, 79, 109, 130, 140, 145, 148, 153, 159, 169, 172, 244, 273–275, 375
 x^2-z^2 , 160–165
 XOR gate, 458, 465
 X-ray absorption (EXAFS, XANES), 93, 375
 X-ray diffraction, 94, 186, 292–295, 303, 381, 383
 X-ray magnetic circular dichroism (XMCD), 61, 93–94
 XY anisotropy, 135, 185
 xy, xz orbital, 5, 15, 21, 28–36, 109, 129, 145, 148, 153, 163–165, 169, 239, 272–275

Y

y^2 orbital, 21, 163–165
 yz orbital, 5, 15, 21, 28–36, 47, 129, 145, 153,
163–165, 169, 272–275

Z

Zeeman, P., 3
coefficients, 96, 109

effect, 92, 97, 108, 128–131, 139, 173, 194,
452, 464

Hamiltonian, 105, 128, 173, 199

Zero field splitting (ZFS), 128–132, 140, 193

Zerner's Intermediate Neglect of Differential
Overlap (ZINDO) method, 63

z^2 orbital, 5, 28–36, 130, 153, 169,
273–275